

MATERIALS-CHIRALITY

VOLUME 24

ADVISORY BOARD

GUY BERTRAND, *Paul Sabatier University, Toulouse, France*

HENRI BRUNNER, *University of Regensburg, Regensburg, Germany*

DAVID E. CANE, *Brown University, Providence, Rhode Island, USA*

GAUTAM R. DESIRAJU, *University of Hyderabad, Hyderabad, India*

FRANÇOIS DIEDERICH, *Eidgenössische Technische Hochschule, Zurich, Switzerland*

ERNEST L. ELIEL, *University of North Carolina/Chapel Hill, Chapel Hill, North Carolina, USA*

MARK M. GREEN, *Polytechnic University, Brooklyn, New York, USA*

CLAYTON H. HEATHCOCK, *University of California/Berkeley, Berkeley, California, USA*

KENDALL N. HOUK, *University of California/Los Angeles, Los Angeles, CA, USA*

DANIEL S. KEMP, *Massachusetts Institute of Technology, Cambridge, Massachusetts, USA*

JEAN-MARIE LEHN, *Université Louis Pasteur, Strassbourg, France*

STEVEN V. LEY, *Cambridge University, Cambridge, England*

EIICHI NAKAMURA, *University of Tokyo, Tokyo, Japan*

RYOJI NOYORI, *Nagaya University, Nagoya, Japan*

NED A. PORTER, *Vanderbilt University, Nashville, Tennessee, USA*

STUART L. SCHREIBER, *Harvard University, Cambridge, Massachusetts, USA*

K. BARRY SHARPLESS, *Scripps Institute, La Jolla, California, USA*

DAVID M. WALBA, *University of Colorado/Boulder, Boulder, Colorado, USA*

MATERIALS-CHIRALITY

EDITED BY

**MARK M. GREEN
R. J. M. NOLTE
E. W. MEIJER**

VOLUME 24

**TOPICS IN
STEREOCHEMISTRY**

Series Editors

**SCOTT E. DENMARK
JAY SIEGEL**

 **WILEY-
INTERSCIENCE**

A JOHN WILEY & SONS, INC., PUBLICATION

Copyright © 2003 by John Wiley & Sons, Inc. All rights reserved.

Published by John Wiley & Sons, Inc., Hoboken, New Jersey.
Published simultaneously in Canada.

No part of this publication may be reproduced, stored in a retrieval system, or transmitted in any form or by any means, electronic, mechanical, photocopying, recording, scanning, or otherwise, except as permitted under Section 107 or 108 of the 1976 United States Copyright Act, without either the prior written permission of the Publisher, or authorization through payment of the appropriate per-copy fee to the Copyright Clearance Center, Inc., 222 Rosewood Drive, Danvers, MA 01923, 978-750-8400, fax 978-750-4470, or on the web at www.copyright.com. Requests to the Publisher for permission should be addressed to the Permissions Department, John Wiley & Sons, Inc., 111 River Street, Hoboken, NJ 07030, (201) 748-6011, fax (201) 748-6008, e-mail: permreq@wiley.com.

Limit of Liability/Disclaimer of Warranty: While the publisher and author have used their best efforts in preparing this book, they make no representations or warranties with respect to the accuracy or completeness of the contents of this book and specifically disclaim any implied warranties of merchantability or fitness for a particular purpose. No warranty may be created or extended by sales representatives or written sales materials. The advice and strategies contained herein may not be suitable for your situation. You should consult with a professional where appropriate. Neither the publisher nor author shall be liable for any loss of profit or any other commercial damages, including but not limited to special, incidental, consequential, or other damages.

For general information on our other products and services please contact our Customer Care Department within the U.S. at 877-762-2974, outside the U.S. at 317-572-3993 or fax 317-572-4002.

Wiley also publishes its books in a variety of electronic formats. Some content that appears in print, however, may not be available in electronic format.

Library of Congress Catalog Card Number: 67-13943

ISBN 0-471-05497-6

Printed in the United States of America.

10 9 8 7 6 5 4 3 2 1

INTRODUCTION TO THE SERIES

Since its first appearance in 1967, the *Topics in Stereochemistry* series has stood as the standard-bearer for advances in the broad field of stereochemistry. The visionary founders of the series anticipated, with remarkable foresight, the extraordinary growth and impact that stereochemistry has had on all reaches of the chemical enterprise. Fortunately, there is no cease of interest in the importance of stereochemistry as the discipline of chemistry evolves and its borders expand and diffuse into the related fields of biology, medicine, physics, materials science, chemical engineering, and environmental science.

The field of stereochemistry serves as a unifying theme for the expanded definition and diversification of chemistry. The consequences of molecular and macromolecular shape and topology are central to issues of chemical reactivity, physical properties, and biological function. With that view, the importance of stereochemistry had never been greater, and it is hoped that this series will provide a forum for documentation of significant advances in all of these subdisciplines of chemistry.

The *Topics in Stereochemistry* series has set itself apart by maintaining a remarkable balance of chapters that are both definitive, standing the test of time, and current, addressing the impact of stereochemistry at the most exciting frontiers. As a student and researcher, I have often turned to chapters in *Topics in Stereochemistry* for the foundations and the state of the art in new areas of interest. It is my hope that the series continue to enjoy that level of confidence in the chemistry community and that it retain, in this second incarnation, the esteem that the founders have worked so hard to establish.

I am fortunate in having been able to enlist the help and guidance of an international board of editorial advisors who have provided great assistance by suggesting chapter topics and suitable authors for articles both here and in future volumes. While I am grateful for the assistance of this editorial advisory board, it is the editor and the authors who are solely responsible for any shortcomings of *Topics in Stereochemistry*.

S. E. DENMARK

FOREWORD

This volume, dedicated entirely to the field of materials science, signals the scientific, conceptual as well as editorial evolution of this series. In my introduction to the 1999 relaunch of this series, I noted that, more than ever, stereochemistry serves as a unifying theme for the expanded influence of chemistry on the "... related fields of biology, medicine, physics, materials science, chemical engineering and environmental science." Volumes 22 and 23 have been consciously composed to represent a range of areas in which chirality plays a central role in the understanding and practice of the enterprise. However, the importance of molecular and macromolecular stereochemistry is perhaps most evident in the general field of materials science. Indeed, two earlier chapters in this series by Goodman (Volume 2) and Farina (Volume 17) have treated individual aspects of polymer stereochemistry.

When Professor Mark Green joined the editorial board, he suggested that a single volume dedicated to Materials-Chirality would be both timely and of broad interest to the chemistry community. Better still, he volunteered to serve as volume editor along with Bert Meijer and Roeland Nolte after he and Dave Walba had organized an ACS Symposium dedicated to Mario Farina a few years before under the title Materials-Chirality. This idea intrigued me as there had been only one thematic volume in this series, the one in 1981 dedicated to inorganic stereochemistry edited by Professor Gregory Geoffroy.

After reading the chapters in this volume, it is clear that the editors have not only done a spectacular job but have also chosen authors whose expertise and writing skill are certain to capture the imagination of practitioners in the field and generalists alike. The regular readers of this series, whose focus may reside primarily in small-molecule stereochemistry, will find a fascinating world wherein chirality takes on even greater significance in the relationship of structure with physical and chemical properties. This volume is destined to become the definitive resource of the state of the art in Materials-Chirality

SCOTT E. DENMARK

June 2003

PREFACE

Materials take us beyond the small molecule into a world characterized by very large molecules and by arrangements among molecules, a world from which the concept of chirality found its origin. There is no better example of this connection between materials and chirality than the famous experiment of Pasteur in which his hands, on dissolving the separate tartrate crystals, took us from the observation of chirality as a material characteristic to chirality directly derived from a molecular property. This volume demonstrates that the continuing evolution of the ideas of chirality is returning us to the world of materials, to a domain beyond the chiral properties of individual molecules, and in doing so is providing us with new ideas that were not previously accessible. Let's take a quick overview of the origins of chiral ideas before we find out how chiral materials, while obeying the familiar rules, are offering a stereochemistry not previously imagined.

The best source we know for the historical development of the chirality concept is in T. M. Lowry's text, *Optical Rotatory Power*, published originally in 1935 and republished by Dover Press in 1964. This classic treatment of the subject informs us of the roles of Jean Baptiste Biot (1774–1862) and Augustin Fresnel (1788–1827), who investigated the nature of rotatory polarization of light, and how Biot reported in 1815 that the light phenomenon investigated in quartz crystals could be reproduced in organic substances, “oils of turpentine [sic], laurel, and lemon, and in alcoholic solutions of camphor.” Biot's interest in exploring the rotatory phenomenon across the spectrum of the states of matter was shown in early experiments, which ran the gamut from the glassy states formed by sugars to the gaseous state formed by turpentine. The latter led to a famous accident. In 1817, in trying to understand the effect of dilution on the rotatory power of turpentine, he convinced the peers of an ancient church to allow him to conduct an experiment in their cloister. Biot needed the space to construct an apparatus in which he would fill a long tube with turpentine vaporized from the liquid using the heat from a boiler. He set the church on fire when the boiler exploded, but not before he recorded the fact that the vapor had rotatory power, the first demonstration of this effect in the gas state.

By 1815 Biot had extended his observations to tartaric acid, the molecule later to be the subject of Pasteur's critical investigations. As described by Lowry, by 1832 Biot's studies of tartaric acid allowed him to report “that an aqueous solution of tartaric acid, containing approximately 50 per cent by

weight of the acid, gave a rotation of $+8.5^\circ$ (for white light with its optical center of gravity in the yellow), but that its rotation was 'stronger for the less refrangible rays.'

Pasteur was twenty-six years old in 1848 when he carried out the experiment that introduced the concept of "molecular dissymmetry." The experiment is best described in Pasteur's own words, given to us in translation by Lowry: "I hastened therefore to reinvestigate the crystalline form of Mistscherlich's two salts. I found, as a matter of fact, that the tartrate was hemihedral, like all the other tartrates which I had previously studied, but, strange to say, the paratartrate was hemihedral also. Only the hemihedral faces, which in the tartrate were all turned the same way, were inclined in the paratartrate sometimes to the right and sometimes to the left. I carefully separated the crystals which were hemihedral to the right from those hemihedral to the left, and examined their solutions separately in the polarizing apparatus. I then saw with no less surprise than pleasure that the crystals hemihedral to the right deviated the plane of polarization to the right, and that those hemihedral to the left deviated to the left."

Molecular theory in 1848 could not yield understanding of the relationships among the solid salts, the solutions they formed, and the optical activity. But Pasteur was able to ask a question that pointed everyone in the correct direction. Again taking Pasteur in translation by Lowry: "Are the atoms of the dextro-acid grouped on the spirals of a dextrogyrate helix, or placed at the summits of an irregular tetrahedron, or disposed according to some particular dissymmetric grouping or other?"

Just as Pasteur was a child when Biot reported the detailed nature of the rotatory power of tartaric acid in 1832, Joseph Achille Le Bel (1847–1930) and Hemricus Jacobus van't Hoff (1852–1911) were children when Pasteur asked the question quoted above. But both gave detailed answers to Pasteur's question when they were both about the same age as Pasteur was when he separated the hemihedral crystals of sodium ammonium tartrate. In 1874 Le Bel published a memoir in French in which he stated two general principles introducing the structural basis of optical activity arising from tetrahedral carbon while in the same year van't Hoff independently published a pamphlet in Dutch introducing these concepts in more detail. How influential van't Hoff's pamphlet was at the time is attested to by its rapid translation into both French and German. The latter translation subjected van't Hoff to severe criticism from Kolbe, who occupied a distinguished position in chemistry at the time, but in fact the last word on van't Hoff's work is best given to Lowry writing in 1935: "In spite of the criticisms with which the German translation was assailed by Kolbe, the space-chemistry of carbon compounds, as set out in van't Hoff's pamphlet, has held good, without correction and almost without addition, during a period of at least half a century; and even today it is so

sound that modern electronic formulae may be judged very largely by their conformity to the principles laid down by van't Hoff in 1874.”

Now more than 128 years later this concept endures and has been one of the foundations of chemistry inspiring and guiding chemists in their endeavors to design and study molecular architectures of increasing complexity. Although unexpected in those early years in the development of chemistry, the concept connecting the three-dimensional arrangements of atoms in space to isomerism and chiral optical phenomena has been critical in both the development of polymer science and later in supramolecular chemistry. These fields can be gathered under the descriptor materials-chirality, a term first created in 1996 for an American Chemical Society symposium honoring the memory of Mario Farina. Professor Farina played an early role in the understanding of how the formation of isotactic polymers required chiral information in the catalyst, a key piece of the puzzle leading to the Nobel Prize for Ziegler and Natta. His chapter in *Topics in Stereochemistry* in 1987 still stands as a masterpiece in this field. And chirality is no less important in the field of supramolecular chemistry, another area distinguished by Nobel Prizes to Pederson, Cram, and Lehn. It was thought timely to focus in Volume 24 of this series on these two fields and organize a volume of *Topics in Stereochemistry* titled *Materials-Chirality*.

The different chapters in Volume 24 have been arranged in such a way that some justice is given to history and the chronological order of events in materials-chirality.

Chapter 1, by Guerra, Cavallo, and Corradini, discusses in detail both the historical and modern aspects of stereoregular olefin polymerization, a field that arose with the first uses of the catalyst that came to be known as Ziegler-Natta, and a field that these authors greatly contributed to and therefore write about with an intimate knowledge.

De Rosa's overview in Chapter 2 effectively links up with the first chapter in that polymer crystallinity yielded the essential first insight into the workings of the Ziegler-Natta catalyst. This chapter provides a penetrating analysis of the origins of the helical conformations found in stereoregular polymers in the solid state, including newly discovered phenomena, such as frustration and symmetry-breaking effects, which regulate the crystal packing of polymer chains.

Many studies, the first of which began shortly after the discovery of stereoregular polymerization of olefins, demonstrated that macromolecules could adopt stable helical conformations not only in the solid state but also in solution. These efforts have led to the realization that certain helical polymers reach a level of chiral recognition adequate for commercial development as an important aspect of chromatography. Researchers from the leading laboratory in this field, Okamoto, Yashima, and Yamamoto, have written Chapter 3 painting a detailed picture of the current status and future possibilities in this

field. The authors provide insights into the origins of the chiral separations and the mechanisms of the recognition processes found between the racemates and the chiral polymeric materials.

Optically active poly(silanes) constitute a special and intriguing class of helical polymers because they contain a sigma-conjugated main chain. As a result of this conjugation, polymers and copolymers of this type display very interesting chiroptical properties, which are analyzed and discussed together with other features of poly(silanes) in a state-of-the-art account by Fujiki, Koe, Nakashima, and Toyoda in Chapter 4. There are several other classes of helical polymers with fascinating chiral properties, which were not included in this volume but which can be recommended for study. Among these are the polyisocyanates, which are responsible for quantitatively defining the cooperative characteristics of chiral amplification but which have been adequately reviewed in recent years, and as such do not require incorporation in this volume.

Well into the twentieth century, chemists and physicists struggled with the problem of whether very large molecules could exist. Staudinger contributed greatly to resolving this quandary by a series of elegant experiments demonstrating that macromolecules are held together with the same kinds of bonds as in small molecules. It is interesting to note that with the advent of supramolecular chemistry we discover how the physical bonding forces so vigorously but incorrectly defended as solely responsible for the formation of polymers can, in fact, lead to macromolecules via self-assembly and self-organization. These phenomena have led to new and sometimes unexpected architectures with interesting properties, sometimes reminiscent of those found in nature. The next chapters bring us into this area.

In Chapter 5, Spector, Selinger, and Schnur describe such supramolecular architectures, which are formed in water from compounds derived from natural materials that have been altered in their ability to pack. Chirality plays an essential role in this area. However, there are the questions as to why these supramolecular structures are formed, the answers to which can improve approaches to control their architectures and dimensions. These authors evaluate several theories proposed to answer these fundamental questions.

The number of building blocks for supramolecular self-assembly is virtually unlimited. Chapter 6, by Brunsveld, Rowan, Nolte, and Meijer, describes studies on disk-shaped molecules which are programmed to stack in a helical fashion, leading to novel kinds of twisted fibers as well as lyotropic and thermotropic liquid crystalline materials.

In Chapter 7, Gottarelli and Spada extend further the theme of liquid crystalline materials. They note that although much is understood, important mysteries remain about the relationships between the handedness of cholesteric liquid crystalline phases and the chirality of the constituting building blocks. This may seem surprising given the intense interest in these materials, including their

widespread commercial use, but it testifies to the subtlety of chiral interactions. Their chapter provides a detailed analysis with directions pointed to for further study and with the conclusion that the problem is far from being solved.

This volume of *Topics in Stereochemistry* could not be complete without hearing about ferroelectric liquid crystals, where chirality is the essential element behind the wide interest in this mesogenic state. In Chapter 8, Walba, a pioneering contributor to this area, provides a historical overview of the earlier key developments in this field and leads us to the discovery of the unique banana phases. This discussion is followed by a view of the most recent results, which involve, among others, the directed design of chiral ferroelectric banana phases, which display spontaneous polar symmetry breaking in a smectic liquid crystal.

Nonlinear optical techniques are extremely useful in characterizing the chiral properties of materials, as is pointed out by Verbiest and Persoons in Chapter 9. These authors give an in-depth discussion of this tool, both from an experimental and theoretical point of view, paying special attention to the characterization of chiral surfaces and thin films. In the second part of their contribution they highlight the role chiral materials can play in the field of nonlinear optics and photonics, which opens the way for a variety of applications.

The idea of a *Topics in Stereochemistry* volume on materials-chirality was conceived following the 1996 American Chemical Society meeting entitled Materials-Chirality dedicated to the memory of Mario Farina noted above. One hundred and twenty-five years after van 't Hoff and Le Bel, chirality in its various forms has pervaded all molecular science and now is finding its way increasingly into fields under the heading of materials. It is rewarding to see that the various contributions of the authors bear out this increasing importance of chirality in the materials area. We hope that the nine chapters in this volume will inspire many readers and act as seeds of inspiration which grow into sparkling ideas, in particular for the younger generation of chemists who are supposed to take the lead in the further development of science, in a similar way that Pasteur and then van 't Hoff and Le Bel did as young scientists in their time.

As a final note, there was a tenth chapter intended for this volume to be written by André Collet. He had agreed to write this chapter but could not, adding one additional loss among many of far greater importance arising from the death of this eminent stereochemist and gentleman and friend to so many.

July, 2003

MARK M. GREEN
BERT MEIJER
ROELAND NOLTE

CONTENTS

CHIRALITY OF CATALYSTS FOR STEREOSPECIFIC POLYMERIZATIONS	1
<i>By Gaetano Guerra,* Luigi Cavallo[†] and Paolo Corradini[†]</i>	
<i>*Dipartimento di Chimica, Università di Salerno, Via Salvador Allende, I-84081 Salerno, Italy</i>	
<i>[†]Dipartimento di Chimica, Università di Napoli Federico II, Complesso Monte S. Angelo, Via Cintia, I-80126 Napoli, Italy</i>	
CHAIN CONFORMATION, CRYSTAL STRUCTURES, AND STRUCTURAL DISORDER IN STEREOREGULAR POLYMERS	71
<i>By Claudio De Rosa</i>	
<i>Dipartimento di Chimica, Università di Napoli "Federico II" Complesso Monte S. Angelo, Via Cintia, 80126 Napoli, Italy</i>	
OPTICALLY ACTIVE POLYMERS WITH CHIRAL RECOGNITION ABILITY	157
<i>By Yoshio Okamoto, Eiji Yashima, and Chiyo Yamamoto</i>	
<i>Department of Applied Chemistry, Graduate School of Engineering, Nagoya University, Nagoya, Japan 464-8603</i>	
CHIRALITY IN THE POLYSILANES	209
<i>By Michiya Fujiki,* Hiroshi Nakashima,[†] Seiji Toyoda[‡] and Julian R. Koe,[§]</i>	
<i>*Graduate School of Materials Science, Nara Institute of Science and Technology, 8916-5 Takayama, Ikoma, Nara 630-0101, Japan</i>	
<i>[†]NTT Photonics Laboratories, NTT Corporation, 3-1 Wakamiya, Morinosato, Atsugi, Kanagawa 243-0198, Japan</i>	
<i>[‡]NTT Basic Research Laboratories, NTT Corporation, 3-1 Wakamiya, Morinosato, Atsugi, Kanagawa 243-0198, Japan</i>	
<i>[§]Department of Chemistry, International Christian University, 3-10-2 Osawa, Mitaka, Tokyo 181-8585, Japan</i>	

CHIRAL MOLECULAR SELF-ASSEMBLY	281
<i>By Mark S. Spector, Jonathan V. Selinger, and Joel M. Schnur Naval Research Laboratory, Center for Bio/Molecular Science and Engineering, 4555 Overlook Avenue SW, Washington, D.C. 20375-5348</i>	
CHIRAL DISCOTIC MOLECULES: EXPRESSION AND AMPLIFICATION OF CHIRALITY	373
<i>By L. Brunsveld*, A. E. Rowan[†], R. J. M. Nolte,[†] and E. W. Meijer*</i>	
<i>*Laboratory of Macromolecular and Organic Chemistry, Eindhoven University of Technology, Eindhoven, The Netherlands</i>	
<i>[†]Laboratory of Organic Chemistry, Department of Organic Chemistry, NSRIM, University of Nijmegen, Nijmegen, The Netherlands</i>	
SOME CORRELATIONS BETWEEN MOLECULAR AND CHOLESTERIC HANDEDNESS	425
<i>By Giovanni Gottarelli and Gian Piero Spada Alma Mater Studiorum—Università di Bologna, Dipartimento di Chimica Organica “A. Mangini,” Via S. Donato 15, 40127 Bologna, Italy</i>	
FERROELECTRIC LIQUID CRYSTAL CONGLOMERATES	457
<i>By David M. Walba University of Colorado, Boulder, Colorado 80309-0215</i>	
NONLINEAR OPTICS AND CHIRALITY	519
<i>By Thierry Verbiest and André Persoons KU Leuven, Celestijnenlaan 200 D, B-3001 Leuven, Belgium</i>	
SUBJECT INDEX	571
CUMULATIVE AUTHOR INDEX, VOLUMES 1–24	595
CUMULATIVE TITLE INDEX, VOLUMES 1–24	601

Chapter 1

Chirality of Catalysts for Stereospecific Polymerizations

GAETANO GUERRA, LUIGI CAVALLO

*Dipartimento di Chimica, Università di Salerno, Via Salvador Allende,
I-84081 Salerno, Italy*

PAOLO CORRADINI

*Dipartimento di Chimica, Università di Napoli Federico II, Complesso Monte
S. Angelo, Via Cintia, I-80126 Napoli, Italy*

- 1 Introduction
- 2 Polymerization Mechanisms and Elements of Chirality
- 3 Chirality in Site-Controlled Stereospecific Polymerizations
 - 3.1 Homogeneous Polymerization Catalysts: Metallocenes
 - 3.1.1 Stereoselectivity: Mechanism of Chiral Orientation of Growing Chain
 - 3.1.2 Stereospecificity
 - 3.1.3 Stereoselectivities of Regioirregular Insertions
 - 3.1.4 Implications of Relative Stereoselectivities for Primary and Secondary Insertions
 - 3.2 Heterogeneous Polymerization Catalysts
 - 3.2.1 Traditional Catalytic Systems Based on TiCl_3
 - 3.2.2 Catalytic Systems Supported on MgCl_2
 - 3.3 Comparison Between Models for Heterogeneous and Homogeneous Stereospecific Catalysts
- 4 Chirality in Chain-End Controlled Stereospecific Polymerization
 - 4.1 Olefin Polymerization
 - 4.1.1 Chain-End Stereocontrol for Primary 1-Alkene Insertions
 - 4.1.2 Chain-End Stereocontrol for Secondary 1-Alkene Insertions
 - 4.2 Styrene and Substituted Styrene Syndiotactic Polymerization
 - 4.3 Conjugated Diene Polymerizations
- 5 Final Remarks
- References

Materials-Chirality: Volume 24 of Topics in Stereochemistry,
Edited by Mark M. Green, R.J.M. Nolte, and E.W. Meijer
ISBN 0-471-05497-6 Copyright © 2003 John Wiley & Sons, Inc.

1 INTRODUCTION

Ziegler–Natta catalysts are formed from reactions involving transition metal compounds of groups 4–10 (mainly titanium, vanadium, zirconium) with alkyl, aryl, or hydrides of groups 1–4 under inert conditions.^{1–3} These catalysts are of great industrial relevance since they are used for the production of several polymeric materials: thermoplastics like high-density polyethylene (HDPE), linear low-density polyethylene (LLDPE), and isotactic polypropylene (and, in much smaller volumes, isotactic poly-1-butene and poly-4-methyl-pentene) and rubbers like polybutadiene, polyisoprene, and ethene–propene copolymers. Ziegler discovered these catalytic systems in 1953,⁴ while Natta and co-workers discovered the synthesis of stereoregular polymers in 1954 by using similar catalytic systems.⁵

According to International Union of Pure and Applied Chemistry (IUPAC) nomenclature we define as a *regular polymer* a linear polymer whose molecules can be substantially described by a unique species of constitutional units in a unique sequential arrangement. We define a polymer as *stereoregular* if the succession of configurations is regular too (we mean by configuration the spatial arrangement of the various bonds without considering the multiplicity of arrangements which arise from rotation around single bonds).

Cellulose, guttapercha, and natural rubber are examples of stereoregular polymers which nature is able to synthesize. Research conducted in the three decades after 1922, when Staudinger first proposed the term *macromolecule*, led to the synthesis of semicrystalline polymers—nylons by polycondensation and low-density polyethylene by polyaddition, for example—all polymers of great practical importance. These are regular polymers whose constitutional units can have only a unique configuration. Consequently, they do not show problems of stereoregularity. On the other hand, the vinyl polymers already known at the time—poly(vinyl chloride) or polystyrene obtained by radical polymerization processes, for example—resulted substantially or totally amorphous at a roentgenographic examination even if they had a quite regular constitution. In any case, the researchers of those years, in general, did not recognize that the lack of crystallinity was to be related to the lack of regularity in the succession of configurations.

In the early 1950s there was the quite contemporary discovery—in three different laboratories—of processes for the polymerization of ethene at low pressure using solid catalysts: The catalyst used by the Standard Oil of Indiana was Mo(VI) oxide supported on aluminum oxide; the one by Phillips Petroleum was Cr(VI) oxide still supported on silica/alumina; the catalyst studied by Ziegler and his co-workers at the Max Planck Institute at Mühlheim

resulted from the reaction between AlEt_3 and TiCl_4 . Nowadays it is hypothesized that the mechanism of polymerization (insertion of a monomer molecule into a metal-carbon bond) is quite similar for all the three catalytic systems.

The polyethylene obtained (the already cited HDPE) is more highly crystalline and more rigid and dense and has a much more regular structure than the one previously known and obtainable at very high temperature and pressure and which had been industrially produced in the previous 15 years (now called low-density polyethylene, LDPE). The latter shows macromolecules with both long and short branches and is consequently less crystalline than the almost completely linear HDPE. It is obvious that polyethylene does not present tertiary carbon atoms in its constitutional unit, hence it does not show problems of stereoisomerism.

In the laboratories of Natta in Milan it was found that the Ziegler catalysts could polymerize (besides ethene) propene, styrene, and several α -olefins to high linear polymers. These polymers appeared crystalline when examined by X-ray diffraction techniques and were able to give oriented fibers. In less than one year since the preparation of the first polymer of propene, Natta was able to communicate, in the meeting of the Accademia dei Lincei of December 1954 in Rome, that a new chapter had been disclosed in the field of macromolecular chemistry, due to the discovery of processes to obtain polymers with an extraordinary regularity in their structure in terms of both chemical constitution and configuration of the successive monomeric units along the chain of each macromolecule.

This regularity is particularly impressive considering that each propene monomer unit can be inserted in a polymer molecule in four (constitutionally and/or configurationally) different ways. It follows that a chain molecule with 1000 monomer units, for instance, can be built up in $4^{1000} \approx 10^{600}$ different ways. The lattice constants of several new crystalline polymers like polypropylene, poly-1-butene, and polystyrene were determined by X-ray studies. The identity period along the chain axis, as determined by fiber diffraction patterns, resulted to be of the order of 6.5 Å and could be attributed to a chain segment containing three monomeric units. Therefore, it was to be excluded that the crystallinity could have originated from a regular alternance of monomeric units characterized by enantiomeric steric configurations. On the contrary, it was evident that the polymeric chains had to be constituted by regular successions of monomeric units with the same steric configuration.⁵ This kind of structure was denominated *isotactic* (from the greek words *isos*, "the same", and *tassein*, "to put in order"). The examination of the crystal structure of isotactic polymers showed that the chain conformation of these polymers is always helical.

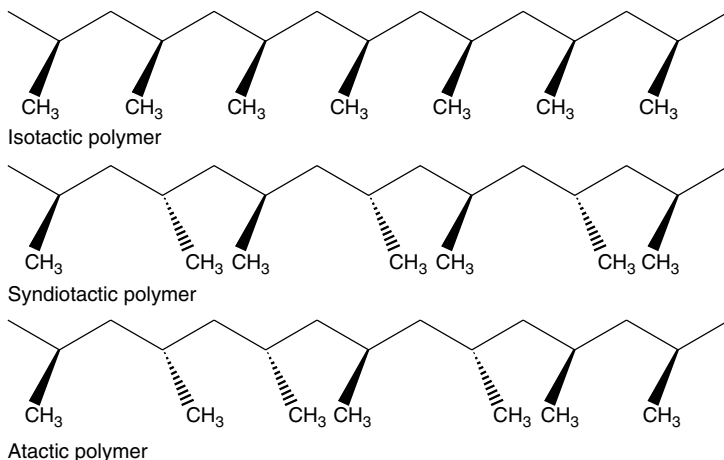


Figure 1.1 Schematic representation of configuration of isotactic, syndiotactic, and atactic vinyl polymers.

Figure 1.1 shows the typical representation proposed to distinguish easily between the different types of stereoisomerism present in vinyl polymers. Viewing the main chains as lying down on a plane, there are (i) isotactic sequence of configurations, (ii) syndiotactic sequence of configurations, and (iii) no order present, atactic sequence of configurations.

It can be useful to represent the possible successions of configurations for a vinyl polymer on the grounds of relative local configurations. As it results from Figure 1.2, two monomeric units in sequence (constituting a “diad”) can have two nonequivalent relative configurations; in analogy with the classic case of tartaric acids, these relative configurations are indicated as *meso* (abbreviation *m*) and *racemic* (abbreviation *r*), respectively. A polymer will be ideally isotactic if all the diads are *m*; it will be ideally syndiotactic if all the diads are *r*. In general, and according to the catalytic system, intermediate situations can occur.

Figure 1.3 shows a model of the chain of polypropylene, in two orthogonal projections, along the axis and perpendicularly to the axis of the chain. It is seen that a ternary helix with three monomeric units per repeating unit is formed by the alternation of carbon–carbon bonds in *gauche* and *trans* conformations. Helicoidal chain structures in a polymer allow the repetition of identical configurational units in such a way that they take equivalent conformations in respect to an axis. It may be interesting to recall that at the beginning of the 1950s the application of similar principles led Pauling to suggest the α -helix model for polyamino acid and Watson and Crick to propose the double helix model for deoxyribonucleic acid (DNA).

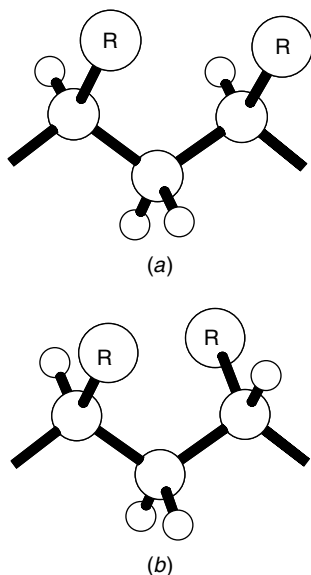


Figure 1.2 (a) The *meso* (*m*) and (b) *racemic* (*r*) relative configurations in constitutionally regular (head-to-tail) vinyl polymer.

At the beginning of the 1960s, the feeling was that nothing better than a clarification and a better control of the stereospecificity mechanism could be obtained in the research on the catalysts. The art (if not the science) of preparing TiCl_3 catalysts with the highest possible surface activity appeared to be well consolidated. However, at the end of this decade new catalytic systems for the polymerization of ethene were implemented in which the titanium chloride is supported on a matrix as magnesium oxide or chloride, for instance. These new catalysts show a very high activity in the polymerization of ethene, with yields of the order of 10^6 instead of 10^4 g polymer/g titanium. In the second-generation plants for the production of HDPE, the use of these catalysts avoids the expensive process of separating the catalyst from the polymer.

However, the new supported catalysts were unsatisfactory for the polymerization of propene, where a control of the succession of the *m* versus the *r* configurations along the polymer chain is necessary. The isotacticity index (the insoluble fraction in boiling *n*-heptane) of polypropylenes, which can be obtained with high yields using catalysts for ethene polymerization of the above kind, is in fact in the range of 30–60%. This means that approximately one-half of the macromolecules have a fraction of relative *m* configurations lower than 95%, so that the most interesting technological characteristics of the polymer are heavily damaged. In the 1980s, the research to design a

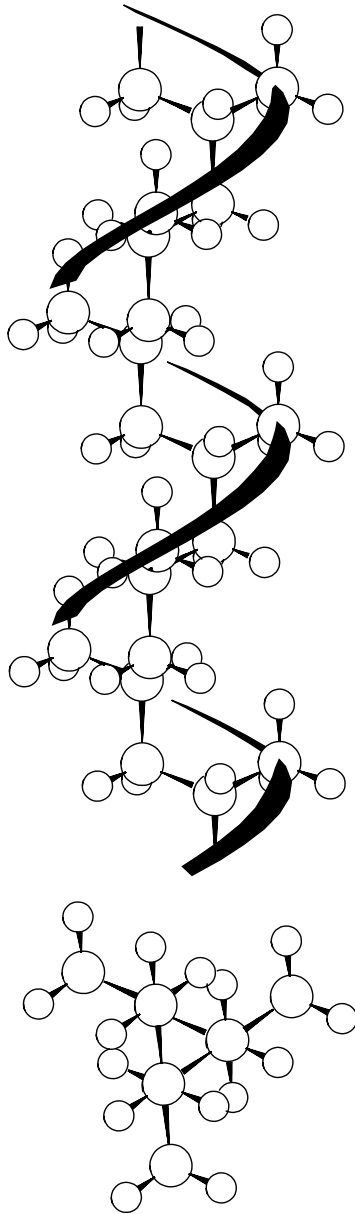


Figure 1.3 Chain conformation of isotactic polypropylene in its crystalline phases.

high-yield supported catalyst also for the isotactic polymerization of propene has led, with the help of the previous experience in the field, to the implementation in industrial research laboratories of a new catalytic system capable of such high yields (thousands of kilograms of polymer per gram of titanium) that the depuration process can be eliminated in the production plants; however, the isotacticity is so high that the heavy cost of the extraction of the amorphous fraction can be considerably reduced.⁶

Also in the 1980s, the discovery of homogeneous stereospecific catalysts for the polymerization of 1-alkenes has opened up new prospects for research on stereospecific polymerization and stereoregular polyolefins. Ewen and co-workers⁷⁻⁹ achieved this discovery on the basis of earlier research on metallocenes in combination with alkyl-Al-oxanes by Sinn and Kaminsky.¹⁰

Depending on the specific metallocene π -ligands used, these systems present completely different stereospecific behaviors. For instance, catalytic systems containing the metallocene stereorigid ligand ethylene-bis(1-indenyl) or ethylene-bis(4,5,6,7-tetrahydro-1-indenyl) [in the following $C_2H_4(1-Ind)_2$ and $C_2H_4(H_4-1-Ind)_2$, respectively] polymerize α -olefins to isotactic polymers⁷ while catalytic systems comprising the metallocene stereorigid ligand isopropyl(cyclopentadienyl-9-fluorenyl), $Me_2C(Cp)(9-Flu)$ in the following, instead polymerize α -olefins to syndiotactic polymer.⁸ Hence, it has been possible to tune the structure of these catalysts to obtain a series of new stereoregular polymers, in particular a series of new crystalline syndiotactic polymers.

A main feature of the new homogeneous catalytic systems is that they can be "single site"; that is, they can include all identical catalytic sites. This can be a great advantage with respect to the heterogeneous catalytic systems, for which several sites with different reactivities and regio- and stereospecificities are present. In particular, single-site catalytic systems can also allow better control of the molecular mass distribution as well as, for copolymers, better control of the comonomer composition and distribution. Several aspects relative to the catalytic behavior of these "single-site" stereospecific catalysts have been described in some recent reviews.^{11,12}

It is generally accepted that the stereospecificity of Ziegler-Natta catalysts is due to chirality of the environment of the catalytic transition metal which imposes, mainly through nonbonded interactions, a chiral coordination of prochiral monomers. Cossee and his group in the 1960s¹³ and subsequently Allegra¹⁴ and Corradini and co-workers¹⁵ made some evaluation of the nonbonded interactions between propene and chiral catalytic sites, suggested as suitable for heterogeneous isospecific catalysis. The detailed structure of these models, based on crystallochemistry considerations relative to possible terminations of crystals of $TiCl_3$, was, of course, only hypothetical. However, the proposed polymerization mechanism¹³ and the derived mechanism

of stereoselectivity, which involves the growing chain orientation,¹⁵ agree well with a large number of experimental facts for the first generation (TiCl₃ based) as well as for the high-yield MgCl₂-supported catalytic systems.

The discovery of new stereospecific homogeneous catalysts based on metallocenes in combination with alkyl-Al-oxanes^{7-10,16,17} gave the stimulating opportunity to investigate much better defined catalysts. In fact, the coordination of the π -ligands in the catalytic models can be reasonably assumed to be similar to those observed in crystal structures of precursor metallocenes, which are often well described. In fact, in the last decade, experimental as well as molecular modeling studies relative to metallocene-based catalytic systems have been conducted by several research groups and have given relevant contributions to the comprehension of different aspects of the stereospecific polymerization mechanisms.

In this review, contributions of selected experimental and molecular modeling studies to the elucidation of even fine details relative to the stereospecificity of polymerization catalytic systems are outlined.

In Section 2 a brief description of the generally assumed polymerization mechanism and the elements of chirality for the stereospecific olefin polymerization is presented.

Section 3 will deal with catalytic systems whose stereospecificity is mainly controlled by the chirality of the environment of the transition metal, independently of the possible chirality of the growing chain (chiral site stereocontrol). In particular, in Section 3.1 the chirality and stereospecificity of homogeneous catalytic systems based on metallocenes of different symmetries and in different experimental conditions will be reviewed. In Section 3.2 the chirality of model catalytic sites, which have been supposed for isospecific first-generation TiCl₃-based and high-yield MgCl₂-supported catalysts, is described. In Section 3.3 we will present a comparison between model catalytic sites proposed for heterogeneous and homogeneous stereospecific site-controlled catalysts.

Section 4 will deal with catalytic systems whose stereospecificity is controlled principally by the chirality of the closest tertiary carbon atom of the growing chain (chain-end stereocontrol). In Section 4.1 possible mechanisms for chain-end controlled isospecific and syndiospecific propene polymerizations will be reviewed. In Section 4.2 informations relative to the mechanism of chain-end controlled syndiospecific polymerization of styrene and substituted styrenes will be reviewed. In Section 4.3 chain-end controlled mechanisms for the isospecific and syndiospecific *cis*-1,4 and 1,2 polymerizations of dienes will be presented.

A large part of the stereospecific behavior of polymerization catalysts presented in this review can be rationalized in the framework of a stereoselectivity mechanism involving a *chiral orientation of the growing chain*. The discovery

of this stereoselectivity mechanism, never considered before (even as only possible in principle), constitutes, in our opinion, the main contribution of molecular modeling to the comprehension of stereospecific polymerizations. The experiments often designed to verify the possible validity of this mechanism are also shortly reviewed.

2 POLYMERIZATION MECHANISMS AND ELEMENTS OF CHIRALITY

The basic assumptions common to most mechanism studies relative to transition metal catalyzed polymerizations are as follows: (i) The mechanism is essentially monometallic and the active center is a transition metal–carbon bond.^{13–15,18,19} (ii) The mechanism is in two stages: coordination of the olefin to the catalytic site followed by insertion into the metal–carbon bond through a *cis* opening of the olefin double bond.^{13,20,21}

Possible elements of chirality in stereospecific polymerizations will be briefly recalled in order to indicate the used terminology. First of all, upon coordination, a prochiral olefin such as propene gives rise to not superposable *si* and *re* coordinations.²² According to the mechanism described, the isotactic polymer is generated by a large series of insertions of all *si*- or all *re*-coordinated monomers, while the syndiotactic polymer would be generated by alternate insertions of *si*- and *re*-coordinated monomers.

A second element of chirality is the configuration of the nearest tertiary carbon atom of the growing chain, and a third element of chirality is the chirality of the catalytic site, which, in particular, can be of two different kinds:

(i) *Chirality Arising from Coordinated Ligands* (other than alkene monomer and growing chain). For the case of ligands which may be prochiral (*i'*), it is possible to use the notation (*R*) or (*S*), in parentheses, according to the Cahn–Ingold–Prelog rules²³ extended by Schlögl.²⁴ For instance, the (*R, R*) chirality of coordination of the C₂H₄(1-Ind)₂ ligand, which is labeled according to the absolute configurations of the bridgehead carbon atoms (marked by arrows), is shown in Figure 1.4. For complexes with two bidentate ligands (*i''*), like those proposed for the heterogeneous Ziegler–Natta catalysis^{13–15} (Figure 1.5), the relative orientations of the two bidentate ligands can be chiral and labeled with the notation Λ or Δ (15), defined for octahedral coordination compounds with at least two bidentate chelating agents.²⁵

(ii) *Intrinsic Chirality at Central Metal Atom* (which for tetrahedral or assimilable to tetrahedral situations can be labeled with the notation *R* or *S*, by the extension of the Cahn–Ingold–Prelog rules, as proposed by Stanley and Baird²⁶. For instance, the two diastereoisomers with intrinsic chirality at

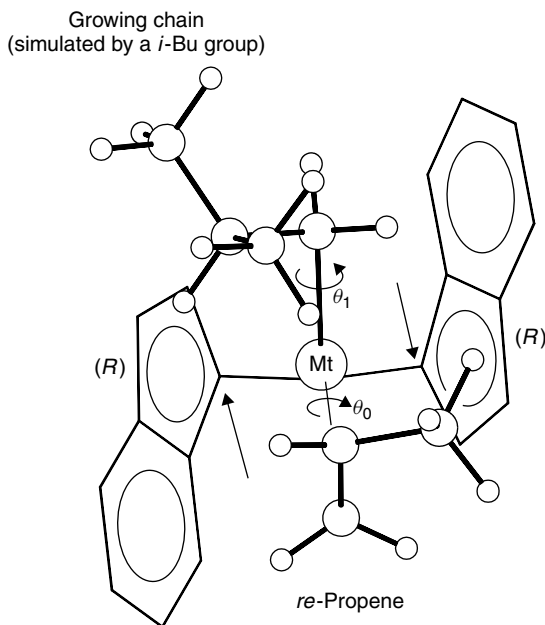


Figure 1.4 Model catalytic complex comprising isopropyl-bis(1-indenyl) ligand, propene molecule *re* coordinated, and isobutyl group (simulating a growing primary polypropylene chain). Chirality of coordination of bridged π -ligand is (*R*, *R*), labeled according to absolute configurations of bridgehead carbon atoms which are marked by arrows. Coordinated bridged π -ligand presents local C_2 symmetry axis, and two coordination positions which are available for monomer and growing chain are homotopic. For sake of clarity, for bridged π -ligand only C–C bonds are sketched and carbon atoms of methyl groups of isopropyl bridge are omitted. Dihedral angles θ_0 and θ_1 (see text), used in energy plots of Figures 1.9 and 1.7, respectively, are also indicated.

the central metal atom *R* and *S* are shown in Figures 1.6*a* and *b*, respectively, for the case of a metallocene with a $\text{Me}_2\text{C}(\text{Cp})(9\text{-Flu})$ ligand.

As will be shown in detail in the following sections, one or both of these kinds of chirality of the site can be present in the catalytic complexes. However, for the case of catalytic complexes in which two carbon polyhapto ligands are tightly connected through chemical bonds and which we shall call thereafter “stereorigid,” only the chirality of kind (ii) can change during the polymerization reaction.

In the simpler cases, the discrimination between the two faces of the prochiral monomer may be dictated by the configuration of the asymmetric tertiary C atom of the last inserted monomer unit (*chain-end stereocontrol*) or by the chirality of the catalytic site (*chiral site stereocontrol*). The distribution of steric defects along the polymer chain may be indicative of which kind

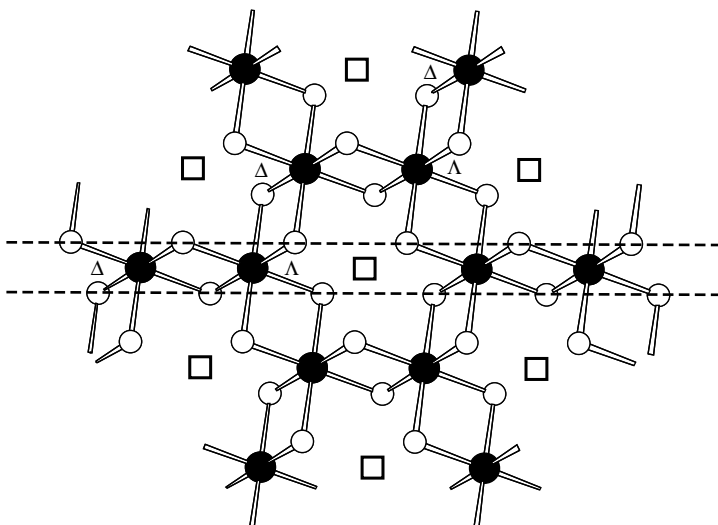


Figure 1.5 Schematic drawing of structural layer of violet TiCl_3 . Titanium atoms (full circles) are bonded to six chlorine atoms (empty circles) and occupy only two-thirds of octahedral positions; vacant octahedral positions are indicated by squares. Chirality (Λ or Δ) of some metal atoms are also labeled. Dashed lines correspond to possible lateral cut, later shown in Figure 1.13.

of stereocontrol is operating. Bernoullian statistics have been shown²⁷ to be consistent with a chain-end stereocontrol while non-Bernoullian distributions originate from a chiral site stereocontrol.^{28,29} The difference can be readily realized for isotactic propagation. Intuitively, in the case of chain-end stereocontrol an occasional change in the configuration of the last inserted monomer unit tends to be perpetuated (as in Scheme 1.1*a*), while in the case of enantiomorphic site stereocontrol the same occasional change, having no effect on site chirality, tends to remain isolated (as in Scheme 1.1*b*). It is generally assumed that the stereoselectivity of stereospecific polymerizations is connected with the energy differences between diastereoisomeric situations which originate from a combination of two or more of the above elements of chirality.

Molecular modeling studies have contributed to the definition of the polymerization mechanisms, and in particular to the stereospecificity mechanisms, through (i) the recognition of "stable" geometries of the relevant diastereoisomers; (ii) the choice, among these, of geometries which are as near as possible to the transition states of the insertion reactions; and (iii) comparative estimates of the corresponding activation energies. Internal energies are minimized with respect to the relevant dihedral angles determining the positions of the

atoms in the vicinity of the catalytic center. In particular, for models for olefin polymerizations, θ_0 is associated with rotations of the olefin around the axis connecting the metal to the center of the double bond, while θ_1 is associated with the rotation around the bond between the metal atom and the first carbon atom of the growing chain (Figure 1.4). At θ_0 near 0° the olefin is oriented in a way suitable for primary insertion, while θ_0 near 180° corresponds to an orientation suitable for secondary insertion. The angle θ_1 near 0° corresponds to the conformation having the first C–C bond of the growing chain eclipsed with respect to the axis connecting the metal atom to the center of the double bond of the olefin. For instance, the situation depicted in Figure 1.4 corresponds to $\theta_0 \approx 0^\circ$ and $\theta_1 \approx -60^\circ$.

Intermediates corresponding to the coordination step are considered as sufficiently close to transition states of the insertion reaction, and hence as suitable *preinsertion intermediates*, only if the insertion can occur through a motion of the nuclei that is near to the least—principle of *least nuclear motion*.^{13,30,31} For instance, for alkene polymerizations preinsertion intermediates correspond to geometries with (a) a double bond of the olefin nearly parallel to the metal growing chain bond and (b) the first C–C bond of the chain nearly perpendicular to the plane defined by the double bond of the monomer and by the metal atom ($50^\circ < \theta_1 < 130^\circ$, rather than $\theta_1 \approx 180^\circ$; see below).

3 CHIRALITY IN SITE-CONTROLLED STEREOSPECIFIC POLYMERIZATIONS

3.1 Homogeneous Polymerization Catalysts: Metallocenes

Different kinds of homogeneous catalysts based on group 4 metallocene–MAO (MAO = methylalumoxane) systems have been discovered. Depending on the kind of metallocene π -ligands, these systems present completely different stereospecific behaviors.

For instance, catalytic systems comprising the metallocene stereorigid ligand $C_2H_4(1-Ind)_2$ or $C_2H_4(H_4-1-Ind)_2$ polymerize propene to isotactic polymer with a non-Bernoullian distribution of steric defects, consistent with a prevalingly chiral site stereocontrol.^{7,16,17} Catalytic systems comprising the metallocene stereorigid ligand isopropyl $Me_2C(Cp)(9-Flu)$ polymerize, instead, propene to syndiotactic polymer, again consistently with a prevalingly chiral site stereocontrol.⁸

The cationic character of the active site, proposed as long ago as 1961,³² has recently been confirmed by the synthesis of a wide series of group 4 metallocene cations able to polymerize ethene and propene without any aluminum cocatalyst.^{33–36} The finding by Ewen that $C_2H_4(1-Ind)_2ZrCl_2/MAO$

and $C_2H_4(1-Ind)_2ZrCH_3^+B(C_6F_5)_4^-$ produce isotactic polypropylene with the same microstructural defects is the best available proof for the cationic nature of the active species.⁹

The generally assumed models of the alkene-bound intermediates are metal complexes containing a π -coordinated alkene molecule, a σ -coordinated growing chain, and the π -coordinated ligands of the precursor metallocenes. Geometries of coordination of the π -ligands similar to those observed in the crystal structures of the precursor metallocenes have been generally assumed as starting points for energy minimizations.

3.1.1 Stereoselectivity: Mechanism of Chiral Orientation of Growing Chain

A necessary (but not sufficient) prerequisite for models of stereospecific catalytic systems is the stereoselectivity of each monomer insertion step. The possible origin of stereoselectivity for models of several kinds of catalytic systems has been investigated through molecular modeling.

Let us first consider models relative to preinsertion intermediates like those described in the previous section. Figures 1.7*a,b* plot as a function of θ_1 the optimized energy for the catalytic site models of Figures 1.4 and 1.6*a*, respectively. These models coordinate to a zirconium atom a propene molecule, an isobutyl group (simulating a primary growing chain), and a stereorigid π -ligand, being (*R,R*)-coordinated *rac*- $C_2H_4(1-Ind)_2$ or $Me_2C(Cp)(9-Flu)$ with *R* chirality at the metal. The starting points for the energy optimizations are conformations with $\theta_0 = 0^\circ$. Whatever the energy, the absolute value of θ_0 for the optimized conformations is never higher than 20° . Hence, these models simulate preinsertion intermediates for primary insertion of propene into a primary polypropylene growing chain. The full and dashed lines refer to *re*- and *si*-coordinated propene, respectively.

The absolute-energy minima labeled as *a* in Figures 1.7*a,b* correspond to $\theta_1 \approx -60^\circ$ for the *re* monomer coordination and are sketched in Figures 1.4 and 1.6*a*, respectively. These models minimize the interactions between the growing chain (at $\theta_1 \approx -60^\circ$) and the methyl of the propene monomer (*re* coordinated). Therefore, these are assumed to be preinsertion intermediates suitable for the *re* monomer primary insertions.

The minimum-energy situations labeled as *b* in Figure 1.7 have similar θ_1 values but opposite monomer enantiofaces and are slightly higher in energy (1–2 kcal/mol). However, since the methyl group of propene and the second carbon atom (and its substituents) of the growing chain are on the same side with respect to the plane defined by the Zr–C bonds, the corresponding models are assumed to be unsuitable for the successive monomer insertion (see below).

The minimum-energy situations labeled as *c* in Figure 1.7, corresponding to the opposite monomer enantioface, minimize the interactions between the

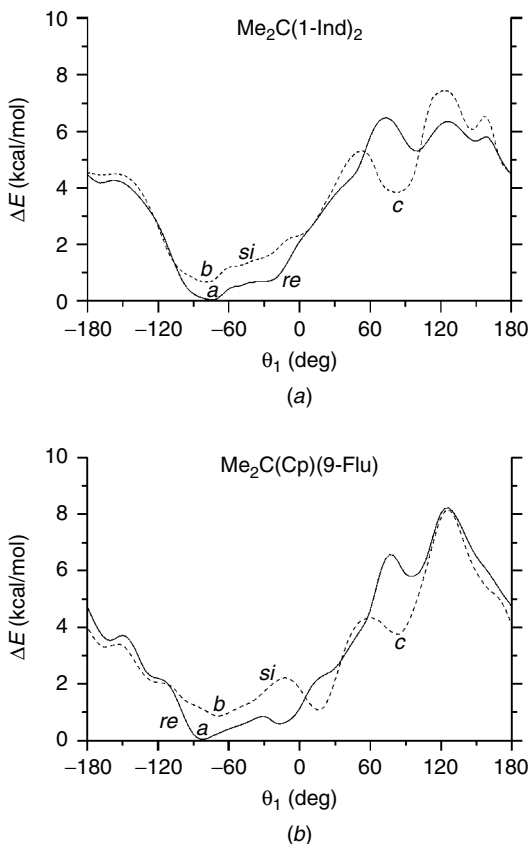


Figure 1.7 Optimized energies plotted as function of θ_1 for model complexes comprising (a) (*R,R*)-coordinated isopropyl-bis(1-indenyl) ligand, i.e., **5** in Scheme 1.2; (b) isopropyl(cyclopentadienyl-9-fluorenyl) ligand, i.e., **30** in Scheme 1.2, for *R* chirality at metal atom. Full and dashed lines refer to *re*- and *si*-coordinated propene, respectively. In both cases chirality of site favors negative values of θ_1 , which in turn favor *re* coordination of propene. Models of preinsertion intermediates corresponding to absolute energy minima, labeled *a* in (a) and (b), are sketched in Figures 2.4 and 2.6a, respectively. For model complex comprising isopropyl(cyclopentadienyl-9-fluorenyl) ligand, for *S* chirality at metal atom chirality of site favors positive values of θ_1 , which in turn favor *si* coordination of propene (corresponding minimum-energy preinsertion intermediate is shown in Figure 1.6b).

methyl group of the propene monomer and the growing chain ($\theta_1 \approx +60^\circ$ for *si*-coordinated monomer). Therefore, as discussed in previous papers,^{15,37} they are also assumed to be suitable for the successive insertion reaction. However, these models are strongly disfavored by repulsive interactions of the growing chain with one of the six-membered rings of the ligands. In our framework,

the energy difference $E_c - E_a$ gives an approximation of the stereoselectivity of the primary (ΔE_{enant}) insertion step.

Hence, this analysis indicates that the stereoselectivity of these models is due, not to direct interactions of the π -ligands with the monomer, but to interactions of the π -ligands with the growing chain, determining its chiral orientation ($\theta_1 \approx -60^\circ$ preferred to $\theta_1 \approx +60^\circ$), which in turn discriminates between the two prochiral faces of the propene monomer.^{15,37}

Molecular mechanics calculations have been performed also on approximated transition states originating from the preinsertion intermediates labeled as *a*, *b*, and *c*, in Figure 1.7. The approximated transition states originating from the preinsertion intermediates labeled as *b*, presenting the methyl group of propene and the second carbon atom (and its substituents) of the growing chain on the same side with respect to the plane defined by the Zr-C bonds, are always of higher energy. An additional kind of evaluation of the stereoselectivities for the primary insertions ($\Delta E_{\text{enant}}^*$) is hence obtained by energy differences between transition states following preinsertion intermediates labeled as *a* and *c* in Figure 1.7. The approximated transition states corresponding to the preinsertion intermediates labeled as *a* in Figures 1.7*a,b* (sketched in Figures 1.4 and 1.6*a*) are sketched in Figures 1.8*a,b*, respectively.

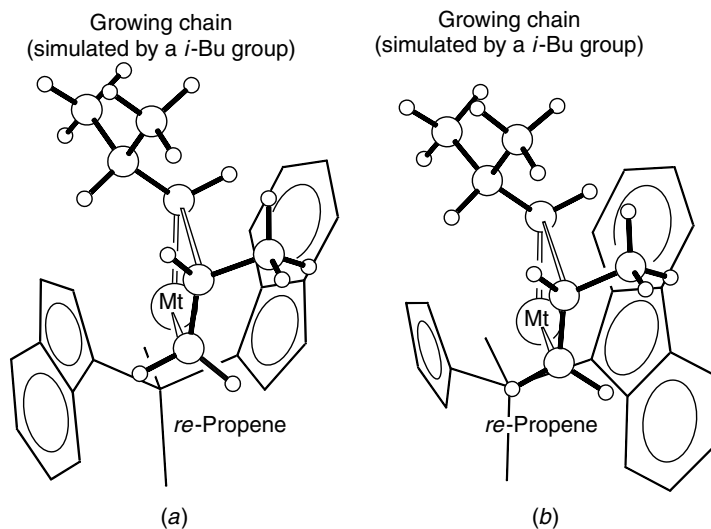


Figure 1.8 Approximated transition states for primary propene insertion for model complexes with (a) isopropyl-bis(1-indenyl) ligand (isospecific) for the (*R,R*) coordination and (b) isopropyl(cyclopentadienyl-9-fluorenyl) ligand (syndiospecific) for the *R* chirality at metal atom. Corresponding preinsertion intermediates, labeled *a* in Figures 1.7*a,b*, are sketched in Figures 1.4 and 1.6*a*, respectively.

The stereoselectivities as evaluated from preinsertion intermediates and transition states (ΔE_{enant} and $\Delta E_{\text{enant}}^*$, respectively) are collected in Table 1.1 for stereorigid models based on the π -ligands sketched in Scheme 1.2. In the table, the local symmetry of the coordinated bridged π -ligand (C_2 , C_1 , or C_s), the possible chirality of coordination of the π -ligand (which does not change during the polymerization reaction), and, for C_1 or C_s local symmetries, the possible chirality at the central metal atom (which generally is inverted at each insertion step, see next section) are also indicated. It is apparent that the values of the stereoselectivities obtained by the two above-described methods (ΔE_{enant} and $\Delta E_{\text{enant}}^*$) are generally similar.

Molecular modeling studies relative to both preinsertion intermediates and insertion states indicate that for all the metallocenes from **1** to **39** of Scheme 1.2 (independent of their structure and symmetry), when a substantial stereoselectivity is calculated for primary monomer insertion, this is mainly due to nonbonded energy interactions of the methyl group of the chirally coordinated monomer with the chirally oriented growing chain.

According to analogous molecular mechanics analyses,³⁸ this stereoselectivity mechanism would also operate for catalytic systems with oscillating stereocontrol, leading to atactic–isotactic stereoblock polymers,^{39,40} like those based on two unbridged 2-phenyl-indenyl ligands.⁴⁰

This mechanism of stereoselectivity is in agreement with several available experimental data. In this respect, it may be of interest to recall that a relevant experimental proof of the importance of the role played by the growing chain in determining the steric course of the insertion reaction was given, by Zambelli and co-workers,^{41,42} by the observation of the stereospecificity in the first step of polymerization. In fact, analyses by ¹³C nuclear magnetic resonance (NMR) techniques of the polymer end groups have shown that in the first step of polymerization, when the alkyl group bonded to the metal is a methyl group, the propene insertion is essentially nonenantioselective, whereas when the alkyl group is an isobutyl group, the first insertion is enantioselective as the successive insertions, both for heterogeneous⁴¹ and homogeneous Ziegler–Natta catalysts.⁴² The results of molecular mechanics calculations on the proposed metallocene models relative to possible initiation steps are in perfect agreement with these experimental findings^{41,42} and are also able to rationalize⁴³ the partial stereoselectivity of a catalytic system based on the bis(1-indenyl) ligand for 1-butene insertion at a Mt–CH₃ bond.⁴²

This enantioselective mechanism is also in accordance with the elegant analysis and optical activity measurements by Pino et al.^{44,45} on the saturated propene oligomers obtained under suitable conditions with this kind of catalysts, proving that the *re* insertion of the monomer is favored in case of (*R*, *R*) chirality of coordination of the C₂H₄(1-Ind)₂ ligand.

Table 1.1
 Calculated Nonbonded Energy Contributions to Enantioselectivity for Preinsertion
 Intermediates (ΔE_{enant}) and Approximated Transition States ($\Delta E_{\text{enant}}^{\ddagger}$)

Ligand ^a	Metal Atom	Chirality of Coordination of π -Ligand	Propene Coordination Position	ΔE_{enant}	$\Delta E_{\text{enant}}^{\ddagger}$	Favored Propene Enantioface	$E_{\text{out}} - E_{\text{inw}}$
C ₂ -Symmetric Ligands							
1	Zr	(R, R)	—	0.1	—	<i>si</i>	
2	Zr	(R, R)	—	3.3	—	<i>re</i>	
3	Zr	(R, R)	—	7.0	5.9	<i>re</i>	
4	Zr	(R, R)	—	3.7	—	<i>re</i>	
5	Zr	(R, R)	—	3.8	2.3	<i>re</i>	
6	Zr	(R, R)	—	3.6	—	<i>re</i>	
7	Zr	(R, R)	—	0.0	—	—	
8	Zr	(R, R)	—	4.3	4.3	<i>si</i>	
9	Zr	(R, R)	—	0.0	—	—	
10	Zr	(R, R)	—	3.7	—	<i>re</i>	
11	Zr	(R, R)	—	6.4	5.0	<i>re</i>	
12	Zr	(R, R)	—	4.4	—	<i>re</i>	
13	Zr	(R, R)	—	4.9	3.0	<i>re</i>	
14	Zr	(R, R)	—	4.8	3.2	<i>re</i>	
15	Zr	(R, R)	—	0.1	0.3	<i>re</i>	
16	Zr	(R, R)	—	4.0	2.4	<i>si</i>	
17	Zr	(R, R)	—	5.3	3.1	<i>re</i>	
18	Zr	(R, R)	—	5.9	5.7	<i>re</i>	
19	Zr	(R, R)	—	5.5	3.8	<i>re</i>	
20	Zr	(R, R)	—	5.6	—	<i>re</i>	
21	Zr	(R, R)	—	5.3	—	<i>re</i>	
22	Zr	(R, R)	—	5.1	3.8	<i>re</i>	
23	Zr	(R, R)	—	4.3	3.5	<i>re</i>	
23	Ti	(R, R)	—	5.6	3.5	<i>re</i>	
24	Zr	(R, R)	—	5.7	4.7	<i>re</i>	
24	Ti	(R, R)	—	7.4	—	<i>re</i>	
25	Zr	(R, R)	—	1.4	1.3	<i>re</i>	
26	Zr	(R, R)	—	5.7	3.2	<i>re</i>	
27	Zr	(R, R)	—	6.1	10.1	<i>re</i>	
28	Zr	(R, R)	—	1.9	—	<i>re</i>	
29	Zr	(R, R)	—	4.7	—	<i>re</i>	
C _s -Symmetric Ligands							
30	Zr	—	<i>R</i>	3.7	2.1	<i>re</i>	
31	Zr	—	<i>R</i>	3.2	1.6	<i>re</i>	
32	Zr	—	<i>R</i>	2.3	—	<i>re</i>	
33	Zr	—	<i>R</i>	4.8	—	<i>re</i>	

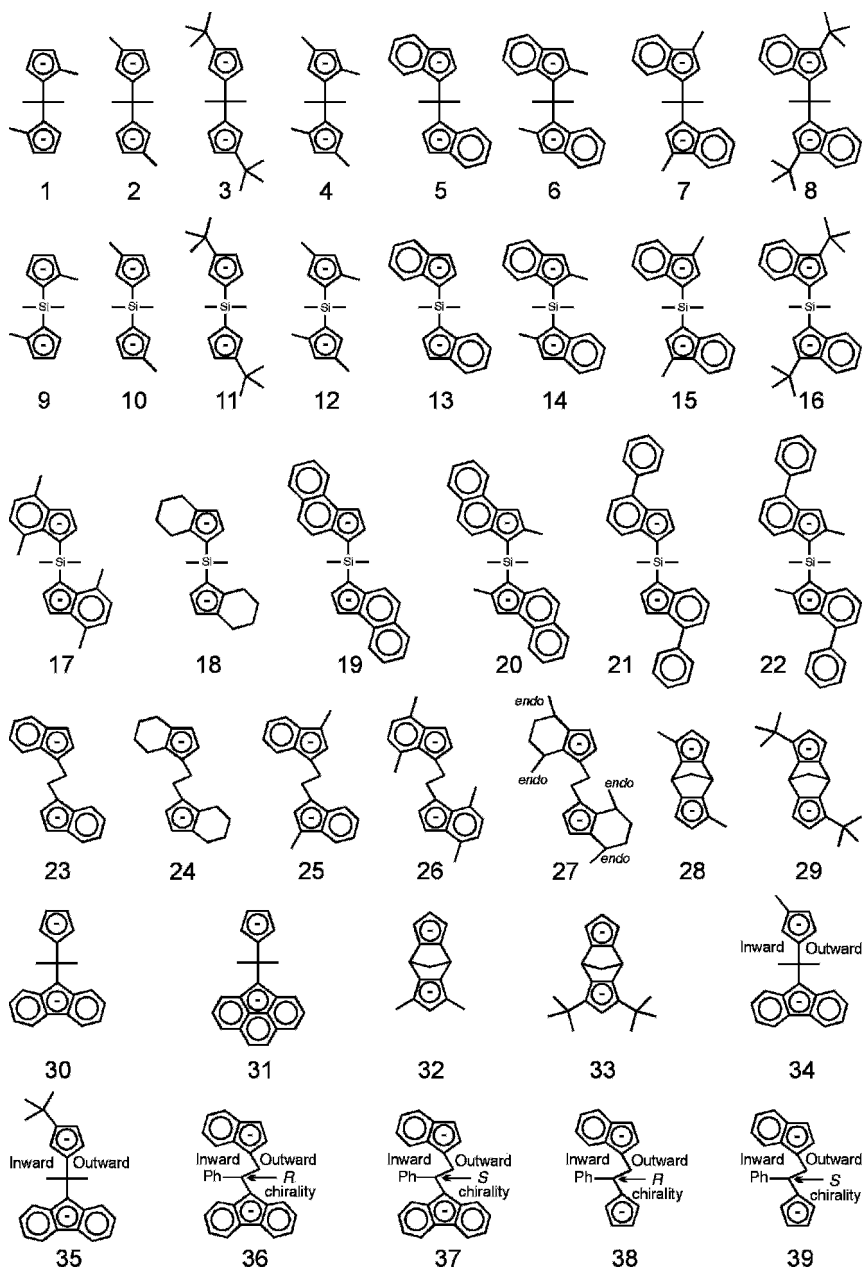
Table 1.1
(continued)

Ligand ^a	Metal Atom	Chirality of Coordination of π -Ligand	Propene Coordination Position	ΔE_{enant}	$\Delta E_{\text{enant}}^{\ddagger}$	Favored Propene Enantioface	$E_{\text{out}} - E_{\text{inw}}$
C ₁ -Symmetric Ligands							
34	Zr	(<i>R</i>)	<i>R</i> \equiv inward	4.6		<i>re</i>	2.9
			<i>S</i> \equiv outward	1.1		<i>si</i>	2.9
35	Zr	(<i>R</i>)	<i>R</i> \equiv inward	7.6		<i>re</i>	4.6
			<i>S</i> \equiv outward	2.1		<i>re</i>	4.6
36	Zr	(<i>R</i>)	<i>R</i> \equiv inward	6.3		<i>re</i>	3.1
			<i>S</i> \equiv outward	2.2		<i>re</i>	3.1
37	Zr	(<i>R</i>)	<i>R</i> \equiv inward	4.4		<i>re</i>	3.4
			<i>S</i> \equiv outward	1.5		<i>si</i>	3.4
38	Zr	(<i>R</i>)	<i>S</i> \equiv inward	0.1		<i>re</i>	-0.9
			<i>R</i> \equiv outward	3.8		<i>re</i>	-0.9
39	Zr	(<i>R</i>)	<i>S</i> \equiv inward	0.3		<i>re</i>	-0.9
			<i>R</i> \equiv outward	2.6		<i>re</i>	-0.9

^a See Scheme 1.2.

Moreover, studies on simultaneous deuteration and deuteriooligomerization of 1-alkenes using catalysts based on (*R, R*) C₂H₄(H₄-1-Ind)₂ zirconium derivatives have shown that in all studied dimerizations and oligomerizations of 1-alkenes (propene, 1-pentene, 4-methyl-pentene) the *R* enantioface of the olefin is predominantly involved; in all studied deuteration of 1-alkenes (1-pentene, styrene) the *S* enantioface is favored.⁴⁵ These results confirm that the growing chain plays a primary role in enantioface discrimination for stereospecific polymerization catalyses. On the other hand, the presence of opposite stereoselectivities in deuteration and oligomerization has also been rationalized by molecular mechanics calculations analogous to those previously described, thus constituting a further valuable support to the proposed catalytic models and stereoselective mechanism.⁴⁶ More recent results by Bercau and co-workers relative to deuteration and deuterodimerization experiments on isotopically chiral 1-pentene are also in agreement with a mechanism involving a chiral orientation of the growing chain.⁴⁷

It is worth noting that the proposed preinsertion intermediates, like those of Figures 1.4 and 1.6, are suitable for the formation of an α -agostic bond between the metal and the hydrogen atom on the opposite side with respect to the incoming monomer.⁴⁸ In fact, the transition state for the insertion step in nonchiral scandium-based⁴⁹ and chiral zirconium-based⁵⁰ catalysts has been found to be α -agostic stabilized. According to our energy calculations,



Scheme 1.2 π -ligands coordinated to the metal atom for the catalytic models whose calculated stereoselectivities have been reported in Table 1.1.

the formation of an α -agostic bond is adjuvant but not always crucial for the stereoselectivity of monomer insertion. In fact, the conformation with $|\theta_1| \approx 60^\circ$, which discriminates between *re* and *si* monomer enantiofaces, is often imposed by the chiral environment, even in the absence of a possible α -agostic bond. Moreover, as described in detail in Ref. 37d, the observed stereoselectivity of the primary propene insertion into a secondary growing chain $[\text{Mt}-\text{CH}(\text{CH}_3)\text{CH}_2-]$ for a catalytic system based on ligands **23** and **24** has been rationalized on the basis of preinsertion intermediates, which do not involve α -agostic bonds.

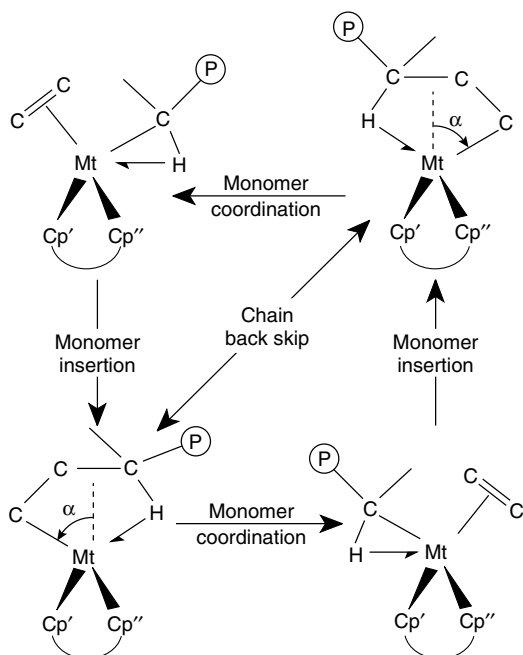
3.1.2 Stereospecificity

3.1.2.1 Chain Migratory Insertion Mechanism. For a given catalytic model, the stereoselectivity of each insertion step does not assure its stereospecificity (i.e., to lead to a stereoregular polymer). In fact, the possible presence as well as the kind of stereospecificity depends on possible differences between stereostructures of transition states of two successive insertion steps.

These stereostructures are related to the best geometry of coordination of the growing chain at the site in the absence of the monomer molecule (as at the end of each polymerization step) as well as to the stability of such geometry before the coordination of a new monomer molecule.

According to simple quantum mechanical considerations by Hoffman and co-workers, for d_0 , d_1 , d_3 , or low-spin d_2 complexes of the kind MtCp_2L ,⁵¹ $\text{Cp} = \text{C}_5\text{H}_5$, the best coordination of L is not the one (most symmetrical and presumably sterically most favorable) along the symmetry axis which relates the two bent cyclopentadienyl rings. This is confirmed by more recent and complete calculations by Ziegler and co-workers relative to homogeneous $[\text{Cp}_2\text{ZrCH}_3]^+$ and $[\text{CpSiH}_2\text{NHTiCH}_3]^+$ systems.⁵² According to these calculations, energy minimum situations would correspond to angular deviations $\alpha \approx 60^\circ$ from the symmetry axis, and an additional stabilization of geometries with $\alpha \neq 0^\circ$ at the unsaturated metal center could occur because of an agostic interaction of a hydrogen in the γ -position,⁵² analogous to that postulated by Brookhart and Green⁵³ (see Scheme 1.3). Note that a geometry with $\alpha \neq 0^\circ$ makes the metal atom chiral in the cation $(\text{MtCp}'\text{Cp}''\text{L})^+$ if the two cyclopentadienyl ligands Cp' and Cp'' are different.

On the basis of the chain migratory insertion mechanism^{8,13,37c} (polymerization scheme reported in Scheme 1.3), at the end of each polymerization step the growing chain occupies the coordination site previously occupied by the alkene monomer. Hence, if the rate of rearrangement of the ligands is much lower than the rate of insertion of new monomer molecules, most consecutive polymerization steps correspond to models obtained by exchanging the relative positions of the growing chain and of the incoming monomer. This



Scheme 1.3 Polymerization scheme showing the *migratory insertion mechanism* as well as the possible occurrence of the *chain back-skip*. The possible formation of agostic Mt–H bonds is indicated by half-arrows.

is extremely relevant for the stereospecific behavior of the models since, if a chirality at the central metal atom (i.e. of type ii) exists, it is inverted at most polymerization steps, as shown in Scheme 1.3.

In the framework of the chain migratory insertion mechanism (Scheme 1.3), the stereospecific behavior of the model sites depends on the relationship between the two situations obtained by exchanging, in the coordination step, the relative positions of the growing chain and the incoming monomer. Depending on the local symmetry of the coordinated bridged π -ligand, these two situations can be as follows:

(i) *Identical* (i.e., two available coordination positions are homotopic⁵⁴). These model sites, if the insertion step is enantioselective, are consequently isospecific. Model sites presenting a C_2 symmetry axis, which locally relates the atoms which are relevant to the nonbonded interactions with the monomer and the growing chain, were proposed by Allegra several years ago for the heterogeneous catalysis on $TiCl_3$.¹⁴

Analogous models based on metallocenes with C_2 symmetry axes relating the atoms of the stereorigid π -ligand (like **1–29** of Scheme 1.2 and Table 1.1)

account for the isospecific behavior of corresponding metallocene-based catalytic systems.^{7,37} In fact, the calculated stereoselectivity values compare well with the observed tacticities of polypropylene samples obtained by the corresponding catalytic systems.

For instance, by considering **1–27** as bridged and substituted bis(cyclopentadienyl) ligands, substituents in position 2 (and 2') are not sufficient to give stereoselectivity (**1** and **9**), substituents in position 3 (and 3') give substantial stereoselectivities (**2–6**, **10–14**, **17–24**, **27**), while substituents of similar encumbrances in positions 3 and 4 (and 3' and 4') produce again poor stereoselectivities (**7** and **15**). These computational results^{31,55} agree well with the experimental findings relative to catalytic systems based on analogous C_2 -symmetric π -ligands.^{9,56,57}

Of course, the stereoselectivity (and hence the isospecificity) of the catalytic models strongly depends on the encumbrance of the π -ligand, increasing along the following series: 3-methyl-cyclopentadienyl (e.g., 3.7 kcal/mol for **10**), indenyl (e.g., 4.9 kcal/mol for **13**), 4,7-dimethyl-indenyl (e.g., 5.3 kcal/mol for **17**), and tetrahydroindenyl (e.g., 5.9 kcal/mol for **18**). This is in good qualitative agreement, for instance, with the percent of *mmmm* pentads evaluated for polypropylene samples obtained for different catalytic systems in strictly similar conditions by Resconi and co-workers.⁵⁸

The calculation results listed in Table 1.1 are also able to account for the influence of the bridge on the isospecificity. In fact, in agreement with the experimental results,⁵⁸ the calculated stereoselectivities for a given π -ligand are generally smaller for the case of the $-C(CH_3)_2-$ (**2–6**) than for the $-Si(CH_3)_2-$ bridge (**10–14**), while for the case of the $-CH_2-CH_2-$ bridge the stereoselectivities are often intermediates (compare, e.g., **5**, **13**, and **23**).

It is worth noting that the calculations on models with 3-*t*-butyl-1-indenyl ligand (**16**) predict a substantial stereoselectivity but in favor of the opposite monomer enantioface [*si* and *re* for (*R*, *R*)- and (*S*, *S*)-coordinated π -ligand, respectively].

(ii) *Enantiomeric* (i.e., two available coordination positions are enantiotopic⁵⁴). These model sites, if the insertion step is enantioselective, are consequently syndiospecific. Model sites based on metallocenes with C_s symmetry planes, relating the atoms of the stereorigid π -ligand (like **30–33** of Table 1.1),^{37b,59} account for the syndiospecific behavior of corresponding metallocene-based catalytic systems.^{8,9,60}

It is worth noting that the lower syndiospecificity of catalytic systems based on **31**, with respect to those based on **30**,⁹ is accounted for by these calculations. This is easily rationalized in the framework of the enantioselective mechanism which imposes to the growing chain (both in the preinsertion intermediate and in the approximated transition state) a chiral orientation toward

the cyclopentadienyl ligand and favors the insertion of the propene enantioface presenting the methyl group closer to the bulkier π -ligand (as shown in Figures 1.6 and 1.8*b*, respectively). In fact, the two additional aromatic carbon atoms which are present in **31**, with respect to **30**, generate direct interactions with the propene coordinated with the right enantioface, thus reducing the stereoselectivity.

(iii) *Diastereomeric* (i.e., two available coordination positions are diastereotopic⁵⁴). These model sites would be prevalingly isospecific (or syndiospecific) if these two situations are enantioselective in favor of a same (or opposite) monomer enantioface and tendentially hemi-isospecific⁶¹ if only one of the two situations is enantioselective.

The calculated stereoselectivities relative to the C_1 -symmetric models of Table 1.1 qualitatively agree with the stereospecific behavior of corresponding catalytic systems. In particular, for instance, the calculations relative to the model complexes with ligands **35** and **34** well account for the isospecificity and hemi-isospecificity of corresponding catalytic systems.^{9,62} The calculations are also able to qualitatively account for the stereospecificities of catalytic systems based on ligands differing only in the chirality at the tertiary carbon atom of the bridge.⁶³ As described in detail in Ref. 64, this chirality imposes the chirality of the ethylene bridge conformation (λ or δ for *S* or *R*, respectively), which, for crowded complexes (like those based on **36** and **37**), has a substantial influence on the stereospecific behavior of propene polymerization. In fact, both models **36** and **37** are enantioselective for the inward monomer coordination while both present a reduced stereoselectivity for the propene outward coordination; however, this stereoselectivity is in favor of the same or opposite monomer enantioface, respectively. This is in good agreement with measured tacticities of corresponding catalytic systems (46% vs. 15% of *mmmm* pentads, respectively).⁶³ According to the calculations, this influence of chirality relative to the bridge conformation on the stereoselectivity would also be mainly mediated by the chiral orientation of the growing chain.⁶⁴

For noncrowded complexes, the influence of the ethylene bridge conformation (and hence of the chirality of the tertiary carbon atom of the bridge) on the stereospecific behavior is poor (compare calculations for ligands **38** and **39**, in Table 1.1). This is in qualitative agreement with measured stereospecificities of corresponding catalytic systems (39% vs. 34% of *mmmm* pentads, respectively).⁶³

In summary, characterizations of stereosequences in polymers obtained by catalytic systems based on well-characterized metallocene complexes have produced a general acceptance of the chain migratory insertion mechanism and of models described in i–iii.

3.1.2.2 Possible Back-Skip of Growing Chain. Several experimental facts relative to propene polymerization behavior of different metallocene-based catalytic systems can be rationalized by considering a disturbance of the chain migratory insertion mechanism due to a kinetic competition between the monomer coordination in the alkene-free state and a back-skip of the growing chain to the other possible coordination position (see Scheme 1.3).

The possible occurrence of a back-skip of the chain for catalytic systems based on C_2 -symmetric metallocenes would not change the chirality of the transition state for the monomer insertion and hence would not influence the corresponding polymer stereostructure. On the contrary, for catalytic systems based on C_s -symmetric metallocenes, this phenomenon would invert the chirality of the transition state for the monomer insertion, and in fact it has been invoked to rationalize typical stereochemical defects (isolated *m* diads) in syndiotactic polypropylenes.^{9,37b,60} This mechanism of formation of stereoregularities has been confirmed by their increase in polymerization runs conducted with reduced monomer concentrations.⁶⁵ In fact, it is reasonable to expect an increase in the frequency of chain back-skip by reducing the monomer concentration and hence the frequency of monomer insertion.

For the case of catalytic systems based on C_1 -symmetric metallocenes, a driving force for the occurrence of the back-skip phenomenon related to the energy difference between the two diastereomeric situations obtained by exchanging the relative positions of monomer and chain can be added. The energy differences between minima corresponding to diastereomeric preinsertion intermediates with different chiralities at the central metal atom ($E_{\text{out}} - E_{\text{inv}}$) for several catalytic models with C_1 -symmetric metallocenes are listed in the column 7 of Table 1.1. It is worth noting that, when there are substantial energy differences between minimum-energy diastereomeric intermediates, lower energies correspond to the monomer coordination in the (more crowded) inward coordination position.⁶⁴

Of course, the probability of occurrence of a chain back-skip in the alkene-free state is only indirectly dependent on this energy difference. It is, in fact, dependent on the difference between the activation energy for the chain back-skip and the activation energy for the formation of the high-energy alkene-bound intermediate (Scheme 1.3). However, since the degree to which empirical force fields can be used for prediction of transition states is not well established and since the activation energy for the formation of the high-energy alkene-bound intermediate is expected to increase with increasing E_{out} , for the sake of simplicity, we take $E_{\text{out}} - E_{\text{inv}}$ as a semiquantitative evaluation of the driving force for the chain, back-skip.⁶⁴

In particular, it is reasonable to expect that, for the models with large $E_{\text{out}} - E_{\text{inv}}$ values (34–37), the growing chain in successive coordination steps can frequently occupy the (less crowded) outward coordination position, leaving

the inward position free for monomer coordination. For all these models, the lower energy diastereomer with inward monomer coordination is more enantioselective than the higher energy diastereomer with outward monomer coordination.

The results of Table 1.1 are in good qualitative agreement with several experimental results. In particular, the appreciable probability of two successive additions at the enantioselective catalytic face and the near-zero probability of two successive additions at the nonenantioselective catalytic face, observed for the essentially hemi-isospecific catalytic system based on **34**,^{9,61} are rationalized in terms of the lower energies for the single minimum of the enantioselective steps with respect to the two minima of the nonenantioselective steps.⁶⁴ The increased stereoregularity at decreasing monomer concentration (i.e., increasing the frequency of the chain back-skip) for catalytic systems based on **36** and **37** (not shown by systems based on **38** and **39**⁶³) can be explained on similar grounds.⁶⁴

3.1.2.3 Cyclopolymerization of Nonconjugated Dienes. Cyclopolymerization is an addition polymerization that leads to introduction of cyclic structures into the main chain of the polymer. Nonconjugated dienes are the most deeply studied monomers for cyclopolymerization and for cyclocopolymerizations with alkene monomers.⁶⁶ In general, (substituted and unsubstituted) dienes with double bonds that are linked by less than two or more than four atoms cannot undergo efficient cyclization and result in crosslinked materials.¹² In fact, efficient cyclopolymerization processes have been described, for instance, for α,ω -dienes like 1,5-hexadiene, 2-methyl-1,5-hexadiene, 1,6-heptadiene, and 1,7-octadiene,⁶⁷⁻⁷³ which lead to formation of homopolymers and copolymers containing methylene-1,3-cycloalkane units.

As for the stereochemistry, for the case of complete cyclization, besides the usual tacticity (possibly, isotactic or syndiotactic, referred to relative configurations of equivalent stereogenic carbons of subsequent monomeric units), the *cis* or *trans* configuration of the 1,3-cycloalkane rings which are present in the polymer main chain also has to be considered.^{70,74}

According to a widely accepted cyclopolymerization mechanism,^{67,75} there are two distinct stereochemical events for these cyclopolymerizations: the already discussed stereoselectivity and stereospecificity of olefin insertion, which determine the tacticity of the polymer, and the stereoselectivity of the cyclization step, which determines the *cis* or *trans* configuration of the rings.

In general, these stereochemical events are completely independent. For instance, isospecific catalysts like the heterogeneous ones (based on TiCl_3 or on TiCl_4 supported on MgCl_2) as well as C_2 symmetric metallocenes [e.g., based on *rac*- $\text{C}_2\text{H}_4(\text{H}_4\text{-1-Ind})_2\text{ZrCl}_2$] can present extremely poor *cis/trans*

selectivity. On the other hand, aspecific catalysts based on C_{2v} -symmetric metallocenes like Cp_2ZrCl_2 (Cp = cyclopentadienyl) or $Cp_2^*ZrCl_2$ (Cp^* = pentamethylcyclopentadienyl) present *trans* or *cis* selectivity, respectively, which can be larger than 90% for polymerizations conducted at $-78^\circ C$.⁷⁰

The stereoselectivity of the cyclization step in the cyclopolymerization of 1,5-hexadiene with homogeneous catalysts based on zirconocene–MAO systems has been investigated in detail through the analysis of the non-bonded interactions on model catalytic sites analogous to those proposed for α -olefin polymerizations. According to the calculations, the relative stability of diastereoisomeric cyclic intermediates, corresponding to the cyclization step, are substantially altered by steric interactions with the π -ligands. In particular, the *trans* and *cis* selectivities observed for cyclopolymerization of 1,5-hexadiene with catalytic systems based on Cp_2ZrCl_2 and $Cp_2^*ZrCl_2$ have been rationalized in terms of minimum-energy cyclic intermediate presenting a *trans* configuration in a chair conformation and a *cis* configuration in a twist conformation, respectively.⁷⁵

3.1.3 Stereoselectivities of Regioirregular Insertions

Molecular mechanics analyses of the kind described in previous sections are able to rationalize not only the stereoselectivity (and stereospecificity) of regioregular primary insertion steps but also the stereoselectivities relative to occasional secondary monomer insertions as well as relative to primary insertions following these secondary insertions.^{37d}

For instance, Figure 1.9a plots as a function of θ_0 the optimized energies for the model complex **5**, that is, a π -ligand with C_2 symmetry with (*R, R*) chirality of coordination of the bridged π -ligand. Let us recall that, in our framework, energy minima with $\theta_0 \approx 0^\circ$ or $\theta_0 \approx 180^\circ$ can correspond to preinsertion intermediates suitable for primary and secondary monomer insertions, respectively.

The energy minima labeled as *a*, *b*, and *c* in Figure 1.9a, corresponding to $\theta_0 \approx 0^\circ$, are coincident with those labeled with the same letters in the energy plot of Figure 1.7a. As already cited, the absolute minimum energy (labeled *a*) corresponds to the preinsertion intermediate for propene primary insertion with *re* enantioface, which is sketched in Figure 1.4.

As for situations possibly suitable for secondary propene insertion ($\theta_0 \approx 180^\circ$), the optimized energy for the *si* monomer coordination, labeled *e* in Figure 1.9a, is higher by nearly 2 kcal/mol with respect to the absolute minimum. The corresponding model sketched in Figure 1.10a is considered suitable for *si* monomer secondary insertion. The energy corresponding to $\theta_0 = 180^\circ$ is much higher for the *re* monomer coordination (*d* in Figure 1.9a) due to the repulsive interactions of the methyl group of propene with the six-membered rings of one of the indenyl ligands.

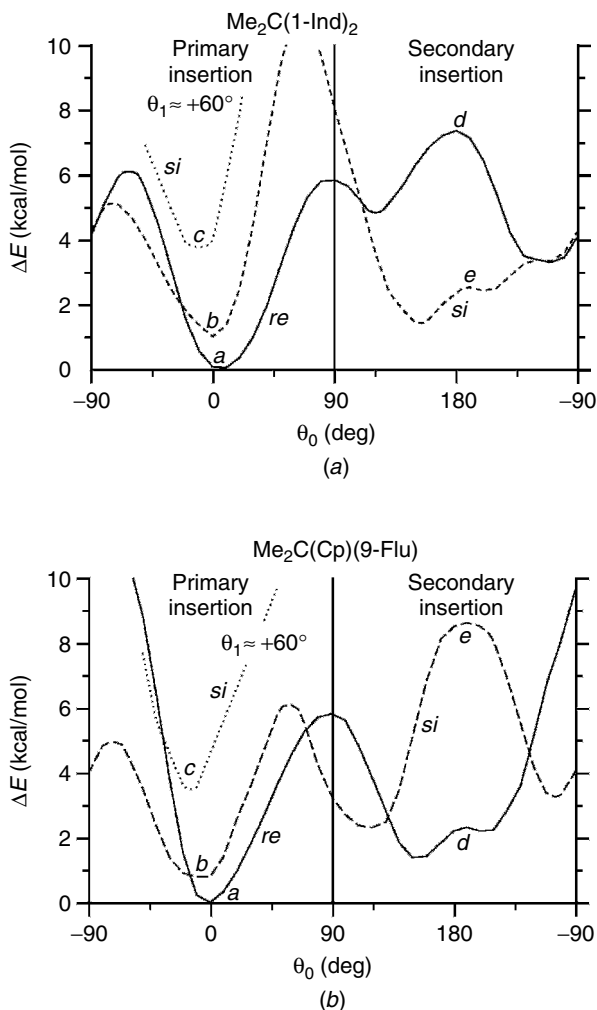


Figure 1.9 Optimized energies plotted as function of θ_0 for model complexes comprising (a) (*R,R*)-coordinated isopropyl-bis(1-indenyl) ligand and (b) isopropyl(cyclopentadienyl-9-fluorenyl) ligand for *R* chirality at metal atom. Full and dashed lines refer to *re*- and *si*-coordinated propene, respectively. Dotted lines are parts of optimized energy curves obtained by requiring, for *si*-coordinated monomer, that methyl group of propene and second carbon atom (and its substituents) of growing chain are on opposite sides with respect to plane defined by Zr-C bonds (i.e., requiring $\theta_1 \approx +60^\circ$ rather than $\theta_1 \approx -60^\circ$). Minimum-energy preinsertion intermediates for primary insertion ($\theta_0 \approx 0^\circ$), labeled *a* in parts (a) and (b), are sketched in Figures 1.4 and 1.6a, respectively. Minimum-energy preinsertion intermediates for secondary insertion ($\theta_0 \approx 180^\circ$), labeled *e* and *d* in parts (a) and (b), are sketched in Figures 1.10a,b, respectively.

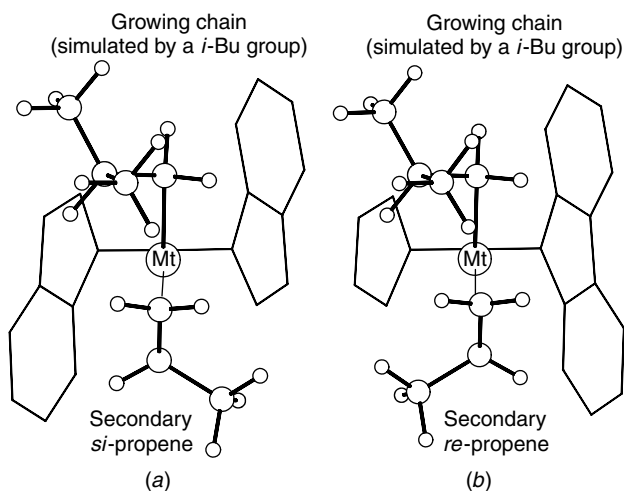


Figure 1.10 Preinsertion intermediates for secondary propene insertion into primary polypropylene chain for (a) isospecific model complex based on (*R,R*)-coordinated isopropyl-bis(1-indenyl) ligand and (b) syndiospecific model complex based on isopropyl(cyclopentadienyl-9-fluorenyl) ligand for *R* chirality at metal atom. Stereoselectivity of isospecific model site is in favor of opposite monomer prochiral faces for primary and secondary insertions (cf. Figures 1.4 and 1.10a). Stereoselectivity of syndiospecific model site is in favor of same monomer prochiral face for primary and secondary insertions (cf. Figures 1.6a and 1.10b).

In summary, there is substantial stereoselectivity of this isospecific C_2 symmetric catalytic model for the lower energy (and experimentally observed) primary monomer insertion, and the stereoselectivity would also be higher for the higher energy (minor but experimentally detected) secondary monomer insertion. It is worth noting that the *stereoselectivity of the isospecific model site is in favor of opposite monomer prochiral faces for primary and secondary insertions.*^{37d}

This result is in perfect agreement with the observed microstructure of polypropylene chains obtained by isospecific catalytic systems, including the aforementioned as well as analogous bridged π -ligands.^{76,77} It is also worth noting that the nonbonded interactions generating stereoselectivity are those between the methyl substituent of the coordinated propene and the chiral oriented growing chain in the case of primary insertion and between the propene methyl group and one of the six-membered rings of the π -ligand in the case of secondary insertion.^{37d}

For the case of catalytic model sites based on metallocenes **23**, a detailed molecular mechanics analysis has also been conducted for the case of primary or secondary propene insertions on secondary polypropylene chains

(for which the last propene insertion has been secondary).^{37d} According to this analysis, the stereoselectivities observed after an occasional secondary monomer insertion are easily accounted for in the framework of the mechanism of the *chiral orientation of the growing chain*. In fact, substituting the usual primary growing chain with a secondary growing chain reduces the bulkiness of the substituents of the second carbon atom of the chain (which is secondary carbon for the secondary chain but is the tertiary carbon for the primary chain). Correspondingly, the energy differences between conformations with positive and negative values of θ_1 (which determines the stereoselectivity in the framework of our model; see before) are reduced, leading to a less pronounced stereoselectivity.^{37d} These results are able to rationalize the probability distributions of stereochemical configurations of regioirregular units in isotactic polymer samples prepared in the presence of corresponding catalytic systems.^{76,77}

Syndiospecific catalytic systems based on metallocenes are highly regioirregular. As a consequence, their stereoselectivity in possible regioirregular insertions has been experimentally investigated for propene copolymers only.^{78,79} However, an analysis of the stereoselectivity of possible secondary propene insertions on syndiospecific catalytic models based on C_s -symmetric metallocenes is reported here, also due to its relevance to the rationalization of the dependence of regiospecificity on the type of stereospecificity (see Section 3.1.4.1).⁸⁰

As an example, Figure 1.9*b* plots as a function of θ_0 the optimized energies for the model complex **30**, that is, a π -ligand with C_s symmetry, for the polymerization step involving an *R* chirality at the metal atom. The energy minima labeled *a*, *b*, and *c* of Figure 1.9*b*, corresponding to $\theta_0 \approx 0^\circ$, are coincident with those labeled with the same letters in the energy plot of Figure 1.7*b*. The absolute minimum energy (labeled *a*) corresponds to the preinsertion intermediate for propene primary insertion with *re* enantioface which is sketched in Figure 1.6*a*.

As for situations possibly suitable for secondary propene insertion ($\theta_0 \approx 180^\circ$), the optimized energy for the *re* monomer coordination (*d* in Figure 1.9*b*) is higher by nearly 2 kcal/mol with respect to the absolute minimum. The corresponding model sketched in Figure 1.10*b* is considered suitable for *re* monomer secondary insertion. Much higher is the energy corresponding to $\theta_0 = 180^\circ$ for the *si* monomer coordination (*e* in Figure 1.9*b*) due to repulsive interactions of the methyl group of propene with a six-membered ring of the fluorenyl ligand.

In summary, there is a substantial stereoselectivity of this syndiospecific C_s -symmetric catalytic model for the lower energy (and experimentally observed) primary monomer insertion as well as for the higher energy (experimentally undetected) secondary monomer insertion. It is worth noting that the

stereoselectivity of the syndiospecific model site is in favor of the same monomer prochiral face for primary and secondary insertions (contrary to the isospecific model sites).⁸⁰

The preferred primary and secondary insertions of opposite monomer prochiral faces into isospecific C_2 -symmetric catalysts, and of a same prochiral face into syndiospecific C_s -symmetric catalysts, have been confirmed by recent characterization studies on propene–ethene–styrene terpolymers.⁷⁹

3.1.4 Implications of Relative Stereoselectivities for Primary and Secondary Insertions

3.1.4.1 Dependence of Regiospecificity on Metallocene Symmetry. The regiospecificity of metallocene-based catalytic systems is generally very high. In fact, in most polypropylene samples obtained by these catalytic systems, regioirregularities cannot be detected by standard NMR characterization methods. In particular, highly regioregular polymer samples are obtained by catalytic systems based on titanocenes as well as by syndiospecific or aspecific catalytic systems based on zirconocenes and hafnocenes.^{8,44,80,81} On the contrary, isotactic polypropylene samples from catalytic systems based on zirconocenes and hafnocenes contain isolated secondary (2,1 insertions, usually 0–2%) propene units and isolated 3,1 propene units (arising from the unimolecular isomerization of 2,1 units, 0–5%) in the isotactic sequences of primary propene insertions.^{76–77,82–88} Regioirregularities have been observed not only for isospecific catalytic systems based on C_2 -symmetric π -ligands but also for isospecific catalytic systems based on C_1 -symmetric π -ligands, like **35** of Table 1.1.⁸⁹

The regioirregularities can also be reduced for isospecific catalysts based on *ansa*-zirconocenes and hafnocenes when at each cyclopentadienyl ligand, in addition to a substituents in the 4 (β) positions (which is determining for the stereoselectivity), the C_2 -symmetric ligand contains an alkyl group in the 2 (α) position.^{56,57,90} Moreover, the regioirregularities are substantially absent for catalytic systems based on C_2 -symmetric ligands with a *t*-butyl substituted in the 3 (β') position.⁹¹ On the other hand, the regioirregularities are increased for isospecific catalysts based on *ansa*-zirconocenes when the indenyl ligands are substituted in both positions 4 and 7.⁹² This effect is particularly strong (leading to amounts of regioirregularities larger than 20%) for the case of the catalytic system based on $C_2H_4(4,7-Me_2-H_2Ind)_2ZrCl_2$.^{88,93}

Molecular mechanics calculations similar to those described in the previous sections allow us to evaluate energy differences between catalytic models (preinsertion intermediates and transition states) suitable for primary and secondary insertions. This energy difference, in the framework of the assumed mechanism, can give a rough estimate of the nonbonded energy contribution

to the regiospecificity of the insertion reaction. Although the main contribution to the energy differences determining the regiospecificity could be electronic in most cases, analysis of the nonbonded energy contribution has allowed us to rationalize the dependence of regiospecificity not only on the nature and position of alkyl substituents⁹⁰ of the π -ligands but also on the type of stereospecificity.⁸⁰ In the present review we will confine our attention only to the latter aspect.

As previously recalled, while the syndiospecific and aspecific zirconocene-based catalytic systems are highly regiospecific, isospecific systems produce substantial amounts of regioirregular monomeric units, independently of the nature of the π -ligands and of the bridge between them (unless suitable substitutions of the ligands are involved). This dependence of the degree of regiospecificity on the symmetry rather than on the nature of the π -ligand is, of course, not easy to rationalize by invoking differences in the electronic contributions to the regiospecificity.

On the other hand, the molecular mechanics analysis of the previous section indicates that the nonbonded energy contribution to the differences between the minimum-energy secondary and primary preinsertion intermediates for zirconocene-based catalytic models is poorly dependent on the symmetry of the π -ligands and hence on their stereospecificity (in Figure 1.9a, $E_d - E_a \approx 2$ kcal/mol; in Figure 1.9b, $E_e - E_a \approx 2$ kcal/mol). A similar energy difference has also been calculated for the analogous C_{2v} -symmetric model for aspecific propene polymerization (based on two bridged cyclopentadienyl ligands).⁸⁰

However, for the enantioselective (syndiospecific and isospecific) model complexes, this energy difference between secondary and primary preinsertion intermediates for a given chirality of coordination of the monomer largely changes with the symmetry of the π -ligands. In particular, for isospecific (C_2 -symmetric as well as C_1 -symmetric) and for the syndiospecific (C_s -symmetric) model complexes, the nonbonded energy contribution to the regiospecificity is particularly large for the enantioface which is right (with reference to Figure 1.9a, $E_d - E_a \approx 8$ kcal/mol) and wrong (with reference to Figure 1.9b, $E_e - E_b \approx 8$ kcal/mol) for primary insertion, respectively.

Schematic plots of the internal energy versus the reaction coordinate for both primary and secondary insertions and for generic aspecific, syndiospecific, and isospecific model complexes are sketched in Figures 1.11a, b, and c, respectively. The minima at the centers and at the ends of the energy curves correspond to alkene-free intermediates, including a growing chain with n and $n + 1$ monomeric units, respectively. Movements from the central minima toward the left and the right correspond to possible reaction pathways leading to primary and secondary insertions, respectively. For the enantioselective complexes the reaction pathways for monomer enantiofaces being

right and wrong for primary insertion are different and are indicated by full and dashed lines, respectively. The two energy barriers encountered for each pathway correspond to the coordination and insertion steps.

The energy minima between the energy barriers for the monomer coordination and insertion correspond to alkene-bound intermediates of the kind simulated by our molecular mechanics calculations (Figures 1.7 and 1.9). The possible dissociation of the monomer coordinated with the wrong enantioface can lead back to the alkene-free intermediate or, directly, to the alkene-bound intermediate with the right enantioface (through some isomerization mechanism, for which the monomer does not leave the coordination sphere of the metal).

The preinsertion intermediates of our molecular mechanics analysis (when different from the coordination intermediates) would correspond to situations closer to the transition state for the insertion reactions. For an easier comparison, the labels (*a–e*) used for coordination and preinsertion intermediates in Figures 1.7*a* and *b* are also reported close to the schematic energy plots of Figures 1.11*a* and *b*, respectively.

For the sake of simplicity, the minimum-energy pathways (which according to our calculations on coordination and preinsertion intermediates are expected to be similar) are assumed identical, independent of the symmetry (stereospecificity) of the catalyst. However, the plots for the syndiospecific (Figure 1.11*b*) and isospecific (Figure 1.11*c*) models are different since, as previously discussed, the stereoselectivities for the primary and secondary insertions are in favor of the same or opposite monomer enantiofaces, respectively.

In this framework, the lower regioselectivity of the isospecific catalytic systems can be rationalized by assuming that the activation energy for the rotation of the coordinated monomer around θ_0 between the orientations suitable for the primary and secondary insertions (schematically shown by dotted lines in Figure 1.11) is in general lower than (or comparable to) the activation energy for the secondary insertion.⁸⁰

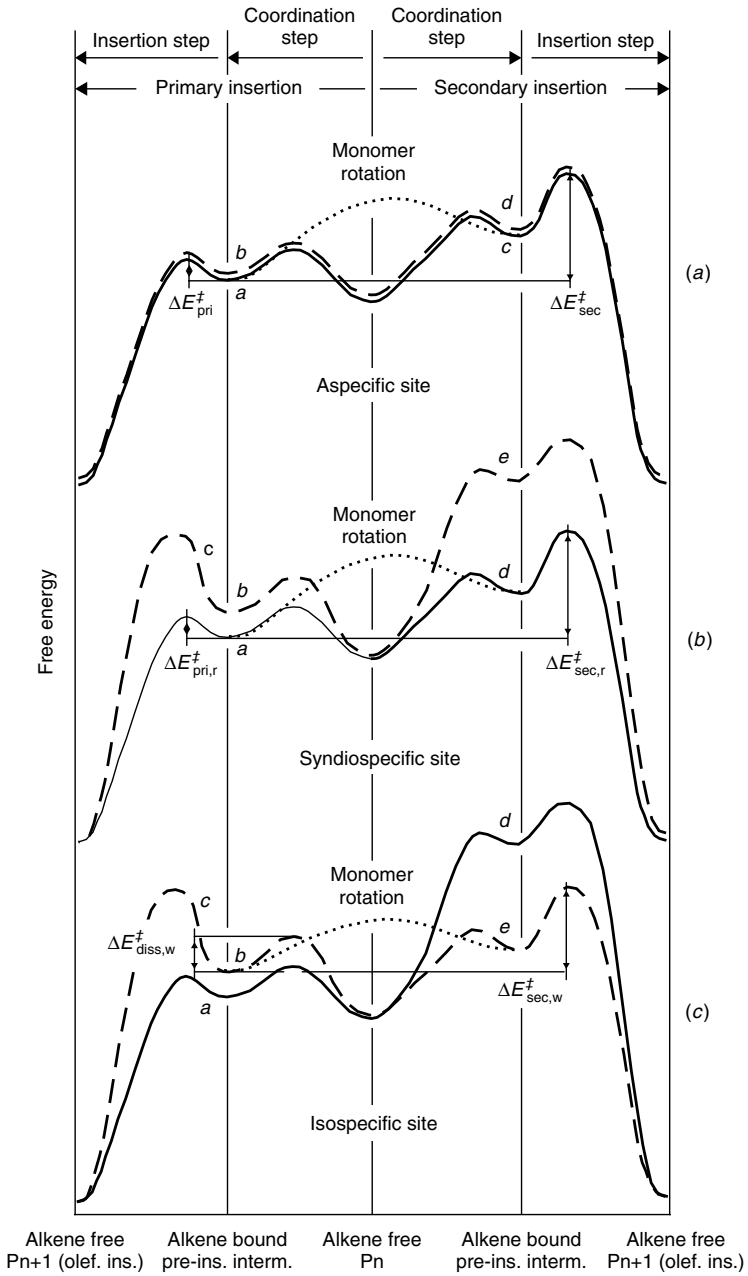
For syndiospecific model complexes, since their stereoselectivity is in favor of the same monomer enantioface for both primary and secondary insertions, when the coordination of the monomer with the wrong enantioface for the primary insertion occurs (situation *b* in Figures 1.9*b* and 1.11*b*), the most probable event is the dissociation of the coordinated monomer. It is also possible, with low probability, the primary insertion of the wrong enantioface, which introduces a stereoirregularity in the polymer chain. Secondary insertions with the wrong enantioface are expected to be essentially absent (see the high energy of situation *e* in Figures 1.9*b* and 1.11*b*). In the assumption of a low-energy barrier for the monomer rotation around θ_0 , the regioselectivity would be simply determined by the difference between the activation energies for the secondary and primary insertions of the more suitable enantioface ($\Delta E_{\text{sec,r}}^{\#} - \Delta E_{\text{pri,r}}^{\#}$) (and independent of the energy barrier for the monomer

coordination). Moreover, the regiospecificity is expected to be high and similar to that of the corresponding aspecific catalytic complex.⁸⁰

For isospecific model complexes, since their stereoselectivity is in favor of opposite monomer enantiofaces for primary and secondary insertions, when the coordination of the monomer with the enantioface unsuitable for primary insertion occurs (situation *b* or *e* in Figures 1.9*a* and 1.11*c*), besides the dissociation of the coordinated monomer and a low-probability primary insertion (generating the stereoirregularities), a low-probability secondary insertion (generating the regioirregularities) would also be possible. This is due to the fact that the barrier for the dissociation of the coordinated monomer is expected to be not negligible with respect to the activation energy for the secondary insertion. Hence, for these isospecific model complexes, the amount of regioirregularities in the polymer chains would not be determined (as for the cases of aspecific and syndiospecific model complexes) by the differences between the activation energies for the secondary and primary insertions but would be related to the difference between the activation energies for the dissociation of the monomer (coordinated with the wrong enantioface) and the activation energy for its secondary insertion ($\Delta E_{\text{sec,w}}^{\#} - \Delta E_{\text{diss,w}}^{\#}$).

3.1.4.2 Dependence on Metallocene Symmetry of *E-Z* Selectivity for 2-Butene Copolymerizations. We have seen in the Section 3.1.3 that opposite enantiofaces are favored for primary and secondary propene insertion on C_2 -symmetric metallocenes, whereas the same enantioface is favored for primary and secondary insertion on C_s -symmetric metallocenes. In this framework, if the same steric interactions which rule the enantioselectivity of primary and secondary propene insertions hold for 2-butene, the insertion of

Figure 1.11 Schematic plots of internal energy versus reaction coordinate for both primary and secondary insertions for (a) generic aspecific, (b) syndiospecific, and (c) isospecific model complexes. Minima at centers and at ends of energy curves correspond to alkene-free catalytic intermediates including growing chain with n and $n + 1$ monomeric units, respectively. Movements from central minima toward left and right correspond to possible reaction pathways leading to primary and secondary insertions, respectively. For enantioselective complexes (b,c), reaction pathways for monomer enantiofaces being right and wrong for primary insertion are different and are indicated by full and dashed lines, respectively. Two energy barriers encountered for each pathway correspond to coordination and insertion steps. Energy minima between energy barriers for monomer coordination and insertion correspond to alkene-bound catalytic intermediates of the kind simulated by our molecular mechanics calculations (e.g., Figures 1.7 and 1.9). In particular, labels *a–e* close to curves of parts (b) and (c) correspond to coordination and preinsertion intermediates of Figures 1.9*b* and 1.9*a*, respectively. Dotted lines indicate rotation of coordinated monomer around θ_0 whose activation energy is assumed to be lower than (or comparable to) activation energy for secondary insertion. Activation energies, which in this framework are relevant to regiospecificity, are also indicated.



(*Z*)-butene should be favored with C_2 -symmetric metallocenes, whereas insertion of (*E*)-butene should be favored with C_s -symmetric metallocenes.

To investigate this idea, which would confirm and summarize a large class of widely accepted mechanisms, the insertion reactions of (*Z*)- and (*E*)-butene with catalytic systems based on the C_2 -symmetric $\text{Me}_2\text{Si}(\text{1-Ind})_2$ ligand and on the C_s -symmetric $\text{Me}_2\text{Si}(\text{Cp})(\text{9-Flu})$ ligand have been recently studied. A double approach based on combined quantum mechanics/molecular mechanics (QM/MM) techniques and on selected ethene/2-butene copolymerization runs has recently been utilized.⁹⁴

The QM/MM transition states for (*Z*)- and (*E*)-butene insertion into the Zr–C(*n*-propyl) bond of the C_2 -symmetric metallocene **5** are reported in Figures 1.12*a* and *b*, respectively. According to the mechanism of the chiral orientation of the growing chain,^{15,37} the *n*-propyl group used to simulate a polyethylenic growing chain assumes a conformation which minimizes repulsive interactions with the C_2 -symmetric ligand, and the head methyl group (see also Scheme 1.4) is put on the opposite side relative to the growing chain to minimize steric interactions with the growing chain. This orientation of the head methyl group implies that the (*Z*)-butene tail methyl group (see Scheme 1.4) is located far from the indenyl ligand, whereas the (*E*)-butene tail methyl group feels severe steric repulsion with an indenyl ligand. As a consequence, (*Z*)-butene insertion is favored relative to (*E*)-butene insertion.

The QM/MM transition states for (*Z*)- and (*E*)-butene insertion into the Zr–C bond of the C_s -symmetric metallocene **30** are reported in Figures 1.12*c* and *d*, respectively. Also in this case, the *n*-propyl group assumes a conformation to minimize repulsive interactions with the π -ligand, and the head methyl group is put on the opposite side relative to the growing chain. Now, the (*Z*)-butene tail methyl group feels severe steric repulsion with the fluorenyl ligand, whereas the (*E*)-butene tail methyl group is located in an uncrowded region. As a consequence, (*E*)-butene insertion is favored relative to (*Z*)-butene insertion.

According to the reported calculations, (*Z*)-butene insertion on the C_2 -symmetric metallocene is favored relative to insertion of (*E*)-butene by 1.6 kcal/mol, while (*E*)-butene insertion on the C_s -symmetric metallocene is favored relative to insertion of (*Z*)-butene by 1.8 kcal/mol. Finally, it is worth noting that (*Z*)-butene coordination would be preferred for both C_2 - and C_s -symmetric metallocenes.⁹⁴

In agreement with the theoretical analysis, C_2 - and C_s -symmetric metallocenes scarcely insert (*E*)- and (*Z*)-butene, respectively, whereas C_2 - and C_s -symmetric metallocenes insert relevant fractions of (*Z*)- and (*E*)-butene, respectively. Moreover, in agreement with QM/MM analysis, when copolymerization experiments are run with a 40% (*Z*)-2-butene–60% (*E*)-2-butene mixture, the presence of the better coordinating (*Z*)-butene inhibits the reaction

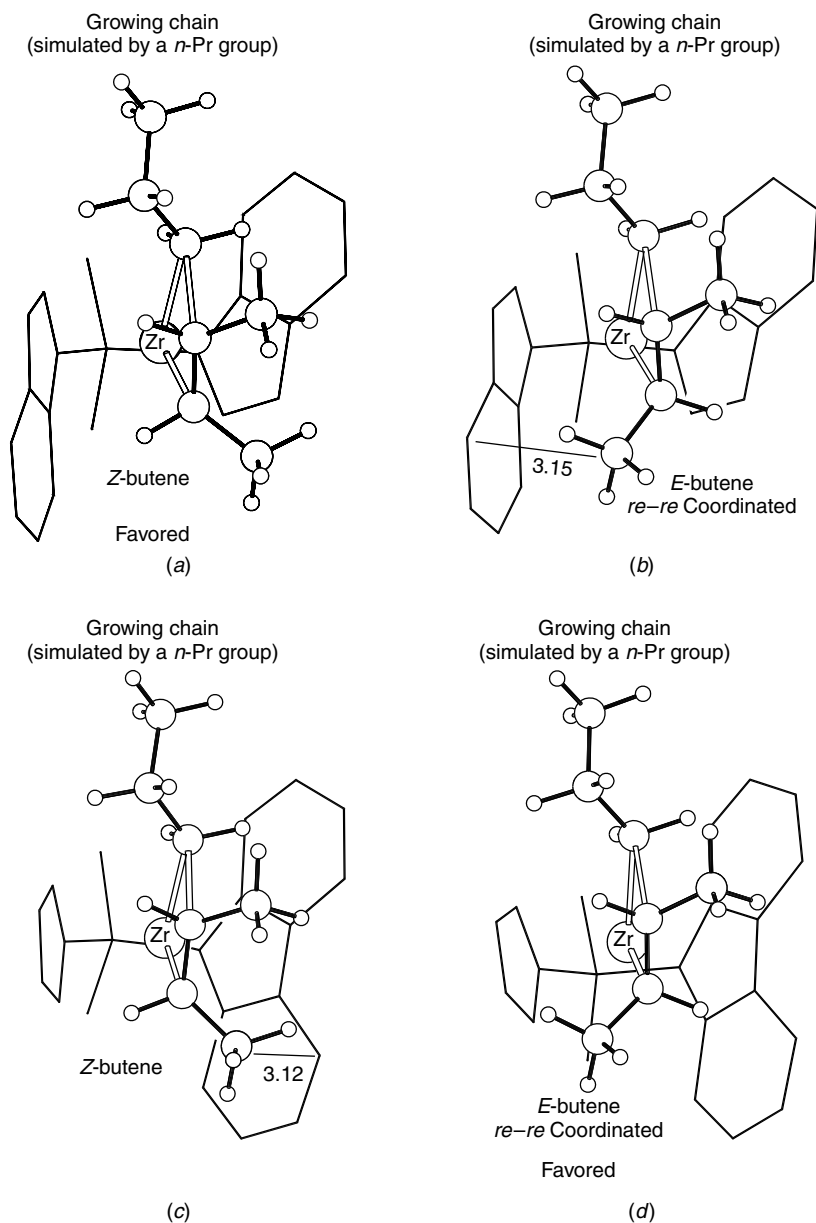
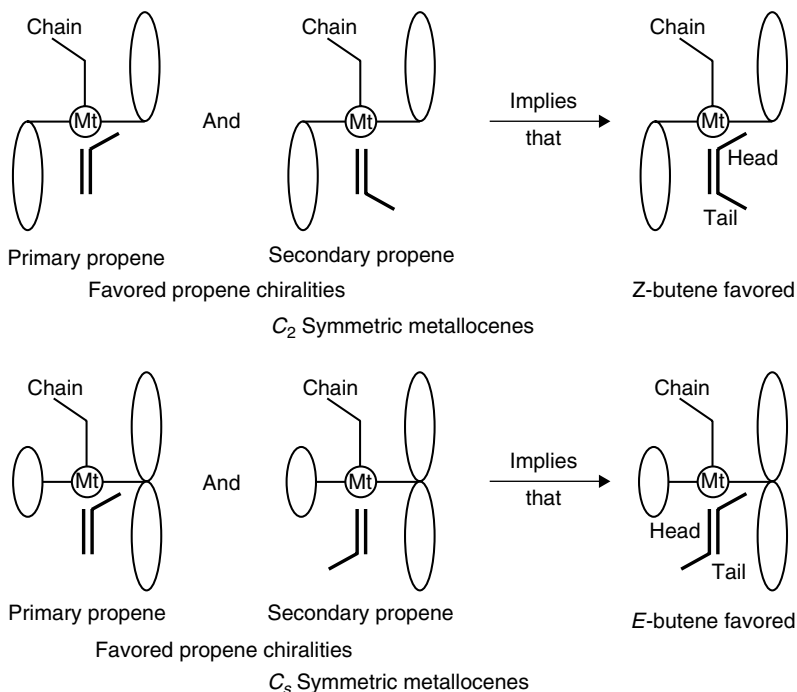


Figure 1.12 QM/MM transition states for insertion into polyethylene chain of (*Z*) and (*E*) isomers of 2-butene for (a,b) C_2 - and (c,d) C_s -symmetric metallocenes. Molecular modeling studies have predicted preference of C_2 - and C_s -symmetric metallocenes for (*Z*) and (*E*) isomers of 2-butene, respectively.



Scheme 1.4 Schematic presentation of the favored propene chiralities of coordination, which are suitable for primary and secondary insertions for C_2 and C_s symmetric metallocenes. The models sketched on the right show that *Z* and *E* butene coordinations are expected to be favored for C_2 and C_s symmetric metallocenes, respectively.

of (*E*)-butene with the C_s -symmetric metallocene, while the presence of the poorer coordinating (*E*)-butene is only able to reduce the amount of (*Z*)-butene insertions with the C_2 -symmetric metallocene.⁹⁴

In summary, the prediction that (*E*)-(Z) selectivity in the ethene/internal olefins copolymerization with group 4 metallocenes can be achieved by using ligands of suitable symmetry has been proved. In particular, it has been shown that C_2 - and C_s -symmetric metallocenes are able to copolymerize ethene with (*Z*)- and (*E*)-butene, respectively.

3.2 Heterogeneous Polymerization Catalysts

The world market for polypropylene is currently over 30×10^6 tons, and more than 80% of the global polymer is obtained with heterogeneous Ziegler–Natta catalysts. Over the years, these catalysts have evolved from simple $TiCl_3$ crystals into the current systems based on $MgCl_2$ as a support for $TiCl_4$.

3.2.1 Traditional Catalytic Systems Based on TiCl_3

On the basis of the microstructure of the prevailing isotactic polymer chains, it is well established that the steric control of the heterogeneous Ziegler–Natta catalysts is due to the chirality of the catalytic site and not to the configuration of the last inserted monomer unit.^{28,29,95}

Natta first hypothesized that the steric control is due to the structure of catalytic sites on the border of crystal layers of TiCl_3 .⁹⁶ This idea was thoroughly developed by Arlman and Cossee.¹³ The structure of violet titanium trichlorides as well as that of other transition metal trichlorides effective as components of Ziegler–Natta catalysts (e.g., VCl_3 , CrCl_3) is built up of layers of the kind shown in Figure 1.5 piled one on top of the other according to a close packing of the chlorine atoms. The various known crystalline modifications^{97,98} correspond to different ways in which the piling may be obtained. Within each layer, the metal atoms occupy in an ordered arrangement two-thirds of the octahedral positions. As a result, neighboring metal atoms (bridged by two Cl atoms) have opposite chirality¹⁴ which may be designated with the symbols Λ and Δ .¹⁵

On the basis of crystallochemistry consideration and taking into account electron microscopy observations of the surface of crystals upon which some polymer was formed,⁹⁹ Arlman and Cossee¹³ concluded that the active sites are located on crystal surfaces different from the basal (001) ones. In particular, these authors considered in detail active sites located on crystal surfaces parallel in the direction **a** – **b** of the unit cell defined as in Ref. 98. Figure 1.13 illustrates that, if we cut a TiCl_3 layer parallel to the direction defined above, which corresponds to the line connecting two bridged Ti atoms, electroneutrality conditions impose that each Ti atom at the surface of the cut be bonded

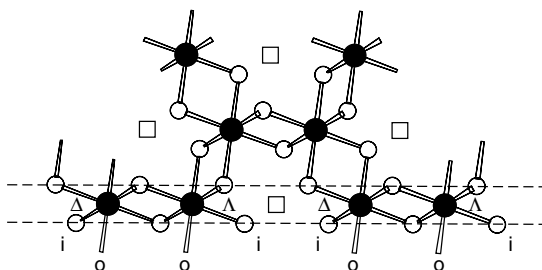


Figure 1.13 Schematic drawing of possible lateral cut of TiCl_3 structural layer. Chirality of Ti atoms on termination of layer is indicated. Electroneutrality conditions impose that metal atoms on this lateral cut are bonded to four Cl atoms bridge bonded to further metal atoms and one Cl atom not bridge bonded and that coordination position is left free. Two nonequivalent coordination positions, which will become available to monomer and growing polymer chain, inward and outward, are indicated by i and o, respectively (see text).

to five Cl atoms only. Four of these are bridged to further metal atoms and are then more strongly bonded. The fifth Cl atom, nonbridged, may be replaced by an alkyl group. The octahedral position which is still left free may π coordinate an alkene. For these sites, the two positions accessible to the growing chain and to the monomer are nonequivalent. As shown in Figure 1.13, one (indicated as inward) is further in than the other (indicated as outward) with respect to the lateral cut.

Active sites located on crystal surfaces different from the basal (001) ones were also proposed by Allegra¹⁴ for which the Ti atom at the surface of the cut would be bonded to four Cl atoms only (bridged to further metal atoms) (Figure 1.14). In this case both octahedral sites of coordination for the monomer and growing chain (indicated by arrows in Figure 1.14) are equivalent because the surface atoms with relevant nonbonded interactions at the catalytic site are locally related by a twofold axis (dashed line in Figure 1.14). It is worth noting that this model site presents a local C_2 symmetry as the isospecific metallocenes of the previous section.

Corradini et al. examined in some detail by molecular mechanics¹⁵ and density functional studies¹⁰⁰ the polymerization mechanism proposed by Cossee and the catalytic sites on $TiCl_3$ surfaces, including those proposed by Arlman and Cossee¹³ and by Allegra.¹⁴ According to the calculations, for all these octahedral active sites a similar general mechanism of stereoselectivity occurs which is very similar to the one established several years later for stereospecific metallocenes (see previous section). The chirality of the site would determine a chiral orientation of the first C–C bond of the chain (for a Λ site,

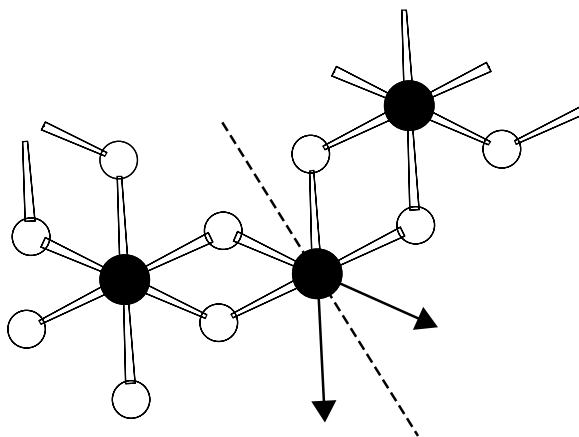


Figure 1.14 Different lateral cut of $TiCl_3$ structural layer as proposed by Allegra.¹⁴ Two coordination positions available for polymerization reaction (indicated by arrows) are equivalent. In fact, they are locally related by a twofold axis (dashed line).

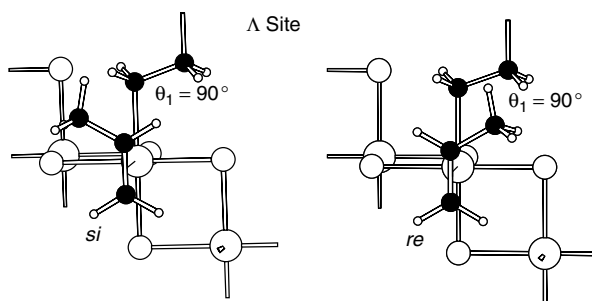


Figure 1.15 Perspective drawing of two possible chiral coordinations of propene (*si* and *re*), suitable for primary insertion, on a Δ site of the kind of Figure 1.14. In both cases conformation $\theta_1 \approx +90^\circ$ of growing chain corresponds to energy minimum; however, lower energy corresponds to model A presenting methyl group of propene and second carbon atom of growing chain on opposite sides with respect to plane defined by Ti-C bonds.

values for θ_1 near $+90^\circ$ would be allowed while values near -90° would be forbidden) (Figure 1.15). This orientation was identified as an essential factor in determining the isospecificity. Indeed, as shown in Figure 1.15, the alkyl group of the 1-alkene and the second carbon atom of the growing chain for the *si* monomer coordination are on opposite sides with respect to the plane defined by the Ti-C bonds, while for the *re* coordination they are on the same side. This would determine a lower activation energy and henceforth favor the insertion of the *si*- with respect to the *re*-coordinated alkene on a Δ site. The opposite, of course, holds for a Δ site.

The analysis by ^{13}C NMR techniques of the chain-end groups resulting from the initiation steps on ^{13}C -enriched Ti-alkyl bonds performed some years later⁴¹ and already described in Section 3.1.1 pointed out that the chiral site is able to discriminate between *si* and *re* insertions of the monomer only when alkyl groups with at least two C atoms are initially bound to the Ti atom, thus confirming the essential role of the chain in conferring the isospecific behavior. Indeed, specific calculations relative to the steric control in the first steps of propene polymerization¹⁰¹ showed that for these octahedral model sites the insertion of the first monomer unit is nonstereospecific into an initial Ti-Me bond, partially stereospecific into an initial Ti-Et bond, and totally stereospecific into an initial Ti- t Bu bond, in agreement with experiments.

Alternative octahedral sites on the basal or lateral surface of violet TiCl_3 crystals, presenting two vacancies accessible to the incoming monomer, were also proposed.¹⁰² The main reason for these suggestions was, in the proponents' opinion, that in the Cossee model access of the monomer to the only vacancy at the metal atom would be largely hindered by the growing chain. These model sites, besides the unlikelihood of two chlorine ligands being removed from the same metal atom, require the helicity of the chain as an

element of chirality in order to account for the stereospecificity, which is definitely in contrast with many experimental observations. Moreover, at least for single-vacancy sites in relief with respect to lateral surfaces, calculations in the presence of a long polypropylene chain¹⁰³ showed that, although able to discriminate between the two faces of the prochiral alkene, this does not severely hinder access of the monomer to the vacancy, thus overcoming the previously discussed criticism to the single-vacancy sites.

The chiral sites which are able to rationalize the isospecific polymerization of 1-alkenes are also able, in the framework of the mechanism of the chiral orientation of the growing polymer chain, to account for the stereoselective behavior observed for chiral alkenes in the presence of isospecific heterogeneous catalysts.¹⁰⁴ In particular, the model proved able to explain the experimental results relative to the first insertion of a chiral alkene into an initial Ti–methyl bond,¹⁰⁵ that is, the absence of discrimination between *si* and *re* monomer enantiofaces and the presence of diastereoselectivity [preference for *S*(*R*) enantiomer upon *si* (*re*) insertion]. Upon *si* (*re*) coordination of the two enantiomers of 3-methyl-1-pentene to the octahedral model site, it was calculated that low-energy minima only occur when the conformation relative to the single C–C bond adjacent to the double bond, referred to the hydrogen atom bonded to the tertiary carbon atom, is nearly anticlinal minus, A^- (anticlinal plus, A^+). Thus one can postulate the reactivity only of the A^- conformations upon *si* coordination and of the A^+ conformations upon *re* coordination (Figure 1.16). In other words, upon *si* coordination, only the synperiplanar methyl conformation would be accessible to the *S* enantiomer and only the (less populated) synperiplanar ethyl conformation to the *R* enantiomer; this would favor the *si* attack of the *S* enantiomer with respect to the same attack of the *R* enantiomer, independent of the chirality of the catalytic site. This result is in agreement with a previous hypothesis of Zambelli and co-workers based only on the experimental reactivity ratios of the different faces of C-3-branched 1-alkenes.¹⁰⁵

3.2.2 Catalytic Systems Supported on $MgCl_2$

Different routes have been developed for the preparation of the supported catalysts. The mechanical route is based on comilling $MgCl_2$, $TiCl_4$, and a Lewis base (the so-called internal donor) for several hours. Alternatively, chemical routes can be used both to generate active $MgCl_2$ and to incorporate the Ti compound and the Lewis base. Usually, a $MgCl_2$ precursor is treated with the Lewis base and excess $TiCl_4$ above 80°C. Among internal donors, aromatic esters (ethyl benzoate in particular), alkoxysilanes, and diethers have been shown to be particularly suitable. Finally, the catalyst is activated by addition of alkylating reducing species— $Al(C_2H_5)_3$ being most used—possibly mixed

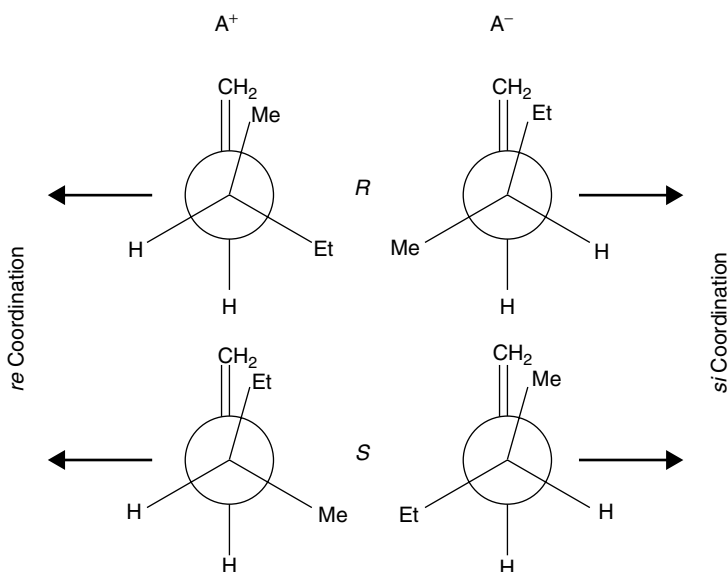


Figure 1.16 Newman projections of energy minimum conformations for (*R*)-3-methyl-1-pentene and (*S*)-3-methyl-1-pentene upon coordination on a site of the kind of Figure 1.14 or 1.15. Energy minimum conformations for *si* coordination are shown on right while those for *re* coordination are on left.

with a second electron donor (the so-called external donor). The resulting active system is of extreme chemical complexity, and the intimate nature of the active sites is still a matter of debate.

The characterization of heterogeneous Ziegler–Natta catalysts has been attempted by means of several experimental approaches,^{106–120} but definitive answers have not been achieved yet. As for the support structure, the primary particles of activated MgCl_2 are composed of a few irregularly stacked Cl–Mg–Cl sandwiches of the kind shown in Figure 1.17. Observations of MgCl_2 microcrystals by optical microscopy¹⁰⁶ and transmission electron microscopy¹¹² confirmed the proposed^{15c} copresence of (100) and (110) lateral cuts. For electroneutrality reasons, these two lateral cuts contain coordinatively unsaturated Mg^{2+} ions with coordination numbers 4 and 5 on the (110) and (100) cuts, respectively, as shown in Figure 1.17.

Magnesium chloride has a crystal structure very similar to violet titanium trichloride. This dictates the possibility of an epitaxial coordination of TiCl_4 units (or TiCl_3 units, after reduction) on the lateral coordinatively unsaturated faces of MgCl_2 crystals, giving rise to relieves crystallographically coherent with the matrix.^{15c}

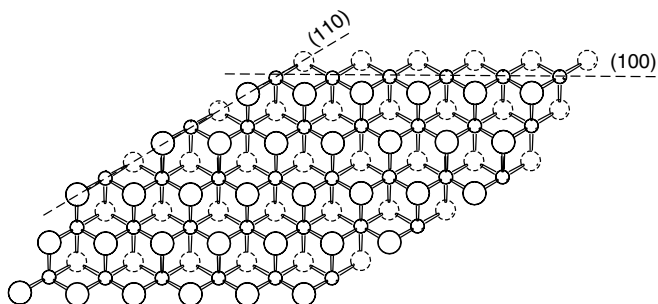


Figure 1.17 Schematic drawing of structural layers of MgCl_2 . Full-line Cl atoms represent Cl atoms above plane of Mg atoms, whereas dashed Cl atoms represent Cl atoms below plane of Mg atoms. Possible (100) and (110) lateral cuts with 5- and 4-coordinated Mg atoms are also indicated.

As for the Ti oxidation state after reduction with alkylaluminum compounds, literature reports are often contradictory, owing to the different catalysts and analytical methods used.^{108,110,113–117} The only reasonable conclusion is that under polymerization conditions a considerable reduction of Ti(IV) takes place, not only to Ti(III) but to Ti(II) as well. However, Ti(II) is usually considered not to be active for propene polymerization.¹¹⁶

Useful information on the nature of the active sites can also be obtained by ^{13}C NMR analyses of the polymers produced. These analyses indicate that some active sites can interconvert in a time shorter than the average time of chain growth^{118–120} and that at least one of the active sites has an environment of C_1 symmetry.¹¹⁹

Although the whole framework is extremely complicated, some theoretical studies have been devoted to investigations of interactions occurring between TiCl_4 and/or Lewis bases and MgCl_2 clusters.^{121–125} In particular, a systematic density functional theory investigation¹²³ of the interactions possibly occurring between TiCl_4 molecules and TiCl_3 fragments with both (100) and (110) lateral cuts of MgCl_2 clusters has pointed to the possible occurrence of various possible adsorbed Ti species. Several structures of similar energy would be consistent with a family of polymerization sites with different local symmetries (from C_1 to C_2 -like to almost C_2), steric environment, and hence different stereospecific properties (from substantially aspecific sites to isospecific ones). In fact, besides monomeric and dimeric species,^{15c} polynuclear Ti(III) species¹¹⁵ on the (100) lateral cut of MgCl_2 are possible and appear to be energetically favored, independent of the number of unpaired spins. This result could rationalize experiments indicating that most of Ti(III) is Electronic Spin Resonance (ESR) silent.

The epitactic placement of Ti_2Cl_6 and $\text{Ti}_4\text{Cl}_{12}$ units on the (100) face of MgCl_2 is, for instance, shown in Figure 1.18. It is immediately apparent that

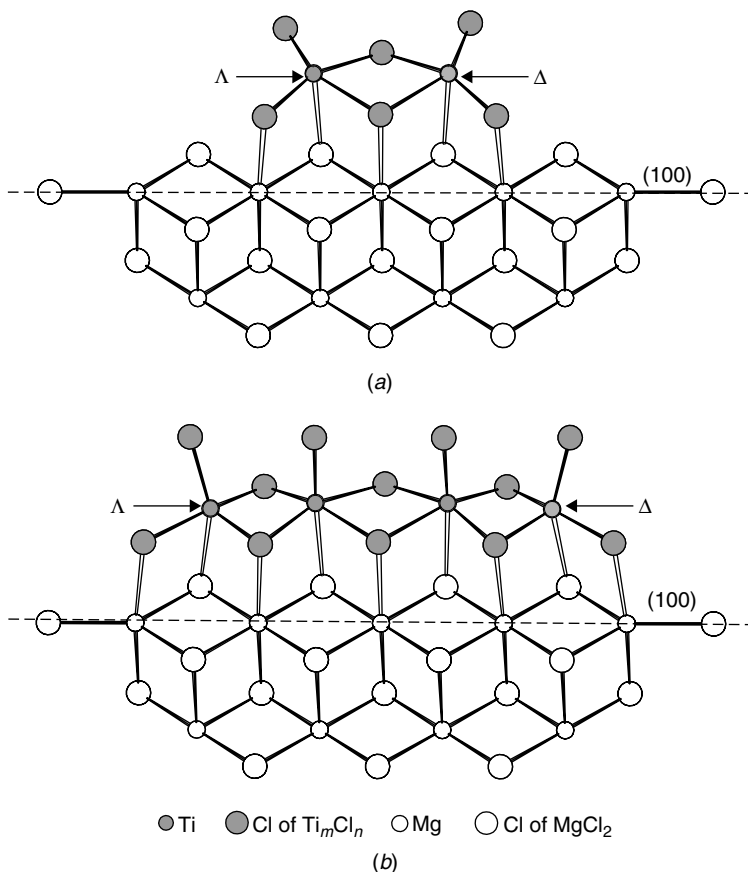


Figure 1.18 Detailed view of Ti_2Cl_6 and Ti_4Cl_{12} groups placed on (100) cut of $MgCl_2$. Chiral environments of metal atoms are explicitly labeled.

the environment of the unsaturated Ti atoms is chiral and that Ti_2Cl_6 sites on the (100) cut are very similar to the C_1 -symmetric sites proposed by Cossee,¹³ while polynuclear Ti_nCl_{3n} sites (with $n > 2$) are extremely similar to the C_2 -symmetric sites proposed by Allegra for $TiCl_3$ -based catalytic systems.¹⁴ Calculations of nonbonded interactions showed that these sites can have stereoregulating ability, the main factor determining their stereospecific behavior being again the fixed chiral orientation into which the growing polymer chain appears to be forced.^{15c}

On the (110) face there are many possibilities. In fact, although an isolated $TiCl_3$ unit adsorbed on the (110) face can be thought to produce a poorly stereoregular polymer with a prevalence of syndiotactic diads,¹⁰³ C_1 - and

C_2 -symmetric species, which can produce isotactoid and isotactic polymers, are obtainable by occupation of one and two vicinal positions.¹²³ An easy switch between these three polymerization modes has recently been proposed on the basis of a high-resolution ^{13}C NMR microstructural analysis.^{119d}

Of course, the calculated minimum-energy Ti species supported on different lateral faces of MgCl_2 layers can only represent a basis for the description of the real effective catalyst, since the relative distribution, interconversion, and stereospecificity of the various Ti species are sensitively modified by the presence of alkylaluminum compounds and, particularly, by the added Lewis bases.

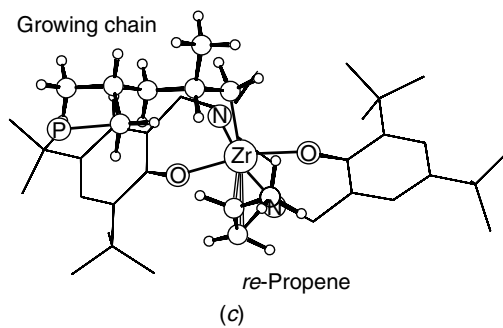
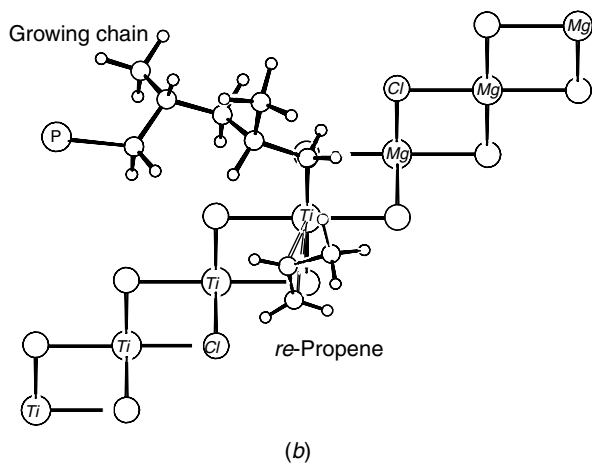
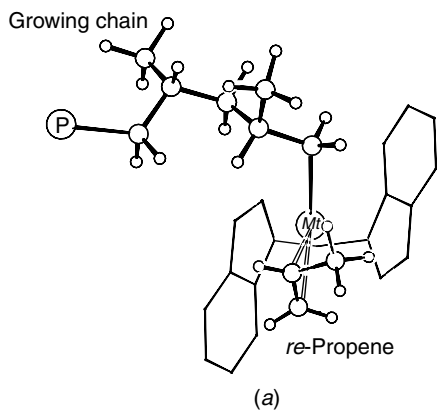
Some studies relative to the influence of Lewis bases,^{124–127} 1,3-diethers in particular,^{125–127} and the MgCl_2 support have also been recently reported. The dependence of the industrially relevant isotactic indexes on the chemical structure of the 1,3-diether donor has been rationalized in the assumption that donor coordination competes with Ti catalytic species formation and xylene-insoluble (highly isotactic) and xylene-soluble (poorly isotactic) fractions are mainly obtained by polymerization on (100) and (110) cuts, respectively.¹²⁷

3.3 Comparison Between Models for Heterogeneous and Homogeneous Stereospecific Catalysts

The models for heterogeneous and homogeneous stereospecific Ziegler–Natta polymerization of olefins, which have been described in the two previous sections, present a general pattern of similarity. In particular, for all the proposed stereospecific models the chiral orientation of the first C–C bond of the growing chain, imposed by the chirality of the site, seems to be crucial in determining the stereoselectivity. This mechanism of stereoselectivity agrees well with a large number of experimental facts, some of which result from experiments designed to test its validity.

As an example, C_2 -symmetric isospecific models for homogeneous catalytic systems based on the (*R,R*)-coordinated isopropyl-bis(1-indenyl) ligand and for heterogeneous catalytic systems based on TiCl_4 supported on MgCl_2 are compared in Figure 1.19. These models correspond to minimum-energy preinsertion intermediates calculated to be suitable for primary propene insertion

Figure 1.19 Minimum-energy preinsertion intermediates suitable for primary propene insertion for isospecific models of (a) homogeneous catalytic systems based on (*R,R*)-coordinated isopropyl-bis(1-indenyl) ligand; (b) heterogeneous catalytic systems based on TiCl_4 supported on MgCl_2 (catalytic model site is located on lateral termination of structural layer and presents Δ chirality); and (c) homogeneous catalytic systems based on dianionic tetradentate chelating ligands.¹³⁰ In all models methyl group of propene and second carbon atom (and its substituents) of growing chain are on opposite sides with respect to plane defined by Zr–C bonds (i.e., θ_1 in range $[-60^\circ, -90^\circ]$ and *re* monomer).



and clearly show a similarity in the positions and relative orientations of the growing chain and incoming monomer.

A closer similarity exists between the C_2 -symmetric octahedral isospecific model sites, which have been proposed for the heterogeneous polymerization catalysts,¹³⁻¹⁵ and some slightly distorted octahedral metal complexes, including bidentate or tetradentate ligands, which have recently been described as active in isospecific olefin polymerization in the presence of MAO.¹²⁸⁻¹³⁰ In fact, all these catalytic systems can be described in terms of racemic mixtures of active species with Λ or Δ chiralities.

For the sake of comparison, the minimum-energy preinsertion intermediate suitable for primary propene insertion, calculated for the isospecific catalytic complex based on a dianionic tetradentate chelating ligand,¹³⁰ is shown in Figure 1.19c. It is already apparent on inspection of these catalytic models (presenting a Δ chirality) that there are similar locations of chlorine atoms (Figure 1.19b) and *tert*-butyl substituents (Figure 1.19c), which are symmetry related by a C_2 axis and impose a chiral orientation of the growing chain ($\theta_1 \approx -60^\circ$ preferred to $\theta_1 \approx +60^\circ$), which in turn discriminates between the monomer enantiofaces (*re* monomer coordination and insertion are favored).

4 CHIRALITY IN CHAIN-END CONTROLLED STEREOSPECIFIC POLYMERIZATION

4.1 Olefin Polymerization

The chain-end stereocontrol for olefin polymerizations leads generally to lower stereoselectivities (differences in activation energy for insertion of the two enantiofaces generally lower than 2 kcal/mol) than the chiral site stereocontrol.^{18,131,132} For this reason, the corresponding catalytic systems have not reached industrial relevance for propene homopolymerization. However, some of them are widely used for propene copolymerization with ethene.

Since the 1960s the syndiospecific chain-end controlled polymerization of propene in the presence of homogeneous vanadium-based catalytic systems has been known. For these systems, it has been well established by the work of Zambelli and co-workers that the polymerization is poorly regioselective and the stereoselective (and possibly syndiospecific) step is propene insertion into the metal secondary carbon bond with formation of a new secondary metal-carbon bond.^{133,134}

Chain-end controlled isospecificity and syndiospecificity for 1-alkene polymerizations at low temperatures with achiral metallocenes have also been reported.^{2,16a,81,131,135} The polymerization with these catalysts is highly regio-specific in favor of primary monomer insertion.

A syndiospecific chain-end controlled propene polymerization by Brookhart-type¹³⁶ Ni(II) catalysts at low temperatures, also occurring through a primary

monomer insertion, has also been reported.¹³⁷ The polymerization is even less regioselective than in the case of V-based catalysts, but a prevailing primary monomer insertion has been assessed by ¹³C NMR analysis of suitably labeled polymer end groups formed in both the initiation and termination steps and confirmed by the structure of low-molecular-weight samples.¹³⁷

Recently, bis(imino)pyridyl Fe(II)-based catalysts have been reported to afford isospecific chain-end controlled propene polymerization occurring through secondary monomer insertion.^{138,139} Even more recently, catalytic systems based on the octahedral bis(salicylaldiminato)Ti complex have been reported to afford syndiospecific chain-end controlled propene polymerization,¹⁴⁰ which possibly occurs through secondary monomer insertion.¹⁴¹

Possible mechanisms for chain-end stereocontrol for catalytic systems presenting primary and secondary 1-alkene (mainly propene) insertion will be described in Sections 4.1.1 and 4.1.2, respectively.

4.1.1 Chain-End Stereocontrol for Primary 1-Alkene Insertions

The models considered in this section refer to catalytic systems for which the polymerization reaction occurs by primary insertion of the 1-alkene and neither chirality of coordination of the aromatic ligands nor chirality at the central metal atom exists.

Diastereoisomeric transition states calculated for propene primary insertion in a model of the Ewen achiral metallocenes are shown in Figure 1.20. The two possible diastereomeric transition states correspond to *si* (Figure 1.20a) and *re* (Figure 1.20b) insertions of the monomer for the case of a *si* chain (i.e., a growing chain in which the last monomeric unit has been obtained by a *cis* addition of a *si*-coordinated monomer molecule) and are suitable for *like* (isotactic) and *unlike* (syndiotactic) propagations, respectively.^{142,143}

Diastereoisomeric transition states calculated for propene insertion in a model for a Brookhart-type Ni(II) catalyst, based on diacetylbis(2,6-diisopropylphenylimine)nickel derivative,^{143,144} are shown in Figure 1.21. Diastereomeric transition states for *si* (Figure 1.21a) and *re* (Figures 1.21b,c) monomer insertions into a *si* chain correspond to *like* (isotactic) and *unlike* (syndiotactic) propagations, respectively.^{144,143}

According to our calculations, these transition states are geometrically similar to those found for stereorigid metallocenes. In fact, not only do they present the methyl group of propene and the second carbon atom (and its substituents) of the growing chain on opposite sides with respect to the plane defined by the Mt–C bonds but also the dihedral angles θ_0 , θ_1 are similar to those found for the stereorigid metallocenes, like those of Figure 1.8.

However, for the transition states of Figures 1.20 and 1.21, the energy differences between models for *si* and *re* monomer insertions, corresponding to

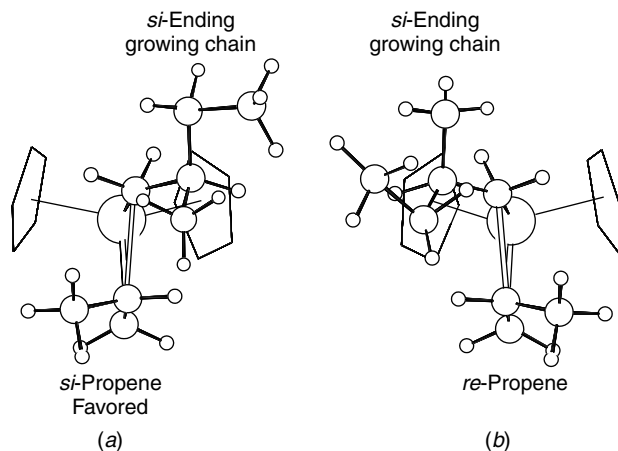


Figure 1.20 Minimum-energy transition states for primary propene insertion on model site comprising two cyclopentadienyl ligands, primary coordination of propene molecule, and primary growing chain. Growing chain is labeled as *si* chain since chirality of its tertiary carbon atom closest to metal has been obtained by primary insertion of *si*-coordinated propene. Conformational freedom of growing chain is higher for model corresponding to (a) *like* (isospecific) propagation where chain (atoms C3, C4, ...) points away from olefin, while is lower for model corresponding to (b) *unlike* (syndiospecific) propagation, where it points toward olefin.

$\theta_1 \approx +60^\circ$, -60° , respectively, are much smaller and essentially depend only on the different conformational freedom of the growing chain for positive or negative θ_1 values. In particular, a *si*-ending chain has higher conformational freedom in transition states presenting $\theta_1 \approx +60^\circ$ (Figure 1.20a) for the model of the Ewen catalyst and $\theta_1 \approx -60^\circ$ (Figures 1.21b,c) for the model of the Brookhart-type Ni(II) catalyst. Specifically for the latter model, for the *like* insertion there is only one transition state with $\theta_1 \approx +70^\circ$ and $\theta_3 \approx 180^\circ$ (Figure 1.21a), while for the *unlike* insertion there are two energetically nearly equivalent transition states for $\theta_1 \approx -70^\circ$ and $\theta_3 \approx 180^\circ$, -60° (Figures 1.21b,c). This preference of a *si* chain for $\theta_1 \approx +60$ and $\theta_1 \approx -60$, in turn, determines the preference for *si* and *re* monomer insertion and hence the *like* and *unlike* stereoselectivity (and hence isospecificity and syndiospecificity) of the model catalytic systems of Figures 1.20 and 1.21, respectively.

Both above-described mechanisms for chain-end control of isotacticity and syndiotacticity are critically dependent on the growing chain conformation and in particular on the value of the dihedral angle relative to the first C–C bond of the growing chain (θ_2 in Figures 1.20 and 1.21). In fact, models imposing a chain conformation with the first tertiary H atom pointing toward the metal ($\theta_2 \approx 0^\circ$), like the model of Figure 1.20, show an easier *like* monomer insertion, while models imposing a chain conformation with the first tertiary H

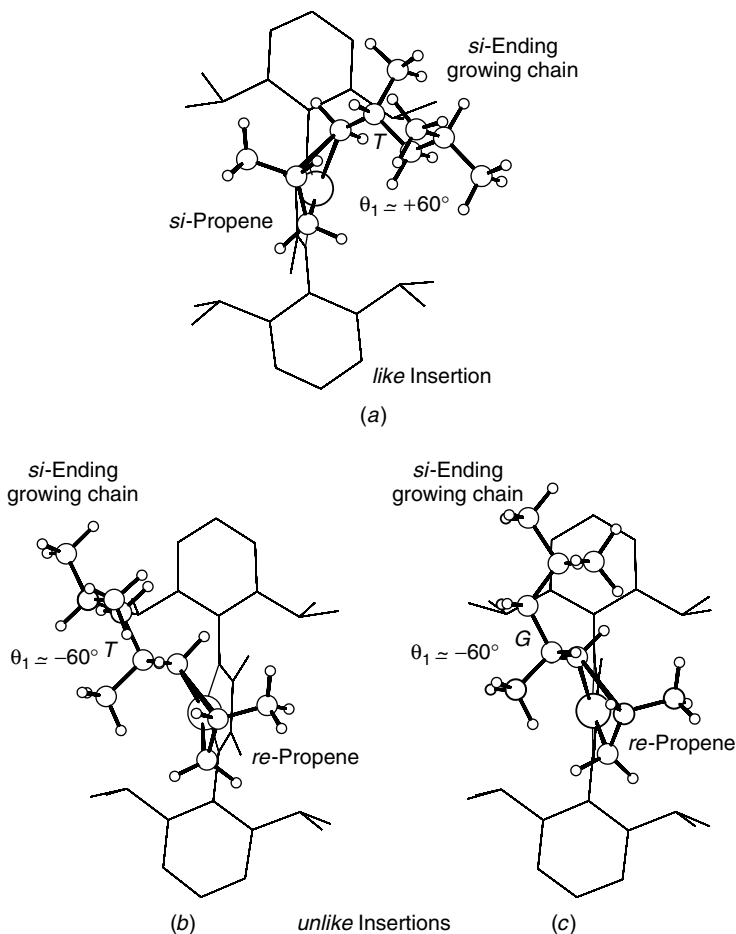


Figure 1.21 Minimum-energy transition states for primary propene insertion on Brookhart-type Ni(II) catalyst for the model including *si* growing chain (whose last monomeric unit was generated by insertion of *si*-coordinated monomer). (a) There is only minimum-energy transition state for insertion of *si*-propene (*like* insertion) while (b,c) there are two nearly energetically equivalent minimum-energy transition states for insertion of *re*-propene (*unlike* insertion).

atom pointing toward the monomer ($\theta_2 \approx 100^\circ$), like the model of Figure 1.21, show an easier *unlike* monomer insertion.¹⁴³

4.1.2 Chain-End Stereocontrol for Secondary 1-Alkene Insertions

The problem of the origin of chain-end stereocontrol for secondary 1-alkene insertions has been relatively little investigated up to now. The only reported

studies refer to the syndiospecific polymerization of propene in the presence of homogeneous V-based catalytic systems. As previously discussed (Section 3.2.3), there is experimental evidence that the polymerization is not completely regiospecific and that the only syndiospecific step is propene insertion into a metal–secondary carbon bond with formation of a new secondary metal–carbon bond. A chain-end stereocontrol is also well established.

All the proposed models for syndiotactic propagation suppose that the active center is a vanadium–carbon bond and that the monomer first coordinates to the metal. Moreover, all of them attribute the stereospecificity to steric factors. However, different driving forces for the syndiospecificity have been proposed.

According to an early model,^{13d} there are two adjacent accessible positions at the catalytic site, each favoring the coordination of the prochiral monomer with one of its two faces; if the growing polymer chain alternates between the two positions at each insertion step, syndiotactic propagation is ensured. Due to the successive finding of a chain-end stereocontrol, this model has to be rejected.

Most models^{18,145,146} favored the hypothesis that syndiotacticity could arise from direct steric repulsions between the methyl group of the complexed propene and the last inserted monomer unit of the growing chain. One of these models¹⁴⁵ is no more suitable, since it assumed a primary monomer insertion. Other papers^{18,145} suggested that such steric repulsions could occur in an activated four-center complex, resulting from propene secondary insertion into a metal–secondary carbon bond, although this model has not been subjected to quantitative examination.

A detailed catalytic model with a pentacoordinated metal (V) atom was proposed by Zambelli and Allegra¹³⁴ that is able to account for several experimental observations concerning the homo- and copolymerization of propene and other 1-alkenes in the presence of the syndiospecific catalyst systems under consideration. However, the authors pointed out that the steric repulsions between the methyl group of a coordinated propene molecule and the last inserted propene unit of the growing chain do not generate energy differences between diastereoisomeric situations in the hypothesized catalytic complex, so that steric interferences with the growing chain during monomer approach to the catalyst were suggested as the source of the syndiospecific control.

A completely different model of the origin of the syndiospecificity which involves the formation of a fluxional chiral site has also been proposed.¹⁴⁷ According to this mechanism, the chirality of the growing chain determines the chirality of the fluxional site, which in turn discriminates between the two monomer enantiofaces. In particular, the assumed model site consists of a hexacoordinated metal (V) atom surrounded by four chlorine atoms assumed to be bridge bonded to other metal (i.e., Al) atoms^{147–149} (Figures 1.22a,b).

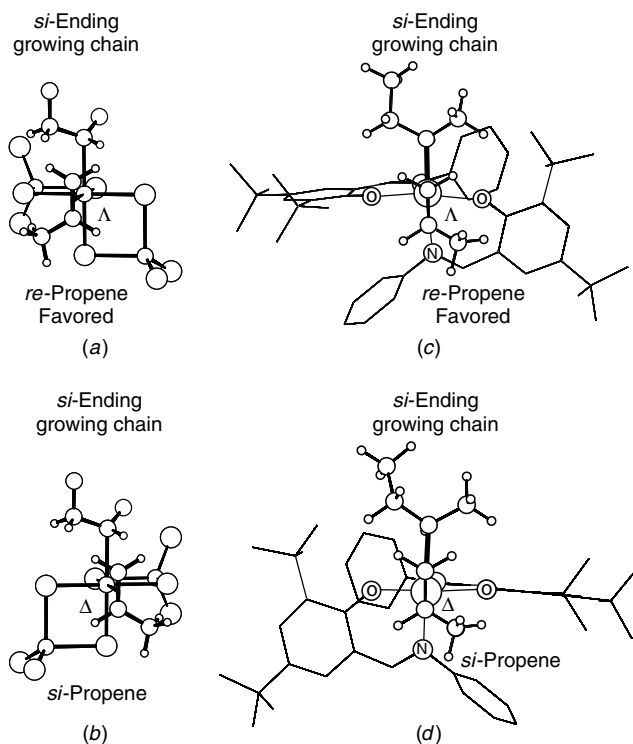


Figure 1.22 Minimum-energy diastereoisomeric intermediates for secondary propene insertion into secondary growing chain presenting *si* chirality (that is, generated secondary insertion of *si*-coordinated propene): (a,b) for model site comprising hexacoordinated V atom; (c,d) for octahedral bis(salicylaldiminato)Ti complex. Models for *unlike* (syndiospecific) propagation (a,c) include fluxional sites of Δ chirality which impose *re*-propene coordination while models for *like* (isospecific) propagation (b,d) include fluxional sites of Δ chirality which impose *si*-propene coordination. Model (b) is of higher energy with respect to model (a) due to repulsive interactions of first methyl group of growing chain with Cl atom of Δ site.

The catalytic site is chiral and analogous to that proposed for the isospecific heterogeneous catalysts (Section 3.2), but, unlike the heterogeneous model site, interconversion between enantiomeric complexes is assumed to be possible, after each insertion step, when the metal atom is pentacoordinated.^{147,149} The analysis of the nonbonded interactions at the catalytic site showed that a *si* chain favors the formation of the Δ complex, which in turn favors the *re* coordination and insertion of the successive monomer unit, thus assuring the syndiospecific propagation of the chain.

A possible support to the latter model comes from its geometrical similarity with the octahedral bis(salicylaldiminato)Ti complex (Figures 1.22c,d)

which has been recently reported to afford syndiospecific chain-end controlled propene polymerization¹⁴⁰ through secondary insertion.¹⁴¹ It is also worth noting that a recent quantum mechanical density functional study of ethene coordination and insertion has calculated, for the hexacoordinated models of Figures 1.22a,b, a reasonable reaction pathway involving a low activation energy.¹⁴⁹

A similar mechanism could operate also for bis(imino)pyridyl Fe(II)-based catalysts which have been reported to afford isospecific chain-end controlled propene polymerization occurring through secondary monomer insertion.^{138,139} In fact, preliminary calculations indicate that the chirality of the growing chain would determine a chiral conformation of the bis-pyridyl ligand, which in turn would discriminate between the two monomer enantiofaces.

4.2 Styrene and Substituted Styrene Syndiotactic Polymerization

Syndiotactic polystyrene is a new polymeric material^{150–152} of industrial relevance since it shows a high melting point (270°C) and high crystallization rates.¹⁵³ Syndiotactic polystyrene is a highly stereoregular polymer which can be obtained by using several soluble titanium and, to a less extent, zirconium compounds.

Among titanium-based precursors, monocyclopentadienyl compounds of the type CpTiCl₃ or Cp*TiCl₃ activated by MAO or B(C₆F₅)₃ showed the best performance, although several substituted mono-Cp or indenyl derivative and Cp-free compounds as Ti(CH₂Ph)₄ and Ti(OR)₄ (R = alkyl, aryl) are quite active as well. In short, practically any soluble titanium compound can be used as precatalyst.^{154–158}

Although there is some debate about the exact nature of the species active in polymerization,^{159–163} many characteristics of the polymerization mechanism have been addressed beyond any doubt. Elegant NMR experiments have clearly indicated that polymerization of styrene to syndiotactic polymer occurs through a Ziegler–Natta polyinsertion mechanism.^{164,165} In particular, these experiments have shown that (i) the insertion mechanism occurs through the *cis* opening of the monomer double bond¹⁶⁶, (ii) the regiochemistry of styrene insertion is secondary^{167,168}, and (iii) the stereoselectivity of the insertion step is controlled by the chirality of the growing chain end. This is clearly indicated by the analysis of the stereochemical composition of the syndiotactic polymer, which shows the presence of the *rmr* tetrad, which is consistent with chain-end stereocontrol, and the substantial absence of the *rmm* tetrad, which is consistent with site stereocontrol.^{169–171}

Despite the many experimental studies which have contributed to clarify even details of the polymerization mechanism, only recently has theoretical study (a combined quantum mechanics/molecular mechanics, QM/MM) of the

mechanisms of polymerization and of stereocontrol in the syndiospecific polymerization of styrene been afforded.^{172,173} In particular, insertion of styrene on the $\text{CpTi}^{\text{III}}\text{CH}_2\text{Ph}^+$ active species, in which the achiral $-\text{CH}_2\text{Ph}$ group has been used to simulate the growing chain, was investigated. This choice allowed to explore details of the insertion reaction delaying the complications due to the presence of a chiral growing chain.¹⁷² After the basic features of the insertion step have been clarified, the issue of stereoselectivity was afforded. In order to contribute to establish a possible mechanism of growing chain stereocontrol, the insertion of styrene on the $\text{CpTi}^{\text{III}}\text{CH}(\text{CH}_3)\text{Ph}^+$ active species, which contains a chiral growing chain, has been investigated.¹⁷³

According to these calculations, the most stable styrene-free but solvent-coordinated structure is characterized by a coordination scheme in which the benzyl-type chain end is η^3 coordinated to the metal atom. The most stable coordination intermediate is characterized by a fluxionality in the hapticity of coordination of the growing chain (from η^3 to η^7) and of the styrene monomer (from η^4 to η^2). The monomer uptake energy amounts to roughly 20 kcal/mol and is comparable to the uptake energy calculated for ethene coordination to group 4 metallocenes. The insertion reaction can proceed through a transition state which is characterized by the classical four-center transition state geometry proposed for olefin polymerization with Ziegler–Natta catalysts. A rearrangement of the benzyl-type chain end from the η^7 coordination to an almost σ -bonding scheme between the metal atom and the C atom of the CH_2 group of the chain end is required to facilitate the insertion reaction. Moreover, the styrene molecule is almost *cis*- η^4 coordinated at the transition state. The energy barrier with respect to the most stable coordination intermediate is 11.2 kcal/mol.

The mechanism of stereoselectivity, which was deduced by the calculations, involves the formation of a fluxional chiral site, as for the case of stereoselective chain-end controlled propene polymerizations which involve secondary monomer insertion (Section 4.1.2). According to this mechanism, the chirality of the growing chain determines the chirality of the fluxional site, which in turn discriminates between the two monomer enantiofaces. In particular, the diastereoisomeric transition states consist of a pseudotetrahedral metal (Ti) atom whose chirality can be defined by extension of the Cahn–Ingold–Prelog nomenclature²³ to organometallic compounds, as proposed by Stanley and Baird.²⁶ In order of priority, the four different substituents used to define the chirality at the pseudotetrahedral metal atom are (i) the center of mass of the ancillary aromatic Cp or C_6H_6 ligand, (ii) the center of mass of the two C atoms of the aromatic ring of the styrene which are coordinated to the metal, (iii) the center of mass of the monomer double bond, and (iv) the C_α atom of the growing chain. Within this choice, *R* is the chirality at the metal atom in Figure 1.23*a*, while it is *S* in Figure 1.23*b*.

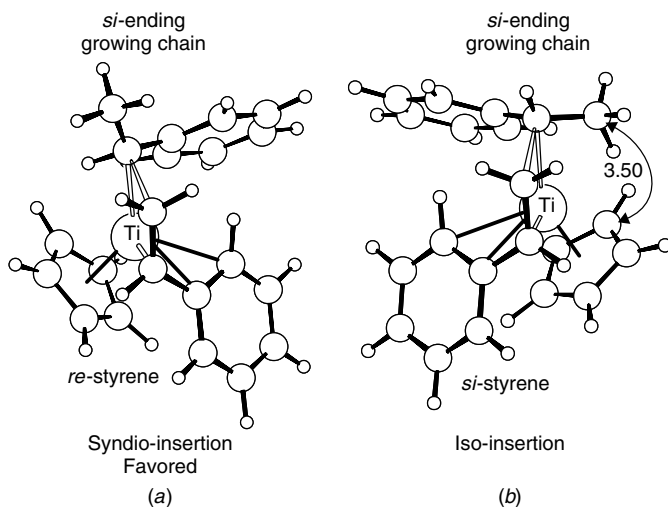


Figure 1.23 Transition states for secondary insertion of styrene into secondary growing chain presenting *si* chirality (that is, generated secondary insertion of *si*-coordinated styrene). (a) Model for *unlike* (syndiospecific) propagation includes fluxional site of *R* chirality at metal atom, which imposes *re*-propene coordination, while (b) model for *like* (isospecific) propagation includes fluxional sites of *S* chirality at metal, which imposes *si*-propene coordination. Syndiospecific transition state (a) is favored because smallest substituent on C_α atom of chain, the H atom, can be pointed toward Cp ligand, whereas isospecific transition state (b) is of higher energy because C_β of growing chain is oriented toward Cp ring.

According to our calculations, this chirality at the metal atom is able to discriminate between monomer enantiofaces. In particular, a *re*-coordinated styrene is energetically feasible only in the presence of a *R* chirality at the metal atom, while a *si*-coordinated only in the presence of a *S* chirality. Moreover, in case of a *si*-ending chain, the diastereoisomeric transition state with a *S* chirality at the metal (Figure 1.23b) is favored because the smallest substituent on the C_α atom of the chain, the H atom, can be pointed toward the Cp ligand, whereas the diastereoisomeric transition state with a *R* chirality at the metal (Figure 1.23a) is of higher energy because one group between the aromatic ring on the C_α atom of the growing chain or the C_β and following of the growing chain must be oriented toward the Cp ring. Energetically, the transition state leading to the syndiotactic diad is favored by 1.2 kcal/mol with respect to the one leading to the isotactic diad (Figure 1.23). The calculated ΔE^\ddagger in favor of the *r* diad is in good agreement with the experimental difference between the apparent energies of activation leading to *r* and *m* diads, ΔE_a , which has been determined to be 1.5–2 kcal/mol.¹⁷⁰

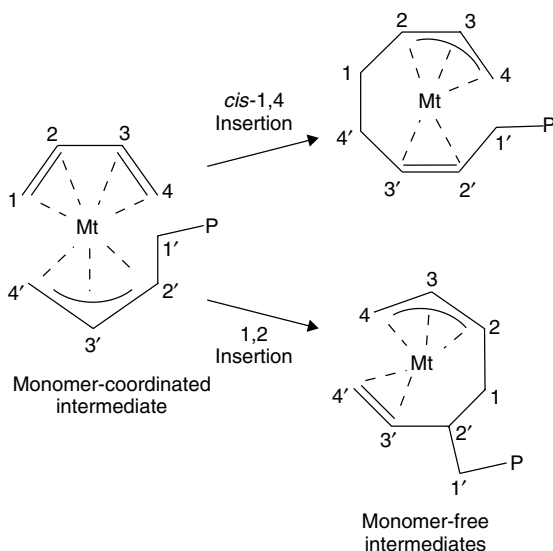
It is also worthy to note that the most preferred structure (Figure 1.23b) is characterized by a θ_1 value, $|35^\circ|$, not far from the θ_1 values, $|60^\circ|$, we

calculated to be the preferred ones in the polymerization of propene with group 4 metallocenes (Section 3.1.1).

4.3 Conjugated Diene Polymerizations

The polymerization of conjugated dienes with transition metal catalytic systems is an insertion polymerization, as is that of monoalkenes with the same systems. Moreover, it is nearly generally accepted that for diene polymerization the monomer insertion reaction occurs in the same two steps established for olefin polymerization by transition metal catalytic systems: (i) coordination of the monomer to the metal and (ii) monomer insertion into a metal-carbon bond. However, polymerization of dienes presents several peculiar aspects mainly related to the nature of the bond between the transition metal of the catalytic system and the growing chain, which is of σ type for the monoalkene polymerizations, while it is of the allylic type in the conjugated diene polymerizations.¹⁷⁴⁻¹⁸³

Several experimental facts have been rationalized in terms of different π -allyl insertion mechanisms, depending on the nature of the catalytic systems and the diene monomer, mainly by the extensive work of Porri and co-workers, as reviewed in Refs. 181 and 182, and Taube and co-workers, as reviewed in Ref. 183. A widely accepted scheme for *cis*-1,4 and 1,2 polymerizations of conjugated dienes is reported in Scheme 1.5. In particular, it has been



Scheme 1.5 Monomer coordinated and monomer free intermediates of a widely accepted mechanism for *cis*-1,4 and 1,2 polymerizations of conjugated dienes.

suggested that 1,2 units and *cis*-1,4 units can derive from an intermediate including a *s-cis*- η^4 -coordinated diene monomer as well as a η^3 -coordinated allyl terminal of the growing chain presenting an *anti* structure.^{181–183} This kind of arrangement of the ligands would give rise to *cis*-1,4 or to 1,2 units, depending on whether the incoming monomer reacts at the terminal C4' or internal C2' allyl carbon, respectively. The labels for the carbon atoms presented in Scheme 1.5 should help to visualize 1,4 and 1,2 enchainments.

While in olefin polymerization the monomer-free intermediates could only be stabilized by weak agostic interactions (β or γ),¹⁸⁴ in diene polymerization the monomer-free intermediates could be stabilized by the higher coordination energies connected with the back-biting of double bonds present along the growing chain^{183,185–187} (as sketched for the monomer-free intermediates of Scheme 1.5). The existence of complexes with polydienyl chains coordinated to a transition metal through the terminal allyl group as well as by one or two double bonds along the chain (back-biting coordination) has been proved by NMR and X-ray diffraction studies.^{188–192} Moreover, it is well known that also in the absence of cocatalysts, complexes containing back-biting π -allyl ligands can be active in the polymerization of conjugated dienes.^{189,192}

The iso- and syndiotactic isomerism in the insertion polymerization of dienes (for 1,2 polymerization of generic dienes and for *cis*-1,4 polymerization of 4-monosubstituted or of 1,4-disubstituted monomers) would be determined, according to the polymerization scheme proposed by Porri and co-workers,^{181–182} by the relative orientations of the two ligands (diene monomer and allyl terminal of the growing chain) in the preinsertion catalytic intermediates.

According to molecular mechanics¹⁸⁶ and a density functional studies¹⁹³ relative to the CpTiCl₃–MAO system reported by some of us, minimum-energy preinsertion catalytic intermediates leading to 1,2 and *cis*-1,4 polymerizations are those shown in Figure 1.24. In particular, for the absolute minimum of Figure 1.24a, the diene and of the allyl group present an *endo–endo* orientation, that is, their concavities are oriented in opposite direction with respect to the Cp ligand, while for the intermediate of Figure 1.24b, which is higher in energy by nearly 2 kcal/mol, the orientation can be defined *endo–exo*, that is, the concavity of the allyl is toward the Cp whereas the diene is in the opposite direction. In the framework of the polymerization scheme proposed by Porri and co-workers^{181,182} and as also indicated in Figure 1.24, diene insertion starting from the *endo–endo* intermediate leads to 1,4-*like* or 1,2-*unlike* enchainments through C–C bond formation between the C1 of butadiene (1 in Figure 1.24) and the C4' of the allyl and between the C1 of butadiene (4 in Figure 1.24) and the C2' of the allyl, respectively. On the other hand, diene insertions starting from the *endo–exo* intermediate leads to 1,4-*unlike*

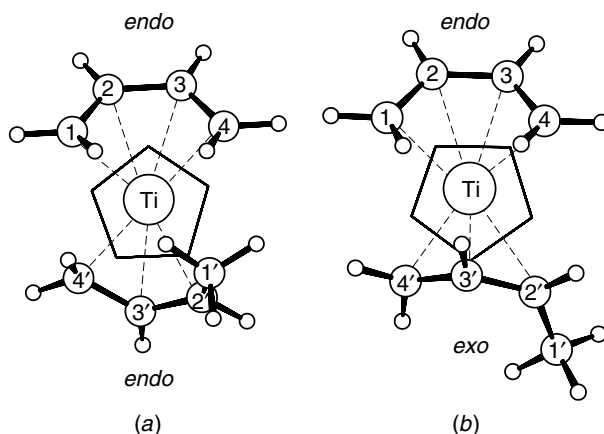


Figure 1.24 Minimum-energy preinsertion catalytic intermediates leading to 1,2 and *cis*-1,4 polymerizations. In particular, (a) absolute minimum-energy intermediate, for which diene and of allyl group present an *endo-endo* orientation (that is, their concavities are oriented in opposite direction with respect to Cp ligand), can lead to 1,2-*unlike* or *cis*-1,4-*like* insertions, while (b) higher energy intermediate, for which diene and allyl group present an *endo-exo* orientation (that is, the concavity of allyl is toward Cp whereas diene is in opposite direction) can lead to 1,2-*like* or *cis*-1,4-*unlike* insertions.

or 1,2-*like* enchainments, through C-C bond formation between the C1 of butadiene (1 and 4 in the figure) and allyl atoms C4' and C2', respectively.

According to the same studies,^{186,193} *iso*- and *syndiotactic* isomerism in the insertion polymerization of diene could also be determined by substantial energy differences between monomer-free intermediates, presenting a back-biting coordination of the growing chain. The minimum-energy geometries of the diastereoisomeric monomer-free intermediates for butadiene polymerization catalyzed by titanium complexes presenting a Cp group as the ancillary ligand are shown in Figure 1.25. The chiralities of coordination of the allyl groups (assumed to be *si*) and of the back-biting double bonds (*si* or *re*) are also indicated in Figure 1.25 in order to easily visualize the possible stereoregularity (*iso* or *syndio*) of the model chains. In fact, *like* and *unlike* chiralities would possibly lead to isotactic and syndiotactic enchainments, respectively.

Lower and similar energies correspond to the 1,4-*like* and 1,2-*unlike* (Figures 1.25a,b) intermediates. The higher energy of the 1,4-*unlike* and 1,2-*like* (Figures 1.25c,d) intermediates are associated with the orientation of the η^2 back-biting double bond, which is roughly orthogonal with respect to the allyl plane.

The relative energies of the preinsertion intermediates of Figure 1.24 and the diastereoisomeric monomer-free intermediates of Figure 1.25 are in

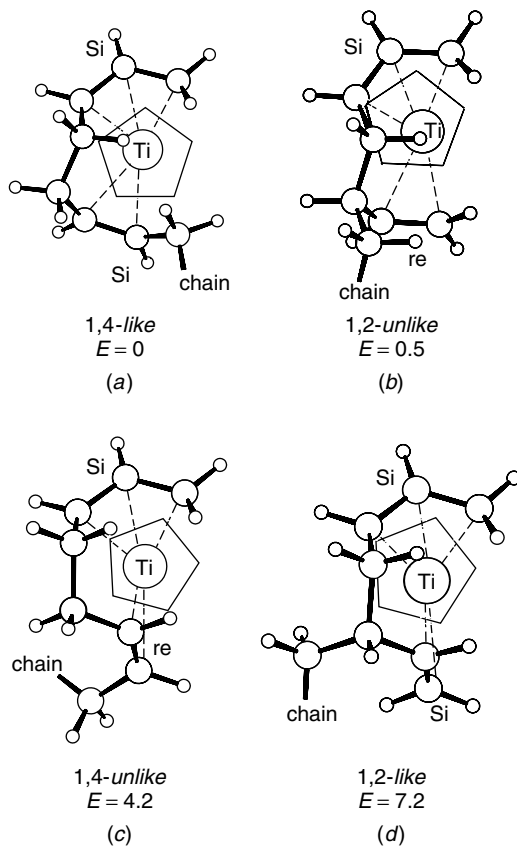


Figure 1.25 Minimum-energy diastereoisomeric monomer free intermediates for butadiene polymerization catalyzed by titanium complexes presenting Cp group as ancillary ligand. Chiralities of coordination of allyl groups (assumed to be *si*) and back-biting double bonds (*si* or *re*) are indicated, in order to easily visualize possible stereoregularity (iso or syndio) of model chains. In fact, *like* and *unlike* chiralities would possibly lead to isotactic and syndiotactic enchainments, respectively.

qualitative agreement with several experimental facts. In particular, systems based on CpTiX_3 ($\text{X} = \text{Cl}$,^{194,195} F ,¹⁹⁵ CH_3 ,¹⁹⁵ OR ¹⁹⁶) polymerize butadiene to products containing prevalingly 1,4 units ($\sim 85\%$) and 1,2 units ($\sim 10\%$), whose ratio is in qualitative agreement with the energy difference between the monomer-free structures **1.25a** and **1.25b**. Moreover, the small energy difference between intermediates **1.25a** and **1.25b**, which lead to 1,4 and 1,2 enchainments, respectively, could be responsible for the strong dependence of chemoselectivity on the kind of diene monomer.

As for the stereoselectivity, the frequently observed syndiotacticity for 1,2 polydienes and the frequently observed isotacticity for *cis*-1,4 polymers (of 4-substituted dienes) by using catalytic systems based on CpTiX_3 ($X = \text{F}, \text{Cl}, \text{CH}_3$), Cp^*TiCl_3 , Cp^*TiCl_2 , Cp_2TiCl_2 , and Cp_2TiCl ^{194,197} agree well with the lower energy of 1,2-*unlike* and 1,4-*like* monomer-free intermediates with respect to 1,2-*like* and 1,4-*unlike* intermediates.

5 FINAL REMARKS

The examination of models for stereospecific Ziegler–Natta polymerizations indicate the importance of the nonbonded interactions for the stereoselectivity mechanisms.

The mechanisms of stereoselectivity for all *chiral site* stereocontrolled Ziegler–Natta (heterogeneous and homogeneous) polymerizations of olefins (Section 3), all involving a primary monomer insertion, present a general pattern of similarity. For all the proposed stereospecific models, the chiral orientation of the first C–C bond of the growing chain, imposed by the chirality of the site, seems to be crucial in determining the stereoselectivity. In particular, the chirality of the site discriminates between the two possible growing chain conformations suitable for the formation of transition states involving an α -hydrogen agostic bond, thus determining the internal rotation angle relative to the metal–carbon bond θ_1 being close to $+60^\circ$ or -60° , which in turn would determine preferred insertion of a *re*- or a *si*-propene enantioface, respectively. This mechanism of stereoselectivity, which involves a *chiral orientation of the growing chain*, agrees well with a large number of experimental facts, some of which result from experiments designed to test its validity.

Nonbonded energy interactions are able to rationalize not only the stereospecificities observed for different metallocene-based catalytic systems (ispecific, syndiospecific, hemi-isospecific, and with oscillating stereocontrol) but also the origin of particular stereodefects and their dependence on monomer concentration as well as stereostructures associated with regioirregular insertions. Nonbonded energy analysis also allowed to rationalize the dependence of regiospecificity on the type of stereospecificity of metallocene-based catalysts.

As for olefins different from propene, molecular modeling studies have also been able to rationalize the dependence on metallocene symmetry of *E–Z* selectivity for 2-butene copolymerization as well as the stereoselectivity of the cyclization step, which determines the *cis* or *trans* configuration of the rings, for cyclopolymerization of nonconjugated dienes.

The mechanisms for *chain-end* stereoselectivity (ispecific and syndiospecific) for *primary* monomer insertion (Section 4.1.1) present relevant analogies with the well-established mechanism of chiral site controlled stereoselectivity (Section 3). In fact, for both mechanisms, the selection between the two

monomer prochiral faces is operated by the chiral orientation of the growing chain. This chiral orientation of the growing chain, which for chiral site stereocontrolled catalysts is strictly imposed by the chirality of the site, for chain-end stereocontrolled catalysts can be determined by the chain-end chirality. On this basis, we suggest that the mechanisms of chain-end controlled stereoselectivity, both *like* and *unlike* for primary propene insertion, could be considered as a subcase of the more general mechanism of the *chiral orientation of the growing chain* (Section 3.1.1).

The mechanisms of stereoselectivity which have been proposed for chain-end stereocontrolled polymerizations involving *secondary* monomer insertion also present a general pattern of similarity. In fact, molecular modeling studies suggest that for olefin polymerizations (both syndiospecific and isospecific, Section 4.1.2) as well as for styrene polymerization (syndiospecific, Section 4.2), the chirality of the growing chain would determine the chirality of a fluxional site, which in turn would discriminate between the two monomer enantiofaces.

The stereoselectivity mechanisms for polymerizations of dienes present several peculiar aspects mainly related to the nature of the bond between the transition metal of the catalytic system and the growing chain, which is of allylic type rather than of σ type, as for the monoalkene polymerizations. There is experimental evidence, also supported by molecular modeling studies, that a relevant role for chemoselectivity and stereoselectivity is also played by the chirality of the back-biting coordination to the metal of the double bond of the polydienyl chain closest to the coordinated allyl group.

ACKNOWLEDGMENTS

We thank A. Zambelli, P. Longo, C. Pellecchia, G. Milano, G. Monaco, and C. Costabile of the University of Salerno, M. Toto and G. Minieri of the University of Naples, and L. Resconi, G. Morini, and G. Moscardi of Giulio Natta Research Center of Basell for useful discussions. This work has been supported by the Ministero della Ricerca Scientifica e Tecnologica of Italy within PRIN 2002 fundings, by Basell, and by the National Research Council of Italy.

REFERENCES

1. Tait, P. J. T. Monoalkene Polymerization: Ziegler–Natta and Transition Metal Catalysts. In *Comprehensive Polymer Science*, Vol. 4. Eastmond, G. C.; Ledwith, A.; Russo, S.; Sigwalt, P. (Eds.). Pergamon, Oxford, 1989, Chapter 1.
2. Corradini, P.; Busico, V.; Guerra, G. Monoalkene Polymerization: Stereospecificity. In *Comprehensive Polymer Science*, Vol. 4. Eastmond, G. C.; Ledwith, A.; Russo, S.; Sigwalt, P. (Eds.). Pergamon, Oxford, 1989, Chapter 3.



3. Porri, L.; Giarrusso G. Conjugated Diene Polymerization. In *Comprehensive Polymer Science*, Vol. 4. Eastmond, G. C.; Ledwith, A.; Russo, S.; Sigwalt, P. (Eds.). Pergamon, Oxford, 1989, Chapter 5.
4. Ziegler, K.; Holzkamp, E.; Breil, H.; Martin, H. *Angew. Chem.* **1955**, *67*, 541.
5. Natta, G. *Science* **1965**, *147*, 261.
6. Barbé, P. C.; Cecchin, G.; Noristi, L. *Adv. Polym. Sci.* **1986**, *81*, 1.
7. Ewen, J. A. *J. Am. Chem. Soc.* **1984**, *104*, 6355.
8. Ewen, J. A.; Jones, R. L.; Razavi, A.; Ferrara, J. D. *J. Am. Chem. Soc.* **1988**, *110*, 6255.
9. Ewen, J. A.; Elder, M. J.; Jones, R. L.; Haspeslagh, L.; Atwood, J. L.; Bott, S. G.; Robinson, K. *Makromol. Chem. Symp.* **1991**, *48/49*, 253.
10. Sinn, H.; Kaminsky, W. *Adv. Organometal. Chem.* **1980**, *18*, 99.
11. Resconi, L.; Cavallo, L.; Fait, A.; Piemontesi, F. *Chem. Rev.* **2000**, *100*, 1253.
12. Coates, G. W. *Chem. Rev.* **2000**, *100*, 1223.
13. (a) Cossee, P. *Tetrahedron Lett.* **1960**, *17*, 12. (b) Cossee, P. *J. Catal.* **1964**, *3*, 80. (c) Arlman, E. J.; Cossee, P. *J. Catal.* **1964**, *3*, 99. (d) Cossee, P. In *The Stereochemistry of Macromolecules*, Vol. 1. Ketley, A. D. (Ed.). Marcel Dekker, New York, 1964, Chapter 3.
14. Allegra, G. *Makromol. Chem.* **1971**, *145*, 235.
15. (a) Corradini, P.; Barone, V.; Fusco, R.; Guerra, G. *Eur. Polym. J.* **1979**, *15*, 133. (b) Corradini, P.; Barone, V.; Fusco, R.; Guerra, G. *J. Catal.* **1982**, *77*, 32. (c) Corradini, P.; Barone, V.; Fusco, R.; Guerra, G. *Gazz. Chim. Ital.* **1983**, *113*, 601.
16. (a) Ewen, J. A. In *Catalytic Polymerization of Olefins, Studies in Surface Science and Catalysis*, Vol. 25. Keii, T.; Soga, K. (Eds.). Elsevier, New York, 1986, p. 271. (b) Ewen, J. A.; Haspeslagh, L.; Atwood, J.; Zhang, H. *J. Am. Chem. Soc.* **1987**, *109*, 6544.
17. (a) Kaminsky, W.; Külper, K.; Brintzinger, H.; Wild, F. *Angew. Chem. Int. Ed. Engl.* **1985**, *24*, 507. (b) Kaminsky, W. *Angew. Makromol. Chem.* **1986**, *145/146*, 149.
18. Zambelli, A.; Tosi, C. *Fortschr. Hochpolym-Fortsch. (Adv. Polym. Sci.)* **1974**, *15*, 31.
19. Boor, J., Jr. *Ziegler-Natta Catalysts and Polymerizations*, Academic, New York, 1979.
20. Natta, G.; Farina, M.; Peraldo, M. *Chim. Ind. (Milan)* **1960**, *42*, 255.
21. Zambelli, A.; Giongo, M. G.; Natta, G. *Makromol. Chem.* **1968**, *112*, 183.
22. Hanson, K. R. *J. Am. Chem. Soc.* **1966**, *88*, 2731.
23. (a) Cahn, R. S.; Ingold, C.; Prelog, V. *Angew. Chem. Int. Ed. Engl.* **1966**, *5*, 385. (b) Prelog, V.; Helmchem, G. *Angew. Chem. Int. Ed. Engl.* **1982**, *21*, 567.
24. Schlögl, K. *Top. Stereochem.* **1966**, *1*, 39.
25. Nomenclature of Inorganic Chemistry, *Pure Appl. Chem.* **1971**, *18*, 77.
26. Stanley, K.; Baird, M. C. *J. Am. Chem. Soc.* **1975**, *97*, 6598.
27. Bovey, F. A.; Tiers, G. V. D. *J. Polym. Sci.* **1960**, *44*, 173.
28. Sheldon, R. A.; Fueno, T.; Tsunetsugu, T.; Furukawa, J. *J. Polym. Sci., Part B* **1965**, *3*, 23.
29. Doi, Y.; Asakuru, T. *Makromol. Chem.* **1975**, *176*, 507.
30. (a) Hine, J. *J. Org. Chem.* **1966**, *31*, 1236. (b) Hine, J. *Adv. Phys. Org. Chem.* **1977**, *15*, 1.
31. Corradini, P.; Cavallo, L.; Guerra, G. In *Metallocene-Based Polyolefins*, Vol. 2. Scheirs, J.; Kaminsky, W. (Eds.). Wiley, Chichester, UK, 2000, Chapter 1.
32. Dyachkovsky, F. S.; Shilova, A. J.; Shilov, E. *J. Polym. Sci., Part C* **1967**, *16*, 2333.
33. Eisch, J. J.; Piotrovsky, A. H.; Brownstein, S. K.; Gabe, E. J.; Lee, F. J. *J. Am. Chem. Soc.* **1985**, *107*, 7219.
34. Jordan, R.; Bajgur, C.; Willet, R.; Scott, B. *J. Am. Chem. Soc.* **1986**, *108*, 7410.

35. Bochmann, M.; Jaggar, A.; Nicholls, J. *Angew. Chem. Int. Ed. Engl.* **1990**, *29*, 780.
36. Xinmin, Y.; Stern, C.; Marks, T. J. *J. Am. Chem. Soc.* **1991**, *113*, 3623.
37. (a) Corradini, P.; Guerra, G.; Vacatello, M.; Villani, V. *Gazz. Chim. Ital.* **1988**, *118*, 173. (b) Cavallo, L.; Corradini, P.; Guerra, G.; Vacatello, M. *Macromolecules* **1991**, *24*, 1784. (c) Corradini, P.; Guerra, G. *Prog. Polym. Sci.* **1991**, *16*, 239. (d) Guerra, G.; Cavallo, L.; Moscardi, G.; Vacatello, M.; Corradini, P. *J. Am. Chem. Soc.* **1994**, *116*, 2988.
38. (a) Pietsch, M. A.; Rappé, A. *J. Am. Chem. Soc.* **1996**, *118*, 10908. (b) Cavallo, L.; Guerra, G.; Corradini, P. *Gazz. Chim. Ital.* **1996**, *126*, 463.
39. Chien, J. C. W.; Llinas, G. H.; Rausch, M. D.; Lin, G. Y.; Winter, H. H.; Atwood, J. L.; Bott, S. G. *J. Am. Chem. Soc.* **1991**, *113*, 8569.
40. Coates, G. W.; Waymouth, R. M. *Science* **1995**, *267*, 217.
41. Zambelli, A.; Sacchi, M. C.; Locatelli, P.; Zannoni, G. *Macromolecules* **1982**, *15*, 211.
42. Longo, P.; Grassi, A.; Pellicchia, C.; Zambelli, A. *Macromolecules* **1987**, *20*, 1015.
43. Cavallo, G.; Guerra, G.; Oliva, L.; Vacatello, M.; Corradini, P. *Polym. Commun.* **1989**, *30*, 16.
44. Pino, P.; Cioni, P.; Wei, J. *J. Am. Chem. Soc.* **1987**, *109*, 6189.
45. Pino, P.; Galimberti, M.; Prada, P.; Consiglio, G. *Makromol. Chem.* **1990**, *191*, 1677.
46. Cavallo, G.; Guerra, G.; Vacatello, M.; Corradini, P. *Chirality* **1991**, *3*, 299.
47. Gilchrist, J. H.; Bercaw, J. E. *J. Am. Chem. Soc.* **1996**, *118*, 12021.
48. Brookhart, M.; Green, M. L. H.; Wong, L. *Prog. Inorg. Chem.* **1988**, *36*, 1.
49. Piers, W. E.; Bercaw, J. E. *J. Am. Chem. Soc.* **1990**, *112*, 9406.
50. Kraudelat, H.; Brintzinger, H. H. *Angew. Chem. Int. Ed. Eng.* **1990**, *29*, 1412.
51. Lauher, J. W.; Hoffman, R. *J. Am. Chem. Soc.* **1976**, *98*, 1729.
52. Woo, T.; Fan, L.; Ziegler, T. *Organometallics* **1994**, *13*, 2252.
53. Brookhart, M.; Green, M. L. H. *J. Organometal. Chem.* **1983**, *250*, 395.
54. Mislow, K.; Raban, M. *Top. Stereochem.* **1967**, *1*, 1.
55. Cavallo, L.; Corradini, P.; Guerra, G.; Vacatello, M. *Polymer* **1991**, *32*, 1329.
56. Mise, T.; Miya, S.; Yamazaki, H. *Chem. Lett.* **1989**, 1853.
57. (a) Röhl, W.; Brintzinger, H. H.; Rieger, B.; Zolk, R. *Angew. Chem. Int. Ed. Eng.* **1990**, *29*, 279. (b) Stehling, V.; Diebold, J.; Kirsten, R.; Röhl, W.; Brintzinger, H. H. *Organometallics* **1994**, *13*, 964.
58. Several data are collected in Ref. 11 and in Table 1 of Ref. 80.
59. Cavallo, L.; Corradini, P.; Guerra, G.; Resconi, L. *Organometallics* **1996**, *15*, 2254.
60. Veghini, D.; Henling, L. M.; Burkhardt, T. J.; Bercaw, J. E. *J. Am. Chem. Soc.* **1999**, *121*, 564.
61. Farina, M.; Di Silvestro, G.; Sozzani, P. *Macromolecules* **1993**, *26*, 946.
62. Ewen, J. A. *Macromol. Symp.* **1995**, *89*, 181.
63. Rieger, B.; Jani, G.; Fawzi, R.; Steiman, M. *Organometallics* **1994**, *13*, 647.
64. Guerra, G.; Cavallo, L.; Moscardi, G.; Vacatello, M.; Corradini, P. *Macromolecules* **1996**, *29*, 4834.
65. Ewen, J. A.; Elder, M. J.; Jones, R. L.; Curtis, S.; Cheng H. N. In *Catalytic Olefin Polymerization*. Keii, T.; Soga, K. (Eds.). Kodansha, Tokyo, 1990, p. 439.
66. For extensive reviews, see: (a) Butler, G. B. *Acc. Chem. Res.* 1982, *15*, 370. (b) Butler, G. B. In *Encyclopedia of Polymer Science and Engineering*, Vol. 4, 2nd ed. Kroschwitz, J. I. (Ed.). Wiley, New York, 1986, p. 543.

67. (a) Marvel, C. S.; Stille, J. K. *J. Am. Chem. Soc.* **1958**, *80*, 1740. (b) Marvel, C. S.; Garrison, W. E., Jr. *J. Am. Chem. Soc.* **1959**, *81*, 4737.
68. Makowski, H. S.; Shim, B. K. C.; Wilchinsky, Z. W. *J. Polym. Sci., Part A* **1964**, *2*, 1549.
69. Cheng, H. N.; Khasat, N. P. *J. Appl. Polym. Sci.* **1988**, *35*, 825.
70. (a) Resconi, L.; Waymouth, R. M. *J. Am. Chem. Soc.* **1990**, *112*, 4953. (b) Coates, G. W.; Waymouth, R. M. *J. Am. Chem. Soc.* **1991**, *113*, 6270. (c) Kesti, M. R.; Waymouth, R. M. *J. Am. Chem. Soc.* **1992**, *114*, 3565. (d) Coates, G. W.; Waymouth, R. M. *J. Mol. Catal.* **1992**, *76*, 189. (e) Coates, G. W.; Waymouth, R. M. *J. Am. Chem. Soc.* **1993**, *115*, 91.
71. Schaverien, C. J. *Organometallics* **1994**, *13*, 69.
72. Jeremic, D.; Wang, Q. Y.; Quyoum, R.; Baird, M. C. *J. Organometal. Chem.* **1995**, *497*, 143.
73. Mitani, M.; Oouchi, K.; Hayakawa, M.; Yamada, T.; Mukaiyama, T. *Chem. Lett.* **1995**, 905.
74. Structural characterization of crystalline phases of poly(methylene-1,3-cyclopentane) samples of different microstructures have also been reported: (a) Ruiz de Ballesteros, O.; Venditto, V.; Auriemma, F.; Guerra, G.; Resconi, L.; Waymouth, R. M.; Mogstad, A. L. *Macromolecules* **1995**, *28*, 2383. (b) Ruiz de Ballesteros, O.; Cavallo, L.; Auriemma, F.; Guerra, G. *Macromolecules* **1995**, *28*, 7355.
75. Cavallo, L.; Guerra, G.; Corradini, C.; Resconi, L.; Waymouth, R. M. *Macromolecules* **1993**, *26*, 260.
76. Grassi, A.; Zambelli, A.; Resconi, L.; Albizzati, E.; Mazzocchi, R. *Macromolecules* **1988**, *21*, 617.
77. Mizuno, A.; Tsutsui, T.; Kashiwa, N. *Polymer* **1992**, *33*, 254.
78. Busico, V.; Cipullo, R.; Malarico, G.; Segre, A. L.; Caporaso, L. *Macromolecules* **1998**, *31*, 8720.
79. (a) Caporaso, L.; Izzo, L.; Oliva, L. *Macromolecules* **1999**, *32*, 7323. (b) Caporaso, L.; Zappile, S.; Izzo, L.; Oliva, L. *Macromolecules* **2000**, *33*, 7275.
80. Guerra, G.; Longo, P.; Cavallo, L.; Corradini, P.; Resconi, L. *J. Am. Chem. Soc.* **1997**, *119*, 4394.
81. Zambelli, A.; Ammendola, P.; Grassi, A.; Longo, P.; Proto, A. *Macromolecules* **1986**, *19*, 2703.
82. Soga, K.; Shiono, T.; Takemura, S.; Kaminsky, W. *Makromol. Chem. Rapid Commun.* **1987**, *8*, 305.
83. Cheng, H.; Ewen, J. *Makromol. Chem.* **1989**, *190*, 1931.
84. Tsutsui, T.; Ishimaru, N.; Mizuno, A.; Toyota, A.; Kashiwa, N. *Polymer* **1989**, *30*, 1350.
85. Tsutsui, T.; Mizuno, A.; Kashiwa, N. *Makromol. Chem.* **1989**, *190*, 1177.
86. Rieger, B.; Mu, X.; Mallin, D.; Rausch, M.; Chien, J. *Macromolecules* **1990**, *23*, 3559.
87. Busico, V.; Cipullo, R. *J. Organometal. Chem.* **1995**, *497*, 113.
88. Spaleck, W.; Antberg, M.; Aulbach, M.; Bachmann, B.; Dolle, V.; Haftka, S.; Küber, F.; Rohrmann, J.; Winter, A. In *Ziegler Catalysts*. Fink, G.; Mühlhaupt, R.; Brintzinger, H. H. (Eds.). Springer-Verlag, Berlin, 1995, p. 83.
89. Razavi, A.; Vereeke, D.; Petres, L.; Den Davw, K.; Nafpliotis, L.; Atwood, J. L. In *Ziegler Catalysts*. Fink, G.; Mühlhaupt, R.; Brintzinger, H. H. (Eds.). Springer, Berlin, 1995, p. 111.
90. Toto, M.; Cavallo, L.; Corradini, P.; Moscardi, G.; Resconi, L.; Guerra, G. *Macromolecules* **1998**, *31*, 3431.

91. (a) Resconi, L.; Piemontesi, F.; Nifant'ev, I. E.; Ivichenko, P. V. *PCT Int. Appl.* **1996**, WO 9622995 A1. (b) Resconi, L.; Balboni, D.; Baruzzi, G.; Fiori, C.; Guidotti, S.; Mercandelli, P.; Sironi, A. *Organometallics* **2000**, *19*, 420.
92. Resconi, L.; Piemontesi, F.; Camurati, I.; Balboni, D.; Sironi, A.; Moret, M.; Rychlicki, H.; Ziegler, R. *Organometallics* **1996**, *15*, 5046.
93. Resconi, L.; Moscardi, G. *Polym. Prep.* **1997**, *38*, 832.
94. (a) Guerra, G.; Longo, P.; Corradini, P.; Cavallo, L. *J. Am. Chem. Soc.* **1999**, *121*, 8651. (b) Longo, P.; Grisi, F.; Guerra, G.; Cavallo, L. *Macromolecules* **2000**, *33*, 4647.
95. (a) Zambelli, A.; Locatelli, P.; Sacchi, M. C.; Crain, W. O., Jr.; Roberts, J. D. *Macromolecules* **1971**, *4*, 475. (b) Zambelli, A.; Zannoni, G.; Bovey, F. A. *Macromolecules* **1978**, *11*, 923.
96. Natta, G. *Inorg. Nucl. Chem.* **1958**, *8*, 589.
97. Natta, G.; Corradini, P.; Allegra, G. *J. Polym. Sci.* **1961**, *51*, 399.
98. Allegra, G. *Nuovo Cimento* **1962**, *23*, 502.
99. (a) Hargitay, B.; Rodriguez, L.; Miotto, M. *J. Polym. Sci.* **1959**, *35*, 599. (b) Rodriguez, L. A.; Gabant, A. *J. Polym. Sci. Part C* **1964**, *4*, 125.
100. Cavallo, L.; Guerra, G.; Corradini, P. *J. Am. Chem. Soc.* **1998**, *120*, 2428.
101. Corradini, P.; Barone, V.; Guerra, G. *Macromolecules* **1982**, *15*, 1242.
102. Kissin, Y. V.; Chirkov, N. M. *Eur. Polym. J.* **1970**, *6*, 525.
103. Corradini, P.; Guerra, G.; Barone, V. *Eur. Polym. J.* **1984**, *20*, 1177. See particularly Figures 6 and 9.
104. (a) Ammendola, P.; Guerra, G.; Villani, V. *Makromol. Chem.* **1984**, *185*, 2599. (b) Corradini, P.; Guerra, G.; Villani, V. *Macromolecules* **1985**, *18*, 1401.
105. (a) Zambelli, A.; Ammendola, P.; Sacchi, M. C.; Locatelli, P.; Zannoni, G. *Macromolecules* **1983**, *16*, 341. (b) Zambelli, A.; Ammendola, P.; Longo, P.; Grassi, A. *Gazz. Chim. Ital.* **1987**, *117*, 579.
106. Giannini, U.; Giunchi, G.; Albizzati, E. *NATO ASI Series, Series C: Mathematical and Physical Sciences* 1987, *215*, 473.
107. Auriemma, F.; Talarico, G.; Corradini, P. In *Progress and Development of Catalytic Olefin Polymerization*. Sano, T.; Uozumi, T.; Nakatani, H.; Terano, M. (Eds.). Technology and Education Publisher, Tokyo, 2000, p. 7.
108. Jones, P. J. V.; Oldman, R. J. In *Transition Metals and Organometallics as Catalysts for Olefin Polymerization*. Kaminsky, W.; Sinn, H. (Eds.). Springer, Berlin, 1988, p. 337.
109. Popatov, A. G.; Kriventsov, V. V.; Kochubey, D. I.; Bukatov, G. D.; Zakharov, V. A. *Macromol. Chem. Phys.* **1997**, *198*, 3477.
110. (a) Magni, E.; Somorjai, G. A. *Catal. Lett.* **1995**, *35*, 205. (b) Magni, E.; Somorjai, G. A. *Appl. Surf. Sci.* **1996**, *89*, 187. (c) Magni, E.; Somorjai, G. A. *Surf. Sci.* **1996**, *1*, 345. (d) Magni, E.; Somorjai, G. A. *J. Phys. Chem.* **1998**, *102*, 8788. (e) Koranyi, T. I.; Magni, E.; Somorjai, G. A. *Top. Catal.* **1999**, *7*, 179.
111. Hasebe, K.; Mori, H.; Terano, M. *J. Mol. Catal.* **1997**, *11*, 124.
112. (a) Mori, H.; Hasebe, K.; Terano, M. *Macromol. Chem. Phys.* **1998**, *199*, 2709. (b) Mori, H.; Sawada, M.; Higuchi, T.; Hasebe, K.; Otsuka, N.; Terano, M. *Macromol. Rapid Commun.* **1999**, *20*, 245.
113. (a) Chien, J. C. W.; Wu, J. C. *J. Polym. Sci., Part A: Polym. Chem.* **1982**, *20*, 2461. (b) Chien, J. C. W.; Hu, Y. *J. Polym. Sci., Part A: Polym. Chem.* **1989**, *27*, 897.

- (c) Weber, S.; Chien, J. C. W.; Hu, Y. *J. Polym. Sci., Part A: Polym. Chem.* **1989**, *27*, 1499.
114. Sergeev, S. A.; Polubayarov, V. A.; Zakharov, V. A.; Anufrienko, U. F.; Bukatov, G. D. *Makromol. Chem.* **1985**, *186*, 243.
115. (a) Brant, P.; Specca, A. N. *Macromolecules* **1987**, *20*, 2740. (b) Brant, P.; Specca, A. N.; Johnston, D. C. *J. Catal.* **1988**, *113*, 250.
116. Kashiwa, N.; Yoshitake, J. *Makromol. Chem.* **1984**, *185*, 1133.
117. Fuhrmann, H.; Herrmann, W. *Macromol. Chem. Phys.* **1994**, *195*, 3509.
118. Paukkeri, R. V. T.; Lehtinen, A. *Polymer* **1993**, *34*, 2488.
119. (a) Busico, V.; Corradini, P.; De Martino, L. *Makromol. Chem. Rapid Commun.* **1990**, *11*, 49. (b) Busico, V.; Cipullo, R.; Corradini, P.; Landriani, L.; Vacatello, M.; Segre, A. L. *Macromolecules* **1995**, *28*, 1887. (c) Busico, V.; Cipullo, R.; Talarico, G.; Segre, A. L.; Chadwick, J. C. *Macromolecules* **1997**, *30*, 4787. (d) Busico, V.; Cipullo, R.; Monaco, G.; Talarico, G.; Vacatello, M.; Chadwick, J. C.; Segre, A. L.; Sudmeijer, O. *Macromolecules* **1999**, *32*, 4173.
120. Randall, J. C. *Macromolecules* **1997**, *30*, 803.
121. (a) Puhakka, E.; Pakkanen, T. T.; Pakkanen, T. A. *Surf. Sci.* **1995**, *334*, 289. (b) Puhakka, E.; Pakkanen, T. T.; Pakkanen, T. A.; Iiskola, E. *J. Organometal. Chem.* **1996**, *19*, 511. (c) Puhakka, E.; Pakkanen, T. T.; Pakkanen, T. A. *J. Mol. Catal.* **1996**, *120*, 143. (d) Puhakka, E.; Pakkanen, T. T.; Pakkanen, T. A. *J. Chem. Phys.* **1997**, *101*, 6063. (e) Puhakka, E.; Pakkanen, T. T.; Pakkanen, T. A. *J. Mol. Catal.* **1997**, *123*, 171.
122. (a) Boero, M.; Parrinello, M.; Terakura, K. *J. Am. Chem. Soc.* **1998**, *120*, 2746. (b) Boero, M.; Parrinello, M.; Terakura, K. *Surf. Sci.* **1999**, *1*, 438. (c) Boero, M.; Parrinello, M.; Hüffer, S.; Weiss, H. *J. Am. Chem. Soc.* **2000**, *122*, 501.
123. Monaco, G.; Toto, M.; Guerra, G.; Corradini, P.; Cavallo, G. *Macromolecules* **2000**, *33*, 8953.
124. (a) Barino, L.; Scordamaglia, R. *Macromol. Symp.* **1995**, *89*, 111. (b) Barino, L.; Scordamaglia, R. *Macromol. Theory Simul.* **1998**, *7*, 407.
125. Iiskola, E.; Pelkonen, A.; Kakkonen, H.; Pursiainen, J.; Pakkanen, T. *Makromol. Chem. Rapid Commun.* **1993**, *14*, 133.
126. Barino, L.; Scordamaglia, R. *Macromol. Theory Simul.* **1998**, *7*, 399.
127. Toto, M.; Morini, G.; Guerra, G.; Corradini, P.; Cavallo, L. *Macromolecules* **2000**, *33*, 1134.
128. van der Linden, A.; Schaverien, C. J.; Meijboom, N.; Ganter, C.; Orpen, A. G. *J. Am. Chem. Soc.* **1995**, *117*, 3008.
129. Volkis, V.; Shmulinson, M.; Averbuj, C.; Lisovskii, A.; Edelman, F. T.; Eisen, M. S. *Organometallics* **1998**, *17*, 3155.
130. Tshuva, E. Y.; Goldberg, I.; Kol, M. *J. Am. Chem. Soc.* **2000**, *122*, 10706.
131. Resconi, L.; Abis, L.; Franciscano, G.; *Macromolecules* **1992**, *25*, 6814.
132. Erker, G.; Fritze, C. *Angew. Chem. Int. Ed. Eng.* **1992**, *31*, 199.
133. (a) Zambelli, A.; Tosi, C.; Sacchi, C. *Macromolecules* **1972**, *5*, 649. (b) Zambelli, A.; Locatelli, P.; Rigamonti, E. *Macromolecules* **1979**, *12*, 156.
134. Zambelli, A.; Allegra, G. *Macromolecules* **1980**, *13*, 42.
135. Ammendola, P.; Pellicchia, C.; Longo, P.; Zambelli, A. *Gazz. Chim. Ital.* **1987**, *117*, 65.

136. (a) Johnson, L. K.; Killian, C. M.; Brookhart, M. S. *J. Am. Chem. Soc.* **1995**, *117*, 6414. (b) Killian, C. M.; Templ, D. J.; Johnson, L. K.; Brookhart, M. *J. Am. Chem. Soc.* **1996**, *118*, 11664.
137. (a) Pellecchia, C.; Zambelli, A.; Oliva, L.; Pappalardo, D. *Macromolecules* **1996**, *29*, 6990. (b) Pellecchia, C.; Zambelli, A. *Macromol. Chem. Rapid Commun.* **1996**, *17*, 333. (c) Pellecchia, C.; Zambelli, A.; Mazzeo, M.; Pappalardo, D. *J. Mol. Catal. A: Chem.* **1998**, *128*, 229.
138. (a) Small, B. L.; Brookhart, M. *Polym. Prepr.* **1998**, *39*, 213. (b) Small, B. L.; Brookhart, M. *Macromolecules* **1999**, *32*, 2120.
139. Pellecchia, C.; Mazzeo, M.; Pappalardo, D. *Macromol. Chem. Rapid Commun.* **1998**, *19*, 651.
140. (a) Matsui, S.; Mitani, M.; Saito, J.; Tohi, Y.; Makio, H.; Matsukawa, N.; Takagi, Y.; Tsuru, K.; Nitabaru, M.; Nakano, T.; Tanaka, H.; Kashiwa, N.; Fujita, T. *J. Am. Chem. Soc.* **2001**, *123*, 6847. (b) Tian, J.; Coates, G. W. *Angew. Chem., Int. Ed.* **2000**, *39*, 3626. (c) Tian, J.; Hustad, P. D.; Coates, G. W. *J. Am. Chem. Soc.* **2001**, *123*, 5134.
141. (a) Lamberti, M.; Pappalardo, D.; Zambelli, A.; Pellecchia, C. *Macromolecules* **2002**, *35*, 658. (b) Milano, G.; Cavallo, L.; Guerra, G. *J. Am. Chem. Soc.* **2002**, *124*, 13368.
142. Venditto, V.; Guerra, G.; Corradini, P.; Fusco, R. *Polymer* **1990**, *31*, 530.
143. Milano, G.; Fiorello, G.; Guerra, G.; Cavallo, L. *Macromol. Chem. Phys.* **2002**, *203*, 1564.
144. Milano, G.; Guerra, G.; Pellecchia, C.; Cavallo, L. *Organometallics* **2000**, *19*, 1343.
145. Boor, J., Jr.; Youngman, E. A. *J. Polym. Sci., Part A1*, **1966**, *4*, 1861.
146. Takegami, Y.; Suzuki, T. *Bull. Chem. Soc. Jpn.* **1970**, *43*, 1484.
147. Corradini, P.; Guerra, G.; Pucciariello, R. *Macromolecules* **1985**, *18*, 2030.
148. Zambelli, A.; Pasquon, I.; Signorini, R.; Natta, G. *Makromol. Chem.* **1968**, *112*, 160.
149. Zambelli, A.; Sessa, I.; Grisi, F.; Fusco, R.; Accomazzi, P. *Macromol. Rapid Commun.* **2001**, *22*, 297.
150. Ishihara, N.; Seimiya, T.; Kuramoto, M.; Uoi, M. *Macromolecules* **1986**, *19*, 2464.
151. Ishihara, N.; Kuramoto, M.; Uoi, M. *Macromolecules* **1988**, *21*, 3356.
152. Ammendola, P.; Pellecchia, C.; Longo, P.; Zambelli, A. *Gazz. Chim. Ital.* **1987**, *117*, 65.
153. Guerra, G.; Vitagliano, V. M.; De Rosa, C.; Petraccone, V.; Corradini, P. *Macromolecules* **1990**, *23*, 1539.
154. Ewart, S. W.; Baird, M. C. In *Metallocene Based Polyolefins, Preparation, Properties and Technology*, Vol. 1. Scheirs, J.; Kaminsky, W. (Eds.). Wiley, New York, 2000, p. 119.
155. Ewart, S. W.; Baird, M. C. *Top. Catal.* **1999**, *7*, 1.
156. Pellecchia, C.; Grassi, A. *Top. Catal.* **1999**, *7*, 125.
157. Po, R.; Cardi, N. *Prog. Polym. Sci.* **1996**, *21*, 47.
158. Tomotsu, N.; Ishihara, N.; Newman, T. H.; Malanga, M. T. *J. Mol. Catal. A* **1998**, *128*, 167.
159. Chien, J. C. W.; Salajka, Z.; Dong, S. *Macromolecules* **1992**, *25*, 3199.
160. Grassi, A.; Pellecchia, C.; Oliva, L.; Laschi, F. *Macromol. Chem. Phys.* **1995**, *196*, 1093.
161. Grassi, A.; Zambelli, A.; Laschi, F. *Organometallics* **1996**, *15*, 480.
162. Grassi, A.; Saccheo, S.; Zambelli, A.; Laschi, F. *Macromolecules* **1998**, *31*, 5588.
163. Williams, E. F.; Murray, M. C.; Baird, M. C. *Macromolecules* **2000**, *33*, 261.
164. Pellecchia, C.; Pappalardo, D.; Oliva, L.; Zambelli, A. *J. Am. Chem. Soc.* **1995**, *117*, 6593.
165. Wang, Q.; Quyoum, R.; Gillis, D. J.; Tudoret, M.-J.; Jeremic, D.; Hunter, B. K.; Baird, M. C. *Organometallics* **1996**, *15*, 693.

166. Longo, P.; Grassi, A.; Proto, A.; Ammendola, P. *Macromolecules* **1988**, *21*, 24.
167. Pellecchia, C.; Longo, P.; Grassi, A.; Ammendola, P.; Zambelli, A. *Makromol. Chem. Rapid Commun.* **1987**, *8*, 277.
168. Zambelli, A.; Longo, P.; Pellecchia, C.; Grassi, A. *Macromolecules* **1987**, *20*, 2035.
169. Grassi, A.; Pellecchia, C.; Longo, P.; Zambelli, A. *Gazz. Chim. Ital.* **1987**, *117*, 249.
170. Longo, P.; Proto, A.; Zambelli, A. *Macromol. Chem. Phys.* **1995**, *196*, 3015.
171. Zambelli, A.; Pellecchia, C.; Oliva, L.; Han, S. *J. Polym. Sci.* **1988**, *26*, 365.
172. Minieri, G.; Corradini, P.; Zambelli, A.; Guerra, G.; Cavallo, L. *Macromolecules* **2001**, *34*, 2459.
173. Minieri, G.; Corradini, P.; Guerra, G.; Zambelli, A.; Cavallo, L. *Macromolecules* **2001**, *34*, 5379.
174. Porri, L.; Natta, G.; Gallazzi, M. C. *Chim. Ind. (Milan)* **1964**, *46*, 428.
175. Natta, G.; Porri, L.; Carbonaro, A.; Greco, A. *Makromol. Chem.* **1964**, *71*, 207.
176. Wilke, G.; Bogdanovich, B.; Hardt, P.; Heimbach, P.; Keim, W.; Kromer, M.; Oberkirch, W.; Tanaka, K.; Steinrucke, E.; Walter, D.; Zimmermann, H. *Angew. Chem. Int. Ed. Engl.* **1966**, *5*, 151.
177. Marconi, W. In *Stereochemistry of Macromolecules*, Vol. 1. Ketley, A. D. (Ed.). Dekker, New York, 1967, p. 239.
178. Natta, G.; Porri, L. In *Polymer Chemistry of Synthetic Elastomers*, Part II. Kennedy, J. P.; Tornquist, E. (Eds.). Wiley-Interscience, New York, 1969, p. 597.
179. Teyssie, P.; Dawans, F. In *The Stereo Rubbers*. Saltman, W. M. (Ed.). Wiley, New York, 1977, p. 79.
180. Porri, L. In *Structural Order in Polymers*. Ciardarelli, F.; Giusti, P. (Eds.). Pergamon, Oxford, 1981, p. 51.
181. Porri, L.; Giarrusso, A. In *Comprehensive Polymer Science*, Vol. 4, Part II. Eastmond, G. C.; Ledwith, A.; Russo, S.; Sigwalt, P. (Eds.). Pergamon, Oxford, 1989, p. 53.
182. Porri, L.; Giarrusso, A.; Ricci, G. *Prog. Polym. Sci.* **1991**, *16*, 405.
183. Taube, R.; Windisch, H.; Maiwald, S. *Macromol. Symp.* **1995**, *89*, 393.
184. Woo, T.; Fan, L.; Ziegler, T. *Organometallics* **1994**, *13*, 2252.
185. Tobish, S.; Bögel, H.; Taube, R. *Organometallics* **1996**, *15*, 3563.
186. Guerra, G.; Cavallo, L.; Corradini, P.; Fusco, R. *Macromolecules* **1997**, *30*, 677.
187. Peluso, A.; Improta, R.; Zambelli, A. *Organometallics* **1998**, *19*, 411.
188. Natta, G.; Giannini, U.; Pino, P.; Cassata, A. *Chim. Ind. (Milan)* **1965**, *47*, 525.
189. Taube, R.; Wache, S.; Sieler, J. *Organometal. Chem.* **1993**, *459*, 335.
190. Ciajolo, R.; Jama, M. A.; Tuzi, A.; Vitagliano, A. *J. Organometal. Chem.* **1985**, *295*, 233.
191. Corradini, P.; Guerra, G.; Jama, M. A.; Zhi, G.; Tuzi, A. *Polym. Commun.*, **1985**, *26*, 175.
192. Allegra, G.; Lo Giudice, F.; Natta, G.; Giannini, U.; Fagherazzi, G.; Pino, P. *Chem. Commun.* **1967**, 1263.
193. Costabile, G.; Milano, G.; Cavallo, L.; Guerra, G. *Macromolecules*. **2001**, *34*, 7952.
194. Longo, P.; Oliva, P.; Proto, A.; Zambelli, A. *Gazz. Chim. Ital.* **1996**, *126*, 377.
195. Zambelli, A.; Caprio, M.; Grassi, A.; Bowen, D. E. *Macromol. Chem. Phys.* **2000**, *201*(4), 393.
196. Ricci, G.; Porri, L.; Giarrusso, A. *Macromol. Symp.* **1995**, *89*, 383.
197. Ricci, G.; Italia, S.; Porri, L. *Macromolecules* **1994**, *27*, 868.

Chapter 2

Chain Conformation, Crystal Structures, and Structural Disorder in Stereoregular Polymers

CLAUDIO DE ROSA

*Dipartimento di Chimica, Università di Napoli "Federico II" Complesso
Monte S. Angelo, Via Cintia, 80126 Napoli, Italy*

- 1 Constitution and Configuration of Crystalline Polymers
 - 2 Conformation of Polymer chains in Crystalline State
 - 2.1 Basic Principles
 - 2.2 Helical Conformations in Isotactic and Syndiotactic Polymers
 - 2.3 Conformational Energy Calculations in Isotactic and Syndiotactic Polymers
 - 2.4 Helical Conformation and Optical Activity
 - 2.5 Polydienes
 - 2.6 Disordered Conformations
 - 2.7 Alternating Copolymers
 - 3 Packing of Macromolecules in Polymer Crystals
 - 3.1 General Principles
 - 3.2 Symmetry Breaking
 - 3.3 Frustrated Polymer Crystal Structures
 - 3.4 Disorder in Polymer Crystals
 - 3.5 Examples of Positional Disorder with Long-Range Three-Dimensional Periodicity Maintained Only for Some Characterizing Points of Structure
 - 3.5.1 Disorder in Positioning of Right- and Left-Handed Helical Chains
 - 3.5.2 Disorder in Positioning of Up and Down Chains
 - 3.5.3 Disorder in Stacking of Ordered Layers of Macromolecules Along One Lattice Direction
 - 3.5.4 Conformational Kink-Band Disorder
 - 3.6 Solid Mesomorphic Forms
 - 3.7 Chiral Crystallization of Polymers with Helical Chain Conformations
- References

Materials-Chirality: Volume 24 of Topics in Stereochemistry,
Edited by Mark M. Green, R.J.M. Nolte, and E.W. Meijer
ISBN 0-471-05497-6 Copyright © 2003 John Wiley & Sons, Inc.

1 CONSTITUTION AND CONFIGURATION OF CRYSTALLINE POLYMERS

The crystalline state is characterized by the presence of three-dimensional order. It is well known that the general requirement for the crystallizability of polymers is the regularity in the chemical constitution and in the configuration of long sequences of monomeric units.^{1,2} This implies that, for long sequences of polymerized monomers, all the repeating units have the same chemical structure. In addition, whenever a monomeric unit may assume different configurations, the succession of configurations must be regular.

Copolymers of different monomeric units which are able to cocrystallize in the same lattice may be considered as possible exceptions to the need of the regularity in the chemical constitution. For instance, in the case of vinyl polymers it is possible to accommodate into the crystalline lattice different comonomeric units having lateral groups with different shape and dimensions. Copolymers of butene and 3-methylbutene³ or copolymers of styrene and *o*-fluorostyrene⁴ are crystalline in the whole range of composition, provided that the copolymers are isotactic, whereas propene and 1-butene comonomeric units are able to cocrystallize at any composition in syndiotactic copolymers.^{5,6} Isomorphism of comonomeric units also occurs in copolymers of acetaldehyde and *n*-butyraldehyde, which are crystalline over the whole range of composition.⁷ Analogous isomorphism of comonomeric units has been observed in *trans*-1,4-copolymers of butadiene and 1,3-pentadiene⁸ or in copolymers of vinylidene fluoride and vinyl fluoride.⁹ These examples indicate that the requirement concerning the regularity in the configuration (stereoregularity) is more stringent than those concerning the regularity in the chemical constitution in order for a polymer be crystalline.¹ However, it has been recently clarified that even stereoirregular polymers are able to crystallize. The role played by the disorder in the crystallization of polymers will be discussed in the next sections.

The formation of chiral objects, such as macromolecules in helical conformations, from nonchiral monomers as a consequence of the stereospecific polymerization¹⁰ is strictly related to the regularity of the configuration of the stereoisomeric centers along the chain. A useful way of classifying the possible configurations is associated with the chirality of the chemical bonds rather than that of the atoms.¹ Let l_1 and l_2 be two bonds adjacent to the carbon atom C_i , which carries two different substituents R_1 and R_2 (Figure 2.1). The two bonds l_1 and l_2 are chiral even though the carbon atom C_i is not asymmetric. A bond adjacent to a stereoisomeric center C_i along a chain $C_{i-1}-C_i-C_{i+1}$ is defined with a (+) sign when, looking along the $C_{i-1}-C_i$ or $C_{i+1}-C_i$ bond, we see the substituents R_1, R_2, C_{i+1} or R_1, R_2, C_{i-1} succeeding each other clockwise,¹ with the convention that R_1 is bulkier than R_2 ¹¹ (Figure 2.1). If

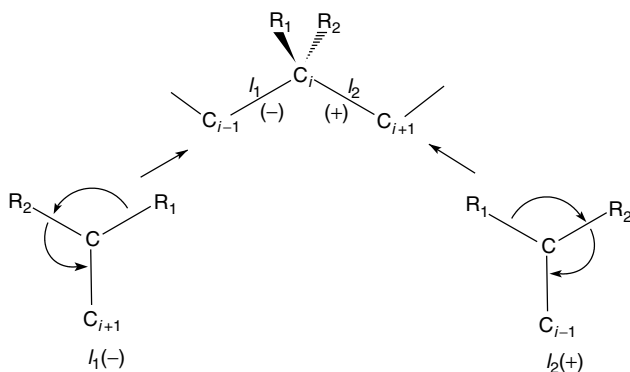


Figure 2.1 Definition of (-) and (+) bonds adjacent to tetrahedral stereoisomeric center.

these substituents succeed each other counterclockwise, the bond is defined with the (-) sign.¹ It is apparent from Figure 2.1 that if the bond l_1 has a (+) character with respect to the stereoisomeric center C_i , l_2 must have a (-) character and vice versa. Two monomeric units have the same configuration if the bonds adjacent to the tetrahedral stereoisomeric centers are characterized by the same (+) and (-) character; they are enantiomorphous if the signs (+) and (-) are reversed (Figure 2.2a).¹ The stereoregularity of a polymer chain implies a regular succession of couples of (+) and (-) bonds. Isotactic polymers are characterized by a regular enchainment of monomeric units having the same configuration, hence by a regular succession of (+) and (-) bonds (Figure 2.2b). Syndiotactic polymers are characterized by a regular enchainment of monomeric units having alternatively enantiomorphous configurations, which produces couples of adjacent bonds having the same sign (Figure 2.2c).¹

Although the definitions of isotactic, syndiotactic, and atactic polymers according to International Union of Pure and Applied Chemistry (IUPAC) rules are well established in terms of succession of *meso* (m) or *racemic* (r) dyads,¹² the symbolism of (+) and (-) bonds allows the easy treatments of possible configurations in cases of any complexity.¹ Moreover, the (+) or (-) character of the bonds in a polymer chain is strictly related to the accessibility of *gauche*⁺ or *gauche*⁻ conformations of the bonds and, therefore, to the formation of right-handed or left-handed helical conformations.¹

When a monomeric unit contains more than one tetrahedral stereoisomeric center, the relative configuration of the centers has to be defined. In the case of two adjacent stereoisomeric centers, for instance, $-\text{CHA}-\text{CHB}-$, with $A \neq B$, two configurational signs can be assigned to the bonds connecting the centers (Figure 2.3a). The pairs (+, +) or (-, -) define a relative *threo* configuration,

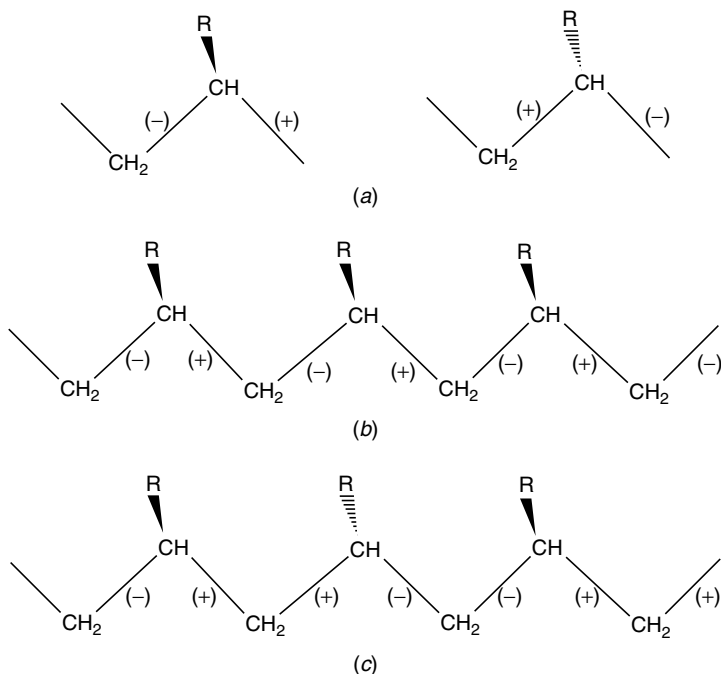


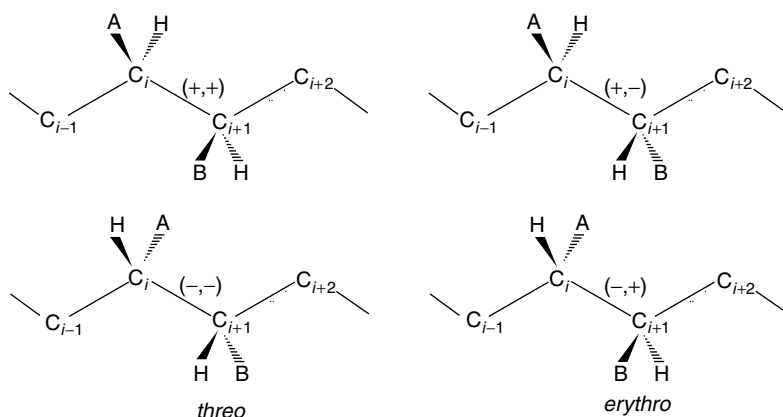
Figure 2.2 (a) Vinyl units with enantiomorphous configurations and sequences of (+) and (-) bonds in (b) isotactic and (c) syndiotactic polymers.

whereas the pairs $(-, +)$ or $(+, -)$ define a relative *erythro* configuration¹ (Figure 2.3a). Stereoregular polymers of the kind $-(\text{CHA}-\text{CHB})_n-$ may be ditactic.¹³ A regular alternating succession of $(+, +)$ and $(-, -)$ bonds corresponds to a *threo* diisotactic polymer, the regular succession of $(+, -)$ bonds corresponds to the *erythro* diisotactic polymer, and the succession $\dots(-, -)(+, -)(+, +)(-, +)\dots$ corresponds to the syndiotactic polymer (Figure 2.3b).^{12,13}

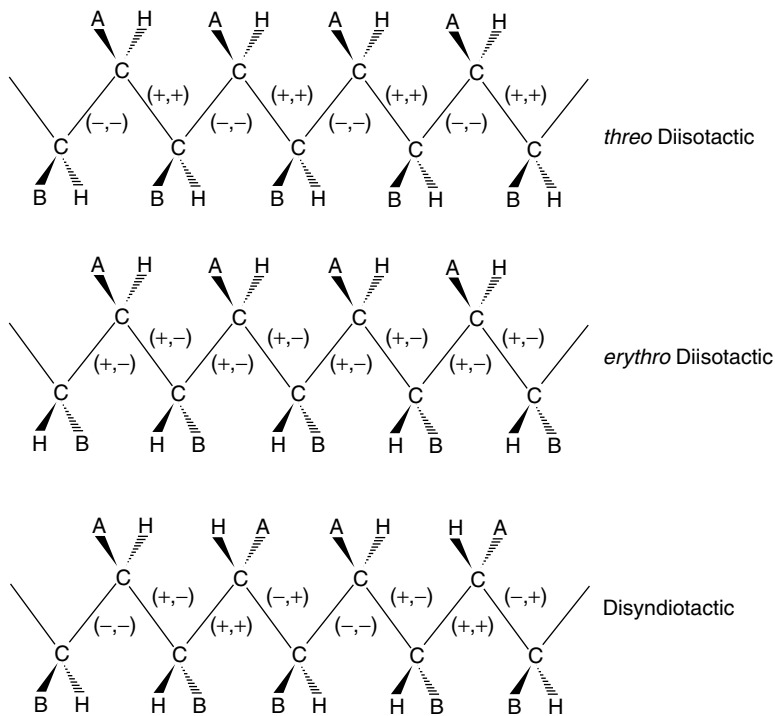
2 CONFORMATION OF POLYMER CHAINS IN CRYSTALLINE STATE

2.1 Basic Principles

The conformation assumed by polymer chains in the crystalline state depends on the configuration of the stereoisomeric centers present along the chains and is defined by two basic principles^{1,2,14-16}:



(a)



(b)

Figure 2.3 (a) The *threo* and *erythro* relative configurations and (b) succession of (+) and (-) bonds in *threo*-diisotactic, *erythro*-diisotactic, and disyndiotactic polymers.

1. *Equivalence Principle.* The conformation of a polymer chain in the crystalline state is defined by a succession of equivalent structural units which occupy geometrically (not necessarily crystallographically) equivalent positions with respect to the chain axis. The chain axis is parallel to a crystallographic axis of the crystal.
2. *Principle of Minimum Internal Conformational Energy.* The conformation of a polymer chain in a crystal approaches one of the minima of the internal conformational energy, which would be taken by an isolated chain subjected to the restrictions imposed by the equivalence principle.

The necessary geometrical equivalence of structural units along an axis allows defining the possible types of geometrical symmetry that a linear macromolecule may achieve in the crystalline state. The conformation of a macromolecule is generally defined in terms of its symmetry and, precisely, of the line repetition symmetry group.^{1,12,17} Thirteen line repetition groups have been defined.¹ The possible symmetry elements for a chain conformation must be compatible with the chemical constitution and configuration. For instance, the screw (*s*) and the glide plane (*c*) symmetries corresponding to the line repetition groups $s(M/N)$, $s(M/N)2$, tc , and tc_m are the only ones possible for a vinyl polymer.¹⁸ The screw repetition of M structural units in N turns of the helix is characterized by a rotation of $t = 2\pi(N/M)$ (unit twist) around the chain axis (*c*) and by a translation of $h = c/M$ (unit height) along the chain axis. The chain symmetry $s(M/N)$ is compatible only with an isotactic configuration, whereas the line repetition symmetries $s(M/N)2$, tc , and tc_m are compatible only with a syndiotactic configuration.¹

Polymers showing crystalline mesomorphic modifications, characterized by chains in disordered conformations, are exceptions to the equivalence principle. Examples of these cases are shown in Section 2.6.

Once the symmetry of the chain of a crystalline polymer having a given regular configuration has been assigned using the equivalence principle, the actual conformation assumed by the chain is determined by energetic factors, as defined by the principle of minimum internal conformational energy. In saturated molecules, the bond orientation effect favors staggered conformations of the bonds (*trans* and *gauche*).¹⁹ Deviations from staggered conformations can be induced by intramolecular interactions between neighboring atoms, as in isotactic polymers with bulky side groups. Packing effects generally do not influence the conformation of the chains as long as the conformational energy of the isolated chain corresponds to a deep energy minimum. When the energy differences between different conformations of an isolated chain are low, the intermolecular interactions may influence the choice of the conformation in the crystal.

The helical conformations found in the crystals of isotactic polymers may be easily justified by the application of these principles. In the case of isotactic polypropylene (iPP), the configuration corresponds to an alternating succession of (+) and (-) bonds (Figure 2.4a). If θ_1 and θ_2 are the torsion angles of two successive bonds of the chain, the equivalence principle imposes that successive monomeric units take equivalent conformations in the crystalline state and hence successive bonds assume the same torsion angles θ_1 and θ_2 . According to the principle of the staggered bonds, the torsion angles θ_1 and θ_2 tend to be *trans* (T) or *gauche* (G). Intramolecular interactions impose some well-established constraints¹; in particular, (+) bonds tend to assume only G⁺ or T conformations, whereas (-) bonds tend to assume only G⁻ or T conformations.¹ Moreover, G⁺ bonds cannot be followed by G⁻ bonds, and the pair of torsion angles θ_1 and θ_2 adjacent to a methylene carbon atom cannot

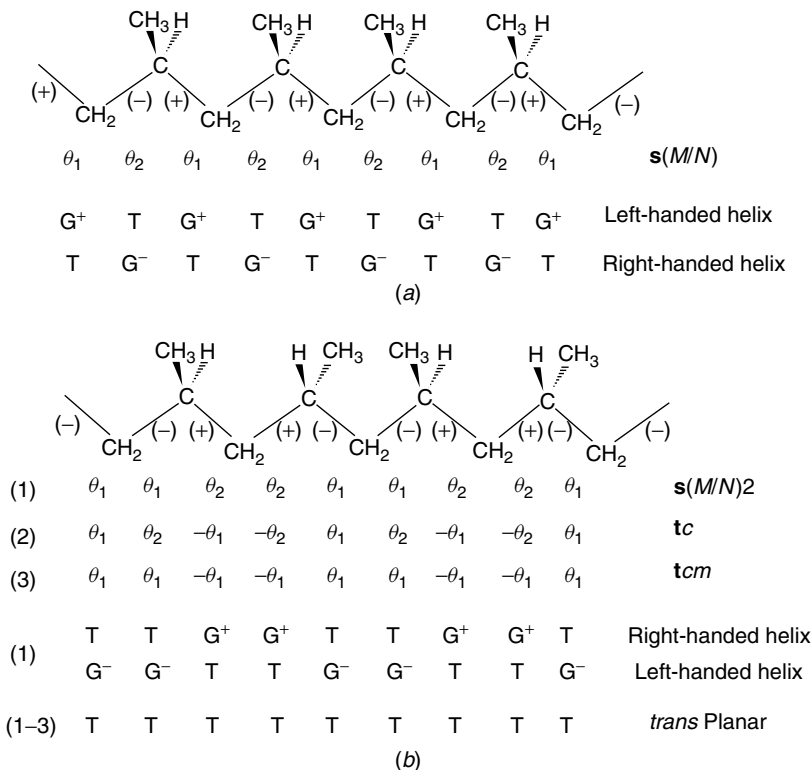


Figure 2.4 Line repetition symmetries, according to equivalence principle, and corresponding possible conformations, according to minimum conformational energy, for (a) isotactic and (b) syndiotactic polypropylene (T = *trans*, G = *gauche*).

be TT for an isotactic polymer and cannot be TG or GT for a syndiotactic polymer. These conditions impose that the only possible conformations for isotactic polypropylene are $(TG^-)_n$ and $(G^+T)_n$, corresponding to right-handed and left-handed threefold helical conformations, respectively.²⁰

In the case of syndiotactic polypropylene (sPP), the configuration corresponds to an alternating succession of couples of (+), (+) and (-), (-) bonds (Figure 2.4*b*). If θ_1 and θ_2 are the torsion angles of two successive bonds of the chain, the equivalence principle imposes that the only possible successions of torsion angles are those shown in Figure 2.4*b*, $\dots\theta_1\bullet\theta_1|\theta_2\bullet\theta_2|\theta_1\bullet\theta_1|\theta_2\bullet\theta_2\dots\dots$, $\dots\theta_1\bullet\theta_2|-\theta_1\bullet-\theta_2|\theta_1\bullet\theta_2|-\theta_1\bullet-\theta_2\dots\dots$, and $\dots\theta_1\bullet\theta_1|-\theta_1\bullet-\theta_1|\theta_1\bullet\theta_1|-\theta_1\bullet-\theta_1\dots\dots$, corresponding to the $s(M/N)2$, tc , and tc_m symmetries (dots and vertical bars indicate placement of CH₂ and CH groups, respectively). In the $s(M/N)2$ symmetry two successive monomeric units are related by a twofold rotation axis perpendicular to the chain axis centered on the methylene carbon atoms. According to the principle of minimum conformational energy, the possible conformations are $(TTG^+G^+)_n$ and $(G^-G^-TT)_n$, corresponding to right-handed and left-handed twofold helical conformations, respectively, found in the crystals of the most stable polymorphic forms of sPP,^{21,22} and $(TTTT)_n$, corresponding to the *trans* planar conformation.^{23,24} In the tc and tc_m symmetries two successive monomeric units are related by a glide plane parallel to the chain axis, so that the torsion angles θ_1 and θ_2 in two successive monomeric units have opposite values. When a mirror plane perpendicular to the chain axis, crossing the methine carbon atom, is also present (tc_m symmetry), $\theta_2 = \theta_1$. Since G^+G^- and TG successions are forbidden, the minimum conformational energy principle imposes that, for the tc and tc_m symmetries, the only possible conformation is $(TTTT)_n$, corresponding to the fully extended *trans* planar conformation (Figure 2.4*b*).

2.2 Helical Conformations in Isotactic and Syndiotactic Polymers

Interesting geometrical differences between helical conformations in isotactic and syndiotactic polymers have recently been found.²⁵⁻²⁷

Maps of the values of the unit twist ($|t|$) and unit height (h) as a function of the torsion angles θ_1 and θ_2 , are reported for generic isotactic [$s(M/N)$ symmetry] and syndiotactic [$s(M/N)2$ symmetry] vinyl polymers in Figures 2.5 and 2.6, respectively. It is apparent that only one set of symmetry-related curves corresponds to any given value of the unit twist $|t|$ (different from 180°) for the isotactic polymer, while there are two such sets for the syndiotactic polymers.²⁷

The curves corresponding to a given $|t|$ value (like those of Figure 2.5) generally intersect the curves corresponding to a given h value (like those of Figure 2.6) into four different points for isotactic polymers and into eight points for syndiotactic polymers. These intersection points correspond to one

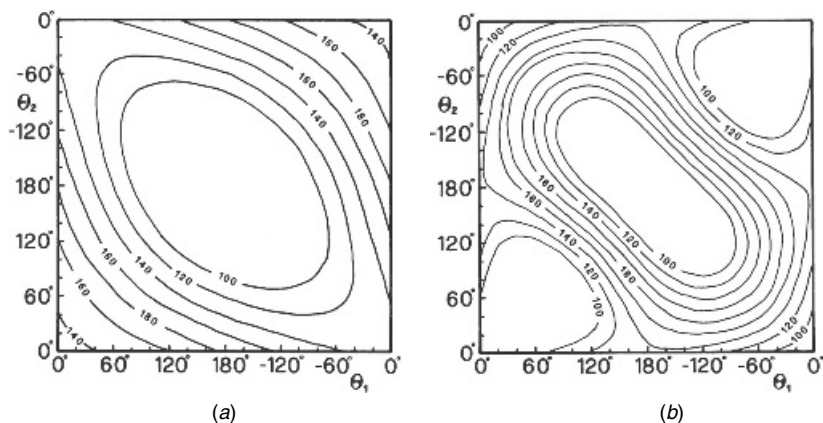


Figure 2.5 Maps of absolute value of unit twist $|t|$ as function of backbone torsion angles θ_1 and θ_2 for (a) isotactic and (b) syndiotactic polymers.²⁷ Curves corresponding to $|t| = 180^\circ, 160^\circ, 140^\circ, 120^\circ, 100^\circ$ are reported. (Reproduced with permission from Ref. 27. Copyright 1992 by the Società Chimica Italiana.)

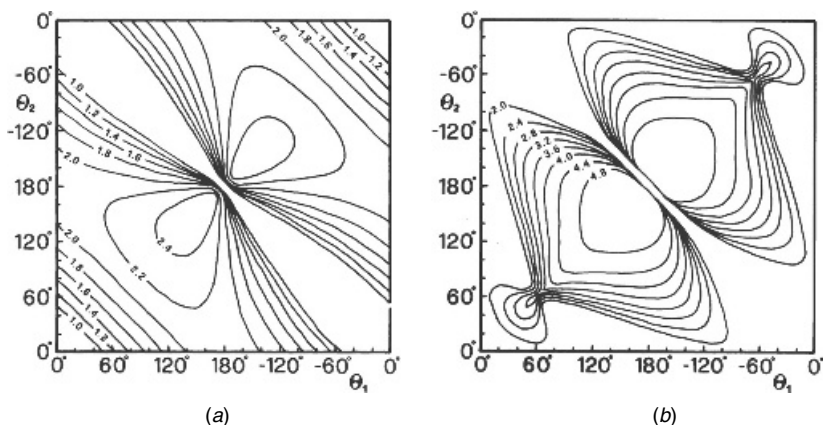


Figure 2.6 Maps of unit height h as function of backbone torsion angles θ_1 and θ_2 for (a) isotactic and (b) syndiotactic polymers.²⁷ Curves corresponding to values of unit height h in the range 1.0–2.4 Å for isotactic polymers and in the range 2.0–4.8 Å for syndiotactic polymers are reported. (Reproduced with permission from Ref. 27. Copyright 1992 by the Società Chimica Italiana.)

set or two sets (for isotactic and syndiotactic polymers, respectively) of four pairs of dihedral angles of the kind:

- (a) (θ_1, θ_2) (b) (θ_2, θ_1)
 - (ā) $(-\theta_2, -\theta_1)$ (b̄) $(-\theta_1, -\theta_2)$
- 1**

The pairs of torsion angles (\bar{a}) and (\bar{b}) correspond to chains which are enantiomorphous with respect to the chains corresponding to the pairs (a) and (b), respectively.

As an example, for a generic isotactic polymer, the curves corresponding to $|t| = 144^\circ$ and $h = 2.0 \text{ \AA}$ are reported in Figure 2.7a; analogously, for a generic syndiotactic polymer, the curves corresponding to $|t| = 144^\circ$ and $h = 4.0 \text{ \AA}$ are reported in Figure 2.7b. The latter h and $|t|$ values are those found for the chain conformation of form II of syndiotactic poly(1-butene) (sPB).^{25,28} For the isotactic polymer (Figure 2.7a), there are four intersection points corresponding to the four conformations indicated in **1** with $\theta_1 = 28^\circ$, $\theta_2 = -156^\circ$. The two conformations (a) (with $\theta_1 = 28^\circ$, $\theta_2 = -156^\circ$) and (b) (with $\theta_1 = -156^\circ$, $\theta_2 = 28^\circ$) are geometrically equivalent because they correspond to energy minima for two possible equivalent configurations of the isotactic chain, shown in the Schemes 2.1a,b, respectively.

Hence, without loss of generality, we can consider only the chain of the Scheme 2.1a and the enantiomorphous helices corresponding to the intersections (a) and (\bar{a}), which are shown in Figure 2.8.

By associating two vectors perpendicular to the chain axis, having origin on the chain axis and crossing two consecutive methylene carbon atoms, it is immediately apparent that the helix with conformation (a) ($\theta_1 = 28^\circ$, $\theta_2 = -156^\circ$) is characterized by a unit twist $t = 216^\circ = -144^\circ$, while the helix with conformation (\bar{a}) ($\theta_1 = 156^\circ$, $\theta_2 = -28^\circ$) is characterized by $t = 144^\circ$.

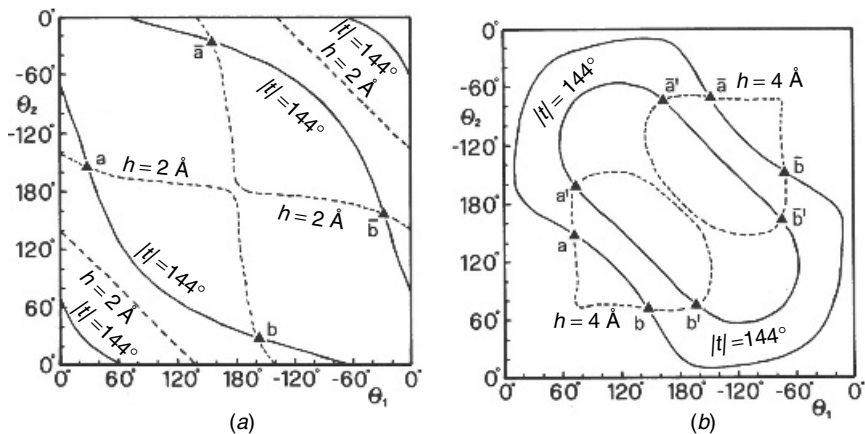
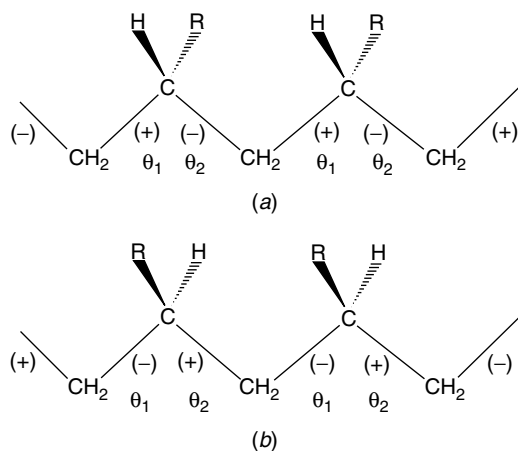


Figure 2.7 Maps as function of backbone torsion angles θ_1 and θ_2 of loci of points for which absolute value of unit twist $|t|$ is equal to 144° (continuous lines) and unit height h is (a) 2.0 \AA for an isotactic polymer and (b) 4.0 \AA for a syndiotactic polymer (dashed lines). Intersection points are indicated by triangles.²⁷ (Reproduced with permission from Ref. 27. Copyright 1992 by the Società Chimica Italiana.)



Scheme 2.1

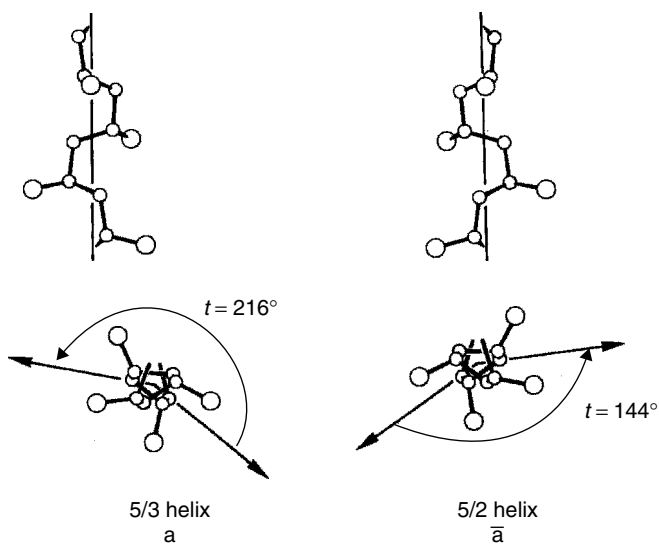
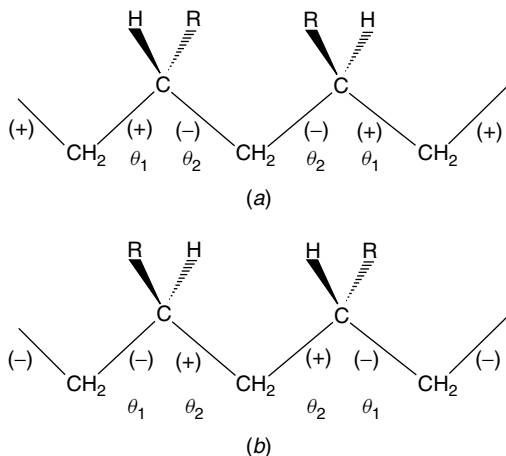


Figure 2.8 Side views and projections along chain axis of two enantiomorphous hypothetical helices of isotactic polymer having unit height of 2 Å and unit twist $|t| = 144^\circ$, corresponding to intersection points of Figure 2.7a: a, left-handed helix with $s(5/3)1$ symmetry and $t = -144^\circ = 216^\circ$; \bar{a} , right-handed helix with $s(5/2)1$ symmetry and $t = 144^\circ$.²⁷ (Reproduced with permission from Ref. 27. Copyright 1992 by the Società Chimica Italiana.)

The helix (a) is therefore left handed with $5/3$ symmetry ($t = 2\pi 3/5$), whereas the helix (\bar{a}) is right-handed with $5/2$ symmetry ($t = 2\pi 2/5$). A right-handed helix grows along the chain axis counterclockwise, whereas a left-handed helix grows clockwise. According to this convention, for a helix $s(M/N)$, the unit twist $t = 2\pi N/M$ should be defined as the angle of the counterclockwise rotation to go from an atom with coordinate $z = z_0$ to the helically equivalent atom having coordinate $z = z_0 + h$, where h is the unit height $h = c/M$. In Figure 2.8, the right-handed screw sense of the main-chain carbon atom bonds is associated with a value of t lower than 180° , $t = 2\pi 2/5 = 144^\circ$, and, hence, with a $5/2$ symmetry. In the case of the left-handed helix, in order to go from an atom at $z = z_0$ to the corresponding atom related by the helix operator, it is necessary to rotate in the same direction by an angle higher than 180° , $t = 216^\circ$. This implies that a complete repetition occurs after three counterclockwise turns of the helix (Figure 2.8). Therefore, the left-handed screw sense is associated with $t = 2\pi 3/5 = 216^\circ$ and the $5/3$ symmetry.

For the syndiotactic polymer [$s(M/N)2$ symmetry], in Figure 2.7b there are eight intersection points (a), (\bar{a}), (a'), (\bar{a}'), (b), (\bar{b}), (b'), and (\bar{b}'), corresponding to two nonequivalent sets of conformations of the kind **1** with (a) $\theta_1 = 72^\circ$, $\theta_2 = 147^\circ$ and (a') $\theta_1 = 74^\circ$, $\theta_2 = -164^\circ$.

Also in this case the conformations (a) and (a') are energetically feasible for the chirality of the bonds present in the chain of Scheme 2.2a, while the conformations (b) and (b') are feasible for the chirality of the bonds in the Scheme 2.2b. Therefore, the conformations (b) and (b') can be disregarded because the configurations of the two chains of Scheme 2.2 are



Scheme 2.2

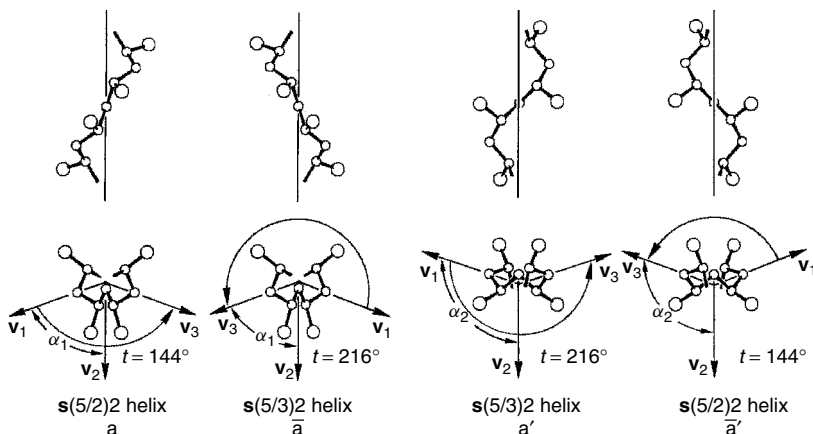


Figure 2.9 Side views and projections along chain axis of helices of syndiotactic polymer having unit height of 4.0 Å and unit twist $|t| = 144^\circ$ observed for form II of syndiotactic poly(1-butene),^{25,28} corresponding to intersection points of Figure 2.7b: a, right-handed helix with $s(5/2)2$ symmetry ($t = 144^\circ$ and $\alpha_1 = 72^\circ$); \bar{a} , left-handed helix with $s(5/3)2$ symmetry ($t = 216^\circ$, $\alpha_1 = 72^\circ$); a' , left-handed helix with $s(5/3)2$ symmetry ($t = 216^\circ$ and $\alpha_2 = 108^\circ$); \bar{a}' , right-handed helix with $s(5/2)2$ symmetry ($t = 144^\circ$ and $\alpha_2 = 108^\circ$).²⁷ (Reproduced with permission from Ref. 27. Copyright 1992 by the Società Chimica Italiana.)

equivalent. Hence, without loss of generality, we can consider only the chain of Scheme 2.2a and the pair of enantiomorphous helices corresponding to the intersections (a), (\bar{a}) and (a'), (\bar{a}') reported in Figure 2.9.

It is apparent from Figure 2.9 that the two pairs of enantiomorphous helices (a), (\bar{a}) and (a'), (\bar{a}') are not geometrically equivalent. While for isotactic polymers there exists only one pair of M/N and $M/(M - N)$ enantiomorphous helices, corresponding to defined values of unit twist and unit height, for syndiotactic polymers two different pairs of helices exist, corresponding to the same values of unit twist and unit height. If unit twist is defined as the angle of counterclockwise rotation to go from an atom with coordinate $z = z_0$ to the helically equivalent atom having coordinate $z = z_0 + h$, as for isotactic polymers, the difference between these pairs of helices can be evidenced in the following way.

For a $s(M/N)2$ symmetry the structural units related by the helical symmetry correspond to two monomeric units, which, in turn, are related by twofold rotation axes perpendicular to the chain axis and crossing the methylene carbon atoms. Let us associate vectors along these twofold axes having directions which bisect alternatively the H–C–H bond angle (\mathbf{v}_1 and \mathbf{v}_3 in Figure 2.9) and the C–C–C bond angle at the methylene carbon atoms (\mathbf{v}_2 in Figure 2.9). Let α be the angle between two successive twofold axes (\mathbf{v}_1 and \mathbf{v}_2 in Figure 2.9). The unit twist t is the angle between two corresponding atoms

of neighboring structural units, that is, the angle between two consecutive twofold axes connected by the helix symmetry (\mathbf{v}_1 and \mathbf{v}_3 in Figure 2.9). The relationship between the unit twist t and the angle α is either $t = 2\alpha$ or $t = 360 - 2\alpha$, depending on the relative orientation of the twofold axes and on the values of unit twist. According to the definition of unit twist, it is apparent that the conformations (a) and (\bar{a}) are enantiomorphous helices. The conformation (a) has $t = 144^\circ$ and $\alpha_1 = t/2 = 72^\circ$ and therefore is a right-handed 5/2 helix, whereas the conformation (\bar{a}) has $t = 216^\circ$, $\alpha_1 = (360 - t)/2 = 72^\circ$ and is a left-handed 5/3 helix. The conformations (a') and (\bar{a}') are another pair of enantiomorphous 5/3 and 5/2 helices, respectively, characterized by a different value of α . The conformation (a') has $t = 216^\circ$ and $\alpha_2 = t/2 = 108^\circ$ and therefore is a left-handed 5/3 helix, whereas the conformation (\bar{a}') has $t = 144^\circ$, $\alpha_2 = (360 - t)/2 = 108^\circ$ and is a right-handed 5/2 helix. Therefore, for syndiotactic polymers there exist two different M/N helical conformations characterized by different values of backbone torsion angles but the same values of unit twist and unit height and hence the same number of structural units M and turns N of the helix per chain repeat. The only difference is related to the different orientation of two successive twofold axes perpendicular to the chain axis, that is, the different values of α (Figure 2.9).

The four kinds of helices defined in terms of M structural units (M repeating pairs of monomeric units) in N turns can be differentiated with reference to the screwing of the single monomeric units. In fact, a (5/2)2 helix may have 10 monomeric units in two (10/2 helix) or seven (10/7 helix) turns, and a (5/3)2 helix may have 10 monomeric units in three (10/3 helix) or eight (10/8 helix) turns. With reference to Figure 2.9 we note that, looking at the CH atoms, the right-handed 5/2 helix (a) may be considered as having a mean twist angle $t = \alpha_1 = 360(2/10) = 72^\circ$ and then 10 monomeric units in two turns, while the right-handed 5/2 helix (a') may be considered as having a mean twist angle $t = \alpha_2 = 360(7/10) = 252^\circ = -108^\circ$ and then 10 monomeric units in seven turns. The left-handed 5/3 helix (\bar{a}) may be considered as having a mean twist angle $t = \alpha_1 = 360(8/10) = 288^\circ = -72^\circ$ and then 10 monomeric units in eight turns, while the left-handed 5/3 helix (a') may be considered as having a mean twist angle $t = \alpha_2 = 360(3/10) = 108^\circ$ and then 10 monomeric units in three turns.

2.3 Conformational Energy Calculations in Isotactic and Syndiotactic Polymers

The conformation of the chains of isotactic polymers in the crystalline state is generally helical and corresponds to a succession of nearly *trans* and *gauche* torsion angles, the exact values depending on the bulkiness of the side groups. Molecular mechanics calculations have been extensively used for the prediction of the chain conformation of polymers in the crystal.²⁹

Calculations of the conformational energy are performed according to the equivalence principle and, as a consequence, a succession of backbone torsion angles $\dots\theta_1\theta_2\theta_1\theta_2\theta_1\theta_2\dots$ is generally assumed for isotactic polymers.

The conformational energy maps as a function of the torsion angles θ_1 and θ_2 for iPP,³⁰ isotactic polystyrene (iPS),³¹ polybutene (iPB),^{31,32} and poly(4-methyl-1-pentene) (iP4MP)³³ are reported in Figure 2.10. It is apparent the presence in the map of iPP of two equivalent energy minima, corresponding to the right-handed $(G^-T)_n$ ($\theta_1 = -60^\circ, \theta_2 = 180^\circ$) and left-handed $(TG^+)_n$ ($\theta_1 = 180^\circ, \theta_2 = 60^\circ$) threefold helical conformation (Figure 2.10b). In the case of iPS, besides the two absolute minima corresponding to the threefold helical conformation found in the most stable crystalline form of iPS,³⁴ a

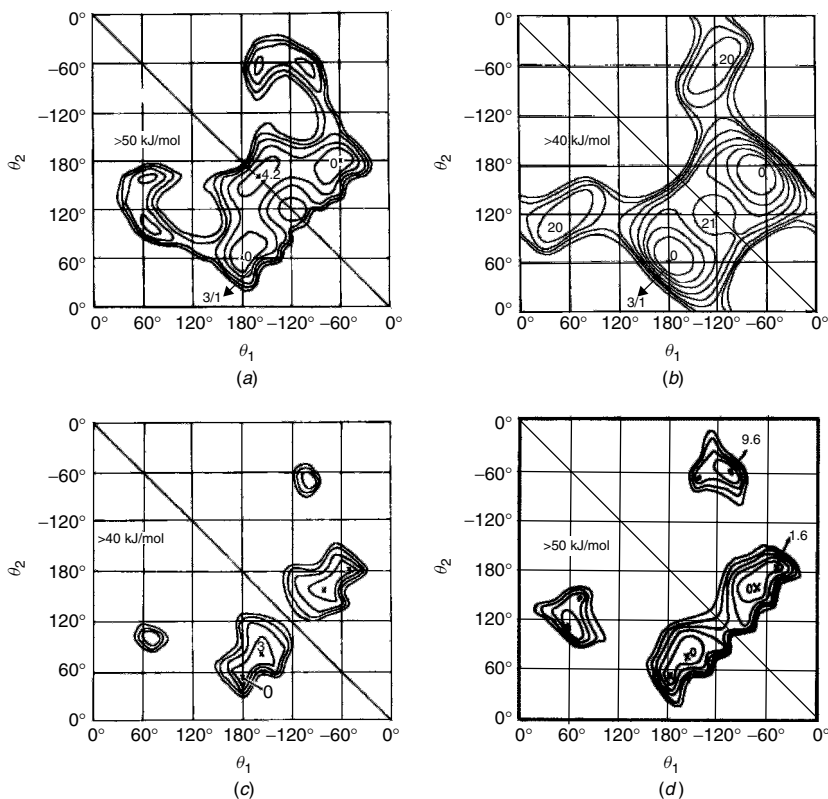


Figure 2.10 Maps of conformational energy of various isotactic polymers as function of backbone torsion angles θ_1 and θ_2 : (a) Isotactic polystyrene, (b) polypropylene, (c) poly(1-butene), and (d) poly(4-methyl-1-pentene). Succession of torsion angles $\dots\theta_1\theta_2\theta_1\theta_2\dots$ [$s(M/N)$ symmetry] has been assumed. Isoenergetic curves are reported every 10 (a,c,d) or 5 (b) kJ/mol of monomeric units with respect to absolute minimum of each map assumed as zero.

minimum of higher energy in the region of the *trans* planar conformation is also present (Figure 2.10a). This is due to the planarity of the benzene rings, which makes the *trans* planar conformation energetically feasible. This energy minimum is absent for iPP, iPB, and iP4MP because of the greater repulsions between the nonplanar side groups.

In the energy maps of iPB the energy minimum in the region of the helical conformation (TG) is split into two minima (Figure 2.10c). The absolute minimum corresponds to the 3/1 helix, found in form I of iPB³⁵, while the second minimum comprises both the 11/3 and 4/1 helical conformations found in forms II and III, respectively.^{29,32,36,37} These helical (T'G')_n conformations are characterized by values of the torsion angles θ_1 and θ_2 slightly deviated from the exact *trans* (180°) and *gauche* (60°) values typical of the 3/1 helix, due to the steric interaction between the bulky side groups. These interactions induce a similar distortion of the two backbone torsion angles,³⁸ $\theta_1 = 180^\circ + \delta_1$, $\theta_2 = 60^\circ + \delta_2$ for a left-handed helix and $\theta_1 = -60^\circ - \delta_1$, $\theta_2 = 180^\circ - \delta_2$ for a right-handed helix, with $\delta_1 \approx \delta_2$.

The same isodistortion of the torsion angles θ_1 and θ_2 is observed for iP4MP (Figure 2.10d). The increased bulkiness of the side groups in iP4MP makes the distorted helical conformations (T'G')_n more stable than the 3/1 helix. The absolute minimum is close to the 7/2 and 4/1 helical conformations, found in form I^{39,40} and forms II and III of iP4MP.^{33,41,42,247} The relative energy minimum (Figure 2.10d) corresponds to the 3/1 helical conformation, found in the less stable form IV of iP4MP.^{43,44} A greater distortion of the torsion angles occurs for the 4/1 helix, as revealed by the lower value of unit height (1.97 Å for the 7/2 helix and 1.74 Å for the 4/1 helix).³³

Data concerning the chain conformations of isotactic polymers are reported in Table 2.1. In all the observed cases the torsion angles do not deviate more than 20° from the staggered (60° and 180°) values and the number of monomeric units per turn *M/N* ranges between 3 and 4. Chains of 3-substituted polyolefins, like poly(3-methyl-1-butene), assume a 4/1 helical conformation (T'G')₄,^{45,46} while 4-substituted polyolefins, like poly(4-methyl-1-pentene), have less distorted helices with 7/2 symmetry (T'G')_{3.5}.³⁹ When the substituent on the side group is far from the chain atoms, as in poly(5-methyl-1-hexene), the polymer crystallizes again with a threefold helical conformation (Table 2.1). Models of the chain conformations found for the polymorphic forms of various isotactic polymers are reported in Figure 2.11.

Recently, a similar analysis of the conformational energy has been performed also for various new syndiotactic polymers.^{27,47} The conformational energy maps of syndiotactic polypropylene (sPP),⁴⁸ polystyrene (sPS),⁴⁹ polybutene (sPB),²⁵ and poly(4-methyl-1-pentene) (sP4MP)²⁶ are reported in Figure 2.12. A line repetition group s(*M/N*)2 for the polymer chain, and, hence, a succession of the torsion angles ... θ_1 , θ_1 , θ_2 , θ_2 , ..., has been

Table 2.1
Structural Data of Isotactic (*it*) and Syndiotactic (*st*) Polymers

Polymer	Chain Axis (Å)	Chain Symmetry	Space Group	References
<i>it</i> -Polypropylene α -form	6.5	s(3/1)	$P2_1/c, C2/c$	20, 173, 174
<i>it</i> -Polypropylene β -form	6.5	s(3/1)	$P3$	154, 158, 159
<i>it</i> -Polypropylene γ -form	6.5	s(3/1)	$Fddd$	141, 142
<i>it</i> -Polybutene form I	6.5	s(3/1)	$R3c, R\bar{3}c$	35
<i>it</i> -Polybutene form II	21.05	s(11/3)	$P\bar{4}$	32, 36
<i>it</i> -Polybutene form III	7.56	s(4/1)	$P2_12_12_1$	37
<i>it</i> -Poly(3-methyl-1-butene)	6.8	s(4/1)	$P2_1/b$	45, 46
<i>it</i> -Poly(1-pentene)	6.6	s(3/1)	—	220
<i>it</i> -Poly(<i>(S)</i> -3-methyl-1-pentene)	6.80	s(4/1)	$I4_1$	66
<i>it</i> -Poly(4-methyl-1-pentene) form I	13.8	s(7/2)	$P\bar{4}b2$	39, 40
<i>it</i> -Poly(4-methyl-1-pentene) form II	7.13	s(4/1)	$P2_1/b$	41, 247
<i>it</i> -Poly(4-methyl-1-pentene) form III	7.02	s(4/1)	$I4_1$	33, 153
<i>it</i> -Poly(4-methyl-1-pentene) form IV	6.5	s(3/1)	—	44
<i>it</i> -Poly(1-hexene)	13.7	s(7/2)	—	243
<i>it</i> -Poly(<i>(S)</i> -4-methyl-1-hexene)	13.8	s(7/2)	$P\bar{4}, P1$	39a
<i>it</i> -Poly(<i>(R)</i> , <i>(S)</i> -4-methyl-1- hexene)	13.8	s(7/2)	$P\bar{4}$	39a
<i>it</i> -Poly(5-methyl-1-hexene)	6.33	s(3/1)	$P2_1$	129
<i>it</i> -Poly(<i>(S)</i> -5-methyl-1-heptene)	6.36	s(3/1)	$P2_1$	65, 129b,c
<i>it</i> -Poly(<i>(R)</i> , <i>(S)</i> -5-methyl-1- heptene)	38.76	s(19/6)	$P\bar{4}$	129b,c
<i>it</i> -Polystyrene	6.65	s(3/1)	$R3c, R\bar{3}c$	34
<i>it</i> -Poly(<i>o</i> -methylstyrene)	8.1	s(4/1)	$I4_1cd$	134
<i>it</i> -Poly(<i>m</i> -methylstyrene)	21.7	s(11/3)	$P\bar{4}$	128
<i>it</i> -Poly(<i>o</i> -fluorostyrene)	6.63	s(3/1)	$R3c$	132
<i>it</i> -Poly(<i>p</i> -fluorostyrene)	8.25	s(4/1)	$P2_12_12_1$	45, 244
<i>it</i> -Poly(vinylcyclohexane) form I	6.5	s(4/1)	$I4_1/a$	136, 137
<i>it</i> -Poly(vinylcyclohexane) form II	44.6	s(24/7)	$I\bar{4}$	221
<i>it</i> -Poly(α -vinyl-naphthalene)	8.1	s(4/1)	$I4_1cd$	135
<i>it</i> -Poly(vinyl methyl ether)	6.5	s(3/1)	$R\bar{3}$	133
<i>it</i> -Poly(vinyl isopropyl ether)	35.5	s(17/5)	—	222
<i>it</i> -Poly(vinyl isobutyl ether)	6.5	s(3/1)	—	223
<i>it</i> -Poly(<i>t</i> -butylacrylate)	6.5	s(3/1)	$P3_1$	130
<i>it</i> -1,2-Poly(1,3-butadiene)	6.5	s(3/1)	$R3c, R\bar{3}c$	131
<i>it</i> -1,2-Poly(4-methyl-1,3- pentadiene)	36.5	s(18/5)	$I\bar{4}c2$	245

(continued overleaf)

Table 2.1
(continued)

Polymer	Chain Axis (Å)	Chain Symmetry	Space Group	References
<i>st</i> -Polypropylene form I	7.4	s(2/1)2	<i>Ibca</i> , <i>P2₁/a</i>	59, 146
<i>st</i> -Polypropylene form II	7.4	s(2/1)2	<i>C222₁</i>	22
<i>st</i> -Polypropylene form III	5.06	tc	<i>P2₁cn</i>	23, 24
<i>st</i> -Polypropylene form IV	11.6	t2	<i>P1</i> , <i>C2</i>	148, 149
<i>st</i> -Polybutene form I	7.73	s(2/1)2	<i>C222₁</i>	25, 60
<i>st</i> -Polybutene form II	20.0	s(5/3)2	<i>P2₁/a</i>	25, 28
<i>st</i> -Poly(4-methyl-1-pentene)	46.9	s(12/7)2	<i>P4</i>	26, 61
<i>st</i> -Polystyrene α -form	5.1	tc	<i>P3</i>	53, 150
<i>st</i> -Polystyrene β -form	5.1	tc	<i>P2₁2₁2₁</i>	54, 55
<i>st</i> -Polystyrene γ -form	7.7	s(2/1)2	—	50
<i>st</i> -Polystyrene δ -form	7.7	s(2/1)2	<i>P2₁/a</i>	58a
<i>st</i> -Polystyrene δ -form (clathrate forms)	7.7	s(2/1)2	<i>P2₁/a</i>	57, 58
<i>st</i> -Poly(<i>p</i> -methylstyrene) form I	7.8	s(2/1)2	—	224
<i>st</i> -Poly(<i>p</i> -methylstyrene) form II	7.8	s(2/1)2	—	224
<i>st</i> -Poly(<i>p</i> -methylstyrene) clathrate forms	7.8	s(2/1)2	<i>P2₁/a</i>	225
<i>st</i> -Poly(<i>p</i> -methylstyrene) form III	5.12	tc <i>m</i>	<i>Pnam</i>	226
<i>st</i> -1,2-Poly(1,3-butadiene)	5.1	tc <i>m</i>	<i>Pcam</i>	139
<i>st</i> -1,2-Poly(4-methyl-1,3-pentadiene) form I	11.73	t2	<i>P1</i>	227
<i>st</i> -1,2-Poly(4-methyl-1,3-pentadiene) form II	5.05	tc	—	227

assumed.²⁷ All the maps of Figure 2.12 present energy minima into the regions corresponding to the highly extended *trans* planar ($\theta_1 \approx \theta_2 \approx T = 180^\circ$) and helical conformations ($\theta_1 \approx 60^\circ$ and $\theta_2 \approx 180^\circ$ or $\theta_1 \approx 180^\circ$ and $\theta_2 \approx -60^\circ$).

In the case of sPS (Figure 2.12a), the absolute minimum present in a region of the *trans* planar conformation corresponds to the conformation found in the α - and β -forms,^{50–55} while the minimum in the region of the twofold helical conformation (TTGG)₂, with s(2/1)2 symmetry ($\theta_1 \approx 60^\circ$, $\theta_2 \approx 180^\circ$ or $\theta_1 \approx 180^\circ$, $\theta_2 \approx -60^\circ$), corresponds to the conformation found in the γ - and δ -forms of sPS.^{50,56–58} The same energy minima are present in the map of sPP (Figure 2.12b) and correspond to the twofold helical conformation, found in forms I and II,^{21,22,59} and the *trans* planar conformation, found in form III of sPP.^{23,24}

In the case of sPB and sP4MP, having bulkier side groups, deep energy minima are present only in the region of the helical conformation, the minimum in the *trans* planar region being of higher energy. According to these calculations,

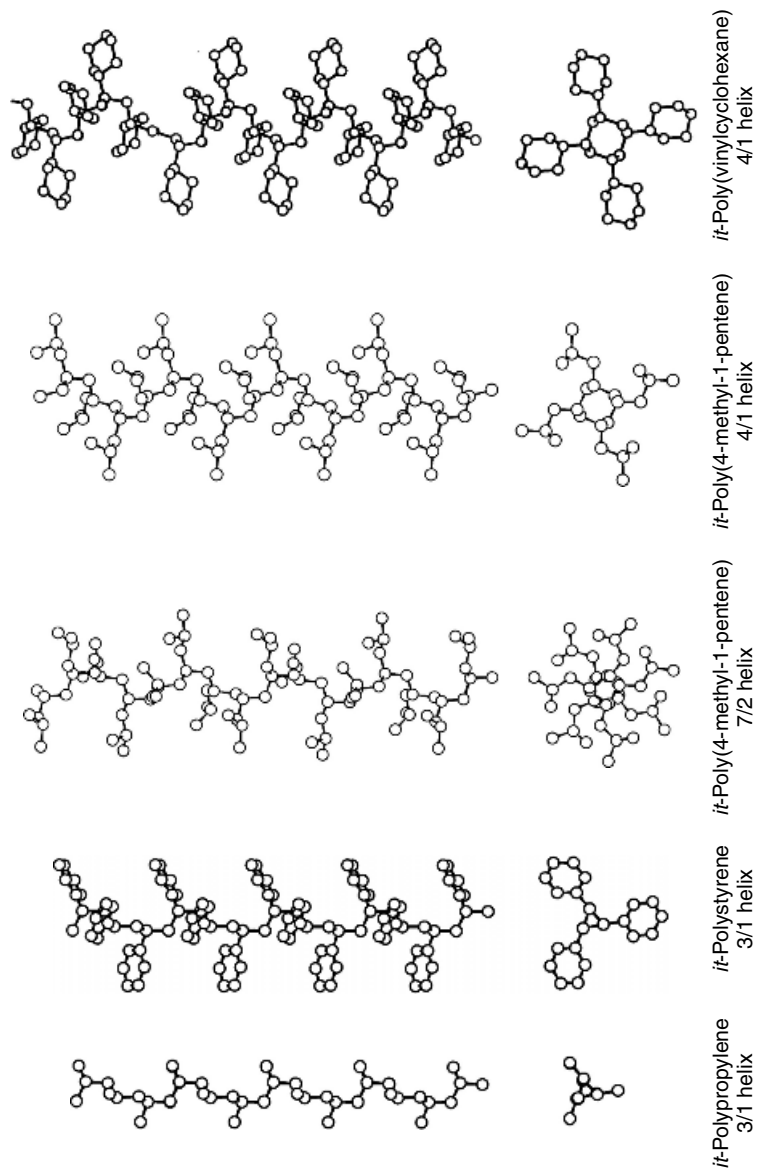


Figure 2.11 Models for helical conformations of chains of various isotactic (*it*) polymers.

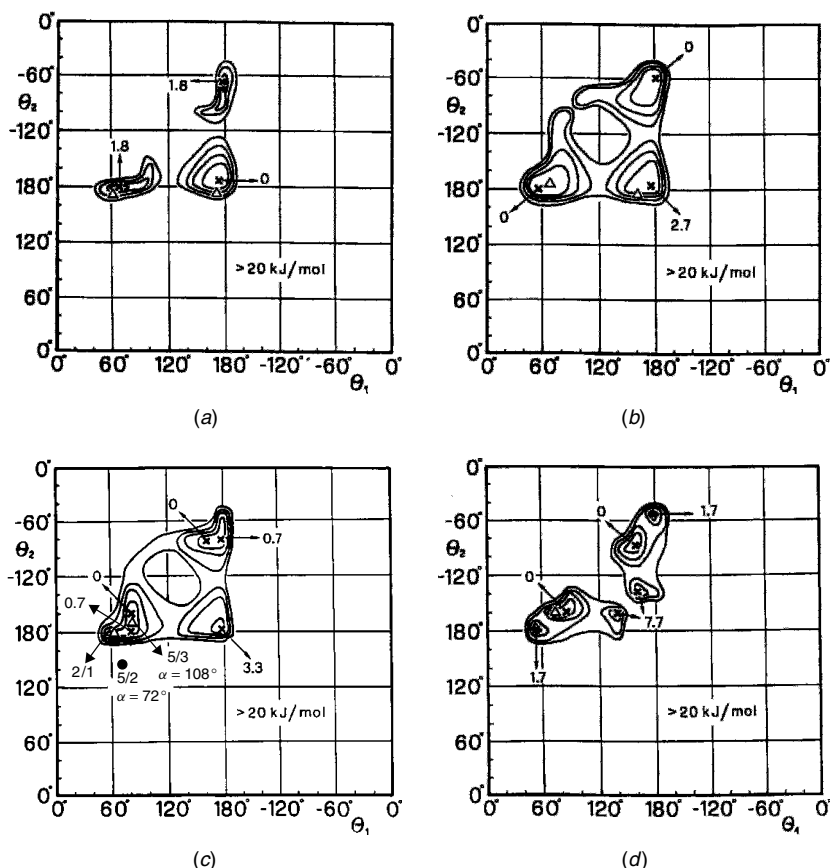


Figure 2.12 Maps of conformational energy of various syndiotactic polymers as function of backbone torsion angles θ_1 and θ_2 ²⁷: (a) syndiotactic polystyrene, (b) polypropylene, (c) poly(1-butene), and (d) poly(4-methyl-1-pentene). Succession of torsion angles $\dots\theta_1\theta_1\theta_2\theta_2\dots$ [s(M/N)2 symmetry] has been assumed. Isoenergetic curves are reported every 5 kJ/mol of monomeric units with respect to absolute minimum of each map assumed as zero. Values of energies corresponding to minima (x) are also indicated. Experimental conformations observed for different polymorphic forms of polymers are indicated by triangles. (Reproduced with permission from Ref. 27. Copyright 1992 by the Società Chimica Italiana.)

it was found that for sPS the two crystalline forms with the chains in the *trans* planar conformation are the most stable ones,⁵⁰ while the crystalline form of sPP with chains in the *trans* planar conformation is metastable,^{23,24} and no crystalline forms with chains in *trans* planar conformation have been observed for sPB²⁵ and sP4MP.²⁶

In the case of sPB and sP4MP (Figures 2.12c,d), the energy minimum in the region of the helical conformations is split into two minima of nearly

equal energy, as occurs in the maps of the corresponding isotactic polymers (Figure 2.10). The first minimum correspond to the twofold (TTGG)_n helical conformation s(2/1)2, characterized by staggered values for the torsion angles $\theta_1 \approx 60^\circ$ and $\theta_2 \approx 180^\circ$. The second minimum corresponds to distorted helical conformations (T'T'G'G')_n, characterized by values of the torsion angles deviated from the staggered values; $\theta_1 = G' = 60^\circ + \delta$; $\theta_2 = T' = 180^\circ + \delta$. According to these calculations, two crystalline forms of sPB have been found,^{25,28,60} the most stable form I with chains in the s(2/1)2 helical conformation^{25,60} and the metastable form II characterized by chains in the helical conformation with s(5/3)2 symmetry.^{25,28} The only crystalline form found for sP4MP is characterized by chains in the helical conformation with s(12/7)2 symmetry,^{26,61} which corresponds to the absolute energy minimum in the map of Figure 2.12d.

These data indicate that the principle of similar distortions of the torsion angles of the main chain from the staggered values 180° and 60° , due to the bulkiness of the side groups and observed in various isotactic polyolefins,³⁸ is also valid for the chain conformations of syndiotactic polymers. While the isodistortion gives rise to a shortening of the unit height for isotactic polymers, it induces an increase of the unit height for syndiotactic polymers.²⁷ Data concerning the chain conformations of syndiotactic polymers are also reported in Table 2.1.

As discussed in Section 2.2, in the case of syndiotactic polymers there exist two different kinds of helical conformations, characterized by the same s(M/N)2 symmetry, but different values of the angle α between two consecutive binary axes perpendicular to the chain axis. It is apparent from the map of Figure 2.12c that the conformation found for form II of sPB [s(5/3)2 symmetry with $\theta_1 = 74^\circ$, $\theta_2 = -164^\circ$, $\alpha = 108^\circ$, conformation (a') in Figures 2.7b and 2.9]^{25,28} corresponds to an energy minimum. The second possible conformation, compatible with the observed unit height and unit twist, with s(5/2)2 symmetry and $\alpha = 72^\circ$ [$\theta_1 = 72^\circ$, $\theta_2 = 147^\circ$, conformation (a) in Figures 2.7b and 2.9] does not correspond to an energy minimum, and a much higher energy is involved.

Models of the chain conformations found in the various polymorphic forms of syndiotactic polymers are reported in Figure 2.13.

The unusual “double *gauche*” conformation assumed by the lateral groups in the twofold helical chain of sPB in the form I is worth mentioning. In this conformational assignment the methyl groups are in a *gauche* arrangement with respect to both the closest methylene groups of the main chain (Figure 2.13). This conformation was predicted by conformational energy calculations^{25,27} and confirmed by complete determination of the crystal structure of form I of sPB⁶⁰ and by solid-state ¹³C nuclear magnetic resonance (NMR) analysis of form I.⁶²

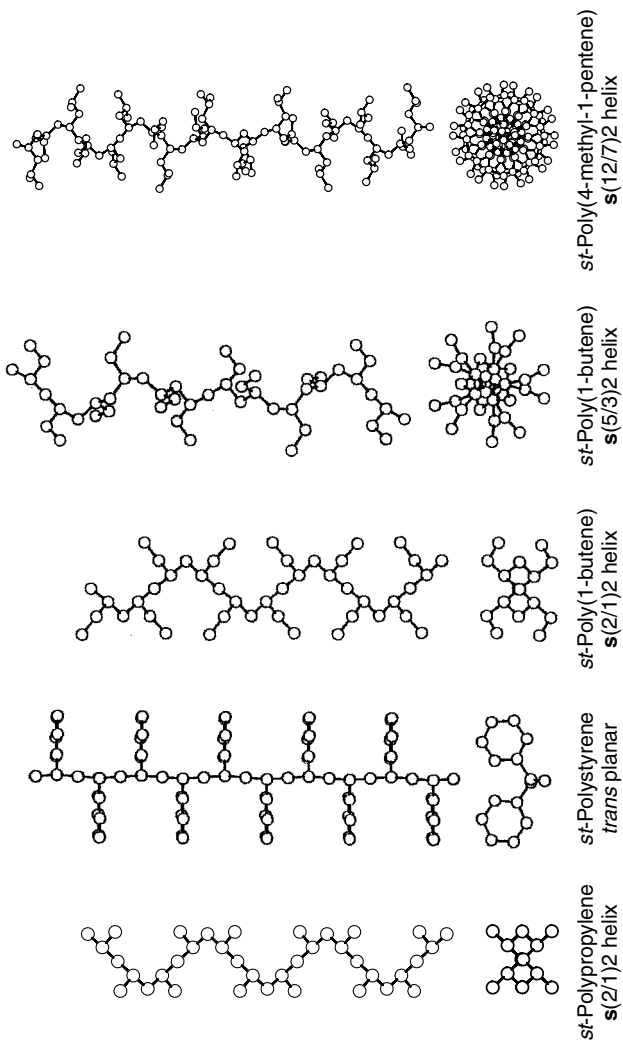


Figure 2.13 Models for helical conformations of chains of various syndiotactic (*st*) polymers.

2.4 Helical Conformation and Optical Activity

An isotactic chain of a vinyl polymer is chiral as long as the chain ends are different. Isotactic polyolefins are generally not optically active because in a very long polymer chain the chain ends are indistinguishable.⁶³ The manifestation of chirality, such as optical activity, is precluded by the high molecular weight of polymers, which makes the chain ends an unimportant part of the chain structure. Isotactic polymers belong, therefore, to a class of molecules in which the chirality is buried,⁶³ leading to a cryptochiral state.⁶⁴ Optical activity may be produced in these polymers in another manner.

One possibility is the presence of chiral, nonracemic lateral groups,⁶⁵ as in the case of isotactic poly((*S*)-3-methyl-1-pentene) [iP(*S*)3MP].⁶⁶ It has been shown that the conformation of the chain is influenced not only by the steric hindrance of the lateral group but also by its configuration. The conformational energy maps of iP(*S*)3MP in the regions of the minimum-energy right-handed G^-T and left-handed TG^+ helical conformations are reported in the Figure 2.14.²⁹ The two energy minima present in each map correspond to the 3/1 and 4/1 helical conformations, the latter being the conformation found in the crystal structure.⁶⁶ Because of the chirality of the lateral group,

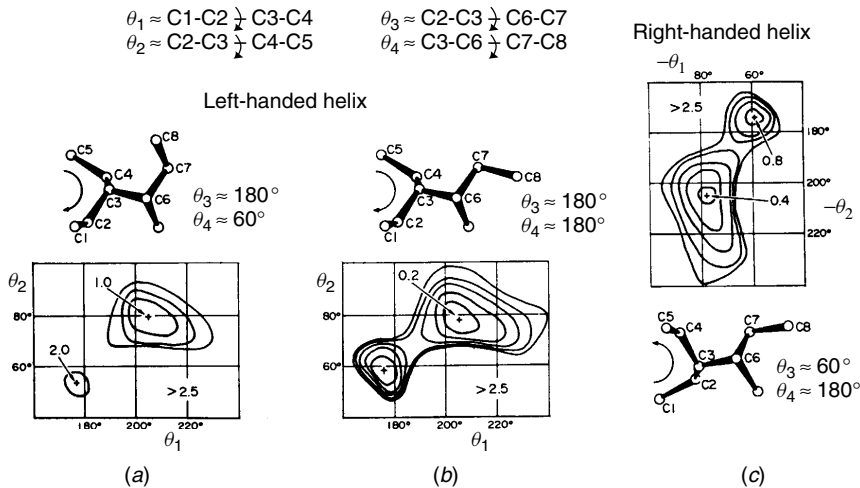


Figure 2.14 Maps of conformational energy as function of backbone torsion angles θ_1 and θ_2 of a chain of isotactic poly((*S*)-3-methyl-1-pentene) for (a,b) left-handed helix and (c) right-handed helix.²⁹ For each pair of θ_1 and θ_2 , reported energy corresponds to minimum obtained by varying torsion angles of lateral group θ_3 and θ_4 . Curves are reported at intervals of 0.5 kcal/mol of monomeric unit. Values of energies corresponding to minima are also indicated. (Reprinted with permission from Ref. 29. Copyright 1976 by Elsevier Science.)

right-handed and left-handed helices of iP(S)3MP are not equivalent, as instead generally occurs for isotactic polymers. In fact, two low-energy conformations of the chiral lateral group, with $\theta_4 \approx 60$ and 180° , are possible for the left-handed helix (Figures 2.14*a,b*), while only one low-energy conformation, with $\theta_4 \approx 180^\circ$, is possible for the right-handed helix (Figure 2.14*c*). The left-handed helix of iP(S)3 MS is, therefore, favored over the right-handed one. In the crystal structure the chains of iP(S)3MP assume a 4/1 helical conformation⁶⁶ and only left-handed helices are included in the tetragonal unit cell, with lateral groups which may take statistically both conformations of minimum energy.²⁹ The chirality of the lateral groups induces the crystallization of isochiral helices.

The chirality of the lateral group influences the conformation of the chain not only in the crystalline state. The experimental observation that vinyl polymers having optically active lateral groups show optical activity also in solution and that the optical activities show nonlinear relationships between the configurational enantiomeric characteristics of the monomeric units and the optical activity of the derived polymer⁶⁵ suggests that a prevailing spiralization sense of the helical chains is present in solution. In the case of iP(S)3MP in solution or in the melt, a local left-handed helical conformation should prevail in length over the right-handed one for entropic reason,⁶⁷ because of the higher numbers of possible low-energy conformational states accessible to the lateral groups when the helical chains are left handed.

2.5 Polydienes

Double bonds present along a polymer chain are stereoisomeric centers, which may have a *cis* or *trans* configuration. Polymers of 1,3-dienes with 1,4 additions of the monomeric units contain double bonds along the chains and may contain up to two stereoisomeric tetrahedral centers. Stereoregular polymers can be *cis* or *trans* tactic, isotactic or syndiotactic, and diisotactic or disyndiotactic if two stereoisomeric tetrahedral centers are present. In the latter case *erythro* and *threo* structures are defined depending on the relative configurations of two chiral carbon atoms.¹

All the possible line repetition groups for *cis* and *trans* polydienes compatible with the isotactic or syndiotactic configurations are reported in Figure 2.15.^{47,68} In order to consider only the possible conformations assumed in the crystalline state, the torsion angle of the central single bond is assumed to be 180° (*trans*) in both the *cis* and *trans* polydienes. This condition produces conformations sufficiently extended to be packed in a crystalline lattice for each value of the torsion angles θ_1 and θ_2 (Figure 2.15).

The line repetition group $s(M/N)$ is general for *cis* and *trans* polydienes, whichever the A and B substituents, and corresponds to a succession

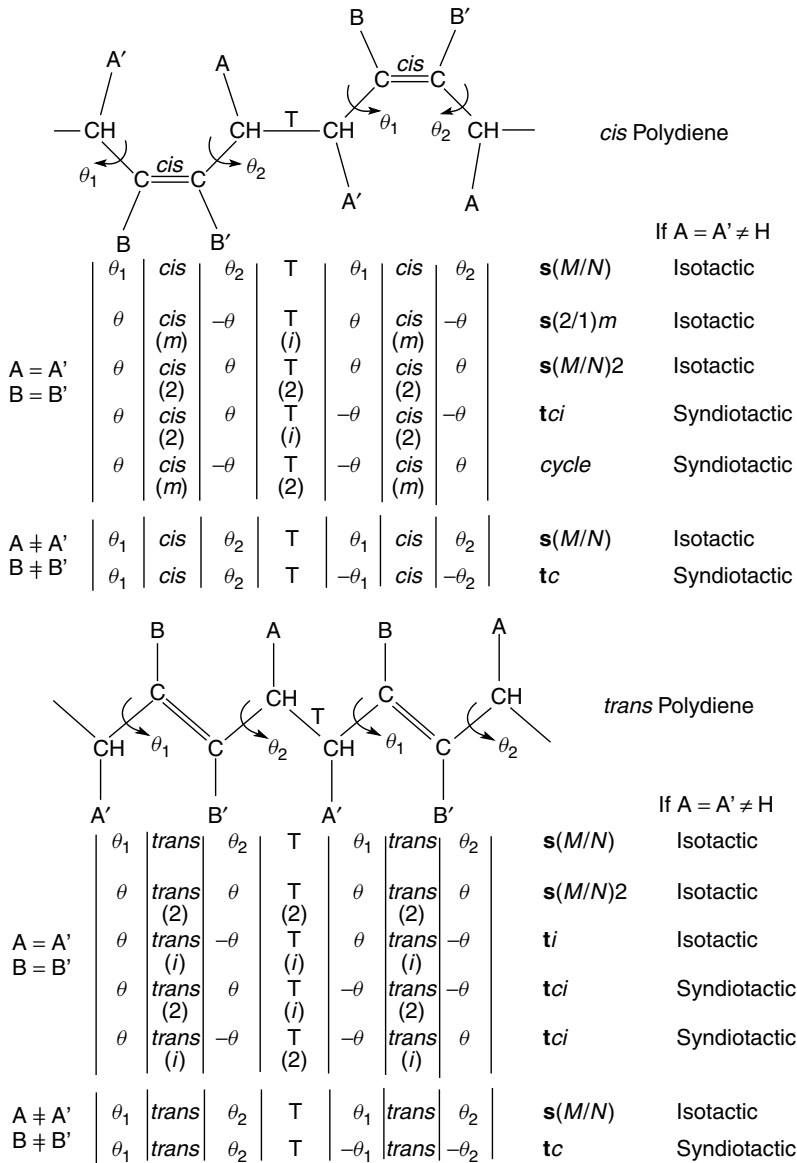


Figure 2.15 Line repetition symmetry groups and corresponding sequences of torsion angles for cis and trans polydienes. Position of mirror planes (m), inversion centers (i), and binary axes (2) along polymer chain are also indicated. Torsion angle of single bond, CHA–CHA', is assumed to be trans (T) in both cis and trans polydienes.

of torsion angles $(\theta_1 cis \theta_2 T)_n$ and $(\theta_1 trans \theta_2 T)_n$. When $A = A'$ and $B = B'$, the *cis* polymer may present mirror planes or binary axes perpendicular to the chain axis in correspondence with the double bonds, whereas inversion centers and binary axes may be present in the *trans* polymer. Inversion centers in the center of the $CHA-CHA'$ single bond or binary axes crossing the same bond and perpendicular to the chain axis may also be present in both *cis* and *trans* polymers (Figure 2.15). As a consequence, line repetition groups $s(2/1)m$, $s(M/N)2$, and tci are possible for *cis* polydienes, whereas $s(M/N)2$, ti , and tci line repetition groups are possible for *trans* polydienes.^{47,68-70} When $A = A' \neq H$, line repetition groups $s(2/1)m$ and $s(M/N)2$ are compatible for *cis* isotactic chains, while $s(M/N)2$ and ti symmetries for *trans* isotactic polydienes, and only the tci line repetition group is possible for syndiotactic *cis* or *trans* polymers. In these cases only one torsion angle (θ in Figure 2.15) in the backbone is independent for each line repetition group.⁴⁷ In the case of *cis* polymers, if mirror planes perpendicular to the chain axis, bisecting the double bonds, and binary axes perpendicular to the chain axis, crossing the $CHA-CHA'$ single bond, are both present, a conformation of the kind $(\theta cis - \theta T - \theta cis \theta T)_n$ is produced and the chain degenerates in a cycle.^{69,47}

When $A \neq A'$ or $B \neq B'$, the symmetry is lower and the only possible line repetition groups are $s(M/N)$ and tc for isotactic and syndiotactic polymers, respectively, in both *cis* and *trans* configurations. In these cases, two independent torsion angles in the main chain define the regular conformation (θ_1 and θ_2 in Figure 2.15).

Also for polydienes the actual conformation assumed by the chain under the constraint of the equivalence principle is determined by energetic factors as defined by the principle of minimum conformational energy. The torsion angles of single bonds adjacent to double bonds preferentially assume values equal to 120° or -120° . In fact, the intrinsic torsional energy is still described by a threefold function, but the energy minima are at values of the torsion angles 120° , -120° , and 0° (anticlinal A^+ and A^- and *cis*).¹² The minima are separated by a barrier energy lower than that in the torsional energy function of single bonds adjacent to single bonds. For these reasons, in polydienes deviations from the equilibrium torsion angles are possible at lower cost of energy, and moreover, the packing energy may play an important role in determining the chain conformation in the crystalline state.

Figure 2.16 reports the conformational energy maps as a function of the torsion angles θ_1 and θ_2 of the two single bonds adjacent to the double bonds for $\theta_3 = T = 180^\circ$ for *cis*-1,4-poly(1,3-butadiene) (*cis*PBD),⁶⁹ *trans*-1,4-poly(1,3-butadiene) (*trans*PBD),⁷⁰ *cis*-1,4-poly(isoprene) (*cis*PI),⁶⁸ *trans*-1,4-poly(isoprene) (*trans*PI),⁷¹ *cis*-1,4-poly(2,3-dimethyl-1,3-butadiene) (*cis*PMBD),⁶⁸ and *trans*-1,4-poly(2,3-dimethyl-1,3-butadiene) (*trans*PMBD).⁶⁸ These polymers are representative examples of polydienes with $A = A' = H$

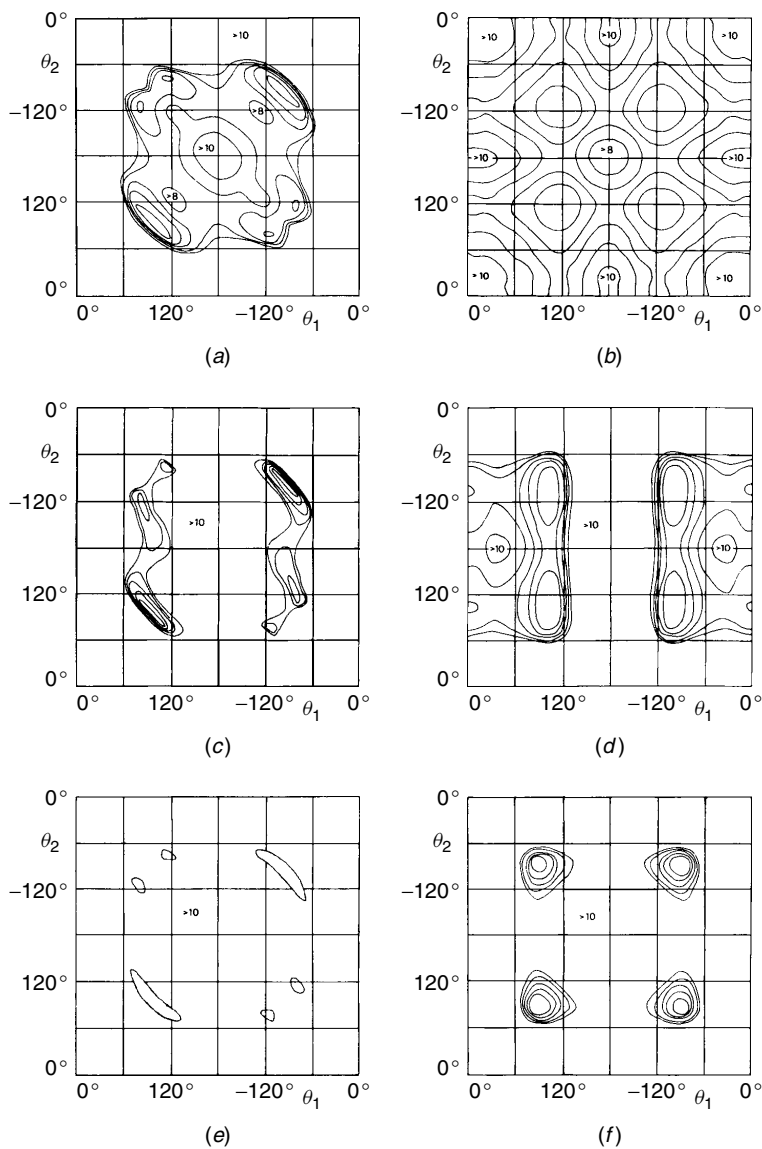


Figure 2.16 Maps of conformational energy of various *cis* and *trans* polydienes as function of torsion angles θ_1 and θ_2 ⁶⁸: (a) *cis*-1,4-poly(1,3-butadiene), (b) *trans*-1,4-poly(1,3-butadiene), (c) *cis*-1,4-poly(isoprene), (d) *trans*-1,4-poly(isoprene), (e) *cis*-1,4-poly(2,3-dimethyl-1,3-butadiene), and (f) *trans*-1,4-poly(2,3-dimethyl-1,3-butadiene). Isoenergetic curves are reported every 2 kJ/mol of monomeric units with respect to absolute minimum of each map assumed as zero. (Reproduced with permission from Ref. 68. Copyright 1986 by the Società Chimica Italiana.)

and B or B' equal to H or CH₃ and show the effect of the presence of the methyl groups adjacent to the double bonds on the conformational energy. The maps present various energy minima for values of θ_1 and θ_2 close to the torsional minima A⁺, A⁻, and *cis* (120°, -120°, and 0°) (Table 2.2). The conformations found in the crystals and the values of the chain axes are also reported in Table 2.2.

In the case of *cis*PBD (A = B = H) (Figure 2.16a), the absolute minimum is localized in the two equivalent regions (A⁺*cis*A⁺T) = (A⁻*cis*A⁻T), while two nearly isoenergetic minima were found in the regions (A⁺*trans*A⁺T) = (A⁻*trans*A⁻T) and (A⁺*trans*A⁻T) = (A⁻*trans*A⁺T) in the case of *trans*PBD (Figure 2.16b). On the basis of the minima present in the map of the *cis* polymer, the possible conformations corresponding to the line repetition groups s(2/1)*m*, *tci*, and s(M/N)2 are characterized by the succession of torsion angles (A⁺*cis*A⁻T)_n, (A⁺*cis*A⁺TA⁻*cis*A⁻T)_n and (A⁺*cis*A⁺T)_n, respectively.⁶⁹ The periodicity of the *tci* conformation (A⁺*cis*A⁺TA⁻*cis*A⁻T)_n corresponds to the chain axis *c* = 8.6 Å found in the crystalline form of *cis*PBD⁷² (Table 2.2).

For *trans*PBD, the possible conformations corresponding to the s(M/N)2, *ti*, and s(M/N) symmetries are (A⁺*trans*A⁺T)_n, (A⁺*trans*A⁻T)_n, and (C*trans*A⁺T)_n, respectively.⁷⁰ The *ti* conformation (A⁺*trans*A⁻T)_n corresponds to that found in the stable polymorphic form of *trans*PBD (form I) with a chain periodicity *c* = 4.83 Å.^{2,73-75}

In the case of *cis*PI (A = A' = H and B = CH₃ and B' = H), the two conformations corresponding to the two nonequivalent energy minima in the map of Figure 2.16c,⁶⁸ (A⁺*cis*A⁻T)_n [s(2/1) symmetry] and (A⁺*cis*A⁺TA⁻*cis*A⁻T)_n (*tc* symmetry), correspond to the conformations of the chains in the crystal structure of *cis*PI proposed by Nyburg⁷⁶ and Bunn,⁷⁷ respectively. The X-ray diffraction data are, however, better accounted for by a disordered conformation, proposed by Corradini and co-workers,^{72,78} characterized by a statistical succession of monomeric units which assume these two energy minimum conformations.

For *trans*PI, among the possible s(M/N) conformations (A⁺*trans*A⁺T)_n, (A⁺*trans*A⁻T)_n, and (C*trans*A⁺T)_n, the succession (A⁺*trans*A⁻T)_n, with *c* = 4.72 Å and *t1* symmetry, corresponds to the conformation found in the β form of *trans*PI.^{73,77} The three possible *tc* conformations (A⁺*trans*A⁺TA⁻*trans*A⁻T)_n, (A⁺*trans*A⁻TA⁻*trans*A⁺T)_n, (C*trans*A⁺TC*trans*A⁻T)_n give chain periodicities similar to the experimental chain axis of 8.77 Å of the α-form of *trans*PI,⁷⁹ but the conformation (C*trans*A⁺TC*trans*A⁻T)_n gives the best packing in the proposed space group,⁷¹ as actually found in the crystal structure.⁷⁹

In the case of *cis*PMBD and *trans*PMBD (A = A' = H and B = B' = CH₃), the maps present narrow minima in correspondence to θ_1 and θ_2 close to 90°. The *tci* and *ti* conformations were found in the crystals of *cis*PMBD⁸⁰ and *trans*PMBD,⁸¹ respectively (Table 2.2). The values of the torsion angles lower

Table 2.2
Structural Data of Polydienes

Polymer	Energy Minima	c (Å)	Conformation in Crystalline State	Chain Symmetry	Space Group	References
<i>cis</i> -1,4-Poly(1,3-butadiene)	$A^\pm cis A^\pm T$; $A^\pm cis A^\mp T$	8.6	$(A^+ cis A^+ TA^- cis A^- T)_n$	<i>tci</i>	$C2/c$	72
<i>trans</i> -1,4-Poly(1,3-butadiene) form I	$A^\pm trans A^\pm T$; $A^\pm trans A^\mp T$ <i>Ctrans</i> $A^\pm T$; $A^\pm trans CT$;	4.83	$(A^+ trans A^- T)_n$	<i>ti</i>	$P2_1/a$	2, 73–75
<i>trans</i> -1,4-Poly(1,3-butadiene) form II	$A^\pm cis A^\pm T$; $A^\pm trans A^\pm T$; $A^\pm trans A^\mp T$; <i>Ctrans</i> $A^\pm T$	4.66	$\dots A^\pm trans A^\pm T \dots$ <i>Ctrans</i> $A^\pm T \dots$	Dis.	—	2, 70, 74, 111, 112
<i>cis</i> -1,4-Poly(isoprene)	$A^\pm cis A^\pm T$; $A^\pm cis A^\mp T$	8.10	$\dots A^\pm cis A^\pm TA^\mp cis A^\pm T \dots$	Dis.	$Pbca$	72, 76–78
<i>trans</i> -1,4-Poly(isoprene) α -form	$A^\pm trans A^\pm T$; $A^\pm trans A^\mp T$; <i>Ctrans</i> $A^\pm T$	8.77	$(Ctrans A^+ TCtrans A^- T)_n$	<i>tc</i>	$P2_1/c$	73, 71, 79
<i>trans</i> -1,4-Poly(isoprene) β -form		4.72	$(A^+ trans A^- T)_n$	<i>tl</i>	$P2_1 2_1 2_1$	73, 77
<i>cis</i> -1,4-Poly(2- <i>t</i> -butyl-1,3-butadiene)		15.3		<i>s</i> (11/3)	—	228
<i>cis</i> -1,4-Poly(2,3-dimethyl-1,3-butadiene)	$A^\pm cis A^\pm T$; $A^\pm cis A^\mp T$	7.0	$(A^+ cis A^+ TA^- cis A^- T)_n$	<i>tci</i>	$C2/c$	80, 68
<i>trans</i> -1,4-Poly(2,3-dimethyl-1,3-butadiene)	$A^\pm cis A^\pm T$; $A^\pm cis A^\mp T$	4.35	$(A^+ trans A^- T)_n$	<i>ti</i>	—	81, 68
<i>it-cis</i> -1,4-Poly(1,3-pentadiene)	$A^- cis A^- T$; $A^- cis A^+ T$	8.17	$(A^- cis A^+ T)_n$	<i>s</i> (2/1)	$P2_1 2_1 2_1$	96–98, 82
<i>it-trans</i> -1,4-Poly(1,3-pentadiene)	$A^- trans A^+ T$; $A^- trans A^- T$	4.85	$(A^- trans A^+ T)_n$	<i>tl</i>	$P2_1 2_1 2_1$	73, 84, 90–94

(continued overleaf)

Table 2.2
(continued)

Polymer	Energy Minima	c (Å)	Conformation in Crystalline State	Chain Symmetry	Space Group	References
<i>st-cis</i> -1,4-Poly(1,3-pentadiene)	$A^- cis A^+ T$; $A^- cis A^- T$	8.5	$(A^- cis A^- TA^+ cis A^+ T)_n$	tc	$P2_1/c$	99, 83
<i>it-cis</i> -1,4-Poly(2-methyl-1,3-pentadiene) α -form	$A^- cis A^+ T$; $A^- cis A^- T$	7.87	$(A^- cis A^+ T)_n$	$s(2/1)$	$Pbca$	85
<i>it-cis</i> -1,4-Poly(2-methyl-1,3-pentadiene) β -form	$A^- cis A^+ T$	7.90	$(A^- cis A^+ T)_n$	$s(2/1)$	$P2_12_12_1$	85
<i>it-trans</i> -1,4-Poly(2-methyl-1,3-pentadiene)	$A^- trans A^+ T$; $A^- trans A^- T$	4.82	$(A^- trans A^+ T)_n$	$t1$	$P2_1/c$	95, 86
<i>it-cis</i> -1,4-Poly(3-methyl-1,3-pentadiene)	$A^- cis A^+ T$; $A^- cis A^- T$	8.0	$(A^- cis A^+ T)_n$	$s(2/1)$	—	239
<i>st-cis</i> -1,4-Poly(3-methyl-1,3-pentadiene)	$A^- cis A^+ T$; $A^- cis A^- T$	8.6	$(A^- cis A^- TA^+ cis A^+ T)_n$	tc	—	87
<i>it-trans</i> -1,4-Poly(1,3-hexadiene)	$A^- trans A^+ T$	4.85	$(A^- trans A^+ T)_n$	$t1$	$P2_12_12_1$	240
<i>it-cis</i> -1,4-Poly(1,3-hexadiene)	$A^- cis A^+ T$	8.0	$(A^- cis A^+ T)_n$	$s(2/1)$	—	241
<i>it-trans-erythro</i> -Poly(methylsorbate)	$A^- trans A^+ T$; $A^- trans A^- T$	4.8	$(A^- trans A^+ T)_n$	$t1$	—	103–105
<i>it-trans-threo</i> -Poly(methylsorbate)	$A^- trans A^+ T$; $A^- trans A^- T$	9.4	$(A^+ trans A^- TA^- trans A^+ T)_n$	$s(M/N)$	—	102, 105
<i>trans</i> -Polypentamer	$A^+ trans A^- T$	11.9	$(A^+ trans A^- T)_2$	$s(2/1)m$	—	242
<i>trans</i> -Polyheptamer	$A^+ trans A^- T$	17.1	$(A^+ trans A^- T)_4$	$s(2/1)m$	—	242
<i>trans</i> -Polyoctamer	$A^+ trans A^- T$	9.85	$(A^+ trans A^- T)_5$	$t1$	—	242
<i>trans</i> -Polydodecamer	$A^+ trans A^- T$	14.85	$(A^+ trans A^- T)_9$	$t1$	—	242

Note: *it* = isotactic, *st* = syndiotactic.

Note: Dis. = Disordered.

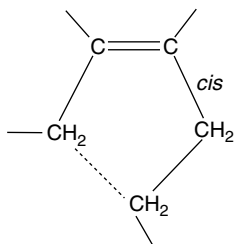
than 120° are in agreement with the lower values of the chain axes in both *cis*PMBD (7.0 \AA^{80}) and *trans*PMBD (4.35 \AA^{81}) with respect to those of *cis* and *trans* poly(1,3-butadiene) and poly(isoprene).

The calculations of Figure 2.16 indicate some features of the conformations of polydienes. Minima in the region of the torsional *cis* minimum (θ_1 and $\theta_2 \approx 0$) are present in the maps of the *trans* polymers (Figures 2.16*b,d*) but disappear in the map of the *cis* polymers (Figures 2.16*a,c*), because of the repulsive nonbonded interactions arising between the atoms in the Scheme 2.3.⁶⁸ The same nonbonded interactions induce slight deviations from the exact anticlinal torsional minimum for the *cis* polymers. Moreover, the large-energy-minimum regions in the case of *cis* and *trans* poly(1,3-butadiene) (Figures 2.16*a,b*) become narrow in poly(isoprene) (Figures 2.16*c,d*) and poly(2,3-dimethylbutadiene) (Figures 2.16*e,f*), due to the presence of the bulky methyl groups. For the same reason, some of these minima disappear in the energy maps of isotactic and syndiotactic poly(1,3-pentadienes) (with $A = H$ and $A' = CH_3$)⁸²⁻⁸⁴ and substituted poly(1,3-pentadienes) (with B or $B' = CH_3$)⁸⁵⁻⁸⁹ (Table 2.2).

According to the conformational energy minima, isotactic *trans*-1,4-poly(1,3-pentadiene)^{73,74,90-94} and *trans*-1,4-poly(2-methyl-1,3-pentadiene)⁹⁵ are characterized by chains in the conformation $(A^-transA^+T)_n$ (**t1** symmetry) and chain axes c values of 4.85 and 4.82 \AA , respectively. The conformation $(A^-cisA^+T)_n$ with **s(2/1)** symmetry characterizes the chains in the structures of isotactic *cis*-1,4-poly(1,3-pentadiene)⁹⁶⁻⁹⁸ and *cis*-1,4-poly(2-methyl-1,3-pentadiene).⁸⁵

For syndiotactic polydienes, experimental data and energy calculations have been reported for *cis*-1,4-poly(1,3-pentadiene)^{83,99,100} and *cis*-1,4-poly(3-methyl-1,3-pentadiene).⁸⁷ In both cases energy minima are obtained for the **tc** conformation $(A^-cisA^-TA^+cisA^+T)_n$,^{47,83,87} according to the observed chain axes of 8.5 and 8.6 \AA .^{87,99}

Examples of ditactic polydienes are provided by a class of crystalline polymers derived from the alkyl-esters of the *trans-trans* isomer of sorbic acid.^{101,102} For example *trans*-poly(methyl sorbate) $(-CH(CH_3)-CH =$



Scheme 2.3

$\text{CH}-\text{CH}(\text{COOCH}_3)_n$ presents two asymmetric carbon atoms ($A = \text{CH}_3$, $A' = \text{COOCH}_3$, $B = B' = \text{H}$). Polymers with prevalingly *erythro* or *threo* configurations have been obtained with different catalytic systems¹⁰². Polymers with *erythro* configuration show chain axis of $c = 4.8 \text{ \AA}$,^{103,104} while polymers with *threo* configuration present a chain periodicity of $c = 9.4 \text{ \AA}$.¹⁰² X-ray diffraction analysis¹⁰⁴ and conformational energy calculations¹⁰⁵ have shown that the polymers with *trans-erythro* configuration are diisotactic with a $t1$ conformation, characterized by a succession of torsion angles $(A^- \text{trans} A^+ T)_n$, whereas polymers with *trans-threo* configuration are diisotactic but with conformation $(A^+ \text{trans} A^- \text{TA}^- \text{trans} A^+ T)_n$.

2.6 Disordered Conformations

As discussed in Section 1, general requirements for the crystallizability of polymers are the regularity of the chemical constitution and of the configuration of long sequences of monomeric units. In these conditions the conformation of the chains is also regular (equivalence principle). However, some three-dimensional long-range (crystalline) order may be maintained even when disorder is present in the conformation of the polymer chains.

Crystalline polymers characterized by disordered conformations of the chains are, for instance, polytetrafluoroethylene (PTFE), *trans*-1,4-poly(1,3-butadiene), and *cis*-1,4-poly(isoprene).

Various polymorphic forms of PTFE characterized by different kinds of structural disorder have been described.¹⁰⁶⁻¹⁰⁷ Form IV is characterized by chains in ordered 15/7 helical conformation^{107a-e} and transforms into form I at temperatures higher than 30°C.^{107a,b} Form I is characterized by chains in disordered conformation, corresponding to the presence of helix reversals along the chain. Ordered portions of chains in right-handed and left-handed 15/7 helical conformation succeed each other statistically along the chain, according to a sequence of torsion angles of the kind $\dots T^+ T^+ T^+ T T^- T^- T^- T T^+ T^+ T^+ \dots$ ($T^+ = +165^\circ$, $T^- = -165^\circ$).¹⁰⁸⁻¹¹⁰ For these sequences of torsion angles, the enantiomorphous helices are connected by at least one bond in *trans* conformation ($T = 180^\circ$). The shape of the chain remains nearly unaltered with respect to the ordered one; moreover, the chain may be maintained exactly straight with small deformations of the torsion and bond angles with a very low cost of energy.¹⁰⁸ In spite of the conformational disorder, a long-range three-dimensional order in the parallelism and positioning of the chain axes is maintained because the atoms are able to maintain a fixed distance from the chain axis, so that the fluorine atoms are confined in cylindrical envelopes having the same size as in the ordered modification.^{109,110}

The high-temperature polymorphic form of *trans*-1,4-poly(1,3-butadiene) (form II) provides another example of conformational disorder.¹¹¹ At

temperatures higher than 76°C the stable form I, characterized by chains in the **ti** conformation $(A^+transA^-T)_n$ ^{2,70,73,75} (Table 2.2), transforms into form II, which is characterized by chains having a lower periodicity ($c = 4.66 \text{ \AA}$), packed in a hexagonal lattice.^{2,74,112} The diffuse X-ray diffraction pattern of form II indicates that disorder is present in the structure. The possibility that chains of polydienes may present disorder in the conformation may be easily explained on the basis of the conformational energy analysis (Figure 2.16 and Table 2.2) reported in the previous section. The conformational energy maps of polydienes (Figure 2.16) present several nonequivalent nearly isoenergetic minima (Table 2.2) because of the low barrier energy which separates the intrinsic torsional energy minima around the single bonds adjacent to the double bonds. Therefore, the configurational repeating units may assume different low-energy conformations, and a succession of repeating units having different conformation is energetically feasible. In the case of *trans*-1,4-poly(1,3-butadiene), the conformational energy map (Figure 2.16b) presents three nonequivalent nearly isoenergetic minima corresponding to the conformations $A^\pm trans A^\pm T$, $A^\pm trans A^\mp T$ and $Ctrans A^\pm T$ (Table 2.2). Therefore, a possible disorder in the conformation may arise from a statistical succession of monomeric units which assume these energy minimum conformations.¹¹¹ The random succession of sequences $\dots A^\pm trans A^\pm T \dots$ and $\dots Ctrans A^\pm T \dots$, characterized by chain periodicities of 4.84 and 4.48 Å, respectively, produces a contraction of the chain axis which matches the observed reduction from form I (4.83 Å) to form II (4.66 Å) for a probability of 25% that the single bonds adjacent to double bonds are in *cis* conformation.^{70,111} This model accounts for the X-ray diffraction data and has been confirmed by the solid-state ¹³C NMR analysis of form II.¹¹³ Also in this case, the chains can be maintained straight, and hence, the crystallinity is maintained, even with a statistical succession of structural units having widely different torsion angles, by allowing small deformations of bond angles.¹¹¹

A similar kind of conformational disorder is present in the crystal structure of *cis*-1,4-poly(isoprene).^{72,78} The conformational energy map (Figure 2.16c) presents two nonequivalent minima corresponding to the sequences (A^+cisA^+T) and (A^+cisA^-T) . Two models of ordered conformation have been proposed. The s(2/1) helical conformation with the sequence $(A^+cisA^-T)_n$ was proposed by Bunn,⁷⁷ while the **tc** conformation with the sequence $(A^-cisA^-TA^+cisA^+T)_n$ was proposed by Nyburg.⁷⁶ The X-ray diffraction data are better accounted for by a different model characterized by a disordered conformation.⁷⁸ The disorder corresponds to a statistical succession along the chain of the four sequences (A^+cisA^+T) , (A^-cisA^-T) , (A^+cisA^-T) , and (A^-cisA^+T) ⁷⁸ (Figure 2.17). In the model of Figure 2.17 the symbols D and U indicate structural units having the double bond down and up, respectively, with respect to the two adjacent single bonds in the *ac* projection. The torsion

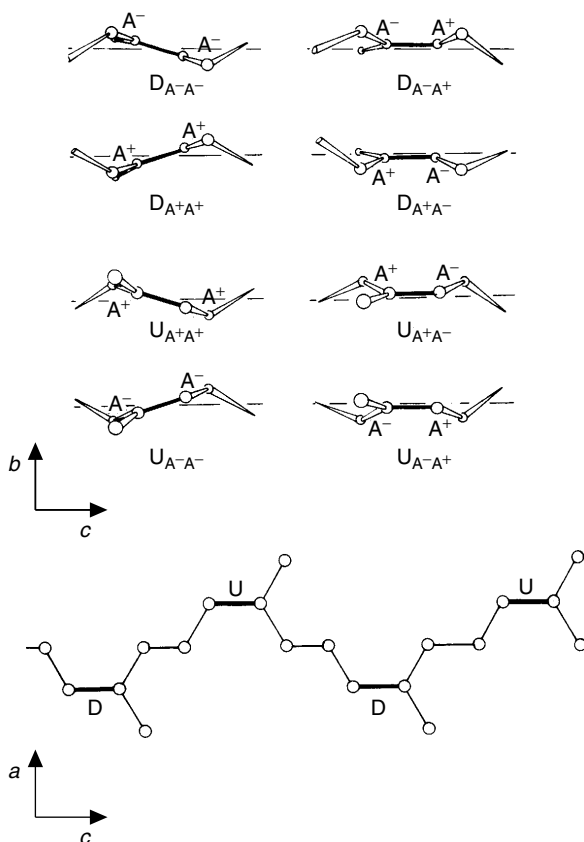


Figure 2.17 Model of disorder for conformation of chains of *cis*-1,4-poly(isoprene). Thick lines indicate double bonds. The symbols D and U indicate structural units having double bond down or up, respectively, with respect to two adjacent single bonds. Subscripts A^+ and A^- indicate torsion angles assumed by two single bonds adjacent to double bonds. Central single bond, $-\text{CH}_2-\text{CH}_2-$, is always in *trans* conformation.

angles of the two single bonds are indicated by the two subscripts A^+ or A^- . In the proposed model,⁷⁸ after a D structural unit only a U unit may follow (Figure 2.17). Moreover, the second subscript of one unit (A^+ or A^-) must be opposite to the first subscript of the successive unit (A^- or A^+ , respectively); for example after a unit $D_{A^-A^+}$ there must be a unit $U_{A^-A^+}$ or $U_{A^-A^-}$. In these conditions, for any succession of the two possible conformations of the three single bonds, (A^+TA^-) or (A^-TA^+), the overall shape of the chain remains unchanged in the *ac* plane of the crystal, as shown in Figure 2.17, and a three-dimensional order is maintained.

This kind of conformational disorder has also been suggested for poly(methyl sorbate).¹⁰⁵ It is therefore not unusual and also explains some properties of these polymers, as, for instance, the low entropy of melting.¹¹⁴

2.7 Alternating Copolymers

Chains of copolymers may keep a regular constitution when the different monomeric units alternate along the chain. One of the monomeric units may present stereoisomeric centers, and, also in this case, crystalline alternating copolymers, having regular configurations, and hence regular conformations, have been synthesized with Ziegler–Natta catalysts¹¹⁵ and, recently, with the new homogeneous metallocene catalysts.¹¹⁶

Alternating copolymers of ethylene with olefins containing double bonds in the *cis* configuration, like *cis*-2-butene, cyclopentene, cycloheptene,¹¹⁵ and norbornene,¹¹⁶ have been described. Recently also copolymers of carbon monoxide with styrene and styrene derivatives, having syndiotactic¹¹⁷ and isotactic¹¹⁸ configurations, have been synthesized and characterized.

In the case of the alternating copolymer of ethylene with *cis*-2-butene, four different stereoregular configurations are possible, according to the relative *threo* and *erythro* configurations of the two adjacent asymmetric carbon atoms and the relative configurations of successive monomeric units along the chain, isotactic or syndiotactic.¹¹⁹ The four possible configurations have been defined *threo*-isotactic and syndiotactic and *erythro*-isotactic and syndiotactic (Figure 2.18).¹¹⁹ However, the terms *threo* and *erythro* have been used to define the relative configurations in monomeric units containing two adjacent asymmetric atoms bound to different substituents, $-\text{CHA}-\text{CHB}-$.^{1,12} In the case of the ethylene-*cis*-2-butene alternating copolymer, the asymmetric carbon atoms are bound to two methyl groups; therefore, the possible configurations should be defined *racemo*-isotactic and syndiotactic and *meso*-isotactic and syndiotactic¹² (Figure 2.18). The experimental chain axis of 9.10 Å and a periodicity per structural unit of 2.27 Å, determined by X-ray diffraction,¹¹⁹ have indicated that two structural units composed of two ethylene and two 2-butene units are included in the chain axis. A conformation of the chain characterized by a succession of torsion angles $\text{TTTG}^+\text{TTTG}^-$ and a *ti* symmetry accounts for the experimental chain axis. This conformation is compatible with a *meso*-diisotactic (*erythro*-diisotactic as defined in Ref. 119) configuration of the chain, as found in the crystal structure¹¹⁹ (Figure 2.19). It is worth noting that this structure is the first case in which an isotactic polymer is characterized by a chain conformation in the crystalline state corresponding to a regular succession of enantiomorphous structural units related by an inversion center instead of a helical conformation characterized by a repetition of isomorphous structural units.

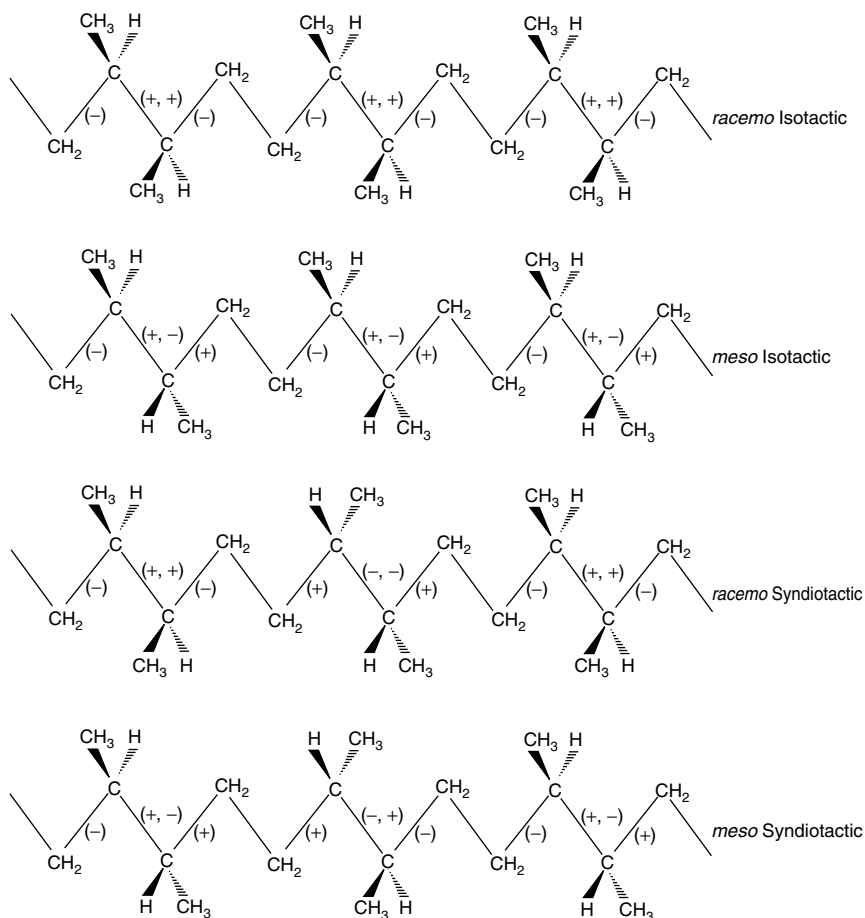


Figure 2.18 Four possible configurations in chain of alternating copolymer between ethylene and *cis*-2-butene. Sequences of (+) and (-) bonds are also indicated. Note that in Ref. 119 relative configurations *racemo* and *meso* were defined as *threo* and *erythro*, respectively.

The synthesis of linear alternating copolymers of styrene and carbon monoxide using soluble organometallic palladium catalysts has been described recently.¹¹⁷ Depending on the catalyst, isotactic or syndiotactic configurations of the styrene units have been obtained. With achiral ligands, chain-end control of the polymerization was considered to be operative¹²⁰ and a syndiotactic configuration of the copolymer was assigned by X-ray diffraction.¹²⁰ Chiral ligands switch the chain-end control to yield the isotactic optically active copolymer.¹¹⁸ Similar values of the chain axes (7.5 Å) have been found

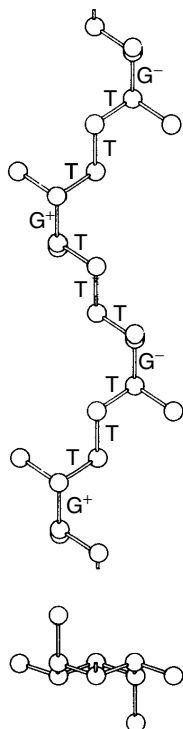


Figure 2.19 Side view and projection along chain axis of conformation of chains in crystals of alternating ethylene-*cis*-2-butene copolymer.¹¹⁹

for both syndiotactic^{120–122} and isotactic copolymers.¹²³ This value indicates nearly extended conformations for the chains of both copolymers.

The constitution of isotactic (i-STCO) and syndiotactic (s-STCO) alternating styrene–carbon monoxide copolymers makes the two directions of the chain intrinsically nonequivalent, so that inversion centers, binary axes, and mirror planes perpendicular to the chain axis can be excluded for both copolymers. The helical and glide plane symmetries can be excluded for the syndiotactic and isotactic copolymers, respectively, because they are incompatible with the corresponding configurations. The only possible line repetition symmetries are *tc* and *s(M/N)* for the syndiotactic and isotactic chains, respectively (Figure 2.20). The sequences of torsion angles are $\dots\theta_1\theta_2\theta_3-\theta_1-\theta_2-\theta_3\dots$ for the *tc* symmetry of s-STCO and $\dots\theta_1\theta_2\theta_3\theta_1\theta_2\theta_3\dots$ for the *s(M/N)* symmetry of i-STCO (Figure 2.20).

For the syndiotactic copolymer, highly extended conformations with *c* values of 7.5–7.6 Å can be obtained for a glide plane symmetry when

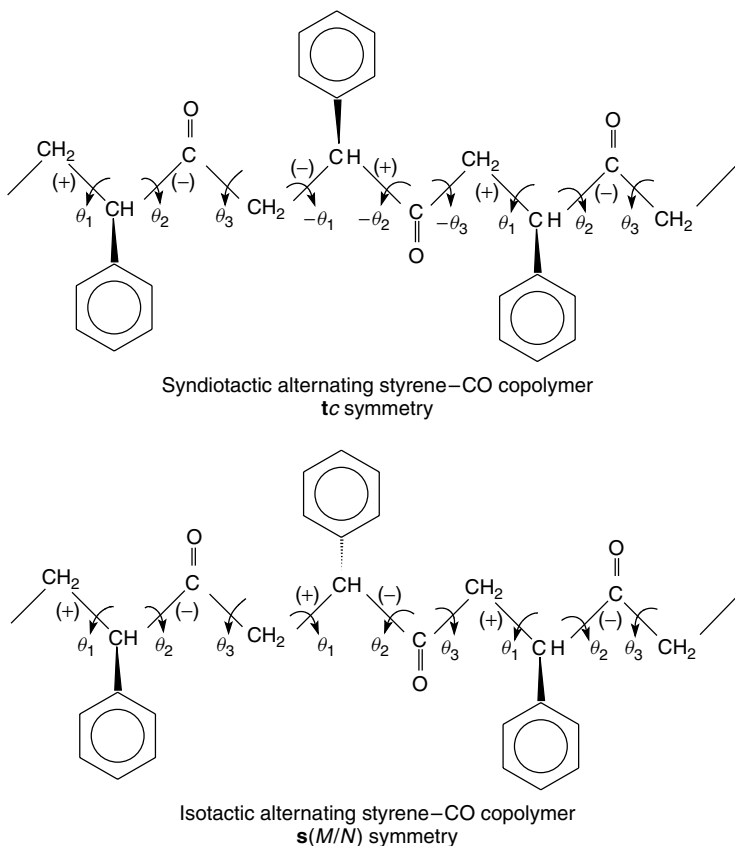


Figure 2.20 Sequences of torsion angles in chains of syndiotactic and isotactic alternating styrene-CO copolymers, according to *tc* and *s(M/N)* symmetries, respectively.

θ_1 , θ_2 , and θ_3 are slightly deviated from 180° , in the range $180^\circ \pm \delta$ with δ being $25\text{--}30^\circ$.¹²¹ The experimental values of the torsion angles found in the crystal structure of s-STCO^{121,122} are indeed $\theta_1 = 170^\circ$, $\theta_2 = -162^\circ$, and $\theta_3 = -150^\circ$. Similar values have been found by conformational energy calculations.¹²⁴

For the isotactic polymer, highly extended chains with chain axis of $7.5\text{--}7.6$ Å can be obtained with a helix repeating after two structural units [*s*(2/1) line repetition group] when θ_1 , θ_2 , and θ_3 are in the range $180^\circ \pm \delta$, with δ being $25\text{--}30^\circ$ and $\delta_1 + \delta_2 + \delta_3 \approx 0$.¹²⁵ The experimental values of the torsion angles found in the crystal structure of i-STCO¹²³ are indeed $\theta_1 = -161.5^\circ$, $\theta_2 = 155.3^\circ$, and $\theta_3 = -171.4^\circ$. Similar values have been found by conformational

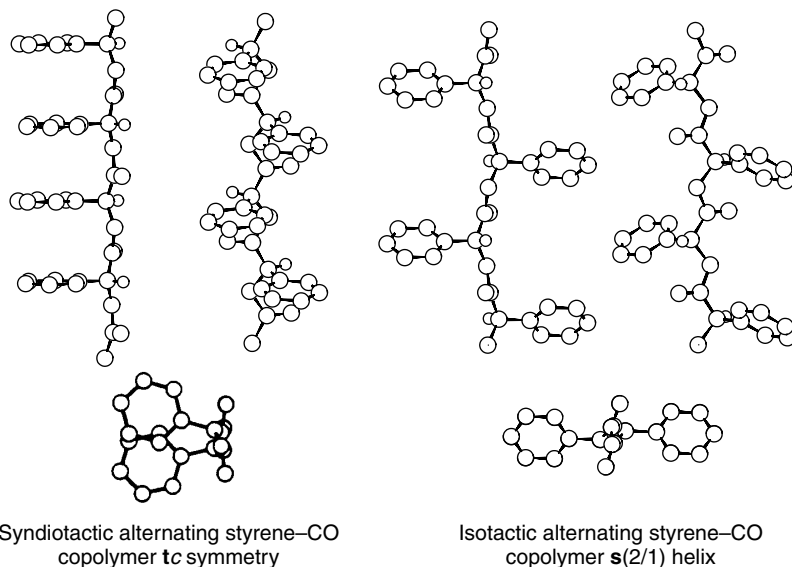


Figure 2.21 Side views and projections along chain axis of conformations of chains in syndiotactic¹²¹ and isotactic¹²³ alternating styrene-CO copolymers.

energy calculations.¹²⁵ Models of the chain conformations of *s*-STCO and *i*-STCO are reported in Figure 2.21.

3 PACKING OF MACROMOLECULES IN POLYMER CRYSTALS

3.1 General Principles

As discussed in the previous sections, the principles of equivalence and of minimum internal conformational energy allow establishing the conformation assumed in the crystalline state by a stereoregular polymer chain. General rules concerning the mode of packing of polymers in the crystals have also been described by Corradini.¹ When no strong electrostatic interactions are present, polymer crystals are generally built up according to the *principle of close packing*,¹²⁶ which establishes that *the packing of molecules in crystals is dominated by the condition that the closest distance between nonbonded atoms is defined by their van der Waals radii*. Kitajgorodskij has shown that, for low-molecular-weight organic compounds, the close packing corresponds to the free-energy minimum, that is, the crystal structure of a molecule corresponds to one of the minima of the multidimensional surface of the energy.¹²⁶

The close-packing principle implies that the energy minima are close to the minima of the multidimensional volume surface, provided that the distances between neighboring atoms of different molecules are not lower than the van der Waals distances.

Besides the energy factors, defined by the close-packing principle, entropic factors are also involved in determining the mode of packing of molecules. *A molecule in a crystal tends to maintain part of its symmetry elements, provided that this does not cause a serious loss of density.* In a more symmetric position a molecule has a greater freedom of vibration, that is, the structure corresponds to a wider energy minimum.¹²⁶

In the case of polymers the application of the principle of close packing is easier than in the case of low-molecular-weight compounds, because the known chain conformation allows determining the structure along the direction corresponding to the chain axis.¹ Moreover, if the elements of symmetry of the chains are compatible with the crystal, they are generally maintained in the crystal lattice, so that the problem is further simplified. In this case, indeed, geometrically equivalent atoms belonging to different structural units of the same chain can assume equivalent positions with respect to the corresponding atoms of neighboring chains, that is, they become crystallographically equivalent.¹ On the basis of these principles, starting from the configuration and the conformation of the chains, it is possible to theoretically predict the mode of packing of polymers.¹

Corradini has shown that almost all the known crystal structures of polymers are easily rationalizable in terms of these principles.¹ In particular, he suggested that the mode of packing of polymer chains first depends on the outside envelope of the chains.¹ Depending on the conformation, the form of a polymer chain may be approximated by a cylinder of radius r , corresponding to the outside envelope of the atoms of the main chain, bearing a periodic helical relief of radius R , corresponding to the atoms of the lateral groups.¹ When the ratio r/R is close to 1, the chains have the form of a uniform cylinder, as in polyethylene,¹²⁷ *trans*-1,4-poly(1,3-butadiene),^{73,75} and polytetrafluoroethylene.^{106,107} In these cases the best mode of packing is the hexagonal arrangement of the chains with coordination number equal to 6. When the ratio r/R is different from 1, the form of the chains may be approximated by a cylinder in which hollows and bulges are periodically repeated, that is, the chains have an outside envelope similar to a screw.¹ If the ratio r/R is very small, close to 0.1–0.2, as for chains in threefold helical conformation, a trigonal packing of enantiomorphous chains may arise. Each 3/1 right-handed helical chain is surrounded by three left-handed chains and vice versa, as in isotactic polystyrene³⁴ and form I of isotactic polybutene.³⁵ Higher values of the ratio r/R , close to $\sqrt{2}-1$, are obtained in the cases of many vinyl polymers with chains in complex helical conformation $s(M/N)$

with a fractional ratio M/N , like form I of isotactic poly(4-methyl-1-pentene) (7/2 helix),³⁹ form II of isotactic poly(1-butene) (11/3 helix),³⁶ and isotactic poly(*m*-methylstyrene) (11/3 helix).¹²⁸ In these cases a tetragonal packing of enantiomorphous chains with coordination number equal to 4 is favored. Each right-handed chain is surrounded by four left-handed chains and vice versa, and a tight fitting of threads into grooves is achieved.¹

The driving force toward this kind of packing is so high that, even in the case of optically active isotactic poly((*S*)-4-methyl-1-hexene), where the chiral group should preferentially stabilize one of the two possible senses of the helix, it has been found that both right- and left-handed 7/2 helical chains are present in the tetragonal unit cell.^{39a} In other optically active polymers, as well as in some polymers from achiral monomers, chiral structures, characterized by all isomorphous helical chains in the unit cell, have been found (see Section 3.7). For instance, in isotactic poly(5-methyl-1-hexene),¹²⁹ isotactic poly(*t*-butylacrylate),¹³⁰ optically active isotactic poly((*S*)-5-methyl-1-heptene),^{129b,c} and poly((*S*)-3-methyl-1-pentene),⁶⁶ chiral pseudohexagonal or tetragonal packing with isomorphous 3/1 or 4/1 helical chains have been found.

Antichiral structures, characterized by the packing of enantiomorphous helical chains, are generally obtained through crystallographic glide planes or inversion centers.¹ Glide planes parallel to the chain axes are able to repeat neighboring enantiomorphous and isoclined chains producing good space filling, whereas inversion centers produce a packing of enantiomorphous and anticlined chains.¹ According to these principles, in the trigonal packing of chains in 3/1 helical conformation, each right-handed chain may be surrounded by three left-handed isoclined or anticlined chains and vice versa (space group $R3c$ or $R\bar{3}$, respectively). This kind of packing has been found, for example, for isotactic polystyrene,³⁴ form I of isotactic poly(1-butene),³⁵ isotactic 1,2-poly(1,3-butadiene),¹³¹ isotactic poly(*o*-fluorostyrene),¹³² and isotactic poly(vinyl methyl ether).¹³³ Chains in 4/1 helical conformation are generally packed in tetragonal lattices, and the possible space groups are $I4_1cd$ or $I4_1/a$, with each right-handed chain surrounded by four left-handed isoclined or anticlined chains, respectively, and vice versa.¹ Structures with $I4_1cd$ symmetry have been found for isotactic poly(*o*-methylstyrene)¹³⁴ and poly(α -vinylnaphthalene),¹³⁵ while the $I4_1/a$ space group has been found for isotactic poly(vinylcyclohexane)^{136,137} and almost all the polyaldehydes.¹³⁸ Similar kinds of packing are obtained with chains in complex M/N helical conformation, with M/N ranging between 3 and 4. In these cases the space group is generally $P\bar{4}$, as in form I of isotactic poly(4-methyl-1-pentene) (7/2 helix),³⁹ form II of isotactic poly(1-butene) (11/3 helix),³⁶ isotactic poly(*m*-methylstyrene) (11/3 helix),¹²⁸ and syndiotactic poly(4-methyl-1-pentene) (12/7 helix).⁶¹

The entropic principle, which establishes that the symmetry of the isolated chains is generally maintained in the lattice, is valid not only for chains in helical conformations but also for other elements of symmetry. For instance, in almost all the known structures of polymers having chain conformations with a glide plane, this symmetry element is maintained in the lattice because it allows a good distribution of bulky substituents of different chains between themselves (e.g., *cis*-1,4-poly(1,3-butadiene),⁷² *cis*-1,4-poly(isoprene),^{72,76-78} syndiotactic 1,2-poly(1,3-butadiene),¹³⁹ and form III of sPP²⁴). In some cases the complete chain symmetry is preserved in the crystal lattice; for instance, in *cis*-1,4-poly(1,3-butadiene) the binary axes perpendicular to the chain axes crossing the double bonds as well as the inversion centers located on the central single bonds (*tci* symmetry) are maintained in the lattice (space group *C2/c*)⁷²; in syndiotactic 1,2-poly(1,3-butadiene) the binary axes centered on the CH₂ groups and the symmetry planes perpendicular to the chain axis are also preserved.¹³⁹

These general principles, which regulate the conformation and the mode of packing of macromolecules, are very useful and valid in the description of ideal, ordered structures, where the chains having regular constitution, configuration, and conformation are regularly packed according to a defined space group. In the description of these ideal structures three principles have been considered for a long time as basic principles of polymer crystallography:

1. A crystalline polymer must be stereoregular.
2. The chains must be parallel.
3. The symmetry of the chain tends to be maintained in the crystalline lattice, and the local symmetry becomes a crystallographic symmetry.

Recently, new interesting phenomena which control the mode of packing of polymers have been found, and the validity of these principles is being weakened. In particular, we know the following:

1. An atactic polymer can crystallize, for instance the case of polyacrylonitrile, whose crystallizability has been explained on the basis of local conformations, which produce extended and straight chains.¹⁴⁰
2. In a crystalline polymer the chains can be nonparallel; for instance, the structure of the γ -form of isotactic polypropylene is characterized by the packing of nearly perpendicular chains.^{141,142}
3. The high symmetry of the chains can be broken in the limit-ordered crystalline lattice of polymers (symmetry breaking).

Moreover, we have already shown in the Section 2.6 that chains characterized by disordered conformation may crystallize. The presence of disorder in polymer crystals is a typical feature, so that the real crystalline forms are generally different from the ideal models. These disordered modifications can,

however, be well studied, and either the nature or the amount of the disorder present in the structure can be described (Section 3.4).

The observation of the lack of symmetry in ordered structures of polymers is strictly related to the possibility of the direct observation of the local arrangements of polymer chains. The study of the crystal structure of polymers, performed with traditional X-ray diffraction, generally leads to models of packing which describe the order in the long range. The local arrangement of the polymer chains is, generally, not accessible by X-ray diffraction. More recently, the use of electron diffraction and solid-state ^{13}C NMR spectroscopy has allowed direct observation of the local arrangement of the chains and new phenomena such as *symmetry breaking* and *frustration* have been revealed as discussed below.

3.2 Symmetry Breaking

The crystal structure of the most stable form of sPP, form I, provides a first example of symmetry breaking. In the ideal ordered structure, chains in the twofold helical conformation are packed in an orthorhombic unit cell.⁵⁹ The space group proposed for this structure is $Ibca$, according to the intensities of the reflections observed in the X-ray and electron diffraction patterns.⁵⁹ This space group corresponds to a lattice having the highest symmetry compatible with the symmetry of the sPP chain, because the local twofold rotation symmetry axes of the $s(2/1)2$ helical chains, perpendicular to the chain axis, are maintained in the lattice as crystallographic symmetry (Figure 2.22a). However, the electron diffraction pattern of single crystals of sPP grown at very high temperature show the presence of the 001 reflection,^{143–145} which is

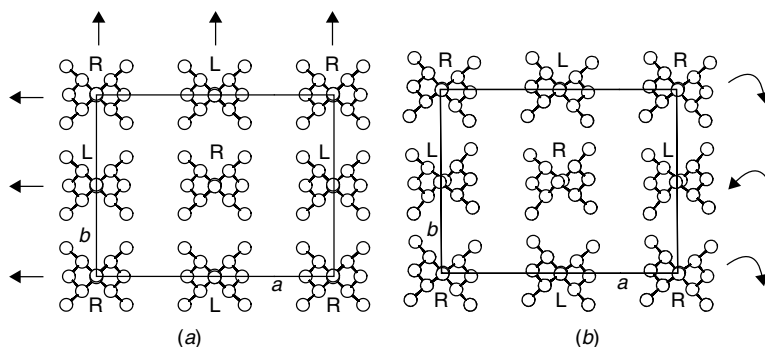


Figure 2.22 Models of packing of chains in form I of sPP according to space groups (a) $Ibca$ ⁵⁹ and (b) $P2_1/a$.¹⁴⁶ Arrows indicate crystallographic twofold axes, present in (a) and lost in (b). In (b) chains are rotated by nearly 5° around chain axes, according to direction indicated by the arrows.

extinct in the space group $Ibca$. This indicates that the symmetry of the space group should be lower than $Ibca$.¹⁴⁶ A general principle may be deduced from these data: *The low symmetry of the unit cell may be revealed even for symmetric single crystals by the asymmetries of the diffraction patterns.*

Moreover, in the solid-state ^{13}C NMR cross-polarization magic angle spinning (CPMAS) spectrum of annealed samples of sPP in form I, the resonance of the methyl carbon atom is split into a doublet.¹⁴⁷ This is a clear evidence that two nonequivalent methyl carbon atoms are present in the unit cell and indicates that the lattice has a symmetry lower than $Ibca$. A lower symmetry can be obtained by removing the crystallographic twofold axes, so that the chains may rotate around their axes and translate along the chain axis.¹⁴⁶ If the chains are slightly rotated around their axes, the local twofold rotation axes of the chains, perpendicular to the chain axis, are lost in the lattice and the symmetry is broken. The space group is monoclinic $P2_1/a$ and two of the four chains included in the unit cell are independent, that is, not related by any element of symmetry (Figure 2.22b).¹⁴⁶ The low-symmetry model accounts for the electron diffraction data and the splitting observed in the solid-state NMR spectrum and corresponds to local packing of the chains. In other words, it describes a local arrangement of the chains, that is, the order at very short distance, which can be detected only by direct observation of a very small area of the diffracting crystals. Owing to possible different setting angles of the chains in different crystalline domains diffracting coherently, the model with higher symmetry $Ibca$ (Figure 2.22a) may be considered, however, as an average model structure, suitable for the description of the structure at long-range distance.

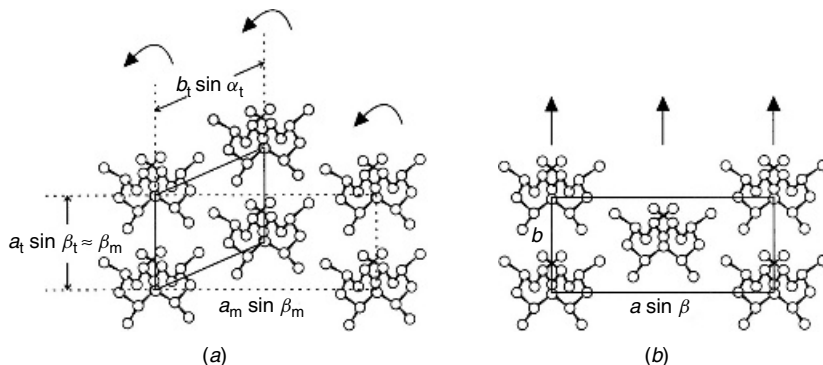


Figure 2.23 Models of packing of chains in form IV of sPP according to space groups (a) $P1$ ¹⁴⁸ and (b) $C2$ ¹⁴⁹. Arrows indicate crystallographic twofold axes, present in (b) and lost in (a). In (a) chains are rotated by 6.5° according to direction indicated by arrows and continuous and dashed lines show triclinic and monoclinic unit cells, respectively.

Form IV of sPP also presents the phenomenon of symmetry breaking. The crystal structure of form IV, as reported by Chatani et al.,¹⁴⁸ is characterized by chains in $(T_6G_2T_2G_2)_n$ helical conformation (t_2 symmetry) packed in a triclinic unit cell according to the space group $P1$ (Figure 2.23a). It has been recently evidenced that the structure could also be described by an analogous model having higher symmetry.¹⁴⁹ In this alternative model, reported in Figure 2.23b, the unit cell is monoclinic and the space group is $C2$.¹⁴⁹ In the monoclinic model (Figure 2.23b) the local twofold rotation axes of the chain, perpendicular to the chain axis, are maintained in the lattice as crystallographic symmetry (space group $C2$). In the triclinic model (Figure 2.23a) all the chains are rotated by the same amount (nearly 6.5°) around the chain axis with respect to the monoclinic model. The crystallographic twofold rotation axes are lost as a consequence of this rotation and the symmetry is broken (space group $P1$). Since in the triclinic model clockwise and counterclockwise rotations are equivalent, the monoclinic model with higher $C2$ symmetry (Figure 2.23b) may be considered as an average model for the structure of form IV, which may describe the order in the long range. The triclinic model (Figure 2.23a) describes a local situation of order, where the symmetry, locally, is broken.

Symmetry breaking has also been found in the structure of the α -form of sPS. Various models of packing have been proposed for this structure.^{51-53,150} The most important feature is that the *trans* planar chains are organized in triplets.⁵¹ The X-ray powder and fiber diffraction patterns^{52,53} as well as the electron diffraction pattern^{51,150} are basically accounted for by a trigonal packing of triplets of *trans* planar chains, according to space groups $P3c1$ or $P3$.^{52,53} Three independent triplets (not related by any element of symmetry) are included in the unit cell. The space group of highest symmetry for the ordered structure would be $P3c1$ if the local glide plane of the *trans* planar chains was maintained in the lattice as crystallographic symmetry⁵² (Figure 2.24a). The analysis of the electron diffraction pattern of single crystals^{51,150} shows that the intensities of $hk0$ and $kh0$ reflections are different. This indicates that the symmetry of the space group should be lower than $P3c1$.^{53,150} These data still show that *low symmetries of the unit cell are revealed even for symmetric single crystals by the asymmetries of the electron diffraction patterns*. The α -form of sPS forms, indeed, standard hexagonal single crystals^{51,150} but a low unit-cell symmetry.⁵³

The removal of the crystallographic glide plane symmetry produces a lowering of the space group symmetry from $P3c1$ to $P3$.⁵³ In the space group $P3$ the triplets of chains may rotate around the threefold axes⁵³ and, in a refined model, the azimuthal orientations of the three independent triplets are found to be different.¹⁵⁰ The crystallographic glide planes are lost because of this rotation and the symmetry is broken (Figure 2.24b). This model should

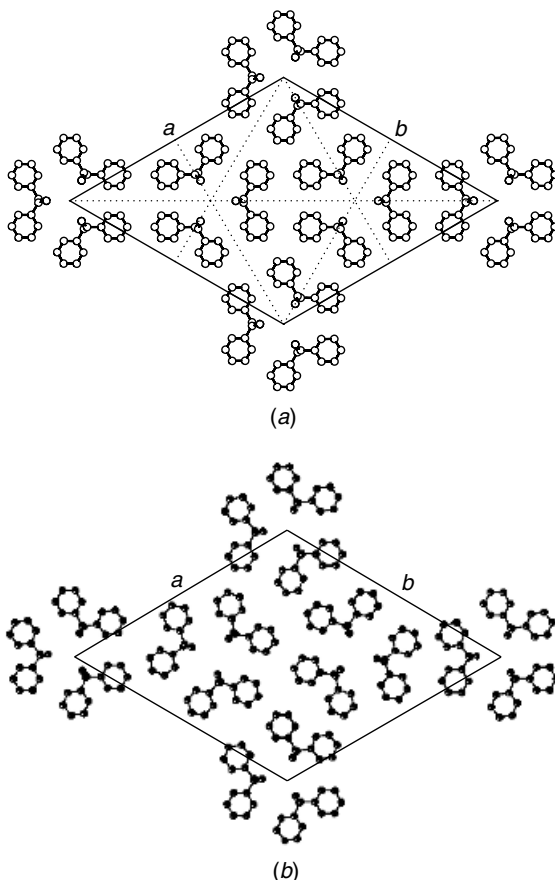


Figure 2.24 Models of packing of chains in α -form of sPS according to space groups (a) $P3c1$ ⁵² and (b) $P3150$. In (a) dotted lines indicate crystallographic glide planes coincident with local glide planes of chains. In (b) triplets of chains are rotated around threefold axes and crystallographic glide planes are lost.

be thought as a local ordered arrangement of the chains and accounts for the different intensities of the $hk0$ and $kh0$ reflections observed in the electron diffraction pattern.^{51,150} Disorder in the setting angles of the triplets, or opposite values of the setting angles of the triplets in different domains of the crystal, may produce packing modes with higher symmetry (Figure 2.24a), which can describe the order in the long range.⁵³

Another example of symmetry breaking is provided by the crystal structure of form III of iP4MP. Electron diffraction patterns of the square single crystals of form III have indicated that chains in fourfold helical conformation

are packed in a tetragonal unit cell.^{42,151} Typical space groups for isotactic polymers with chains in 4/1 helical conformation are $I4_1cd$ and $I4_1/a$ ^{134–138} (Section 3.1).

For form III of iP4MP, however, two experimental data indicate that the symmetry of the space group is lower than $I4_1/a$ or $I4_1cd$. Pradere et al.¹⁵¹ have, indeed, observed different intensities of $hk0$ and $h\bar{k}0$ reflections in the electron diffraction patterns of the square single crystals. Moreover, dark-field imaging has revealed that the square crystals are made of many small microdomains.¹⁵¹ Also in this case, the same principle seems to be valid: *Although the single crystals are highly symmetric, the packing presents low symmetry as revealed by the asymmetry of the electron diffraction pattern.* The diffraction pattern obtained with larger selected area diffraction is symmetric, that is, the intensities of $hk0$ and $h\bar{k}0$ reflections are equal.¹⁵¹ This means that only using a small diffraction aperture and when a very small area of the single crystal is selected can the presence of microdomains and the asymmetry of the diffraction pattern be evidenced. The solid-state CPMAS ¹³C NMR spectrum of form III of iP4MP,¹⁵² reported in Figure 2.25, gives the same evidence of a low symmetry of the packing. The resonances of the methyl carbon atoms show narrow splittings which can be traced back to a packing effect. Two different kinds of methyl C6 and two different kinds of methyl C5 must be present in the unit cell.¹⁵² This also indicates that the symmetry of the space group should be lower than $I4_1/a$ or $I4_1cd$.

On the basis of these experimental observations, the model of packing reported in Figure 2.26 (space group $I4_1$) has been proposed.^{33,153} The low symmetry of the packing comes from the fact that two of the four chains included in the tetragonal unit cell are independent, that is, are not related by

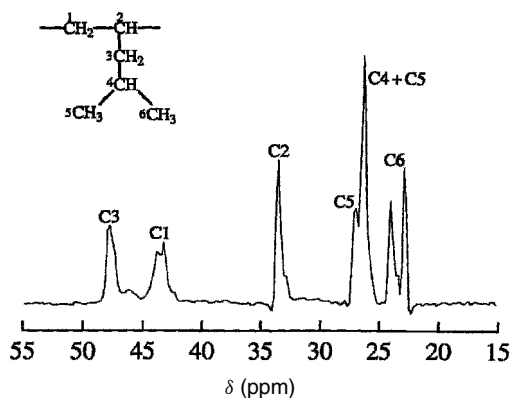


Figure 2.25 Solid-state ¹³C NMR CPMAS spectrum of form III of iP4MP.¹⁵²

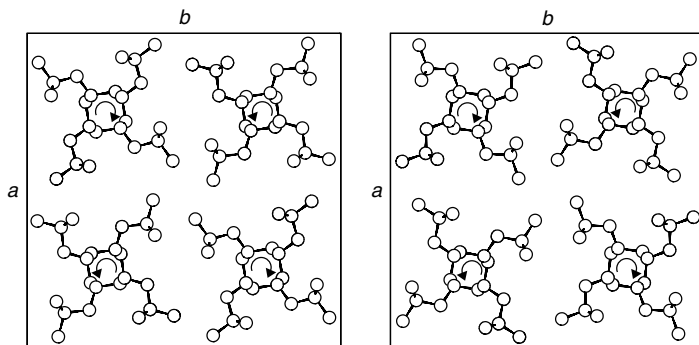


Figure 2.26 Model of packing of chains in form III of iP4MP according to space group $I4_1$.^{33,153} Two equivalent unit cells characterized by chains having opposite azimuthal orientations indicating possible packing in different microdomains of crystal are shown.

any element of symmetry and are present in different azimuthal orientations. This model accounts for the asymmetry of the diffraction patterns and the splitting of the resonances observed in the CPMAS spectrum of Figure 2.25. The methyl carbon atoms of the two independent chains present, indeed, different crystallographic environments since the contact distances with the neighboring atoms are different.¹⁵² The low-symmetry model describes the local arrangement of the chains, which can be detected only by direct observation of a very small area of the diffracting crystals. When larger areas are observed, for example by X-ray diffraction or by electron diffraction with a large selected area aperture,¹⁵¹ different microdomains characterized by different setting angles of the chains (e.g., those shown in Figure 2.26) may diffract coherently and only an average structure with higher symmetry can be seen. A model with higher symmetry, for instance the space group $I4_1/a$, describes the order in the long range and, indeed, accounts for the X-ray diffraction pattern and the symmetric electron diffraction pattern obtained with larger selected area aperture.

3.3 Frustrated Polymer Crystal Structures

As discussed in the Section 3.1, according to the close-packing principle, polymer chains in 3/1 helical conformations are generally packed in trigonal lattices, where the 3/1 symmetry is preserved and enantiomorphous helices are closely packed through glide planes or inversion centers (space group $R3c$ or $R\bar{3}$).¹ Recently a different mode of packing of three fold helical chains in trigonal unit cells has been rationalized in term of the concept of frustration,¹⁵⁴ a new concept in polymer crystallography. The frustrated structures are based on the packing of three isochiral threefold helices in trigonal unit cells. The concept of frustration was introduced in materials science by Toulouse¹⁵⁵ to

describe the mutual orientation of magnetic spins in antiferromagnetic systems. Frustration exists whenever vicinal requirements (e.g., antiparallelism of spins) are incompatible with packing requirements (e.g., close-packed hexagonal lattice). The concept of frustration was introduced in polymer crystallography by Lotz et al.¹⁵⁴ Frustration results from the fact that two of the three helices included in the trigonal unit cell maximize their interactions at the expense of the third one. As a consequence, the crystallographic environment of two chains differs significantly from that of the third one. Frustrated polymer structures have been established for various achiral and chiral polymers,^{156,157} for instance, the β -form of iPP,^{154,158,159} isotactic poly(2-vinylpyridine),^{160,161} the α -form of sPS,¹⁵⁰ isotactic poly(*t*-butylethylene sulfide)^{156,162,163} and the β -form of poly(L-lactide),¹⁶⁴ and for biopolymers, for instance, poly(L-hydroxyproline)^{165,166} and triethylcellulose.^{156,167}

Frustrated polymer crystal structures generally display characteristic morphological features and typical diffraction patterns. Very often a triangular shape of the single crystals has been observed.^{156,168} This is a macroscopic manifestation of the fact that the front and back faces of any crystallographic plane have different topologies. These differences induce unequal front and back growth rates for growth planes and, therefore, result in the triangular, rather than hexagonal, single-crystal morphology.¹⁶⁸ Frustrated structures display $hk0$ diffraction patterns presenting typical asymmetries,^{150,156} which indicate an asymmetry of the content of the unit cell, that is, a different azimuthal orientation of the three $3/1$ helical chains. Moreover, also typical is the relative intensities of some hkl reflections, in particular a weak intensity of the 003 reflection compared to that of the 103 reflection.^{156,163} This indicates that the three helices are not shifted by an exact $c/3$ distance but the c axis shifts of the three helices are uneven. It is worth mentioning that most of these experimental observations have been obtained thanks to the method of epitaxial crystallization of polymers on various substrates, developed by Wittmann and Lotz.¹⁶⁹

The crystal structure of the β -form of isotactic polypropylene is the first example of a frustrated structure.^{154,158,159} The model of packing is reported in Figure 2.27.¹⁵⁸ The trigonal unit cell contains three isochiral threefold chains having different azimuthal settings. It is apparent that the crystallographic environment of two chains is different from that of the third chain. The chain A is surrounded by six nearly equivalent chains (chains B), while the other two chains (chains B) are surrounded by three chains having a given azimuthal orientation (chains A) and three other chains having a different orientation (chains B). Two chains experience strong interactions with the neighbors, whereas the third chain interacts weakly with the neighboring chains, giving rise to the frustration.^{154,158}

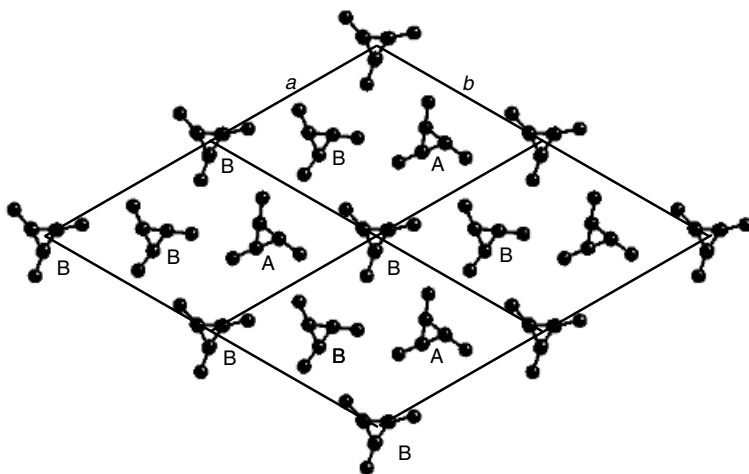


Figure 2.27 Model of packing of chains in β -form of iPP.¹⁵⁸

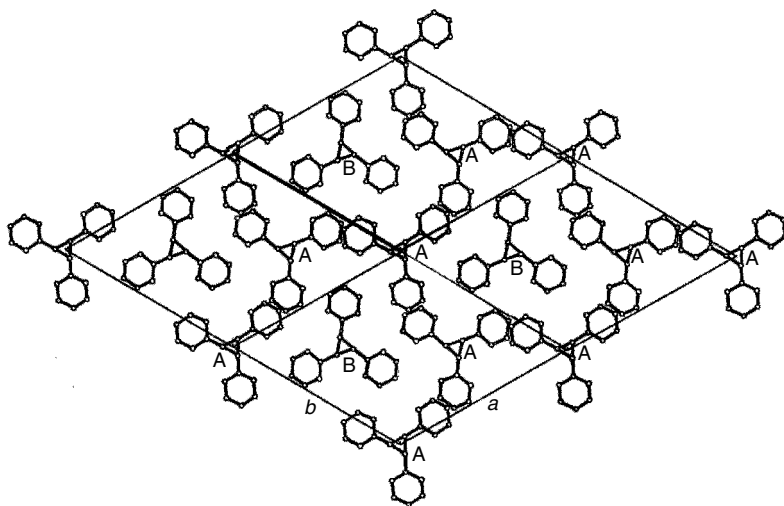


Figure 2.28 Model of packing of chains in poly(vinylpyridine).¹⁶¹

Similar frustration has been evidenced for the crystal structure of isotactic poly(2-vinylpyridine)^{160,161} (Figure 2.28). Also in this case three independent threefold helices are included in the trigonal unit cell and the frustration is related to a different azimuthal orientation of the chains due to the different interactions between the chains.¹⁶⁰ Two chains (chains A in Figure 2.28) maximize their interactions at the expense of the third one (chain B).

The crystal structure of the α -form of sPS, showing symmetry breaking and discussed in the previous section, has been reevaluated by Lotz,¹⁵⁰ who recognized a frustrated packing. The trigonal unit cell contains three triplets of *trans* planar chains having different azimuthal settings (Figure 2.24*b*). The triplets of chains behave like the threefold helical chains in the other frustrated structures. The azimuthal settings and the relative shifts of the triplets indicate that two triplets maximize their interactions while the third one interacts less favorably with the neighbors.

Frustration and symmetry breaking are two different but related concepts. Frustration implies symmetry breaking because it occurs when three isochiral threefold chains having different azimuthal orientations, hence not related by any element of symmetry, are packed in a trigonal lattice. The symmetry breaking is probably a more general concept because it has been found even in the case of orthorhombic and tetragonal unit cells.^{33,146,149}

3.4 Disorder in Polymer Crystals

The examples of polymer crystal structures shown in the previous sections are ideal structures, which can be described with the traditional concepts of the principles of equivalence and close packing or the new concepts of symmetry breaking¹⁴⁶ and frustration.¹⁵⁴ The models of perfect crystals are characterized by a long-range positional order for all the atoms (disregarding thermal motion). The X-ray diffraction patterns of such crystals, oriented with the chain axes along one direction (as in oriented fibers), present sharp reflections organized in layer lines.

Various kinds and amounts of disorder can be present in the crystal structures of polymers, depending on the conditions of crystallization. Lack of order may arise from the presence of defects in the chemical constitution and configuration and mode of packing. When large amounts of chemical defects are present in the polymer molecules, the lack of order is generally complete, leading to amorphous materials. Even in the case of regular constitution, configuration, and conformation, disorder may be present in the crystals due to the presence of defects in the mode of packing. Generally, disorder in the packing of polymer chains may occur while a long-range positional order of some structural feature is maintained.

Different kinds of disorder may affect differently the X-ray diffraction pattern of the crystals. Depending on the features present in the X-ray fiber diffraction pattern, it is useful to distinguish three main classes of disordered structures¹⁷⁰:

- (i) The long-range three-dimensional periodicity is maintained only for some characterizing points of the structure. In this case there is

only a partial three-dimensional order and the X-ray fiber diffraction pattern presents sharp reflections and diffuse halos. Disordered structures belonging to this class may be characterized, for instance, by disorder in the positioning of right- and left-handed helical chains (Section 3.5.1) or disorder in the up-down positioning of conformationally ordered chains (Section 3.5.2) or disorder in the stacking of ordered layers of chains along one crystallographic direction (Section 3.5.3).

- (ii) The long-range positional three-dimensional order is maintained only for some structural features which are not point centered, for example the chain axes. Structures characterized by conformationally disordered chains with a long-range order in the position of the chain axes belong to this class (Sections 2.6 and 3.6). The X-ray fiber diffraction pattern of this kind of disordered structure is characterized by sharp reflections on the equator and diffuse halos on the other layer lines.
- (iii) The long-range positional order is maintained only in two or one dimension, for example only along each chain axis. Examples may be provided by structures characterized by conformationally ordered parallel chains with disorder in the lateral packing of the chains. Short-range correlations between the atoms of neighboring chains may still be present, but long-range order is maintained only along the axis of each chain (Section 3.6). The X-ray fiber diffraction pattern is characterized by well-defined layer lines presenting only diffuse reflections.

Crystalline forms presenting large amounts of disorder of the kind (ii) or (iii) are generally called *mesomorphic* modifications (Section 3.6), in analogy with the ordered liquids (smectic and nematic). In these cases the lack of periodicities in one or two dimensions (e.g., along the chain axes or along the directions normal to the chain axes) prevents the definition of a unit cell. Typical features in the X-ray diffraction patterns of *mesomorphic* forms are diffuse halos on the equator or on the layer lines depending on the kind of disorder present.

It is worth noting that in polymer structures the various kinds of long-range positional order of the equilibrium positions of the structural elements may be lost after not too big numbers of repetitions owing to the presence of lattice distortions (different from the thermal one), which have been called distortions of the second kind. According to Hosemann and Bagchi,¹⁷¹ these forms are called paracrystalline modifications.

Disordered structures belonging to the class (i) are interesting because, in some cases, they may be characterized by disorder which does not induce changes of the lattice dimensions and of the crystallinity, and a unit cell may still be defined. These particular disordered forms are generally not considered as *mesomorphic* modifications. A general concept is that in these cases the order–disorder phenomena can be described with reference to two ideal structures, *limit-ordered and limit-disordered models*, that is, ideal fully ordered or fully disordered models.

In the *limit ordered model*, chains with regular conformations are packed in a crystalline lattice with a perfect three-dimensional order. Examples of limit-ordered models have been described in Sections 3.1–3.3. It is possible to consider models of disordered structures having the same lattice geometry as in the limit-ordered models. Structural disorder may arise while the same unit cell is maintained, for instance, whenever polymer chains, or even layers of chains, may assume different and equivalent positions in the unit cell without, changing the steric interactions with the neighboring chains. In these cases, indeed, the substitution of chains, or layers of chains, does not produce a large disturbance of the packing, so that a high degree of crystallinity and the same lattice geometry are preserved.

A *limit-disordered model* is an ideal fully disordered structure characterized by disorder corresponding to the statistical substitution of chains or layer of chains. Because the single macromolecules in the considered structures have the same periodical conformation, the difference between the entropies of the ideal ordered and disordered structures is small. Examples of limit-ordered and limit-disordered models are shown in Figure 2.29 for the crystal structure of form I of sPP^{59,145,146,172} (see Section 3.2). In the limit-ordered model there is a regular alternation of right- and left-handed twofold helical chains along the *a* and *b* axes of the unit cell⁵⁹ (Figure 2.29*a*); in the limit-disordered model there is a statistical distribution of right- and left-handed chains in the sites of the lattice while the lattice geometry remains unaltered¹⁷² (Figure 2.29*b*). The limit-disordered model can be described by the statistical space group *Bmcm*.¹⁷²

The real crystalline forms are generally intermediate between the limit-ordered and limit-disordered models, the amount of disorder being dependent on the condition of crystallization and thermal and mechanical treatments of the samples. A condition to have more or less disordered modifications, corresponding to the same unit cell, is the substantial equality of steric hindrances in the space regions where a statistical substitution is achieved (Figure 2.29*b*).

Some examples of disordered structures of the class (i) are given in Section 3.5.

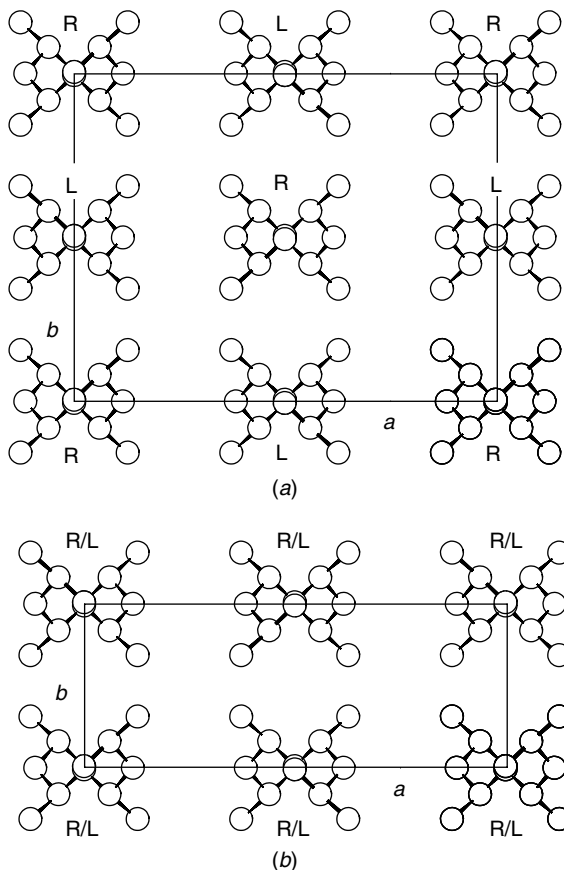


Figure 2.29 (a) Limit-ordered model (space group $Ibca$ or $P2_1/a$) and (b) limit-disordered model (space group $Bmcm$) for crystal structure of form I of sPP¹⁷² (R = right-handed helix, L = left-handed helix).

3.5 Examples of Positional Disorder with Long-Range Three-Dimensional Periodicity Maintained Only for Some Characterizing Points of Structure

3.5.1 Disorder in Positioning of Right- and Left-Handed Helical Chains

As already shown in Figure 2.29a, in the ideal limit-ordered model of form I of sPP, right- and left-handed twofold helical chains alternate along the a and b axes of the orthorhombic unit cell.⁵⁹ In the electron diffraction patterns of single crystals grown at low temperatures, reported by Lovinger et al.,¹⁴⁵ the

211 reflection presents streaks indicating defects in the perfect alternation of enantiomorphous helices. In the X-ray powder diffraction patterns of melt-crystallized samples of sPP, reported in Figure 2.30, the intensity of the 211 reflection at $2\theta = 18.8^\circ$ depends on the crystallization temperature.¹⁷² High intensity of the 211 reflection, corresponding to the limit-ordered modification, characterized by a perfect alternation of enantiomorphous helices along both axes of the unit cell (Figure 2.29a), has been obtained only at high crystallization temperatures. At lower crystallization temperatures, lower intensities of the 211 reflection are observed, indicating disorder in the regular alternation of left- and right-handed helices.¹⁷² The ratio R between the intensities of the 211 and the 020 reflections has been taken as a measure of the degree of order present in the structure.¹⁷² The order parameter R increases with increasing crystallization temperature (Figure 2.31) from $R = 0$, corresponding to a completely disordered structure ($Bmcm$), to a constant value $R = 1$, corresponding to the limit-ordered structure ($Ibca$ or $P2_1/a$).¹⁷² As-prepared samples, or samples crystallized at very low temperatures, showing $R = 0$ (the 211 reflection is absent), are crystallized in disordered modifications close to the limit-disordered model $Bmcm$ (Figure 2.29b), characterized by statistical disorder in the positioning of enantiomorphous helices, although local correlation about the chirality of neighboring chains may still be preserved. Figure 2.31 indicates that form I of sPP is better described by a continuum of disordered modifications, intermediate between the limit-disordered model $Bmcm$ and the limit-ordered model $Ibca$ or $P2_1/a$, the degree of order being dependent on the crystallization temperature.¹⁷²

3.5.2 Disorder in Positioning of Up and Down Chains

A second kind of disorder of class (i) typical of isotactic polymers with chains in helical conformations is the up/down disorder. Detailed structural studies have shown that the α -form of iPP may present a different degree of disorder in the positioning of up and down chains.^{20,173,174} Threefold helical chains of iPP of a given chirality may present the lateral methyl groups up or down with respect to the methine carbon atoms to which they are bound (Figure 2.32). The ideal limit-ordered model proposed for the α -form of iPP (defined α_2 -form)¹⁷⁴ is characterized by an ordered alternation of bilayers of chains composed of all up or all down chains (space group $P2_1/c$, Figure 2.33a). Disorder in the positioning of up and down chains may be present because if up and down chains substitute each other in the same site of the lattice, the same steric interactions with neighboring chains are involved. An ideal-limit disordered model (defined α_1 -form)²⁰ is characterized by a statistical distribution of up and down chains in the lattice (space group $C2/c$) (Figure 2.33b). Samples crystallized or annealed at different

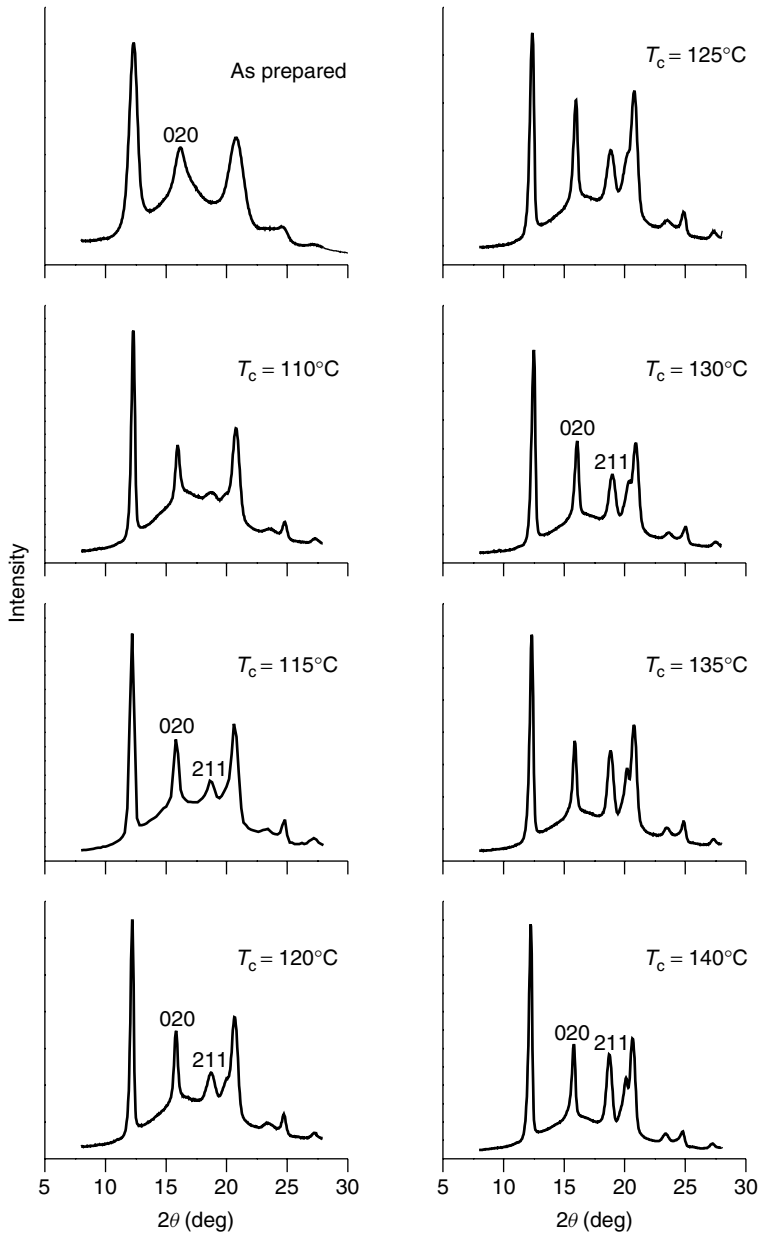


Figure 2.30 X-ray powder diffraction patterns of sPP samples isothermally crystallized from melt at indicated temperatures.¹⁷² Indices of 211 and 020 reflections are given for unit cell of form I of Figure 2.29a.

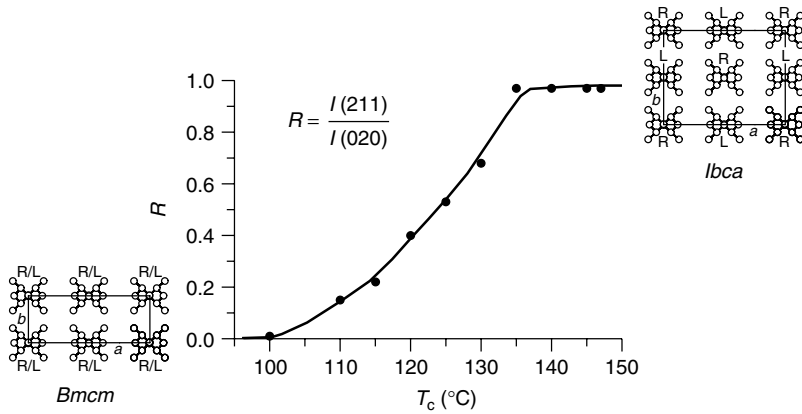


Figure 2.31 Values of order parameter R of sPP samples crystallized from melt reported as function of crystallization temperature T_c .¹⁷²

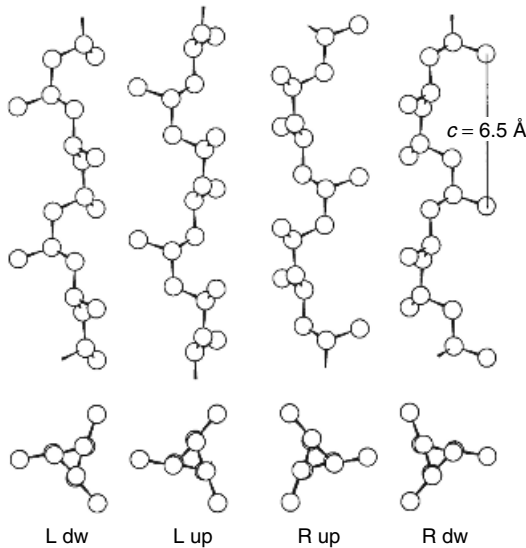


Figure 2.32 Chains of isotactic polypropylene in threefold helical conformation, right-handed (R) up and down (dw) and left-handed (L) up and down.

temperatures show X-ray diffraction patterns with different intensities of hkl reflections with $h + k$ odd,^{175,176} indicating the presence of variable amounts of up/down disorder. The real crystalline modifications are, therefore, intermediate between the two limit-ordered and limit-disordered models, the degree of up/down disorder being dependent on the condition of crystallization.

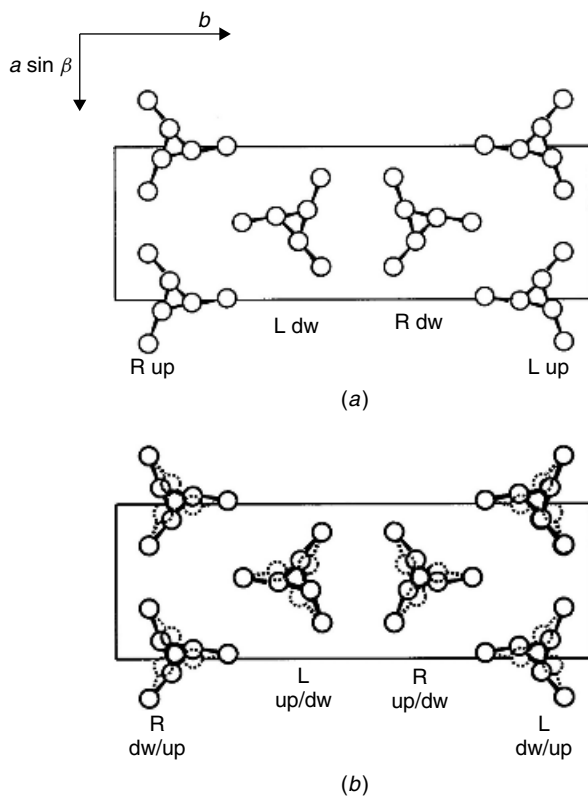


Figure 2.33 (a) Limit-ordered model (space group $P2_1/c$) and (b) limit-disordered model (space group $C2/c$) for crystal structure of α -form of iPP¹⁷⁸ (R = right-handed helix, L = left-handed helix). (Reprinted with permission from Ref. 178. Copyright 2000 by the American Chemical Society.)

The degree of order has been evaluated from the relative intensities of some specific reflections in the X-ray diffraction pattern (Figure 2.34).¹⁷⁵ It has been found that the order parameter R increases with increasing annealing or melt crystallization temperature (Figure 2.35), indicating an increase of the order in the positioning of up and down chains at high annealing or crystallization temperatures.^{175,176} For samples crystallized at high temperatures, structures shown in Figure 2.36a, very close to the ideal limit-ordered model (α_2 -form, Figure 2.33a) are obtained. These modifications present a small percentage of up/down disorder which develops essentially along the b direction.^{177,178} Ordered bilayers of threefold helices composed of enantiomorphous and isoclined chains (all up or all down) follow one another along b

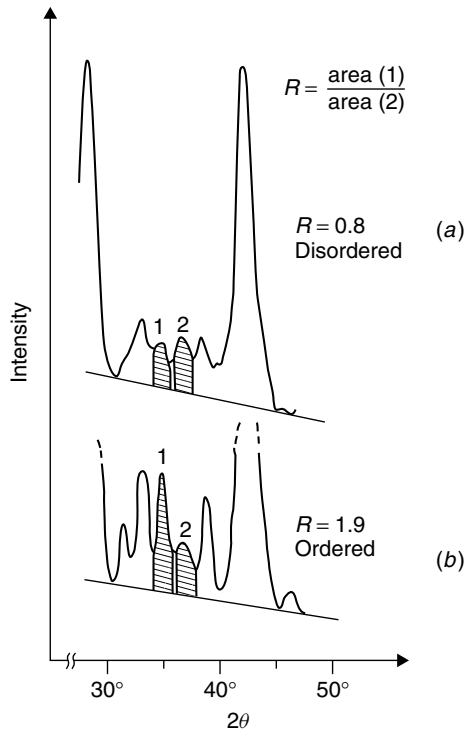


Figure 2.34 Definition of up/down order parameter R from X-ray powder diffraction patterns of iPP samples^{170,175}: (a) unannealed sample; (b) sample annealed at 167°C. (Reprinted with permission from Ref. 170. Copyright 1992 by Springer-Verlag.)

(Figure 2.36a). When $p = 1$, there is a regular succession of bilayers with anticlinal chains and the structure corresponds to the limit-ordered α_2 -form (space group $P2_1/c$, Figure 2.33a). For samples crystallized at low temperatures, the up/down disorder develops also along the a axis and inside the bilayers, so that only in small clusters of chains is the order typical of bilayers preserved (Figure 2.36b).¹⁷⁸ A continuum of intermediate disordered modifications exists between the limit-disordered α_1 -form, corresponding to the space group $C2/c$, and the limit-ordered ideal α_2 form, corresponding to the space group $P2_1/c$.¹⁷⁸

In the crystal structures of many other isotactic polymers, with chains in threefold or fourfold helical conformations, disorder in the up/down positioning of the chains is present. Typical examples are isotactic polystyrene,^{34,179} isotactic poly(1-butene),³⁵ and isotactic poly(4-methyl-1-pentene).^{39,40,153,247}

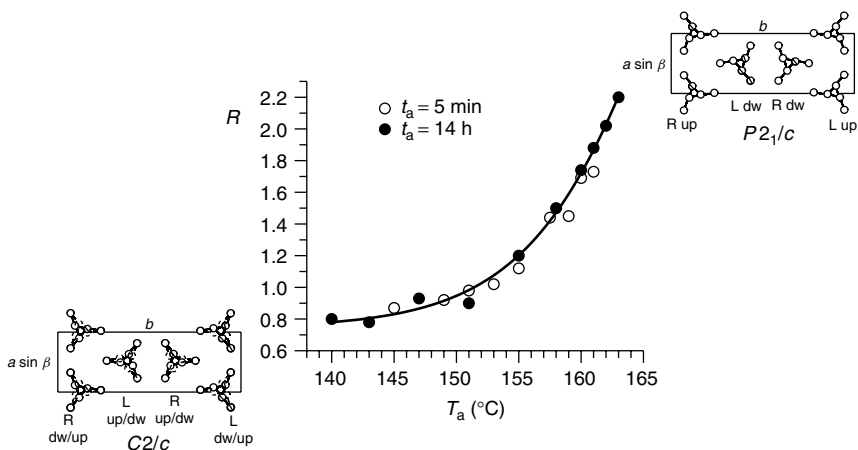


Figure 2.35 Values of order parameter R of annealed samples of iPP reported as function of annealing temperature T_a for different annealing time t_a .¹⁷⁵

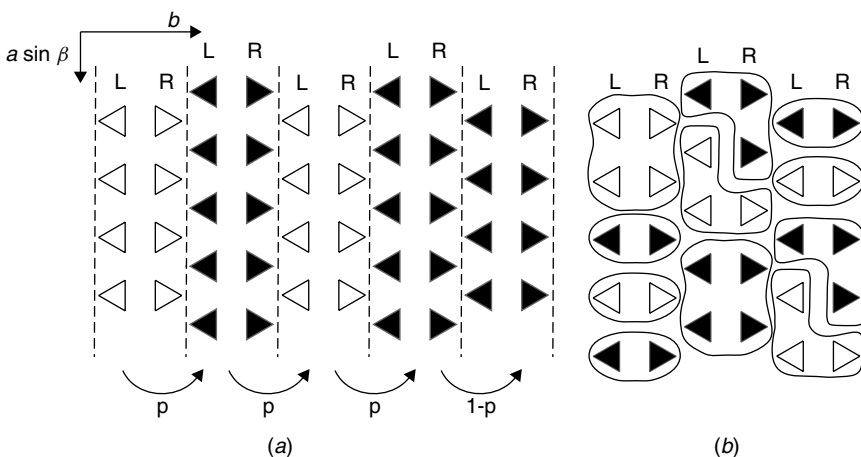


Figure 2.36 Models of packing of right- (R) and left- (L) handed threefold helices of iPP in modifications of α -form having different degrees of up/down disorder.¹⁷⁸ Up and down chains are indicated with black and white triangles, respectively. (a) Ordered bilayers of chains, composed of enantiomorphous and isoclinical chains (all up or all down), succeed along b with probability p that chains are anticlinal (bilayers of up chains alternate with bilayers of down chains) and with probability $1 - p$ that chains are isoclinical; $p = 1$ corresponds to limit-ordered model $P2_1/c$ (α_2 -form, Figure 2.33a). (b) Small clusters of isoclinical (all up or down) chains are packed along a and b with equal probability that neighboring chains are isoclinical or anticlinal. (Reprinted with permission from Ref. 178. Copyright 2000 by the American Chemical Society.)

3.5.3 Disorder in Stacking of Ordered Layers of Macromolecules Along One Lattice Direction

Another kind of disorder corresponding to an important subcase of class (i) can arise from defects in the stacking of ordered layers of macromolecules along one lattice direction. This kind of disorder produces broadening of reflections in the X-ray diffraction patterns and streaks in the electron diffraction patterns of single crystals.

The structure of sPP presents this kind of disorder. Chains of sPP in twofold helical conformation crystallize in two different crystalline forms (I and II), having similar orthorhombic unit cells (Figure 2.37).^{22,59,180,181} As discussed in Section 3.5.1, samples of syndiotactic polypropylene crystallized from the melt in form I at low temperatures present disorder in the alternation of right- and left-handed chains. Lovinger et al.¹⁴⁵ have observed that electron diffraction patterns of single crystals of sPP grown at low temperatures present streaks around the 020 reflection. These data have been interpreted by assuming the presence of disorder in form I characterized by defects in the stacking

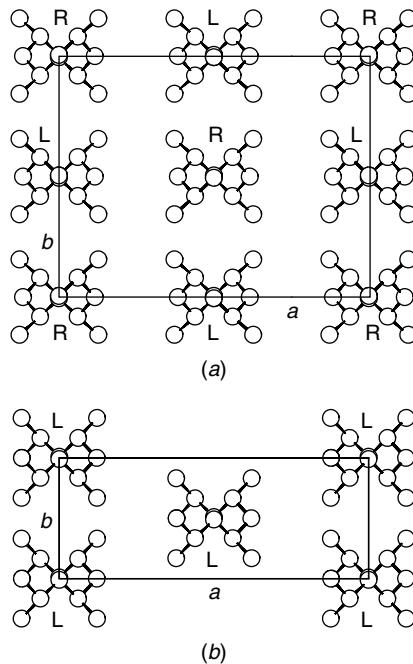


Figure 2.37 Limit-ordered models of packing of twofold helical chains of sPP in (a) form I (space group $Ibca$) and (b) form II (space group $C222_1$).

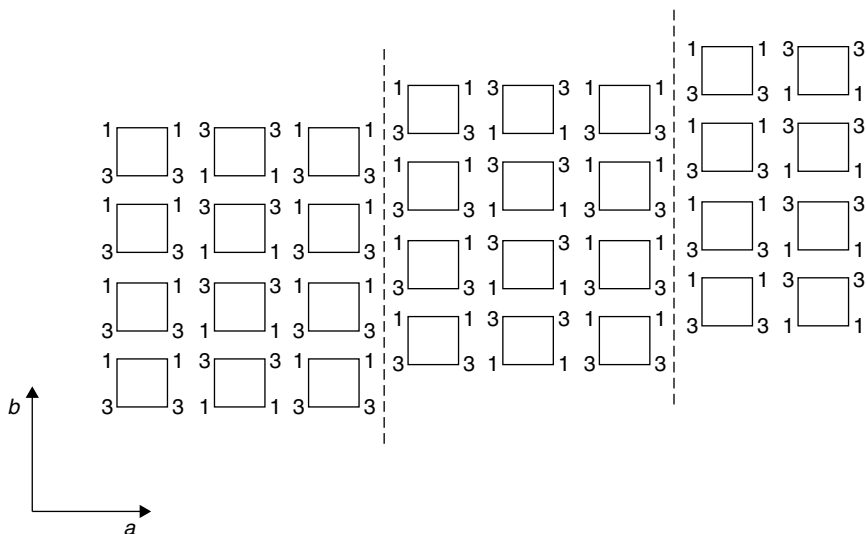


Figure 2.38 Schematic model of packing of chains of sPP in form I showing disorder in stacking of bc layers of chains along a axis. Squares indicate chains of sPP in twofold helical conformation and numbers indicate relative heights of methyl carbons in $c/4$ units. Dashed lines indicate positions of defects which correspond to shift of bc layers of chains of $b/4$ along b axis.

of ordered bc layers of chains along the a axis, implying shifts of $b/4$ between consecutive layers.^{145,182} These defects produce, locally, the C -centered mode of packing of form II (Figure 2.37*b*). A model for this kind of disorder is shown in Figure 2.38; antichiral packing of first neighboring chains may still be preserved but is lost in the long range because of the disorder in the stacking of the layers.^{182,183}

Disorder in the stacking of ordered layers of chains along one lattice direction is present in samples of iPP crystallized in the γ -form. The models of packing of the threefold helical chains of iPP in the α - and γ -forms are reported in Figure 2.39. The structure of the γ -form of iPP is the first example of polymer structure characterized by the packing of nearly perpendicular chains^{141,142} (Figure 2.39*a*). Ordered bilayers of 3/1 helical chains, typical of the α -form (Figure 2.39*b*), are packed along the c_γ axis with the chain axis tilted by 81° ¹⁴¹ (Figure 2.39*a*). The iPP samples prepared with the traditional Ziegler–Natta catalysts generally crystallize in the stable α -form, whereas samples prepared with the homogeneous metallocene catalysts tends to crystallize more easily in the γ -form.^{184–186} X-ray diffraction patterns of iPP samples prepared with a metallocene catalyst and crystallized from the melt are reported in Figure 2.40.¹⁸⁶ The presence of both $(130)_\alpha$ (at $2\theta = 18.6^\circ$) and $(117)_\gamma$ (at $2\theta = 20.1^\circ$) reflections indicate that crystals of α - and γ -forms are present in

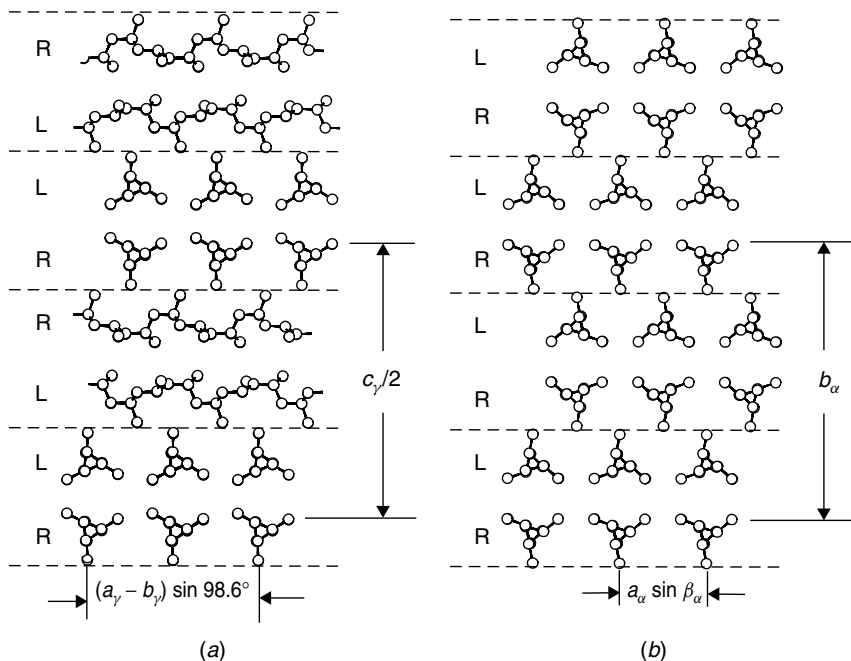


Figure 2.39 Models of packing of threefold helical chains in (a) γ -form and (b) α -form of iPP. Dashed lines delimit bilayers of chains. Subscripts γ and α identify unit-cell parameters of orthorhombic and monoclinic unit cells of γ -¹⁴¹ and α -forms,¹⁷⁴ respectively. R and L identify rows of all right- and all left-handed helices, respectively.¹⁸⁵ (Reprinted with permission from Ref. 185. Copyright 2001 by the American Chemical Society.)

these samples. However, the relative intensities of the reflections and the presence of a diffuse halo in the patterns have been interpreted by assuming that some kind of disorder is also present.^{185–187} The proposed model of the disordered structure is reported in Figure 2.41.^{185,186} The disorder corresponds to the statistical succession along the b_α (c_γ) axis direction of double layers of chains with the chain axes either parallel (as in the α -form) or nearly perpendicular (as in the γ -form). Inside the same crystalline domain local arrangements of the double layers of chains piled along the b_α (c_γ) axis typical of the α -form (with parallel chains) and typical of the γ -form (with chains nearly perpendicular) are present. It has been shown that the amount of disorder present in the structure depends on the microstructure of the chains and the crystallization temperature^{185,186} and, for stretched samples, on the draw ratio.¹⁸⁵ Also in this case the polymorphic behavior and the order–disorder phenomena can be described by a continuum of disordered modifications intermediate between the limit-ordered α - and γ -forms.^{185,186}

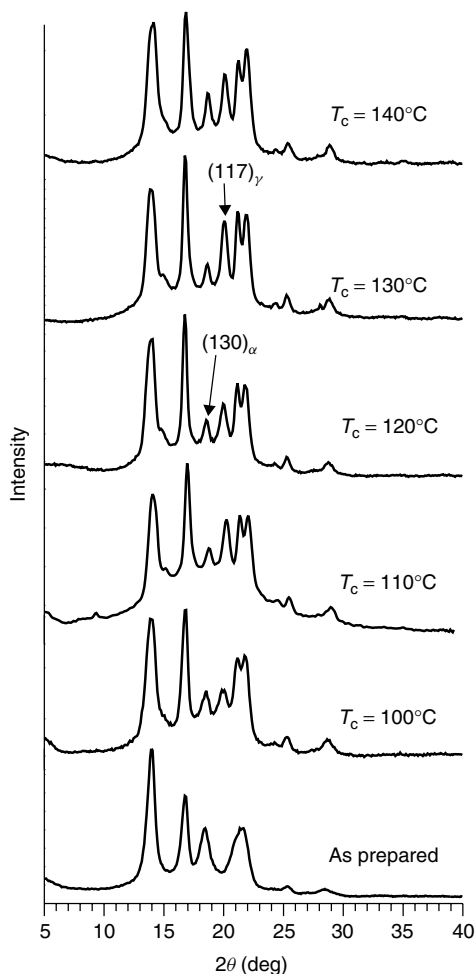


Figure 2.40 X-ray powder diffraction patterns of iPP samples prepared with metallocene catalyst¹⁸⁶ and isothermally crystallized from the melt at the indicated temperatures. The $(130)_\alpha$ and $(117)_\gamma$ reflections at 2θ values of 18.6° and 20.1° , respectively, typical of α - and γ -forms of iPP, respectively, are also indicated.

Disorder in the stacking of ordered layers of chains along one crystallographic direction is also present in the β -form of sPS.⁵⁴ In the crystal structure of the β -form, *trans* planar chains are packed in an orthorhombic unit cell (Figure 2.42a).^{54,55} Disorder in the stacking of ordered *ac* layers of chains along one direction is present, according to X-ray⁵⁴ and electron diffraction patterns.¹⁸⁸ The structure has been described in terms of two limit models; a limit-ordered β'' -form, described by the space group $P2_12_12_1$

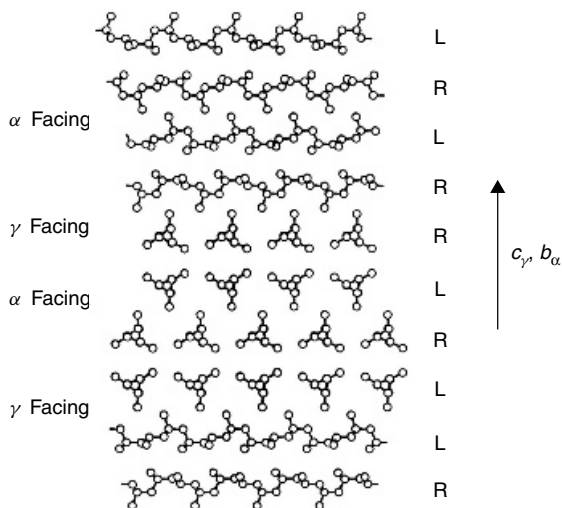


Figure 2.41 Model of α/γ disorder occurring in disordered modifications of iPP intermediate between α - and γ -forms.^{185,186} Consecutive $a_\gamma b_\gamma$ ($a_\alpha c_\alpha$) bilayers of chains are stacked along c_γ (b_α) with chain axes either parallel or nearly perpendicular. R and L identify rows of all right- and left-handed helices, respectively. (Reprinted with permission from Ref. 185. Copyright 2001 by the American Chemical Society.)

(Figure 2.42a), and a limit-disordered β' -form, described by the statistical space group $Cmcm$ (Figure 2.42b), characterized by a statistical positioning of ac layers of chains.^{54,55} Real modifications are intermediate between these ideal models. A model for the intermediate modifications is shown in Figure 2.43. A regular succession of bilayers ABAB... gives rise to the limit-ordered β'' -form, whereas defects in the alternation of bilayers A and B characterize the disordered modification, where a three-dimensional long-range order in the position of the phenyl rings is maintained.⁵⁴

Another important subclass of class (i) of disorder arises from the statistical occurrence of two specific orientations of a group of chains not necessarily organized in layers. This kind of disorder is present, for instance, in the crystal structure of the α -form of sPS (Figure 2.24). *Trans* planar chains of sPS are organized in triplets which may assume two different and isosteric orientations while the positions of the barycenters of the phenyl rings are left unaltered at well-defined positions in the lattice (Figure 2.44). The three-dimensional long-range order in the positioning of the phenyl rings is preserved while disorder in the positions of the atoms of the backbone is present. Also for this polymorphic form of sPS a limit-ordered structure (α'' -form) and a limit-disordered structure (α' -form) have been defined^{50,52,53} according to the presence of this kind of disorder.

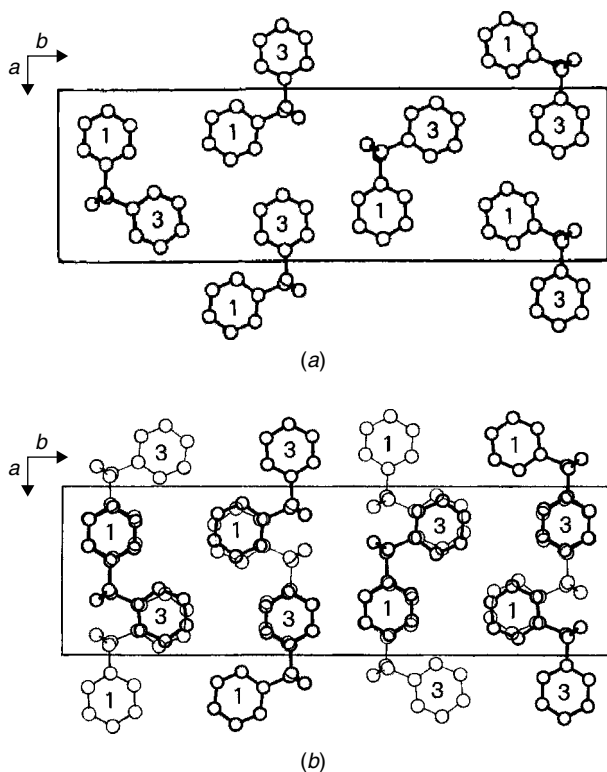


Figure 2.42 (a) Limit-ordered model (β'' -form, space group $P2_12_12_1$) and (b) limit-disordered model (β' -form, space group Cmc_m) for crystal structure of β -form of sPS.⁵⁴ Relative heights of centers of benzene rings are in units $c/4$. In (b) disorder corresponds to statistical disposition of chains in two alternative positions shown as thick and thin lines. (Reprinted with permission from Ref. 54. Copyright 1992 by Elsevier Science.)

3.5.4 Conformational Kink-Band Disorder

A particular kind of disorder, characterized by maintaining three-dimensional long-range periodicity only for some points of the structure, has been found in samples of syndiotactic polypropylene having a relatively low degree of stereoregularity.^{189,190} In these samples the chains present conformational disorder, which produces defects frozen in the crystals.

The X-ray diffraction patterns and the corresponding solid-state ^{13}C NMR spectra of samples of sPP crystallized in forms I and II are reported in Figure 2.45. Samples of sPP which present X-ray powder diffraction pattern typical of the stable form I (Figure 2.45a) show the usual solid-state ^{13}C NMR

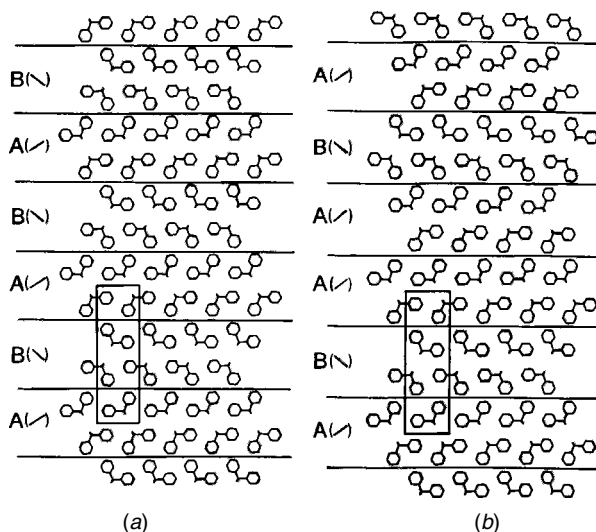


Figure 2.43 Possible models of packing of ac bilayers of chains in β -form of sPS.⁵⁴ (a) Regular succession of bilayers . . .ABAB. . . gives rise to limit-ordered β'' modification. (b) Defects corresponding to pairs of bilayers of the kind AA or BB characterize disordered modifications. (Reprinted with permission from Ref. 54. Copyright 1992 by Elsevier Science.)

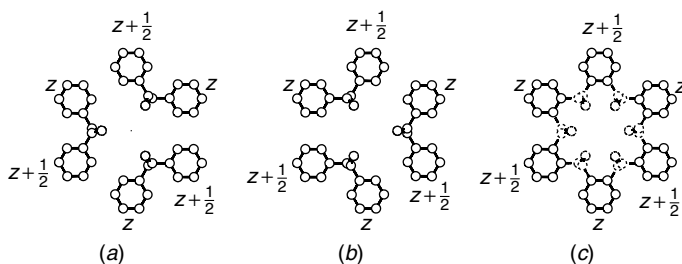


Figure 2.44 (a,b) Two different and isosteric orientations of triplets of *trans* planar chains of sPS as in structure of α -form (Figure 2.24). (c) Atoms of backbone are statistically distributed in six positions around threefold axis, whereas atoms of phenyl rings are in same positions as in (a) and (b).

CPMAS spectrum typical of the regular twofold helical conformation (Figure 2.45b).^{147,191} Samples of sPP which present X-ray powder diffraction patterns typical of the isochiral form II (Figure 2.45c) show a different solid-state ^{13}C NMR spectrum with additional signals in the region of the methylene and methyl carbon resonances (Figure 2.45d). These additional resonances have

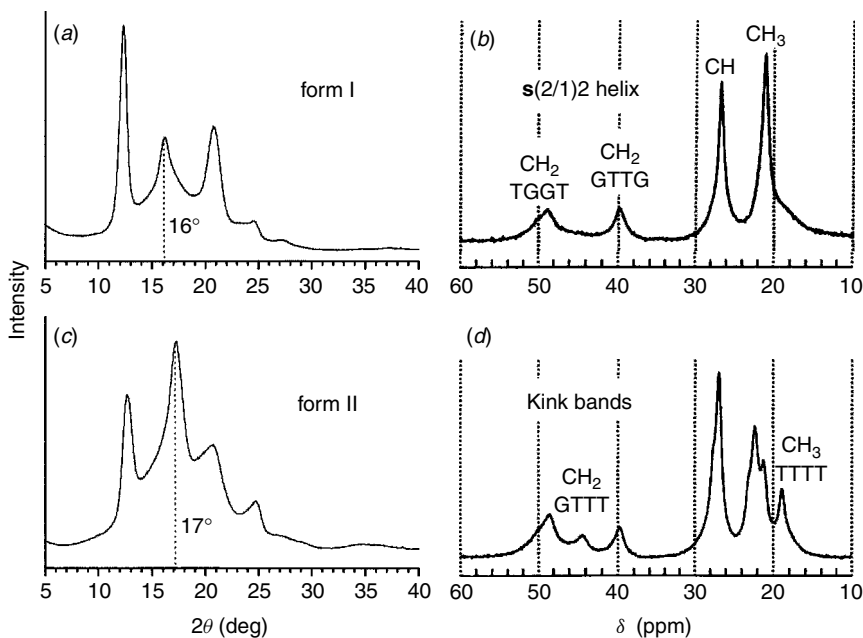


Figure 2.45 X-ray powder diffraction patterns of sPP samples in (a) form I and (b) form II and (c,d) corresponding solid-state ^{13}C NMR CPMAS spectra.

been explained by assuming the presence of conformational disorder characterized by the presence of portions of chain in *trans* planar conformation in a chain having a prevailing twofold helical conformation.^{189,190}

A possible model of disorder which accounts for the X-ray diffraction pattern and the solid-state ^{13}C NMR spectrum of Figures 2.45c,d is shown in Figure 2.46. The defective region, characterized by chains in T_6G_2 conformation, is clustered in planes and forms kink bands. Portions of chains in the regular twofold helical conformation, all having the same chirality, are packed according to the limit-ordered model of form II (Figure 2.37b) and are connected by portion of chains in *trans* planar conformation. The most important feature is that a substantial parallelism among the local chain axes is maintained, so that good packing of the chains is preserved. These kink bands may be regarded as stacking faults cutting the chain axes but preserving a substantial parallelism of the chains. Also in this case the presence of the conformational disorder does not avoid the possibility of crystallization, provided that the parallelism of the chains is preserved. The model of Figure 2.46 describes disordered modifications intermediate between forms II and IV of sPP (Figure 2.47). In the defective regions the chains are packed like in form IV of sPP (Figure 2.47c), while in

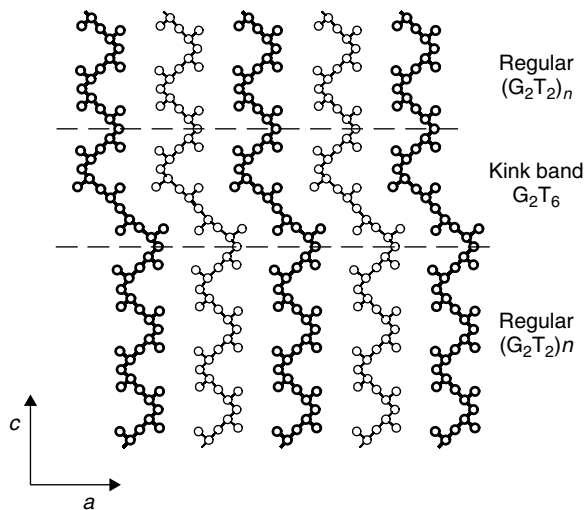


Figure 2.46 Model of packing of conformationally disordered chains of sPP in disordered modifications of form II presenting kink bands.^{189,190} Chains drawn with thick and thin lines are at 0 and 0.5 along b . In the ordered portion of crystal chains are in ordered twofold $(T_2G_2)_n$ helical conformation, whereas in the defective portion (delimited by dashed lines) chains are in $T_2G_2T_6$ conformation.

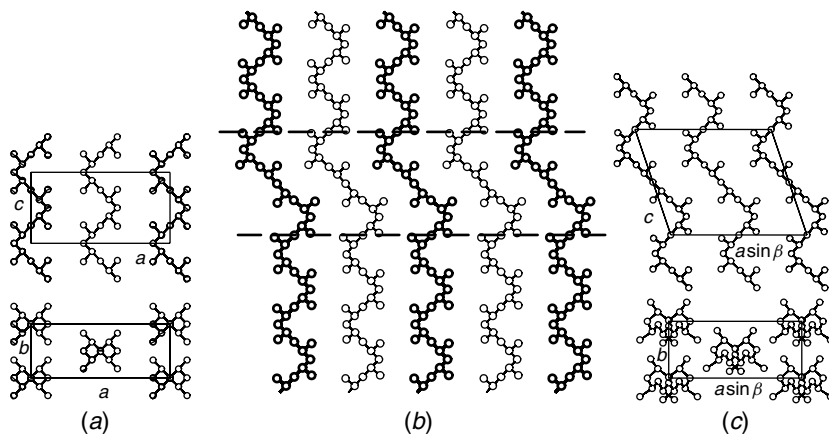


Figure 2.47 Models of packing in limit-ordered forms (a) II and (c) IV of sPP and (b) model of conformationally disordered modification, presenting kink bands, intermediate between limit-ordered models of form II and form IV. In defective region of model (b), delimited by dashed lines, chains are packed as in form IV, whereas in ordered regions chains are packed as in the form II.

the ordered regions the chains are packed like in form II (Figure 2.47a). This suggests that, depending on the condition of crystallization, there exists a continuum of conformationally disordered modifications of sPP containing kink bands intermediate between two limit isochiral structures, the limit-ordered form II and the limit ordered form IV.

Conformational disorder and kink-bands structures have recently been found also in random copolymers of syndiotactic polypropylene with small amounts of ethylene.^{192,193} The ethylene units are included in the crystalline regions¹⁹³ and induce the crystallization of the metastable form II of sPP with conformationally disordered chains characterized by kink bands. Portions of chains containing the ethylene units tend, indeed, to assume a *trans* planar conformation, producing the kink-band defects in chains in the prevailing twofold helical conformation.^{192,193}

3.6 Solid Mesomorphic Forms

As discussed in the Section 3.4, crystalline forms presenting large amounts of disorder of the kind (ii) or (iii) are generally called *mesomorphic* modifications, in analogy with the ordered liquids (smectic and nematic). A notable difference between the solid mesomorphic forms and the ordered liquid mesophases is that the solid mesomorphic forms are crystalline modifications generally characterized by the typical feature of the crystalline order, that is, the packing of parallel chains. The long-range order in the correlations between the atoms of the parallel chains is absent because of the presence of disorder. The long-range order may be lost in one or two dimensions, for example, when conformationally disordered chains are packed with a long-range order in the positions of the chain axes [case (ii)] or for conformationally ordered chains packed with high degree of disorder in the lateral packing [case (iii)]. The presence of these kinds of disorder generally prevents the definition of a unit cell. Typical features in the X-ray diffraction patterns of *mesomorphic* forms are diffuse halos on the equator and/or the layer lines.

Examples of mesomorphic forms characterized by disorder in the conformation of the chains have already been described in Section 2.6. For instance, a mesomorphic form is present in the high-temperature form I of polytetrafluoroethylene.^{106,107} In this phase the chains are in disordered conformation due to the presence of helix reversals along the chains.¹⁰⁸⁻¹¹⁰ Moreover, intermolecular disorder is also present due to the random rotations of the chains around the chain axes.¹⁰⁹ A long-range three-dimensional order is present only in the pseudo-hexagonal placement of the chain axes.^{107,109}

Another example of a conformationally disordered mesomorphic form is the high-temperature phase of *trans*-1,4-poly(1,3-butadiene).^{111,112} As discussed in Section 2.6, in this phase the disorder corresponds to a statistical succession

along the chain of different minimum-energy conformational sequences, while the chains remain practically fully extended and packed in a pseudohexagonal lattice.^{70,111} Similar disorder in the conformation of the chains has been found in the mesomorphic form of poly(ethylene terephthalate).¹⁹⁴ Also in this case the disorder corresponds to the random succession of monomeric units in different minimum-energy conformations.

The polymorphic form of polyethylene stable at high temperature and pressure may be considered as a mesomorphic modification since it has been described as characterized by a pseudohexagonal packing of conformationally disordered chains.¹⁹⁵ A similar mesomorphic pseudohexagonal modification of polyethylene can be obtained at room temperature and atmospheric pressure in ethylene-propylene copolymers having a content of propylene in the range 20–30 mol%.¹⁹⁶ The copolymers crystallize under stretching with the propylene units included in the resulting pseudohexagonal lattice.¹⁹⁶

Many examples of mesomorphic forms characterized by chains in ordered conformation packed in disordered lattices could be provided. Both crystalline forms of the alternating ethylene-tetrafluoroethylene (ETFE) copolymer may be considered as mesomorphic forms.^{197,198} In the low-temperature form the chains are in the ordered *trans* planar conformation and are packed in a polyethylene-like orthorhombic lattice.¹⁹⁷ However, intermolecular order is present only in the *ab* projection of the lattice, any intermolecular correlations in the relative positions of the atoms being absent due to the presence of nearly random relative displacements of neighboring chains along the *c* axis.¹⁹⁸ At high temperatures this orthorhombic mesomorphic phase of ETFE transforms into a hexagonal mesophase characterized by chains still in the ordered *trans* planar conformation, packed in a hexagonal lattice. Besides the disorder in the relative heights of the chains, disorder in the rotations of the chains around their axes develops at high temperature, inducing the hexagonal packing.^{197,199} A long-range three-dimensional order is maintained only along each *trans* planar chain and in the hexagonal arrangement of the chain axes.¹⁹⁹

Mesomorphic forms characterized by conformationally ordered polymer chains packed in lattices with different kinds of lateral disorder have been described for various isotactic and syndiotactic polymers. For instance, for iPP,²⁰⁰ sPP,²⁰¹ sPS,²⁰² syndiotactic poly(*p*-methylstyrene) (sPPMS),²⁰³ and syndiotactic poly(*m*-methylstyrene),²⁰⁴ mesomorphic forms have been found. In all of these cases the X-ray fiber diffraction patterns show diffraction confined in well-defined layer lines, indicating order in the conformation of the chains, but broad reflections and diffuse haloes on the equator and on the other layer lines, indicating the presence of disorder in the arrangement of the chain axes as well as the absence of long-range lateral correlations between the chains.

In the mesomorphic form of iPP, chains in the ordered 3/1 helical conformation are arranged in small domains where only the first neighboring chains

maintain the typical correlations present in the structure of the α -form.²⁰⁰ These correlations and any order in the positioning of the chain axes are lost at longer distances. The mesomorphic forms of sPP,²⁰¹ sPS,^{202a,b} and sPPMS²⁰³ are characterized by chains in ordered *trans* planar conformations packed in small disordered aggregates which maintain the structural features of one of the polymorphic forms of the polymers only up to very short distances. In the case of sPS and sPPMS, the small aggregates of chains are characterized by packing modes very close to those of the α -form of sPS^{202a,b} and form III of sPPMS.²⁰³

3.7 Chiral Crystallization of Polymers with Helical Chain Conformations

Crystallization of polymers in chiral crystals, even in the case of achiral polymers, is quite frequent and strictly related to the occurrence of helical conformations of the chains. The crystallizable polymer consists of a regular sequence of a chemical repeating unit which can be chiral if it presents an asymmetric center or achiral. On the contrary, helical conformations assumed by the polymer chains in the crystalline state are intrinsically chiral, even though the chemical repeat is achiral. Three possible cases can be distinguished:

1. The monomeric repeating unit is truly chiral, containing a “true” asymmetric atom. In this case the chirality of the monomeric units favors the formation of helices of one specific chirality (right or left handed). In fact, when the monomeric units are chiral, enantiomorphous helices are not equivalent, since they have different conformational energies (Section 2.4). This is, for instance, the case of iP(S)3MP, discussed in Section 2.4, where only 4/1 left-handed helical chains are present in the tetragonal unit cell according to the space group $I4_1$.^{29,66} Poly(L-peptides) and polylactides fall in this class of chiral polymers. In particular, polylactides $[-CH(CH_3)-CO-O-]_n$ adopt specific helical hands, imposed by the stereochemistry: left handed for poly(L-lactide) and right handed for poly(D-lactide).^{164,205,206}

2. The monomeric unit presents a stereoisomeric center which is not a true asymmetric carbon because it is linked to two undistinguishable chain segments. This is the case, for instance, for stereoregular vinyl polymers $(-CH_2-C^*HR-)_n$. As discussed in Section 2.4, isotactic polymers are chiral as long as the chain ends are distinguishable; in these polymers the chains form helical conformations, but right- and left-handed helices are equally probable since they are isoenergetic. For this reason these polymers are called *chiral but racemic*, where the chirality is buried,⁶³ that is, resides in a crypt.^{64,207}

3. The monomeric unit is chiral, each individual polymer molecule consists of isochiral monomers, but the macroscopic sample is a *racemate*. Chains

having monomers with opposite absolute configurations form helices of opposite hand; since monomers of opposite configurations occur in equal number, right- and left-handed helical chains are equiprobable. Unlike case 2, where the helices of opposite chirality may in principle interconvert, in this case the helices of opposite chirality are not isoenergetic and cannot interconvert. This is the case, for instance, for the poly(L,D-lactide) stereocomplex, where right-handed threefold helical chains of poly(D-lactide) and left-handed threefold helical chains of poly(L-lactide) are intrinsically blended in the trigonal unit cell of the racemate, according to the space group $R3c$.^{168,208} The structure is similar to that of chiral but racemic polymers, like form I of iPB,³⁵ with the notable difference that the racemate structure is made of different molecular species, whereas the polyolefin structure is made up of a single molecular species which can exist in two energetically equivalent enantiomorphous helices.^{35,209} Another example is provided by form I of isotactic poly(*t*-butylethylene oxide), which presents chiral monomeric units giving two types of optical isomers, rectus (R) and sinister (S).²¹⁰ The tetragonal unit cell contains two left-handed 9/4 helical chains of the rectus polymer and two right-handed 9/4 helical chains of the sinister isomer,²¹⁰ giving a racemic lattice and optical compensation.²¹¹

Optical compensation for polymers with chiral monomeric units may also occur when the racemic polymer consists of crystallites, each composed only of the rectus chains or only of the sinister polymer chains, and a same amount of optical antipode crystallites is present. This intercrystallite optical compensation²¹¹ has been found, for instance, in isotactic poly(propylene sulfide),²¹² poly(β -methylpropiolactone),²¹³ and poly(isopropylethylene oxide),²¹⁴ where isochiral 2/1 helical chains are included in orthorhombic unit cells according to the space group $P2_12_12_1$.

Nonchiral systems belonging to case 2 (chiral but racemic) and consisting of equiprobable right- and left-handed helices may crystallize in chiral space groups in which only helices of a given chirality are present in an individual polymer crystal. Of course, as in the case of intercrystallite optical compensation, equal fractions of crystals of the enantiomorphous space groups will be present. Some examples of polymers displaying chiral modifications are reported in Table 2.3. In principle, the formation of chiral crystals from achiral or racemic helical polymers may be related to the stability of the chiral modification or may be associated with kinetic factors.²¹⁵ It has been suggested that a hexagonal or pseudohexagonal arrangement of helical chains in the crystalline state promotes the chiral crystallization and is, in turn, favored by clustering of isochiral helices.²¹⁵ When a given polymer forms both chiral and nonchiral modifications, the nonchiral structure is probably the most stable one, whereas the chiral form develops under kinetic control.²¹⁵

Table 2.3
Structural Data for Chiral Polymorphic Forms of Selected Polymers

Polymer	Chain Axis (Å)	Chain Symmetry	Space Group	References
<i>it</i> -Polypropylene β -form	6.5	s(3/1)	$P3$	154, 158, 159
<i>it</i> -Polybutene form III	7.56	s(4/1)	$P2_12_12_1$	37
<i>it</i> -Poly((<i>S</i>)-3-methyl-1-pentene)	6.80	s(4/1)	$I4_1$	66
<i>it</i> -Poly(5-methyl-1-hexene)	6.33	s(3/1)	$P2_1$	129
<i>it</i> -Poly((<i>S</i>)-5-methyl-1-heptene)	6.36	s(3/1)	$P2_1$	65, 129b,c
<i>it</i> -Poly(<i>t</i> -butylacrylate)	6.5	s(3/1)	$P3_1$	130
Poly(isobutylene)	18.60	s(8/3)	$P2_12_12_1$	19, 229
Poly(methylene oxide) form I	17.39	s(9/5)	$P3_1$	230
Poly(methylene oxide) form II	3.56	s(2/1)	$P2_12_12_1$	231
<i>it</i> -Poly(propylene oxide)	7.03	s(2/1)	$P2_12_12_1$	246
<i>it</i> -Poly(isopropylethylene oxide)	5.55	s(2/1)	$P2_12_12_1$	214
Poly(thiomethylene)	36.52	s(17/9)	$P1$	232
<i>it</i> -Poly(propylene sulfide)	8.20	s(2/1)	$P2_12_12_1$	212
Poly(selenomethylene) form I	46.25	s(21/11)	$P3_1, P3_112, P3_121$	233
Poly(selenomethylene) form II	4.27	s(2/1)	$P2_12_12_1$	234
<i>it</i> -Poly(β -methylpropiolactone)	5.96	s(2/1)	$P2_12_12_1$	213
<i>it</i> -Poly(β -ethylpropiolactone)	5.56	s(2/1)	$P2_12_12_1$	235
<i>it</i> -Poly(L-lactide) α -form	28.8	s(10/7)	$P2_12_12_1$	205
<i>it</i> -Poly(L-lactide) β -form	8.8	s(3/2)	$P3_2$	164
<i>it</i> -Poly(L-lactide) γ -form	8.8	s(3/2)	$P2_1$	206
Poly(diketene)	7.75	s(2/1)	$P2_12_12_1$	236
Poly(<i>p</i> -benzamide)	12.8	s(2/1)	$P2_12_12_1$	237
Poly(ethylene oxybenzoate) α -form	15.6	s(2/1)	$P2_12_12_1$	238
<i>it-cis</i> -1,4-Poly(1,3-pentadiene)	8.17	s(2/1)	$P2_12_12_1$	82, 96–98
<i>it-cis</i> -1,4-Poly(2-methyl-1,3-pentadiene) β -form	7.90	s(2/1)	$P2_12_12_1$	85
<i>it</i> -Poly(styrene- <i>alt</i> -carbonmonoxide)	7.5	s(2/1)	$P2_1$	123
<i>st</i> -Polypropylene form II	7.4	s(2/1)2	$C222_1$	22
<i>st</i> -Polypropylene form IV	11.6	$t2$	$P1, C2$	148, 149
<i>st</i> -Polybutene form I	7.73	s(2/1)2	$C222_1$	25, 60

Note: *it* = isotactic, *st* = syndiotactic.

However, chiral crystal structures have also been found for nonhexagonal lattices, for instance, in forms II^{22,180,181} and IV^{148,149} of sPP (Figures 2.37*b* and 2.23, respectively) and form I of sPB.⁶⁰ In the structures of form II of sPP and form I of sPB, isochiral twofold helical chains are packed in orthorhombic unit cells according to the space group $C222_1$.^{22,60,180} Form IV of sPP is characterized by a packing of isochiral helices in the $(T_6G_2T_2G_2)_n$ conformation¹⁴⁸ into a triclinic or monoclinic lattice.^{148,149} In the case of sPB the chiral form I is the stable modification^{25,60} and no antichiral modification with chains in 2/1 helical conformation has been found.²⁵ In the case of sPP the isochiral forms II and IV are metastable modifications and are produced on transformations of the *trans* planar form III by different treatments.^{148,180,181} The most stable form of sPP is the antichiral form I, characterized by twofold helical chains of opposite chirality included in the orthorhombic unit cell (Figure 2.22).⁵⁹

The chiral form II of sPP can be obtained only in stretched fibers of sPP initially in the *trans* planar form III through a crystal–crystal phase transition occurring when the tension is removed.¹⁸¹ The transition between the *trans* planar form III and the helical form of sPP is reversible upon successive stretching and relaxing of fiber specimens^{181,216} and is probably responsible of the elastic behavior of sPP.²¹⁶ Only when the *trans* planar form of sPP is obtained by stretching can the chiral form II of sPP be formed by releasing the tension through the spontaneous solid-state transition. When the *trans* planar form of sPP becomes unstable and does not form by stretching, as, for instance, in copolymers of sPP with 1-butene having compositions higher than 5–6 mol % of 1-butene or by stretching at high temperatures, the chiral helical form II of sPP does not form any more.²¹⁷

It has been recently suggested that this crystal–crystal transformation, involving a conformational transition from *trans* planar to helical conformations, is a *cooperative process* imposed by steric constraints.²¹⁸ The cooperativity induces the formation of chains having the same chirality. The chains pack in the orthorhombic lattice forming the metastable isochiral form II, even though the antichiral helical form of sPP (form I) is more stable. A possible mechanism of this transition is shown in Figure 2.48. The generation of helical structures requires the introduction of *gauche*⁺ or *gauche*⁻ bonds in an all-*trans* chain:



This implies a modification of the chain direction and, finally, a generation of a helix with a larger cross section than that of the *trans* planar chain.²¹⁸ Such phase transitions are often associated with the onset of some conformational disorder characterized by the occurrence of kink bands (Figure 2.48*b*), similar to those found in sPP samples quench crystallized from solutions^{189,190} (Figures 2.46 and 2.47) or in polyethylene.²¹⁹ It is apparent from Figure 2.48

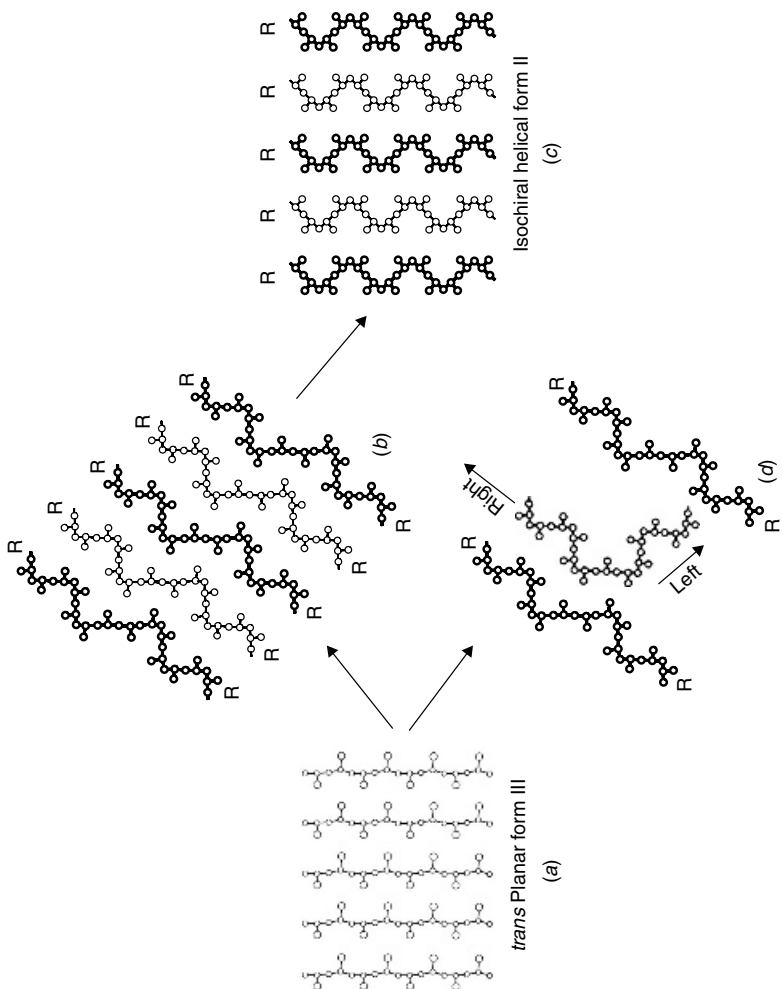


Figure 2.48 Possible cooperative mechanism of crystal-crystal transition from (a) *trans* planar form III of sPP into (c) iso-chiral helical form II. Transition occurs through formation of (b) intermediate conformationally disordered modifications containing kink bands, characterized by helical sequences having same chirality (R = right-handed helix). Formation of helical sequences of opposite chirality (right- and left-handed) produces (d) steric interactions between neighboring chains.

that the formation of right- and left-handed helical stretches appears sterically most unlikely because it would result in two local stem orientations which would diverge on opposite sides of the initial *trans* planar chain (Figure 2.48*d*), producing steric interactions with the neighboring chains. As a consequence, during the transformation helical sequences generated in neighboring chains have the same chirality in order to avoid steric interactions (Figure 2.48*b*). *Gauche* bonds having the same sign are formed cooperatively and the isochiral helical structure forms (Figure 2.48*c*). The generation of helical structures from the *trans* planar chain is, for steric reasons, an isochiral process.²¹⁸ The cooperativity imposed by steric constraints controls the generation of *gauche* bonds and, in the case of sPP, induces the formation of the chiral helical form II, even though the antichiral form I is more stable.

ACKNOWLEDGMENTS

Financial support from the Ministero dell'Università e della Ricerca Scientifica e Tecnologica (PRIN 2002) is gratefully acknowledged. The author thanks Paolo Corradini and Finizia Auriemma for useful discussions and advice.

REFERENCES

1. Corradini, P. In *The Stereochemistry of Macromolecules*, Vol. 3. Ketley, A. D. (Ed.). Marcel Dekker, New York, 1968, p. 1.
2. Natta, G.; Corradini, P. *Nuovo Cimento, Suppl.* **1960**, *15*, 9.
3. Turner Jones, A. *Polymer* **1965**, *6*, 249.
4. Natta, G.; Corradini, P.; Sianesi, D.; Morero, D. *J. Polym. Sci.* **1961**, *51*, 527.
5. Kakugo, M. *Macromol. Symp.* **1995**, *89*, 545.
6. De Rosa, C.; Talarico, G.; Caporaso, L.; Auriemma, F.; Galimberti, M.; Fusco, O. *Macromolecules* **1998**, *31*, 9109.
7. Tanaka, A.; Hozumi, Y.; Hatada, K.; Endo, S.; Fujishige, R. *J. Polym. Sci.* **1964**, *B2*, 181.
8. Natta, G.; Porri, L.; Carbonaro, A.; Lugli, G. *Makromol. Chem.* **1962**, *53*, 52.
9. Guerra, G.; Di Dino, G.; Centore, R.; Petraccone, V.; Obrzut, J.; Karasz, F. E.; MacKnight, W. J. *Makromol. Chem.* **1989**, *190*, 2203.
10. Natta, G. *Atti Accad. Lincei, Memorie* **1955**, *4*(8), 61. *J. Polym. Sci.* **1955**, *16*, 143.
11. Cahn, R. S.; Ingold, C. K.; Prelog, V. *Experientia* **1956**, *12*, 93.
12. IUPAC Commission on Macromolecules Nomenclature, *Pure Appl. Chem.* **1979**, *51*, 1101; **1981**, *53*, 733.
13. Natta, G.; Farina, M.; Peraldo, M.; Corradini, P.; Bressan, G.; Ganis, P. *Rend. Fis. Acc. Lincei* **1960**, *28*, 422.
14. Huggins, M. L. *J. Chem. Phys.* **1945**, *13*, 37.
15. Bunn, C. W. *Proc. Roy. Soc. (London)* **1942**, *A180*, 67.
16. Pauling, L.; Corey, R. B.; Branson, H. R. *Proc. Natl. Acad. Sci. U.S.* **1951**, *37*, 205.

17. Corradini, P. *Rend. Fis. Acc. Lincei* **1960**, 28, 1.
18. Natta, G.; Corradini, P.; Ganis, P. *J. Polym. Sci.* **1962**, 58, 1191.
19. Bunn, C. W.; Holmes, D. R. *Discuss. Faraday Soc.* **1958**, 25, 95.
20. Natta, G.; Corradini, P. *Nuovo Cimento, Suppl.* **1960**, 15, 40.
21. Natta, G.; Pasquon, I.; Corradini, P.; Peraldo, M.; Pegoraro, M.; Zambelli, A. *Rend. Fis. Acc. Lincei* **1960**, 28, 539.
22. Corradini, P.; Natta, G.; Ganis, P.; Temussi, P. A. *J. Polym. Sci., Part C* **1967**, 16, 2477.
23. Natta, G.; Peraldo, M.; Allegra, G. *Makromol. Chem.* **1964**, 75, 215.
24. Chatani, Y.; Maruyama, H.; Noguchi, K.; Asanuma, T.; Shiomura, T. *J. Polym. Sci., Part C* **1990**, 28, 393.
25. De Rosa, C.; Venditto, V.; Guerra, G.; Pirozzi, B.; Corradini, P. *Macromolecules* **1991**, 24, 5645.
26. De Rosa, C.; Venditto, V.; Guerra, G.; Corradini, P. *Macromolecules* **1992**, 25, 6938.
27. Corradini, P.; De Rosa, C.; Guerra, G.; Pirozzi, B.; Venditto, V. *Gazz. Chim. Ital.* **1992**, 122, 305.
28. De Rosa, C.; Scaldarella, D. *Macromolecules* **1997**, 30, 4153.
29. Corradini, P.; Petraccone, V.; Pirozzi, B. *Eur. Polym. J.* **1976**, 12, 831.
30. Natta, G.; Corradini, P.; Ganis, P. *J. Polym. Sci.* **1962**, 58, 1191.
31. Corradini, P.; De Rosa, C.; Zhi, G.; Napolitano, R.; Pirozzi, B. *Eur. Polym. J.* **1985**, 21, 635.
32. Petraccone, V.; Pirozzi, B.; Frasci, A.; Corradini, P. *Eur. Polym. J.* **1976**, 12, 323.
33. De Rosa, C.; Borriello, A.; Venditto, V.; Corradini, P. *Macromolecules* **1994**, 27, 3864.
34. Natta, G.; Corradini, P. *Makromol. Chem.* **1955**, 16, 77; Natta, G.; Corradini, P.; Bassi, I. W. *Nuovo Cimento, Suppl.* **1960**, 15, 68.
35. Natta, G.; Corradini, P.; Bassi, I. W. *Nuovo Cimento, Suppl.* **1960**, 15, 52.
36. Turner Jones, A. *J. Polym. Sci.* **1963**, B1, 455; *Polymer* **1966**, 7, 23.
37. Cojazzi, G.; Malta, V.; Celotti, G.; Zannetti, R. *Makromol. Chem.* **1976**, 177, 915.
38. Corradini, P.; Pasquon, I. *Rend. Fis. Acc. Lincei* **1955**, 19, 453.
39. (a) Bassi, I. W.; Bonsignori, O.; Lorenzi, G. P.; Pino, P.; Corradini, P.; Temussi, P. A. *J. Polym. Sci. Phys. Ed.* **1971**, 9, 193. (b) Frank, F. C.; Keller, A.; O'Connor, A. *Philos. Mag.* **1959**, 8, 200.
40. Kusanagi, H.; Takase, M.; Chatani, Y.; Tadokoro, H. *J. Polym. Sci., Polym. Phys. Ed.* **1978**, 16, 131.
41. Takayanagi, M.; Kawasaki, N. *J. Macromol. Sci. Phys.* **1967**, B1, 741.
42. Charlet, G.; Delmas, G.; Revol, F. J.; Manley, R. St. *J. Polymer* **1984**, 25, 1613.
43. Rastogi, S.; Newman, M.; Keller, A. *Nature* **1991**, 353, 55; *J. Polym. Sci. Polym. Phys. Ed.* **1993**, 31, 125.
44. De Rosa, C. *Macromolecules* **1999**, 32, 935.
45. Natta, G.; Corradini, P.; Bassi, I. W. *Gazz. Chim. Ital.* **1959**, 89, 784.
46. Corradini, P.; Ganis, P.; Petraccone, V. *Eur. Polym. J.* **1970**, 6, 281.
47. Napolitano, R.; Pirozzi, B. *Macromol. Theory Simul.* **1999**, 8, 15.
48. Pirozzi, B.; Napolitano, R. *Eur. Polym. J.* **1992**, 28, 703. Corradini P.; Napolitano R.; Petraccone, V.; Pirozzi, B.; Tuzi, A. *Macromolecules* **1982**, 15, 1207.
49. Corradini, P.; Napolitano, R.; Pirozzi, B. *Eur. Polym. J.* **1990**, 26, 157.

50. Guerra, G.; Vitagliano, V. M.; De Rosa, C.; Petraccone, V.; Corradini, P. *Macromolecules* **1990**, *23*, 1539.
51. Greis, O.; Xu, Y.; Asano, T.; Petermann, J. *Polymer* **1989**, *30*, 590.
52. De Rosa, C.; Guerra, G.; Petraccone, V.; Corradini, P. *Polym. J.* **1991**, *23*, 1435.
53. De Rosa, C. *Macromolecules* **1996**, *29*, 8460.
54. De Rosa, C.; Rapacciuolo, M.; Guerra, G.; Petraccone, V.; Corradini, P. *Polymer* **1992**, *33*, 1423.
55. Chatani, Y.; Shimane, Y.; Ijitsu, T.; Yukinari, T. *Polymer* **1993**, *34*, 1625.
56. Immirzi, A.; De Candia, F.; Iannelli, P.; Vittoria, V.; Zambelli, A. *Makromol. Chem. Rapid Commun.* **1988**, *9*, 761.
57. Chatani, Y.; Shimane, Y.; Inagaki, T.; Ijitsu, T.; Yukinari, T.; Shikuma, H. *Polymer* **1993**, *34*, 1620. Chatani Y.; Inagaki, T.; Shimane, Y.; Shikuma, H. *Polymer* **1993**, *34*, 4841.
58. (a) De Rosa, C.; Guerra, G.; Petraccone, V.; Pirozzi, B. *Macromolecules* **1997**, *30*, 4147. (b) De Rosa, C.; Rizzo, P.; Ruiz de Ballesteros, O.; Petraccone, V.; Guerra, G. *Polymer* **1999**, *40*, 2103.
59. Lotz, B.; Lovinger, A. J.; Cais, R. E. *Macromolecules* **1988**, *21*, 2375.
60. De Rosa, C.; Venditto, V.; Guerra, G.; Corradini, P. *Makromol. Chem.* **1992**, *193*, 1351.
61. De Rosa, C.; Venditto, V.; Guerra, G.; Corradini, P. *Polymer* **1995**, *36*, 3619.
62. De Rosa, C.; Guerra, G.; Grassi, A. *Macromolecules* **1996**, *29*, 471.
63. Farina, M. *Top. Stereochem.* **1987**, *17*, 1.
64. Mislow, K.; Bickart, P. *Israel J. Chem.* **1976/1977**, *15*, 1.
65. Pino, P.; Ciardelli, F.; Lorenzi, G. P.; Montagnoli, G. *Makromol. Chem.* **1963**, *61*, 207. Pino, P. *Adv. Polym. Sci.* **1965**, *4*, 393. Pino, P.; Lorenzi, G. P. *J. Am. Chem. Soc.* **1960**, *82*, 4745. Luisi, P. L.; Pino, P. *J. Phys. Chem.* **1968**, *72*, 2400.
66. Petraccone, V.; Ganis, P.; Corradini, P.; Montagnoli, G. *Eur. Polym. J.* **1972**, *8*, 99.
67. Allegra, G.; Corradini, P.; Ganis, P. *Makromol. Chem.* **1966**, *90*, 60.
68. Napolitano, R.; Pirozzi, B. *Gazz. Chim. Ital.* **1986**, *116*, 323.
69. Corradini, P.; Napolitano, R.; Petraccone, V.; Pirozzi, B.; Tuzi, A. *Eur. Polym. J.* **1981**, *17*, 1217.
70. De Rosa, C.; Napolitano, R.; Pirozzi, B. *Polymer* **1985**, *26*, 2039.
71. Napolitano, R.; Pirozzi, B. *Makromol. Chem.* **1986**, *187*, 1993.
72. Natta, G.; Corradini, P. *Angew. Chem.* **1956**, *68*, 615; Natta, G.; Corradini, P. *Nuovo Cimento, Suppl.* **1960**, *15*, 111.
73. Natta, G.; Corradini, P.; Porri, L. *Rend. Fis. Acc. Lincei* **1956**, *20*, 728.
74. Natta, G.; Porri, L.; Corradini, P.; Morero, D. *Chim. Ind.* **1958**, *40*, 362.
75. Iwayanagi, S.; Sakurai, I.; Sakurai, T.; Seto, T. *J. J. Macromol. Sci., Phys.* **1970**, *B2(2)*, 163.
76. Nyburg, S. C. *Acta Crystallogr.* **1954**, *7*, 385.
77. Bunn, C. W. *Proc. Roy. Soc.* **1942**, *A180*, 40.
78. Benedetti, E.; Corradini, P.; Pedone, C. *Eur. Polym. J.* **1975**, *11*, 585.
79. Takahashi, Y.; Sato, T.; Tadokoro, H.; Tanaka, Y. *J. Polym. Sci., Polym. Phys. Ed.* **1973**, *20*, 728.
80. Yen, T. F. *J. Polym. Sci. Lett.* **1959**, *35*, 533. Pirozzi, B.; Napolitano, R.; Petraccone, V.; Esjosito, S. *Makromol. Rapid Commun.* **2003**, *24*, 392.
81. Yen, T. F. *J. Polym. Sci. Lett.* **1962**, *38*, 272.

82. Napolitano, R. *Makromol. Chem.* **1990**, *191*, 355.
83. Napolitano, R. *Makromol. Chem.* **1990**, *191*, 2435.
84. Napolitano, R. *Macromolecules* **1988**, *21*, 622.
85. Cabassi, F.; Porzio, W.; Ricci, G.; Bruckner, S.; Meille, S. V.; Porri, L. *Makromol. Chem.* **1988**, *189*, 2135. Bruckner, S.; Meille, S. V.; Porzio, W.; Ricci, G. *Makromol. Chem.* **1989**, *189*, 2145. Ferro, D. R.; Bruckner, S.; Meille, S. V.; Ragazzi, M. *Macromolecules* **1992**, *25*, 5231;
86. Napolitano, R. *Macromolecules* **1989**, *22*, 233.
87. Venditto, V.; De Rosa, C.; Guerra, G.; Napolitano, R. *Polymer* **1992**, *33*, 3547.
88. Ricci, G.; Zetta, L.; Porri, L.; Meille, S. V. *Macromol. Chem. Phys.* **1995**, *196*, 2785.
89. Meille, S. V.; Capelli, S.; Allegra, G.; Ricci, G. *Macromol. Rapid Commun.* **1995**, *16*, 329.
90. Natta, G.; Porri, L.; Corradini, P.; Zanini, G.; Ciampelli, F. *Rend. Fis. Acc. Lincei* **1960**, *29*, 257.
91. Natta, G.; Porri, L.; Corradini, P.; Zanini, P.; Ciampelli, F. *J. Polym. Sci.* **1961**, *51*, 463.
92. Bassi, I. W.; Allegra, G.; Scordamaglia, R. *Macromolecules* **1971**, *4*, 575.
93. Neto, N.; Minuz-Miranda, M.; Benedetti, E. *Macromolecules* **1980**, *13*, 1302.
94. Bruckner, S.; Di Silvestro, G.; Porzio, W. *Macromolecules* **1986**, *19*, 235.
95. Bruckner, S.; Luzzati, S.; Porzio, W.; Sozzani, P. *Macromolecules* **1987**, *20*, 585.
96. Natta, G.; Porri, L.; Stoppa, G.; Allegra, G.; Ciampelli, F. *J. Polym. Sci. Part B* **1963**, *1*, 67.
97. Natta, G.; Porri, L.; Carbonaro, A.; Stoppa, G. *Makromol. Chem.* **1964**, *77*, 114.
98. Purevsuren, B.; Allegra, G.; Meille, S. V.; Farina, A.; Porri, L.; Ricci, G. *Polymer J.* **1998**, *30*, 431.
99. Natta, G.; Porri, L.; Carbonaro, A.; Ciampelli, F.; Allegra, G. *Makromol Chem.* **1962**, *51*, 229.
100. Ricci, G.; Italia, C.; Cominati, C.; Porri, L. *Polym. Commun.* **1991**, *32*, 514.
101. Natta, G.; Farina, M.; Donati, M. *Makromol. Chem.* **1961**, *43*, 251.
102. Farina, M.; Grassi, M.; Di Silvestro, G.; Zetta, L. *Eur. Polym. J.* **1985**, *21*, 71.
103. Natta, G.; Farina, M.; Corradini, P.; Peraldo, M.; Donati, M.; Ganis, P. *Chim. Ind.* **1960**, *42*, 1361.
104. Natta, G.; Corradini, P.; Ganis, P. *J. Polym. Sci. Part A* **1965**, *3*, 11.
105. Corradini, P.; Napolitano, R.; Petraccone, V.; Pirozzi, B.; Tuzi, A. *Eur. Polym. J.* **1985**, *21*, 65.
106. Bunn, C. W.; Howells, E. R. *Nature* **1954**, *174*, 549.
107. (a) Clark, E. S.; Muus, L. T. *Z. Kristallogr.* **1962**, *117*, 119. (b) Sperati, C. A.; Starkweather, H. W., Jr., *Adv. Polym. Sci.* **1961**, *2*, 465. (c) Kilian, H. G. *Kolloid Z. Z. Polym.* **1962**, *185*, 13. (d) Weeks, J. J.; Clark, E. S.; Eby, R. K. *Polymer* **1981**, *22*, 1480. (e) Farmer, B. L.; Eby, R. K. *Polymer* **1985**, *26*, 1944. (f) Yamamoto, T.; Hara, T. *Polymer* **1982**, *23*, 521.
108. Corradini, P.; Guerra, G. *Macromolecules* **1977**, *10*, 1410.
109. Corradini, P.; De Rosa, C.; Guerra, G.; Petraccone, V. *Macromolecules* **1987**, *20*, 3043.
110. De Rosa, C.; Guerra, G.; Petraccone, V.; Centore, R.; Corradini, P. *Macromolecules* **1988**, *21*, 1174.
111. Corradini, P. *J. Polym. Sci. Polym. Lett. Ed.* **1969**, *7*, 211.
112. Suehiro, K.; Takayanagi, M. *J. J. Macromol. Sci., Phys.*, **1970**, *B4*(1), 39.

113. Schilling, F. C.; Gomez, M. A.; Tonelli, A. E.; Bovey, F. A.; Woodward, A. E. *Macromolecules* **1987**, *20*, 2954.
114. Robert, P. E.; Mandelkern, L. *J. Am. Chem. Soc.* **1955**, *77*, 781.
115. Natta, G.; Dall'Asta, G.; Mazzanti, G.; Pasquon, I.; Valvassori, A.; Zambelli, A. *Makromol. Chem.* **1962**, *54*, 95; *J. Am. Chem. Soc.* **1961**, *83*, 3343.
116. Kaminsky, W. *Macromol. Chem. Phys.* **1996**, *197*, 3907. McKnight, L.; Waymouth, R. M. *Chem. Rev.* **1998**, *98*, 2586.
117. Drent, E. *Eur. Pat. Appl.* 0229408, **1986**. Barasacchi, M.; Consiglio, G.; Medici, L.; Petrucci, G.; Suter, U. V. *Angew. Chem., Int. Ed. Engl.* **1991**, *30*, 989. Brookhart, M.; Rix, F. C., De Simone J. M.; Barborak, J. M. *J. Am. Chem. Soc.* **1992**, *114*, 5894. Sen, A. *Acc. Chem. Res.* **1993**, *26*, 303. Sen, A.; Jiang, Z. *Macromolecules* **1993**, *26*, 911.
118. Bartolini, S.; Carfagna, C.; Musco, A. *Makromol. Chem. Rapid Commun.* **1995**, *16*, 9. Brookhart, M.; Wagner, M. I.; Bolavoine, G. G. A.; Haddon, H. A. *J. Am. Chem. Soc.* **1994**, *116*, 3641. Jiang, Z.; Adams, S. E.; Sen, A. *Macromolecules* **1994**, *27*, 2694.
119. Natta, G.; Allegra, G.; Bassi, I. W.; Corradini, P.; Ganis, P. *Makromol. Chem.* **1962**, *58*, 242. Corradini, P.; Ganis, P. *Makromol. Chem.* **1963**, *62*, 97.
120. Corradini, P.; De Rosa, C.; Panunzi, A.; Petrucci, G.; Pino, P. *Chimia* **1990**, *44*, 52.
121. De Rosa, C.; Corradini, P. *Eur. Polym. J.* **1993**, *29*, 163.
122. Trifuoggi, M.; De Rosa, C.; Auriemma, F.; Corradini, P. *Macromolecules* **1994**, *27*, 3553.
123. Bruckner, S.; De Rosa, C.; Corradini, P.; Porzio, W.; Musco, A. *Macromolecules* **1996**, *29*, 1535.
124. Napolitano, R.; Pirozzi, B. *Macromolecules* **1995**, *28*, 2406.
125. De Rosa, C. *Macromolecules* **1997**, *30*, 5494.
126. Kitajgorodskij, A. I. *Acta Crystallogr.* **1965**, *18*, 585; *Molecular Crystals and Molecules Academic*, New York, **1973**.
127. Bunn, C. W. *Trans. Faraday Soc.* **1939**, *35*, 482.
128. Corradini, P.; Ganis, P. *J. Polym. Sci.* **1960**, *43*, 311.
129. (a) Natta, G.; Corradini, P.; Bassi, I. W. *Rend. Fis. Accad. Lincei* **1955**, *19*, 404. (b) Natta, G. *Makromol. Chem.* **1960**, *35*, 94. (c) Corradini, P.; Martuscelli, E.; Montagnoli, G.; Petraccone, V. *Eur. Polym. J.* **1970**, *6*, 1201.
130. Natta, G.; Corradini, P. *Chim. Ind. (Milano)* **1963**, *45*, 299.
131. Natta, G.; Corradini, P.; Bassi, I. W. *Rend. Fis. Accad. Lincei* **1957**, *23*, 363.
132. Natta, G.; Corradini, P.; Bassi, I. W. *Nuovo Cimento, Suppl.* **1960**, *15*, 83.
133. Corradini, P.; Bassi, I. W. *J. Polym. Sci. Part C* **1968**, *16*, 3233.
134. Corradini, P.; Ganis, P. *Nuovo Cimento, Suppl.* **1960**, *15*, 96.
135. Corradini, P.; Ganis, P. *Nuovo Cimento, Suppl.* **1960**, *15*, 104.
136. Natta, G.; Corradini, P.; Bassi, I. W. *Makromol. Chem.* **1959**, *33*, 247.
137. De Rosa, C.; Borriello, A.; Corradini, P. *Macromolecules* **1996**, *29*, 6323.
138. Natta, G.; Corradini, P.; Bassi, I. W. *J. Polym. Sci.* **1961**, *51*, 505.
139. Natta, G.; Corradini, P.; Bassi, I. W. *J. Polym. Sci.* **1956**, *20*, 251.
140. Rizzo, P.; Auriemma, F.; Guerra, G.; Petraccone, V.; Corradini, P. *Macromolecules* **1996**, *29*, 8852.
141. Bruckner, S.; Meille, S. V. *Nature* **1989**, *340*, 455.
142. Meille, S. V.; Bruckner, S.; Porzio, W. *Macromolecules* **1990**, *23*, 4114.
143. Lovinger, A. J.; Lotz, B.; Davis, D. D. *Polymer* **1990**, *31*, 2253.

144. Lovinger, A. J.; Davis, D. D.; Lotz, B. *Macromolecules* **1991**, *24*, 552.
145. Lovinger, A. J.; Lotz, B.; Davis, D. D.; Padden, F. J. *Macromolecules* **1993**, *26*, 3494.
146. De Rosa, C.; Auriemma, F.; Corradini, P. *Macromolecules* **1996**, *29*, 7452.
147. Sozzani, P.; Simonutti, R.; Galimberti, M. *Macromolecules* **1993**, *26*, 5782.
148. Chatani, Y.; Maruyama, H.; Asanuma, T.; Shiomura, T. *J. Polym. Sci., Polym. Phys. Ed.* **1991**, *29*, 1649.
149. Auriemma, F.; De Rosa, C.; Ruiz de Ballesteros, O.; Vinti, V.; Corradini, P. *J. Polym. Sci. Polym. Phys. Ed.* **1998**, *36*, 395.
150. Cartier, L.; Okihara, T.; Lotz, B. *Macromolecules* **1998**, *31*, 3303.
151. Pradere, P.; Revol, J. F.; Manley, R. St. J. *Macromolecules* **1988**, *21*, 2747.
152. De Rosa, C.; Capitani, D.; Cosco, S. *Macromolecules* **1997**, *30*, 8322.
153. De Rosa, C.; Auriemma, F.; Borriello, A.; Corradini, P. *Polymer* **1995**, *36*, 4723.
154. Lotz, B.; Kopp, S.; Dorset, D. L. *C. R. Acad. Sci. Paris* **1994**, *319*, 187.
155. Toulouse, G. *Commun. Phys.* **1977**, *2*, 115.
156. Cartier, L.; Spassky, N.; Lotz, B. *C. R. Acad. Sci. Paris* **1996**, *322*, 429.
157. Lotz, B. *Polym. Prepr. Am. Chem. Soc., Div. Polym. Chem.* **1996**, *37*, 430.
158. Dorset, D. L.; McCourt, M. P.; Kopp, S.; Schumacher, M.; Okihara, T.; Lotz, B. *Polymer* **1998**, *39*, 6331. Stocker, W.; Schumacher, M.; Graff, S.; Thierry, A.; Wittmann, J.-C.; Lotz, B. *Macromolecules* **1998**, *31*, 807.
159. Meille, S. V.; Ferro, D. R.; Bruckner, S.; Lovinger, A.; Padden, F. J. *Macromolecules* **1994**, *27*, 2615.
160. Okihara, T.; Cartier, L.; Alberda van Ekenstein, G. O. R.; Lotz, B. *Polymer* **1998**, *40*, 1.
161. Puterman, M.; Kolpak, F. J.; Blackwell, J.; Lando, J. B. *J. Polym. Sci., Polym. Phys. Ed.* **1977**, *15*, 805.
162. Matsubayashi, H.; Chatani, Y.; Tadokoro, H.; Dumas, P.; Spassky, N.; Sigwalt, P. *Macromolecules* **1977**, *10*, 996.
163. Cartier, L.; Spassky, N.; Lotz, B. *Macromolecules* **1998**, *31*, 3040.
164. Puiggali, J.; Ikada, Y.; Tsuji, H.; Cartier, L.; Okihara, T.; Lotz, B. *Polymer* **2000**, *41*, 8921.
165. Sasisekharan, V. *Acta Crystallogr.* **1959**, *12*, 903.
166. Cartier, L.; Lotz, B. *Macromolecules* **1998**, *31*, 3049.
167. Zugenmaier, P. *J. Appl. Polym. Sci., Appl. Polym. Symp.* **1983**, *37*, 223.
168. Cartier, L.; Okihara, T.; Lotz, B. *Macromolecules* **1997**, *30*, 6313.
169. Wittmann, J. C.; Lotz, B. *Prog. Polym. Sci.* **1990**, *15*, 909.
170. Corradini, P.; Guerra, G. *Adv. Polym. Sci.* **1992**, *100*, 183.
171. Hosemann, R.; Bagchi, S. N. *Direct Analysis of Diffraction by Matter*. North-Holland, Amsterdam, 1962.
172. De Rosa, C.; Auriemma, F.; Vinti, V. *Macromolecules* **1997**, *30*, 4137.
173. Mencik, Z. *J. Macromol. Sci. Phys.* **1972**, *6*, 101.
174. Hikosaka, M.; Seto, T. *Polym. J.* **1973**, *5*, 111.
175. Guerra, G.; Petraccone, V.; Corradini, P.; De Rosa, C.; Napolitano, R.; Pirozzi, B.; Giunchi, G. *J. Polym. Sci., Polym. Phys. Ed.* **1984**, *22*, 1029. De Rosa C.; Guerra, G.; Napolitano, R.; Petraccone, V.; Pirozzi, B. *Eur. Polym. J.* **1984**, *20*, 937.
176. De Rosa, C.; Guerra, G.; Napolitano, R.; Pirozzi, B. *J. Thermal Anal.* **1985**, *30*, 1331.

177. Corradini, P.; Giunchi, G.; Petraccone, V.; Pirozzi, B.; Vidal, H. M. *Gazz. Chim. Ital.* **1980**, *110*, 413.
178. Auriemma, F.; Ruiz de Ballesteros, O.; De Rosa, C.; Corradini, P. *Macromolecules* **2000**, *33*, 8764.
179. Petraccone, V.; De Rosa, C.; Tuzi, A.; Fusco, R.; Oliva, L. *Eur. Polym. J.* **1988**, *24*, 297.
180. De Rosa, C.; Corradini, P. *Macromolecules* **1993**, *26*, 5711.
181. De Rosa, C.; Auriemma, F.; Vinti, V. *Macromolecules* **1998**, *31*, 7430.
182. Auriemma, F.; De Rosa, C.; Corradini, P. *Macromolecules* **1993**, *26*, 5719.
183. Auriemma, F.; De Rosa, C.; Corradini, P. *Rend. Fis. Acc. Lincei* **1993**, *4*, 287.
184. Alamo, R. G.; Kim, M.-H.; Galante, M. J.; Isasi, J. R.; Mandelkern, L. *Macromolecules* **1999**, *32*, 4050. Thomann, R.; Wang, C.; Kressler, J.; Mulhaupt, R. *Macromolecules* **1996**, *29*, 8425.
185. Auriemma, F.; De Rosa, C.; Boscato, T.; Corradini, P. *Macromolecules* **2001**, *34*, 4815.
186. Auriemma, F.; De Rosa, C. *Macromolecules* **2002**, *35*, 9057. De Rose, C.; Auriemma, F.; Circelli, T.; Waymouth, R. M. *Macromolecules* **2002**, *35*, 3622.
187. Meille, S. V.; Philips, P. J.; Mzghani, K.; Bruckner, S. *Macromolecules* **1996**, *29*, 795.
188. Tosaka, M.; Hamada, N.; Tsuji, M.; Kohjiya, S.; Ogawa, T.; Isoda, S.; Kobayashi, T. *Macromolecules* **1997**, *30*, 4132; **1997**, *30*, 6888; **1997**, *30*, 6592; **1999**, *32*, 4905; *Polymer* **1998**, *39*, 5273.
189. Auriemma, F.; Born, R.; Spiess, H. W.; De Rosa, C.; Corradini, P. *Macromolecules* **1995**, *28*, 6902. Auriemma, F.; Lewis, R. H.; Spiess, H. W., De Rosa C. *Macromol. Chem.* **1995**, *196*, 4011.
190. Auriemma, F.; De Rosa, C.; Ruiz de Ballesteros, O.; Corradini, P. *Macromolecules* **1997**, *30*, 6586.
191. Bunn, A.; Cudby, E. A.; Harris, R. K.; Packer, K. J.; Say, B. J. *J. Chem. Soc. Chem. Commun.* **1981**, 15.
192. De Rosa, C.; Auriemma, F.; Vinti, V.; Grassi, A.; Galimberti, M. *Polymer* **1998**, *39*, 6219.
193. De Rosa, C.; Auriemma, F.; Talarico, G.; Busico, V.; Caporaso, L.; Capitani, D. *Macromolecules* **2002**, *35*, 1314. De Rose, C.; Auriemma, F.; Fanelli, E.; Talarico, G.; Gejitani, D. *Macromolecules* **2003**, *36*, 1850.
194. Auriemma, F.; Corradini, P.; De Rosa, C.; Guerra, G.; Petraccone, V.; Bianchi, R.; Di Dino, G. *Macromolecules* **1992**, *25*, 2490.
195. Basset, D. C. In *Developments in Crystalline Polymers*, Vol. 1. Basset, D. C. (Ed.) Applied Science Publishers, London, p. 115.
196. Ruiz de Ballesteros, O.; Auriemma, F.; Guerra, G.; Corradini, P. *Macromolecules* **1996**, *29*, 7141.
197. Wilson, F. C.; Starkweather, H. W. Jr., *J. Polym. Sci., Polym. Phys. Ed.* **1973**, *11*, 919. Tanigami, T.; Yamaura, K.; Matsuzawa, S.; Ishikawa, M.; Mizoguchi, K.; Miyasaka, K. *Polymer* **1986**, *27*, 999; **1986**, *27*, 1521.
198. Petraccone, V.; De Rosa, C.; Guerra, G.; Iuliano, M.; Corradini, P. *Polymer* **1992**, *33*, 22.
199. Iuliano, M.; De Rosa, C.; Guerra, G.; Petraccone, V.; Corradini, P. *Makromol. Chem.* **1989**, *190*, 827.
200. Corradini, P.; Petraccone, V.; De Rosa, C.; Guerra, G. *Macromolecules* **1986**, *19*, 2699.
201. Nakaoki, T.; Ohira, Y.; Hayashi, H.; Horii, F. *Macromolecules* **1998**, *31*, 2705. Vittoria, V.; Guadagno, L.; Comotti, A.; Simonutti, R.; Auriemma, F., De Rosa C. *Macromolecules*

- 2000**, 33, 6200; De Rosa C.; Auriemma, F.; Ruiz de Ballesteros O. *Polymer* **2001**, 42, 9729.
202. (a) Petraccone, V.; Auriemma, F.; Dal Poggetto, F.; De Rosa, C.; Guerra, G.; Corradini, P. *Makromol. Chem.* **1993**, 194, 1335. (b) Auriemma, F.; Petraccone, V.; Dal Poggetto, F.; De Rosa, C.; Guerra, G.; Manfredi, C.; Corradini, P. *Macromolecules* **1993**, 26, 3772. (c) Manfredi, C.; De Rosa, C.; Guerra, G.; Rapacciuolo, M.; Auriemma, F.; Corradini, P. *Macromol. Chem. Phys.* **1995**, 196, 2795.
203. Ruiz de Ballesteros, O.; Auriemma, F.; De Rosa, C.; Floridi, G.; Petraccone, V. *Polymer* **1998**, 39, 3523.
204. De Rosa, C.; Buono, A.; Caporaso, L.; Petraccone, V. *Macromolecules* **2001**, 34, 7349.
205. Hoogsteen, W.; Postema, A. R.; Pennings, A. J.; tenBrinke, G.; Zugenmaier, P. *Macromolecules* **1990**, 23, 634. De Santis P.; Kovacs, J. *Biopolymers* **1968**, 6, 299. Miyata, T.; Masuko, T. *Polymer* **1997**, 38, 4003. Kobayashi, J.; Asahi, T.; Ichiki, M.; Okikawa, A.; Suzuki, H.; Watanabe, T.; Fukada, E.; Shikinami, Y. *J. Appl. Phys.* **1995**, 77, 2957. Aleman, C.; Lotz, B.; Puiggali, J. *Macromolecules* **2001**, 34, 4795.
206. Cartier, L.; Okihara, T.; Ikada, Y.; Tsuji, H.; Puiggali, J.; Lotz, B. *Polymer* **2000**, 41, 8909.
207. Green, M. M.; Park, J.-W.; Sato, T.; Teramoto, A.; Lifson, S.; Selinger, R. L. B.; Selinger, J. V. *Angew. Chem. Int. Ed.* **1999**, 38, 3138.
208. Okihara, T.; Tsuji, M.; Kawagushi, A.; Katayama, K. I.; Tsuji, H.; Hyon, S. H.; Ikada, Y. *J. Macromol. Sci. Phys.* **1991**, B30, 119.
209. Lotz, B. *Eur. Phys. J.* **2000**, E3, 185.
210. Sakakihara, H.; Takahashi, Y.; Tadokoro, H.; Oguni, N.; Tani, H. *Macromolecules* **1973**, 6, 205.
211. Tadokoro, H. *Polymer* **1984**, 25, 147.
212. Sakakihara, H.; Chatani, Y.; Tadokoro, H.; Sigwalt, P.; Spassky, N. *Macromolecules* **1969**, 2, 515.
213. Yokouchi, M.; Chatani, Y.; Tadokoro, H.; Teranishi, K.; Tani, H. *Polymer* **1973**, 14, 267.
214. Takahashi, Y.; Tadokoro, H.; Hirano, T.; Sato, A.; Tsuruta, T. *J. Polym. Sci., Polym. Phys. Ed.* **1975**, 13, 285.
215. Meille, S. V.; Allegra, G. *Macromolecules* **1995**, 28, 7764.
216. Auriemma, F.; Ruiz de Ballesteros, O.; De Rosa, C. *Macromolecules* **2001**, 34, 4485.
217. De Rosa, C.; Auriemma, F.; Orlando, I.; Talarico, G.; Caporaso, L. *Macromolecules* **2001**, 34, 1663. De Rosa, C.; Gargiulo, M. C.; Auriemma, F.; Ruiz de Ballesteros, O.; Razavi, A. *Macromolecules* **2002**, 35, 9083.
218. Lotz, B.; Mathieu, C.; Thierry, A.; Lovinger, A. J.; De Rosa, C.; Ruiz de Ballesteros, O.; Auriemma, F. *Macromolecules* **1998**, 31, 9253.
219. Attenburrow, G. E.; Bassett, D. C. *J. Mater. Sci.* **1979**, 14, 2679. Bassett, D. C. *Principles of Polymer Morphology*. Cambridge Polymer Press, Cambridge, 1981.
220. Natta, G. *Makromol. Chem.* **1955**, 16, 213; Turner-Jones A.; Aizlewood, J. M. *J. Polym. Sci.* **1963**, B1, 471.
221. Noether, H. D. *J. Polym. Sci. Part C* **1967**, 16, 725.
222. Dall'Asta, G.; Otto, N. *Chim. Ind. (Milan)* **1960**, 42, 1234.
223. Natta, G.; Bassi, I. W.; Corradini, P. *Makromol. Chem.* **1956**, 18–19, 455.
224. De Rosa, C.; Petraccone, V.; Guerra, G.; Manfredi, C. *Polymer* **1996**, 37, 5247.

225. Petraccone, V.; La Camera, D.; Pirozzi, B.; Rizzo, P.; De Rosa, C. *Macromolecules* **1998**, *31*, 5830. Petraccone, V., La Camera D.; Caporaso, L., De Rosa C. *Macromolecules* **2000**, *33*, 2610.
226. De Rosa, C.; Petraccone, V.; Dal Poggetto, F.; Guerra, G.; Pirozzi, B.; De Lorenzo, M. L.; Corradini, P. *Macromolecules* **1995**, *28*, 5507.
227. Meille, S. V.; Capelli, S.; Ricci, G. *Makromol. Chem. Rapid Commun.* **1995**, *16*, 891. Immirzi, A.; Tedesco, C.; Meille, S. V.; Famulari, A.; van Smaalen, S. *Macromolecules* **2003**, *36*, 3666.
228. Cesari, M. *J. Polym. Sci.* **1962**, *B2*, 453.
229. Liquori, A. M. *Acta Crystallogr.* **1955**, *8*, 345. Wasai, G.; Saegusa, T.; Furukawa, J. *Makromol. Chem.* **1965**, *86*, 1. Allegra, G.; Benedetti, B.; Pedone, C. *Macromolecules* **1970**, *3*, 727. Tanaka, T.; Chatani, Y.; Tadokoro, H. *J. Polym. Sci. Polym. Phys. Ed.* **1974**, *12*, 515.
230. Tadokoro, H.; Yasumoto, T.; Murahashi, S.; Nitta, I. *J. Polym. Sci.* **1960**, *44*, 266. Carazzolo, G. *J. Polym. Sci.* **1963**, *A1*, 1573. Tadokoro, H. *J. Polym. Sci.* **1966**, *C15*, 1. Uchida, T.; Tadokoro, H. *J. Polym. Sci. Polym. Phys. Ed.* **1967**, *5*, 63. Takahashi, Y.; Tadokoro, H. *J. Polym. Sci. Polym. Phys. Ed.* **1978**, *16*, 1219; **1979**, *17*, 123.
231. Carazzolo, G.; Mammì, M. *J. Polym. Sci., Part A* **1963**, *1*, 965.
232. Carazzolo, G.; Valle, G. *Makromol. Chem.* **1966**, *90*, 66.
233. Carazzolo, G.; Valle, G. *J. Polym. Sci., Part A* **1965**, *3*, 4013.
234. Carazzolo, G.; Mammì, M. *Makromol. Chem.* **1967**, *100*, 28.
235. Yokouchi, M.; Chatani, Y.; Tadokoro, H.; Tani, H. *Polym. J.* **1974**, *6*, 248.
236. Yokouchi, M.; Chatani, Y.; Tadokoro, H. *J. Polym. Sci., Polym. Phys. Ed.* **1976**, *14*, 81.
237. Tashiro, K.; Kobayashi, M.; Tadokoro, H. *Macromolecules* **1977**, *10*, 413.
238. Kusanagi, H.; Tadokoro, H.; Chatani, Y.; Suehiro, K. *Macromolecules* **1977**, *10*, 405.
239. Ricci, G.; Zetta, L.; Porri, L.; Meille, S. V. *Macromol. Chem. Phys.* **1995**, *196*, 2785. Meille, S. V.; Capelli, S.; Allegra, G.; Ricci, G. *Macromol. Rapid Commun.* **1995**, *16*, 329.
240. Perego, G.; Bassi, I. W. *Makromol. Chem.* **1963**, *61*, 198.
241. Ricci, G.; Zetta, L.; Meille, S. V. *Gazz. Chim. Ital.* **1996**, *126*, 401.
242. Natta, G.; Dall'Asta, G.; Bassi, I. W.; Carella, G. *Makromol. Chem.* **1966**, *91*, 87.
243. Turner-Jones, A. *Makromol. Chem.* **1964**, *71*, 1.
244. Farmer, B. L.; Lando, J. B. *J. Macromol. Sci. Phys.* **1974**, *10*, 403.
245. Natta, G.; Corradini, P.; Bassi, I. W.; Fagherazzi, G. *Eur. Polym. J.* **1968**, *4*, 297.
246. Cesari, M.; Perego, G.; Marconi, W. *Makromol. Chem.* **1966**, *94*, 194.
247. De Rosa, C. *Macromolecules* **2003**, *36*, in press.

Chapter 3

Optically Active Polymers with Chiral Recognition Ability

YOSHIO OKAMOTO, EIJI YASHIMA, AND CHIYO YAMAMOTO

Department of Applied Chemistry, Graduate School of Engineering, Nagoya University, Nagoya, Japan 464-8603

- 1 Introduction
- 2 Optically Active Polymers with Chiral Recognition Ability
- 3 Vinyl Polymers
 - 3.1 Polymethacrylates
 - 3.2 Other Vinyl Polymers
- 4 Polyamides
- 5 Other Synthetic Polymers
- 6 Natural Polymers and Their Derivatives
 - 6.1 Proteins
 - 6.2 Polysaccharides
 - 6.2.1 Cellulose Esters
 - 6.2.2 Cellulose and Amylose Phenylcarbamates
 - 6.2.3 Cellulose and Amylose Arylalkylcarbamates
 - 6.2.4 Cellulose and Amylose Cycloalkylcarbamates
 - 6.2.5 Oligosaccharides and Cyclodextrins
 - 6.2.6 Other Phenylcarbamates of Polysaccharides
 - 6.3 Mechanism of Chiral Recognition on Polysaccharide Derivatives
 - 6.3.1 Chromatographic Studies
 - 6.3.2 NMR Studies
 - 6.3.3 Computational Studies
- 7 Conclusions
- References

1 INTRODUCTION

In living systems, optically active macromolecules, such as proteins, nucleic acids, and polysaccharides, are extensively involved in life processes. These macromolecules often possess specific conformational and higher

Materials-Chirality: Volume 24 of Topics in Stereochemistry,
Edited by Mark M. Green, R.J.M. Nolte, and E.W. Meijer
ISBN 0-471-05497-6 Copyright © 2003 John Wiley & Sons, Inc.

order structures associated with their chiral properties; their structures are deeply connected with their properties and functions, including the ability for chiral recognition. For one example in which the properties of naturally occurring macromolecules have been used *in vitro*, enantioselective reactions with enzymes as chiral catalysts have been used to produce chiral nonracemic molecules of practical importance. To mimic the enantioselective characteristics of enzymes, various optically active polymers have been designed and synthesized.^{1,2} These optically active polymers are usually prepared through the polymerization of optically active monomers or through the modifications of a polymer with chiral molecules or are based on natural polymers.

One of the most practical and widely accepted applications of both natural and synthetic optically active polymers is that for the chiral separation of racemic compounds by high-performance liquid chromatography (HPLC) using these polymers as chiral stationary phases (CSPs).^{3–11} In the past two decades, a remarkable change has been observed in the methods used for the determination of optical purity, that is, enantiomer composition. Figure 3.1*a* shows the distribution of the methods reported in the journal *Tetrahedron Asymmetry* in 2000. The methods are classified into five categories: (1) chiral HPLC; (2) chiral gas chromatography (GC); (3) nuclear magnetic resonance (NMR) methods using chiral derivatizing agents, chiral solvating agents, and chiral lanthanide shift reagents; (4) optical rotation measurements; and (5) others involving the indirect determination of enantiomeric excess with achiral HPLC and GC methods. As Figure 3.1*a* shows, most organic chemists are now using mainly three methods: chiral HPLC, chiral GC, and NMR. The polarimetric method, which had been the main method before 1980, has already become minor.¹²

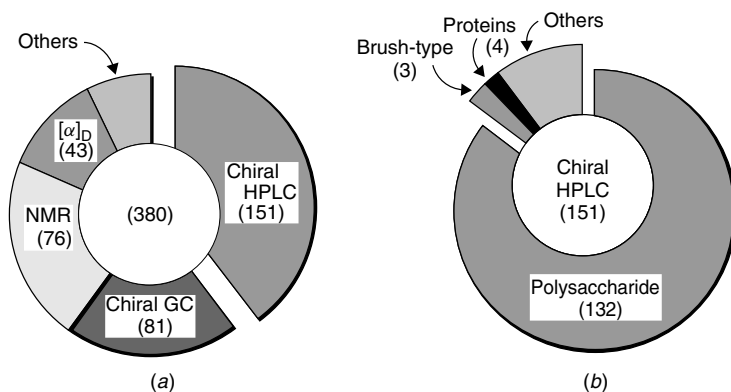


Figure 3.1 Distribution of (a) methods and (b) CSPs for HPLC for determination of enantiomer composition appeared in *Tetrahedron Asymmetry* in 2000. Figures represent number of paper counted.

The CSPs for HPLC have been prepared with both optically active small molecules^{8,13,14} and polymers with chiral recognition ability. The small molecules are usually bonded onto silica gel. However, polymers can also be used as CSPs by coating on silica gel because of their low solubility in the solvent normally used for HPLC separations. Chiral recognition by small-molecule CSPs depends mainly on that of the small molecules themselves, but polymer CSPs often show chiral recognition that significantly depends on the higher order structure of the polymers, which makes understanding of chiral recognition mechanisms by polymeric CSPs difficult. Many small-molecule and polymeric CSPs have been commercialized since the early 1980s. Today, as shown in Figure 3.1*b*, the most popular CSPs are derivatives of polysaccharides, mainly because of the very broad applicability of these CSPs.^{12,15–19} Therefore, in this chapter, we will describe optically active polymers, especially polysaccharide derivatives as CSPs for HPLC, emphasizing the correlation between their structure and recognition.

2 OPTICALLY ACTIVE POLYMERS WITH CHIRAL RECOGNITION ABILITY

Both synthetic and naturally occurring polymers have been used as CSPs. Figure 3.2 shows typical CSPs prepared from optically active polymers (**1–18**); **1–15** are totally synthetic polymers, including vinyl polymers (**1–7**), polyamides (**8–12**), polyurethanes (**13**), polyacetylene (**14**), and polysaccharide analogue (**15**). The CSPs **16–18** are based on natural polymers, proteins (**16**), and polysaccharides (**17, 18**).

In addition, crosslinked polymer gels possessing chiral cavities have been prepared by a molecular imprinting method using an optically active template moiety of a monomer or template molecule; their chiral recognition abilities have been evaluated.^{20–22} Figure 3.3 shows template monomers having a removable chiral moiety. The obtained gels resolve the racemate with a higher affinity for the templated enantiomer.

The chiral recognition ability of a CSP is quantitatively evaluated from the results of chromatographic separation of enantiomers. Figure 3.4 shows a chromatogram of the resolution of benzoin (**19**) on cellulose tris(3,5-dimethylphenylcarbamate). The (+)-isomer elutes first followed by the (–)-isomer; complete baseline separation is achieved. The results of the separation can be expressed by three parameters—capacity factors (k'), separation factor (α), and resolution factor (R_s)—defined as follows:

$$k'_1 = \frac{t_1 - t_0}{t_0} \quad k'_2 = \frac{t_2 - t_0}{t_0} \quad \alpha = \frac{t_2 - t_0}{t_1 - t_0} = \frac{k'_2}{k'_1} \quad R_s = \frac{2(t_2 - t_1)}{w_1 + w_2}$$

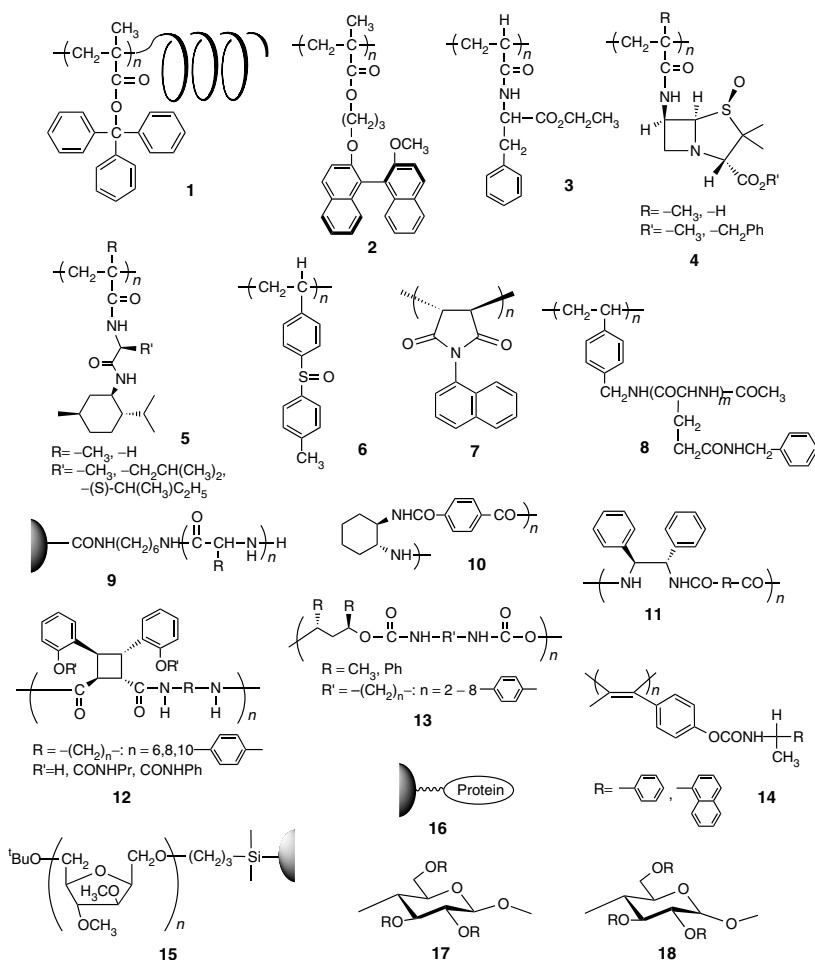


Figure 3.2 Chiral polymer stationary phases for HPLC.

where t_1 and t_2 are retention times of the enantiomers, t_0 is dead time (retention time of nonretained compound), and w_1 and w_2 are bandwidths of the peaks. In a chromatographic separation, α is directly related to the chiral recognition ability of a CSP and R_s is correlated to both the chiral recognition ability of a CSP and column efficiency (theoretical plate number). The energy difference ($\Delta\Delta G$) for the interactions between a CSP and a pair of enantiomers can be estimated from an α value by using the equation $\Delta\Delta G = -RT \ln \alpha$. A separation factor of $\alpha = 1.20$ corresponds to $\Delta\Delta G = -0.11$ kcal/mol, which is usually enough for baseline separation of enantiomers.

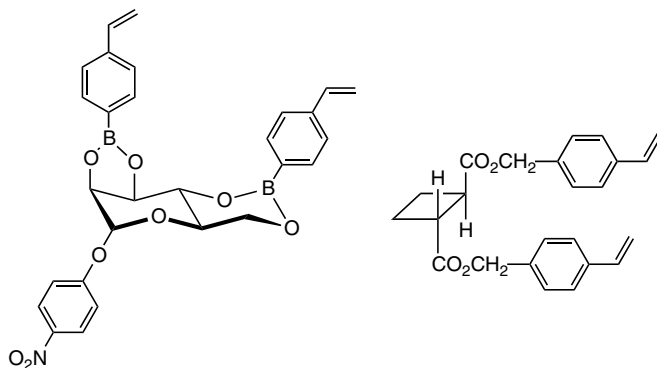


Figure 3.3 Structures of chiral template monomers.

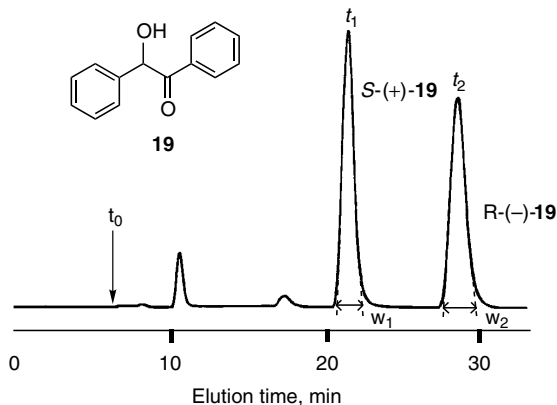


Figure 3.4 Optical resolution of **19** on cellulose tris(3,5-dimethylphenylcarbamate) column: 25×0.46 (i.d.) cm; eluent: hexane/2-propanol (90/10); flow rate: 0.5 ml/min (i.d. = inside diameter).

3 VINYL POLYMERS

3.1 Polymethacrylates

A bulky methacrylate, triphenylmethyl methacrylate (TrMA), is a unique monomer which gives an almost 100% isotactic polymer in anionic polymerization with *n*-butyllithium both in nonpolar and polar solvents. Moreover, even free-radical polymerization affords a highly isotactic polymer from this monomer.²³ The isotactic specificity of TrMA polymerization is ascribed to the helical formation of the main chain. When TrMA is polymerized in toluene at -78°C

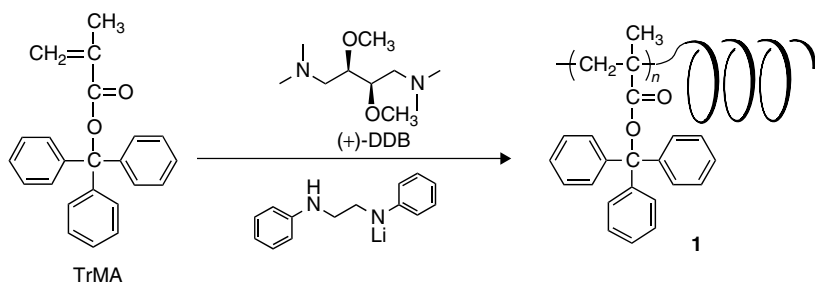


Figure 3.5 Asymmetric polymerization of TrMA.

with a chiral anionic initiator, for instance, (+)- or (–)-2,3-dimethoxy-1,4-bis(dimethylamino)butane (DDB)–lithium amide complex, it gives a one-handed helical polymer showing a high optical activity (Figure 3.5).²⁴ The helical handedness of the polymer can be controlled by changing the chiral sense of the ligand of the initiation system. The helical conformation is maintained by steric repulsion of the bulky side groups; therefore, the optical activity of **1** disappears when the bulky triphenylmethyl groups are removed by hydrolysis of the ester linkage.

The optically active poly(TrMA) shows a large optical activity and intense circular dichroism (CD) due both to the triphenylmethyl group, indicating that this group has a chiral propeller structure, and to the helicity. Poly(TrMA) of degree of polymerization (DP) over 80 is insoluble in common organic solvents.

The chiral recognition ability of the insoluble (+)-**1** was estimated by HPLC using a column packed with small particles of **1**.²⁵ However, this column showed a poor efficiency because of a low theoretical plate number. This defect was overcome by coating soluble poly(TrMA) with a DP of ≈ 50 on macroporous silica gel.²⁶ The **1**-coated silica gel had higher resistance against compression and longer lifetime than the CSP of insoluble **1**. Moreover, the two **1**-based CSPs show quite different chiral recognition for several racemates, which may be attributed to the different orientation of **1** in bulk and on the surface of the silica gel.²⁷

The one-handed helical poly(TrMA) shows high chiral recognition abilities toward various types of compounds. However, optically active polymethacrylates bearing a simple chiral side chain such as the (*S*)-1-phenylethyl group show almost no chiral recognition ability.²⁷ This suggests that the chiral recognition by **1** is a special case and is attributed to the rigid helical structure accompanying a chiral propeller triphenylmethyl group.

The **1**-coated silica gel has resolved more than 200 racemic compounds so far; some of them are shown in Figure 3.6. The CSP is especially useful for the resolution of stereochemically interesting compounds without

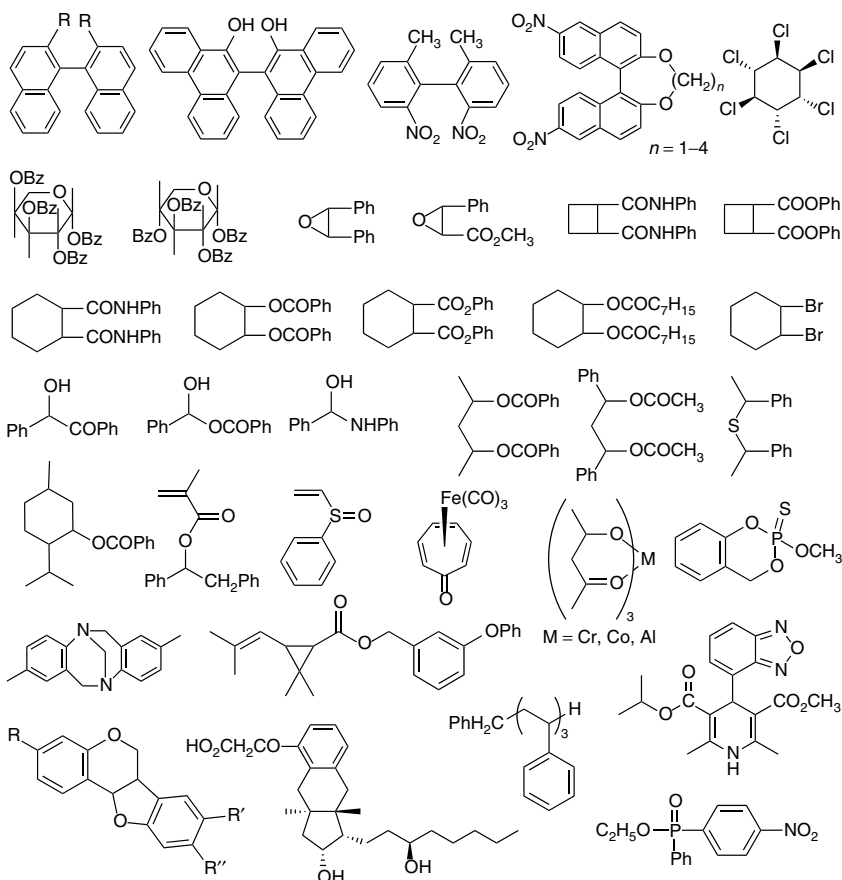


Figure 3.6 Compounds resolved on optically active 1.

functional groups whose resolution would be difficult by other methods (Figure 3.7).^{25,28–44} The most important recognition site of **1** is probably the triphenylmethyl group with a chiral propeller structure.²⁷ In most cases, a polar eluent such as methanol or a methanol–water mixture gives better results for enantiomer separations than a nonpolar eluent. This indicates that nonpolar or hydrophobic interactions between **1** and a nonpolar group of an analyte is important for achieving effective chiral recognition.

In the resolution of racemates having a C_2 axis and two aromatic groups using (+)-**1**, the more retained enantiomers have *P*-helicity with respect to their aromatic groups if one looks at the molecules from the direction perpendicular to a C_2 axis (Figure 3.8). This could suggest that (+)-**1** has *P*-helicity; that is, a right-handed helical conformation.⁴⁵

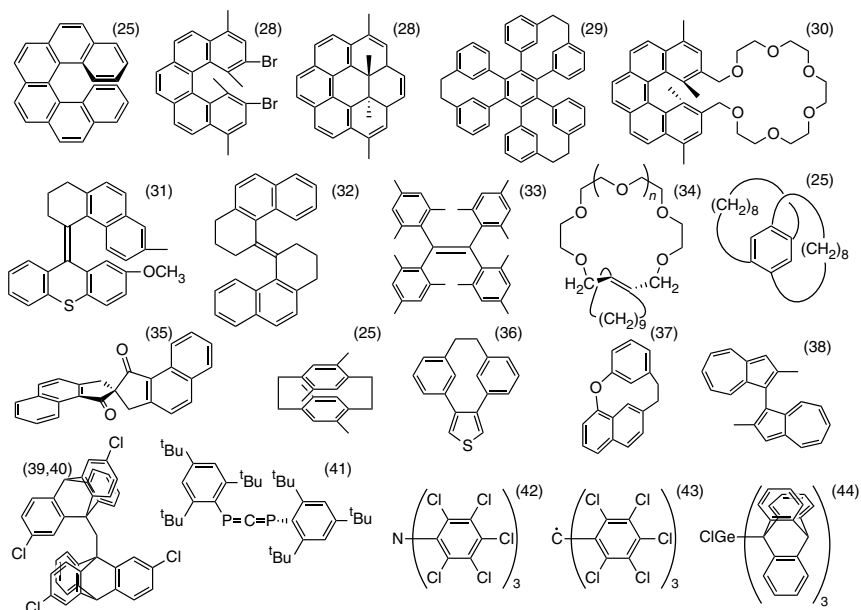


Figure 3.7 Stereochemically interesting compounds resolved on optically active **1**.

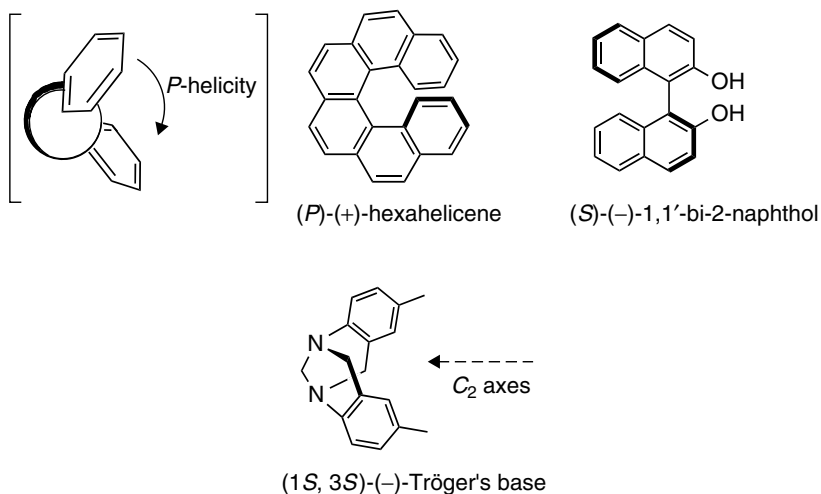


Figure 3.8 Enantiomers adsorbed more strongly on (+)-**1**.

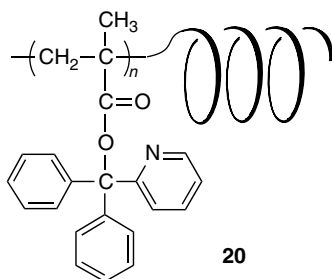


Figure 3.9 Structure of optically active **20**.

Although methanol is a good eluent for CSP, the triphenylmethyl groups of **1** are slowly solvolyzed in methanol. In order to counter this defect, a pyridyl group was introduced in place of a phenyl group in **1**. Diphenyl-2-pyridylmethyl methacrylate also afforded an optically active polymer (**20**) (Figure 3.9) with a one-handed helical structure by helix-sense-selective polymerization with a chiral anionic initiator.^{46–48} Stability of optically active **20**-coated silica gel against solvolysis by methanol is 16-fold higher than that of **1**-coated silica gel.⁴⁹ The chiral recognition by **20** is basically similar to that by **1**; many racemic compounds have also been resolved via HPLC based on **20**.⁴⁹

An optically active polymethacrylate (**2**) having a binaphthol moiety in the side chain was synthesized by radical polymerization. This polymer coated on silica gel resolved several racemates.⁵⁰ However, no data on the influence of the stereoregularity of the main chain on resolution have been reported. The chiral recognition by this polymer may simply arise from the binaphthyl group.

3.2 Other Vinyl Polymers

Blaschke and co-workers succeeded in resolving many chiral drugs by using optically active polyacrylamides (**3**) and polymethacrylamides^{51–53} and evaluated the difference in pharmacological behaviors between the enantiomers. It is particularly meaningful that they pointed out the more pronounced teratogenic effect of (*S*)-thalidomide over the (*R*)-isomer.⁵⁴ They also mentioned that only the polymers prepared by the radical polymerization of optically active monomers exhibit high chiral recognition and that the same polymer prepared by the reaction of poly(acrylic acid) with the corresponding chiral amine has a low chiral recognition ability.⁵¹ This indicates that chiral recognition sites with high ability are constructed only by the polymerization process. Similar behavior has also been observed for cellulose triacetate; its chiral recognition ability is associated with its higher order structure. This will be mentioned in Section 6.2.1 in detail.

Other polyacrylamides and polymethacrylamides (**4**, **5**)^{55,56} have been prepared and their chiral recognition abilities as CSPs have been evaluated. Chiral stationary phase **5** shows high recognition for several drugs.

An optically active styrene derivative (**6**) with a chiral sulfoxide moiety can resolve several alcohols and amines having an aryl group.⁵⁷ Poly(*N*-1-naphthylmaleimide) (**7**) obtained by asymmetric anionic polymerization with organometal/chiral ligand complexes showed chiral recognition for several racemates, including 1,1'-bi-2-naphthol.⁵⁸ This polymer has predominant (*R,R*) or (*S,S*) configuration of the main chain produced by *trans* opening of the maleimide monomer. The polymer likely has a helical structure arising from the main-chain asymmetry.^{59,60}

4 POLYAMIDES

Several optically active polyamides including poly(α -amino acid)s have been prepared to be used as CSPs. Poly(*N*-benzyl-L-glutamine) chemically bonded to polystyrene beads (**8**) resolved mandelic acid and hydantoin derivatives.^{61,62} The main chain of the immobilized poly(*N*-benzyl-L-glutamine) takes an α -helical structure, which seems to be responsible for the chiral recognition ability. The dimer with $m = 2$ showed no chiral recognition. However, polymers with m values of 14 or 36 achieved baseline separation, but the polymer with $m = \approx 250$ showed lower recognition. These results suggest that the vicinities of a helical chain end may recognize enantiomers. Porous beads have been prepared with poly(L-leucine) and poly(γ -methyl-L-glutamate) and used for the resolution of some α -amino acids. The beads showed broad chromatograms probably because of the formation of nonuniform adsorbing sites. The CSPs containing poly(L-leucine) or poly(L-phenylalanine) chemically bonded to poly(methyl acrylate) macroporous beads (**9**) exhibit chiral recognition for some amino acid derivatives.⁶³

Polyamides **10**,⁶⁴ **11**,⁶⁵ and **12**⁶⁶⁻⁶⁸ prepared from chiral diamines or chiral dicarboxylic acids can separate polar racemates capable of hydrogen bonding to the CSP. The chiral recognition ability of **12** (R' = methylene groups) was affected by the crystallizability of **12**, which depended on the number of methylene groups. The polyamide **12** having an even number of methylene groups shows higher recognition ability than those having an odd number of methylene groups.

5 OTHER SYNTHETIC POLYMERS

Polyurethanes (**13**) have been prepared with optically active diols and various diisocyanates.⁶⁹ Chiral recognition depends on the diisocyanate

residues. Polyurethanes derived from 1,3-diphenylpropanediol and aliphatic diisocyanates showed better chiral recognition abilities for 1,1'-bi-2-naphthol derivatives than those from aromatic diisocyanates.

Polyacetylenes have a structure of alternating double and single bonds and, therefore, there exist at least four possible structures with respect to these bonds: *cis*-transoid, *cis*-cisoid, *trans*-transoid, and *trans*-cisoid. By using a rhodium catalyst, phenylacetylene derivatives often produce stereoregular polymers with an almost completely *cis*-transoidal structure.⁷⁰ Polyphenylacetylene derivatives (**14**) with optically active substituents at the *para* position have been prepared to examine the chiral recognition ability as CSPs.^{71,72} The polymers show intense CD peaks due to the main-chain conjugated structure, indicating that the polymers possess a one-handed helical conformation. The CSP resolved several enantiomers, including Tröger's base. This ability must be ascribed to the stereoregular structure because the stereoirregular polymer produced with a tungsten catalyst exhibited very low chiral recognition. Several chiral polyacetylenes have been prepared to be used as solid membranes to separate enantiomers.

Polysaccharide analogue, polyether **15**, prepared through anionic cyclo-polymerization, was chemically bonded to silica gel.⁷³ The CSP resolved several α -amino acids; the chiral recognition abilities of the analogue of **15** have been evaluated.⁷⁴

6 NATURAL POLYMERS AND THEIR DERIVATIVES

6.1 Proteins

Proteins are stereoregular as a consequence of the nonracemic nature of the amino acids from which they are formed. There exist many kinds of proteins in nature. Structural proteins such as wool, silk, and human hair usually show very low chiral recognition. However, most proteins have chiral recognition ability to some extent. So far, the following proteins have been evaluated as CSPs for HPLC: albumins such as bovine serum albumin (BSA)⁷⁵ and human serum albumin (HSA),⁷⁶ glycoproteins such as α_1 -acid glycoprotein (AGP),⁷⁷ ovomucoid from chicken egg whites (OMCHI),⁷⁸ ovoglycoprotein from chicken egg whites (OGCHI),⁷⁹ avidin (AVI),⁸⁰ and riboflavin binding protein (RfBP) (or flavoprotein),⁸¹ enzymes such as trypsin,⁸² α -chymotrypsin,⁸³ cellobiohydrolase I (CBH I),⁸⁴ lysozyme,⁸⁵ pepsin,⁸⁶ and amyloglucosidase⁸⁷ and other proteins such as ovotransferrin (or conalbumin)⁸⁸ and β -lactoglobulin.⁸⁹ Among those proteins, BSA, HSA, AGP, OMCHI, AVI, CBH I, and pepsin have been commercialized as CSPs. These CSPs often show high chiral recognition toward chiral basic organic

drugs under reversed-phase conditions with aqueous mobile phases. This may be the most significant feature for these CSPs.

The protein phases also have several demerits such as low loading capacity and low stability as CSPs. It is not easy to elucidate the chiral recognition mechanisms for proteins. Moreover, the defects noted above come from the fact that proteins are copolymers of various α -amino acids and conformationally not stable under all conditions. For the protein-based CSPs, retention and enantioselectivity for racemates are significantly affected by chromatographic conditions such as eluent, temperature, and pH, which can vary protein conformation. The protein-based CSPs are useful for analytical purposes, but not for preparative separation because of the very low loading capacity due to the limited number of recognition sites. Various experiments have been carried out to improve the performance of the protein-based CSPs. The stability of the CSPs has been enhanced through crosslinking of the proteins.⁹⁰ The protein fragment or protein domain, which plays the central role for chiral recognition, has been used to increase the loading capacity of CSPs and to understand the chiral recognition site of protein-based CSPs.^{91–93} In the future, it might become possible to prepare more suitable protein-based CSPs for a target molecule by genetic technology.

6.2 Polysaccharides

Polysaccharides such as cellulose and amylose are the most readily available optically active polymers. Although these polymers have stereoregular sequences consisting of D-glucose, their chiral recognition abilities are not large enough that one can use them as CSPs. However, these polysaccharides have hydroxy groups which can be readily converted to esters and carbamates through the reaction with suitable reagents. The derivatized polysaccharide-based CSPs offer much better chromatographic and enantioselective properties than the native polysaccharides. At present, more than 10 CSPs derived from polysaccharide derivatives have been marketed and, as previously mentioned, have been extensively used for both analytical and preparative separation of enantiomers.

6.2.1 Cellulose Esters

The first practical CSP derived from polysaccharides is cellulose triacetate (**21**, Figure 3.10) prepared by Hesse and Hagel in 1973.^{94,95} Since this derivative was prepared by the heterogeneous acetylation of native microcrystalline cellulose (Avicel) in benzene, it has been postulated that its structure is closely related to that of native cellulose (form I). This has been called “microcrystalline cellulose triacetate” (CTA-I). CTA-I shows characteristic chiral

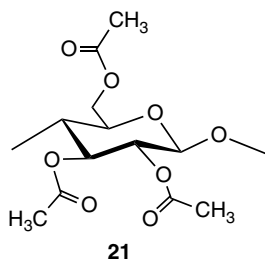


Figure 3.10 Structure of cellulose triacetate (**21**).

recognition associated with its structure. Hesse and Hagel pointed out that the microcrystallinity of CTA-I is essential for chiral recognition, because the resolving ability is substantially reduced and, in some cases, the reversal of elution order of enantiomers occurs when once CTA-I is dissolved in a solvent. CTA-I has been used for the resolution of a wide range of racemates, especially nonpolar compounds and aromatic pharmaceuticals, using an ethanol–water mixture as the eluent.^{51,53,96} Stereochemically interesting compounds completely separated on CTA-I are shown in Figure 3.11.^{97–104} The loading capacity of CTA-I is quite high and, therefore, this CSP is one of the most usable CSPs for large-scale separation of pharmaceuticals. When CTA-I was coated on silica gel for HPLC from a solution, it gave another CSP whose chiral recognition ability is completely different from that of CTA-I as mentioned above.^{105,106} For example, Tröger's base enantiomers eluted in reversed order on the two cellulose triacetate columns (Figure 3.12).¹⁰⁵ This

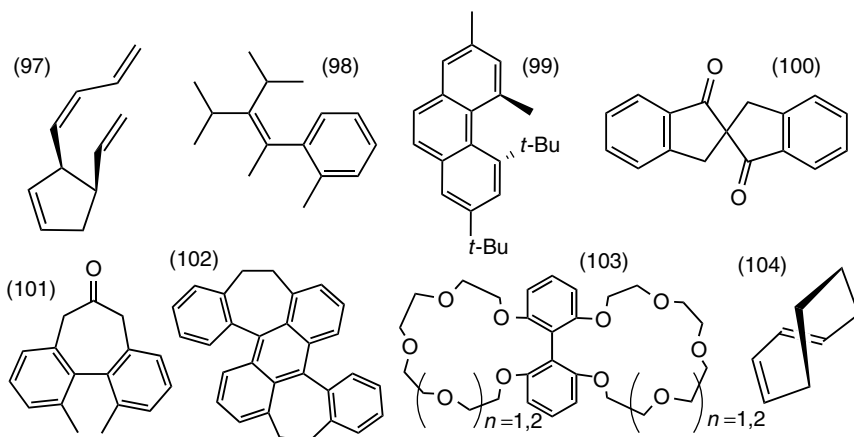


Figure 3.11 Compounds resolved on microcrystalline cellulose triacetate (CTA I).

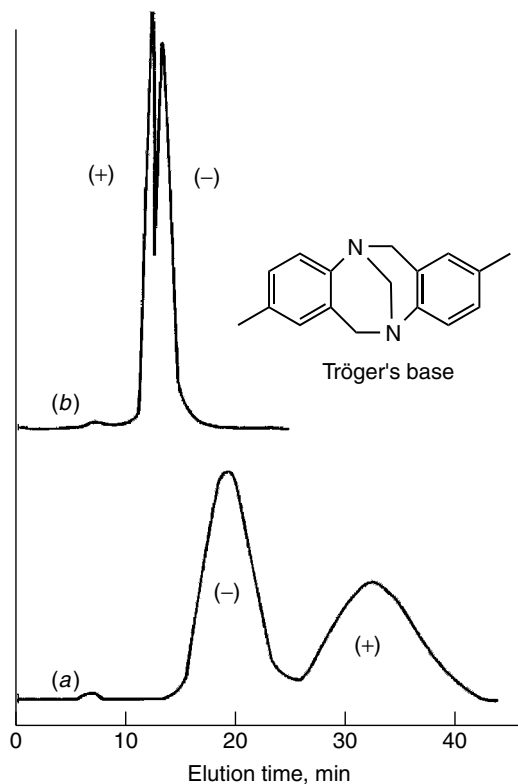


Figure 3.12 Enantioseparation of Tröger's base on (a) microcrystalline cellulose triacetate (CTA I) and (b) **21** coated on silica gel. Column, 25×0.46 (i.d.) cm; eluent: ethanol–H₂O (7/3); flow rate, 0.5 ml/min).

difference has been attributed to the different higher order structures or the different supramolecular structures of the two cellulose triacetates.

The influence of substituents, such as alkyl, halogen, trifluoromethyl, and methoxy groups, on the phenyl groups of cellulose tribenzoate (**22**) has been systematically investigated (Figure 3.13).¹⁰⁷ The main chiral-adsorbing site of cellulose tribenzoates is considered to be the polar carbonyl groups of esters, and the inductive effect of the substituents may change the polarity of carbonyl groups. The benzoate derivatives having electron-donating substituents, such as the methyl group, showed a better chiral recognition ability than those having electron-withdrawing substituents, such as a halogen group. Among the benzoates, cellulose tris(4-methylbenzoate) (**22b**) showed a high chiral recognition ability for various racemates. Some racemates, including stereochemically interesting compounds resolved on **22b**, are shown in Figure 3.14.^{108–118} Nonaromatic compounds (Figure 3.15) are sufficiently

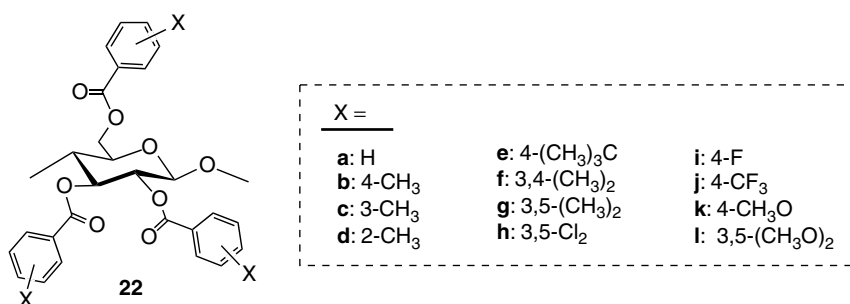


Figure 3.13 Structures of cellulose tribenzoates (**22**).

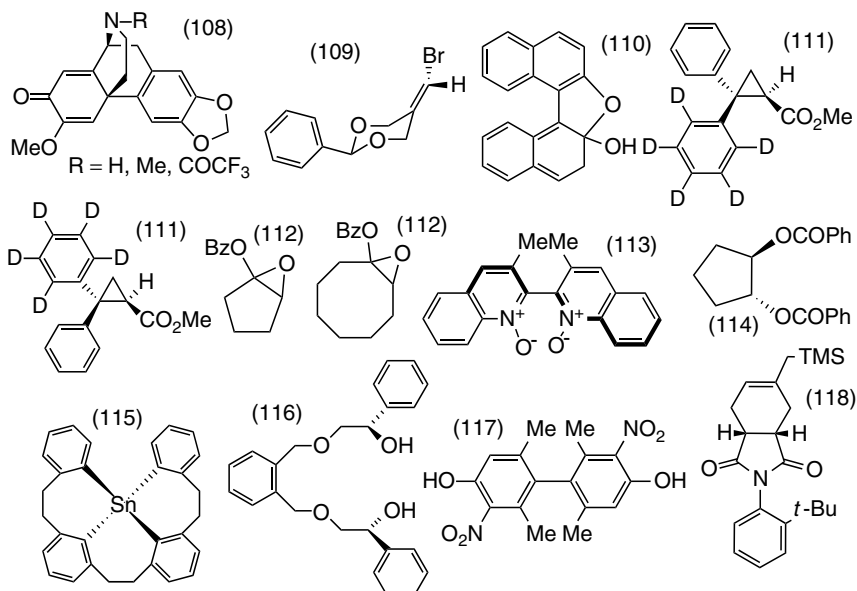


Figure 3.14 Compounds resolved on cellulose tris(4-methylbenzoate) (**22b**).

resolved on **22a**.^{96,119–123} These CSPs have been prepared by coating the benzoates dissolved in a solvent such as methylene dichloride on silica gel. The chiral recognition of **22a** was significantly influenced by the solvents in which **22a** was dissolved for coating.^{96,107,124} The higher order structure of **22a** coated on silica gel must depend on the coating solvents. Tribenzoates of amylose showed much lower chiral recognition ability than the cellulose tribenzoates.¹⁰⁷

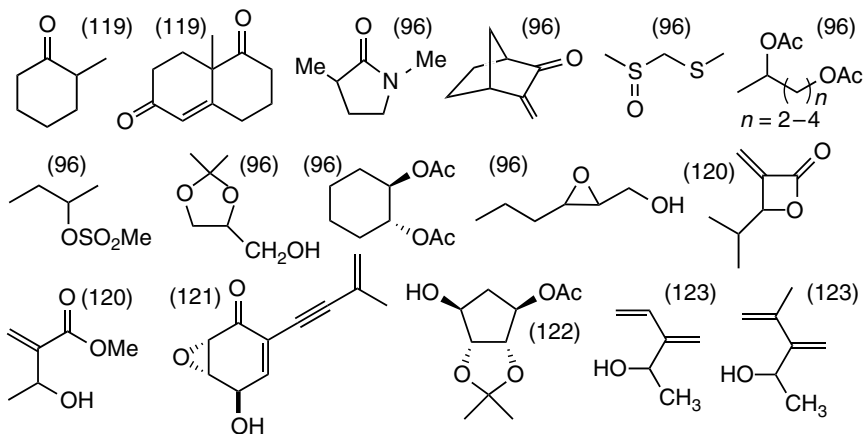


Figure 3.15 Nonaromatic compounds resolved on cellulose tribenzoate (**22a**).

Rimböck et al.¹²⁵ prepared microcrystalline cellulose tribenzoate powders and Francotte et al.^{126–128} prepared spherical beads of cellulose tribenzoate derivatives; they found that these derivatives are useful CSPs with a high loading capacity.

6.2.2 Cellulose and Amylose Phenylcarbamates

Cellulose is easily converted to various trisphenylcarbamate derivatives (**23**) by the reaction with corresponding phenyl isocyanates (Figure 3.16). These derivatives can be used as CSPs by coating on silica gel. Until now, many cellulose phenylcarbamate derivatives have been prepared to study the effect of the substituents on chiral recognition,^{129,130} and some derivatives have been on the market as practical CSPs. These phenylcarbamate derivatives can separate a wide range of racemates with various functional groups. Their chiral recognition abilities are greatly influenced by the substituents on the phenyl group. Generally, the introduction of an electron-donating methyl group or an electron-withdrawing halogen at the 3- and/or 4- position of a phenyl ring improves the chiral recognition ability for many racemates, but 2-substituted phenylcarbamate derivatives, such as **23o**, **23u**, and **23ac**, show low chiral recognition. The derivatives having a polar substituent, such as methoxy and nitro groups, also show poor chiral recognition abilities.¹³⁰ The phenylcarbamate derivatives having both an electron-donating methyl group and an electron-withdrawing chloro or fluoro group on the phenyl moieties, especially **23aj**, **23am**, and **23aq**, also exhibit high chiral recognition abilities for many racemates.^{131–134}

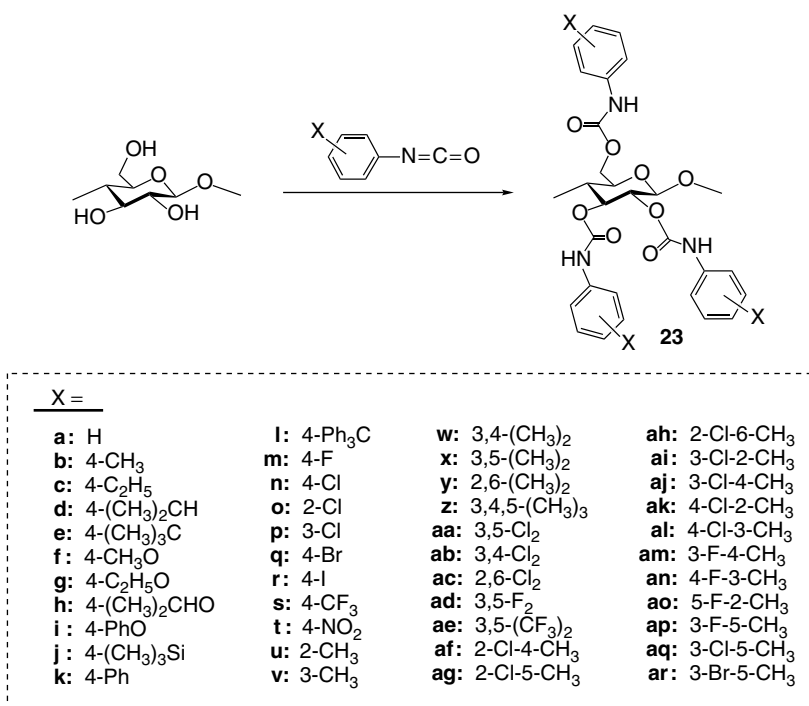


Figure 3.16 Structures of cellulose trisphenylcarbamates (**23**).

Amylose has also been converted to phenylcarbamate derivatives (**24**) (Figure 3.17). Similar to the cellulose derivatives, the chiral recognition abilities of amylose phenylcarbamate derivatives are improved by introducing methyl or chloro groups on the phenyl moieties.¹³⁵ However, contrary to the cellulose derivatives, 2-substituted amylose phenylcarbamates such as **24t** showed high chiral recognition ability.¹³² In addition, the 4-methoxyphenylcarbamate derivative of amylose (**24e**) exhibited relatively high chiral recognition.¹³⁶ These results may be ascribed to their different higher order structures. Zugenmaier et al. proposed left-handed 3/2^{137,138} and 4/3¹³⁹ helical chain conformations for tris(phenylcarbamate)s of cellulose and amylose, respectively. This structural difference seems to be responsible for the different influence of the substituents on the chiral recognition ability.

Among the many tris(phenylcarbamate) derivatives of cellulose and amylose prepared so far, 3,5-dimethylphenylcarbamate derivatives, **23x** and **24n**, respectively, exhibit excellent chiral recognition ability for a wide range of racemates, including many stereochemically interesting organic compounds and drugs. Examples resolved on **23x** and **24n** are shown in Figures 3.18^{140–151}

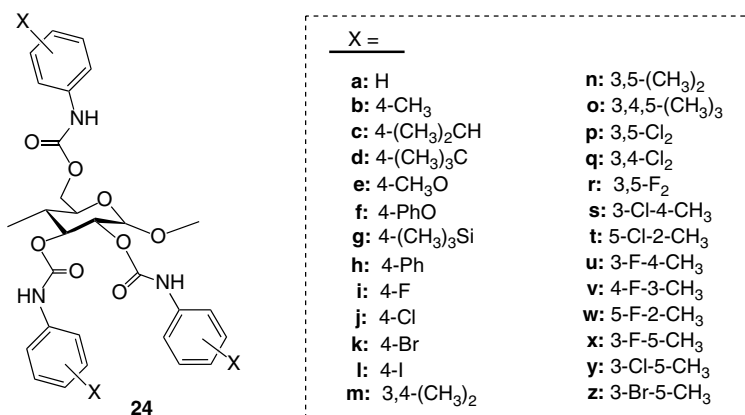


Figure 3.17 Structures of amylose trisphenylcarbamates (**24**).

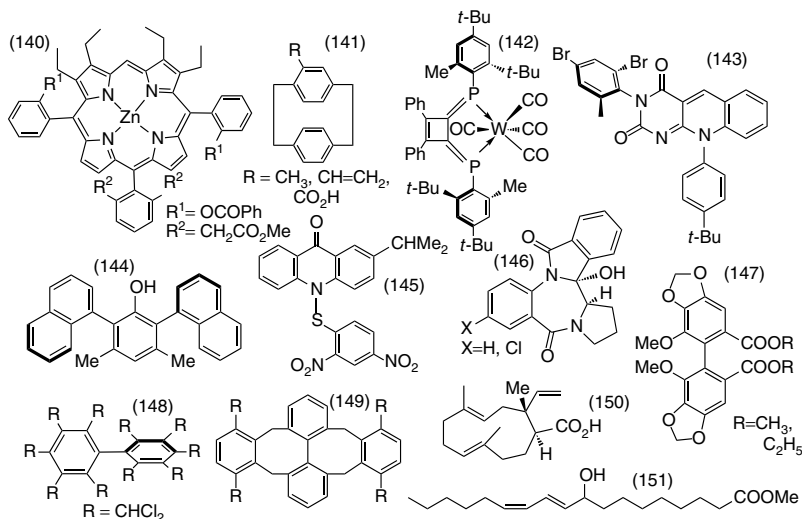


Figure 3.18 Compounds resolved on cellulose tris(3,5-dimethylphenylcarbamate) (**23x**).

and 3.19,^{152–162} respectively. Cellulose tris(3,5-dichlorophenylcarbamate) (**23aa**) also shows a unique chiral recognition ability and resolves, for instance, methacrylates and acrylates having a bulky ester group¹³⁰ and the stereoisomers of oligo(methyl methacrylates) (Figure 3.20).^{163,164} This oligomer separation made it possible to explain the mechanism of helix-sense-selective polymerization of triphenylmethyl methacrylate leading to an optically active, one-handed helical polymer. Recently, **23aa** was found

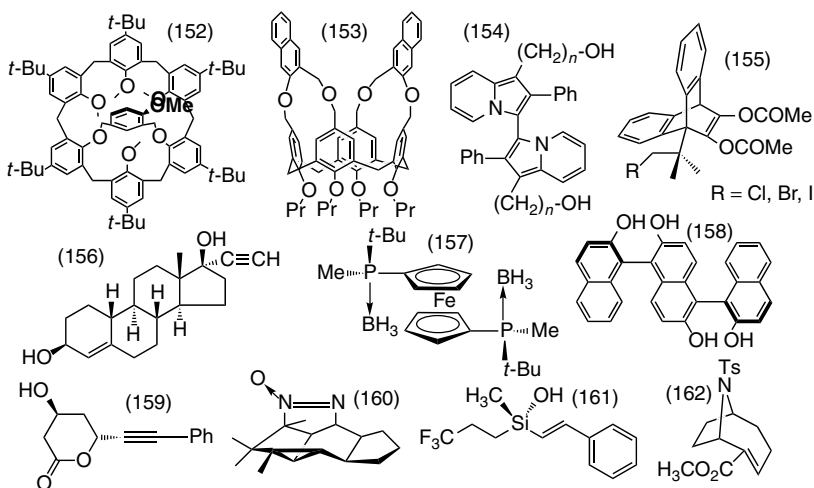


Figure 3.19 Compounds resolved on amylose tris(3,5-dimethylphenylcarbamate) (**24n**).

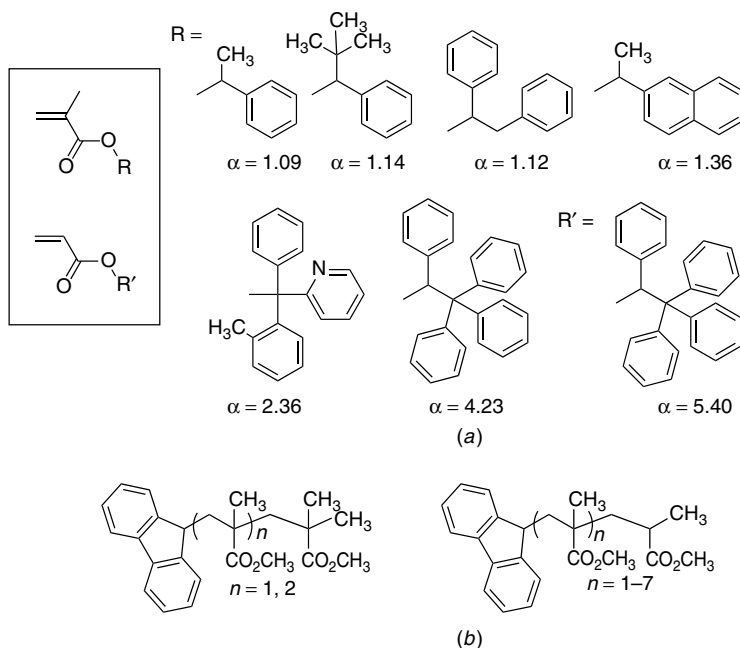


Figure 3.20 Structures of (a) methacrylates and an acrylate having a bulky ester group and (b) stereoisomers of oligo(methyl methacrylate)s well resolved on **23aa**. Eluent: (a) hexane–2-propanol (98/2), (b) hexane–2-propanol (95/5).

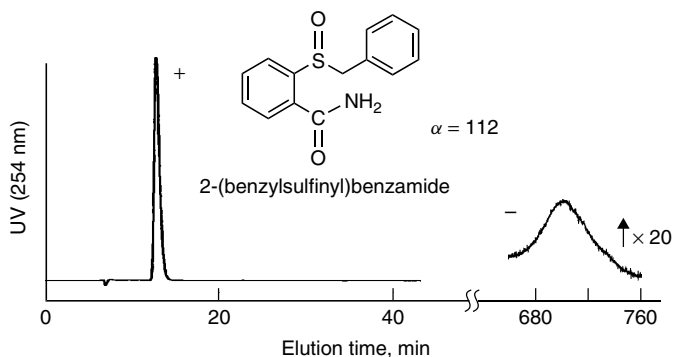


Figure 3.21 Enantioseparation of 2-(benzylsulfinyl)benzamide on **23aa** using 2-propanol as an eluent. Column: 25 × 0.46 (i.d.) cm; flow rate: 0.5 ml/min. (Reprinted with permission from Ref. 165. Copyright 2000 by the Chemical Society of Japan.)

to show high chiral recognition by using alcohol as an eluent.^{165–167} For example, a very high enantioseparation factor exceeding 110 was obtained in the enantioseparation of 2-(benzylsulfinyl)benzamide on **23aa** with 2-propanol as an eluent (Figure 3.21).¹⁶⁵ This α value may be the highest among the enantioseparations on polysaccharide derivatives by HPLC. Although **23aa** is insoluble in polar solvents such as alcohols, acetonitrile, and water, it is soluble in hexane containing 10–20% 2-propanol. This higher solubility of **23aa** limits its application as a CSP. This defect is overcome by chemically bonding **23aa** to silica gel.¹⁶⁸ This high solubility is in marked contrast to that of **23x**, which is totally insoluble in any component mixtures of hexane and 2-propanol or ethanol.

Eluents often significantly influence the resolution of a racemate, and therefore, the selection of a suitable eluent for a target racemic compound is important.¹⁶⁹ A mixture of hexane and 2-propanol or ethanol is usually the most useful eluent for the separation. The alternation of an alcohol from 2-propanol to polar ethanol leads to a shorter retention and sometimes better separation. For the separation of an acidic analyte, addition of a small amount of a strong acid such as trifluoroacetic acid often improves the separation,¹⁷⁰ probably because the strong acid can be preferentially adsorbed on the non-stereospecific basic sites existing on silica gel. When an analyte is basic, the addition of a small amount of an amine such as diethylamine is recommended for efficient resolution.¹⁷¹ Aqueous eluents are also useful for investigating the pharmacokinetics and pharmacodynamics of chiral drugs in living systems.^{19,172,173} Polysaccharide-based CSPs can also be used for supercritical-fluid chromatography (SFC) using carbon dioxide and alcohols as a mobile phase.^{174–177}

However, other solvents such as tetrahydrofuran (THF), chloroform, and ethyl acetate, in which polysaccharide derivatives are dissolved or swollen, cannot be used as the main component of an eluent because the CSPs coated on silica gel are damaged. To overcome this defect, several chemically bonded-type CSPs have been prepared. Polysaccharide derivatives were randomly and regioselectively chemically bonded to 3-aminopropylsilanized silica gel at the 2-, 3-, and 6-positions of glucose units using diisocyanates (Figure 3.22a).^{168,178} These chemically bonded-type CSPs can be used with most eluents which cannot be used for the coated CSPs. However, these CSPs show slightly lower chiral recognition than the corresponding coated-type

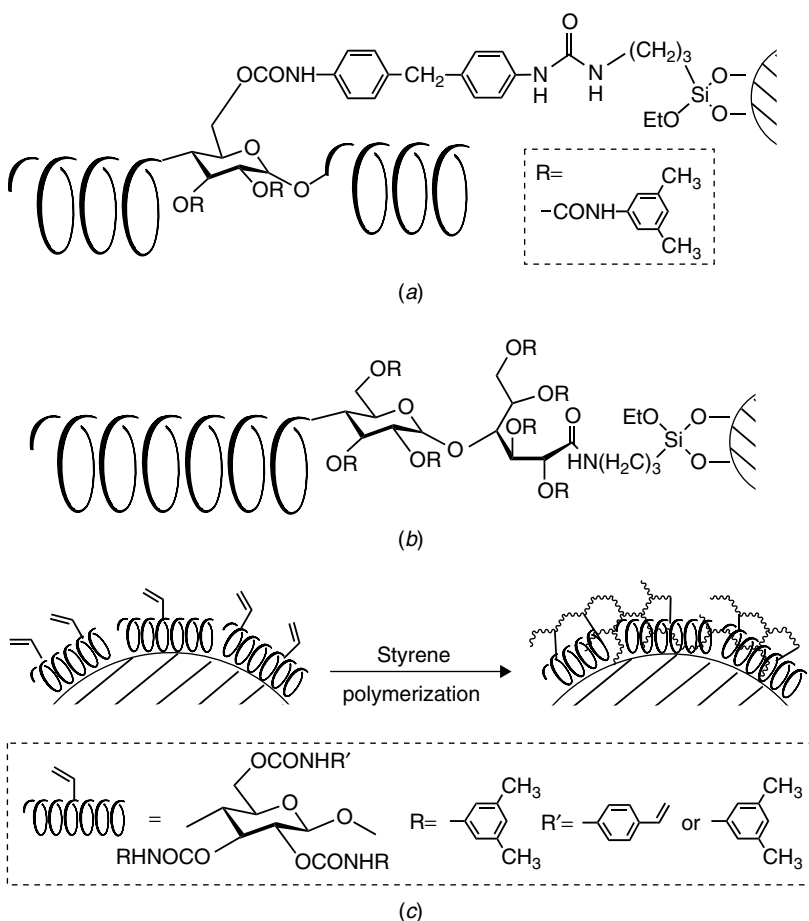


Figure 3.22 Polysaccharide derivative immobilized CSPs.

CSPs. This deterioration of chiral recognition ability may be caused by the alteration of regular higher order structures of the polysaccharides. The structure regularity may be reduced. An ideal chemically bonded-type CSP has been prepared by immobilizing a polysaccharide derivative at a chain end to silica gel. As shown in Figure 3.22*b*, **24n** was chemically bonded to silica gel only at the reducing terminal residue of amylose by the enzymatic polymerization of α -D-glucose 1-phosphate dipotassium salt using a phosphorylase.¹⁷⁹ This bonded-type CSP of **24n** showed an excellent resolving ability similar to that of the coated-type CSP and can be used with many organic solvents including THF and chloroform. Other immobilization methods such as the photochemical crosslinking of **23x**¹⁸⁰ and the polymerization of 3,5-dimethylphenylcarbamates of cellulose, amylose, and chitosan having a 10-undecenoylcarboxylate group have been reported.^{181–183} Recently, cellulose phenylcarbamate derivatives having a styryl or methacryloyl group at a part of the 6-position were synthesized and immobilized onto silica gel via radical polymerization with styrene (Figure 3.22*c*). The chiral recognition ability of this immobilized CSP was similar to that of the coated-type CSP of **23x**.¹⁸⁴

Some racemates (Figure 3.23) are more efficiently resolved on the bonded-type CSP than the coated-type CSP by using chloroform as a component of the eluent. On the bonded-type CSP of **24n**, topologically interesting catenanes and molecular knots are successfully resolved using a hexane–chloroform–2-propanol mixture.¹⁸⁵ The first direct HPLC resolution of the smallest chiral

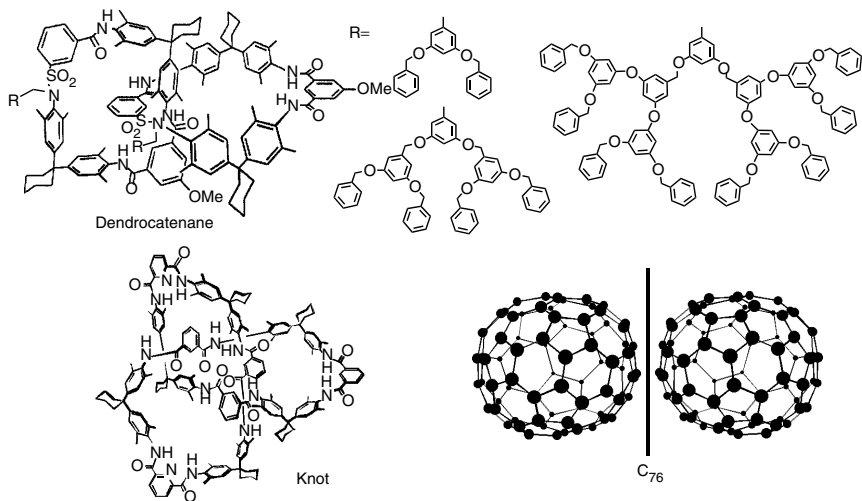


Figure 3.23 Structures of dendrocatenanes, molecular knot, and C₇₆ resolved on chemically bonded-type CSP of **24n**.

fullerene C_{76} was also achieved on this CSP using a hexane–chloroform mixture (80 : 20) as the eluent.¹⁸⁶ In this case, to obtain high enantiomeric purity recycling was necessary because of the low degree of resolution.

The enantiomers of many compounds are eluted in reverse order on the 3,5-dimethylphenylcarbamates of cellulose (**23x**) and amylose (**24n**), suggesting that these two CSPs may be complementary in recognizing chirality. Many enantiomers unresolved on **23x** can be resolved on **24n**, and vice versa. Consequently, when two **23x** and **24n** columns were used for the resolution of 500 racemates, nearly 80% of the racemates were separated into enantiomers at least on either of **23x** and **24n**.

6.2.3 Cellulose and Amylose Arylalkylcarbamates

Several tris(arylalkylcarbamate)s of cellulose and amylose (Figure 3.24) exhibit characteristic resolving abilities different from those of the phenylcarbamates. Among the five arylalkylcarbamates in Figure 3.24, only 1-phenylethylcarbamates (**25b**, **26b**) and 1-phenylpropylcarbamates (**25c**, **26c**) show high chiral recognition abilities.^{187,188} Other less bulky and more bulky arylalkylcarbamates exhibit very low recognition abilities. In the CD spectra of the films of these arylalkylcarbamates, intense peaks are observed only for **25b**, **25c**, **26b**, and **26c**, while other arylalkylcarbamates show much weaker peaks (Figure 3.25).¹⁸⁸ These results suggest that **25b**, **25c**, **26b**, and **26c** probably possess more regular higher order structures than the other derivatives and that too-small groups such as benzyl and too-bulky groups such as 2-methyl-1-phenylpropyl and 1,1-diphenylmethyl seem to disturb the higher order structure of the carbamate derivatives.

The chiral recognition abilities of the 1-phenylethylcarbamate derivatives depend greatly on the chirality of the 1-phenylethyl group. For the cellulose derivatives, (*R*)- and (*RS*)-**25b** show higher resolving abilities than (*S*)-**25b**. On the other hand, amylose 1-phenylethylcarbamates **26b** generally show higher

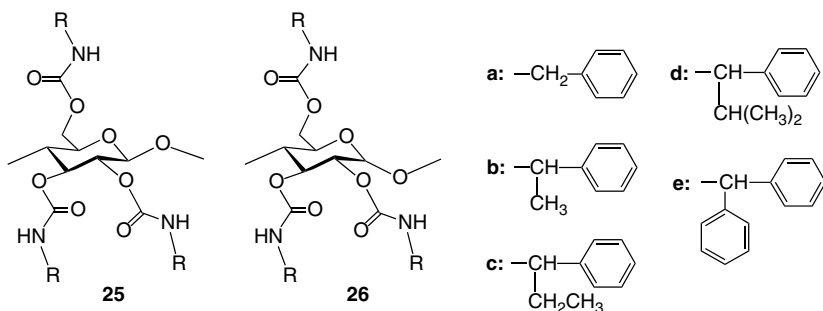


Figure 3.24 Structures of arylalkylcarbamates of cellulose (**25**) and amylose (**26**).

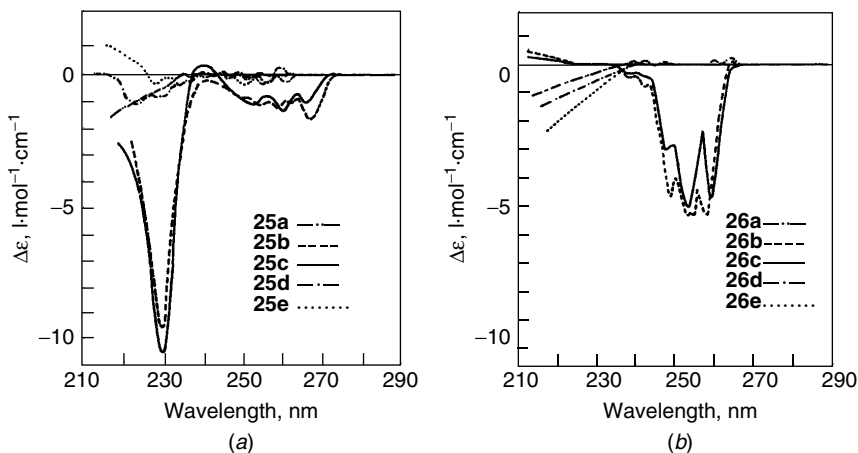


Figure 3.25 CD spectra of (a) arylalkylcarbamates of cellulose (**25**) and (b) amylose (**26**) cast from THF solution. (Reprinted with permission from Ref. 188. Copyright 1993 by Elsevier Science.)

chiral recognition abilities than the cellulose derivatives, and (*S*)-**26b** and (*RS*)-**26b** exhibit higher abilities than (*R*)-**26b**, in contrast to the cellulose derivatives. The elution order of enantiomers is sometimes affected by the chirality of the side chain, and a reversed elution order occurs between (*R*)-**25b** and (*S*)-**25b** and also between (*R*)-**26b** and (*S*)-**26b**. These results suggest that not only the chirality of the glucose unit but also the chirality of the 1-phenylethyl group plays an important role in the chiral recognition. (*S*)-**26b** shows high chiral recognition, especially for β -lactams¹⁸⁹ and 3-hydroxy-2-cyclopentanone¹⁹⁰ derivatives. Racemates resolved well on (*S*)-**26b** are shown in Figure 3.26.

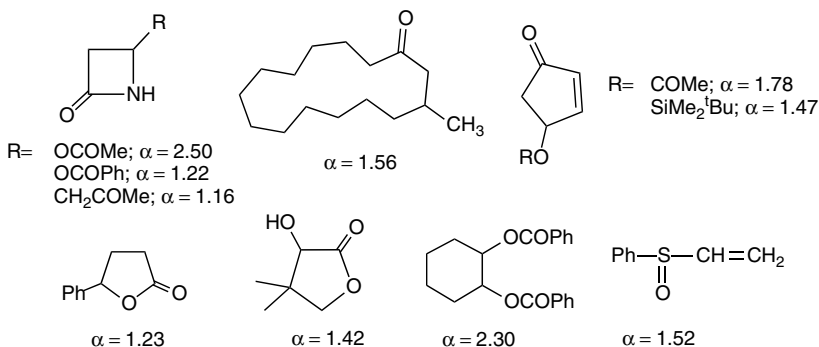


Figure 3.26 Compounds resolved on amylose tris(*S*)-1-phenylcarbamate [(*S*)-**26b**].

6.2.4 Cellulose and Amylose Cycloalkylcarbamates

Alkylcarbamates, such as methyl- and isopropylcarbamates, show very low chiral recognition as CSPs. These derivatives do not form a lyotropic liquid crystalline phase¹³⁰ and probably do not have a regular higher order structure, which may be important for these derivatives to show high chiral recognition. However, cycloalkylcarbamate derivatives such as cyclohexyl- and norbornylcarbamates (**27**, **28**, Figure 3.27) of cellulose and amylose were found to exhibit high chiral recognition for a wide range of racemates.¹⁹¹ Their chiral recognition abilities are comparable to those of 3,5-dimethylphenylcarbamate derivatives **23x** and **24n**. These cycloalkylcarbamates of cellulose exhibit high crystallinity when cast from solution. Most of the cellulose tris(phenylcarbamate) derivatives form a similar lyotropic liquid crystalline phase in a highly concentrated solution and also show high crystallinity under a polarizing microscope when they are cast from solution.^{130,192} This means that the carbamates coated on the silica surface from solution also have an ordered structure in which carbamates are regularly arranged. Such an ordered structure seems to be very important for efficient recognition of chirality by CSPs derived from polymers.

The cycloalkylcarbamates do not absorb UV light above 220 nm and therefore can be used as the CSPs for thin-layer chromatography (TLC).¹⁹¹ The TLC chromatogram was readily detected by UV radiation at 254 nm and showed the resolution of racemates into each enantiomer. The TLC results can be compared with those obtained by HPLC with the same CSP. The α values in HPLC are slightly larger than those in TLC, although a good correlation is observed between these α values. The cycloalkylcarbamates can be very useful CSPs for TLC as well as for HPLC resolution.

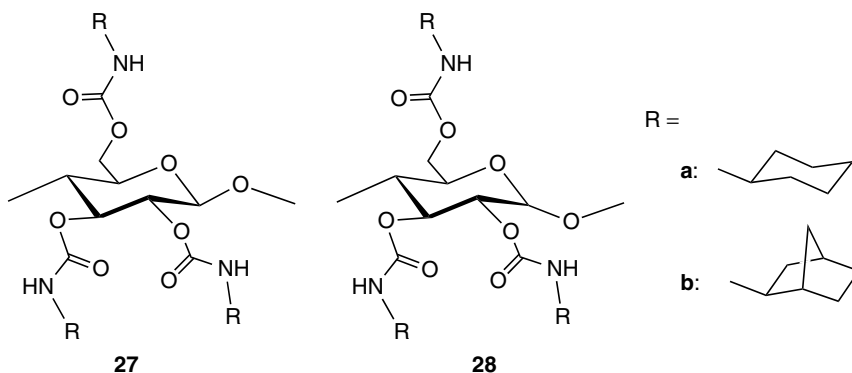


Figure 3.27 Structures of cycloalkylcarbamates of cellulose (**27**) and amylose (**28**).

6.2.5 Oligosaccharides and Cyclodextrins

3,5-Dimethylphenylcarbamates of linear oligomers of D-glucose, cellooligosaccharides (**29**) and maltooligosaccharides (**30**), and cyclic oligomers, α -, β -, and γ -cyclodextrins (**31**, $n = 6-8$), were prepared (Figure 3.28) and their chiral recognition abilities as CSPs were evaluated to investigate the influence of the degree of polymerization and higher order structure of the polysaccharide derivatives on chiral recognition.¹⁹³ The chiral recognition abilities of cellooligosaccharide ($n = 2, 4$) derivatives were much lower than that of the corresponding cellulose derivative (**23x**), and the dimer ($n = 2$) showed almost no recognition, indicating that the chiral recognition of the cellulose derivative is not due to a few glucose residues. Among the maltooligosaccharide derivatives ($n = 2-7$), the dimer and trimer also showed almost no recognition, but higher oligomers, 5- to 7-mer, exhibited similar chiral recognition abilities to each other, and their recognition abilities were not significantly different from that of the corresponding amylose derivative (**24n**). These results indicate that cellooligosaccharide derivatives may have different structures from that of cellulose derivative **23x**, whereas the maltooligosaccharides with $n \geq 5$ may have a similar ordered structure to that of amylose derivative **24n**. This assumption was supported through conformational studies of the oligomers by CD spectroscopy. The intensities of the CD spectra of the cellooligosaccharide derivatives are quite different from that of **23x** (Figure 3.29a), while the CD patterns of the maltooligosaccharides, except for the dimer, are similar to that of **24n** (Figure 3.29b).¹⁹³ Consequently, the high chiral recognition abilities of cellulose and amylose must be due to a higher order structure, probably helical structures. Such an ordered structure seems to start at a rather low degree of

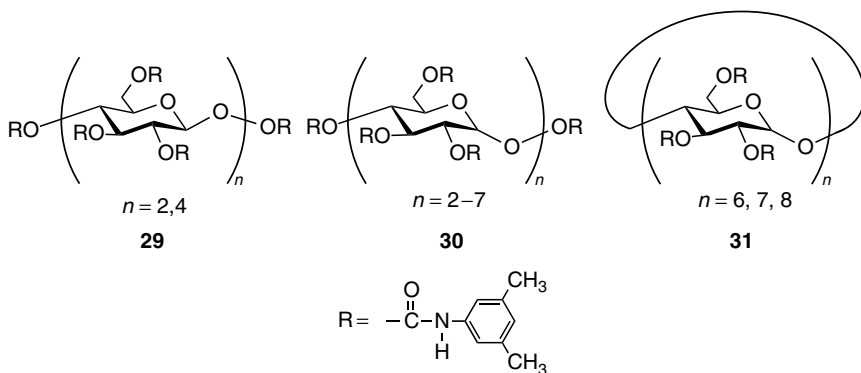


Figure 3.28 Structures of 3,5-dimethylphenylcarbamates of cellooligosaccharides (**29**), maltooligosaccharides (**30**), and cyclodextrins (**31**).

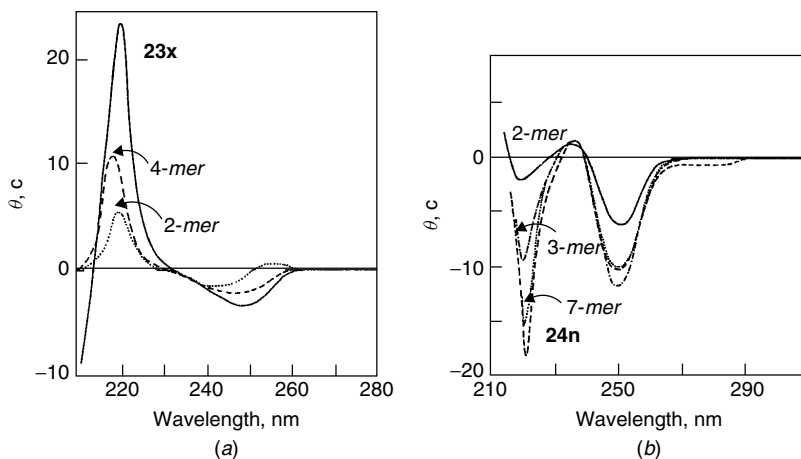


Figure 3.29 CD spectra of (a) 3,5-dimethylphenylcarbamates of celooligosaccharides (**29**) and **23x** and (b) maltooligosaccharides (**30**) and **24n** in THF. Concentration ≈ 1 mg/ml. (Reprinted with permission from Ref. 193. Copyright 1990 by the Chemical Society of Japan.)

polymerization for the amylose derivatives but may be at higher values for the cellulose derivatives.

On the other hand, 3,5-dimethylphenylcarbamates of cyclodextrins showed quite different chiral recognition abilities from those of **24n** and the maltooligosaccharide derivatives.¹⁹³ The cyclodextrin derivatives must have conformations different from those of the maltooligosaccharide derivatives. Actually the CD spectra of the cyclodextrin derivatives are different from that of **24n** (Figure 3.30). The CD patterns of three cyclodextrin derivatives differed slightly from each other in the aromatic region, suggesting that the conformation of these derivatives may also be different. The possible structures of β -cyclodextrin and its 3,5-dimethylphenylcarbamate derivative **31** ($n = 6$) are shown in Figure 3.31. The chiral recognition by the cyclodextrin phenylcarbamate derivatives may mainly occur on its polar carbamate residues.

Two different CSPs consisting of β -cyclodextrin 3,5-dimethylphenylcarbamate have been prepared by immobilizing it on silica gel at different positions of the glucose unit. One is immobilized through the 6-position¹⁹⁴ and the other through the 2- and/or 3-position.¹⁹⁵ The chiral recognition abilities of the two CSPs are different, and the latter CSP shows slightly higher chiral recognition.¹⁹⁶

6.2.6 Other Phenylcarbamates of Polysaccharides

3,5-Dimethyl- and 3,5-dichlorophenylcarbamates of other polysaccharides¹⁹⁷ such as curdlan (**32**), dextran (**33**), xylan (**34**), chitosan (**35**), galactosamine

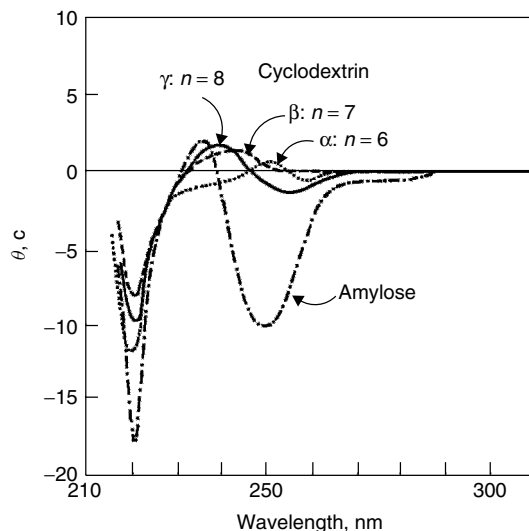


Figure 3.30 CD spectra of 3,5-dimethylphenylcarbamates of cyclodextrins (**31**) and **24n** in THF. Concentration ~ 1 mg/ml. (Reprinted with permission from Ref. 193. Copyright 1990 by the Chemical Society of Japan.)

(**36**), chitin (**37**),¹⁹⁸ and inulin (**38**) were prepared (Figure 3.32), and their chiral recognition abilities as CSPs for HPLC have been evaluated and compared with those of the corresponding phenylcarbamate derivatives of cellulose and amylose. Among these phenylcarbamate derivatives, 3,5-dimethylphenylcarbamates of xylan (**34a**), chitosan (**35a**), and chitin (**37a**) and 3,5-dichlorophenylcarbamates of galactosamine (**36b**) and chitin (**37b**) showed relatively high chiral recognition abilities. Especially, several chiral acidic drugs such as ketoprofen and ibuprofen were efficiently resolved on **37b** with high α values.¹⁹⁸ Other carbamates showed high resolution for a few specific racemates and better resolved them than the cellulose and amylose derivatives.

As might be expected, enantioselectivity and the elution order of enantiomers differ in these polysaccharides with different sugar units, linkage position, and linkage type. As already mentioned, several pairs of enantiomers are eluted in the reversed order on 3,5-dimethylphenylcarbamates of cellulose (**23x**) and amylose (**24n**). Cellulose and amylose are different only in the linkage type, α -linkage and β -linkage. Similar reversed enantioselectivities were also observed for a few racemates between **35a** β -(1 \rightarrow 4) and **36a** α -(1 \rightarrow 4) consisting of D-glucosamine units and between **35b** and **36b**.¹⁹⁷ This indicates that these pairs of CSPs are different in chiral recognition and may be complementary to each other to some extent.

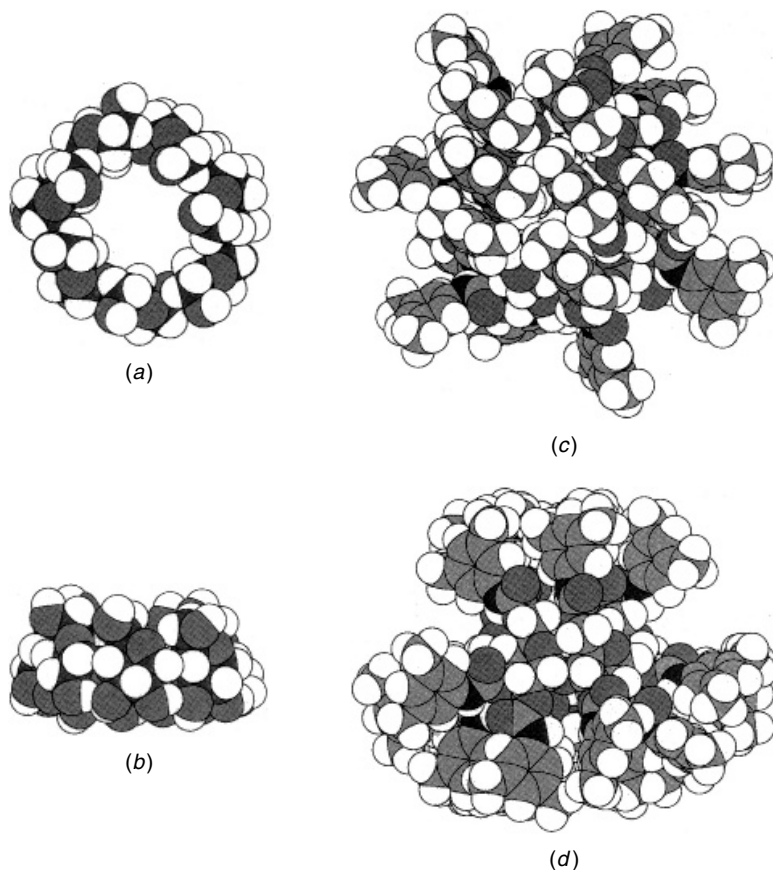


Figure 3.31 (a, c) Plan and (b, d) side views of (a, b) crystal structure of β -cyclodextrin and (c, d) possible structure of 3,5-dimethylphenylcarbamoylated β -cyclodextrin **31** ($n = 7$) optimized by MM and MD calculations.

6.3 Mechanism of Chiral Recognition on Polysaccharide Derivatives

An understanding of the recognition of chirality at a molecular level has become of interest in many fields of chemistry and biology. In the past decade, many attempts to clarify the mechanism of chiral recognition on CSPs for liquid chromatography have been made by means of chromatography, NMR spectroscopy,^{199–202} X-ray analysis, and computational methods.^{203–206} The successful studies have been mostly carried out for the small-molecule CSPs, especially cyclodextrin-based CSPs and Pirkle-type (brush-type) CSPs. In contrast, only a few mechanistic studies on chiral discrimination at the molecular

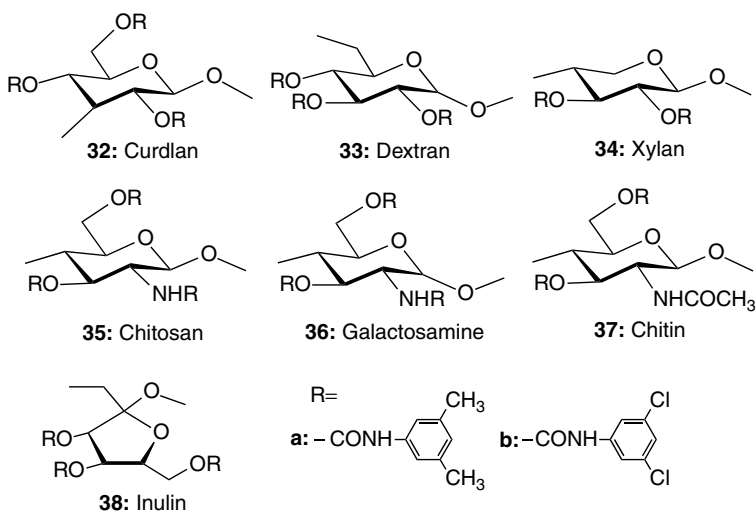


Figure 3.32 Structures of trisphenylcarbamate of polysaccharides (**32–38**).

level have been performed for polymeric CSPs, probably because the chiral polymers usually have a number of different binding sites with a different affinity to enantiomers and the determination of their exact structures in both the solid and in solution is not easy.

Although the polysaccharide-based CSPs have been commercialized and used for the resolution of a wide range of racemates, the chiral recognition mechanism has been investigated mainly through the analysis of chromatographic data and has not yet been satisfactorily elucidated at a molecular level. Recently, in order to understand chiral recognition at a molecular level, spectroscopic^{207–209} and computational approaches^{210,211} have been carried out on the polysaccharide-based CSPs.

6.3.1 Chromatographic Studies

As previously mentioned above, the chiral recognition abilities of the phenyl-carbamates of polysaccharides are greatly influenced by the substituents on the phenyl groups. In order to evaluate the effect of the substituents on the interaction between CSPs and solutes, the retention times of acetone and the first-eluted isomer of 1-(9-anthryl)-2,2,2-trifluoroethanol (**39**) on 3- and 4-substituted CSPs are plotted against the Hammett parameter σ of the substituents (Figure 3.33).¹³⁰ The retention times of acetone tend to increase as the electron-withdrawing power of the substituents increases, whereas those of the first-eluted isomer of **39** tend to decrease. These results indicate that

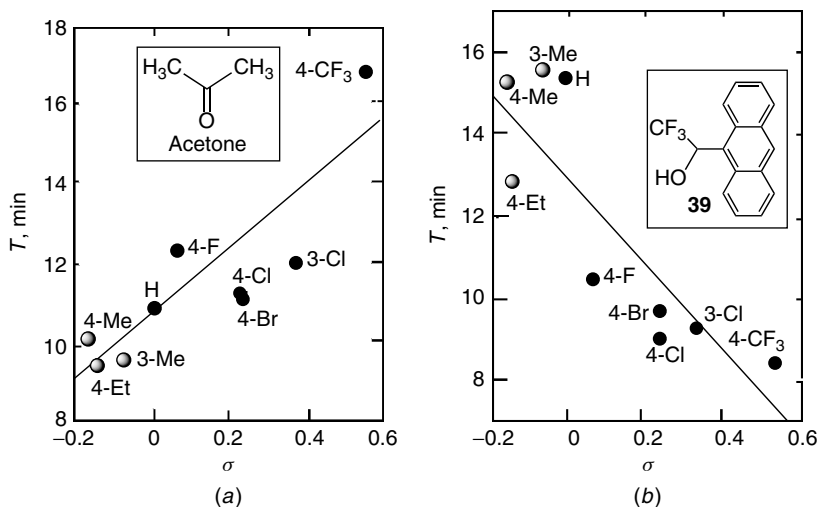


Figure 3.33 Plots of retention times t of (a) acetone and (b) first enantiomer of **39** to elute on cellulose tris(phenylcarbamate) derivatives against Hammett parameter σ of substituents. (Reprinted with permission from Ref. 130. Copyright 1986 by Elsevier Science.)

the main chiral interaction sites are probably the polar carbamate groups, which can interact with a racemate via hydrogen bonding on NH and C=O groups and the dipole–dipole interaction on C=O. Figure 3.34 shows the schematic interaction of carbamate residues and solutes. Information about the effect of the substituents can also be obtained from the ¹H NMR spectra of the phenylcarbamates of polysaccharides in solution. The NH protons of the phenylcarbamates move downfield as the electron-withdrawing power of the substituent increases. This means that the acidity of the NH proton increases with an increase of the electron-withdrawing power of the substituents. Probably, acetone is mainly adsorbed on the stationary phases via hydrogen bonding with an NH proton, and this interaction must be stronger when the proton is more acidic. On the other hand, the electron density at the carbonyl oxygen atom of the carbamates increases when the electron-donating power of the substituents is strong, and therefore the alcohol must be more strongly adsorbed on the CSPs via hydrogen bonding when the substituent is electron donating.

Figure 3.35 shows stable structures of **23a** and **23x** optimized by molecular-mechanics calculations on the basis of the X-ray crystal structure of **23a** proposed by Zugenmaier.^{137,138} These optimized structures have similar left-handed 3/2 helixes and the glucose residues are regularly arranged along the helical axis. A chiral helical groove with polar carbamate groups exists along the main chain. The polar carbamate groups are preferably located inside, and

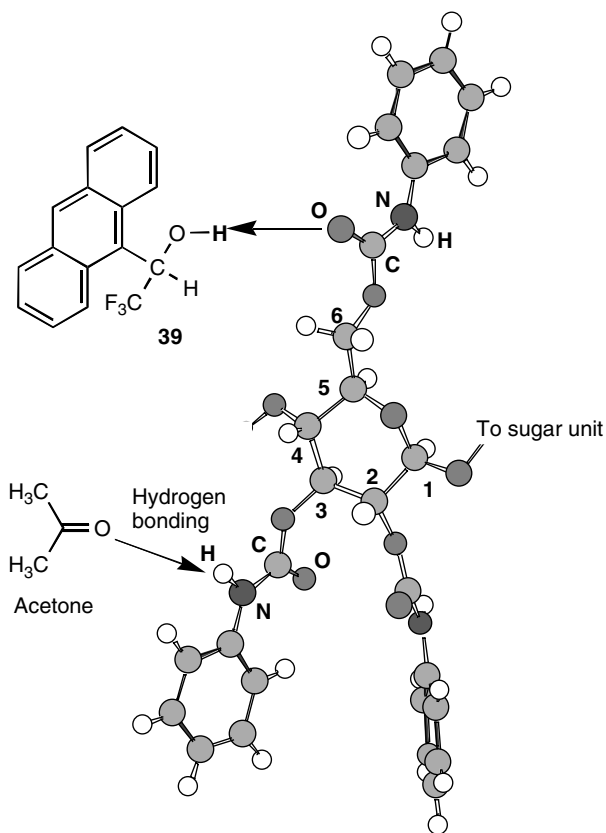


Figure 3.34 Possible interaction sites of cellulose trisphenylcarbamates.

hydrophobic aromatic groups are located outside the polymer chain, so that polar enantiomers may predominantly interact with the carbamate residues in the groove through hydrogen bond formation. When a substituent on the phenyl group itself is polar, like the methoxy or nitro group, racemates may also interact with the polar substituent, which should reduce chiral recognition ability because the substituent is too far from a chiral glucose unit that is the origin for chiral recognition. Therefore, when a substituent is a more bulky alkoxy group, such as isopropoxy or isobutoxy, the bulky substituent can prevent racemates from interacting with the ether oxygen of the alkoxy group to improve the chiral recognition ability.¹³⁶

The substituents on the phenyl group can also sterically influence the chiral recognition ability. The main-chain structures of **23a** and **23x** look similar, but the conformations of side groups are not the same. Three aromatic groups of

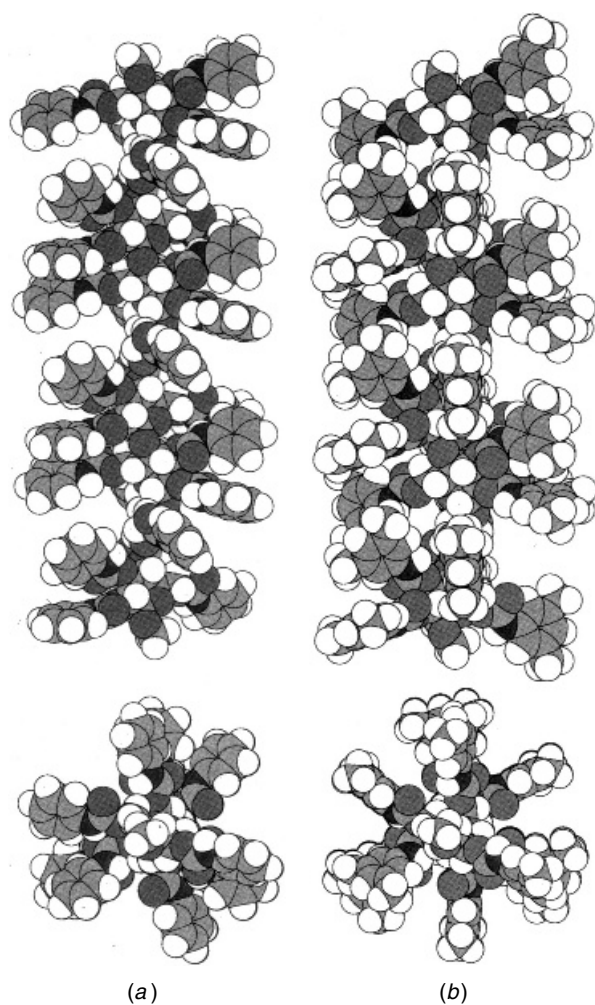


Figure 3.35 Optimized structures of (a) phenylcarbamate **23a** and (b) 3,5-dimethylphenylcarbamate **23x** derivatives of cellulose. View along helix axis (top) and perpendicular to helix axis (bottom).

23x appear to form a group affording a quite different chiral space from that of **23a**. This may be responsible for the different enantioselectivity of **23a** and **23x** toward some racemates.

The phenylcarbamates of polysaccharides also separate several nonpolar aromatic compounds,¹⁴¹ which cannot interact with the carbamate group through polar interaction. This indicates that, besides the polar interactions,

a nonpolar interaction, such as π - π interaction between the phenyl groups of phenylcarbamate derivative and an aromatic group of a solute, may play some role in chiral recognition, particularly in a reversed-phase mode HPLC separation.

6.3.2 NMR Studies

Nuclear magnetic resonance spectroscopy is one of the most powerful tools for revealing chiral recognition mechanisms. However, most phenylcarbamate derivatives of polysaccharides with a high chiral recognition ability as CSPs are soluble only in polar solvents, such as acetone, pyridine, and THF, in which chiral discrimination of enantiomers by NMR is hardly detected because the solvents preferentially interact with the polar carbamate residues. Hence, it was difficult to elucidate the mechanism for chiral discrimination of enantiomers on most phenylcarbamate derivatives by NMR spectroscopy in these solvents. However, a few phenylcarbamate derivatives, for instance, tris(4-trimethylsilylphenylcarbamate)s (**23j**, **24g**)^{207,208} and tris(5-fluoro-2-methylphenylcarbamate)s (**23ao**, **24 w**)^{133,209} of cellulose and amylose, were found to be soluble in chloroform and showed chiral recognition for many racemates as detected by ¹H and ¹³C NMR in solution as well as in HPLC. These findings made it possible to investigate interactions occurring in solution using NMR spectroscopy.

Figure 3.36 shows the ¹H NMR spectra of (\pm)-*trans*-stilbene oxide (**40**) in the absence (Figure 3.36a) and presence (Figure 3.36b) of **23j**. The signal for the methine proton of **40**, which appears as a singlet at δ 3.871, was enantiomerically separated into two singlet peaks in the presence of **23j**, and only the (–)-isomer is shifted downfield. This clearly indicates that **23j** can recognize the enantiomer even in solution. In the chromatographic enantioseparation of (\pm)-**40** on CSP **23j**, the (+)-isomer eluted first followed by (–)-isomer, and complete baseline separation was achieved ($\alpha = 1.55$). This elution order is associated with the downfield shift of the (–)-isomer observed in ¹H NMR.^{207,208} The chemical shift difference $\Delta\Delta\delta$ of the methine proton of **40** increased with an increase in the amount of **23j**, and 40 mg of **23j** was found to be enough for almost baseline separation of (\pm)-**40** at 22°C (Figure 3.36c).²⁰⁸ As mentioned above, the most important adsorbing site for chiral discrimination on the phenylcarbamate derivatives is the polar carbamate residue. For **40**, the oxygen atom of the oxirane ring may interact with the NH proton of the carbamate residue via hydrogen bonding. Therefore, addition of a compound capable of hydrogen bonding with the NH proton prevented the interaction between **23j** and **40**, and the splitting of the methine proton signal of **40** disappeared (Figure 3.36d). A similar change was also induced by the addition of 2-propanol in place of acetone. Interestingly, the signals for the

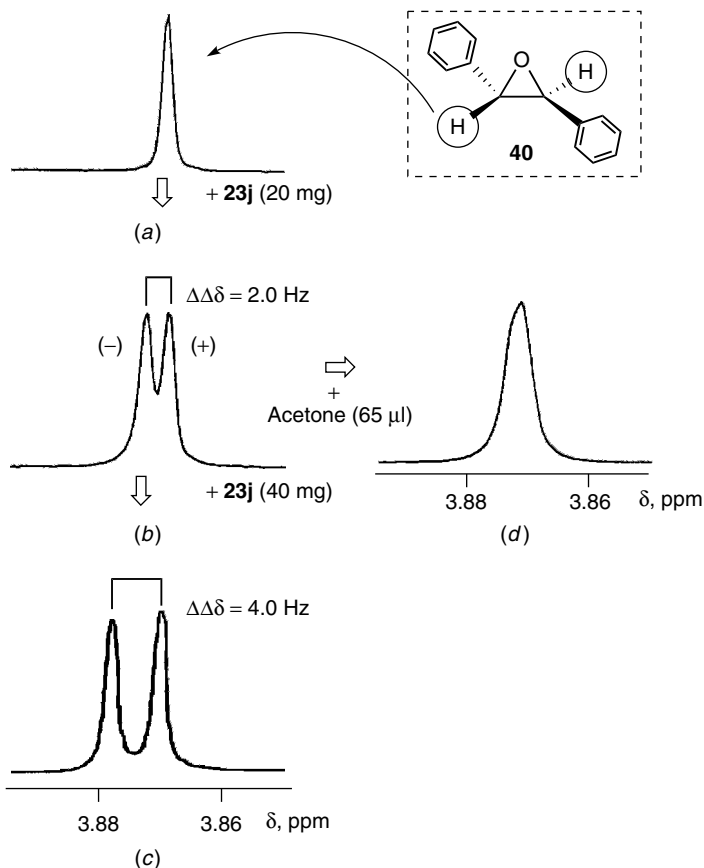


Figure 3.36 Proton NMR spectra of **40** in CDCl_3 (1.0 ml) at 22°C . **23j**: (a) 0, (b, d) 20, and (c) 40 mg; acetone: (a, b, c) 0 and (d) 65 μl .

methyl groups of 2-propanol were shifted upfield from the original signal and split into a pair of doublets in the presence of **23j** (Figure 3.37), indicating that two methyl groups are not magnetically equivalent in the presence of **23j**. The chirality of **23j** seems to force 2-propanol to bind in a diastereotopic environment, allowing the recognition of enantiotopic methyl groups.²⁰⁸

The phenylcarbamate derivative **23j** also showed chiral recognition for many racemates in CDCl_3 (Figure 3.38). Figure 3.39 shows the ^1H NMR spectra of (\pm)-2-butanol in the absence and presence of **23j**. In the case of secondary alcohols, such as 2-butanol, 2-heptanol, and 2-octanol, the methyl protons at the end of the longer chain and remote from the stereogenic center were enantiomerically separated in the presence of **23j**, and the methine and

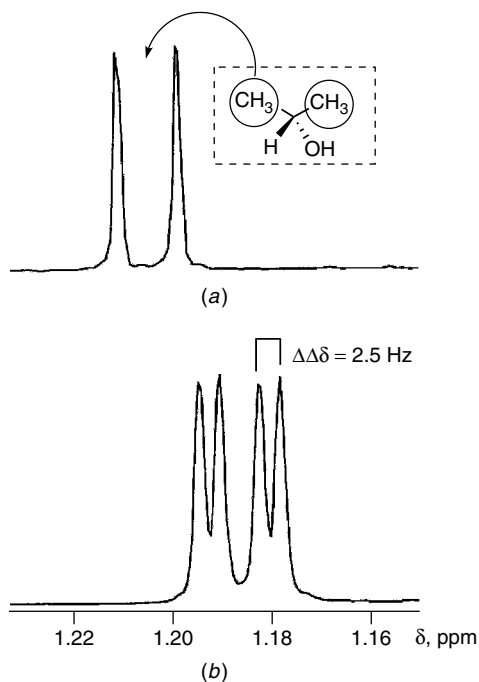


Figure 3.37 Proton NMR spectra of 2-propanol (3 μ l) in CDCl_3 (1.0 ml) with **40** (5 mg) in (a) absence and (b) presence of **23j** (20 mg).

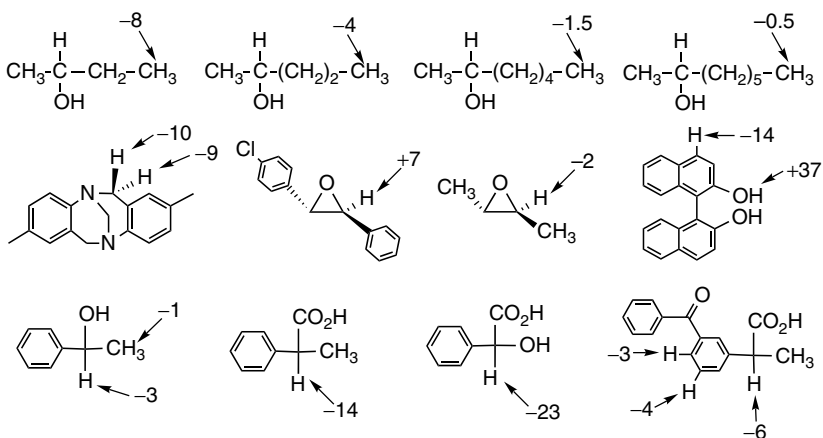


Figure 3.38 Compounds enantiomerically recognized by **23j** in ^1H NMR. Protons marked with arrow indicate recognized ones and figures represent $\Delta\Delta\delta$ (ppb). Negative value indicates upfield shift.

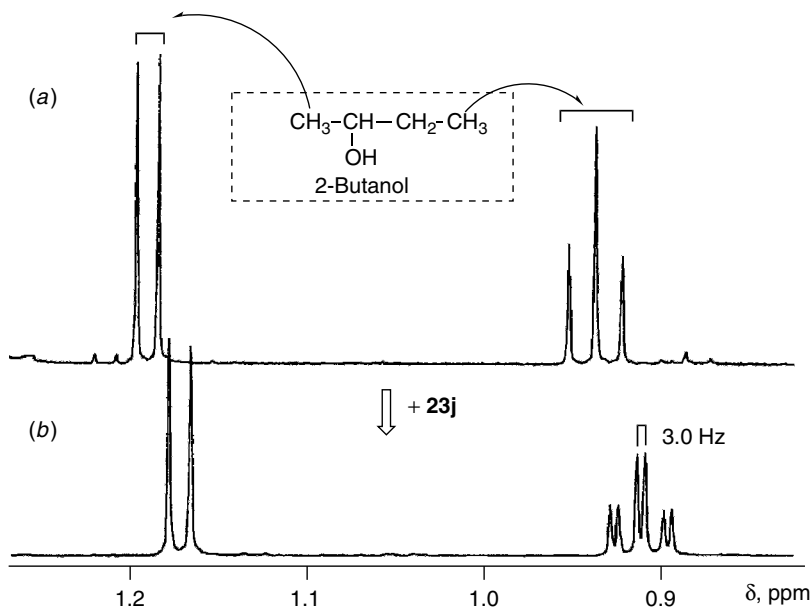


Figure 3.39 The 500-MHz ^1H NMR spectra of (\pm)-2-butanol (3 ml) in (a) absence and (b) presence of **23j** (20 mg) in CDCl_3 (1.0 ml) at 22°C .

its adjacent methyl protons were not recognized, suggesting that the methyl protons of the alkyl chains may be specifically located near chiral **23j**.²⁰⁸

Cellulose tris(5-fluoro-2-methylphenylcarbamate) (**23ao**) could discriminate the enantiomers of 1,1'-bi-2-naphthol (**41a**) with a large separation factor ($\alpha = 4.23$) in HPLC.²⁰⁹ Figure 3.40 shows a chromatogram for the resolution of **41a** on **23ao**; a complete baseline separation was achieved and the (*R*)-isomer was eluted first followed by the (*S*)-isomer. Hydrogen-bonding interaction through the hydroxy groups of **41a** is considered to be the main force for its retention and separation, because mono- (**41b**) and di-*O*-methylated (**41c**) derivatives were hardly resolved on **23ao**. Analogue **42** was also completely resolved with a large α value (3.22), and the same (*S*)-isomer was more retained as observed for **41a**.

In addition, **23ao** discriminated between the enantiomers of **41a** and **42** in ^1H and ^{13}C NMR spectroscopies.²⁰⁹ Figure 3.41 shows the 500-MHz ^1H NMR spectra of (*RS*)-**41a** in the absence and presence of **23ao** in CDCl_3 . Each of the hydroxy and naphthyl protons (H4 and H6) of **41a** were significantly separated into two peaks for the enantiomers in the presence of **23ao**. The signal for the OH protons of (*S*)-**41a** was more largely shifted downfield with accompanying line broadening than the corresponding (*R*)-**41a**-OH; the signals

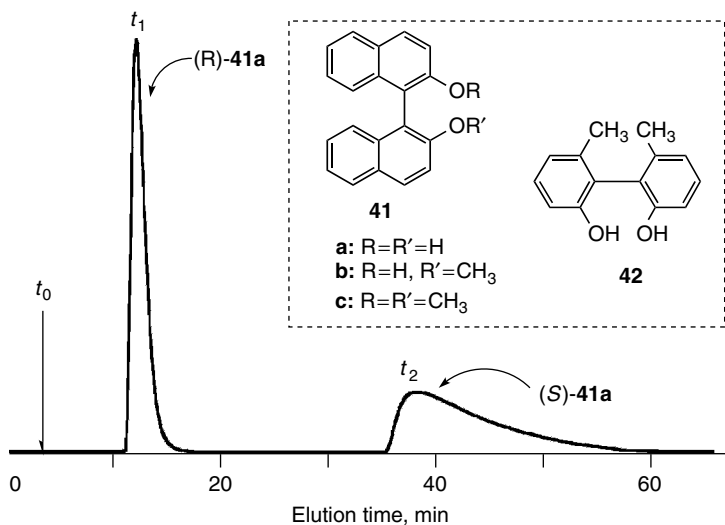


Figure 3.40 Chromatogram of enantioseparation of **41a** on **23ao** with hexane–2-propanol (90/10) as eluent. (Reprinted with permission from Ref. 209. Copyright 1996 by the American Chemical Society.)

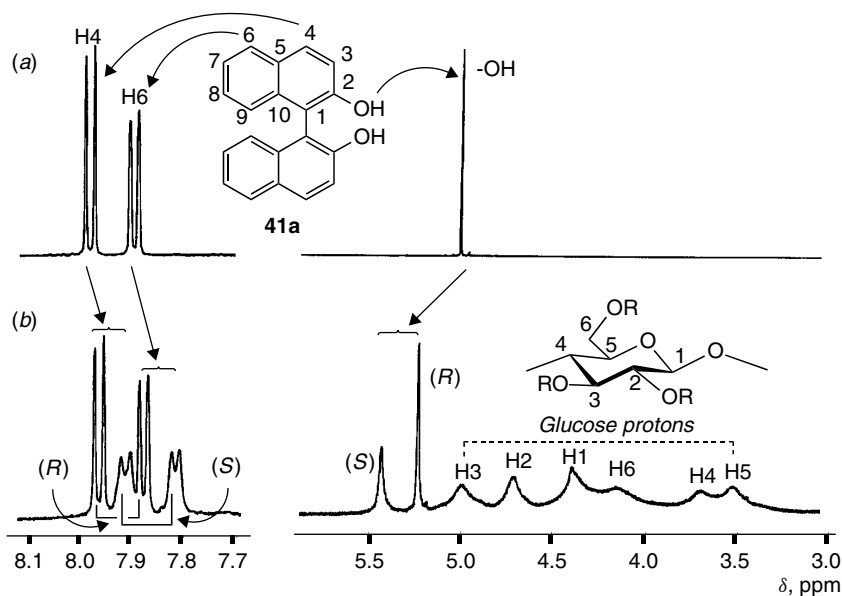


Figure 3.41 Proton NMR spectra of selected region of (*RS*)-**41a** in (a) absence and (b) presence of **23ao** in CDCl₃ at 23°C. (Reprinted with permission from Ref. 209. Copyright 1996 by the American Chemical Society.)

for the H4 and H6 protons of (*S*)-**41a** exhibited upfield shift and broadening, indicating that (*S*)-**41a** interacts more strongly with **23ao**. The downfield shift of the OH resonances is ascribed to hydrogen bonding, and the upfield shifts for the aromatic protons are probably due to π -stacking or shielding effect by a neighboring aromatic ring of **23ao**. The larger chemical shift movement and broadening of (*S*)-**41a** resonances than (*R*)-**41a** observed in ^1H NMR is associated with the chromatographic elution order of the enantiomers. Similar discrimination of enantiomers in ^1H NMR was also observed for (*RS*)-**42** in the presence of **23ao**, and the OH proton resonances of (*S*)-**42** were largely shifted downfield. These NMR results also support the importance of the hydrogen bonding through the two hydroxy groups for chiral discrimination, as seen in the HPLC separation.

Similar splittings of **41a** and **42** into enantiomers in the presence of **23ao** were observed in ^{13}C NMR spectroscopy (Figure 3.42).²⁰⁹ Interestingly, the carbons separated into enantiomers belong to the ring A bearing hydroxy groups, indicating that the ring A may be favorably located close to the chiral glucose residue. This means that (*S*)-**41a** may insert into the chiral groove of **23ao** to form hydrogen bonding. Spin-lattice relaxation time (T_1), which is sensitive to molecular motions, was measured for the enantiomers of **41a** in the absence and presence of **23ao**.²⁰⁹ The T_1 of all carbon atoms of (*R*)- and (*S*)-**41a** becomes shorter in the presence of **23ao** than those of free **41a**, and the T_1 values for (*S*)-**41a** are always shorter than the corresponding values for (*R*)-**41a**. In particular, a remarkable reduction in T_1 is observed for the C1–C5

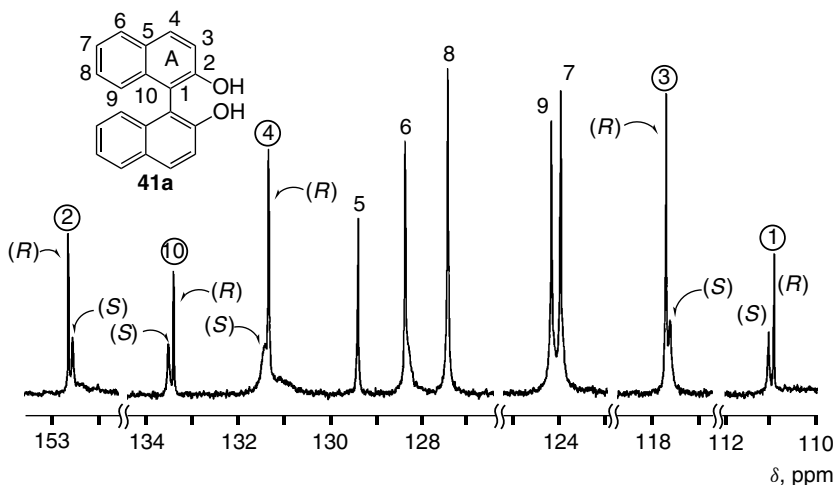


Figure 3.42 Carbon-13 NMR spectrum of (*RS*)-**41a** in presence of **23ao** in CDCl_3 at 23°C . (Reprinted with permission from Ref. 209. Copyright 1996 by the American Chemical Society.)

and C10 carbon atoms attached to ring A. This indicates that the mobility of ring A is restricted due to the binding of the OH groups to the C=O of **23ao**.

Information about the binding site of **23ao** and the stoichiometry of the complexation can be obtained by ^1H NMR titrations of **23ao** with (*S*)- and (*R*)-**41a** and the continuous variation plot (Job plot) for the **23ao**–(*S*)-**41a** complex.²⁰⁹ The H2 proton resonance of a glucose unit of **23ao** was dramatically affected by addition of (*S*)-**41a** and shifted upfield with binding, while the other glucose proton resonances only moved slightly. This significant upfield shift of the H2 proton resonance indicates that a naphthyl ring of (*S*)-**41a** may be closely located above the H2 proton. The chemical shift movement of the glucose protons induced by addition of (*R*)-**41a** was relatively small. In the Job plot, the maximal complex formation occurred at around 0.5 mol fraction of the glucose residue of **23ao**.²⁰⁹ This result indicates that each glucose unit of **23ao** may have the same binding affinity to (*S*)-**41a** due to the regular structure of **23ao** in solution. The regular structure of **23ao** must be responsible for the efficient chiral recognition capability in the NMR as well as in HPLC.

The two-dimensional(2D) NMR technique is a powerful tool for constructing the structures of biopolymers and synthetic polymers and also for elucidating the interaction occurring in a host–guest system. Especially, 2D NOESY spectroscopy is very useful to obtain interproton distances. Figure 3.43 shows the NOESY (Nuclear Overhauser Effect Spectroscopy) spectra of **23ao**–(*R*)-**41a** and **23ao**–(*S*)-**41a** (molar ratio 2 : 1) systems in the regions between the aromatic protons (**23ao** and **41a**) and the methyl protons on the phenyl group of **23ao**.²⁰⁹ For the **23ao**–(*R*)-**41a** system, many cross peaks are observed.

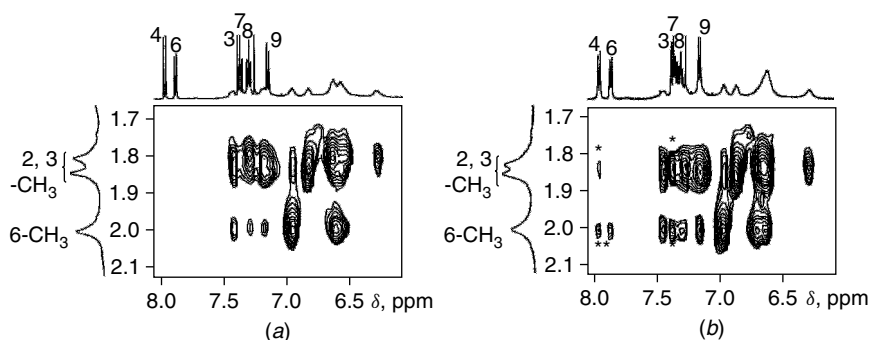


Figure 3.43 Expanded NOESY spectra (CDCl_3 , 30°C) of the mixtures of (a) (*R*)-**41a** and **23ao** and (b) (*S*)-**41a** and **23ao** (molar ratio 1 : 2) in region between aromatic protons (**41a** and **23ao**) and methyl protons on phenyl moiety of **23ao**. (Reprinted with permission from Ref. 209. Copyright 1996 by the American Chemical Society.)

However, this spectrum is very similar to that of free **23ao** and no intermolecular NOE (Nuclear Overhauser Effect) cross peaks between **23ao** and (*R*)-**41a** are observed. The interaction between them must be weak. On the other hand, some clear intermolecular NOE cross peaks, represented by asterisks in the figure, are observed between the aromatic H4, H6, and H7 protons of (*S*)-**41a** and the methyl protons of **23ao**. These data indicate that (*S*)-**41a** binds or interacts more strongly with **23ao** than (*R*)-**41a**, and the naphthyl protons of (*S*)-**41a** are located closely to the methyl protons of **23ao**, probably within less than 5 Å. These results are in good agreement with those of HPLC and 1D NMR experiments.

The enantioselectivities (α) and the thermodynamic parameters ΔH^\ddagger , ΔS^\ddagger , and ΔG^\ddagger for the more stable complex **23ao**–(*S*)-**41a** and the difference in Gibbs energy ($\Delta\Delta G^\ddagger$) in the chiral discrimination process can be separately determined by ^1H NMR titrations in solution and by HPLC.²⁰⁹ On the basis of the HPLC and NMR data combined with the structural data of **23a** determined by X-ray analysis, a model structure of the **23ao**–(*S*)-**41a** complex can be proposed, as shown in Figure 3.44.²⁰⁹ The (*S*)-**41a** is placed in a chiral groove of **23ao** so as to sufficiently explain these HPLC and NMR data. A naphthyl group of (*S*)-**41a** exists above the H2 proton of the glucose, and two OH protons of (*S*)-**41a** form hydrogen bonds with the carbonyl oxygens of the carbamate groups at the 2- and 3-positions on two different glucose units, and the naphthyl protons (H4, H6, and H7) are located close to the methyl protons on the phenyl groups of **23ao**. Therefore, this interaction model can satisfactorily explain all NMR data, including the intermolecular NOE data and the titration results.

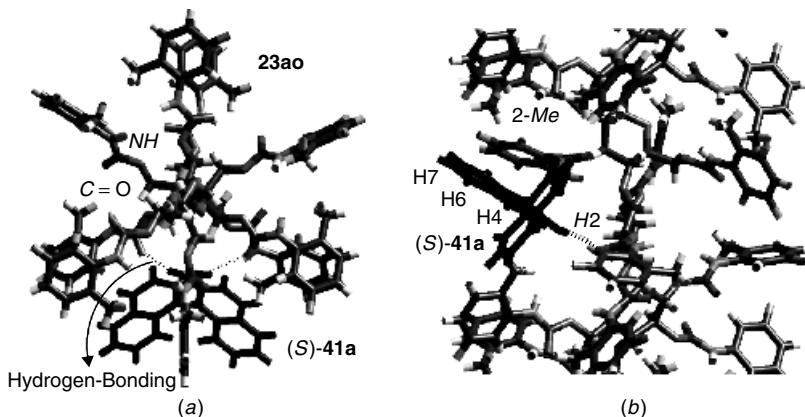


Figure 3.44 Calculated structure of complex **23ao**–(*S*)-**41a**. (a) View perpendicular to helix axis and (b) expanded region of same structure model as viewed along helix axis. (Reprinted with permission from Ref. 209. Copyright 1996 by the American Chemical Society.)

3,5-Dimethylphenylcarbamates of cellotetraose, maltooligosaccharides, and cyclodextrins are also soluble in CDCl_3 . Figure 3.45 shows the 500-MHz NMR spectra of **40** in the absence (*a*) and presence (*b–f*) of the 3,5-dimethylphenylcarbamates of oligosaccharides (**29**: $n = 4$, **30**: $n = 3, 5, 6$) and cyclodextrin (**31**: $n = 6$).²⁰⁸ The methine proton signal of **40** was split into two singlets and that of (–)-**40** was shifted downfield in the presence of **29** or **30**. The $\Delta\Delta\delta$ value tends to increase as the degree of polymerization (n) of **30** increases. This may be due to an increase in the regularity of the higher order structure of the maltooligosaccharides in the order 3-mer, 5-mer, and 6-mer. On the other hand, the same enantiomer of **40** shifted upfield in the presence of the cyclodextrin derivatives. These results indicate that the structures of

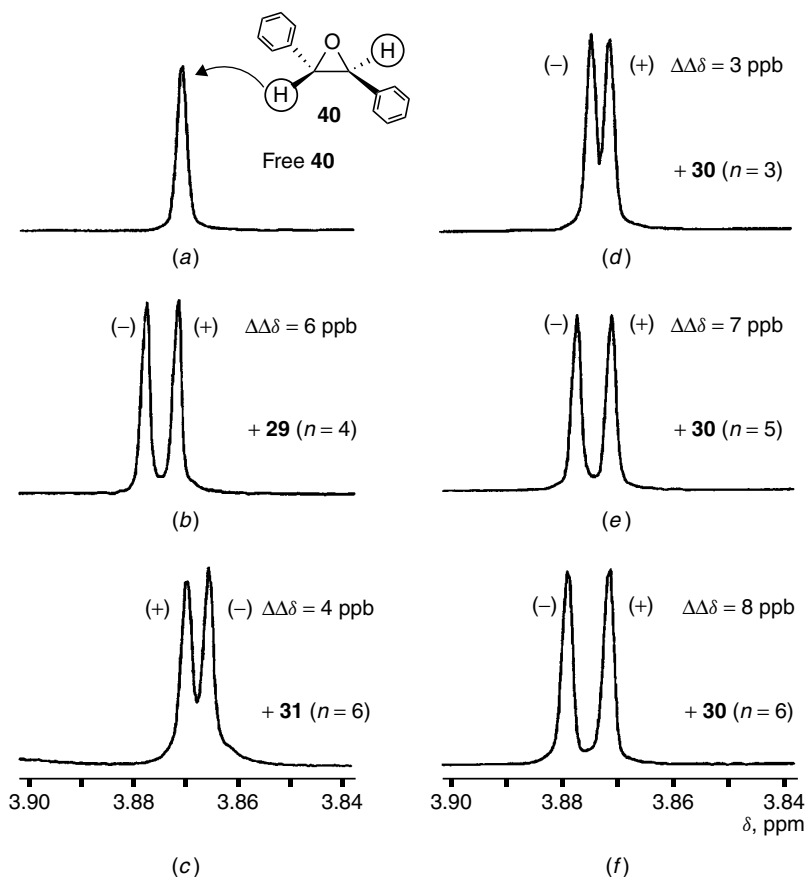


Figure 3.45 The 500-MHz ^1H NMR spectra of **40** in CDCl_3 : (a) free **40**, (b) **40** with **29** ($n = 4$), (c) **31** ($n = 6$), and (d–f) **30** ($n = 3, 5, 6$).

the 3,5-dimethylphenylcarbamates of linear- and cyclic-oligosaccharides are quite different, which is associated with the results obtained in HPLC and CD spectral measurements of **30**. The shift of the methine protons of (–)-**40** observed in ¹H NMR is consistent with the elution order of the enantiomers of **40** in chromatographic enantioseparation. The methine protons of (+)-**40** scarcely changed.

6.3.3 Computational Studies

Most phenylcarbamates of the polysaccharides with a high resolving ability are soluble only in polar solvents, such as pyridine, THF, and DMF, in which the interaction between the solvent and the phenylcarbamate is too strong to detect the interaction between the phenylcarbamate and a racemate. Therefore, NMR spectroscopy often cannot be utilized for the investigation of a chiral recognition mechanism. For these CDCl₃-insoluble phenylcarbamate derivatives, a computer simulation involving molecular-mechanics (MM) and molecular dynamics (MD) calculations may be a useful and effective approach for elucidating the mechanism for the chiral recognition and for predicting the elution order of enantiomers. Lipkowitz et al. have extensively been studying the chiral recognition mechanism on small-molecule CSPs from theoretical viewpoints with the aid of chromatography on CSPs.^{203,204} The interaction energies between the CSPs and enantiomers were calculated by MM, MD, and quantum mechanics calculations, and the chiral recognition mechanisms have been proposed on the basis of the calculation results.

The interaction energy calculations between cellulose tris(phenylcarbamate) (**23a**) or tris(3,5-dimethylphenylcarbamate) (**23x**) and *trans*-stilbene oxide (**40**) or benzoin (**19**) were performed by various methods using different force fields to gain insight into the mechanism for the chiral recognition on CDCl₃-insoluble phenylcarbamate derivatives.²¹¹ A good candidate for this study is **23a** because it exhibits a high chiral recognition ability as the CSP as well as **23x** and its structure has been postulated on the basis of X-ray data. In a chromatographic enantioseparation, **40** was completely resolved on both CSPs [**23a** ($\alpha = 1.46$), **23x** ($\alpha = 1.68$)]. However, the enantiomer elution order is reversed; the (*R,R*)-isomer elutes first on **23a**, whereas the (*S,S*)-isomer elutes first on **23x**. On the other hand, **19** is completely resolved on **23x** ($\alpha = 1.58$) but is not resolved on **23a**.

The methods used for calculating the interaction energy are roughly divided into the following two types, which differ in the enantiomer generation method:

1. Enantiomers were generated and tumbled at specific angles around each NH proton and the C=O oxygen at the 2-, 3-, and 6-positions of the carbamoyl group of **23a** and **23x**, which are considered to be the most important adsorbing sites from chromatographic resolution and NMR studies,

and then the interaction energy was calculated at each point of a grid on **23a** and **23x** molecules using all possible combinations of the rotation angles of the enantiomer. The calculation results were evaluated by the lowest interaction energy and the distribution of the interaction energy.

2. Enantiomers with a particular orientation were randomly generated by the Monte Carlo method on the surface of **23a** and **23x** defined by the particular van der Waals radius using the reported technique of “blowing up” the atomic radii.²¹² Molecular-mechanics calculations between the molecules were then performed step by step. The results of these calculations were evaluated with the averaged interaction energy.

The structures of **23a** and **23x** used in the calculations are octamer or nanomer constructed based on X-ray data for **23a**. Enantiomers were generated on the middle part of the polymers in order to avoid the influence of the end groups of polymers, because **23a** and **23x** used as the CSPs are polymers with degree of polymerization of ~ 200 .

The results of both calculations were in good agreement with the chromatographic resolution data for **40** and **19**.²¹¹ The lowest or averaged interaction energy between **23a** and (*S,S*)-**40** obtained in the calculation is lower than that between **23a** and (*R,R*)-**40**, whereas an opposite enantiomer preference was observed for **23x** and **40**.

Figure 3.46 shows the computer graphics of the interaction between **23a** and (*S,S*)-**40** having the lowest interaction energy.²¹¹ The (*S,S*)-**40** is bound

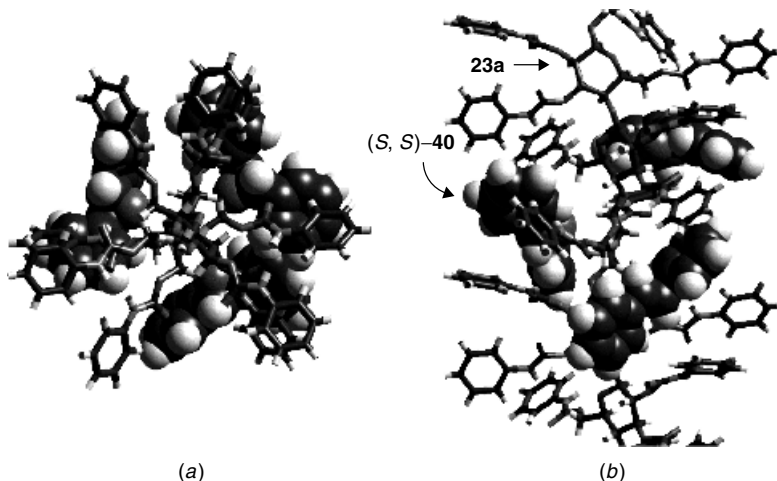


Figure 3.46 Calculated structure of **23a**–(*S,S*)-**40** complex formed through hydrogen bondings. (a) View perpendicular to helix axis and (b) along helix axis. (Reprinted with permission from Ref. 211. Copyright 1999 by the Chemical Society of Japan.)

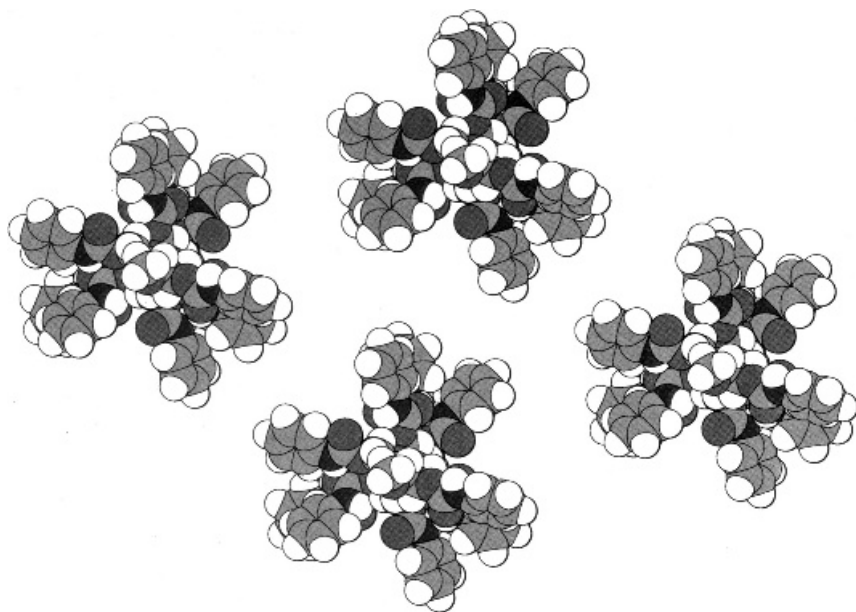


Figure 3.47 Calculated structures of **23a** aggregates as viewed perpendicular to helix axis.

in a chiral groove to form a hydrogen bond between the ether oxygen of **40** and the NH proton of the carbamate group of **23a**, and each phenyl group appears to interact with the phenyl groups of **23a** through π - π interactions. Although the same calculation was performed for benzoin and **23a**, almost no difference in interaction energies were observed for the enantiomers.

In the above calculations, the interactions between a single polysaccharide chain and an enantiomer are taken into consideration, because polar racemates should preferentially come into a chiral groove of the polymer chain with polar carbamate residues. However, besides these polar interactions, the π - π interaction between the phenyl group of the phenylcarbamate derivatives and the aromatic groups of a solute may contribute to the chiral recognition. Especially under reversed-phase conditions using aqueous eluents, the hydrophobic chiral space existing between the polymer chains may play an important role for chiral recognition. In this case, the calculation must be carried out in the system composed of several polymer chains, as shown in Figure 3.47.

7 CONCLUSIONS

In this chapter, the chiral recognition by optically active polymers has been reviewed in connection with polymer structures. Most of the polymers showing

high chiral recognition as CSPs for HPLC possess regular higher order structures, which seems to be the most important factor for efficient chiral recognition by polymeric CSPs. In order to achieve efficient chiral separation on a CSP, the same interaction between a CSP and an enantiomer must be regularly repeated. This can be achieved effectively on the polymer with a regular conformation.

Among optically active polymers, polysaccharide derivatives are particularly valuable. Polysaccharides such as cellulose and amylose are the most readily available optically active polymers and have stereoregular sequences. Although the chiral recognition abilities of native polysaccharides are not remarkable, they can be readily converted to the esters and carbamates with high chiral recognition abilities. The chiral recognition mechanism of these derivatives has been clarified to some extent.

REFERENCES

1. Akelah, A.; Sherrington D. C., *Chem. Rev.* **1981**, *81*, 557–587.
2. Kobayashi, N. *J. Syn. Org. Chem. Jpn.* **1981**, *39*, 181–191.
3. Allenmark, S. *Chromatographic Enantioseparation*. Ellis Horwood, Chichester, 1988.
4. Subramanian G. (Ed.) *A Practical Approach to Chiral Separations by Liquid Chromatography*, VCH, New York, 1994.
5. Ahuja, S. *Chiral Separations: Applications and Technology*, American Chemical Society, Washington, D.C., 1997.
6. Yashima, E.; Okamoto Y. In *Advances in Liquid Chromatography*. Hanai, K.; Hatano, H. (Eds.). World Scientific, Singapore, 1996, pp. 231–254.
7. Okamoto, Y.; Yashima E. In *Macromolecular Design of Polymeric Materials*, Hatada, K.; Kitayama, T.; Vogl, O. (Eds.). Dekker, New York, 1997, pp. 731–746.
8. Taylor, D. R.; Maher, K. *J. Chromatogr. Sci.* **1992**, *30*, 67–85.
9. *J. Chromatogr. A* **1994**, *666*. Special Volume for Chiral Separations.
10. *J. Chromatogr. A* **2001**, *906*. Special Volume for Chiral Separations.
11. Okamoto, Y. *CHEMTEC* **1987**, 176–181.
12. Yashima, E.; Yamamoto, C.; Okamoto, Y. *Synlett* **1998**, 344–360.
13. Pirkle, W. H.; Pochapsky, T. C. *Chem. Rev.* **1989**, *89*, 347–362.
14. Welch, C. J. *Adv. Chromatogr.* **1995**, *35*, 171–197.
15. Okamoto, Y.; Kaida, Y. *J. Chromatogr. A.* **1994**, *666*, 403–419.
16. Yashima, E.; Okamoto, Y. *Bull. Chem. Soc. Jpn.* **1995**, *68*, 3289–3307.
17. Okamoto, Y.; Yashima, E. *Angew. Chem. Int. Ed.* **1998**, *37*, 1020–1043.
18. Yashima, E. *J. Chromatogr. A.* **2001**, *906*, 105–125.
19. Tachibana, K.; Ohnishi, A. *J. Chromatogr. A.* **2001**, *906*, 127–154.
20. Wulff, G. *Angew. Chem. Int. Ed. Engl.* **1995**, *34*, 1812–1832.
21. Remcho, V. T.; Tam, Z. J. News and Features, *Anal. Chem.*, **1999**, *71*, 248A–255A.
22. Kriz, D.; Ramstrom, O.; Mosbach, K. *Anal. Chem.* **1997**, *69*, 345A–349A.

23. Yuki, H.; Hatada, K.; Niinomi, T.; Kikuchi, Y. *Polym. J.* **1970**, *1*, 36–45.
24. Okamoto, Y.; Shohi, H.; Yuki, H. *J. Polym. Sci., Polym. Lett. Ed.* **1983**, *21*, 601–607.
25. Yuki, H.; Okamoto, Y.; Okamoto, I. *J. Am. Chem. Soc.* **1980**, *102*, 6356–6358.
26. Okamoto, Y.; Honda, S.; Okamoto, I.; Yuki, H.; Murata, S.; Noyori, R.; Tanaka, H. *J. Am. Chem. Soc.* **1981**, *103*, 6971–6973.
27. Okamoto, Y.; Hatada, K. *J. Liq. Chromatogr.* **1986**, *9*, 369–384.
28. Yamamoto, K.; Ueda, T.; Yumioka, H.; Okamoto, Y.; Yoshida, T. *Chem. Lett.* **1984**, 1977–1978.
29. Kissener, W.; Vögtle, F. *Angew. Chem. Int. Ed. Engl.* **1985**, *24*, 222–223.
30. Nakazaki, M.; Koji, K.; Ikeda, T.; Kitsuki, T.; Okamoto, Y. *J. Chem. Soc., Chem. Commun.* **1983**, 787–788.
31. Feringa, B. L.; Jager, W. F.; de Lange, B.; Meijer, E. W. *J. Am. Chem. Soc.* **1991**, *113*, 5468–5470.
32. Harada, N.; Saito, A.; Koumura, N.; Roe, D. C.; Jager, W. F.; Zijlstra, R. W. J.; de Lange, B.; Feringa, B. L. *J. Am. Chem. Soc.* **1997**, *119*, 7249–7255.
33. Gur, E.; Kaida, Y.; Okamoto, Y.; Biali, S.; Rappoport, Z. *J. Org. Chem.* **1992**, *57*, 3689–3693.
34. Yamamoto, K.; Noda, K.; Okamoto, Y. *J. Chem. Soc., Chem. Commun.* **1985**, 1421–1422.
35. Harada, N.; Iwabuchi, J.; Yokota, Y.; Uda, H.; Okamoto, Y.; Yuki, H.; Kawada, Y. *J. Chem. Soc., Perkin Trans. 1* **1985**, 1845–1848.
36. Meurer, K.; Aigner, A.; Vögtle, F. *J. Inclusion Phen.* **1985**, *3*, 51–54.
37. Duchene, K.-H.; Vögtle, F. *Angew. Chem. Int. Ed. Engl.* **1985**, *24*, 885–886.
38. Tajiri, A.; Fukuda, M.; Hatano, M.; Morita, T.; Takase, K. *Angew. Chem. Int. Ed. Engl.* **1983**, *22*, 870–871.
39. Kawada, Y.; Iwamura, H.; Okamoto, Y.; Yuki, H. *Tetrahedron Lett.* **1983**, *24*, 791–794.
40. Kawada, Y.; Okamoto, Y.; Iwamura, H. *Tetrahedron Lett.* **1983**, *24*, 5359–5362.
41. Yoshifuji, M.; Toyota, K.; Niitsu, T.; Inamoto, N.; Okamoto, Y.; Aburatani, R. *J. Chem. Soc., Chem. Commun.* **1986**, 1550–1551.
42. Okamoto, Y.; Yashima, E.; Hatada, K.; Mislow, K. *J. Org. Chem.* **1984**, *49*, 557–558.
43. Irurre, J.; Santamaria, J.; Gonzalez-Rego, M. C. *Chirality* **1995**, *7*, 154–157.
44. Chance, J. M.; Geiger, J. H.; Okamoto, Y.; Aburatani, R.; Mislow, K. *J. Am. Chem. Soc.* **1990**, *112*, 3540–3547.
45. Okamoto, Y.; Okamoto, I.; Yuki, H. *Chem. Lett.* **1981**, 835–838.
46. Okamoto, Y.; Ishikura, H.; Hatada, K.; Yuki, H. *Polym. J.* **1983**, *15*, 851–853.
47. Okamoto, Y.; Mohri, H.; Hatada, K. *Chem. Lett.* **1988**, 1879–1882.
48. Okamoto, Y.; Mohri, H.; Nakano, T.; Hatada, K. *Chirality* **1991**, *3*, 277–284.
49. Okamoto, Y.; Mohri, H.; Hatada, K. *Polym. J.* **1989**, *21*, 439–445.
50. Tamai, Y.; Qian, P.; Matsunaga, K.; Miyano, S. *Bull. Chem. Soc. Jpn.* **1992**, *65*, 817–823.
51. Blaschke, G. *Angew. Chem. Int. Ed. Engl.* **1980**, *19*, 13–24.
52. Blaschke, G.; Bröcker, W.; Frankel, W. *Angew. Chem. Int. Ed. Engl.* **1986**, *25*, 830–833.
53. Blaschke, G. *J. Liq. Chromatogr.* **1986**, *9*, 341–368.
54. Blaschke, G.; Kraft, H.-P.; Fickentscher, K.; Köhler, F. *Arzneim. Forsch.* **1979**, *29*, 1640–1642.
55. Saotome, Y.; Miyazawa, T.; Endo, T. *Chromatographia* **1989**, *28*, 505–508.

56. Arlt, D.; Bomer, B.; Grosser, R.; Lange, W. *Angew. Chem. Int. Ed. Engl.* **1991**, *30*, 1662–1664.
57. Kunieda, N.; Chakihara, H.; Kinoshita, M. *Chem. Lett.* **1990**, 317–318.
58. Oishi, T.; Isobe, Y.; Onimura, K.; Tsutsumi, H. *Polym. Prep. Jpn.* **1999**, *48*, 1850–1851.
59. Oishi, T.; Yamasaki, H.; Fujimoto, M. *Polym. J.* **1991**, *23*, 795–804.
60. Okamoto, Y.; Nakano, T.; Kobayashi, H.; Hatada, K. *Polym. Bull.* **1991**, *25*, 5–8.
61. Doi, Y.; Kiniwa, H.; Nishikaji, T.; Ogata, N. *J. Chromatogr.* **1987**, *396*, 395–398.
62. Kiniwa, H.; Doi, Y.; Nishikaji, T.; Ogata, N. *Makromol. Chem.* **1987**, *188*, 1851–1860.
63. Hirayama, C.; Ihara, H.; Tanaka, K. *J. Chromatogr.* **1988**, *450*, 271–276.
64. Okamoto, Y.; Nagamura, Y.; Fukumoto, T.; Hatada, K. *Polym. J.* **1991**, *23*, 1197–1207.
65. Saigo, K.; Chen, Y.; Kubota, N.; Yashibana, K.; Yonezawa, N.; Hasegawa, M. *Chem. Lett.* **1986**, 515–518.
66. Saigo, K. *Prog. Polym. Sci.* **1992**, *17*, 35–86.
67. Saigo, K.; Nakamura, M.; Adegawa, Y.; Noguchi, S.; Hasegawa, M. *Chem. Lett.* **1989**, 337–340.
68. Saigo, K.; Shiwaku, T.; Hayashi, K.; Fujioka, K.; Sukegawa, M.; Chen, Y.; Yonezawa, N.; Hasegawa, M.; Hashimoto, T. *Macromolecules* **1990**, *23*, 2830–2836.
69. Kobayashi, T.; Kakimoto, M.; Imai, Y. *Polym. J.* **1993**, *25*, 969–975.
70. Kishimoto, Y.; Eckerle, P.; Miyatake, T.; Kainosho, M.; Ono, A.; Ikariya, T.; Noyori, R. *J. Am. Chem. Soc.* **1999**, *121*, 12035–12044.
71. Yashima, E.; Huang, S.; Okamoto, Y. *J. Chem. Soc. Chem. Commun.* **1994**, 1811–1812.
72. Yashima, E.; Matsushima, T.; Nimura, T.; Okamoto, Y. *Korea Polym. J.* **1996**, *4*, 139–146.
73. Kakuchi, T.; Satoh, T.; Kanai, H.; Umeda, S.; Hatakeyama, T.; Yokota, K. *Enantiomer* **1997**, *2*, 273–276.
74. Umeda, S.; Satoh, T.; Saitoh, K.; Yokota, K.; Kakuchi, T. *J. Polym. Sci. Part A: Polym. Chem.* **1998**, *36*, 901–909.
75. Allenmark, S.; Bomgren, B.; Borén, H. *J. Chromatogr.* **1983**, *264*, 63–68.
76. Domenici, E.; Bertucci, C.; Salvadori, P.; Felix, G.; Cahagne, I.; Montellier, S.; Wainer, I. W. *Chromatographia* **1990**, *29*, 170–176.
77. Hermansson, J. *J. Chromatogr.* **1983**, *269*, 71–80.
78. Miwa, T.; Ichikawa, M.; Tsuno, M.; Hattori, T.; Miyakawa, T.; Kayano, M.; Miyake, Y. *Chem. Pharm. Bull.* **1987**, *35*, 682–686.
79. Haginaka, J.; Seyama, C.; Kanasugi, N. *Anal. Chem.* **1995**, *67*, 2539–2547.
80. Miwa, T.; Miyakawa, T.; Miyake, Y. *J. Chromatogr.* **1988**, *457*, 227–233.
81. Mano, N.; Oda, Y.; Asakawa, N.; Yoshida, Y.; Sato, T. *J. Chromatogr.* **1992**, *623*, 221–228.
82. Theolohan, S.; Jadaud, P.; Wainer, I. W. *Chromatographia* **1989**, *28*, 551–555.
83. Wainer, I. W.; Jadaud, P.; Schombaum, G. R.; Kadodkar, S. V.; Henry, M. P. *Chromatographia* **1988**, *25*, 903–907.
84. Erlandsson, P.; Marle, I.; Hansson, L.; Isaksson, R.; Pettersson, C.; Pettersson, G. *J. Am. Chem. Soc.* **1990**, *112*, 4573–4574.
85. Haginaka, J.; Murashima, T.; Seyama, C. *J. Chromatogr. A* **1994**, *666*, 203–210.
86. Haginaka, J.; Miyano, Y.; Saizen, Y.; Seyama, C.; Murashima, T. *J. Chromatogr. A* **1995**, *708*, 161–168.

87. Nyström, A.; Strandberg, A.; Aspergren, A.; Behr, S.; Karlsson, A. *Chromatographia* **1999**, *50*, 209–214.
88. Mano, N.; Oda, Y.; Asakawa, N.; Yoshida, Y.; Sato, T. *J. Chromatogr.* **1992**, *603*, 105–109.
89. Massolini, G.; De Lorenzi, E.; Lloyd, D. K.; McGann, A. M.; Caccialanza, G. *J. Chromatogr. B* **1998**, *712*, 83–94.
90. Haginaka, J.; Seyama, C.; Yasuda, H.; Fujima, H.; Wada, H. *J. Chromatogr.* **1992**, *592*, 301–307.
91. Erlandsson, P.; Nilsson, S. *J. Chromatogr.* **1989**, *482*, 35–51.
92. Marle, I.; Jönsson, S.; Isaksson, R.; Pettersson, C.; Pettersson, G. *J. Chromatogr.* **1993**, *648*, 333–347.
93. Pinkerton, T. C.; Howe, W. J.; Ulrich, E. L.; Comiskey, J. P.; Haginaka, J.; Murashima, T.; Walkenhorst, W. F.; Westler, W. M.; Markley, J. L. *Anal. Chem.* **1995**, *67*, 2354–2367.
94. Hesse, G.; Hagel, R. *Chromatographia* **1973**, *6*, 277–280.
95. Hesse, G.; Hagel, R. *Liebigs Ann. Chem.* **1976**, 966–1008.
96. Shibata, T.; Okamoto, I.; Ishii, K. *J. Liq. Chromatogr.* **1986**, *9*, 313–340.
97. Boland, W.; Niedermeyer, U.; Jaenicke, L.; Görisch, H. *Helv. Chim. Acta* **1985**, *68*, 2062–2073.
98. Pettersson, I.; Berg, U. *J. Chem. Res. Synop.* **1984**, 208–209.
99. Koller, H.; Rimböck, K.-H.; Mannschreck, A. *J. Chromatogr.* **1983**, *282*, 89–94.
100. Schlögl, K.; Widhalm, M. *Chem. Ber.* **1982**, *115*, 3042–3048.
101. Schlögl, K.; Werner, A.; Widhalm, M. *J. Chem. Soc. Perkin Trans. 1* **1983**, 1731–1735.
102. Agranat, I.; Suissa, M. R.; Cohen, S.; Isaksson, R.; Sandström, J.; Dale, J.; Grace, D. *J. Chem. Soc. Chem. Commun.* **1987**, 381–383.
103. Lindsten, G.; Wennerström, O.; Isaksson, R. *J. Org. Chem.* **1987**, *52*, 547–554.
104. Isaksson, R.; Rochester, J.; Sandström, J.; Wistrand, L.-G., *J. Am. Chem. Soc.* **1985**, *107*, 4074–4075.
105. Okamoto, Y.; Kawashima, M.; Yamamoto, K.; Hatada, K. *Chem. Lett.* **1984**, 739–742.
106. Ichida, A.; Shibata, T.; Okamoto, I.; Yuki, Y.; Namikoshi, H.; Toda, Y. *Chromatographia* **1984**, *19*, 280–284.
107. Okamoto, Y.; Aburatani, R.; Hatada, K. *J. Chromatogr.* **1987**, *389*, 95–102.
108. Hara, H.; Komoriya, S.; Miyashita, T.; Hoshino, O. *Tetrahedron Asymmetry* **1995**, *6*, 1683–1692.
109. Amadji, M.; Vadeкарd, J.; Plaquevent, J.-C.; Duhamel, L.; Duhaniel, P. *J. Am. Chem. Soc.* **1996**, *118*, 12483–12484.
110. Cavazza, M.; Zandomenighi, M.; Ouchi, A.; Koga, Y. *J. Am. Chem. Soc.* **1996**, *118*, 9990–9991.
111. Kimata, K.; Kobayashi, M.; Hosoya, K.; Araki, T.; Tanaka, N. *J. Am. Chem. Soc.* **1996**, *118*, 759–762.
112. Feng, X.; Shu, L.; Shi, Y. *J. Am. Chem. Soc.* **1999**, *121*, 11002–11003.
113. Nakajima, M.; Sasaki, Y.; Shiro, M.; Hashimoto, S. *Tetrahedron Asymmetry* **1997**, *8*, 341–344.
114. Nozaki, K.; Nakano, K.; Hiyama, T. *J. Am. Chem. Soc.* **1999**, *121*, 11008–11009.
115. Okada, K.; Minami, M.; Oda, M. *Chem. Lett.* **1993**, 1999–2002.

116. Takeuchi, S.; Ohira, A.; Miyoshi, N.; Mashio, H.; Ohgo, Y. *Tetrahedron Asymmetry* **1994**, *5*, 1763–1780.
117. Vizitiu, D.; Lazar, C.; Halden, B. J.; Lemieux, R. P. *J. Am. Chem. Soc.* **1999**, *121*, 8229–8236.
118. Corey, E. J.; Letavic, M. A. *J. Am. Chem. Soc.* **1995**, *117*, 9616–9617.
119. Ichida, A.; Shibata, T. In *Chromatographic Chiral Separations*. Zief, M.; Crane, L. J. (Eds.). Marcel Dekker, New York, 1990, Chapter 9, pp. 219–243.
120. Adam, W.; Groer, P.; Saha-Mölller, C. R. *Tetrahedron Asymmetry* **1997**, *8*, 833–836.
121. Miller, M. W.; Johnson, C. R. *J. Org. Chem.* **1997**, *62*, 1582–1583.
122. Biadatti, T.; Esker, J. L.; Johnson, C. R. *Tetrahedron Asymmetry* **1996**, *7*, 2313–2320.
123. Adam, W.; Diaz, M. T.; Saha-Mölller, C. R. *Tetrahedron Asymmetry* **1998**, *9*, 791–796.
124. Shibata, T.; Sei, T.; Nishimura, H.; Deguchi, K. *Chromatographia* **1987**, *24*, 552–554.
125. Rimböck, K.-H.; Kastner, F.; Mannschreck, A. *J. Chromatogr.* **1986**, *351*, 346–350.
126. Francotte, E.; Wolf, R. M. *Chirality* **1991**, *3*, 43–55.
127. Francotte, E.; Wolf, R. M. *J. Chromatogr.* **1992**, *595*, 63–75.
128. Francotte, E.; Zhang, T. *J. Chromatogr. A* **1995**, *718*, 257–266.
129. Okamoto, Y.; Kawashima, M.; Hatada, K. *J. Am. Chem. Soc.* **1984**, *106*, 5357–5359.
130. Okamoto, Y.; Kawashima, M.; Hatada, K. *J. Chromatogr.* **1986**, *363*, 173–186.
131. Chankvetadze, B.; Yashima, E.; Okamoto, Y. *J. Chromatogr. A* **1994**, *670*, 39–49.
132. Chankvetadze, B.; Yashima, E.; Okamoto, Y. *J. Chromatogr. A* **1995**, *694*, 101–109.
133. Yashima, E.; Yamamoto, C.; Okamoto, Y. *Polym. J.* **1995**, *27*, 856–861.
134. Chankvetadze, B.; Chankvetadze, L.; Sidamonidze, S.; Kasashima, E.; Yashima, E.; Okamoto, Y. *J. Chromatogr. A* **1997**, *787*, 67–77.
135. Okamoto, Y.; Aburatani, R.; Fukumoto, T.; Hatada, K. *Chem. Lett.* **1987**, 1857–1860.
136. Okamoto, Y.; Ohashi, T.; Kaida, Y.; Yashima, E. *Chirality* **1993**, *5*, 616–621.
137. Steinmeier, H.; Zugenmaier, P. *Carbohydr. Res.* **1987**, *164*, 97–105.
138. Vogt, U.; Zugenmaier, P. *Ber. Bunsenges. Phys. Chem.* **1985**, *89*, 1217–1224.
139. Vogt, U.; Zugenmaier, P. Communication at the European Science Foundation Workshop on Specific Interaction in Polysaccharide Systems, Uppsala, Sweden, 1983.
140. Mizutani, T.; Ema, T.; Tomita, T.; Kuroda, Y.; Ogoshi, H. *J. Am. Chem. Soc.* **1994**, *116*, 4240–4250.
141. Hopf, H.; Grahn, W.; Barrett, D. G.; Gerdes, A.; Hilmer, J.; Hucker, J.; Okamoto, Y.; Kaida, Y. *Chem. Ber.* **1990**, *123*, 841–844.
142. Yoshifuji, M.; Ichikawa, Y.; Toyota, K.; Kasashima, E.; Okamoto, Y. *Chem. Lett.* **1997**, 87–88.
143. Ohno, A.; Kunitomo, J.; Kawai, Y.; Kawamoto, T.; Tomishima, M.; Yoneda, F. *J. Org. Chem.* **1996**, *61*, 9344–9355.
144. Saito, S.; Kano, T.; Muto, H.; Nakadai, M.; Yamamoto, H. *J. Am. Chem. Soc.* **1999**, *121*, 8943–8944.
145. Ben-David Blanca, M.; Yamamoto, C.; Okamoto, Y.; Biali, S. E.; Kost, D. *J. Org. Chem.* **2000**, *65*, 8613–8620.
146. Griesbeck, A. G.; Kramer, W.; Lex, J. *Angew. Chem. Int. Ed.* **2001**, *40*, 577–579.
147. Liu, Y.; Lao, W.; Zhang, Y.; Jiang, S.; Chen, L. *Chromatographia* **2000**, *52*, 190–194.

148. Biali, S. E.; Kahr, B.; Okamoto, Y.; Aburatani, R.; Mislow, K. *J. Am. Chem. Soc.* **1988**, *110*, 1917–1922.
149. Eshdat, L.; Shabtai, E.; Saleh, S. A.; Sternfeld, T.; Saito, M.; Okamoto, Y.; Rabinovitz, M. *J. Org. Chem.* **1999**, *64*, 3532–3537.
150. Corey, E. J.; Kania, R. S. *J. Am. Chem. Soc.* **1996**, *118*, 1229–1230.
151. Martini, D.; Iacazio, G. *J. Chromatogr. A* **1997**, *790*, 235–241.
152. Otsuka, H.; Shinkai, S. *Supramol. Chem.* **1996**, *3*, 189–205.
153. Ikeda, A.; Yoshimura, M.; Lhotak, P.; Shinkai, S. *J. Chem. Soc. Perkin Trans. 1* **1996**, 1945–1950.
154. Theil, F.; Sonnenschein, H.; Kreher, T. *Tetrahedron Asymmetry* **1996**, *7*, 3365–3370.
155. Toyota, S.; Akinaga, T.; Kojima, H.; Aki, M.; Oki, M. *J. Am. Chem. Soc.* **1996**, *118*, 11460–11466.
156. Kummer, M.; Werner, G. *J. Chromatogr. A* **1998**, *825*, 107–114.
157. Tsuruta, H.; Imamoto, T. *Tetrahedron Asymmetry* **1999**, *10*, 877–882.
158. Sugimura, T.; Inoue, S.; Tai, A. *Tetrahedron Lett.* **1998**, *39*, 6487–6490.
159. Henkel, B.; Kunath, A.; Schick, H. *Tetrahedron Asymmetry* **1994**, *5*, 17–18.
160. Exner, K.; Prinzbach, H. *Chem. Commun.* **1998**, 749–750.
161. Mori, A.; Toriyama, F.; Kajiro, H.; Hirabayashi, K.; Nishihara, Y.; Hiyama, T. *Chem. Lett.* **1999**, 549–550.
162. Trost, B. M.; Oslob, J. D. *J. Am. Chem. Soc.* **1999**, *121*, 3057–3064.
163. Nakano, T.; Okamoto, Y.; Hatada, K. *J. Am. Chem. Soc.* **1992**, *114*, 1318–1329.
164. Nakano, T.; Okamoto, Y.; Hatada, K. *Polym. J.* **1995**, *27*, 882–891.
165. Chankvetadze, B.; Yamamoto, C.; Okamoto, Y. *Chem. Lett.* **2000**, 1176–1177.
166. Chankvetadze, B.; Yamamoto, C.; Okamoto, Y. *J. Comb. Chem. High Throughput Scr.* **2000**, *3*, 497–508.
167. Chankvetadze, B.; Yamamoto, C.; Okamoto, Y. *J. Chromatogr. A* **2001**, *922*, 127–137.
168. Okamoto, Y.; Aburatani, R.; Miura, S.; Hatada, K. *J. Liq. Chromatogr.* **1987**, *10*, 1613–1628.
169. Dingenen, J. In *A Practical Approach to Chiral Separations by Liquid Chromatography*, Subramanian, G. (Ed.), VCH, New York, 1994, Chapter 6, pp. 115–181.
170. Okamoto, Y.; Aburatani, R.; Kaida, Y.; Hatada, K. *Chem. Lett.* **1988**, 1125–1128.
171. Okamoto, Y.; Kawashima, M.; Aburatani, R.; Hatada, K.; Nishiyama, T.; Masuda, M. *Chem. Lett.* **1986**, 1237–1240.
172. Ikeda, K.; Hamasaki, T.; Kohno, H.; Ogawa, T.; Matsumoto, T.; Sakai, J. *Chem. Lett.* **1989**, 1089–1090.
173. Ishikawa, A.; Shibata, T. *J. Liq. Chromatogr.* **1993**, *16*, 859–878.
174. Kaida, Y.; Okamoto, Y. *Bull. Chem. Soc. Jpn.* **1992**, *65*, 2286.
175. Petersson, P.; Markides, K. E. *J. Chromatogr. A* **1994**, *666*, 381–394.
176. Bargmann-Leyder, N.; Tambuté, A.; Caude, M. *Chirality* **1995**, *7*, 311–325.
177. Terfloth, G. *J. Chromatogr. A* **2001**, *906*, 301–307.
178. Yashima, E.; Fukaya, H.; Okamoto, Y. *J. Chromatogr. A* **1994**, *677*, 11–19.
179. Enomoto, N.; Furukawa, S.; Ogasawara, Y.; Akano, H.; Kawamura, Y.; Yashima, E.; Okamoto, Y. *Anal. Chem.* **1996**, *68*, 2789–2804.
180. Francotte, E. R.; Zhang, T. PCT WO 97/040411, February 6, 1997.

181. Oliveros, L.; Lopez, P.; Minguillón, C.; Franco, P. *J. Liq. Chromatogr.* **1995**, *18*, 1521–1532.
182. Franco, P.; Senso, A.; Minguillón, C.; Oliveros, L. *J. Chromatogr. A* **1998**, *796*, 265–272.
183. Franco, P.; Senso, A.; Oliveros, L.; Minguillón, C. *J. Chromatogr. A* **2001**, *906*, 155–170.
184. Kubota, T.; Kusano, T.; Yamamoto, C.; Yashima, E.; Okamoto, Y. *Chem. Lett.* **2001**, 724–725.
185. Reuter, C.; Pawlittzki, G.; Wörsdörfer, U.; Plevvoets, M.; Mohry, A.; Kubota, T.; Okamoto, Y.; Vögtle, F. *Eur. J. Org. Chem.* **2000**, 3059–3067.
186. Yamamoto, C.; Hayashi, T.; Okamoto, Y.; Ohkubo, S.; Kato, T. *Chem. Commun.* **2001**, 925–926.
187. Okamoto, Y.; Kaida, Y.; Hayashida, H.; Hatada, K. *Chem. Lett.* **1990**, 909–912.
188. Kaida, Y.; Okamoto, Y. *J. Chromatogr.* **1993**, *641*, 267–278.
189. Kaida, Y.; Okamoto, Y. *Chirality* **1992**, *4*, 122–124.
190. Kaida, Y.; Okamoto, Y. *Chem. Lett.* **1992**, 85–88.
191. Kubota, T.; Yamamoto, C.; Okamoto, Y. *J. Am. Chem. Soc.* **2000**, *122*, 4056–4059.
192. Vogt, U.; Zugenmaier, P. *Makromol. Chem., Rapid Commun.* **1983**, *4*, 759–765.
193. Aburatani, R.; Okamoto, Y.; Hatada, K. *Bull. Chem. Soc. Jpn.* **1990**, *63*, 3606–3610.
194. Armstrong, D. W.; Stalcup, A. M.; Hilton, M. L.; Duncan, J. D.; Faulkner, J. R., Jr.; Chang, S.-C. *Anal. Chem.* **1990**, *62*, 1610–1615.
195. Hargitai, T.; Okamoto, Y. *J. Liq. Chromatogr.* **1993**, *16*, 843–858.
196. Hargitai, T.; Kaida, Y.; Okamoto, Y. *J. Chromatogr.* **1993**, *628*, 11–22.
197. Okamoto, Y.; Noguchi, J.; Yashima, E. *React. Funct. Polym.* **1998**, *37*, 183–188.
198. Yamamoto, C.; Hayashi, T.; Okamoto, Y.; Kobayashi, S. *Chem. Lett.* **2000**, 12–13.
199. Feibush, B.; Fitueroa, A.; Charles, R.; Onan, K. D.; Feibush, P.; Karger, B. L. *J. Am. Chem. Soc.* **1986**, *108*, 3310–3318.
200. Lohmiller, K.; Bayer, E.; Koppenhoefer, B. *J. Chromatogr. A* **1993**, *634*, 65–77.
201. Pirkle, W. H.; Welch, C. J. *J. Chromatogr. A* **1994**, *683*, 347–353.
202. Pirkle, W. H.; Murray, P. G.; Rausch, D. J.; McKenna, S. T. *J. Org. Chem.* **1996**, *61*, 4769–4774.
203. Lipkowitz, K. B. In *A Practical Approach to Chiral Separations by Liquid Chromatography*, Subramanian, G. (Ed.), VCH, New York, 1994, Chapter 2, pp. 19–55.
204. Lipkowitz, K. B. *J. Chromatogr. A* **1995**, *694*, 15–37.
205. Topiol, S.; Sabio, M.; Moroz, J.; Caldwell, W. B. *J. Am. Chem. Soc.* **1990**, *110*, 8367–8376.
206. Lipkowitz, K. B.; *J. Chromatogr. A* **2001**, *906*, 417–442.
207. Yashima, E.; Yamada, M.; Okamoto, Y. *Chem. Lett.* **1994**, 579–582.
208. Yashima, E.; Yamada, M.; Yamamoto, C.; Nakashima, M.; Okamoto, Y. *Enantiomer* **1997**, *2*, 225–240.
209. Yashima, E.; Yamamoto, C.; Okamoto, Y. *J. Am. Chem. Soc.* **1996**, *118*, 4036–4048.
210. Yashima, E.; Yamada, M.; Kaida, Y.; Okamoto, Y. *J. Chromatogr. A* **1995**, *694*, 347–354.
211. Yamamoto, C.; Yashima, E.; Okamoto, Y. *Bull. Chem. Soc. Jpn.* **1999**, *72*, 1815–1825.
212. Theodorou, D. N.; Suter, U. W. *Macromolecules* **1985**, *18*, 1467–1478.

Chapter 4

Chirality in the Polysilanes

MICHIYA FUJIKI

*Graduate School of Materials Science, Nara Institute of Science and
Technology, 8916-5 Takayama, Ikoma, Nara 630-0101, Japan*

HIROSHI NAKASHIMA

*NTT Photonics Laboratories, NTT Corporation, 3-1 Wakamiya, Morinosato,
Atsugi, Kanagawa 243-0198, Japan*

SEIJI TOYODA

*NTT Basic Research Laboratories, NTT Corporation, 3-1 Wakamiya,
Morinosato, Atsugi, Kanagawa 243-0198, Japan*

JULIAN R. KOE

*Department of Chemistry, International Christian University, 3-10-2 Osawa,
Mitaka, Tokyo 181-8585, Japan*

- 1 Historical Background and Introduction
 - 1.1 Optically Active Synthetic Polymers
 - 1.2 Optically Active Polysilanes
 - 1.3 Preparation of Polysilanes
 - 1.4 Helical Polysilane and Circular Dichroism Spectroscopy
 - 1.5 Preferential Screw Sense Helical Ordering of Polysilanes
 - 1.6 Correlation Between Global Conformation and Optical Characteristics of Polysilanes
- 2 Optically Active Dialkylpolysilanes
 - 2.1 Preferential Screw Sense Homopolymers with Enantiopure Chiral Side Chains
 - 2.2 Imaging of Rodlike Polysilane Single Molecule

Materials-Chirality: Volume 24 of Topics in Stereochemistry,
Edited by Mark M. Green, R.J.M. Nolte, and E.W. Meijer
ISBN 0-471-05497-6 Copyright © 2003 John Wiley & Sons, Inc.

- 2.3 Optically Active Polysilanes with Diastereomeric Helicities Containing Opposite Screw Senses and Different Screw Pitches
 - 2.4 Copolymers with Preferential Screw Sense and “Sergeants-and-Soldiers” Principle
 - 2.5 Copolymers with Preferential Screw Sense and “Majority Rule” Principle
 - 2.6 Enantiopure Chiral Termini Effects and Sergeants-and-Soldiers Cooperativity
 - 2.7 Switching Preferential Screw Sense by Helix–Helix Transition
 - 2.8 Summary and Conclusions for Dialkylpolysilanes
 - 3 Optically Active Alkyl(alkoxyphenyl)polysilane
 - 3.1 Alkyl(alkoxyphenyl)polysilane Bearing Enantiopure Chiral Side Chains
 - 3.2 Control of Optical Properties and Global–Local Conformations
 - 3.2.1 Substituent Effects and Cooperative Helical Order Effect
 - 3.2.2 Control of Main-Chain Helicity by Position of Remote Chiral Group
 - 3.3 Poly{alkyl(alkoxyphenyl)silane} Chiral Aggregates
 - 3.3.1 Switch and Memory of Chiroptical Properties
 - 3.3.2 Chiroptical Properties
 - 3.3.3 Temperature Effects
 - 3.3.4 Solvent Effects
 - 3.4 Molecular Chirality Recognition of Poly{alkyl(alkoxyphenyl)silane}
 - 4 Optically Active Alkyl(phenyl)polysilane
 - 4.1 UV Absorption, Fluorescence Spectra, and Fluorescence Anisotropy of Optically Inactive Homopolymers
 - 4.2 UV and CD Spectra of Copolymers Bearing Chiral–Achiral Substituents
 - 4.3 Molecular Mechanics Calculation
 - 4.4 Comparison of UV and CD Spectra of Copolymers
 - 4.5 Analysis of CD Spectra Based on Ising Model
 - 4.6 Summary of Poly(alkyl(aryl)silane)s
 - 5 Optically Active Diarylpolysilanes
 - 5.1 CD and UV Spectroscopy of Homopolymers
 - 5.2 Molecular Mechanics Calculations
 - 5.3 CD and UV Spectroscopy and Cooperativity in Copolymers
 - 5.4 Thermo-Driven Helix–Helix Transition
 - 5.5 Poly(diarylsilane) Aggregates
 - 5.6 Circularly Polarized Photoluminescence
 - 5.7 Summary and Conclusions for Diarylpolysilanes
- References

1 HISTORICAL BACKGROUND AND INTRODUCTION

1.1 Optically Active Synthetic Polymers

Ever since the beginning of life on primitive Earth, biopolymers and biomolecules have essentially comprised optically active constituents because of the natural selection of *l*-amino acids and *d*-sugars. Although the origin of this biomolecular handedness is a long debated issue among biologists, chemists, physicists, and astronomers,^{1–5} it is accepted that our life is a consequence of the chemistry of homochiral biosubstances. Deoxyribonucleic acid (DNA) is a classic example of a chiral biopolymer. Its chirality is essentially characterized

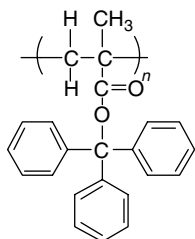
by (i) the incorporation of enantiopure chiral sugars connecting the achiral bases and (ii) the double-stranded, stiff helical conformation along with base pairing and base stacking. Concerning synthetic materials, the synthesis of single-strand stiff helical polymers with single screw sense and their quantitative conformational analysis by spectroscopic and physicochemical characterization have long been of interest in the areas of modern synthetic polymer stereochemistry and chiral chemistry.⁶⁻¹²

In the early studies of helical polymer stereochemistry two or three decades ago, outside of the realm of biologically related polymers, a few polymers were reported to adopt a predominantly single-screw-sense helical main chain in solution at room temperature. For example, poly(*t*-butyl isocyanides),¹³ poly(triphenylmethyl methacrylate),¹⁴ polyisocyanate,¹⁵ and poly- α -olefins¹⁶ were successfully obtained using specialized monomers and/or stereospecific catalysts under controlled polymerization conditions. The helical structures are maintained through side group interactions. Although many artificial optically active chromophoric polymers bearing chiral and/or bulky side groups or chiral additives have been investigated so far (Chart 4.1), including polyisocyanides,¹⁷ polyisocyanates,^{8,18} polyacetylenes,^{9,19} polythiophenes,²⁰ poly(*p*-phenylenevinylene)s,²¹ polycarbodiimides (or polyguanidines),²² polydiacetylenes,²³ polypyrroles,²⁴ polyanilines,²⁵ poly(*p*-phenylene)s,²⁶ polyfluorenes,²⁷ and polysilanes,²⁸⁻³² investigation of the relationship between global and local conformational structures, electronic structures, photophysical properties, and functionality are still ongoing subjects.

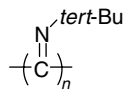
1.2 Optically Active Polysilanes

Even if an optically active polymer can be obtained from an enantiopure monomer, it is generally difficult to identify whether the main chain in the resulting polymer in solution at a given temperature has an enantiopure helical conformation with either purely *P* (plus, right-handed) or *M* (minus, left-handed) screw sense, or is composed of a collection of pseudodiastereomeric mixed helical motifs containing *P* and *M* screw senses. Fluorescence (FL) studies combined with circular dichroism (CD), ultraviolet (UV), and nuclear magnetic resonance (NMR) spectra of the main-chain constitute a powerful probe in identifying the main-chain chirality (screw sense, uniformity, and rigidity) of optically active polymers, since the photoexcited energy above the optical band gap should relax to the lowest energetic domain in a polymer chain and then be emitted from that domain.

Helical polysilanes whose optical activity is induced by chiral side chains are particularly suitable chiroptical polymers for elucidating the inherent nature of the polymer helix since they embody a fluorophoric and chromophoric main chain, exhibiting intense UV, CD, and FL bands due to the $\text{Si}\sigma\text{-Si}\sigma^*$



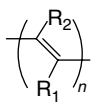
Poly(triphenylmethacrylate)

Poly(*t*-butylisocyanide)

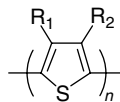
Inherently stable helix with achiral side groups



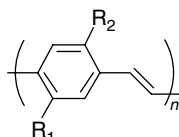
Polyisocyanate



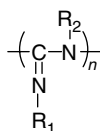
Polyacetylene



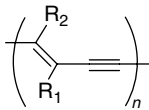
Polythiophene



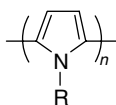
Poly(phenylenevinylene)



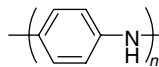
Polycarbodiimide



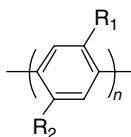
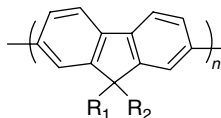
Poly(diacetylene)



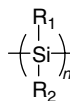
Polypyrrole



Polyaniline

Poly(*p*-phenylene)

Polyfluorene



Polysilane

Preferential screw sense helix induced by chiral side groups and/or chiral chemical influence

Chart 4.1 Typical optically active chromophoric polymers.

transition around 300–400 nm. Moreover, samples of any desired molecular weight can be obtained by fractional precipitation since the molecular weights of helical polysilanes are widely distributed in the range from 10^3 to 10^7 . Compared with other optically active π -conjugating polymers, these unique properties of helical polysilanes may permit a more straightforward analysis of

the helix–property–functionality relationship. Recently, it has been reported that the spectral characteristics of several helical polysilane homopolymers and copolymers, including intensity, spectral width, peak position, Stokes shift, and linewidth, vary sensitively with changes in the main-chain stiffness, population of *P*- and *M*-helical motifs and helix reversals, degree of polymerization, temperature, and solvent polarity.³²

Although main-chain chirality refers to both polymers with stereogenic centers in the main chain (configurational main-chain chirality) and polymers with main chains consisting of helical stereogenic bonds induced by chiral side groups or end termini (conformational main-chain chirality), in this chapter we mainly focus on polysilanes exhibiting the latter type of chirality.

1.3 Preparation of Polysilanes

The synthesis of polysilanes with a high degree of stereogenic control is still a challenging issue, with relatively reports,³³ in contrast to the well-documented and successful methods in organic polymer chemistry. Thus, most organopolysilanes, including poly(dialkylsilane)s, poly(alkylarylsilane)s, and poly(diarylsilane)s, are still prepared by the Wurtz-type condensation of the corresponding dichlorodiorganosilanes with sodium in inert solvent.^{28–32,33,34} This reaction is essentially identical to the procedure of Kipping more than 75 years ago,³⁵ as shown in Chart 4.2. Although the reaction is highly exothermic and usually carried out in hot toluene, an advanced modification of the reaction is to use a small amount of crown ether or diglyme as an additive, leading to significant improvement of polymerization yields, shortening of polymerization times, and modification of molecular weight distributions.^{29,36}

1.4 Helical Polysilane and Circular Dichroism Spectroscopy

In the case of synthetic optically active polymers, the intuitive meaning of a CD signal intensity is very similar to that of UV spectroscopy, with the additional dimension of the subtracted absorption between left and right circularly polarized light.³⁷ Absorption of light obeys the Beer–Lambert law, and thus CD intensity is defined as $\Delta\varepsilon = \varepsilon_L - \varepsilon_R = (A_L - A_R)/cl$, where $\Delta\varepsilon$ is the

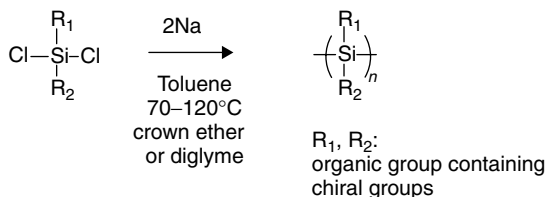


Chart 4.2 Wurtz-type reduction preparation of optically active polysilanes.

molar circular dichroism intensity, ϵ_L and ϵ_R are the molar absorptivities for left and right circularly polarized light, respectively, A_L and A_R are the absorbances of left and right light, c is the molar concentration per repeat unit, and l is the path length. CD bands are commonly referred to as either positive or negative Cotton effects and the peaks as extrema. It is now useful to express a ratio of the strength of CD (polarized) to strength of UV (unpolarized) absorptions. This is formalized in the dimensionless parameter, Kuhn's dissymmetry ratio, $g_{\text{abs}} = 2\Delta\epsilon/(\epsilon_L + \epsilon_R) = \Delta\epsilon/\epsilon$, where ϵ is the molar absorptivity per repeat unit. The dissymmetry ratio is also a function of the magnetic and electric dipole moments (m and μ , respectively) and the angle θ between them, such that $g_{\text{abs}} = 4 \cdot R/D = 4|m||\mu| \cos\theta(m^2 + \mu^2)^{-1}$, where R is the rotatory strength, D is the dipole strength, and both R and D are normalized to one repeat unit. For chromophoric helical polymers, this g_{abs} ratio provides information on the helical characteristics (screw pitch and sense, and diastereomeric and/or enantiomeric purities). For the polysilanes constituting the chromophoric main chain, the observation of CD signal thus indicates chirality in the main chain with a preferential screw sense helical conformation. The idealized CD and UV spectra for single P and M screw sense polymers (arbitrarily assigned to P - and M -CD signals) are illustrated in Figure 4.1a. However, particular attention should be paid to the interpretation of g_{abs} due to the possibility of segments of opposite screw sense and helix reversals. This is because, if absorptions of P and M occur at the same wavelength, the magnitude of g_{abs} would result in a smaller, or possibly zero value, as illustrated in Figure 4.1b.

Bisignate Cotton CD signals have two possible origins. First, in a polymer containing both P and M screw senses with slightly different absorption wavelengths, the positive and negative Cotton effects will be slightly offset with respect to each other, resulting in an apparent bisignate signal.^{28e} Second, for two adjacent chromophores, coupling between the stronger electronic dipole moments will occur to give bisignate split-type CD signals: the so-called exciton couplet signal.³⁸ This could be classified as either an intramolecular interaction in the same molecule at a kink or upon chain folding or an intermolecular interaction in aggregate phases. The sign of an exciton couplet bisignate signal affords a simple, direct method for determining the absolute configuration (right-handed or left-handed configuration) of the two interacting chromophores.

1.5 Preferential Screw Sense Helical Ordering of Polysilanes

Although the main-chain conformations of polysilanes have been described as random coil, 7_3 - (deviant helical), 15_7 - (transoid helical), and 2_1 - (all anti, planar) structures, it is now generally accepted that most polysilanes tend to adopt helical main-chain structures, regardless of side groups and temperature.³⁹ It

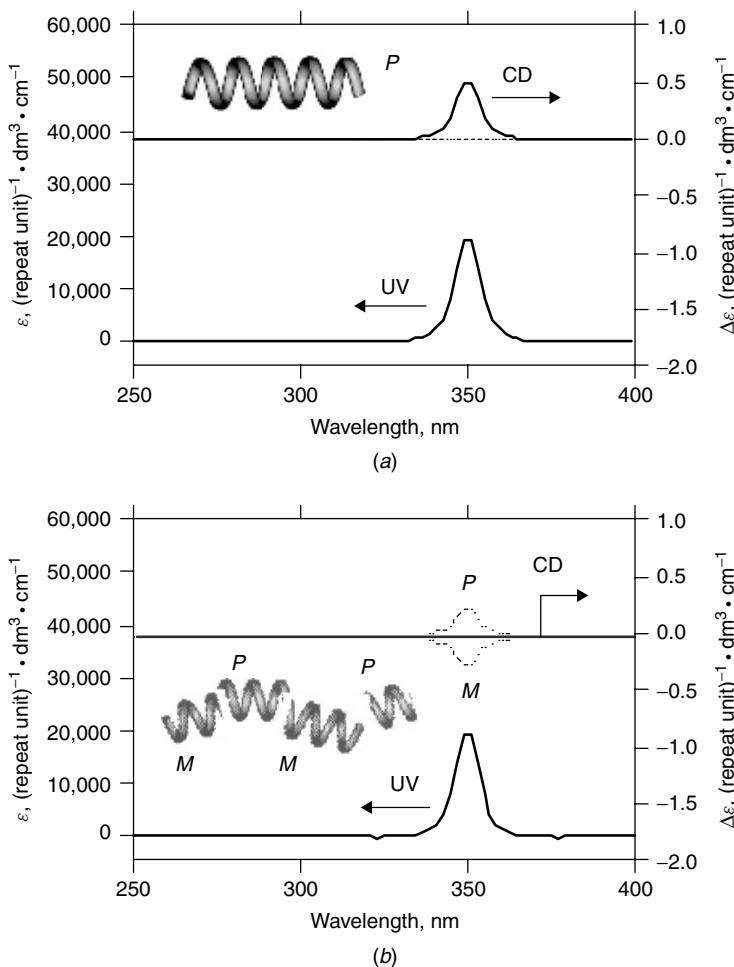


Figure 4.1 Illustrations of coincident CD and UV absorptions for chromophoric main chain with (a) *P* screw sense and (b) equal proportion of *P* and *M* screw senses.

was recently shown that poly(dichlorosilane) can have an all-anti conformation in the solid state by single-crystal X-ray diffraction.⁴⁰ However, the vast majority of polysilanes do not show any Cotton effects in their CD spectra, due to the adoption of equal numbers of *P* and *M* segments, resulting in an average racemic helical conformation and optical inactivity. If the helical main chain is driven by a chiral chemical influence to adopt a preferential screw sense with an enantiomeric excess of either *P* or *M* screw sense, a Cotton effect can be seen in the CD spectrum. Thus the interaction between side

groups, solvents, temperature, and helical main-chain structures of polysilane in isotropic solution may be probed by means of CD spectroscopy, combined with UV, FL, and ^{29}Si NMR spectroscopies and viscometry.

The main-chain chirality and helicity of polypeptides is inherent since the stereogenic centers are incorporated into the main chain. In poly(triphenylmethyl methacrylate) and polyisocyanide synthesized by screw-sense-selective polymerization, the helical structures are maintained through the stereochemical locking effect of bulky achiral side groups, while poly(triphenylmethyl methacrylate) contains stereogenic centers in the main chain associated with the tacticity.^{7a} In the cases of polyisocyanates, polyacetylenes, polythiophenes, polyphenylenevinylenes, polycarbodiimides, and polysilanes, their main-chain helical structures are induced by chiral side chains. Such optically active helical polymers can be obtained in a number of ways,^{7a,7b,8,9,32} including (a) polymerization with enantiopure chiral catalyst or initiator, (b) chiral doping of optically inactive polymers with enantiopure chiral ions, (c) separation of a racemic mixture of enantiomeric helices using chiral stationary-phase chromatography for nondynamic helical systems, (d) chiral complexation of achiral or racemic polymers with nonracemic chiral ligands, (e) postpolymerization functionalization with chiral moieties, (f) incorporation of enantiopure chiral end groups, (g) polymerization of nonracemic chiral monomers, (h) copolymerization of nonracemic chiral monomers with achiral monomers or with nonracemic monomers, and (i) circularly polarized irradiation of polymers bearing racemic sensitizers. In the case of optically active polysilanes, synthetic techniques from (e) to (h) have been carried out.

1.6 Correlation Between Global Conformation and Optical Characteristics of Polysilanes

The conformational mobility of a chromophoric main-chain polymer is often connected to its electronic structure. Therefore, changes in the UV–visible absorption spectra and/or chiroptical properties are spectroscopically observable as thermo-, solvato-, piezo-, or electrochromisms. It is widely reported that σ -conjugating polysilanes exhibit these phenomena remarkably clearly.³⁴ However, their structural origins were controversial until recently, since limited information was available on the correlation between the conformational properties of the main chain, electronic state, and (chir)optical characteristics. In 1996, we reported that in various polysilanes in tetrahydrofuran (THF) at 30°C, the main-chain peak intensity per silicon repeat unit, ϵ (Si repeat unit)⁻¹ · dm³ · cm⁻¹, increases exponentially as the viscosity index, α , increases.⁴¹ Although conventional viscometric measurements often requires a wide range of low-dispersity molecular-weight polymer samples, a size exclusion chromatography (SEC) machine equipped with a viscometric detector can afford

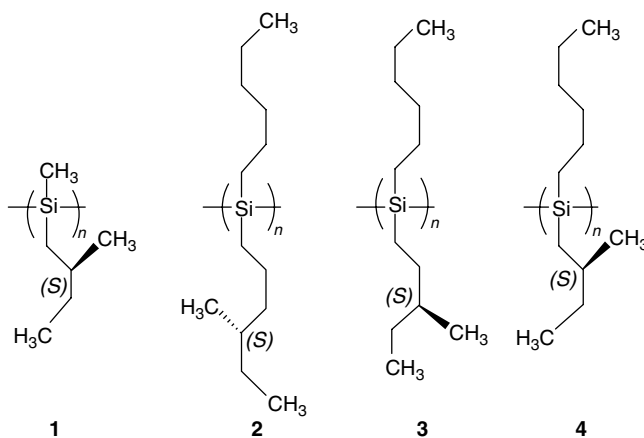
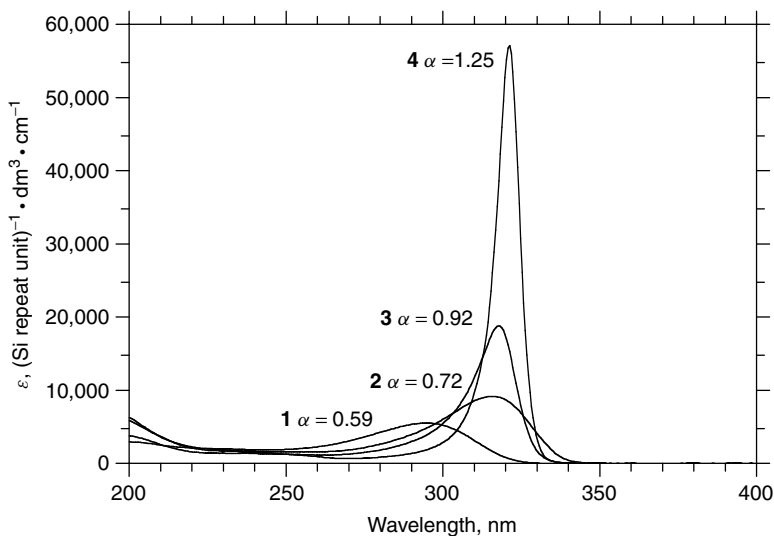


Figure 4.2 Comparison of UV absorption spectra of four optically active polysilanes in THF at 30°C: poly{methyl-(*S*)-2-methylbutylsilane} (**1**, α of 0.59), poly{*n*-hexyl-(*S*)-4-methylpentylsilane} (**2**, α of 0.75), poly{*n*-hexyl-(*S*)-3-methylpentylsilane} (**3**, α of 0.92), and poly{*n*-hexyl-(*S*)-2-methyl-butylsilane} (**4**, α of 1.25).

the intrinsic viscosity (η) as a function of the molecular weight of the polymer, M_w , in real time, from the Mark–Houwink–Sakurada plot.

Figure 4.2 shows the UV absorption spectra of four optically active poly(dialkylsilane)s bearing different chiral side groups in THF at 30°C.^{32a} It is evident that as the value of α increases from 0.59 to 1.25, the UV

absorption intensity increases, whereas the full width at half maximum (FWHM) decreases. These results led to the finding of the semiempirical relationship between the main-chain absorption characteristics and the global conformation of various polysilanes in solution.

Figure 4.3 shows a correlation between the values of ϵ , FWHM, and α of various poly(dialkylsilane)s and poly(alkylarylsilane)s in THF at 30°C.⁴¹ The polymers include seven optically active poly(dialkylsilane)s with 4 different types of chiral β -, γ -, or δ -branched alkyl substituent, 11 optically inactive poly(dialkylsilane)s with 6 different types of achiral β -, γ -, or δ -branched substituent, an optically inactive poly(dialkylsilane) with racemic chiral side groups, and 2 optically inactive poly(alkylphenylsilane)s. It is evident that, for the polysilanes whose λ_{\max} ranges from 290 to 352 nm, the value of ϵ increases exponentially with an increase in the α value, but on the other hand, the value of the FWHM decreases exponentially. Thus, the degree of σ -conjugation, global conformation, and UV absorption characteristics in polysilanes are controllable by the choice of side groups. For example, poly{methyl-(*S*)-2-methylbutylsilane} (**1**) has the most shrunken shape with $\alpha = 0.59$, whereas its longer *n*-alkyl chain derivative, poly{*n*-hexyl-(*S*)-2-methylbutylsilane} (**4**) takes a rigid rodlike conformation with $\alpha = 1.25$. Poly{*n*-hexyl-(*S*)-4-methylpentylsilane} (**2**) with $\alpha = 0.75$ has a random coiled conformation similar to conventional optically inactive polysilanes. Poly{*n*-hexyl-(*S*)-3-methylpentylsilane} (**3**) with $\alpha = 0.92$ is stiff (semirigid or semiflexible) and shows intermediate properties between **2** and **4**.

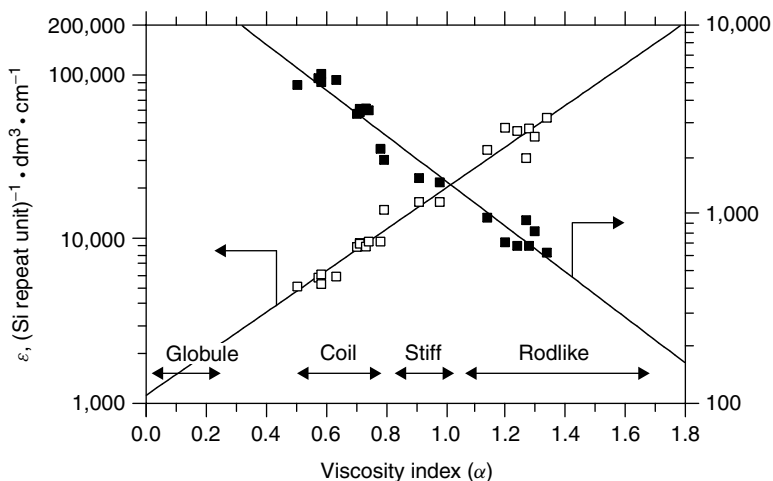


Figure 4.3 Correlation between UV peak intensity (ϵ), full width at half maximum (FWHM), and α of various poly(dialkylsilane)s and poly(alkyl(aryl)silane)s in THF at 30°C.

From the semiempirical ϵ - α -FWHM relationship, either value of ϵ or FWHM gives information on the degree of chain coiling in solution at a given condition and is useful for discussing the global conformational properties of polysilane in any condition. Also, the relationship assists in predicting the upper limit of the ϵ value for an ideal rigid rod polysilane. From the extrapolation of the ϵ - α relationship, it is expected that the ϵ value may reach $150,000 (\text{Si repeat unit})^{-1} \cdot \text{dm}^3 \cdot \text{cm}^{-1}$ since the maximum α value for the ideal rigid rod polymer is 1.7 – 1.8 ^{32a,41} and indeed the ϵ value for rodlike optically active poly(6,9,12-trioxatetradecyl-(*S*)-2-methylpropyl)silane) (**5**) in ethanol progressively increases from 42,000 with an FWHM of 800 cm^{-1} (8 nm) at 323 nm to 102,000 with a FWHM of 400 cm^{-1} (4 nm) at 318 nm when the temperature is cooled from 25 to -104°C .^{28k} This ϵ value, the highest among all polysilanes, is believed to correspond to an almost perfect rigid rod structure.

2 OPTICALLY ACTIVE DIALKYLPOLYSILANES

2.1 Preferential Screw Sense Homopolymers with Enantiopure Chiral Side Chains

From 1992–1994, two research groups independently reported the synthesis and chiroptical properties of poly(dialkylsilane)s bearing (*S*)-2-methylbutyl side groups. Copolymers were studied originally by Möller, Matyjaszewski, and co-workers,^{28a–c} and homopolymers were prepared by our group.^{28d–g, 28k–w} Since most of the fundamental features are clarified in a series of our works concerning poly(*n*-decyl-(*S*)-2-methylbutylsilane) (**6**) and its derivatives,^{28d,28f,28l,28q} we describe first our results concerning dialkyl homopolymers derived from monomers with enantiopure chiral alkyl substituents.

Polymer **6** showed the ideal UV, CD, and FL spectral characteristics of a rodlike chromophore and fluorophore due to the single-screw-sense helical structure induced by preferential side group interactions in dilute isooctane at 20°C . As is evident in Figures 4.4*a,b,c* (i) **6** exhibits a very intense, narrow UV absorption at 323 nm, with $\epsilon = 55,000 (\text{Si repeat unit})^{-1} \cdot \text{dm}^3 \cdot \text{cm}^{-1}$ and an FWHM value of 8 nm [ϵ is about six times greater and the FWHM narrower by one sixth than conventional random coil poly(dialkylsilane)s]; (ii) its CD spectral profile at 323 nm fits completely within the UV spectrum; (iii) the FL spectral profile at 328 nm is the mirror image of the UV and CD band profiles, and (iv) the FL anisotropy (FLA) value around the 323-nm UV–CD bands reaches the theoretical limit of 0.4 expected for the random distribution of a rigid rod chromophore being collinear with the fluorophore in a rigid medium. These novel UV–CD–FL characteristics of **6** could be the first demonstration

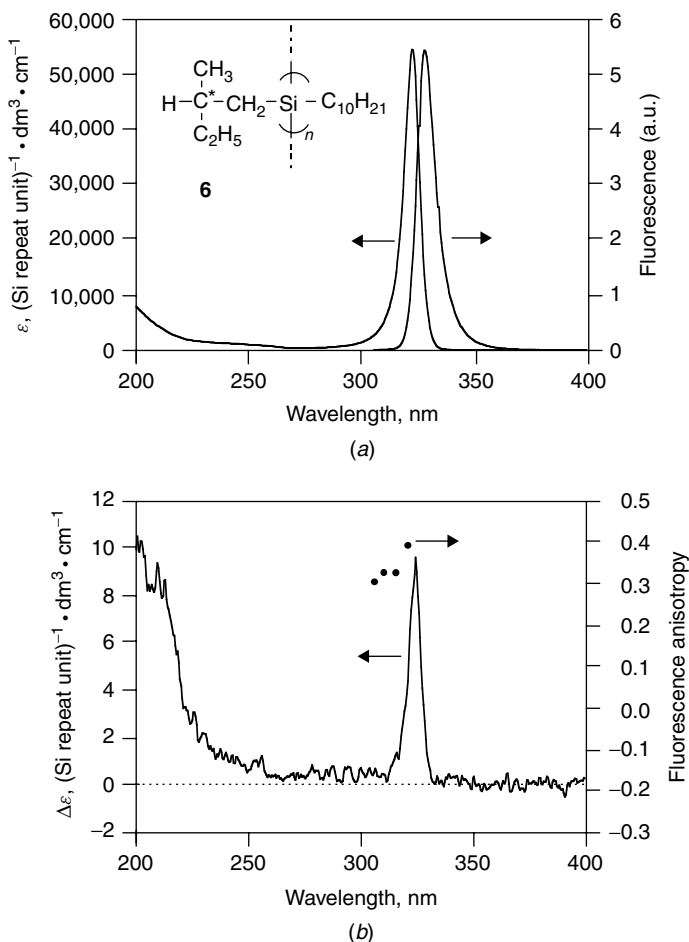
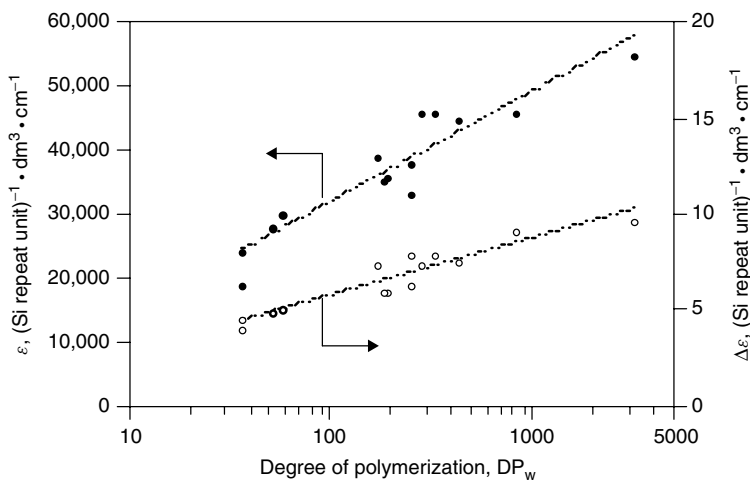


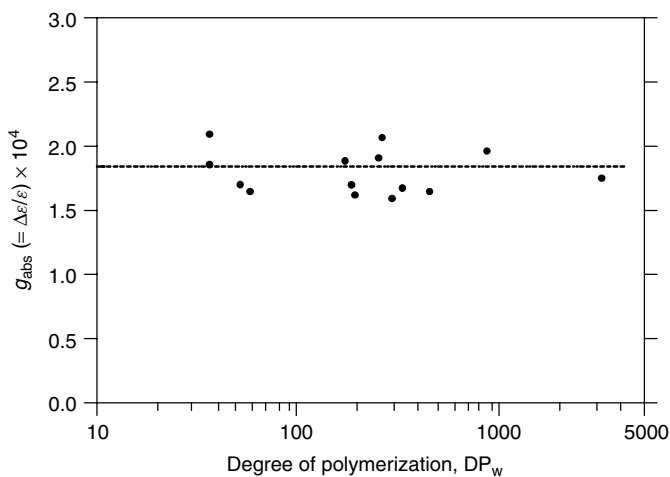
Figure 4.4 (a) UV and CD spectra and (b) FL spectrum and FL anisotropy of poly(*n*-decyl-(*S*)-2-methylbutylsilane) (6, $M_w = 5,330,000$, $M_n = 4,110,000$, $\alpha = 1.35$ in THF at 30°C) in isooctane at 20°C.

of uniqueness among other optically active polysilanes and optically active organic polymers.

Additionally, in a series of poly(*n*-alkyl(*S*)-2-methylbutylsilane)s, the UV, CD, FL, and FL excitation (FLE) spectral characteristics in isooctane at 20°C were investigated in more detail to clarify the effects of the *n*-alkyl side group and main-chain length.^{28f} It was found that the rigid rodlike helical structure was maintained even if the *n*-alkyl side group length was increased from *n*-propyl to *n*-dodecyl and the main-chain length is increased from 20



(a)



(b)

Figure 4.5 Characteristics of UV and CD intensities at around 323 nm in isoctane at 20°C of 14 samples isolated from 9 poly(*n*-alkyl(*S*)-2-methylbutylsilane) derivatives as a function of the degree of polymerization (DP_w) in isoctane at 20°C: (a) ϵ and $\Delta\epsilon$ and (b) the dissymmetry ratio.

to 3000 Si units. This idea was supported by the unique UV–CD–FL–FLE spectroscopic features characteristic of **4** and the fact that the g_{abs} value of $\sim 1.9 \times 10^{-4}$ was almost independent of both *n*-alkyl side group length and Si main-chain repeat length, as is evident in Figure 4.5b. On the other hand, the peak intensities of UV and CD bands at 323 nm increased nonlinearly

as the main-chain repeat number increased, as shown in Figure 4.5a, while the respective values of the UV peak wavelength and FWHM of the band converged to limiting values of 322 and 8 nm in isoctane at 20°C.

It is noted that the dipole strength of the UV absorption band is independent of the *n*-alkyl side group length and main-chain repeat numbers. Actually, integration of the 323-nm UV absorption band of the poly(*n*-alkyl(*S*)-2-methylbutylsilane) derivatives depends very weakly on the repeat numbers. These results led to the important idea that in the case of optically active polysilanes, the g_{abs} value should be used to characterize helical parameters such as the population of *P* and *M* motifs and their regularity, rather than the values of $\Delta\epsilon$ or optical rotation. Recently, it was determined that the persistence length q of **4** is as large as 85 nm in isoctane at 20°C by Terao et al.²⁸ⁿ This high q value is greater than that of polyisocyanate ($q = 76$ nm) bearing β -branched (*R*)-2,6-dimethylheptyl groups.^{18s}

2.2 Imaging of Rodlike Polysilane Single Molecule

Although chain dimensional parameters such as persistence length in solution can be evaluated by well-established light-scattering and viscometric techniques, molecular imaging of individual polymer chains is an important issue in the design and control of the inherent optoelectronic properties of functional polymers and nanomaterials. Fortunately, recent advances in atomic force microscopy (AFM) and scanning tunneling microscopy (STM) have now enabled the direct observation of single-molecule images of such insulating polymers as cyclic DNAs, random coiled polystyrene–block–poly(methyl methacrylate) on mica, monolayer images of soluble poly(*para*-phenylene) on a gold surface, and twinned chiral polyacetylene placed on a highly oriented pyrolytic graphite substrate.⁴²

Ebihara et al. observed the first molecular AFM images of a single molecule of a high-molecular-weight sample ($M_w = 5,330,000$, $M_n = 4,110,000$) of **6** deposited on an ultraflat sapphire surface.^{43a} It was found that, although the total molecular contour length of **6** reached about 2000 nm in length, the chain consisted of several segments separated by kinks. The individual molecular image appears to indicate rodlike structures accompanied by slight structural fluctuations. The longest segment length between the kinks reached about 800 nm and the shortest was about 150 nm. Such very long segment structures might be responsible for the unique UV–CD–FL spectroscopic features of **6** and its *n*-alkyl derivatives. Recently, Furukawa, Ebata, and co-workers successfully obtained a similar AFM molecular image of **6**, one end terminus of which had been chemically immobilized on a silicon substrate, as well as of other flexible polysilanes immobilized on solid substrates.^{43b–e}

2.3 Optically Active Polysilanes with Diastereomeric Helicities Containing Opposite Screw Senses and Different Screw Pitches

In a series of poly(alkyl(*S*)-2-methylbutylsilane)s, only **1** exhibited a very different CD spectrum around the UV absorption at 300 nm^{28d,28e}. An apparent bisignate CD band with positive and negative signals was observed, as shown in Figure 4.6a. From a deconvolutional analysis of the CD, and UV spectra, it was considered that both tight *P*- and loose *M*-helical segments may coexist in

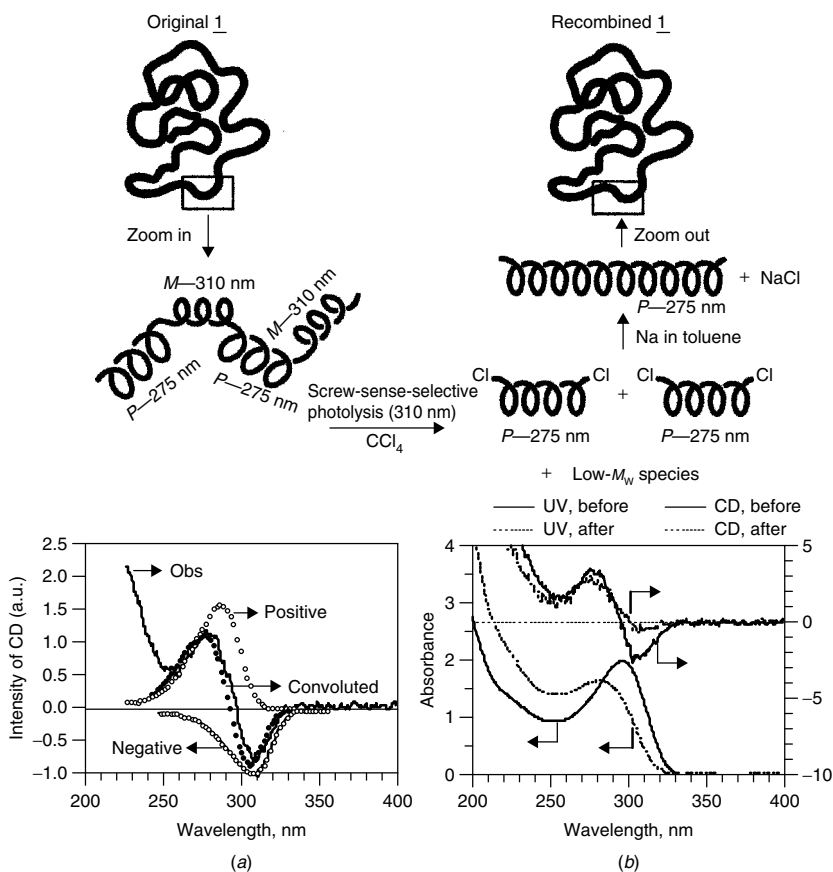


Figure 4.6 (a) Original and deconvoluted CD spectra of original **1**, (b) change in UV and CD spectra of original and recombined **1** in isoctane at 25°C using cut-and-paste technique. Key ideas for recombination of **1** with single screw sense from original **1** with diastereomeric helicities with opposite screw sense by cut-and-paste technique, featuring (i) *M* screw-sense-selective photolysis in CCl_4 , (ii) formation of *P* screw sense telomers with Si-Cl termini, and (iii) Na-mediated recondensation of telomers in hot toluene.

the same main chain of **1** in a diastereomeric helical block containing opposite screw senses and different screw pitches. From the Mark–Houwink–Sakurada plot of **1**,⁴⁴ the α value of 0.59 in THF at 30°C is typical of a coiled global conformation. Based on this assumption, a screw-sense-selective “cut-and-paste” experiment allowed a modified **1** to be recombined containing an almost single *P* screw sense.^{28e}

The cut-and-paste technique has two steps: (i) *M* (or *P*) screw-sense-selective photolysis at the longer λ_{\max} region in CCl₄ to form *P* (or *M*) screw sense telomers with Si–Cl termini, and (ii) Na-mediated recondensation of the telomers in hot toluene. Formation of an optically active helical polysilane with an almost single screw sense was evidenced by significant changes in the UV and CD spectra after the cut-and-paste technique, as shown in Figure 4.6*b*.

This knowledge and understanding may be helpful to characterize local conformations of other optically active polysilanes in solution. For example, poly(methyl-(*-*)- β -pinanylsilane) [(+)-**7**; $M_w = 10,200$] prepared by Shinohara and co-workers,²⁸ⁱ showed a bisignate CD band at 280 and 303 nm, associated with a broad UV absorption at 300 nm in chloroform at 15°C. Since the spectroscopic features are quite similar to those of **1**,^{28d,28e} it is possible that the main chain in **7** may contain diastereomeric helical motifs with opposite screw senses and different screw pitches.

2.4 Copolymers with Preferential Screw Sense and “Sergeants-and-Soldiers” Principle

The most striking cooperative feature concerning preferential screw sense helical ordering in optical active copolymers is the “sergeants-and-soldiers” phenomenon named by Green et al.^{18b} In this effect, a minority of enantiopure chiral side groups determines the overall screw sense (*P* or *M*) of a helical main chain bearing a majority of achiral side groups. Since the first report of this phenomenon in poly- α -olefin copolymers by Pino et al.,^{8b,16a} it has also been established in poly(alkyl isocyanate)s^{8c,18b,18q} and poly(aryl isocyanate).^{18p}

In the field of polysilane chemistry, although Möller, Matyjaszewski, and co-workers originally prepared two types of copolymers, poly[[*bis*{(*S*)-2-methylbutyl}silane]-*co*-(*di-n*-pentylsilane)] (**8**) and poly[[*bis*{(*S*)-2-methylbutyl}silane]-*co*-{(*S*)-2-methylbutyl-*n*-pentylsilane}] (**9**),^{28b,28c} these copolymers revealed an almost linear increment of CD intensity around 320 nm in cyclohexane with an increase of the molar fraction of the silicon repeat unit with chiral side chains, indicating no significant sergeants-and-soldiers phenomenon due to very limited chiral side-chain interactions.

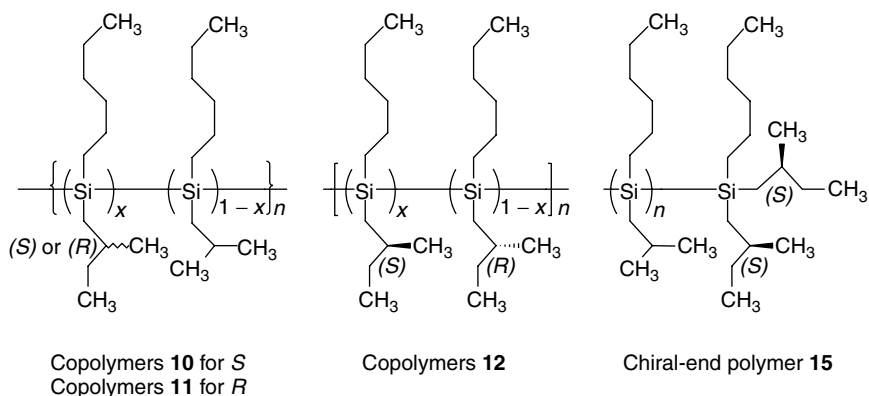


Chart 4.3 Chemical structure of poly(dialkylsilane)s (**10–12** and **15**) comprising chiral and achiral groups.

On the other hand, noticeable cooperative preferential screw sense induction was reported in rodlike polysilane copolymers bearing (*S*)-2-methylbutyl and 2-methylpropyl groups (**10**) and (*R*)-2-methylbutyl and 2-methylpropyl groups (**11**) in isooctane (Chart 4.3). Since the UV–CD spectral features of the polysilane copolymers are almost identical with those of **4–6** and the λ_{\max} varies sensitively with changes in the molar fraction of chiral substituents and temperature,^{28g} the copolymer systems are suitable for testing the sergeants-and-soldiers phenomenon by their CD–UV spectra.

Figure 4.7 compares the UV and CD spectra of homopolymer **4** and copolymer **10** with 10 mol % of (*S*)-2-methylbutyl and 90 mol % of 2-methylpropyl side groups in isooctane at -5°C . The UV–CD spectra of **10** are almost identical to those of **4**, with the CD signal profile matching the corresponding UV absorption, except for their λ_{\max} values. As expected, the UV and CD spectra of copolymers **11** bearing (*R*)-2-methylbutyl side groups reveal almost identical features to those in copolymers **10**, except for the sign of the CD band.

The g_{abs} values in copolymers **10** and **11** as a function of the molar fraction of *n*-hexyl-(*S*)-2-methylbutylsilane or *n*-hexyl-(*R*)-2-methylbutylsilane are plotted in Figure 4.8a. It is apparent that only 5–10 mol % chiral moieties in **10** and **11** almost completely determines the screw sense. Moreover, even as little as 0.6 mol % of chiral side groups induces a marked preferential screw sense helical conformation in the copolymers at temperatures below 0°C . We ascribe the reason for the lack of sergeants-and-soldiers effect in **8** and **9** to the greater flexibility of the di-*n*-pentylsilane moieties, since the α value of poly(di-*n*-pentylsilane) may be similar to that of random coil poly(di-*n*-butylsilane) ($\alpha \sim 0.71$) and poly(di-*n*-hexylsilane) ($\alpha \sim 0.74$).⁴¹ Structural

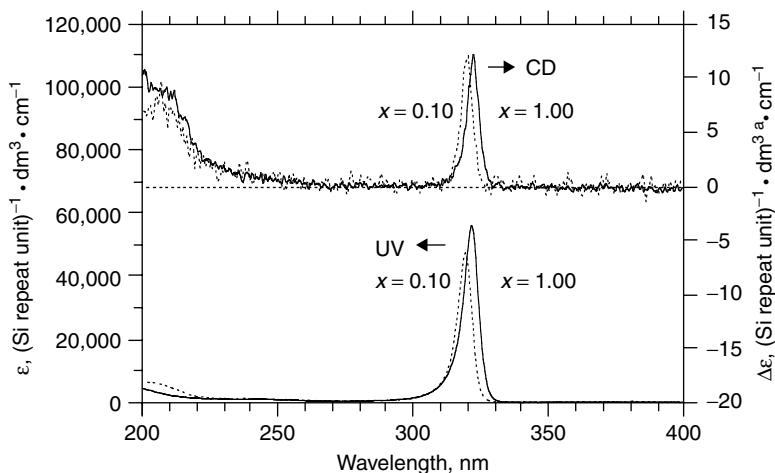


Figure 4.7 UV and CD spectra of polysilane homopolymer **4** (solid lines) and copolymer **10** (dotted lines) containing 10 mol % of (*S*)-2-methylbutyl and 90 mol % of 2-methylpropyl groups in isoctane at -5°C .

similarity between chiral and branched achiral side groups and stiffer main chains in copolymer systems may be needed to reveal effective sergeants-and-soldiers cooperativity.

The λ_{max} values of **10** and **11** as a function of the molar fraction of *n*-hexyl(*S*)-2-methylbutylsilane or *n*-hexyl(*R*)-2-methylbutylsilane are shown in Figure 4.8*b*. The value of λ_{max} redshifts slightly, but progressively, with increase in the fraction of the silane with chiral side chains in the copolymers. These features are considered to be associated with a decrease in screw pitch of the main chain because the $\text{Si}\sigma\text{-Si}\sigma^*$ absorption of polysilanes is shown from ab initio calculations⁴⁵ to blueshift progressively with change in the main chain dihedral angle from planar all-anti (180°) to 4_1 helix (60°).

2.5 Copolymers with Preferential Screw Sense and “Majority Rule” Principle

Another significant cooperativity effect in preferential helical screw sense optically active copolymers is the “majority rule” phenomenon.^{18h,18q} In this case, the screw sense of a helical main chain with unequal proportions of opposite chirality enantiopure chiral side groups is controlled by the enantiomeric excess only. Since this phenomenon was first reported from poly- α -olefins made of vinyl co-monomers bearing nonenantio pure chiral moieties by Green et al.^{8b} and Pino et al.,^{16b} this majority rule has been established in

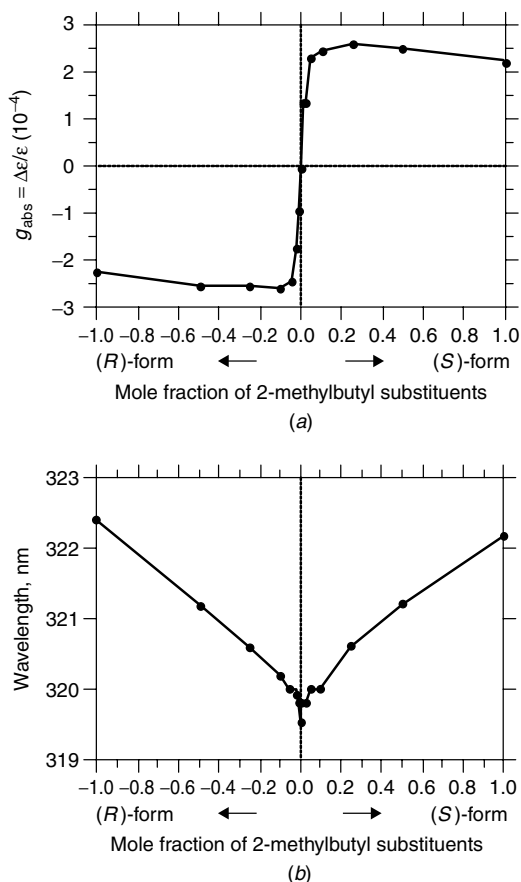


Figure 4.8 Values of (a) dissymmetry ratio (g_{abs}) and (b) λ_{max} in a series of copolymers **10** and **11** as function of mole fraction of *n*-hexyl-(*S*)-2-methylbutylsilane and *n*-hexyl-(*R*)-2-methylbutylsilane in isoctane at -5°C .

stiff polyisocyanates bearing nonenantio pure chiral side chain.^{8c,18h,18q} Similarly, noticeable majority rule effects were also found in rodlike polysilane copolymer **12** containing (*S*)- and (*R*)-2-methylbutyl side groups in different proportions.^{28g,32a,32b}

A comparison of the UV and CD spectra between homopolymer **4** and copolymer **12** with 60 mol % of (*S*)- and 40 mol % of (*R*)-2-methylbutyl side groups [20% (*S*)-*ee*] in isoctane at -5°C is shown in Figure 4.9. The UV and CD spectra of **12** are almost identical to those of **4**, the CD peak profile almost matching the corresponding UV absorption, including their λ_{max} values. As expected, the UV and CD spectra of the corresponding (*R*)-rich **12**

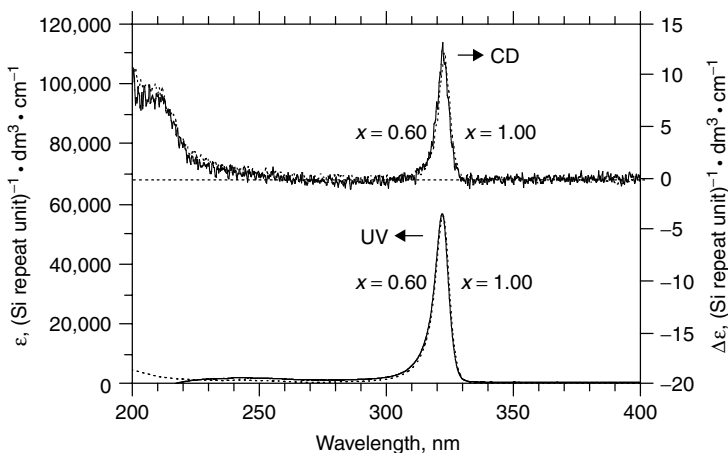


Figure 4.9 UV and CD spectra of polysilane homopolymer **4** (solid lines) and copolymers **12** (dotted lines) containing 60 mol % of *n*-hexyl-(*S*)-2-methylbutylsilane and 40 mol % of *n*-hexyl-(*R*)-2-methylbutylsilane in isoctane at -5°C .

copolymer containing 40 mol % of (*S*)- and 60 mol % of (*R*)-2-methylbutyl side groups [20% (*R*) *ee*, where *ee* is enantiomeric excess] exhibit almost identical features to those in the (*S*)-rich **12** copolymer, except for the sign of the CD band.

As shown in Figure 4.10a, from the plot of the g_{abs} values of **12** as a function of the molar fraction of *n*-hexyl-(*S*)-2-methylbutyl or *n*-hexyl-(*R*)-2-methylbutylsilane, it is evident that only 20% *ee* of (*R*) or (*S*)-2-methylbutyl group in **12** completely determines the overall screw sense and even only 6% *ee* of (*R*) or (*S*)-2-methylbutyl group induces a significant preferential screw sense helical conformation in the copolymers. The structural identity between the (*S*)- and mirror image (*R*)-chiral side group and stiffer main chain in the copolymer systems appear essential to induce an effective majority rule phenomenon. Also, as shown in Figure 4.10b, from the plot of the λ_{max} value of **12** as a function of the molar fraction of *n*-hexyl-(*S*)-2-methylbutylsilane or *n*-hexyl-(*R*)-2-methylbutylsilane, it is seen that the value of λ_{max} is very weakly blueshifted, though the enantiopurity of *n*-hexyl-2-methylbutylsilane changes from 100 to 0% *ee* in the copolymers, indicating minimal change in the screw pitch of the main chain, in accordance with the ab initio calculation.⁴⁵

2.6 Enantiopure Chiral Termini Effects and Sergeants-and-Soldiers Cooperativity

Kira and co-workers described the first single-crystal X-ray structure, CD, and UV spectra of hexasilane oligomers with preferential screw sense induced by

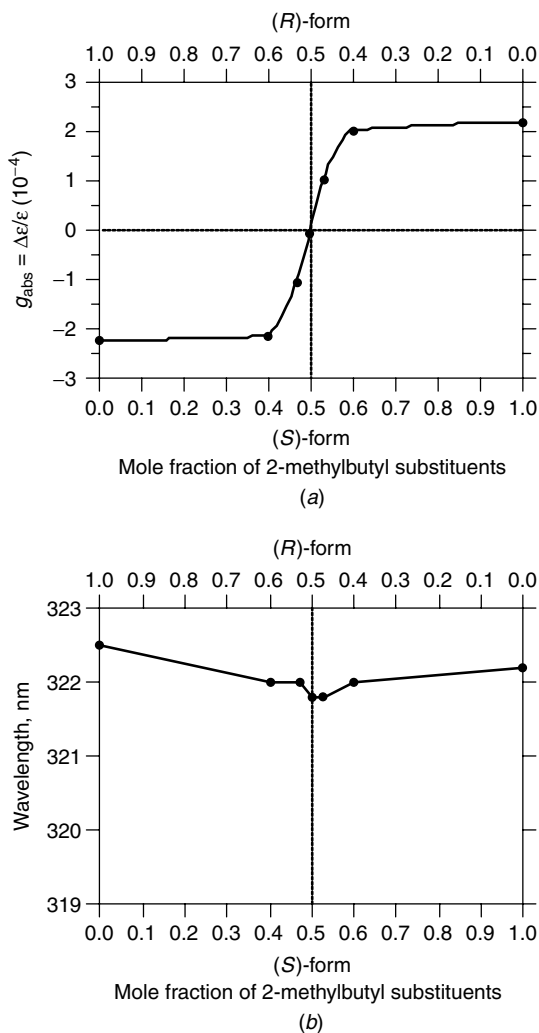


Figure 4.10 Values of (a) dissymmetry ratio and (b) λ_{max} in a series of copolymers **12** as function of mole fraction of *n*-hexyl-(*S*)-2-methylbutylsilane and *n*-hexyl-(*R*)-2-methylbutylsilane in isoctane at -5°C .

cooperativity between achiral side chains and chiral chain termini (**13**).^{28h} They also extended the cooperativity system to high-molecular-weight poly(*di-n*-hexylsilane) with the same chiral termini (**14**).^{28j} Their works provide important experimental evidence for the adoption of a 15_7 helical conformation in solution at lower temperature for **14**, which was long believed to adopt

an all-anti conformation in solution.^{34,39} Apparent bisignate Cotton effects observed for the oligomers below 153 K and the polymers below 233 K are interpreted in terms of an exciton couplet for two spatially interacting polysilane chromophores.^{28j} They considered that **14** at low temperatures is composed of loose helical segments divided by one-handed approximately 90° preferential kinks.

We also reported an intriguing chiral termini effect in rodlike poly(*n*-hexyl-(2-methylpropyl)silane) with (*S*)-2-methylbutyl termini (**15**).^{28g} Although the value of g_{abs} is only $+1 \times 10^{-5}$, which indicates a very weak preferential screw sense in **15**, it is noted that the preferential screw sense of **15** was opposite to that of **4**, bearing the same (*S*)-2-methylbutyl side groups.^{28d,28f,28k}

2.7 Switching Preferential Screw Sense by Helix–Helix Transition

The design and controlled synthesis of helical polymers with dynamic properties are currently challenging issues. Successful polymer systems include polyisocyanates and certain recently established polyacetylenes bearing aryl and alkyl ester moieties. However, the most striking dynamic property of a helical polymer may be a helix–helix (*PM*) transition in response to external physical and/or chemical stimuli, affording almost mirror image helical motifs. Although biochemists originally discovered this phenomenon almost three decades ago and recently in synthetic DNA (driven by a change in NaCl concentration),⁴⁶ poly(*l*-aspartic acid ester)s (driven by changes in temperature and organic acid),⁴⁷ and a calf thymus DNA,⁴⁸ several artificial polymers^{18n,18t,19g,19k,19l,19n,20c,20d,49–51} have now also been found to undergo the *PM* transition. This might be due to limited knowledge and understanding of the nature of *PM* transition characteristics. Recently, we found that certain poly(dialkylsilane) homopolymers and copolymers^{28m,28q,28u,28w,28x} and a poly(diarylsilane) copolymer^{30b,30c} undergo a thermo-driven *PM* transition in solution by controlling their composition and side chains. This section highlights the poly(dialkylsilane)s^{28m} for quantitatively discussing thermo-responsive *PM* transition characteristics.

Poly{(*S*)-3,7-dimethyloctyl-3-methylbutylsilane} (**16**) may be classified as a rodlike helical main-chain polymer bearing enantiopure alkyl side groups. The polymer affords an intense, narrow UV absorption band, completely matching the corresponding CD and FL band mirror image profiles, similar to the rigid rodlike helical polysilanes described above. The occurrence of the *PM* transition is spectroscopically detectable as an inversion of the CD band profile. Figures 4.11*a* and *b* compare the CD and UV absorption spectra of **16** at -40 and -5°C and of poly{(*S*)-3,7-dimethyloctyl-2-methylpropylsilane} (**17**) at -82 and $+80^\circ\text{C}$ in isoctane. The positive-signed CD spectrum of **16** with λ_{ext} of 320 nm at -40°C is almost the inverse of the negative-signed CD spectrum

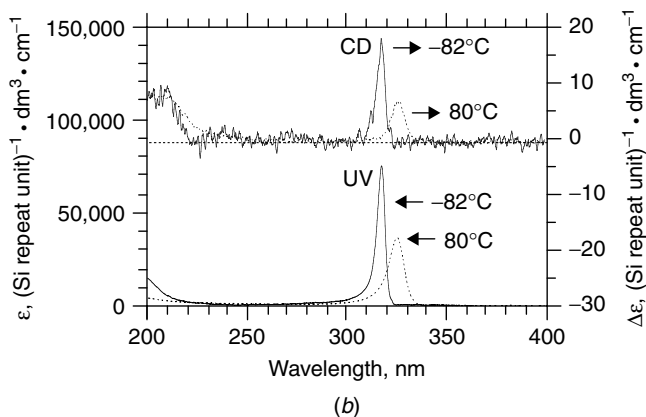
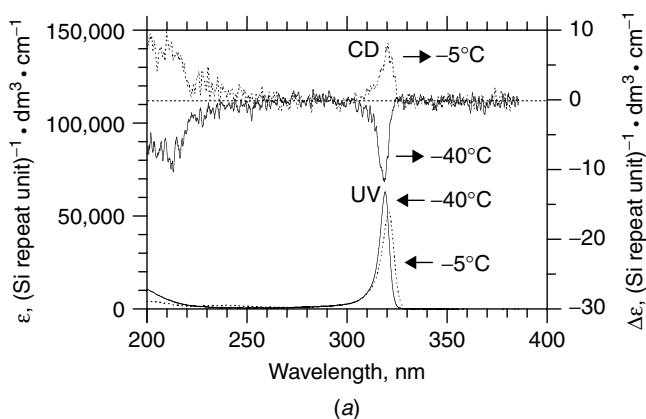


Figure 4.11 (a) CD and UV absorption spectra of poly{(*S*)-3,7-dimethyloctyl-3-methylbutylsilane} (**16**, $M_w = 1.6 \times 10^6$ and $M_w/M_n = 1.53$) at -40°C (solid line) and -5°C (dotted line) in isooctane; (b) CD and UV absorption spectra of poly{(*S*)-3,7-dimethyloctyl-2-methylpropylsilane} (**17**, $M_w = 4.2 \times 10^4$ and $M_w/M_n = 1.51$) at -82°C (solid line) and 80°C (dotted line) in isooctane.

with λ_{ext} of 322 nm at -5°C . It is evident that **16** undergoes a *PM* transition between the two temperatures, though the helical motifs at -40 and -5°C are energetically and spectroscopically nonequivalent. On the other hand, neither **17** nor its mirror image poly{(*R*)-3,7-dimethyloctyl-2-methylpropylsilane} (**18**) undergo any such inversion of the CD spectra in isooctane between -90 and $+80^\circ\text{C}$.

Moreover, introduction of additional silane with chiral/achiral side groups to the **16**-based copolymers permits fine control of the transition temperature (T_c) between -64 and $+79^\circ\text{C}$. These results may open new methodologies in

designing *PM* transition polymers that may be promising in diverse screw-sense-related applications, such as thermo-driven chiroptical switch and memory, a thermo-driven switching chiral separation column, and molecular recognition ability.

Polysilanes **6**, **16**, and **17** are thought to adopt rodlike 7_3 -helical conformations (dihedral angle of about 150° or 210°) in solution, since these λ_{\max} near 320 nm are almost identical to that of poly(di-*n*-butylsilane) (**19**) adopting a 7_3 -helical form in the solid state.³⁴ The rodlike behavior of these materials is evidenced by the high values of α ; for **16** and **17** in CHCl_3 at 30°C , the α values reached 1.11 and 1.29, respectively, and for **6** in THF at 30°C , the α value was 1.35. However, **16** might be more flexible than **17** (and **18**), according to the following ^{29}Si NMR results.

Figure 4.12 displays the ^{29}Si NMR spectra of **16**, **17**, and **6** in CDCl_3 at 30°C . Since these polysilanes have two different types of side groups attached to the main chain, they may essentially comprise isotactic (*it*-), syndiotactic (*st*-), and heterotactic (*ht*-) sequences. Nevertheless, both **16** and **17** exhibit single ^{29}Si NMR signals near -23 to -25 ppm, implying mainly *it*- or *st*-sequences. On the other hand, **6** exhibits a major signal at -22.2 ppm and a weak signal at -23.1 ppm, suggesting an almost single configurational sequence with a minor fraction of another sequence in the same main chain. It is noted that a remarkable difference in ^{29}Si NMR linewidth ($\Delta\nu_{1/2}$) between **16**, **17**, and **6** can be seen. The greater flexibility of **16** compared to **17** and

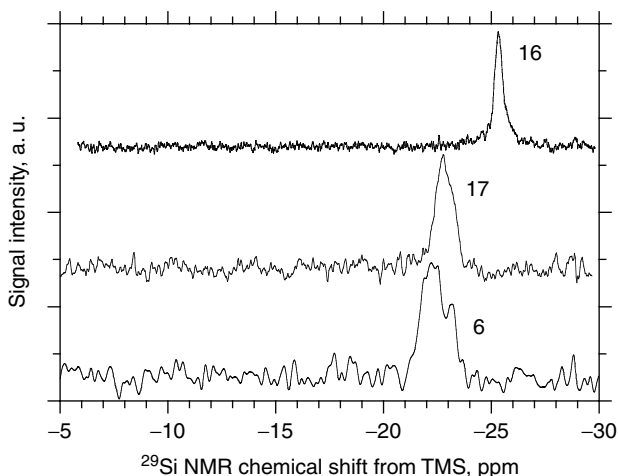


Figure 4.12 Comparison of ^{29}Si NMR spectra between (top) poly{(S)-3,7-dimethyloctyl-3-methylbutylsilane} (**16**), (middle) poly{(S)-3,7-dimethyloctyl-2-methylpropylsilane} (**17**), and (bottom) poly(*n*-decyl-(S)-2-methylbutylsilane) (**6**) in CDCl_3 at 30°C .

6 is suggested by the narrower $\Delta\nu_{1/2}$: for **16**, $\Delta\nu_{1/2} = 29$ Hz at -25.3 ppm, while for **17**, $\Delta\nu_{1/2} = 65$ Hz at -22.7 ppm and for **6**, $\Delta\nu_{1/2} = 90$ Hz at -22.3 ppm. Although homopolymers bearing two γ -branched side groups per repeat unit can undergo a *PM* transition, polymers with a combination of β - and nonbranched side groups do not undergo a *PM* transition. Thus, subtle modification in the side groups of polysilanes definitively determines the capability of the *PM* transition and CD inversion characteristics.

Considering the temperature dependence of the λ_{ext} , λ_{max} , and intensities of $\Delta\varepsilon$ and ε of **16** and **17** in isoctane, it is apparent that the λ_{ext} and λ_{max} values of **16** and **17** linearly blueshift from 325 to 318 nm, and the ε values of **16** and **17** increase monotonically from 40,000 to 80,000, as the temperature decreases from $+80$ to -82°C . The former may be ascribed to a slight decrease in screw pitch, deviating from an ideal 7_3 -helical structure, and the latter is due to a progressive increase in dimension of the main chain. However, the $\Delta\varepsilon$ value of **16** monotonically increases from ca. 3 at 80°C to ca. 8 at -5°C , goes to zero abruptly at -20°C , and then decreases monotonically to ca. -15°C , while that of **17** monotonically increases from 7 to 18°C . Mutual cancellation of positive and negative CD signals is indeed occurring at T_c , resulting from an equal population of *P*- and *M* motifs with the same λ_{ext} and λ_{max} values.

To quantitatively characterize the *PM* populations using chiroptical characteristics, it may be useful to use the g_{abs} values of **16** at each temperature with reference to the regression curve of these g_{abs} values in **17**, which is assumed to adopt a purely *P* 7_3 -helical structure, instead of the $\Delta\varepsilon$ value. The analysis is based on the assumption that the weak temperature dependence of the g_{max} for **17** is due to a minute modification in the screw pitch of the *P* helix, rather than any formation of the *M*-helical motif.

Figure 4.13 plots the temperature dependence of the dissymmetry ratios and the *PM* populations in three different M_w samples of **16** in isoctane based on the above analysis. It is evident that although the *PM* populations in the three samples depend slightly on M_w , a steep *PM* transition clearly occurs at -20°C . The highest M_w polymer contains 12% *P* and 88% *M* motifs at -90°C , while at 25°C these values are 84% *P* and 16% *M* motifs. The medium and lower M_w samples contain 15% *P* and 85% *M* motifs at -90°C , while at 25°C these values are 76% *P* and 24% *M* motifs. However, the transition temperature width (ΔT_c) tends to slightly broaden as M_w decreases. It is concluded that the *PM* transition characteristics including T_c , ΔT_c , and *PM* populations weakly depend on the molecular weight, and the *PM* transition characteristics may vary with segment length, for segments shorter than 50 silicon repeat units and/or the nature of the chiral termini.

Although the origin of the *PM* transition remains obscure, the differences in potential energy curves and main-chain stiffness between **16** and **17** may be critical. Figure 4.14 shows the main-chain dihedral angle dependence on the

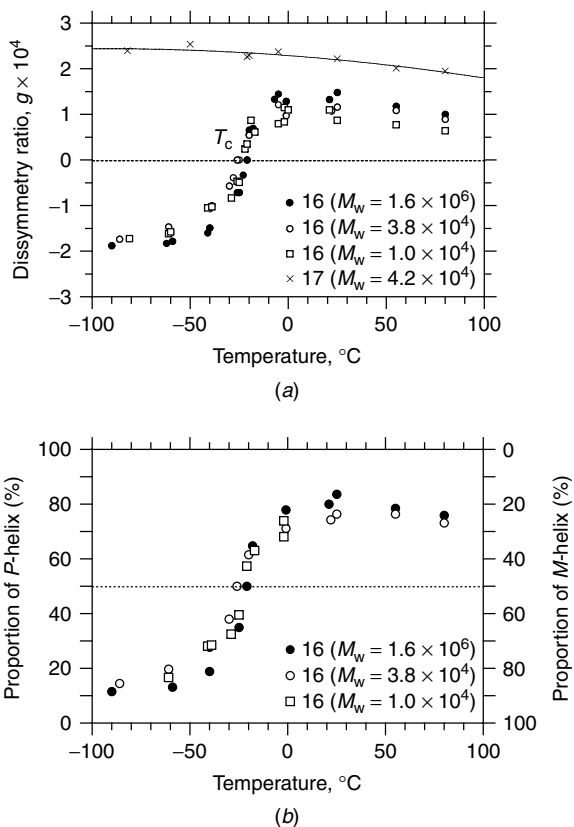


Figure 4.13 (a) Temperature dependence of dissymmetry ratios of poly{(*S*)-3,7-dimethyloctyl-3-methylbutylsilane} (**16**) (three different M_w samples) and poly{(*S*)-3,7-dimethyloctyl-2-methylpropylsilane} (**17**) (a purely *P* helix) in isoctane. (b) Temperature dependence of *P* and *M* populations of **16** in isoctane by reference to the regression curve of g_{abs} values in **17**.

potential energy of (*S*)-3,7-dimethyloctyl-3-methylbutylsilane (31 repeat units with hydrogen termini) (**20**) and (*S*)-3,7-dimethyloctyl(2-methylpropyl)silane (31 repeat units with hydrogen termini) (**21**) for their *it*- and *st*- sequences, respectively. An *it*-**20** clearly shows a double-well potential curve, that is, two local energy minima with almost enantiomeric helices at dihedral angles of *P* 157° and *M* 210° . The global minimum *M* is slightly more stable than that of *P* by about 0.67 kcal per repeat unit, and the barrier heights of the *M* and *P* screw senses are 2.3 and 1.7 kcal per repeat unit, respectively.

It is noted that *st*-**20** also has a similar double-well potential curve at about *P* 160° and *M* 200° dihedral angles and the global minimum *M* is slightly

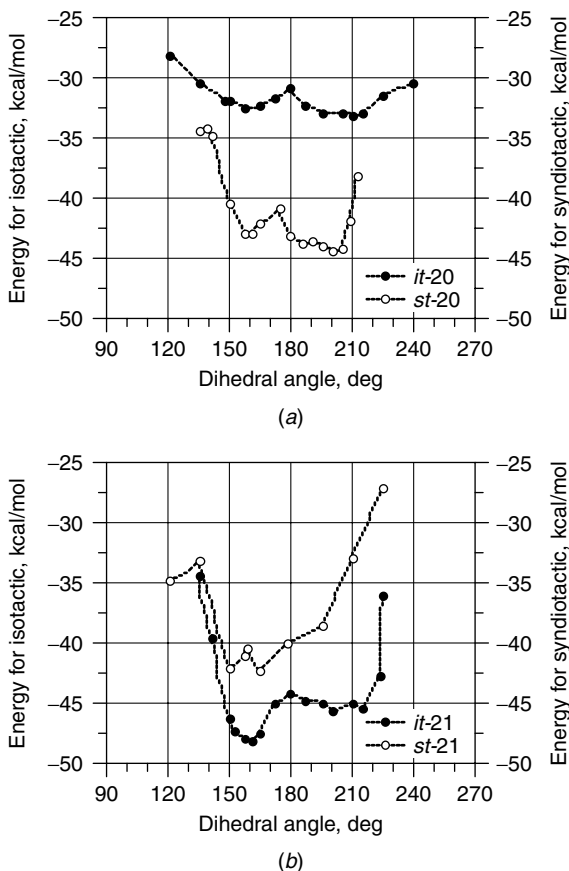


Figure 4.14 Results of molecular mechanics calculation. Main-chain dihedral angle dependence on the potential energy of (a) *it*- and *st*-(*S*)-3,7-dimethyloctyl-3-methylbutylsilane 31 repeat units with hydrogen termini (**20**), and (b) *it*- and *st*-(*S*)-3,7-dimethyloctyl-2-methyl-propylsilane 31 repeat units with hydrogen termini (**21**).

more stable than the corresponding *P* by about 1.3 kcal per repeat unit. The barrier heights for the respective *M* and *P* screw senses are about 4.6 and 3.4 kcal per repeat unit. Thus, the calculation of **21** suggests that both pseudoenantiomeric *P* and *M* motifs are likely to stably coexist in the same main chain at any temperature, regardless of tacticity.

Contrarily, *it*-**21** shows an unclear double well potential curve with minima at dihedral angles of about *P* 160° and *M* 200°. The *P* helix is much more stable compared to the corresponding *M* by about 2.3 kcal per repeat unit. The barrier heights of the respective *M* and *P* are about 3.9 and 1.4 kcal per

repeat unit, leading to the idea that *P* helix might be more stable. A *st*-**21** has an almost single-well potential curve with dihedral angles of *P* 160°. These calculations assume that the *P* motifs of **16** and **17** are more stable at all temperatures, regardless of tacticity.

The origin of the *PM* transition may be discussed using very simple energy parameters of the *P* and *M* states of **20** and **21**. Here, ΔG is the difference in free energy between the *P* and *M* states. Similarly, ΔH and ΔS are the differences in enthalpy and entropy between the *P* and *M* states, respectively.

$$\Delta G = G_P - G_M = \Delta H - T\Delta S = H_P - H_M - T(S_P - S_M), \quad (1)$$

where

$$\Delta H = H_P - H_M, \Delta S = S_P - S_M \quad (2)$$

$$\text{at } T_c, \Delta G = 0, \text{ then } T_c = \Delta H / \Delta S \quad (3)$$

Using the value of $T_c = 253$ K from **16** and $\Delta H = -0.67$ kcal per repeat unit for its model **20**, then $\Delta S = -2.6$ cal \cdot K⁻¹ at T_c . Since the sign of the ΔG term below T_c is negative, *P* is more stable than *M*, and vice versa. To design a thermo-driven *PM* transition polysilane for switching at a desired temperature, it seems to be essential that the polysilane has a double-well potential curve, small ΔH , and small potential barrier height. If the ΔS term is responsible for the inversion of preferential screw sense, *P* polysilane in a low entropy state below T_c may have a highly ordered packing structure of side groups, whereas *M* polysilane in a high entropy state above T_c may have a disordered arrangement of side groups. Entropy considerations may also need to

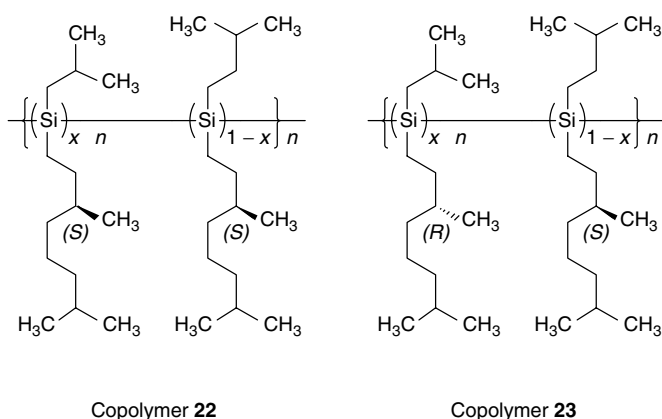


Chart 4.4 Chemical structures of poly(dialkylsilane) copolymers (**22** and **23**) with *PM* transition ability.

consider solvent interactions. Thus, semiempirical understanding of *PM* transition characteristics and main-chain stiffness of rodlike polysilanes leads to the new idea that minute structural modification of the achiral and chiral alkyl side groups could critically modify the transition characteristics, as indeed demonstrated in a series of **16**-based copolymers, poly{((*S*)-3,7-dimethyloctyl-3-methylbutylsilane)-*co*-((*S*)-3,7-dimethyloctyl-2-methylpropylsilane)} (**22**) and poly{((*S*)-3,7-dimethyloctyl-3-methylbutylsilane)-*co*-((*R*)-3,7-dimethyloctyl-2-methylpropylsilane)} (**23**) (see Chart 4.4).

Figure 4.15 shows the temperature dependence of the g_{abs} values and *PM* populations in **22** (with 80 mol % of **16** and 20 mol % of **17**), **16**, and **23** (with 80 mol % of **16** and 20 mol % of **18**) in isoctane between -82 and $+80^\circ\text{C}$. It

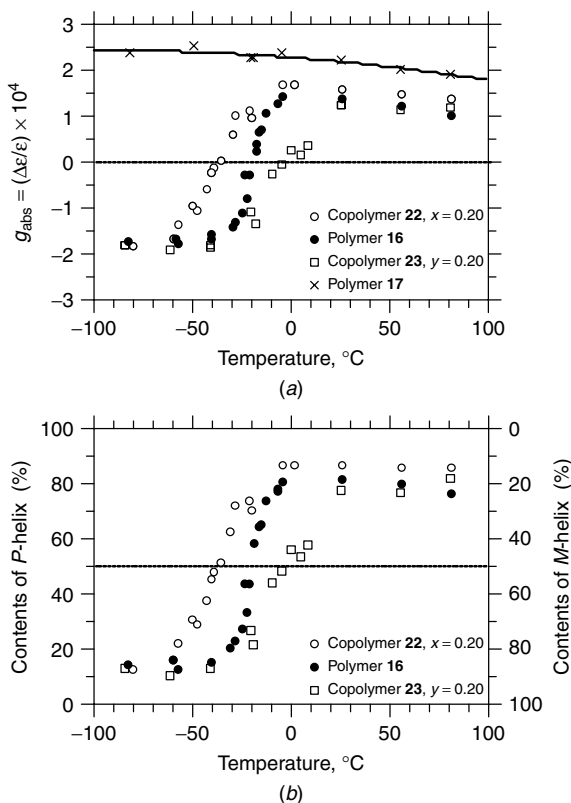


Figure 4.15 (a) Temperature dependence of the g_{abs} values of **22** (with 80% of **16** and 20% of **17**, $M_w = 5.0 \times 10^4$, open squares), **16** ($M_w = 3.8 \times 10^4$, filled circles), **23** (with 80% of **16**, 20% of **18**, $M_w = 4.8 \times 10^4$, open circles), and **17** ($M_w = 4.2 \times 10^4$, crosses and solid curve) in isoctane. (b) Temperature dependence of the populations of *P*(%) and *M*(%) of the **22**, **16**, and **23** samples in isoctane by reference to the regression curve of g_{abs} values in **17**.

is evident that, compared to the T_c of **16**, that of **22** containing two identical (*S*)-chiral side groups is lower by 16°C , whereas that of **23** containing the opposite (*S*)- and (*R*)-chiral side groups is higher by 16°C . The CD spectral profile for the respective copolymers still matches the corresponding UV absorption spectrum at all temperatures. However, as introduction of **17** or **18** moieties to pure **16** causes an increase of ΔT_c , presumably, the randomness of the two silane repeat units in the same copolymers significantly affects the ΔT_c .

Figure 4.16 plots the values of T_c and ΔT_c as a function of the molar fraction of **17** in **22** and **18** in **23**. It is obvious that, as the molar fraction of **17** in **22** and **18** in **23** increases, the value of T_c changes nonlinearly from -64 to $+79^\circ\text{C}$ and the value of ΔT_c is nonlinearly broadened. Although a further mechanistic study will be needed to clarify the true origin of the transition, as demonstrated in stiff poly(alkyl isocyanate) copolymer systems,^{18t} the presence of two local free-energy minimum potentials with respect to the helical dihedral angle and entropy term in the free-energy stability may be responsible for the transition characteristics. In addition, the coexistence of *P* and *M* motifs in the same main chain at any temperature, even sufficiently low below T_c and high above T_c , may be essential for the polymers able to undergo the *PM* transition.

2.8 Summary and Conclusions for Dialkylpolysilanes

In this section, we comprehensively focused on the controlled synthesis, chiroptical characterization, and manipulation of optically active poly(dialkylsilane)s. Although many artificial polymers adopting preferential screw sense

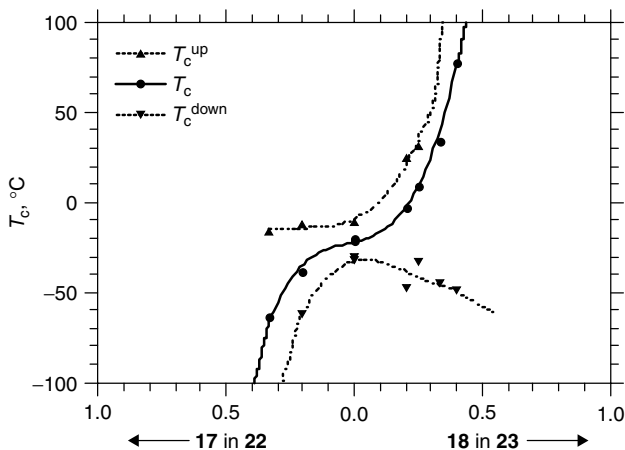


Figure 4.16 Values of T_c and ΔT_c as a function of molar fraction of **17** in **22** and **18** in **23** in isooctane. The M_w values in all copolymers ranged from 8.5×10^4 to 3.5×10^4 .

helical structure have been investigated, optically active poly(dialkylsilane)s bearing chiral side chains may be among the most suitable to elucidate the inherent nature of the helical structure, since these polymers offer powerful spectroscopic probes due to their ideal chromophoric and fluorophoric main-chain properties around 300–330 nm. We presented the helix–property–functionality relationship between side-chain structure, global and local main-chain conformation, control of (chir)optical and electronic properties, several helical cooperative phenomena, the effect of temperature, and molecular imaging. The present knowledge and understanding of the nature of the polysilanes should assist in designing new types of helical polymers directed to diverse screw-sense-related properties and applications in the future.

3 OPTICALLY ACTIVE ALKYL(ALKOXYPHENYL)POLYSILANE

3.1 Alkyl(alkoxyphenyl)polysilane Bearing Enantiopure Chiral Side Chains

The conformational structures of polysilane main chains at the macro- and microscopic levels are controllable by suitable choice of the side-chain structures. Similarly, it is also the side chain which control the optoelectronic properties by their effects on the optical band gap.^{28–32} In the case of phenyl-substituted polysilanes, electronic interaction between the delocalized Si chain σ -bonding orbitals and the π orbitals of the aryl groups causes a dramatic modification of both the band gap and conformational properties.^{29,30,52} These aryl-containing polysilanes may be potential candidates for applications in a molecular-based chiroptical switch and memory in the UV/visible region. On the other hand, the precise control of helical polymers is now a subject of great interest and importance due to the technological importance of polymeric materials in the analysis and preparation of chiral drugs. Indeed, a few synthetic helical polymers are able to act as chiral selectors tuned for a particular chiral drug and its mirror image substance.^{7a,53} Aiming at chiral selection, it is necessary to introduce some functional groups capable of discriminating between a pair of the guest enantiomers through intermolecular physicochemical interactions such as hydrogen bonding, phenyl π – π , dipole–dipole, ionic, and acid–base interactions. Helical poly(alkyl-(alkoxyphenyl)silane)s bearing chiral side-chains are potential candidates for use as a chiral selector since the polysilanes have multiple chiral recognition sites such as aryl groups, oxygen atoms, enantiopure chiral groups, and a chiral matrix due to the preferential helical conformation of the main chain. Therefore, this type of polysilane may open new concepts in the design of new polymer-based chiral stationary phases in gas or liquid chromatography or in molecular chirality sensors.

3.2 Control of Optical Properties and Global–Local Conformations

3.2.1 Substituent Effects and Cooperative Helical Order Effect

The absorption spectra of poly(alkyl(alkoxyphenyl)silane)s are sensitive to substituent effects such as charge transfer from the phenyl ring to Si main chain ($\pi \rightarrow \sigma$ mixing), the position of the electron-donating alkoxy group on the phenyl ring, or the introduction of enantiopure chiral groups.^{29,52} We systematically investigated the UV absorption properties in THF at 20°C of a series of achiral poly(alkyl(alkoxyphenyl)silane)s with different degree of chain coiling, which are easily controlled by a combination of the alkyl substituents and the position of the methoxy group on the phenyl ring,^{29,29e,29g,52e} as shown in Chart 4.5.

As shown in Figure 4.17, these absorption properties mainly depend on the polysilane global conformation (from a shrunk random coil to an extended

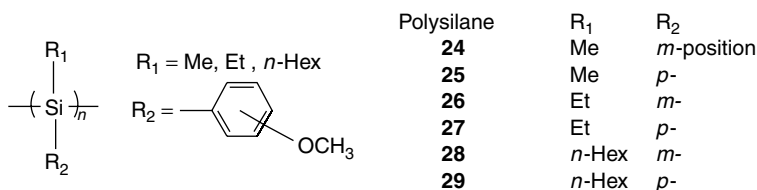


Chart 4.5 Chemical structures of poly{alkyl(alkoxyphenyl)silane}s (**24–29**).

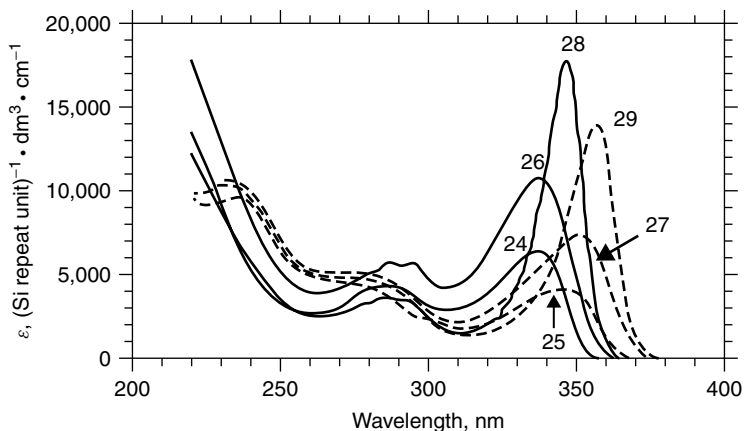


Figure 4.17 UV spectra of poly(alkyl(methoxyphenyl)silane) derivatives **24–29** in THF at 20°C. The value of α in THF at 30°C and polysilane are $\alpha = 0.45$ for **24**, $\alpha = 0.35$ for **25**, $\alpha = 0.63$ for **26**, $\alpha = 0.64$ for **27**, $\alpha = 0.96$ for **28**, and $\alpha = 0.94$ for **29**.

stiffer structure on increase of the alkyl side chain length) and also the positional effect of the electron-donating alkoxy moiety in the phenyl ring (*m* or *p* position).

Additionally, copolymers of **30**–**37** containing 20% enantiopure chiral silane units (see Chart 4.6) are optically active helical polymers which obey the sergeants-and-soldiers principle, as shown in Figure 4.18.^{29g} Interestingly, from the observation of the CD sign in the phenyl region, the arrangement of phenyl

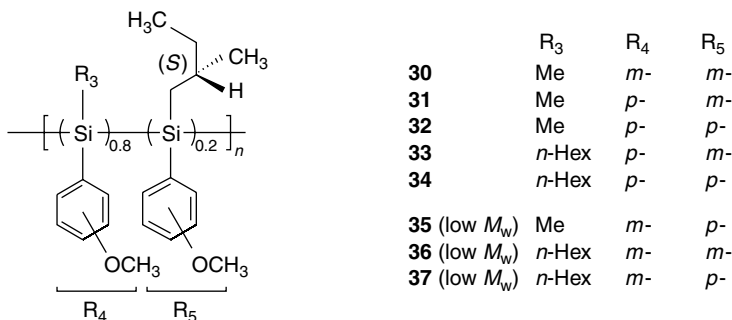


Chart 4.6 Chemical structures of poly{alkyl(alkoxyphenyl)silane} copolymers (**30**–**37**).

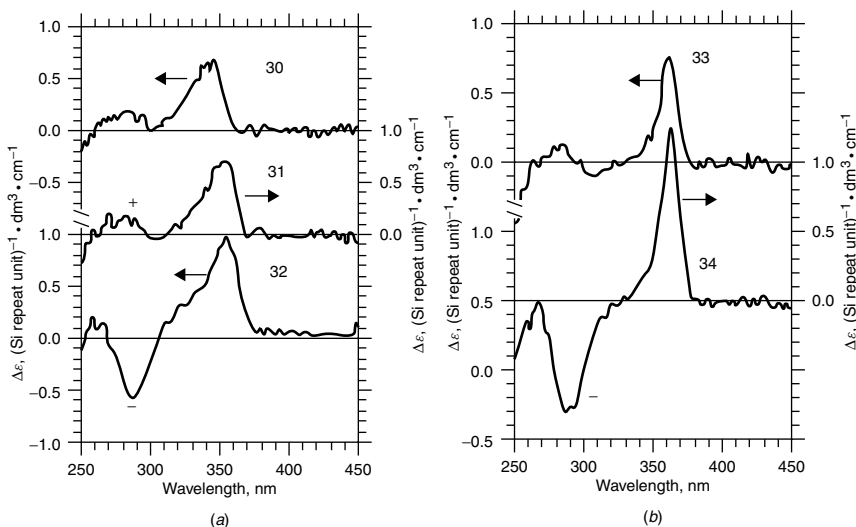


Figure 4.18 CD spectra of (a) poly{methyl(methoxyphenyl)silane}-co-*(S)*-2-methylbutyl(methoxyphenyl)silane}s (**30**–**32**) and (b) poly[*n*-hexyl(methoxyphenyl)silane]-co-*(S)*-2-methylbutyl(methoxyphenyl)silane}s (**33** and **34**) in THF at 20°C.

side chains, which may be either along the Si main-chain screw sense or orthogonal, could be controlled by the methoxy group position of only chiral monomer units without change of the preferential Si main-chain helical screw sense.

3.2.2 Control of Main-Chain Helicity by Position of Remote Chiral Group

The helical main-chain structures of poly{alkyl(alkoxyphenyl)silane}s bearing a remote enantiopure chiral group on the phenyl ring (a series of poly{methyl((*S*)-2-methylbutoxyphenyl)silane}s) are significantly affected by the position of the chiral alkoxy substituent, even though the chiral substituent is far from the main chain.^{29c} The CD spectrum of the *m* derivative (**38**) shows a marked negative peak at around 310 nm in the region between the two UV bands, indicating that the chiral steric effect locks the Si main chain conformation in a particular helical screw sense, even though it may be strongly distorted, twisted, and folded due to the steric imbalance between the methyl and bulky *m*-(*S*)-2-methylbutoxyphenyl side chains, as shown in Figure 4.19*a*.

By contrast, in the CD spectrum of the *p* derivative (**39**), no bands were observed even at -80°C , as shown in Figure 4.19*b*. This is because the Cotton band of the *p* derivative is canceled by an oppositely signed CD band originating in an equivalent proportion of opposite screw sense helical segments (which may be referred to as “masked helicity” or “masked circular dichroism”). The difference between the helical conformations of *m* and *p* derivatives may be due to the degree of steric hindrance of (*S*)-2-methylbutoxyphenyl rings, since the *p* derivative may have enough space to freely rotate the

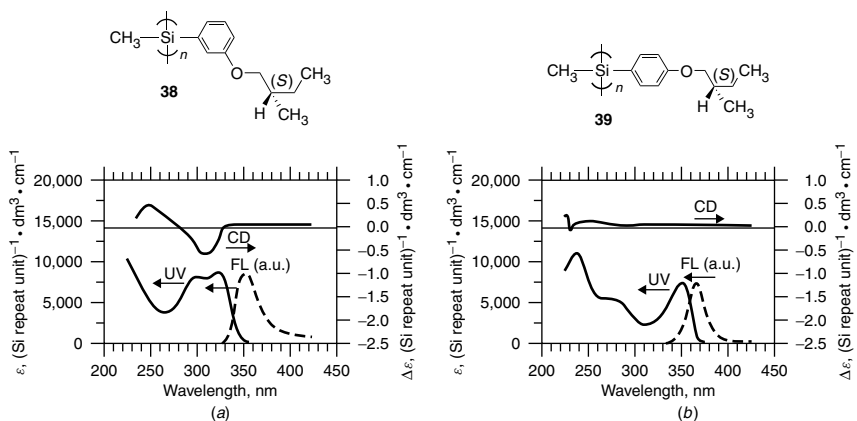


Figure 4.19 UV, CD, and FL spectra of (a) poly{methyl(*m*-(*S*)-2-methylbutoxyphenyl)silane} (**38**) and (b) poly{methyl(*p*-(*S*)-2-methylbutoxyphenyl)silane} (**39**) in THF at 23–25°C.

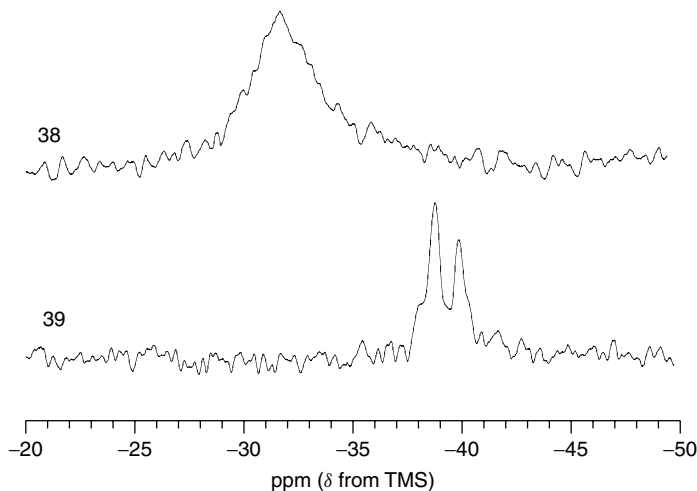


Figure 4.20 ^{29}Si -NMR spectra of poly[methyl(*S*)-2-methylbutoxyphenyl]silane)s (**38** and **39**) in benzene- d_6 at 50°C .

p-(*S*)-2-methylbutoxyphenyl group, main chains in these systems are not conformationally locked.

The different Si helical main-chain structures are apparent in their ^{29}Si NMR spectra,^{29c} as shown in Figure 4.20. In these spectra, a broad signal (around -32 ppm, $\Delta\nu_{1/2}$ about 240 Hz) is observed for the *m* derivative (**38**), and two sharp signals (about -39 ppm and -40 ppm, $\Delta\nu_{1/2}$ about 76 and 85 Hz, respectively) and one shoulder (about -38 ppm) are observed for the *p* derivative (**39**). (The two sharp signals may reflect the tacticity of the Si main chain, with *st*-, *it*-, and *ht*- triads).^{34,54} The broad signal of **38** suggests that the mobility of the Si main chain is considerably restrained due to chiral steric locking in one predominant helical screw sense. Contrarily the sharpness of the NMR signal of **39** indicates that the Si main chain is in fast motion, thus *P*- and *M*-helical segments can exchange easily without locking into a partial screw sense. Consistent with this, it was recently reported that ^1H NMR linewidths of poly(alkyl isocyanate)s are directly related to the degrees of mobilities of the main chain and side chains and interconversion between *P* and *M* screw senses.^{18r}

3.3 Poly{alkyl(alkoxyphenyl)silane} Chiral Aggregates

3.3.1 Switch and Memory of Chiroptical Properties

Poly{alkyl(alkoxyphenyl)silane}s bearing enantiopure chiral substituents in the *para* position on the phenyl ring, in contrast to poly(dialkylsilane)s or

poly(diarylsilane)s, are optically inactive in dilute solution due to the presence of equivalent proportions of *P*- and *M*-helical segments.^{29,29e} However, it is well established for several π -conjugated polymers bearing chiral side chains that, even though the polymer may be optically inactive in the single-molecule state, optical activity may be observed in an aggregated form due to greater ordering. Interestingly, aggregation of polymers bearing chiral side chains into chiral superstructures considerably influences the optical and chiroptical properties. For instance, the sign and magnitude of the bisignate CD signal switching of polythiophene^{20,20d,20g,20i} or poly(*l*-aspartate)⁵⁰ aggregates and/or liquid crystals in response to the cooling rate and/or temperature of the thin film or the ratio of good/poor co-solvents have been described. The poly{alkyl(alkoxyphenyl)silane}s aggregates also show switchable and memorizable CD properties in good/poor co-solvent systems, controllable by various experimental factors, such as solvent polarity, solvation, solubility, solvent addition order, thermal effects and polysilane structure and stereochemistry.²⁹ Detailed experimental investigations of polysilane aggregates may help in the design of future generations of synthetic polymers with unique and functional chiroptical properties.

3.3.2 Chiroptical Properties

The CD spectra of poly[*n*-hexyl(*p*-(*S*)-2-methylbutoxyphenyl)silane] (**40**) aggregates exhibit a well-resolved bisignate CD signal in a THF/methanol co-solvent system, although no CD signal is evident in pure THF solution.^{29e} The observed positive Cotton effect in excess THF became a negative Cotton effect above 60% methanol, and the bisignate CD intensities changed continuously with increasing methanol concentration (Figure 4.21a), the CD reversal point occurring at ca. 50%/50% THF/methanol. Previously, thermally reversible aggregation and gelation were reported for stiff poly(*n*-hexyl isocyanate)^{18b,55a} and also intermolecular association and supramolecular organization of poly(*p*-biphenylmethyl-*l*-glutamate) in solution has been investigated by means of light scattering and optical activity.⁵⁵ Those results mean that the polysilane, while optically inactive in a good solvent, forms optically active chiral aggregates in a good/poor mixed-solvent system. In addition the chirality of the aggregates is switchable by the solvent polarity, as has also been reported for a polythiophene.^{20d} The bisignate nature of the CD spectra is considered to be characteristic of exciton coupling between closely situated transition dipole moments on neighboring polymer segments in chiral configurations.³⁸ The CD splitting results mainly from the *intermolecular* interaction between neighboring polysilane helices since the CD spectra originate from the micrometer-scale chiral aggregate particles (as shown by filtration experiments using several different pore size filters).

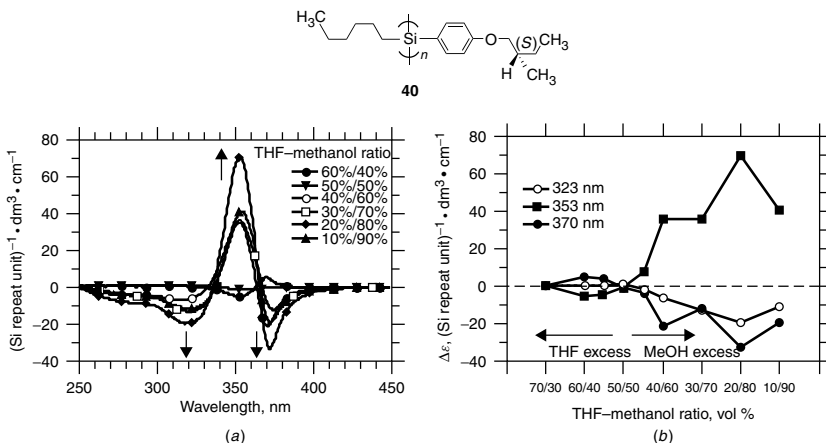


Figure 4.21 (a) CD spectra and (b) plot of CD intensities of poly[n-hexyl(p-S)-2-methylbutoxyphenyl)silane] (40) aggregates at different THF/methanol ratios at 20°C.

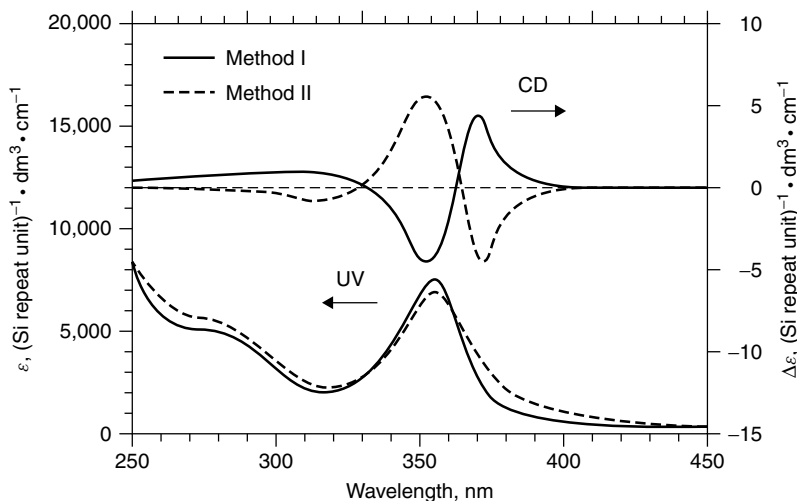


Figure 4.22 UV-Vis and CD spectra of poly[n-hexyl(p-S)-2-methylbutoxyphenyl)silane] (40) aggregates prepared by methods I and II at 55%/45% THF/methanol volume ratio at 20°C.

In addition, the CD sign of chiral aggregates around the CD reversal point (THF/methanol 55%/45%) is easily switchable, depending on the solvent addition order: either method I (methanol added into THF solution of the polysilane) or method II (THF solution of the polysilane added into methanol) (Figure 4.22). This CD switching may be related to the dependence of the

chirality of the “seed” aggregates on the solvent polarity in the initial stage of the aggregation process.

Two possible origins of the CD switching phenomenon (relating to the oppositely oriented chiral aggregates) dependent on solvent polarity are proposed^{29c}: (i) First, the dynamic equilibrium between *P*- and *M*-helical screw senses in **40** may incline to a preferential helical screw sense upon aggregation by locking effects of the *p*-chiral ether moieties, while the solvent polarity may control the slight preference of the polysilane for *P* or *M* helicity. Consequently, the preferred chiral orientation of the aggregates may be a result of the preferred helicity of single molecules of the polysilane, as shown in Figure 4.23. (ii) Second, the helix angle ϕ may govern the handedness of the packing between the preferential helical main chains of contiguous polysilane chains (there is no helical inversion of the single main chain), as shown in Figure 4.24. In this model, the handedness of the superhelix depends on only two critical factors: the ratio of polymer helical screw pitch, p , to helical diameter, d , as has also been proposed for cholesteric liquid crystal phases of DNA.⁵⁶ Concerning polysilane aggregates in a good/poor co-solvent system, the screw pitch (p) of the preferential helicity could be largely dependent on the amount of poor solvent since the polysilane chains may shrink and fold (p becomes shorter) in excess poor solvent.

3.3.3 Temperature Effects

Chiral aggregates of **40** were subjected to multiple cycles of heating (50°C) and cooling (−10°C) to investigate the thermal stability of the aggregate chirality.^{29c} In the CD spectra of the aggregates at 60%/40% THF/methanol, the bisignate Cotton effect observed at 20°C completely disappears at 50°C

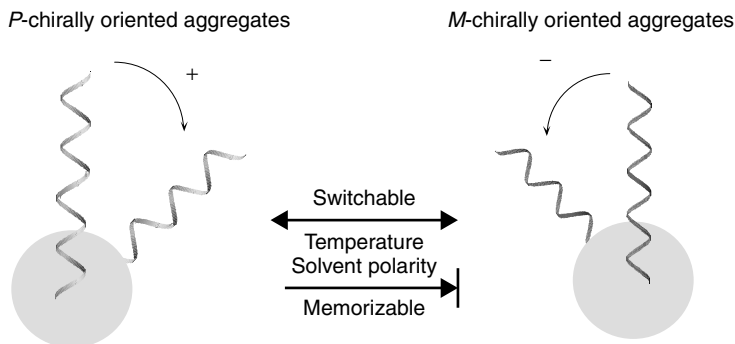


Figure 4.23 Chiral orientation of the preferred helicity of single molecules of the polysilane for the origin of bisignate Cotton effect.

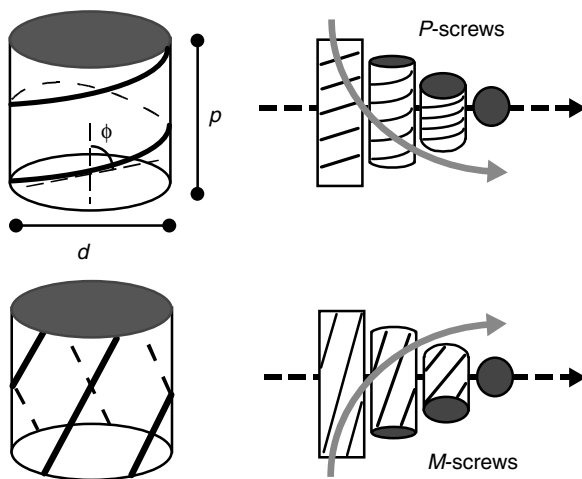


Figure 4.24 Superhelix with helix angle ϕ governing handedness of packing between preferential helical main chains of contiguous polysilane chains for origin of Cotton effect of polysilane aggregates.

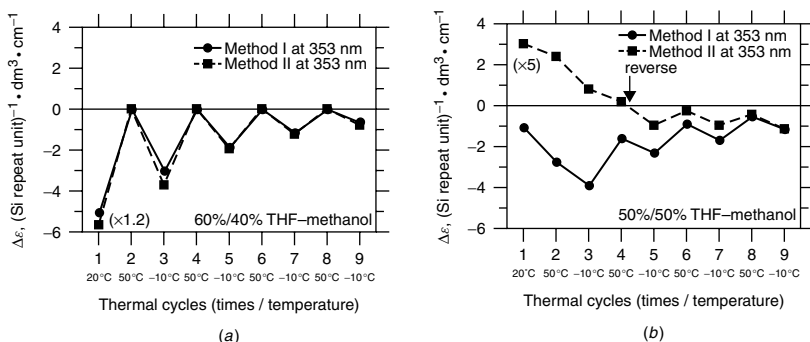


Figure 4.25 Change of CD intensity of poly(*n*-hexyl(*p*-*S*)-2-methylbutoxyphenyl)silane) (**40**) aggregates prepared by methods I and II at (a) 60%/40% and (b) 55%/45% THF/methanol volume ratios in multiple thermal cycles of heating to 50°C and cooling to -10°C.

due to dissolution of the aggregates and appears again at -10°C on the cooling run with similar λ_{ext} and sign to that at 20°C (Figure 4.25a). These CD profiles are reproducible after several thermal cycles. In contrast, at 50%/50% THF/methanol (CD reversal point), the CD spectra of the aggregates for only method II (THF solution of **40** added into methanol) are reversed after four thermal cycles and the CD profiles finally showed similar CD λ_{ext} , signs and

intensities to those obtained by method I (Figure 4.25*b*). This CD switching for method II results from the transformation of a metastable chiral aggregate to an energetically more stable opposite chiral state on application of the thermal stimulus.

3.3.4 Solvent Effects

The solvent polarity and solvation mode may be critical factors in the determination of the polysilane chiral aggregate structures. Polysilane **40** in toluene (low dielectric constant of 2.4, good solvent)/acetonitrile (high dielectric constant of 35.9, poor solvent) forms aggregates due to the effect of the poorly solvating, polar acetonitrile, and shows much white precipitation in the bottom of the cell, especially at a high acetonitrile ratio.^{29e} Poly{alkyl(alkoxyphenyl)silane} has a polar oxygen in the side chain, and thus a better affinity for methanol than acetonitrile, though both are poor solvents.

The formation of stable chiral aggregates also depends critically on the polysilane structure and stereochemistry. The less sterically hindered *p*-substituted **39** exhibits a weak, bisignate, nonswitchable CD signal in only the toluene/acetonitrile system, and no CD signals are evident in pure toluene or THF due to no preferential screw sense, as shown in Figure 4.26*a*. In contrast, although the even less sterically hindered, less polar *m*-substituted **38** does show optical activity when molecularly dispersed in a THF or toluene solution, as shown in Figure 4.26*b*, the CD signal disappears on formation of aggregates in good/poor co-solvent systems. These methyl-substituted polysilanes have sterically imbalanced side chains, a small methyl group and a bulky (*S*)-2-methylbutoxyphenyl group, and may adopt conformations with macroscopically random and shrunk coils. In contrast, **40** adopts a stiffer coil, and therefore the more extended Si main-chain conformation and greater spatial freedom between the bulky side chains may favor the formation of well-balanced, chirally oriented aggregates and permit chirality switching.

3.4 Molecular Chirality Recognition of Poly{alkyl(alkoxyphenyl)silane}

A few synthetic helical polymers are known to act as chiral selectors.^{7a,9,18d,18k,19d-19h} and are widely used as chiral stationary phases (CSP) in gas or liquid chromatography.^{7a,53} Recently, it has been reported that the preference of one helical sense in isotropic solution can be induced by some interaction between optically inactive polymers and chiral solvents/additives. Examples of this include poly(*n*-hexyl isocyanate)^{18d,18k} and poly(phenylacetylene)s bearing functional group.^{19d-19h} The polysilane derivatives also show chiral recognition ability in solution at room temperature. Poly(methyl- β -pinanylsilane) includes two chiral centers per bulky hydrophobic pinanyl side group²⁸ⁱ and

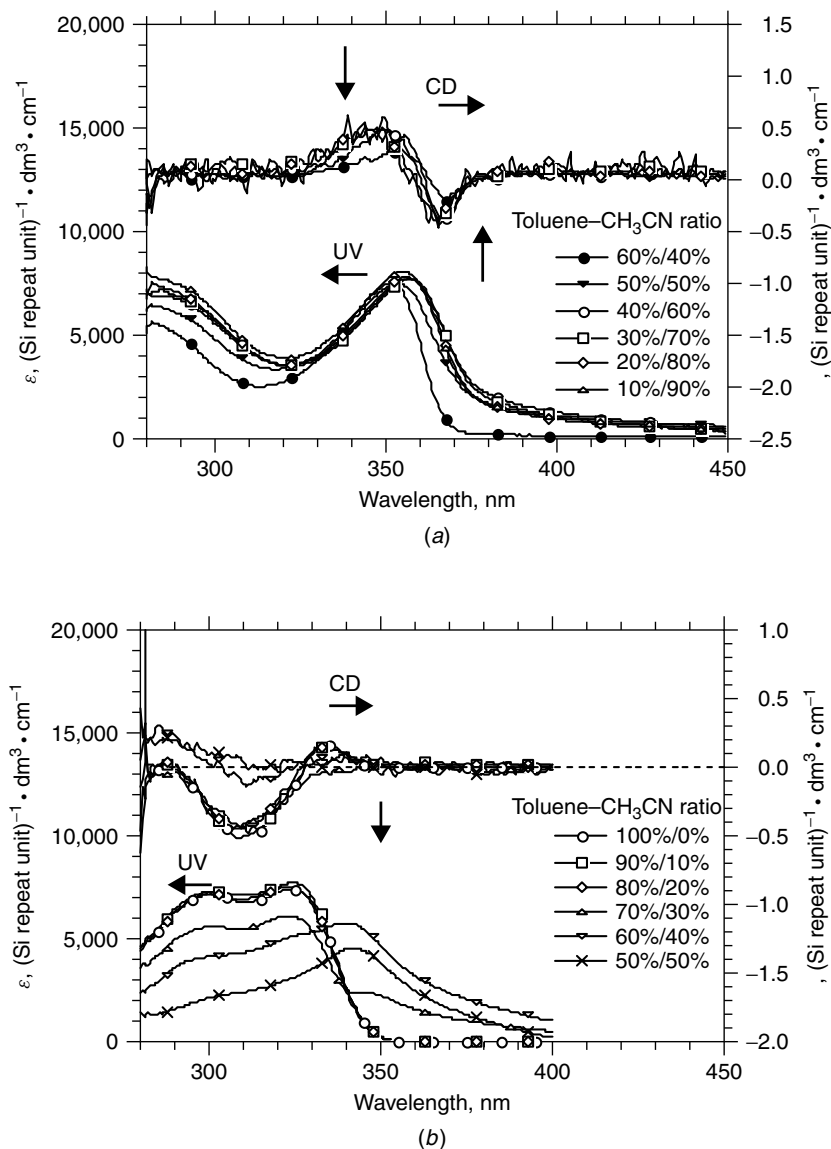


Figure 4.26 UV-Vis and CD spectra of (a) poly[methyl(*p*-(*S*)-2-methylbutoxyphenyl)silane] (**39**) and (b) poly[methyl(*m*-(*S*)-2-methylbutoxyphenyl)silane] (**38**) aggregates prepared at various toluene/acetonitrile ratios at 20°C.

exhibits an enantio-recognition ability for hydrophobic β -pinene, but none for hydrophilic methanol. We also demonstrated the chiral recognition of chiral alcohols using aggregates^{29g} of optically inactive, chromophoric poly[*n*-hexyl(*p* - *n*-propoxyphenyl)silane] (**41**). Aggregates of this polysilane complexed with various chiral alcohols exhibit remarkable, bisignate induced circular dichroism (ICD) based on amplified chiral ordering as shown in Figure 4.27*a*. Additionally, the sign of the ICD depends on the absolute configuration of the chiral alcohol, indicating clearly that the polysilane forms chiral-oriented aggregates due to the transfer of chiral information by the weak hydrogen-bonding interaction between the ether oxygen moieties of the polysilane and the OH group of the chiral alcohols. The chiral polysilane aggregates showed a linear relation between the enantiomeric excess (*ee*) of chiral 2-butanol and the ICD intensities (Figure 4.27*b*): This system can thus determine the optical purity of chiral targets quantitatively.

Interestingly, when we focused on a series of (*S*)-chiral primary alkyl alcohols with monotonically increasing numbers of methylene spacer groups, the ICD sign of the polysilane aggregates oscillated according to the number of methylene carbons from the OH group to the chiral center (Figure 4.28). Such CD phenomena have been referred to as the “odd–even” effect and have been observed in certain helical superstructures.^{17g,20g} From exciton theory and model studies, it is empirically suggested that the odd–even effect originates in the transition between *P*- and *M*-handed supramolecular helicity,

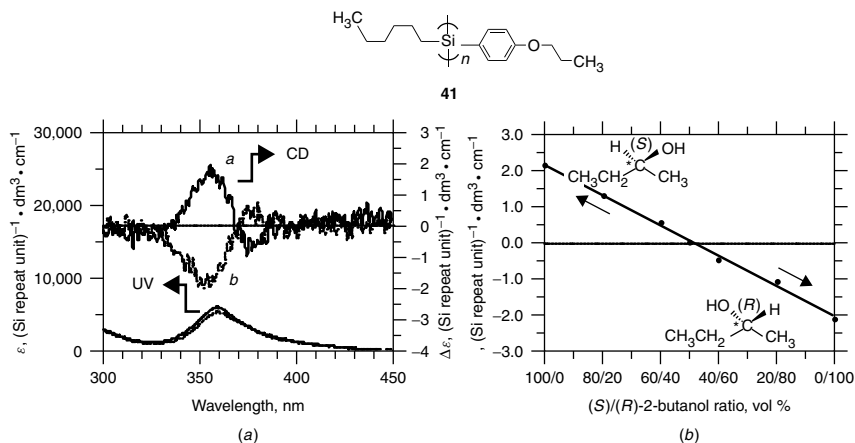


Figure 4.27 (a) CD and UV spectra of poly[*n*-hexyl(*p*-*n*-propoxyphenyl)silane] (**41**) aggregates in toluene/(*S*)- (*a*; solid line) or (*R*)-2-butanol (*b*; dotted line)/methanol mixtures at 20°C and (b) plot of CD intensities at 354 nm of the polysilane aggregates in toluene/various ratio of (*S*)/(*R*)-2-butanol/methanol mixtures at 20°C.

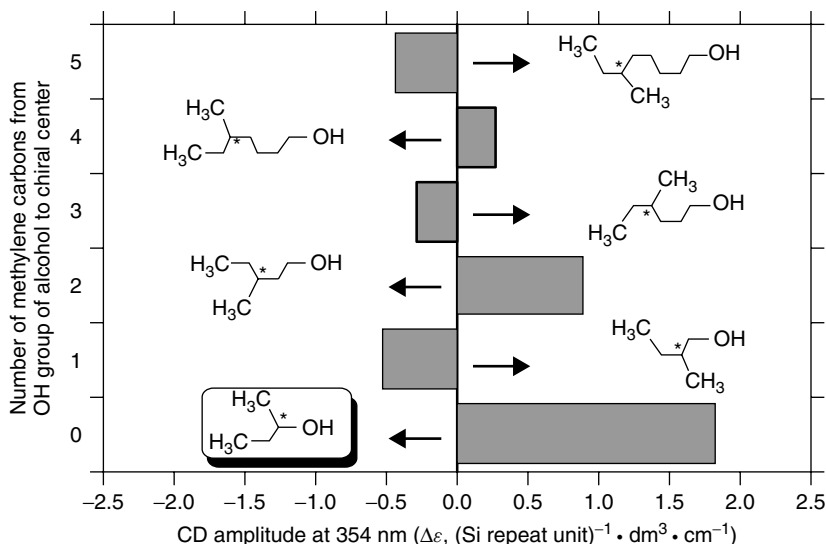


Figure 4.28 Plot of CD intensities of poly[*n*-hexyl(*p*-*n*-propoxyphenyl)silane] (**41**) aggregates in toluene/series of (*S*)-primary chiral alkyl alcohols/methanol mixtures at 20°C. [For comparison, CD intensity with (*S*)-2-butanol is inserted.].

and therefore these results mean that the position of the chiral center might govern the chirality of the polysilane aggregates. The preparation of a library by screening against various chiral guests (by combinatorial techniques) using **41** aggregates might assist in the design of new polymer-based CSPs or chiral sensors.

4 OPTICALLY ACTIVE ALKYL(PHENYL)POLYSILANE

In this section, the effect of the cooperative helical ordering in poly(alkyl(alkyl-phenyl)silane) copolymers with a minor portion of chiral and major portion of achiral moieties is described.^{29b,29f} First, the conformation of the structure was analyzed to determine the main-chain solution state conformation. This is because, although well-established light-scattering and viscosity measurements provide information on the global conformation such as the radius of gyration and the value of α ,⁴⁴ these methods cannot determine whether a local conformation is helical. The main-chain conformation of poly(alkyl(aryl)silane)s, however, is not fully understood because the main-chain peak wavelength (λ_{max}) depends not only on the main-chain conformation and the Si repeat number^{33,34} but also on the effect of σ - π mixing between the phenyl groups

and the Si main chain.^{52a} Second, poly(alkyl(aryl)silane) copolymers with an increasing proportion of chiral pendant to achiral side chains were investigated.^{29b,29f} The preferential single screw sense in the main chain of these helical polymers was induced nonlinearly as regards the incorporated chiral moiety ratio, which is consistent with a cooperative response of the conformational properties^{16a,18b,18p,18q} to the chiral information.

A series of optically active poly{alkyl(phenyl)silane} derivative copolymers with different chiral molar composition **44** and **45**, are shown in Chart 4.7, along with homopolymers poly(methyl(phenyl)silane) (**42**) and poly(n-hexyl(m-tolyl)silane) (**43**).

4.1 UV Absorption, Fluorescence Spectra, and Fluorescence Anisotropy of Optically Inactive Homopolymers

The UV absorption, FL, and FLA spectra of optically inactive homopolymers **42** and **43** are shown in Figures 4.29*a* and *b*, respectively. There are two bands around 280 and 320–360 nm in both absorption spectra. The latter absorption is due to their silicon main chain, while the former is due to their phenyl $\pi-\pi^*$ transition. However, a comparison of the UV absorption, FL, and FLA spectra of **42** and **43** reveals great differences.

For **42**, the FL spectral profile with an FWHM of 30 nm is not the mirror image of the 340-nm absorption band, and the photoexcitation wavelength depends strongly on the FLA around the 340-nm exciton band, ranging from 0.00 at 300 nm to 0.36 at 350 nm. By contrast, for **43**, the FL spectral profile with an FWHM of 15 nm is the mirror image of the 350-nm absorption band; the photoexcitation wavelength, however, has a similar FLA dependence around the 350-nm exciton band, ranging from 0.00 at 300 nm to

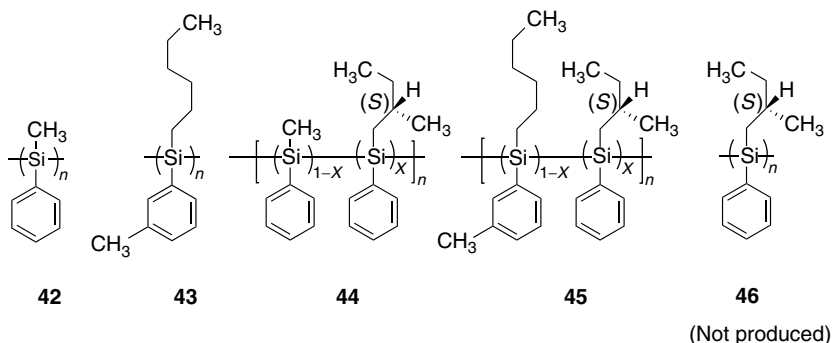


Chart 4.7 Chemical structures of poly{alkyl(alkylphenyl)silane} derivatives, including homopolymers **42** and **43**, and copolymers **44** ($x = 0.05, 0.10, 0.25, 0.30,$ and 0.50) and **45** ($x = 0.05, 0.10, 0.20,$ and 0.50).

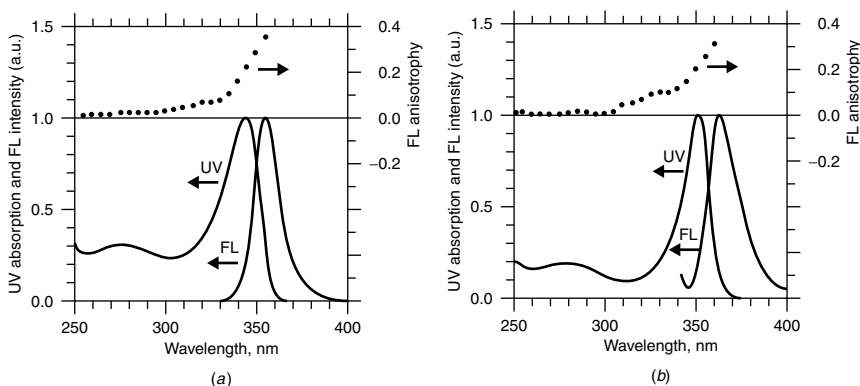


Figure 4.29 UV absorption, FL, and FLA spectra of (a) **42** and (b) **43** in THF.

0.31 at 360 nm. These properties relate to the conformational structure. The polysilane absorption spectra result from a convolution of the spectra of the various segmented chromophores with different excitation energies. Therefore, when segments with higher energy absorption are excited, the photoexcited electron–hole pair migrates into a segment of lower energy from which the emission occurs. Consequently, the mirror image relation and narrower absorption show that the main-chain conformation of **43** has a more regular spatial conformation than that of **42**. This is consistent with the idea that **42** and **43** have random-coil and stiff global conformational structures, respectively, in dilute solution from the absorptivity–viscosity index–FWHM correlation.⁴¹

4.2 UV and CD Spectra of Copolymers Bearing Chiral–Achiral Substituents

The UV absorption and CD spectra of copolymers with chiral–achiral substituents **44** ($x = 0.25$) and **45** ($x = 0.20$) in THF at 23–25°C are shown in Figures 4.30*a,b*. The positive-sign CD spectral profile around 340 nm almost traces the corresponding 340-nm UV absorption profile for both copolymers. This is consistent with local helical conformations for both **44** and **45**. This is because, if **44** and **45** have an achiral, *trans* planar conformation, a zero, or far smaller, CD signal should be observed. If **44** and **45** have partly *trans* planar moieties not responsible for a CD signal in the main chain, the CD band will not completely match the apparent UV band. All the spectral profiles for all the copolymers involving monomer units bearing chiral side chains were almost identical except for the magnitude of the CD band. Therefore, this led to the idea that the local conformations of the optically active **44** and **45** are helical with a preferential screw sense independent of the incorporated

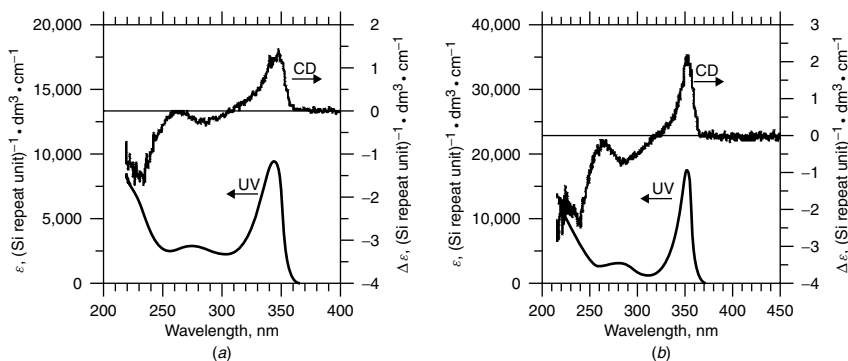


Figure 4.30 UV absorption and CD spectra of (a) copolymers **44** ($x = 0.25$) and (b) copolymers **45** ($x = 0.20$) in THF at 23–25°C.

monomer unit with chiral pendant, and therefore by extrapolation, that even optically inactive **42** and **43** may have a latent helical structure,^{7c} but without a preferential screw sense.

4.3 Molecular Mechanics Calculation

The idea that the most stable conformation of **42** and **43** may be helical is supported by a molecular mechanics calculation using Discover III with a PCFF force field (MSI, ver. 3.00). Figure 4.31a shows the total energy of a **42** oligomer with 21 Si repeat units as a function of the Si–Si–Si–Si dihedral angle. The respective *P*- and *M*-helical conformations of **42** near dihedral angles of 160° and 200° are more stable than a *trans* planar conformation of

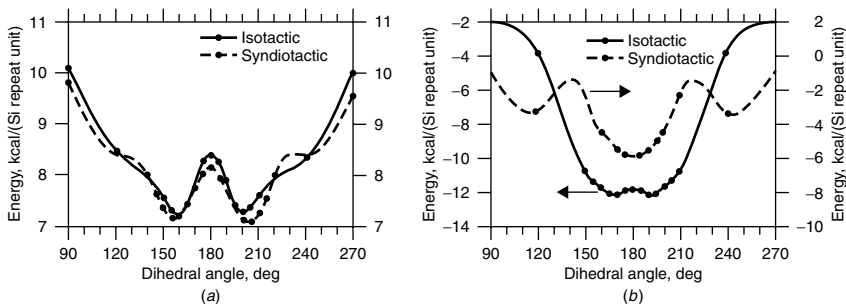


Figure 4.31 Total energy per Si repeat unit of (a) methyl(phenyl)silane oligomer **42** with 21 Si repeat units and (b) *n*-hexyl(phenyl)silane oligomer **46** as a model of **43** with 31 Si repeat units as a function of the Si–Si–Si–Si dihedral angle.

180° regardless of the *it*- and *st*- configuration. The thermodynamic excess energy of the kinetic barrier between the *P*- and *M*-helical states reached about 1 kcal/mol. We also calculated the total energy of *n*-hexyl(phenyl)silane oligomer (**46**) with 31 Si repeat units instead of **43** for simplicity. The conformations of **45** and **46** are almost the same because the UV absorption and FL spectral profiles of **46** trace those of **45**. Figure 4.31*b* shows the total energy of **46** as a function of the dihedral angle. The respective *P*- and *M*-helical conformations of *it*-**46** near 170° and 190° are more stable than a *trans* planar conformation at 180°, although the conformations of the *st* configuration of **46** are stable near 180° for a *trans* planar conformation. If we assume that the total energy of the *st*- configuration is about 4 kcal/mol less stable than that of the *it*- conformation at any dihedral angle, actual **45** is likely to contain mainly *it*- sequences rather than *st* sequences. These calculations and considerations led to the idea that **42** and **43** are most stable in helical conformations rather than *trans* planar structure, regardless of their optical activity.

4.4 Comparison of UV and CD Spectra of Copolymers

In order to discuss the preferential screw sense capability qualitatively in a series of **44** and **45** helical copolymers with chiral–achiral side chains, we compared the UV and CD spectral characteristics of **44** and **45** as a function of the chiral molar composition in detail.

The chiral molar composition dependences of the peak wavelengths in the UV and FL spectra in **44** and **45** are shown in Figure 4.32. As the molar composition of monomer unit with chiral groups changes from 0.00 to 0.50, these

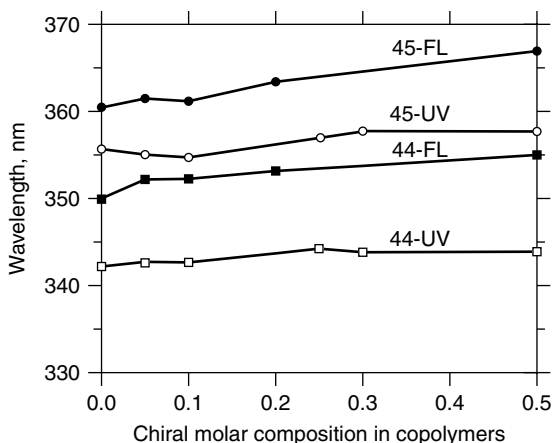


Figure 4.32 UV and FL peak wavelength dependence on molar composition of monomer unit with chiral groups in copolymers **44** and **45** in THF at 23–25°C.

peak wavelengths are only slightly red-shifted: the UV and FL peak wavelengths of **44** change from 342 to 344 nm, and 350 to 355 nm, respectively, while the UV and FL peak wavelengths of **45** change from 356 to 358 nm, and 360 to 367 nm, respectively. As for the overall compositions of monomer with chiral side chains, there were no significant changes in either the UV and FL peak wavelengths or intensities. This means that the introduction of the chiral moiety causes an imbalance between the *P*- and *M*-screw-senses populations only in their helical main chain but does not have a significant effect on their global conformation or local main-chain helical structure.

4.5 Analysis of CD Spectra Based on Ising Model

Figure 4.33 show the values of the Kuhn dissymmetry ratio, g_{abs} in a series of **44** and **45** at CD–UV peak absorption wavelengths as a function of the chiral molar composition. It is already established that the g_{abs} value in a range of optically active polysilanes^{28–32} is very sensitive to changes in both helical pitch and *P*- and *M*-helix population (see Sections 2.5 and 2.6). Although the g_{abs} value for both **44** and **45** increases nonlinearly as the molar composition of the chiral units increases, there is a significant difference in the relation between the g_{abs} value and the chiral composition. The g_{abs} value of **45** increases almost linearly as the chiral composition increases from 0 to 30 mol % and eventually converges at a chiral composition of 30 mol %. In contrast, the g_{abs} value of **44** increases nonlinearly with a convex curvature as the chiral composition increases from 0 to 50 mol %. Although

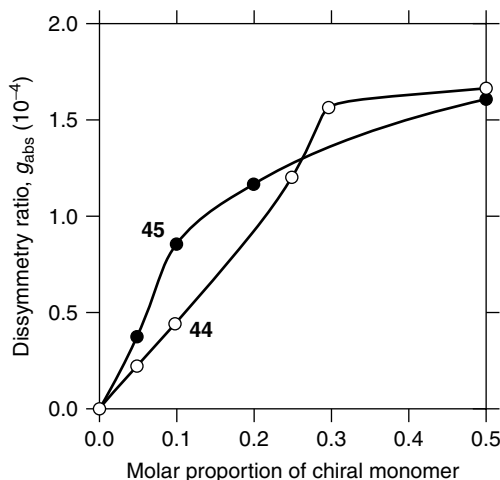


Figure 4.33 Dissymmetry ratios ($g = \Delta\epsilon/\epsilon$) of **44** and **45** in THF at 23–25°C.

poly{(*S*)-2-methylbutyl(phenyl)silane} homopolymer was not produced, probably because of the great steric effect of (*S*)-2-methylbutyl moieties attached to the main chain, we consider these differences to originate from differences in the chain stiffness and/or persistence length between **44** and **45**.

However, the introduction of (*S*)-2-methylbutyl substituents does not cause any great change in their global or local main-chain conformations including the dihedral angle, as discussed above. The population of *P* and *M* motifs, therefore, changes nonlinearly as regards the chiral unit composition. We may call these relations between g_{abs} value and the chiral composition a positive cooperative effect (“a good sergeant–good soldiers effect”) for preferential screw sense helix induction, as already established in poly(alkyl isocyanate) copolymers bearing chiral and achiral side chains.^{18b,18c}

The g_{abs} value in a series of rigid rodlike poly(dialkylsilane)s with a single screw sense helix reaches about $+1.8(\pm 0.2) \times 10^{-4}$, at the UV peak absorption wavelength,^{28f} while that of **44** ($x = 0.30$) is slightly lower, 1.6×10^{-4} at the UV peak absorption. Unfortunately, poly[(*S*)-2-methylbutyl(phenyl)silane] homopolymer (**46**) was not produced, probably because of the great steric effect of (*S*)-2-methylbutyl moieties attached to the main chain. If we assume that the maximum value of poly(alkyl(aryl)silane) derivatives (**44** and **45**) with a single screw sense (100% enantiopure *P* or *M* helix) is $+1.8 \times 10^{-4}$ by extrapolation, the introduction of a 30% chiral unit composition can sufficiently induce an approximately 90% positive Cotton effect helix and a 10% negative Cotton effect helix, which corresponds to an 80% diastereomeric excess for a helix with a positive CD band, into the overall main-chain structure of **45**.

It is considered that, if ideal, optically active poly(alkyl(aryl)silane) homopolymer and copolymer systems could be obtained which had stiffer main-chain structures with longer persistence lengths, it should be possible to clarify the relationship between the g_{abs} value and the chiral molar composition. The magnitude of the chirality of the polyisocyanates allowed precise correlations with the cooperativity models.^{18q} In the theory of the cooperative helical order in polyisocyanates, the polymers are characterized by the chiral order parameter *M*, which is the fraction of the main chain twisting in one helical sense minus the fraction of the main chain twisting in the opposing sense. This order parameter is equal to the optical activity normalized by the value for an entirely one-handed helical polymer. The theory predicts

$$M = \tanh(\Delta G_{\text{h}} Lr / RT) \quad (4)$$

where ΔG_{h} , L , r , T are the helical reversal energy, the helical domain size, the composition of the polymers, and temperature, respectively. Figure 4.34 shows the degree of preferential helical order as a function of chiral molar

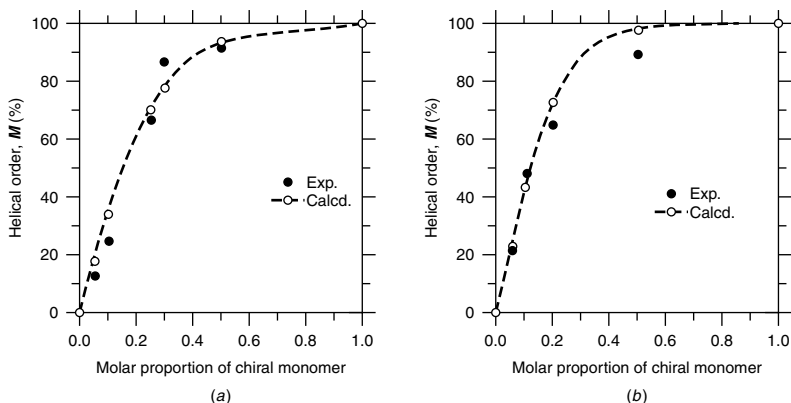


Figure 4.34 Degree of preferential helical order (M) and estimated as a function of chiral molar composition in (a) copolymers **44** and (b) copolymers **45**.

composition in copolymers **44** and **45**. Closed circles are estimated % ee (enantiomeric excess) of helix and open circles are calculated % ee using Eq. (4). Here, the g_{abs} value in Figure 4.33 was normalized, assuming a saturated value is 1.8×10^{-4} by extrapolation. The data were fitted to the function $a \tanh br$, where a is the saturated value and b is $\Delta G_{\text{h}}/RT$. The results are $b = 3.9$ and 3.6 for polymers **44** and **45**, respectively. Here, we could not estimate ΔG_{h} because the L value, which is related to the persistence of the helical conformation against defects allowing change of handedness, is unknown. The b value is much smaller than that of polyisocyanates, which show a sharp response to a small portion of chiral pendant.^{18q} Polysilanes with larger L and ΔG_{h} by modifying their substituents might show a sharper response to a small enantiomeric excess in future.

4.6 Summary of Poly(alkyl(aryl)silane)s

In this part, two series of **44** copolymers with coiled main-chain structures and **45** copolymers with stiff main-chain conformations were described. It was concluded that both optically inactive **42** and **43** adopt helical conformations with an equal proportion of P and M screw senses by means of UV and CD spectra as well as molecular mechanics calculations. A marked “positive” cooperative induction effect of the preferential screw sense in **44** and **45** copolymers was found. However, there is a marked difference in the helical cooperativity between **44** and **45**, probably because of the differences in their global and local conformations. This difference can be related to the persistence of the helical conformation against defects allowing change of

handedness as seen originally in the work of the Italian school on isotactic vinyl polymers^{16a} and later in the polyisocyanates.^{8,12}

5 OPTICALLY ACTIVE DIARYLPOLYSILANES

Among the polysilanes, those with two aryl rings directly attached to the main chain exhibit the longest wavelength UV absorption—typically around 400 nm. The actual value depends on the other aryl ring substituent(s). For reasonable solubility, alkyl chains of four or more carbon atoms should be attached to the aryl rings—and the longer the chain, the longer the wavelength of the absorption maximum. It is recognized that both opening of the silicon main-chain dihedral angles and interaction of the phenyl ring orbitals with those of the silicon chain result in a decreased highest occupied molecular orbital–lowest unoccupied molecular orbital (HOMO–LUMO) gap and hence longer absorption wavelengths^{45,52} For many years the conformation of the diarylpolyisilanes was accordingly discussed in terms of a fully extended, all-*anti* silicon main chain (commonly referred to as all-*trans*) from both theoretical^{39,52a} and experimental⁵⁹ perspectives. However, single-crystal X-ray studies on diphenylsilane oligomers⁵⁷ revealed helical main chains (dihedral angles between 150° and 160° and our molecular mechanics calculations^{30c} on 30-mer chains were consistent with this (see below), affording nonminimum potential energies for all-*anti* structures. To further investigate the higher order structure of diarylpolyisilanes and determine experimentally whether they adopt helical or all-*anti* main-chain conformations, we synthesized a series of homopolymers^{30a} and copolymers bearing chiral and achiral side chains^{30b,30c} containing enantiopure chiral alkyl substituents on the aryl rings. According to this strategy, if the main chain is indeed helical, the presence of the enantiopure chiral substituents should induce a preferential screw sense in the helix, which can then be analyzed by CD and UV spectroscopy, since the main chain itself is chromophoric due to delocalization of the silicon σ and σ^* orbitals. We present first the diarylpolyisilane homopolymers, as these illustrate the general principles, and second the copolymers, which exhibit some more surprising helix inversion phenomena.^{30b} We then discuss the properties and structure of the aggregates formed when poor solvents are added to solutions of such polymers and present the first example of circularly polarized luminescence (CPL) from a polysilane.⁵⁸

5.1 CD and UV Spectroscopy of Homopolymers

The chemical structures of the homopolymers **47–52** are shown in Chart 4.8. The polymers were obtained in yields typically in the range of 5–10%.

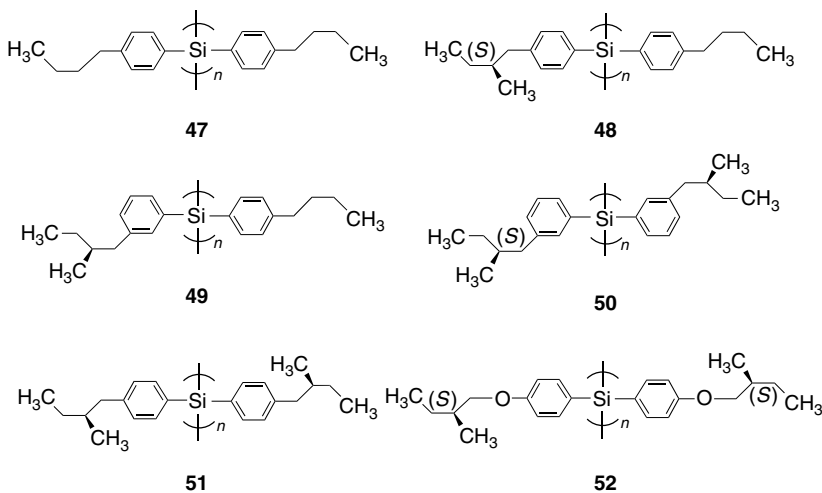
Chart 4.8 Chemical structures of diarylpolysilanes **47–52**.

Table 4.1
Selected Data^a for Homopolymers at 20°C

Cpd	T ^a (°C)	UV ^b (ε/λ _{max} /FWHM)	CD ^b (Δε/λ _{ext})	g _{abs} (10 ⁻⁴)	FL ^a (λ _{max})	M _w ^c (10 ³)
47	20	13,300/394/16	0/—	0	407	434
48	20	10,500/396/19	0.5/395	0.48	408	333
49	20	7,900/397/22	0.27/396	0.34	411	254
50	20	7,400/386/27	-1.60/382	-2.16	404	5
51	20	8,400/395/19	-1.47/384	-0.35	406	240
52	20	4,100/402/22 6,000/327/—	-0.87/397 —	-2.10 —	419	2000

^a UV and CD data in isoctane at -10 and 20°C; fluorescence (FL) data in toluene at room temperature (21°C).

^b ε and Δε units: (Si repeat unit)⁻¹ dm³ cm⁻¹; λ_{max} and λ_{ext} units: nm; FWHM = full width (nm) at half maximum of λ_{max}.

^c Molecular weights determined by SEC and relative to polystyrene standards; eluent: THF.

Table 4.1 lists synthetic and spectroscopic data for **47–52**. It may be seen that the molecular weights (*M_w*) and UV absorption maxima of the polymers are broadly similar, except for **50**, which has a markedly lower *M_w*, and a weaker, broader, slightly blueshifted UV absorption. This difference appears to result from the structure in that the (*S*)-2-methylbutyl groups in

meta positions on the aryl rings afford a less soluble polymer, which consequently self-terminates due to precipitation during synthesis at a relatively low M_w .

Since for the diarylpolysilanes, as for all polysilanes, the main chain is chromophoric due to the electronic transition between the delocalized silicon σ and σ^* orbitals, the electronic spectroscopies of CD, UV-Vis, and FL are particularly powerful probes of the structures of these materials. The magnitude of dimensionless quantity, g_{abs} , is perhaps the most useful in comparing the CD spectra of optically active poly(diarylsilane)s.

The polymers show relatively narrow ($\Delta\nu_{1/2}$ ca. 16 nm) UV absorptions (peak maximum ca. 396 nm) due to the conjugated Si main-chain σ - σ^* transition, mirror image FL emission spectra, small Stokes' shifts (ca. 13 nm) and FLA in the range of 0.20-0.38, indicating regular, semiflexible polymer molecules with long segment lengths.^{28d} Variable temperature CD and UV-Vis studies in dilute solution (1×10^{-4} M in toluene, isoctane or THF) were carried out over the temperature range of -70 to $+80^\circ\text{C}$ and indicated that polymers **48** and **49**, bearing one enantiopure chiral group per monomer unit, afforded a positive Cotton effect in the CD spectrum, coincident with the UV-Vis absorption due to the σ - σ^* transition of the silicon main chain.

Figure 4.35 shows the CD and UV spectra for **48** in isoctane. The observation of the Cotton effect indicates that the chromophore in the polymer, which is a main-chain segment over which the silicon σ and σ^* orbitals are electronically delocalized, exists in a chiral structure: a helix.

The adoption of this higher order helical structure presumably results from the preferential stereorelationship between phenyl ring alkyl substituents on neighboring silicon atoms. While the UV spectra of the polymers are similar,

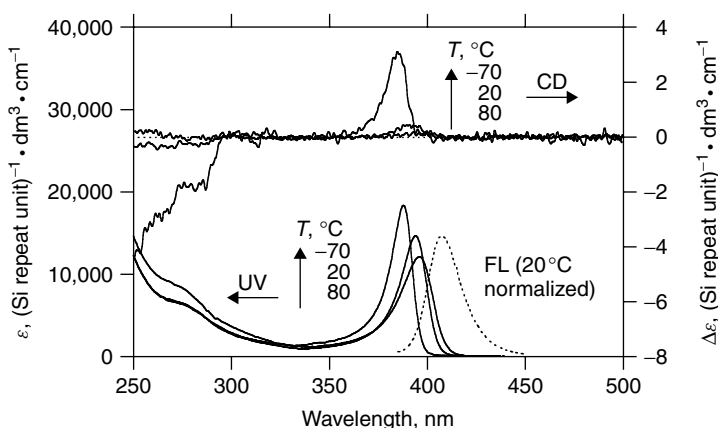


Figure 4.35 CD, UV-Vis, and FL spectra of **48** in isoctane.

the CD spectra depend strongly on the polymer composition. At low temperature, the Cotton effect is greatest, though as the temperature is raised it decreases until around 80°C, when it is typically zero. This indicates that the conformation of the silicon chain is dynamically switching between the two helical screw senses and that, while at low temperature this process is slow and the preferential screw sense emerges, at high temperature the process is fast, effectively equilibrating the populations of the two screw senses. The corollary of the reduction in Cotton effect intensity at high temperature is an increase in $\Delta\epsilon$ with decrease in temperature (in the absence of helical inversion), which has also been observed by other workers.^{18f} Green et al. demonstrated that the optical activity of poly(alkyl isocyanate)s increases with decreasing temperature due to a diminishing number of helix reversals, allowing greater cooperation of main-chain units.^{18b}

Similarly to **48**, the CD spectrum of **49**, the asymmetric homopolymer bearing one *m*-(*S*)-2-methylbutylphenyl and one *p* - *n*-butylphenyl group per silicon atom, exhibits a positive Cotton effect (396 nm) at the lowest energy UV transition, indicating that the main chain adopts the same preferential helical screw sense as that for **48**, although the small Kuhn dissymmetry ratio, g_{abs} , suggests the preference is small. It could be argued that a small g_{abs} value, as in the case of **47**, is the result of an almost planar all-*anti* main-chain conformation; however, an all-*anti* main chain would be expected to have a significantly red-shifted absorption due to the dependence of $\sigma-\sigma^*$ transition energy on a dihedral angle.^{34b,45} Since the CD extrema are almost the same, it is reasonable to suggest that the small g_{abs} value stems rather from a main chain of similar screw pitch, but weaker helical screw sense preference such that partial cancellation of oppositely signed CD bands of major and opposite minor screw sense pseudodiastereomeric helical segments occurs. The weaker screw sense preference in the case of **49** may be a result of the greater ability to mitigate steric congestion by phenyl ring rotation to minimize interaction between the *meta* chiral alkyl groups on nearest and next nearest silicon atoms.

In contrast, the CD spectra of **50**, **51**, and **52** exhibit negative Cotton effects, as shown in Figure 4.36 for **50**. This implies a helical conformation, but of the *opposite* preferential screw sense to **48** and **49**, even though the enantiopure chiral moiety in all cases is the (*S*)-2-methylbutyl group. Similarly, the Cotton effect is of greatest magnitude (negative) at low temperature and almost very much reduced at 80°C.

It is thus apparent that despite the fact that only (*S*)-chiral substituents are employed, polymers exhibiting either positive or negative CD spectra may be obtained, corresponding to helical polymers with opposing screw senses. This finding is significant in that to obtain homopolymers with opposing screw senses it is not necessary to use both enantiomeric forms of the chiral group.

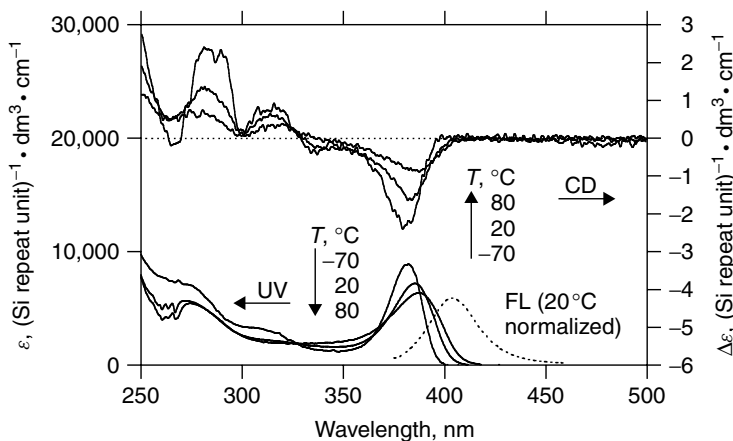


Figure 4.36 CD, UV, and FL spectra of **50** in isoctane.

In any potential applications, the cheaper enantiomer [usually (*S*), due to its procurement from natural sources] may therefore be employed.

It is possible that the helicity is a result of the chiral substitution itself and that the polymers with achiral substituents have, in fact, all-*anti* conformations. While this possibility cannot be directly ruled out, comparison of the spectroscopic data for the polymers with chiral substituents and achiral substituents, for example, **47** and **48**, respectively, indicates similar main-chain dihedral angles, since the UV absorption maxima are so similar. Both polymers should therefore be latent helical, that is, contain segments of opposite screw sense separated by strong kinks (helix reversal points), with the difference being that in the case of **47** the overall numbers of *P* and *M* turns are equal, whereas for **48**, one of the screw senses predominates, resulting in net helicity and optical activity.

One other possible factor affecting CD and UV data is the helical domain size (polymer chain length divided by number of helix reversals, the latter possibly reducing conjugation): where the helical domain size is larger than the effective conjugation length of the silicon main chain, there should be no significant effect on the UV energy or intensity, although the resultant CD will depend on the position of the helix reversal. Where, however, steric constraints impose a helical domain size shorter than the effective conjugation length, the UV peak should undergo a blue shift and possibly broaden. The CD wavelength would also undergo a blue shift, though the sign of the effect should depend rather more on the relative proportions of *P*- and *M*-screw-sense domains, rather than the size of the domain. Unambiguous experimental support for these hypotheses, however, is still required.

5.2 Molecular Mechanics Calculations

For polymers with achiral substituents, molecular mechanics calculations (Discover 3, ver. 4.00; simple minimization) by us of potential energy as a function of dihedral angle afforded symmetrical multi-well-potential curves, with non-minimum 180° values, as shown in Figures 4.37a and 4.37b for H-(Ph₂Si)₃₀-H and H-[(*p-n*-BuPh)₂Si]₃₀-H, respectively.

These predicate helical main-chain conformations, and since the curves are symmetrical, equal proportions of *P* and *M* turns should exist, resulting in overall optical inactivity from the internal racemate. This indication of helicity is in contrast to literature reports, which suggested an all-*anti* conformation⁵⁹ for perphenylated oligosilanes, but in agreement with our experimental observations. When we performed calculations for a polysilane with small substituents, that is, Cl-(Cl₂Si)₃₀-Cl, we did obtain an all-*anti* conformation³¹ in agreement with a single-crystal X-ray diffraction study,⁴⁰ with a potential energy minimum at 180° , though with all other, bulkier, substituents (aryl and aliphatic), helical structures are predicted.^{28d,30c} Calculations of diarylpoly silane models bearing enantiopure chiral substituents, however, afforded nonsymmetrical potential energy dependence on dihedral angle,^{30c} as seen in Figures 4.38a and b, which show plots for the model compounds H-[(*p-n*-BuPh)(*p*-(*S*)-2-MeBuPh)Si]₃₀-H and H-[*p*-(*S*)-2-MeBuPh]₂Si]₃₀-H, bearing one and two chiral groups per monomer unit, respectively. These plots suggest that both *P*- and *M*-screw-sense turns should coexist, but that the lower energy *M* turns should be in greater abundance, resulting in an excess of these and consequent optical activity, corroborating our experimental conclusions from CD studies of helicity. In contrast to experiment, though, the calculations did not indicate opposite screw sense preferences for models with one and two enantiopure chiral groups per monomer unit.

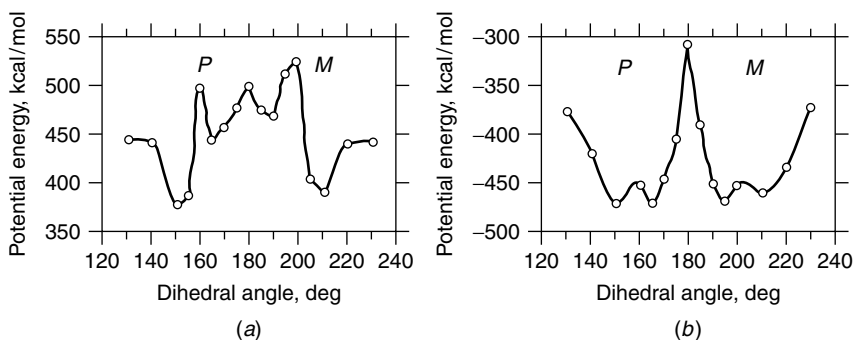
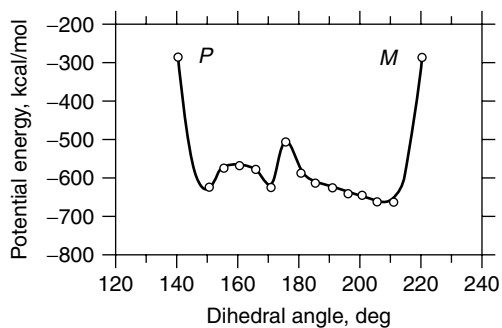
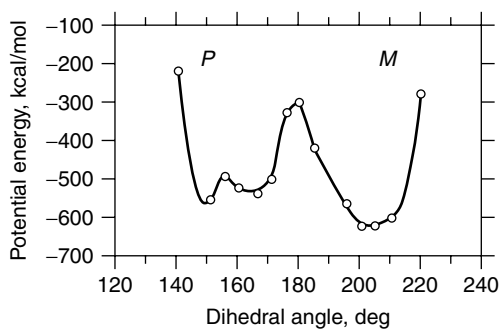


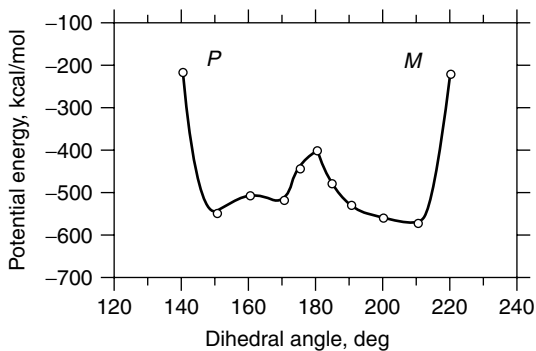
Figure 4.37 Potential energy as function of Si-Si-Si-Si dihedral angle for model diarylpoly silanes with achiral substituents (a) H-(Ph₂Si)₃₀-H and (b) H-[(*p-n*-BuPh)₂Si]₃₀-H.



(a)



(b)



(c)

Figure 4.38 Potential energy as function of Si-Si-Si-Si dihedral angle for mono- and dienantiopure chiral alkyl-substituted model diarylpolsilanes (a) $H-(Ar^*_2Si)_{30}-H$, (b) $st-H-(ArAr^*Si)_{30}-H$, and (c) $it-H-(ArAr^*Si)_{30}-H$ (where Ar = 4-*n*-butylphenyl, and Ar* = 4-(*S*)-2-methylbutylphenyl).

5.3 CD and UV Spectroscopy and Cooperativity in Copolymers

One point of great interest concerning polymers with supramolecular helicity is the effect on the conformation of “diluting” the chiral content by incorporation of achiral monomer units to give chiral–achiral copolymers. It is now well established for the helical polyisocyanates^{8,12} that interactions between side chains in neighboring monomer units can result in stereochemical conformational locking within polymer segments (i.e., between major kinks or helix reversals) and that chiral monomer units can exert stereochemical control over the helicity of adjacent achiral monomer units. Termed the “sergeants-and-soldiers effect” to describe the nonlinear relation between the specific optical rotation of the polymer and the *ee* of the chiral units,^{8,16} this phenomenon has also been observed very clearly in the dialkylpolysilanes, where even 0.6 mol % was effective to induce almost complete helical screw sense selection^{28g,32} (see Sections 2.4 and 2.5). It was of interest to us to investigate whether such an effect could also be observed for the diarylpolysilanes since in any device application, considerable saving in costs could be achieved if preferential screw sense helical polymers could be obtained from largely achiral materials.

The spectroscopy data of the copolymers, **53**–**58**^{30c} (see Chart 4.9), which are similar to the data for **48**–**52**, are listed in Table 4.2.

As for the homopolymers, dilute solution (1×10^{-4} M in toluene, isoctane or THF) spectroscopic studies were carried out over the temperature range of -70 to $+80^\circ\text{C}$. The CD spectrum of **54** (Figure 4.39), containing 50% *p*-(*S*)-2-methylbutylphenyl-substituted monomer units, exhibits a positively signed Cotton effect (389 nm), almost coincident with the lowest energy main-chain electronic transition (σ – σ^*) in the 20°C UV spectrum (394 nm). The CD spectra of **53** and **55** show similar features to that of **54**, and the similarity

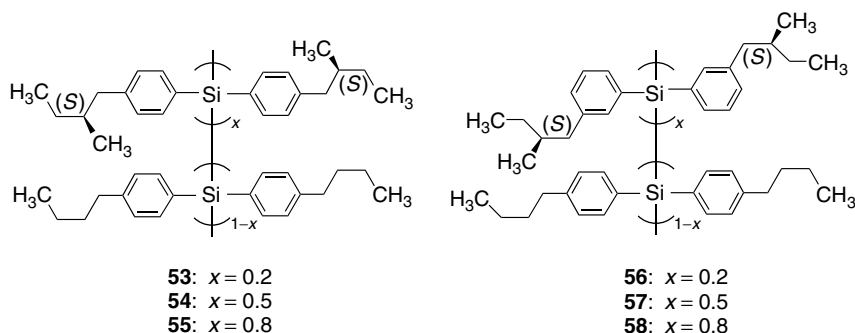


Chart 4.9 Chemical structure of optically active poly(diarylsilane) copolymers.

Table 4.2
Selected Data^a for Copolymers **53**–**58** at 20°C

Cpd	UV ^b (ϵ/λ_{\max} /FWHM)	CD ^b ($\Delta\epsilon/\lambda_{\text{ext}}$)	g_{abs} (10^{-4})	FL ^a (λ_{\max})	M_w^c (10^3)
53	10,900/393/17	0.45/391	0.41	407	162
54	17,400/394/15	1.73/389	0.99	407	186
55	14,700/395/17	0.81/394	0.55	407	247
56	24,300/397/14	0.24/393	0.10	409	474
57	25,700/399/15	-0.61/400	-0.24	411	271
58	10,400/393/19	-1.06/392	-1.02	408	8

^a UV and CD data in isoctane at -10 and 20°C; FL data in toluene at room temperature (21°C).

^b ϵ and $\Delta\epsilon$ units: (Si repeat unit)⁻¹ dm³ cm⁻¹; λ_{\max} and λ_{ext} units: nm; FWHM = full width (nm) at half maximum of λ_{\max} .

^c Molecular weights determined by SEC and relative to polystyrene standards; eluent: THF.

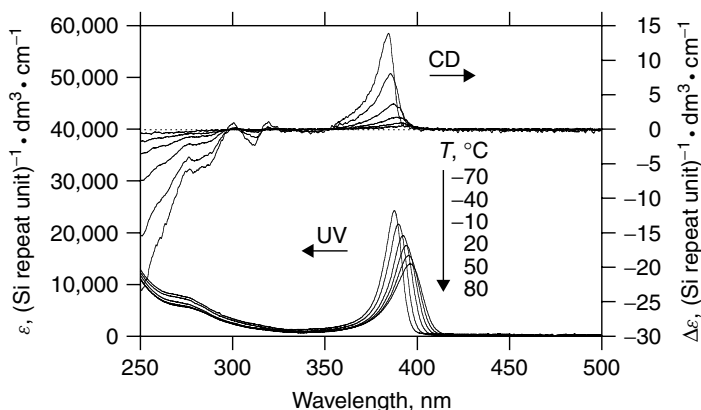


Figure 4.39 Variable temperature CD and UV spectra of **54** in isoctane.

of these data with those for the homopolymers indicates that the copolymers can therefore also be expected to adopt helical conformations in a segmented structure, the individual segments of which comprise helical turns of alternating helicity. As for the homopolymers above, the preference for one screw sense over the other leads to net helicity and optical activity.

To investigate cooperativity in these copolymers, the g_{abs} ratios were evaluated. The dissymmetry ratio, g_{abs} , is displayed as a function of chiral content for **47**, **50**, **51**, and **53**–**58** at 20°C in Figure 4.40. It is evident that the absolute magnitudes of $|g_{\text{abs}}|$ (i.e., independent of sign) for the *para*-phenyl-substituted

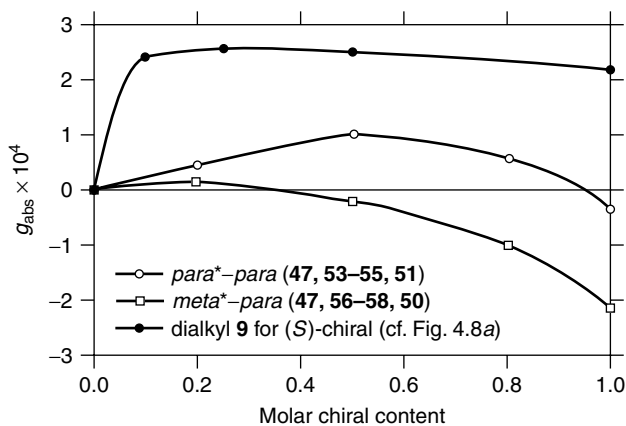


Figure 4.40 Dissymmetry ratio g_{abs} as a function of chiral content for **50**, **51**, and **53–58** at 20°C.

copolymers **53–55** exceed those for enantiopure chirally substituted homopolymer **51**. Since the spectroscopic data (UV, FL, FLE, and FLA) are similar for all the polymers (see Tables 4.1 and 4.2), it is reasonable to assume that polymer main-chain dihedral angles are also similar, so that an increase in g_{abs} should thus imply greater helical screw sense selectivity. The larger g_{abs} values for copolymers **53–55** compared with homopolymer **51** may therefore indicate that the cooperative effect in the *para*-phenyl-substituted copolymer cases is such as to induce helical main-chain conformations with greater screw sense selectivity than the enantiopure-substituted poly(diarylsilane) homopolymer, in which there is assumed to be a minor presence of segments of the less favored, opposite, chiral sense, resulting in a lower dissymmetry ratio.

Among **53–55**, **54** with a chiral–achiral ratio of 0.5 : 0.5 shows the greatest absolute dissymmetric ratio. At higher chiral content than this, the dissymmetric ratio decreases again, becoming negative for the bis-chiral homopolymer **51**,^{30a,30c} indicating a change of preferential screw sense. This cooperativity is unusual and contrasts with that observed in other optically active copolymer systems such as poly(alkyl isocyanate)s,^{18b} poly(aryl isocyanate),^{18p} and poly(dialkylsilane)s.^{28a–c,28g} In these latter cases, the screw sense is determined by a small minority of enantiopure chiral repeat units, and the dissymmetric ratio is constant or only slightly increases at greater chiral content levels.^{28g} The CD and UV spectra of all three polymers **53–55** exhibit temperature dependence as is evident for **54** in Figure 4.39 and presented graphically for all the copolymers in Figures 4.41a and b (which show plots of UV and CD λ_{max} intensities vs. temperature, respectively), the UV λ_{max} shifting to slightly longer values at higher temperatures with generally a concomitant reduction

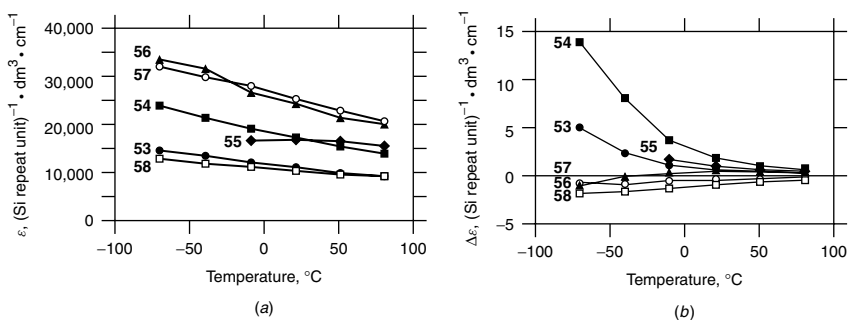


Figure 4.41 Plots of (a) UV and (b) CD λ_{\max} intensities vs. temperature in toluene.

in intensity and the CD intensity dropping in most cases to near zero at about 80°C. This is consistent with the loss of helical screw sense preference due to the thermal energy exceeding that of the conformational fixing effect and consequent partial cancellation of oppositely signed CD bands.

In contrast, however, the CD spectrum of **57**, containing 50% bis-*m*-(*S*)-2-methylbutylphenyl units, exhibits very weak negative CD bands (dissymmetry ratio at -10°C , $g_{\text{abs}} = -0.23 \times 10^{-4}$), lower by a factor of 4–8 than those of **53**–**55**, indicating that there is only a weak cooperative effect in the *meta* case, the main chain adopting the opposite screw sense to the *para*-substituted cases, presumably resulting from the better alleviation of steric hindrance afforded. Two possible, nonexclusive, reasons can be considered to account for the lower dissymmetry ratio: (i) The polymer main-chain dihedral angles are very close to 180° , resulting in a looser helix. (ii) Although the main chain is helical, there is less dominant screw sense selectivity, thus giving rise to weaker Cotton effects through partial cancellation of oppositely signed CD bands.^{30c} This may result from the greater ability of **57** to mitigate steric congestion by phenyl ring rotation, minimizing interaction between the *meta* chiral alkyl group and *p*-*n*-butyl or *m*-(*S*)-2-methylbutyl groups on neighboring silicon atoms. As can be seen by comparing the data in Table 4.2, the room temperature spectroscopic data (excluding CD) for all the polymers are similar, though **57** exhibits a longer UV absorption maximum (indicative of more open main-chain dihedral angles)^{59b} than **53** and **55**. Although it is not possible at present to definitively state the origin of the weaker Cotton effects observed for **57**, we suggest that both factors outlined above are responsible, viz. **57** has a loose helical structure (near to all *anti*) in which *P*- and *M*-sense helical turns coexist but in unequal proportions. For copolymer **58**, similar spectral features to **57** are evident, though with increasing negative dissymmetry ratios and in the *meta*-phenyl-substituted series, it is the homopolymer (**50**) which evidences the highest dissymmetry ratio.

5.4 Thermo-Driven Helix–Helix Transition

In the case of **56**, containing 20% *m*-(*S*)-2-methylbutylphenyl-substituted monomer units, as can be seen in Figure 4.42, the CD spectrum shows a negative Cotton effect at -70°C , whereas at 50°C , the effect is positive and at -10°C the signal is approximately zero.^{30b} This indicates a change in the main chain from one prevailing helical screw sense to the other—a rare example of a temperature-driven helical inversion of a polymer in dilute solution. There are only a few other reports of such solution state inversions; these concern, for example, certain poly(α -amino acid ester)s,⁴⁷ poly(β -phenethyl *l*-aspartate),^{49,50} a poly(aryl isocyanate),^{18p} poly(dialkylsilane)s,^{28m,28o,28q,28u,28w} and most recently, some polyisocyanate copolymers.^{18t}

The dissymmetric ratio, g_{abs} , is small for **56** at the temperature listed in Table 4.2 (20°C), since this is close to the transition temperature. However, at -70°C , g_{abs} is -0.38×10^{-4} , greater than that for **57** (-0.27×10^{-4}), but less than that for **58** (-1.57×10^{-4}). By comparison, g_{abs} for the related homopolymer **50** at 20°C is -2.00×10^{-4} .^{30a} The lower dissymmetric ratios for the bis(*m*-(*S*)-2-methylbutylphenyl}-silane copolymers **56–58**, therefore, are most probably the consequence of the coexistence of both helical screw senses in **56–58** at all temperatures.

Consistent with the above suggestion, at -10°C , the CD spectrum of **56** actually has a small negative component at ~ 401 nm in addition to the small positive peak at 390 nm. We ascribe these two bands to the two different screw senses, which should be characterized by different screw pitches.^{28e} It is not possible, however, to associate a particular screw sense with the sign of the Cotton effect. The maximum magnitude of the positive Cotton effect for **56** occurs around 50°C , but it is less than the maximum negative magnitude, as may be seen from the plot of CD intensity $\Delta\epsilon$ vs. T in Figure 4.43.

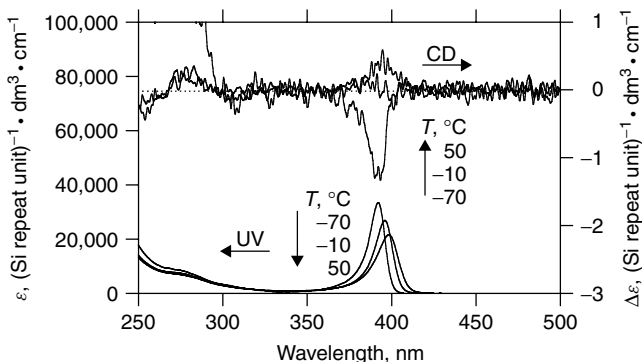


Figure 4.42 CD and UV spectra for *PM* transition diarylpolyisilane **56**.

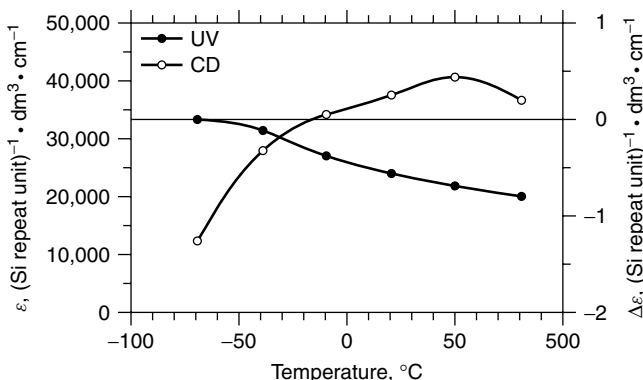


Figure 4.43 CD (right ordinate) and UV (left ordinate) intensities vs. temperature for **56**, showing *PM* transition in toluene.

Above 50°C, the CD signal intensity decreases again, a feature in common with the other poly(diarylsilane)s,^{30c} which we attribute to thermal population of the higher energy screw sense state, but additionally, though to a much lesser degree, to thermal broadening of the bands as a result of slight bond length increase (the molar absorptivities for UV and CD spectra decrease with increasing temperature).

A temperature cycling experiment comprising three cycles of -70/50°C with CD and UV spectra recorded at each temperature for **56** indicated that the transition is reversible, with negative and positive Cotton effects being observed at the low and high temperatures, respectively, as is evident in Figure 4.44.

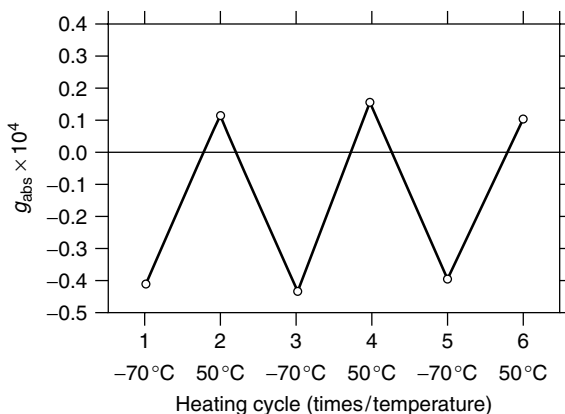


Figure 4.44 Temperature cycling experiment for **56** in toluene.

Despite the fact that the diarylpolysilanes are among the most robust polysilanes, indefinite cycling would not be possible, as the polymers are photosensitive and degrade by Si–Si bond scission. Excluding CD results, the data for the homologous copolymer **57**, with a ratio of enantiopure chiral monomer to achiral monomer of 0.5 : 0.5, are similar to those of **56**. Copolymer **58** (chiral–achiral = 0.8 : 0.2) with lower *M* (due to lower solubility during synthesis) has slightly lower UV molar absorptivity but is otherwise also comparable to **56**, indicating similar polymer structures for **56–58**. The CD data, however, are markedly different: whereas **56** shows negative Cotton effects at low temperature and positive at high temperature, indicating a transition from one helical screw sense to the other, **57**, **58**, and the above-mentioned related homopolymer, **50**, show only negative Cotton effects at all temperatures and thus do not exhibit this phenomenon; that is, this function is specific to **56**.

It is apparent, therefore, that a subtle interplay of factors permits such a *PM* transition, presumably as a result of the enthalpy and entropy terms in the Gibbs free-energy equation being of the same sign, such that the free-energy difference changes sign as a function of temperature, as was proposed in discussions of *PM* transitions for certain polyisocyanates.^{18m,18t} In the present case, since we consider that both *P* and *M* screw senses coexist in these polymer systems, the transition may be considered to reflect the gradual thermodynamic stabilization of one screw sense relative to the other, as the populations alter with temperature, rather than an abrupt switch.

5.5 Poly(diarylsilane) Aggregates

Aggregates—microprecipitates of tens to thousands of polymer molecules—are formed for the poly(diarylsilane)s when a poor solvent such as methanol is added to a molecularly disperse solution of the polymer in a good solvent, such as toluene or THF. Aggregates can be invisible to the naked eye or appear as a faint cloudiness in the solution and are amenable to study by many solution techniques such as solution state CD and UV spectroscopy. Since aggregates are the first stage of a solid precipitate, they are also therefore useful as model materials of the solid bulk state polymers. Here we describe briefly our initial investigations of poly(diarylsilane) aggregates.^{57a}

The UV and CD spectra of **48** in toluene after addition of methanol are shown in Figure 4.45 and are typical of the spectra obtained for poly(diarylsilane)s under such conditions. The typical polysilane aggregate UV spectrum is similar to the solution state spectrum, although often the intensity of the absorption is reduced, and absorption tails into the visible as some light is effectively prevented from reaching the detector (by scattering and absorption), resulting in nonflat baselines. The polysilane aggregate CD spectrum, however, is markedly different from the solution state spectrum, and instead of a single

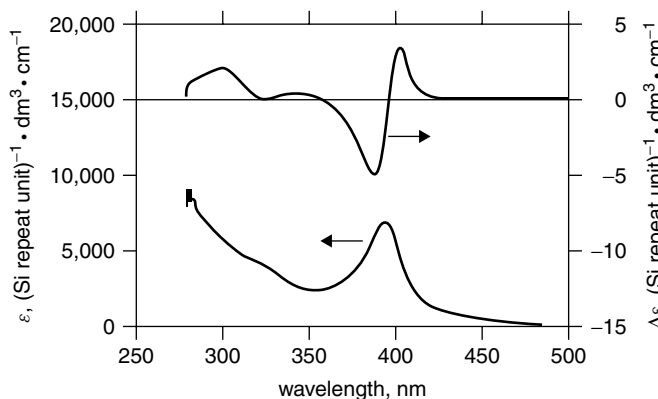


Figure 4.45 Aggregates of **48** in toluene/MeOH (normal addition); upper curves CD, lower curves UV.

Cotton effect of positive or negative sign coincident with the UV spectrum, a bisignate Cotton effect is produced as a result of coupled excitonic interactions (Davidov coupling). By convention, a bisignate Cotton effect takes the sign of the longer wavelength extremum; thus in Figure 4.45, the bisignate Cotton effects are positive.

The poly(diarylsilane) aggregate CD and UV appearances are similar to those for the poly[alkyl(alkoxyphenyl)silane]s, although shifted to longer wavelength due to the presence of two phenyl rings. However, while the latter contain an oxygen atom, allowing effective interaction with solvents and guest molecules, the former do not, and are thus less responsive to their environment.

5.6 Circularly Polarized Photoluminescence

Photoluminescence (PL) in the polysilanes is well documented,^{34b,34c} and for the poly(diarylsilane)s occurs typically with a small Stokes shift and almost mirror image profile of the UV absorption.⁵⁹ This is due to the similarity of the chromophore and fluorophore structures in the ground and excited states, respectively, which is a result of the fact that little structural change occurs on excitation of the electrons from the σ to the σ^* orbitals. As PL is the emissive counterpart to UV, the emissive counterpart to CD is circularly polarized photoluminescence (CPPL). Where the fluorophore is chiral, then the photoexcited state can return to the ground state with emission of circularly polarized light, the direction of polarization of which depends on the relative intensities of the right-handed and left-handed emissions (I_R and I_L , respectively), which in turn depends on the chirality of the material, or more accurately, the chirality

of the photoexcited state of the material.³⁷ Preliminary investigations⁵⁸ have shown that CPPL can indeed be observed, although the intensity is low.

Accordingly, an aggregate phase of **48** in toluene and methanol (1 : 1) at 20°C was prepared by the normal addition method, and the CPPL emission spectrum was measured while irradiating at 350 nm, on the higher frequency side of the positive/negative extremum centered at 395 nm. The CPPL λ_{max} occurs at 412 nm, matching the emission peak, and is negative in sign. The luminescence dissymmetric ratio, g_{lum} , is approximately -1.8×10^{-3} for aggregates of **54**,⁶⁰ which is similar in magnitude to the g_{abs} value (1.4×10^{-3}) for CD in UV at 390 nm, indicating that the helical characteristics of the polymer are similar in excited and ground states. This constitutes the first observation of CPPL for a polysilane and is a promising indicator of the possibility of circularly polarized electroluminescent (CPEL) emission from these polymers.

5.7 Summary and Conclusions for Diarylpolysilanes

This section describes the preparation of the first optically active diarylpolysilanes with preferential screw sense helical main-chain conformations in solution and extended main-chain structures. These polymers are soluble, semiconducting materials with strong FL emission. It is seen that homopolymers of either screw sense (and thus sign of the Cotton effect in the CD spectrum, both positive and negative), containing only the (*S*)-2-methylbutylphenyl group as a chiral moiety, are accessible, depending on the number of chiral moieties per Si repeat unit. In the copolymers, temperature-dependent cooperative side-chain interactions are evident, the most important of which is the occurrence of an inversion of sign of optical activity for one particular polymer with temperature, arising from a transition from one helical screw sense to the other.

The side-chain–main-chain relationships and observation of CPL discussed here should provide insight into the design of CP (circularly polarized), CPL (CP photoluminescence), and CPEL (CP electroluminescence) devices using only single-handed enantiopure chiral moieties. The results concerning the *PM* transition polymer are particularly significant since materials with higher order structural regularity which exhibit physical responses to external stimuli are being designed and prepared for use in devices.

ACKNOWLEDGMENTS

The authors thank Hiromi Tamoto-Takigawa and Masao Motonaga for CD, UV, FL, and SEC measurements. Prof. Kyozauro Takeda (Waseda University), Dr. Hiroyuki Teramae (ATR), Dr. Masaie Fujino, Dr. Hiroaki Isaka,

Dr. Keisuke Ebata, and Dr. Kazuaki Furukawa are thanked for valuable discussions on the electronic structure and optoelectronic properties of polysilanes at NTT. Prof. Nobuo Matsumoto (Shonan Institute of Technology), and Drs. Masao Morita, Kei-ichi Torimitsu, and Hideaki Takayanagi are acknowledged for encouragement and generous support at NTT during the course of this study.

Prof. Mark M. Green (Polytechnic University) is acknowledged for inviting us into the world of the cooperative science of helical polymers. Prof. Akio Teramoto (Ritsumeikan University), Prof. Takahiro Sato (Osaka University), Prof. Naotaka Nakamura (Ritsumeikan University), Prof. Junji Watanabe (Tokyo Institute of Technology), Prof. Shoji Furukawa (Kyushu Institute of Technology), Prof. Eiji Yashima (Nagoya University), Prof. Yoshihisa Inoue (Osaka University), Prof. Masashi Kunitake (Kumamoto University), Dr. Ken Terao (formerly from CREST-JST, now Gunma University), Ikuyo Terakawa (CREST-JST), and Yoshimi Iwamoto-Terao (CREST-JST) are gratefully acknowledged for collaboration and fruitful discussion on the global conformational structure and energy of polysilanes in solution. Drs. Hong-Zhi Tang (CREST-JST) and Zhong-Biao Zhang (formerly from CREST-JST, now University of Southern California) are grateful for fruitful discussion on optically activity of polysilanes.

Finally, Prof. Hideki Sakurai (Science University of Tokyo), Prof. Yoshio Okamoto (Nagoya University), Prof. Toyoki Kunitake (University of Kitakyushu), Prof. Masaki Hasegawa (Toin University of Yokohama), and Dr. Katsuhiko Kuroda (CREST-JST) are acknowledged for their encouragement and Yukiko Shimamura (CREST-JST) for able assistance.

REFERENCES

1. (a) Mason, S. F. *Nature* **1984**, *311*, 19. (b) Mason, S. F. *Chemical Evolution: Origin of the Elements, Molecules, and Living Systems*. Oxford, London, 1991. (c) Mason, S. F. In *Circular Dichroism: Principles and Applications*, 2nd ed. Berova, N.; Nakanishi, K.; Woody, R. W. (Eds.). Wiley-VCH, New York, 2000, Chapter 2.
2. (a) Bonner, W. A.; Kavasmaneck, P. R.; Martin, F. S.; Flores, J. J. *Science* **1975**, *186*, 143. (b) Bonner, W. A. *Chirality*, **2000**, *12*, 114.
3. (a) Avalos, M.; Babiano, R.; Cintas, P.; Jiménez, J. L.; Palacios, J. C. *Tetrahedron: Asymmetry* **1997**, *8*, 2997. (b) Avalos, M.; Babiano, R.; Cintas, P.; Jiménez, J. L.; Palacios, J. C.; Barron, L. D. *Chem. Rev.* **1998**, *98*, 2391.
4. (a) Quack, M. *Angew. Chem. Int. Ed. Engl.* **1989**, *28*, 571. (b) Berger, R.; Quack, M. *ChemPhysChem*. **2001**, *1*, 57.
5. (a) Cline, D. B. (Ed.) *Physical Origin of Homochirality in Life*. American Institute of Physics, Woodbury, NY, 1996. (b) Hasegawa, M. *Proc. Jpn. Acad.* **1992**, *68B*, 9.
6. Farina, M. *Top. Stereochem.* **1987**, *17*, 1.

7. (a) Okamoto, Y.; Nakano, T. *Chem. Rev.* **1994**, *94*, 349. (b) Nolte, R. J. M. *Chem. Soc. Rev.* **1994**, *23*, 11. (c) Zabrodsky, Z.; Peleg, S.; Avnir, D. *J. Am. Chem. Soc.* **1993**, *115*, 8278. (d) Fowler, P. W. *Nature* **1992**, *360*, 626. (e) Nakano, T.; Okamoto, Y. *Chem. Rev.* **2001**, *101*, 4013. (f) Cornelissen, J. J. L. M.; Rowan, A. E.; Nolte, R. J. M.; Sommerdijk, N. A. J. M. *Chem. Rev.* **2001**, *101*, 4039.
8. (a) Green, M. M.; Peterson, N. C.; Sato, T.; Teramoto, A.; Cook, R.; Lifson, S. *Science* **1995**, *268*, 1860. (b) Green, M. M.; Park, J.-W.; Sato, T.; Teramoto, A.; Lifson, S.; Selinger, R. L. B.; Selinger, J. V. *Angew. Chem. Int. Ed.* **1999**, *38*, 3138. (c) Green, M. M. In *Circular Dichroism: Principles and Applications*, 2nd ed. Berova, N.; Nakanishi, K.; Woody, R. W. (Eds.). Wiley-VCH, New York, 2000, Chapter 17. (d) Green, M. M.; Cheon, K.-P.; Yang, S.-Y.; Park, J.-W.; Swanburg, S.; Liu, W. *Acc. Chem. Res.* **2001**, *34*, 672.
9. Yashima, E.; Okamoto, Y. In *Circular Dichroism: Principles and Applications*, 2nd ed. Berova, N.; Nakanishi, K.; Woody, R. W. (Eds.). Wiley-VCH, New York, 2000, Chapter 18.
10. Berova, N.; Nakanishi, K.; Woody, R. W. (Eds.), *Circular Dichroism: Principles and Applications*, 2nd ed., Wiley-VCH, New York, 2000.
11. Pu, L. *Acta Polym.* **1997**, *48*, 116.
12. (a) Teramoto, A. *Prog. Polym. Sci.* **2001**, *26*, 667. (b) Teramoto, A. *Rep. Prog. Polym. Phys. Jpn.* **1998**, *41*, 25.
13. (a) Nolte, R. J. M.; van Beijnen, A. J. M.; Drenth, W. *J. Am. Chem. Soc.* **1974**, *96*, 5932. (b) van Beijnen, A. J. M.; Nolte, R. J. M.; Drenth, W.; Hezemans, A. M. F. *Tetrahedron* **1976**, *32*, 2017.
14. (a) Okamoto, Y.; Suzuki, K.; Ohta, K.; Hatada, K.; Yuki, H. *J. Am. Chem. Soc.* **1979**, *101*, 4768. (b) Nakano, T.; Okamoto, Y. *Macromol. Rapid Commun.* **2000**, *21*, 603.
15. Goodman, M.; Chen, S.-C. *Macromolecules* **1971**, *4*, 625.
16. (a) Carlini, C.; Pino, P.; Ciardelli, F. *Makromol. Chem.* **1968**, *119*, 244. (b) Pino, P.; Ciardelli, F.; Montagnoli, G.; Pieroni, O. *J. Polym. Sci., Polym. Lett. Ed.* **1967**, *5*, 307.
17. (a) Kamer, P. C. J.; Cleij, M. C.; Nolte, R. J. M.; Harada, T.; Hezemans, A. M. F.; Drenth, W. *J. Am. Chem. Soc.* **1988**, *110*, 1581. (b) Green, M. M.; Gross, R. A.; Schilling, F. C.; Zero, K.; Crosby III, C. C. *Macromolecules* **1988**, *21*, 1839. (c) Deming, T. J.; Novak, B. M. *J. Am. Chem. Soc.* **1992**, *114*, 7926. (d) Ito, Y.; Ihara, E.; Murakami, M. *Angew. Chem. Int. Ed. Engl.* **1992**, *31*, 1509. (e) Kauranen, M.; Verbiest, T.; Boutton, C.; Teerenstra, M. N.; Clays, K.; Schouten, A. J.; Nolte, R. J. M.; Persoons, A. *Science* **1995**, *270*, 966. (f) Takei, F.; Yanai, K.; Onitsuka, K.; Takahashi, S. *Angew. Chem. Int. Ed. Engl.* **1996**, *35*, 1554. (g) Ramos, E.; Bosch, J.; Serrano, J.-L.; Sierra, T.; Veciana, J. *J. Am. Chem. Soc.* **1996**, *118*, 4703. (h) Amabilino, D. B.; Ramos, E.; Serrano, J.-L.; Sierra, T.; Veciana, J. *J. Am. Chem. Soc.* **1998**, *120*, 9126. (i) Ito, Y.; Miyake, T.; Hatano, S.; Shima, R.; Ohara, T.; Suginome, M. *J. Am. Chem. Soc.* **1998**, *120*, 11880. (j) Takei, F.; Hayashi, H.; Onitsuka, K.; Kobayashi, N.; Takahashi, S. *Angew. Chem. Int. Ed. Engl.* **2001**, *41*, 4092.
18. (a) Green, M. M.; Andreola, C.; Muñoz, B.; Reidy, M. P.; Zero, K. *J. Am. Chem. Soc.* **1988**, *110*, 4043. (b) Green, M. M.; Reidy, M. P.; Johnson, R. J.; Darling, G.; O'Leary, D. J.; Willson, G. *J. Am. Chem. Soc.* **1989**, *111*, 6452. (c) Okamoto, Y.; Matsuda, M.; Nakano, T.; Yashima, E. *Polym. J.* **1993**, *25*, 391. (d) Green, M. M.; Khatri, C.; Peterson, N. C. *J. Am. Chem. Soc.* **1993**, *115*, 4941. (e) Müller, M.; Zentel, R. *Macromolecules* **1994**, *27*, 4404. (f) Maxein, G.; Zentel, R. *Macromolecules* **1995**, *28*, 8438. (g) Maeda, K.; Matsuda, M.; Nakano, T.; Okamoto, Y. *Polym. J.* **1995**, *27*, 141. (h) Green, M. M.; Garetz, B. A.; Munoz, B.; Chang, H.-P. *J. Am. Chem. Soc.* **1995**, *117*, 4181. (i) Müller, M.; Zentel, R. *Macromolecules* **1996**, *29*, 1609. (j) Guenet, J. M.; Jeon, H. S. J.; Khatri, C.; Jha, S. K.; Balsara, N. P.; Green, M. M.; Brulet, A.; Thierry, A. *Macromolecules* **1997**, *30*, 4590.

- (k) Khatri, C. A.; Pavlova, Y.; Green, M. M.; Morawetz, H. *J. Am. Chem. Soc.* **1997**, *119*, 6991. (l) Mayer, S.; Maxein, G.; Zentel, R. *Macromolecules* **1998**, *31*, 8522. (m) Maeda, K.; Okamoto, Y. *Macromolecules* **1998**, *31*, 5164. (n) Maeda, K.; Okamoto, Y. *Macromolecules* **1998**, *31*, 5924. (o) Mayer, S.; Maxein, G.; Zentel, R. *Macromolecules* **1998**, *31*, 8522. (p) Maeda, K.; Okamoto, Y. *Macromolecules* **1999**, *32*, 974. (q) Jha, S. K.; Cheon, K.-S.; Green, M. M.; Selinger, J. V. *J. Am. Chem. Soc.* **1999**, *121*, 1665. (r) Ute, K.; Fukunishi, Y.; Jha, S. K.; Cheon, K. S.; Munoz, B.; Hatada, K.; Green, M. M. *Macromolecules* **1999**, *32*, 1304. (s) Gu, H.; Nakamura, Y.; Sato, T.; Teramoto, A.; Green, M. M.; Andreola, C. *Polymer* **1999**, *40*, 849. (t) Cheon, K. S.; Selinger, J. V.; Green, M. M. *Angew. Chem. Int. Ed.* **2000**, *39*, 1482. (u) Li, J.; Schuster, G. B.; Cheon, K.-S.; Green, M. M.; Selinger, J. V. *J. Am. Chem. Soc.* **2000**, *122*, 2603.
19. (a) Pieroni, O.; Matera, F.; Ciardelli, F. *Tetrahedron Lett.* **1972**, *7*, 597. (b) Ciardelli, F.; Lanzillo, S.; Pieroni, O. *Macromolecules* **1974**, *7*, 174. (c) Moore, J. S.; Gorman, C. B.; Grubbs, R. H. *J. Am. Chem. Soc.* **1991**, *113*, 1704. (d) Yashima, E.; Matsushima, T.; Okamoto, Y. *J. Am. Chem. Soc.* **1995**, *117*, 11596. (e) Yashima, E.; Nimura, T.; Matsushima, T.; Okamoto, Y. *J. Am. Chem. Soc.* **1996**, *118*, 9800. (f) Yashima, E.; Matsushima, T.; Okamoto, Y. *J. Am. Chem. Soc.* **1997**, *119*, 6345. (g) Yashima, E.; Maeda, K.; Okamoto, Y. *J. Am. Chem. Soc.* **1998**, *120*, 8895. (h) Yashima, E.; Maeda, K.; Okamoto, Y. *Nature* **1999**, *399*, 449. (i) Nakako, H.; Nomura, R.; Tabata, M.; Masuda, T. *Macromolecules* **1999**, *32*, 2861. (j) Aoki, T.; Kobayashi, Y.; Kaneko, T.; Oikawa, E.; Yamamura, Y.; Fujita, Y.; Teraguchi, M.; Nomura, R.; Masuda, T. *Macromolecules*, **1999**, *32*, 79. (k) Maeda, K.; Okamoto, Y. *Macromolecules* **1999**, *32*, 974. (l) Nakako, H.; Nomura, R.; Masuda, T. *Macromolecules* **2001**, *34*, 1496. (m) Nomura, R.; Tabei, J.; Masuda, T. *J. Am. Chem. Soc.* **2001**, *123*, 8430. (n) Yashima, E.; Maeda, K.; Sato, O. *J. Am. Chem. Soc.* **2001**, *123*, 8159.
20. (a) Lemaire, M.; Delabouglise, D.; Garreau, R.; Guy, A.; Roncali, J. *J. Chem. Soc. Chem. Commun.* **1988**, 658. (b) Andersson, M.; Ekeblad, P. O.; Hjertberg, T.; Wennerström, O.; Inganäs, O. *Polymer Commun.* **1991**, *32*, 546. (c) Bouman, M. M.; Meijer, E. W.; *Adv. Mater.* **1995**, *7*, 385. (d) Bidan, G.; Guillerez, S.; Sorokin, V. *Adv. Mater.* **1996**, *8*, 157. (e) Langeveld-Voss, B. M. W.; Janssen, R. A. J.; Christiaans, M. P. T.; Meskers, S. C. J.; Dekkers, H. P. J. M.; Meijer, E. W. *J. Am. Chem. Soc.* **1996**, *118*, 4908. (f) Andreani, F.; Angiolini, L.; Caretta, D.; Salatelli, E. *J. Mater. Chem.* **1998**, *8*, 1109. (g) Lermo, E. R.; Langeveld-Voss, B. M. W.; Janssen, R. A. J.; Meijer, E. W. *Chem. Commun.* **1999**, 791. (h) Yashima, E.; Goto, H.; Okamoto, Y. *Macromolecules* **1999**, *32*, 7942. (i) Langeveld-Voss, B. M. W.; Waterval, R. J. M.; Janssen, R. A. J.; Meijer, E. W. *Macromolecules* **1999**, *32*, 227.
21. (a) Peeters, E.; Christiaans, M. P. T.; Janssen, R. A. J.; Schoo, H. F. M.; Dekkers, H. P. J. M.; Meijer, E. W. *J. Am. Chem. Soc.* **1997**, *119*, 9909. (b) Peeters, E.; Delmotte, A.; Janssen, R. A. J.; Meijer, E. W. *Adv. Mater.* **1997**, *9*, 493.
22. (a) Goodwin, A.; Novak, B. M. *Macromolecules* **1994**, *27*, 5520. (b) Nieh, M.-P.; Goodwin, A. A.; Stewart, J. R.; Novak, B. M.; Hoagland, D. A. *Macromolecules* **1998**, *31*, 3151. (c) Schiltzer, D. S.; Novak, B. M. *J. Am. Chem. Soc.* **1998**, *120*, 2196. (d) Heintz, A. M.; Novak, B. M. *Polym. Prepr. (Am. Chem. Soc., Div. Polym. Chem.)* **1998**, *39*(2), 429.
23. (a) Fuhrhop, J.-H.; Blumtritt, P.; Lehmann, C.; Luger, P. *J. Am. Chem. Soc.* **1991**, *113*, 7437. (b) Frankel, D. A.; O'Brien, D. F. *J. Am. Chem. Soc.* **1994**, *116*, 10057. (c) Schnur, J. M.; Ratna, B. R.; Selinger, J. V.; Singh, A.; Jyothi, G.; Easwaran, K. R. K. *Science* **1994**, *264*, 945. (d) Drake, A. F.; Udvarhelyi, P.; Ando, D. J.; Bloor, D.; Obhi, J. S.; Mann, S. *Polymer* **1989**, *30*, 1043.
24. (a) Salmon, M.; Bidan, G. *J. Electrochem. Soc.* **1985**, *132*, 1897. (b) Delabouglise, D.; Garnier, F. *Synth. Met.* **1990**, *39*, 117.

25. (a) Majidi, M. R.; Kane-Maguire, L. A. P.; Wallace, G. G. *Polymer* **1994**, *35*, 3113. (b) Innis, P. C.; Norris, I. D.; Kane-Maguire, L. A. P.; Wallace, G. G. *Macromolecules* **1995**, *31*, 6521. (c) Su, S.-J.; Kuramoto, N. *Chem. Lett.* **2001**, 504. (d) Su, S.-J.; Kuramoto, N. *Macromolecules* **2001**, *34*, 7249.
26. Fiesel, R.; Scherf, U. *Acta Polym.* **1998**, *49*, 445.
27. (a) Oda, M.; Nothofer, H.-G.; Lieser, G.; Scherf, U.; Meskers, S. C.; Neher, D. *Adv. Mater.* **2000**, *12*, 362. (b) Oda, M.; Meskers, S. C. J.; Nothofer, H. G.; Scherf, U.; Neher, D. *Synth. Met.* **2000**, *111–112*, 575. (c) Tang, H.-Z.; Fujiki, M.; Motonaga, M.; Torimitsu, K. *Polym. Prepr. (Am. Chem. Soc., Div. Polym. Chem.)* **2001**, *42*(1), 440. (d) Leclerc, M. J. *Polym. Sci. A: Polym. Chem.*, **2001**, *39*, 2867. (e) Neher, D. *Macromol. Rapid Commun.* **2001**, *22*, 1365.
28. For optically active dialkylpolysilanes, (a) Matyjaszewski, K. *J. Inorg. Organomet. Polym.* **1992**, *2*, 5. (b) Frey, H.; Möller, M.; Matyjaszewski, K. *Macromolecules* **1994**, *27*, 1814. (c) Frey, H.; Möller, M.; Turetskii, A.; Lots, B.; Matyjaszewski, K. *Macromolecules* **1995**, *28*, 5498. (d) Fujiki, M. *J. Am. Chem. Soc.* **1994**, *116*, 6017. (e) Fujiki, M. *J. Am. Chem. Soc.* **1994**, *116*, 11976. (f) Fujiki, M. *Appl. Phys. Lett.* **1994**, *65*, 3251. (g) Fujiki, M. *Polym. Prepr. (Am. Chem. Soc. Polym. Sci. Div.)* **1996**, *37*(2), 454. (h) Obata, K.; Kabuto, C.; Kira, M. *J. Am. Chem. Soc.* **1997**, *119*, 11345. (i) Shinohara, K.; Aoki, T.; Kaneko, T.; Oikawa, E. *Chem. Lett.* **1997**, 361. (j) Obata, K.; Kira, M. *Macromolecules* **1998**, *31*, 4666. (k) Fujiki, M.; Toyoda, S.; Yuan, C.-H.; Takigawa, H. *Chirality* **1998**, *10*, 667. (l) Ichikawa, T.; Yamada, Y.; Kumagai, J.; Fujiki, M. *Chem. Phys. Lett.* **1999**, *306*, 275. (m) Fujiki, M. *J. Am. Chem. Soc.* **2000**, *122*, 3336. (n) Terao, K.; Terao, Y.-I.; Teramoto, A.; Nakamura, N.; Sato, T.; Fujiki, M. *Macromolecules* **2001**, *34*, 2682. (o) Fujiki, M. *Macromol. Rapid Commun.* **2001**, *22*, 669. (p) Watanabe, J.; Kamee, H.; Fujiki, M. *Polym. J.* **2001**, *33*, 495. (q) Fujiki, M.; Koe, J. R.; Nakashima, H.; Motonaga, M.; Terao, K.; Teramoto, A. *J. Am. Chem. Soc.* **2001**, *123*, 6253. (r) Terao, K.; Terao, Y.-I.; Teramoto, A.; Nakamura, N.; Sato, T.; Fujiki, M. *Macromolecules* **2001**, *34*, 2682. (s) Terao, K.; Terao, Y.; Teramoto, A.; Nakamura, N.; Fujiki, M.; Sato, T. *Macromolecules* **2001**, *34*, 4519. (t) Terao, K.; Terao, Y.-I.; Teramoto, A.; Nakamura, N.; Fujiki, M.; Sato, T. *Macromolecules* **2001**, *34*, 6519. (u) Teramoto, A.; Terao, K.; Terao, Y.; Nakamura, N.; Sato, T.; Fujiki, M. *J. Am. Chem. Soc.* **2001**, *123*, 12303. (v) Natsume, T.; Wu, L.; Sato, T.; Terao, K.; Teramoto, A.; Fujiki, M. *Macromolecules* **2001**, *34*, 7899. (w) Fujiki, M.; Motonaga, M.; Tang, H.-Z.; Torimitsu, K.; Zhang, Z.-B.; Koe, J. R.; Watanabe, J.; Terao, K.; Sato, T.; Teramoto, A. *Chem. Lett.* **2001**, 1218. (x) Fujiki, M.; Tang, H.-Z.; Motonaga, M.; Torimitsu, K.; Koe, J. R.; Watanabe, J.; Sato, T.; Teramoto, A. *Silicon Chem.* **2002**, *1*, 67.
29. For optically active alkylarylpolysilanes, (a) Terunuma, D.; Nagumo, K.; Kamata, N.; Matsuoka, K.; Kuzuhara, H. *Chem. Lett.* **1998**, 681. (b) Toyoda, S.; Fujiki, M. *Chem. Lett.* **1999**, 699. (c) Nakashima, H.; Fujiki, M.; Koe, J. R. *Macromolecules* **1999**, *32*, 7707. (d) Terunuma, D.; Nagumo, K.; Kamata, N.; Matsuoka, K.; Kuzuhara, H. *Polym. J.* **2000**, *32*, 113. (e) Nakashima, H.; Fujiki, M.; Koe, J. R.; Motonaga, M. *J. Am. Chem. Soc.* **2001**, *123*, 1963. (f) Toyoda, S.; Fujiki, M. *Macromolecules* **2001**, *34*, 640. (g) Nakashima, H.; Koe, J. R.; Torimitsu, K.; Fujiki, M. *J. Am. Chem. Soc.* **2001**, *123*, 4877.
30. For optically active diarylpolysilanes, (a) Koe, J. R.; Fujiki, M.; Nakashima, H. *J. Am. Chem. Soc.* **1999**, *121*, 9734. (b) Koe, J. R.; Fujiki, M.; Nakashima, H. *Chem. Commun.* **2000**, 389. (c) Koe, J. R.; Fujiki, M.; Motonaga, M.; Nakashima, H. *Macromolecules* **2001**, *34*, 1082.
31. For optically active dialkoxypolysilane, Koe, J. R.; Motonaga, M.; Fujiki, M.; West, R. *Macromolecules* **2001**, *34*, 706.

32. For a review and books of optically active dialkylpolysilanes and diarylpolysilanes, (a) Fujiki, M. *Macromol. Rapid Commun.* **2001**, *22*, 539. (b) Fujiki, M.; Koe, J. R. In *Silicon-Containing Polymers: The Science and Technology of Their Synthesis and Applications*. Kluwer, Dordrecht, 2000, Chapter 24. (c) Koe, J. R.; Fujiki, M.; Nakashima, H.; Motonaga, M. In *Synthetic Macromolecules with Higher Structural Order*. Khan, I. (Ed.). ACS Symposium Series 812. American Chemical Society, Washington, DC, 2002.
33. (a) Jones, R. G.; Holder, S. J. In *Silicon-Containing Polymers: The Science and Technology of Their Synthesis and Applications*. Kluwer, Dordrecht, 2000, Chapter 12. (b) Sakurai, H.; Yoshida, M. In *Silicon-Containing Polymers: The Science and Technology of Their Synthesis and Applications*. Kluwer, Dordrecht, 2000, Chapter 13. (c) Yamaguchi, S.; Tamao, T. In *Silicon-Containing Polymers: The Science and Technology of Their Synthesis and Applications*. Kluwer, Dordrecht, 2000, Chapter 17.
34. For reviews and books, (a) West, R. *J. Organomet. Chem.* **1986**, *300*, 327. (b) Miller, R. D.; Michl, J. *Chem. Rev.* **1989**, *89*, 1359. (c) Ziegler, J. M.; Fearson, F. W. G. (Eds.). *Silicon-Based Polymer Science*, Advances in Chemistry Series, Vol. 224, American Chemical Society, Washington, DC, 1990. (d) Michl, J.; West, R. In *Silicon-Containing Polymers: The Science and Technology of Their Synthesis and Applications*. Kluwer, Dordrecht, 2000, Chapter 18.
35. (a) Kipping, F. S. *J. Chem. Soc.* **1921**, *119*, 830. (b) Kipping, F. S. *J. Chem. Soc.* **1924**, *125*, 2291.
36. Fujino, M.; Isaka, H. *J. Chem. Soc., Chem. Commun.* **1989**, 466.
37. (a) Riehl, J. P.; Richardson, F. S. *Chem. Rev.* **1986**, *86*, 1. (b) Dekkers, H. P. J. M. *Circular Dichroism: Principles and Applications*, 2nd ed. Berova, N.; Nakanishi, K.; Woody, R. W. (Eds.). Wiley-VCH, New York, 2000, Chapter 7.
38. (a) Harada, N.; Nakanishi, K. *Circular Dichroic Spectroscopy: Exciton Coupling in Organic Chemistry*. University Science Books, Oxford, 1983. (b) Berova, N.; Nakanishi, K. *Circular Dichroism: Principles and Applications*, 2nd ed. Berova, N.; Nakanishi, K.; Woody, R. W. (Eds.). Wiley-VCH, New York, 2000, Chapter 12.
39. (a) Zink, R.; Magnera, T. F.; Michl, J. *J. Phys. Chem. A* **2000**, *104*, 3829. (b) Ottosson, C.-H.; Michl, J. *J. Phys. Chem. A* **2000**, *104*, 3367. (c) Michl, J.; West, R. *Acc. Chem. Res.* **2000**, *33*, 821. (d) Michl, J.; and West, R. In *Silicon-Containing Polymers: The Science and Technology of Their Synthesis and Applications*. Kluwer, Dordrecht, 2000, Chapter 18.
40. Koe, J. R.; Powell, D. R.; Buffy, J. J.; Hayase, S.; West, R. *Angew. Chem. Int. Ed.* **1998**, *37*, 1441.
41. Fujiki, M. *J. Am. Chem. Soc.* **1996**, *118*, 7424.
42. (a) Hansma, H. G.; Vesenka, J.; Siegerist, C.; Kelderman, G.; Morrett, H.; Sinsheimer, R. L.; Elings, V.; Bustamante, C.; Hansma, P. K. *Science* **1992**, *256*, 1180. (b) Samori, B.; Nigro, C.; Gordan, A.; Muzzalupo, I.; Quagliarillo, C. *Angew. Chem. Int. Ed. Engl.* **1996**, *35*, 529. (c) Kumaki, J.; Nishikawa, Y.; Hashimoto, T. *J. Am. Chem. Soc.* **1996**, *118*, 33213. (d) Steiner, U. B.; Rehahn, M.; Caseri, W. R.; Suter, U. W. *Macromolecules* **1994**, *27*, 1983. (e) Shinohara, K.; Yasuda, S.; Kato, G.; Fujita, M.; Shigekawa, H. *J. Am. Chem. Soc.* **2001**, *123*, 3619.
43. (a) Ebihara, K.; Koshihara, S.; Yoshimoto, M.; Maeda, T.; Ohnishi, T.; Koinuma, H.; Fujiki, M. *Jpn. J. Appl. Phys.* **1997**, *36*, L1211. (b) Ebata, K.; Furukawa, K.; Matsumoto, N. *J. Am. Chem. Soc.* **1998**, *120*, 7367. (c) Ebata, K.; Furukawa, K.; Matsumoto, N.; Fujiki, M. *Polym. Prepr. (Am. Chem. Soc. Polym. Sci. Div.)* **1999**, *40*(2), 157. (d) Furukawa, K.; Ebata, K.; Fujiki, M. *Adv. Mater.* **2000**, *12*, 1033. (e) Furukawa, K.; Ebata, K. *Appl. Phys. Lett.* **2000**, *77*, 4289.

44. Lovell, P. A. *Comprehensive Polymer Science*, Vol. 1. Booth, C.; Price, C. (eds.) Pergamon, Oxford, 1989, Chapter 9.
45. Teramae, H.; Takeda, K. *J. Am. Chem. Soc.* **1989**, *111*, 1281.
46. Pohl, F. M.; Jovin, T. M. *J. Mol. Biol.* **1972**, *67*, 375.
47. Bradbury, E. M.; Carpenter, B. G.; Goldman, H. *Biopolymers* **1968**, *6*, 837.
48. Mahadevan, S.; Palaniandavar, M. *Chem. Commun.* **1996**, 2547.
49. Toriumi, H.; Saso, N.; Yasumoto, Y.; Sasaki, S.; Uematsu, I. *Polym. J.* **1979**, *11*, 977.
50. (a) Watanabe, J.; Okamoto, S.; Abe, A. *Liq. Cryst.* **1993**, *15*, 259. (b) Watanabe, J.; Okamoto, S.; Satoh, K.; Sakajiri, K.; Furuya, H.; Abe, A. *Macromolecules* **1996**, *29*, 7084.
51. Okamoto, Y.; Nakano, T.; Ono, E.; Hatada, K. *Chem. Lett.* **1991**, 525.
52. (a) Takeda, K.; Teramae, H.; Matsumoto, N. *J. Am. Chem. Soc.* **1986**, *108*, 8186. (b) Harrah, L. A.; Zeigler, J. M. *Macromolecules* **1987**, *20*, 601. (c) Kakimoto, M.; Ueno, H.; Kojima, H.; Yamaguchi, Y.; Nishimura, A. *J. Polym. Sci. Part A: Polym. Chem.* **1996**, *34*, 2753. (d) Cleij, T. J.; King, J. K.; Jennekens, L. W. *Macromolecules* **2000**, *33*, 89. (e) Nakashima, H.; Fujiki, M. *Macromolecules* **2001**, *34*, 7558.
53. (a) Pirkle, W. H.; Pochapsky, T. C. *Chem. Rev.* **1989**, *89*, 347. (b) Blaschke, G. *J. Liq. Chromatogr.* **1986**, *9*, 341. (c) Okamoto, Y.; Yashima, E. *Angew. Chem. Int. Ed. Engl.* **1998**, *37*, 1020. (d) Yashima, E.; Kasashima, E.; Okamoto, Y. *Chirality* **1997**, *9*, 63. (e) Okamoto, Y.; Honda, S.; Okamoto, I.; Yuki, H.; Murata, S.; Noyori, R.; Takaya, H. *J. Am. Chem. Soc.* **1981**, *103*, 6971.
54. Fossum, E.; Matyjaszewski, K. *Macromolecules* **1995**, *28*, 1618.
55. (a) Guenet, J.-M.; Jeon, H. S.; Khatri, C.; Jha, S. K.; Balsara, N. P.; Green, M. M.; Brûlet, A.; Thierry, A. *Macromolecules* **1997**, *30*, 4590. (b) Yue, S.; Berry, G. C.; Green, M. M. *Macromolecules* **1996**, *29*, 6175.
56. Gottarelli, G.; Spada, G. P. In *Circular Dichroism: Principles and Applications*, 2nd ed. Berova, N.; Nakanishi, K.; Woody, R. W. (eds.). Wiley-VCH, New York, 2000, Chapter 19.
57. (a) Ovchinnikov, Y. E.; Shklover, V. E.; Struchkov, Y. T.; Dement'ev, V. V.; Frunze, T. M.; Antipova, B. A. *J. Organomet. Chem.* **1987**, *335*, 157. (b) Ovchinnikov, Y. E.; Dement'ev, V. V.; Shklover, V. E.; Struchkov, Y. T.; Frunze, T. M.; Antipova, B. A.; Igonin, V. A. *Makromol. Chem.* **1989**, *190*, 3195.
58. Koe, J. R.; Motonaga, M.; Fujiki, M. In preparation.
59. (a) Miller, R. D.; Sooriyakumaran, R. *Macromolecules* **1988**, *21*, 3122. (b) Michl, J. *Synth. Met.* **1992**, *49–50*, 367.
60. Due to the noisiness of the signal, it was difficult to accurately ascertain the CPPL intensity.

Chapter 5

Chiral Molecular Self-Assembly

MARK S. SPECTOR, JONATHAN V. SELINGER,
AND JOEL M. SCHNUR

*Naval Research Laboratory, Center for Bio/Molecular Science and
Engineering, 4555 Overlook Avenue SW, Washington, D.C. 20375-5348*

- 1 Introduction
- 2 Carbohydrate Amphiphiles
 - 2.1 Aldonamides
 - 2.2 Glycolipids
 - 2.3 Cerebrosides
- 3 Peptide-based Amphiphiles
 - 3.1 Amino Acid Amphiphiles
 - 3.2 Peptides
- 4 Phospholipids
 - 4.1 Diacetylenic Phospholipids
 - 4.2 Diacetylenic Phosphonate Lipids
 - 4.3 Phospholipid Mixtures
- 5 Related Chiral Systems
 - 5.1 Nucleotides
 - 5.2 Steroid-Based Systems
 - 5.3 Gemini Surfactants
- 6 Models of Chiral Self-Assembly
 - 6.1 Nonchiral Models
 - 6.1.1 Electrostatics
 - 6.1.2 Elasticity of Orientational Order
 - 6.1.3 Spontaneous Curvature
 - 6.2 Chiral Models: Molecular Approach
 - 6.3 Continuum Elastic Theory: Membranes with Uniform Tilt Direction
 - 6.4 Membranes with Variations in Tilt Direction
 - 6.5 Cylindrical Versus Gaussian Curvature
 - 6.6 Chiral Symmetry-Breaking
 - 6.7 Biased Chiral Symmetry-Breaking
- 7 Conclusion
- References

Materials-Chirality: Volume 24 of Topics in Stereochemistry,
Edited by Mark M. Green, R.J.M. Nolte, and E.W. Meijer
ISBN 0-471-05497-6 Copyright © 2003 John Wiley & Sons, Inc.

1 INTRODUCTION

The self-assembly of molecules into helical aggregates is ubiquitous in nature. The key characteristic of chirality in biological systems is enantiomeric specificity, which has an enormous impact on the pharmaceutical industry.^{1,2} Awareness of the differential effects of enantiomers on physiological processes and, therefore, the necessity for single-enantiomer drugs have driven this critically important industry in new directions. From the amusing differing smells of the enantiomers of certain terpenes to the tragedy of thalidomide, one finds a great deal of evidence to support the differing interplay between mirror image isomers and biochemical processes. This is hardly surprising considering that biological polymers are constructed of enantiomerically pure chiral units, the L-amino acids and D-sugars, leading proteins and nucleic acids to take on chiral secondary structures such as helical conformations, which take up a single-handed sense under a specified set of conditions.

On the other hand, cellular membranes are composed of chiral molecules such as phospholipids and cholesterol, but the homochirality of these constituents is not obviously manifested in the membrane's structure. However, in certain cases biological membranes exhibit a distinct helical or twisted structure, which is a very conspicuous sign of the chirality of the supramolecular aggregate. These chiral supramolecular aggregates are the subject of this chapter.

Researchers have used the process of biological self-assembly as a model for the development of novel materials for use in diverse applications such as biosensors, lithography, and drug delivery.^{3,4} In contrast to covalently bonded polymers, these systems aggregate in aqueous solution because of the competition between hydrophilic and hydrophobic interactions.⁵ Such aggregates are often bilayers, with the hydrophilic head groups of the molecules exposed to water and the hydrophobic tails shielded from water. One would normally expect the lowest energy state of the bilayers to be flat or to be large spherical vesicles with the minimum curvature needed to close off the hydrophobic region from the water, as is usually the case. However, experiments have found that under the right circumstances chiral molecules assemble into helical aggregates whose topology reflects the underlying handedness of the individual constituents. The helicity of the mesoscopic aggregate is often revealed using electron microscopy and can be probed spectroscopically using circular dichroism. When the handedness of the molecules is reversed, the helicity of the aggregate also changes. Interestingly, in some cases racemic mixtures lead to chiral discrimination, where equal numbers of left- and right-handed aggregates are formed, and produce completely different morphologies in others.

This chapter will review the self-assembly of chiral amphiphiles in aqueous solvents. We will focus on the ways in which individual molecules can pack

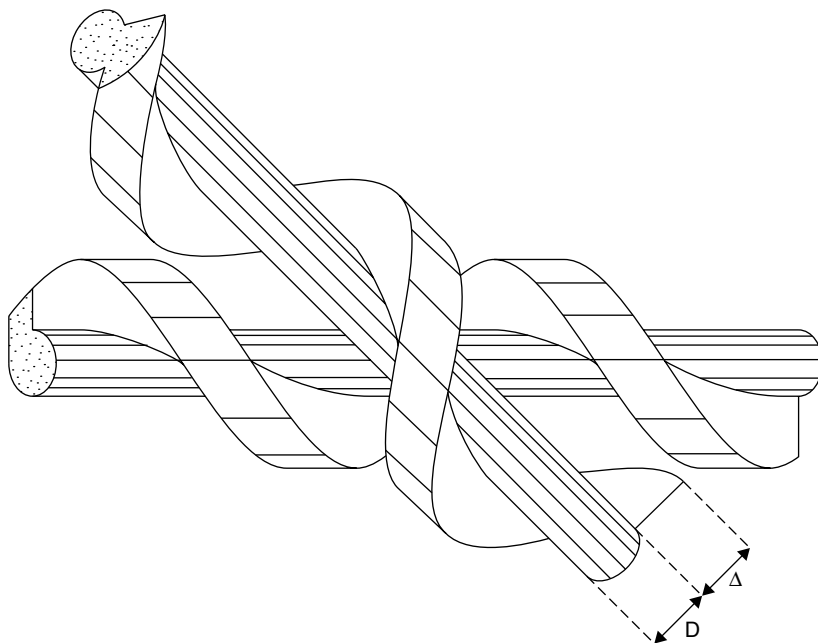


Figure 5.1 Packing of two threaded rods illustrating that minimal approach distance requires that the principal axis of upper rod be rotated clockwise with respect to axis of lower, leading to nonparallel packing. Reprinted from Ref. 6 with permission of the author. Copyright 1976 by the American Physical Society.

into chiral supramolecular aggregates. In considering this topic, one might consider the way in which two screws are forced to pack in a nonparallel fashion as they come closer together, as illustrated in Figure 5.1. In the case of the screws, their packing will be determined by the pitch of the threads, the depth of the ridges, and the minimum approach distance.⁶ If the screws have the same helical sense, then close packing will force nonparallel alignment. For molecules the situation is more complex since there are no real threads. In this case one must consider the shape of the molecule carefully.^{7,8} While a molecule's stereocenter has traditionally been associated with a carbon atom bonded to four different chemical species, in general, it can describe any molecular region that lacks inversion symmetry.⁹ It is clear that geometric considerations lead chiral molecules to pack in an asymmetric fashion. The consequences of this for crystallization have been known since the time of Pasteur. It is only more recently that the importance of molecular chirality in the case of self-assembled materials has been recognized. While one can easily quantify the chirality of a screw in terms of its pitch, diameter, and

tooth depth, it is not simple to quantitatively describe the chirality of single molecules and determine how this affects intermolecular interactions.^{10–13}

This review will explore the way in which small chiral molecules pack together into chiral aggregates. Our purpose is not to discuss the many cases where the supramolecular architecture does not depend on the molecule's handedness but rather to focus on those cases where it does. This review will focus on systems where hydrophobic interactions are the primary driving force toward aggregation (in polar solvents). Often, it is the additional interactions due to hydrogen bonding or steric effects that play an important role in driving the chiral self-assembly. At the same time many of these molecules form interesting arrangements in organic solvents, often leading to gels. This work has been reviewed elsewhere and will not be discussed here.¹⁴ This review will also not cover related phenomena in thermotropic liquid crystals and polymers, which are covered elsewhere in this volume. We will consider different classes of molecules and the way in which their chirality affects the formation of chiral aggregates. It is quite interesting to note that most of these molecules are biologically derived.

Studies of chiral self-assembled systems were reviewed in the early 1990s.^{15–17} Therefore, we will focus on more recent results, although we will introduce earlier work. One of the earliest observations of helical molecular aggregates occurred in lubricating grease where surfactants were found to crystallize into morphologies variously described as twisted ribbons and helical ropes. Hotten and Birdsall first pointed out that lithium 12-hydroxystearate assembles into intertwined micellar fibers that all twist with the same handedness.¹⁸ The definite sense of handedness was confirmed by Tachibana and Kambara who found the D-enantiomer always assembles into right-handed assemblies, while the L-enantiomer forms left-handed fibers and the racemic mixture forms platelets.¹⁹ Detailed studies of these structures using electron microscopy further revealed the opposite sense of handedness in the acid form, with D-12-hydroxystearic acid forming left-handed fibrils and the L-acid having left-handed twist.²⁰ The handedness of the fibers could further be manipulated through the cation with Rb and Cs giving the opposite handedness as Li, while Na and K give a mixture of left- and right-handed assemblies.²¹ This suggests that changing the cation size affects the packing and, hence, helical sense of the aggregate. Variations in solvent, in particular alcohols, also affected the helical morphology.²¹ This is an early example of the effects of hydration and molecular packing on the chiral interactions, a recurring theme in the discussions below.

Relatively little work on chiral assemblies was reported over the next 15 years until a resurgence in activity in the mid-1980s with nearly simultaneous reports of chiral morphologies in gluconamides,²² amino acid amphiphiles,^{23,24} and diacetylenic phospholipids.^{25,26} These systems will be discussed in

Sections 2, 3, and 4, respectively. Other lipid systems (nucleoside conjugates and bile mixtures) as well as chiral aggregation in gemini surfactants will be discussed in Section 5.5. What common features set these molecules apart from the many other chiral amphiphiles that do not self-assemble into helical aggregates? This review will attempt to point out common features in this class of chirally aggregating molecules. For the case of gluconamides and amino acid amphiphiles, hydrogen bonding appears to play an important role in the aggregation process. On the other hand, the acyl chains of the diacetylenic lipids have a kinked shape which leads to a nonparallel packing arrangement that prefers twisted bilayers. In all cases, the helical twisting induced by the intermolecular interactions is biased by the molecular chirality leading to asymmetric (handed) supramolecular morphologies. It then appears that some sort of secondary intermolecular interaction is necessary in addition to the primary hydrophilic interactions between the molecules and polar solvent.

The challenge for theory is to explain the formation of tubules and helical ribbons in this range of systems. One would like to construct a theory based on symmetry considerations that apply to all the materials. This theory should have some material-dependent parameters which would predict the behavior of any particular system. Through such a theory, one would explain the tubules and helical ribbons that have been observed, and one would learn how to control the dimensions of the aggregates through changes in the molecular structure or processing conditions. Section 5.6 reviews progress in the theory of tubules and helical ribbons.

The observations of bioderived chiral aggregates and their subsequent characterizations and understanding about the phenomena have led to advances in the ability to control their dimensions, stability, and yield. This now makes feasible the use of these structures for a number of applications. Controlled-release, high-strength composites based upon designed submicrometer particles, new opportunities for catalysis, and advanced electromagnetic materials are all possibilities for technological exploitation. Recent work on diacetylenic lipid tubules has clearly demonstrated the feasibility of some of these technological possibilities.

The submicrometer-diameter, hollow cylindrical morphology presented by lipid tubules offers attractive possibilities for applications in controlled-release and electroactive composites. However, since the constituent lipid membranes are held together by weak hydrophobic forces, their technological utility is limited by a lack of mechanical strength and temperature stability. An electroless metallization technique, which allows the tubules to be clad with such metals as copper, gold, iron, and nickel, has been developed to increase the mechanical strength of lipid tubules.²⁷ Micrographs of metal-coated microtubules are shown in Figure 5.2. In the top of the figure, a scanning electron micrograph of copper-plated microtubules illustrates the uniformity in diameter and the

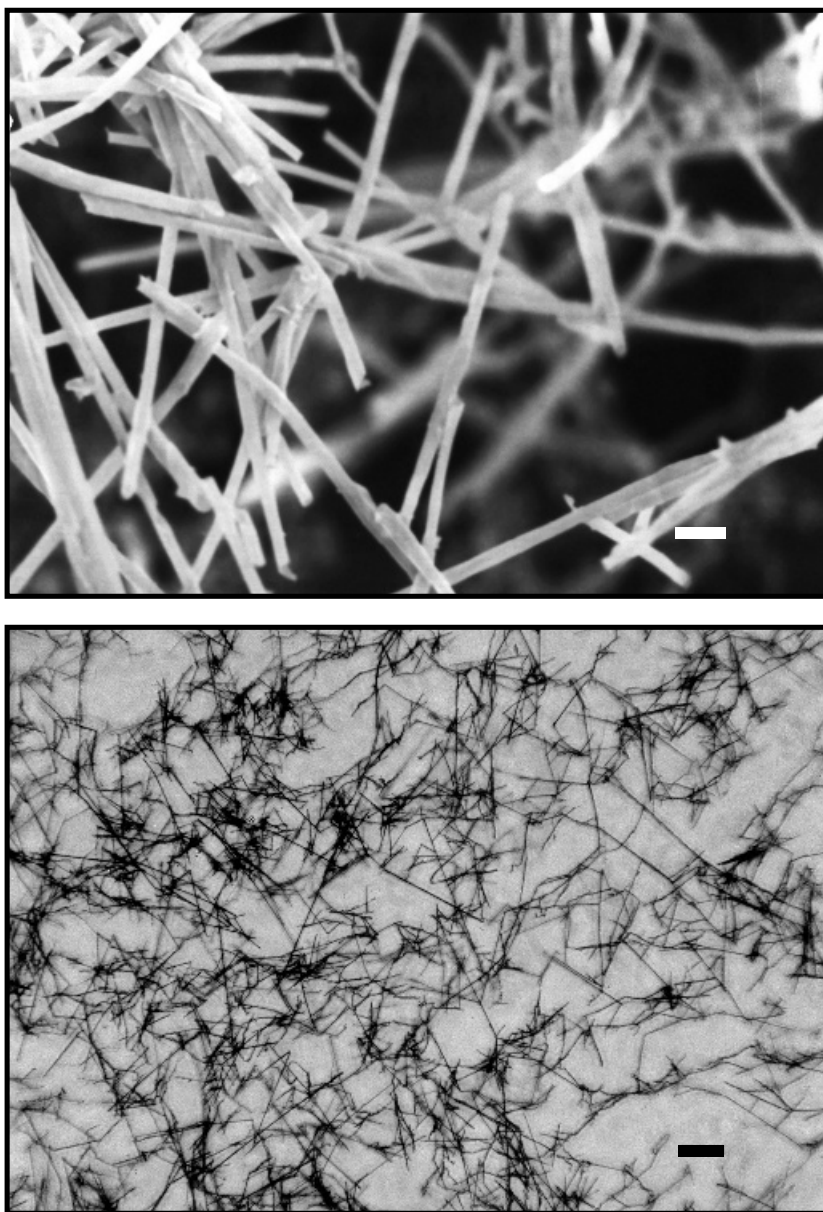


Figure 5.2 Micrographs of metal-coated lipid tubules. Top panel shows scanning electron micrograph of copper-plated microtubules (bar = 2.0 μm), while bottom panel shows optical micrograph of iron-coated microtubules embedded in acrylic-urethane clear coating (bar = 25 μm). Reprinted from Ref. 135 with permission of Wiley-VCH.

relatively straight morphology of the tubules. The lower optical micrograph illustrates iron-coated microtubules which have an average length in excess of 50 μm embedded in an acrylic/urethane clear coating. Novel composites containing such metal-clad tubules are currently being produced commercially for use as high-dielectric-loss materials.²⁸ Metal-coated tubes have also successfully been demonstrated for long-term controlled-release applications in nonmedical scenarios.²⁹

2 CARBOHYDRATE AMPHIPHILES

Polysaccharides such as cellulose and chitin are the principal structural components of plants and invertebrates.³⁰ On the other hand, sugars are the principal source of cellular energy. While sugars exist largely in cyclic form in vivo, surfactants of alkylated, open-chain sugars are among the most widely studied of chirally assembling molecules. Glycolipids, carbohydrates covalently linked to a lipid, often reside in the outer membrane of cells where they play an important role in molecular recognition. These sugar-based amphiphiles will be the topic of this section.

2.1 Aldonamides

Alkyl aldonamides consist of open-chain carbohydrates connected to a hydrocarbon chain through an amide linkage. In aqueous dispersions, these surfactants aggregate into helical ropes, tubules, and ribbons. The first studies by Pfnemüller and Welte of *N*-alkyl-D-gluconamides found a viscous gel consisting of highly ordered helical rope forms at concentrations as low as 1%.²² Electron microscopy of *N*-octyl-D-gluconamide (D-Glu-8, **1**) showed that these ropes had diameters of about 125 Å with pitch of 180 Å. Figure 5.3a shows helical rods formed from D-Glu-8.³¹ As with hydroxystearic acid, the pure enantiomers aggregate with stereospecificity. For the case of D-Glu-8, only right-handed helices were observed, whereas left-handed helices are seen in the L-enantiomer.³² Untwisted platelets were found in a racemic mixture of octyl-D-gluconamide. Fuhrhop and co-workers have described the requirement of enantiomeric purity for the formation of chiral aggregates as the "chiral bilayer effect."³²

In these materials the strong hydrogen bonding of the amide groups plays an important role in the supramolecular morphology and was postulated to direct the formation of helical fibers.^{22,32} An alternative view is that the molecular structure is primarily responsible for the twisted morphology, with the hydrogen bonding stabilizing the structure. In either case, at high temperatures the hydrogen bonding is disrupted and only spherical micelles are seen.

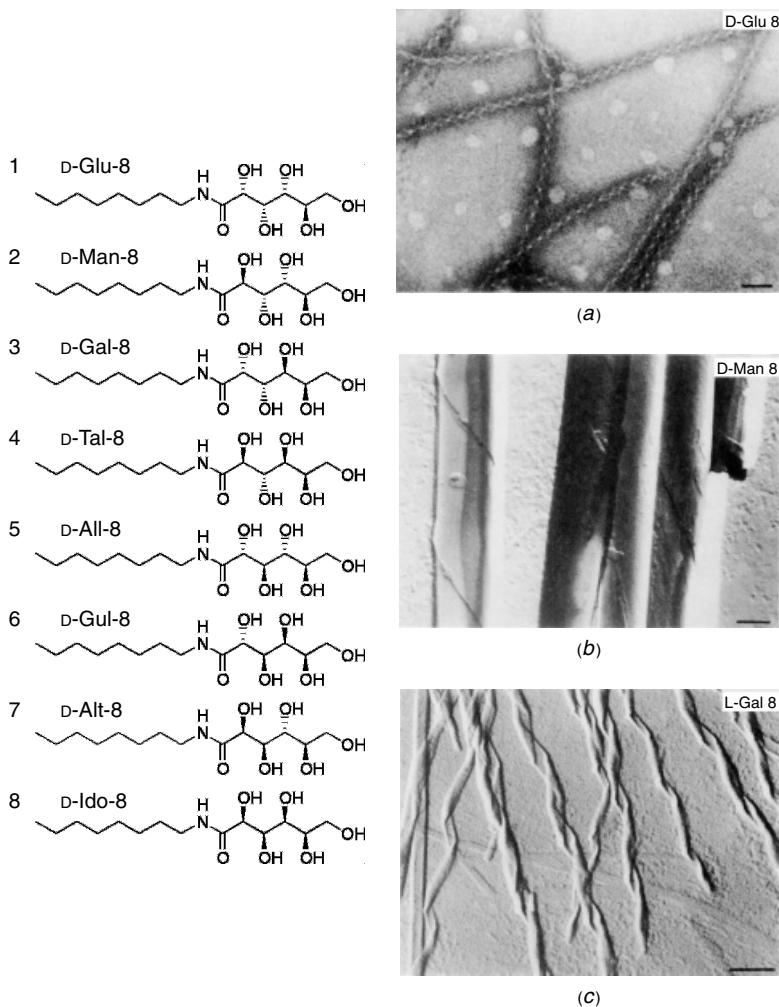


Figure 5.3 Electron micrographs of diastereomers of *N*-octyl-D-aldonamide: (a) helical rods from D-Glu-8 (1, bar = 50 nm), (b) rolled-up sheets from D-Man-8 (2, bar = 300 nm), and (c) twisted ribbons from D-Gal-8 (3, bar = 300 nm). Reprinted with permission from Ref. 31. Copyright 1990 by the American Chemical Society.

Below the melting temperature ($T_m \sim 68^\circ\text{C}$ for D-Glu-8), helical aggregates of increasing complexity are formed, yielding a white gel as the final product. While decreasing the alkyl chain length decreases the melting temperature and has a small effect on diameter, it does not appear to change the overall morphology. Chain lengths longer than 10 hydrocarbons result in crystalline needles.²² If D-Glu-8 is mixed with *N*-dodecyl-L-gluconamide (L-Glu-12),

a gel consisting of a mixture of right- and left-handed fibers made from Glu-8 and Glu-12, respectively, is formed, indicating chain-length-induced resolution.³¹ However, these fibers are short lived and quickly grow into multilayer platelets. Diamine-linked glucose derivatives were also synthesized by Pfannemüller and Welte.²² When the two amide linkages have opposite orientation, as in *N*-octyl-*N'*-gluconoyl-ethylenediamine, smooth ribbons with widths of 600–800 Å are observed. Methylating one of the amides resulted in helical ropes similar to the gluconamides.

Extensive studies on the effect of the head group stereochemistry on aggregate morphology were carried by Fuhrhop and co-workers.³³ The eight diastereomers shown in Figure 5.3 were found to assemble into fibers, ribbons, tubes, needles, and platelets. Aldonamides with a carbohydrate backbone favoring all-*trans* conformation (galactose and mannose) give bilayer structures. In the case of mannoamides, the bilayers curl up into tubulelike structures, as shown in Figure 5.3*b* for *N*-octyl-*D*-mannonamide (*D*-Man-8, **2**). On the other hand, Figure 5.3*c* shows twisted ribbons formed from *N*-octyl-*D*-galactonamide (*D*-Gal-8, **3**). One pair of 1,3-*syn* hydroxyl groups in the hexose backbone (glucose and talose) gives highly curved, micellar-type aggregates. Gulanoamides (all *syn*) formed nonchiral, crystalline sheets (platelets) in water. Allonamides, altronamides, and idonamides were very soluble in water and did not form helical aggregates.

The morphology of these assemblies was correlated with the conformation of the head group.³³ Galactonamide and mannonamide, with a fully extended, all-*trans* conformation, are able to satisfy their hydrogen bonds in flat bilayers. On the other hand, the highly soluble aldonamides (allon, altron, idon, gulon) have two *gauche* bonds leading to an extremely bent conformation, which prevents the formation of extended hydrogen bonding and aggregation. The intermediate case of gluconamide and talonamide, with one *gauche* bond, forms a bent structure which favors packing into a twisted micellar fiber. These head group conformations were confirmed by nuclear magnetic resonance (NMR).³⁴ Thus, although the primary force for aggregation is the molecular amphiphilicity, the morphological polymorphism results from interplay between the hydrogen bonding and steric constraints of the carbohydrate head groups. Mixtures of *D*- and *L*-glucon-, mannon-, and galactonamides with different chain lengths resulted in chain-length-induced resolution.³¹ Figure 5.4 shows the demixing of *D*-Glu-12 helices from *L*-Man-8 tubules. This system is quite interesting in that the two distinguishable bilayer morphologies remain connected. Mixtures of *D*-Glu-8 and *L*-Man-8 tubules resolved into separate helical and tubular fibers, while mixtures of *D*-Glu-8 and *D*-Man-8 rapidly formed flat platelets.

On the basis of computer-enhanced electron micrographs, Fuhrhop et al. proposed a structure of two intertwined bilayer micelles, termed “bulgy double



Figure 5.4 Electron micrograph showing demixing of D-Glu-12 helices from L-Man-8 tubules to form heterogeneous structures (bar = 500 nm). Reprinted with permission from Ref. 31. Copyright 1990 by the American Chemical Society.

helix.”³² High-resolution, negative-stain electron microscopy revealed additional electron density inside the bulges, leading to the proposed quadruple helix structure.³⁵ This morphology, shown in Figure 5.5, consists of four bilayer membranes, each with thickness 3.6 nm, wrapped in a helical bundle having a radius of 5.0 nm and a pitch of 22.4 nm. Boettcher and co-workers further elaborated the structure of these helices through detailed cryo-electron microscopy (EM) studies.³⁶ Three-dimensional computer reconstructions of vitrified samples suggest that the helical structures consist of six stacked bilayers, rather than four. The cryo-EM data also suggest that the twisted helices are left handed, the opposite of the fibers described in earlier work.^{22,32} This implies that additives such as staining material influence the fiber morphology.

Structural information about the gluconamide fibers was also obtained from X-ray diffraction³⁷ and solid-state NMR.^{38–40} While X-ray diffraction on *N*-octyl-*D*-gluconamide crystals showed a monolayer with head-to-tail packing, high-resolution cross polarization³⁸ and rotational echo double-resonance NMR⁴⁰ provided evidence for bilayer, tail-to-tail packing in the hydrated fibers. In particular, the double-resonance NMR showed that the fourth carbon

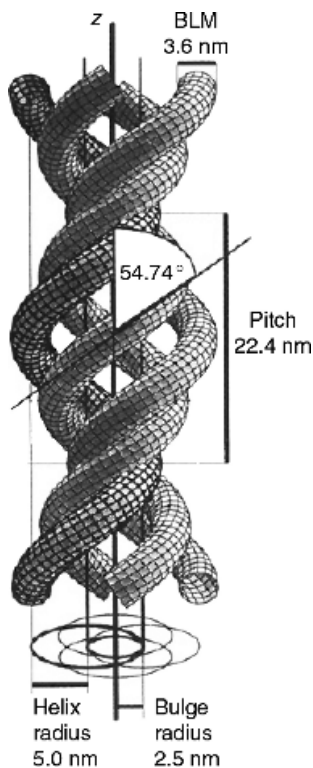


Figure 5.5 Computer-generated model of quadruple helix structures made of D-Glu-8 (I) based upon image-processed electron micrograph of helical fibers. Reprinted with permission from Ref. 35. Copyright 1993 by the American Chemical Society.

from the nitrogen in the glucose head group (C4) was closer to the nitrogen in the fiber morphology than in the crystalline (all-*trans*) state.⁴⁰ This indicates a *gauche* conformation of the C2–C3 bond giving the molecule the sickle shape shown in Figure 5.6. These studies also showed that the alkyl chain has an all-*trans* conformation. The bent shape of this molecule thus leads to a hydrogen-bonded state that favors a twisted packing in the fiber which does not exist in the crystalline state.

Atomic force microscopy (AFM) can be used to obtain high-resolution imagery of molecular orientation and ordering for materials adsorbed onto substrates. Early AFM studies on gluconamides were hampered by the tendency of the fibers to unravel on substrates forming bilayer sheets.⁴¹ These layers showed the head-to-tail packing of a monolayer which is similar to the crystal structure reported for anhydrous gluconamides.³⁸ A procedure to retain the fiber networks on surfaces with the addition of a small fraction of

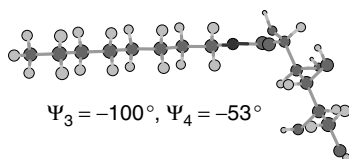


Figure 5.6 Steric view of sickle structure of D-Glu-8 (**1**) in helical fibers based upon measurements made using rotational echo double-resonance NMR experiments. The N–C3 torsion angle (Ψ_3) is -100° , while the C1–C4 torsion angle (Ψ_4) is -53° . Reprinted from Ref. 40 with permission of The Royal Society of Chemistry on behalf of PCCP Owner Societies.

ionic detergent (sodium dodecyl sulfate) was recently reported.⁴² An AFM image of a network of D-Glu-8 fibers adsorbed to silicon this way is shown in Figure 5.7. The high-resolution image in Figure 5.7*b* shows the quadruple helix structure of these aggregates. Similar results were found on mica, but the larger van der Waals attraction to gold leads to flattening of the fibers even in the presence of sodium dodecyl sulfate.

Nolte and co-workers have extensively examined the aggregation of aldonoamides in organic solvents and found that they also aggregate and gel in solvents such as chloroform and 1,2-xylene.⁴³ They also synthesized a derivative of octyl-D-gluconamide containing a metal-coordinating imidazole group (**9**).⁴⁴ The protonated compound (pH 4.5) assembled into vesicles, while **9** formed long fibers and hollow tubules of pH 8.5. In a 1 : 4 copper complex at pH 8.5, helices with diameters of 330 nm were formed.

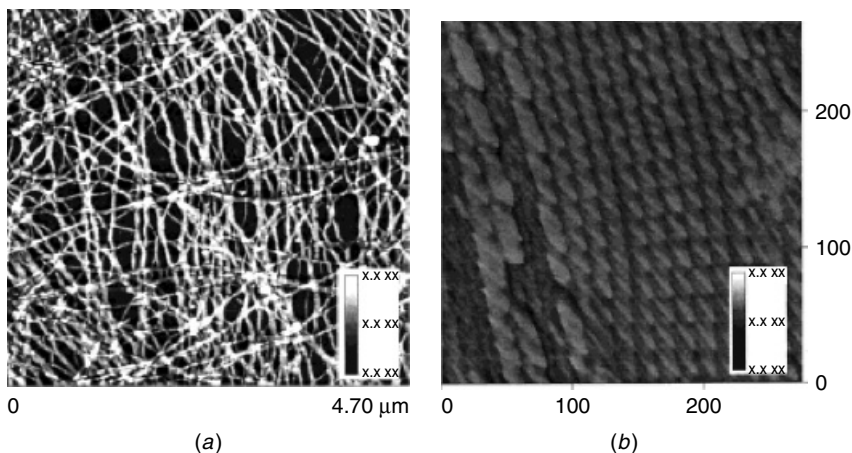


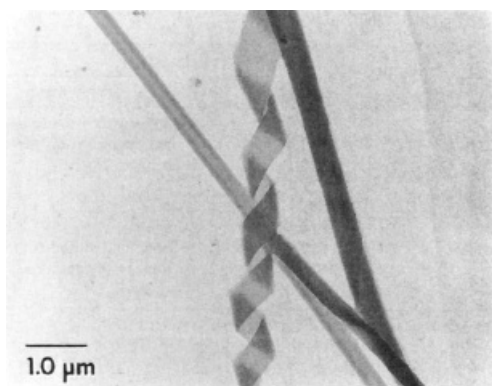
Figure 5.7 AFM images of fibrous aggregates of D-Glu-8 (**1**) lying directly on silicon surfaces: (a) network of fibers; (b) high-resolution phase image of quadruple helices. Reprinted with permission from Ref. 42. Copyright 2000 by the American Chemical Society.

Incorporation of a diacetylenic group in the alkyl chain of the gluconamide was found to cause the formation of tubules rather than the chiral helices seen for saturated chains.^{45,46} The diacetylene moiety results in highly ordered and kinked alkyl chains and had previously been found to induce chiral tubules in phospholipids,²⁵ as discussed in Section 5.4.1. In extensive studies, Frankel and O'Brien synthesized a variety of diacetylenic butyl-, pentyl-, hexyl-, and heptyl-aldonamides.⁴⁷ Similar to the diacetylenic gluconamides, *N*-dodeca-5,7-diyne-D-galactonamide (**10**) formed helices and tubules as shown in Figure 5.8*a*, while the aldopentose *N*-dodeca-5,7-diyne-L-arabonamide (**11**) assembled into the braided fibers seen in Figure 5.8*b*. The formation of different aggregates in the diacetylenic aldonamides compared to their saturated counterparts indicates that the interaction between the acyl chains and π -orbital overlap of the diacetylenes is an important force.²⁵ A combination of microscopy and molecular modeling led the authors to conclude that two packing arrangements are possible, either head-to-head bilayer packing, which results in planar, nonchiral aggregates, or head-to-tail and "dromic" hydrogen-bonding patterns, which favors chiral fibers.

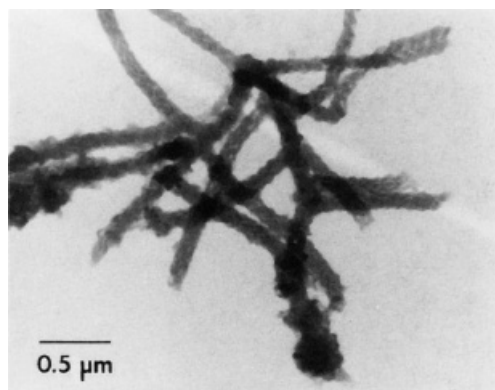
2.2 Glycolipids

Anionic glucophospholipids were synthesized by attaching a double-tailed chain through a phosphate linkage to a glucose head group.^{48,49} Both the hydrogenated (**12**) and partially fluorinated (**13**) amphiphiles were found to form tubular microstructures when dispersed in water. No tubules were seen in galactose or mannose derivatives. Electron microscopy revealed that the tubules are hollow having an outer radius of 140 Å and a wall thickness of 105 Å, as shown in Figure 5.9.⁵⁰ Heating the tubules to 60°C causes the tubules to melt into spherical vesicles. A novel amphiphile containing a glycopyranosyl head group linked to a diacetylenic chain via a tetrapeptide was recently reported to form tubules and helical ribbons.⁵¹

Bolaamphiphiles which consist of two hydrophilic groups connected via a hydrophobic spacer tend to form stable monolayer membranes.⁵² *Archaea species*, microbes which are able to survive in harsh environments such as high temperatures or acidic conditions, contain bolaamphiphiles in their plasma membranes. Synthetic bolaamphiphiles with amide-linked head groups have been developed to increase the stability of bilayer membranes.⁵³ In addition to tuning the membrane interactions by the choice of head group, unsymmetric head groups can give rise to interesting morphologies. Figure 5.10 shows a schematic overview of the supramolecular aggregates observed using bolaamphiphiles. Bolaamphiphiles containing glucosamide head groups at each end of an alkyl chain were found to also assemble into helical ribbons by Shimizu and Masuda.⁵⁴ Allowing hot aqueous solutions of Glc-NC(*n*)CN-Glc (**14**)



(a)



(b)

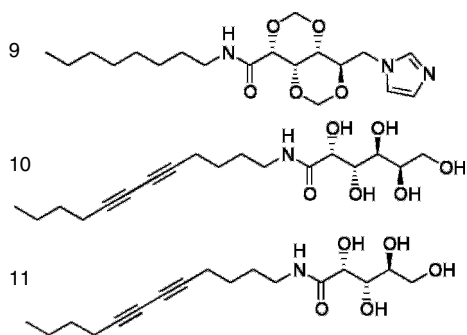
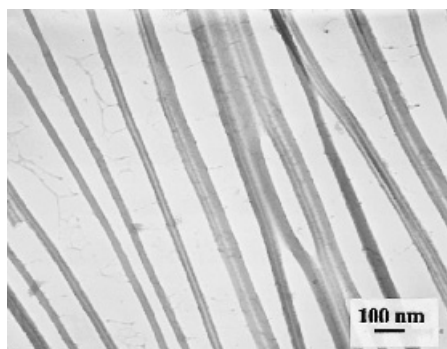
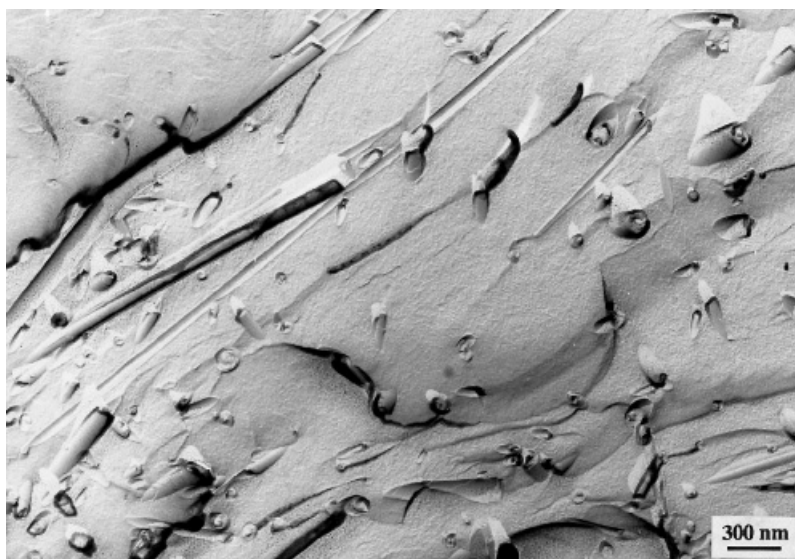


Figure 5.8 Electron micrographs of (a) right-handed helices and tubules from *N*-dodeca-5,7-diyne-D-galactonamide (**10**) and (b) braided fibers from *N*-dodeca-5,7-diyne-L-arabonamide (**11**). Reprinted with permission from Ref. 47. Copyright 1994 by the American Chemical Society.



(a)



(b)

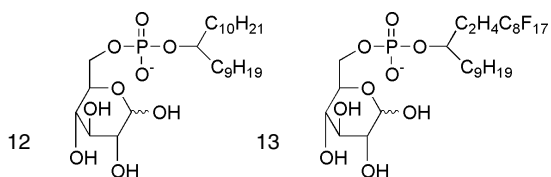


Figure 5.9 Transmission electron microscopy (TEM) photographs of 3 wt % fluorinated glucophospholipid (**13**) dispersion at room temperature: (a) cryo TEM; (b) freeze-fracture TEM. Reprinted from Ref. 50 with permission of Academic Press.

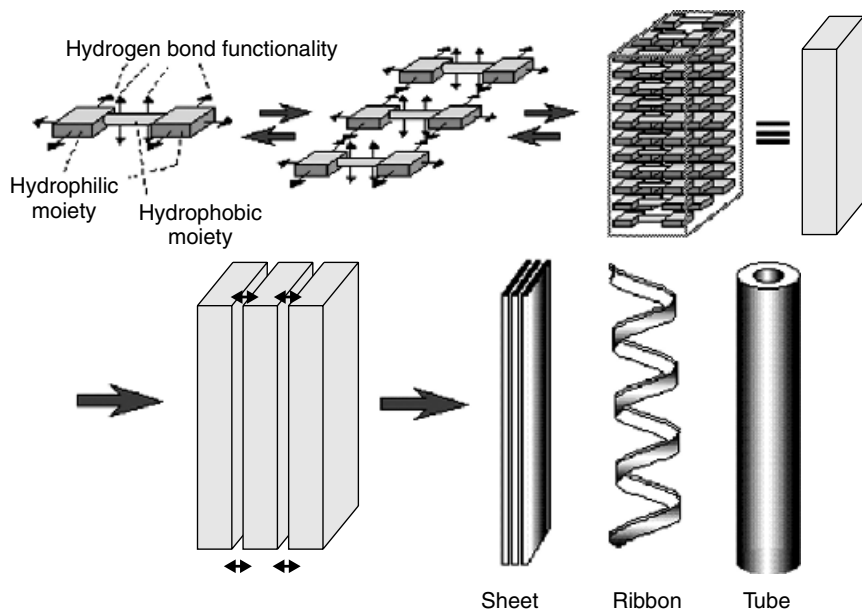
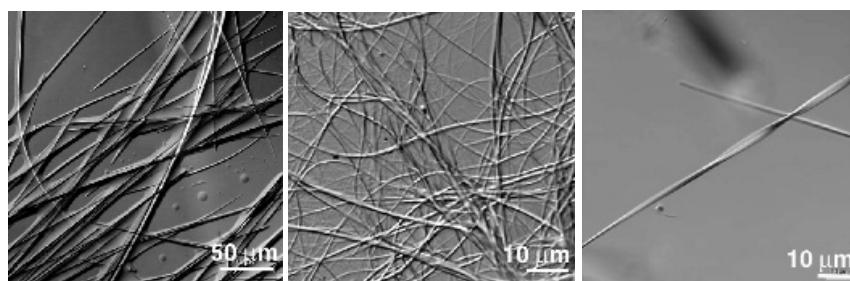


Figure 5.10 Schematic overview of self-assembly process of high-axial-ratio nanostructures using bolaamphiphilic monomers. Arrows indicate hydrogen bond functionalities. Reprinted from Ref. 53 with permission of Wiley-VCH.

to slowly cool and equilibrate at room temperature resulted in a variety of nanometer-sized fibers. Due to the relative orientation of the two carbonyl dipoles, the aggregate morphology was found to strongly depend on whether the alkyl spacer had an odd or even number of methylenes, n . Elongated fiber morphologies were observed for n even, while crystal platelets were seen for odd n . Needle like fibers for $n = 6$, flexible fibers for $n = 10$, and right-handed helical fibers for $n = 12$ are shown in Figures 5.11a, b, and c, respectively. Constrained hydrogen bond networks require deviation of the chain from an all-*trans* conformation in the helical aggregates. Fourier transform infrared (FTIR) studies on the methylene stretch bands revealed a partially *gauche* conformation for the short-chain homologues ($n < 10$) and all-*trans* conformation for longer derivatives, as seen in Figure 5.12a. Similar effects are found in side-chain polymers, where crystallization is found in poly(n -alkyl methacrylates) having 10 or more methylenes in the side chain.⁵⁵ In addition, the amide bands of Glc-NC(n)CN-Glc aggregates showed an odd–even effect for longer chain lengths ($n > 11$), as shown in Figure 5.12b, indicating bolaamphiphiles with even n had weaker hydrogen bonding between the amide groups than those with odd n .⁵⁴



(a)

(b)

(c)

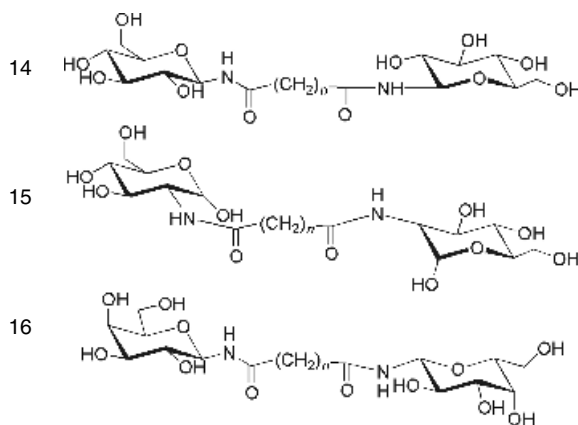


Figure 5.11 Confocal laser scanning micrographs of self-assembled helical fibers made of glucosamide bolaamphiphiles Glc-NC(*n*)CN-Glc (**14**): (a) *n* = 6, (b) *n* = 10, and (c) *n* = 12. Reprinted from Ref. 53 with permission of Wiley-VCH.

Connecting the amide-linked hydrocarbon bridge to the C2 positions of the glucopyranose rings gave a series of bolaamphiphiles that were far less soluble than their C1-linked counterparts discussed above.⁵⁶ However, these bolaamphiphiles (**15**) showed a similar odd–even effect, with twisted fibers forming for *n* = 10, 12, 14 and amorphous sheets and ribbons observed for *n* = 11, 13. However, the morphology observed in the two cases appears to differ, with the C1-linked bolaamphiphiles showing a coiled or helical wrapping and the C2-linked ones having a twisted topology. The topological difference between these two cases will be further discussed in Section 5.6.5. Changing the glucose head groups to galactose (**16**) introduced a kink in the alkylene bridge, leading to a significant change in the layer packing arrangement and the formation of crystalline needles.⁵⁷ Incorporation of butadiynes into the hydrocarbon bridge of the acetylated glucosamide bolaamphiphiles led to the formation of an amorphous gel lacking the chiral twisting observed in **14**.⁵⁸

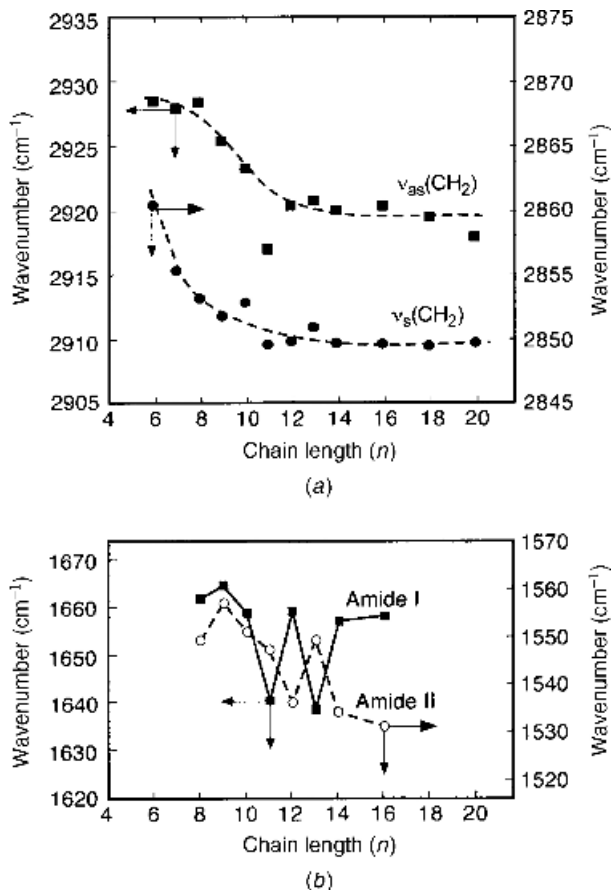
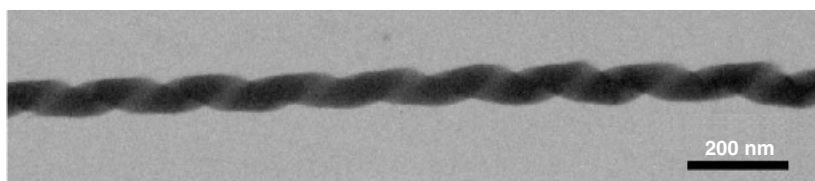
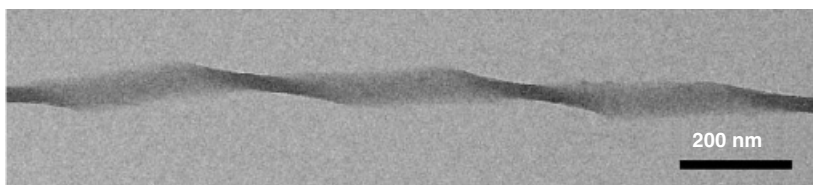


Figure 5.12 Dependence of peak frequencies in infrared spectrum of glucosamide bolaamphiphiles NC(n)GN-GLC (**14**) on methylene spacer length n . (a) The CH_2 antisymmetric ν_{as} and symmetric ν_{s} stretching vibrations reveal *gauche*-included conformation for short chains and an all-*trans* conformation for longer chains. (b) Amide I and II frequencies show an even-odd effect for $n \geq 10$. Reprinted from Ref. 53 with permission of Wiley-VCH.

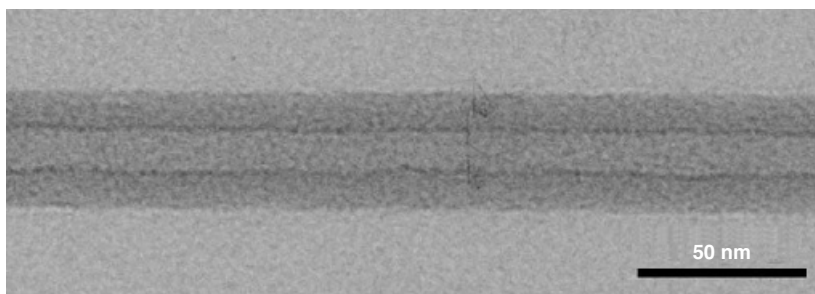
The formation of helical fibers from synthetic lipids synthesized from plant-derived cardanol was recently reported.⁵⁹ Coupling this natural, long-chain phenol (obtained from *Anacardium occidentale* L, a by-product of the cashew industry) with aldopyranose gave a glucoside mixture. This system produced helically coiled ribbons, as shown in Figure 5.13a, after gradual cooling from high temperature and 1–2 days of incubation at room temperature. These ribbons converted into the nanotubes shown in Figure 5.13c after several days. The saturated homologue (**17**) alone was found to assemble into twisted



(a)



(b)



(c)

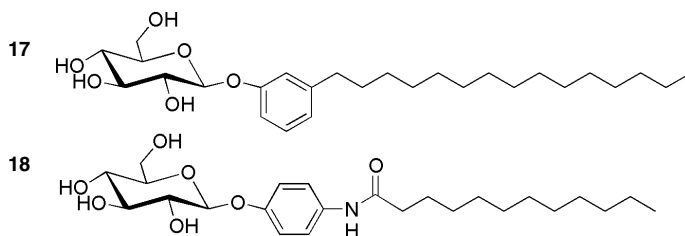


Figure 5.13 TEM images of (a) an individual helically coiled nanofiber from cardanyl glucoside mixtures, (b) a helically twisted nanofiber from saturated glucoside (**17**), and (c) an individual nanotube from cardanyl glucoside mixtures. Reprinted from Ref. 53 with permission of Wiley-VCH.

nanofibers (Figure 5.13*b*), which did not convert into the tubular structure. A related compound containing an amide linkage between the hydrocarbon and acyl chain (**18**) was found to form a three-dimensional network of 20–500-nm-diameter puckered fibrils.⁶⁰

2.3 Cerebrosides

Sphingolipids, derivatives of the long-chain amino acid sphingosine, are naturally occurring lipids that can assemble into cochleate cylinders, nanotubes, and fiberlike microstructures.³⁰ Cerebrosides are alkyl derivatives with a single sugar moiety as the head group and, thus, form a special class of glycolipids that will be discussed in this section. Galactocerebrosides, also called galactosylceramides, have a β -D-galactose head group and are thought to provide structural rigidity to membranes because of their intermolecular interactions. Naturally occurring galactocerebrosides (GalCer) were first observed to form helical ribbonlike structures within the cells of patients afflicted with globoid cell leukodystrophy.⁶¹ Archibald and co-workers performed the first detailed studies of bovine brain GalCer and its two major components, hydroxy fatty acid cerebroside (HFA-Cer, **19**) and nonhydroxy fatty acid cerebroside (NFA-Cer, **20**).^{62,63} When dehydrated with 1,2-ethanediol, they observed cochleate cylindrical structures for HFA-Cer and helical ribbons for NFA-Cer. They called these aggregates high-axial-ratio microstructures (HARMs).

Studies into the self-assembly of individual molecular species of galactocerebrosides have been carried out in aqueous solution by Brown and co-workers^{64,65} and in water–dimethylformamide (DMF) by Yager and co-workers.^{66,67} Manipulations of the acyl chain or head group were found to play a significant role in modulating cylindrical microstructure formation. The saturated version of the 24-carbon acyl chain (*N*-24:0) nonhydroxy GalCer (**20**) formed undulating ribbons in water that occasionally showed a twisted region.⁶⁴ Introduction of just one *cis* double bond at carbon 15 (*N*-24:1 Δ^{15}) to the acyl chain of **20** resulted in the nanotubular structures shown in Figure 5.14 for 24:1 GalCer (**21**) in water. Similar morphologies were also found for the same glycolipid in water–DMF solutions.⁶⁶ Shortening the chain length to 20 carbons, with one double bond (20:1 Δ^{11}), resulted in the formation of right-handed helical ribbons.⁶⁵ The bulkier zwitterionic phosphocholine head group was found to inhibit the formation of tubules.⁶⁴

The work of Kulkarni et al. suggests that the anisotropic chiral interactions thought to be necessary for bilayer nanotube formation are optimal not only when the acyl chain of GalCer is long and unsaturated but also when the *cis* bond location marginally disrupts chain–chain packing.⁶⁵ This work also leads to the conclusion that stabilization of helical ribbons or edges sealing to form tubes are dependent upon experimental conditions as described by the model of Schnur et al.⁶⁸

Head group structural modifications have been observed to influence the morphology of glycolipid assemblies.^{66,67} Replacement of the galactose head group with *N*-acetyl-glycine yielded long, thin fibers, whereas the *N*-acetyl-proline analogue gave amorphous assemblies.⁶⁶ Glucose leads to needlelike

3 PEPTIDE-BASED AMPHIPHILES

Proteins are the central class of biomacromolecules that catalyze and regulate the chemical reactions necessary for life. Central to their function is the hierarchical structure which often arises due to subtle interactions between the amino acids along the protein backbone.⁶⁹ Hydrogen bonding between the amide and carbonyl groups in the backbone stabilizes the secondary structures of proteins, as it also does with the twisted ribbons assembled from aldonamides. This section will explore two classes of molecules that use the hydrogen bonding of natural amino acids with the amide bond in an amphiphilic molecule for control of chiral aggregation.

3.1 Amino Acid Amphiphiles

Amphiphiles using amino acids as the connecting group between acyl chains and the polar head group were originally studied by Kunitake and co-workers as analogues of natural bilayer-forming molecules.^{16,70} Single-, double-, triple-, and quadruple-chain compounds can readily be synthesized using an amino acid-linking group. Chiral diacyl ammonium amphiphiles synthesized from alanine and glutamic acid were found to form bilayer membrane vesicles in water.⁷¹ In such systems, Kunitake's group pioneered the use of circular dichroism (CD) spectroscopy as a powerful tool to study the structure of self-assembled chiral molecules. Circular dichroism, the difference in absorption of right and left circularly polarized light, arises from the chirality of the molecular architecture. This chirality can arise from either the structure of individual molecules or the chiral packing of molecules into larger aggregates. With the addition of an aromatic chromophore to the glutamic acid head group of chiral amphiphiles, Kunitake et al. were able to monitor the temperature dependence of the CD.⁷² They observed a 60-fold decrease of the CD when the vesicles were heated above the chain melting temperature, $T_m \sim 30^\circ\text{C}$. In addition, the bisignate nature of the CD peak below T_m indicates exciton coupling of the adjacent chromophores.⁷³ The presence of exciton coupling implies these bilayers are more highly ordered than their glycerol-backboned counterparts, due to the hydrogen bonding between the amide and carbonyl groups.

Further studies of chiral glutamic-acid- and aspartic-acid-derived amphiphiles found the appearance of helical aggregates.^{23,24} Double-chain, amino-acid-derived ammonium amphiphiles produced bilayer vesicles when dispersed in water by sonication.²³ After several hours, flexible filaments of 5–50 μm in length were observed in dispersions of $2\text{C}_{12}\text{-L-GluC}_{11}\text{N}^+$ (**22**), as shown in Figure 5.15. The helical sense of the L-enantiomer was always right handed, while the D-enantiomer was left handed. Rod like aggregates are observed in a racemic mixture. When the filaments are heated above the melting temperature, $T_m = 34^\circ\text{C}$, the helices are transformed into tubes which immediately

Helical morphologies were observed in amphiphiles with oligo-L-aspartic acid⁷⁵ and oligo-L-proline head groups.⁷⁶ Lee et al. reported similar results on several glutamic acid dialkyl amides with short peptides in their head group.⁷⁷ Long fibers were found to rapidly form by thermal cycling of the compounds in either aqueous buffer or buffer containing methanol or ethanol. In particular, the proline derivative (Pro)₃-Glu(NHC₁₂H₂₅)₂ (**25**) formed helical ribbons similar to those observed by Shimizu and Hato.⁷⁶ However, slow cooling through T_m , unlike incubation at room temperature, was found to cause direct self-assembly resulting in more stable helical morphologies.⁷⁷ A related system with the alkyl chains connected to the α -carboxylate and α -amino group of the amino acid was studied by Cescato et al.⁷⁸ This left the side groups free for further functionalization. Aqueous dispersion of such amphiphiles with either glutamic acid (**26**) or arginine (**27**) residues formed spherically vesicles above T_m . Upon cooling the sample to room temperature, helical and tubular assemblies with diameters of tens of micrometers slowly appeared after several hours to days. Based upon CD studies, the authors suggest that these helical structures are conformationally more ordered than vesicles.

Multilamellar tubules and helical ribbons formed in solutions of *N*-dodecanoyl-L-serine (**28**) when cooled from 80°C to room temperature.⁷⁹ The cryo-electron micrographs shown in Figure 5.16 show that tubules formed at pH 6.4 have helical markings, while those at pH 4.9 do not. Right-handed aggregates are seen for L-serinamide and left-handed ones for D-serinamide, with the racemic mixture forming nonchiral platelets. The authors speculate that a hydrogen bond pattern between neighboring hydroxyl groups may be responsible for the formation of helical aggregates. Earlier studies of *N*-undecanoyl-L-serine (one methylene shorter than **28**) found helical ribbons and tubules in organic solvents (e.g., chloroform) but only nonchiral aggregates in water.⁸⁰ On the other hand, *N*-undecynoyl-L-histidine (**29**) assembled into spherical and helical aggregates in water but was insoluble in chloroform. Studies on a series of diacyl tripeptide derivatives with ammonium head groups found spectroscopic evidence of a parallel β -sheet structure in the bilayers.^{81,82} However, the resulting needlelike assemblies were not helical.

The helical nature of the amino acid aggregates was revealed by embedding an aromatic chromophore to the surface of filaments of 2C₁₂-L-GluC₁₁N⁺.⁸³ A very large induced CD arises from strong exciton coupling among chromophores bound to the chiral bilayer surface. The large dissymmetry factor $g \equiv \Delta\epsilon/\epsilon = 0.026$ implies that the chromophore is well oriented by the chiral matrix. Interestingly, the induced CD disappears completely 5 degrees below the melting temperature, as shown in Figure 5.17. Similar exciton coupling was induced in dyes arranged on helical bilayer membranes of L-glutamic-acid-derived amphiphiles.⁸⁴ The opposite sign of the CD spectra was observed in membranes of the corresponding D-isomers, while no induced

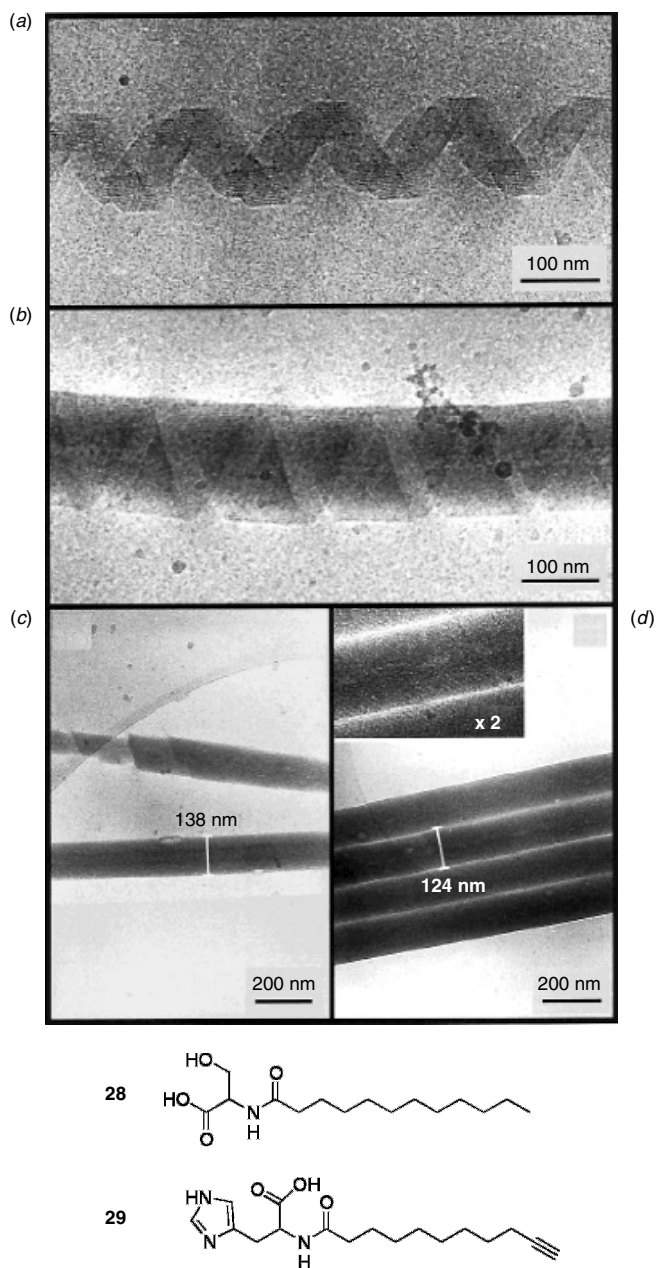


Figure 5.16 Cryo-transmission electron micrograph of (a, b) helical ribbons and (c, d) multi-lamellar tubules in aqueous dispersions of *N*-dodecanoyl-L-serine (**28**) at pH 6.4 (a–c) and 4.9 (d). Reprinted with permission from Ref. 79. Copyright 2001 by the American Chemical Society.

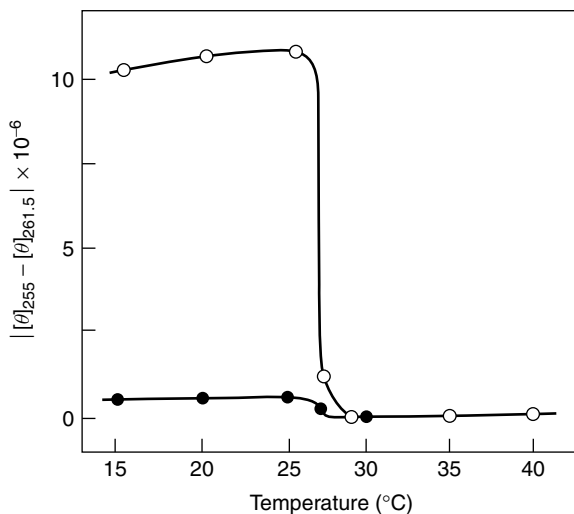


Figure 5.17 Temperature dependence of induced CD of 9-anthracenecarboxylate bound to chiral filaments of $2C_{12}$ -L-GluC₁₁N⁺ (**22**). Reprinted with permission from Ref. 83. Copyright 1994 by the American Chemical Society.

CD was observed in the corresponding ester-type amphiphiles which did not produce helices.

Incorporation of the photopolymerizable 2,4-hexadienoyl groups into an L-glutamic acid derivative also produced helical structures.⁸⁵ Because they were believed to promote helical aggregates, whereas ester linkages were thought to be more likely to form vesicles, amide bonds were used to connect the alkyl groups to the amino acid backbone.⁸⁶ Helical fibers were observed when an aqueous suspension of lipid **30** was cooled into the gel phase. The fibers showed very strong exciton coupling in their CD spectra below the phase transition temperature, as shown in Figure 5.18. Irradiation decreased the absorption of the 2,4-hexadienoyl groups and induced a morphological transition from helical lamellar to tubular aggregates at temperatures below the lipid melting temperature T_m and to twisted fibrous aggregates above T_m . Related diacetylenic glutamate lipids (DGLs) did not assemble into chiral aggregates.⁸⁷ The bilayers of these DGLs were easily polymerized and X-ray diffraction indicated the acyl chains were tilted approximately 30° in the bilayer.

A series of amphiphiles containing a polygalactosylated tris(hydroxymethyl) aminomethane (Tris) linked to a diacyl aspartic acid (**31**) were synthesized by Polidori and co-workers.⁸⁸ These compounds had a peptidic spacer for control of the hydrophilic/lipophilic balance as well as providing intermolecular hydrogen bonding. The mono- and digalactosylated (**31a**, **31b**) derivatives

were multilamellar vesicles. The authors proposed a possible explanation for this phenomenon based upon slow protonation of the terminal anions first promoting the tubular morphology, with subsequent nucleation of vesicles at defects in the inner surface.⁵³ Similar bolaamphiphiles containing two different amino acid end groups, alanine and lysine, only formed helical fibers when the spacer had an even number of methylenes and both peptides were the same enantiomer.⁹³ A diastereomer with L-Lys and D-Ala formed ribbons with almost no twist.

Stevens and co-workers have developed a series of polymerizable amino-acid-derivatized diacetylenic lipids for use as colorimetric sensors.^{94,95} The polymerized liposomes respond to thermal and pH changes through a blue-to-red color change, with hydrophobic amino acid head groups being more sensitive than hydrophilic ones. They found both vesicles and helical structures could be formed from the same amide-linked amino acid diacetylenes,⁹⁵ in contradiction to the earlier proposal by Ihara et al.⁸⁶ The chemical structure of the head group and preparation procedure were found to play an important role in determining the microstructure's morphology. Examples of the morphologies observed in methanol–water solutions are shown in electron micrographs in Figure 5.20. Figure 5.20*a* shows a gel consisting of twisted ribbons using the glutamic acid–polydiacetylene (Glu–PDA) lipid (**34**), while Figures 5.20*b* and *c* show similar structures in Gln–PDA (**35**). The Gln–PDA ribbons are more uniform in width and length. They suggest that molecular chirality and hydrogen-bonding interactions in the head group regions control the growth of the helical aggregates.⁹⁵ However, head group size also plays an important role since Phe–PDA (**36**), with its bulky aromatic ring, only forms nonchiral platelets. Many of the observations in this system parallel those for the aldonamides discussed in Section 2.1.

A bolaamphiphile diacetylenic lipid based on the L-glutamic acid discussed above but with an additional carbonyl group on the other end of the chain was subsequently synthesized and found to assemble into right-handed twisted ribbons.⁹⁶ The tricarboxylate functionalities were expected to bring unique properties to the assemblies and respond to pH elevation in a more sensitive manner than Glu–PDA. The lipid L-Glu-Bis-3 (**37**) assembled into stable helical ribbons in an aqueous environment under mild conditions, as shown in Figure 5.21.⁹⁷ These ribbons are up to tens of micrometers in length, with widths of 10–100 nm and thicknesses of 5–10 nm. In contrast to probe sonication and subsequent low-temperature incubation that were used to promote helices in monofunctional Glu–PDA, vortexing and room temperature incubation were sufficient to ensure formation of stable supramolecular assemblies of L-Glu-Bis-3. Ultraviolet irradiation of these assemblies results in rapid polymerization of L-Glu-Bis-3, indicating high structural order and good alignment of the diacetylene units. High-resolution AFM data suggest that flat ribbons and highly twisted ribbons correlate with hexagonal and pseudorectangular

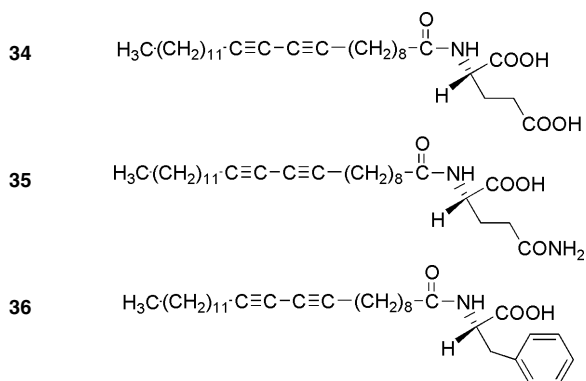
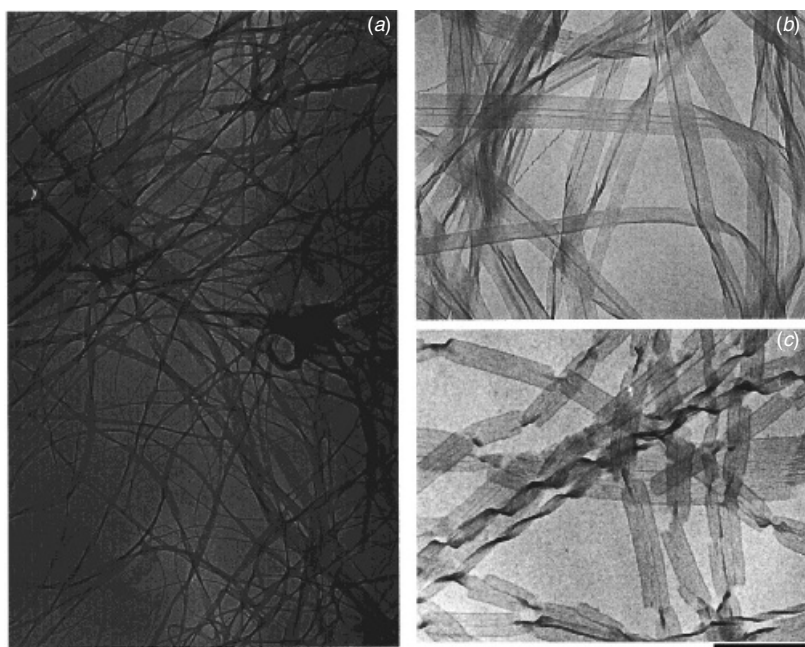


Figure 5.20 TEM images of twisted ribbons observed in diacetylenic amino-acid-derivatized lipids in methanol–water solution: (a) Glu-PDA (**34**); (b, c) Gln-PDA (**35**). Bar = 0.6 μm . Reprinted with permission from Ref. 95. Copyright 2000 by the American Chemical Society.

packing arrangements on the atomic level, respectively.⁹⁶ Increasing the pH from 7.5 to 9 caused the ribbons to fray into thin, randomly coiled nanofibers. At the same time, a blue-to-red colorimetric shift and a decrease in the CD intensity were observed. Both the AFM and spectroscopic results support theories of chiral packing which will be discussed in detail in Section 6.

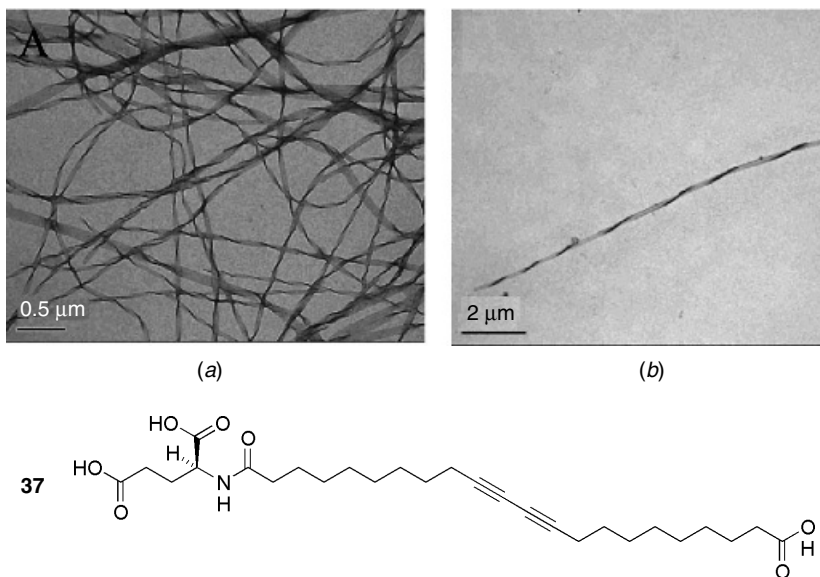
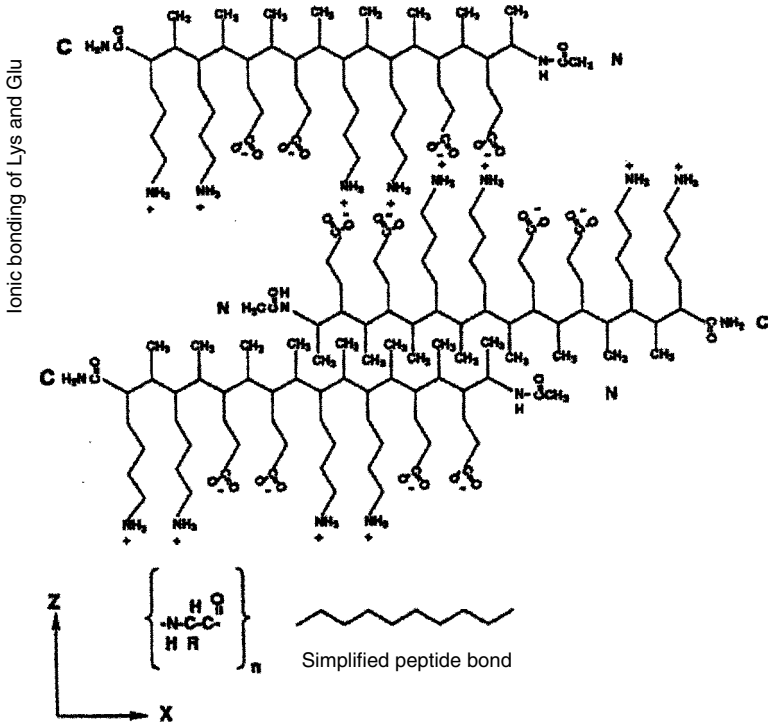


Figure 5.21 Transmission electron micrographs showing right-handed helical ribbons of L-Glu-Bis-3 (**37**) in aqueous environment. Reprinted with permission from Ref. 97. Copyright 2002 by Elsevier Science.

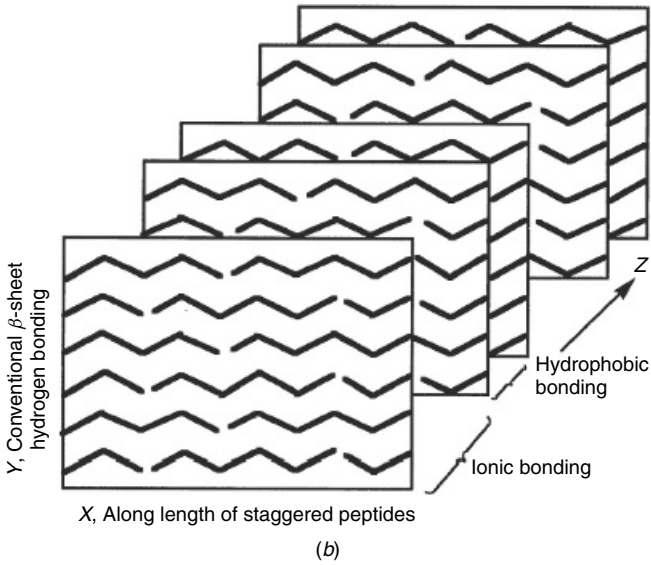
Addition of 5% ganglioside G_{M1} into the L-Glu-Bis-3 resulted in the appearance of vesicles along with twisted ribbons, while addition of nonchiral 10,12-docosadienedioic acid caused the formation of platelets.⁹⁷ These results affirm the importance of packing geometry, along with head group chirality, for the formation of helical structures.

3.2 Peptides

While the folded structure of proteins arise from hydrogen bonding, electrostatic and hydrophobic interactions, and disulfide bonds,^{69,98} the secondary structure of peptides is determined by the periodicity of polar and nonpolar residues.⁹⁹ For example, peptides of alternating hydrophilic and hydrophobic amino acids tend to adopt a β -sheet motif. However, hydrogen bonding between the amide and carbonyl groups in the backbone of neighboring peptides typically leads to higher order assembly. Short peptides designed to adopt β -sheet structure are, thus, found to self-assemble into helical filaments in polar solvents.^{100,101} These structures closely resemble amyloid and prion fibrils associated with neurodegenerative diseases such as Alzheimer's and Creutzfeldt–Jakob (mad cow disease).^{102,103} In these diseases, normally



(a)



(b)

soluble proteins convert into insoluble plaques having a well-defined fibril structure, termed amyloids. The proteins fold into β -strands that are oriented perpendicular to the fibril axis. The chiral aggregation of these peptide systems is similar to the mixed-lipid systems and gemini surfactants, described in Sections 4.3 and 5.3, respectively.

Zhang and co-workers first reported fibril formation in a designed peptide $\text{CH}_3\text{CO}-(\text{Ala}-\text{Glu}-\text{Ala}-\text{Glu}-\text{Ala}-\text{Lys}-\text{Ala}-\text{Lys})_2-\text{CONH}_2$, called EAK16, based upon a repetitive segment in the yeast protein Zuotin.¹⁰⁰ This peptide consists of alternating hydrophobic (alanine-A) and ionic (positive lysine-K and negative glutamic acid-E) residues and is thus amphiphilic in nature. The hydrogen bonding of the peptide backbone leads the peptides to self-assemble into β -sheets in aqueous solution with the hydrophobic side chains on one surface of the fiber and the ionic side chains on the opposite, hydrophilic surface. The resulting hydrophobic and electrostatic interactions then give rise to higher order assembly in saline solution, leading to a three-dimensional hydrogel which has been shown to support cell attachment and growth.¹⁰⁴ This scenario is schematically described in Figure 5.22. When the alanines are replaced by more hydrophobic residues such as phenylalanine, the self-assembly occurs in the absence of salt. In particular, the peptide $\text{NH}_3^+-\text{Lys}-\text{Phe}-\text{Glu}-\text{Phe}-\text{Lys}-\text{Phe}-\text{Glu}-\text{Phe}-\text{CO}_2^-$, called EFK8, has been found to have interesting mechanical properties.¹⁰⁵ The mechanical strength of this peptide assembled in water is proportional to its concentration with a Young's modulus of 15 kPa at 1.0%, comparable to that of collagen gel.

In related work, Boden and co-workers designed peptides to self-assemble into β -sheets in moderately polar (e.g., methanol) and aqueous solvents.^{101,106} These peptides were designed to include interstrand attraction and lateral recognition through rational placement of charged and hydrophobic chains in order to obtain the favored anti-parallel β -sheet structures. In particular, the 11-residue peptide $\text{CH}_3\text{CO}-\text{Gln}-\text{Gln}-\text{Arg}-\text{Phe}-\text{Gln}-\text{Trp}-\text{Gln}-\text{Phe}-\text{Glu}-\text{Gln}-\text{Gln}-\text{CONH}_2$ (DN1) was found to aggregate into tapes, ribbons, fibrils, and fibers with increasing peptide concentration. Figure 5.23 shows the variety of aggregates formed in solutions of this peptide. Although this peptide does not contain the alternating hydrophobic/hydrophilic pattern used by Zhang et al., the residues Phe4, Trp6, and Phe8 are expected to promote β -sheets

Figure 5.22 Model of fibril formation in designed peptides. (a) View perpendicular to β -sheet, which is y axis. Three peptide molecules form three layers of antiparallel β -sheet, held together on one side by bonding between hydrophobic residues facing each other and the other by oppositely charged residues facing each other. (b) Stacking of β -sheets. Staggered peptides are oriented along x axis. The z axis has complementary ionic and hydrophobic bonds. The y axis contains conventional β -sheet hydrogen bonds from amino acid backbone. Reprinted with permission from Ref. 100. Copyright 1993 by the National Academy of Sciences, U.S.A.

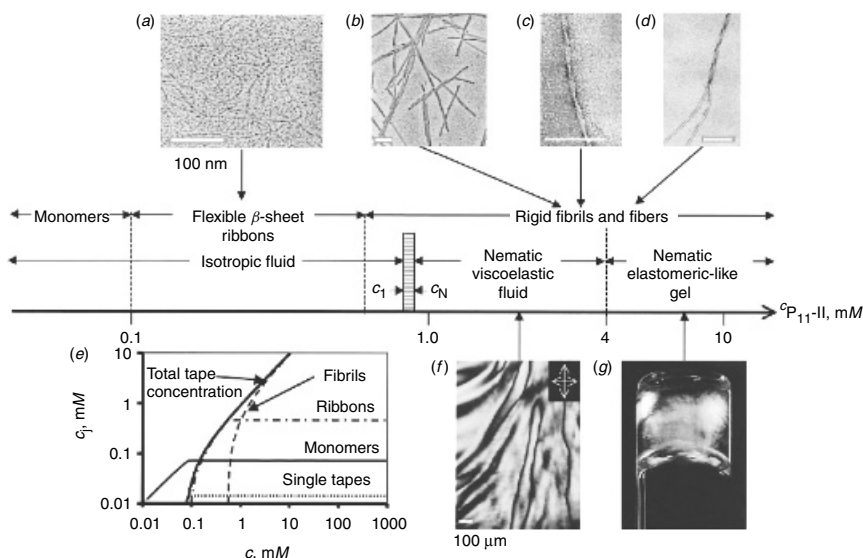


Figure 5.23 Aggregate structures and liquid crystalline phase behavior observed in solutions of 11-residue peptide DN1 in water with increasing concentration (log scale). Electron micrographs of (a) ribbons ($c = 0.2$ mM) and (b) fibrils ($c = 6.2$ mM) were obtained with 4-month-old solution after platinum rotary shadowing. (c, d) Micrographs obtained with 1-month-old 6.2 mM solution after uranyl acetate negative staining. The TEM micrographs show principal aggregate structures whose populations change with peptide concentration, as depicted in (e), based on model described in Ref. 109. (f) Polarizing optical micrograph shows thick threadlike texture observed for solution with $c = 3.7$ mM. (g) Self-supporting birefringent gel ($c = 6.2$ mM) in inverted 10-mm-o.d. glass tube viewed between crossed polarizers. Bars = 100 nm (a, b, c, and d), 100 μ m (f). Reprinted with permission from Ref. 109. Copyright 2001 by the National Academy of Sciences, U.S.A.

through side-chain π - π interactions, while Arg3 and Glu9 promote antiparallel alignment.¹⁰⁷ In order to explain this hierarchical aggregation, Nyrkova et al. developed a statistical model to describe the competition between the attractive forces between ribbons and the elastic distortions caused by aggregation of twisted ribbons.^{108,109} The phase diagram predicted by this theory, shown in Figure 5.24, resembles the complicated hierarchy observed in the assembly of peptide DN1.

Intermediate structures in fibril assembly were observed by Marini et al. in the peptide $\text{CH}_3\text{CO-Phe-Lys-Phe-Glu-Phe-Lys-Phe-Glu-CONH}_2$ (KF8).¹¹⁰ Under acidic conditions, the kinetics of aggregation was significantly slowed down allowing for the deposition of early-stage ribbons on mica substrates and subsequent imaging using AFM. Figure 5.25 shows the observed aggregates at different times.¹¹⁰ The ribbons observed after a few

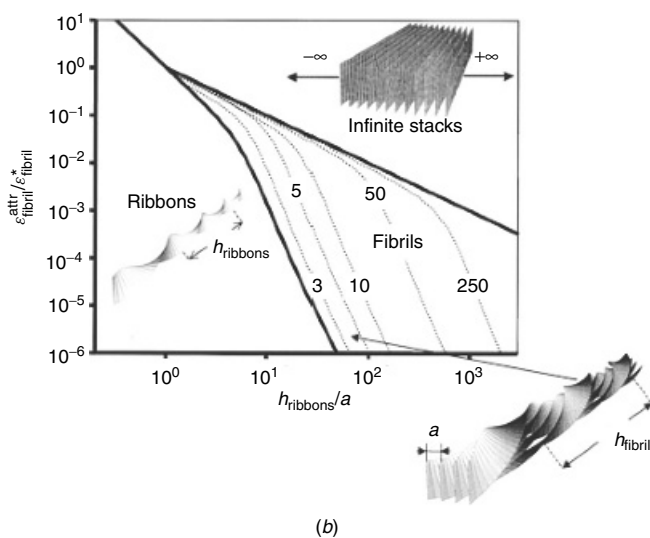
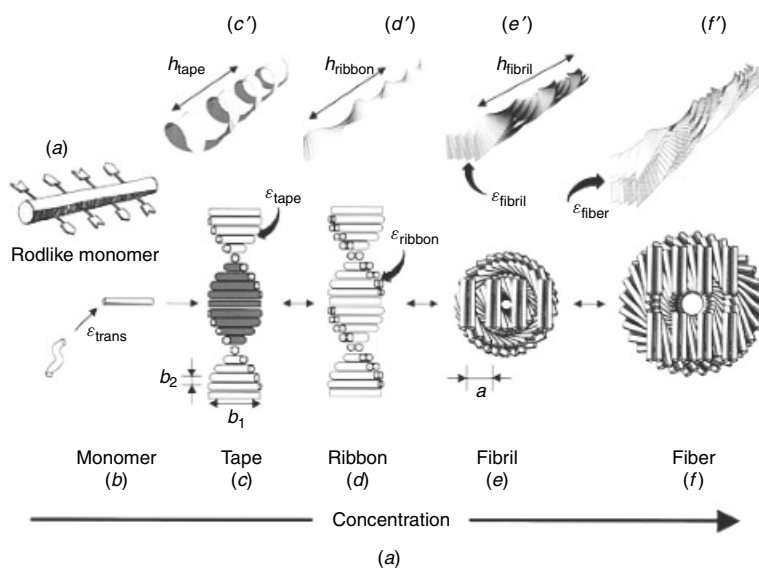


Figure 5.24 Model of hierarchical self-assembly of chiral rodlike monomers.¹⁰⁹ (a) Local arrangements (c–f) and corresponding global equilibrium conformations (c'–f') for hierarchical self-assembling structures formed in solutions of chiral molecules (a), which have complementary donor and acceptor groups, shown by arrows, via which they interact and align to form tapes (c). Black and the white surfaces of rod (a) are reflected in sides of helical tape (c), which is chosen to curl toward black side (c'). (b) Phase diagram of solution of twisted ribbons that form fibrils. Scaled variables: relative helix pitch of isolated ribbons h_{ribbon}/a , relative side-by-side attraction energy between fibrils $\epsilon^{\text{attr}}/\epsilon^*$. Reprinted with permission from Ref. 109. Copyright 2001 by the National Academy of Sciences, U.S.A.

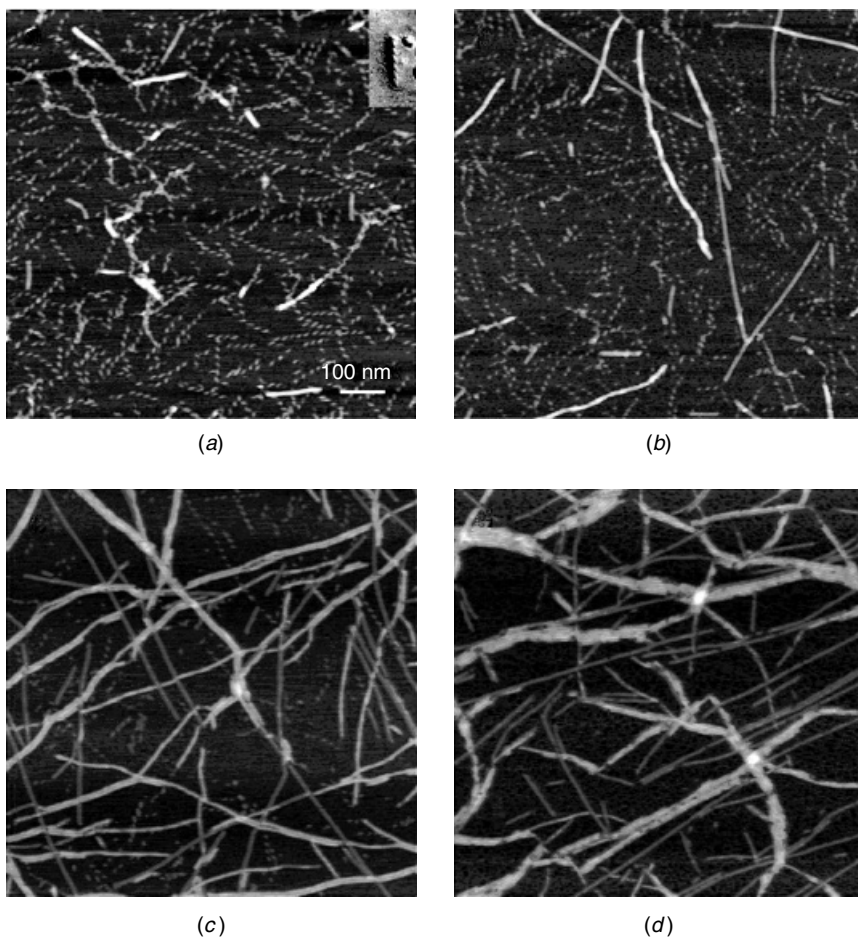


Figure 5.25 AFM images of intermediate structures in self-assembly of peptide KFE8 in aqueous solution deposited on freshly cleaved mica surface: (a) 8 min after preparation of solution. Inset: electron micrograph of sample of peptide solution obtained using quick-freeze deep-etch technique; (b) 35 min, (c) 2 h, and (d) 30 h after preparation. Reprinted with permission from Ref. 110. Copyright 2002 by the American Chemical Society.

minutes are all left handed with 7 nm diameter and 19 nm pitch. Fibrillar structures of 8 nm diameter appear at later stages. Dibenzofuran-based peptides were also found to have a rich polymorphism in their aggregate structure which can be manipulated by the pH, buffer composition, and ionic strength.¹¹¹

Recently, a series of surfactant-like peptides were found to form helical nanotubes.¹¹² The anionic peptide monomers were composed of a head group of one or two aspartic acids and a hydrophobic tail containing six residues

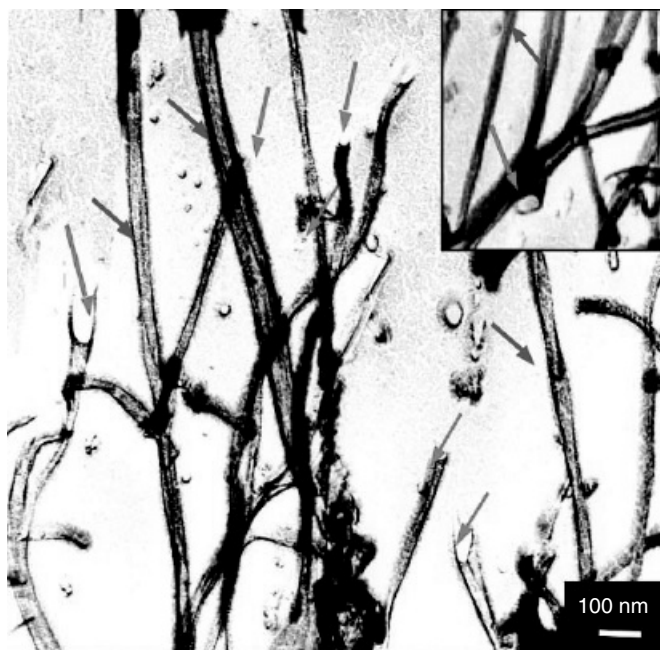


Figure 5.26 TEM image of surfactant-like peptide A_6D dissolved in water (4.3 mM at pH 7) obtained using quick-freeze deep-etch technique. Image shows dimensions, 30–50 nm in diameter with openings of nanotube ends (arrows). Inset: Opening ends in more detail. Reprinted with permission from Ref. 112. Copyright 2002 by the National Academy of Sciences, U.S.A.

of alanine, valine, or leucine. The peptides assemble into a cross-linked network of tubular aggregates in water. Figure 5.26 shows a freeze-etch electron micrograph of $\text{CH}_3\text{CO}-(\text{Ala})_6-\text{Asp}-\text{CO}_2^-$ (A_6D) which reveals the hollow, tubular structure. These tubules have multiple junctions and appear much less rigid than the phospholipid tubules discussed in Section 4.1. In related work, Ghadiri and co-workers synthesized a series of cyclic peptides that self-assemble into tubular structures hundreds of nanometers long, with internal diameters of less than a nanometer.^{113,114} However, these nanotubes are composed of L- and D-amino acids and show no chiral features.

4 PHOSPHOLIPIDS

Lipids encompass a wide class of amphiphilic molecules which, along with proteins, form the biological membranes necessary to support cellular function. While the simplest lipids, fatty acids and triglycerides, are not

chiral, the majority are. The most commonly occurring membrane lipids are diacyl-glycerophospholipids, commonly referred to as phospholipids. Most long-chain phospholipids self-assemble into spherical, multibilayer aggregates known as liposomes.³ However, certain naturally occurring, synthetic, or mixed-lipid systems can form chiral aggregates. Synthetic phospholipids will be discussed in this section, while naturally occurring cerebrosides and mixtures of lipids and bile salts are discussed in Sections 2.3 and 5.2, respectively.

4.1 Diacetylenic Phospholipids

Phospholipids with photopolymerizable diacetylenic moieties in the acyl chains were first synthesized to increase the durability of liposomes^{115,116} and for the modification of polymer surfaces.¹¹⁷ However, some diacetylenic lipids were found to self-assemble into hollow, cylindrical structures.^{25,26} Tubules formed upon cooling the lipid bilayer from the fluid L_α phase, where the chains are disordered, into the ordered L_β' gel phase. The important feature of these lipids is the multiple carbon triple bonds in the acyl chains which introduce a kink in the chains and make them unusually rigid. Infrared,^{118,119} Raman,^{120,121} and NMR spectroscopy,¹²² as well as X-ray diffraction,^{123,124} show that the acyl chains are highly ordered and tilted in tubules. The tubules observed by Yager and Schoen assembled from aqueous dispersions of 1,2-bis(tricoso-10,12-diynoyl)-*sn*-glycero-3-phosphocholine (**38**).²⁵ This lipid is designated DC_{8,9}PC because it has eight methylenes between the ester and diacetylene group and nine methylenes between the diacetylene and the terminal methyl group. Tubules formed from DC_{8,9}PC have an average diameter of 0.5 μm and lengths of 20 μm to more than a millimeter. The chirality of these tubules is often reflected in helical markings visible in electron micrographs and large peaks observed in their CD spectra.⁶⁸ Both of these techniques reveal an inversion of handedness when the opposite enantiomer lipid is used.¹²⁵ The scanning electron micrograph of a copper-plated lipid tubule in Figure 5.27 shows that they are hollow and contain spiral wrappings.

Several methods have been reported for the formation of tubules from diacetylenic lipids. The first involves thermal cycling of multilamellar vesicles formed by hydrating the lipids with pure water above the chain melting temperature T_m .¹²⁶ The size and stability of DC_{8,9}PC tubules formed in water are sensitive to preparation conditions and thermal history. Longer and more robust tubules can be formed by first dissolving the lipids in alcohol and then mixing with water above their melting temperature ($T_m \sim 37^\circ\text{C}$) and slowly cooling the mixture.¹²⁷ Several studies have found that the length distribution and thickness of tubules depend on the alcohol used, while the diameter appears independent of preparation conditions. Decreasing the cooling rate through T_m has been shown to greatly increase the average length of



Figure 5.27 Scanning electron micrograph of copper-coated DC_{8,9}PC (**38**) tubules. Tubules are hollow with diameter of approximately 0.5 μm (bar = 0.5 μm). Helical wrappings evident in some tubules are all right handed. Reprinted with permission from Ref. 125. Copyright 1998 by the American Chemical Society.

tubules and decrease the wall thickness in ethanol–water solutions.¹²⁴ Tubules formed in mixtures of methanol and water at low lipid concentration consist of single-bilayer walls and are of maximal length at 85% methanol, while those in ethanol–water contain more than five bilayers and are longest at 70% ethanol.¹²⁸ Calorimetric studies of concentrated ethanol–water tubules indicate a maximum in the enthalpy of the melting transition also in a solution of 70% ethanol.¹²⁹

Lipid tubules were also found to have intense peaks in their CD spectra indicating large chiral correlations in the molecular packing.^{68,130} This chiral order can no longer be maintained when the chains disorder above T_m , and the tubules melt, leading to a decrease in CD peak intensity by four orders of magnitude. Further CD experiments revealed that, in addition to chiral packing within the bilayer, chiral correlations exist between bilayers in multibilayer tubules.¹³¹ Representative CD spectra from tubules of varying thickness are shown in Figure 5.28. For single-bilayer tubules formed in methanol–water solution (Figure 5.28c), a sharp peak at 195 nm ($\pi \rightarrow \pi^*$ of the diacetylene chromophore, $\epsilon_{197} = 8020 \text{ cm}^{-1} \text{ M}^{-1}$ in methanol) associated with chiral packing of the diacetylene group is the predominant spectral feature, while a broader peak at 202 nm is seen from multibilayer tubules formed in ethanol–water (Figure 5.28a). The large magnitude of this CD

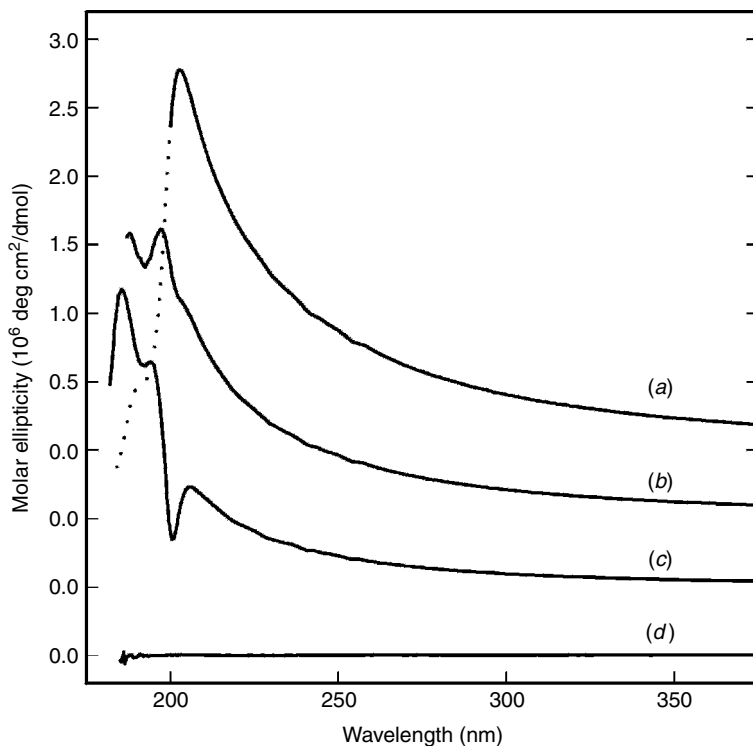


Figure 5.28 Circular dichroism spectra of DC_{8,9}PC tubules prepared in (a) ethanol–water (7:3), (b) methanol–ethanol–water (35:35:20), and (c) methanol–water (70:30) and (d) DC_{8,9}PC liposomes above melting temperature. All samples were prepared at lipid concentration of 2.0 mg/ml and spectra for tubules were recorded at 25°C. Liposome spectrum was recorded at 40°C and peak intensity is about 10⁴ smaller than that from tubules.

($\Delta\epsilon_{195} = 660 \text{ cm}^{-1} \text{ M}^{-1}$) gives a dissymmetry factor $g = 0.08$, among the largest measured for a self-assembled system. The loss of chiral order in the L_{α} phase is reflected in the CD spectrum shown in Figure 5.28d for DC_{8,9}PC liposomes above the lipid melting temperature, where the peak magnitude is 10⁴ times smaller than that from the tubule ($L_{\beta'}$) phase. Such observations showed the usefulness of CD as a tool to investigate tubule morphology and allowed for optimization of DC_{8,9}PC tubules for technological applications.¹²⁵ Tubules with an optimal thickness of two bilayers can be formed by either increasing the lipid concentration or using mixed alcohol solutions. The CD spectrum from two-bilayer tubules made in a solution of methanol, ethanol, and water is shown in Figure 5.28b. It has both a large peak at 195 nm and a broad shoulder indicating an additional peak near 205 nm.

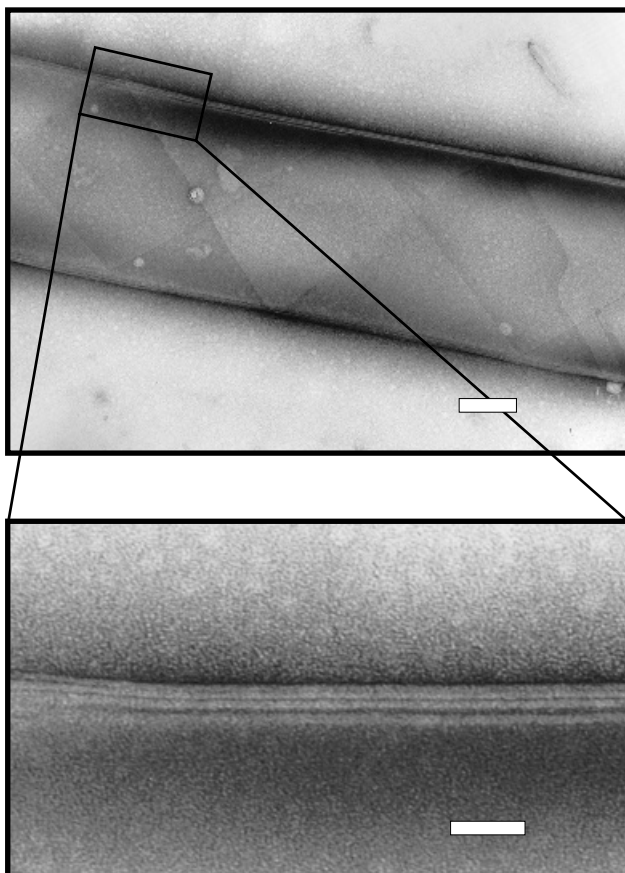


Figure 5.29 Negative-stained electron micrograph of DC_{8,9}PC tubule from 5-mg/ml sample in methanol–water (85 : 15). Solvent conditions and lipid concentration were adjusted to obtain sample of two-bilayer tubules as shown in enlargement of tubule edge in bottom panel. Bar = 200 nm (top); 50 nm (bottom). Reprinted with permission from Ref. 125. Copyright 1998 by the American Chemical Society.

Tubules with an average length in excess of 100 μm and a thickness of two bilayers can also be formed by varying the lipid concentration in methanol–water.¹²⁵ An electron micrograph of a double-bilayer tubule is shown in Figure 5.29. Helical markings are observed in the top panel. Such markings are characteristic of multiple-bilayer ethanol–water tubules but are not seen in single-bilayer methanol–water tubules. These markings may be associated with defects in the tilt direction of the lipid molecules on the tubules¹³² or they may be the edges of helical ribbons wrapped around the

inner tubule core. Although it is sometimes difficult to differentiate the helical markings from the top and bottom bilayers, observation of the tubule ends or taking stereo pairs of micrographs occasionally allows unambiguously the determination of the handedness of the helical markings. Only right-handed helices are observed for the L-enantiomer in single-component systems.^{125,133}

The question then arises as to whether other saturated lipid bilayers have enhanced chiral order in the $L_{\beta'}$ phase. In fact, Walde and Blöchliger found enhanced CD in liposomes below the melting temperature.¹³⁴ For the saturated lipid 1,2-dipalmitoyl-*sn*-glycero-3-phosphocholine (L-DPPC, **39**), a CD peak at 218 nm ($n \rightarrow \pi^*$ of the ester chromophore) is observed to decrease upon heating the liposomes through the main transition temperature (41°C), as shown in curve 2 of Figure 5.30. In the case of partially unsaturated L-POPC (1-palmitoyl-2-oleoyl-*sn*-glycero-3-phosphocholine, **40**) with $T_m = -3^\circ\text{C}$, liposomes in the fluid phase also show a measurable CD peak (curve 3 in Figure 5.30) at least 30 times larger than that for monomeric lipids in methanol. They were also able to probe the hydrophobic domain of the liposomes by solubilizing a water-insoluble dye in the liposomes.¹³⁴ The induced CD spectrum showed a similar but sharper decrease at T_m . If the opposite enantiomer, D-DPPC is used, both the normal and induced CD show a change

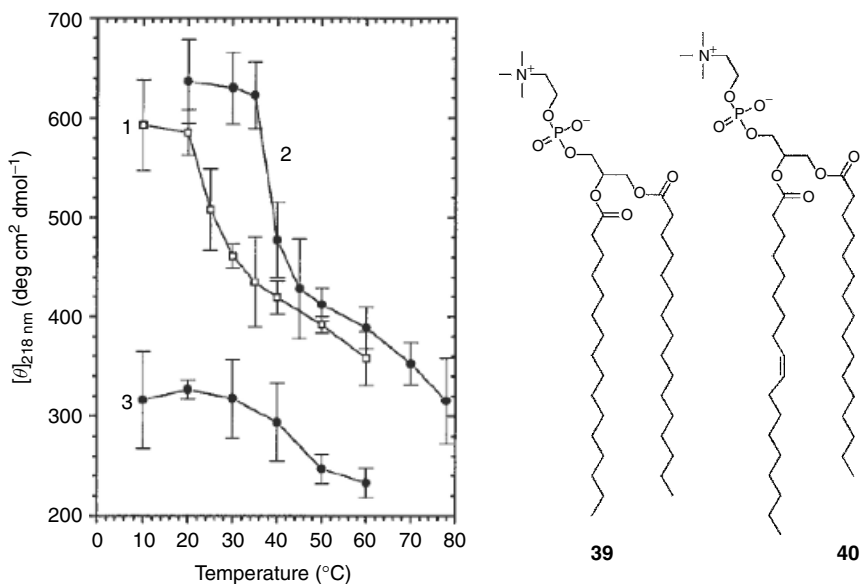


Figure 5.30 Temperature dependence of molar ellipticity at 218 nm for liposomes prepared from L-DMPC, L-DPPC (**39**), and L-POPC (**40**). Reprinted with permission from Ref. 134. Copyright 1997 by the American Chemical Society.

of sign in the spectrum. Thus, enhanced CD in these spherical assemblies of chiral molecules does reflect the change in packing of the head groups at the chain melting temperature. However, the approximate doubling of the peak magnitude below the melting temperature is far less than the 10^4 increase seen for the diacetylenic lipid upon tubule formation.¹³⁵

Investigations of the thermodynamics of tubule melting were carried out by Nounesis et al. using magnetic birefringence and calorimetry.¹³⁶ They found that single-bilayer tubules melt continuously, while multiple-bilayer tubules melt discontinuously. This difference was attributed to a dimensional crossover, whereby single-bilayer tubules are effectively two-dimensional systems that melt through a second-order defect-unbinding transition, while multiple-bilayer tubules are three-dimensional systems that melt through a conventional first-order transition. Further studies at the Naval Research Laboratory on a broader range of alcohol fraction and lipid concentration using CD and calorimetry¹³⁷ did not agree with the model of Nounesis et al. They found that the melting can be explained in terms of two distinct thermodynamic processes. The discontinuous melting is a first-order transition of the lipid bilayers from the ordered $L_{\beta'}$ phase to the disordered L_{α} phase, while the continuous melting reflects an increase in the lipid solubility with temperature. This behavior is illustrated in Figure 5.31, where the concentration dependence of the melting curves for tubules prepared in 70:30 ethanol–water is shown. The top panel of Figure 5.31 shows the temperature dependence of the peak molar ellipticity for DC_{8,9}PC tubules, while the bottom panel shows corresponding specific heat measurements. A crossover from discontinuous to continuous melting is seen in both the ellipticity and specific heat as the lipid concentration is lowered from 5 mg/ml. For continuous melting, the transition temperature is seen to decrease with lipid concentration, reflecting an increase in the lipid solubility with temperature. Electron microscopy showed multibilayer tubules for all concentrations in this system.

The diameter of tubules formed from negatively charged diacetylenic lipids, synthesized by enzymatically replacing the choline portion with glycols, was found to be altered by varying the pH and ionic strength of the solution and the anion of added salt.¹³⁸ Depending on the exact conditions, single populations of either larger or smaller diameter tubules as well as tubules with bimodal distributions of diameters were formed. Studies of positional isomers of diacetylenic phospholipids found that variations of the position of the diacetylene in the acyl chain had very little effect on the diameter of the tubules.^{119,127} At the same time, infrared and calorimetry data indicated an odd–even effect in the packing of the isomers. It was later found using CD spectroscopy and electron microscopy that when the number of methylenes between the glycerol ester and diacetylene group was even, single-bilayer tubules were seen in a methanol–water mixture, while multiple-bilayer

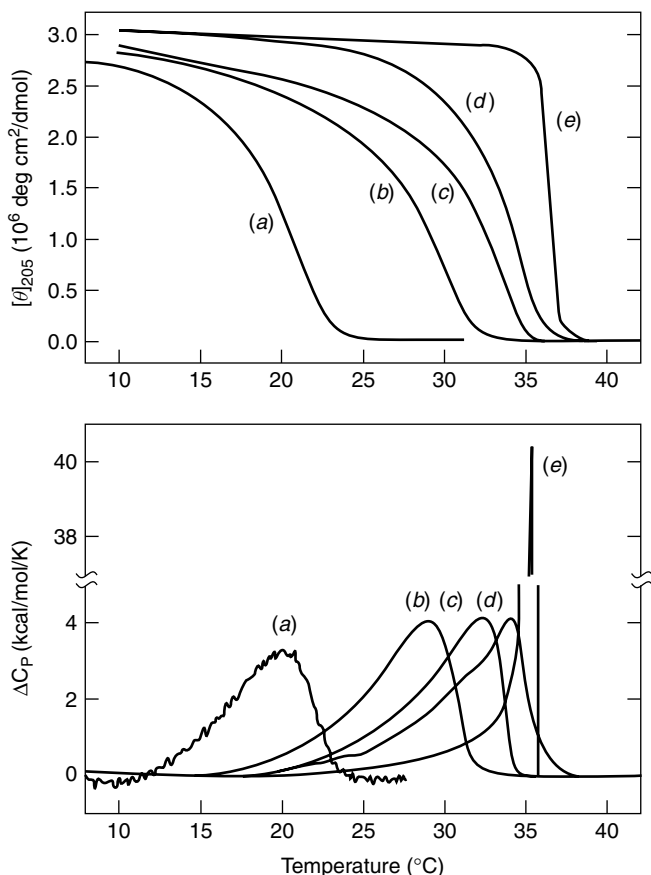


Figure 5.31 Concentration dependence of CD spectra at 205 nm (top) and specific heat (bottom) of DC_{8,9}PC tubules prepared in ethanol–water (70:30) at lipid concentrations of (a) 0.2, (b) 0.5, (c) 1.0, (d) 2.0, and (e) 5.0 mg/ml. These results show crossover from continuous to discontinuous melting as lipid concentration is increased. Reprinted with permission from Ref. 137. Copyright 1997 by the American Chemical Society.

tubules were seen for an odd number.¹²⁵ The alternation between even- and odd-segment lengths can have a substantial effect on the molecular packing leading to variations in the arrangement of the head group spacing which affects interbilayer interactions.

In experiments on diacetylenic lipid tubules formed from mixed L- and D-lipids, the tubule radius did not change as a function of enantiomeric excess. Rather, tubules formed from the mixed enantiomers have approximately the same diameter, length, and density as tubules of the pure chiral lipid.¹²⁵ Electron microscopy shows that the mixed enantiomers form mixtures of tubules

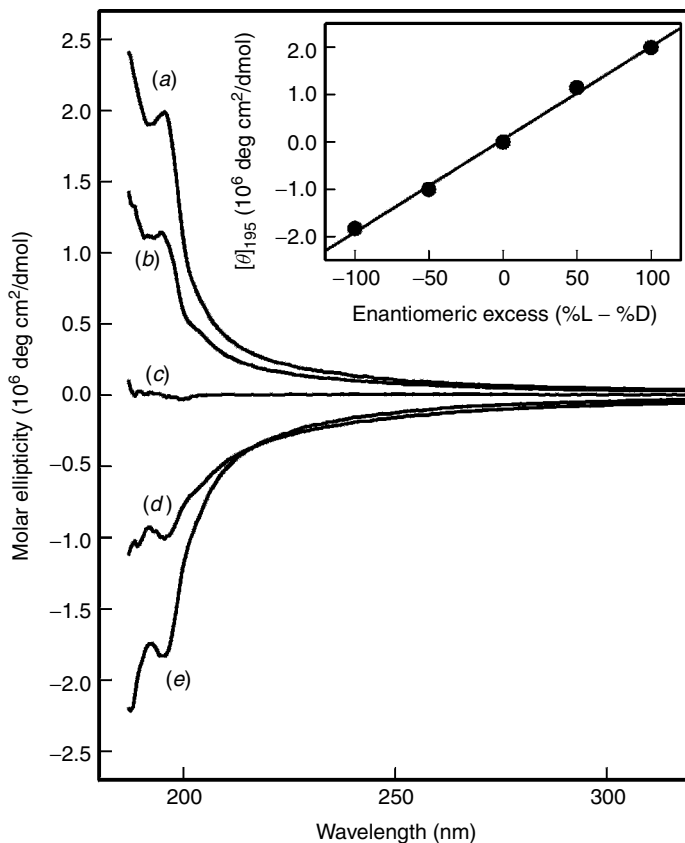


Figure 5.32 Circular dichroism spectra of tubules made from mixtures of opposite enantiomers of DC_{8,9}PC in 80:20 methanol–water. Spectra shown correspond to mixtures of (a) 100:0, (b) 75:25, (c) 50:50, (d) 25:75, and (e) 0:100 L-/D-DC_{8,9}PC. Inset shows dependence of peak molar ellipticity on enantiomeric excess along with linear fit of data. Reprinted with permission from Ref. 125. Copyright 1998 by the American Chemical Society.

with right- and left-handed markings as well as right- and left-handed helical ribbons.¹³³ Circular dichroism spectra from tubules composed of mixtures of L- and D-enantiomers in a methanol–water solution are shown in Figure 5.32. Spectra from tubules made purely from the L- and D-enantiomers are nearly identical but of opposite sign. This reflects the opposite handedness of packing in tubules composed of lipids with opposite chirality. In addition, tubules made from mixtures of opposite enantiomers show comparable spectra with the magnitude and sign scaling with the enantiomeric excess. By analyzing the measured peak molar ellipticity as a function of enantiomeric excess (inset

to Figure 5.32), it was determined that a linear dependence implies complete phase separation, so that each tubule is nearly pure of D- or L-lipids.¹³⁹ This differs from the gluconamides and amino acid amphiphiles, discussed in Sections 2 and 3, respectively, where the mixed bilayers of opposite enantiomers lead to noncylindrical aggregates. It also can be contrasted with the case of chiral polymers, where the cooperativity forced by the covalent bonds leads to chiral amplification, with a highly nonlinear dependence of CD signal on enantiomeric excess.¹⁴⁰

A novel approach to imaging the chiral patterns on lipid tubules was developed by Lvov and co-workers.¹⁴¹ Silica nanospheres were assembled onto the tubules after the sequential adsorption of oppositely charged polymers. For purely diacetylenic lipid tubules, caps containing 50–100 silica spheres were observed at the end of the tubules. Electron micrographs of tubules containing 2% anionic lipid showed helices of nanoparticles winding around the interior of the tubules in addition to the end caps, as shown in Figure 5.33.¹⁴¹ The high-magnification image (Figure 5.33*b*), clearly shows the nanoparticles are inside the tubules and the outside of the tubules appears smooth. Earlier experiments by Burkett and Mann found similar results through the reduction of H₂AuCl₄ onto preformed tubules.¹⁴² However, in this case the gold nanoparticles formed in helical patterns on the outside of the tubules. On the other hand, Letellier et al. observed that magnetic nanoparticles of maghemite iron nanoparticles entered into the interior of DC_{8,9}PC tubules and filled them uniformly in acidic media, where the particles are positively charged.¹⁴³ By contrast, at neutral pH, the particles were negatively charged and did not enter into the tubule interior. In neither case did they find the end caps or nanoparticle helices observed by Lvov et al.¹⁴¹

Thomas et al. studied the kinetics of tubule formation in highly concentrated solutions of a single enantiomer of DC_{8,9}PC.¹⁴⁴ In the early stages of tubule formation, they observed both right- and left-handed helices in roughly equal proportions. In the later stages, they saw only a single helical sense on the outer bilayers of multilamellar tubules, but they still found both helical senses in the inner bilayers. This experiment seems to violate the expected connection between the chirality of the molecules and the helical sense of the tubules. One explanation for these observations is that highly concentrated solutions lead to longer equilibration times, thus making possible the observation of intermediate states. As discussed in Section 6.6, this argument implies that the molecular packing has two possible states which are approximately mirror images of each other. These states are both local minima of the free energy, but one is the stable minimum while the other is only metastable. Hence, in the early stages of tubule formation under some conditions, both states might be populated, but at later stages most tubules would transform into the favored helical sense.

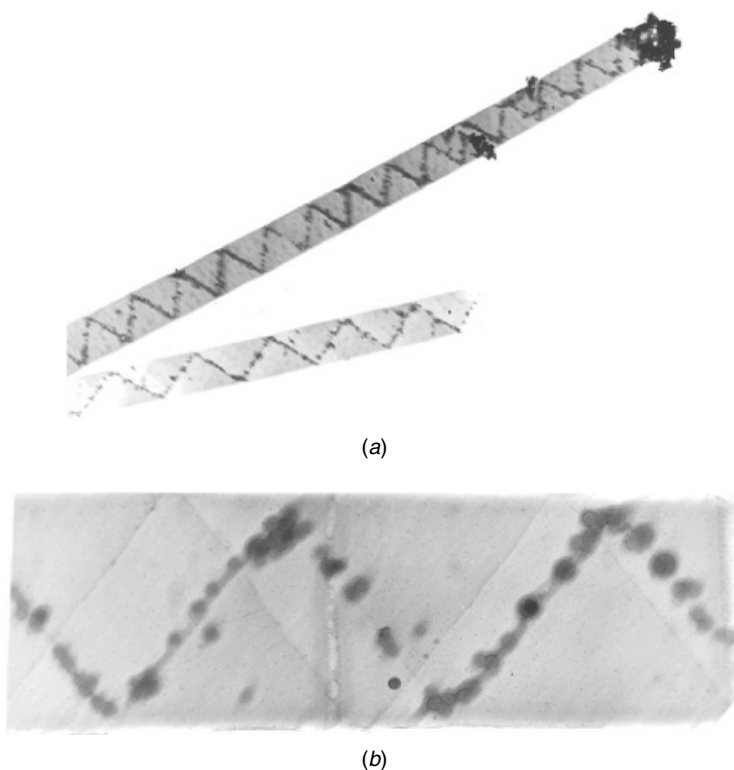


Figure 5.33 Electron micrographs of nanoparticle helices inside tubules of DC_{8,11}PC+ 2% DC_{8,9}PEOH after sequential absorption of charged polymers followed by treatment with 45-nm silica spheres. Reprinted with permission from Ref. 141. Copyright 2000 by the American Chemical Society.

4.2 Diacetylenic Phosphonate Lipids

Thomas and co-workers have synthesized analogues of DC_{8,9}PC where the phosphate linkage between the choline head group and glycerol backbone is replaced by a phosphonate.^{145,146} Tubule formation with these phosphonate lipids (**41**, **42**) was determined using the ethanol–water preparation conditions described above. X-ray diffraction and microscopy revealed these tubules have diameters of about 1 μm , twice that of DC_{8,9}PC tubules, in ethanol–water solutions. The tubules of the phosphonate appeared shorter, more fragile, and thinner walled. They were also polymerized rapidly in comparison with those of DC_{8,9}PC. The phosphonate lipids were designated C3 (**41**) and C4 (**42**), in reference to the respective three or four carbons in their molecular

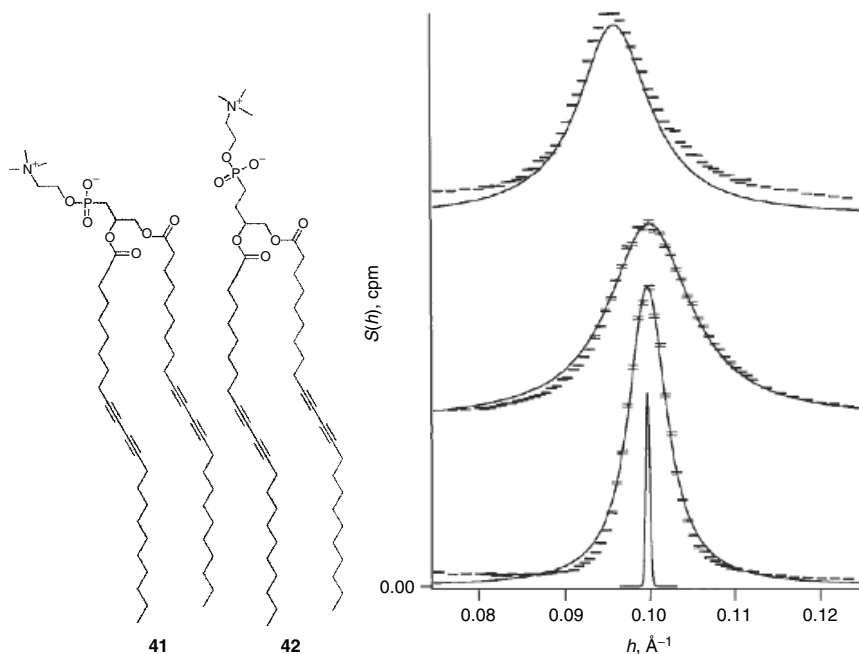


Figure 5.34 Small-angle X-ray scattering showing interlamellar fundamental peaks from C4 phosphonate (**42**) tubules (top), C3 phosphonate (**41**) tubules (middle), and DC_{8,9}PC (**38**) tubules (bottom). Solid trace is 0.0007 Å⁻¹ full width at half maximum instrument resolution. Reprinted with permission from Ref. 146. Copyright 2002 by the American Chemical Society.

backbone. The small-angle X-ray scattering data in Figure 5.34 shows that the interlamellar spacings of the tubules from the three compounds are quite similar despite the difference in diameter.¹⁴⁶ However, the broader peaks observed for the phosphonate tubules indicates the correlation length is about half that for DC_{8,9}PC tubules due to their thinner walls.

Tubules derived from the phosphonate lipids appeared more flexible than those made of DC_{8,9}PC. The optical micrograph in Figure 5.35 clearly shows bending of a C3 (**41**) tubule over a few micrometers. Similar pictures show DC_{8,9}PC tubules to be rigid on length scales of hundreds of micrometers.¹⁷ Atomic force microscopy showed that the phosphonate tubules were more deformable than those of DC_{8,9}PC and flattened upon drying.¹⁴⁶ A small portion of the phosphonate is in the form of stable open helices which were imaged using liquid mode AFM. Surprisingly, Thomas et al. found helices with both senses of handedness in an enantiomerically pure sample.¹⁴⁵ Figure 5.36 shows AFM images of a right-handed (top) and left-handed (bottom) helix formed from the C4 phosphonate analogue (**42**). This is in contrast with the DC_{8,9}PC tubules

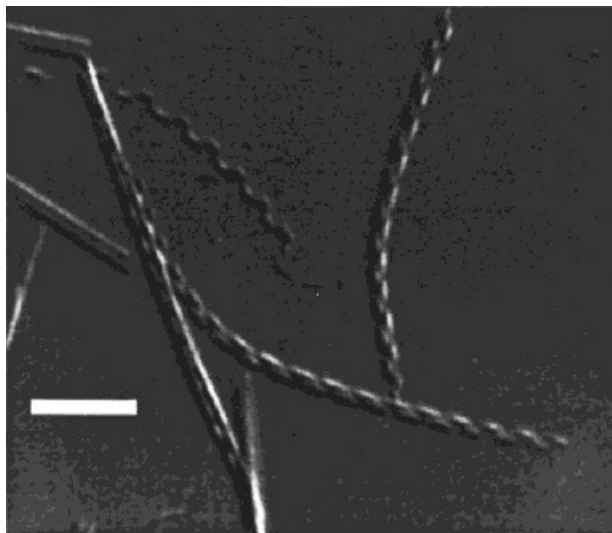


Figure 5.35 Nomarski differential interference contrast micrograph of C3 phosphonate (**41**) tubules. Note gentle bending of tubule axes and unwinding occurring at tubule ends. Vertical tubule found at right of figure and diagonal tubule it touches appear to have opposite handedness. Bar = 5 μm . Reprinted with permission from Ref. 146. Copyright 2002 by the American Chemical Society.

discussed in Section 4.1, where all the helices had the same handedness for a given enantiomer.

These experiments on phosphonate tubules raise two issues. The first issue is how to explain the increased diameter of the phosphonate tubules compared with $\text{DC}_{8,9}\text{PC}$ tubules. The chemical structure of the phosphonate lipid is similar to that of $\text{DC}_{8,9}\text{PC}$, except for a small change in the structure of the glycerol backbone. However, the differences in bond lengths and bond angles associated with this chemical change can modify the packing of neighboring molecules.¹⁴⁶ This modification is small enough that tubules can still form but large enough to increase the tubule diameter by a factor of 2. This connection between chemical structure and tubule-forming properties is a great benefit derived from synthetic effort in this area.

The second issue is how to explain the observation of both left- and right-handed helices in the phosphonate material. While Thomas et al. found both helical senses in the early stages of formation of $\text{DC}_{8,9}\text{PC}$ tubules, they found both helical senses even in the equilibrium state of the phosphonate. In the previous section, we attributed their results on tubule formation kinetics to a biased chiral symmetry-breaking in which the molecular packing has two possible states which are approximately mirror images of each other. The

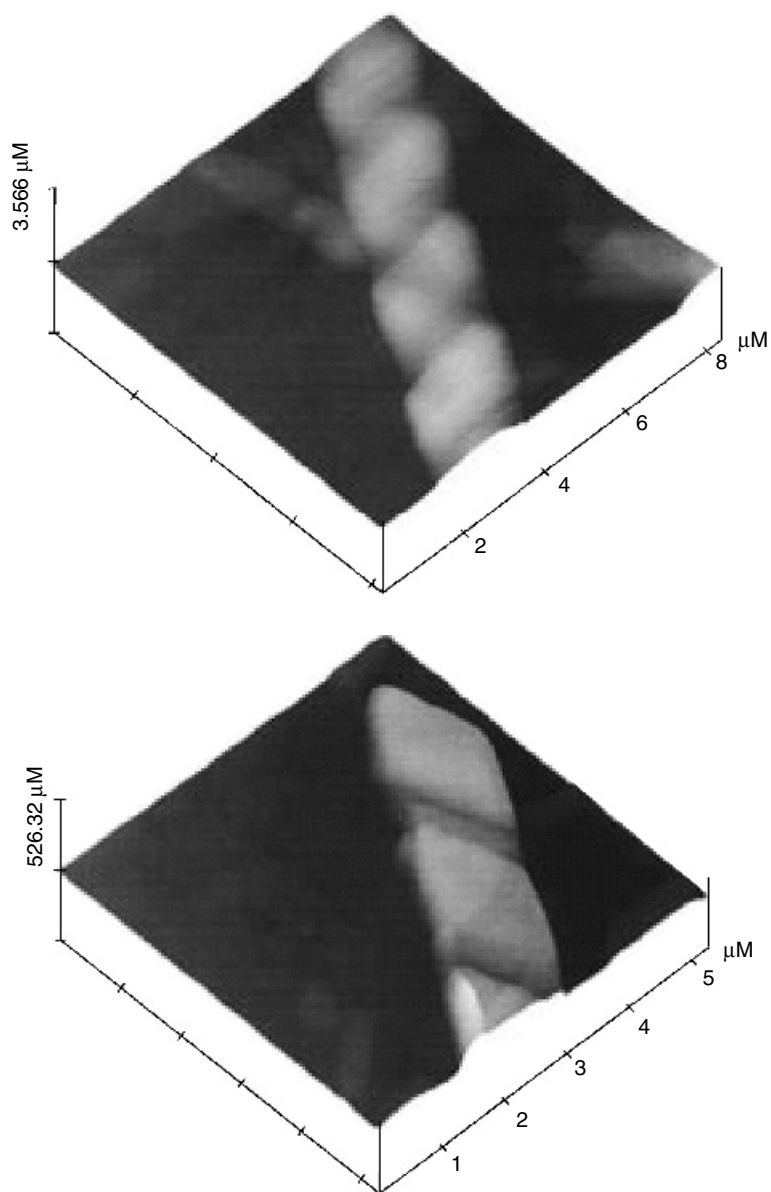


Figure 5.36 Pseudo-three-dimensional perspective of right-handed (top) and left-handed (bottom) C₄ phosphonate (**42**) helices obtained with underwater contact-mode AFM. Reprinted with permission from Ref. 145. Copyright 1998 by the American Chemical Society.

molecular chirality breaks the symmetry between these two states and selects one as the stable minimum. In DC_{8,9}PC, the influence of molecular chirality is apparently large enough to cause almost all tubules to take the favored helical sense in the equilibrium state. In the phosphonate, either the influence of molecular chirality is much smaller, so that both helical senses occur in equilibrium, or there are two conformers of the head group that favor opposite helical twist. This view is supported by the observation that the ratio of left- and right-handed helices was sensitive to the rate of formation in the phosphonate system.¹⁴⁵ The theory of biased chiral symmetry-breaking will be discussed further in Section 6.6.

4.3 Phospholipid Mixtures

The mixing of nematogenic compounds with chiral solutes has been shown to lead to cholesteric phases without any chemical interactions.¹⁴⁷ Milhaud and Michels describe the interactions of multilamellar vesicles formed from dilauryl-phosphatidylcholine (DLPC) with chiral polyene antibiotics amphotericin B (amB) and nystatin (Ny).¹⁴⁸ Even at low concentrations of antibiotic (molar ratio of DLPC to antibiotic >130) twisted ribbons are seen to form just as the CD signals start to strengthen. The results support the concept that chiral solutes can induce chiral order in these lyotropic liquid crystalline systems and are consistent with the observations for thermotropic liquid crystal systems. Clearly the lipid membrane can be chirally influenced by the addition of appropriate solutes.

Addition of the protein lysozyme to DC_{8,9}PC dispersions resulted in the formation of conical tubules in ethanol–water solution.¹⁴⁹ The scanning electron micrograph in Figure 5.37 shows that precipitate from this system is primarily composed of these cones, with a smaller number of cylinders. The cones exhibit more pronounced helical ridges on their exteriors than pure lipid cylinders, suggesting that protein selectively associates to the helical defects in a similar manner as the colloidal particles discussed above.

In an attempt to stabilize lipid tubules through photopolymerization, Singh and co-workers found that addition of short-chain lipid spacers to diacetylenic lipid tubules significantly enhances polymerization efficiency when the length of the acyl chains in the spacer lipid is matched to the number of methylenes in the upper segment (closer to the head group) of the diacetylenic acyl chains.¹⁵⁰ This is probably due to geometric considerations in the mixed-lipid bilayer, namely an increase in the average area to volume ratio of the lipids. Surprisingly, a gellike network of twisted fibers was found to form in an equimolar mixture of DC_{8,9}PC and dinonanoyl-phosphatidylcholine (DNPC).¹⁵¹ Further studies found that a new, nanotubular morphology consisting of cylinders with diameters around 50 nm preceded the formation of twisted ribbons.¹⁵²

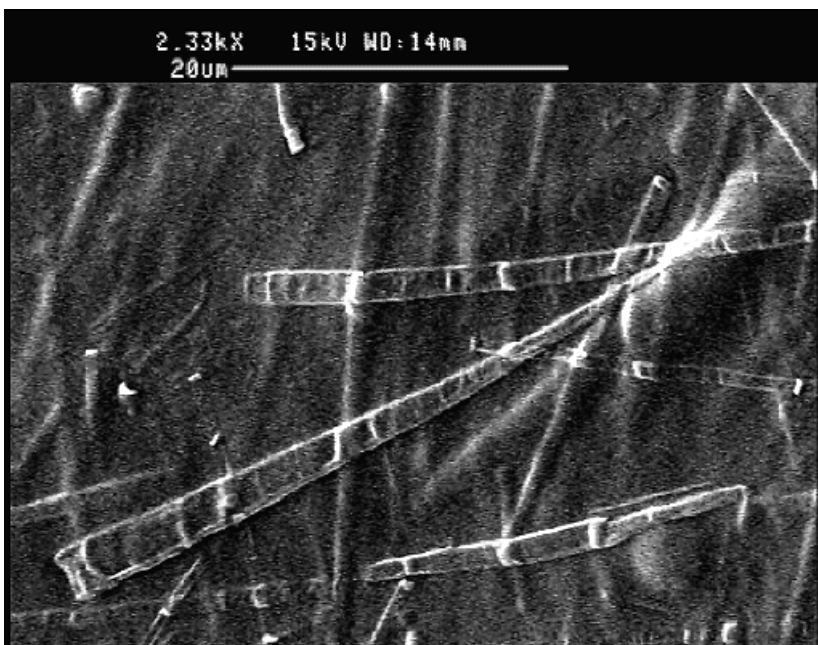
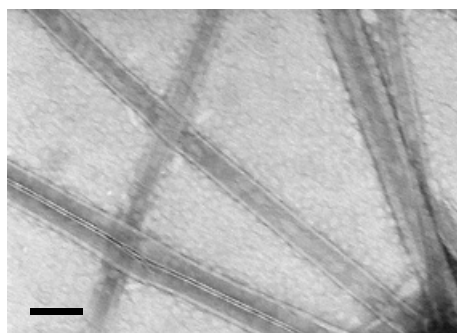


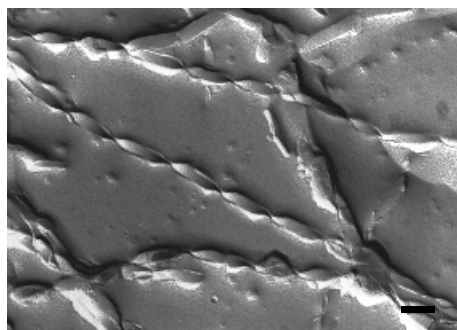
Figure 5.37 Scanning electron micrograph of phospholipid/protein cones lying atop dried bed of lysozyme-DC_{8,9}PC mixture. Reprinted with permission from Ref. 145. Copyright 2002 by the American Chemical Society.

Figure 5.38 shows electron micrographs of the nanotubes and ribbons in this system. While these nanotubes were transformed into the ribbon gel after a few hours at ambient temperature, they appeared to be stable at 4°C.

Circular dichroism spectroscopy suggests that chiral packing of the lipids drives both nanotubule and twisted-ribbon formation.¹⁵³ Nuclear magnetic resonance shows that the molecular composition remains unchanged during the transition between these morphologies, while CD indicates a significant change in molecular packing as shown in Figure 5.39. A large positive peak at 195 nm and a negative peak at 202 nm, as shown in the top panel of Figure 5.39, characterize the CD spectra of DC_{8,9}PC/DNPC nanotubules. This spectrum is indicative of a splitting in the $\pi-\pi^*$ excitation of the diacetylene moiety which usually shows a UV absorption at 198 nm.¹³¹ The bisignate nature of this peak reveals strong coupling of the electric transition moments of neighboring diacetylenic groups.⁷³ Such exciton coupling is not observed in the CD spectra of DC_{8,9}PC microtubules, as shown in Figure 5.28, which suggests tighter packing in the mixed-lipid nanotubules. In the twisted-ribbon phase, only one negative peak is observed at 198 nm (Figure 5.39, curve *e*). The loss



(a)



(b)

Figure 5.38 (a) Negative-stained transmission electron micrograph of nanotubes formed from equimolar mixture of DC_{8,9}PC and DNPC (2 mM total lipid concentration) stored at 4°C just prior to deposition. (b) Freeze-fracture electron micrograph of twisted ribbons at 27°C. Bars = 100 nm. Reprinted with permission from Ref. 153. Copyright 2001 by the American Chemical Society.

of exciton coupling at the transition temperature indicates a substantial change in the molecular packing of the twisted-ribbon phase. This is consistent with earlier calorimetric studies where a change in morphology from nanotubes to twisted ribbons was identified at 25.4°C.¹⁵²

5 RELATED CHIRAL SYSTEMS

5.1 Nucleotides

The well-known double-helical structure of DNA (deoxyribonucleic acid) is derived from the specificity of the Watson–Crick base pairing.¹⁵⁴ Yanagawa and co-workers first addressed the issue of whether mononucleotide units could be

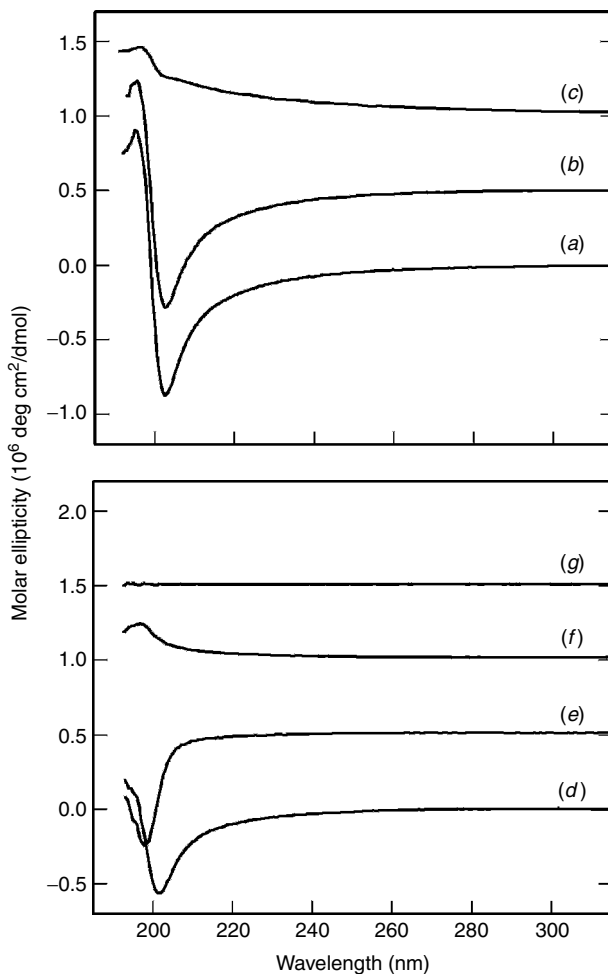


Figure 5.39 Circular dichroism spectra of equimolar mixture of DC_{8,9}PC and DNPC (2 mM total lipid concentration). Top panel: In nanotubule phase at (a) 4°C and (b) 20°C. (c) Also shown is spectra from pure DC_{8,9}PC microtubules in water at 20°C. Bottom panel: (d) In nanotubule phase at 25°C, (e) in twisted ribbon phase at 26°C, (f) in microtubule phase at 38°C, and (g) completely melted at 40°C. Curves have been offset vertically for display. Reprinted with permission from Ref. 153. Copyright 2001 by the American Chemical Society.

constructed that are capable of self-assembling into chiral aggregates similar to DNA structures.¹⁵⁵ They enzymatically synthesized phospholipid–nucleoside conjugates wherein the nucleotidyl residue is covalently linked to two acyl chains. Initial results on dimyristoyl-5'-phosphatidylcytidine (DMPC, **43a**) found the formation of linear helical strands at low KCl concentrations and

vesicular structures at higher concentrations ($>0.5 M$). Electron microscopy of dimyristoyl-5'-phosphatidyldeoxycytidine (**43b**) revealed that the helical duplex strands consisted of a duplex with approximately 110 Å diameter and 240 Å pitch which further formed a superhelical structure.¹⁵⁶ Double-duplex helices of the same dimensions were also observed. The authors propose that hydrophobic interactions between the nucleic acid base and the alkyl chain result in a bent conformation for the phospholipid–nucleoside conjugates in the helical aggregates. This is a common feature shared with the gluconamides and diacetylenic phospholipids previously discussed.

Tojima et al. continued this work with the synthesis and characterization of conjugates of all four nucleosides and variations of the chain length.¹⁵⁷ Neutral and alkaline solutions of dimyristoyl-5'-phosphatidyladenosine (DMPA, **44**) were also observed to form helical strands as shown in Figure 5.40. The CD spectrum of these aggregates was sensitive to aggregate morphology reflecting the chiral nature of the assembly. The efficiency of helix formation was found to decrease with decreasing chain length, with shorter chains forming extended tape structures. Acidic systems caused a dramatic change in morphology in aggregates of **44** to cigarlike scrolls consisting of many double-helical strands. Dimyristoyl-5'-phosphatidyluridine (DMPU, **45**) produced achiral, crystalline platelets in both alkaline and acidic pH. An equimolar mixture of DMPA and DMPU resulted in the formation of thick, helical ribbons which were not found in mixtures of DMPC and DMPA, suggesting complementary base pairing in the adenosine–uridine system. Bonaccio et al. found that using partially unsaturated chains in phosphatidyl-nucleosides resulted in the formation of nonchiral liposomes due to the depression of the melting temperature below ambient.¹⁵⁸ They also reported an interesting disk morphology in mixtures of cytidine and inosine phospholipids.

Recent studies of nucleobase bolaamphiphiles begin to shed some light on the role of chiral interactions in these systems and the subsequent formation of double helices. Shimizu et al. synthesized nucleobase-appended bolaamphiphiles in which thymine or adenine derivative is homoditopically or heteroditopically connected to both ends of an alkyl chain.¹⁵⁹ The bolaamphiphile T-10-T (**46**) produced fibrous assemblies shown in Figures 5.41*a–c* in 10% ethanol solutions after incubation for a few days, whereas A-10-A (**47**) formed only microcrystalline solids. The fibers were double-helical ropes 1–2 μm in width and several hundred micrometers long. Equimolar mixtures of T-10-T and A-10-A produced nanofibers 15–30 nm in width, rather than the helices, as shown in Figure 5.41*e*. The heteroditopic T-12-A (**48**) bolaamphiphile also formed supramolecular fibers (Figure 5.41*f*).

The double-helical rope formation in T-10-T was unexpected, since neither T-10-T nor its precursor thymine is chiral, as verified by CD spectroscopy. The authors speculate that photodimerization of two thymine derivatives leads

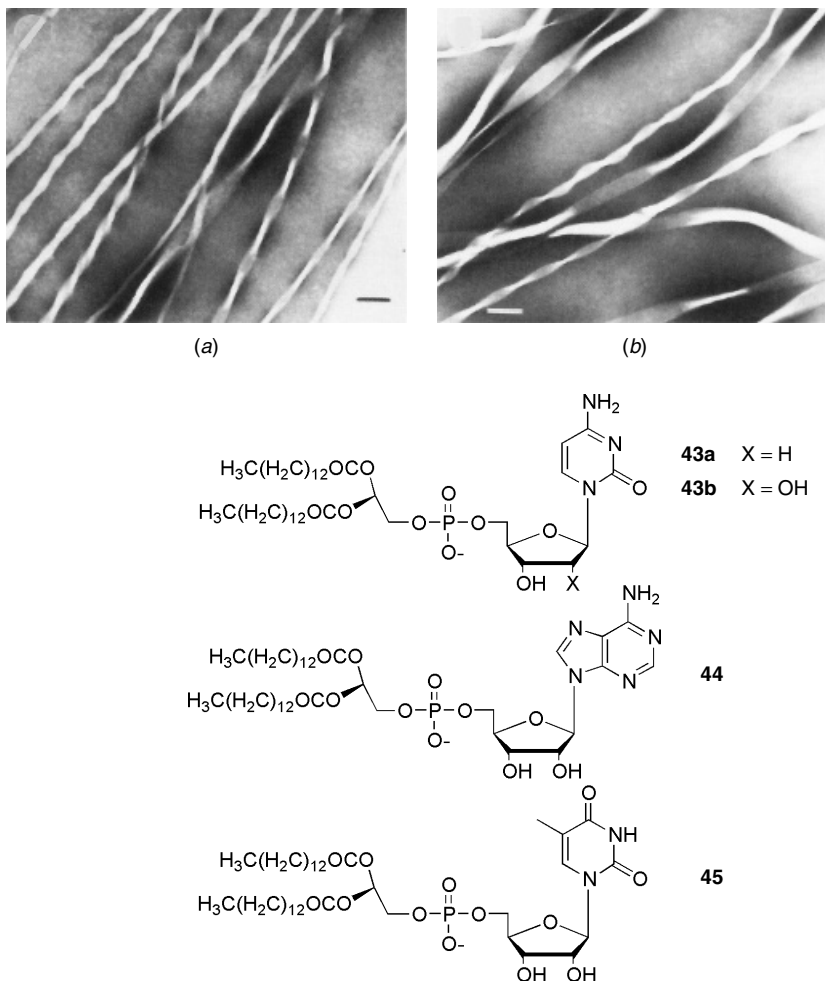


Figure 5.40 Electron micrographs of extended ribbon structure from DMPA (**44**) in 50 mM Tris-HCl buffer (pH 8.0): (a) after aging at 25°C and (b) gel of ribbons after aging at 25°C for 1 month. Bars = 0.1 μm . Reprinted with permission from Ref. 157. Copyright 1992 by the American Chemical Society.

to four stereoisomers, among which two are chiral, leading to helical aggregation. Indeed, both left- and right-handed double-helical ropes were present in approximately equal number. In the dark, the self-assembly of 10-T-10 produced no helical ropes. This hypothesis is also consistent with the observation in the case of the mixtures of T-10-T and A-10-T. The complementary base pairing of the thymine and adenine hinders the photodimerization discussed above, so no helices are formed.

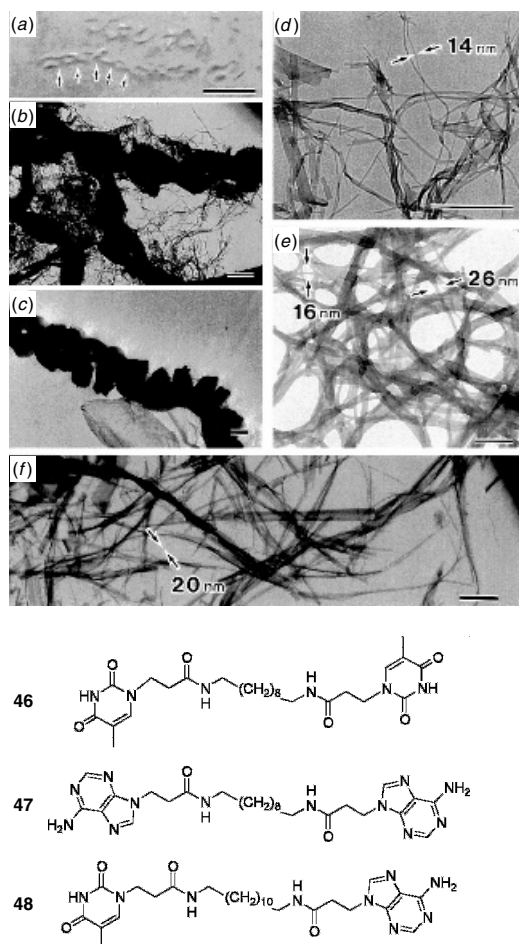


Figure 5.41 (a) Dark-field light micrograph of double-helical ropes formed from homoditopic bolaamphiphile T-10-T (**46**) at 25°C in 10% ethanolic–aqueous solutions (bar = 5 μm). Arrows denote representative interwoven portions of helical ropes. Electron micrographs of (b, c) double-helical ropes (bar = 1 μm), (d) nanofibers as constituent of helical ropes (bar = 5 μm), (e) nanofibers formed from equimolar mixture of T-10-T and A-10-A (**47**) (bar = 200 nm), and (f) nanofibers formed from heteroditopic T-12-A (**48**) (bar = 1 μm). Reprinted with permission from Ref. 159. Copyright 2001 by the American Chemical Society.

5.2 Steroid-Based Systems

Helical ribbons were found to be metastable intermediates in the process of cholesterol crystallization from bile in the gallbladder.¹⁶⁰ Since gallstones result from the formation of cholesterol monohydrate crystals in supersaturated

bile, Chung and co-workers explored the supramolecular aggregates formed in native and synthetic biles.¹⁶¹ The model biles consisted of a three-component mixture, a bile salt (e.g., sodium taurocholate), lecithin, and cholesterol, in a molar ratio of 97.5:0.8:1.7. It is important to note that all three components are chiral. The model systems initially formed micelles with mean radii 17 Å when initially solvated at high concentration (70 mg/ml). Upon dilution the system evolved through a number of metastable phases as shown in Figure 5.42. Within a few hours, filamentous structures formed followed by the appearance of helices, tubules, and platelike crystals within a few days. These helices had high pitch angles ($\sim 54^\circ$) and disappeared within weeks when low-pitch-angle ($\sim 11^\circ$) helices began to appear independently. All the helical structures were right handed. This behavior was observed in all model biles with unsaturated lecithin. In the absence of lecithin, only needlelike crystals are found.¹⁶⁰

In further studies, Zastavker et al. established that the formation of helical ribbons with two distinct pitch angles is a general phenomenon observed in a wide variety of multicomponent systems containing a sterol.¹⁶² High-pitch (54°) and low-pitch (11°) helices were observed in almost all of the

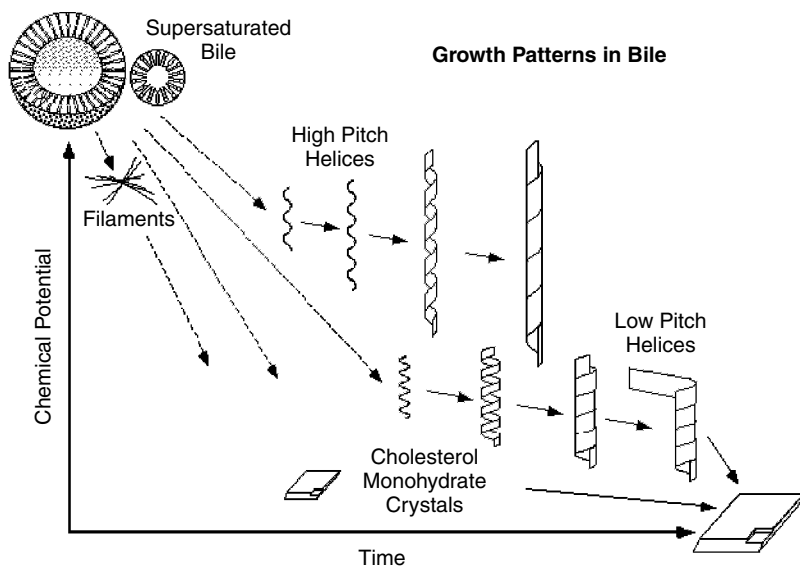


Figure 5.42 Sequence and relative stability in growth pattern of bile showing formation of metastable intermediates as function of time after supersaturation. Less stable structures have higher chemical potential. Solid and dotted arrows represent observed and presumed transitions, respectively. Reprinted with permission from Ref. 161. Copyright 1993 by the National Academy of Sciences, U.S.A.

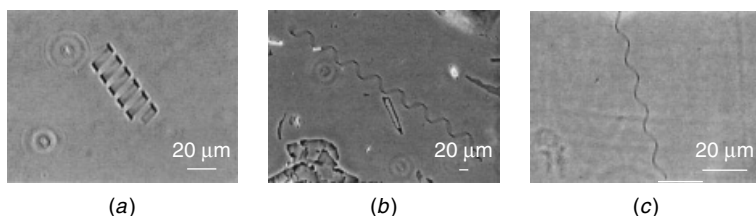


Figure 5.43 Phase contrast optical micrographs of typical helical structures in chemically defined lipid concentrate system. (a) Low-pitch helical ribbon with pitch angle $\psi = 11 \pm 2^\circ$. (b) High-pitch helical ribbons with pitch angle $\psi = 54 \pm 2^\circ$. (c) Intermediate-pitch helical ribbons with pitch angle $\psi = 40.8 \pm 3.8^\circ$. Reprinted with permission from Ref. 162. Copyright 1999 by the National Academy of Sciences, U.S.A.

systems studied, as shown in Figure 5.43. Most systems also produced small amounts of helices with intermediate pitch. Of note, in 7 of the 16 enantiomerically pure systems studied, both right- and left-handed helices were observed, although less than 5% of the total helical ribbons were left handed. In the cases where the only chiral component was cholesterol, all the helices were right handed. Neither the specific structure of lecithin and fatty acids nor the presence of charged groups on surfactant molecules seemed to affect helix formation. However, differences in the sterols did affect helix structure. In fact, the commercially available system, chemically defined lipid concentrate (CDLC), formed helical ribbons in high yields with good reproducibility, as seen in Figure 5.43.¹⁶²

Recent work by this group has focused upon elastic deformation of these helices and their response to uniaxial forces.¹⁶³ Under sufficient tension, a low-pitch helix reversibly separates into a straight domain with a pitch angle of 90° and a helical domain with a pitch angle of 16.5° , as shown in Figure 5.44.

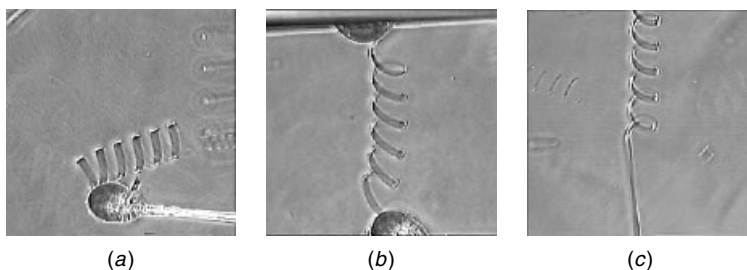


Figure 5.44 Elastic deformations of CDLC helices. (a) Low-pitch helix free from external force attached to glass rod at one end, (b) same helix attached at both ends and slightly extended, and (c) helix extended beyond 16.5° and allowed to come to equilibrium with respect to the straightening transition (helix ends are off screen). Reprinted from Ref. 163 with permission of the author. Copyright 2001 by the American Physical Society.

They developed a continuum elastic-free energy model that suggests these observations can be explained as a first-order mechanical phase transition. In other recent work on steroids, Terech and co-workers reported the formation of nanotubes in single-component solutions of the elementary bile steroid derivative lithocholic acid, at alkaline pH,¹⁶⁴ although these tubules do not show any chiral markings indicating helical aggregation.

5.3 Gemini Surfactants

A novel system wherein the chirality comes from the counterion to an ionic, achiral surfactant was investigated by Oda and co-workers.¹⁶⁵ The chirality in this system could be controlled by variations of the enantiomeric excess of the chiral counterion allowing for continuous variation in the pitch of the aggregates. Gemini surfactants consist of two identical cationic surfactants joined by a hydrocarbon spacer.¹⁶⁶ The cationic gemini surfactant ethylene-1,2-bis(cetyl-dimethylammonium) (**50**) with the chiral counterion *L*-tartrate (**49**) was found to form gels in both water and organic solvents.¹⁶⁷ These gels consisted of multilamellar twisted ribbons, shown in Figure 5.45c.

The twisted ribbons formed from **50** and *L*-tartrate were right handed, while those formed using *D*-tartrate as the counterion were left handed. When the two enantiomers were mixed, helices with continually varying pitch and width are formed, with the widest ribbons found in racemic mixtures having infinite pitch (Figure 5.45a).¹⁶⁵ This is the first example of using chiral counterions for control of supramolecular chirality. Changing the counterion to *L*-malate (**51**), with only one hydroxyl group, weakened the hydrogen bonding, resulting in the formation of flat, nonchiral membranes. Using *D*-glucarate (**52**) as the counterion also resulted in untwisted bilayers due to the spacing mismatch between the negative charges and the ethylene bridged gemini surfactant. Thus, the ability to form anisotropic structures appears directly linked to the dimeric character of the molecule. This implies long-range alignment of molecules through a hydrogen-bonding network of the tartrate counterions.¹⁶⁷

Furthermore, Oda et al. pointed out that there are two topologically distinct types of chiral bilayers, as shown in Figure 5.46.¹⁶⁵ Helical ribbons (helix A) have cylindrical curvature with an inner face and an outer face and are the precursors of tubules. These are, for example, the same structures that are observed in the diacetylenic lipid systems discussed in Section 4.1. By contrast, twisted ribbons (helix B) have Gaussian saddlelike curvature, with two equally curved faces and a *C*₂ symmetry axis. They are similar to the aldonamide and peptide ribbons discussed in Sections 2 and 3, respectively. The twisted ribbons in the tartrate-gemini surfactant system were found to be stable in water for alkyl chains with 14–16 carbons. Only micelles form

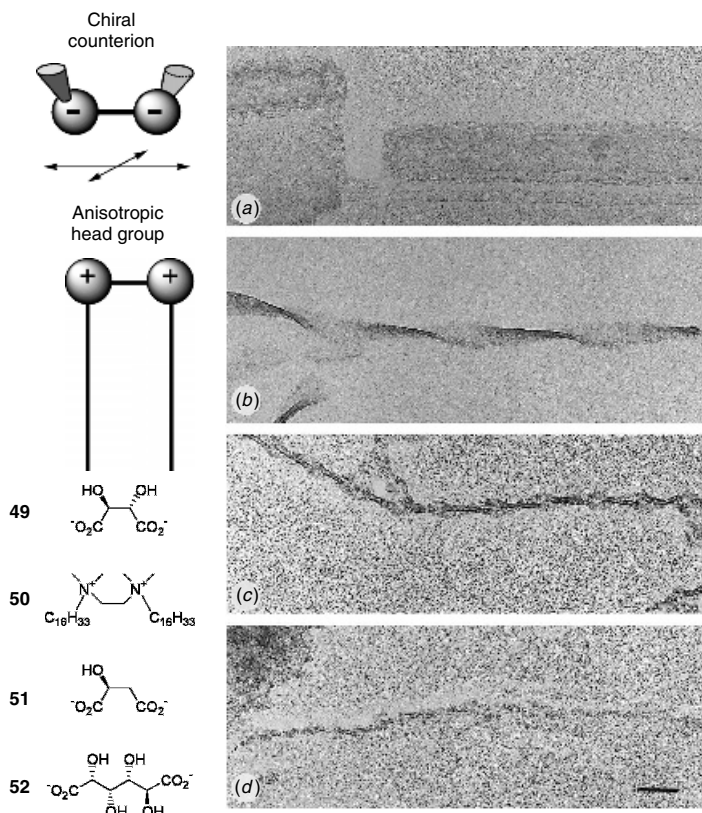


Figure 5.45 Cationic gemini amphiphiles having chiral counterions. TEM images of representative twisted ribbons formed by 16-2-16 tartrate (**49** + **50**) at 0.1% in water for various values of enantiomeric excess: (a) 0 (racemate); (b) 0.5; (c) 1 (pure L); (d) 1 (pure L) in presence of 1 eq sodium L-tartrate. Bar = 100 nm. Reprinted with permission from Ref. 165. Copyright 1999 by Macmillan Magazines.

in shorter chain surfactants and chains with 18 hydrocarbons lead to helical ribbons. They developed a model which suggests that more ordered (solid-like) membranes form helical ribbons while less ordered (fluid) membranes form twisted ribbons. The longer chain surfactants, with higher chain melting temperatures, are more highly ordered than shorter chains and, hence, form helical ribbons. This interpretation is consistent with IR and Raman experiments that show high chain ordering in DC_{8,9}PC, which indeed forms only helical ribbons and tubules.^{118,120} The details of this model will be discussed more in Section 6.5.

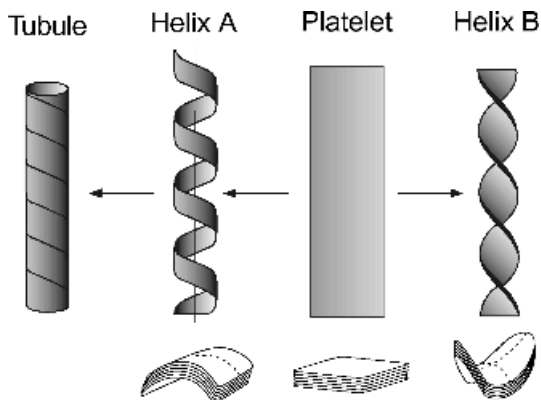


Figure 5.46 Schematic representation of helical and twisted ribbons as discussed in Ref. 165. Top: Platelet or flat ribbon. Helical ribbons (helix A), precursors of tubules, feature inner and outer faces. Twisted ribbons (helix B), formed by some gemini surfactant tartrate complexes, have equally curved faces and C₂ symmetry axis. Bottom: Consequences of cylindrical and saddlelike curvatures in multilayered structures. In stack of cylindrical sheets, contact area from one layer to next varies. This is not the case for saddlelike curvature, which is thus favored when the layers are coordinated. Reprinted with permission from Ref. 165. Copyright 1999 by Macmillan Magazines.

6 MODELS OF CHIRAL SELF-ASSEMBLY

The experiments discussed in this chapter have shown that a variety of chiral molecules self-assemble into cylindrical tubules and helical ribbons. These are indeed surprising structures because of their high curvature. One would normally expect the lowest energy state of a bilayer membrane to be flat or to have the minimum curvature needed to close off the edges of the membrane. By contrast, these structures have a high curvature, with a characteristic radius that depends on the material but is always fairly small compared with vesicles or other membrane structures. Thus, the key issue in understanding the formation of tubules and helical ribbons is how to explain the morphology with a characteristic radius.

To address this issue, several researchers have developed models of chiral self-assembly. In this section, we review these models. We begin with models based on nonchiral mechanisms and argue that they all have limitations in identifying a mechanism to select a particular tubule radius. We then discuss models based on the elastic properties of chiral membranes and argue that they provide a plausible approach to understanding the formation of tubules and helical ribbons. Most of this discussion was previously presented in our recent theoretical review article.¹³⁹

6.1 Nonchiral Models

In this section, we review models for the self-assembly of tubules and helical ribbons that are *not* based on chiral elastic properties. Our overall assessment is that these models have not been successful in explaining the characteristic length scale for the curvature of tubules and helical ribbons.

6.1.1 Electrostatics

The earliest approach to explain tubule formation was developed by de Gennes.¹⁶⁸ He pointed out that, in a bilayer membrane of chiral molecules in the $L_{\beta'}$ phase, symmetry allows the material to have a net electric dipole moment in the bilayer plane, like a chiral smectic- C liquid crystal.¹⁶⁹ In other words, the material is ferroelectric, with a spontaneous electrostatic polarization P per unit area in the bilayer plane, perpendicular to the axis of molecular tilt. (Note that this argument depends on the chirality of the molecules, but it does not depend on the chiral elastic properties of the membrane. For that reason, we discuss it in this section, rather than with the chiral elastic models in the following sections.)

De Gennes applied this electrostatic argument to predict the buckling of a bilayer membrane in solution. Consider a bilayer ribbon with length l and width w , as shown in Figure 5.47. The electrostatic polarization P gives a net separation of positive and negative charges across the width of the ribbon. Along one edge of the ribbon, there is a line with charge $\sigma = Pw$ per unit length, and along the opposite edge there is the opposite charge $-\sigma$. Because these opposite charges attract, they favor a buckling of the bilayer, which allows them to be closer together. If the bilayer buckles with a curvature radius $r \gg w$, the electrostatic energy decreases by

$$\frac{\Delta F_{\text{elec}}}{lw} = -\frac{\sigma^2 w}{12\epsilon r^2} \quad (1)$$

where ϵ is the dielectric constant of the solvent. However, this curvature costs a bending energy¹⁷⁰

$$\frac{\Delta F_{\text{bend}}}{lw} = \frac{\kappa}{2r^2} \quad (2)$$

where κ is the bending modulus of the membrane. Comparing these expressions shows that a flat ribbon becomes unstable to a buckling instability whenever $w > 6\epsilon\kappa/\sigma^2$. This crossover width sets a length scale of order micrometers for the resulting curved structure.

The electrostatic argument describes a situation that could occur in some bilayer systems. However, there are two problems with this argument as an

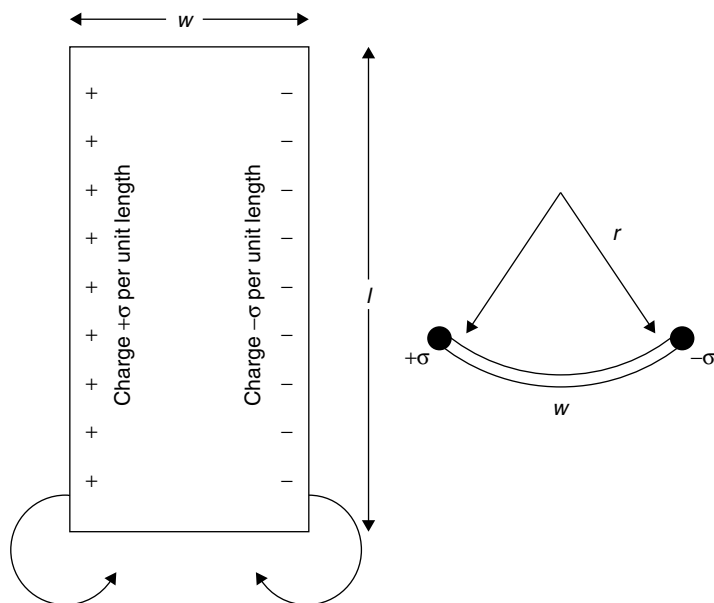


Figure 5.47 Electrostatic model for buckling of bilayer ribbon of length l and width w based on attraction between lines of charge on opposite edges.¹⁶⁸ Left: Side view. Right: Top view of curvature of ribbon. Reprinted with permission from Ref. 139. Copyright 2001 by the American Chemical Society.

explanation for the tubules that have been studied experimentally. First, it does not explain the helical markings that are often observed on tubules or the helical ribbons that are often precursors to tubule formation. Rather, it predicts buckling along the length of a narrow ribbon, presumably leading to a straight seam along the length of a tubule. This problem might be addressed by modifications of the electrostatic model.¹⁷¹ A more fundamental problem is that any electrostatic model predicts that tubule formation depends on interactions that can be screened by electrolytes in solution. Thus, it predicts that low concentrations of electrolytes should increase the tubule diameter and higher concentrations should suppress tubule formation. This prediction was tested experimentally for diacetylenic lipid tubules by Chappell and Yager.¹⁷² They found that adding electrolytes to the solution does not affect the formation or radius of the resulting tubules. Certain specific electrolytes had some effects on tubule wall thickness, but the general electrostatic effects predicted by the model were not observed. From this experiment, one can conclude that tubule formation is not primarily controlled by electrostatic interactions transmitted through the solvent. Rather, it must depend on some internal properties of the membrane.

6.1.2 Elasticity of Orientational Order

Another approach to explain tubule formation was taken by Lubensky and Prost as part of a general theoretical study of the relationship between orientational order and vesicle shape.¹⁷³ These authors note that a membrane in an $L_{\beta'}$ phase has orientational order within the membrane which is lacking in the L_{α} phase. The clearest source of orientational order is the tilt of the molecules with respect to the local membrane normal: The molecules select a particular tilt direction, and hence the local elastic properties of the membrane become anisotropic. A membrane might also have other types of orientational order. For example, if it is in a hexatic phase, it has order in the orientations of the intermolecular “bonds” (not chemical bonds but lines indicating the directions from one molecule to its nearest neighbors in the membrane).

Lubensky and Prost showed that any type of orientational order is coupled to the shape of the membrane, because certain shapes require topological point defects in the orientational order. For example, a sphere must have 2 defects of topological charge +1 in tilt order or 12 defects of charge $+\frac{1}{6}$ in hexatic bond orientational order. Because these topologically required defects cost elastic energy, they can change the relative energies of different membrane shapes. These considerations lead to a phase diagram in terms of various elastic constants, which shows the competition between several possible shapes: a flat sheet, a sphere with or without pores, a torus, and a cylinder. The cylinder is favored when the elastic constant for in-plane variations of the orientational order is large because the cylinder does not require such variations. This cylindrical regime was suggested as a possible explanation for tubule formation.

The main problem with this explanation for tubule formation arises from its prediction for the dimensions of the cylinder. In this model, the energy of a cylinder comes from two sources: the curvature of the entire membrane and the edge energy of the membrane edge exposed to the solvent. These mechanisms give

$$F = \frac{S\kappa}{2r^2} + 4\pi r\gamma \quad (3)$$

where $S = 2\pi rl$ is the cylinder's surface area and γ is the edge energy per unit length. Minimizing this expression over r for fixed S gives the cylinder radius and length

$$r = \left(\frac{S\kappa}{4\pi\gamma} \right)^{1/3} \quad \text{and} \quad l = \left(\frac{S^2\gamma}{2\pi^2\kappa} \right)^{1/3} \quad (4)$$

These expressions predict a scaling between radius and length: For an ensemble of cylinders containing different numbers of molecules and hence having

different surface area, the model predicts $r \propto l^{1/2}$. This scaling is not observed in any of the experimental systems discussed in this chapter. Rather, those systems all show tubules with a particular radius that is highly monodisperse, independent of the cylinder length, which is quite polydisperse. Thus, there must be some mechanism to select a particular cylinder radius, which is not included in this model.

6.1.3 Spontaneous Curvature

A further attempt to explain tubule formation without reference to chirality was made by Chen.¹⁷⁴ His model is based on a particular kinetic pathway for tubule formation. In this scenario, lipid molecules initially self-assemble out of solution into spherical vesicles in the high-temperature L_α phase. Once they are in spherical vesicles, the molecules redistribute between the inner and outer monolayers of the bilayer membrane, with more lipid going into the outer monolayer. The redistribution breaks the bilayer symmetry and gives the membrane a spontaneous curvature. In other words, the curvature free-energy density becomes $\frac{1}{2}\kappa(c - c_0)^2$, where c is the mean curvature ($2/r_{\text{sph}}$ for a sphere, $1/r_{\text{cyl}}$ for a cylinder) and c_0 is the spontaneous curvature. The favored value of c_0 is $2/r_{\text{ves}}$, where r_{ves} is the radius of the particular spherical vesicle. When the vesicle is cooled to the low-temperature L_β' phase, with orientational order in the membrane, the membrane rigidity becomes anisotropic—it becomes harder to bend the membrane along the tilt direction than normal to the tilt direction. In order to reduce the free energy, the membrane distorts from a spherical vesicle into a cylindrical tubule. To keep the same spontaneous curvature, the tubule radius must be half of the spherical vesicle radius.

One problem with this argument is that it assumes tubules are nonequilibrium structures which only form through a particular kinetic pathway, that is, out of preexisting spherical vesicles. This is not the case experimentally. Tubules are sometimes formed by cooling spherical vesicles, but they can also be formed directly from dissolved lipid in an isothermal process. A further problem is that this argument predicts that tubules form with half the radius of the preexisting spherical vesicles. Experimentally, the radius of tubules is normally much smaller than the radius of spherical vesicles, and the radius of tubules is monodisperse while the radius of spherical vesicles is polydisperse. Moreover, if a single tubule forms out of a single vesicle, with half the radius of the vesicle, then the tubule length must be just eight times the tubule radius in order to conserve lipid. Experimentally, the tubule length is always much greater than the tubule radius. (Of course, vesicles might merge to form longer tubules, but if they can merge, then it is not clear that they should keep the same spontaneous curvature.) Finally, this argument does not really explain

the radius of tubules; it only changes the problem of predicting the radius of tubules into a problem of predicting the radius of spherical vesicles. Thus, like the model in the previous section, this model is missing a mechanism to select a particular tubule radius.

More recently, Smith et al. have developed another model based on spontaneous curvature.¹⁶³ Their analysis is motivated by a remarkable experimental study of the elastic properties of individual helical ribbons formed in model bile. As mentioned in Section 5.2, they measure the change in pitch angle and radius for helical ribbons stretched between a rigid rod and a movable cantilever. They find that the results are inconsistent with the following set of three assumptions: (a) The helix is in equilibrium, so that the number of helical turns between the contacts is free to relax. (b) The tilt direction is uniform, as will be discussed below in Section 6.3. (c) The free energy is given by the chiral model of Eq. (5). For that reason, they eliminate assumption (c) and consider an alternative model in which the curvature is favored not by a chiral asymmetry but by an asymmetry between the two sides of the bilayer membrane, that is, by a spontaneous curvature of the bilayer. With this assumption, they are able to explain the measurements of elastic properties.

Although this modified assumption explains the elastic measurements, it leads to other questions. First, the origin of the spontaneous curvature is not clear. Smith et al. speculate that it arises from a difference in surface tension of fatty acids coating the two sides of the membrane but do not explain why this coating should be asymmetrical. That issue is important because it is the fundamental mechanism that leads to curvature and determines the radius of helical ribbons. Second, because this modified assumption does not involve chirality, it predicts equal free energies for right- and left-handed ribbons. Hence, contrary to the statement of Smith et al., the model does not explain the experimental observation that only right-handed ribbons form in this model bile. For those reasons, we think there are still unresolved issues in understanding these experiments. Future work should reexamine assumption (a) to consider the possibility that the number of helical turns is out of equilibrium and assumption (b) to investigate whether a tilt modulation changes the elastic properties of helical ribbons (as will be discussed below in Section 6.4). Through this work, it may be possible to reconcile the measurements of elastic properties with the chiral models presented below.

6.2 Chiral Models: Molecular Approach

The basic concept behind all models of chiral self-assembly can be stated as follows. In general, chiral molecules do not pack parallel to their neighbors but rather pack at a slight angle with respect to their neighbors. This favored packing can be visualized by the packing of hard screws,⁶ as illustrated in

Figure 5.1, although the details can be more subtle.^{13,175} It can arise from repulsive interactions (such as steric forces), attractive interactions (such as hydrogen bonding), or a combination thereof. As a result, chirality favors a twist in the orientation of the molecules, with a characteristic chiral length scale $2\pi/q$, where q is the angle between the orientations of neighboring molecules divided by the distance between their centers of mass. In liquid crystals, this chiral packing gives the cholesteric phase and other, more complex modulated phases.¹⁷⁶ In our present context of self-assembled structures in solution, chiral molecules form bilayer membranes and have some favored tilt with respect to the local membrane normal. The only way for molecules to twist with respect to their neighbors is for the entire membrane to twist. Hence, the chiral packing of molecules favors a twist of the membrane with a characteristic length scale. This chiral length scale can select a radius for tubules and helical ribbons.

To transform this intuitive argument into a quantitative theory, there are two fundamentally distinct steps. First, on a microscopic length scale, one must model how chiral molecules pack together to form a chiral membrane with certain elastic constants. This modeling begins with the shape and chemical structure of the molecules and ends with numerical values of the elastic constants that describe the membrane. Second, on a more macroscopic length scale, one must calculate how the membrane bends to form a tubule, helical ribbon, or other structure. This calculation begins with a continuum elastic free energy expressed in terms of the membrane elastic constants and ends with a prediction for the morphology. Note that the first step depends on the details of molecular structure, while the second step concentrates on the longer length scale degrees of freedom that are relevant in all membranes.

So far, there has only been limited progress toward microscopic modeling of chiral aggregates. In particular, a model for the packing of chiral amphiphilic molecules has been developed by Nandi and Bagchi.^{177,178} In this model, they regard each molecule as a single chiral carbon bonded to four inequivalent groups. Hence, they represent the molecule as a distorted tetrahedron consisting of four inequivalent spheres. The size of each sphere depends on the space-filling volume of the actual chemical group. The model molecules interact through an effective pair potential derived from the sum of Lennard–Jones interactions between the spheres. The authors minimize this effective pair potential to find the most efficient packing of the molecules. They present this calculation for two specific examples of chiral amphiphiles as well as their enantiomers. This calculation shows explicitly that the molecules of the same handedness pack at an angle with respect to their neighbors, leading to the formation of a helical aggregate. Furthermore, the calculation gives the geometric parameters of the aggregate, including the radius and the helical sense, and these are consistent with experiments on the same amphiphiles.

The work of Nandi and Bagchi is an important step toward the goal of deriving properties of self-assembled aggregates from the chiral structure of the molecules. We do not see any problems with their calculations or with the comparison between theory and experiment that they have achieved for certain amphiphiles. However, their model seems too simple to predict the properties of large-scale aggregates in the wide range of systems that form tubules. Representing the molecules by distorted tetrahedra is a very drastic approximation, because most amphiphilic molecules have an elongated structure that is quite different from a tetrahedron. Neglecting thermal fluctuations in the orientation of the molecules is another drastic approximation, because such fluctuations are known to have a large effect on chiral packing of liquid crystals.^{13,175} Thus, we believe there is much more work to do in this area.

Another model for the self-assembly of chiral molecules into helical aggregates has been developed by Nyrkova and co-workers.^{108,109} This model is expressed on a somewhat larger length scale than the work of Nandi and Bagchi. While Nandi and Bagchi begin with assumptions about the chemical structure of molecules, Nyrkova et al. begin with geometric parameters that characterize the favored packing of neighboring chiral molecules. From these geometric parameters, they calculate the optimum radius of tapes and higher order helical aggregates. This is a reasonable approach for molecular modeling, but we emphasize that more work needs to be done in this area. First, the relationship between the chemical structure of the molecules and the geometric packing parameters should be elucidated, at least for some sample molecules. Furthermore, the role of thermal fluctuations should be clarified for this model, because thermal fluctuations may again change the geometric packing parameters.

Because of the difficulty of microscopic modeling, most theoretical research on tubule formation has focused on the more macroscopic issue of calculating the structures formed by a chiral membrane. The earliest model was proposed by Helfrich, who argued that chirality leads to a spontaneous torsion of the edges of a ribbon, giving the ribbon a helical shape.¹⁷⁹ Soon thereafter, this model was extended by Helfrich and Prost, who showed that there is an intrinsic bending force in any bilayer membrane of chiral molecules with tilt order.¹⁸⁰ Subsequently, other investigators developed more detailed models that extend this approach in different ways. In the following sections, we review these models, present the similarities and differences among them, and discuss the theoretical considerations that are involved in each.

6.3 Continuum Elastic Theory: Membranes with Uniform Tilt Direction

The simplest model of tubule formation based on chiral elastic properties was developed by Helfrich and Prost.¹⁸⁰ They considered the elastic free energy of

a bilayer membrane of chiral molecules with orientational order in the molecular tilt. In a cylindrical geometry, the curvature is just $1/r$, and the orientation of the molecular tilt is represented by the unit vector $\mathbf{m} = (\cos \phi, \sin \phi)$. As shown in Figure 5.48, \mathbf{m} is the projection of the three-dimensional molecular director \mathbf{n} into the local tangent plane normalized to unit magnitude. The Helfrich–Prost model considers the case in which \mathbf{m} is uniform. The lowest order elastic free energy for membranes with cylindrical curvature can then be written as

$$F = \int dS \left[\frac{1}{2} \kappa \left(\frac{1}{r} \right)^2 - \lambda_{\text{HP}} \left(\frac{1}{r} \right) \sin \phi \cos \phi \right] \quad (5)$$

The first term in this free energy is the standard isotropic curvature rigidity. The second term is a chiral term with coefficient λ_{HP} , which can exist only in chiral membranes and is prohibited by reflection symmetry in nonchiral membranes. This term favors curvature in a direction 45° from \mathbf{m} . Thus, it gives an intrinsic bending force in any membrane with both chirality and tilt order.

To find the optimum tubule structure, Helfrich and Prost minimized the free energy over the radius r and the tilt direction ϕ . This minimization

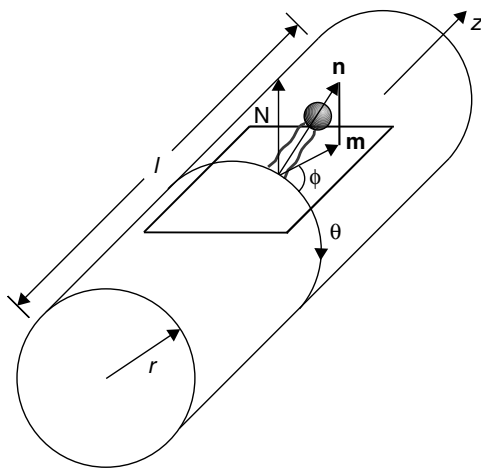


Figure 5.48 Geometry discussed in Section 6.3 for tubule formation based on chiral elastic properties. Here, r is tubule radius, l is tubule length, \mathbf{n} is molecular director, \mathbf{m} is projection of \mathbf{n} into local tangent plane (normalized to unit magnitude), ϕ is angle in tangent plane between \mathbf{m} and curvature direction (equator running around cylinder), and \mathbf{N} is local normal vector. Adapted from Ref. 132 with permission of the author. Copyright 1996 by the American Physical Society.

gives explicitly

$$r = \frac{2\kappa}{\lambda_{\text{HP}}} \quad \text{and} \quad \phi = \pm 45^\circ \quad (6)$$

with the favored sign of ϕ determined by the sign of λ_{HP} . From those results, we can draw three conclusions. First, the chiral mechanism selects a particular optimum radius for the tubules. Second, the optimum radius scales inversely with the chiral coefficient λ_{HP} and diverges in the nonchiral limit $\lambda_{\text{HP}} \rightarrow 0$. This shows explicitly that chirality is essential in this model for tubule formation. Third, the optimum structure has the tilt oriented at an angle $\phi = \pm 45^\circ$ from the curvature direction (the equator of the cylinder), as shown in Figure 5.49. This result is reasonable, because the tubule structure would have

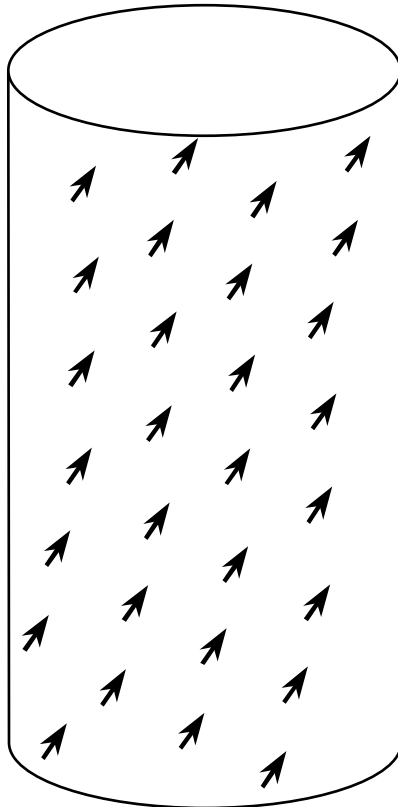


Figure 5.49 Schematic view of tubule with uniform tilt direction $\mathbf{m} = (\cos \phi, \sin \phi)$, as indicated by arrows. Adapted from Ref. 132 with permission of the author. Copyright 1996 by the American Physical Society.

a reflection symmetry if the tilt direction were at either $\phi = 0^\circ$ or $\phi = \pm 90^\circ$. The intermediate orientation of $\phi = 45^\circ$ gives the maximally chiral state, and $\phi = -45^\circ$ gives the mirror image.

The Helfrich–Prost model was extended in a pair of papers by Ou-Yang and Liu.^{181,182} These authors draw an explicit analogy between tilted chiral lipid bilayers and cholesteric liquid crystals. The main significance of this analogy is that the two-dimensional membrane elastic constants of Eq. (5) can be interpreted in terms of the three-dimensional Frank constants of a liquid crystal. In particular, the λ_{HP} term that favors membrane twist in Eq. (5) corresponds to the term in the Frank free energy that favors a helical pitch in a cholesteric liquid crystal. Consistent with this analogy, the authors point out that the typical radius of lipid tubules and helical ribbons is similar to the typical pitch of cholesteric liquid crystals. In addition, they use the three-dimensional liquid crystal approach to derive the structure of helical ribbons in mathematical detail. Their results are consistent with the three conclusions from the Helfrich–Prost model outlined above.

Before moving on, we should discuss two issues related to the models in this section. The first issue is the scaling of the chiral elastic constant λ_{HP} . Even without a detailed molecular model of a membrane, we can make two statements about λ_{HP} purely on the basis of symmetry. First, if we replace all molecules in a system by their enantiomers, then the entire membrane transforms into its mirror image, and λ_{HP} must change sign. Hence, the tubule radius r remains the same but the tilt orientation ϕ is reversed, giving the mirror image tubule structure. Second, because λ_{HP} depends on the chiral order of the membrane, we should be able to reduce it by diluting chiral effects. If chiral molecules are mixed with their enantiomers, λ_{HP} should scale linearly with the enantiomeric excess *for small enantiomeric excess*. If chiral molecules are mixed with analogous achiral molecules, λ_{HP} should scale linearly with the chiral fraction *for small chiral fraction*. (This point was first made explicitly by Nelson and Powers^{183,184} in work discussed below but it is implicit in the earlier studies.) Thus, both of the models presented so far predict that the tubule radius should scale inversely with enantiomeric excess in a mixture of enantiomers or inversely with chiral fraction in a chiral–achiral mixture. However, there could be exceptions to this scaling if the molecules phase separate or if the system undergoes spontaneous chiral symmetry-breaking, as discussed below.

The second issue concerns the anisotropy of the membrane. The models presented in this section all assume that the membrane has the symmetry of a chiral smectic-*C* liquid crystal, so that the only anisotropy in the membrane plane comes from the direction of the molecular tilt. With this assumption, the membrane has a twofold rotational symmetry about an axis in the membrane plane, perpendicular to the tilt direction. It is possible that a membrane

might have a different source of anisotropy other than molecular tilt. For example, Chappell and Yager developed a scenario in which the direction of one-dimensional chains of molecules defines a favored orientation within the membrane.¹⁸⁵ The direction of these one-dimensional chains, or any other vector order parameter, can play the role of molecular tilt in the theoretical calculations presented above. The predictions for ϕ would then give the favored direction of the chains rather than the favored orientation of molecular tilt.

It is also possible that a membrane might have an even lower symmetry than a chiral smectic-*C* liquid crystal; in particular, it might lose the twofold rotational symmetry. This would occur if the molecular tilt defines one orientation in the membrane plane and the direction of one-dimensional chains defines *another* orientation. In that case, the free energy would take a form similar to Eq. (5) but with additional elastic constants favoring curvature. The argument for tubule formation presented above would still apply, but it would become more mathematically complex because of the extra elastic constants. As an approximation, we can suppose that there is one principal direction of elastic anisotropy, with some slight perturbations about the ideal twofold symmetry. In that approximation, we can use the results presented above, with ϕ representing the orientation of the principal elastic anisotropy.

6.4 Membranes with Variations in Tilt Direction

Some researchers have generalized the model for tubule structure by eliminating the assumption that the tilt direction is uniform everywhere on the tubule and allowing it to vary. The earliest model with tilt variations was developed by Nelson and Powers, who considered thermal fluctuations in the tilt direction.^{183,184} They generalized the free energy of Eq. (5) to include terms giving the energy cost of variations in the tilt direction as well as the energy cost of membrane curvature. Their free energy includes a very large number of terms allowed by symmetry, and we will not reproduce it here. They then performed a renormalization-group calculation to determine how the effective coefficients of these terms evolve as the length scale increases. This calculation is mathematically analogous to calculations in string theory. The main conclusion from the renormalization-group calculation is that the effective chiral elastic constant λ_{HP} on the length scale L evolves as a power law,

$$\lambda_{\text{HP,eff}}(L) = \lambda_{\text{HP}} \left(\frac{L}{L_0} \right)^{-k_B T / 4\pi\kappa_{\text{eff}}} \quad (7)$$

where L_0 is the molecular length scale. Note that the exponent of this power law is a nonuniversal function of temperature T and membrane rigidity κ and that this exponent vanishes in the limit $T \rightarrow 0$ when thermal fluctuations are

suppressed. Using this result on the length scale of the tubule radius r implies that $r = 2\kappa_{\text{eff}}(r)/\lambda_{\text{HP,eff}}(r)$, and hence

$$r \propto (\lambda_{\text{HP}})^{-(1+k_B T/4\pi\kappa_{\text{eff}})} \quad (8)$$

Thus, the model predicts that thermal fluctuations in the tilt and curvature change the way that the tubule radius scales with chiral elastic constant—instead of $r \propto (\lambda_{\text{HP}})^{-1}$, the scaling has an anomalous, temperature-dependent exponent. This anomalous exponent might be detectable in the scaling of tubule radius as a function of enantiomeric excess in a mixture of enantiomers or as a function of chiral fraction in a chiral–achiral mixture.

A very different model of tubules with tilt variations was developed by Selinger et al.^{132,186} Instead of thermal fluctuations, these authors consider the possibility of systematic modulations in the molecular tilt direction. The concept of systematic modulations in tubules is motivated by modulated structures in chiral liquid crystals. Bulk chiral liquid crystals form cholesteric phases, with a helical twist in the molecular director, and thin films of chiral smectic- C liquid crystals form striped phases, with periodic arrays of defect lines.¹⁷⁶ To determine whether tubules can form analogous structures, these authors generalize the free-energy of Eq. (5) to consider the expression

$$F = \int dS \left[\frac{1}{2}\kappa \left(\frac{1}{r}\right)^2 + \frac{1}{2}\kappa' \left(\frac{1}{r}\right)^2 \cos^2 \phi - \lambda_{\text{HP}} \left(\frac{1}{r}\right) \sin \phi \cos \phi - \lambda_{\text{LS}} \mathbf{N} \cdot \nabla \times \mathbf{m} + \gamma \left(\frac{1}{r}\right) \nabla \cdot \mathbf{m} + \frac{1}{2}c[(\mathbf{N} \cdot \nabla \times \mathbf{m})^2 + (\nabla \cdot \mathbf{m})^2] \right] \quad (9)$$

This expression does not contain a complete list of the terms permitted by symmetry but rather includes terms that generate distinct physical effects: κ gives the isotropic rigidity of the membrane, κ' gives the anisotropy of the rigidity, λ_{HP} is the chiral term favoring curvature, λ_{LS} is another chiral term favoring bend of the director \mathbf{m} (as in liquid crystal films¹⁷⁶), γ is a coupling between curvature and splay of \mathbf{m} , and c is the two-dimensional Frank free-energy cost of variations in \mathbf{m} . The authors then minimize this expression to determine the optimal tubule radius r and the optimal configuration of the molecular tilt.

This calculation shows that molecular chirality has two effects: It favors formation of cylinders with a radius scaling as $r \propto (\lambda_{\text{HP}})^{-1}$, and it favors the formation of a striped modulation in the molecular tilt direction. The

stripes wind around the tubule in a helical fashion, as shown in Figure 5.50, and they are separated by sharp defect lines. Furthermore, the modulation in the molecular tilt induces a higher order modulation in the curvature, thus giving ripples that wind around the tubule, also shown in Figure 5.50. This modulation is stable as long as the free-energy gain from the λ_{LS} and γ terms exceeds the free-energy cost of the defect lines; for smaller values of λ_{LS} and γ the uniform state of Figure 5.49 is favored.

The authors draw three conclusions from this calculation. First, the lowest free-energy state of tubules can have a helically modulated structure, with alternating stripes and defect lines. This structure provides a possible explanation of the helical markings that are often seen in electron micrographs of tubules. Second, the same mechanism that stabilizes the striped pattern can also stabilize helical ribbons, with a modulation in the tilt direction across the width of a ribbon. Thus, helical ribbons can be stable structures for some range of the energetic parameters. Third, the pitch angle of the helical stripes can be calculated in this model, and it is different from the average tilt direction ϕ .

This model for the modulated state of tubules leads to an interesting speculation on the kinetic evolution of flat membranes or large spherical vesicles into tubules.^{68,132} In this scenario, when a flat membrane or large spherical

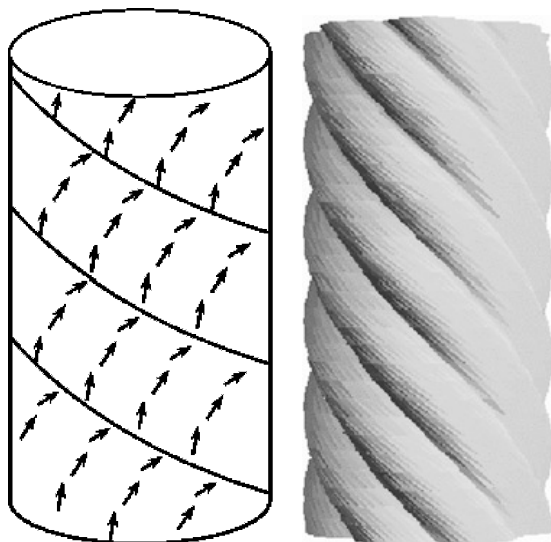


Figure 5.50 Schematic view of modulated state of tubule. Left: Modulation in direction of molecular tilt, as indicated by arrows. Right: Ripples in tubule curvature (greatly exaggerated for clarity). Adapted from Ref. 132 with permission of the author. Copyright 1996 by the American Physical Society.

vesicle is cooled from an untilted phase into a tilted phase, it develops tilt order. Because of the chirality, the tilt order forms a series of stripes separated by domain walls, as shown in Figure 5.51*a*. The domain walls are weak lines in the membrane, and the membrane can fall apart along these lines, leading to a series of narrow ribbons. These ribbons are free to twist in solution to form helices, as shown in Figure 5.51*b*. These helices may remain as stable helical ribbons or, alternatively, may grow wider to form tubules, as shown in Figure 5.51*c*. This mechanism might be called “molecular disassembly and reassembly.”

The concept of systematic modulations in the tilt direction was developed into a more detailed model of helical ribbons in steroid-based systems by Komura and Ou-Yang.¹⁸⁷ They argue that helical ribbons should have a boundary condition that the tilt direction is aligned with the ribbon edges. This boundary condition implies that there should be two types of ribbons: ribbons with the tilt pointing in the same direction along the two ribbon edges (“parallel packing”) and ribbons with the tilt pointing in opposite directions along the two edges (“antiparallel packing”). The parallel ribbons have a uniform tilt direction across the width of the ribbon, but the antiparallel ribbons have a variation in the tilt direction that can be derived by minimizing the elastic free energy. Komura and Ou-Yang show that this scenario leads to structures consistent with the observed helical ribbons in bile, discussed in Section 5.2. The parallel ribbons correspond to the structures with a pitch angle of 54° and the antiparallel ribbons to the structures with a pitch angle of 11° . (More recent

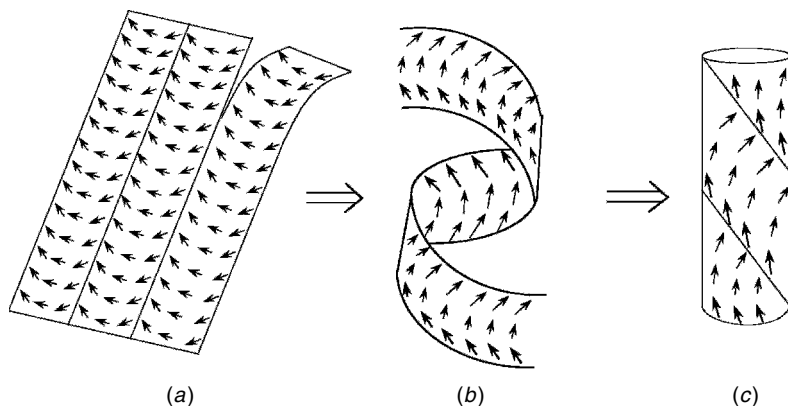


Figure 5.51 Scenario for kinetic evolution of flat membranes into tubules.^{68,132} (a) When membrane is cooled into tilted phase, it develops stripes in tilt direction and then breaks up along domain walls to form ribbons. (b) Each ribbon twists in solution to form helix. (c) Helical ribbon may remain stable or may grow wider to form tubule. Reprinted with permission from Ref. 139. Copyright 2001 by the American Chemical Society.

experiments also find rarer structures with intermediate pitch angles.¹⁶² They might correspond to more unusual situations in which the boundary condition is violated.)

To discuss the models in this section, we should mention two issues. First, the models assume the membrane is sufficiently soft that the tilt direction can vary with an energy cost that scales as $(\nabla\phi)^2$. This is appropriate if the membrane is in a fluid phase like a smectic-*C* liquid crystal, with order in the tilt direction but not in the positions of the molecules. It is also appropriate if the membrane is in a tilted hexatic phase, with order in the orientations of the intermolecular “bonds” as well as the tilt. However, this assumption is not appropriate if the membrane is in a crystalline phase, because the tilt direction would be locked to the crystalline axes, and varying it would cost more energy than $(\nabla\phi)^2$.

The assumption of membrane softness is supported by a theoretical argument of Nelson et al., who showed that a flexible membrane cannot have crystalline order in thermal equilibrium at nonzero temperature, because thermal fluctuations induce dislocations, which destroy this order on long length scales.^{188,189} The assumption is also supported by two types of experimental evidence for diacetylenic lipid tubules. First, Treanor and Pace found a distinct fluid character in NMR and electron spin resonance experiments on lipid tubules.¹⁹⁰ Second, Brandow et al. found that tubule membranes can flow to seal up cuts from an atomic force microscope tip, suggesting that the membrane has no shear modulus on experimental time scales.¹⁹¹ However, conflicting evidence comes from X-ray and electron diffraction experiments on diacetylenic lipid tubules. These experiments found sharp diffraction peaks, which indicate crystalline order in tubule membranes, at least over the length scales probed by the diffraction techniques.^{123,192,193}

It is possible that some membranes might be either fluid or hexatic, while others might have crystalline order over the relevant experimental length and time scales, with the Nelson et al. argument applying only on length scales that are much larger than a tubule. In the latter case, the models for variations in the tilt direction would need to be modified to take into account the locking of the tilt direction to the crystalline axes. One possible consequence is that the resulting tubules would simply have a uniform tilt direction, as discussed in the previous section. Alternatively, they might have grain boundaries in which the tilt direction jumps from alignment along one crystalline axis to alignment along another axis.

The second issue is simply that the models in this section have never been fully unified. As discussed above, the model of Nelson and Powers considers thermal fluctuations in the curvature and the tilt direction about a uniform state but neglects the possibility of systematic modulations. By comparison, the models of Selinger et al. and Komura and Ou-Yang consider systematic

modulations in the lowest free-energy state of tubules but do not consider thermal fluctuations. It would be very interesting to see a model that combines these features by considering thermal fluctuations about the modulated state. This calculation remains to be done.

6.5 Cylindrical Versus Gaussian Curvature

In the preceding sections, we have investigated how chirality can favor the formation of cylindrical tubules and helical ribbons, which are both high-curvature structures, compared with low-curvature structures like flat membranes or large spherical vesicles. One can also ask: Among all possible high-curvature structures, are tubules and helical ribbons the most favored? Or would chiral membranes prefer to form twisted ribbons with Gaussian curvature? The distinction between helical ribbons and twisted ribbons is shown in Figure 5.46. Helical ribbons have cylindrical curvature (mean curvature in the terminology of differential geometry) and can be precursors of tubules. By comparison, twisted ribbons have Gaussian or saddlelike curvature.

The competition between cylindrical and Gaussian curvature has been addressed in recent work by Oda et al.,¹⁶⁵ which we discussed in Section 5.3. In the experimental part of their study, these authors investigate charged gemini surfactants with chiral counterions and find that these molecules can aggregate into either helical or twisted ribbons. Helical ribbons are favored for long-chain surfactants (which should form an ordered membrane phase), while twisted ribbons are favored for shorter chain surfactants (which should form a more disordered membrane phase). Similarly, Spector et al. found that mixed bilayers of saturated and diacetylenic phospholipids undergo a transition from twisted ribbons to cylindrical tubules, as discussed in Section 4.3.¹⁵³ To explain these observations, Oda et al.¹⁶⁵ extend the Helfrich–Prost model of Eq. (5) to include the possibility of Gaussian rather than cylindrical curvature. Their calculations show that, for a membrane in a fluid phase, a twisted ribbon always has a lower free energy than a helical ribbon. In their model, the only way to stabilize a helical ribbon is to have crystalline order in a membrane, because crystalline order is incompatible with Gaussian curvature.¹⁸⁸ Thus, they conclude that twisted ribbons are associated with fluid membranes and helical ribbons with crystalline membranes—not only in gemini surfactants but generally for all chiral membranes.

The argument of Oda et al. implies that helical ribbons are in a crystalline phase, and it suggests that tubules are also in a crystalline phase because they can grow out of helical ribbons. By contrast, in Section 6.4 we presented a theoretical argument that tubules and helical ribbons are *not* in a crystalline phase. As noted in that section, there is experimental evidence both for and against crystallinity. Thus, it is not yet clear how to reconcile the

conflicting arguments. The resolution may involve the fact that membranes can have multiple bilayers. Locally, multiple bilayers with Gaussian curvature pack together very efficiently. However, this packing must be distorted on the longer length scale of the helical pitch, and the distortion might increase the free energy of twisted ribbons above helical ribbons, even for noncrystalline membranes. Alternatively, the resolution may involve a modulation in the direction of the molecular tilt, which was not considered in the model of Oda et al. and which may play a role in stabilizing one structure compared with the other. This remains an important subject for theoretical research.

6.6 Chiral Symmetry-Breaking

So far we have considered the formation of tubules in systems of fixed molecular chirality. It is also possible that tubules might form out of membranes that undergo a chiral symmetry-breaking transition, in which they spontaneously break reflection symmetry and select a handedness, even if they are composed of achiral molecules. This symmetry breaking has been seen in bent-core liquid crystals which spontaneously form a liquid conglomerate composed of macroscopic chiral domains of either handedness.¹⁹⁴ This topic is extensively discussed in Walba's chapter elsewhere in this volume. Some indications of this effect have also been seen in experiments on self-assembled aggregates.^{195,196}

A specific model for chiral symmetry-breaking leading to tubule formation was proposed by Seifert et al.¹⁹⁷ They point out that each monolayer of a bilayer membrane is characterized by its own direction of molecular tilt, \mathbf{m}_+ and \mathbf{m}_- . These monolayer tilt directions are usually aligned with each other, but under some circumstances the molecules might pack with a relative angle of α between \mathbf{m}_+ and \mathbf{m}_- . If α is neither 0° nor 180° , then this packing spontaneously breaks reflection symmetry: The states with packing angle $\pm\alpha$ are distinct mirror images of each other, even if the individual molecules are not chiral. A chiral order parameter characterizing the magnitude and sign of the symmetry breaking can be written as $\psi = (\mathbf{m}_+ \times \mathbf{m}_-) \cdot \mathbf{N} = \sin \alpha$. The authors show explicitly that this spontaneous chiral ordering leads to a term in the free energy equivalent to the λ_{HP} term discussed in the previous sections, which favors curvature of a membrane to form a tubule.

This model of bilayer tilt differences has certainly identified one possible mechanism for chiral symmetry-breaking in membranes. However, we suggest that the argument can be made more general, analogous to a model for chiral symmetry-breaking in Langmuir monolayers by Selinger et al.¹⁹⁸ That paper points out that Langmuir monolayers can break reflection symmetry in various ways, including the formation of a tilted hexatic phase with a fixed relative angle between the tilt and bond directions, the packing of molecules on a two-dimensional surface in two distinct ways that are mirror images of each other,

and the phase separation of a racemic mixture. Any of these mechanisms can be characterized by a chiral order parameter ψ —for example, in the phase separation of a racemic mixture, ψ is the difference in densities of the two enantiomers. Likewise, a flexible membrane can break reflection symmetry in any of these ways, and any such mechanism would be characterized by a chiral order parameter ψ . Once the symmetry is broken through any mechanism, the membrane will tend to bend, and the molecular tilt direction will also tend to bend, just as in a system of chiral molecules.

Following the notation of Eq. (9), a general free energy for chiral symmetry-breaking in membranes can be written as

$$\begin{aligned}
 F = \int dS \left[\frac{1}{2}\kappa \left(\frac{1}{r}\right)^2 + \frac{1}{2}\kappa' \left(\frac{1}{r}\right)^2 \cos^2 \phi - \lambda'_{\text{HP}}\psi \left(\frac{1}{r}\right) \sin \phi \cos \phi \right. \\
 \left. - \lambda'_{\text{LS}}\psi \mathbf{N} \cdot \nabla \times \mathbf{m} + \gamma \left(\frac{1}{r}\right) \nabla \cdot \mathbf{m} + \frac{1}{2}c [(\mathbf{N} \cdot \nabla \times \mathbf{m})^2 \right. \\
 \left. + (\nabla \cdot \mathbf{m})^2] + \frac{1}{2}K(\nabla\psi)^2 + \frac{1}{2}t\psi^2 + \frac{1}{4}u\psi^4 \right] \quad (10)
 \end{aligned}$$

Here, the final three terms are a Ginzburg–Landau expansion in powers of ψ . The coefficient t varies as a function of temperature and other control variables. When it decreases below a critical threshold, the system undergoes a chiral symmetry-breaking transition at which ψ becomes nonzero. The membrane then generates effective chiral coefficients $\lambda_{\text{HP}} = \lambda'_{\text{HP}}\psi$ and $\lambda_{\text{LS}} = \lambda'_{\text{LS}}\psi$, which favor membrane curvature and tilt modulations, respectively. Although this free energy has not yet been studied in detail, it shows that any mechanism for chiral symmetry-breaking can lead to the formation of tubules in membranes of achiral molecules.

6.7 Biased Chiral Symmetry-Breaking

In the previous section, we considered a situation in which a system has two ground states which are mirror images of each other and which have exactly the same free energy. In that case, the system randomly selects one of these ground states, giving a spontaneous symmetry-breaking. Now, let us consider a slight bias that “tips the balance” and favors one state compared to the other. Such a bias could arise in a material where the constituent molecules are chiral or in a mixture where the concentrations of right- and left-handed molecules are slightly different. In that case, the system would have two states which are approximately mirror images of each other, and one of these states would be stable while the other would be metastable.

There are two reasons to think this situation might occur. The first reason is experimental. As discussed in Sections 2–5, in *most* experiments on chiral materials, tubules and helical ribbons are observed with only one sense of handedness. However, there are a few exceptions in experiments on diacetylenic phospholipids,¹⁴⁴ diacetylenic phosphonate lipids,^{145,146} and bile.¹⁶² In these exceptional cases, some helices are observed with the opposite sense of handedness from the majority. In the work on diacetylenic phospholipids, the minority handedness was observed only during the kinetic process of tubule formation at high lipid concentration,¹⁴⁴ which is a condition that should promote metastable states. Hence, these experiments may indeed show a case of biased chiral symmetry-breaking in which the molecular chirality favors a state of one handedness and disfavors a mirror image state.

The second reason to consider biased chiral symmetry-breaking is an issue of molecular theory. One can ask the question: Why do diacetylenic lipids form tubules, while many other chiral lipids do not? A possible answer was proposed by Spector et al.¹²⁵ These authors argue that the most striking feature of diacetylenic lipids is that the diacetylene group puts a kink into the acyl chain of the molecules, which can be seen in the space-filling model of Figure 5.52*a*. This kink imposes a steric hindrance to the molecules packing parallel to each other. Hence, the optimum packing of two neighboring molecules can have either of the two arrangements shown in Figure 5.52*b*. If the molecule had no stereocenter, those two arrangements would be degenerate. Because the molecule is chiral, the degeneracy between the two arrangements is lifted, and one of them is favored. That favored packing of the molecules causes the favored twist of the lipid bilayer. This argument implies that a kink in the molecular structure is very important for tubule formation because it determines the possible arrangements of neighboring molecules, and the molecular chirality only selects between those possible arrangements. Chiral lipids without a kink would presumably pack at only a very slight angle with respect to their neighbors, which would give only a slight tendency toward membrane curvature, and hence tubules would not be seen in such systems.

The concept of biased chiral symmetry-breaking has been studied quantitatively in the context of polymer science.^{140,199} In the present situation of tubule-forming membranes, we should express the scenario in terms of continuum elastic theory. In this scenario, the molecular kinks lead to chiral symmetry-breaking, as discussed in Section 6.6. In particular, the net amount of right-handed minus left-handed molecular packing can be characterized by the chiral order parameter ψ . If the molecules were not chiral, the membrane could be described by the free energy of Eq. (10). However, because the molecules have a stereocenter, there is a bias in favor of one sign of ψ . This bias can be described by a chiral field h acting on ψ , giving the

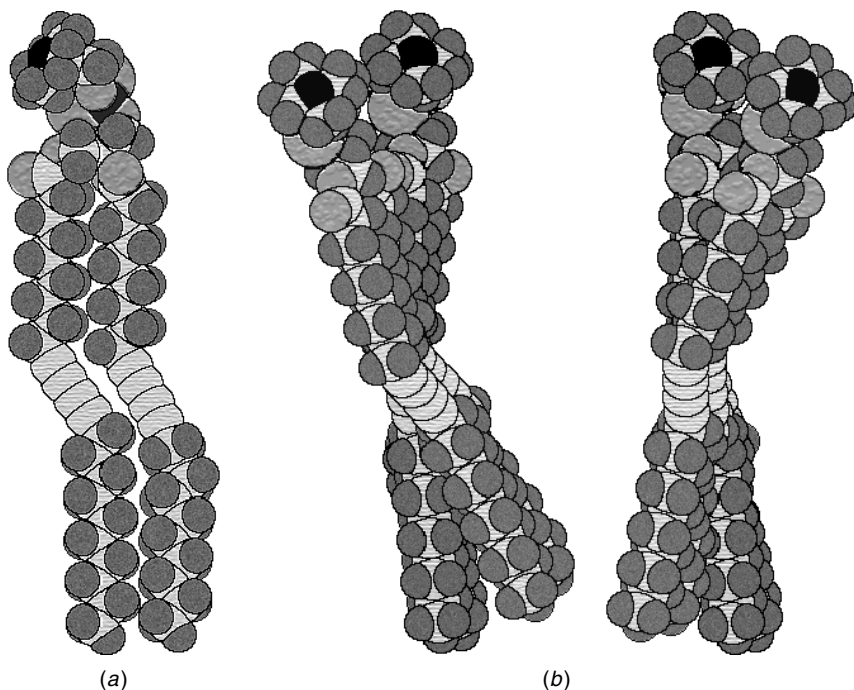


Figure 5.52 (a) Space-filling model of three-dimensional structure of diacetylenic lipid DC_{8,9}PC (38) and (b) schematic showing nonparallel packing of neighboring molecules in right-handed or left-handed fashion.¹²⁵ Chirality causes one orientation to be energetically preferred over the other.

free energy

$$\begin{aligned}
 F = \int dS \left[\frac{1}{2} \kappa \left(\frac{1}{r} \right)^2 + \frac{1}{2} \kappa' \left(\frac{1}{r} \right)^2 \cos^2 \phi - \lambda'_{\text{HP}} \psi \left(\frac{1}{r} \right) \sin \phi \cos \phi \right. \\
 \left. - \lambda'_{\text{LS}} \psi \mathbf{N} \cdot \nabla \times \mathbf{m} + \gamma \left(\frac{1}{r} \right) \nabla \cdot \mathbf{m} + \frac{1}{2} c [(\mathbf{N} \cdot \nabla \times \mathbf{m})^2 \right. \\
 \left. + (\nabla \cdot \mathbf{m})^2] + \frac{1}{2} K (\nabla \psi)^2 + \frac{1}{2} t \psi^2 + \frac{1}{4} u \psi^4 - h \psi \right] \quad (11)
 \end{aligned}$$

According to this argument, diacetylenic lipids do not have an unusually high value of the chiral field h compared with other lipids. Rather, diacetylenic lipids have an unusual negative value of the coefficient t , which gives a free

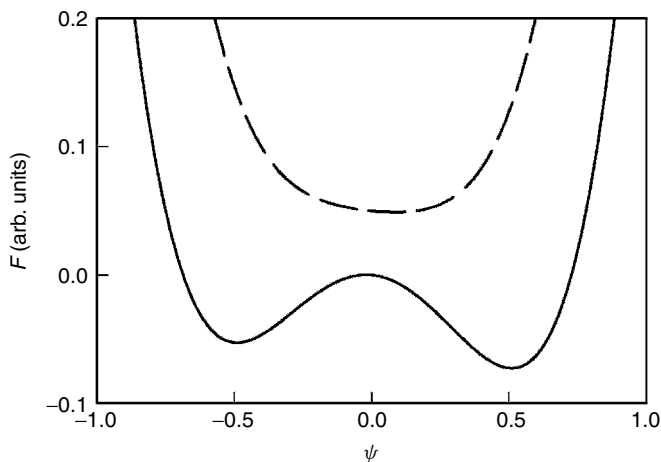


Figure 5.53 Schematic plot of free energy F as function of chiral order parameter ψ for biased chiral symmetry-breaking discussed in Section 6.7. Solid line shows free energy for $t < 0$, with two local minima representing two types of packing shown in Figure 5.52. Molecular chirality favors one minimum over the other. System therefore has large value of ψ , corresponding to membrane with high chiral order. Dashed line shows free energy for $t > 0$, which has only one minimum with much smaller value of ψ , corresponding to membrane with much lower chiral order. Reprinted with permission from Ref. 139. Copyright 2001 by the American Chemical Society.

energy of the form shown by the solid line in Figure 5.53. This free energy has two local minima corresponding to the two types of molecular packing in Figure 5.52*b*. The chiral field h favors one packing over the other. For that reason, the system has a high value of the chiral order parameter ψ , hence high values of the effective chiral coefficients $\lambda_{\text{HP}} = \lambda'_{\text{HP}}\psi$ and $\lambda_{\text{LS}} = \lambda'_{\text{LS}}\psi$, and therefore it forms tubules with a small radius. By contrast, other lipids have positive values of t , giving the free energy of the form shown by the dashed line in Figure 5.53, which has only one minimum with a much lower value of ψ . In those systems, λ_{HP} and λ_{LS} are much smaller, and tubules would have a much larger radius—or perhaps tubules would not form at all if the favored radius is larger than the size of a molecular aggregate.

This scenario for molecular packing leading to biased chiral symmetry-breaking is quite speculative. However, it makes an important point for molecular modeling of lipid membranes: The unusual feature of diacetylenic lipids does not have to be associated with the stereocenter of the molecules but rather may be a broken symmetry in the packing of the kinks in the acyl chains. This speculation needs to be investigated by detailed molecular modeling calculations.

7 CONCLUSION

In this chapter, we have surveyed a wide range of chiral molecules that self-assemble into helical structures. The molecules include aldonamides, cerebrosides, amino acid amphiphiles, peptides, phospholipids, gemini surfactants, and biological and synthetic biles. In all of these systems, researchers observe helical ribbons and tubules, often with helical markings. In certain cases, researchers also observe twisted ribbons, which are variations on helical ribbons with Gaussian rather than cylindrical curvature. These structures have a large-scale helicity which manifests the chirality of the constituent molecules.

A key question that we have discussed throughout the chapter is: Why do some molecules form helical aggregates while other molecules do not? Molecular chirality is clearly part of the answer. The molecules that form helical aggregates are almost all chiral, in that one of their carbons is a stereocenter. The few exceptions seem to be interesting cases of chiral symmetry-breaking in the larger scale aggregate. However, chirality of the molecules (or spontaneous chirality of the aggregate) cannot be the whole answer, because there are many chiral molecules that do not form helical aggregates. For example, most lipids form spherical bilayer vesicles but not tubules or helical ribbons.

As we have discussed, the molecules that form helical aggregates seem to have other features in common, in addition to chirality. One important feature is intramolecular rigidity, as measured by spectroscopy experiments. Each molecule has a distinct shape, which may be kinked, as in the glucenamides and diacetylenic phospholipids. Another important feature is strong intermolecular interactions, which can be transmitted through hydrogen bonding or other noncovalent forces. Because of these interactions, the molecular shape strongly affects the way that neighboring molecules pack together, giving a strong preference for nonparallel alignment of the molecules.

An important point about these issues of intramolecular rigidity and intermolecular interactions is that they are not directly related to chirality. It is certainly possible to have high rigidity and strong interactions in systems of achiral molecules. However, there is one important difference between systems of achiral and chiral molecules. In achiral systems, there is an overall reflection symmetry. Hence, if achiral molecules have a favored right-handed packing from molecule to molecule, they must also have a favored left-handed packing. By contrast, in chiral systems, the molecular handedness breaks the reflection symmetry and favors one handedness of the packing. Thus, one part of the molecule far from the stereocenter may determine the possible types of intermolecular packing, and a slight influence from the chirality may select among them.

We close our theoretical discussion with the concept of biased chiral symmetry-breaking because it sums up this speculation about the interplay

between different parts of a molecule. Most theoretical work on helical aggregates is based on the concept of chiral packing of molecules, which leads to chiral elastic constants in the continuum free energy of a membrane. This theoretical work then predicts the overall shape of chiral membranes. Indeed, it is successful in predicting the range of experimentally observed shapes, including tubules, helical ribbons, and twisted ribbons. However, theoretical work of this type does not address the question of why some materials form chiral aggregates and others do not, except by saying that the chiral elastic constants are bigger in some materials than in others. The concept of biased chiral symmetry-breaking makes a reasonable proposal to address this question. It suggests that the special feature of certain molecules is not the stereocenter itself, but rather the strong preference for some nonparallel packing of the molecules. The molecular chirality then selects a particular type of packing. We believe that this concept will provide a worthwhile basis for further experimental and theoretical research in the coming years.

ACKNOWLEDGMENTS

Our research has benefited tremendously from discussions and collaborations with many colleagues at the Naval Research Laboratory (NRL) and at other institutions. At NRL, we would particularly like to thank Yuri Lvov, Ronald Price, B. R. Ratna, Alan Rudolph, Paul Schoen, R. Shashidhar, and Alok Singh. At other institutions, our thanks go to George Benedek and Shuguang Zhang (Massachusetts Institute of Technology), Noel Clark and David Walba (University of Colorado), Mark Green (Polytechnic University), Tom Lubensky and Phil Nelson (University of Pennsylvania), Fred MacKintosh (Vrije Universiteit, Amsterdam), Phil Messersmith (Northwestern University), Reiko Oda (Institut Européen de Chimie et Biologie, Bordeaux), Jacques Prost (Institut Curie, Paris), and Britt Thomas (Louisiana State University). The authors would also like to thank Ms. Linda Norton at the NRL library for technical assistance. This work was supported by the Office of Naval Research and the Naval Research Laboratory.

REFERENCES

1. Stinson, S. C. *Chem. Eng. News* **2000**, 78, 55–78.
2. Barreiro, E. J.; Ferreira, V. F.; Costa, P. R. R. *Quim. Nova* **1997**, 20, 647–656.
3. Lasic, D. D. *Liposomes: From Physics to Applications*. Elsevier, Amsterdam, 1993.
4. Schnur, J. M.; Peckerar, M. (Eds.). *Synthetic Microstructures in Biological Research*. Plenum, New York, 1992.
5. Tanford, C. *Physical Chemistry of Macromolecules*, Wiley, New York, 1961.

6. Straley, J. P. *Phys. Rev. A* **1976**, *14*, 1835–1841.
7. Buda, A. B.; Derheyde, T. A.; Mislow, K. *Angew. Chem.-Int. Edit. Engl.* **1992**, *31*, 989–1007.
8. Mislow, K. In *Topics in Stereochemistry*, Vol. 22. Denmark, S. E. (ed.). Wiley, New York, 1999.
9. Jacques, J.; Collet, A.; Wilen, S. H. *Enantiomers, Racemates, and Resolutions*, Krieger, Malabar, 1994.
10. Buda, A. B.; Mislow, K. *J. Am. Chem. Soc.* **1992**, *114*, 6006–6012.
11. Kuz'Min, V. E.; Stel'Kakh, I. B.; Bekker, M. B.; Pozigun, D. V. *J. Phys. Org. Chem.* **1992**, *5*, 295–298.
12. Osipov, M. A.; Pickup, B. T.; Dunmur, D. A. *Mol. Phys.* **1995**, *84*, 1193–1206.
13. Harris, A. B.; Kamien, R. D.; Lubensky, T. C. *Rev. Mod. Phys.* **1999**, *71*, 1745–1757.
14. Terech, P.; Weiss, R. G. *Chem. Rev.* **1997**, *97*, 3133–3159.
15. Fuhrhop, J. H.; Helfrich, W. *Chem. Rev.* **1993**, *93*, 1565–1582.
16. Kunitake, T. *Angew. Chem.-Int. Edit.* **1992**, *31*, 709–726.
17. Schnur, J. M. *Science* **1993**, *262*, 1669–1676.
18. Hotten, B. W.; Birdsall, D. H. *J. Colloid Sci.* **1952**, *7*, 284–294.
19. Tachibana, T.; Kambara, H. *J. Am. Chem. Soc.* **1965**, *87*, 3015–3016.
20. Tachibana, T.; Kambara, H. *Bull. Chem. Soc. Jpn.* **1969**, *42*, 3422–3424.
21. Tachibana, T.; Kitazawa, S.; Takeno, H. *Bull. Chem. Soc. Jpn.* **1970**, *43*, 2418–2421.
22. Pfannemüller, B.; Welte, W. *Chem. Phys. Lipids* **1985**, *37*, 227–240.
23. Nakashima, N.; Asakuma, S.; Kim, J. M.; Kunitake, T. *Chem. Lett.* **1984**, 1709–1712.
24. Yamada, K.; Ihara, H.; Ide, T.; Fukumoto, T.; Hirayama, C. *Chem. Lett.* **1984**, 1713–1716.
25. Yager, P.; Schoen, P. E. *Mol. Cryst. Liq. Cryst.* **1984**, *106*, 371–381.
26. Leaver, J.; Alonso, A.; Durrani, A. A.; Chapman, D. *Biochim. Biophys. Acta* **1983**, *732*, 210–218.
27. Schnur, J. M.; Price, R.; Schoen, P.; Yager, P.; Calvert, J. M.; Georger, J.; Singh, A. *Thin Solid Films* **1987**, *152*, 181–206.
28. Browning, S. L.; Lodge, J.; Price, R. R.; Schelleng, J.; Schoen, P. E.; Zabetakis, D. *J. Appl. Phys.* **1998**, *84*, 6109–6113.
29. Schnur, J. M.; Price, R.; Rudolph, A. S. *J. Control Release* **1994**, *28*, 3–13.
30. Voet, D.; Voet, J. G. *Biochemistry*. Wiley, New York, 1990.
31. Fuhrhop, J. H.; Boettcher, C. *J. Am. Chem. Soc.* **1990**, *112*, 1768–1776.
32. Fuhrhop, J. H.; Schnieder, P.; Rosenberg, J.; Boekema, E. *J. Am. Chem. Soc.* **1987**, *109*, 3387–3390.
33. Fuhrhop, J. H.; Schnieder, P.; Boekema, E.; Helfrich, W. *J. Am. Chem. Soc.* **1988**, *110*, 2861–2867.
34. Svenson, S.; Kirste, B.; Fuhrhop, J. H. *J. Am. Chem. Soc.* **1994**, *116*, 11969–11975.
35. Köning, J.; Boettcher, C.; Winkler, H.; Zeitler, E.; Talmon, Y.; Fuhrhop, J. H. *J. Am. Chem. Soc.* **1993**, *115*, 693–700.
36. Boettcher, C.; Stark, H.; vanHeel, M. *Ultramicroscopy* **1996**, *62*, 133–139.
37. Zabel, V.; Mullerfahrnow, A.; Hilgenfeld, R.; Saenger, W.; Pfannemüller, B.; Enkelmann, V.; Welte, W. *Chem. Phys. Lipids* **1986**, *39*, 313–327.
38. Svenson, S.; Koning, J.; Fuhrhop, J. H. *J. Phys. Chem.* **1994**, *98*, 1022–1028.

39. Buntkowsky, G.; Sack, I.; Limbach, H. H.; Kling, B.; Fuhrhop, J. *J. Phys. Chem. B* **1997**, *101*, 11265–11272.
40. Sack, I.; Macholl, S.; Fuhrhop, J. H.; Buntkowsky, G. *Phys. Chem. Chem. Phys.* **2000**, *2*, 1781–1788.
41. Tuzov, I.; Cramer, K.; Pfannemüller, B.; Magonov, S. N.; Whangbo, M. H. *New J. Chem.* **1996**, *20*, 37–52.
42. Messerschmidt, C.; Svenson, S.; Stocker, W.; Fuhrhop, J. H. *Langmuir* **2000**, *16*, 7445–7448.
43. Hafkamp, R. J. H.; Feiters, M. C.; Nolte, R. J. M. *J. Org. Chem.* **1999**, *64*, 412–426.
44. Hafkamp, R. J. H.; Feiters, M. C.; Nolte, R. J. M. *Angew. Chem.-Int. Edit. Engl.* **1994**, *33*, 986–987.
45. Frankel, D. A.; O'Brien, D. F. *J. Am. Chem. Soc.* **1991**, *113*, 7436–7437.
46. Fuhrhop, J. H.; Blumtritt, P.; Lehmann, C.; Luger, P. *J. Am. Chem. Soc.* **1991**, *113*, 7437–7439.
47. Frankel, D. A.; O'Brien, D. F. *J. Am. Chem. Soc.* **1994**, *116*, 10057–10069.
48. Giulieri, F.; Guillod, F.; Greiner, J.; Krafft, M. P.; Riess, J. G. *Chem.-Eur. J.* **1996**, *2*, 1335–1339.
49. Zarif, L.; Gulikkrzywicki, T.; Riess, J. G.; Pucci, B.; Guedj, C.; Pavia, A. A. *Colloid Surf. A-Physicochem. Eng. Asp.* **1994**, *84*, 107–112.
50. Imae, T.; Funayama, K.; Krafft, M. P.; Giulieri, F.; Tada, T.; Matsumoto, T. *J. Colloid Interface Sci.* **1999**, *212*, 330–337.
51. Reichel, F.; Roelofsen, A. M.; Geurts, H. P. M.; van der Gaast, S. J.; Feiters, M. C.; Boons, G. J. *J. Org. Chem.* **2000**, *65*, 3357–3366.
52. Fuhrhop, J. H.; David, H. H.; Mathieu, J.; Liman, U.; Winter, H. J.; Boekema, E. *J. Am. Chem. Soc.* **1986**, *108*, 1785–1791.
53. Shimizu, T. *Macromol. Rapid Commun.* **2002**, *23*, 311–331.
54. Shimizu, T.; Masuda, M. *J. Am. Chem. Soc.* **1997**, *119*, 2812–2818.
55. Plate, N. A.; Shibaev, V. P.; Petrukhi B. S.; Zubov, Y. A.; Kargin, V. A. *J. Polym. Sci., Part A1, Polym. Chem.* **1971**, *9*, 2291.
56. Nakazawa, I.; Masuda, M.; Okada, Y.; Hanada, T.; Yase, K.; Asai, M.; Shimizu, T. *Langmuir* **1999**, *15*, 4757–4764.
57. Shimizu, T.; Masuda, M.; Shibakami, M. *Chem. Lett.* **1997**, 267–268.
58. Masuda, M.; Hanada, T.; Yase, K.; Shimizu, T. *Macromolecules* **1998**, *31*, 9403–9405.
59. John, G.; Masuda, M.; Okada, Y.; Yase, K.; Shimizu, T. *Adv. Mater.* **2001**, *13*, 715–718.
60. Jung, J. H.; John, G.; Masuda, M.; Yoshida, K.; Shinkai, S.; Shimizu, T. *Langmuir* **2001**, *17*, 7229–7232.
61. Yunis, E. J.; Lee, R. E. *Science* **1970**, *169*, 64.
62. Archibald, D. D.; Yager, P. *Biochemistry* **1992**, *31*, 9045–9055.
63. Archibald, D. D.; Mann, S. *Chem. Phys. Lipids* **1994**, *69*, 51–64.
64. Kulkarni, V. S.; Anderson, W. H.; Brown, R. E. *Biophys. J.* **1995**, *69*, 1976–1986.
65. Kulkarni, V. S.; Boggs, J. M.; Brown, R. E. *Biophys. J.* **1999**, *77*, 319–330.
66. Goldstein, A. S.; Lukyanov, A. N.; Carlson, P. A.; Yager, P.; Gelb, M. H. *Chem. Phys. Lipids* **1997**, *88*, 21–36.
67. Goldstein, A. S.; Gelb, M. H.; Yager, P. *Chem. Phys. Lipids* **2001**, *109*, 1–14.
68. Schnur, J. M.; Ratna, B. R.; Selinger, J. V.; Singh, A.; Jyothi, G.; Easwaran, K. R. *Science* **1994**, *264*, 945–947.

69. Branden, C.; Tooze, J. *Introduction to Protein Structure*, 2nd ed. Garland, New York, 1999.
70. Kunitake, T.; Okahata, Y. *J. Am. Chem. Soc.* **1977**, *99*, 3860–3861.
71. Kunitake, T.; Nakashima, N.; Hayashida, S.; Yonemori, K. *Chem. Lett.* **1979**, 1413–1416.
72. Kunitake, T.; Nakashima, N.; Shimomura, M.; Okahata, Y.; Kano, K.; Ogawa, T. *J. Am. Chem. Soc.* **1980**, *102*, 6642–6644.
73. Harada, N.; Nakanishi, K. *Circular Dichroic Spectroscopy: Exciton Coupling in Organic Stereochemistry*. University Science Books, Mill Valley, CA 1983.
74. Nakashima, N.; Asakuma, S.; Kunitake, T. *J. Am. Chem. Soc.* **1985**, *107*, 509–510.
75. Ihara, H.; Fukumoto, T.; Hirayama, C.; Yamada, K. *Polym. Commun.* **1986**, *27*, 282–285.
76. Shimizu, T.; Hato, M. *Biochim. Biophys. Acta* **1993**, *1147*, 50–58.
77. Lee, K. C.; Lukyanov, A. N.; Gelb, M. H.; Yager, P. *Biochim. Biophys. Acta Biomembr.* **1998**, *1371*, 168–184.
78. Cescato, C.; Walde, P.; Luisi, P. L. *Langmuir* **1997**, *13*, 4480–4482.
79. Boettcher, C.; Schade, B.; Fuhrhop, J. H. *Langmuir* **2001**, *17*, 873–877.
80. Rangunathan, K. G.; Bhattacharya, S. *Chem. Phys. Lipids* **1995**, *77*, 13–23.
81. Yamada, N.; Koyama, E.; Kaneko, M.; Seki, H.; Ohtsu, H.; Furuse, T. *Chem. Lett.* **1995**, 387–388.
82. Yamada, N.; Ariga, K.; Naito, M.; Matsubara, K.; Koyama, E. *J. Am. Chem. Soc.* **1998**, *120*, 12192–12199.
83. Nakashima, N.; Ando, R.; Muramatsu, T.; Kunitake, T. *Langmuir* **1994**, *10*, 232–234.
84. Hachisako, H.; Ihara, H.; Hirayama, C.; Yamada, K. *Liq. Crystallogr.* **1993**, *13*, 307–311.
85. Ihara, H.; Takafuji, M.; Hirayama, C.; O'Brien, D. F. *Langmuir* **1992**, *8*, 1548–1553.
86. Ihara, H.; Yamaguchi, M.; Takafuji, M.; Hachisako, H.; Hirayama, C.; Yamada, K. *Nippon Kagaku Kaishi* **1990**, 1047–1053.
87. Rhodes, D. G.; Frankel, D. A.; Kuo, T. M.; O'Brien, D. F. *Langmuir* **1994**, *10*, 267–275.
88. Polidori, A.; Pucci, B.; Zarif, L.; Lacombe, J. M.; Riess, J. G.; Pavia, A. A. *Chem. Phys. Lipids* **1995**, *77*, 225–251.
89. Zarif, L.; Polidori, A.; Pucci, B.; Gulik-Krzywicki, T.; Pavia, A. A.; Riess, J. G. *Chem. Phys. Lipids* **1996**, *79*, 165–170.
90. Polidori, A.; Pucci, B.; Zarif, L.; Riess, J. G.; Pavia, A. A. *Macromol. Rapid Commun.* **1996**, *17*, 229–238.
91. Shimizu, T.; Kogiso, M.; Masuda, M. *Nature* **1996**, *383*, 487–488.
92. Kogiso, M.; Ohnishi, S.; Yase, K.; Masuda, M.; Shimizu, T. *Langmuir* **1998**, *14*, 4978–4986.
93. Schneider, J.; Messerschmidt, C.; Schulz, A.; Gnade, M.; Schade, B.; Luger, P.; Bombicz, P.; Hubert, V.; Fuhrhop, J. H. *Langmuir* **2000**, *16*, 8575–8584.
94. Cheng, Q.; Stevens, R. C. *Langmuir* **1998**, *14*, 1974–1976.
95. Cheng, Q.; Yamamoto, M.; Stevens, R. C. *Langmuir* **2000**, *16*, 5333–5342.
96. Song, J.; Cheng, Q.; Kopta, S.; Stevens, R. C. *J. Am. Chem. Soc.* **2001**, *123*, 3205–3213.
97. Song, J.; Cheng, Q.; Stevens, R. C. *Chem. Phys. Lipids* **2002**, *114*, 203–214.
98. Dill, K. A. *Biochemistry* **1990**, *29*, 7133–7155.
99. Xiong, H. Y.; Buckwalter, B. L.; Shieh, H. M.; Hecht, M. H. *Proc. Natl. Acad. Sci. U.S.A.* **1995**, *92*, 6349–6353.
100. Zhang, S. G.; Holmes, T.; Lockshin, C.; Rich, A. *Proc. Natl. Acad. Sci. U.S.A.* **1993**, *90*, 3334–3338.

101. Aggeli, A.; Bell, M.; Boden, N.; Keen, J. N.; Knowles, P. F.; McLeish, T. C. B.; Pitkeathly, M.; Radford, S. E. *Nature* **1997**, *386*, 259–262.
102. Prusiner, S. B. *Proc. Natl. Acad. Sci. U.S.A.* **1998**, *95*, 13363–13383.
103. Dobson, C. M. In *From Protein Folding to New Enzymes*. Berry, A.; Radford, S. (eds.). Portland Press, Portland, 2001, pp. 1–26.
104. Zhang, S. G.; Holmes, T. C.; Dipersio, C. M.; Hynes, R. O.; Su, X.; Rich, A. *Biomaterials* **1995**, *16*, 1385–1393.
105. Leon, E. J.; Verma, N.; Zhang, S. G.; Lauffenburger, D. A.; Kamm, R. D. *J. Biomater. Sci.-Polym. Ed.* **1998**, *9*, 297–312.
106. Aggeli, A.; Bell, M.; Boden, N.; Keen, J. N.; McLeish, T. C. B.; Nyrkova, I.; Radford, S. E.; Semenov, A. *J. Mater. Chem.* **1997**, *7*, 1135–1145.
107. Smith, C. K.; Regan, L. *Science* **1995**, *270*, 980–982.
108. Nyrkova, I. A.; Semenov, A. N.; Aggeli, A.; Bell, M.; Boden, N.; McLeish, T. C. B. *Eur. Phys. J. B* **2000**, *17*, 499–513.
109. Aggeli, A.; Nyrkova, I. A.; Bell, M.; Harding, R.; Carrick, L.; McLeish, T. C. B.; Semenov, A. N.; Boden, N. *Proc. Natl. Acad. Sci. U.S.A.* **2001**, *98*, 11857–11862.
110. Marini, D. M.; Hwang, W.; Lauffenburger, D. A.; Zhang, S. G.; Kamm, R. D. *Nano Lett.* **2002**, *2*, 295–299.
111. Lashuel, H. A.; LaBrenz, S. R.; Woo, L.; Serpell, L. C.; Kelly, J. W. *J. Am. Chem. Soc.* **2000**, *122*, 5262–5277.
112. Vauthey, S.; Santoso, S.; Gong, H. Y.; Watson, N.; Zhang, S. G. *Proc. Natl. Acad. Sci. U.S.A.* **2002**, *99*, 5355–5360.
113. Ghadiri, M. R.; Granja, J. R.; Milligan, R. A.; McRee, D. E.; Khazanovich, N. *Nature* **1993**, *366*, 324–327.
114. Ghadiri, M. R. *Adv. Mater.* **1995**, *7*, 675–677.
115. Johnston, D. S.; Sanghera, S.; Pons, M.; Chapman, D. *Biochim. Biophys. Acta* **1980**, *602*, 57–69.
116. Hub, H. H.; Hupfer, B.; Koch, H.; Ringsdorf, H. *Angew. Chem.-Int. Edit. Engl.* **1980**, *19*, 938–940.
117. Regen, S. L.; Kirszensztejn, P.; Singh, A. *Macromolecules* **1983**, *16*, 335–338.
118. Rudolph, A. S.; Burke, T. G. *Biochim. Biophys. Acta* **1987**, *902*, 349–359.
119. Rudolph, A. S.; Singh, B. P.; Singh, A.; Burke, T. G. *Biochim. Biophys. Acta* **1988**, *943*, 454–462.
120. Schoen, P. E.; Yager, P. *J. Polym. Sci. Pt. B-Polym. Phys.* **1985**, *23*, 2203–2216.
121. Schoen, P. E.; Nagumo, M.; Singh, A. *Chem. Phys. Lipids* **1994**, *69*, 251–257.
122. Easwaran, K. R. K.; Balasubramanian, S. V.; Singh, A. *Chem. Phys. Lipids* **1994**, *69*, 161–165.
123. Caffrey, M.; Hogan, J.; Rudolph, A. S. *Biochemistry* **1991**, *30*, 2134–2146.
124. Thomas, B. N.; Safinya, C. R.; Plano, R. J.; Clark, N. A. *Science* **1995**, *267*, 1635–1638.
125. Spector, M. S.; Selinger, J. V.; Singh, A.; Rodriguez, J. M.; Price, R. R.; Schnur, J. M. *Langmuir* **1998**, *14*, 3493–3500.
126. Burke, T. G.; Rudolph, A. S.; Price, R. R.; Sheridan, J. P.; Dalziel, A. W.; Singh, A.; Schoen, P. E. *Chem. Phys. Lipids* **1988**, *48*, 215–230.
127. Georger, J. H.; Singh, A.; Price, R. R.; Schnur, J. M.; Yager, P.; Schoen, P. E. *J. Am. Chem. Soc.* **1987**, *109*, 6169–6175.

128. Ratna, B. R.; Baral-Tosh, S.; Kahn, B.; Schnur, J. M.; Rudolph, A. S. *Chem. Phys. Lipids* **1992**, *63*, 47–53.
129. Rudolph, A. S.; Testoff, M. A.; Shashidar, R. *Biochim. Biophys. Acta* **1992**, *1127*, 186–190.
130. Pons, M.; Johnston, D. S.; Chapman, D. *Biochim. Biophys. Acta* **1982**, *693*, 461–465.
131. Spector, M. S.; Easwaran, K. R. K.; Jyothi, G.; Selinger, J. V.; Singh, A.; Schnur, J. M. *Proc. Natl. Acad. Sci. U.S.A.* **1996**, *93*, 12943–12946.
132. Selinger, J. V.; MacKintosh, F. C.; Schnur, J. M. *Phys. Rev. E* **1996**, *53*, 3804–3818.
133. Singh, A.; Burke, T. G.; Calvert, J. M.; Georger, J. H.; Herendeen, B.; Price, R. R.; Schoen, P. E.; Yager, P. *Chem. Phys. Lipids* **1988**, *47*, 135–148.
134. Walde, P.; Blöchliger, E. *Langmuir* **1997**, *13*, 1668–1671.
135. Spector, M. S.; Price, R. R.; Schnur, J. M. *Adv. Mater.* **1999**, *11*, 337–340.
136. Nounesis, G.; Ratna, B. R.; Shin, S.; Flugel, R. S.; Sprunt, S. N.; Singh, A.; Litster, J. D.; Shashidhar, R.; Kumar, S. *Phys. Rev. Lett.* **1996**, *76*, 3650–3653.
137. Spector, M. S.; Selinger, J. V.; Schnur, J. M. *J. Am. Chem. Soc.* **1997**, *119*, 8533–8539.
138. Markowitz, M. A.; Schnur, J. M.; Singh, A. *Chem. Phys. Lipids* **1992**, *62*, 193–204.
139. Selinger, J. V.; Spector, M. S.; Schnur, J. M. *J. Phys. Chem. B* **2001**, *105*, 7157–7169.
140. Green, M. M.; Park, J. W.; Sato, T.; Teramoto, A.; Lifson, S.; Selinger, R. L. B.; Selinger, J. V. *Angew. Chem.-Int. Edit.* **1999**, *38*, 3139–3154.
141. Lvov, Y. M.; Price, R. R.; Selinger, J. V.; Singh, A.; Spector, M. S.; Schnur, J. M. *Langmuir* **2000**, *16*, 5932–5935.
142. Burkett, S. L.; Mann, S. *Chem. Commun.* **1996**, 321–322.
143. Letellier, D.; Sandre, O.; Menager, C.; Cabuil, V.; Lavergne, M. *Mater. Sci. Eng. C-Biomimetic Mater. Sens. Syst.* **1997**, *5*, 153–162.
144. Thomas, B. N.; Lindemann, C. M.; Clark, N. A. *Phys. Rev. E* **1999**, *59*, 3040–3047.
145. Thomas, B. N.; Corcoran, R. C.; Cotant, C. L.; Lindemann, C. M.; Kirsch, J. E.; Persichini, P. J. *J. Am. Chem. Soc.* **1998**, *120*, 12178–12186.
146. Thomas, B. N.; Lindemann, C. M.; Corcoran, R. C.; Cotant, C. L.; Kirsch, J. E.; Persichini, P. J. *J. Am. Chem. Soc.* **2002**, *124*, 1227–1233.
147. Friedel, G. *Ann. Phys. (Paris)* **1922**, *18*, 273.
148. Milhaud, J.; Michels, B. *Chem. Phys. Lipids* **1999**, *101*, 223–235.
149. Mishra, B. K.; Thomas, B. N. *J. Am. Chem. Soc.* **2002**, *124*, 6866–6871.
150. Singh, A.; Gaber, B. P. In *Applied Bioactive Polymeric Materials*. Gebelein, C. G.; Carraher, C. E.; Forster, V. R. (Eds.). Plenum, New York, 1988, pp. 239–249.
151. Markowitz, M. A.; Singh, A.; Chang, E. L. *Biochem. Biophys. Res. Commun.* **1994**, *203*, 296–305.
152. Svenson, S.; Messersmith, P. B. *Langmuir* **1999**, *15*, 4464–4471.
153. Spector, M. S.; Singh, A.; Messersmith, P. B.; Schnur, J. M. *Nano Lett.* **2001**, *1*, 375–378.
154. Watson, J. D.; Crick, F. H. C. *Nature* **1953**, *171*, 737–738.
155. Yanagawa, H.; Ogawa, Y.; Furuta, H.; Tsuno, K. *Chem. Lett.* **1988**, 269–272.
156. Yanagawa, H.; Ogawa, Y.; Furuta, H.; Tsuno, K. *J. Am. Chem. Soc.* **1989**, *111*, 4567–4570.
157. Itojima, Y.; Ogawa, Y.; Tsuno, K.; Handa, N.; Yanagawa, H. *Biochemistry* **1992**, *31*, 4757–4765.
158. Bonaccio, S.; Wessicken, M.; Berti, D.; Walde, P.; Luisi, P. L. *Langmuir* **1996**, *12*, 4976–4978.

159. Shimizu, T.; Iwaura, R.; Masuda, M.; Hanada, T.; Yase, K. *J. Am. Chem. Soc.* **2001**, *123*, 5947–5955.
160. Konikoff, F. M.; Chung, D. S.; Donovan, J. M.; Small, D. M.; Carey, M. C. *J. Clin. Invest.* **1992**, *90*, 1155–1160.
161. Chung, D. S.; Benedek, G. B.; Konikoff, F. M.; Donovan, J. M. *Proc. Natl. Acad. Sci. U.S.A.* **1993**, *90*, 11341–11345.
162. Zastavker, Y. V.; Asherie, N.; Lomakin, A.; Pande, J.; Donovan, J. M.; Schnur, J. M.; Benedek, G. B. *Proc. Natl. Acad. Sci. U.S.A.* **1999**, *96*, 7883–7887.
163. Smith, B.; Zastavker, Y. V.; Benedek, G. B. *Phys. Rev. Lett.* **2001**, *87*, 278101.
164. Terech, P.; de Geyer, A.; Struth, B.; Talmon, Y. *Adv. Mater.* **2002**, *14*, 495.
165. Oda, R.; Huc, I.; Schmutz, M.; Candau, S. J.; MacKintosh, F. C. *Nature* **1999**, *399*, 566–569.
166. Zana, R.; Talmon, Y. *Nature* **1993**, *362*, 228–230.
167. Oda, R.; Huc, I.; Candau, S. J. *Angew. Chem.-Int. Edit.* **1998**, *37*, 2689–2691.
168. De Gennes, P. G. C. *R. Acad. Sci. Paris* **1987**, *304*, 259–263.
169. Meyer, R. B.; Liebert, L.; Strzelecki, L.; Keller, P. *J. Phys. Lett.* **1975**, *36*, L69–L71.
170. Helfrich, W. *Z. Naturforsch. (C)* **1973**, *C28*, 693–703.
171. Chappell, J. S.; Yager, P. *Chem. Phys.* **1991**, *150*, 73–79.
172. Chappell, J. S.; Yager, P. *Biophys. J.* **1991**, *60*, 952–965.
173. Lubensky, T. C.; Prost, J. *J. Phys. II* **1992**, *2*, 371–382.
174. Chen, C. M. *Phys. Rev. E* **1999**, *59*, 6192–6195.
175. Harris, A. B.; Kamien, R. D.; Lubensky, T. C. *Phys. Rev. Lett.* **1997**, *78*, 1476–1479.
176. Kamien, R. D.; Selinger, J. V. *J. Phys.: Condens. Matter* **2001**, *13*, R1–R22.
177. Nandi, N.; Bagchi, B. *J. Am. Chem. Soc.* **1996**, *118*, 11208–11216.
178. Nandi, N.; Bagchi, B. *J. Phys. Chem. A* **1997**, *101*, 1343–1351.
179. Helfrich, W. *J. Chem. Phys.* **1986**, *85*, 1085–1087.
180. Helfrich, W.; Prost, J. *Phys. Rev. A* **1988**, *38*, 3065–3068.
181. Ou-Yang, Z.-C.; Liu, J.-X. *Phys. Rev. Lett.* **1990**, *65*, 1679–1682.
182. Ou-Yang, Z.-C.; Liu, J.-X. *Phys. Rev. A* **1991**, *43*, 6826–6836.
183. Nelson, P.; Powers, T. *Phys. Rev. Lett.* **1992**, *69*, 3409–3412.
184. Nelson, P.; Powers, T. *J. Phys. II* **1993**, *3*, 1535–1569.
185. Chappell, J. S.; Yager, P. *Chem. Phys. Lipids* **1991**, *58*, 253–258.
186. Selinger, J. V.; Schnur, J. M. *Phys. Rev. Lett.* **1993**, *71*, 4091–4094.
187. Komura, S.; Ou-Yang, Z.-C. *Phys. Rev. Lett.* **1998**, *81*, 473–476.
188. Nelson, D. R.; Peliti, L. *J. Phys.* **1987**, *48*, 1085–1092.
189. Seung, H. S.; Nelson, D. R. *Phys. Rev. A* **1988**, *38*, 1005–1018.
190. Treanor, R.; Pace, M. D. *Biochim. Biophys. Acta* **1990**, *1046*, 1–11.
191. Brandow, S. L.; Turner, D. C.; Ratna, B. R.; Gaber, B. P. *Biophys. J.* **1993**, *64*, 898–902.
192. Rhodes, D. G.; Blechner, S. L.; Yager, P.; Schoen, P. E. *Chem. Phys. Lipids* **1988**, *49*, 39–47.
193. Lando, J. B.; Sudiwala, R. V. *Chem. Mat.* **1990**, *2*, 594–599.
194. Walba, D. M.; Korblova, E.; Shao, R.; MacLennan, J. E.; Link, D. R.; Glaser, M. A.; Clark, N. A. *Science* **2000**, *288*, 2181–2184.
195. Singh, A.; Schoen, P. E.; Schnur, J. M. *J. Chem. Soc.-Chem. Commun.* **1988**, 1222–1223.

196. Lindsell, W. E.; Preston, P. N.; Seddon, J. M.; Rosair, G. M.; Woodman, T. A. J. *Chem. Mat.* **2000**, *12*, 1572–1576.
197. Seifert, U.; Shillcock, J.; Nelson, P. *Phys. Rev. Lett.* **1996**, *77*, 5237–5240.
198. Selinger, J. V.; Wang, Z. G.; Bruinsma, R. F.; Knobler, C. M. *Phys. Rev. Lett.* **1993**, *70*, 1139–1142.
199. Selinger, J. V.; Selinger, R. L. B. *Phys. Rev. Lett.* **1996**, *76*, 58–61.

Chapter 6

Chiral Discotic Molecules: Expression and Amplification of Chirality

L. BRUNSVELD AND E. W. MEIJER

Laboratory of Macromolecular and Organic Chemistry, Eindhoven University of Technology, P.O. Box 513, 5600 MB, Eindhoven, The Netherlands

A. E. ROWAN AND R. J. M. NOLTE

Laboratory of Organic Chemistry, Department of Organic Chemistry, NSRIM, University of Nijmegen, Toernooiveld 1, 6525 ED, Nijmegen, The Netherlands

- 1 Introduction
 - 1.1 Liquid Crystals
 - 1.2 Discotic Liquid Crystals
- 2 Objective
- 3 Chiral Thermotropic Discotic Liquid Crystals
 - 3.1 Chiral Induction in N_D Mesophase
 - 3.2 Chiral Columns Formed by Helical Self-Assembly
 - 3.2.1 Helical Core
 - 3.2.2 Polymer Backbone–Controlled Helicity
 - 3.2.3 Side-Chain Packing
 - 3.3 Discotics with Chiral Core
 - 3.4 Ferroelectricity
 - 3.4.1 Flat Discotics
 - 3.4.2 Cone-Shaped Molecules
- 4 Chiral Lyotropic Discotic Liquid Crystals and Self-Assembly of Chiral Discotics in Dilute Solution
 - 4.1 Self-Assembly of Chiral Discotics
 - 4.1.1 Self-Assembly of Chiral Discotics Without Expression of Chirality
 - 4.1.2 Noncooperative Self-Assembly into Chiral Columns
 - 4.1.3 Cooperative Self-Assembly into Chiral Columns

Materials-Chirality: Volume 24 of Topics in Stereochemistry,
Edited by Mark M. Green, R.J.M. Nolte, and E.W. Meijer
ISBN 0-471-05497-6 Copyright © 2003 John Wiley & Sons, Inc.

- 4.2 Self-Assembly of Guanine- and Pterine-Related Molecules
- 4.3 Self-Assembly of Helices
- 5 Conclusions and Outlook
- References

1 INTRODUCTION

Chiral liquid crystals are currently one of the very few organic materials that have found widespread application in electronic devices.¹ The chiral liquid crystals exploited for these systems are primarily calamitic or rodlike in nature. Discotic liquid crystals were discovered 25 years ago,² and it was envisaged that certain properties, such as their electrical and photoconductivity, viscosity, and temperature stability,³ would be more beneficial in application when compared to the calamitic liquid crystals. Initially, the thermotropic organization of the discotics was the main focus of research, and as a result full control over the mesophases and their temperature regimes was achieved. This precise control was obtained via variation of the core type, its size, and by varying the peripheral side chains. In addition to their thermotropic behavior, the properties of this type of molecule have also been investigated in the lyotropic or gel phase and in dilute solution. The large aromatic cores of the molecules were shown to induce strong intermolecular interactions in both polar and apolar solvents. Before setting the stage for the studies described in this chapter, we will—in short—describe the basic aspects of liquid crystals in general and that of discotic liquid crystals in particular.

1.1 Liquid Crystals

Reinitzer discovered liquid crystallinity in 1888; the so-called fourth state of matter.⁴ Liquid crystalline molecules combine the properties of mobility of liquids and orientational order of crystals. This phenomenon results from the anisotropy in the molecules from which the liquid crystals are built. Different factors may govern this anisotropy, for example, the presence of polar and apolar parts in the molecule, the fact that it contains flexible and rigid parts, or often a combination of both. Liquid crystals may be thermotropic, being a state of matter in between the solid and the liquid phase, or they may be lyotropic, that is, ordering induced by the solvent. In the latter case the solvent usually solvates a certain part of the molecule while the other part of the molecule helps induce aggregation, leading to mesoscopic assemblies. The first thermotropic mesophase discovered was a chiral nematic or cholesteric phase (N^*)⁴ named after the fact that it was observed in a cholesterol derivative. In hindsight, one can conclude that this was not the simplest mesophase possible. In fact, this mesophase is chiral, since the molecules are ordered in

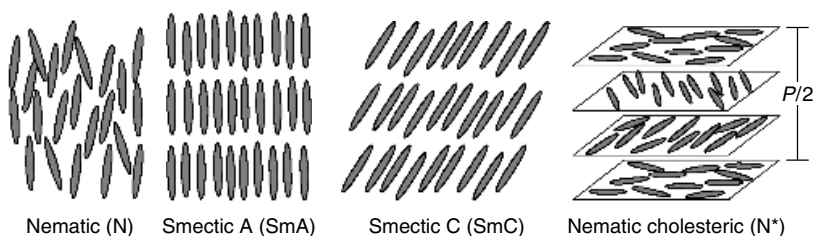


Figure 6.1 Schematic representation for some different mesophases formed by calamitic mesogens. $P/2$ is half of cholesteric pitch.

different layers which are rotated with respect to one another, giving rise to an overall helical pitch within the material. The least ordered mesophase is the nematic phase (N), in which there is only orientational order, with the molecules aligned in one direction, but without positional order. When lateral order is present, the mesophase is called smectic (Sm). During the last century a large variety of smectic mesophases have been identified of which smectic A (SmA) and C (SmC) are the least ordered ones (Figure 6.1). In smectic B (SmB), for example, the molecules are ordered in a hexagonal array. All these mesophases and the property of liquid crystallinity, in general, were identified for calamitic mesogens, that is, molecules having the shape of a rod. It was not until 1977 that liquid crystals from molecules with another molecular shape were discovered² and named discotic liquid crystals after their disklike structure.

1.2 Discotic Liquid Crystals

Although the concept had been proposed before,⁵ Chandrasekhar synthesized the first discotic liquid crystals in 1977.² Using X-ray diffraction, it was established that the molecules stack to form columnar structures in the mesophase due to a phase separation between the flexible aliphatic side chains and the rigid aromatic core. In the first years after the discovery of discotics, the general principles of discotic liquid crystals were further developed by several groups in France.^{6,7} At present, the number of discotic molecules showing mesomorphism is rapidly expanding as more research is carried out.³ Discotic molecules can be characterized as having a rigid and usually planar aromatic core provided with flexible chains at the periphery and typically rotational symmetry. The radial anisotropy within the molecules generally induces an assembly of the molecules into columns. The molecules within these columns can stack in a variety of orientations and the columns themselves can further self-assemble in a variety of ways. Some of the most common examples are the

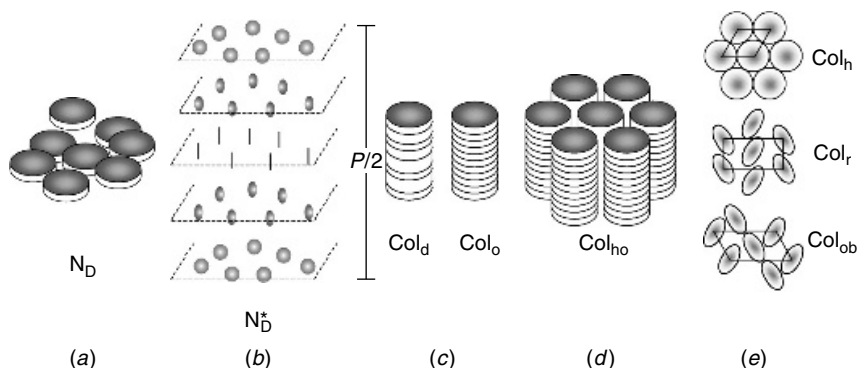


Figure 6.2 Discotic molecules in a (a) nematic state N_D , (b) twisted nematic discotic state N_D^* ($P/2$ is half of cholesteric pitch), (c) columnar state, ordered D_0 and disordered D_d , (d) hexagonal ordered columnar state D_{ho} ; two-dimensional packing arrays for columnar structures in (e) hexagonal, Col_h ; rectangular, Col_r ; oblique, Col_{ob} .

hexagonal columnar (Col_h), rectangular columnar (Col_r), and oblique columnar (Col_{ob}) mesophases (with the last being tilted columnar mesophases). Another subdivision can be made into ordered and disordered (Col_{ho} and Col_{hd} , respectively) mesophases, which is used to define whether the interdisk stacking of the discotics is fixed or more liquidlike throughout the column (Figure 6.2). Apart from the highly ordered columnar mesophases, less ordered mesophases exist, primarily, the nematic discotic (N_D), in which there is only orientational order, similar to that present in conventional nematic liquid crystals. Discotic molecules may form phases that show polymorphism, and the determination of the mesophases is not always unambiguous due to the fact that only very slight differences in molecule geometry are required to significantly alter the mesophase.

2 OBJECTIVE

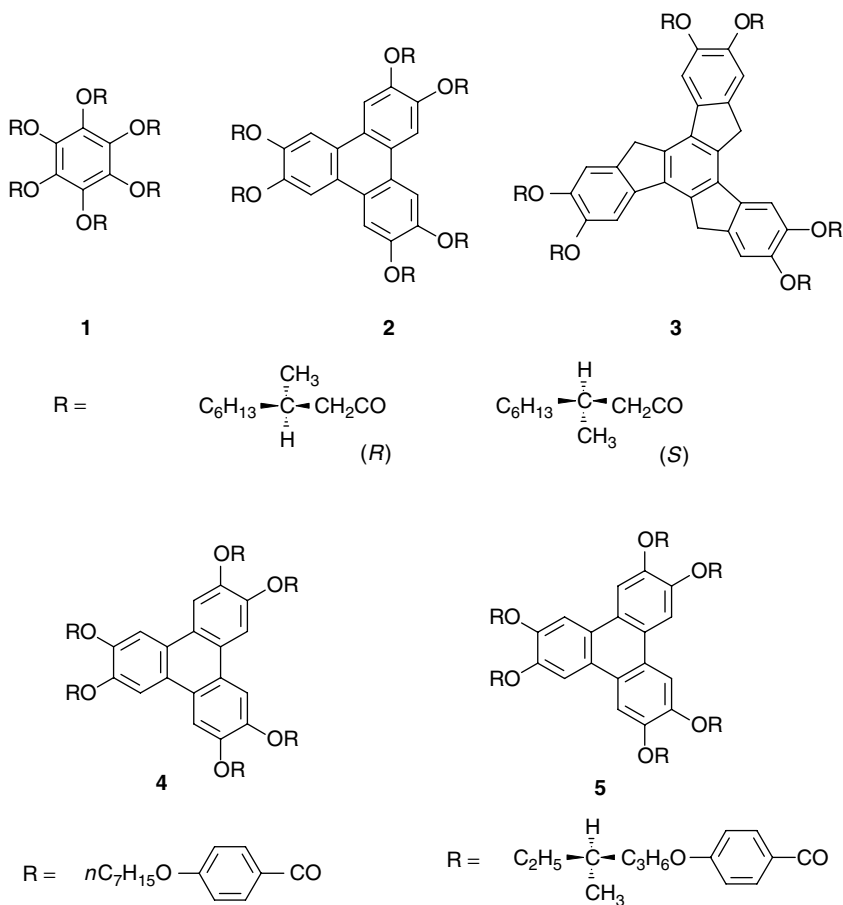
It was quickly recognized that chirality would play an important role in discotic liquid crystals, not only for the possibility of creating cholesteric and ferroelectric liquid crystals but also as a tool for studying the self-assembly of these molecules as a whole, both in solution and in the solid state. However, initial studies revealed that expression of chirality in discotic liquid crystals was not as straightforward as for liquid crystals derived from calamitic molecules. More recently, with the increase in interest in self-assembly and molecular recognition, considerably more attention has been directed to the study of chiral discotics and their assemblies in solution. The objective of this chapter is

to summarize and elucidate *how molecular chirality can be expressed in discotic supramolecular architectures* both in the liquid crystalline state and in solution. A more intriguing question related to the self-assembly of discotic systems is the question of how this chirality can be passed on from one discotic molecule to another, and how this molecular chirality can be amplified upon assembly. This complex question has significant bearing on the fundamental issue of the origin of homochirality throughout nature.

To understand how chirality is expressed, it is important to first describe the different thermotropic mesophase assemblies which can be formed by chiral discotics. Even though expression of chirality has been observed in thermotropic mesophases, the chiral expression occurs in a rather uncontrolled manner, and systems which are suitable for applications, for example, easily switchable columns/ferroelectric discotic liquid crystals, consequently have not yet been developed. Hence, the assembly of discotics in solution has received considerable attention. Supramolecular assemblies of discotic molecules in solution are still in their infancy and have not yet found commercial application, but they are of fundamental importance since they allow a detailed and focused investigation of the specific interactions that are required to express chirality at higher levels of organization. As such, the fundamental knowledge acquired from supramolecular assemblies in solution might formulate the design criteria for thermotropic chiral discotic mesophases and provide the necessary tools for the creation of functional systems.

3 CHIRAL THERMOTROPIC DISCOTIC LIQUID CRYSTALS

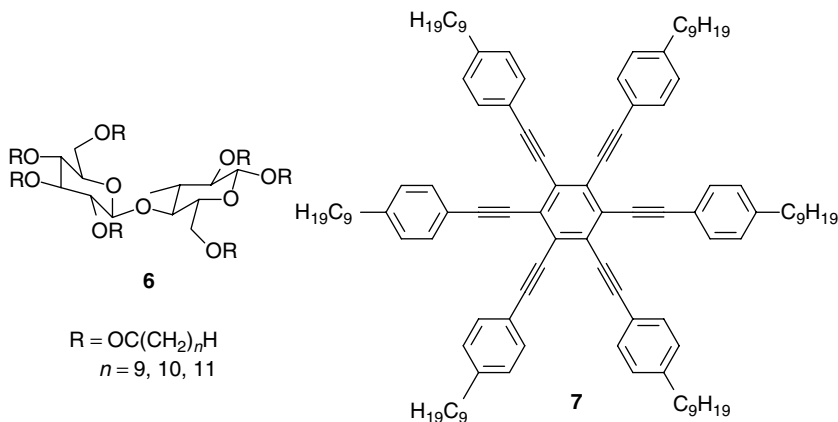
After the discovery of the nematic discotic (N_D) mesophase,^{8,9} it was soon questioned whether the corresponding cholesteric phase could also exist, in analogy to calamitic liquid crystals.¹⁰ Destrade and co-workers investigated this question using chiral benzenes, triphenylenes, and truxenes esters (**1–3**) as mesogens. These compounds showed columnar mesomorphism, but initially, no indications of chirality at the mesoscopic level were observed. Mixing of these esters with the 2,3,6,7,10,11 hexa-*n*-heptyloxybenzoate of triphenylene (**4**), however, gave rise to cholesteric textures. The chiral molecules were able to twist the N_D mesophase of **4** into a chiral phase. The resulting mesophase was labeled N_D^* , and is a twisted nematic discotic mesophase. A schematic figure of this mesophase is shown in Figure 6.2*b*. In a logical extension of this work, chiral triphenylene derivative **5** was also prepared and was the first pure chiral discotic that exhibited cholesteric behavior.¹¹ The chiral side chains attached at the periphery induce a twist in the nematic discotic phase. As a consequence of this twist, triphenylene **5** was the first discotic molecule to show a chiral (N_D^*) mesophase. It was also reported that the



cholesteric properties were strongly dependent on the structure of the chiral chains, since a variety of related derivatives failed to exhibit similar properties. The twisting of the N_D phase of **4** by the addition of small amount of **2** and the observation of a N_D^* phase for **5** stimulated the authors to carefully reexamine the two columnar mesophases they had previously observed for **2**.¹² Cooling of isotropic free droplets gave rise to fan-shaped textures, with the two enantiomers of **2** showing mirror images of the chiral points. Upon further cooling, spiralization of the medium took place. These triphenylenes thus were the first true chiral discotic compounds forming columnar mesophases with expression of their molecular chirality at the mesoscopic level. In the following sections, chirality in thermotropic discotic liquid crystals will be dealt with in a more systematic order, with the chiral compounds classified according to their unique physical properties.

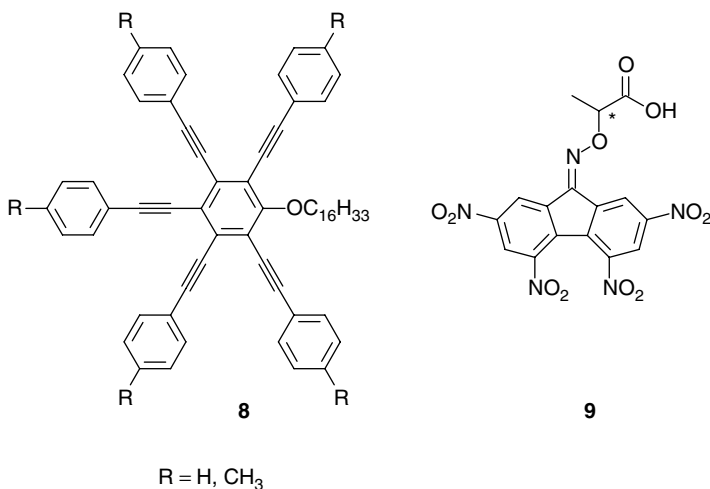
3.1 Chiral Induction in N_D Mesophase

The observation of a nematic discotic (N_D) mesophase first occurred in 1979.⁸ It is the least ordered of all discotic mesophases. One year later the first example of induction of chirality in N_D mesophases was demonstrated, by mixing a chiral triphenylene (2) with an achiral molecule (4).¹⁰ The chiral triphenylene alone was found to form a chiral columnar mesophase. After this first example of a chiral N_D mesophase, compound 4 was slightly modified to give chiral 5, which as mentioned above, alone formed a chiral N_D mesophase, denoted as N_D^* .⁹ This chiral N_D^* mesophase was completely miscible with a nonchiral N_D mesophase, highlighting the structural similarities between the two phases. Furthermore, it was observed that the chiral mesophase could be oriented in a magnetic field.¹¹ The helical twisting power [$HTP = 1/pc$, where p is the helical pitch in microns (μm) and c is the relative concentration of chiral dopant] of this chiral discotic molecule is not large, and consequently cellobiose derivatives (6) were designed as chiral dopants for discotic nematic host 7.^{13,14} The small pitches induced by these molecules were found to be comparable to those observed for calamitic chiral dopants, which allowed selective reflection of visible light. Intriguingly, the authors also observed blue phases at certain concentrations of chiral dopants, indicating the high degree of chirality expressed in the system.

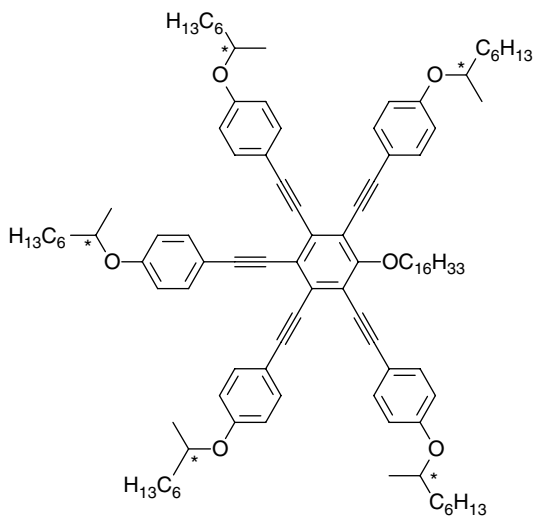
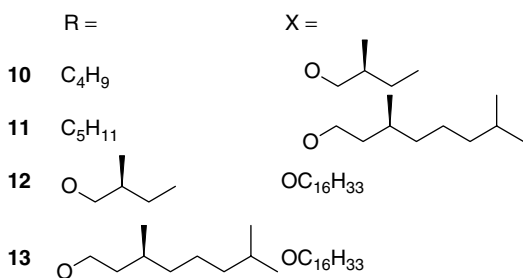
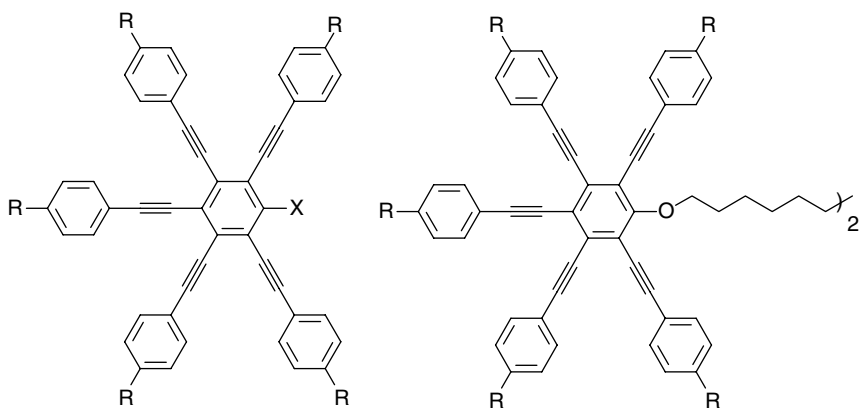


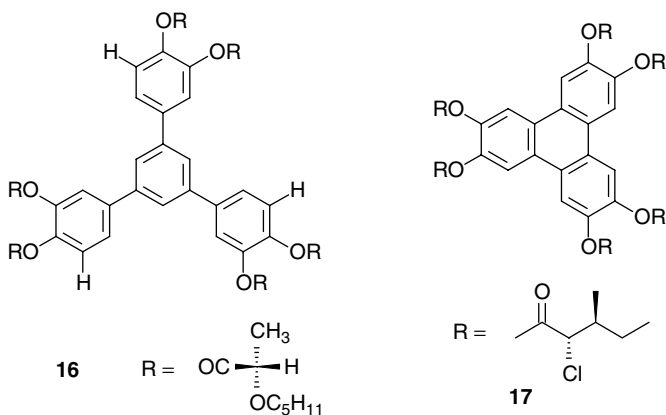
Induction of chirality in N_D phases was also shown to be possible using charge transfer interactions, via π - π stacking. The binary mixture of mesogen 8, which is electron rich, with chiral electron-deficient molecule 9 was shown to induce a twist in the mesophase.¹⁵ Furthermore, nonmesogenic 8 gave rise to a cholesteric mesophase, denoted as being of the columnar type (N_C^*), when present in a ternary system with TNF (trinitrofluorenone, an electron acceptor)

and chiral electron-deficient component **9** (the columnar N_C^* phase resembles the calamitic variety displayed in Figure 6.1, but with the single molecules replaced by columns). It was also reported that when the π - π interactions are strong enough, it is possible to induce twisted nematic (N^*) phases within a lyotropic phase.¹⁶ As such, these molecules are able to form both thermotropic as well as lyotropic phases.



Using structurally similar chiral pentaynes (**10–14**), it was shown that a small helical pitch or a temperature-induced helix inversion could be induced by variation of the lateral substituents.¹⁷ The temperature of the helix inversion remained unaltered when a nonchiral nematic discotic was added, indicating that the effect primarily arose from a molecular property of the chiral compound alone. Of great interest was the fact that addition of a different cholesteric pentayne mesogen caused a shift of the helical inversion temperature linearly with the relative composition. This phenomenon indicates that the helical twisting power of chiral compounds in a cholesteric discotic system is additive and highlights that for these pentaynes, the interactions are not cooperative. The helical twisting powers reported for these systems are relatively weak ($pc \sim 1000 \mu\text{m} \cdot \text{wt} \%$); however, significant improvement of this value could be obtained by mixing the chiral pentayne **15** with achiral host **7**, giving similar values to those reported for the cellobiose derivatives ($pc \sim 8 \mu\text{m} \cdot \text{wt} \%$).¹⁸ This result arose great interest given the fact that the chiral pentayne **15** is not liquid crystalline. Similarly, chiral 1,3,5-triphenylbenzene **16**, which is nonmesogenic, is also capable of inducing a cholesteric phase in hexayne **7** ($pc \sim 150 \mu\text{m} \cdot \text{wt} \%$).¹⁹ More recently, it was also observed that chiral triphenylene **17** can induce a cholesteric phase in





hexayne **7**,²⁰ and it was found that a chiral diplatinum complex exhibits a cholesteric nematic discotic mesophase.²¹ The induction of chirality in the N_D mesophase of triphenylenes has been investigated for compensation films for twisted liquid crystal films.²²

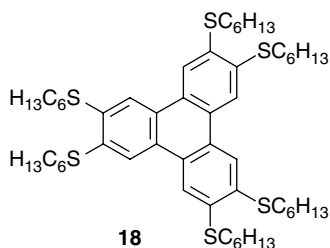
3.2 Chiral Columns Formed by Helical Self-Assembly

The most famous example of helical order in columns can be found in nature, in deoxyribonucleic acid (DNA).²³ In this biopolymer, the subsequent base pairs are rotated giving rise to helical columns. The rotational and positional order of the base pairs is ensured via the chiral sugar–phosphate backbone. Most chiral and achiral discotic molecules do not form helical columns. Generally, the chirality of chiral discotic liquid crystals is located in the side chains, and the flat core is usually nonchiral in nature. As the interactions between the chiral side chains are usually not significant enough to induce helicity, the majority of self-assembled columns are nonhelical. However, if the core molecules have an intrinsic shape that gives rise to stacking with a preferred rotation, helical columns are invariably formed. The chirality in the side chains of these molecules then can express itself within the column because it merely induces an energy difference in packing between a left- and right-handed column. The examples to be presented in the following section illustrate the above-mentioned situation.

3.2.1 Helical Core

The first observed example of helical order in a discotic mesophase was found in hexa-hexylthiotriphenylene (**18**).^{24–26} Molecule **18** has two mesophases, at high temperature a Col_hd mesophase and at low temperature a Col_ho

mesophase. The low-temperature phase consists of a triangular array of columns with a periodic, positional, and unequal helical intracolumn order. The helicity within the columns formed by **18** is the result of the steric bulk of the sulfur atoms linking the tails to the core. In contrast to the oxygen analogs, the triphenylenes with sulfur atoms cannot stack precisely on top of each other due to the large van der Waals radius of the sulfur (1.85 Å). Hence a rotation of the discs occurs in such a way that the sulfur atoms of neighboring discotic molecules are forced to move away from each other in order to preserve the arene–arene interactions. This hindered stacking severely limits the rotation of the discs within the columns and thus induces positional and ultimately helical order.



The second example of helical stacks reported in the literature is based on discotics **19–22**, which have threefold symmetry and possess an extended core planarized via intramolecular hydrogen bonding.²⁷ The three wedges are connected to the central aromatic benzene via a single bond and can rotate out of the plane of the core, resulting in the molecule having a propellerlike geometry (Figure 6.3). X-ray diffraction measurements on compounds **19–22**

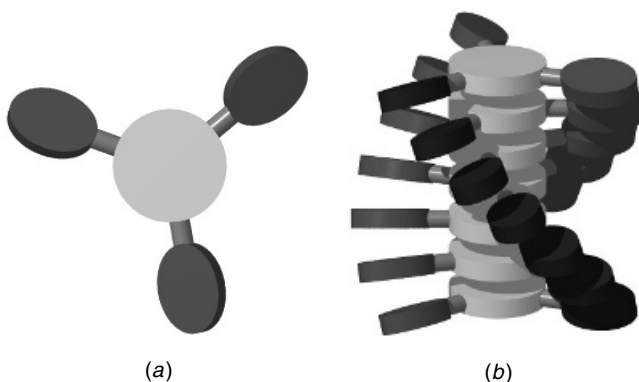
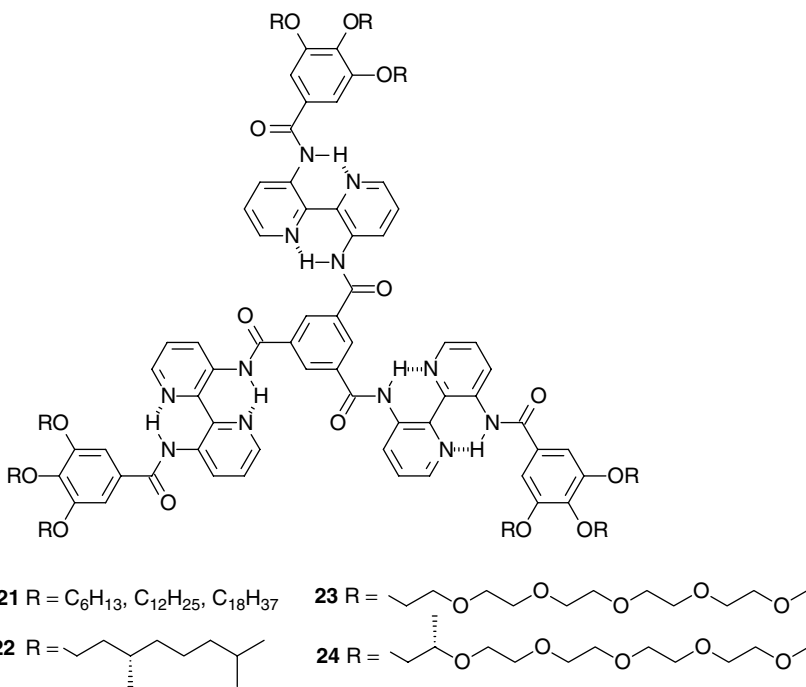


Figure 6.3 (a) Cartoon representation of propellerlike conformation attained by C_3 -symmetrical molecules **19–24**; (b) cartoon representation of helical columns formed by these discotics.

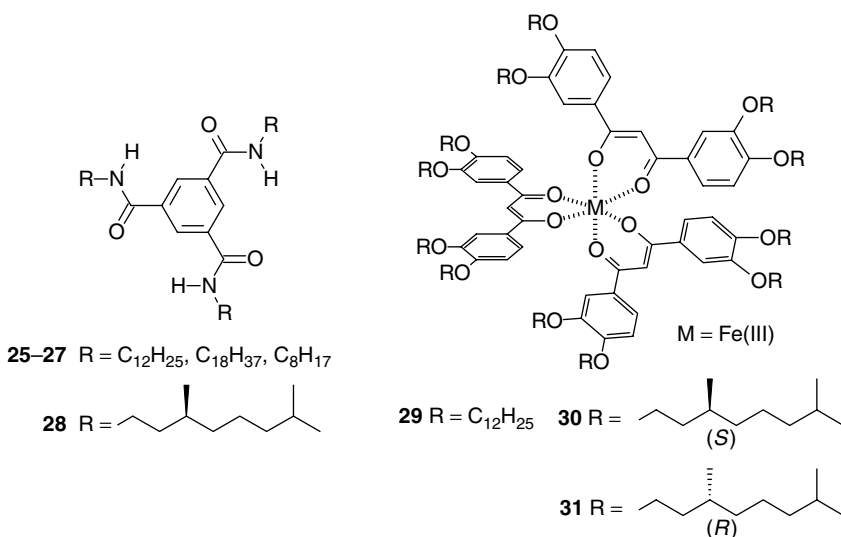


revealed that in the solid state the molecules form columnar hexagonally ordered mesophases. Quadruplet splitted signals are observed in the X-ray diffraction patterns of all compounds, whether chiral or achiral, when the columns in the mesophase were aligned by shearing. This splitting is due to the twist induced into the column by the nonperpendicular positioning of the three wedges of the aromatic core with respect to the columnar axis (Figure 6.3). In analogy with DNA,²³ this splitting indicates the presence of a pitch in the columns and thus that the molecules stack into helical columns. This result was further verified by circular dichroism (CD) spectroscopy on the chiral solid. Whereas the mesogenic state arising from the achiral molecules is CD silent, the liquid crystalline state of chiral **22** showed a strong Cotton effect for the chromophore of the core. In addition to the propellerlike arrangement of the molecules, intermolecular hydrogen bonding also plays a prominent role in the positional order of the wedges within the helical columns. The role of the alkyl tails in this system is limited. The replacement of these aliphatic tails by glycol chains (**23** and **24**) does not influence the helical arrangement of the molecules within the columns. Compounds **23** and **24** similarly formed columnar mesophases with helicity in the columns.^{28,29}

It might be good to point out at this stage that although compounds **19–21** are achiral on a molecular basis, the supramolecular columns they form are

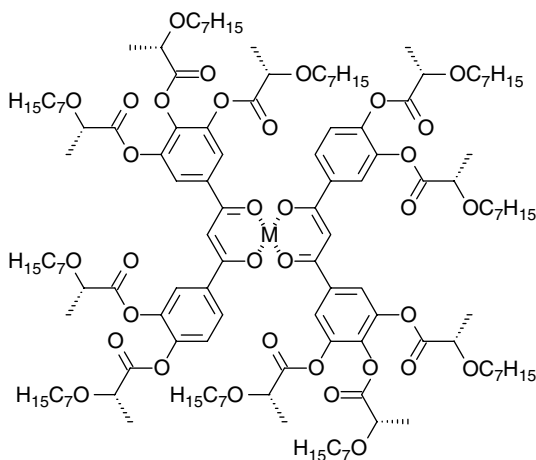
helical. The absence of molecular chiral information in **19–21** results in these supramolecular columns being of both left- and right-handed nature, overall yielding a racemic mixture. The chiral information of compound **22**, which is located in the side chains, biases the helicity of the columns and makes them homochiral. It is therefore good to note the difference we have to make in this chapter between chiral *versus* achiral and racemic *versus* homochiral. Whereas on a molecular level we usually deal with either achiral or chiral molecules, on a supramolecular level we often have to refer to racemic or homochiral structures, due to the intrinsic helical nature of the architectures. However, if the supramolecular columns formed by the individual achiral building blocks are nonhelical in nature, they are achiral as well.

Positional ordering by a threefold intermolecular hydrogen bonding network has also been observed for another, more simple, class of C_3 -symmetric molecules (**25–28**). The molecules which consist of only one aromatic ring functionalized with three amide groups were observed to form helical columns.^{30,31} The molecules arrange themselves in columns via arene–arene interactions of the aromatic cores and, more importantly, via threefold intermolecular hydrogen bonding as proven by X-ray, infrared, and CD spectroscopy.^{32,33} As a consequence of the benzenes stacking at a distance of ca. 3.5 Å, the longer intermolecular hydrogen bonds (~4.2 Å) have to rotate out of the plane, thus inducing helicity in the columns. For the achiral compounds **25–27**, this results in the formation of a racemic mixture of left- and right-handed columns, whereas for chiral **28**, all the columns have a preferred helicity due to the chirality bias imparted by the side chains.



Trzaska and co-workers showed a similar propeller mechanism for the formation of helical columns from disclike metallomesogens (**29–31**).³⁴ These metallomesogens also have C_3 symmetry and **30** and **31** are provided with chiral side chains. In the hexagonal columnar mesophase these chiral side chains induce a Cotton effect in the chromophore of the helically arranged core. Heating the mesophase to the isotropic liquid results in the disappearance of the Cotton effect because of the loss of helical order. This effect illustrates the need for the molecules to be positionally ordered in order for the side-chain chirality to be transferred to the supramolecular column.

A helical arrangement within columns was also found for other metal β -diketonate complexes provided with chiral side chains (**32**) by Serrano and co-workers.^{35,36} These compounds form rectangular columnar mesophases with helical order within the columns. A spin-coated sample of **32** showed a positive exciton-splitting signal in the CD spectra, which was interpreted as a left-handed (*M*) helix. Annealing of the film resulted in much higher optical activities and a shift of the absorption maxima. The observed optical changes clearly point to a chiral organization of the columns in the mesophase.



32 M = VO(IV), Cu(II), Pd(II)

Nuckolls and Katz have synthesized discotic liquid crystalline molecules in which the core is a helix in its own right.³⁷ Nonracemic helicene **33** was found to assemble into a columnar mesophase in which the helicenes stack on top of each other. CD spectroscopy showed a strong increase of the Cotton effect upon going from the molecularly dissolved state to the aggregated state, exhibiting an amplification of chirality. These helical columns give rise to a strong expression of chirality because the intrinsic shape of the helicenes

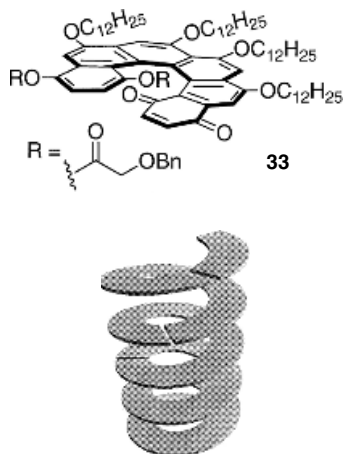
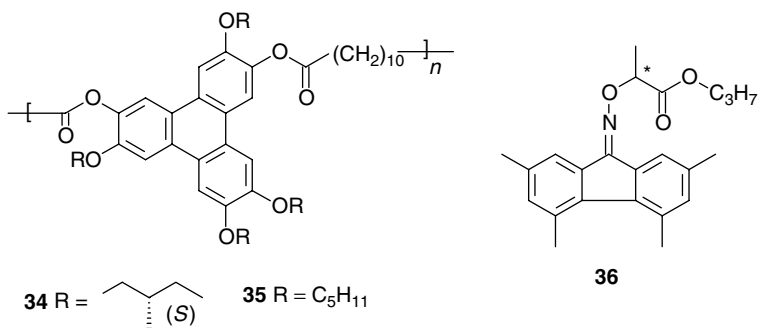


Figure 6.4 Graphical representation of mode of association of helicene **33** into helical columns. (Katz, T. J. *Angew. Chem. Int. Ed. Engl.* **2000**, *39*, 1921–1923, reproduced by permission of John Wiley & Sons, Inc.)

generates a tight “intertwined” fit (Figure 6.4). These chiral discotic systems have been proven to be extremely promising materials for second-order nonlinear optics due to their high chirality expression. They form highly organized Langmuir–Blodgett films in which the second-order nonlinear optics (NLO) susceptibility is approximately 30 times larger for the nonracemic material than for the racemic material with the same chemical structure.³⁸

3.2.2 Polymer Backbone–Controlled Helicity

Green and co-workers³⁹ were the first to demonstrate the use of a polymeric backbone for the positional locking of flat discotic molecules. They showed that polymer **34**, which possesses covalently attached chiral triphenylenes, folds into a helical polymer in which the side chains induce the helical bias.³⁹ The polymeric backbone is necessary to obtain a precisely ordered helix because without it, the triphenylenes would simply rotate around their stacking axis. Remarkably, the backbone is still long and flexible enough to allow for the incorporation of electron acceptors between the chiral triphenylenes. It was nicely demonstrated that incorporation of chiral electron acceptor **36** in achiral polymer **35** resulted in a helical bias of the columns. These results indicate that the achiral polymer intrinsically forms helical columns. Incorporation of a chiral molecule modifies the energy difference between the two helical forms, resulting in the preference of one, which is in turn expressed in a Cotton effect.



More recently, it was shown that helical self-assembled columns can also be formed via cooperative stacking of hydrogen-bonded pairs.⁴⁰ Self-complementary hydrogen bonding molecules were provided with aliphatic or glycol chains and linked via a spacer (**37**–**40**). These molecules dimerize via quadruple complementary hydrogen bonding forming a large disc which is connected to two other discs, above and below, via the spacers. In this way a supramolecular polymer is formed. The discs stack on top of each other in a helical fashion since the linker prevents free rotation but is of a long enough length to allow a twist in the stacking of the dimers (Figure 6.5). The chiral nature of the side chains is what induces a preferred handedness in the overall helix.

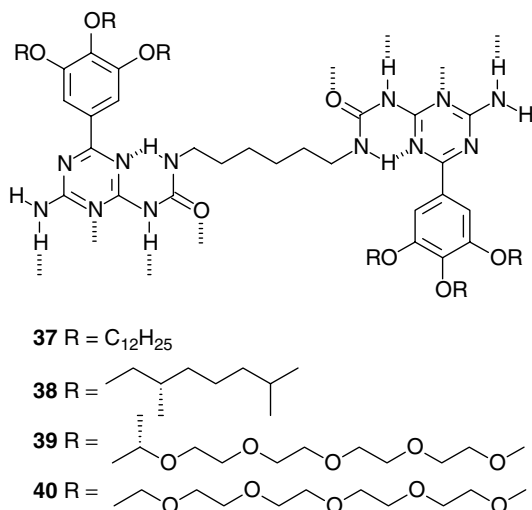


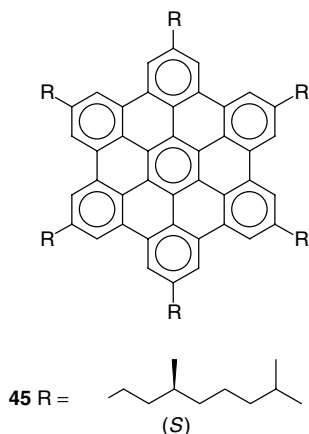


Figure 6.5 Graphical representation of polymerization of **37**–**40** into helical columns.

3.2.3 Side-Chain Packing

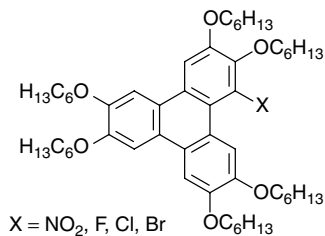
As mentioned earlier, the first example of a chiral columnar mesophase was observed for a chiral triphenylene in 1982.¹² Achiral analogs of this triphenylene do not display any helical arrangements, thus the chiral side chains must induce the homochiral helicity via packing effects. Spiess and co-workers have shown for chiral triphenylene **41** that steric effects, due to the out-of-plane conformation of the ester, have a strong, stabilizing influence on the intermolecular interactions and hinder rotation of the molecules.^{41,42} Similarly, it has been shown that chiral centers present in the side chain of phthalocyanines induce chirality in the mesoscopic system, even though the phthalocyanines normally form only nonhelical columns. Cho and Lim described in 1988 the synthesis of chiral phthalocyanine **42**⁴³ and showed that the chirality present in the molecule not only lowered the melting temperature of PcH_2 's but also that the overall mesomorphic behavior of the discotic liquid crystal had changed with respect to the achiral compound. The authors observed a cholesteric-like texture in which a transition from a platelet (blue phase) to a fan-shaped texture was observed.

Van Nostrum and co-workers first published evidence for a chiral superstructure in the discotic mesophase of chiral phthalocyanines in 1993.⁴⁴ Homochiral phthalocyanine **43** was compared with its racemic analog **44**. Whereas **44** showed a normal Col_{ho} phase and did not form helical columns, the homochiral side chains of **43** gave rise to a helical packing of the discotics



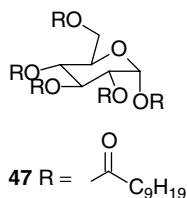
3.3 Discotics with Chiral Core

Praefcke et al.⁴⁷ and Boden et al.⁴⁸ have both synthesized triphenylene derivatives with halogens attached to the core (**46**). It was assumed that the resulting chirality would express itself more strongly than chirality present in the side chains. These halogenated compounds could be readily modified to give the hepta-alkylated triphenylenes; however, in spite of calculations which revealed that the triphenylene core indeed becomes helical, no expression of the helicity at the mesoscopic level could be achieved.



46

Discotic liquid crystals based on carbohydrates are intrinsically chiral due to the chiral nature of their core.^{49,50} Numerous discotic liquid crystals derived from these mesogens have been reported; however, the expression of chirality in the subsequent mesophases has only rarely been seen. An example of the latter is the α -anomer of penta-*O*-decanoylglucopyranose (**47**), which forms a discotic mesophase in which the molecules pack helically in the columns

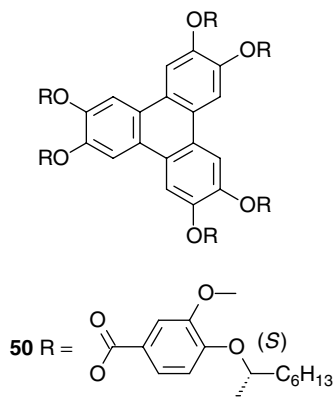
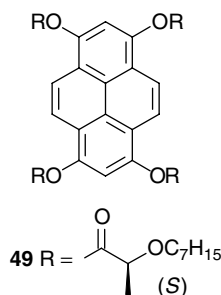
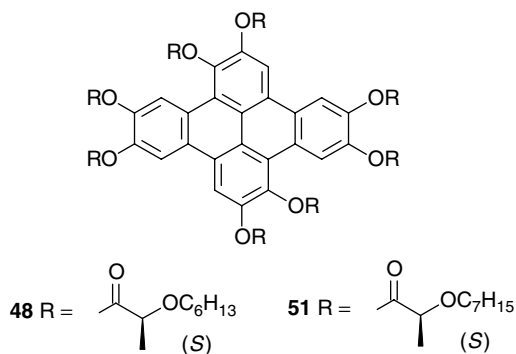


as suggested by X-ray diffraction experiments.⁵¹ Pyrene added as a guest to **47** showed a liquid-crystalline-induced circular dichroism effect, indicating a helical arrangement of the sugar molecules in the mesophase. The helicity of this system was found to be extremely sensitive to changes in the alkyl chains. Even slight modifications in the chains or the use of the β -anomers resulted in the loss of helicity.

3.4 Ferroelectricity

3.4.1 Flat Discotics

In 1981, it was predicted that ferroelectricity should be possible in rectangular columnar mesophases if the molecules themselves are chiral.⁵² In such phases, each column has a spontaneous polarization perpendicular to its axis. The phase is ferroelectric whenever the polarizations do not neutralize each other. In 1984, however, it was suggested that steric hindrance between the columns would prevent ferroelectric switching.⁵³ This apparent contradiction was resolved by Bock and Helfrich in 1992, who synthesized a ferroelectrically switchable columnar liquid crystal based on a dibenzopyrene core (**48**).⁵⁴ They first showed that the previously studied chiral triphenylene **2** indeed does not show an electro-optical effect. However, by placing the stereocenter one methylene unit closer to the core, a small switching effect of one degree was observed. It was concluded that although the columns are tilted, their polarizations are canceled out. The tilt-induced molecular dipole moment is not strong enough to enable a high electric field to rotate the tilt direction of the columns. A new dibenzopyrene was subsequently designed (**48**), in order to obtain mesophases with a large tilt-induced dipole moment. The dibenzopyrene **48** displayed a columnar phase from 84 to 124°C. At 90°C the “Maltese crosses” observed under the polarization microscope, switched between + and -20° , when a field strength of $8 \cdot 10^4$ V/cm was applied. Partial switching, a novel feature of ferroelectric switching, was also shown to be possible since the transition from one preferred state to the other is slow. The same authors reported similar features for a chiral pyrene (**49**).⁵⁵ More recently, chiral triphenylene derivatives (e.g., **50**) were also reported to exhibit ferroelectrically switchable columnar mesophases or a cholesteric blue phase.⁵⁶ Furthermore,

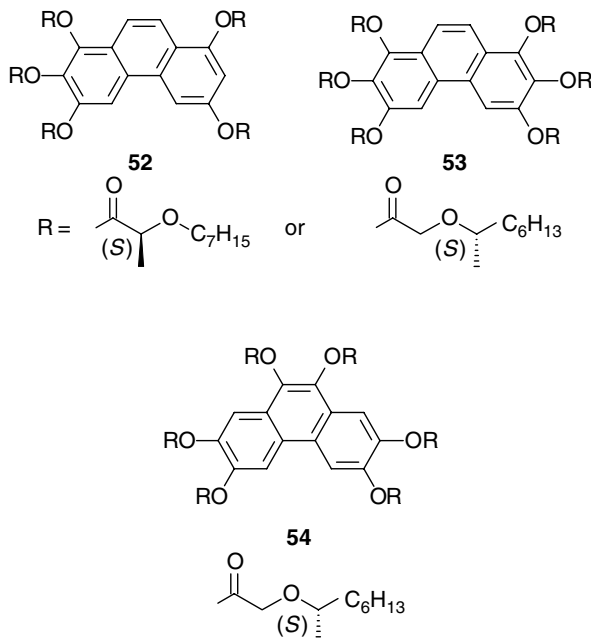


adding dodecane could reduce the viscosity of the system, thereby decreasing the response time of the system.⁵⁷ With these lyotropic mesophases switching at temperatures as low as room temperature was even possible.

A homologous dibenzopyrene compound **51**, which differs from **48** only in side-chain length, was studied by the same authors and shown to have two ferroelectric phases.^{58,59} The coexistence of the two columnar phases depended

on the applied electric field. Compound **51** was furthermore investigated for electromechanical effects.⁶⁰ It was shown that the electromechanical responses are orders of magnitude weaker than those seen for SmC* liquid crystals. It was proposed that this decrease in response is due to the sample breaking up into small domains during switching. Dibenzopyrene **51** has also been dispersed in a polymer film.⁶¹ Analysis of these films indicated that the molecules self-assemble within small cavities present in the polymer. By shearing the films, the columns could be uniformly oriented and bistable, and linear switching effects were observed. In addition the field-induced orientation could be stored by cooling the system below the melting point.

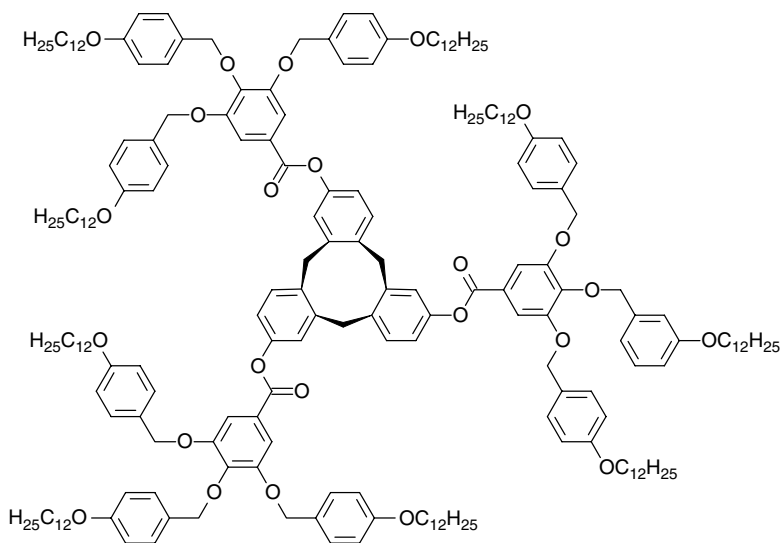
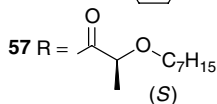
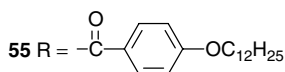
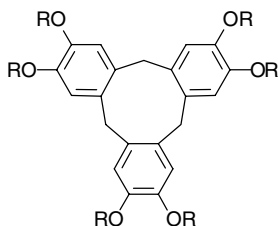
Another class of molecules showing ferroelectric switching in the columnar phase is based on chiral phenanthrenes (**52** and **53**). Scherowsky and Chen showed that penta- (**52**) and hexa- (**53**) substituted chiral phenanthrenes exhibit tilted columnar phases, displaying a linear electro-optical effect.⁶² By changing the substitution pattern, they obtained a phenanthrene derivative (**54**), which no longer formed tilted phases but could be induced to tilt by the addition of **53**. The resulting mixed mesophase also exhibited ferroelectrical switching.⁶³ Together with Levelut the authors discussed the electro-optical behavior of **54** on the bases of several structural features.⁶⁴ They showed that the behavior they observed could be linked to the several possible different orientational geometries in a triangular lattice of columns.



Finally, ferroelectricity has been shown for columnar metallomesogens.³⁵ Serrano and co-workers have shown that metal β -diketonates, provided with chiral side chains (e.g., **32**), form helical columns (vide supra), which can also be switched under an alternating electric field.

3.4.2 Cone-Shaped Molecules

The first reports on the liquid crystalline properties of pyramidal or cone-shaped materials appeared in 1985.⁶⁵ It was discovered that compounds with



56

a rigid pyramidal core are able to display mesomorphism of the columnar type. Even though the initially studied molecules lacked centers of chirality, it was recognized that the mesophases formed by this type of molecules might also exhibit ferroelectricity. The core of the molecule has an overall electric dipole moment and stacking of the molecules in a column is most favored when the dipoles are parallel, giving rise to a mesoscopic electric dipole. Depending on the ordering of the columns, this would result in either paraelectric, ferroelectric, or antiferroelectric mesophases. It was then shown by Levelut et al. that a more densely substituted cone (**55**) could give rise to a helical structure of the columns.⁶⁶ The columns themselves, however, were arranged in an imperfect three-dimensional lattice and no intercolumnar correlation between the stacking of the cores existed. As a consequence the observed mesophase was not ferroelectric. Malthete and Collet further developed the system and synthesized a chiral cyclotribenzylene (**56**), in order to study the racemization rate of the cones in the columnar mesophase (i.e., the rate with which the cone inverts).⁶⁷ The rate of racemization was found to be highly dependent on the temperature. At 3°C below the isotropization temperature the rate of racemization was estimated to be ca. 4 min, starting from enantiomerically pure cones. It was, however, not until 1997 that indications of ferroelectricity in columnar mesophases of pyramidal molecules were observed.⁶⁸ The tris-benzocyclononene core was functionalized with six chiral side chains (**57**) and a homeotropic alignment of the columnar phase was achieved by cooling the film in the presence of an electrical field. For these films a transient optical effect was observed upon electric field reversal. To date, however, no examples are known of unambiguous ferroelectricity in pyramidal liquid crystals.

4 CHIRAL LYOTROPIC DISCOTIC LIQUID CRYSTALS AND SELF-ASSEMBLY OF CHIRAL DISCOTICS IN DILUTE SOLUTION

Self-assembly of molecules in solution is an active field of research in supramolecular chemistry.⁶⁹ Depending on the nature of the interactions and the shape of the molecules involved, a large variety of architectures can be formed. Structures ranging from random coil polymers to intertwined helices and discrete multimolecular structures have been obtained. A typical feature of these assemblies is the dynamic behavior of the molecules within the aggregates. The molecules can migrate in and out of the aggregates very fast as is similar to micelles, but they can also largely exist within the assemblies, as in vesicles. The molecules located in the aggregates may still be mobile, or have some positional order. Supramolecular polymers, that is, polymers of which the monomeric units are held together by directional and reversible noncovalent interactions, are a special class of self-assembled systems. Discotics fall into

this class, as their assembly is a one-dimensional process yielding polymeric architectures with a columnar or rodlike shape.

Compounds that form discotic liquid crystals in the bulk are highly suited for the formation of supramolecular polymers in solution because of the strong π - π interactions that are possible between their cores. These interactions make them prone to aggregate in, for example, polar or apolar solvents, forming rod- or wormlike polymers. Due to the polarizability of the planar aromatic system and the good intermolecular contacts, attractive intermolecular stacking interactions occur, which can be further strengthened by additional solvophobic forces in the case of poor solvents. In apolar solvents π - π stacking interactions best describe the association, although in very apolar solvents solvophobic effects also play a role. In polar solvents like water and alcohols, the association merely comes from a hydrophobic/solvophobic effect of the apolar core. In this chapter we will use the general term arene-arene interactions, but it should be noted that solvophobic effects could be stronger than these π - π stacking interactions.

Discotic mesogens are the only type of mesogens able to form linear stacked architectures in dilute solution. Other types of mesogens can have intermolecular interactions of the same order of magnitude, but these are operative in several directions. This gives rise to gels at high concentrations, that is, uncontrolled growth of the aggregates, whereas at lower concentrations the intermolecular interactions generally are too weak to generate well-defined polymeric architectures. In discotics, the interdisk stacking interaction is several orders of magnitude stronger than the intercolumnar interactions, due to the phase separation induced by the side chains. In general, the best ordered structures are obtained for discotics that have strong and specific intracolumnar interactions, either via a large aromatic core or via interactions such as hydrogen bonding. The combination of two or more of such interactions leads to the formation of highly ordered columns. Only at higher concentrations do the intercolumnar interactions become prominent and superstructure formation or gelation occurs, followed by the generation of a thermotropic liquid crystalline phase. An illustrative picture displaying the self-assembly of discotic molecules into supramolecular polymers is given in Figure 6.6.

In this section we will address the issue of chirality in self-assembled discotic molecules in dilute solution. We will show how and why chirality is expressed at the mesoscopic level of the self-assembly and make clear that unique information concerning expression of chirality can be gathered from assemblies of discotics in solution.

4.1 Self-Assembly of Chiral Discotics

With respect to the self-assembly of chiral discotics into columns, two different cases can be distinguished, differing in the order that is present in the

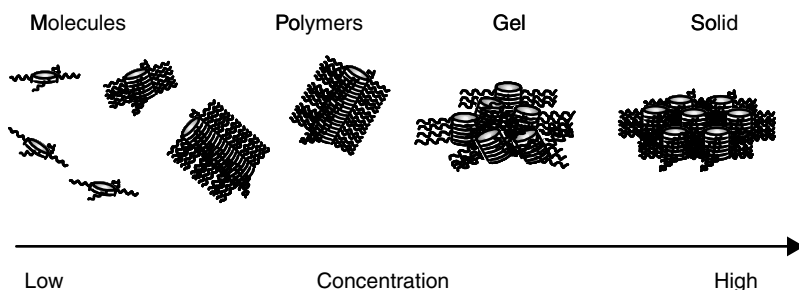


Figure 6.6 Self-assembly of discotics. Different stages of aggregation are given as function of concentration.

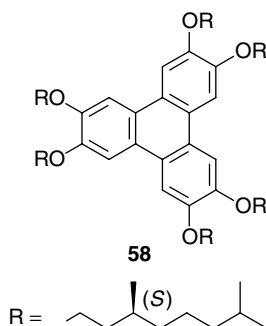
supramolecular columns. First of all, the chiral discotics can self-assemble in columnar aggregates that lack mesoscopic chirality. For these aggregates the molecular chirality, being in the side chains or the core, is not expressed at the supramolecular level, due to the absence of specific intermolecular interactions. The second case involves aggregates in which the chirality of the molecules is transferred to the mesoscopic level. Here a subdivision can be made in cooperative and noncooperative transfer of the molecular chirality. In the latter case the molecular chirality is only expressed in the specific chiral molecule involved and is not transferred nor amplified to neighboring molecules. In the case of the cooperative expression of the molecular chirality, interactions between the molecules in the column are present that allow the molecular chirality of one single molecule to be expressed in many molecules of the supramolecular assembly. The chirality is transferred to neighboring molecules, resulting in cooperative amplification of chirality from a molecular level to a mesoscopic level.

4.1.1 Self-Assembly of Chiral Discotics Without Expression of Chirality

It has been shown frequently that without the presence of strong intermolecular interactions, discotic molecules are highly mobile in the liquid crystalline state.¹ They undergo both lateral as well as rotational translations, resulting in the absence of positional order. Similarly, such discotics also freely rotate in the columnar aggregates they form in solution. This lack of positional order in the columns accounts for the absence of chiral or helical supramolecular order. We will demonstrate this characteristic using results obtained for triphenylenes.

Using small-angle neutron scattering (SANS), it was shown that alkoxy-substituted triphenylenes associate in deuterated hexadecane.⁷⁰ At low concentrations small aggregates are formed and at higher concentrations (10^{-3} M)

rodlike aggregates. The molecules thus form columnar supramolecular polymers due to the stacking of the aromatic cores. The intercore distance was determined to be $\sim 6 \text{ \AA}$, a value that is significantly larger than the stacking distance of $\sim 3.5 \text{ \AA}$ found in the liquid crystalline state, indicating that the molecules are loosely stacking. The formation of columns by triphenylenes in dodecane was also visualized using optical techniques. Increase of the concentration of a solution of an alkoxy-substituted triphenylene resulted in a broadening of the ultra violet–visible (UV-Vis) spectrum and an increase of the absorbance.⁷¹ Evidence for the “loose” stacking of the molecules in the columns is the absence of a Cotton effect as was shown for dodecane solutions of triphenylene **58** provided with chiral alkoxy side chains.⁷² This demonstrates that the chirality of the side chains is not expressed in the supramolecular assembly, a phenomenon typical for molecules arranged in an unordered assembly. Due to the absence of specific intermolecular interactions, the triphenylenes are highly mobile in the columns as well as in the liquid crystalline state and undergo both rotation and lateral translation.



For the triphenylenes discussed above, the only interactions that are involved in the formation of the columns are the arene–arene interactions which, although being strong, are generic and do not have positional information. Additional specific interactions are necessary to keep the molecules positionally ordered with respect to each other and to create chiral columns, as will be discussed in the next sections.

4.1.2 Noncooperative Self-Assembly into Chiral Columns

Supramolecular chirality can be introduced in columns of discotic molecules by using specific interactions, apart from the arene–arene interactions. To achieve this, a study with chiral dopants has been performed.⁷³ Hexa-*n*-hexyloxytriphenylenes were mixed in dodecane solutions with a variety of chiral electron-deficient dopants and the resulting charge transfer complexes

were found to be CD active in the region of the charge transfer bands. However, only the largest electron acceptor, that is, the one derived from (-)-menthol 3,5-dinitrobenzoate, gave rise to an induced CD effect in the chromophore of the triphenylene molecule. Apparently, only the bulky menthol derivative is capable of inducing a helical twist into the column because of the steric intercalation of the menthol group with the alkyl side chains of the triphenylene (Figure 6.7). In mixtures with smaller chiral electron acceptors, the molecules are able to maintain their rotational freedom within the column. These results indicate that the positional locking of the triphenylenes within the columns is a noncooperative process and that, even though chiral supramolecular columns can be built up from triphenylenes, these molecules alone do not give rise to helical architectures.

A second example of homochiral columns formed by discotics are the complexes of tetrazoles (**59** and **60**) with 1,3,5-tris(4,5-dihydroimidazol-2-yl)benzene (**61**).⁷⁴ Four molecules self-assemble to give a supramolecular disc and these discs subsequently form columns in nonpolar solvents. Chiral discs were obtained from the self-assembly of the chiral tetrazole (**60**) with **61**. The chirality of the side chains was found to induce a bias in the helicity of the supramolecular assembly. “Sergeants-and-soldiers” measurements⁷⁵ were performed for which chiral (**60**) and achiral (**59**) molecules were mixed. The experiments showed no amplification of chirality, thus revealing that in these systems chirality transfer from the side chains into the column is

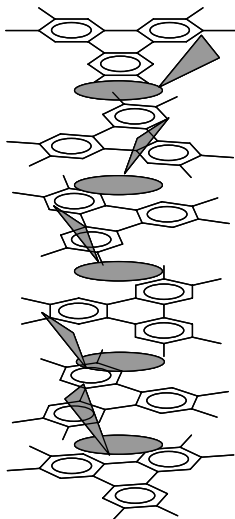
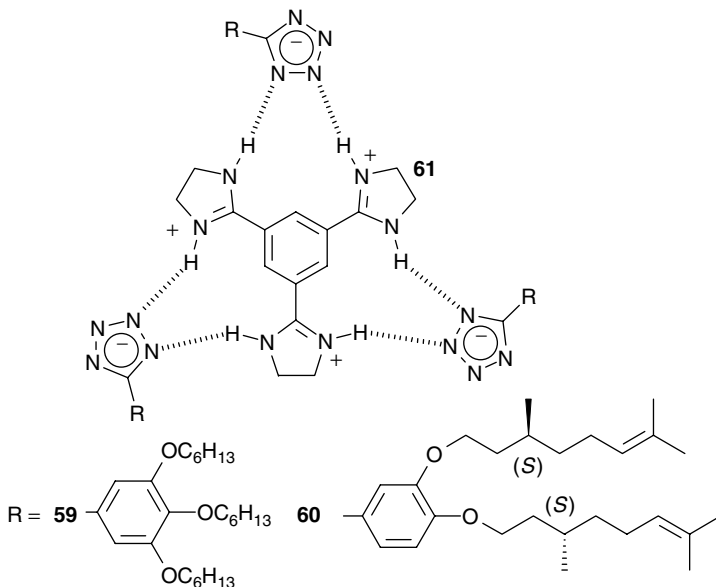


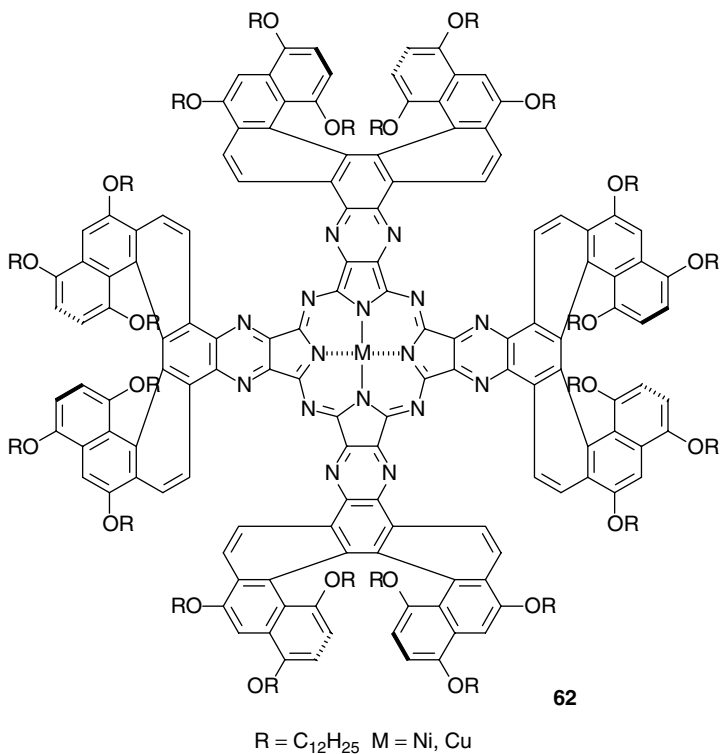
Figure 6.7 Helical columns based on a donor–acceptor system of alkoxytriphenylenes and menthol 3,5-dinitrobenzoates.

a noncooperative process and that columns only become completely helical when exclusively molecules with chiral side chains are used; molecules with achiral side chains form nonhelical columns.



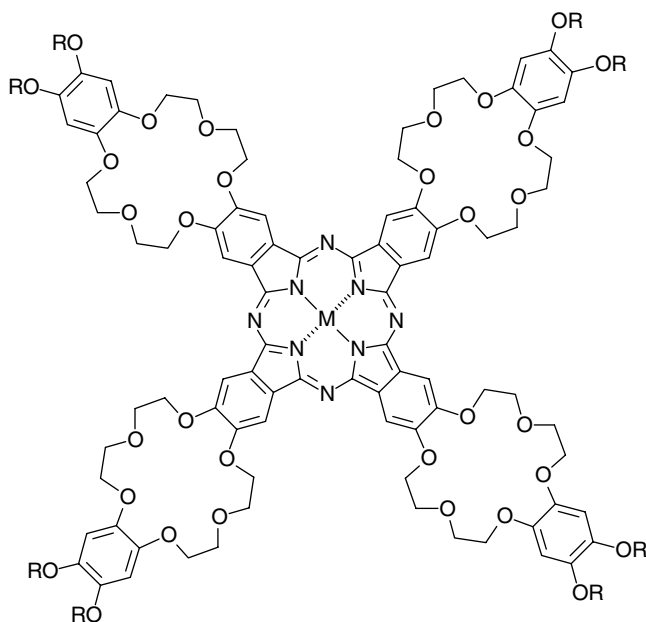
Metal phthalocyanines functionalized with four helicenes (**62**) have also been reported to form chiral columnar aggregates.⁷⁶ In chloroform solutions of these metal phthalocyanines aggregation into columns occurred upon addition of ethanol, as was observed by UV-Vis spectroscopy. CD spectroscopy revealed that the chromophores within the columnar aggregates are in a chiral environment, implying that the chirality of the peripheral helicenes has been transferred to the supramolecular aggregates. These phthalocyanines stack with a typical intermolecular distance of 3.4 Å, and calculations have indicated that to allow this distance the two phthalocyanine moieties have to be rotated because of the bulkiness of the helicenes. It can easily be imagined that a phthalocyanine provided with both *R* and *S* helicenes cannot stack in such a defined manner because of the steric interactions between the nonconform helicenes.

Phthalocyanines provided with crown ethers and chiral alkyl side chains (**64**) have also been reported to self-assemble in nonpolar solvents.⁷⁷ These molecules form helical columns as could be deduced from the presence of a Cotton effect upon aggregation. To investigate the expression of chirality at the mesoscopic level, sergeants-and-soldiers experiments⁷⁵ were performed. Chiral phthalocyanine molecules **64** were used as the sergeants and achiral



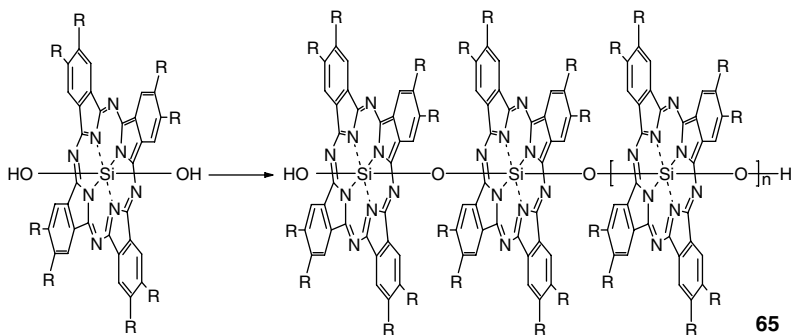
molecules **63** as the soldiers. The experiments showed no amplification of chirality. In fact, it appeared that at least two sergeants have to stack next to each other in order to give rise to a helical packing, pointing to an anticooperative effect. These results show that the achiral phthalocyanines **63** stack without an intrinsic helicity (achiral columns are present) and that the chiral side chains of **64** introduce a helical perturbation in the stacking of the chiral molecules. The helicity of the columns could be “turned-off” by the addition of potassium salt. The potassium ions bind to two crown ethers of two phthalocyanines and overrule the twist imposed by the chiral side chains to give a nonassociating achiral dimer (Figure 6.8). Interestingly, in the covalent columnar polymer **65** the chirality remains present upon the addition of potassium ions. As the single phthalocyanines break up into dimerized species upon addition of salt, the polymer cannot, which results in a staggered conformation of the monomeric units in the latter and a lowering of the repulsive cationic interactions. This staggered conformation increases the Cotton effect.

Already at very low concentrations phthalocyanine **64** forms gels made up of long left handedly twisted fibers as seen by electron microscopy. The



M = 2H

63 R = C₁₀H₂₁ **64** R = (S)



chiral discotics initially stack to form right-handed chiral columns that subsequently further self-assemble to form left-handed supercoils (Figure 6.8). The large phthalocyanine surface induces self-assembly, while the chiral tails induce a preferential twist in the aggregate due to steric interactions. The inversion of the chirality upon aggregation of the fibers can be readily understood by the following model. A fiber with a right-handed twist (Figure 6.9a) has a “grooved” exterior, and, in order to maximize the van der Waals contact

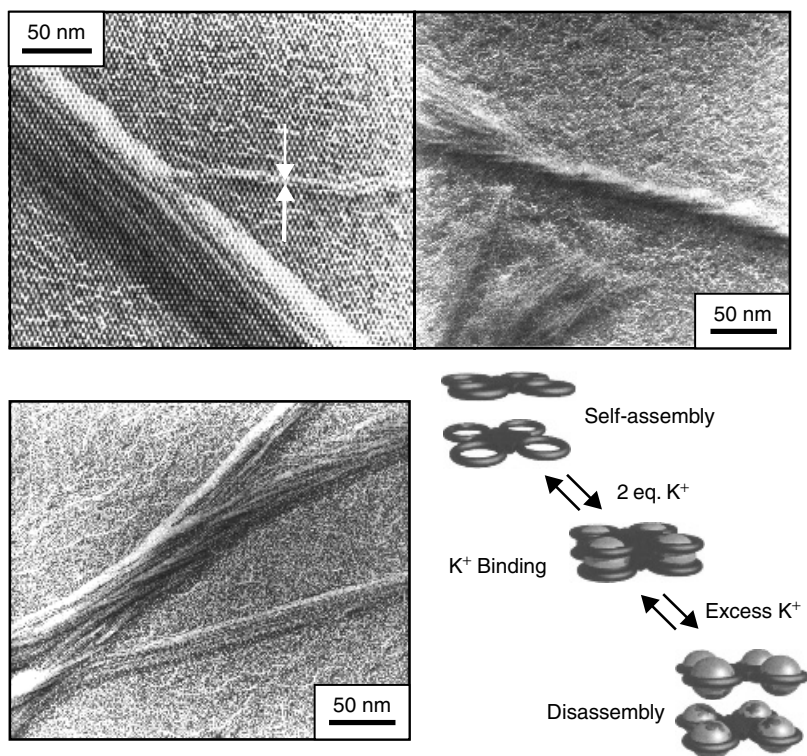


Figure 6.8 Phthalocyanine **63** self-assembles in chloroform to give bundles of micrometer length fibers. Single fibers have diameter of 50 Å (highlighted between arrows) and can be envisaged as nanowires (top left). Chiral derivative **64** forms left-handed super helices (top right) due to chirality within side chains. This chiral expression can be “turned-off” by addition of K⁺ ions, which bind within the crown-ether part of the molecule, forcing the phthalocyanines to be stacked directly on top of each other, resulting in straight wires (bottom left).

between two fibers twisted around each other, each of them has to bend in order to fit into the groove of the other fiber, as shown in Figure 6.9a. The tilting angle between the two fibers is called the *inter axial, crossing, or crossover* angle. If only steric interactions are taken into account, this angle is double the angle β of the groove with respect to the stacking axis, which in turn depends on the diameter D of the molecule, and the staggering angle ϕ and the stacking distance d between two monomers. From Figure 6.8b, the crossing angle α is plotted as a function of the staggering angle ϕ according to this equation, with $D = 60 \text{ \AA}$ and $d = 3.4 \text{ \AA}$. In this graph, three possibilities arise, indicated by the dotted lines. At staggering angles smaller than 6.5° , the crossing angle is smaller than 90° , which results in a superhelix with the

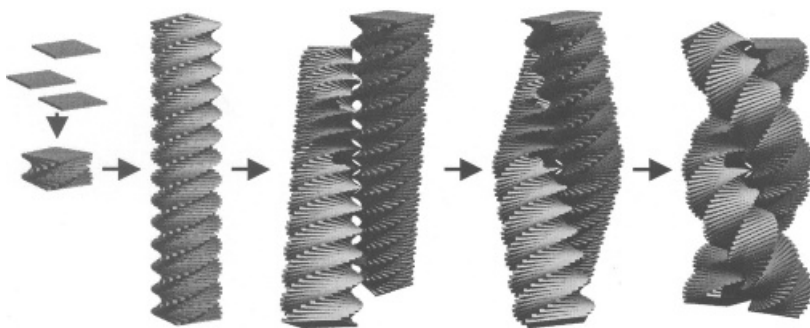


Figure 6.9 Schematic representation of hierarchical self-assembly process for chiral phthalocyanine **64**. Phthalocyanine molecules self-assemble into helical columns with right-handed screw sense (left). These right-handed helices subsequently aggregate to give left-handed super-helices.

same handedness. At larger staggering angles, the crossing angle exceeds 90° , and the superhelix will be of opposite handedness. When the crossing angle is close to 90° (at the intersection of the dotted lines), the superhelix can go either way. In other words of all staggering angles available, only about 14% result in a superhelix with the same handedness.

As mentioned above, the helicity of this aggregate can be “turned off” by the addition of potassium salts. Coordination of potassium ions to the crown ether rings results in face-to-face stacking and unwinding of the helical aggregate. The twist imposed by the chiral side chains is overruled by this stronger ion–dipole interaction, locking two molecules to each other in such a way that they are exactly on top of each other without a twist. The resulting complex forms linear fibers. Similarly, the aggregates formed by the achiral counterparts (**63**) are not helical because the phthalocyanines stack intrinsically nonhelical.⁷⁸ The fact that already at very low concentrations fibers and gels are formed by these phthalocyanine dimers points to a very high association constant. The large energy gain upon self-assembly possibly overrules the much weaker side-chain interactions for transfer of chirality, as it prevents a helical arrangement of the dimers.

A final example of noncooperative formation of chiral columns is found in the aggregation of hexakis-porphyrinato benzenes (**66**). Six porphyrins are arranged in three pairs giving rise to a propeller-shaped molecule (Figure 6.10). These molecules are molecularly dissolved in chloroform but aggregate upon the addition of a nonsolvent such as methanol, resulting in a red shift of the UV–Vis absorption bands and the detection of an intense Cotton effect (G value = 0.09). In order to investigate whether the columns formed by **66** are intrinsically helical due to the propeller shape of the molecules or whether the aggregation is a noncooperative process in which the propeller structure

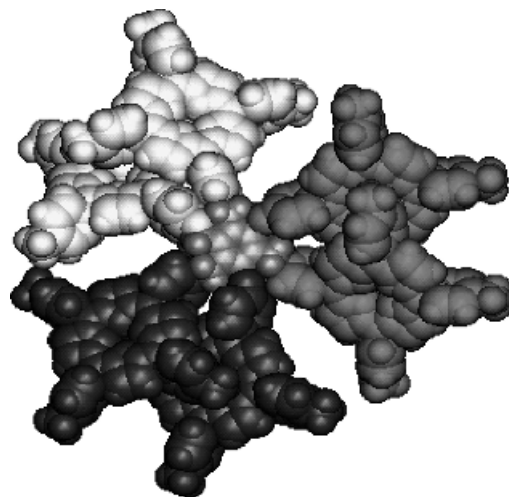
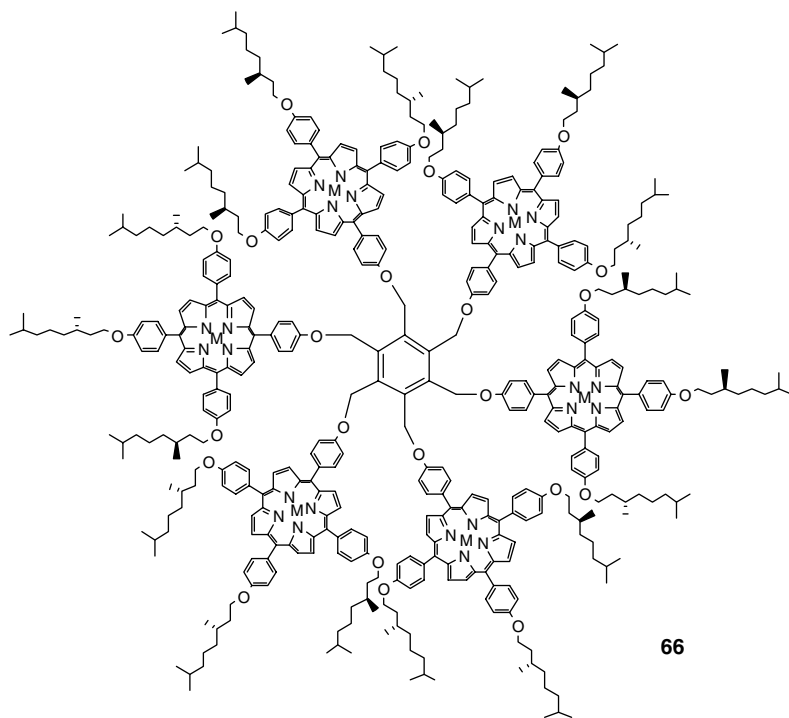


Figure 6.10 Chiral hexakis-porphyrinato benzene compound **66**, which possesses propellerlike structure and can self-assemble to form helical arrays.

is not maintained in the aggregates, sergeants-and-soldiers experiments were performed by mixing **66** with its achiral analog possessing C₁₆ alkyl tails. Similar as for the chiral phthalocyanines discussed above, a negative bias of the chirality was found, indicating that the chiral molecules need to interact with themselves to achieve chirality at the mesoscopic level; it furthermore proves the absence of a cooperative effect.

4.1.3 Cooperative Self-Assembly into Chiral Columns

Molecules that are most suited for the creation of helical architectures are those that have a large aromatic core, allowing for stacking, and in addition to that the possibility of structuring interactions such as hydrogen bonding. The C₃-symmetrical disc-shaped molecules **19–22** feature these requirements.²⁷ These discotic molecules form polymeric structures with a rigid-rod character in very dilute solution (10⁻⁶ M in hexane), due to their large association constant ($K_a = 10^8$ l/mol).⁷⁹ The aggregation of the discs in hexane is a cooperative process; the molecules attain a chiral, propellerlike conformation (Figure 6.3), and the conformation of subsequent discotics is biased toward a propeller with the same handedness. The optimization of the stacking interactions results in a helical column. The chirality placed in the side chains accounts for the formation of homochiral columns via the transfer of the side-chain chirality into the supramolecular helical structure. When chiral and achiral molecules are blended in solution, mixed columns are formed. Surprisingly, these sergeants-and-soldiers⁸⁰ experiments showed that only one chiral disc on, on the average, every 80 achiral discs is enough to bias the helicity of a complete columnar stack into one particular sense (Figure 6.11). This result can be explained by a strong intracolumnar cooperative effect in which the directional hydrogen bonding of the chiral seed molecule is used to orient the subsequent stacking of the achiral discs, leading to a homochiral superstructure. These experiments show that the formation of the helical columns is a highly cooperative process, in which there is a high energetic penalty for helix reversal within the column.

Lateral interactions between the columns arise at higher concentrations resulting in the formation of a lyotropic liquid crystalline phase.⁸¹ Because of the chiral propellerlike conformation of the molecules, the columns have a dipole moment along their axis, which allows alignment and switching of the columns in the gel phase by an electric field. This alignment of chiral discotics has great potential in the design and construction of new devices.

Polar, water-soluble analogs of these molecules (**23** and **24**) have also been studied and have been shown to form helical columns in a variety of polar solvents such as methanol, butanol, acetonitrile, and water, by virtue of solvophobic interactions between the large aromatic cores.^{82,83} A stepwise association process is observed when alcohol solutions of **24** are cooled. The

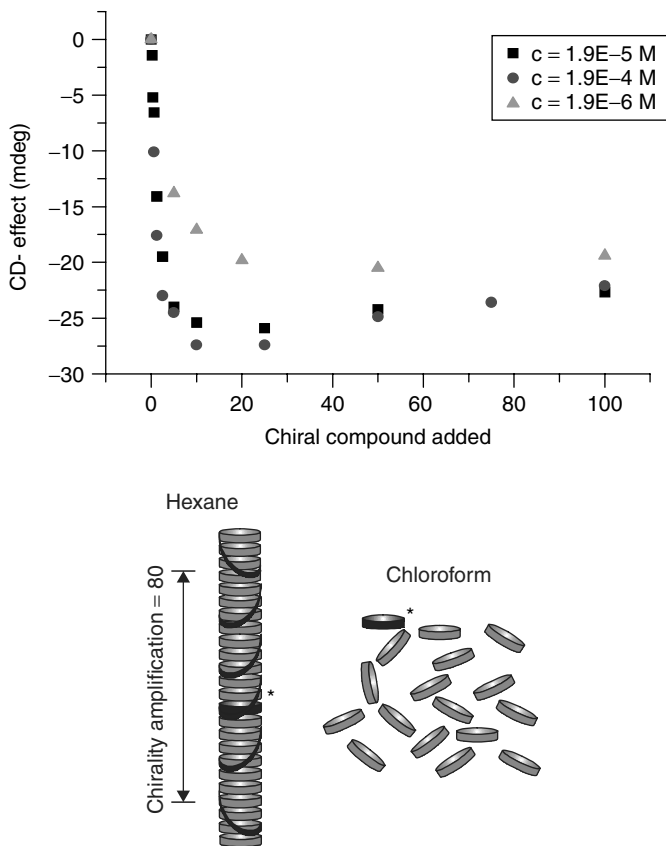


Figure 6.11 (Top) Plot showing chiral induction via sergeants and soldiers experiment, expressed in terms of Cotton effect (mdeg), as function of fraction of sergeants added. At higher concentrations maximum Cotton effect has been reached after addition of only 10% sergeant **22** to soldiers **20**. (Bottom) Graphical representation of columns formed by **22** (*) and **20** in hexane with 80-fold amplification of chirality and molecular dissolved nature in chloroform.

molecules first assemble into achiral columns, which have a small degree of polymerization (DP). This process is governed by the generic arene–arene interactions of the aromatic core. Subsequently, these achiral columns become helical via a phase transition coinciding with a strong growth spurt of the column size rendering a $DP > 1000$ (Figure 6.12).⁸⁴ During this transition specific intermolecular hydrogen bonding interactions arise within the column, ordering the molecules in a helical fashion. In water, the helicity of the columns is lost at higher temperatures, but aggregation is maintained. Due to the increased strength of the arene–arene interactions and lower critical

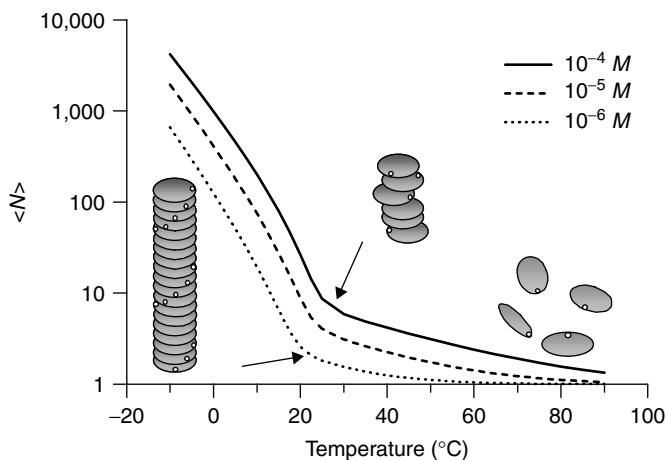


Figure 6.12 Self-assembly process of **24** from single molecules into helical columns via nonhelical intermediates. The average number of molecules, $\langle N \rangle$, participating in one column in *n*-butanol at three different concentrations is given as function of temperature. Arrows mark transition from achiral to helical aggregates.

solution temperature (LCST) of the side chains at higher temperature, long columns remain even at 90°C as proven by SANS. This stepwise growth and increase of order within the column shows great similarity to the self-assembly of the tobacco mosaic virus without the ribonucleic acid strand.⁸⁵

The amplification of chirality within the columns in both water and in *n*-butanol was studied using sergeants and soldiers experiments.^{75,80} In *n*-butanol the average distance between helix reversals in columns containing both **23** and **24** was found to exceed 400 molecules. The long length of uniform helicity results in strong (400-fold) amplification of chirality. In water the helix inversions were found to occur after, on the average, every 12 discs, indicating that the helical order within the columns is highly solvent dependent. Water interferes with the interactions that create the helical order at all temperatures, resulting in a lower energy barrier for helix inversions.

A model, rationalizing the experimentally observed self-assembly data, has been formulated.⁸⁴ In this model the standard theory of linear self-assembly was modified through adopting a two-state model for the molecules in the aggregates. The cooperative transition from achiral to chiral columns could be well described by the Zimm–Bragg theory for the helix–coil transition in polymers. The model provides a description of both the length of the column and the state of helicity as a function of concentration and temperature. Since the two binding strengths in the model can simply be adjusted, it might serve as a general tool for the description of helical columnar systems.

The previously discussed tris-amides **25–28** self-assemble into single columns via hydrogen bonding interactions only.^{30–32} Achiral compounds **25–27** form an equimolar mixture of left- and right-handed helical columns, but the homochiral side chains of chiral discotic **28** introduce an energy difference between left- and right-handed columns and bias the helicity.³³ The chiral columns have a high DP even in very dilute solution (10^{-6} M in hexane), due to their large association constant ($K_a = 5 \cdot 10^8$ l/mol). When chiral and achiral molecules are blended, mixed columns are formed and, surprisingly, only one chiral disc on circa 200 achiral discs is enough to bias the helicity of a complete column of discotics into one helix direction. These results are explained by a strong intracolumnar cooperative effect via directional hydrogen bonding in stacks with a very high DP. At higher concentrations, the length of the helical columns is long enough to gelate the solvent.^{30,31} Lateral interactions between the supramolecular columnar polymers result in the formation of a lyotropic liquid crystalline gel. This process is reminiscent of the behavior of rigid-rod polymers such as polyaramides and poly(γ -benzyl-L-glutamate), which also form lyotropic mesophases at higher concentrations.⁸⁶

Helical columns based on chiral discotics formed by dimerization of two halves have also been studied. Two molecules **67** dimerize via quadruple intermolecular hydrogen bonding resulting in an extended core, which is mesogenic. In apolar solvents such as dodecane, the dimerized molecules stack and form columns.⁴⁰ Within these columns the discotics are rotating freely. As a result the side-chain chirality is not expressed in the supramolecular assembly. When two hydrogen bonding units are connected via a short spacer, a bifunctional molecule **38** is obtained, which is capable of forming hydrogen-bonded, supramolecular polymers in chloroform, in analogy with bifunctional ureidopyrimidinones.⁸⁷ The polymer consists of an array in which discs and spacers alternate and the discs stack in apolar solvents forming long columns. The columns are helical, in contrast to those formed by monofunctional molecules. The presence of a covalent linkage between consecutive layers of the column prevents rotation of the discs. A comparison might be made here to the function of the sugar–phosphate backbone in DNA. The intrinsic helicity of the columns formed by the bifunctional compounds allows chiral side chains to induce a preferred handedness and thus express their chirality in the supramolecular architecture. The induction of chirality in the helical columns is a cooperative process: achiral **37** forms a racemic mixture of helical columns, but their helicity is biased when end capped with monofunctional chiral **67** (Figure 6.13). The columns formed by bifunctional **38** in dodecane are longer than those formed by monofunctional **67**, as could be observed by SANS. This results in an increased thermostability of the lyotropic mesophase in dodecane and is due to the hexamethylene linker covalently connecting two discs.

4.2 Self-Assembly of Guanine- and Pterine-Related Molecules

Impressive work on the self-assembly of chiral discotics has been performed by Gottarelli and co-workers on guanine- and pterine-related molecules.⁸⁸ These molecules organize in lamellae in the solid state^{89,90} but form chiral disc-shaped tetramers in solution via intermolecular hydrogen bonding. The subsequent stacking of the discs into helical columns has been studied in great detail. The system is of interest because of the strong similarities to DNA and other biopolymers.^{91,92}

Oligomeric deoxyguanosines **69** all assemble into columns in water.⁹³ Using SANS, the average length of the columns (DP) of freshly prepared samples was determined to be around 6 nm at a concentration of 1% in D₂O.⁸⁸ Increase of the temperature resulted in the loss of the cylindrical aggregates. When the sodium salt was used, subsequent cooling did not result in the reformation of the cylindrical polymers. In contrast, the potassium salt did allow for reversible self-assembly. The addition of extra potassium salt even increased the DP. It binds to the inner carbonyls of the G-tetramer and stabilizes the tetramer.⁹⁴

The formation of lyotropic liquid crystalline mesophases by a deoxyguanosine derivative in water was reported in 1988,⁹⁵ after which this behavior was also observed for other monomers and oligomers of deoxyguanosine phosphate.⁹⁶ The microscopic textures indicated that cholesteric and hexagonal phases were present at lower and higher concentrations, respectively. The polymeric columns are generated in a hierarchical manner: first a well-defined “barrel” is formed by the assembly of four oligodeoxyguanosine oligomers and then these “barrels” stack on top of each other to give the columns (Figure 6.14).^{88,93} This stepwise self-assembly process was elucidated with the help of CD experiments, which revealed two melting transitions. It was furthermore shown that the formation of the liquid crystalline phase depends on the amount of repulsive electrostatic interactions from the phosphate groups and on the hydrophilic/hydrophobic balance.

Not only guanosine but also pterine derivatives give rise to supramolecular polymers in water.⁹⁷ Similar to the guanosines, folic acid **70** assembles in disc-shaped tetramers in water. The addition of sodium or potassium salts aids the tetramerization and induces the aggregation into columns.⁹⁸ At the relatively high concentration of 4% w/w these columns have an average DP of 9 discs. Highly interesting were the melting experiments performed in water and in the presence of salt. The intensity of the Cotton effect was followed as a function of temperature, which is an indication of the amount of chirality present in the columns. In pure water a single melting transition was detected, whereas in the presence of salt two melting transition were visible, indicating hierarchical assembly.⁹⁹

Gottarelli and co-workers have prepared apolar guanosine derivatives **71** and **72** for the study of the above-mentioned processes in organic solvents. In

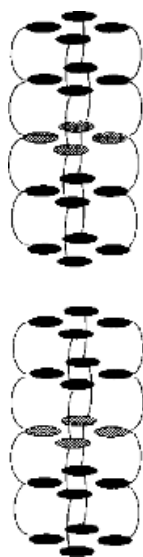
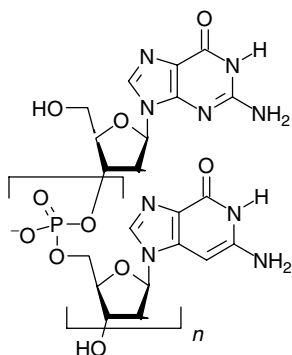
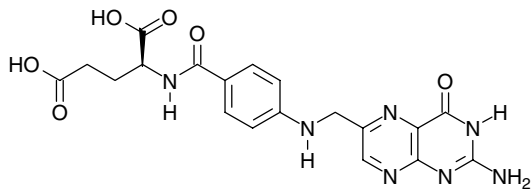


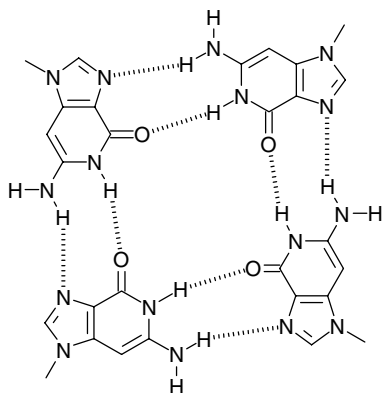
Figure 6.14 Mode of aggregation of eight *d*(GpGpApGpG) molecules. First self-assembly in “barrels” occurs, followed by stacking of these barrels in columns. (Gottarelli, G.; Masiero, S.; Spada, G. P. *J. Chem. Soc., Chem. Commun.* **1995**, 2555–2557. Reproduced by permission of the Royal Society of Chemistry.)

dilute solution in the presence of potassium ions, disc-shaped structures were formed.¹⁰⁰ In chloroform compound **72** was molecularly dissolved, but upon contact of the organic layer with an aqueous layer containing potassium salts, **72** was found to extract the potassium into the organic layer. An octameric potassium complex is formed, consisting of two stacked G-quartets between which a potassium ion is sandwiched via interactions with the carbonyls of the guanosines (Figure 6.15).^{101,102} Upon the addition of more salt the octamers polymerized into a columnar architecture. In this polymer potassium ions and G-quartets alternate in the stacking.¹⁰³ The Cotton effect observed for the polymer indicated the presence of helical columns. Apart from the formation of octamers, also the formation of decamers has been observed.¹⁰⁴

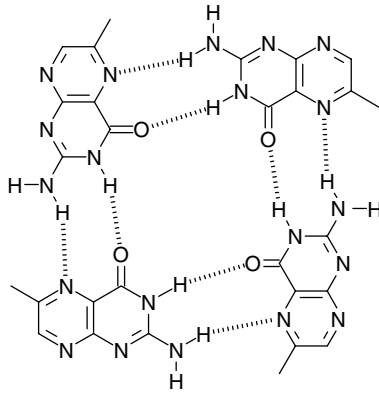
Compound **72** was shown to display enantioselectivity in the extraction of chiral potassium salts from water into the organic phase.¹⁰⁵ The supramolecular polymer possesses a homochiral helical architecture onto which one of the anionic enantiomers preferentially binds. Intriguingly, for some of the anions the octamer and polymer showed opposite selectivity, illustrating the difference in supramolecular chirality of the two systems. Furthermore, the polymer was capable of inducing a Cotton effect in the achiral compound potassium *N*-(2,4-dinitrophenyl)glycinate. Since the apolar side chains would

69: $n = 1, 2, 3, 5$ 

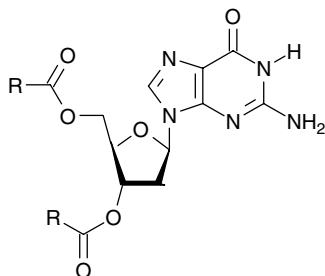
70



Tetrameric discs of 69



Tetrameric discs of 70

71: $R = C_9H_{19}$ 72: $R = p-(C_{12}H_{25}O)C_6H_4$

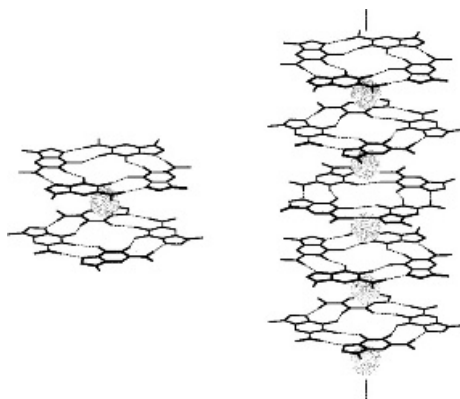
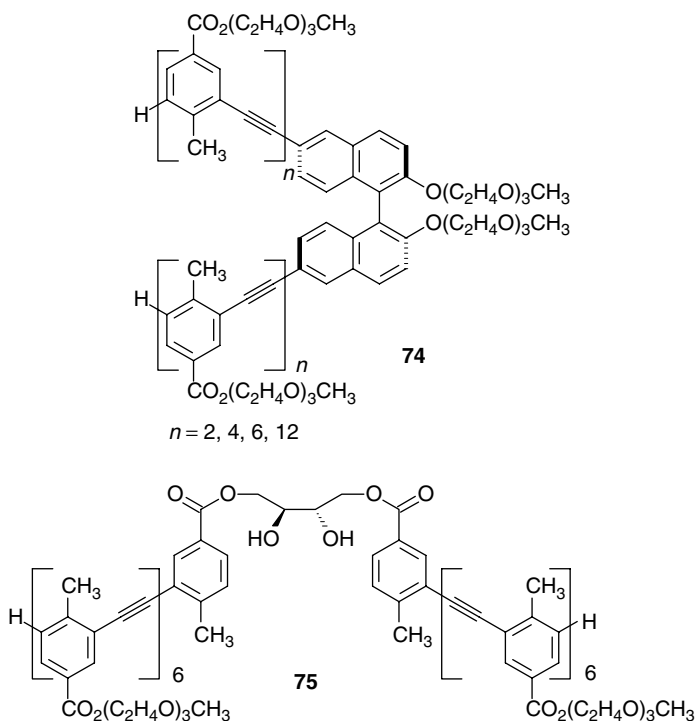


Figure 6.15 Self-assembly of apolar deoxyguanosines **72** in octamers and polymers upon the addition of potassium ions. (Masiero, S.; Gottarelli, G.; Pieraccini, S. *Chem. Commun.* **2000**, 1995–1996. Reproduced by permission of John Wiley & Sons, Inc.)

allow incorporation into a membrane, the use of these polymers as artificial ion channels is currently under investigation.^{102,106} These helical columns may also be ideal supramolecular polymeric architectures for the creation of functional arrays. The guanosines were derivatized with porphyrins, and they were shown to self-assemble into columns with a periphery of porphyrins in chloroform.¹⁰⁷ The creation of such functional columns with the help of external stimuli offers a unique approach for the creation of bio-inspired self-assembled polymers.

4.3 Self-Assembly of Helices

In the phthalocyanines decorated with helicenes (**62**) the positional order for helicity was governed by the chiral helicenes at the periphery. Helicenes themselves have also been used as mesogens in discotic liquid crystals (**33**).³⁷ The helical shape of the rigid cores allows the molecules to stack and form helical supramolecular columns. The molecules maintain their supramolecular columnar ordering in apolar solvents as indicated by UV–Vis spectroscopy. Upon going from the molecular dissolved state in dilute solution to the polymeric state at higher concentrations, an increase of the Cotton effect in the CD spectrum is observed. The formation of a helical column thus gives rise to a stronger expression of chirality. The formation of the rigid rod polymers upon increasing the concentration is accompanied by an increase in the viscosity. More detailed measurements have been performed on a non-liquid crystalline helicene. This compound self-assembles to give helical columnar architectures.^{108–110} A strong increase of the Cotton effect was observed upon



the overall helical sense (**76**). Solvent denaturation studies revealed that the helix was formed via a hierarchical growth process, in which only in the last stages of the folding process chirality is transferred from the side chains to the backbone. The side-chain chirality is only expressed once a well-defined architecture, that is, a helix, is formed. In good solvents the oligomers are present as random coils, but in solvents of intermediate polarity, such as acetonitrile, the oligomers fold into the helix structure. Increasing the polarity by addition of water (a nonsolvent for the backbone) resulted in the formation of columns of stacked helices (Figure 6.17).¹¹⁶ The study of columns consisting of both achiral (**73**) and chiral oligomers (**76**) showed that the stacking is a cooperative process: the chiral, helically folded oligomers create a chiral platform for the achiral oligomers and in this way induce chirality in the achiral oligomers. The chirality of the chiral oligomers is thus amplified to the achiral oligomers.

Apolar *m*-phenylene ethynylene oligomers **77** fold in apolar solvents, such as alkanes, into helices.¹¹⁷ Due to the strongly favored arene–arene interactions in this solvent type, the folding into a helical oligomer coincides with stacking of the folded oligomers into helical columnar polymers and a strong

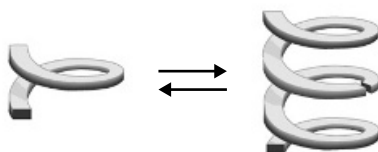
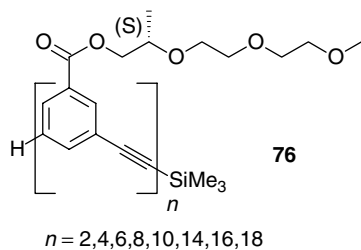
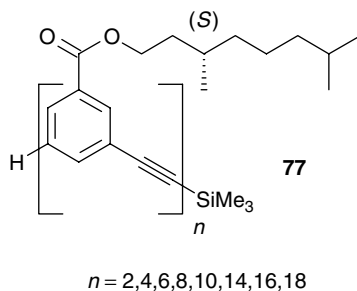


Figure 6.17 Schematic representation of the formation of helical columns by stacking of individual oligomers.



enhancement of the Cotton effect is observed. The formation of supramolecular columns stabilizes in a cooperative fashion the chiral helical conformation of the individual oligomers.

5 CONCLUSIONS AND OUTLOOK

Chirality is an essential property of life, which can be found throughout all biological self-assembled and self-organized architectures. Over many millennia nature has, through trial and error, learned how to utilize the chiral properties of the small building blocks, for example, amino acids and nucleic acids and how to express this structural property in a hierarchical process at the quaternary level. This expression of chirality at the quaternary level in turn

modifies the material and functional properties of the resulting architecture, that is, enantioselective catalysis. In comparison with nature the control of chiral expression within discotic assemblies is still in its infancy. The precise guidelines needed to amplify the chirality of one molecule to other molecules through specific molecular recognition interactions are, however, gradually being developed. In a process analogous to natural systems, the combination of several interactions, viz. π - π interactions, hydrogen bonding, solvophobic interactions has enabled researchers to develop chiral discotic molecules which upon self-assembly are able to pass on their molecular information to hundreds of achiral neighbors, in a molecular amplification process. These exciting first tentative steps hold great promise for the development of even better systems in the future, and for the study of the relationship between the functional liquid crystalline properties and the chirality expression. In a recent study achiral discotic molecules were used to induce a preferred handedness at the supramolecular level due to macroscopic influence,¹¹⁸ leading to insights into the origin of chirality. More of these and related studies will be disclosed in the not too far future, all making use of the unique features of chiral discotic liquid crystals and their self-assembly into well-defined objects.

ACKNOWLEDGMENT

The authors like to express their warm thanks to the many co-workers from our laboratories and our collaborators who participated in the work reported here for their enthusiasm to be actively involved in the field of chiral discotic liquid crystalline materials. Also the continuing discussions to unravel the many features of these systems are highly acknowledged. Their names appear in the list of references.

REFERENCES

1. Demus, D.; Goodby, J.; Gray, G. W.; Spiess, H. W.; Vill, V. (Eds.). *Handbook of Liquid Crystals*. Wiley-VCH, Weinheim, 1998.
2. Chandrasekhar, S.; Sadashiva, B. K.; Suresh, K. A. *Pranama* **1977**, 9, 471-480.
3. Demus, D.; Goodby, J.; Gray, G. W.; Spiess, H. W.; Vill, V. (Eds.). *Handbook of Liquid Crystals*, Vol. 2B. Wiley-VCH, Weinheim, 1998.
4. Reinitzer, F. *Monath. Chem.* **1888**, 9, 421.
5. Vorländer, D. *Zeitschr. Physik. Chem.* **1923**, 105, 211.
6. Billard, J.; Dubois, J. C.; Tinh, N. H.; Zann, A. *Nouv. J. Chim.* **1978**, 2, 535-540.
7. Destrade, C.; Mondon, M. C.; Malthete, J. *J. Phys.* **1979**, 3, 17-21.
8. Tinh, N. H.; Destrade, C.; Gasparoux, H. *Phys. Lett.* **1979**, 72A, 251-254.

9. Levelut, A. M.; Hardouin, F.; Gasparoux, H.; Destrade, C.; Tinh, N. H. *J. Phys.* **1981**, *42*, 147–152.
10. Destrade, C.; Tinh, N. H.; Malthete, J.; Jacques, J. *Phys. Lett.* **1980**, *79A*, 189–192.
11. Malthete, J.; Destrade, C.; Tinh, N. H.; Jacques, J. *Mol. Crystallogr. Liq. Crystallogr. Lett.* **1981**, *64*, 233–238.
12. Malthete, J.; Jacques, J.; Tinh, N. H.; Destrade, C. *Nature* **1982**, *298*, 46–48.
13. Krüerke, D.; Kitzrow, H.-S.; Heppke, G.; Vill, V. *Ber. Bunsenges. Phys. Chem.* **1993**, *97*, 1371–1375.
14. Hauser, A.; Thieme, M.; Saupe, A.; Heppke, G.; Krüerke, D. *J. Mater. Chem.* **1997**, *7*, 2223–2229.
15. Praefcke, K.; Singer, D.; Eckert, A. *Liq. Crystallogr.* **1994**, *16*, 53–65.
16. Usol'tseva, N.; Praefcke, K.; Singer, D.; Gündogan, B. *Liq. Crystallogr.* **1994**, *16*, 617–623.
17. Langner, M.; Praefcke, K.; Krüerke, D.; Heppke, G. *J. Mater. Chem.* **1995**, *5*, 693–699.
18. Booth, C. J.; Krüerke, D.; Heppke, G. *J. Mater. Chem.* **1996**, *6*, 927–934.
19. Frackowiak, E.; Scherowsky, G. *Z. Naturforsch.* **1997**, *52b*, 1539–1543.
20. Yelamaggad, C. V.; Prasad, V.; Manickam, M.; Kumar, S. *Mol. Crystallogr. Liq. Crystallogr.* **1998**, *325*, 33–41.
21. Eran, B. B.; Singer, D.; Praefcke, K. *Eur. J. Inorg. Chem.* **2001**, 111–116.
22. Sergan, T.; Sonpatki, M.; Kelly, J.; Chien, L.-C. *Mol. Crystallogr. Liq. Crystallogr.* **2001**, *359*, 259–267.
23. Saenger, W. *Principles of Nucleic Acid Structure*. Springer, New York, 1984.
24. Kohne, B.; Poules, W.; Praefcke, K. *Chem. Zeit.* **1984**, *108*, 113.
25. Fontes, E.; Heiney, P. A.; de Jeu, W. H. *Phys. Rev. Lett.* **1988**, *61*, 1202–1205.
26. Heiney, P. A.; Fontes, E.; de Jeu, W. H.; Riera, A.; Carroll, P.; Smith, A. B. III *J. Phys. France* **1989**, *50*, 461–483.
27. Palmans, A. R. A.; Vekemans, J. A. J. M.; Fischer, H.; Hikmet, R. A.; Meijer, E. W. *Chem. Eur. J.* **1997**, *3*, 300–307.
28. Brunsveld, L.; Vekemans, J. A. J. M.; Janssen, H. M.; Meijer, E. W. *Mol. Crystallogr. Liq. Crystallogr.* **1999**, *331*, 449–456.
29. Brunsveld, L.; Zhang, H.; Glasbeek, M.; Vekemans, J. A. J. M.; Meijer, E. W. *J. Am. Chem. Soc.* **2000**, *122*, 6175–6182.
30. Yasuda, Y.; Iishi, E.; Inada, H.; Shirota, Y. *Chem. Lett.* **1996**, 575–576.
31. Hanabusa, K.; Koto, C.; Kimura, M.; Shirai, H.; Kakehi, A. *Chem. Lett.* **1997**, 429–430.
32. Lightfoot, M. P.; Mair, F. S.; Pritchard, R. G.; Warren, J. E. *Chem. Commun.* **1999**, 1945–1946.
33. Brunsveld, L.; Schenning, A. P. H. J.; Broeren, M. A. C.; Janssen, H. M.; Vekemans, J. A. J. M.; Meijer, E. W. *Chem. Lett.* **2000**, 292–293.
34. Trzaska, S. T.; Hsu, H.-F.; Swager, T. M. *J. Am. Chem. Soc.* **1999**, *121*, 4518–4519.
35. Serrano, J. L.; Sierra, T. *Chem. Eur. J.* **2000**, *6*, 759–766.
36. Barberá, J.; Iglesias, R.; Serrano, J. L.; Sierra, T.; de la Fuente, M. R.; Palacios, B.; Pérez-Jubindo, M. A.; Vázquez, J. T. *J. Am. Chem. Soc.* **1998**, *120*, 2908–2918.
37. Nuckolls, C.; Katz, T. J. *J. Am. Chem. Soc.* **1998**, *120*, 9541–9544.
38. Verbiest, T.; Van Elshocht, S.; Karuanen, M.; Heliemans, L.; Snauwaert, J.; Nuckolls, C.; Katz, T. J.; Persoons, A. *Science* **1998**, *282*, 913–915.

39. Green, M. M.; Ringsdorf, H.; Wagner, J.; Wüstefeld, R. *Angew. Chem.* **1990**, *102*, 1525–1528.
40. Hirschberg, J. H. K. K.; Brunsveld, L.; Ramzi, A.; Vekemans, J. A. J. M.; Sijbesma, R. P.; Meijer, E. W. *Nature* **2000**, *407*, 167–170.
41. Werth, M.; Vallerien, S. U.; Spiess, H. W. *Liq. Crystallogr.* **1991**, *10*, 759–770.
42. Möller, M.; Wendorff, J. H.; Werth, M.; Spiess, H. W. *J. Non-Crystallogr. Sol.* **1994**, *170*, 295–299.
43. Cho, I.; Lim, Y. *Mol. Crystallogr. Liq. Crystallogr.* **1988**, *154*, 9–26.
44. van Nostrum, C. F.; Bosman, A. W.; Gelinck, G. H.; Picken, S. J.; Schouten, P. G.; Warman, J. M.; Schouten, A.-J.; Nolte, R. J. M. *J. Chem. Soc., Chem. Commun.* **1993**, 1120–1122.
45. van Nostrum, C. F.; Bosman, A. W.; Gelinck, G. H.; Schouten, P. G.; Warman, J. M.; Kentgens, A. P. M.; Devillers, M. A. C.; Meijerink, A.; Picken, S. J.; Sohling, U.; Schouten, A.-J.; Nolte, R. J. M. *Chem. Eur. J.* **1995**, *1*, 171–182.
46. Fechtenkötter, A.; Tchebotareva, N.; Watson, M.; Müllen, K. *Tetrahedron* **2001**, *57*, 3769–3783.
47. Praefcke, K.; Eckert, A.; Blunk, D. *Liq. Crystallogr.* **1997**, *22*, 113–119.
48. Boden, N.; Bushby, R. J.; Cammidge, A. N.; Duckworth, S.; Headdock, G. *J. Mater. Chem.* **1997**, *7*, 601–605.
49. Jeffrey, G. A.; Wingert, L. M. *Liq. Crystallogr.* **1992**, *12*, 179–202.
50. Demus, D.; Goodby, J.; Gray, G. W.; Spiess, H. W.; Vill, V. (Eds.). *Handbook of Liquid Crystals*, Vol 3. Wiley-VCH, Weinheim, 1998, pp. 305–340.
51. Morris, N. L.; Zimmermann, R. G.; Jameson, G. B.; Dalziel, A. W.; Reuss, P. M.; Weiss, R. G. *J. Am. Chem. Soc.* **1988**, *110*, 2177–2185.
52. Prost, J. *Comptes Rendus du Colloge Pierre Curie: Symmetries and Broken Symmetries*. Boccara, N. (Ed.). Inst. Dev. Sci, Educ. Technol., Paris, 1981, pp. 159–181.
53. Levelut, A. M.; Oswald, P.; Ghanem, A.; Malthete, J. *J. Phys., Paris* **1984**, *44*, 745–754.
54. Bock, H.; Helfrich, W. *Liq. Crystallogr.* **1992**, *12*, 697–703.
55. Bock, H.; Helfrich, W. *Liq. Crystallogr.* **1995**, *18*, 707–713.
56. Heppke, G.; Krüerke, D.; Löhning, C.; Löttsch, D.; Moro, D.; Müller, M.; Sawade, H. *J. Mater. Chem.* **2000**, *10*, 2657–2661.
57. Krüerke, D.; Rudquist, P.; Lagerwall, S. T.; Sawade, H.; Heppke, G. *Ferroelectrics* **2000**, *243*, 207–220.
58. Bock, H.; Helfrich, W. *Liq. Crystallogr.* **1995**, *18*, 387–399.
59. Heppke, G.; Krüerke, D.; Müller, M.; Bock, H. *Ferroelectrics*, **1996**, *179*, 203–209.
60. Jákli, A.; Müller, M.; Krüerke, D.; Heppke, G. *Liq. Crystallogr.* **1998**, *24*, 467–472.
61. Kitzerow, H.-S.; Bock, H. *Mol. Cryst. Liq. Crystallogr.* **1997**, *299*, 117–128.
62. Scherowsky, G.; Chen, X. H. *Liq. Crystallogr.* **1994**, *17*, 803–810.
63. Scherowsky, G.; Chen, X. H. *J. Mater. Chem.* **1995**, *5*, 417–421.
64. Scherowsky, G.; Chen, X. H.; Levelut, A. M. *Liq. Cryst.* **1998**, *24*, 157–162.
65. Zimmermann, H.; Poupko, R.; Luz, Z.; Billard, J. *Z. Naturforsch.* **1985**, *40a*, 149–160.
66. Levelut, A. M.; Malthete, J.; Collet, A. *J. Phys.* **1986**, *47*, 351–357.
67. Malthete, J.; Collet, A. *J. Am. Chem. Soc.* **1987**, *109*, 7544–7545.
68. Jákli, A.; Saupe, A.; Scherowsky, G.; Chen, X. H. *Liq. Crystallogr.* **1997**, *22*, 309–316.
69. J.-M. Lehn (Ed.). *Comprehensive Supramolecular*. 11 issues Pergamon, Oxford, UK, 1996.

70. Sheu, E. Y.; Liang, K. S.; Chiang, L. Y. *J. Phys. France* **1989**, *50*, 1279–1295.
71. Gallivan, J. P.; Schuster, G. B. *J. Org. Chem.* **1995**, *60*, 2423–2429.
72. Brunsveld, L.; Palmans, A. R. A.; Vekemans, J. A. J. M.; Meijer, E. W. Unpublished results.
73. Gallivan, J. P.; Schuster, G. B. *J. Org. Chem.* **1995**, *60*, 2423–2429.
74. Kraft, A.; Osterod, F.; Fröhlich, R. *J. Org. Chem.* **1999**, *64*, 6425–6433.
75. Green, M. M.; Reidy, M. P.; Johnson, R. D.; Darling, G.; O'Leary, D. J.; Wilson, G. *J. Am. Chem. Soc.* **1989**, *111*, 6452–6454.
76. Fox, J. M.; Katz, T. J.; van Elshocht, S.; Verbiest, T.; Kauranen, M.; Persoons, A.; Thongpanchang, T.; Krauss, T.; Brus, L. *J. Am. Chem. Soc.* **1999**, *121*, 3453–3459.
77. Engelkamp, H.; Middelbeek, S.; Nolte, R. J. M. *Science* **1999**, *284*, 785–788.
78. van Nostrum, D. F.; Picken, S. J.; Nolte, R. J. M. *Angew. Chem. Int. Ed. Engl.* **1994**, *33*, 2173–2175.
79. Palmans, A. R. A.; Vekemans, J. A. J. M.; Havinga, E. E.; Meijer, E. W. *Angew. Chem. Int. Ed. Engl.* **1997**, *36*, 2648–2651.
80. Green, M. M.; Peterson, N. C.; Sato, T.; Teramoto, A.; Lifson, S. *Science* **1995**, *268*, 1860–1866.
81. Palmans, A. R. A.; Vekemans, J. A. J. M.; Hikmet, R. A.; Fischer, H.; Meijer, E. W. *Adv. Mater.* **1998**, *10*, 873–876.
82. Brunsveld, L.; Zhang, H.; Glasbeek, M.; Vekemans, J. A. J. M.; Meijer, E. W. *J. Am. Chem. Soc.* **2000**, *122*, 6175–6182.
83. Brunsveld, L.; Lohmeijer, B. G. G.; Vekemans, J. A. J. M.; Meijer, E. W. *Chem. Commun.* **2000**, 2305–2306.
84. van der Schoot, P.; Michels, M. A. J.; Brunsveld, L.; Sijbesma, R. P.; Ramzi, A. *Langmuir* **2000**, *16*, 10076–10083.
85. Klug, A. *Angew. Chem.* **1983**, *95*, 579–596.
86. *Encyclopedia of Polymer Science and Engineering*, Vol 9. Wiley, New York, 1987.
87. Sijbesma, R. P.; Beijer, F. H.; Brunsveld, L.; Folmer, B. J. B.; Hirschberg, J. H. K. K.; Lange, R. F. M.; Lowe, J. K. L.; Meijer, E. W. *Science* **1997**, *278*, 1601–1604.
88. For a review on guanosine and pterine self-assembly until 1996 see Gottarelli, G.; Spada, G. P.; Garbesi, A. In *Comprehensive Supramolecular Chemistry*, Vol. 9. Lehn, J.-M. (Ed.). Pergamon, Oxford, UK, 1996, pp. 483–506.
89. Kanie, K.; Yasuda, T.; Ujiie, S.; Kato, T. *Chem. Commun.* **2000**, 1899–1900.
90. Gottarelli, G.; Masiero, S.; Mezzina, E.; Pieraccini, S.; Rabe, J. P.; Samorí, P.; Spada, G. P. *Chem. Eur. J.* **2000**, *6*, 3242–3248.
91. de Groot, F. M. H.; Gottarelli, G.; Masiero, S.; Proni, G.; Spada, G. P.; Dolci, N. *Angew. Chem., Int. Ed. Engl.* **1997**, *36*, 954–955.
92. Proni, G.; Gottarelli, G.; Mariani, P.; Spada, G. P. *Chem. Eur. J.* **2000**, *6*, 3249–3253.
93. Bonazzi, S.; Capobianco, M.; DeMorais, M. M.; Garbesi, A.; Gottarelli, G.; Mariani, P.; Ponzi Bossi, M. G.; Spada, G. P.; Tondelli, L. *J. Am. Chem. Soc.* **1991**, *113*, 5809–5816.
94. Proni, G.; Spada, G. P.; Gottarelli, G.; Ciuchi, F.; Mariani, P. *Chirality* **1998**, *10*, 734–741.
95. Spada, G. P.; Carcuro, A.; Colonna, F. P.; Garbesi, A.; Gottarelli, G. *Liq. Crystallogr.* **1988**, *3*, 651–654.
96. Mariani, P.; Mazabard, C.; Garbesi, A.; Spada, G. P. *J. Am. Chem. Soc.* **1989**, *111*, 6369–6373.

97. Bonazzi, S.; DeMorais, M. M.; Gottarelli, G.; Mariani, P.; Spada, G. P. *Angew. Chem. Int. Ed. Engl.* **1993**, *32*, 248–250.
98. Ciuchi, F.; Di Nicola, G.; Franz, H.; Gottarelli, G.; Mariani, P.; Ponzi Bossi, Spada M. G., G. P. *J. Am. Chem. Soc.* **1994**, *116*, 7064–7071.
99. Gottarelli, G.; Mezzina, E.; Spada, G. P.; Carsughi, F.; Di Nicola, G.; Mariani, P.; Sabatucci, A.; Bonazzi, S. *Helv. Chim. Acta* **1996**, *79*, 220–234.
100. Gottarelli, G.; Masiero, S.; Spada, G. P. *J. Chem. Soc., Chem. Commun.* **1995**, 2555–2557.
101. Marlow, A. L.; Mezzina, E.; Spada, G. P.; Masiero, S.; Davis, J. T.; Gottarelli, G. *J. Org. Chem.* **1999**, *64*, 5116–5123.
102. Forman, S. L.; Fettinger, J. C.; Pieraccini, S.; Gottarelli, G.; Davis, J. T. *J. Am. Chem. Soc.* **2000**, *122*, 4060–4067.
103. Mezzina, E.; Mariani, P.; Itri, R.; Masiero, S.; Pieraccini, S.; Spada, G. P.; Spinozzi, F.; Davis, J. T.; Gottarelli, G. *Chem. Eur. J.* **2001**, *7*, 388–395.
104. Cai, M.; Sidorov, V.; Lam, Y.-F.; Flowers II, R. A.; Davis, J. T. *Org. Lett.* **2000**, *2*, 1665–1668.
105. Andrisano, V.; Gottarelli, G.; Masiero, S.; Heijne, E. H.; Pieraccini, S.; Spada, G. P. *Angew. Chem. Int. Ed.* **1999**, *38*, 2386–2388.
106. Sidorov, V.; Kotch, F. W.; El-Kouedi, M.; Davis, J. T. *Chem. Commun.* **2000**, 2369–2370.
107. Masiero, S.; Gottarelli, G.; Pieraccini, S. *Chem. Commun.* **2000**, 1995–1996.
108. Nuckolls, C.; Katz, T. J.; Castellanos, L. *J. Am. Chem. Soc.* **1996**, *118*, 3767–3768.
109. Lovinger, A. J.; Nuckolls, C.; Katz, T. J. *J. Am. Chem. Soc.* **1998**, *120*, 264–268.
110. Nuckolls, C.; Katz, T. J.; Katz, G.; Collings, P. J.; Castellanos, L. *J. Am. Chem. Soc.* **1999**, *121*, 79–88.
111. Nelson, J. C.; Saven, J. G.; Moore, J. S.; Wolynes, P. G. *Science* **1997**, *277*, 1793–1796.
112. Prince, R. B.; Barnes, S. A.; Moore, J. S. *J. Am. Chem. Soc.* **2000**, *122*, 2758–2762.
113. Gin, M. S.; Yokozawa, T.; Prince, R. B.; Moore, J. S. *J. Am. Chem. Soc.* **1999**, *121*, 2643–2644.
114. Gin, M. S.; Moore, J. S. *Org. Lett.* **2000**, *2*, 135–138.
115. Prince, R. B.; Brunsveld, L.; Meijer, E. W.; Moore, J. S. *Angew. Chem. Int. Ed.* **2000**, *39*, 228–230.
116. Brunsveld, L.; Meijer, E. W.; Prince, R. B.; Moore, J. S. *J. Am. Chem. Soc.* **2001**, *123*, 7978–7984.
117. Brunsveld, L.; Prince, R. B.; Meijer, E. W.; Moore, J. S. *Org. Lett.* **2000**, *2*, 1525–1528.
118. Ribo, J. M.; Crusats, J.; Sagués, F.; Claret, J.; Rubires, R. *Science* **2001**, *292*, 2063–2066.

Chapter 7

Some Correlations Between Molecular and Cholesteric Handedness

GIOVANNI GOTTARELLI AND GIAN PIERO SPADA

Alma Mater Studiorum—Università di Bologna, Dipartimento di Chimica Organica “A. Mangini,” Via S. Donato 15, 40127 Bologna, Italy

- 1 Introduction
 - 2 Methods
 - 3 Lyotropic Cholesterics Formed by Helical Polymers
 - 4 Thermotropic-Induced Cholesterics
 - 4.1 Empirical Approach
 - 4.2 Theoretical Approach
 - 4.3 Biaryl Moiety
 - 4.4 Chiral Molecules Different from Biaryls
 - 5 Conclusions
- References

1 INTRODUCTION

Liquid crystalline phases¹ can be divided into two classes: thermotropic phases are obtained by temperature variations and exist in a limited temperature interval (see Figure 7.1); lyotropic phases are instead formed by mixing two or more substances, for example, water and amphiphilic compounds or polymers and a solvent. Especially for amphiphilic compounds in water, temperature may play a role in determining the phase behavior.

Thermotropic cholesterics were officially discovered² in 1888 by the Austrian botanist Friederich Reinitzer, while studying the melting of cholesterol esters: cholesteryl benzoate first melted to give a cloudy liquid that, at higher temperature, turned into an ordinary clear liquid. The cloudy liquid (the mesophase) was a thermotropic cholesteric liquid crystal. These phases

Materials-Chirality: Volume 24 of Topics in Stereochemistry,
Edited by Mark M. Green, R.J.M. Nolte, and E.W. Meijer
ISBN 0-471-05497-6 Copyright © 2003 John Wiley & Sons, Inc.

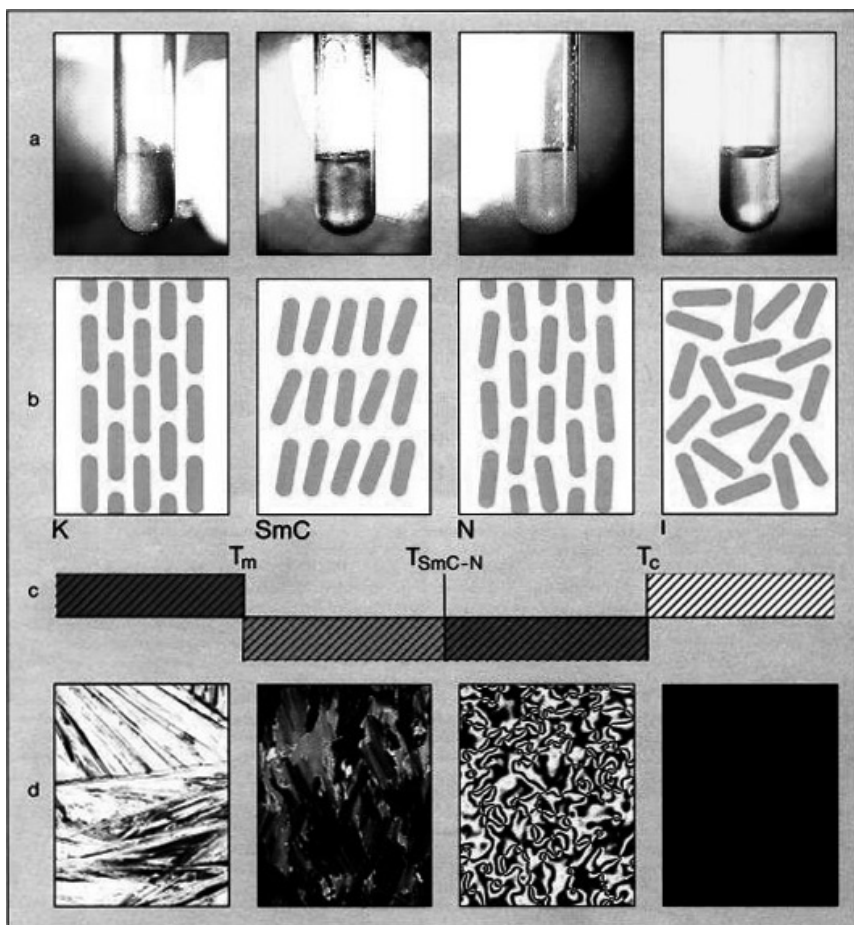


Figure 7.1 Illustration of different aggregation states obtained (from left to right) by increasing temperature: crystal (K), smectic C (SmC), nematic (N) and isotropic (I). Row a shows macroscopic appearance of samples; in row b, short-range microscopic ordering is represented (each bar represents a molecule); thermotropic phase diagram of row c illustrates relevant transition temperatures (T_m ; melting temperature; T_{SmC-N} ; transition temperature between SmC and N; T_c ; clearing temperature); row d shows different texture of different states as seen through polarizing microscope (with crossed polars, isotropic phase appears black).

are described as composed of helical aggregates of molecules; the helical arrays arise from the chirality of the individual molecules, the energy of the molecular interactions being minimized by adopting a skewed orientation.

The cholesteric helices can be right-handed or left-handed and usually have a temperature-dependent pitch; also, in a few cases the sense of the helix

may change with temperature. The definition of cholesteric handedness has created some confusion in the literature as chemists and physicists often adopt opposite conventions. In the following, we shall use the chemist's convention: a cholesteric is right-handed if, on going from the molecule nearest to the observer to its next neighbor, one must carry out a clockwise rotation (see Figure 7.2).

Cholesteric mesophases (twisted nematics) can be formed also by the addition of small quantities of a chiral, resolved guest molecule to an achiral nematic host; one refers to this case as induced cholesteric phases. This phenomenon was discovered at the beginning of the last century,³ but it was forgotten for almost 50 years, and only during the 1960s did the second study appear.⁴ For both ordinary and induced cholesteric phases, on passing from one chiral molecule to its enantiomer, the cholesteric helix sense is reversed; however, it is still almost unknown why a given absolute molecular configuration gives a certain cholesteric handedness.

Cholesteric mesophases have interesting physical properties: The phase is fluid and the orientation of the molecules can be modified by several factors, such as by surface effects (by rubbing or coating the walls of the cell which contains the compound), or by applying magnetic or electric fields. The change of molecular orientation with electric fields is the basis of the liquid crystal (LC) displays. A striking property is the reflection of circularly polarized light (CPL) with wavelength related to the helical pitch ($\lambda = np$, where n is the refractive index and p the pitch)⁵; in particular, right-handed cholesterics reflect right-handed CPL and transmit left-handed CPL. If λ is in the visible region, the chiral phase appears brightly colored in reflection; if the pitch is temperature-dependent, the color changes with temperature. The bands observed [either in circular dichroism (CD) or in absorption spectroscopy], related to this phenomenon, will be referred to as the reflection bands.

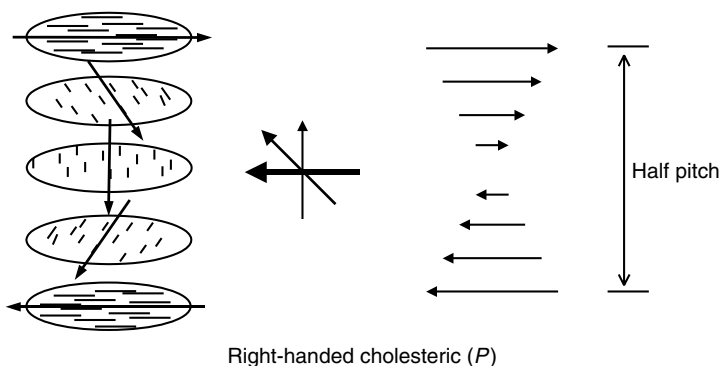


Figure 7.2 Helical arrangement of director in right-handed cholesteric phase.

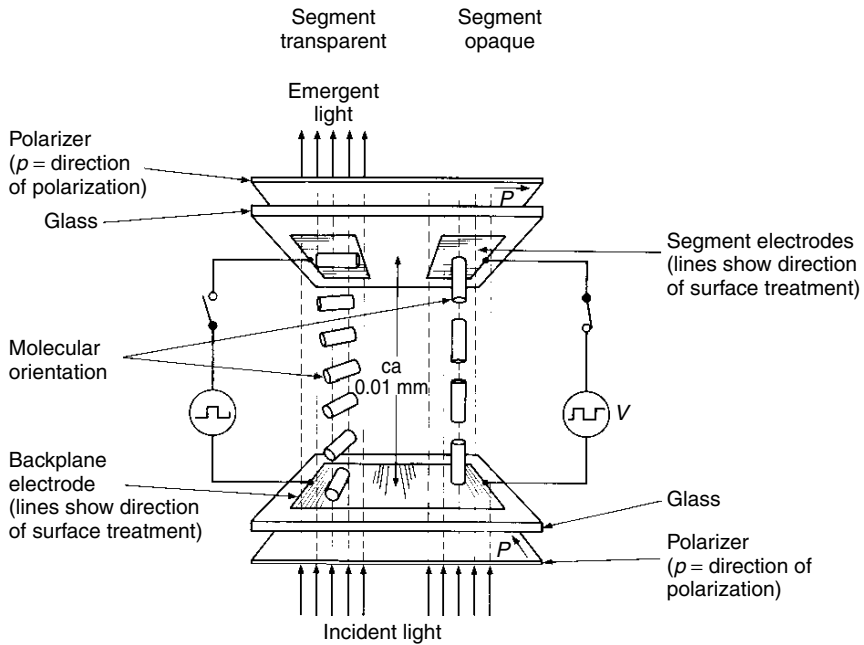
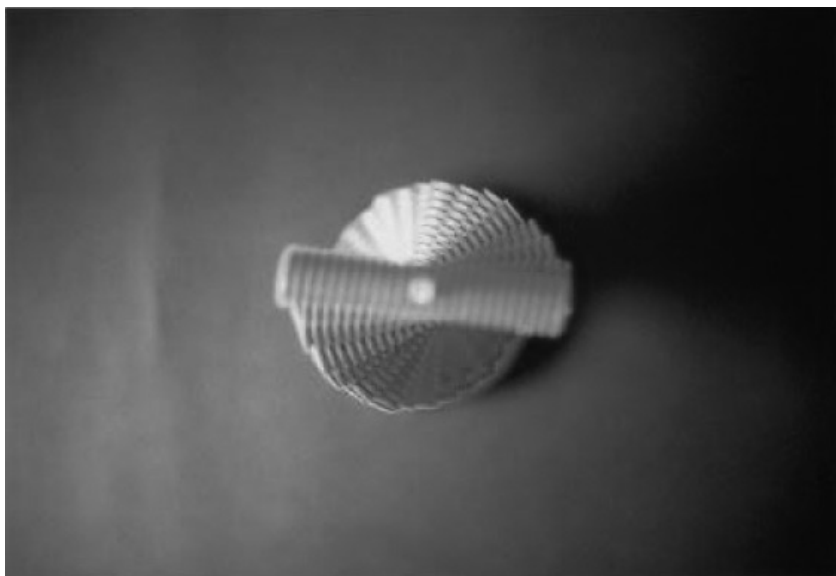


Figure 7.3 Operation of twisted nematic display in transmissive mode. Liquid crystal is contained between two parallel glass plates, each of which has a polarizer on outside and transparent electrodes (defining, e.g., character segments) on inside. Surfaces of electrodes in contact with LC are treated to produce striations which have effect of aligning molecules along striations. Striations of top and bottom sets of electrodes lie at 90° to each other. Light incident on bottom plate is plane-polarized by polarizer and then passes through LC. Where electric circuit is open (left side, OFF state), the plane of polarization follows molecular twist. Top polarizer is arranged to be at 90° to bottom polarizer; light passes through cell unattenuated and segment defined by electrode is invisible. If suitable voltage is applied between electrodes (right-side, ON state), molecules align with field. Spiral is then broken and direction of polarization is unaltered as light traverses cell; in this case, light is blocked by top polarizer and segment defined by electrode geometry becomes visible.

Thermotropic cholesterics have several practical applications, some of which are very widespread. Most of the liquid crystal displays produced use either the twisted nematic (see Figure 7.3) or the supertwisted nematic electrooptical effects.⁶ The liquid crystal materials used in these cells contain a chiral component (effectively a cholesteric phase) which determines the twisting direction. Cholesteric LCs can also be used for storage displays utilizing the dynamic scattering mode.⁷ Short-pitch cholesterics with temperature-dependent selective reflection in the visible region show different colors at different temperatures and are used for popular digital thermometers.⁸

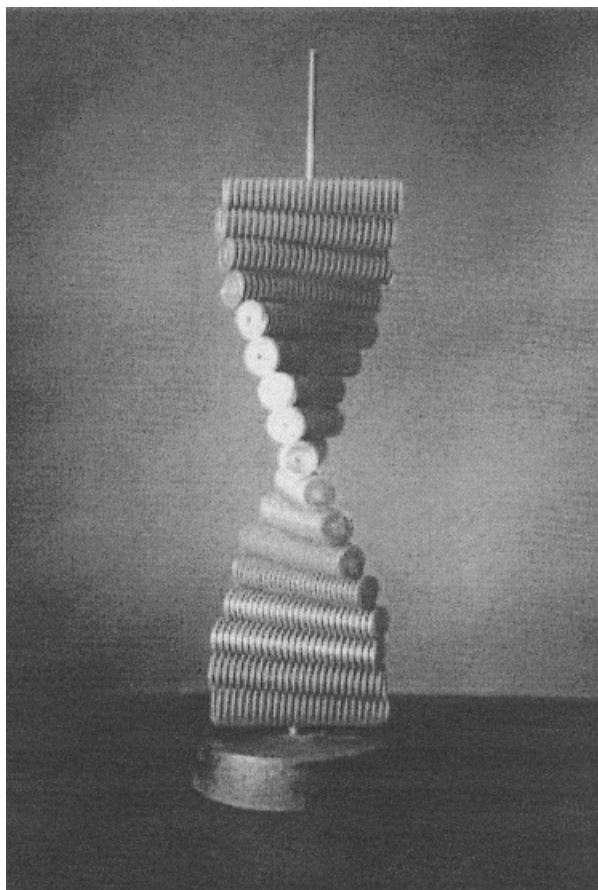
Cholesteric lyotropic phases were discovered later. In 1958, Robinson,⁹ working at Courtaulds (a textile industry), found that solutions of poly- γ -benzyl-L-glutamate (PBLG) in organic solvents (dioxan, dichloromethane, chloroform) gave birefringent solutions characterized by “equi-spaced alternate dark and light lines.” Also solutions of deoxyribonucleic acid (DNA) in 0.1 *M* NaCl were birefringent and, after standing several days, formed the periodic lines observed for glutamate (the origin of these lines will be discussed in Section 2). Both DNA and PBLG are helical polymers and the cholesteric phases can be schematized with the screw model depicted in Figure 7.4.

The individual objects that compose the model are screws which simulate the molecules of the helical polymer; their individual chirality is responsible for the spontaneous formation of the overall helical structure. In the model, the screws are left-handed and have a rather compact thread, that is, the pitch-to-diameter ratio of the individual screws is small: In this case, left-handed screws generate a left-handed overall helical structure. If instead the thread is loose, left-handed screws may generate a right-handed superstructure (see discussion in Section 3).



(a)

Figure 7.4 Simplified macroscopic model for cholesteric: (a) lateral and (b) top view of left-handed superhelix (photographs display a half-pitch length) composed of left-handed helical screws with pitch-to-diameter ratio much smaller than π . (Reprinted with permission of John Wiley & Sons from *Circular Dichroism—Principles and Applications*, 2nd ed., N. Berova, K. Nakanishi, R. W. Woody, Eds., Copyright © 2000.)



(b)

Figure 7.4 (continued).

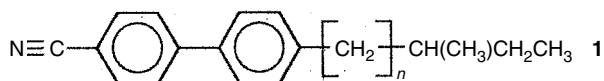
Several natural¹⁰ and synthetic (e.g., polyisocyanates¹¹) polymers form lyotropic cholesterics with the appropriate solvent; also micellar systems formed by amphiphilic molecules and water, if chirality is introduced by either using a chiral amphiphile or adding a chiral dopant, can give cholesteric phases.¹²

Lyotropic cholesteric phases seem to be relevant also in living organisms: Bouligand et al. have pointed out the striking similarity between cholesteric structures and the supramolecular organization of DNA in the dinoflagellate chromosome,¹³ and this observation might be extended to other cases.^{14,15} The bright iridescent color of some beetles seems to originate from a cholesteric

arrangement of chitin in their exocuticle.¹⁶ Collagen fibrils are frequently arranged in a structure which resembles that of a cholesteric mesophase, and the formation of a cholesteric phase seems to be involved in the construction of their suprafibrillar architecture.¹⁷ Also, some virus suspensions may exhibit, in some cases, a cholesteric order.¹⁸ The cholesteric supramolecular order observed *in vivo* in cells and tissues has been reviewed by Giraud-Guille.¹⁹

Surprisingly, very little work concerning the relationships between molecular and the cholesteric handedness has been published, even if this theme is not only intellectually stimulating but also considerably interesting for its applications.

In the field of thermotropic phases, the first empirical attempt to correlate the absolute configuration of chiral dopants to the sense of induced cholesterics appeared in 1975.²⁰ In a pioneering research, Gray and McDonnell²¹ found an interesting correlation between the handedness of cholesteric phases and the number of methylene units connecting the stereocenter to the aromatic core of the nematogen. In particular, derivative **1** with an *S* configuration gives a right-handed cholesteric when *n* is odd or a left-handed cholesteric when *n* is even; however, this does not allow one to predict the absolute configuration of cholesteric phases.



Recently, a promising theoretical treatment was introduced by Ferrarini et al.²² which, in selected cases, leads to the effective calculation of the helical sense and pitch of the induced cholesteric phases.²³ Attempts to relate the cholesteric handedness of lyotropic cholesterics to the helical sense of the polymers were first reported by Sato and co-workers.¹¹

In this report, we shall attempt to review critically works correlating the molecular chirality to the cholesteric handedness.

2 METHODS

Before attempting to develop any theory correlating molecular to cholesteric handedness, one must be completely sure of the experimental data. A cholesteric phase is fully described by its handedness and pitch, and often also knowledge of the pitch variations with temperature is fundamental. In particular, the determination of the handedness is quite a delicate matter. Before discussing the methods currently used to determine handedness and pitch, the principal textures of the cholesteric phase must be briefly reviewed: The planar or Grandjean textures are obtained in thin cells by rubbing the cell walls (with

or without surface treatment) before introducing the sample; in this way, long molecular axes are parallel to the rubbing direction, and the cholesteric helical axes are perpendicular to the cell windows (Figure 7.5, top). In the fingerprint texture, which is observed in thicker cells, the helix axes are instead parallel to the windows (in the scheme of Figure 7.5, bottom, the cholesteric axes are aligned; this can be obtained by applying an external magnetic field).

The planar texture has little or no birefringence and displays strong optical activity: If CPL impinges perpendicularly to the cell walls, its direction of propagation is parallel to the cholesteric helical axis, and this situation maximizes the interaction between the light and the cholesteric phase. It can be used for optical measurements and in particular for optical rotation and circular dichroism measurements²⁴: Both should give the cholesteric handedness, and CD also the pitch value, if the reflection band²⁵ is at an instrumentally accessible wavelength.²⁶ It should be stressed that the wavelength of the reflection band is independent of the nature of the chromophoric groups composing the phase and is related solely to the pitch and the refractive index. It is also possible to determine the cholesteric handedness from the CD measured in the chromophoric absorption region, which is usually accessible to all commercial dichrographs. The validity of CD measurements in the absorption region for determining cholesteric handedness has been confirmed by

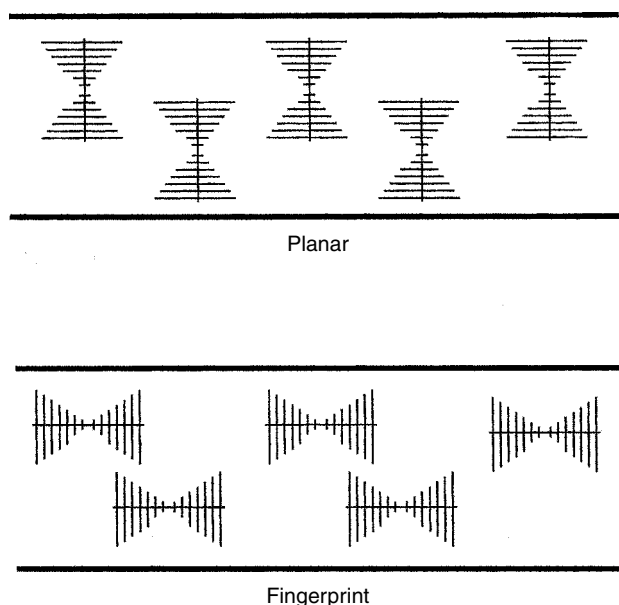


Figure 7.5 Orientation of cholesteric helices in planar and fingerprint alignment.

comparison of the results with those obtained with a nonspectroscopic technique (the Grandjean–Cano wedge method, *vide infra*).²⁹ Information on the cholesteric handedness can be obtained also from optical rotation measurements, carried out, as before, on the planar texture. In this case, several measurements are required on samples with different thicknesses or concentrations; these multiple measurements are necessary for strong optical rotations, such as those of cholesteric samples, which lead to rotations of the analyzer of several radians.²⁷ Both types of measurements (CD and optical rotation) are delicate and should be carried out with great care; linear dichroism and birefringence can lead to wrong results, and one should always check that the sample orientation is planar with a polarizing microscope.

The fingerprint texture shows typical striations (in some cases the sample can be oriented with a magnetic field giving a large area of linear striations), whose distance is one half of the pitch (Figure 7.6)^{24,28}. In Figure 7.6 the fingerprint texture corresponds to the situation depicted in Figure 7.5, bottom, that is, the cholesteric helices are parallel to the cell walls and aligned along a fixed direction by a magnetic field.



Figure 7.6 Fingerprint texture of lyotropic cholesteric: double-headed arrow corresponds to pitch.

An extremely useful technique for determining both handedness and pitch is the Grandjean–Cano wedge method.²⁹ This method is used mainly with thermotropic cholesterics with long pitch. In the most practical arrangement,^{30,31} a plano-convex lens and a flat piece of glass are used, both treated (by coating and/or rubbing) to orient molecules in a planar way, parallel to the same direction. The cholesteric sample is introduced between the two surfaces; the cholesteric helices have their axes perpendicular to the surfaces, and a series of concentric circular disclinations can be seen with a microscope (Figure 7.7). The origin of the disclinations is explained in Figure 7.7: Rubbing forces the molecules on the surfaces to be aligned in the same direction; the cholesteric helices are undisturbed only when the distance between the two surfaces corresponds to an integral number of half a pitch. On either side of these regions, the cholesteric helix is distorted since the pitch must be longer or shorter than the natural value in order to fit between the surfaces. Roughly midway between these regions, the number of half turns must change by one: This causes a defect which is visible as a sharp line under the microscope.

From the diameter of the disclinations, the pitch can be measured³⁰; furthermore, clockwise rotation of the lens generates a shrinking or an expansion of the circles, according to the cholesteric handedness; from this, the helical handedness can be deduced.³¹ It should be stressed that this is not a spectroscopic method and gives results completely independent from those obtained with CD or optical rotation.

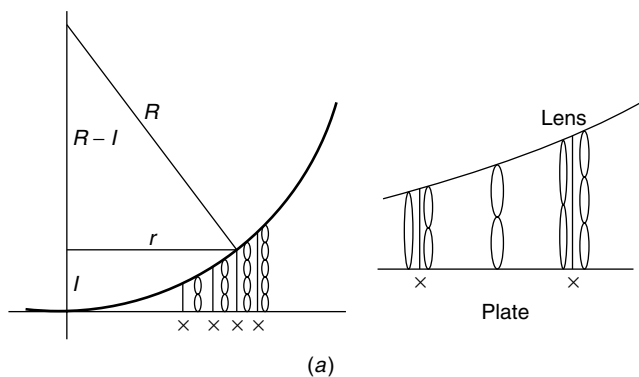
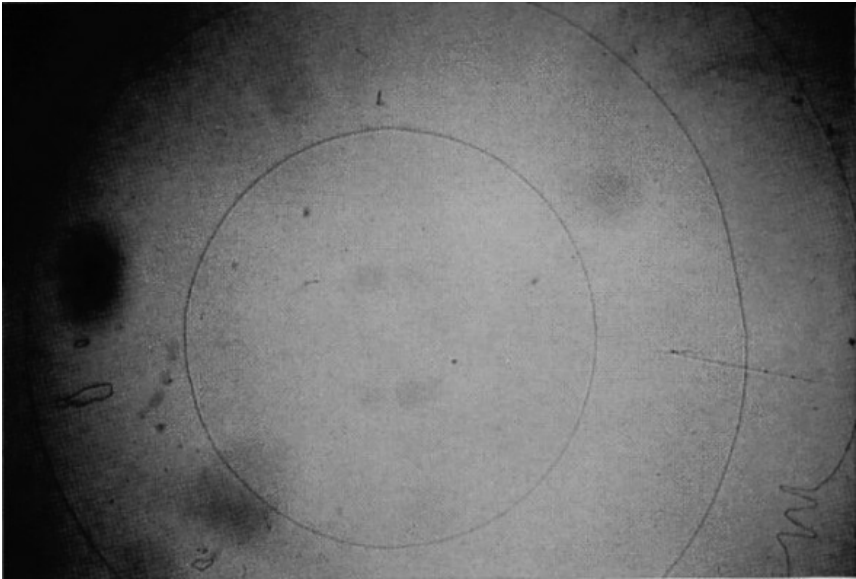
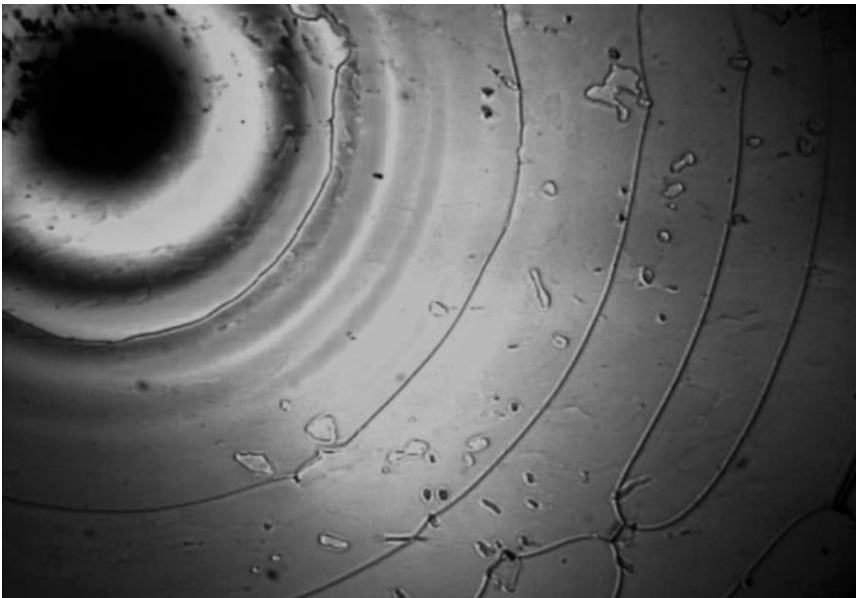


Figure 7.7 (a) Schematic representation of origin of Grandjean–Cano disclination lines which appear when cholesteric is inserted between plano-convex lens and glass plate (a). Surfaces of both lens and plate are treated to produce striations which have effect of aligning molecules along striations; striations of top and bottom surfaces lie parallel to each other. In correspondence of the x 's, the number of half-turns change by one and this causes defects which are visible as sharp lines of circular shape. Radii r of circular Grandjean–Cano disclinations are function of only curvature radius R of lens and of pitch of cholesteric phase. The pictures shown in (b) and (c) are taken in natural and polarized light, respectively.



(b)



(c)

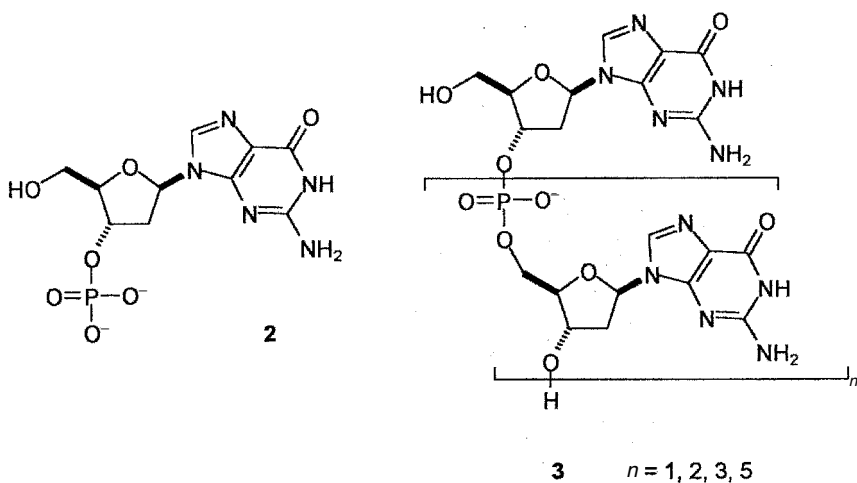
Figure 7.7 (continued).

Another technique widely used to measure the cholesteric pitch is based on the Bragg scattering of monochromatic light (obtained by a helium–neon laser) from fingerprint or planar textures of the cholesteric³²: Its angular dependence is strictly related to the cholesteric pitch.

Other possible methods of measuring the pitch are reviewed in Refs. 33 and 34.

3 LYOTROPIC CHOLESTERIC FORMED BY HELICAL POLYMERS

Several natural and synthetic helical macromolecules such as DNA, polypeptides, and polyisocyanates form, in the appropriate solvent, cholesteric mesophases. Also self-assembled supramolecular systems formed by guanosine derivatives **2** and **3** (G-wires), which are essentially four-stranded helices (Figure 7.8), behave in a similar way.³⁵



Some of these cholesteric systems are well-characterized: The structure and handedness of the macromolecule is unequivocally known and so is the pitch and handedness of the cholesteric phase. A few attempts were made to correlate the polymer structure to the cholesteric handedness.

The screw model of Figure 7.4, a modified version of that originally proposed by Straley³⁶ and Cothia et al.,³⁷ seems attractive to have a rough estimate of chiral steric effects (but not of the elastic response of the system); however, the model is not as simple as it looks and some specifications are needed. The model consists of screws with ridges and grooves on their surface; these screws are packed with the ridges of one in the groove of another. The

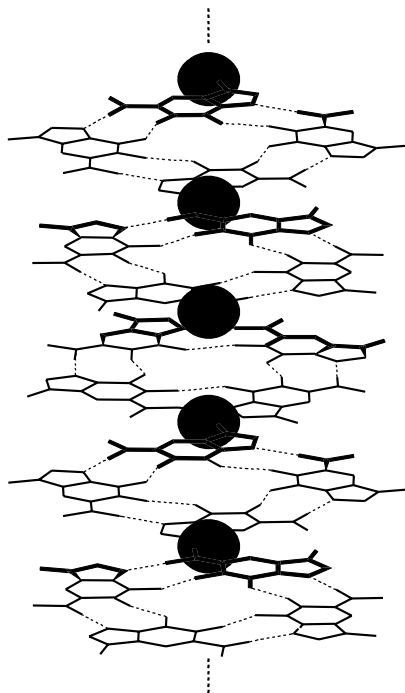


Figure 7.8 Schematized structure of four-stranded helix of G-wire; only G-quartet core is shown.

handedness of the packing depends not only on the screw chirality but also on the inclination of the thread with respect to the helix axis (see Figure 7.9).²⁴ The inclination depends on the pitch-to-diameter ratio. For an idealized helix, if this ratio is smaller than π , right-handed screws pack in a right-handed way; if it is greater than π , right-handed screws pack in a left-handed way; if the ratio is π , the screws are at 90° and their disposition is not chiral.^{24,38} If the diameter of the screw is small with respect to the dimension of the groove, one can consider a simplified screw-cylinder interaction model in which right-handed screws always pack in a left-handed arrangement.^{11,39}

Sato et al.¹¹ realized that for these lyotropic systems, whose phase boundaries have little temperature dependence, an investigation of the handedness in the widest possible temperature interval should be carried out. As the cholesteric handedness in a few cases is opposite at different temperatures, the data at a single temperature are meaningless. Using a simple thermodynamic analysis, they proposed a plot of the cholesteric wavenumber q_c (the reciprocal pitch) as a function of the reciprocal temperature $1/T$ [Eq. (1)]

$$q_c = H_q/T + S_q \quad (1)$$

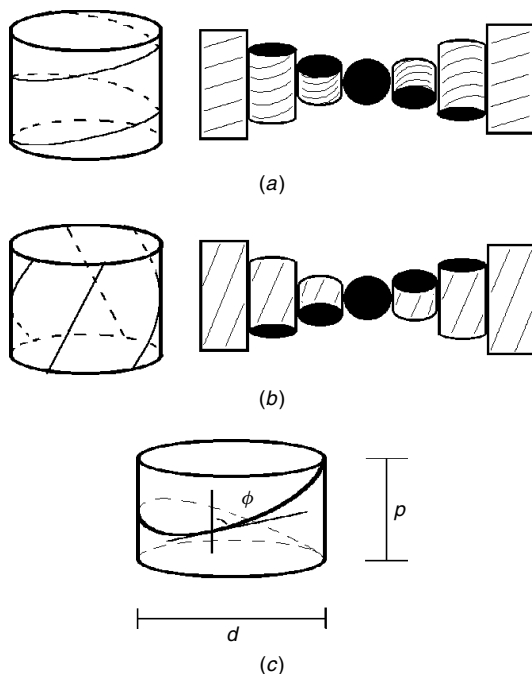


Figure 7.9 Different handedness of packing of right-handed helices with different pitch-to-diameter ratios. Right-handed helices with $p/d < \pi$ interact to give right-handed superhelix, while when $p/d > \pi$, superhelix is left-handed. (Reprinted with permission of Wiley-VCH from *Chemistry—A European Journal*, Vol. 6, p. 3249 ad ff., copyright © 2000.)

In several cases, the experimental plots were indeed linear. According to a molecular theory,^{11,39,40} the slope H_q and the intercept S_q are related to the chiral dispersion forces and to the entropic gain obtained by a twisted relationship between the polymer molecules (Figure 7.4), respectively. The value of S_q reflects the fact that the helices take up less space when packed in a helical arrangement and should be related to the hard-core steric contribution to the twist. Positive or negative values of S_q should be related to a right- or left-handed twist between the polymer molecules, respectively, and should be determined solely by steric effects.

The screw models of Figure 7.4 are, of course, an abstraction, and real macromolecules are much more complex. In particular, apart from DNA and G-wires, which have sugar-phosphate backbones as external ridges, but are also charged, most natural and synthetic polymers have external side chains which could generate a secondary chiral surface, which might interfere with the chirality of the polymer backbone.²⁸ Even if the qualitative estimate of S_q based on the models of Figure 7.4 seems rather primitive, the estimate of H_q

is unfortunately even more complex, and theoretical calculations do not seem applicable to practical cases.⁴¹

With very few exceptions, the most common polymer geometry is similar to that of Figure 7.9a, that is, with $p/d < \pi$. Poly(*R*)-2,6-dimethylheptyl isocyanate is a left-handed helical polymer, and its lyotropic cholesteric (right-handed at room temperature)⁴² has negative S_q (and positive H_q). It, therefore, seems to follow the model of Figure 7.9a: left-handed screws packed in a left-handed way. Schizophyllan is a right-handed triple-helical polysaccharide; its cholesteric phase has negative S_q (and positive H_q), therefore it follows the model of Figure 7.9b.¹¹ This seems in agreement with the very steep inclination of the threads of this polymer (see Figure 7.10).⁴³

The danger of comparing chirality data at a single temperature is particularly evident in the following examples. The cholesteric phase formed by B-DNA (a right-handed double helix) in water is left-handed at room temperature. Right-handed G-wires (a four-stranded right-handed helix as determined by CD spectroscopy^{24,35} and single-crystal X-ray diffraction⁴⁴) give instead right-handed cholesterics at room temperature.⁴⁵ Inspection of X-ray data does not show substantial difference in the inclination of the sugar–phosphate thread in both cases (see Figure 7.11).

However, temperature dependence of the twist (the pitch was determined from fingerprint textures) follows Eq. (1) and in both cases gives positive

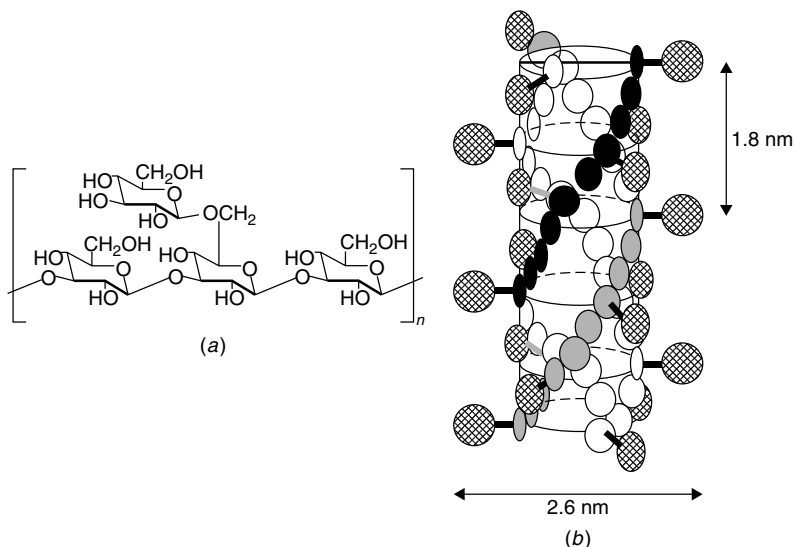


Figure 7.10 Repeating unit of (a) schizophyllan and its representative model of the (b) triple-helix. (Reprinted with permission of American Chemical Society from *Journal of American Chemical Society*, Vol. 122, p. 4520 and ff., copyright © 2000.)

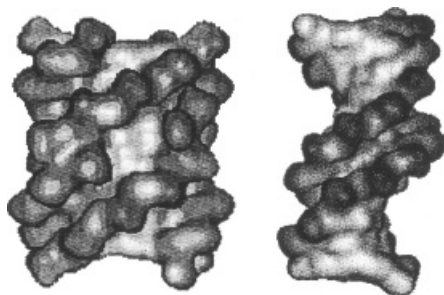


Figure 7.11 Pictures obtained with high-resolution X-ray diffraction data of G-wire of d(TG₄T) (left) and the B-DNA duplex of d(CGCGAATTCGCG). (Reprinted with permission of Wiley—VCH from *Chemistry—A European Journal*, Vol. 6, p. 3249 ad ff., copyright © 2000.)

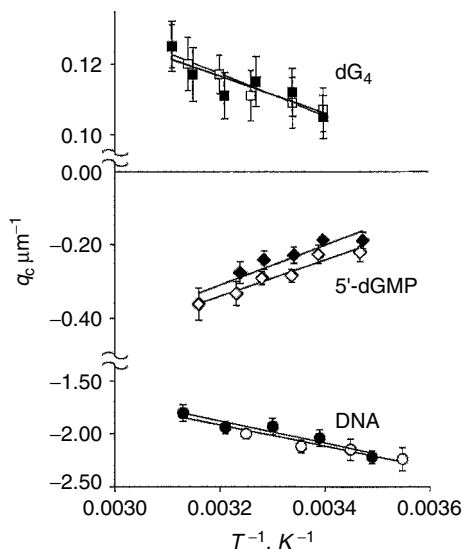


Figure 7.12 Plots of q_c vs. T^{-1} for cholesteric aqueous solutions of short fragments of DNA, 5'-dGMP, and dG₄: Filled symbols refer to heating scans, while open symbols to cooling scans. While DNA and the G-wire of dG₄ are right-handed, the G-wire of 5'-dGMP is left-handed: Slopes and intercepts reflect the polymer stereochemistry. (Reprinted with permission of Wiley—VCH from *Chemistry—A European Journal*, Vol. 6, p. 3249 ad ff., copyright © 2000.)

S_q and negative H_q (Figure 7.12), so the handedness of the polymers are correlated to those of the cholesteric phases and the apparent discrepancy depends only on the comparison of the two results at a single temperature. Also in these cases the most common model of Figure 7.9a seems to be followed.⁴⁶ It should be remarked that in all these cases, H_q and S_q have opposite signs.⁴¹

To summarize, in the field of lyotropic cholesterics formed by helical polymers of known geometry, it is possible to predict qualitatively only the entropic contribution to the cholesteric twist: The prediction relies on the model of Figure 7.4 and should be compared to the experimental S_q data obtained by extrapolation of the twist to $1/T = 0$. A practical model for calculating the often dominant dispersion contribution is not yet available.

4 THERMOTROPIC-INDUCED CHOLESTERICIS

In the transfer of chiral information from the molecular to the mesophase level, there is a passage from molecular to supramolecular macroscopic chirality, and the molecular dissymmetry is, in some way, amplified⁴⁷; this is shown, for example, by the very strong CD and optical rotation of the cholesteric phases. In 1968, Penot et al.⁴⁸ at the College de France detected the spontaneous resolutions of racemates doping a nematic with a single crystal: In that case the crystals were too small to allow an optical rotation measurement, but big enough to induce cholesteric mesophases in nematics and hence to allow the detection of chirality. Later, several studies described the use of the cholesteric induction for detecting traces of chiral dopants^{49,50} or to detect compounds with very low optical rotation.⁵¹

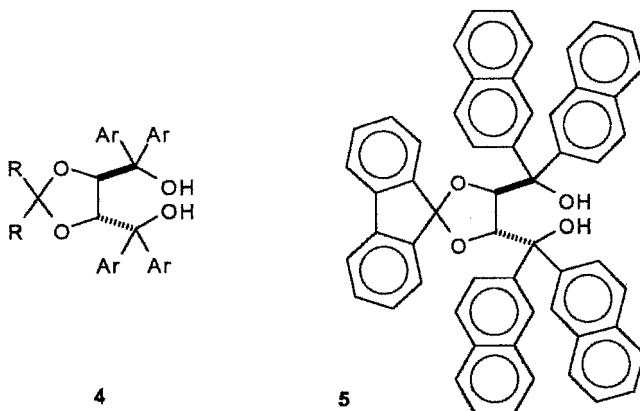
The study of the cholesteric mesophases obtained by doping thermotropic nematics with chiral, nonracemic compounds, has lead to relevant information about the stereochemistry of the dopants. Chiral interactions change the structure of the phase and therefore molecular chirality can be mapped onto an achiral (nematic) phase to yield a superstructural phase chirality. In 1984 Sol-ladié and Zimmermann published the first review summarizing the state of the art at that time.⁵² Later on, several review articles updated this subject.⁵³⁻⁵⁵

A quantitative study of the cholesteric induction and of the chiral transfer from dopant to phase requires the definition of the helical twisting power β . This quantity expresses the ability of a chiral dopant to twist a nematic phase and can be numerically expressed in Eq. (2) where p is the cholesteric pitch, c the dopant molar fraction, and r its enantiomeric excess; its sign is taken to be positive or negative for right-handed (P), or left-handed (M) cholesterics, respectively. This relation holds for molar fractions $<0.01-0.05$:

$$\beta = (pcr)^{-1} \quad (2)$$

From the stereochemical point of view, β characterizes a chiral compound similar to the classical rotatory power $[\alpha]_D$. However, the two quantities have a different origin: The optical rotation is a consequence of the chiral interaction between light and matter, while the cholesteric induction originates from a

solute–solvent chiral interaction. Therefore, one can expect to obtain different and independent information from LC techniques and chiroptical spectroscopic techniques; the former should be more sensitive to molecular shape. Chiral dopants can exhibit a different ability to twist the nematic phase spanning from weak inducer ($\beta < 1 \mu\text{m}^{-1}$) to strong inducer ($\beta > 20 \mu\text{m}^{-1}$); to our knowledge, the strongest chiral dopants investigated are $\alpha,\alpha,\alpha',\alpha'$ -tetraaryl-1,3-dioxolane-4,4-dimethanol (TADDOL) derivatives **4**, typically showing twisting powers in the range $300\text{--}400 \mu\text{m}^{-1}$.⁵⁶ A record of $534 \mu\text{m}^{-1}$ was achieved with **5** in the nematic phase 4'-pentyl-4-cyanobiphenyl.⁵⁷



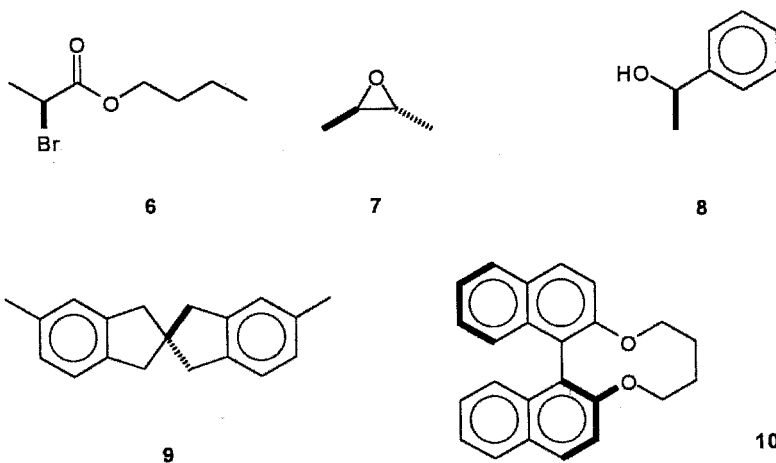
From a cholesteric induction experiment, one can obtain chiral information on the induced cholesteric (namely, pitch and handedness) and therefore the helical twisting power of the dopant in that solvent (at a certain temperature). If a model or molecular theory relating molecular chirality to mesophase chirality is available, one can infer stereochemical information about the dopant (absolute configuration, preferred conformation).

4.1 Empirical Approach

As mentioned in the introduction, the first empirical correlation between the absolute configuration of dopants and the handedness of induced cholesterics was proposed in 1975.²⁰ The first attempt to find a general correlation was a few years later: Krabbe et al.⁵⁸ related the sense of the cholesteric to a stereochemical descriptor of the dopant based on the effective volume of the substituents and listed many compounds following this rule. However, exceptions were described at that time,⁵⁹ and, furthermore, this approach neglects the role of the structure of the nematic solvent in determining the sense of the cholesteric. It is well known that chiral compounds may induce cholesterics of opposite handedness in different nematics.^{60,61}

A satisfactory understanding of the relation existing between molecular and phase handedness would require the knowledge of how the chiral information is transferred from the dopant to the bulk of the solvent.

The first theoretical treatments of the helical twisting power⁶² are too complex to allow the extraction of terms containing molecular parameters useful for a practical investigation of stereochemical problems. Only in recent years (*vide infra*) have several authors obtained reliable calculations of the helical twisting power of selected compounds. At the beginning of the '1980s, we followed an empirical approach based on the analysis of many helical twisting power determinations with the aim of determining the structural features associated to high values of β in both the dopant and the solvent. The results, summarized in Ref. ⁵³, indicated that the most typical structural feature of the dopant associated to high twisting power is the presence of two (or more) (quasi-)planar moieties chirally disposed one with respect to the other(s). For example, while aliphatic compounds with one or two stereocenters **6** and **7**, derivative **8** with one aromatic ring: and spiro-compound **9** with two almost perpendicular benzene rings have helical twisting powers not exceeding $1 \mu\text{m}^{-1}$, biaryl **10** has β around $60 \mu\text{m}^{-1}$ in the same (or similar) solvent.⁵³



The recognition that this molecular feature is only connected to a high efficient transfer of chirality does not allow the prediction of the sense of the induced cholesteric: Some molecular models are therefore required. In the first model proposed,^{20,63} the solvent molecules are considered achiral rigid rods, and the role of the chiral dopant is to prevent the parallel alignment of the host nematic molecules leading to the helicoidal arrangement (see Figure 7.13). Although this model has been used to assign the configuration of a few series of compounds,^{20,63} it is too simplistic; in fact, the value of β

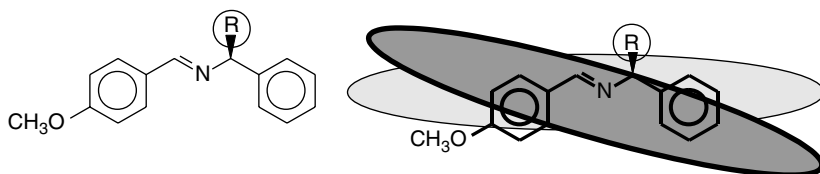


Figure 7.13 Chiral molecule prevents the parallel alignment of two adjacent solvent molecules (idealized as uniaxial rodlike objects).

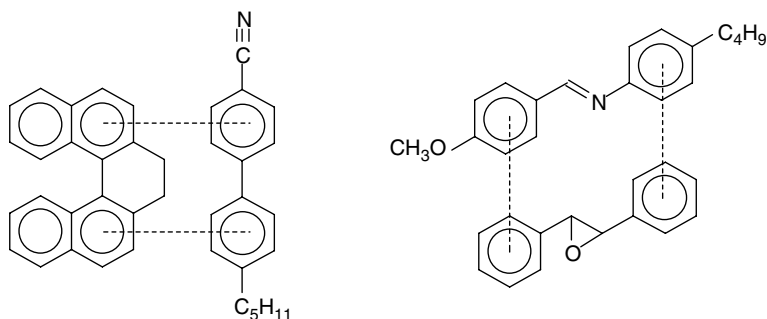


Figure 7.14 Structural similarity between a biaryl derivative and nematic phase K15, and between *trans*-stilbene oxide and the nematic MBBA.

(and sometimes its sign^{60,61}) strongly depends on the nature of the solvent and is higher when the chemical structure of the solute and solvent molecules are similar.⁶⁴ As a general finding, biaryl dopants show the highest value of β in biaryl solvents (e.g., cyanobiphenyl nematics),⁶⁵ while *trans*-diaryl oxiranes (and related molecules) exhibit the highest β 's in 4-methoxybenzylidene-4'-butylaniline (MBBA, a nematic molecule with a two-atom spacer between the two aryls, as in the dopant)⁶⁶ (see Figure 7.14). Furthermore, the ability to twist the nematic also depends on the conformational mobility of the host, and in a rigid core solvent the values of β are generally smaller.⁶⁷

These results allowed the proposal, at the beginning of the 1980s, of a different molecular model for cholesteric induction.^{65,66} This model is sketched in Figure 7.15 in the case when both nematic host and chiral guest have a biaryl structure. Nematic molecules exist in chiral enantiomorphic conformations of opposite helicity in fast interconversion. The chiral dopant has a well-defined helicity (*M* in Figure 7.15) and stabilizes the homochiral conformation of the solvent: In this way, the *M* chirality is transferred from the dopant to the near molecule of the solvent and from this to the next near one and so on. This

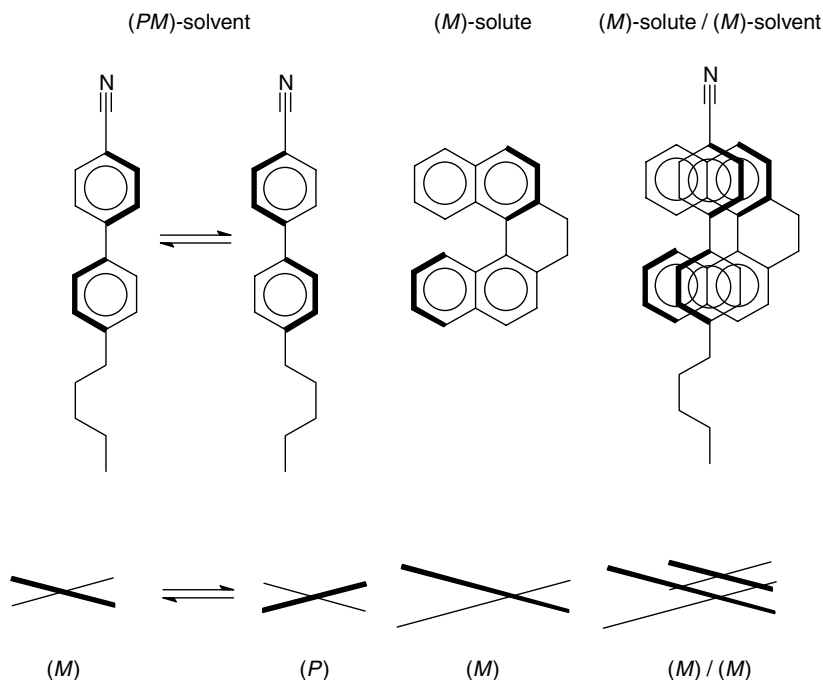
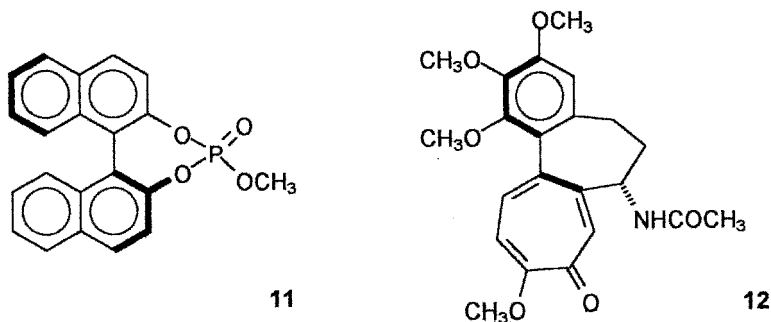


Figure 7.15 Chirality transfer from dopant to solvent. Chiral inducer with an (*M*)-helicity aligned with its biaryl axis parallel to biphenyl axis of solvent can have close contact only with molecules of solvent having same helicity: Chirality is therefore transferred from dopant to near solvent molecule and from this to next near one and so on, via chiral conformations.

leads to a deracemization of the nematic solvent and its transformation into a *M* cholesteric.⁶⁸

The role of the chiral conformation of the solvent in the chiral transfer is important also in chiral SmC, a fundamental phase for obtaining new LC displays with fast response to electric fields.⁶⁹ The mechanism of Figure 7.15 has been supported by rotatory power measurements in isotropic solutions.⁷⁰ Binaphthyl **11**, a compound with positive twisting power ($\beta = +73 \mu\text{m}^{-1}$ in E7, a mixture of biaryl derivatives), in nonmesogenic biphenyl solvents displays a rotatory power ($+762^\circ$, in 4-pentylbiphenyl), which is much more positive than in acetonitrile ($+469^\circ$); colchicine (**12**) has a positive β ($+54 \mu\text{m}^{-1}$ in E7) and is laevorotatory in acetonitrile (-162°), while in biphenyl solvents it displays a small negative rotation (-9°). These data can be interpreted assuming that the right-handed twisting compounds **11** and **12** in biaryl solvents induce an excess of molecules in the *P* conformation; their contribution

to the rotatory power is positive. Molecular statistical calculations support this chirality transfer.⁷⁰



4.2 Theoretical Approach

The understanding of the molecular mechanisms at the base of cholesteric induction has been approached also with theoretical tools. Statistical mechanics and computer simulation techniques are widely used to describe the behavior of many-body systems. However, these methods are forced to use simple idealized objects.^{68,71} Recently, a Monte Carlo technique for the prediction of the twisting power of chiral dopants has been presented: It is based on an atomistic representation of chiral dopants; the agreement between the experimental and calculated β 's is excellent; however, the computational cost is very high.⁷² The recent activity of Ferrarini and co-workers at Padua University aims to set up theoretical methods capable of accounting for the behavior of liquid crystals by using a realistic picture of the chemical constituents in terms of molecular geometry, charge distribution, and polarizability. This theoretical approach²² is based on a shape model accounting for the chirality and anisotropy (affecting the orientational capability) of the interaction between solute and solvent and has been shown to interpret the twisting power of several classes of compounds.⁷³ The handedness and the pitch of induced chiral nematics are determined by the coupling between the molecular helicity (which is different along the different molecular directions) and the orientational behavior of the dopant (which tends to impart a preferential alignment with respect to the nematic director). For example, heptalene derivatives are characterized by helicities which are opposite along the x and y directions (see Figure 7.16): These two helicities have been experimentally differentiated by the handedness of the chiral nematics induced by heptalenes **13** and **14**, whose substitution patterns favor the x or y orientation, respectively, along the director.⁷⁴

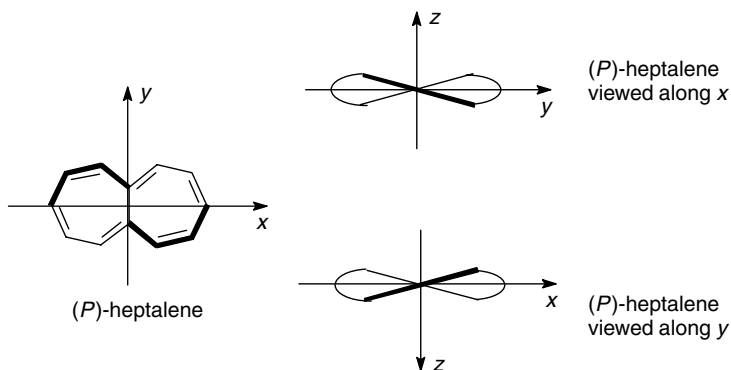
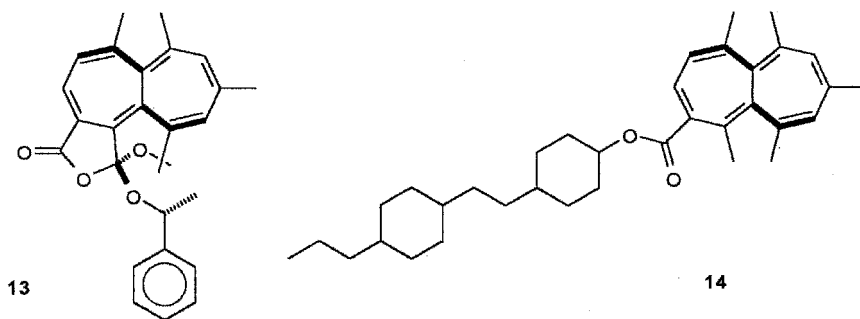


Figure 7.16 Chiral (*P*)-heptalene as seen along the *y* and *x* directions. The helicities along these two axes are opposite.

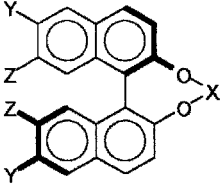


4.3 Biaryl Moiety

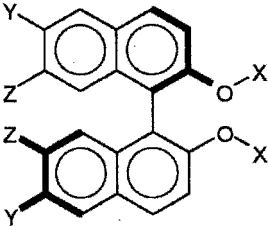
Several stereochemical applications of cholesteric induction have been described.^{52–55} Reliable results are obtained especially when the dopant has a high twisting power. One of the molecular fragments associated to a high value of twisting power is, as anticipated above, the biaryl unit; therefore many experiments have been done on compounds containing this unit.

The main factor in determining the handedness of the cholesterics induced by bridged 1,1'-binaphthyls is the helicity (*P* or *M*) of the solute, and this observation is the basis of many configurational studies of chiral binaphthyls. All the homochiral (*aR*)-binaphthyls **15–19** have an *M* helicity of the core, and all induce, in biphenyl nematics, *M* cholesterics.^{65,75} By systematic structural variations of the covalent bridge, it is possible to obtain 1,1'-binaphthalenes with dihedral angles ranging from 60° to 96° (see series **20–24**); the handedness of the cholesteric phase always matches the helicity

of the binaphthyl unit (see Table 7.1).⁶⁰ It should be noticed that derivatives **23** and **24** have helicity (*P*, *s-trans*) opposite to all the other derivatives, hence they induce opposite-handed cholesterics.

	X	Y	Z	
	15	CH ₂	H	H
	16	CH ₂	H	Br
	17	CH ₂	H	BzO
	18	(CH ₂) ₃	H	H
	19	(CH ₂) ₄	H	H
	20	CH ₂	6-Acetamido-2-pyridyl	BzO
	21	(CH ₂) ₂ N(CO ₂ C ₂ H ₅)(CH ₂) ₂	6-Acetamido-2-pyridyl	BzO
	22	(CH ₂) ₂ N(CH ₃)(CH ₂) ₂	6-Acetamido-2-pyridyl	BzO
	23	CH ₂ CCCH ₂	6-Acetamido-2-pyridyl	BzO
	24	CH ₂ (<i>m</i> -C ₆ H ₄)CH ₂	6-Acetamido-2-pyridyl	BzO

This finding allows one to obtain useful information also on the conformation of nonbridged binaphthyls in solution.^{75,76} In the case of (*aS*)-binaphthyls, *s-cis* and *s-trans* conformations are characterized by opposite helicities along the biaryl axis. Therefore, one may expect the induction of left-handed or right-handed cholesterics depending on the dominant conformation in solution. In fact, binaphthyls **25–27** (with substituents able to stabilize the *s-cis* conformation) exhibit opposite-signed β with respect to binaphthyls **28–32** (with the bulkiest substituents stabilizing the *s-trans* conformation) (Table 7.2).

	X	Y	Z	
	25	H	H	H
	26	H	H	BzO
	27	H	Br	H
	28	H	H	Br
	29	CH ₃	H	Br
	30	C ₂ H ₅	H	H
	31	C ₂ H ₅	Br	H
	32	Bz	H	H

In contrast to binaphthyls, chiral biphenyl derivatives are challenging systems because their twist ability shows a strong dependence on the molecular structure, which does not conform to the empirical correlation rule described above. In fact, homochiral biphenyls **33–40** are characterized by *P* helicity along the biphenyl axis. In spite of this common feature, the twisting power spans from a highly positive value for **33–45** to a relatively negative value

Table 7.1
Helical Twisting Powers of Compounds **15–24** Determined at Room Temperature in Biphenyl Nematics^{60,65,75a}

	15	16	17	18	19	20	21	22	23	24
β	-85	-68	-80	-80	-79	-33.6	-65.6	-2.5	+40.0	+95.2
	<i>s-cis</i>	<i>s-cis</i>	<i>s-cis</i>	<i>s-cis</i>	<i>s-cis</i>	<i>s-cis</i>	<i>s-cis</i>	<i>s-cis/s-trans</i>	<i>s-trans</i>	<i>s-trans</i>
Core helicity	<i>M</i>	<i>M</i>	<i>M</i>	<i>M</i>	<i>M</i>	<i>M</i>	<i>M</i>	—	<i>P</i>	<i>P</i>

^a Also the conformation around the binaphthyl bond⁵⁸ is reported.

Table 7.2
Helical Twisting Powers of Compounds **25–32** Determined at Room Temperature in Biphenyl Nematics^{75,76a}

	25	26	27	28	29	30	31	32
β	-32	-5	-15.5	+26.1	+6.8	+10	+19	+22
	<i>s-cis</i>	<i>s-cis</i>	<i>s-cis</i>	<i>s-trans</i>	<i>s-trans</i>	<i>s-trans</i>	<i>s-trans</i>	<i>s-trans</i>
Core helicity	<i>M</i>	<i>M</i>	<i>M</i>	<i>P</i>	<i>P</i>	<i>P</i>	<i>P</i>	<i>P</i>

^a Also the conformation around the binaphthyl bond⁶⁰ is reported.

for **37–40**, passing through an almost negligible value for **36**.^{52,77,78} The differences between the dopants are mainly due to their orientational behaviors induced by the substitution in the central biphenyl core: The different orientational behavior (compounds **33–35** are similar to discs, while compounds **37–40** resembles rods) correspond to a different averaging of the chiral interaction sensed by the solvent⁷⁸ (Table 7.3).

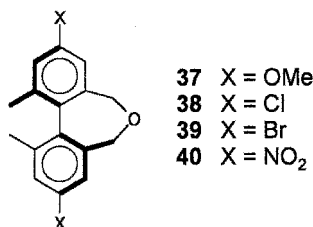
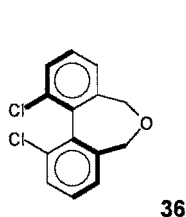
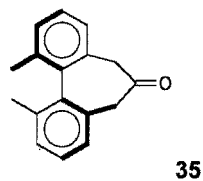
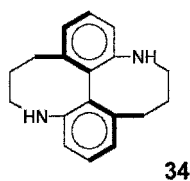
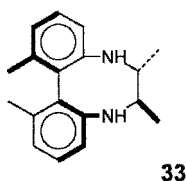


Table 7.3
Helical Twisting Powers of Compounds **33–40** Determined at Room Temperature in
Biphenyl Nematics^{52,77,78}

	33	34	35	36	37	38	39	40
β	+21	+20	+15	-1.5	-11.4	-17.2	-19.3	-20.3

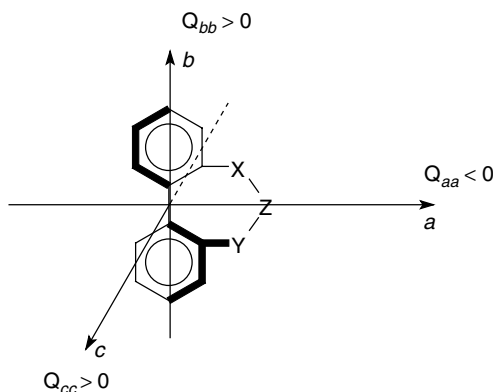


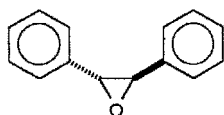
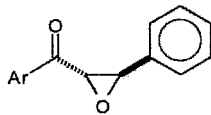
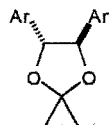
Figure 7.17 The sign of the chirality tensor Q_{ii} along the molecular axes.

Theoretical computations based on the shape model introduced by di Matteo and co-workers support this view.⁷⁸ The chirality of the bridged biphenyls, as measured by a chirality tensor, is substantially the same (positive along the c and b directions and negative along the a direction; see Figure 7.17). However, the order matrix is strongly dependent on the substituents present: The introduction of substituents in the 4, 4' positions transforms the disc-shaped molecules (which tend to align on the normal of the molecular plane perpendicular to the director) into more elongated rodlike compounds (which tend to align on the long molecular axis along the director). The dopant helicity experienced by the solvent is therefore different in the two limiting cases: positive (helicity along c) for dislike molecules and negative (average negative value of the helicities along a and b) for rodlike molecules.

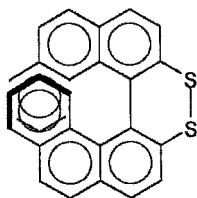
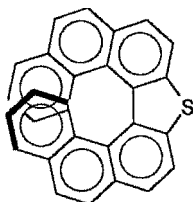
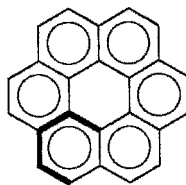
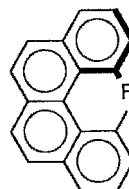
4.4 Chiral Molecules Different from Biaryls

Although biaryl-based chiral molecules are the most extensively studied, also other molecular frameworks are associated to high twisting powers and thus suitable for stereochemical studies. One of the first chiral structures used in

nematic doping was the oxirane ring with two aromatic moieties: Homochiral compounds **41–44** induce cholesterics of the same left-handedness.⁶⁶ These compounds are similar in shape but differ from the spectroscopic point of view: From their chiroptical features, it is not easy to obtain a reliable correlation of configuration, while the nematic doping approach allows a correct configuration assignment. Similar configurational studies have been performed on 4,5-diaryl-1,3-dioxolanes **45**.^{61,79}

**41****42** Ar = Ph**43** Ar = 2-thienyl**44** Ar = 3-thienyl**45** Ar, Ar' = Ph, *p*-R-Ph, Np

A last example of a dopant whose chirality has been investigated by the LC technique is represented by helicenes and related molecules. Once again, compounds very different spectroscopically, such as **46–49**, and hence hardly comparable with chiroptical techniques, are very similar in shape and give helical twisting powers of the same sign and of comparable intensity⁸⁰; the twisting powers of helicenes have been successfully calculated by the shape model of Ferrarini et al.⁷³

**46****47****48****49**

5 CONCLUSIONS

In this report, we have summarized some attempts to correlate molecular to cholesteric chirality both in thermotropic and lyotropic fields. In the former case, we have described only cholesteric induction, while in the lyotropic field, only cholesterics formed by helical polymers have been dealt with, as chiral micellar systems, for the moment, are too complex.

Despite its wide interest, this problem is still far from being solved and requires further theoretical and experimental work. This is not surprising as phenomena connected to chirality are very complex: For example, in chiroptical

spectroscopy, even if a general theory is available and accepted, practical calculations of CD spectra are possible only in limited cases.

In the field of thermotropic cholesterics, the most promising approach seems to be that reported by Nordio and Ferrarini^{22,23} for calculating helical twisting powers. It allows one to tackle real molecules with rather complex structures and to describe them in detail. The model is currently being extended to include a better description of nematic solvents and specific solute–solvent interactions. Once tested also for conformationally mobile molecules, this model could allow the prediction of the handedness of single-component cholesterics, and, in the field of induced cholesterics, very interesting information on solute molecules could be obtained.

ACKNOWLEDGMENTS

We would like to thank all the people who have contributed to the work described in this report and in particular the co-workers who are individually recognized in the cited references. Financial support from MIUR and University of Bologna is gratefully acknowledged.

REFERENCES

1. Collings, P. J. *Liquid Crystals*, Adam Hilger, Bristol, 1990, Chapter 2, for an interesting discussion on the story of the liquid crystal.
2. Reinitzer, F. *Monatsh. Chem.* **1888**, 9, 421.
3. Friedel, G. *Ann. Phys. Paris* **1922**, 18, 273.
4. Buckingham, A. D.; Ceasar, G. P.; Dunn, M. B. *Chem. Phys. Lett.* **1969**, 3, 540.
5. McDonnel, D. G. In *Thermotropic Liquid Crystals*. Gray, G. W. (Ed.). Wiley, Chichester, 1987, pp. 120–125, gives a clear discussion of this phenomenon.
6. Scheffer, T.; Nehring, J. In B. Bahadur (Ed.). *Liquid Crystals—Applications and Uses*, Vol. 1. World Scientific, Singapore, 1990, pp. 231–270.
7. Collings, P. J., *Liquid Crystals*, Adam Hilger, Bristol, 1990, p. 104.
8. McDonnel, D. G. In *Thermotropic Liquid Crystals*, Gray, G. W. (Ed.). Wiley, Chichester, 1987, pp. 125–130.
9. Robinson, C. *Tetrahedron* **1961**, 13, 219. Robinson, C.; Ward, J. C.; Beevers, R. B. *Discuss. Faraday Soc.* **1958**, 25, 29.
10. Livolant, F. *J. Phys.* **1986**, 47, 1605.
11. Sato, T.; Sato, Y.; Umemura, Y.; Teramoto, A.; Nagamura, Y.; Wagner, J.; Weng, D.; Okamoto, Y.; Hatada, K.; Green, M. M. *Macromolecules* **1993**, 26, 4551.
12. Boidart, M.; Hochapfel, A.; Peretti, P. *Mol. Cryst. Liq. Crystallogr.* **1989**, 172, 147.
13. Bouligand, Y.; Soyer, M. O.; Puisseux-Dao, S. *Chromosoma* **1969**, 24, 251.
14. Livolant, F. *Physica A* **1991**, 176, 117.
15. Reich, Z.; Wachtel, E. J.; Minsky, A. *Science* **1994**, 264, 1460.

16. Neville, A. C.; Caveney, S. *Biol. Rev.* **1969**, *44*, 531.
17. Martin, R.; Farjanel, J.; Eichenberger, D.; Colige, A.; Kessler, E.; Hulmes, D. J. S.; Giraud-Guille, M.-M. *J. Mol. Biol.* **2000**, *301*, 11.
18. Dogic, Z.; Fraden, S. *Langmuir* **2000**, *16*, 7820.
19. Giraud-Guille, M.-M. *Int. Rev. Cytol.* **1996**, *166*, 59.
20. Gottarelli, G.; Samorì, B.; Marzocchi, S.; Stremmenos, C. *Tetrahedron Lett.* **1975**, *24*, 1981.
21. Gray, G. W.; McDonnell, D. G. *Mol. Cryst. Liq. Cryst.* **1977**, *34*, 211.
22. Ferrarini, A.; Moro, G. J.; Nordio, P. L.; Luckhurst, G. R. *Mol. Phys.* **1992**, *77*, 1.
23. Ferrarini, A.; Moro, G. J.; Nordio, P. L. *Mol. Phys.* **1996**, *87*, 485. Ferrarini, A.; Moro, G. J.; Nordio, P. L. *Phys. Rev. E* **1996**, *53*, 681. Ferrarini, A.; Nordio, P. L. *J. Chem. Soc. Perkin Trans. 2*, **1998**, 455.
24. Gottarelli, G.; Spada, G. P. In *Circular Dichroism—Principles and Applications*. Berova, N.; Nakanishi, K.; Woody, R. W. (Eds.). Wiley-VCH, New York, 2000, pp. 547–561.
25. De Vries, A. *Acta Crystallogr.* **1951**, *4*, 219.
26. Korte, E. H.; Schrader, B.; Bualek, S. *J. Chem. Res. (S)* **1978**, 236; *J. Chem. Res. (M)* **1978**, 3001.
27. Radley, K.; Catey, H. *Mol. Cryst. Liq. Cryst.* **1994**, *250*, 167–175.
28. Dupré, D. B.; Samulski, R. T. In *Liquid Crystals—the Fourth State of Matter*. Saeva, F. D., (Ed.). Marcel Dekker, New York, 1979, pp. 203–247.
29. Grandjean, F. *C. R. Acad. Sci.* **1921**, *172*, 71. Cano, R. *Bull. Soc. Fr. Mineral.* **1968**, *91*, 20.
30. Heppke, G.; Oestreicher, F. *Z. Naturforsch.* **1977**, *32A*, 899–901.
31. Heppke, G.; Oestreicher, F. *Mol. Cryst. Liq. Cryst.* **1978**, *41*, 245–249.
32. Kahn, F. J. *Phys. Rev. Lett.* **1970**, *24*, 209–212.
33. Hakemi, H.; Varanasi, P. P. *Liq. Cryst.* **1986**, *1*, 63–71.
34. Chilaya, G. S.; Lisetski, L. N. *Mol. Cryst. Liq. Cryst.* **1986**, *140*, 243–286.
35. Bonazzi, S.; Capobianco, M.; De Morais, M. M.; Garbesi, A.; Gottarelli, G.; Mariani, P.; Ponzi Bossi, M. G.; Spada, G. P.; Tondelli, L. *J. Am. Chem. Soc.* **1991**, *113*, 5809.
36. Straley, J. P. *Phys. Rev.* **1976**, *14*, 1835.
37. Cothia, C.; Levitt, M.; Richardson, D. *Proc. Natl. Acad. Sci. (USA)* **1977**, *74*, 4130–4134.
38. Harris, A. B.; Kamien, R. D.; Lubensky, T. C. *Rev. Mod. Phys.* **1999**, *71*, 1745.
39. Green, M. M.; Peterson, N. C.; Sato, T.; Teramoto, A.; Cook, R.; Lifson, S. *Science* **1995**, *268*, 1860.
40. Kimura, H.; Hoshino, M.; Nakano, H. *J. Phys. Soc. Jpn.* **1982**, *51*, 1584.
41. Osipov, M. A. *Nuovo Cimento* **1988**, *D10*, 1249.
42. Green, M. M.; Zanella, S.; Gu, H.; Sato, T.; Gottarelli, G.; Jha, S. K.; Spada, G. P.; Shooevaars, A. M.; Feringa, B.; Teramoto, A. *J. Am. Chem. Soc.* **1998**, *120*, 9810.
43. Sakurai, K.; Shinkai, S. *J. Am. Chem. Soc.* **2000**, *122*, 4520.
44. Laughlan, G.; Murchie, A. I. H.; Norman, D. G.; Moore, M. H.; Moody, P. C. E.; Lilliey, D. M. J.; Luisi, B. *Science* **1994**, *265*, 520–524.
45. Proni, G.; Gottarelli, G.; Mariani, P.; Spada, G. P. *Chem. Eur. J.* **2000**, *6*, 3249–3253.
46. For an electrostatic interpretation of the formation of the cholesteric phase of DNA, which does not give, however, a stereochemical correlation between the macromolecular and cholesteric handedness, see Kornyshev, A. A.; Leikin, S. *Phys. Rev. Lett.* **2000**, *84*.

47. Proni, G.; Spada, G. P. *Enantiomer* **2001**, *6*, 171–179. Kuball, H.-G.; Höfer, T. In *Chirality in Liquid Crystals*. Bahr, C.; Kitzerow, H.-S. (Eds.). Springer, Heidelberg, **2001**, pp. 67–100.
48. Penot, J. P.; Jacques, J.; Billard, J. *Tetrahedron Lett.* **1968**, *9*, 4013.
49. Korte, E. H. *Appl. Spectr.* **1978**, *32*, 568.
50. Bertocchi, G.; Gottarelli, G.; Prati, R. *Talanta*, **1984**, *31*, 138.
51. Gottarelli, G.; Samorì, B.; Fuganti, C.; Grasselli, C. *J. Am. Chem. Soc.* **1981**, *103*, 471.
52. Solladié, G.; Zimmermann, R. G. *Angew. Chem. Int. Ed. Eng.* **1984**, *23*, 348–362.
53. Gottarelli, G.; Spada, G. P. *Mol. Cryst. Liq. Cryst.* **1985**, *123*, 377.
54. Gottarelli, G.; Spada, G. P.; Solladié, G. *Nouv. J. Chim.* **1986**, *10*, 691–696.
55. Spada, G. P.; Proni, G. *Enantiomer*, **1998**, *3*, 301–314.
56. Kuball, H.-G.; Weiss, B.; Beck, A. K.; Seebach, D. *Helv. Chim. Acta* **1997**, *80*, 2507–2514.
57. Seebach, D.; Beck, A. K.; Heckel, A. *Angew. Chem. Int. Ed.* **2001**, *40*, 92–138.
58. Krabbe, H. J.; Heggemeier, H.; Schrader, B.; Korte, E. H. *Angew. Chem. Int. Ed. Eng.* **1977**, *16*, 791. Krabbe, H. J.; Heggemeier, H.; Schrader, B.; Korte, E. H. *J. Chem. Res. (S)* **1978**, *238*; *J. Chem. Res. (M)* **1978**, 3023.
59. Gottarelli, G.; Samorì, B.; Folli, U.; Torre, G. *J. Phys. (C)* **1979**, *40*, 3–25.
60. Proni, G.; Spada, G. P.; Lustenberger, P.; Welti, R.; Diederich, F. *J. Org. Chem.* **2000**, *65*, 5522–5527.
61. Superchi, S.; Donnoli, M. I.; Proni, G.; Spada, G. P.; Rosini, C. *J. Org. Chem.* **1999**, *64*, 4762–4767.
62. Goossens, W. J. A. *Mol. Cryst. Liq. Cryst.* **1971**, *12*, 237. Stegemeyer, H.; Finkelmann, H. *Naturwiss.* **1975**, *62*, 436. Van der Meer, B. W.; Vertogen, G. *Phys. Lett.*, **1979**, *71A*, 486. Allen, M. P. *Phys. Rev. E* **1993**, *47*, 4611.
63. Rinaldi, P. L.; Wilk, M. *J. Org. Chem.* **1983**, *48*, 2141.
64. Mioskowski, C.; Bourguignon, J.; Candau, S.; Solladié, G. *Chem. Phys. Lett.* **1976**, *38*, 456.
65. Gottarelli, G.; Hibert, M.; Samorì, B.; Solladié, G.; Spada, G. P.; Zimmermann, R. *J. Am. Chem. Soc.* **1983**, *105*, 7318.
66. Gottarelli, G.; Mariani, P.; Spada, G. P.; Samorì, B.; Forni, A.; Solladié, G.; Hibert, M. *Tetrahedron* **1983**, *39*, 1337.
67. Gottarelli, G.; Spada, G. P.; Varech, D.; Jacques, J. *Liq. Cryst.* **1986**, *1*, 29.
68. Memmer, R.; Kuball, H. G.; Schönhofer, A. *Mol. Phys.* **1996**, *89*, 1633–1649.
69. Lemieux, R. P. *Acc. Chem. Res.* **2001**, *34*, 845–853.
70. Gottarelli, G.; Osipov, M. A.; Spada, G. P. *J. Phys. Chem.* **1991**, *95*, 3879.
71. Allen, M. P. *Phys. Rev. E* **1993**, *47*, 4611–4614.
72. Cook, M. J.; Wilson, M. R. *J. Chem. Phys.* **2000**, *112*, 1560.
73. Ferrarini, A.; Nordio, P. L.; Shibaev, P. V.; Shibaev, V. P. *Liq. Cryst.* **1998**, *24*, 219–227. Ferrarini, A.; Gottarelli, G.; Nordio, P. L.; Spada, G. P. *J. Chem. Soc. Perkin Trans 2* **1999**, 411–417.
74. Gottarelli, G.; Hansen, H. J.; Spada, G. P.; Weber, R. H. *Helv. Chim. Acta* **1987**, *70*, 430–435.
75. Bandini, M.; Casolari, S.; Cozzi, P. G.; Proni, G.; Schmohel, E.; Spada, G. P.; Tagliavini, E.; Umami Ronchi, A. *Eur. J. Org. Chem.* **2000**, 491.
76. Gottarelli, G.; Spada, G. P.; Bartsch, R.; Solladié, G.; Zimmermann, R. *J. Org. Chem.* **1986**, *51*, 589. Rosini, C.; Rosati, I.; Spada, G. P. *Chirality* **1995**, *7*, 353. Deussen, H. J.;

- Shibaev, P. V.; Vinokur, R.; Bjornholm, T.; Schaumburg, K.; Bechgaard, K.; Shibaev, V. P. *Liq. Cryst.* **1996**, *21*, 327.
77. Gottarelli, G.; Spada, G. P.; Seno, K.; Hagishita, S.; Kuriyama, K. *Bull. Chem. Soc. Jpn.* **1986**, *56*, 1607. Williams, V. E.; Lemieux, R. P. *Chem. Commun.* **1996**, 2260.
78. di Matteo, A.; Todd, S. M.; Gottarelli, G.; Solladié, G.; Williams, V. E.; Lemieux, R. P.; Ferrarini, A.; Spada, G. P. *J. Am. Chem. Soc.* **2001**, *123*, 7842–7851.
79. Rosini, C.; Spada, G. P.; Proni, G.; Masiero, S.; Scamuzzi, S. *J. Am. Chem. Soc.* **1997**, *119*, 506.
80. Gottarelli, G.; Proni, G.; Spada, G. P.; Fabbri, D.; Gladiali, S.; Rosini, C. *J. Org. Chem.* **1996**, *61*, 2013.

Chapter 8

Ferroelectric Liquid Crystal Conglomerates

DAVID M. WALBA

University of Colorado, Boulder, Colorado 80309-0215

- 1 Introduction
- 2 Liquid Crystals and Supermolecular Stereochemistry
 - 2.1 What Is a Molecule? What Is a Liquid Crystal?
 - 2.2 INAC Phase Sequence
- 3 SmC* Phase and Ferroelectric Liquid Crystals
- 4 SmC_A* Phase and Antiferroelectric Liquid Crystals
- 5 Reflection Symmetry Breaking in Organic Materials
 - 5.1 Crystal Conglomerates
 - 5.2 Spontaneous Reflection Symmetry Breaking in Liquid Crystals
- 6 Chiral Liquid Crystals from Achiral Molecules: Banana Phases
 - 6.1 Bilayer Smectics and First Achiral Antiferroelectric LC
 - 6.2 Bent-Core Mesogens
 - 6.3 Matsunaga Diesters
 - 6.4 Banana Mania
 - 6.5 B4 Phase
 - 6.6 B2 Phase: Spontaneous Reflection Symmetry Breaking in Fluid Smectic
 - 6.7 SmCP Phases
 - 6.8 SmC_SP_A and SmC_AP_A Antiferroelectric Phases
 - 6.9 Stereogenic Elements in SmCP Phases: SmCP Supermolecular Diastereomers
 - 6.10 Ferroelectric Banana by Design
 - 6.11 Ferroelectric “Macroscopic Racemate” from Unichiral Mesogen
- 7 Conclusion
- References

1 INTRODUCTION

Macroscopic polarity (polar symmetry) in materials is an extremely important structural feature providing a dizzying array of useful properties including

Materials-Chirality: Volume 24 of Topics in Stereochemistry,
Edited by Mark M. Green, R.J.M. Nolte, and E.W. Meijer
ISBN 0-471-05497-6 Copyright © 2003 John Wiley & Sons, Inc.

ferro-, pyro-, and piezoelectricity and second-order nonlinear optical susceptibility. In the context of liquid crystal (LC) science, chirality and polarity have been closely coupled since Meyer's theoretical prediction of macroscopic electric polarization in the chiral smectic C (SmC^*) phase.¹ This led first to a demonstration of spontaneous polarization in an actual SmC^* material,² then to Clark and Lagerwall's elegant approach for control of the macroscopic structure of the system to create fluid ferroelectrics, and their demonstration of fast electro-optics in SmC^* ferroelectric liquid crystals (FLCs).³ Until 1996, however, chiral LCs always contained enantiomerically enriched compounds, and polar smectic LCs were always chiral. As implied by these statements, smectic LCs composed of achiral or racemic compounds were never polar.

This situation changed dramatically in 1996 with the discovery of strong electro-optic (EO) activity in smectics composed of "bent-core," "bow-shaped," or "banana-shaped" achiral molecules.⁴ Since then, the "banana-phases" exhibited by such compounds have been shown to possess a rich supermolecular stereochemistry, with examples of both macroscopic racemates and conglomerates represented. Indeed, the chiral banana phases formed from achiral or racemic compounds represent the first known bulk fluid conglomerates, identified 150 years after the discovery of their organic crystalline counterparts by Pasteur. A brief introduction to LCs as supermolecular self-assemblies, and in particular SmC^* ferroelectric and SmC_A^* antiferroelectric LCs, followed by a snapshot of the rapidly evolving banana-phase stereochemistry story, is presented here.

2 LIQUID CRYSTALS AND SUPERMOLECULAR STEREOCHEMISTRY

At the most basic level, stereochemistry is about molecular *structure* and *isomerism*. This seems straightforward, but even simple molecular stereochemistry language and thinking is rife with ambiguity. This stems from the fact that most molecules are not rigid Euclidean geometrical objects but rather flexible objects, often sampling a large number of configurations (conformations) on the free-energy hypersurface under conditions where a macroscopic ensemble of such molecules possesses a distinct identity as a "pure compound." This topological aspect of stereochemistry⁵ couples with the Euclidean constraints on molecular geometry in a rich and complex way that is often oversimplified.

For many chemists LCs are mysterious and complex materials, their very definition defying a simple understanding. The basic idea behind this discussion of stereochemistry in LCs is that molecules and LCs represent the same phenomenon. Liquid crystals are "supermolecules" in a different way than are supramolecular assemblies. Indeed, LCs can be composed of supramolecular

assemblies—the latter maintaining their distinct identity as components of the supermolecular LC.

2.1 What Is a Molecule? What Is a Liquid Crystal?

At a basic level, molecules are simply collections of atoms caught in a well on the free-energy configurational hypersurface. The plot in Figure 8.1 represents a slice of the hypersurface indicating two molecules, A and B, corresponding to isomeric compounds at room temperature. The concept that every well on this hypersurface represents an isomer, while defensible, seems singularly useless in the case of molecules that sample a large number of configurations, such as decane. At room temperature it is certainly useful to think of pure *n*-decane as a compound, rather than a mixture of thousands of interconverting isomers. What is a molecule of *n*-decane, then? It is a collection of 10 carbon atoms and 22 hydrogen atoms caught in a well, which itself contains a great many local minima, as indicated by the group of configurations A in Figure 8.1. The group of configurations B has a distinct identity at room temperature, representing, for example, isodecane (2-methylnonane). These collections of atoms are inherently dynamic in nature at room temperature, with a time-average symmetry and structure.

Of course, we consider the fact that the atoms are covalently bonded as a key feature of the structure, but the work of Cram and Lehn, among others, served to formalize the notion that assemblies of molecules can form supramolecular structures which behave very much like molecules, even though not all of the atoms are covalently connected.⁶ In fact Wasserman's discussion of molecular linked rings (catenanes) presaged host–guest chemistry.⁷ In his way of thinking, Wasserman even considered the two unlinked rings to be an “isomer” of the catenane. While disconnected macrocycles, or host and guest, are not typically considered isomeric with the related catenane or complex, this idea cuts to the heart of what is a molecule. An ensemble of molecules has an identity as a compound, with unique and

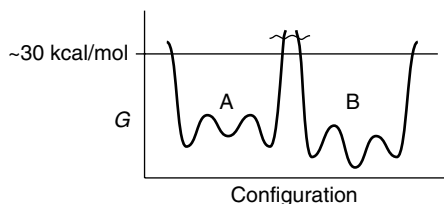


Figure 8.1 Simplified representation of slice of free-energy hypersurface for $C_{10}H_{22}$ is shown. Free energy vs. configuration (conformation) for two molecules, ensembles of which represent two isomeric compounds: *n*-decane (A) and isodecane (B) are given.

identifiable physical properties, under some defined conditions of observation. Separated host and guest are thus clearly not “a molecule” that is isomeric with the host–guest complex but rather two molecules, which may be in equilibrium with the complex. The complex can be reasonably considered a supramolecule. This seems intuitively clear but can be put on a slightly more secure footing by considering the following most basic of thermodynamic equations:

$$\Delta G = \Delta H - T \Delta S \quad (1)$$

$$K = e^{-\Delta G/RT} \quad (2)$$

The equilibrium constant observed for a pair of isomers is related to the free-energy difference between the two (a statistical average quantity). For a macroscopic sample, the free energy of the species on the two sides of the equilibrium equation can be measured and cast in “per molecule” units. The equilibrium constant is given by Eq. (2). In the case of the host and guest example, the relevant free energy for the complex is a “per complex” quantity. For macroscopic samples, the equilibrium constant does not depend strongly upon the number of molecules in the sample. In a complexation process or an isomerization reaction, the smallest collection of atoms reasonably considered as a “molecule” is the collection whose free energy is used to determine the equilibrium constant.

By this definition the host–guest complex is a molecule—let us call it a supramolecular assembly since it is composed of groups of atoms, which are not all covalently connected. In this case the catenane is also a supramolecular assembly. In a way, however, this focus on covalent bonding is somewhat arbitrary, though undeniably useful. Why are collections of atoms that are covalently bonded so strongly considered as entities with their own identity that when two such entities are inextricably joined, as in the catenane, the whole is still supramolecular? This, of course, derives from the “bond energy band gap” nature has given us. That is, interactions between nonionic atoms seem to fall into two classes—covalent “bonds,” which are highly “pairwise,” and typically strong (>60 kcal/mol), and noncovalent interactions such as those connecting host and guest, which are typically much weaker. This is the basic reason for our focus on molecules, and it works because relevant free energies for determining equilibrium constants, for example, are “molecular.”

Liquid crystals are thermodynamic phases composed of a great many molecules. These molecules, termed *mesogens*, possess a free energy of formation, of course. LCs (their structure, properties, everything that gives them their unique identity), however, are not defined at the level of the constituent molecules any more than a molecule is defined at the level of its constituent atoms. LCs are supermolecules. How do they differ from supramolecular

assemblies? Supramolecular assemblies are composed of a small number of molecules to produce a well-defined supramolecule with a relevant free-energy/supramolecule. LCs, of course, have a “free energy per molecule,” but this free energy does not determine the equilibrium constant between different LC phases exhibited by the same mesogens. The free energy of LCs is collective; given by the free energy/molecules multiplied by a very large number of molecules necessary to define the phase (the collective volume).

At the most basic level the LC is the same phenomenon as the molecule—a collection of atoms caught in a well on the configurational hypersurface, this time sampling an infinity of configurational minima. This collection of atoms has a time-average symmetry and structure, just as a flexible molecule does, and a unique identity and set of physical properties deriving from this structure. There is a key difference between molecules and LC phases, however. The relevant free energy determining the equilibrium constant between two molecules is a per molecule quantity, while the corresponding free-energy difference for phases is a “per collective volume” quantity.

This point can be illustrated by the plot shown in Figure 8.2. Here the free energy of two entities (molecules or phases) is plotted with respect to temperature over a fairly narrow temperature range (say from 0 to 100°C). The plot is linear, with the slope = $-S$ for each species. It is quite evident that at higher temperature the more “disordered” molecule or phase, with higher entropy, will have the lowest average free energy. At some temperature, however, the curves representing the two entities cross, and the more “ordered” species, with lower entropy, becomes the thermodynamic minimum.

If these curves represent equilibrating molecular isomers, at the point where the curves cross ($\Delta G = 0$), there are equal concentrations of the two isomers present. Increasing the temperature by a few degrees will perturb the equilibrium in favor of the higher entropy isomer, but a considerable concentration of both isomers will be present since ΔG is typically small relative to kT at this slightly higher T . If the plot represents LC phases, however, the situation

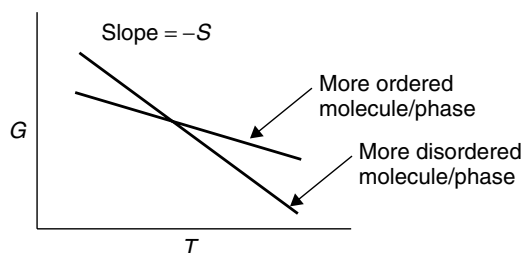


Figure 8.2 Plot of free energy vs. temperature for two species (molecules or LC phases) with different entropies of formation.

is different in an important way. The lines now represent the more disordered and more ordered LCs. With respect to equilibrium between the two, the relevant thermodynamic quantities are collective and not molecular. In this case the free energies are so huge that in theory an infinitesimal change in temperature away from the point where $\Delta G = 0$ causes one or the other of the phases to have a much lower free energy relative to kT , and the entire system takes on the structure of the thermodynamic minimum, with none of the other structure present. This, of course, is standard behavior for a first-order phase transition.⁸

2.2 INAC Phase Sequence

The above-described formalism is applied to the typical calamitic (rod-shaped) mesogen **PYP 906** (2-[4-(hexyloxy)phenyl]-5-nonylpyrimidine, **1**) in Figure 8.3. **PYP 906**, the prototype of the class of phenylpyrimidine LCs, which form the foundation of most commercial SmC^* materials, possesses the phase sequence on heating: X–SmC–SmA–N–I, where X is a crystalline

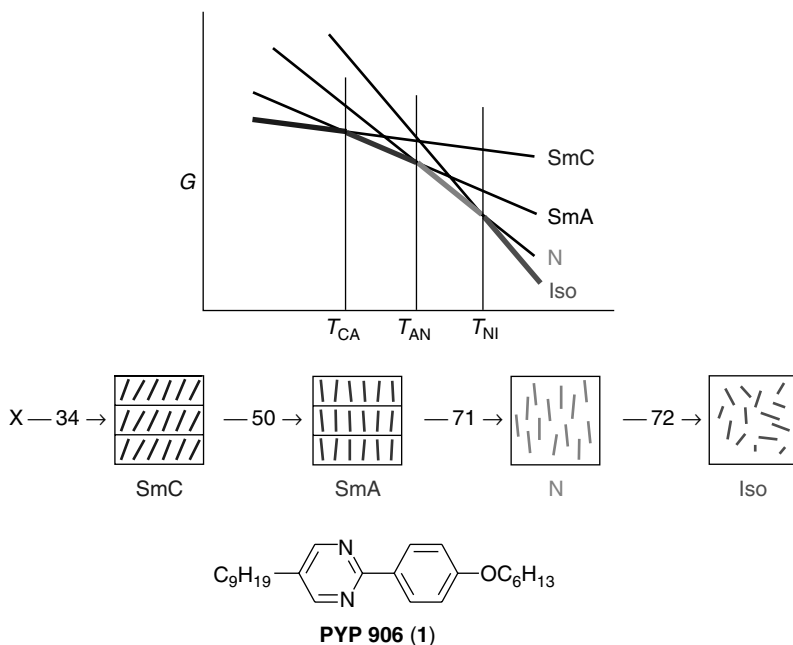


Figure 8.3 Phase sequence and transition temperatures of a pure sample of the mesogen **PYP 906**. Plot illustrates relative entropy of various fluid phases, showing how each becomes thermodynamic minimum in some temperature range.

solid phase, SmC is the smectic C liquid crystal phase, SmA is the smectic A phase, N is the nematic phase, and I is the isotropic liquid phase. The X–SmC transition temperature is said to be the melting point, and the N–I transition temperature is termed the clearing point.

Representations of the structures of the thermodynamic fluid phases exhibited by **PYP 906** are given in Figure 8.3, along with the transition temperatures and plots of the free energy vs. temperature for the four phases; the anisotropic fluids being, of course, LCs. These plots are not meant to represent actual data but rather simply to illustrate the basic thermodynamics of the system. In fact, the SmA–SmC transition for **PYP 906** is second order, and the free energy of the SmC structure has no meaning at temperatures above T_{CA} . For the sake of simplicity, the diagram indicates a hypothetical material where the SmA–SmC transition is first order.

The isotropic phase has the highest entropy of the four fluid phases, and thus the steepest negative slope in the G vs. T plot. It necessarily has the lowest free energy of any of the phases at the high-temperature limit. As the temperature is lowered, the N phase, with a lower entropy, becomes the thermodynamic global minimum at the transition temperature T_{NI} . In the nematic phase the molecular rods are more or less parallel, defining an average uniaxial symmetry on length scales much larger than that of the molecules. Macroscopically, this unique axis is termed the director.

On a molecular level the director is not rigorously defined, but the molecular director is typically considered to be the average long axis of the molecules, oriented along the macroscopic director with some order parameter less than one. This type of anisotropic order is often called “long-range orientational order” and, combined with the nonresonant optical properties of the molecules, provides the combination of crystal-like optical properties with liquidlike flow behavior characteristic of liquid crystals.

Referring to the plot of G vs. T for the isotropic and nematic fluids, a unimolecular isomerization process would show the same characteristics if one of the isomers had a higher entropy of formation than the other. In the molecular case, however, the equilibrium constant at a given temperature would derive from the free energies on a per molecule basis, while for the phases this free energy is “per collective volume” of molecules. The similarities to a molecular isomerization, however, are more important than the differences for the purposes of this discussion. The transition from isotropic fluid to nematic LC can be considered a temperature-driven, or thermotropic, isomerization.

With further cooling, the SmA LC, which is more ordered than the nematic, becomes the thermodynamic minimum. In the SmA, there is a spontaneous formation of layers, with long-range positional order normal to the layer planes. Thus, the SmA can be considered a stack of two-dimensional fluid layers with crystalline (long-range positional) order in the third dimension, but no

long-range positional order in the plane of the layers. Of the fluid phases exhibited by **PYP 906**, the SmC, wherein the director is tilted coherently from the layer normal, is the least disordered and occurs in the lower temperature range before crystallization. In an ad hoc but useful adaptation of molecular stereochemistry language, we refer to the isotropic liquid, the nematic and smectic LC phases, and crystalline solid phases as supermolecular constitutional isomers. We consider the wide variety of smectic LC phases, including the simplest examples SmA and SmC, to be supermolecular stereoisomers.

3 SmC* PHASE AND FERROELECTRIC LIQUID CRYSTALS

Polar symmetry (point group $C_{\infty v}$ or lower) is quite familiar at the molecular level as the symmetry required for the existence of a molecular dipole moment. Molecules possessing higher, nonpolar symmetry, cannot possess a permanent molecular dipole moment even when there are bond dipoles. Until the 1970s, no LC phases were known to possess polar symmetry, in spite of the fact that most mesogens are polar.

In describing the symmetry of an LC phase, it is customary to use the point group symmetry of the phase using Schoenflies symbols. In an ad hoc extension of the usual application of this approach, all symmetry elements (time or ensemble average) containing all possible singular points are considered. In the case of smectics, with crystalline order in one dimension, it is also necessary in some cases to include translations of one layer, along the layer normal, to obtain the symmetry of a phase containing an infinite number of layers. Using this technique it can be seen that the SmC phase possesses average C_{2h} symmetry.

Consider the graphic representation of a SmC phase shown in Figure 8.4. It is understood that there are an infinite number of smectic layers, which

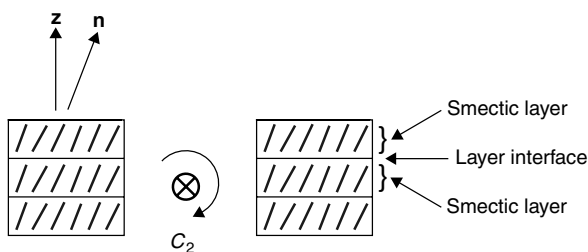


Figure 8.4 Illustration showing layer normal (\mathbf{z}), director (\mathbf{n}), and other parts of the SmC structure. Twofold rotation axis of symmetry of SmC phase for singular point in center of layer is also illustrated. There is also mirror plane of symmetry parallel to plane of page, leading to C_{2h} designation for the symmetry of phase. This phase is nonpolar and achiral.

extend infinitely in the horizontal plane normal to the plane of the page. The horizontal lines in the figure represent the edges of the layer interfaces in projection where they cut the plane of the page. The layer normal is vertical, represented by the unit vector \mathbf{z} in the figure, while the macroscopic director is represented by the unit vector \mathbf{n} . The plane defined by the layer normal and the director is termed the tilt plane; in Figure 8.4 this is the plane of the page.

Picking a singular point either in a layer interface or in the center of a layer, a 180° rotation about an axis containing this point, and perpendicular to the tilt plane, gives an indistinguishable structure, as indicated in Figure 8.4. Note that this assumes no polar order along the director, which is true for the SmC phase and most other LC phases. In addition to the twofold principle rotation axis, the SmC structure possesses a mirror plane of symmetry parallel to the plane of the page, providing the C_{2h} point group mentioned above. In the case of the SmC, glides along the layer normal are not necessary to capture the symmetry of the phase.

Polar structures may have rotation symmetry and reflection symmetry. However, there can be no rotation or reflection normal to the principal rotation axis. Thus, the presence of the mirror plane normal to the C_2 axis precludes any properties in the SmC requiring polar symmetry; the SmC phase is nonpolar.

Molecular chirality, however, proved an extremely powerful tool in the quest for polar LCs. In 1974 Robert Meyer presented to participants of the 5th International Liquid Crystal Conference his now famous observation that a SmC phase composed of an enantiomerically enriched compound (a chiral SmC, denoted SmC*) could possess no reflection symmetry.¹ This would leave only the C_2 symmetry axis for a SmC*; a subgroup of $C_{\infty v}$. The SmC* phase is therefore necessarily polar, with the polar axis along the twofold rotation axis.

This idea is elegant for its simplicity and also for its usefulness. While often in phenomenological theories of materials, control of parameters with molecular structure would provide useful properties, but the parameters are not related in any obvious way to controllable molecular structural features. Meyer's idea, however, is just the opposite. Chemists have the ability to control enantiomeric purity and thus can easily create an LC phase lacking reflection symmetry. In the case of the SmC*, the macroscopic polar symmetry of this fluid phase can lead to a macroscopic electric dipole, and such a dipole was indeed detected by Meyer and his collaborators in a SmC* material, as reported in 1975.²

Figure 8.5 gives the structure of the molecular subject of this classic study, decyloxybenzylideneaminomethylbutylcinnamate (**DOBAMBC**, **2**). **DOBAMBC** possesses the archetypal FLC molecular structural features: A rigid core with two flexible tails, one of which possesses a stereogenic center. A classic theoretical treatment of the SmC phase from 1978 by Durand et al. suggested that a "zigzag" conformation of the LC molecules is important.⁹

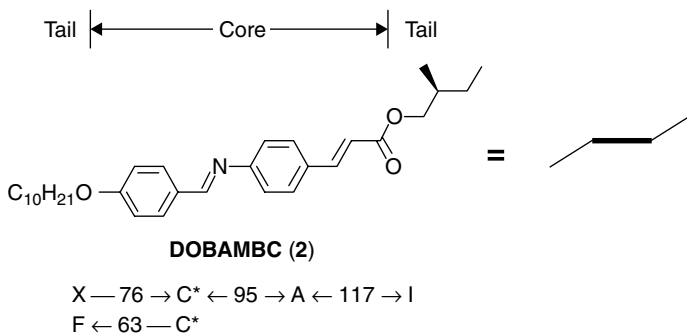


Figure 8.5 Structure and phase sequence of **DOBAMBC** is shown. Terminology used to describe parts of LC mesogen is given, in addition to graphical representation (zigzag structure) of molecule as it exists in tilted smectic phase.

As indicated in Figure 8.5, FLC molecules are often represented by a zigzag of three line segments representing such a conformation of the tail–core–tail structure of the molecules.

On heating from a crystalline phase, **DOBAMBC** melts to form a SmC^* phase, which exists as the thermodynamic minimum structure between 76 and 95°C. At 95°C a thermotropic transition to the SmA phase occurs. Finally, the system clears to the isotropic liquid phase at 117°C. On cooling, the SmC^* phase supercools into the temperature range where the crystalline solid is more stable (a common occurrence). In fact, at 63°C a new smectic phase (the SmF) appears. This phase is metastable with respect to the crystalline solid; such phases are termed *monotropic*, while thermodynamically stable phases are termed *enantiotropic*. The kinetic stability of monotropic LC phases is dependent upon purity of the sample and other conditions such as the cooling rate. However, the appearance of monotropic phases is typically reproducible and is often reported in the phase sequence on cooling. It is assumed that phases appearing on heating a sample are enantiotropic.

The local supermolecular geometry of the SmC^* phase is illustrated in Figure 8.6 for a small volume of the phase. The key geometrical features of the structure are the smectic layer plane, the tilt plane, and the polar plane, the layer normal (\mathbf{z}), the director (\mathbf{n}), the polar axis, and the tilt cone. The smectic layers are normal to the experimentally observed electron density modulation in the phase, the defining characteristic of smectic LCs. Furthermore, in order to avoid using the director as a geometrical foundation of the structure (since the director is not precisely defined, and in fact its geometry depends upon how it is measured), we define the tilt plane to be normal to the twofold symmetry axis. The polar plane is the plane orthogonal to the layer plane and the tilt plane, containing the layer normal and polar axis.

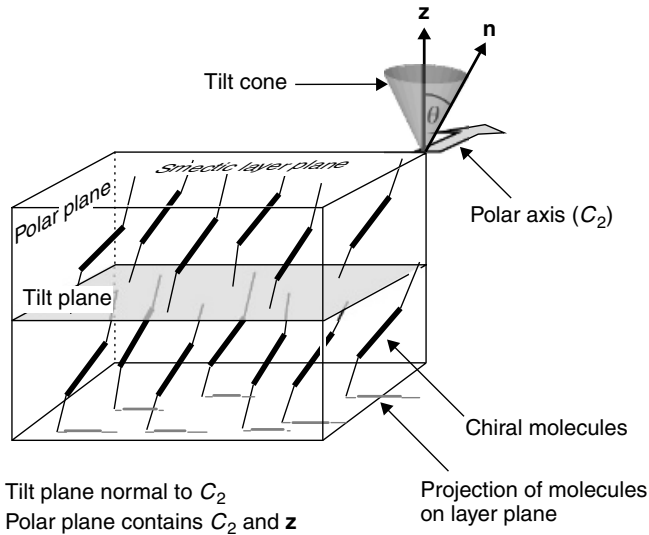


Figure 8.6 Three-dimensional “slice” of C_2 symmetrical SmC^* phase, showing tilt cone, polar axis (congruent with twofold symmetry axis), smectic layer planes, tilt plane, and polar plane.

In general, for a material with polar symmetry, a macroscopic electric dipole will be present. For the SmC^* phase this macroscopic dipole, termed the ferroelectric polarization \mathbf{P} , combined with the layer normal and director, form a chiral macroscopic geometry. That is, the polarization has a handedness. In the FLC field, the chirality descriptor used for this handedness is simply $+$ or $-$. If the polarization (from negative to positive, using the physics convention for the direction of a dipole) is along $\mathbf{z} \times \mathbf{n}$, then it is defined to be positive; if the polarization is opposed to $\mathbf{z} \times \mathbf{n}$, then it is negative. Since this *macroscopic chirality* is a result of the microscopic chirality of the molecules, enantiomers must show equal magnitude but opposite sign of the polarization.

Meyer’s symmetry argument is unassailable. But, it is unsatisfying in the sense that the molecular origins of the polarization (i.e., which dipoles actually contribute to \mathbf{P} and why) is not described. A simple molecular recognition model for the molecular origins of \mathbf{P} in FLCs was described in 1986.¹⁰ Since then, this model has proven strong enough that computational approaches have been demonstrated, which are capable of deriving \mathbf{P} from molecular structure.¹¹ While the details of the molecular origins of \mathbf{P} are still being explored using elegant structure/activity relationship studies,¹² it can be said that a basic understanding of the phenomenon at a molecular level is in hand.

In a bulk SmC material the tilt angle θ is fixed, but the director is free to take up any azimuthal orientation, defining a tilt cone of degenerate azimuthal

orientations, as indicated in Figure 8.6. Locally, all the molecules are tilted on average in the same direction, but the correlation length of this uniform tilt orientational ordering, while “long range,” is relatively short in the bulk. Furthermore, in the chiral SmC^* case, a spontaneous helix in the director field forms, with the helix axis along the layer normal, and a pitch on the order of $1\ \mu\text{m}$. While the layer spacing (related to the molecular length), and helix pitch can vary significantly, one full turn of the helix is on the order of 360 layers thick. Thus, the director precesses on the tilt cone about 1° clockwise or counterclockwise from one layer to the next in a typical bulk SmC^* material. The sign of this helix (clockwise \equiv positive) derives from the molecular structure; enantiomers have equal magnitude and opposite sign of the helix. It should be noted that the sign of the SmC^* helix and the sign of \mathbf{P} are not related (i.e., materials with positive \mathbf{P} can have either positive or negative helical twist).

Since \mathbf{P} must remain normal to \mathbf{z} and \mathbf{n} , the polarization vector forms a helix, where \mathbf{P} is everywhere normal to the helix axis. While locally a macroscopic dipole is present, globally this polarization averages to zero due to the presence of the SmC^* helix. Such a structure is sometimes termed a helical antiferroelectric. But, even with a helix of infinite pitch (i.e., no helix), which can happen in the SmC^* phase, bulk samples of SmC^* material still are not ferroelectric. A ferroelectric material must possess at least two degenerate states, or orientations of the polarization, which exist in distinct free-energy wells, and which can be interconverted by application of an electric field. In the case of a bulk SmC^* material with infinite pitch, all orientations of the director on the tilt cone are degenerate. In this case the polarization would simply line up parallel to an applied field oriented along any axis in the smectic layer plane, with no wells or barriers (and no hysteresis) associated with the reorientation of the polarization. While interesting, such behavior is not that of a true ferroelectric.

In 1980, Clark and Lagerwall reported the first method for achieving a fluid ferroelectric using the SmC^* phase with special boundary conditions.³ In the “surface stabilized FLC” (SSFLC) geometry, the required free-energy wells at two azimuthal orientations of the director on the tilt cone are created by interactions with the surfaces of the bounding plates in thin cells. When the boundary conditions favor the director parallel to the substrates and the layers are more or less perpendicular to the substrates, only two stable orientations of the director on the cone are allowed, as indicated in Figure 8.7. The SSFLC structure shown has the substrates parallel to the plane of the page. The director at the surfaces prefers to tilt right or to tilt left, with other orientations disfavored by the surface interactions. When the cell is thin (on the order of a few microns for FLCs with a helix pitch of $\sim 1\ \mu\text{m}$ or greater), then the LC elastic constants and surfaces combine to favor a more or less uniform director

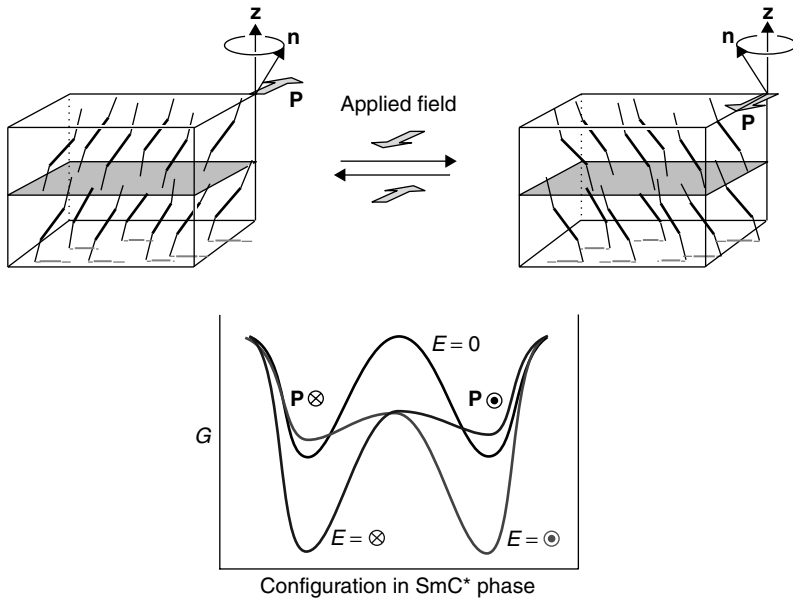


Figure 8.7 Surface-stabilized ferroelectric liquid crystal. Two specially treated glass plates parallel to plane of page, spaced at about $2\ \mu\text{m}$, and with gap filled with SmC^* material, produce a ferroelectric system. Substrates serve to produce two degenerate minimum-energy configurations if the LC director prefers to orient parallel to plates. This situation is illustrated by black curve on free-energy vs. configuration plot. Configuration in this curve represents azimuthal orientation of director on the tilt cone, with two wells differing in this orientation by 180° . Application of an electric field up, above switching threshold, causes free energy of the configurations to change as indicated by the red curve. A down electric field realizes blue curve. Ferroelectric liquid crystals can show essentially infinite bistability in real-world devices.

structure in the bulk of the cell, leading to two stable orientations of \mathbf{P} . In the figure, the polarization of the material illustrated is positive. Thus, when the molecules tilt right, the polarization is “down,” while when the molecules tilt left, the polarization is “up.”

As indicated in the energy diagram in Figure 8.7, these states are degenerate, having the same structure and free energy. The free-energy wells on the diagram are labeled with symbols representing the orientation of the polarization. If an electric field is applied to the sample normal to the plates, the free-energy situation changes dramatically. For molecules with dipole moments, applied electric fields perturb the free energy of the system only slightly. However, the total macroscopic dipole of the FLC sample is large, being a collective dipole arising from polar orientation of a great many molecular dipoles. The orientation where the polarization is parallel to the applied

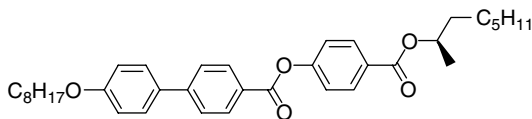
field drops in free energy, while the orientation where the polarization is antiparallel to the applied field increases its free energy. Typically, at readily accessible applied field strengths on the order of a few volts/micrometer, the surface interactions can no longer stop the system from reorienting, and the sample switches to the more stable state.¹³

Removal of the applied field leaves the system unchanged since in the first-order approximation the structure in a well in the presence of a field parallel to \mathbf{P} , or in the absence of an applied field, is not changed. Application of a field of opposite sign, however, causes a reorientation of \mathbf{P} , which becomes parallel to the applied field, by precession of the director 180° around the tilt cone. Since the applied field couples strongly with \mathbf{P} , this switching is relatively fast; on the order of 10–100 μs at room temperature for fields of about 2.5 V/ μm , for highly evolved materials. At small fields, however, the surface-induced barrier prevents switching, even after a long time. Only when the field is increased above a threshold value does the barrier become sufficiently small that the system can switch to the more stable state. This type of thresholded switching behavior leads to hysteresis in the polarization vs. applied field curve, a required property of any ferroelectric. This behavior is often referred to as *bistable switching*.

The optical properties of the cell for the two bistable states illustrated in Figure 8.7 are dramatically different due to the large birefringence of liquid crystals. If the tilt angle is 22.5° , such that the director orientation in the two states differs by 45° for polarized light entering the cell normal to the substrates, then the ferroelectric switching is equivalent to rotation of a waveplate by 45° . If the cell is one half-wave thick, then between crossed polarizers there is an orientation of polarizer and analyzer that provides high-contrast electro-optic switching. This unique combination of fast switching and “in-plane” rotation of the optic axis of the cell provides very attractive optical properties which have actually led to commercial products. At present these include integrated FLC on silicon¹⁴ microdisplays for still digital and video camcorder viewfinder applications.¹⁵ This provides an interesting example of value in consumer electronic products resulting from molecular chirality.

4 SmC_A^* PHASE AND ANTIFERROELECTRIC LIQUID CRYSTALS

Along with the prediction and discovery of a macroscopic dipole in the SmC^* phase and the invention of ferroelectric liquid crystals in the SSFLC system, the discovery of antiferroelectric liquid crystals stands as a key milestone in chiral smectic LC science. Antiferroelectric switching (see below) was first reported for unichiral 4-[(1-methylheptyloxy)carbonyl]phenyl-4'-octyloxy-4-biphenyl carboxylate [MHPOBC, (3)],¹⁶ with structure and phase sequence



(R)-MHPOBC (3)

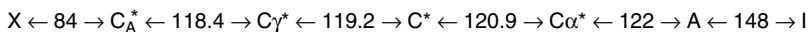


Figure 8.8 Structure and phase sequence of (R)-MHPOBC is shown. One of most famous smectic LCs, antiferroelectric switching in SSFLC cells was first discovered with this material.

shown in Figure 8.8. **MHPOBC** exhibits one of the richest and most interesting phase sequences of any chiral smectic. For the purposes of this discussion, however, the SmC_A^* phase, which occurs at temperatures under the SmC^* and two “ SmC^* subphases,” will be the focus of the discussion. To understand the structure of the SmC_A^* phase, the concept of *clinicity*, a pairwise descriptor for the relationship between two adjacent smectic layers with regard to tilt direction, is useful.

In a typical material possessing an $SmA-SmC^*$ transition, such as **DOBAMBC**, at this transition on cooling from the SmA phase a spontaneous symmetry breaking occurs in which molecules tilt uniformly by less than 90° (and typically less than 45°). As shown at the top of Figure 8.9, the director can tilt counterclockwise from the layer normal. In this case, a material with positive P will have the macroscopic polarization “up,” as indicated in the figure. Regarding two adjacent layers, as shown, the layer interface between them is denoted synclinic, since the molecules are tilting in the same direction in the two layers (with the caveat that in bulk the tilt direction is not exactly the same in the two layers due to the SmC^* helix). If we fix the average geometry of, say, the top layer, and rotate (precess) the director of the bottom layer on the tilt cone, the free energy of the system apparently passes through a maximum, with another, diastereomeric minimum at an azimuthal angle ϕ of about 180° , as shown. When ϕ is 180° , the layer interface is said to be anticlinic.

While the existence of the anticlinic minimum in conventional SmC^* materials has been suggested by experiments with **DOBAMBC**,¹⁷ by far the majority of tilted smectics only exhibit the synclinic structure of the SmC or SmC^* under normal conditions. When the mesogenic compound is unichiral (i.e., enantiomerically pure) or enantiomerically enriched, a macroscopic polarization with the same orientation in each layer is produced, as discussed above. In the SmC_A^* phase of **MHPOBC**, however, the anticlinic structure is the global minimum structure, as shown at the bottom of Figure 8.9. In this case, given that the chirality of the molecules is fixed, the polarization must alternate

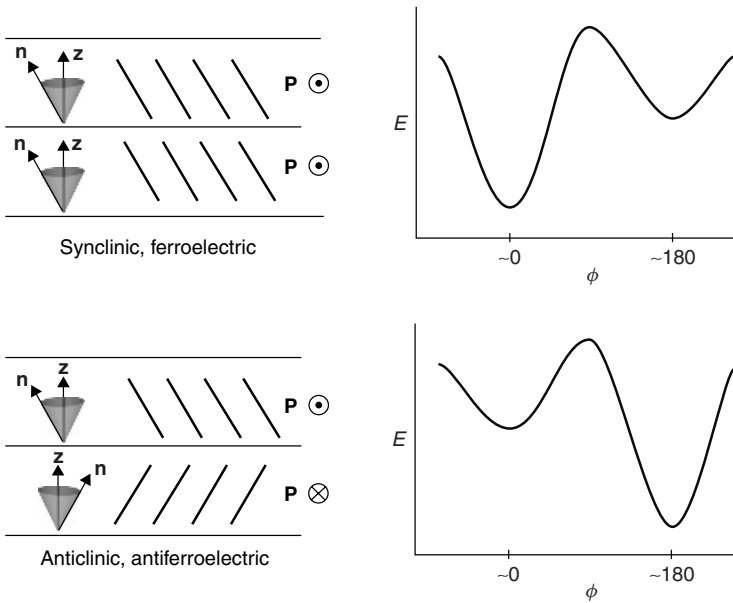


Figure 8.9 Synclinic and anticlinic layer interface configurations, differing in relative azimuthal angle ϕ between director orientations for pair of adjacent layers, are illustrated. It appears that many, if not all, SmC and SmC* materials possess wells for both synclinic and anticlinic configurations. Materials for which anticlinic well is global minimum for system in some temperature range are very rare, however.

between “up” and “down” from layer to layer. This anticlinic structure with enantiomerically enriched molecules leads to nonpolar D_2 symmetry.

In an SSFLC cell, the SmC_A* phase behaves as illustrated in Figure 8.10. At zero applied field there is no net polarization, as required by the nonpolar symmetry of the structure. Application of a small field lowers the free energy of one set of alternate layers and raises the free energy of the other layers, but the barrier illustrated in Figure 8.9 prevents switching. Above a threshold field, switching to a ferroelectric state occurs. The dielectric behavior, and the phases which exhibit it, are termed *antiferroelectric*. While reminiscent of SSFLC switching in a ferroelectric, an antiferroelectric shows the following important differences. First, the barrier to switching is intrinsic to the structure, and not due just to the surface interactions (though the surfaces could contribute). Second, the antiferroelectric is monostable, reverting to the single antiferroelectric ground-state structure at zero field. Finally, while in the case of the ferroelectric SmC* the structure simply reorients during switching, in the case of the antiferroelectric SmC_A* the applied field actually causes an isomerization to a new, diastereomeric structure, termed a *ferroelectric* state.

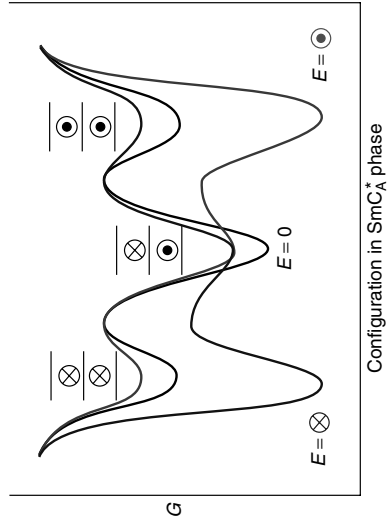
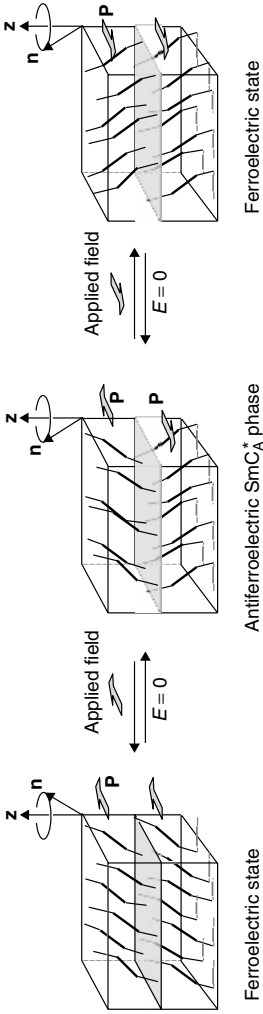


Figure 8.10 Anticlinic, antiferroelectric ground state observed for chiral SmC_A^* material in SSFLC cell, with two degenerate ferroelectric states accessible upon application of electric field, are illustrated. Black curve in plot of free energy vs. configuration shows energetics of system in absence of applied field. Note that ferroelectric wells are necessary on free-energy surface at zero field. Application of up field above switching threshold produces red curve, causing system to switch to ferroelectric state with polarization up. Removal of field allows system to relax to antiferroelectric ground state, though for minority of SmC_A^* antiferroelectrics, well present at zero field causes this relaxation to be quite slow. Application of down field above switching threshold converts system to down ferroelectric state, represented by blue curve.

As mentioned above, the “tilt plane” in the SmC^* phase is defined as normal to the twofold axis of a system with overall C_2 symmetry. Given the three orthogonal twofold axes (D_2) in the SmC_A^* structure, this definition of the tilt plane is ambiguous. For the antiferroelectric SmC_A^* phase, we define the tilt plane as being orthogonal to the polar axis in the ferroelectric state obtained in the presence of a field above the switching threshold. This, of course, is consistent with the term *anticlinic*, suggesting alternate tilt directions in the tilt plane for adjacent layers, this being the plane of the page in Figures 8.9 and 8.10.

5 REFLECTION SYMMETRY BREAKING IN ORGANIC MATERIALS

5.1 Crystal Conglomerates

In the first half of the nineteenth century, it was known that certain minerals, the prime example being quartz, formed chiral crystals. Often, it was seen that rocks could be composed of a physical mixture of small but macroscopic right-handed and left-handed crystals. This kind of mixture, composed of macroscopic chiral domains (crystals) occurring in both enantiomeric forms, was termed a *conglomerate*.

As the story goes, a wine production batch gone bad provided fairly large amounts of a new organic compound, the study of which was deemed of practical importance for the French wine industry. The new material had the same molecular formula as tartaric acid, which to some experts of the time meant it had to be the same as tartaric acid. Solutions of salts of the new material, however, did not rotate the plane of polarization of plane-polarized light, as solutions of salts of tartaric acid were known to do. The new material was named para tartaric acid, or racemic acid (the name racemic acid being derived from the Latin *racemus*: bunch of grapes).

The famous crystallographer/chemist Mysterlich had previously published that crystals of tartaric acid and racemic acid salts were isomorphous (identical in shape). Indeed, in spite of the differing influence of tartaric acid and racemic acid on plane-polarized light, many of the great scientists of the day were convinced that tartaric acid and racemic acid were the same compound. As it turned out, these scientists were both right and wrong.

A young Louis Pasteur observed that many salts of tartaric acid formed chiral crystals (which he knew was related to their ability to rotate the plane of polarization of plane-polarized light). He succeeded in solving the mystery of racemic acid when he found that the sodium ammonium salt of racemic acid could be crystallized to produce a crystal conglomerate. After physical separation of the macroscopic enantiomers with a dissecting needle, Pasteur

found that one of the enantiomeric forms was identical to sodium ammonium tartrate in all respects, while the other was identical except that it caused rotation of plane-polarized light of equal magnitude but opposite sign to that observed for the tartrate.¹⁸ This, of course, was the first resolution of molecular enantiomers, and the first organic crystal conglomerate to be reported in the literature.

Since Pasteur's report, a great many crystal conglomerates composed of achiral or racemic (after racemic acid) compounds have been described. Most of these have been of the Pasteur type, mixtures of macroscopically chiral crystals. More recently, several interesting examples of conglomerate formation in "two-dimensional" systems such as Langmuir films¹⁹ and monolayer crystals on graphite²⁰ have been described. Another extremely interesting example of a two-dimensional conglomerate occurs is involved in the formation of chiral tubules from certain phospholipids, as discussed in Chapter 5 in this volume.

This general phenomenon, the spontaneous formation of chiral objects or systems from achiral or "racemic" initial states, is often termed *spontaneous chiral symmetry breaking*. This phrase, however, can be confusing.²¹ Herein the term *spontaneous reflection symmetry breaking* is used to mean spontaneous breaking of reflection symmetry, producing a chiral object or system from an achiral object or system. While the language may be confusing, the concept is well known, crystal conglomerate formation being one important example. Indeed, the basic phenomenon is actually quite common. For example, calculations show that the global minimum structures of a simple array of either 15 or 16 particles (but no other particle counts less than 21) confined to the surface of a sphere, which interact via a potential that depends logarithmically on their separation, are chiral²²; simply allowing a collection of such particle-laden spheres to relax from achiral starting configurations could lead to the formation of a conglomerate of sorts. A more chemically relevant example of spontaneous reflection symmetry breaking at the molecular level: any reaction of achiral starting materials and reagents, which produces a chiral racemic product. The racemic compound is a "molecular conglomerate," but this phrase is not used. The term *conglomerate* is reserved for a mixture of *macroscopic* chiral domains. A *macroscopic racemate* is composed of achiral domains containing chiral structural elements of opposite handedness, forming an achiral whole.

5.2 Spontaneous Reflection Symmetry Breaking in Liquid Crystals

Spontaneous reflection symmetry breaking in achiral LCs is also well known, driven by specific boundary conditions. A very simple example of this type of chiral domain formation is illustrated in Figure 8.11. Suppose we start with two uniaxial solid substrates, which provide strong "azimuthal anchoring"

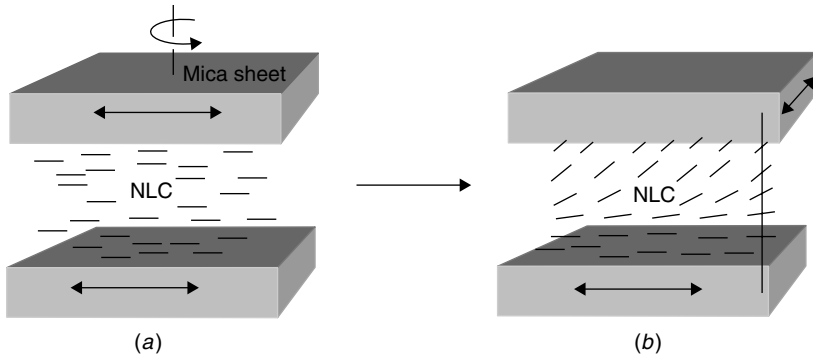


Figure 8.11 Illustration of Mauguin twisted nematic cell, reported in 1911. Substrates are thin mica plates, which are uniaxial with their optic axis parallel to plane of plates. Apparently, uniaxial crystal structure of mica produces strong azimuthal anchoring of nematic “LCs of Lehmann,” such that director is parallel (or perpendicular) to optic axis of mica sheets at both surfaces. Mauguin showed that method of Poincaré could be used to explain optics of system if it was assumed that LC sample created layer of material with uniformly rotating optic axis in twisted cells.

such that uniform orientation of the director parallel to the surface and along the uniaxis of the solid substrates is the minimum energy configuration of the system. If an LC sample is placed between two such plates, which are oriented with their uniaxes parallel, then a uniform achiral director structure will result, as shown in Figure 8.11a. If, however, one plate is rotated relative to the other, a chiral, uniformly twisted director structure may result. If the twist density is low and the birefringence of the LC is high, then the plane of polarization of plane-polarized light incident on the cell parallel to the uniaxis of the first plate will rotate to follow the director orientation, exiting the second plate polarized along its uniaxis.

This is precisely the experiment reported by Mauguin in 1911 using thin mica sheets as the solid substrates!²³ Even though the LC structure was not really understood in 1911, Mauguin intuited that the optic axis of the LC was uniformly rotating in the cell from top to bottom, and using the method of Poincaré (the famous Poincaré sphere had been described about 20 years before), established that the output polarization should rotate with the second plate. In more quantitative terms, the requirement for “adiabatic following” of plane-polarized light in such a twisted nematic (TN) LC cell with a 90° twist is that $\Delta n d \gg \lambda/2\pi$, where Δn is the birefringence of the LC, d is the thickness, and λ is the wavelength of the light. This condition for adiabatic following is called the *Mauguin limit* to this day.

It is interesting to note that Mauguin had discovered the TN LC cell in 1911. Commercialization of this device did not occur for some 75 years, but since then, with the development of thin-film transistor arrays, transparent

conductors, and critically important advances in the properties of the nematic LCs, Mauguin's TN cell has generated over \$1 trillion in revenue and created a cultural revolution of sorts. It is projected that revenues from TN liquid crystal displays (LCDs) will top \$2 trillion by 2005.

Now consider further the case of a 90° twist angle. Starting from parallel plates, then rotating one of them relative to the other by 90° , clearly provides a chiral director structure of a single handedness, as shown in Figure 8.11*b* for counterclockwise twist of the top plate. The configuration of this TN cell is determined by the physical act of twisting one plate relative to the other either clockwise or counterclockwise. But, consider what happens if the uniaxes of the plates are oriented at 90° , the LC is cleared into the isotropic phase, and then the system is allowed to cool into the nematic phase (Mauguin did not report this experiment in his 1911 article).

The starting system is achiral (plates at 90° with isotropic fluid between), but leads to the formation of a chiral TN structure when the fluid becomes nematic. In this case, enantiomeric domains must be formed with equal likelihood; and this is precisely what happens. The size of these domains is determined by the geometry and physics of the system, but they are macroscopic. Though the output polarization is identical for a pair of heterochiral domains, domain walls between them can be easily observed by polarized light microscopy. This system represents a type of spontaneous reflection symmetry breaking, leading to formation of a conglomerate of chiral domains.

Since the walls between heterochiral domains are unacceptable defects in an LC display, enantiomerically enriched dopants are added to the LC to favor one sign of twist over the other in actual devices, providing a monodomain in the TN cell. It should be noted, however, that the chirality of the structure derives from the interaction of the LC director with the surfaces; the molecular chirality serving simply to break the degeneracy between mirror image domains to favor one over the other.

Many other interesting examples of spontaneous reflection symmetry breaking in macroscopic domains, driven by boundary conditions, have been described in LC systems. For example, it is well known that in polymer disperse LCs, where the LC sample is confined in small spherical droplets, chiral director structures are often observed, driven by minimization of surface and bulk elastic free energies.²⁴ We have reported chiral domain structures, and indeed chiral electro-optic behavior, in cylindrical nematic domains surrounded by isotropic liquid (the molecules were achiral).²⁵

In all of these cases the symmetry breaking is derived from the manipulation of surface forces. Prior to 1997, spontaneous reflection symmetry breaking had never been reported in any thermodynamic bulk fluid phase. In the LC field, this empirical fact led to the generally believed assumptions that any LC phase composed of achiral or racemic compounds must be achiral, and

in order to obtain a chiral phase, enantiomerically enriched chiral compounds were necessary. Observation of chiral LC phases has also been considered as proof of molecular enantiomeric enrichment.²⁶

6 CHIRAL LIQUID CRYSTALS FROM ACHIRAL MOLECULES: BANANA PHASES

6.1 Bilayer Smectics and First Achiral Antiferroelectric LC

The situation with regard to spontaneous reflection symmetry breaking in bulk LC phases changed dramatically in 1997. Ironically, this story actually begins with the discovery of the first *achiral* antiferroelectric smectic LC (AFLC), reported by Soto Bustamante and Blinov (working in the Haase labs), at the 61st Bunsen-Kolloquium, Darmstadt, Germany, in February of 1996. While this discovery was exciting, the fundamental phenomena leading to this achiral AFLC were already well understood. These were: (1) The existence of achiral anticlinic SmC_A phases and (2) the existence of bilayer smectics. These supermolecular structural features had never been seen together in an actual mesogenic system, however. A description of how these phenomena presage the achiral AFLCs follows.

Shortly after the discovery of chiral AFLCs (Figure 8.10), the Tokyo Tech group reported the highly interesting result that racemic **MHPOBC** (refer to Figure 8.8) exhibits an achiral SmC_A phase. As was pointed out later in an influential study by Cladis and Brand,²⁷ the achiral anticlinic structure (which they describe as a “chevron” structure) should possess layers of antiparallel electric polarization *in the tilt plane* (sometimes termed *longitudinal polarization*) based purely on symmetry considerations. This interesting concept is illustrated in Figure 8.12 for an idealized highly symmetrical achiral mesogen. Simple inspection of the SmC_A illustration in Figure 8.12 shows the antiparallel polar axes, which would result in sheets of polarized matter alternating in direction with a pitch equal to the layer spacing. Cladis and Brand labeled this structure as an achiral antiferroelectric based upon the symmetry. However, no such SmC_A phase composed of rod-shaped molecules has been shown capable of switching to a ferroelectric state; thus the “calamitic SmC_A ” as illustrated in Figure 8.12 is not antiferroelectric.

In fact, as also indicated in Figure 8.12, an achiral SmC phase possesses antiparallel polarized sheets, in this case with a pitch of half the layer spacing. Photinos and Samulski have made much of this “polar symmetry” of the SmC phase,²⁸ but neither the SmC_A nor the SmC phases have net macroscopic polar symmetry (the SmC_A is D_{2h} while the SmC is C_{2h} , as mentioned above), and thus neither shows properties associated with polar materials (e.g., a pyroelectric effect).

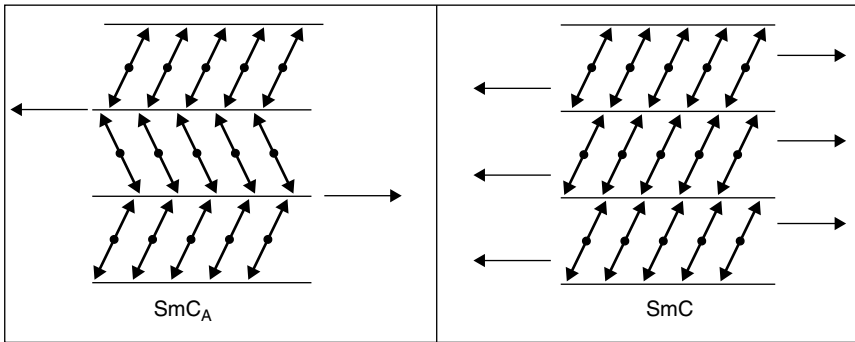


Figure 8.12 Longitudinal sheets with antiparallel polar symmetry are illustrated for achiral SmC_A and SmC phases. Since it is not possible to switch to ferroelectric state in such system upon application of electric field, these structure should not be considered antiferroelectric.

It is now instructive to ask why the achiral calamitic SmC_A (or SmC) is not antiferroelectric. Cladis and Brand propose a possible ferroelectric state of such a phase in which the tails on both sides of the core “tilt” in the same direction, with the cores along the layer normal. Empirically this type of “conformational” ferroelectric minimum on the free-energy hypersurface does not exist in known calamitic LCs. Another type of ferroelectric structure deriving from the SmC_A is indicated in Figure 8.13. Suppose the calamitic molecules in the phase were able to “bend” in the middle to a collective free-energy minimum structure with C_{2v} symmetry. In this ferroelectric state the polar axis is in the plane of the page.

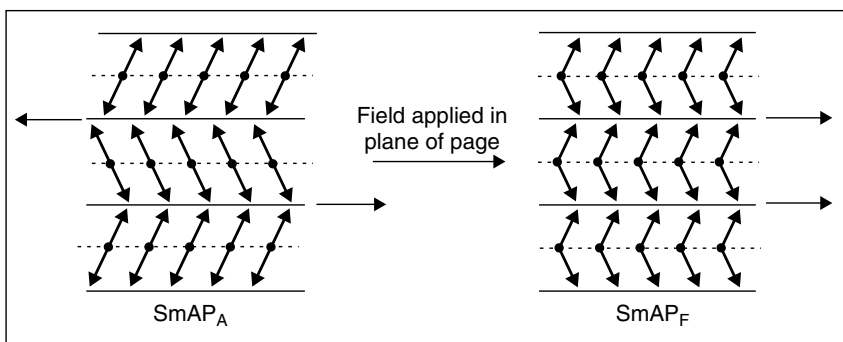


Figure 8.13 Hypothetical smectic mesogen with “hinge” in center of core is illustrated. Such material could in principal switch to ferroelectric state, which we term the $SmAP_F$, upon application of electric field in plane of layers. If this state exists in well on configurational hypersurface, then ground-state structure is antiferroelectric, denoted $SmAP_A$.

By our definition, the tilt plane is normal to the polarization in the ferroelectric state; in the illustration in Figure 8.13 this is a vertical plane normal to the plane of the page. Since there is no tilt of the director projected onto this plane, the phase should be considered a type of SmA. We name this structure SmAP_F (an untilted polar smectic; the subscript F referring to a ferroelectric structure, in this case a ferroelectric state of an antiferroelectric phase). The antiferroelectric phase is therefore also an SmA; denoted SmAP_A (the subscript A for antiferroelectric). While this idea is certainly intriguing, no such antiferroelectric has yet been discovered.

Thus, an achiral anticlinic smectic phase would be ferroelectric if there were a collective minimum, accessible by application of an electric field, with a “bend” (actually another anticlinic layer interface) in the middle of the layers. This has not been seen in any conventional calamitic SmC_A, but it has long been known that *bilayer smectic phases* are produced by some mesogens. Indeed, some of the most well-studied smectics, for example, the SmA phase of *p*-*n*-octyl-*p*'-cyanobiphenyl (8CB), exhibit a layer spacing by X-ray diffraction which is considerably larger than the fully extended molecular length. This result is interpreted to mean that neighboring cyanobiphenyl molecules are strongly correlated such that the phase is essentially composed of antiparallel supramolecular dimers stabilized by dipole–dipole interactions. This leads to a situation where there are two different layer interfaces, one methyl-terminated layer interface and one cyano-rich layer interface. Such a phase is termed a smectic bilayer. While it is not possible to distinguish a bilayer smectic from a monolayer smectic based upon the symmetry of the electron density distribution (i.e., X-ray scattering), it is common practice to assign a bilayer smectic structure to any smectic where the layer spacing is about twice the molecular length of the mesogens.

Now suppose a smectic phase similar to the SmC_A phase indicated in Figure 8.12 were an actual bilayer smectic with alternating synclinic and anticlinic layer interfaces, as illustrated in Figure 8.14*a*. It was already well

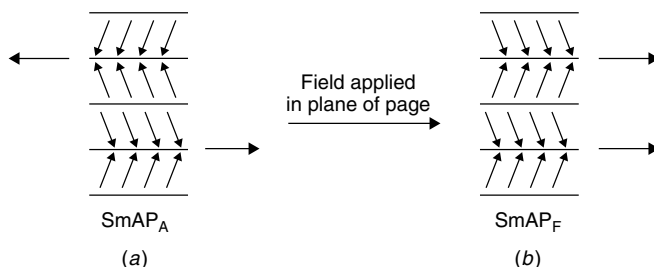


Figure 8.14 Illustration of first achiral antiferroelectric system: bilayer “tilted” smectic with alternating synclinic and anticlinic layer interfaces.

known that anticlinic layer interfaces in an antiferroelectric can switch to an all-synclinc ferroelectric state in response to an applied field. It therefore seems quite reasonable that in the case of the nonpolar structure in Figure 8.14a, with alternating synclinc and anticlinic layer interfaces, application of a field could cause the system to switch to the all-anticlinic ferroelectric state shown in Figure 8.14b. This is similar to the proposal of Cladis and Brand illustrated in Figure 8.13 but now applied to a bilayer smectic phase where the “middle of the *bilayer*” actually can switch to provide the necessary ferroelectric state. Interestingly, Brand, Cladis, and Pleiner proposed the existence of a ferroelectric “chevron” structure identical to that shown in Figure 8.14b.²⁹ Ironically, such an achiral ferroelectric ground state has, to our knowledge, yet to be discovered.

As mentioned above, the first actual realization of these theoretical considerations was demonstrated by Soto Bustamante and Blinov et al.,³⁰ in a very interesting chemical system. In a study of the properties of SmC side-chain polymers containing the interesting resorcyldiene aniline core unit, Soto Bustamante prepared the acrylate monomer **M6R8** (**4**), with the structure and phase sequence shown in Figure 8.15. Polymerization of this monomer gave the expected side-chain LC polymer **PM6R8** (**5**). The monomer possesses a normal SmA phase, while the polymer shows an SmC. Nothing unusual was observed for these achiral smectic phases. But, Soto Bustamante noted unusual behavior in a phase obtained from a mixture containing 90% of the monomer **M6R8**, and 10% of the polymer **PM6R8**.

In detailed studies of this mixture, strong evidence was obtained suggesting that the new achiral smectic phase is antiferroelectric. This consisted mainly of the observation of a double hysteresis loop in the polarization vs. applied electric field curve for the material.³⁰ In addition, it was shown that the mixture is a

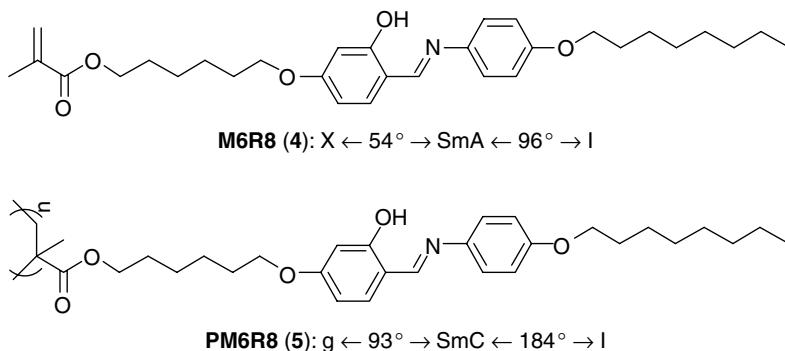


Figure 8.15 Structure and phase sequence of two components of the Soto Bustamante–Blinov achiral antiferroelectric are given.

bilayer smectic by X-ray determination of the layer spacing (much larger than the fully extended mesogen length).³¹ Based upon these results, in addition to apparently pyroelectric behavior of the electric-field-induced state of the new phase, an alternating synclinic–anticlinic bilayer structure, as illustrated in Figure 8.14a, was proposed.

This assignment of the structure of the smectic phase obtained for the **M6R8/PM6R8** blend was confirmed in the Boulder labs using depolarized reflected light microscopy (DRLM) on freely suspended smectic films of the material.³² Most smectic LCs form stable freely suspended films when a sample is “drawn” across a hole in a glass slide. The thickness of such films can be determined with great precision by visible light reflectivity measurements, and with some practice it is possible to obtain films of from 2 to 10 layers in thickness routinely. In some relatively rare cases, even single-layer films can be obtained. Such smectic films with 2 or more layers are typically quite stable, often lasting for several days when undisturbed (of course, the sample must be maintained in the temperature range of the smectic phase).

Freely suspended films provide a “perfect” homeotropic alignment of smectic LCs since the layers always orient parallel to the LC/air interface.³³ The director structure in such films can then be determined by analyzing the optical properties of plane-polarized light reflected from the surface of the films at a slightly oblique angle.³⁴ The technique gains additional power when electrodes are added to the setup, allowing observation of the behavior of the films in the presence of an electric field parallel to the plane of the film.³⁵

Using this method, the **M6R8/PM6R8** blend showed precisely the behavior expected for the achiral SmAP_A structure. Specifically, the optical properties of the films were consistent with a biaxial smectic structure (i.e., two different refractive indices in the layer plane). The thickness of the films was quantized in units of one “bilayer.” Upon application of an electric field, it was seen that films with an even number of bilayers behaved in a nonpolar way, while films with an odd number of bilayers responded strongly to the field, showing that they must possess net spontaneous polarization. Note that the electric fields in this experiment are not strong enough to switch an antiferroelectric to a ferroelectric state. Reorientation of the polarization field (and director structure) of the polar film in the presence of a field can easily be seen, however.

These results are fully consistent with the structural assignment of Soto Bustamante et al.³⁰ As shown in Figure 8.16, the alternating synclinic/anticlinic structure with a finite number of bilayers changes symmetry depending upon the layer number. With an even number of bilayers, the sample is nonpolar with C_{2h} symmetry, as illustrated in the graphic in Figure 8.16a. A film with an odd number of bilayers, however, is polar, with C_{2v} symmetry, as indicated in Figure 8.16b. In the latter case, the polar axis is in the plane of the smectic layers and couples with applied fields in this plane to orient the polarization

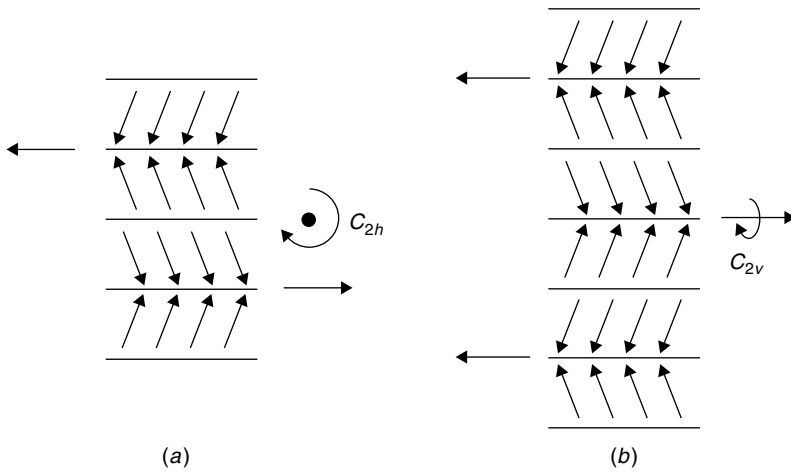


Figure 8.16 Illustration of symmetry of Soto Bustamante–Blinov achiral antiferroelectric smectic LC with finite number of layers. Such systems can be studied using DRLM technique with thin freely suspended smectic films. (a) With even number of bilayers, film has local C_{2h} symmetry, and therefore no net electric polarization. (b) With odd number of bilayers, film has local C_{2v} symmetry and is therefore polar, with net spontaneous electric polarization in plane of layers.

along the field. The biaxial optics of the system allow for observation of this reorientation, which provides a very distinct signature of net polarization in the plane of the layers for the films.

Note that these results in freely suspended films of the **M6R8/PM6R8** blend are identical to those obtained for the SmC_A phase of racemic **MHPOBC**. What, then, is the difference between the SmC_A and SmAP_A phases? The SmAP_A phase is antiferroelectric, while the SmC_A phase is not. That is, in the SmC_A phase the sample cannot switch to a ferroelectric state upon application of a large field (such switching would be observed in an LC cell, not in freely suspended films, since the maximum magnitude of the field which can be applied in the freely suspended film apparatus is too small to cause antiferroelectric–ferroelectric switching). This leads to some lack of precision in the nomenclature. Since there is no unique symmetry axis in the achiral all-anticlinic structure, and there is no ferroelectric state, our definition of the tilt plane fails for the case of the achiral SmC_A . The name of this phase is simply taken from the name of the chiral version, which is antiferroelectric and therefore has a definable tilt plane. Based purely upon the structure of the ground state (and ignoring the difference between a physical layer interface and the plane in the center of the layers cutting molecules “in half”), the SmC_A structure is identical to the SmAP_A ; the tilt plane and director in the SmC_A are ambiguous.

6.2 Bent-Core Mesogens

During the resurgence of interest in liquid crystals brought about by the creation of an LC-based industry starting in the 1960s, most work in thermotropic nematics and smectics was focused on rod-shaped (calamitic) mesogens. Prior to this “modern” era in LC science, however, there was a long history of purely curiosity-driven synthesis and characterization work around the LC phenomenon. One of the most prolific LC synthesis labs in the world was that of Vorländer at Halle University, in Germany. Referring to Vorländer, Pelzl, Wirth, and Weissflog (who today work at Martin-Luther-Universität Halle-Wittenberg—the very same academic institution as Vorländer’s), state “between 1900 and 1937, more than 2000 new mesogenic materials were prepared in his laboratory, representing nearly all of the mesogenic materials known at the time.”^{36a}

In 1929, Vorländer published an interesting study of a series of ortho-, meta-, and para-substituted dihydroxybenzene diesters possessing two azoxybenzene mesogenic units. It is clear from his writing that he was exploring the effect on mesogenicity of changing the geometry of the molecules. The following is taken from an English translation of the abstract of Vorländer’s 1932 paper in *Berichte*, which can be found in *Chemical Abstracts* with SciFinder Scholar (see Figure 8.17):

p-Phenetoleazoxybenzoic acid (I), called phenobenzoic acid. . . , sublimes 205°, m. 234° to a cryst. liquid, seems to be better adapted than any other CO₂H acid to the characterization of alcs., phenols and amines, not only through the m. ps. of the products it forms but also through their cryst.-liquid (c.-l.) properties. *o*-, *m*- and *p*-C₆H₄(OH)₂ (II) have been esterified with I in order to correlate the c.-l. properties of the esters with the directions of the C-O unions in the 3 isomeric II.^{36b}

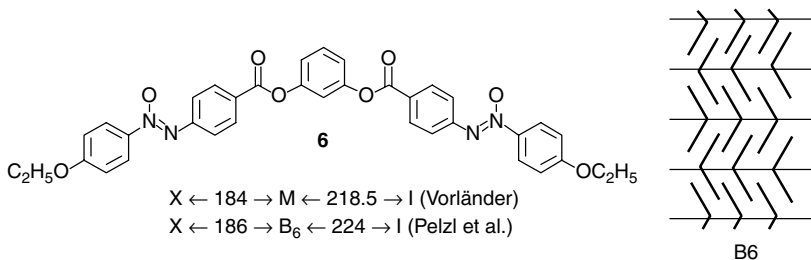


Figure 8.17 Structure and phase sequence of first banana-phase mesogen, reported by Vorländer in 1929, is given. Liquid crystal phase exhibited by this material (actually Vorländer’s original sample) was shown by Pelzl et al.^{36a} to have B₆ structure, illustrated on right, in 2001. Achiral B₆ phase does not switch in response to applied fields in way that can be said to be either ferroelectric or antiferroelectric.

Vorländer found that all three isomers possessed an LC phase. As expected, the linear *p*-isomer showed an extremely stable “crystalline liquid” phase. Indeed, Vorländer reports that this phase decomposes above 200°C without clearing. The *o*- and *m*-isomers had LC phases with narrower temperature ranges; Vorländer’s *m*-isomer, the resorcinol diester **6** (Figure 8.17), is now considered the first banana-phase mesogen. In the context of modern research on the banana phases, Pelzl et al. reinvestigated the bent-core LCs of Vorländer.^{36a} As indicated in Figure 8.17, the resorcinol diester **6** in fact possesses a known banana phase, termed B6. Somewhat surprisingly even today, the LC phase exhibited by the ortho-diester isomer of diester **6** was shown by Pelzl et al.^{36a} to be a nematic phase.

The structure of the B6 phase is also illustrated in Figure 8.17. This achiral, orthogonal smectic phase is one of the class of “intercalated” smectics wherein the layer spacing is actually about half the molecular length. This phase, which has full translational symmetry within the layers, has the same symmetry (D_{2h}), and the same basic structure as the all-anticlinic SmC_A phase. Intercalated SmC_A phases of this type were first described in pioneering work of Watanabe in main-chain polyesters.³⁷

In a model study aimed at elucidating the behavior of the polymers, Watanabe found that the “dimer” polymethylene diol diesters of type **7** (Figure 8.18) formed smectic phases.³⁸ When the “spacer” between the two mesogenic units in the dimer had an odd number of methylene groups (diester **7** has nine methylenes in the spacer), then an intercalated tilted smectic structure with all anticlinic layer interfaces was formed. This structure is often termed “SmC₂” in the literature. As for the B6 phase, all of the layer interfaces in this structure are equivalent, and the X-ray layer spacing is less than half the fully

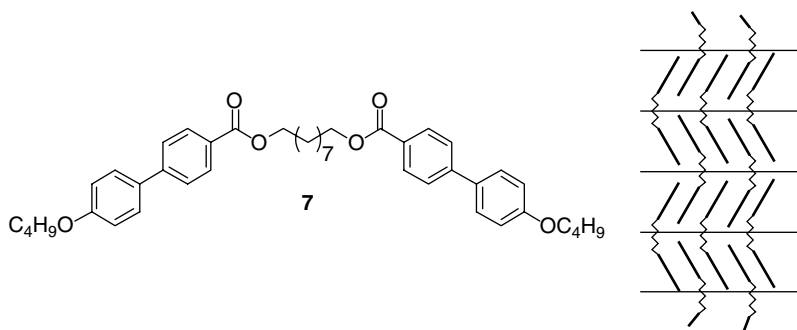


Figure 8.18 “Smectic dimer” of Watanabe, possessing an odd number of methylene units in “linking group.” This material self-assembles into “intercalated” smectic structure very similar to B6 banana phase. As for B6 phase, this achiral phase is also neither ferroelectric nor antiferroelectric.

extended molecular length (less than half due to the tilt of the “director” in the layers). Many additional examples of this type of behavior in dimer or “twin” mesogens have been reported.³⁹ But, typically the phenomenon is the same: A dimeric mesogen with an odd number of atoms in the flexible “spacer” forms a SmC_2 (all anticlinic) structure. Again, the nomenclature for this phase is somewhat confused. The SmC descriptor derives from tilt in the layers. However, the structure is basically the same as an achiral SmC_A , or SmAP_A .

The above discussion shows the great similarity between the SmC_2 phase of Watanabe’s dimers and the B6 banana phase of Vorländer’s diester. Indeed, we have found it particularly useful to consider the bent-core mesogens themselves as **dimers**, wherein two mesogenic units are joined by a rigid “spacer,” in the case of diester **6** the spacer being a resorcinol unit. In this way of thinking, the layer interfaces in the B6 phase contain a random mixture of methyl-terminated chains and resorcinol benzene rings.

6.3 Matsunaga Diesters

After Vorländer’s work of 1929 and 1932, the bent-core mesogens were not revisited again until the 1990s.⁴⁰ Matsunaga et al., referring to Vorländer’s studies, reported on the LC properties of two homologous series of bis-Schiff-base diesters possessing “flipped” Schiff base moieties, diesters **8** and **9**, shown in Figure 8.19. It was found that diesters of type **8** were far superior in mesogenicity to diesters **9**. In addition, an elegant analysis of the X-ray layer spacing observed for 16 homologues of diesters **9** (R = methyl through R = hexadecyl) led Matsunaga to assign a SmC structure to the high-temperature LC phase of all of these homologs. In this analysis, it was found

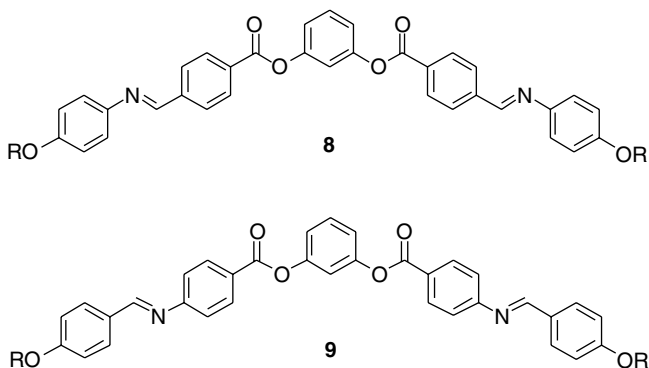


Figure 8.19 Structures of bent-core double-Schiff bases of Matsunaga are given. Mesogenicity of isomers of type **8** was found superior to that of isomers of type **9**.

that the tails are more or less perpendicular to the layers, based upon the incremental increase in layer spacing with each added methylene unit. From the length of the molecular core (distance between the two ether oxygens) estimated with molecular models, a core tilt of over 45° was deduced from the X-ray data.

6.4 Banana Mania

At the 16th International Liquid Crystal Conference (ILCC), held on the campus of Kent State University in June of 1996, Hideo Takezoe started the huge wave of general interest in banana phases in the LC community with his presentation of the unique optical and electro-optical properties of bent-core bis-Schiff bases.⁴¹ The Tokyo Tech group, including Junji Watanabe as coauthor, reported on the LC properties of the Matsunaga compounds as well as a new series of bis-alkyl homologs of the bis-Schiff-base bent-core diesters, published in a pair of pioneering articles in 1996 and 1997.⁴

Four banana phases were described, which now are termed B1, B2, B3, and B4.⁴² For these bis-Schiff bases, the B1 phase occurs only with lower homologs of the alkyl series. The structure and phase sequence of a prototype of the classic bent-core mesogens is given in Figure 8.20. This material, the bis-nonyloxy homolog **8** ($R = n - C_9H_{19}$), given the trivial name **NOBOW** by the Boulder group after the bowl-like (as in bow and arrow) shape of the molecules (NonylOxyBOW), exhibits the B2, B3, and B4 phases. In the context of the topic of this discussion, the B2, B4, and B7 phases are most relevant and are the focus of the following discussion. Pelzl et al. have published an excellent review of all of the banana phases appearing in the literature through 1998.⁴³

At the 1996 ILCC,⁴¹ and in their pioneering works,⁴ the Tokyo Tech group reported two results of special significance. First, these materials exhibit electro-optics in the high-temperature smectic B2 phase (as discussed below, B2 in the banana literature actually refers to a family of phases, often seen in coexistence), strongly suggesting some kind of polar structure; and second, the B4 phase, often termed “blue crystal,” or “SmBlue,” is a crystalline conglomerate with optical activity easily observable in the chiral domains in thin films.

6.5 B4 Phase

The B4 phase is complex; a phase seemingly dominated by defects, similar to the cholesteric blue phase. While the detailed structure is not known, some facts are clear. From the viewpoint of this discussion, the key observation is the chirality of domains of the B4 phase in $4\text{-}\mu\text{m}$ LC cells. This

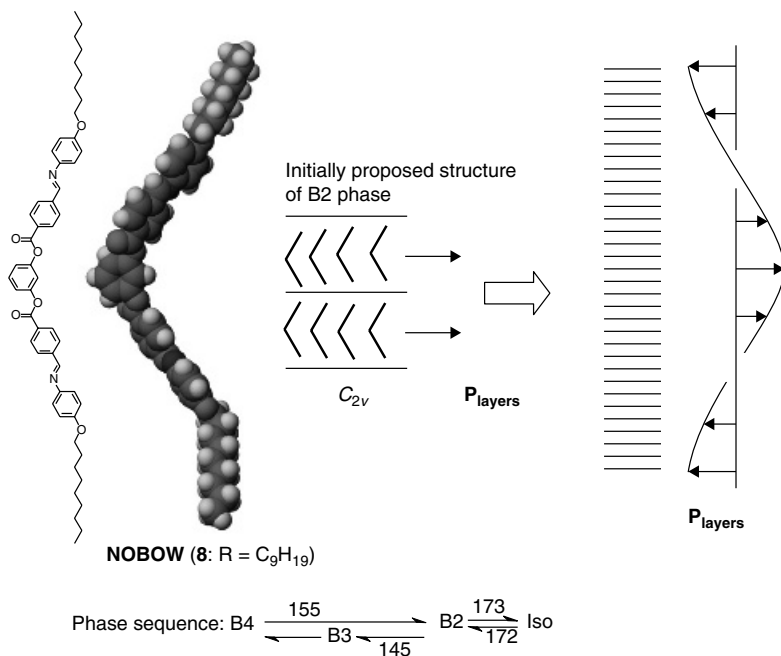


Figure 8.20 Structure and phase sequence of prototypical bent-core mesogen **NOBOW** (**8**) are given, along with space-filling model showing one of many conformational minima obtained using MOPAC with AM1 force field. With observation by Tokyo Tech group of “polar” EO switching for “B2” smectic phases formed by mesogens of this type, banana LC field was born. Achiral, polar C_{2v} layer structure, with formation of macroscopic spontaneous helix in polarization field (and concomitant chiral symmetry breaking), was proposed to account for observed EO behavior.

chirality is manifested as a strong optical activity of macroscopic domains. When observed in transmission between crossed polarizers, the B4 texture of NOBOW is quite smooth, and shows a blue color. There is no extinction in the domains (i.e., the light coming out of the sample is never polarized perpendicular to the analyzer). Upon rotation of the analyzer by about 20° , however, it is possible to cause half the domains to extinguish, while the other half brighten. Rotation of the analyzer in the opposite direction reverses the observed behavior of the domains.

This phenomenology is, of course, consistent with optically active domains in a conglomerate. It should be pointed out that this kind of rotation of plane polarized light in a $4\text{-}\mu\text{m}$ path cannot derive from molecular chirality but should be due to some kind of macroscopic helical chirality.

X-ray scattering data clearly show smectic layering in the B4 phase. Watanabe et al. have suggested⁴⁴ that the layers form a variant of the

well-known twist–grain boundary (TGB) structure in which uniform smectic blocks are joined at twist and grain boundary planes normal to the layers, forming a wall of screw dislocations (the director structure is uniform in these boundary planes).⁴⁵ While the Tokyo Tech suggestion is corroborated by a considerable body of experimental work,⁴⁴ the B4 phase is apparently not identical to other known TGB phases formed by chiral calamitic mesogens.

X-ray scattering from the B4 phase is complex, and there is disagreement in the LC community about the meaning of the data. Observation of a large number of sharp peaks at wide angles has led many workers to suggest that the B4 phase is a kind of crystalline phase with a short coherence length of the three-dimensional positional order due to the presence of defects. Others feel that the B4 phase is a novel liquid crystalline phase. The B4 domains are much smaller than the wavelength of visible light, leading to a smooth texture in the light microscope. These domains are chiral and form a conglomerate of macroscopic unichiral “superdomains” with sizes on the order of hundreds of microns in an LC cell. The observed color and optical activity of these superdomains derives from a combination of birefringence, Mauguin adiabatic following of some kind of macroscopic helical structure, and selective reflection caused by photonic band gaps in the sample.

Efforts aimed at understanding the structure of this fascinating type of conglomerate are in progress. Unfortunately, the most fundamental aspect of the structure of B4—whether it is crystalline or a liquid crystalline—is not firmly established. That is, at this point it is not clear whether the B4 phase is a fluid conglomerate or a very novel version of a crystal conglomerate. This ambiguity, however, is emphatically absent in the B2 electro-optically active family of phases, as discussed below.

6.6 B2 Phase: Spontaneous Reflection Symmetry Breaking in Fluid Smectic

Stimulated by the Tokyo Tech results, several groups began studying similar bent-core mesogens. At the European Conference on Liquid Crystals, held in Zakopane, Poland, in March of 1997, Heppke et al. confirmed the Tokyo Tech results,⁴⁶ and Weissflog et al. did as well, with the important exception that the Halle group found antiferroelectric behavior in the B2 phase.⁴⁷

The Tokyo Tech group assigned a C_{2v} structure for the layers in the B2 phase, and ferroelectric packing of such layers to form a locally polar C_{2v} macroscopic structure, as indicated in Figure 8.20. Other early workers in the field also adopted this structural model for the B2 phase. Brand et al. had discussed a C_{2v} smectic “chevron” structure in their 1992 theoretical study,²⁹ and while they seem to be referring to an all-anticlinic bilayer smectic, their actual graphic is basically identical to that shown in Figure 8.20. Furthermore,

these authors had explicitly considered the possibility of reflection symmetry breaking by suggesting that there could be spontaneous helix formation, which would provide macroscopic regions of left- or right-handed organizations in such a biaxial system. The Tokyo Tech group adopted this helical structure as part of their interpretation of the polarized light microscope textures and EO behavior of the B2 phase. Indeed, they went so far as to suggest such a symmetry breaking was driven by a thermodynamic tendency for “escape from the macroscopic polarization.” In this way they were suggesting formation of a conglomerate structure in the B2 phase.

In order to discuss the nature of these textures, and more generally the supermolecular structure of the banana phases, it has proven useful to adopt some reasonable definitions of aspects of the molecular geometry and to create a symbolic language, similar to Newman projections, to depict the molecular structures. As shown in Figure 8.21, the molecules may be considered to be bow-shaped geometrical objects. This analogy proves useful since we define the molecular director in phases of these molecules as being along the bowstring, as indicated in Figure 8.21 (recall the molecular director is typically indicated by a unit vector \mathbf{n} , but has no “direction,” rather defining the *average*

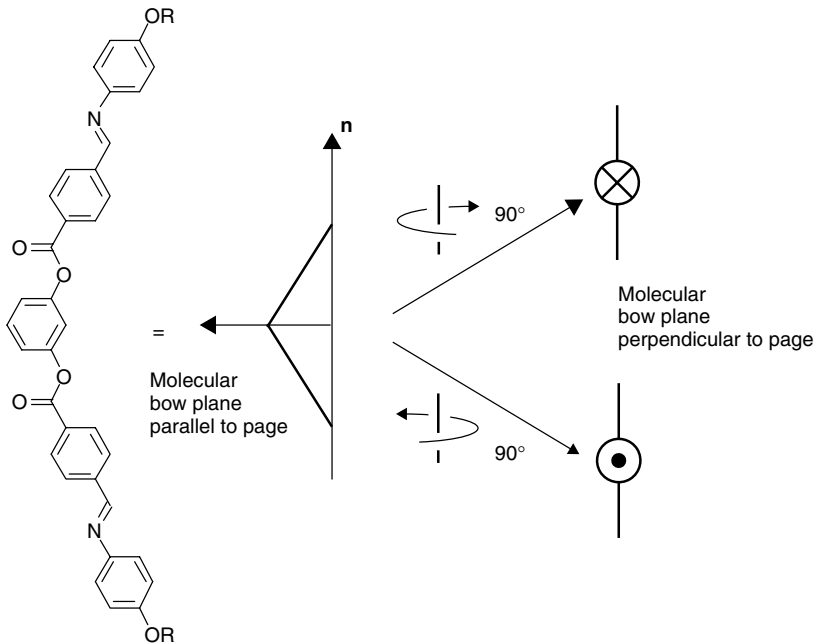


Figure 8.21 Symbolic bow-and-arrow-based representations of bent-core mesogen structures used in this discussion are given.

long axis, or *axis of minimum inertia* of the molecule). For molecules in an LC phase, which are sampling an infinite number of translational and rotational states, and thousands of conformational minima, the molecular director should be considered an ensemble or time-average geometrical object (including end-for-end flips of the molecules).

Returning to the bow and arrow analogy, the polar axis of the C_{2v} symmetrical molecules of the classic bananas is along an arrow fitted to the bow. The *molecular bow plane* is the plane containing the bowstring and the arrow. It is useful to discuss the construct when viewed from a point away from the molecule but in the bow plane. As indicated in Figure 8.21, if the bow and arrow are rotated 90° such that the arrow is pointing directly away from the viewer, a cross inside a circle is used to represent the tail of the arrow; in this view the projection of the bow is simply a straight line. A 90° rotation in the opposite direction has the arrow pointing directly at the viewer, as indicated by a circle with a bullet inside.

Examples of the striking textures and EO behavior of the B2 phase are shown in the photomicrographs of Figure 8.22. In this case the LC cell is composed of glass substrates with indium–tin oxide (ITO) conducting films on the inner surfaces and rubbed nylon alignment layers. On cooling from the isotropic liquid phase, birefringent LC domains grow in as shown in Figure 8.22 (center). In these photomicrographs, the black area is still isotropic (extinguishing between crossed polarizers), and the anisotropic LC is easily seen due to its birefringence. The color of the domains is related to the magnitude of the birefringence and the thickness of the cell, and is independent of the orientation of the input polarized light. Extinction “brushes” (dark regions in the LC domains) occurs when the optic axis of the LC is either parallel or perpendicular to the input polarization.

When formed in this way, the majority (about 90% in our hands) of the LC domains of **NOBOW** show an unusual “stripe” texture, seen on the left in Figure 8.22 (center). This texture is reminiscent of the “fingerprint” texture seen in chiral nematic (cholesteric) LCs when the helix axis is parallel to the substrates. Such stripes might also be expected for a helical banana-phase structure as shown in Figure 8.20, if the layers are perpendicular to the substrates (bookshelf), the director is along the layer normal, and the bow plane and polar axis precess about the layer normal. The nature of the texture clearly indicates that there is no “azimuthal anchoring” of the director in the cell; that is, the layers are locally flat and parallel but curve in complex patterns on macroscopic length scales forming what is called a random focal conic texture. Consistent with the helical structure, it is apparent that the stripes are oriented parallel to the layers in the focal conic texture.

Due to the biaxiality of the molecules in the C_{2v} structure, the refractive index for light polarized parallel to the layers is different depending upon

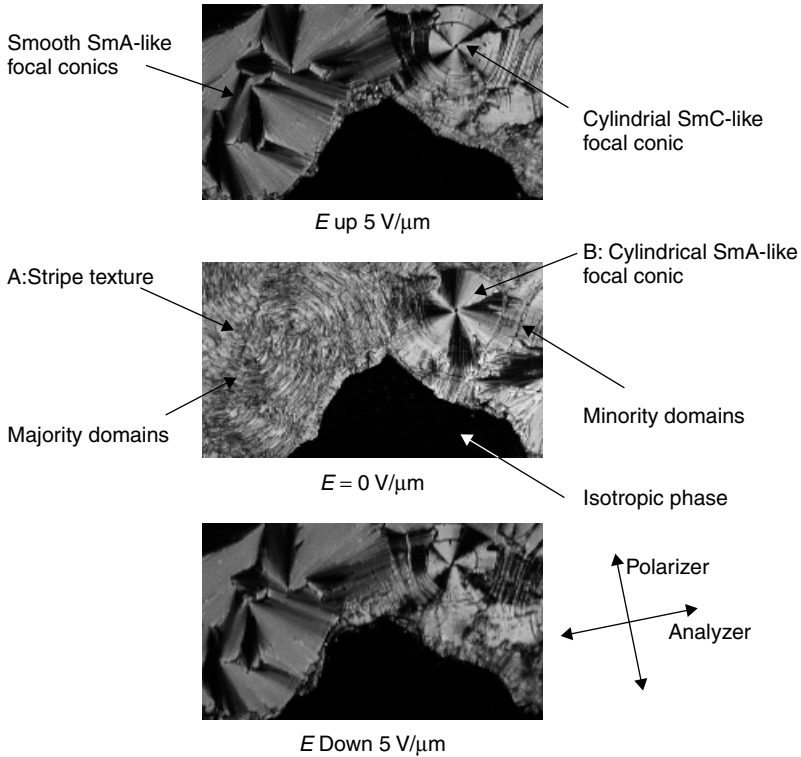


Figure 8.22 Striking electro-optic behavior of **NOBOW** is illustrated with these photomicrographs. At zero field, two types of domains are seen, with dramatically different textures and different birefringence colors. In this case, there are gold stripe domains of type A and green SmA-like focal conics of type B. It was shown that gold birefringence color of type A domains is in Newton's second order, while the green birefringence color in type B domains is first order. Gold texture therefore exhibits a higher average Δn than green texture. Application of electric field normal to plane of substrates causes switching which reverses birefringence of two types of domains. In addition, domains of type B show chiral response to applied field. In this case, extinction brushes of cylindrical SmA-like focal conic domain on right side of field of view rotate counterclockwise in response to up field greater than switching threshold value, forming SmC-like cylindrical focal conic. Upon application of down field of same magnitude, clockwise brush rotation is seen. Other domains of type B in same sample exhibit enantiomorphous behavior.

whether the sample is viewed normal to the bow plane or parallel to it, while light polarized along the layer normal always has the same refractive index. The proposed banana helix would then provide a periodic variation in the birefringence of the sample, leading to a fingerprint texture with some kind of average but periodically varying birefringence color. With the helix axis parallel to the substrates, optical activity would not be expected, nor is it observed.

Application of an electric field above a threshold value of about ± 5 V/ μm causes a dramatic change in the sample, as shown in Figure 8.22 (top and bottom). The layer structure remains unchanged, but the birefringence color and texture changes rapidly (~ 400 μs at 8 V/ μm). This EO switching indicates a field-induced change in the supermolecular structure or orientation. Such fast switching at relatively low field strengths (even at the high temperatures of the B2 phase) is seen as diagnostic of polar order (either ferro- or antiferroelectric) in the phase.

In the cell depicted in Figure 8.22, application of a field causes the stripe texture, which has a gold average birefringence color, to rapidly transform to a smooth focal conic texture with a green birefringence color. This green focal conic is “SmA-like,” meaning that the macroscopic extinction brushes are everywhere parallel or perpendicular to the polarizer, indicating that the microscopic optic axis of the system is along the layer normal (in these photomicrographs the polarizer is oriented about 10° counterclockwise from vertical, with the analyzer crossed by 90° from the polarizer). This texture change is consistent with the helical model, where application of a field “unwinds” the helix (a well-known phenomenon in the SmC* phase), producing a uniform structure with the bow plane perpendicular to the substrates, and the director (and optic axis) along the layer normal.

This proposal has the B2 phase being a SmAP_F structure with a helix, as shown in Figure 8.20, and first proposed by Brand et al.²⁹ Such a system could show “antiferroelectric” polarization reversal current behavior due to the expected barrier for unwinding and reforming of the helix. If the frequency of the applied AC field is faster than is required to allow the helix to reform, then in principle an antiferroelectric polarization reversal behavior could be observed.

However, further analysis of the behavior of the system in LC cells cast doubt on this interpretation. First, while intuitively attractive, the idea that “relaxation” of the polarization by formation of a helielectric structure of the type shown in Figure 8.20 would lower the free energy of the system is not correct. Also, in a thermodynamic helical LC phase the pitch is extremely uniform. The stripes in a cholesteric fingerprint texture are, for example, uniform in spacing, while the stripes in the B2 texture seem quite nonuniform in comparison. Finally, the helical SmAP_F hypothesis predicts that the helical stripe texture should have a smaller birefringence than the uniform texture. Examination of the optics of the system show that in fact the stripe texture has the higher birefringence.

In addition, and most importantly, samples of typical B2 materials always seem to exhibit *minority domains* which behave quite differently from the stripe domains. Specifically, at zero field these minority domains have the lower Δn green birefringence color and show a smooth SmA-like focal conic

texture. A beautiful cylindrical focal conic domain, in which the layers form nested cylinders, can be seen on the right side of the photomicrographs in Figure 8.22. Note that in the zero-field orientation of Figure 8.22 (center), the brushes in the cylindrical focal domain are seen to be parallel and perpendicular to the polarizer, a clear indication that the optic axis is along the layer normal. Application of a field above the switching threshold causes the green SmA-like focal conics of the minority domains to switch to the high birefringence gold color, the changes in Δn being precisely “flipped” relative to those of the majority domains.

The field-induced state in the minority domains also shows a smooth focal conic texture, but in this case the brushes are rotated from the axis of the polarizer, suggesting a tilted smectic. And, application of a field of opposite sign causes the brushes to rotate in the opposite direction. While it is impossible to see this striking behavior in still photos, watching the actual EO switching in response to a slowly ramping triangular driving waveform makes the rotation direction clearly visible. In the minority domain shown in Figure 8.22, application of a positive field (up) causes the brushes to rotate about 40° counterclockwise, while application of a negative field (down) causes the brushes to rotate 40° clockwise. It is also quite apparent visually that the brush rotation is highly nonlinear. That is, most of the rotation occurs as the threshold voltage is approached. Since there is clearly no sign of a helix in the minority domains, this strongly nonlinear EO behavior is suggestive of antiferroelectric switching.

The EO behavior is also clearly chiral: a clockwise response to a force applied perpendicular to the clock face, with a counterclockwise response to a force of opposite orientation. Furthermore, domains of opposite handedness can also be seen in these LC cells. That is, while the brushes in some domains rotate counterclockwise in response to an applied field of positive sign, other domains rotate clockwise in response to the same field. The EO behavior of a pair of such domains is enantiomorphous, implying that the domains themselves are heterochiral.

While such behavior can be seen in achiral LC phases, driven by surface constraints as illustrated in Figure 8.11, further characterization of the phase responsible for the minority domains in the B2 banana phases shows this to be the first unequivocal example of a bulk fluid conglomerate. It is worth noting here that the EO behavior of the majority domains is achiral: Stripes parallel to the layers switch to a SmA-like focal conic texture, which is identical for both signs of the field, as can be seen in Figure 8.22. This EO behavior very clearly appears achiral when observing the switching in motion.

Interestingly, upon heating directly from the B4 phase, when the sample melts into the B2 phase we find chiral domains of B2 texture filling essentially the entire cell. After some hours of switching of the sample at this temperature,

the sample seems to anneal to the same 90:10 mixture of achiral majority domains and chiral minority domains seen immediately upon cooling from the isotropic phase. That a chiral fluid smectic *metastable* phase might form directly upon melting of a chiral crystal or complex LC conglomerate seems reasonable. The fact that the two domains coexist at approximately equal volume fractions in the sample over a wide temperature range is extremely unusual and not currently understood. In any event, under all circumstances (whether the sample had just been melted from the B4 phase or had been allowed to anneal) the polarization vs. applied voltage behavior shows the double-hysteresis-loop characteristic of antiferroelectrics.

6.7 SmCP Phases

All of these rather mysterious and interesting results were explained by elucidation of the structure of the B2 phase, as reported in late 1997.⁴⁸ For the purposes of this discussion, the key question is the following: What is the structural origin of the chirality of the fluid conglomerate phase? The answer can be found by combining the insights of both Matsunaga and the Tokyo Tech group. That is, as proposed by the Tokyo Tech group, within the smectic layers all of the molecular bows are pointing in the same direction (with some order parameter <1) to give a polar layer structure. In addition, as suggested by Matsunaga, the phase is in fact a variation of the SmC, with the director tilted from the layer normal.

These two spontaneous symmetry-breaking events occurring in a smectic LC lead to a polar and chiral layer structure, as shown in Figure 8.23. In this figure the average structure of the fluid smectic phase is illustrated as projected onto the tilt plane of the system. The polar axis is normal to the plane of the page, with the molecular arrows pointing out of the page. The director is tilted with respect to the layer normal in SmC-like fashion.

As can be seen in Figure 8.23, mirror images of this structure (reflected through a vertical mirror perpendicular to the plane of the page in the figure) are nonsuperposable—classic chirality by the Lord Kelvin definition, extended

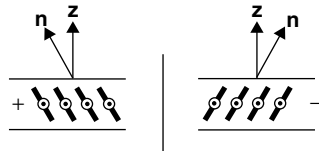


Figure 8.23 Illustration of chiral layer structure proposed for **NOBOW** high-temperature smectic banana phase is given. On left layer with (+) configuration is shown, while on right enantiomeric (-) configuration is illustrated. These mirror image fluid smectic layer configurations are not superposable.

to the time-average symmetry of an LC phase composed, at least in the illustration, of achiral objects. This layer structure has the same symmetry as the $\text{SmC}^* : C_2$. Note that this chirality is not due to any supermolecular helical organization.

A simple approach to describing the chirality of this system was developed. If the molecular arrows are pointing parallel to the cross product of the layer normal and the director ($\mathbf{z} \times \mathbf{n}$), then the layer is said to have positive chirality. If ($\mathbf{z} \times \mathbf{n}$) is opposed to the molecular arrows, then the layer has negative chirality.

Taken from the three spontaneous symmetry-breaking events leading to this layer structure [formation of layers with long-range orientational order of the director (Sm), tilt of the director from the layer normal (C), and polar orientation of the molecular arrows (P)], we term phases of this type SmCP. All of the complex textures and EO behavior of **NOBOW** in the B2 phase can be understood in terms of various stacking modes of SmCP layers as shown in Figure 8.23.

It is interesting to point out here that with all of the theoretical speculation in the literature about polar order (both ferroelectric and antiferroelectric) in bilayer chevron smectics, and about reflection symmetry breaking by formation of a helical structure in a smectic with anticlinic layer interfaces, the first actual LC structure proven to exhibit spontaneous reflection symmetry breaking, the SmCP structure, was never, to our knowledge, suggested prior to its discovery.

6.8 SmC_sP_A and SmC_AP_A Antiferroelectric Phases

One of the key experimental results leading to the elucidation of this overall structural puzzle involved depolarized reflected light microscopy (DRLM) studies on **NOBOW** freely suspended films in the high-temperature SmCP phase.⁴⁸ In the freely suspended films it appears that only one phase is observed, which is assumed to be the phase forming the majority domains in the EO cells. The DRLM experiment provides two key results. First, thin films of any layer number have a uniformly tilted optic axis, suggesting all of the layer interfaces are synclinic. Second, films of even-layer number are non-polar, while films of odd-layer number are polar, with the polar axis oriented normal to the plane of the director tilt (lateral polarization).

These results are consistent with an antiferroelectric structure, as illustrated in Figure 8.24. Two orthogonal projections of the structure are given; on the left the molecules are projected onto the tilt plane, and on the right the molecules are projected onto the polar. Note that when projected onto the polar plane, the molecular bow plane is not parallel to the plane of the page. This tilt of the director out of the polar plane (the plane of the page) is indicated by drawing a thicker line to indicate the part of the bow tilting out, and a thinner line for the part of the bow tilting back.

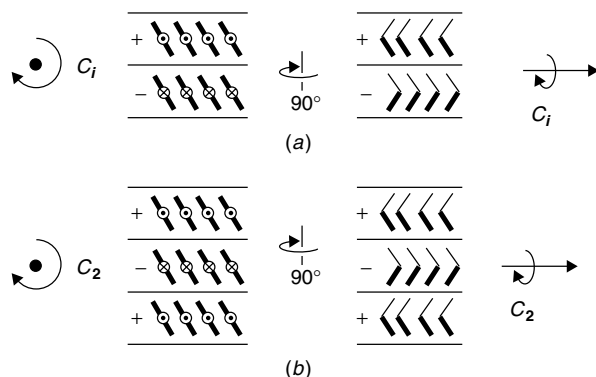


Figure 8.24 Illustration of layer structure and symmetries observed for **NOBOW** thermodynamic phase (majority domains) in freely suspended films. (a) Films of even-layer number have achiral, nonpolar C_i symmetry. (b) Films of odd-layer number have chiral and polar C_2 symmetry, with net polarization normal to tilt plane (lateral polarization).

The layer stacking is synclinic in the tilt plane and antiferroelectric in the polar plane. The phase composed of an infinite number of SmCP layers stacked in this way is termed SmC_SP_A , where the subscripts S and A each refer to a structural feature of the layer interfaces between adjacent pairs of layers. If two adjacent layers are tilted in the same direction, the interface is synclinic (subscript S) in the tilt plane. If two adjacent layers have antiparallel orientation of their polar axes, then the layer interface is said to be antiferroelectric (A) in the polar plane.

As can be seen by examination of Figure 8.24a, with an even number of layers (or an infinite number of layers), the structure has C_i symmetry (a twofold rotation/reflection axis). Note that this is *achiral* (reflection) symmetry. With synclinic tilt and antiferroelectric order in the polar plane, all adjacent pairs of layers must be heterochiral, as indicated in Figure 8.24 by the + and - signs representing the chirality of each layer. One pair of such heterochiral layers is, in fact, achiral, and is superposable on its mirror image. This is analogous to formation of an achiral meso diastereomer in a molecule possessing two stereogenic centers. In the LC case, this phase is termed a *macroscopic racemate*.

The C_i symmetry also means that a freely suspended film possessing an even number of layers is nonpolar, as is observed. When the film possesses a finite and odd number of layers, however, the symmetry of the system is C_2 , as indicated in Figure 8.24b. This structure is both chiral and polar, leading to the observed net polarization in films of **NOBOW** with odd-layer number.

The SmC_SP_A structure for the majority domains of **NOBOW** deduced from the freely suspended film experiments nicely explains the achiral nature of their

EO switching. Since the phase is a macroscopic racemate and achiral, the EO behavior of the SmC_5P_A phase can reasonably be expected to be achiral. But, what of the chiral minority domains?

A complete picture of the phases and EO switching observed for the high-temperature smectic phase of **NOBOW** is given in Figure 8.25.⁴⁸ For most of the polarized light microscopy and EO work accomplished on this system in the Boulder labs, commercial (Displaytech, Inc.) LC cells were used. The substrates in these cells are spaced at about $4\ \mu\text{m}$, with ITO electrodes and parallel-rubbed low-pretilt polyimide alignment layers. Access to a great many cells of the same thickness ($\pm 0.5\ \mu\text{m}$) proved extremely useful in these studies since the birefringence colors of the various domains was constant across the

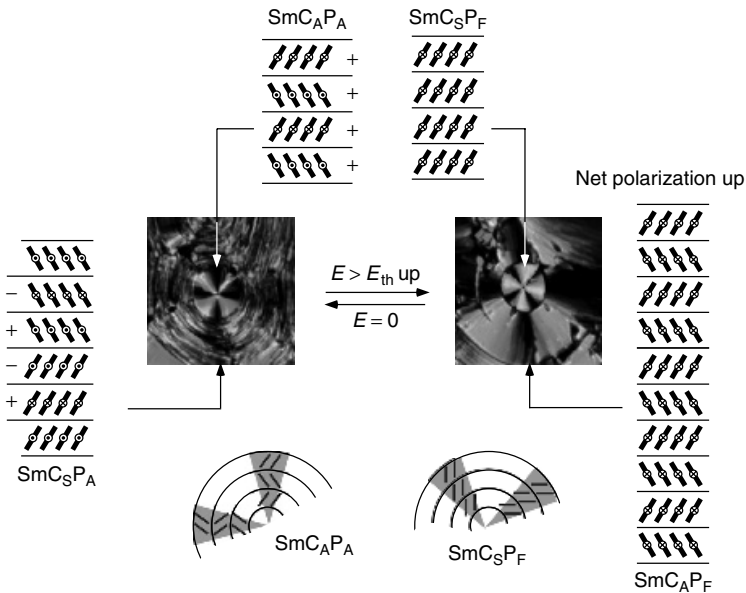


Figure 8.25 Summary of EO observed in SSFLC cells of **NOBOW** is given. Photomicrographs show single large cylindrical focal conic domain. Smectic LC at center of this domain is chiral SmC_AP_A antiferroelectric phase, while achiral SmC_5P_A antiferroelectric domain can be seen at larger diameters, with very sharp domain boundary between them. In this $4\ \mu\text{m}$ SSFLC cell green birefringence color results from higher Δn than purple birefringence color. Proposal for layer structure in green stripe texture is given on far left. Phase is macroscopic racemate (SmC_5P_A), accounting for achiral EO behavior of these domains. Within single SmC_5P_A domain, degenerate synclinc antiferroelectric domains with opposite tilt orientation cause stripe texture visible in photomicrograph. Application of up field gives two ferroelectric states illustrated on right in figure. Illustration of director structure and optic axis orientations in focal conics for chiral SmC_AP_A phase and corresponding SmC_5P_F state resulting from application of field is given at bottom center of figure.

many cells prepared in the course of the work. Since the LC molecules are Schiff bases, the well-known problems with “aging” of the samples, where the transition temperatures and phase coexistence ranges lower and broaden, respectively, with time, are seen. This is presumably due to hydrolysis of the Schiff base moieties and is seen with all Schiff-base-containing LCs. Therefore fresh cells were prepared often during the studies.

In the 4- μm Displaytech cells, the majority domains have a green birefringence color, while the minority domains have a purple birefringence color. This suggests that the birefringence of the majority domains is about $\Delta n = 0.18$ while that of the minority domains is about $\Delta n = 0.12$ at zero field. A proposal for the nature of the stripe texture in the majority domains is indicated on the left of Figure 8.25. The synclinic antiferroelectric SmC_SP_A phase has two possible orientations of the synclinic tilt, which are degenerate. Macroscopic domains of uniform tilt are separated by some kind of defect modulating the transition from domains of one orientation to the other; in the figure this is indicated as a single anticlinic/ferroelectric layer interface. While the details of these transition regions are not understood, the basic picture of the stripe texture shown here seems correct.

The birefringence observed in the majority domains in which the bow plane is perpendicular to the substrates is the highest that can be seen with these molecules in the bookshelf alignment. Incident light polarized parallel to the director excites the polarizable aromatic system, leading to a high “parallel” refractive index. Incident light polarized normal to the director cannot excite the conjugated system, leading to a low “perpendicular” refractive index, and high $\Delta n = n(\text{parallel}) - n(\text{perpendicular})$.

Application of an electric field to the SmC_SP_A phase then causes the system to switch to a ferroelectric state. This could occur in two ways. The molecules in every other layer could simply rotate about the director, leaving the layer clinicity the same but changing the chirality of alternate layers. This would require a locally diastereomeric transition structure where the polarization is not parallel to the layers.

Apparently this switching mode is disfavored since, in fact, the chirality of the layers does not change upon switching to the ferroelectric state; rather the layer interface clinicity changes. This occurs when the molecules in alternate layers simply precess about the tilt cone in a manner exactly analogous to anti-ferroelectric to ferroelectric switching in the chiral SmC_A^* phase. As shown in Figure 8.25, the ferroelectric state obtained from the SmC_SP_A antiferroelectric phase is a SmC_AP_F structure, an achiral macroscopic racemate with anticlinic layer interfaces.

Both “tilt domains” in the green stripe texture switch to the same ferroelectric state in this process, thus causing the stripes to disappear. The anticlinic structure is SmA -like in the sense that the average optic axis is along the layer

normal. In the photomicrograph of the ferroelectric states, this is evidenced by the observed vertical and horizontal extinction brushes (the polarizer was vertical for this experiment). Also, the birefringence is expected to decrease since it is not possible to maximally excite the conjugated aromatic system of all the molecules in an anticlinic smectic, nor to avoid exciting them to some extent, leading to a decrease in $n(\text{parallel})$ (i.e., parallel to the optic axis) and an increase in $n(\text{perpendicular})$, and thus a decrease in Δn .

The photomicrographs in Figure 8.25 also show that the center of the cylindrical focal conic domain, which is the main feature of this area of the sample, has the chiral antiferroelectric structure. At zero field, this domain is SmA -like, with precisely the same birefringence as the ferroelectric SmC_AP_F state, and its optic axis is along the layer normal. This clearly suggests an anticlinic structure for these domains, which are also known to be antiferroelectric. The clear conclusion is that the fluid conglomerate has the SmC_AP_A structure, as shown in Figure 8.25. In this phase all of the layers have the same chirality, positive chirality for the domain shown. The two antiferroelectric structures must exist as separate wells on the free-energy surface, in order to explain their existence within a single focal conic domain.

Application of a field to the SmC_AP_A phase causes switching by precession of the director around the tilt cone in alternate layers, to give a ferroelectric SmC_SP_F state with uniform tilt. In this case, there can be no domains of opposite tilt since such domains would necessarily have their polarization opposing the applied field. This leads to a uniform SmC -like texture with a green birefringence color. The extinction brushes in the cylindrical focal conic rotate counterclockwise when the net tilt rotates clockwise, as indicated in Figure 8.25. As anticipated, the chiral rotation of the brushes is a direct manifestation of the chirality of the phase. Elsewhere in the sample there must be SmC_AP_A domains of opposite handedness, which would possess the opposite sense of tilt for the same sign of the applied field.

It may be noted that simple MOPAC AM1 calculations suggest that the dipole moment of **NOBOW** is oriented antiparallel to the molecular arrow. As indicated in Figure 8.25, this means that for an up field, the molecular arrows are pointing down. Given the definition of the sign of \mathbf{P} in FLCs, this also means that domains of the SmC_AP_A phase with positive chirality have negative ferroelectric polarization, and vice versa.

6.9 Stereogenic Elements in SmCP Phases: SmCP Supermolecular Diastereomers

This interpretation of the properties exhibited by the major EO-active phases of **NOBOW** and the rest of the classic banana mesogens posits the existence of four supermolecular diastereomers, at least two of which, the antiferroelectric phases SmC_SP_A and SmC_AP_A , must exist as separate wells on the

configurational hypersurface in the absence of an applied field. The four diastereomeric structures are built up in a very reasonable way by considering different stacking modes for identical layers. It has proven very useful to borrow the language of molecular stereochemistry to describe this isomerism as follows.⁴⁹

In the SmCP phases, there are three independent stereogenic elements (structural features leading to stereoisomerism), each with two possible configurations. The first of these elements refers to the structure of a single layer, while the other two refer to the interface between adjacent pairs of layers. These are: (1) layer chirality (positive or negative), (2) layer interface clinicity (synclitic or anticlinitic), and (3) layer interface polarity (ferroelectric or antiferroelectric). These elements combine to provide four diastereomers and a total of eight possible isomeric structures. The achiral nature of two of the diastereomers, however, causes a degeneracy leading to the actual observation of six isomeric structures, as shown in Figure 8.26.

There are two macroscopic racemates and two conglomerates possible in this model, each conglomerate showing two enantiomers. This situation is quite analogous to the case of a molecule with three tetrahedral stereogenic

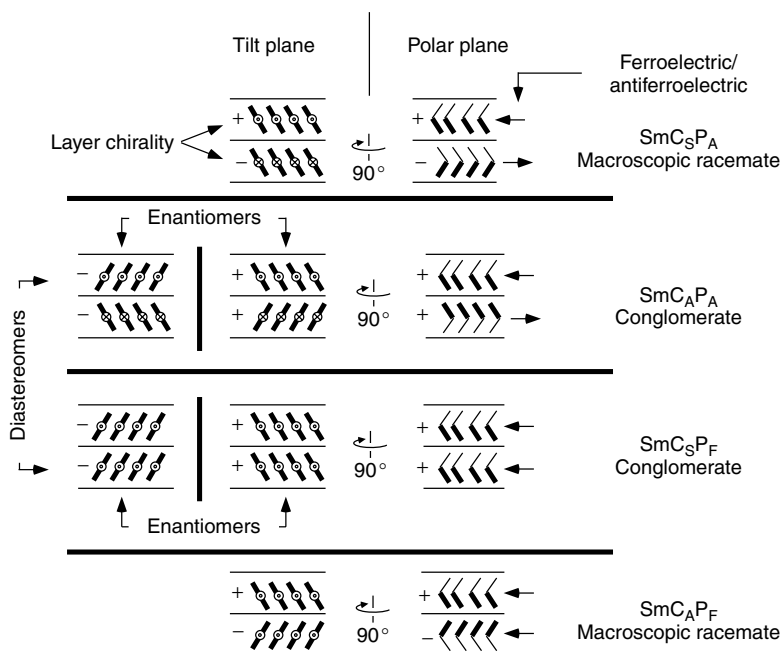


Figure 8.26 Illustration of supermolecular structure and pairwise relationships for isomeric SmCP phases is given.

centers whose symmetry leads to two meso compounds and two *dl* pairs, for a total of six isomers.

6.10 Ferroelectric Banana by Design

The initial reports of polar EO switching in bent-core mesogens, and the discovery of a chiral LC phase from achiral molecules, stimulated a great deal of synthetic effort in the bent-core system.⁴³ However, prior to 2000 all of the known electro-optically active banana phases were apparently antiferroelectric, leading to the question of whether the ferroelectric SmCP diastereomers could exist as global minima on the hypersurface in the absence of an applied field. Some felt that ferroelectric banana phases would never be found, based upon a Coulombic argument supposing an electrostatic preference for antiferroelectric order of the polar axes in the layer stacks. This argument, however, suffers from the same problem as the one suggesting an electrostatic free-energy gain by relaxation of the polarization with a helix; any electrostatic free-energy cost of ferroelectric relative to antiferroelectric bulk polarization in the layers occurs at the edges of the system. A priori there is no difference in the electrostatic energy of these two structures in the bulk.

A consideration of the well-known tendency for smectics to show synclinc layer interfaces suggested an alternative reason for the preference for antiferroelectric bananas. This argument is easily seen by comparing the structures of the two synclinc diastereomers, SmC₅P_A and SmC₅P_F, as shown in Figure 8.27. For the synclinc diastereomers all the molecular bow planes are parallel, defining a macroscopic bow plane. In Figure 8.27 the structures are drawn such that the macroscopic bow plane is vertical in both projections. In the projections on the right, the molecules are shown projected onto this bow plane; in this case, due to the tilt of the director, the layer normal is not in the plane of the page, but tilted out of the page.

As can be easily seen by inspection of these illustrations of the SmC₅P_A and SmC₅P_F phases, while the director tilt in the tilt plane is synclinc for both, the layer interfaces have a different character when observed in projection in the bow plane. The antiferroelectric diastereomer has “synclinc” character at the layer interfaces, while the ferroelectric diastereomer is “anticlinc” in the bow plane. This suggests a very simple reason for the tendency toward *antiferroelectric* bananas, this being basically the same as the tendency toward *ferroelectric* calamitic smectics: preference for synclinc layer interfaces.

A simple consideration of the synclinc banana phases in the context of the prior discovery of the Soto Bustamante–Blinov achiral antiferroelectric bilayer is illuminating. In Figure 8.28, the achiral antiferroelectric SmAP_A bilayer structure is illustrated on the left. The layers are horizontal and normal to the plane of the page, and the tilt plane is vertical and normal to the plane

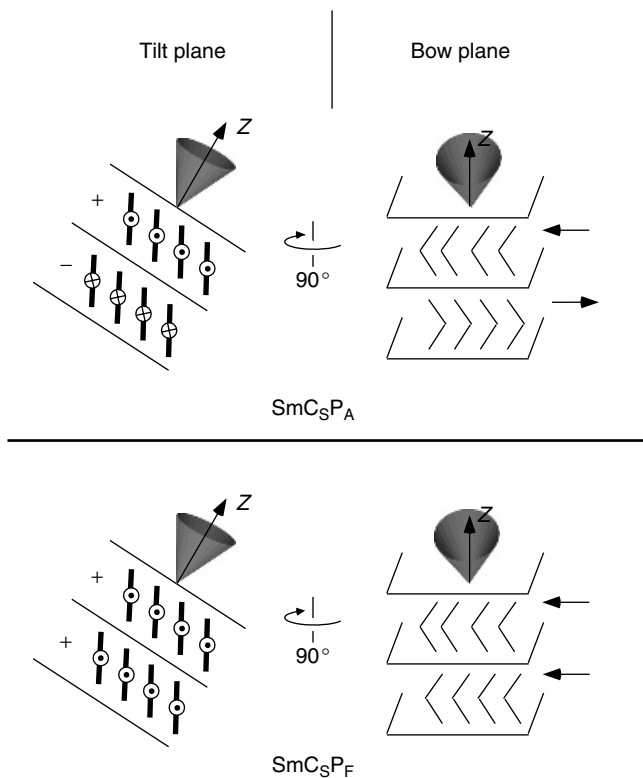


Figure 8.27 Illustrations showing SmC_5P_A and SmC_5P_F supermolecular structures projected onto tilt plane and onto bow plane are given. Projections onto bow plane are meant to illustrate effective synclinal layer interface present in SmC_5P_A phase and corresponding anticlinal layer interface in SmC_5P_F phase, though both are synclinal in tilt plane.

of the page. In this graphic, the “molecular” arrowheads at the anticlinal layer interfaces represent the acrylate ends of the mesogens, while the tails of the arrows at the synclinal layer interfaces represent the methyl-terminated alkoxy ends of the mesogens.

Now suppose these mesogens were “morphed” into covalent dimers with a rigid resorcinol group linking the mesogenic units of the dimers. This leads to a new “bilayer” smectic with alternate layer interfaces “locked” into an anticlinal orientation (indicated by the dashed lines on the right in Figure 8.28), and the other layer interfaces maintaining their synclinal configuration. The morphed structure becomes an $SmCP$ phase if the layers are then tilted to create the chiral layer structure. In this way of thinking, the SmC_5P_A phase is a kind of bilayer smectic with alternating synclinal and anticlinal layer interfaces when

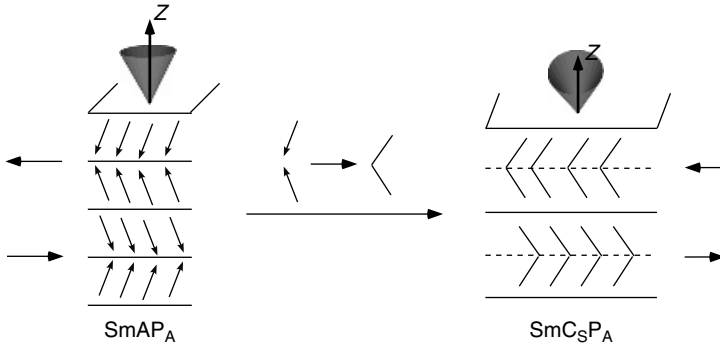


Figure 8.28 Illustration of similarity between achiral antiferroelectric bilayer smectic (SmAP_A) phase and chiral antiferroelectric SmC_SP_A phase is given. In this case, bent-core mesogens are considered kind of dimer, with two rod-shaped mesogenic units joined rigidly by meta-substituted phenyl ring “connecting group.” This connecting group enforces anticlinic configuration at phenyl-rich virtual layer interfaces, while methyl-terminated layer interfaces are free to take up more common synclinic configuration. Apparently, rigid joining of two mesogenic units in bent-core system causes equilibrium tilt of director of molecular bows, making system chiral.

projected on the bow plane, and synclinic tilt of the director of the “dimer mesogens” projected in the tilt plane.

From this discussion the clear similarity between the SmAP_A and SmC_SP_A structures is easily seen. In addition, the suggestion of Brand et al.²⁹ that a bilayer smectic with all anticlinic layer interfaces (the SmAP_F) would produce an achiral ferroelectric smectic follows directly. The unanticipated tilt of the director in the tilt plane, leading to a chiral layer structure, seems to be a general response of the bent-core mesogens to the spontaneous nonpolar symmetry breaking occurring in these rigid dimer structures.

Glaser et al.^{50a} have suggested that this preference is fundamental, involving the entropy of out-of-layer fluctuations in smectic LCs. The basic argument is that synclinic layer interfaces allow some kind of fluctuations of the system which raise its entropy. Anticlinic layer interfaces somehow “freeze out” much of this entropy, increasing the free energy of the anticlinic structure relative to that of the synclinic structure. Whatever the actual reason, the phenomenon in calamitic SmC materials is dramatic: In spite of a large synthesis effort aimed at obtaining chiral antiferroelectric SmC_A^* materials for display applications, such materials remain rare. A vast majority of calamitic tilted smectics display the synclinic SmC or SmC^* phase and do not show the SmC_A or SmC_A^* phase.

Interestingly, a large majority of materials showing the SmC_A or SmC_A^* structure possess a key structural feature of MHPOBC; the 1-methylheptyloxycarbonyl (MHOC) tail, or its close cousin the 1-(1,1,1-trifluoromethyl)heptyloxycarbonyl tail. This unit in calamitic LCs seems quite

unique. Specifically, for most smectic LCs, the tails are apparently less tilted than the cores in tilted smectic phases; a key feature of the Boulder model for the molecular origins of **P**, and a fact experimentally verified for prototypal SmC mesogens.⁵¹ The MHOC tail, however, is apparently more tilted than the core in mesogens such as MHPOBC, according to an analysis of infrared (IR) data by Fukuda and Takezoe et al.⁵²

This seems to be due to intrinsic (gas-phase) conformational properties of the structure, which cause a preference for conformers in which the tail prefers to orient on average at about 90° to the Ar–C=O bond. Whatever its actual origins, this bend in the tail, which might be expected to inhibit the formation of mesophases, instead seems to promote them! Glaser et al.^{50a} have suggested that the large angle between the core and tail favored by the MHOC tail inhibits out-of-layer fluctuations at the level of the molecular structure, thus lowering the entropic cost of anticlinic layer interfaces, and allowing them to become the free-energy minimum in some temperature ranges. This interpretation is consistent with the fact that the anticlinic structures always exist at lower temperatures than the synclinc structures in materials possessing both types (which includes most of the anticlinic LCs), proving that the anticlinic structures indeed have lower entropies than the synclinc structures. Apparently, by lowering the entropic cost of formation of anticlinic structures, the MHOC tail allows some other, more subtle factors favoring anticlinic structures to become dominant. For example, it has been suggested that dipolar interactions between molecules in adjacent layers of mesogens possessing the MHOC tail could favor the anticlinic structures.⁵²

Whatever the origins of the effect, empirically it is true that the MHOC tail is an extremely reliable supermolecular stereochemical control element favoring the formation of anticlinic layer interfaces in calamitic tilted smectics. Given the arguments presented above suggesting that the preference for antiferroelectric ordering in banana phases is simply due to a preference for synclinc methyl-terminated layer interfaces in the bow plane, a very straightforward approach for achieving a ferroelectric banana phase is apparent. As illustrated in Figure 8.29, a bilayer smectic with all anticlinic layer interfaces should be ferroelectric. While such a phase has yet to be described, covalent “dimerization” of the mesogens to create a rigidly enforced anticlinic “virtual” layer interface, in combination with the MHOC tail, known to prefer anticlinic methyl-terminated layer interface, might reasonably be expected to produce a chiral tilted SmC_SP_F as indicated in Figure 8.29.

In order to test this very simple idea, the MHOC tail was incorporated into the prototypical bent-core double-Schiff-base structure, providing as target the mesogen (**Rac**)-MHOBOW (**9**),⁵³ whose structure and phase sequence is shown in Figure 8.30. The racemate was prepared in order to avoid complications in the interpretation of the results caused by molecular enantiomeric

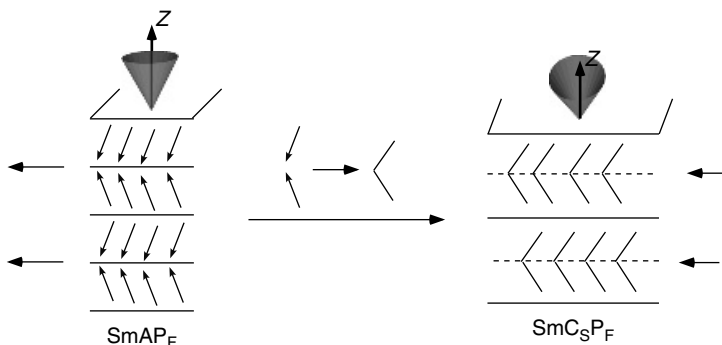


Figure 8.29 Illustration showing how all-anticlinic bilayer smectic should be ferroelectric is given. In case of covalent dimers (bent-core mesogens), equilibrium tilt of director combined with anticlinic layer interfaces in bow plane provides SmC_SP_F ferroelectric banana structure.

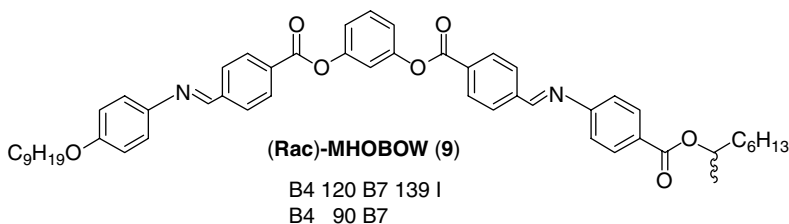


Figure 8.30 Structure and phase sequence of **MHOBOW** are given.

enrichment. This racemate will be referred to as **MHOBOW** in the following discussion.

As indicated in Figure 8.30, **MHOBOW** exhibits the unmistakable and unique B7 texture in the polarized light microscope. This amazing texture, key aspects of which were first reported by Pelzl et al.⁵⁴ has several unique features, as illustrated by the photomicrographs in Figures 8.31–8.33. As the sample cools from the isotropic phase, the LC phase often comes out of the isotropic phase as coiling tubes, as shown in Figure 8.31. These structures grow by a fascinating elongation mechanism, with the tubes growing in length while dynamically coiling, finally giving helical features as indicated in Figure 8.31. About half of the coils are right-handed and half are left-handed, as can easily be seen by direct observation. The helical pitch within a coil appears constant, but differs from coil to coil. Also, in general, it appears that domains with a tighter pitch grow faster.

Interestingly, **MHOBOW** and other B7 materials prefer to form freely suspended fibers instead of films.⁵³ Such fibers, occurring at the LC–air interface,

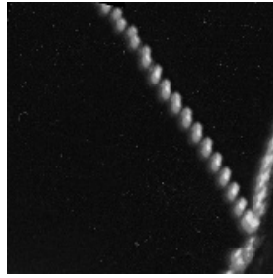


Figure 8.31 Photomicrograph illustrating chiral coiling tubes of smectic LC obtained as B7 phase of **MHOBOW** grows from isotropic melt.

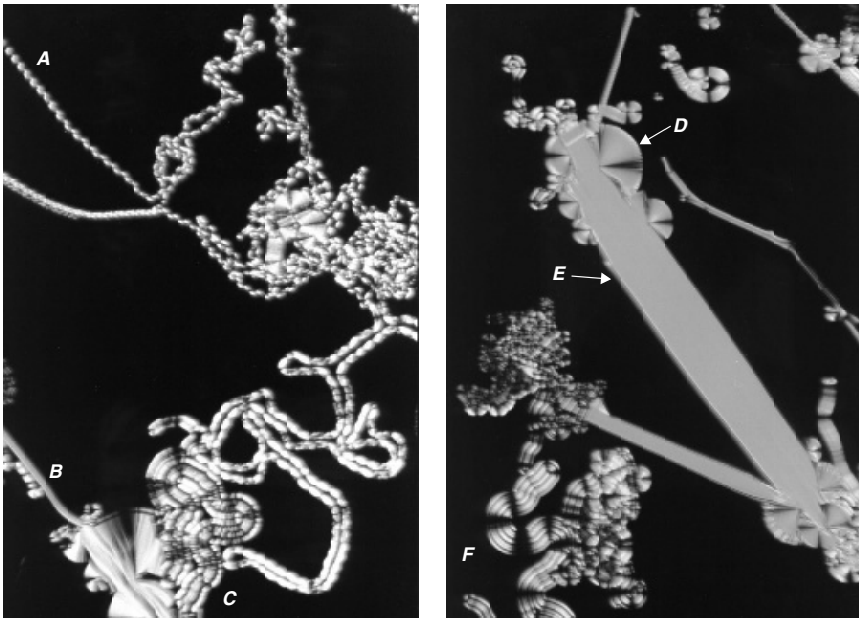


Figure 8.32 Left: Photomicrograph of sample of **MHOBOW** in 4- μm SSFLC cell, illustrating coalescence of coiled tube structures (A) to form gold focal conic domains (C). Small domain of banana leaf (B) can also be seen in this picture. Right: Photomicrograph of similar sample of **MHOBOW** showing large banana leaf domain (E) and several varieties of gold focal conic domains (D, F). Some of latter show a striking regular periodicity along layer normal (F).

are apparently similar to the coiling tubes formed at the isotropic–smectic transition; even showing a tendency to coil into chiral freely suspended structures. In the fibers the layers are parallel to the LC–air interface, forming nested cylinders; and this is the current model for the helical tubes formed from B7

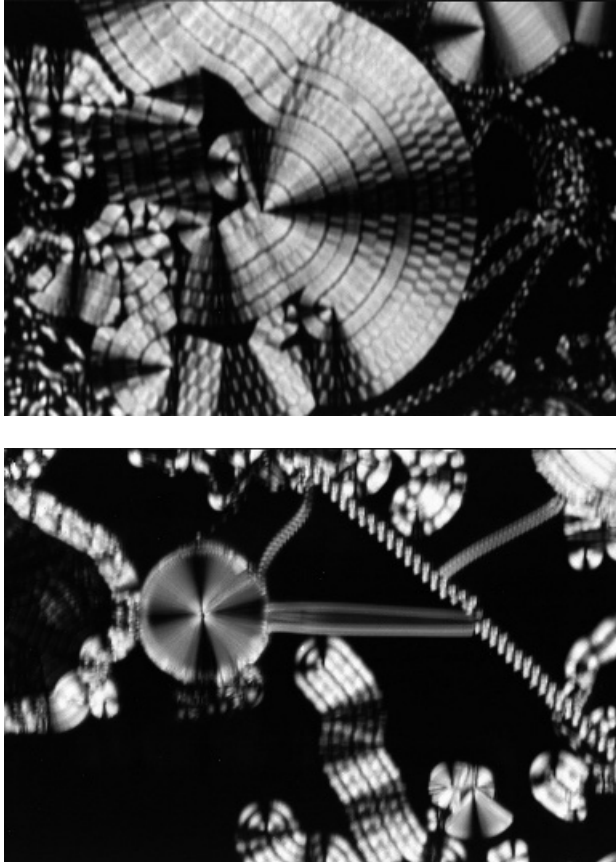


Figure 8.33 Two photomicrographs illustrating more of textures observed for **MHOBOW** and other B7 materials. B7 texture is arguably most complex (and beautiful) LC texture found to date.

materials upon cooling from the isotropic liquid into the B7 phase. It has been suggested in the literature that, in general, the formation of tubes or “filaments” at an isotropic–SmA transition occurs when the director prefers to orient perpendicular, or “homeotropic,” to the isotropic fluid “free surface.”⁵⁵ Such filaments spontaneously form “kinks” as they grow due the unusual physics of the system. This behavior is very rare; the isotropic–Sm transition usually produces focal conic textures, which result when the director prefers to orient parallel to the free surface, as apparently occurs for **NORABOW** and other B2 materials.

Interestingly, it has been suggested that this preference for the layers to form perpendicular to the free surface in smectics forming from the isotropic fluid

phase is caused by the entropy cost of disfavoring out-of-layer fluctuations when the layers form parallel to the free surface.⁵⁶ This is precisely the effect expected from incorporation of the MHOC tail. It must be stressed, however, that calamitic smectics possessing this tail and an SmC_A phase, have not been seen to produce filaments or tubes at the isotropic–Sm transition, but rather form the usual focal conic texture. It is also interesting to note that out-of-layer fluctuations are considered important at the nematic–smectic transition. The occurrence of a nematic phase in LCs possessing the MHOC tail and an SmC_A phase, is extremely rare.

Recently, it has been reported that certain rare B2 materials, showing a mainly conventional focal conic texture and the simple B2 X-ray diffraction behavior, also may exhibit coiled tubes at the isotropic-to-smectic transition.⁵⁷ Given the above discussion, this perhaps suggests that the balance between the free-energy cost of suppression of out-of-layer fluctuations, and other factors, such as an enthalpy gain from smectic order within layers, favoring the layers parallel to the free surface, is very close in B2 and B7 materials. Also, it is reasonable to suggest that the virtual anticlinic layer interfaces in the bow plane themselves might suppress out-of-layer fluctuations by a steric mechanism.

Whatever the physical origins of the effect, the formation of helical tubes in the B7 texture is certainly fascinating. Cases where two such tubes wind around each other in a double helix have been reported.⁵⁸ This novel behavior, however, is just the beginning of the B7 texture story. As the texture continues to grow, the coils, which are often more irregular than the example shown in Figure 8.31, begin to coalesce to form more complex structures which eventually anneal into focal conic domains, as shown in Figure 8.32. In the photomicrograph on the left, twisting tubes or ribbons (Figure 8.32*a*) can be seen to coalesce into complex focal conic domains (Figure 8.32*c*). These domains are SmA -like (the extinction brushes are parallel and perpendicular to the polarizer) and possess much more “fine structure” than would be typical for smectic focal conics. Often, periodic features with the periodicity normal to the layers are seen, as shown in Figure 8.32*c*; more well-defined examples can be seen in Figure 8.32*f*. Often, the focal conics appear relatively smooth, as can be seen in Figure 8.32*d*. At higher magnification, fine structure can be seen in these focal conics, however.

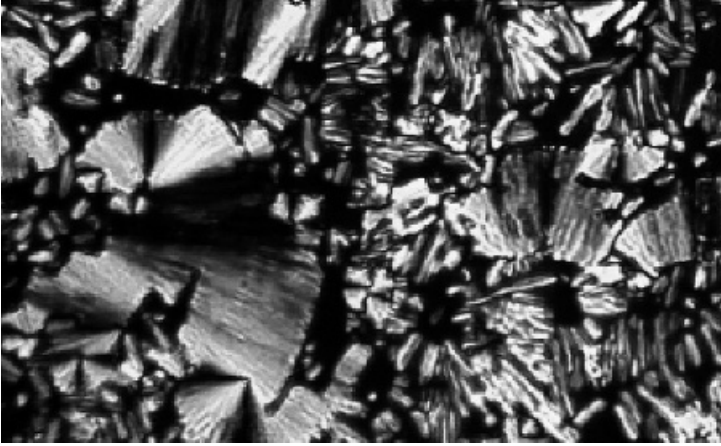
In addition, another distinct texture, which does not form from the tubes, is often seen. A small domain of this texture, termed “banana leaf” by some in the field, can be seen in Figure 8.32*b*. The banana leaf texture appears very smooth in the polarized light microscope, with none of the fine structure apparent in the domains formed by annealing from the twisting tubes. A large banana leaf domain can be seen in Figure 8.32*e*. As can be seen in Figure 8.32, the coils, focal conic domains, and banana leaf domains show gold or yellow birefringence colors in 4- μm cells.

Other textures are also seen at the isotropic–B7 transition, as indicated in Figure 8.33. As shown in the photomicrograph on the left in Figure 8.33, cylindrical focal conic domains with different birefringence colors are sometimes seen. All such focal conics, however, are SmA-like. The photomicrograph on the right in Figure 8.33 shows a beautiful example of a focal conic domain, which formed by annealing of the tubes. Very well defined periodic structures can be seen, with periodicity on a relatively large length scale both parallel and perpendicular to the layers. Very similar B7 textures are shown in the review of Pelzl et al.⁴³

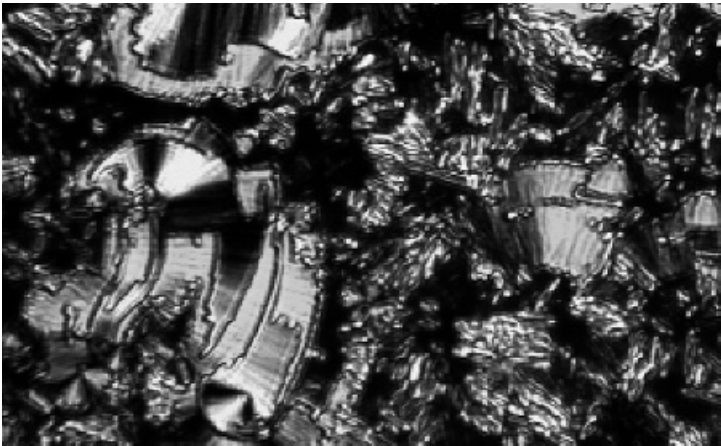
The highly complex and unusual textures observed for B7 materials is complemented by unusual X-ray diffraction behavior. While the beautiful mystery of the B7 texture is not understood in detail, **MHOBOW** shows EO behavior, which allows some definitive statements regarding its nature. Thus, while some B7 materials are reported to be EO-inactive (no EO switching),⁵⁴ and some are reported to exhibit antiferroelectric EO behavior,⁵⁹ **MHOBOW** exhibits a unique texture change upon application of electric fields.

Indicated on the left in Figure 8.34 is a fresh preparation, before application of an electric field. This area of the cell has gold focal conics, which formed by annealing of coiled tubes, in addition to another type of B7 texture termed *accordion*. The birefringence of the gold domains is low ($\Delta n \sim 0.07$), giving a first-order yellow color. The average birefringence of the accordion texture is even lower. The accordion texture is thought to be due to some unusual kind of homeotropic structure.⁶⁰ Application of a 1-Hz triangular driving field peaking at just above a threshold of about 12 V/ μm causes the gold focal conic domains to convert irreversibly, by a well-defined domain-wall-mediated process, to a new texture, termed *bistable blue*. In the photomicrograph on the right in Figure 8.34 bistable blue domains can be easily seen growing in from the gold focal conics. The bistable blue domains show a higher birefringence ($\Delta n \sim 0.14$), leading to a first-order blue birefringence color.

Also, as suggested by their name, the blue domains exhibit bistable EO similar to that observed for a chiral SmC* FLC in the bookshelf alignment. This behavior is illustrated in Figure 8.35 for a nice cylindrical focal conic domain. Application of an electric field “down” causes the sample to switch into the configuration shown on the right in Figure 8.35 (this illustration shows the domain to have positive chirality; negative polarization). The proposed director structure for this brush orientation is illustrated below the photomicrograph of the domain in Figure 8.35. Removal of the applied field causes absolutely no change in the brush orientation, though there is a small, continuous change in Δn as the field is lowered to zero (the birefringence color changes continuously from first-order green to first-order blue).⁵³ Domains of this type are stable for at least several days in the absence of applied fields.



Fresh cell



Cell after application of a field

Figure 8.34 Left: Gold focal conics of **MHOBOW** coexisting with accordion domains in 4- μm SSFLC cell. Cell has not seen electric field. Right: Same area after brief application of field above threshold for causing textural change of focal conics from gold SmA-like to bistable blue SmC*-like. Transition from gold to bistable blue is still incomplete in this photomicrograph; clear domain walls between two textures are easily seen.

Application of a field “up,” however, leads to a dramatic switching of the extinction brushes counterclockwise, to give the configuration shown on the left in Figure 8.35. This dramatic, chiral EO response is mirrored by other domains in the sample of opposite handedness but similar metrics. If the field is then removed, domains of the type shown on the left in Figure 8.35 are

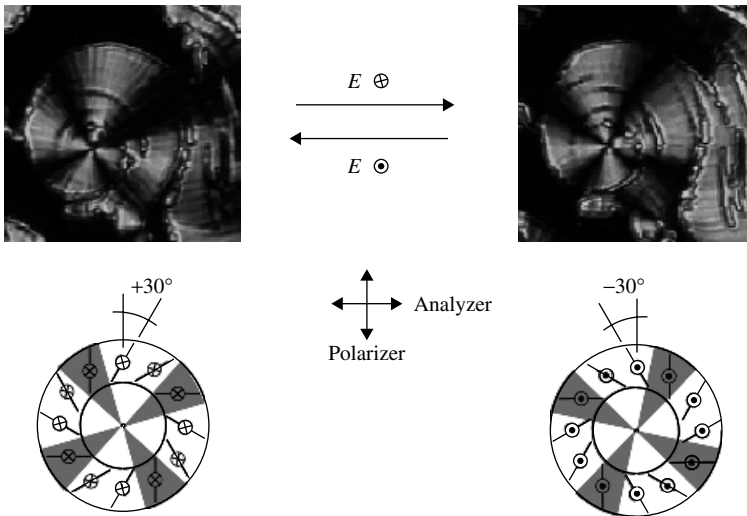


Figure 8.35 Illustration of bistable ferroelectric EO switching observed for blue focal conic domains of **MHOBOW**. SmC_5P_F structure can be assigned for these domains. In this phase director structure in all layers is oriented identically. This structure and corresponding extinction brush orientation for cylindrical focal conic are illustrated at bottom of figure for two bistable ferroelectric states. Note that for material with 30° tilt angle, such as **MHOBOW**, two ferroelectric states look very similar in still photos. In fact, two states result from large rotation of extinction brushes through 60° , as can be easily seen when observing switching in motion.

also stable for long periods of time, leading to their name: bistable blue. As mentioned above, this behavior is strikingly similar to that of a chiral SmC^* material **DOBAMBC** in cylindrical focal conic domains, as reported in the very first study describing SSFLC switching,³ with the exception that in the case of the SmC^* , domains of only one handedness are seen.

At higher threshold fields, the banana leaf and most other B7 textures observed for **MHOBOW** also convert irreversibly to bistable blue, though the picture is still complex, with unusual textures still seen in the cell. Our interpretation of this behavior, however, is simple. The bistable blue texture observed for **MHOBOW** is obtained from an SmC_5P_F conglomerate: the target of the molecular design and synthesis effort.

6.11 Ferroelectric “Macroscopic Racemate” from Unichiral Mesogen

The discussion so far has described the observation of three of the four banana-phase diastereomers shown in Figure 8.26; two antiferroelectric isomers from **NOBOW**, and the ferroelectric banana phase of **MHOBOW**. Interestingly, discovery of the fourth isomer, the ferroelectric macroscopic

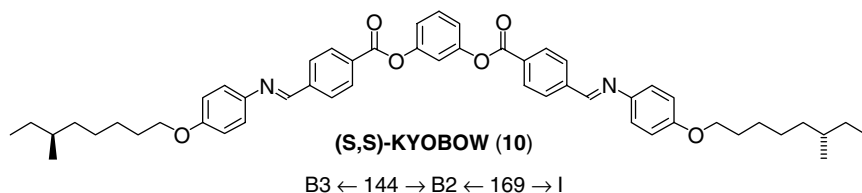


Figure 8.36 Structure and phase sequence of unichiral bent-core mesogen (S,S)-KYOBOW is given.

racemate SmC_AP_F , came from an unexpected place: a unichiral mesogen! As reported by the Tokyo Tech group,⁶¹ the **NOBOW** molecular constitutional isomer **10** (Figure 8.36), which we have dubbed **KYOBOW**, exhibits enantiotropic B3 and “B2” phases. Note that this material was synthesized in unichiral form; the molecules have C_2 symmetry, with both chiral tails possessing the (S) absolute configuration.

KYOBOW exhibited a B2-like focal conic texture, with the majority domains showing SmA -like focal conics. Driving the system with an electric field of alternating sign showed a transient change in birefringence during switching, but no rotation of the optic axis. The polarization vs. applied field curves, however, were indicative of a ferroelectric. In a technical tour de force, the Tokyo Tech workers proved that the SmCP phase of **KYOBOW** is in fact the ferroelectric “racemate”: SmC_AP_F ! The structure of the two ferroelectric states accessed in the switching of **KYOBOW**, and a graphic illustrating the lack of an EO effect in this switching, are shown in Figure 8.37. (While the term *racemate* seems improper when referring to

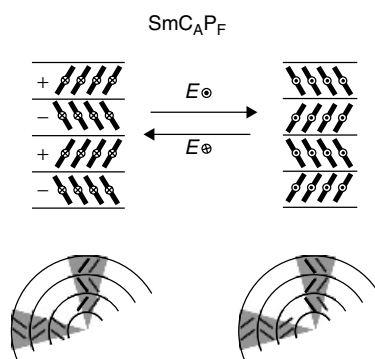


Figure 8.37 Ferroelectric switching and lack of brush rotation illustrated for SmC_AP_F phase exhibited by **KYOBOW** in SSFLC cell.

a phase composed of unichiral molecules, this nomenclature problem has not yet been satisfactorily addressed.)

This rather amazing result at first seems impossible. As indicated in Figure 8.37, the SmC_AP_F structure is composed of heterochiral adjacent layer pairs. By pure symmetry it must be the case that the unichiral molecules have a lower free energy in either the (+) or the (−) layers. The free-energy difference between these diastereomeric layer structures could be small. But, the layers possess a collective free energy. A priori it is expected that the thermodynamic phase would possess only layers of the lower free-energy chirality.

The fact that the thermodynamic global minimum in an SmCP phase of unichiral molecules could be the macroscopic racemate, however, is consistent with the model that *layer interfaces* are critical contributors to the overall free energy of the system. The layer interfaces for the four diastereomeric SmCP isomers are obviously diastereomeric. The layers in an SmCP phase composed of achiral or racemic mesogens are identical, differing only in the structure of their layer interfaces. Indeed, our rationale for design of the SmC_SP_F banana-phase mesogen **MHOBOW** hinged upon control of the layer interface clinicity. While the parsing of free-energy contributions in this way is, of course, arbitrary, we find it useful to consider the **KYOBOW** result as confirming that the free energy of the layer interfaces dominates the thermodynamics of the system in the unichiral mesogen, leading to layer interfaces which are anticlinic in both the tilt plane and the polar plane (SmC_AP_F). In this case, the thermodynamic phase actually possesses diastereomeric layers of differing free energy. A similar phenomenon is known in polymers, as described in Chapter 2 in this volume.

7 CONCLUSION

The first example of spontaneous reflection symmetry breaking in smectic LCs results from a combination of spontaneous nonpolar symmetry breaking and spontaneous tilt in banana phases composed of bent-core mesogens. These symmetry breakings occur in smectic layers which are then seen to stack in such a way that four diastereomeric phases—two conglomerates and two macroscopic racemates—are possible if only synclinic or anticlinic layer interfaces occur. The four diastereomers, comprised of two ferroelectric and two antiferroelectric isomers, were first proposed to explain the electro-optics of a prototypical mesogen in the class: **NOBOW**. This material exhibits the two antiferroelectric phases, with the ferroelectric structures observed only as states in the presence of an applied electric field. Since the initial proposal, however, actual mesogens possessing each of the two possible ferroelectric diastereomers as the ground state have been found; one obtained by design, using layer interface clinicity as the supermolecular stereochemical control element.

ACKNOWLEDGMENTS

The author was supported by the Ferroelectric Liquid Crystal Materials Research Center (National Science Foundation MRSEC award No. DMR-9809555) during the writing of this chapter. The author thanks Professors Tom Lubensky, Leo Radzihovsky, and Joseph Gal for helpful discussions around the issue of terminology for reflection symmetry breaking, and especially Professor Noel Clark for his help on this and many other banana-phase issues. The author also thanks Dr. Renfan Shao for the photomicrographs shown in Figures 8.32 and 8.33.

REFERENCES

1. Meyer, R. B. In abstracts of the *5th International Liquid Crystal Conference*: Stockholm, Sweden, 1974, p. 115.
2. Meyer, R. B.; Liebert, L.; Strzelecki, L.; Keller, P. *J. Phys., Lett. (Orsay, Fr.)* **1975**, *36*, L69–L71.
3. Clark, N. A.; Lagerwall, S. T. *Appl. Phys. Lett.* **1980**, *36*, 899–901.
4. (a) Niori, T.; Sekine, T.; Watanabe, J.; Furukawa, T.; Takezoe, H. *J. Mater. Chem.* **1996**, *6*, 1231–1233. (b) Sekine, T.; Takanishi, Y.; Niori, T.; Watanabe, J.; Takezoe, H. *Jpn. J. Appl. Phys.* **1997**, *36*, L1201–L1203.
5. Walba, D. M. *Tetrahedron* **1985**, *41*, 3161–3212.
6. (a) Cram, D. J. *Science* **1988**, *240*, 760–767. (b) Lehn, J. M. *Angew. Chem., Int. Ed. Engl.* **1990**, *29*, 1304–1319.
7. (a) Wasserman, E. *J. Am. Chem. Soc.* **1960**, *82*, 4433–4434. (b) Wasserman, E. *Sci. Am.* **1962**, *207*, 94–100.
8. Please note this is a simplified discussion of a complex system, and in particular ignores explicit consideration of the contribution of the entropy of mixing to the problem.
9. Bartolino, R.; Doucet, J.; Durand, G. *Ann. Phys. (Paris)* **1978**, *3*, 389–396.
10. (a) Walba, D. M.; Slater, S. C.; Thurmes, W. N.; Clark, N. A.; Handschy, M. A.; Supon, F. *J. Am. Chem. Soc.* **1986**, *108*, 5210–5221. (b) Walba, D. M. In *Advances in the Synthesis and Reactivity of Solids*, Vol. 1. Mallouk, T. E. (Ed.). JAI, Greenwich, CT, **1991**, pp. 173–235.
11. Glaser, M. A.; Ginzburg, V. V.; Clark, N. A.; Garcia, E.; Walba, D. M.; Malzbender, R. *Molec. Phys. Rep.* **1995**, *10*, 26–47.
12. (a) Vizitiu, D.; Lazar, C.; Radke, J. P.; Hartley, C. S.; Glaser, M. A.; Lemieux, R. P. *Chem. Mater.* **2001**, *13*, 1692–1699. (b) Lemieux, R. P. *Acc. Chem. Res.* **2001**, *34*, 845–853.
13. This description of FLC switching behavior is simplified for the sake of clarity. A small minority of FLC materials behave as described; these are termed “bookshelf” materials in the field. For most FLCs, the formation of a chevron layer structure driven by layer shrinkage at the SmA-SmC* transition changes the picture in complex ways. A discussion of this issue, which is not a chirality phenomenon, is outside the scope of this chapter.
14. (a) Drabik, T. J. In *Thin Films for Integrated Optics Applications*, Vol. 392. Wessels, B. W., Marder, S. R., Walba, D. M. (Eds.). Materials Research Society, San Francisco, 1995, pp. 111–122. (b) Cotter, L. K.; Drabik, T. J.; Dillon, R. J.; Handschy, M. A. *Opt. Lett.* **1990**, *15*, 291–293.

15. O'Donnell, P.; Doi, A. *Information Display* **2001**, *17*, 16–19.
16. Chandani, A. D. L.; Gorecka, E.; Ouchi, Y.; Takezoe, H.; Fukuda, A. *Jpn. J. Appl. Phys.* **1989**, *28*, L1265–L1268.
17. Link, D. R.; Natale, G.; MacLennan, J. E.; Clark, N. A.; Walsh, M.; Keast, S. S.; Neubert, M. E. *Phys. Rev. Lett.* **1999**, *83*, 3665–3668.
18. A great account of this story can be found in the citation by the Royal Society of London on the occasion of the awarding of the Rumford Medal to Louis Pasteur by the President, Lord Wrottesley, on December 1, 1856: *Proc. Roy. Soc. London* **1857**, *VII*, 254–257. The text of the citation and more about Pasteur can be found at: <http://www.foundersofscience.net/>, a website created and hosted by Dr. David V. Cohn, Professor of Biochemistry, University of Louisville.
19. (a) Weis, R. M.; McConnell, H. M. *Nature* **1984**, *310*, 47–49. (b) Viswanathan, R.; Zasadzinski, J. A.; Schwartz, D. K. *Nature* **1994**, *368*, 440–443. (c) Eckhardt, C. J.; Peachey, N. M.; Swanson, D. R.; Takacs, J. M.; Khan, M. A.; Gong, X.; Kim, J. -H.; Wang, J.; Uphaus, R. A. *Nature* **1993**, *362*, 614–616. (d) Nassoy, P.; Goldmann, M.; Bouloussa, O.; Rondelez, F. *Phys. Rev. Lett.* **1995**, *75*, 457–460. (e) Weissbuch, I.; Berfeld, M.; Bouwman, W.; Kjar, K.; Als-Nielsen, J.; Lahav, M.; Leiserowitz, L. *J. Am. Chem. Soc.* **1997**, *119*, 933–942.
20. (a) Stevens, F.; Dyer, D. J.; Walba, D. M. *Angew. Chem., Int. Ed. Engl.* **1996**, *35*, 900–901. (b) Walba, D. M.; Stevens, F.; Clark, N. A.; Parks, D. C. *Acc. Chem. Res.* **1996**, *29*, 591–597.
21. The confusion stems from the fact that in the physics community, an object or system with “chiral symmetry” is achiral (i.e., congruent with its mirror image). Chemists using point groups to describe symmetries of objects, however, use the phrase “reflection symmetry” to describe an achiral object. Quoting Mislow’s monograph from the section entitled “Reflection Symmetry—Point Groups” (Mislow, K. *Introduction to Stereochemistry*. R. Breslow (Ed.). Benjamin/Cummings, Reading, MA, 1965, p. 24): “An object is said to have reflection symmetry if it is superimposable on its reflection or mirror image. Reflection symmetry is revealed by the presence of a *rotation–reflection axis* (also called *mirror axis*, *improper axis* or *alternating axis*) S_n : in a molecule having such an axis, reflection in a plane perpendicular to that axis followed by rotation by $360^\circ/n$ will convert the object into itself.” Of course, for the case where $n = 1$ the rotation–reflection axis is a simply a mirror plane.

An object with reflection symmetry has a rotation–reflection axis as at least one of the symmetry elements in its point group. An object lacking reflection symmetry in its point group is chiral. In this context, the phrase *chiral symmetry* most naturally suggests the antonym of *reflection symmetry*, i.e., a chiral object—precisely the opposite of what is meant by chiral symmetry in the phrase *chiral symmetry breaking* as used in physics. While from a chemists point of view it is reasonable to use the term *achiral symmetry breaking* to describe breaking of reflection symmetry, this term is also confusing to a substantial part of the target audience. We feel on balance *reflection symmetry breaking* is the least confusing terminology describing the phenomenon formerly known as *chiral symmetry breaking*.
22. Bergersen, B.; Boal, D.; Palfy-Muhoray, P. *J. Phys. A: Math. Gen.* **1994**, *27*, 2579–2586.
23. Mauguin, C. B. *Soc. Franc. Miner.* **1911**, *34*, 71.
24. Drzaic, P. S. *Liquid Crystal Dispersions*. World Scientific, River Edge, NJ, 1995.
25. Rudquist, P.; Körblova, E.; Walba, D. M.; Shao, R.-F.; Clark, N. A.; MacLennan, J. E. *Liq. Cryst.* **1999**, *26*, 1555–1561.
26. The “necessarily” achiral nature of nematic phases doped with racemic compounds, capable of “de-racemization” by irradiation with circularly polarized light, forms the basis of an

- interesting approach to chiroptical photonic devices: (a) Zhang, Y.; Schuster, G. B. *J. Org. Chem.* **1994**, *59*, 1855–1862. (b) Feringa, B. L.; Huck, N. P. M.; van Doren, H. A. *J. Am. Chem. Soc.* **1995**, *117*, 9929–9930.
27. Cladis, P. E.; Brand, H. R. *Liq. Cryst.* **1993**, *14*, 1327–1349.
28. Photinos, D. J.; Samulski, E. T. *Science* **1995**, *270*, 783–786.
29. Brand, H. R.; Cladis, P. E.; Pleiner, H. *Macromolecules* **1992**, *25*, 7223–7226.
30. (a) Soto Bustamante, E. A.; Yablonskii, S. V.; Ostrovskii, B. I.; Beresnev, L. A.; Blinov, L. M.; Haase, W. *Chem. Phys. Lett.* **1996**, *260*, 447–452. (b) Soto Bustamante, E. A.; Yablonskii, S. V.; Ostrovskii, B. I.; Beresnev, L. A.; Blinov, L. M.; Haase, W. *Liq. Cryst.* **1996**, *21*, 829–839.
31. Ostrovskii, B. I.; Soto Bustamante, E. A.; Sulianov, S. N.; Galyametdinov, Y. G.; Haase, W. H. *Mol. Cryst. Liq. Cryst. Sci. Technol., Sect. C* **1996**, *6*, 171–188.
32. Link, D. R.; Clark, N. A.; Ostrovskii, B. I.; Soto Bustamante, E. A. *Phys. Rev. E* **2000**, *61*, R37–R40.
33. Young, C. Y.; Pindak, R.; Clark, N. A.; Meyer, R. B. *Phys. Rev. Lett.* **1978**, *40*, 773–776.
34. Pindak, R.; Young, C. Y.; Meyer, R. B.; Clark, N. A. *Phys. Rev. Lett.* **1980**, *45*, 1193–1196.
35. Link, D. R.; MacLennan, J. E.; Clark, N. A. *Phys. Rev. Lett.* **1996**, *77*, 2237–2240.
- 36a. Pelzl, G.; Wirth, I.; Weissflog, W. *Liq. Cryst.* **2001**, *28*, 969–972.
- 36b. Vorländer, D.; Apel, A.; Galka, W. *Ber.* **1932**, 1101–1109.
37. Watanabe, J.; Hayashi, M. *Macromolecules* **1989**, *22*, 4083–4088.
38. Watanabe, J.; Komura, H.; Niori, T. *Liq. Cryst.* **1993**, *13*, 455–465.
39. Attard, G. S.; Date, R. W.; Imrie, C. T.; Luckhurst, G. R.; Roskilly, S. J.; Seddon, J. M.; Taylor, L. *Liq. Cryst.* **1994**, *16*, 529–581.
40. Akutagawa, T.; Matsunaga, Y.; Yashuhara, K. *Liq. Cryst.* **1994**, *17*, 659–666.
41. Niori, T.; Sekine, T.; Watanabe, J.; Furukawa, T.; Takezoe, H. *Distinct Ferroelectric Smectic Liquid Crystals Consisting of Achiral Molecules with Banana Shape*; Abstracts of the 16th International Liquid Crystal Conference, Kent State University, Kent, OH, 1996, p. 126.
42. This banana phase nomenclature was established at the first international conference specifically focused on banana phases: Chirality by Achiral Molecules, held in Berlin, Germany, in December, 1997.
43. Pelzl, G.; Diele, S.; Weissflog, W. *Adv. Mater.* **1999**, *11*, 707–724.
44. (a) Sekine, T.; Niori, T.; Sone, M.; Watanabe, J.; Choi, S. -W.; Takanishi, Y.; Takezoe, H. *Jpn. J. Appl. Phys.* **1997**, *36*, 6455–6463. (b) Thisayukta, J.; Takezoe, H.; Watanabe, J. *Jpn. J. Appl. Phys.* **2001**, *40*, 3277–3287.
45. Renn, S. R.; Lubensky, T. C. *Phys. Rev. A* **1988**, *38*, 2132–2147.
46. Heppke, G.; Jákli, A.; Krüerke, D.; Löhning, C.; Löttsch, D.; Paus, S.; Rauch, S.; Sharma, N. K. In *ECLC '97*, Zakopane, Poland, 1997, p. 34.
47. Lischka, C.; Weissflog, W. In *ECLC '97*, Zakopane, Poland, 1997, p. 201.
48. Link, D. R.; Natale, G.; Shao, R.-F.; MacLennan, J. E.; Clark, N. A.; Körblova, E.; Walba, D. M. *Science* **1997**, *278*, 1924–1927.
49. (a) Walba, D. M.; Körblova, E.; Shao, R.-F.; MacLennan, J. E.; Link, D. R.; Glaser, M. A.; Clark, N. A. *J. Phys. Org. Chem.* **2000**, *12*, 830–836. (b) Walba, D. M.; Körblova, E.; Shao, R.-F.; MacLennan, J. E.; Link, D. R.; Clark, N. A. In *Liquid Crystal Materials and Devices*, Vol. 559. Bunning, T., Chen, S., Chien, L.-C., Kajiyama, T., Koide, N., Lien, S.-C. (Eds.). Materials Research Society, San Francisco, **1999**, pp. 3–14. (c) Walba, D. M.; Körblova, E.; Shao, R.-F.; MacLennan, J. E.; Link, D. R.; Clark, N. A.

- In *IDW '98: Fifth International Display Workshops*, SID Japan Chapter, Kobe, Japan, **1998**, pp. 97–100.
50. This idea has not yet been published but has been discussed in the presentations represented by the following abstracts: (a) Maiti, P. K.; Lansac, Y.; Glaser, M. A.; Clark, N. A. *Ordering of Bent-Core Molecules in a Smectic Solvent*; Abstracts of the 8th International Conference on Ferroelectric Liquid Crystals, Washington, D.C., 2001, p. 48. (b) Walba, D. M.; Körblová, E.; Shao, R.-F.; Coleman, D. N.; Chattham, N.; Clark, N. A. *A Bow-Phase Liquid Crystal Exhibiting a General Smectic C Phase*; Abstracts of the 8th International Conference on Ferroelectric Liquid Crystals, Washington, D.C., 2001, p. 29.
 51. Keller, E. N.; Nachaliel, E.; Davidov, D.; Buffel, C. *Phys. Rev. A* **1986**, *34*, 4363–4369.
 52. Miyachi, K.; Matsushima, J.; Takanishi, Y.; Ishikawa, K.; Takezoe, H.; Fukuda, A. *Phys. Rev. E: Stat. Phys., Plasmas, Fluids, Relat. Interdiscip. Top.* **1995**, *52*, R2153–R2156.
 53. Walba, D. M.; Körblová, E.; Shao, R.-F.; MacLennan, J. E.; Link, D. R.; Glaser, M. A.; Clark, N. A. *Science* **2000**, *288*, 2181–2184.
 54. Pelzl, G.; Diele, S.; Jákli, A.; Lischka, C.; Wirth, I.; Weissflog, W. *Liq. Cryst.* **1999**, *26*, 135–139.
 55. Weinan, E.; Palfy-Muhoray, P. *J. Nonlinear Sci.* **1999**, *9*, 417–437.
 56. The author thanks Professor Slobodan Zumer, Department of Physics, University of Ljubljana, for pointing out the effect of the entropy of out-of-layer fluctuations on the I–Sm transition.
 57. Weissflog, W.; Nádasi, H.; Dunemann, U.; Pelzl, G.; Diele, S.; Eremin, A.; Kresse, H. *J. Mater. Chem.* **2001**, *11*, 2748–2758.
 58. Lee, C. K.; Chien, L. C. *Liq. Cryst.* **1999**, *26*, 609–612.
 59. Heppke, G.; Parghi, D. D.; Sawade, H. In *7th International Conference on Ferroelectric Liquid Crystals*; Darmstadt University of Technology, Germany, Darmstadt University of Technology, Germany, 1999; pp. 202–203 (Poster PC205).
 60. Jákli, A.; Krüerke, D.; Sawade, H.; Heppke, G. *Phys. Rev. Lett.* **2001**, *86*, 5715–5718.
 61. Nakata, M.; Link, D. R.; Araoka, F.; Thisayukta, J.; Takanishi, Y.; Ishikawa, K.; Watanabe, J.; Takezoe, H. *Liq. Cryst.* **2001**, *28*, 1301–1308.

Chapter 9

Nonlinear Optics and Chirality

THIERRY VERBIEST AND ANDRÉ PERSOONS

KU Leuven, Celestijnenlaan 200 D, B-3001 Leuven, Belgium

- 1 Introduction
- 2 General background
 - 2.1 Linear Optics
 - 2.2 Optical Activity
 - 2.3 Nonlinear Optics
 - 2.4 Nonlinear Optical Activity in Second-Harmonic Generation
 - 2.5 Nonlinear Optical Activity and Magnetic Dipole Contributions
 - 2.6 Molecular Origin of Nonlinear Optical Activity
- 3 Analysis of nonlinear optical activity
 - 3.1 Theoretical Formalism
 - 3.2 Second-Order Nonlinear Optical Signatures of Chirality
 - 3.2.1 Circular-Difference Effects
 - 3.2.2 Linear-Difference Effects in SHG
 - 3.2.3 Optical Rotation Effects in SHG
 - 3.2.4 Continuous Polarization Measurements
 - 3.3 Experimental Determination of f , g , and h
- 4 Experimental Studies of Nonlinear Optical Activity in SHG
 - 4.1 Comparison of Linearly and Circularly Polarized Probes of Nonlinear Optical Activity of Chiral Surfaces
 - 4.2 Quantitative Determination of Electric and Magnetic Second-Order Susceptibility Tensors of Chiral Surfaces
 - 4.3 Direct Evidence of Failure of Electric Dipole Approximation in Second-Harmonic Generation from Chiral Polymer Film
 - 4.4 Chiral 1,1'-Binaphthyl-Based Helical Polymers as Nonlinear Optical Materials
 - 4.5 Study of Chiral Helicenebisquinone Derivative
 - 4.6 Study of Biological Sample with Nonlinear Optical Activity
- 5 Chiral Materials for Second-Order Nonlinear Optical Applications
 - 5.1 Second-Order Nonlinear Optics in Chiral Isotropic Bulk Media
 - 5.2 Second-Order Nonlinear Optics in Chiral Thin Films
- 6 Conclusions
- References

Materials-Chirality: Volume 24 of Topics in Stereochemistry,
Edited by Mark M. Green, R.J.M. Nolte, and E.W. Meijer
ISBN 0-471-05497-6 Copyright © 2003 John Wiley & Sons, Inc.

1 INTRODUCTION

In linear optics, chiral molecules are known for their different interaction with left- and right-hand circularly polarized light. Furthermore, the circular-difference response changes sign between the two enantiomers of the chiral molecule. These effects give rise to optical activity such as circular dichroism, optical rotation, and optical rotatory dispersion.¹ All these phenomena originate from the interference between electric dipole and weak magnetic dipole transition moments within a molecule. Nevertheless, optical activity effects are routinely used to determine the absolute configuration of chiral molecules, their enantiomeric purity, as well as the secondary structure of proteins and deoxyribonucleic acid (DNA).

Circular-difference effects also occur in nonlinear optics, that is, chiral molecules have a different interaction with left- and right-handed circularly polarized light in a nonlinear optical process. However, the origin of this form of nonlinear optical activity is more complicated than in the linear case: They can both arise from interference between electric dipole transition moments in the molecule and from interference between electric dipole and magnetic dipole transition moments. Nonlinear optical activity effects have been theoretically predicted to occur in sum-and-difference frequency generation and optical-phase conjugation from chiral fluid media.² However, the predicted nonlinear optical activity effects are small and were never experimentally observed, until Meijer et al. demonstrated second-harmonic generation from a centrosymmetric crystal of *R,S-N*-acetyl valine.³ Following these experiments, nonlinear optical activity was demonstrated in second-harmonic generation from chiral surfaces, first from chiral molecules (binaphthol) adsorbed at an air/water interface, and subsequently from Langmuir–Blodgett films of chiral polymers.^{4,5} In this case, the observed circular-difference (CD) effects were large (much larger than in the linear case), and therefore this new experimental technique was put forth as a sensitive tool to study surface chirality. Owing to the similarity with traditional circular dichroism, it is often referred to as second-harmonic generation CD (SHG-CD). The usefulness of SHG-CD is based on the combination of second-harmonic generation and circular dichroism. SHG is inherently surface specific, and therefore SHG-CD is extremely sensitive to surface chirality. The use of $+45^\circ$ and -45° linearly polarized light (with respect to the *p*-polarized direction) can also lead to a difference in second-harmonic intensity and is called second-harmonic generation linear dichroism (SHG-LD). This effect has no analog in linear optics.⁶ Furthermore, a nonlinear analog of optical rotation has also been demonstrated.⁷

The requirements for even-order nonlinear phenomena are particularly stringent because such processes are forbidden in centrosymmetric materials in the electric dipole approximation of the field–matter interaction. For this reason,

materials development in organic nonlinear optics has traditionally focused on the design of conjugated molecules that are substituted with electron donor and acceptor groups to make them noncentrosymmetric.⁸ Furthermore, in order for the noncentrosymmetry to persist at a macroscopic level, the materials have to be oriented by methods such as electric-field poling, crystallization, and the like. However, chiral molecules are inherently noncentrosymmetric, and the noncentrosymmetry persists in the macroscopic state without the requirement of alignment. Hence, chiral materials can be extremely useful in the field of second-order nonlinear optics. Therefore, second-order nonlinear optical processes can be observed in highly symmetric media such as chiral crystals, isotropic liquids, or solutions.⁹

In the following sections we will first in Section 2 briefly discuss the necessary background to understand optical activity effects in linear and nonlinear optics and to illustrate the similarities and differences between both types. In Section 3 we present a more thorough analysis of nonlinear optical effects in second-harmonic generation, both from a theoretical and an experimental point of view. Section 4 deals with experimental examples that illustrate the usefulness of nonlinear optical activity in the study of chiral thin films and surfaces. Finally, in Section 5 we give an overview of the role of chirality in the field of second-order nonlinear optics and show that chiral molecules can be useful for applications in this field.

2 GENERAL BACKGROUND

2.1 Linear Optics

The interaction of light with matter can be described by the influence of its electromagnetic (or electric) field on the electron density. For example, an electric field $E(\omega) = E_0 e^{i(\omega t - k \cdot r)}$ with amplitude E_0 and phase $(\omega t - k \cdot r)$ acting on a molecule (or a material) induces a distortion of the electron density, resulting in an induced dipole moment $\mu(\omega)$ [or polarization $P(\omega)$ on the macroscopic level]. This oscillating dipole moment or polarization acts in turn as an antenna and reemits radiation. For low-intensity light fields, the magnitude of the induced dipole moment or polarization is in general linear with the amplitude of the electric field $E(\omega)$:

$$\mu(\omega) = \alpha E(\omega) \quad (1)$$

$$P(\omega) = \chi^{(1)} E(\omega) \quad (2)$$

The constant α is the molecular polarizability, and the macroscopic constant $\chi^{(1)}$ is known as the linear susceptibility. The molecular polarizability is related

to the macroscopic susceptibility through the relation $\chi^{(1)} = Nf\langle\alpha\rangle$, with N the number density and f a local-field correction factor to take into account the difference between applied field and field experienced by the molecule. The brackets indicate an orientational averaging. The linear proportionality suffices to explain the linear optical properties of the medium, for example, refraction (the real part of $\chi^{(1)}$ is related to the refractive index) and absorption (the imaginary part of $\chi^{(1)}$ is related to the absorption coefficient). However, by adding small perturbations to the polarization, other optical phenomena (optical activity or nonlinear optical properties) can be explained. Note that although the relation between dipole moment (or polarization) and electric field is in general tensorial by nature (α and $\chi^{(1)}$ are second-rank tensors), it is sufficient at present to consider the polarizability and susceptibility as scalar quantities.

2.2 Optical Activity

In order to explain optical activity, the expression for the polarization (and dipole moment) that we used in the previous section does not suffice¹⁰. A convenient way to describe optical activity is to include magnetic dipole contributions to the linear optical properties of the molecule (medium) by defining an induced dipole moment $\mu(\omega)$ [or polarization ($P(\omega)$)] that is also dependent on the magnetic induction field $B(\omega)$. Furthermore, we need to define an induced magnetic moment $m(\omega)$ [or magnetization $M(\omega)$]. Both dipole moment (polarization) and magnetic moment (magnetization) act as sources of radiation. Then, up to first order in the magnetic dipole interaction we can write

$$\mu(\omega) = \alpha^{ee} E(\omega) + \alpha^{em} B(\omega) \quad (3)$$

$$m(\omega) = \alpha^{me} E(\omega) \quad (4)$$

and

$$P(\omega) = \chi^{(1),ee} E(\omega) + \chi^{(1),em} B(\omega) \quad (5)$$

$$M(\omega) = \chi^{(1),me} E(\omega) \quad (6)$$

where α^{ee} is the usual linear polarizability and α^{em} and α^{me} are magnetic dipole polarizabilities, with $\alpha^{em} = -\alpha^{me}$. The superscripts *ee*, *me*, and *em* are used to discriminate between the different polarizabilities and refer to electric dipole (*e*) and magnetic dipole (*m*) interactions. For example, superscript *ee* indicates that a photon at frequency ω is annihilated through an electric dipole interaction and a new photon is created through an electric dipole interaction.

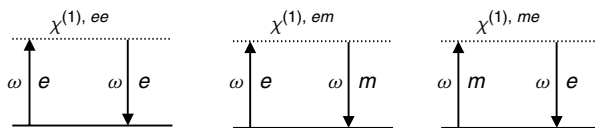


Figure 9.1 Energy diagram for annihilation and creation of photons. For $\chi^{(1),ee}$, input photon (frequency ω) is annihilated and output photon (frequency ω) is created through an electric dipole interaction. For $\chi^{(1),em}$, input photon at frequency ω is annihilated by magnetic interaction whereas other interaction occurs through electric dipole mechanism. On the other hand, for $\chi^{(1),me}$ the output photon is generated through magnetic interaction.

For α^{em} , a photon at frequency ω is annihilated through a magnetic dipole interaction and a new photon is created through an electric dipole interaction. For α^{me} , a photon at frequency ω is annihilated through a magnetic dipole interaction and a new photon is created through an electric dipole interaction. The term $\chi^{(1),ee}$ is the usual electric dipole susceptibility, and $\chi^{(1),em}$ and $\chi^{(1),me}$ are magnetic dipole susceptibilities, with $\chi^{(1),me} = -\chi^{(1),em}$. Important is that α^{em} , α^{me} , $\chi^{(1),me}$, and $\chi^{(1),me}$ change sign between the enantiomers and vanish in achiral or racemic materials. The annihilation and creation of photons through the different mechanisms is illustrated in the energy diagrams of Figure 9.1. These properties allow us to intuitively understand optical rotation. If we consider light that is vertically polarized and incident on a chiral isotropic medium, a vertically directed polarization and magnetization will be created inside the medium. Both polarization and magnetization act as new sources of radiation: The polarization radiates a vertically polarized field, while the magnetization radiates a horizontally polarized field. The sum of both fields is a new field with its polarization rotated over an angle θ , depending on the relative magnitude of P and M . The rotation angle θ has the same magnitude but differs in sign for both enantiomers. In the absence of magnetic interaction, no optical rotation can occur. This is illustrated in Figure 9.2.

2.3 Nonlinear Optics

For weak electric fields the magnitude of the induced polarization is linearly proportional with the amplitude of the electric field. Yet, when the field strength increases, the linear relationship no longer holds, and nonlinear terms have to be taken into account. In this case, the induced dipole moment and polarization can be expressed up to second order in the electric field as¹¹

$$\mu = \alpha E + \beta E E \quad (7)$$

$$P = \chi^{(1)} E + \chi^{(2)} E E \quad (8)$$

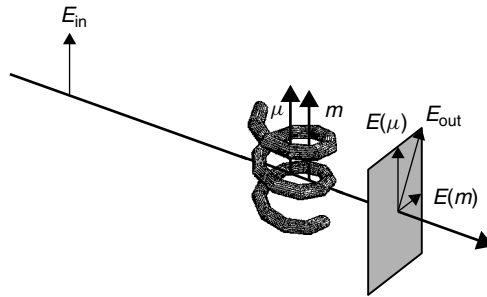


Figure 9.2 Quantitative description of optical rotation. A vertically polarized electric field E_{in} is incident on chiral system and induces vertically directed dipole moment μ and magnetic moment m . Both act as sources of radiation, μ giving rise to vertically polarized field, m giving rise to horizontally polarized field. Sum of both fields is a new field E_{out} with polarization rotated over angle θ .

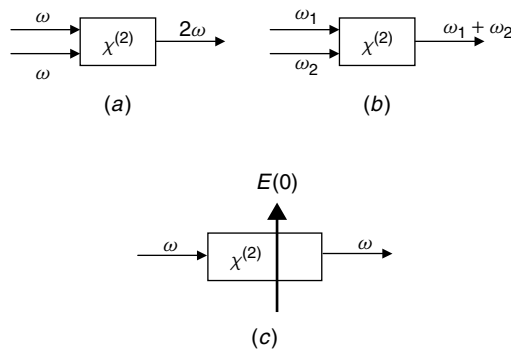


Figure 9.3 Schematic illustration of second-order nonlinear optical effects. (a) Second-harmonic generation. Two light fields at frequency ω are incident on medium with nonvanishing $\chi^{(2)}$. Nonlinear interaction with medium creates new field at frequency 2ω . (b) Frequency mixing. One light field at frequency ω_1 and one at frequency ω_2 is incident on nonlinear medium. Nonlinear interaction with medium creates new field at frequency $\omega_1 + \omega_2$. (c) electro-optic effect. Static electric field $E(0)$ applied over nonlinear medium changes phase of an incoming light field.

The proportionality constants α and β are the linear polarizability and the second-order polarizability (or first hyperpolarizability), and $\chi^{(1)}$ and $\chi^{(2)}$ are the first- and second-order susceptibility. The quadratic terms β and $\chi^{(2)}$ are related by $\chi^{(2)} = Nf(\beta)$ and are responsible for second-order nonlinear optical (NLO) effects such as frequency doubling (or second-harmonic generation), frequency mixing, and the electro-optic effect (or Pockels effect). These effects are schematically illustrated in Figure 9.3. In the remainder of this chapter, we will primarily focus on the process of second-harmonic generation (SHG).

In order to describe second-order nonlinear optical effects, it is not sufficient to treat β and $\chi^{(2)}$ as a scalar quantity. Instead the second-order polarizability and susceptibility must be treated as a third-rank tensors $\beta_{ijk}^{(2)}$ and $\chi_{ijk}^{(2)}$ with 27 components and the dipole moment, polarization, and electric field as vectors. As such, the relations between the dipole moment (polarization) vector and the electric field vector can be defined as:

$$\mu_i = \sum_j \alpha_{ij} E_j + \sum_{j,k} \beta_{ijk} E_j E_k \tag{9}$$

$$P_i = \sum_j \chi_{ij}^{(2)} E_j + \sum_{j,k} \chi_{ijk}^{(2)} E_j E_k \tag{10}$$

where the subscripts ijk refer to Cartesian coordinates. Hence, to fully characterize the second-order nonlinearity of a material, all 27 components would have to be determined. Fortunately, the number of independent tensor components is significantly reduced by taking into account the symmetry of the medium (or molecule).

Symmetry is one of the most important issues in the field of second-order nonlinear optics. As an example, we will briefly demonstrate a method to determine the number of independent tensor components of a centrosymmetric medium. One of the symmetry elements present in such a system is a center of inversion that transforms the coordinates xyz as:

$$x \longrightarrow -x \quad y \longrightarrow -y \quad z \longrightarrow -z$$

Consequently, the quantities of Eq. (10) transform as:

$$\begin{aligned} E_x &\longrightarrow -E_x & E_y &\longrightarrow -E_y & E_z &\longrightarrow -E_z \\ P_x &\longrightarrow -P_x & P_y &\longrightarrow -P_y & P_z &\longrightarrow -P_z \end{aligned}$$

The next step is to examine the effect of the center of inversion for each tensor component. For example, if we assume that all fields only have an x component, the inversion will transform the relation $P_x = \chi_{xxx} E_x E_x$ into

$$-P_x = \chi_{xxx} (-E_x)(-E_x) = \chi_{xxx} E_x E_x$$

Any symmetry operation is required to leave the sign and magnitude of physical properties unchanged and therefore $\chi_{xxx} = 0$. The same line of reasoning can be used to show that all tensor components will vanish under inversion. Hence, second-order nonlinear optical properties are not allowed in centrosymmetric media using the electric dipole approximation. The presence of noncentrosymmetry is one of the most stringent requirements in

second-order nonlinear optics and places considerable restrictions on the materials to be used for NLO applications. For example, the design of NLO crystals in lasers, which are used for frequency doubling of the fundamental laser light, is very critical because they must belong to crystal classes that lack a center of inversion. On the other hand, this property can be exploited in the field of surface science. At any surface, the centrosymmetry is necessarily broken, and second-order nonlinear optical effects can be used to probe the properties of surfaces and interphases. For example, second-harmonic generation has been routinely used to study the symmetry of surfaces and the properties of adsorbates at interfaces and surfaces.¹² Other important systems that are routinely investigated by SHG are noncentrosymmetric thin organic films with in-plane isotropy. They can be prepared by electric field poling, the Langmuir–Blodgett technique or self-assembly, and usually belong to the C_∞ or $C_{\infty v}$ symmetry groups. The C_∞ symmetry is chiral whereas the $C_{\infty v}$ group is achiral. Since the remainder of this work will especially focus on such systems, it is instructive to have a closer look at the nonvanishing tensor components. If we consider a film in the coordinate system shown in Figure 9.4, and after applying the symmetry elements to the susceptibility tensor of the film, we obtain four nonvanishing susceptibility components for the chiral film (C_∞ symmetry) and three nonvanishing components for the achiral film ($C_{\infty v}$ symmetry) (Table 9.1). Important is that the main difference between chiral film and achiral film is the existence of an additional component of the xyz type in the chiral film. The tensor components χ_{xyz} , χ_{xzy} , χ_{yxz} , and χ_{yzx} are only allowed for chiral isotropic surfaces and are designated as chiral tensor components. They change sign between the enantiomers and are responsible for nonlinear optical activity. Because the chiral components have a different sign for each enantiomer, they also vanish in a 50/50 mixture (racemic) of the enantiomers. The remaining components are allowed for all isotropic surfaces and are therefore referred to as achiral tensor components.

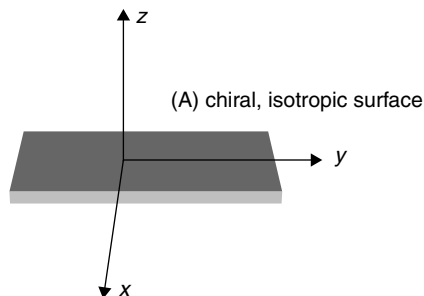


Figure 9.4 Indication of xyz coordinate system. The (a)chiral film surface is in x - y plane. The z -axis is perpendicular to film surface.

Table 9.1
 Nonvanishing Components of Second-Order Susceptibility Tensor for
 Second-Harmonic Generation in Electric-Dipole Approximation for Achiral and
 Chiral Isotropic (i.e. isotropic in the plane of the film) Films^a

	Chiral Isotropic Film	Achiral Isotropic Film
Tensor components χ_{ijk}	zzz $zxx = zyy$ $xxz = yyz = yzy = xzx$ $xyz = -yxz = -yzx = xzy$	zzz $zxx = zyy$ $xxz = yyz = yzy = xzx$

^a The surface is in the x - y plane.

2.4 Nonlinear Optical Activity in Second-Harmonic Generation

Chiral materials are known to be optically active. Linear optical activity includes effects such as optical rotation and circular dichroism, as mentioned in the earlier sections. In addition, they also exhibit nonlinear optical activity, that is, a different response of the NLO process to left- or right-hand circularly polarized light. Such circular-difference effects are predicted for nonlinear optical effects such as sum-and-difference frequency generation.^{13–15} However, they are small and have only been observed experimentally in crystals of racemic compounds. On the other hand, very large (tens of percent) effects have been observed in second-harmonic generation generated in interfaces and films.⁴ For example, the intensity of the frequency-doubled light generated in a chiral film is different for left- and right-hand circularly polarized input light. The effect can be seen as similar to ordinary circular dichroism (CD) and is therefore often referred to as SHG-CD. The use of $+45^\circ$ and -45° linearly polarized light (with respect to the vertically polarized direction) can also lead to a difference in second-harmonic intensity, and is called second-harmonic generation linear dichroism (SHG-LD). This effect has no analog in linear optics.⁶ A nonlinear analog of optical rotation has also been demonstrated experimentally and described theoretically. This effect measures the rotation in the polarization azimuth of the second-harmonic light generated at the surface with respect to that of the fundamental input light.⁷ All three effects are examples of nonlinear optical activity indicative of chirality. They can be used to discriminate between enantiomers because the sign of the effect reverses for the other enantiomer. Furthermore, since SHG is surface sensitive and the nonlinear optical activity effects are specific for chiral materials, the effects can be used as a very sensitive tool to study chiral surfaces. Therefore, techniques based on nonlinear optical activity have been suggested for the study of biological membranes and interfaces.

Without going into too much detail, it is relatively easy to intuitively understand optical rotation in second-harmonic generation from a chiral thin film by simply considering the nonvanishing polarization components generated in a chiral and achiral film. For example, for an achiral thin film with $C_{\infty v}$ symmetry and for the experimental situation shown in Figure 9.5, the nonvanishing components of the polarization can be written as:

$$P_z = \chi_{zzz}^{(2)} E_z E_z + \chi_{zxx}^{(2)} E_x E_x \quad (11)$$

$$P_x = \chi_{xxz}^{(2)} E_x E_z + \chi_{xzx}^{(2)} E_z E_x \quad (12)$$

Both components will radiate, giving rise to second-harmonic radiation polarized in the zx plane. Hence, the polarization of the second-harmonic field is the same as that of the fundamental field.

When the sample becomes chiral (C_{∞} symmetry), the components of the polarization are

$$P_z = \chi_{zzz}^{(2)} E_z E_z + \chi_{zxx}^{(2)} E_x E_x \quad (13)$$

$$P_y = \chi_{yxz}^{(2)} E_z E_x + \chi_{yxz}^{(2)} E_x E_z \quad (14)$$

$$P_x = \chi_{xxz}^{(2)} E_x E_z + \chi_{xzx}^{(2)} E_z E_x \quad (15)$$

The presence of chirality introduces an additional component in the y direction. This component will rotate the polarization of the second-harmonic field with respect to the polarization of the incident radiation. The amount of optical rotation will depend on the relative magnitude of the chiral and achiral susceptibility components. Furthermore, P_y changes sign between the enantiomers

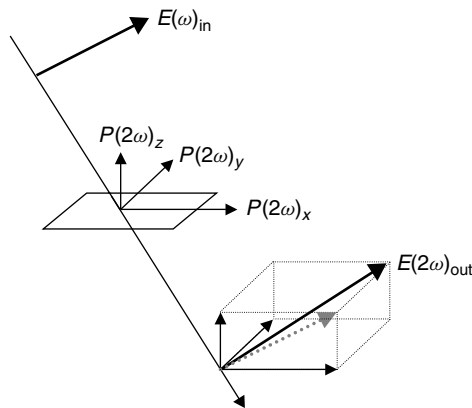


Figure 9.5 Schematic illustration of optical rotation in SHG (see text).

and, consequently, the optical rotation will change sign. Hence, this effect can be taken as a signature of chirality and is in a loose sense the nonlinear analog of optical rotation. An important difference with linear optical rotation is that here we do not rely on magnetic contributions to explain optical rotation.

2.5 Nonlinear Optical Activity and Magnetic Dipole Contributions

Although it is possible to explain nonlinear optical activity within the electric dipole approximation (i.e., by only including electric dipole contributions to the nonlinearity of the medium), experimental results indicate that, depending on the material system, magnetic contributions are nevertheless necessary to accurately explain nonlinear optical activity.^{16,17} In that case, irradiating the sample will induce a nonlinear polarization and magnetization and both will act as sources of second-harmonic radiation. The nonlinear part of the induced dipole moment (polarization), including the magnetic dipole interactions up to first order is now given by:

$$\mu_i(2\omega) = \sum_{j,k} \alpha_{ijk}^{eee} E_j(\omega) E_k(\omega) + \alpha_{ijk}^{eem} E_j(\omega) B_k(\omega) \quad (16a)$$

$$P_i(2\omega) = \sum_{j,k} \chi_{ijk}^{(2),eee} E_j(\omega) E_k(\omega) + \chi_{ijk}^{(2),eem} E_j(\omega) B_k(\omega) \quad (16b)$$

The subscripts refer to Cartesian coordinates in the laboratory coordinate system. The terms $E(\omega)$ and $B(\omega)$ are the electric and magnetic induction fields, respectively. In addition, the nonlinear induced magnetic moment (magnetization) is defined as:

$$m_i(2\omega) = \sum_{j,k} \alpha_{ijk}^{mee} E_j(\omega) E_k(\omega) \quad (17a)$$

$$M_i(2\omega) = \sum_{j,k} \chi_{ijk}^{(2),mee} E_j(\omega) E_k(\omega) \quad (17b)$$

The superscripts e and m , in Eq. (16) and (17), refer to an electric dipole and magnetic dipole interaction, respectively. For example, the superscript eem of the susceptibility tensor $\chi^{(2),eem}$ refers to an interaction where a photon at frequency 2ω is generated through an electric dipole interaction, and two photons are annihilated each by an electric dipole and magnetic dipole interaction, respectively. The energy diagrams for the tensors $\chi^{(2),eee}$, $\chi^{(2),eem}$, and $\chi^{(2),mee}$ are given in Figure 9.6. Note also that we have assumed in Eqs. (16) and (17) that the higher multipole contributions have predominantly a magnetic dipole

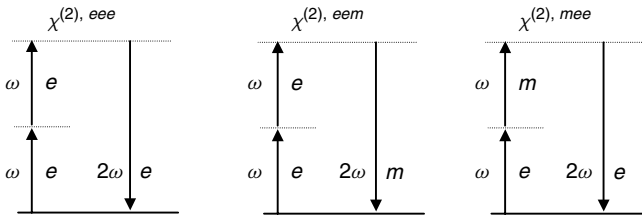


Figure 9.6 Energy diagrams for tensors $\chi^{(2),eee}$, $\chi^{(2),eem}$, and $\chi^{(2),mee}$. For $\chi^{(2),eee}$, input photons (frequency ω) are annihilated and output photon (frequency 2ω) is created through electric dipole interactions. For $\chi^{(2),eem}$, one input photon at frequency ω is annihilated by a magnetic interaction whereas other interactions occur through electric dipole mechanism. On the other hand, for $\chi^{(2),mee}$ output photon is generated through magnetic interaction.

character because the importance of magnetic interactions in chiral media is well established (see Section 2.2).

The nonvanishing components of the tensors $\chi^{(2),eem}$ and $\chi^{(2),mee}$ can be determined by applying the symmetry elements of the medium to the respective tensors. However, in order to do so, one must take into account that there is a fundamental difference between the electric field vector and the magnetic field vector. The first is a polar vector whereas the latter is an axial vector. A polar vector transforms as the position vector for all spatial transformations. On the other hand, an axial vector transforms as the position vector for rotations, but transforms opposite to the position vector for reflections and inversions.⁹ Hence, electric quantities and magnetic quantities transform similarly under rotations, but differently under reflections and inversions. As a consequence, the nonvanishing tensor components of $\chi^{(2),eem}$ and $\chi^{(2),mee}$ can be different from those of $\chi^{(2),eee}$. All nonvanishing components of $\chi^{(2),eem}$, $\chi^{(2),mee}$, and $\chi^{(2),eee}$ for a chiral and achiral isotropic thin film are given in Table 9.2.

2.6 Molecular Origin of Nonlinear Optical Activity

Maki and Persoons¹⁸ described nonlinear optical activity in second-harmonic generation of a chiral molecule using a classical model that is based on a single electron that is bound to a helical path. The helical motion of the electron causes optical activity in the second-order response. This model was used to calculate all the nonvanishing components of the hyperpolarizability tensors β^{eee} , β^{eem} , and β^{mee} . The macroscopic second-order polarization and magnetization were calculated for both an isotropic surface and a liquid of chiral molecules, and the corresponding components of the susceptibility tensors $\chi^{(2),eee}$, $\chi^{(2),eem}$, and $\chi^{(2),mee}$ were given explicitly. Furthermore, the components of the hyperpolarizabilities and susceptibilities were shown to rely upon the pitch and radius of the helix, which can aid in identifying chiral molecules

Table 9.2
 Nonvanishing Components of Second-Order Susceptibility Tensors $\chi^{(2),eee}$, $\chi^{(2),eem}$,
 and $\chi^{(2),mee}$ for Isotropic (a)Chiral Surface for SHG^a

Tensor	Achiral Isotropic Film	Chiral Isotropic Film
$\chi^{(2),eee}$	zzz	zzz
	zxx = zyy	zxx = zyy
	xxz = xzx = yyz = yzy	xxz = xzx = yyz = yzy
$\chi^{(2),eem}$		xyz = -yxz = -yzx = xzy
		zzz
		zxx = zyy
		xxz = yyz
		xzx = yzy
	xyz = -yxz	xyz = -yxz
$\chi^{(2),mee}$	zxy = -zyx	zxy = -zyx
	xzy = -yzx	xzy = -yzx
		zzz
		zxx = zyy
	xyz = xzy = -yxz = -yzx	xxz = xzx = yyz = yzy xyz = xzy = -yxz = -yzx

^a Film is taken to be in the x-y plane.

with large nonlinear optical response or help by providing insight in synthesizing new chiral compounds. In the limit of electric dipole response only, and for an isotropic chiral thin film or surface, the relation between chiral susceptibility components (which are responsible for nonlinear optical activity) and hyperpolarizability is of the form

$$\chi_{xyz}^{eee} = \frac{N_s}{4} (2 \cos^2 \theta - \sin^2 \theta) (\beta_{x'y'z'}^{eee} - \beta_{y'x'z'}^{eee}) \tag{18}$$

with N_s the number density and θ the angle between the helical axis and the normal to the film plane. The terms xyz are the coordinates of the film coordinate system, while $x'y'z'$ are related to the molecular coordinate system (Figure 9.7). The hyperpolarizability components were calculated to be of the form

$$\beta_{x'y'z'}^{eee} = \frac{e^3 \rho^2 \xi}{4\pi m^2 L^4 D^4(\omega)} \tag{19}$$

$$\beta_{y'x'z'}^{eee} = \frac{e^3 \rho^2 \xi}{4\pi m^2 L^4 D(\omega) D(2\omega)} \tag{20}$$

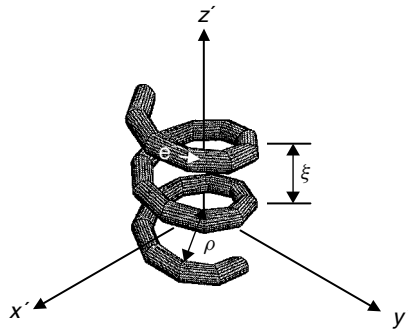


Figure 9.7 Coordinate system for electron bound to helical path of radius ρ and pitch ξ .

with e the charge and m the mass of the electron, L the length of the helical molecule, $D(\omega)$ and $D(2\omega)$ dispersion factors, and ρ and ξ the radius and pitch of the helix. From these relations it is clear that nonlinear optical activity is mainly caused (in the electric dipole approximation) by the figure of merit $(\rho^2\xi)/L^4$.

3 ANALYSIS OF NONLINEAR OPTICAL ACTIVITY

3.1 Theoretical Formalism

The experimental geometry to study nonlinear optical activity in SHG from thin films and surfaces is shown in Figure 9.8. The sample is irradiated with an intense laser beam with frequency ω . The electric field will give rise to a second-harmonic signal at frequency 2ω . The second-harmonic signal will be generated in transmission as well as reflection.¹⁹

To simplify the theoretical formalism, we assume that the thickness of the film is much smaller than the wavelength. Such thin films can be prepared by adsorbing a material on a substrate or interface, or by depositing molecular layers with the Langmuir–Blodgett technique. For such films the efficiency of the second-harmonic signal is of the same order of magnitude for both transmission and reflection. In addition, even though the film may be chiral, the linear optical activity is not expected to mix the p - and s -polarized fundamental and second-harmonic signals because of the thinness of the sample. Furthermore, all indices of refraction are assumed to be equal and unity. The surface of the sample is made up of chiral components and therefore has no mirror planes parallel to the rotation axis that is perpendicular to the film's surface. The film is considered to be isotropic in the plane of the film, that is, full rotational symmetry (C_∞ for a chiral and $C_{\infty v}$ for an achiral film).

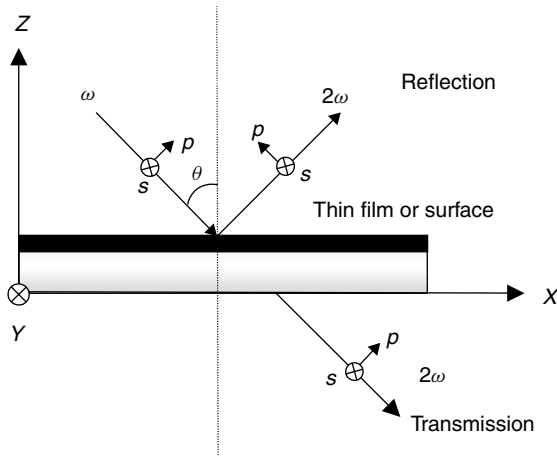


Figure 9.8 Second-harmonic generation from thin film (or surface). Fundamental beam at frequency ω (p or s polarized) is incident on film at angle θ . The p - and s -polarized second-harmonic fields (frequency 2ω) are generated in reflection and transmission.

The second-harmonic field generated in the sample can be calculated by:²⁰

$$E(2\omega) = (n \times P(2\omega)) \times n - n \times M(2\omega) \tag{21}$$

with n the direction of observation and P and M as given in Eqs. (16) and (17). The second-harmonic field is seen to depend linearly on both the polarization and magnetization. In addition, the magnetic induction field depends linearly on the electric field. The fundamental and second-harmonic fields can therefore be expanded in terms of their p - (parallel to the plane of incidence) and s - (perpendicular to the plane of incidence) polarized components, and thus we can write, in a general form

$$E(2\omega) = f E_p(\omega) E_p(\omega) + g E_s(\omega) E_s(\omega) + h E_p(\omega) E_s(\omega) \tag{22}$$

where $E(2\omega)$ represents any component of the second-harmonic signal and $E_p(\omega)$ and $E_s(\omega)$ represent the p - and s -polarized components of the amplitudes of the fundamental electric field, respectively. The coefficients f , g , and h are linear combinations of the second-order susceptibility components. Some of these coefficients may vanish depending on the symmetry of the surface, but there are no more than these three coefficients.

From an experimental point of view, it is more practical to consider the second-harmonic intensity instead of the second-harmonic fields. For simplicity, the intensity is expressed as the square of the amplitude of the electric

field, and with Eq. (22) we can write

$$I(2\omega) \approx |fE_p(\omega)E_p(\omega) + gE_s(\omega)E_s(\omega) + hE_p(\omega)E_s(\omega)|^2 \quad (23)$$

The coefficients f , g , and h in Eq. (23) can only depend on the nonvanishing susceptibility components listed in Table 9.2 and are, for a chiral isotropic surface, given by (a more detailed derivation of these expressions can be found elsewhere)²¹:

$$f_{Ts}^{Rs} = -\sin\theta[-2\chi_{xyz}^{eee}\cos\theta - \chi_{xxz}^{eem} + \chi_{zzz}^{mee}\sin^2\theta + \chi_{zxx}^{mee}\cos^2\theta \mp 2\chi_{xxz}^{mee}\cos^2\theta] \quad (24)$$

$$g_{Ts}^{Rs} = -\sin\theta[\chi_{xxz}^{eem} + \chi_{zxx}^{mee}] \quad (25)$$

$$h_{Ts}^{Rs} = -\sin\theta[2\chi_{xxz}^{eee} - (\chi_{xzy}^{eem} + \chi_{xyz}^{eem})\cos\theta \mp 2\chi_{xyz}^{mee}\cos\theta] \quad (26)$$

$$f_{Tp}^{Rp} = \sin\theta[\chi_{zzz}^{eee}\sin^2\theta + \chi_{zxx}^{eee}\cos^2\theta \mp 2\chi_{xxz}^{eee}\cos^2\theta - \chi_{zxy}^{eem}\cos\theta \pm \chi_{xzy}^{eem}\cos\theta + 2\chi_{xyz}^{mee}\cos\theta] \quad (27)$$

$$g_{Tp}^{Rp} = \sin\theta[\chi_{zxx}^{eee} - \chi_{zxy}^{eem}\cos\theta \mp \chi_{xyz}^{eem}\cos\theta] \quad (28)$$

$$h_{Tp}^{Rp} = -\sin\theta[\mp 2\chi_{xyz}^{eee}\cos\theta + (\chi_{zzz}^{eem} - \chi_{zxx}^{eem})\sin^2\theta \mp (\chi_{xxz}^{eem} + \chi_{xxz}^{eem})\cos^2\theta - 2\chi_{xxz}^{mee}] \quad (29)$$

where θ is the angle of incidence (see Figure 9.8). Equations (24)–(29) show four different coefficients f , g , and h each corresponding to a different experimental geometry. The different experimental geometries that can be distinguished are the detection of the p - (p) and s -polarized (s) components of the second-harmonic signal measured in reflection (R) and transmission (T). Note that the superscript (subscript) on the left-hand side corresponds to the upper (lower) sign on the right-hand side. For example g^{Rp} means the g coefficient for a measurement of the p -polarized second-harmonic signal in reflection.

It is important to note that the coefficients f_p , g_p , and h_s are always nonvanishing, for both achiral and chiral isotropic films. On the other hand, f_s , g_s , and h_p can only be nonvanishing if the isotropic film is chiral (nonracemic) because they completely depend on the chiral susceptibility components. Note that g_s is always equal to zero within the electric dipole approximation. The sign of the chiral expansion coefficients changes between enantiomers, while that of the achiral expansion coefficients stays the same. Experimental determination of all expansion coefficients fully characterizes the nonlinearity and nonlinear optical activity of the sample. Once all expansion coefficients are

known, it is possible to calculate all nonvanishing susceptibility components. Hence, in the next section we will discuss experimental techniques that can be used to determine all the expansion coefficients.

3.2 Second-Order Nonlinear Optical Signatures of Chirality

3.2.1 Circular-Difference Effects

Circular-difference effects in SHG can be understood by taking a closer look at Eq. (23). For *circularly* polarized light that is incident on the sample, we can always write that

$$E_p(\omega) = \pm i E_s(\omega) \quad (30)$$

where the upper (lower) sign corresponds with right-hand (left-hand) circularly polarized light. Substitution of Eq. (30) in Eq. (23) leads to:²²

$$I(2\omega) = |-f + g \pm ih|^2 I^2(\omega) \quad (31)$$

The circular-difference response, that is, a difference in second-harmonic efficiency of the sample for left- and right-hand circularly polarized incident light, is seen to arise from interference between the quantities $(-f + g)$ and h . We recall that, depending on the detected second-harmonic signal, the coefficients f and g are achiral and the coefficient h is chiral or vice versa. Hence, the circular-difference effect can occur only for chiral surfaces and has a different sign for the two enantiomers of the sample. Also, for a circular-difference effect to occur, a phase difference between the achiral and chiral expansion coefficients must exist. Within the electric dipole approximation, this can occur if the fundamental and/or second-harmonic frequencies are tuned close to the resonance frequencies of the material. On the other hand, if magnetic dipole contributions to the nonlinearity are present, the required phase differences can occur also for nonresonant excitation. The magnitude of the SHG-CD effect can be quantified as²³

$$\Delta I(2\omega) = I(2\omega)_{\text{left}} - I(2\omega)_{\text{right}} = 4 \operatorname{Im}\{(f - g)h^*\} I^2(\omega) \quad (32)$$

or as a normalized quantity:

$$\frac{\Delta I}{I} = \frac{2[I(2\omega)_{\text{left}} - I(2\omega)_{\text{right}}]}{I(2\omega)_{\text{left}} + I(2\omega)_{\text{right}}} \quad (33)$$

with $I(2\omega)_{\text{left}}$ and $I(2\omega)_{\text{right}}$ the second-harmonic intensity for left-hand and right-hand circularly polarized input light, respectively. The magnitude of the

SHG-CD effect is equal in magnitude, but opposite in sign, for the two enantiomers. When measured as a function of wavelength, the similarity between ordinary circular dichroism becomes clear. SHG-CD was first observed using the *R* and *S* enantiomers of 2,2'-dihydroxy-1,1'-binaphthyl adsorbed at the air–water interface and solid substrates.^{4,7} The effect was studied as a function of the fundamental wavelength in the 600-nm region, which approaches two-photon resonance with linear–circular dichroism bands of the molecule. In all cases, the maximum value of the circular-difference response was found to be of the order of 100%. This is remarkable considering the fact that the respective circular-difference effect in linear absorbance ($\Delta\varepsilon/\varepsilon$) is typically less than 0.1%, that is, the nonlinear effect is at least three orders of magnitude larger. Similar circular-difference effects have also been observed in a spectroscopic study of the dipeptide Boc-Trp-Trp.²⁴

3.2.2 Linear-Difference Effects in SHG

It is also possible to use appropriately chosen linear input polarizations as nonlinear probes of chirality. For the case of linear polarizations that are rotated by $\pm 45^\circ$ from the *p*-polarized direction, $E_p(\omega)$ and $E_s(\omega)$ are related as:

$$E_p(\omega) = \pm E_s(\omega) \quad (34)$$

An equation similar to Eq. (31) can be derived:²³

$$I(2\omega) = |f + g \pm h|^2 I^2(\omega) \quad (35)$$

This result implies that a different response for these two polarizations can occur when $(f + g)$ and h are simultaneously nonvanishing. Furthermore, the effect changes sign between the enantiomers. In contrast to the circular-difference effect, no phase difference between $(f + g)$ and h is required. Instead these quantities must have appreciable in-phase parts. In this respect, linear-difference effects are complementary to circular-difference effects in SHG (where a phase difference between the expansion coefficients is required).

The magnitude of the linear-difference effect (SHG-LD) can be quantified as:

$$\Delta I(2\omega) = I(2\omega)_{+45^\circ} - I(2\omega)_{-45^\circ} = -4\text{Re}\{(f + g)h^*\} I^2(\omega) \quad (36)$$

or as a normalized quantity:

$$\frac{\Delta I}{I} = \frac{2[I(2\omega)_{+45^\circ} - I(2\omega)_{-45^\circ}]}{I(2\omega)_{+45^\circ} + I(2\omega)_{-45^\circ}} \quad (37)$$

with $I(2\omega)_{+45^\circ}$ and $I(2\omega)_{-45^\circ}$ the second-harmonic intensity for $+45^\circ$ and -45° linearly polarized incident light, respectively.

Linear-difference effects in SHG have been observed from Langmuir–Blodgett films of chiral poly(isocyanide)s.⁶

3.2.3 Optical Rotation Effects in SHG

This effect, which is in a loose sense the nonlinear analog of linear optical rotation, is based on using linearly polarized fundamental light and measuring the direction of the major axis of the ellipse that describes the state of polarization of the second-harmonic light. For a simple description of the effect, we assume that the expansion coefficients are real, as would be the case for nonresonant excitation within the electric dipole approximation.²² In this case, the second-harmonic light will also be linearly polarized in a direction characterized by the angle

$$\phi = \tan^{-1}[R(2\omega)] \quad (38)$$

where the ratio of the s -polarized component to the p -polarized component of the second-harmonic field is

$$R(2\omega) = \frac{E_s(2\omega)}{E_p(2\omega)} = \frac{f_s E_p^2(\omega) + g_s E_s^2(\omega) + h_s E_p(\omega)E_s(\omega)}{f_p E_p^2(\omega) + g_p E_s^2(\omega) + h_p E_p(\omega)E_s(\omega)} \quad (39)$$

In the absence of chirality,

$$R_{\text{achiral}}(2\omega) = \frac{h_s E_p(\omega)E_s(\omega)}{f_p E_p^2(\omega) + g_p E_s^2(\omega)} \neq \frac{E_s(\omega)}{E_p(\omega)} \quad (40)$$

which implies that even an achiral surface will rotate the direction of polarization of the second-harmonic field away from that of the fundamental field. Hence, we can take as a signature of chirality any additional rotation compared with the expression given by Eq. (40). However, this result is problematic in the sense that the chirality of a sample can only be quantified if $R_{\text{achiral}}(2\omega)$ representing a racemic mixture is known. In addition, owing to the nonlinear character of the \tan^{-1} function, the actual polarization rotation angle will not be strictly equal in magnitude (with a change in sign) for the two enantiomers. Fortunately, all these problems can be avoided by choosing the fundamental beam to be p polarized, that is, $E_s(\omega) = 0$. In this case, an achiral sample leads to no polarization rotation and the rotation angle given by

$$\phi = \tan^{-1} \left(\frac{f_s}{f_p} \right) \quad (41)$$

is equal in magnitude and opposite in sign for the two enantiomers of a chiral sample. Hence, a measurement performed using a p -polarized fundamental beam probes surface chirality in an unambiguous way. However, note that the rotation angle is limited to $\pm 90^\circ$. This is an important difference compared with linear optical rotation, which accumulates with no limit in propagation through a chiral medium. Polarization rotation in SHG has been used to investigate 2,2'-dihydroxy-1,1'-binaphthyl and the dipeptide Boc-Trp-Trp adsorbed at different interfaces.^{7,24} In both cases the rotation angle was measured as a function of the fundamental wavelength. The maximum rotation angles were of the order of 50° and 40° , respectively. When measured as a function of fundamental wavelength, the effect is similar to optical rotatory dispersion (ORD) in the linear regime. Therefore, it is often referred to as SHG-ORD.

3.2.4 Continuous Polarization Measurements

Circular- and linear-difference effects and optical rotation in SHG are useful in the sense that they are sensitive to (surface) chirality and that they can be used to discriminate between enantiomers. However, the chirality of the sample is only characterized by a single quantity (rotation angle or intensity-difference effect) that depends on the specific experimental geometry. It would be more useful to determine the fundamental parameters that are responsible for nonlinear optical activity, that is, the different tensor components of the second-order susceptibilities or the different f , g , and h expansion coefficients (which are related to the tensor components). This would allow us to obtain valuable information about the structure–property relationship, which is implicitly present in the different susceptibility components. Recently, a simple technique has been developed to determine the values of the expansion coefficients (and hence the values of the susceptibility components) in a unique way.²⁵ The method is based on continuously varying the state of polarization of the fundamental beam by means of a quarter wave- or half waveplate and to record the intensities of various second-harmonic signals (transmission and reflection, p - and s -polarized signals). A quarter waveplate will convert incoming linearly polarized light into elliptical or circular polarized light. A half waveplate rotates the plane of polarization of incoming linearly polarized light. The polarization patterns obtained in this method can be used to determine (i) the magnitude and sign of the intensity-difference effects and (ii) the magnitude and phase of all expansion coefficients, as well as those of the susceptibility components. In addition, the method is not limited to intensity-difference effects: not only circular-difference and linear-difference effects are indicative of chirality, but also asymmetry in the polarization line shapes and the presence of the chiral expansion coefficients are indicative of chirality. For measurements with

a quarter waveplate, the polarization patterns are described by the equation²³

$$\begin{aligned}
 I(2\omega) = & \frac{1}{16}[f_R - g_R + 4f_I \cos 2\varphi - (f_R - g_R) \cos 4\varphi \\
 & + 2h_I \sin 2\varphi - h_R \sin 4\varphi]^2 I^2(\omega) \\
 & + \frac{1}{16}[f_I - g_I - 4f_R \cos 2\varphi - (f_I - g_I) \cos 4\varphi \\
 & - 2h_R \sin 2\varphi - h_I \sin 4\varphi]^2 I^2(\omega)
 \end{aligned} \tag{42}$$

and for a half waveplate by

$$\begin{aligned}
 I(2\omega) = & \frac{1}{4}[f_R + g_R + (f_R - g_R) \cos 4\varphi + h_R \sin 4\varphi]^2 I^2(\omega) \\
 & + \frac{1}{4}[f_I + g_I + (f_I - g_I) \cos 4\varphi + h_I \sin 4\varphi]^2 I^2(\omega)
 \end{aligned} \tag{43}$$

with φ the angle of rotation of the quarter (half) waveplate, and f_R , g_R , h_R , f_I , g_I , and h_I the real and imaginary parts of the coefficients f , g , and h , respectively. To graphically illustrate the different signatures of chirality in the polarization line shapes, we will consider some different hypothetical situations that are simulated in Figures 9.9*a–f*. The waveplate was a quarter waveplate. Figures 9.9*a* and *d* show that the second-harmonic response of an achiral or racemic film ($f_s = 0$, $h_p = 0$) results in a symmetric line shape (with respect to the 180° rotation angle) without any SHG-CD effect. Since $g_s = 0$ for the s -polarized signal, within the electric dipole approximation, the line shape for an achiral sample depends only on h_s and is always of the form shown in Figure 9.9*a*. It can only vary by a normalization factor. If the line shape deviates from this general shape, the sample has to be chiral (nonracemic). On the other hand, the p -polarized response depends on both expansion coefficients f_p and g_p . Therefore, it is not possible to define a general line shape for the p -polarized second-harmonic signal. However, indications of chirality can also be deduced from the p -polarized line shapes. A chiral surface will always produce an asymmetric (with respect to the 180° rotation angle) line shape as shown in Figures 9.9*e* and *f*. Hence, asymmetry with respect to the 180° rotation angle in the polarization line shape is a unique signature of chirality. Furthermore, the asymmetry becomes more important with increasing enantiomeric content and changes sign as the handedness of the chiral sample is reversed. No asymmetry will be present for a racemic sample.

Note, also, that the presence of a circular-difference effect is not a necessary requirement for chirality. The presence of an intensity difference effect depends on the exact phase relationships between the chiral and achiral expansion coefficients: in-phase coefficients will produce no circular-difference effect (see Figures 9.9*b* and *e*), while out-of-phase components will

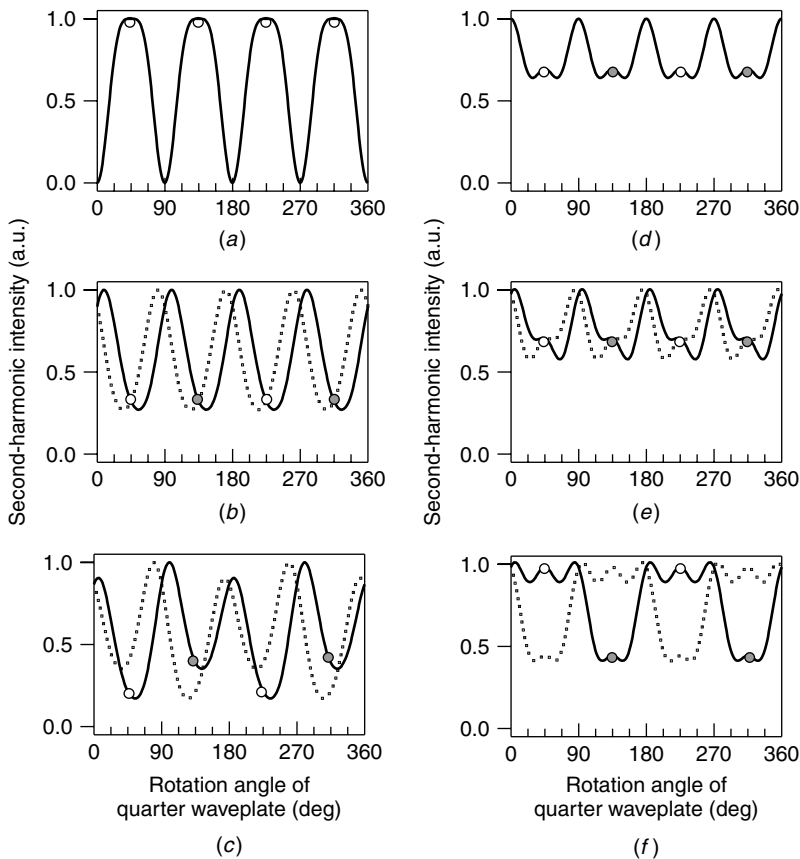


Figure 9.9 Simulated normalized line shapes of *s*-polarized (*a*–*c*) and *p*-polarized (*d*–*f*) second-harmonic signals for quarter waveplate measurements: (*a*) and (*d*) hypothetical achiral surface ($h_s = 0.5$; $f_p = 0.75$, $g_p = -0.5$). (*b*) and (*e*) hypothetical chiral surface with in-phase chiral coefficient ($f_s = \pm 0.75$, $h_s = 0.5$; $f_p = 0.75$, $g_p = -0.5$, $h_p = \pm 0.25$), (*c*) and (*f*) hypothetical chiral surface with out-of-phase chiral coefficient ($f_s = \pm 0.75 \pm 0.25i$, $h_s = 0.5$; $f_p = 0.75$, $g_p = -0.5$, $h_p = \pm 0.25i$). Upper (solid line) and lower (dashed line) sign in expansion coefficients correspond to two enantiomers. Rotation angles of 45° and 225° (135° and 315°) correspond to right-hand (left-hand) circularly polarized light and are indicated for one of enantiomers with open and filled circles, respectively.

give rise to circular-difference effects (see Figures 9.9*c* and *f*). Therefore, the lack of an SHG-CD effect cannot be used to conclude that a surface is achiral. Vice versa, an SHG-CD (or SHG-LD) effect does not originate exclusively from chiral materials. An SHG-LD and SHG-CD effect can also be observed from an achiral *anisotropic* surface.²⁶ This phenomenon can be explained

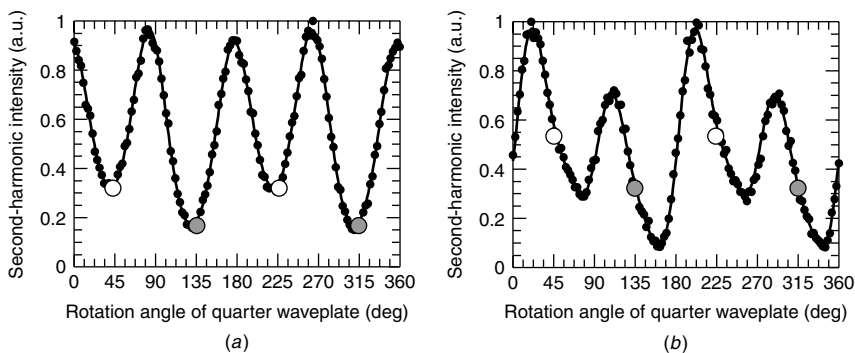


Figure 9.10 (a) and (b) Example of a circular-difference effect from an isotropic Langmuir–Blodgett film composed of enantiomerically pure chiral molecules. Experimental data points are fitted to Eq. (42) (solid curve). (a) The s -polarized second-harmonic signal, fit coefficients: $f_s = 0.87 + 0.39i$ and $h_s = -0.38$. (b) The p -polarized second-harmonic signal, fit coefficients: $f_p = 0.63 - 0.20i$, $g_p = 0.12 + 0.003i$, and $h_p = 1.24$. The right- and left-hand circular polarization are indicated by open and filled circles.

since for certain orientations of an anisotropic sample, the experimental setup can become chiral. Therefore, special care must be taken when interpreting the experimental results. However, it is possible to discriminate between the contributions of anisotropy and chirality. The CD effects that originate from the anisotropy will cancel when averaged over all orientations. On the other hand, there will be a net CD effect when the contributions from the chirality of the sample are averaged over all orientations of the sample.

Figures 9.10a and b show the respective s - and p -polarized components of the second-harmonic intensity recorded from a chiral thin film in transmission. The experimental data points are fitted to Eq. (42) and the values of the expansion coefficients f , g , and h are determined. Note the CD effect observed in both figures. Since f_s , g_s , and h_p are zero for an achiral thin film or surface, $(-f + g)$ and h cannot be simultaneously nonvanishing for a particular experimental arrangement and thus no CD effect can be observed. In Figure 9.11, we compare the second-harmonic response as observed experimentally for a chiral and achiral thin film.

3.3 Experimental Determination of f , g , and h

To determine f , g , and h the second-harmonic intensity is measured as a function of the angle of the quarter waveplate for different experimental geometries. The experimental setup is shown in Figure 9.12. A thin film is irradiated with an infrared Nd:YAG laser (1064 nm, 50 Hz, 8 ns). The polarization of the input beam (p polarized) is continuously varied with a quarter waveplate

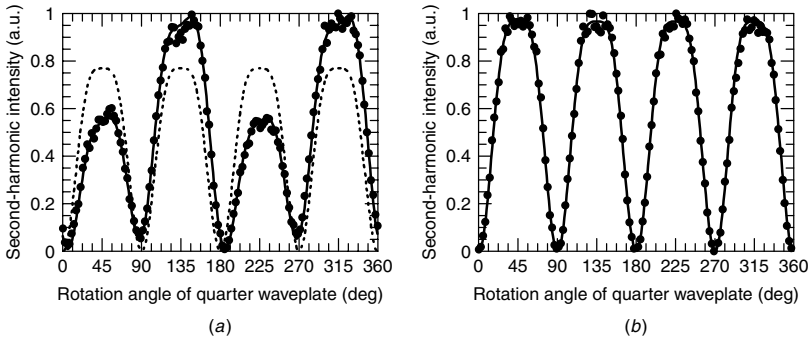


Figure 9.11 (a) and (b) Comparison between the second-harmonic s -polarized signals measured in transmission for (a) an isotropic surface composed of pure enantiomer of chiral poly(isocyanide) (Figure 9.14) and (b) an isotropic surface composed of racemic mixture. Experimental data points are fitted to Eq. (42) (solid curve). Fit coefficients are given by (a) $f_s = -0.091 + 0.24i$ and $h_s = 1.713$ and (b) $h_s = 1.97$. No circular-difference effect can be observed from achiral surface. In (a), the dashed curve represents the line shape with all fit coefficients, except h_s , taken equal to zero. Line shape cannot be reproduced by fitting routine if chiral expansion coefficients are taken to be zero.

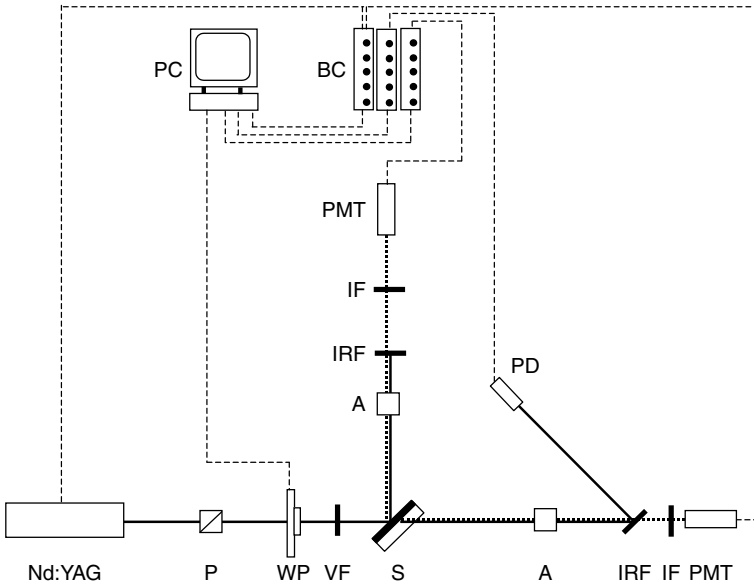


Figure 9.12 Experimental setup: (Nd:YAG) Nd:YAG laser (1064 nm, 50 Hz, 8 ns), (S) sample, (P) polarizer, (A) analyzer, (WP) waveplate (half or quarter rotated by stepper motor), (VF) visible-light-blocking filter, (PD) photodiode, (PMT) photomultiplier tube, (IRF) infrared filter, (IF) 532 nm interference filter, (PC) PC for data recording and control of the setup, (BC) boxcar/gated integrator, solid (dotted) line represents light at 1064 nm (532 nm).

that is rotated by a stepper motor. The intensity of the second-harmonic light is recorded, in transmission and reflection, by a photomultiplier tube as a function of the rotation angle of the quarter waveplate (input polarization). Such measurements are referred to as *polarization measurements*. The analyzer is used to select the polarization component of the second-harmonic signal (*p* or *s* polarization).

Some examples of polarization patterns are presented in Figures 9.13a and b. Figure 9.13a shows the *s*-polarized second-harmonic signal generated in a Langmuir–Blodgett (LB) film of a structure that combines helicenes and Ni–phthalocyanine cores.²⁷ Figure 9.13b shows the *p*-polarized signal detected from an LB film of a similar structure. Note the large CD-SHG effect in both figures, which is the difference between right-hand (rotation angle of quarter waveplate = 45° and 225°) and left-hand (rotation angle of quarter waveplate = 135° and 315°) circularly polarized fundamental excitation. The values for the coefficients *f*, *g*, and *h* are then obtained by fitting the measured SH signal to Eqs. (42) and (43).

To fit the experimental results, it is necessary to fix the overall phase. This can be done, for example, by defining *h* as a real quantity ($h_I = 0$). The values found for the coefficients *f*, *g*, and *h* can then subsequently be used to calculate the values of the components of the second-order susceptibility, $\chi^{(2)}$. This is done in detail for a Langmuir–Blodgett film of a poly(isocyanide) in the following section. Note that both phase and magnitude of all tensor components are relative values. The absolute phase cannot be determined

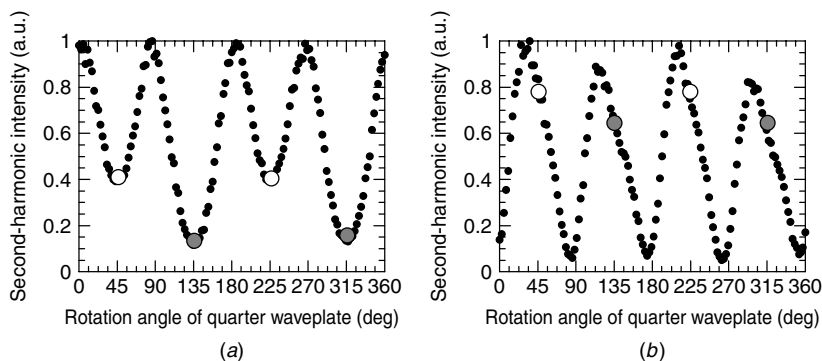


Figure 9.13 (a) and (b) Examples of polarization patterns obtained from quarter waveplate measurements. Transmitted second-harmonic signal is detected as function of angle of quarter waveplate. Second-harmonic intensity (in arbitrary units, a.u.) for right- and left-hand circularly polarized fundamental light is indicated with open and filled circle, respectively. (a) The *s*-polarized second-harmonic signal as measured from chiral LB film of structure that combines helicenes and Ni–phthalocyanine cores. (b) The *p*-polarized signal of structure that combines helicenes and Cu–phthalocyanine cores.

because of the arbitrary choice of $h_I = 0$. In addition, all second-harmonic intensities are recorded in arbitrary units (a.u.), so that no absolute magnitude of a component can be calculated. However, absolute values can be determined by calibration with, for example, a quartz wedge.¹¹

4 EXPERIMENTAL STUDIES OF NONLINEAR OPTICAL ACTIVITY IN SHG

In this section, the experimental techniques described in the previous section are applied to the study of thin Langmuir–Blodgett films of chiral molecules and polymers. We will show in detail how the second-order susceptibility of chiral thin films can be analyzed and discuss the influence of chirality on the nonlinear optical response of these films.

In a first section, the use of continuous polarization measurements with quarter and half waveplates is demonstrated. We examine whether both techniques are complementary and discuss the trade-offs of using either quarter waveplate measurements (circularly polarized light) or half waveplate measurements (linearly polarized light) as a nonlinear optical probe of chirality. In Section 4.2, a more detailed analysis of the second-order susceptibility is offered for a thin film of a chiral poly(isocyanide). The values of the tensor components of the three susceptibilities, χ^{eee} , χ^{eem} , and χ^{mee} , are determined using quarter waveplate measurements. The results suggest the presence of magnetic dipole contributions to the nonlinearity of the material. If such contributions are large compared to the electric dipole contributions, the frequently used electric dipole approximation cannot explain the experimental results and should, for a correct analysis, not be used. However, the indications of magnetic dipole contributions are, for the poly(isocyanide), only obtained by comparing the results of several second-harmonic measurements which makes the procedure sensitive to errors. On the other hand, similar measurements performed on a chiral poly(thiophene) clearly demonstrate these magnetic dipole contributions. In this case, the analysis of single polarization patterns is sufficient to prove the failure of the electric dipole approximation. Inclusion of magnetic dipoles in the theoretical analysis is required to properly explain the recorded experimental data. This is described in Section 4.3. In the following section, we investigate the nonlinear optical properties of thin films of a chiral 1,1'-binaphthyl-based helical polymer. In this case, the sample can be completely described within the electric dipole approximation. In a last section we demonstrate the importance of chiral contributions to the nonlinearity in the field of nonlinear optics. Thin films of a chiral helicenebisquinone derivative have a second-order susceptibility that is dominated by the chiral tensor components. As a result, the second-harmonic signal generated from the pure

enantiomer is several orders of magnitude higher than that of a racemic film of the same material with equal thickness. Therefore, chiral materials can be extremely useful as new materials in the field of nonlinear optics.

4.1 Comparison of Linearly and Circularly Polarized Probes of Nonlinear Optical Activity of Chiral Surfaces

In linear optics, chiral molecules can be studied by measuring the processes of optical rotation and circular dichroism. These linear optical techniques are considered to be complementary because they measure the real and imaginary part of the difference in index of refraction for left- and right-hand circularly polarized light, respectively. In this section, we investigate the nonlinear optical activity in thin films of a chiral chromophore-functionalized poly(isocyanide) with the experimental setup described in Section 3.3. The second-harmonic intensity generated in the film is measured as a function of the polarization of the fundamental light which is continuously varied by means of a half wave or a quarter waveplate.^{23,28,29} Our goal is to examine if both techniques can be considered complementary. We define two quantities as exactly complementary if they measure, respectively, the real and imaginary parts of a more general, complex-valued quantity. In addition, we compare the benefits and disadvantages of both techniques.

The material system is a Langmuir–Blodgett film of the *S* enantiomer of a chiral polymer deposited on a glass substrate. The polymer is a poly(isocyanide)³⁰ functionalized with a nonlinear optical chromophore (see Figure 9.14). In this particular system the optical nonlinearity and chirality are present on two different levels of the molecular structure. The chirality of the polymer is located in the helical backbone whereas the nonlinearity is present in the attached chromophores. Hence, this opens the possibility to optimize both properties independently.

These poly(isocyanide) polymers form rigid, rodlike helices on the surface of water, which can be easily transferred to a solid substrate by means of the LB method. The resulting films have a C_∞ symmetry.

The sample was analyzed using the procedure of continuous polarization measurements described in Section 3.3. The chiral poly(isocyanide) samples respond strongly to both the circular and linear probes of chirality. The full results for excitation using quarter and half waveplates are shown in Figures 9.15 and 9.16, respectively. The second-harmonic signals for left-hand and right-hand circularly polarized fundamental beams are indicated in Figure 9.15. The second-harmonic signals for -45° and $+45^\circ$ linearly polarized fundamental beams are indicated in Figure 9.16. We extracted the measured second-harmonic response at these four cases of input polarization and calculated the magnitude of the circular- and linear-difference effect in

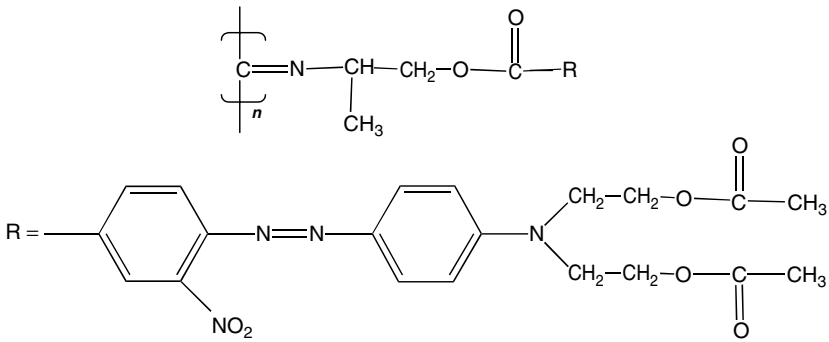


Figure 9.14 Chemical structure of *S*-enantiomer of the chromophore-functionalized poly(isocyanide).

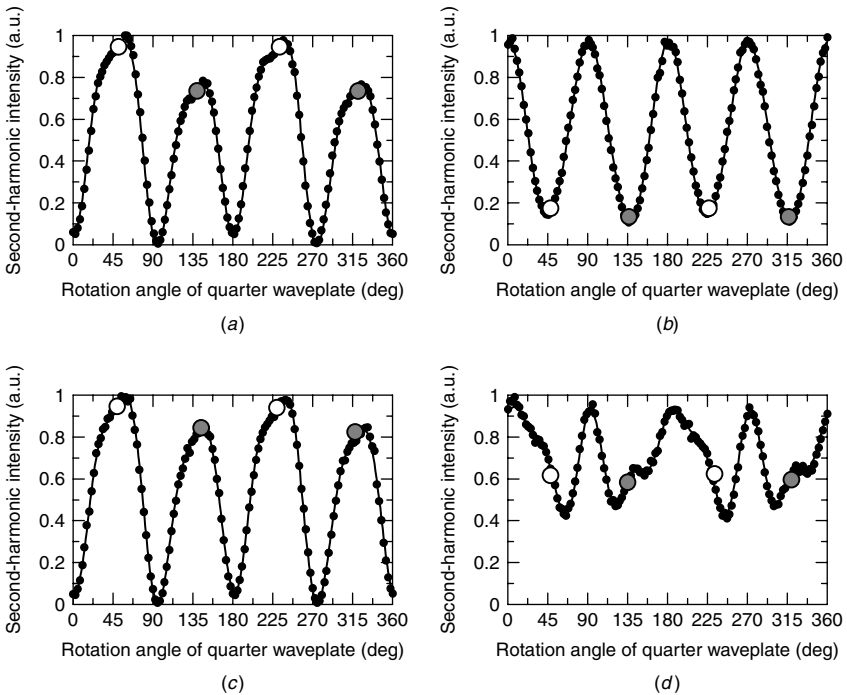


Figure 9.15 Second-harmonic intensity as function of rotation angle of quarter waveplate. (a) Transmitted *s*-polarized SH signal, (b) transmitted *p*-polarized SH signal, (c) reflected *s*-polarized SH signal, and (d) reflected *p*-polarized SH signal. Left- and right-hand circularly polarized input light is indicated with open and filled circles, respectively.

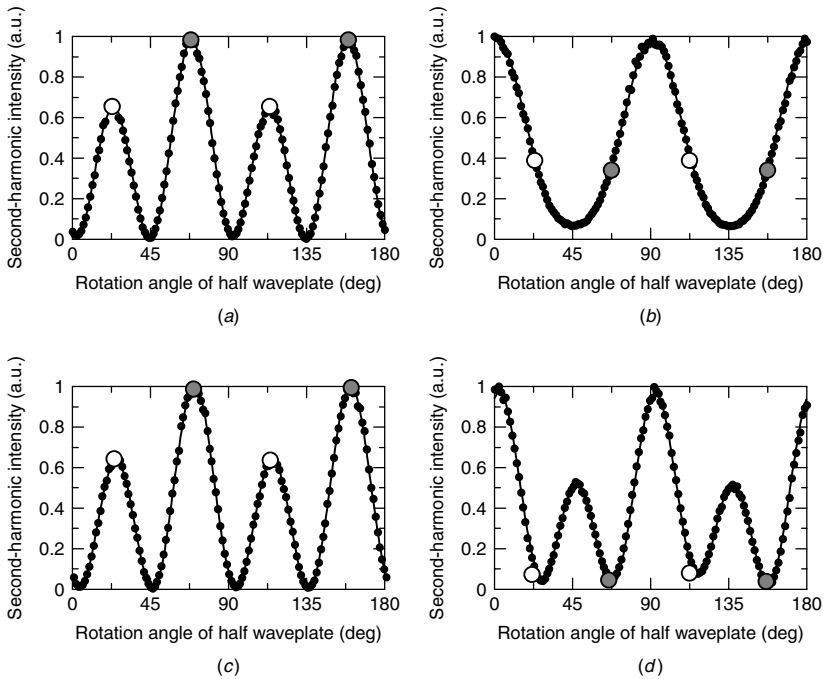


Figure 9.16 Second-harmonic intensity as function of rotation angle of half waveplate. (a) Transmitted *s*-polarized SH signal, (b) transmitted *p*-polarized SH signal, (c) reflected *s*-polarized SH signal, and (d) reflected *p*-polarized SH signal. A $+45^\circ$ and -45° linearly polarized input light (with respect to the *p*-polarized direction) is indicated with open and filled circles, respectively.

the *p* and *s* components of the reflected and transmitted waves. The values are listed in Table 9.3 in the column labeled Measured Asymmetry. Notice the large difference effects (from 15 to 118%) that are observed compared to the effects for their linear optical analogs (e.g., the difference effect $\Delta\varepsilon/\varepsilon$ in circular dichroism is on the order of $\pm 0.1\%$).

Next, the experimental results were fitted to Eqs. (42) and (43), respectively. We choose to set the imaginary part of h (h_I) to zero to fix the overall phase. The second-harmonic intensity is measured in arbitrary units and we normalized the fitting parameter values to the real part of h , that is, $h_R = 1$. Therefore, only the relative values are meaningful. The sets of parameter values found that best fit Eq. (42) to each of the waveplate data curves are given in Table 9.4.

An additional complication occurs in fitting Eq. (43) to the half waveplate data curve. Even with a choice in overall phase, there are four sets of parameter values that give an equally good fit, but only one set is physically correct.²⁵

Table 9.3
Circular- and Linear-Difference Effects for p and s Polarized Components of SHG in Transmission and Reflection^a

Second-Harmonic Wave		Measured Asymmetry		Predicted Value from Quarter-Wave Measurements
Direction	Polarization Component	Circular Difference (%)	Linear Difference (%)	Linear Difference (%)
Reflected	s	+15	-44	-45
Transmitted	s	+23	-40	-37
Reflected	p	+17	+118	+122
Transmitted	p	+22	+25	+26

^a The predicted values of linear difference are each based on the respective quarter waveplate measurements of f , g , and h (see Table 9.4).

Table 9.4
Experimentally Determined Values of f , g , and h for p -Polarized (p) and s -Polarized (s) Components of SHG in Transmission (T) and Reflection (R)^a

	Quarter Waveplate			Half Waveplate		
	f	g	h	f	g	h
R_s	$0.110 + 0.061i$	$0.004 + 0.025i$	1	$0.113 + 0.061i$	$0.000 + 0.052i$	1
T_s	$0.108 + 0.078i$	$-0.013 + 0.020i$	1	$0.102 + 0.065i$	$0.001 + 0.041i$	1
R_p	$-3.358 + 0.033i$	$2.033 - 1.288i$	1	$-3.543 + 0.023i$	$2.202 - 1.352i$	1
T_p	$-8.479 + 4.983i$	$-1.941 + 2.100i$	1	$-6.836 + 6.144i$	$-1.338 + 1.193i$	1

^a Each set of values of f , g , and h is normalized to $h = 1$.

The problem is that one can never know whether a fitting routine has found the physical solution or one of the other solutions. Of course, once the parameter values are determined from the fit to the quarter waveplate data curve, then the physical solution is known and should be recognizable from the four sets of parameter values found to fit the half waveplate data curve. We have done this and give in Table 9.4 the physically correct parameter values that fit the half waveplate data curve. The solid-line curves in Figures 9.15 and 9.16 are plots of Eqs. 42 and 43, respectively, using the parameter values given in Table 9.4. One can see that the solid-line curves provide an excellent fit to the data curves.

The experimental values of f , g , and h determined using quarter and half waveplate excitation agree within 20%, except for the values of the s components of g . The discrepancies in the fit values of g_s for the quarter and

half waveplate data curves, occur not only because the g_s are small but also because of additional problems in fitting the half waveplate data. In addition to the four-solution ambiguity, we found that there is a lack of sensitivity in the half waveplate function [Eq. (43)] to the value of g for the case of the s -polarized data. Fitting the quarter waveplate data, on the other hand, determines the value of g much more sensitively. Overall, we find that the fits to the quarter waveplate data are more sensitive to changes in the exact values of the fit parameters than the fits to the half waveplate data. In support of this, we find that the parameters determined by fitting the quarter waveplate data also provide an excellent fit to the respective half waveplate data, whereas the half-waveplate-determined parameters do not provide as good fits to the respective quarter waveplate data curves. Hence, the rather large discrepancy between the two sets of fit parameters in case of the transmitted p -polarized harmonic is associated with the lack of sensitivity of the half waveplate measurement. In Table 9.3 we have listed the calculated magnitude of the linear-difference effect from the quarter waveplate parameters. The predicted values of the SHG-LD effect from the quarter waveplate measurements are within 4% of the directly measured values.

The fit values of f and g have substantial imaginary components, so are significantly out of phase with h (we set $h = 1$) and, hence, explain the large values of the circular-difference effect. Also there are substantial real components of f and g , which means a significant portion of f and g are in phase with h and, hence, explains the large values of the linear-difference effect.

Comments have been made in the literature^{31,32} that circular-difference probes (e.g., SHG-CD) should work only under resonant conditions, whereas the linear-difference probes (e.g., SHG-LD, SHG-ORD) should work under both nonresonant and resonant conditions, which would be a further example of the probes being complementary. The comments are based on the behavior of the susceptibility components and, thus also, the parameters with detuning from an optical resonance in the limit of only electric dipole response. The real parts of the susceptibility components are dominant, whereas the imaginary parts would be essentially zero. On the other hand, near to a resonance the real and imaginary values would be comparable in value. The presence of magnetic dipole contributions may change this behavior with detuning, though, because the susceptibility components resulting from the magnetic dipole contributions ought to be imaginary valued off resonance and would hence contribute such that SHG-CD occurs off resonance.^{33,34}

We anticipate that, regardless of the detuning from an optical resonance used, the parameters f , g , and h will always be determinable from measurements of SHG as a function of the rotation angle of a quarter waveplate used to set the polarization state of the incident fundamental light. The amount of SHG-CD can be calculated from the parameters or, of course, read directly

from the measured quarter waveplate response curve. Also, the magnitude of the SHG-LD effect can be calculated from the quarter-waveplate-determined parameters as was demonstrated above. Therefore, it is not necessary to perform measurements using a half waveplate to reach -45° and $+45^\circ$ linear-polarization states of the fundamental light. No new information is gained by using half waveplate polarization measurements. However, there is a practical reason to conduct half waveplate measurements. Accurately creating left-hand and right-hand circular polarizations of light is typically far more difficult than creating orthogonal linear polarizations of light. In addition, retardation errors with changes in wavelength are a typical problem when using waveplates, but one does not need a half waveplate to create linearly polarized light. It is true that the fundamental light must be precisely switched between the -45° and $+45^\circ$ orientations of linear polarization with respect to the p -polarized direction, and that the fundamental light must be equal in intensity in both cases, but this can be achieved using broad-band optical components. Therefore, half waveplate measurement promises to be a powerful and simpler to implement technique for measuring chirality as a function of the wavelength of the fundamental light.

4.2 Quantitative Determination of Electric and Magnetic Second-Order Susceptibility Tensors of Chiral Surfaces

In this section, we use continuous polarization measurements with a quarter waveplate (Section 3.3) to study the second-harmonic response in a quantitative way. We calculate the relative values of the three tensors that describe second-harmonic generation, that is, χ^{eee} , χ^{eem} , χ^{mee} up to first order in the magnetic dipole interaction.³⁵ Note that only normalized line shapes of p - and s -polarized signals need to be measured to extract the different components of the susceptibility tensors. This is a distinct advantage compared to similar measurements on achiral surfaces, which require mutually calibrated signals or mixing of p - and s -polarized signals.^{36,37} The measured second-harmonic line shapes are fitted to Eq. (42) to determine the values for f , g , and h . Again, to fix the overall phase and because of the relative character of the values of the tensor components, we define h_I to be zero and $h_R (= h)$ to be unity.

The coefficients f , g , and h are unique for each second-harmonic signal and depend on the three susceptibility tensors. We normalize the relative values of the tensor components to $\chi_{xxz}^{eee} = 1$. The task is then to determine the complex values of the other 14 tensor components (see Table 9.2). A sufficient number of 8 independent measurements is provided by the p - and s -polarized components of the reflected and transmitted second-harmonic signals for the two orientations of the sample shown in Figure 9.17. The change in sample orientation corresponds to a coordinate transformation that reverses the

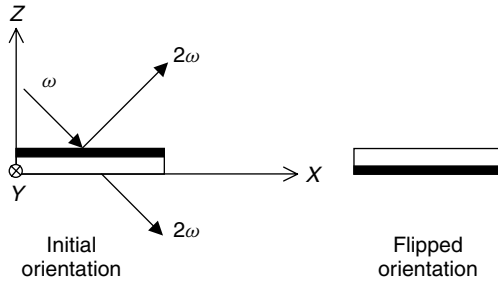


Figure 9.17 Geometry of second-harmonic generation from chiral surface. Two orientations of sample are related by coordinate transformation $x \rightarrow x$, $y \rightarrow -y$, and $z \rightarrow -z$.

sign of certain tensor components. The 8 fitted line shapes are made mutually compatible by scaling each of them by a complex factor to yield 24 complex equations of the type:

$$f_i^{\text{theoretical}}(\chi^{eee}, \chi^{em}, \chi^{mee}) = c_i f_i^{\text{fitted}} \tag{44}$$

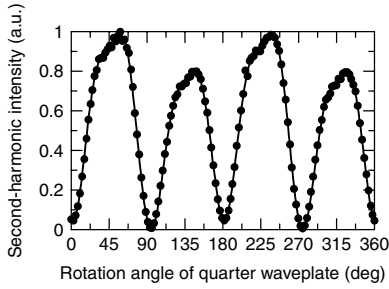
where $f_i^{\text{theoretical}}$ depends linearly on the components of the three tensors, c_i is a complex scaling factor unique to each measured signal, and f_i^{fitted} is the value of the coefficient f for a signal i relative to $h_i^{\text{fitted}} = 1$. The eight scaling factors c_i are additional unknown quantities, which are solved together with the unknown tensor components. The procedure thus has 22 unknowns and 24 equations. The experimental results are shown in Figure 9.18.

We first have attempted to explain the results in the electric dipole approximation. However, the four independent solutions (obtained from different experimental configurations) to the components of χ^{eee} (Table 9.5) are mutually incompatible, and we conclude that the results cannot be explained in the electric dipole approximation.

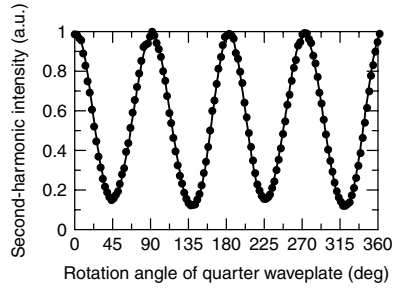
We next include the magnetic contributions to the nonlinearity and the results are given in Table 9.6.

Although this procedure is based on solving a large number of equations, we have good confidence in the obtained results. For example, we found no good solutions if any of the components indicated with an asterisk was assumed to vanish. Further confidence in the results is provided by their excellent agreement with expected results. For example, we observe the common result that the electric dipole components χ_{xxz}^{eee} and χ_{zxx}^{eee} are approximately equal, whereas χ_{zzz}^{eee} is somewhat larger.^{38,39}

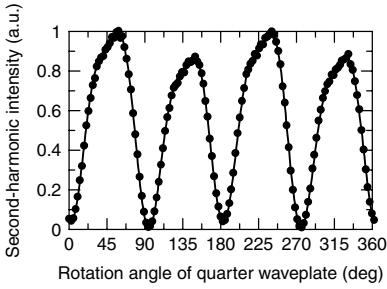
The largest components of the tensors χ^{em} and χ^{mee} are chiral. Furthermore, these components are larger than the chiral component of χ^{eee} . Hence the strongest magnetic quantities are directly associated with the chirality of



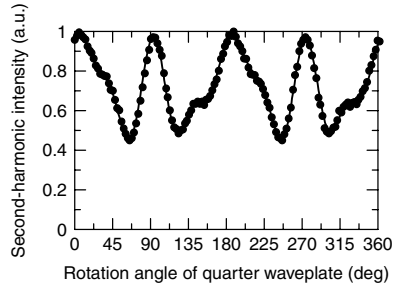
(a)



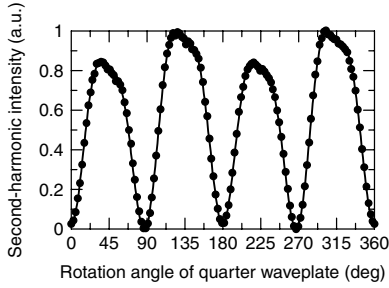
(e)



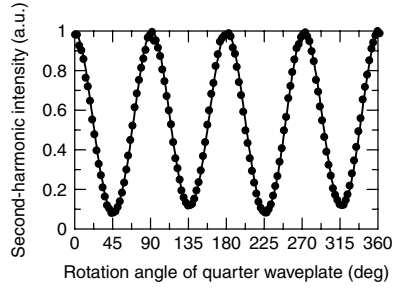
(b)



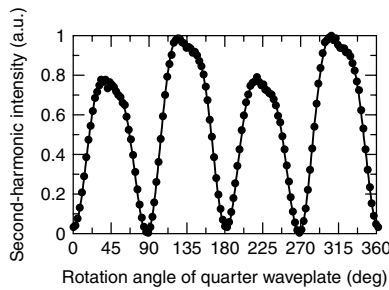
(f)



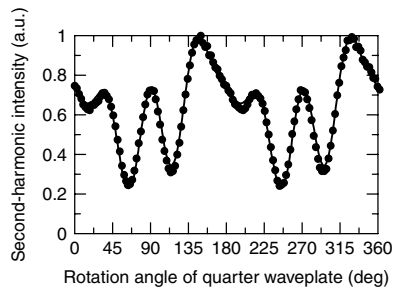
(c)



(g)



(d)



(h)

Table 9.5
 Tensor Components Determined Within the Electric Dipole Approximation and
 Normalized to $\chi_{xxz}^{eee} = 1^a$

Tensor Component ijk	Film Incidence, Transmitted	Film Incidence, Reflected	Glass Incidence, Transmitted	Glass Incidence, Reflected
zzz	$-0.483 + 1.143i$	$1.610 - 0.381i$	$-1.603 + 0.437i$	$0.996 - 0.090i$
xxz	1.00	1.00	1.00	1.00
zxx	$0.991 - 0.050i$	$0.918 - 0.038i$	$0.812 + 0.073i$	$1.174 - 0.331i$
xyz	$0.109 + 0.060i$	$0.129 + 0.038i$	$0.106 + 0.061i$	$0.090 + 0.084i$

^a The four independent solutions were obtained by considering each measured signal separately.

Table 9.6
 Independent Components of Tensors χ^{eee} , χ^{eem} , and χ^{mee} in Geometry of
 Figure 9.17^a

Tensor	Component	Determined Value	Magnitude (%)
χ^{eee}	$zzz(*)$	$1.571 - 0.583i$	100
	$xxz(*)$	1.00	60
	$zxx(*)$	$1.034 - 0.136i$	62
	$xyz(*)$	$0.110 + 0.065i$	7.6
χ^{eem}	$zzz(*)$	$0.354 - 0.152i$	23
	$zxx(*)$	$0.194 - 0.068i$	12
	$xxz(*)$	$0.049 - 0.069i$	5.1
	xxz	$-0.011 + 0.014i$	1.1
	$xyz(*)$	$0.019 - 0.102i$	6.2
	xzy	$-0.015 + 0.223i$	13
	zxy	$0.051 + 0.083i$	5.8
χ^{mee}	$zzz(*)$	$0.163 - 0.195i$	15
	zxx	$-0.001 - 0.004i$	0.3
	xxz	$0.005 - 0.005i$	0.4
	xyz	$0.027 - 0.035i$	2.6

^a Boldface indicates a chiral component. The determined values are normalized to $\chi_{xxz}^{eee} = 1$. The magnitudes are normalized to that of χ_{zzz}^{eee} . An asterisk indicates the tensor components that are essential to our model.

Figure 9.18 Eight measured second-harmonic signals. Waveplate rotation angle of 0° corresponds to p -polarized fundamental field. Dots are experimental data and lines fit to Eq. 42 with polarization control by quarter waveplate. (a–d) Film-side incidence, (e–h) glass-side incidence; (a) and (e) transmitted s -polarized; (b) and (f) transmitted p -polarized; (c) and (g) reflected s -polarized; (d) and (h) reflected p -polarized.

the material. This result is in agreement with the interpretation that large magnetic effects in chiral materials arise from the effective charge displacement along a helical path. For a racemic (50/50) mixture of the two enantiomers, the chiral components would vanish by symmetry, and the relative importance of magnetic contributions would be reduced. The magnitude of the largest magnetic tensor component is $\sim 20\%$ of that of the largest electric component. This large value could be due to a near-random distribution of the nonlinear chromophores in the polymer film that tends to suppress the electric dipole nonlinearity. The absolute magnitude of the χ_{zzz}^{eee} was determined to be on the order of 9 pm/V. Therefore, the highest magnetic dipole component would be on the order of 2 pm/V. The magnitude of this value suggests that magnetic dipole contributions to the nonlinearity can be useful for nonlinear optical applications.

4.3 Direct Evidence of Failure of Electric Dipole Approximation in Second-Harmonic Generation from Chiral Polymer Film

In the previous section, it was shown that in case of Langmuir–Blodgett films of an enantiomerically pure poly(isocyanide) (see also Figure 9.14), magnetic dipole contributions to the nonlinearity must be included to properly explain the experimental results. However, the evidence of contributions beyond electric dipoles in second-harmonic generation was only obtained by a detailed comparison of several different second-harmonic signals. In this section, we investigate second-harmonic generation from thin films of a chiral poly(thiophene) with very strong (linear) optical activity. More specifically we used Langmuir–Blodgett films of the regioregular chiral poly{3-[2-((S)-2-methylbutoxy)ethyl]thiophene} (PT, Figure 9.19). In the LB films of the enantiomerically pure polymer, several individual second-harmonic signals contain direct evidence of significant contributions beyond the electric dipole approximation, which is consistent with the very strong optical activity of the poly(thiophene). This polymer with $M_n = 16,900 \text{ g mol}^{-1}$ possesses a regioselectivity of more than 98% for the head-to-tail coupling.^{40,41} In good solvents, like CHCl_3 , the polymer is in a random coil conformation and does not exhibit optical activity in its $\pi-\pi^*$ transition. However, in the solid state, in poor solvents, or in appropriate combinations of solvents, like CHCl_3 –MeOH, the polymer is aggregated and the chiral side groups induce an enormous optical activity in the $\pi-\pi^*$ transition of the poly(thiophene). This association with a chiral conformation is accompanied by a strong solvatochromism. The Langmuir–Blodgett films have a purple/red color ($\lambda_{\text{max}} = 512 \text{ nm}$), while the random coil conformation has an orange/yellow color ($\lambda_{\text{max}} = 445 \text{ nm}$). The polymer in a 40% CHCl_3 –60% MeOH has an $[\alpha]_{513}^{22} = +140,000$ and a g -value ($\Delta\epsilon/\epsilon$) = 2×10^{-3} . These high values imply that magnetic dipole

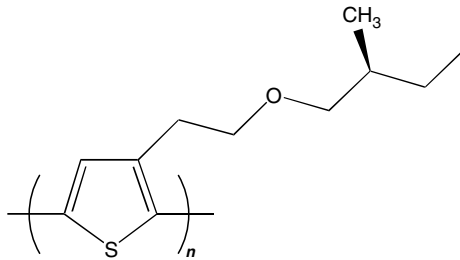


Figure 9.19 Chemical structure of poly{3-[2-((*S*)-2-methylbutoxy)ethyl]thiophene}. Number of repeating units is ~ 50 .

contributions significantly affect the linear optical properties. These strong magnetic effects arise from the character of the $\pi-\pi^*$ transition, which corresponds to the displacement of the electrons along the helical conjugated backbone of the polymer.

To prepare the Langmuir–Blodgett films, the polymer is dissolved in chloroform and spread on the water surface of a Langmuir–Blodgett trough. In chloroform, PT is present in the random coil conformation. However, upon evaporation of the solvent, PT folds into a chiral conformation and changes color from yellow to purple. The surface pressure is increased to 10 mN/m and the polymer forms a rigid layer on the water surface. The layers are transferred on hydrophobic glass substrates by horizontal dipping.⁴² The films used in our experiments consist of 10 layers of PT of good optical quality and deep purple color. The purple color gives a clear indication of the chiral conformation of the associated polymer in the film.

The nonlinearity of the sample was analyzed using the experimental procedure described in Section 3.3: The polarization of the fundamental beam of a YAG laser was continuously varied by means of a quarter waveplate, and the intensity of the second-harmonic signal was measured as a function of the rotation angle of the quarter waveplate. The obtained polarization pattern were then fitted to Eq. (42), which yields the relative values of the expansion coefficients f , g , and h . The experimental results for the transmitted, glass-side-incidence, s -polarized signal are shown in Figure 9.20.

As stated before, the coefficients f , g , and h are linear combinations of the components of the tensors χ^{eee} , χ^{eem} , and χ^{mee} . For a system with C_∞ symmetry (i.e., chiral, isotropic surface symmetry) and s -polarized second-harmonic light detected in transmission, these coefficients are given by: (For the complete set of equations, see previous sections.)

$$f = -\sin \theta [-2\chi_{xyz}^{eee} \cos \theta - \chi_{xzx}^{eem} + \chi_{zzz}^{mee} \sin^2 \theta + \chi_{zxx}^{mee} \cos^2 \theta + 2\chi_{xxz}^{mee} \cos^2 \theta] \quad (45)$$

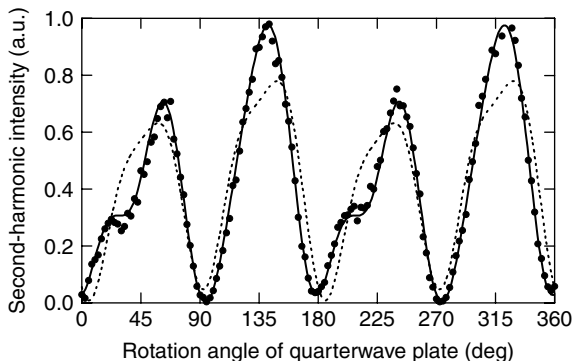


Figure 9.20 Intensity of *s*-polarized second-harmonic signal generated in transmitted direction for glass-side incidence as function of rotation angle of quarter waveplate. Note significant difference in response for right- (45° and 225°) and left-hand (135° and 315°) circularly polarized light. Points represent experimental data, solid line fit to the model described in Section 3 with nonvanishing g , and the dashed line the fit with vanishing g .

$$g = -\sin\theta[\chi_{xxz}^{em} + \chi_{zxx}^{me}] \quad (46)$$

$$h = \sin\theta[2\chi_{xxx}^{ee} - (\chi_{xzy}^{em} + \chi_{xyz}^{em})\cos\theta + 2\chi_{xyz}^{me}\cos\theta] \quad (47)$$

where θ is the angle of incidence and the surface normal is along the z direction. It is clear from Eqs. (45)–(47) that only the coefficient g depends exclusively on magnetic dipole contributions and must vanish in the electric dipole approximation. Therefore, a value of g different from zero provides direct evidence of the failure of the electric dipole approximation and of the presence of magnetic dipole contributions to the nonlinearity of the film.

The experimental results are fitted to the model described in Section 3 with f , g , and h as free complex parameters. Since we are only interested in the relative values of the coefficients, we finally normalize $h = 1$. This fit has been shown to be unique within an overall phase factor. The best fit is obtained for $f = -(0.055 \pm 0.004) - (0.098 \pm 0.004)i$, $g = -(0.378 \pm 0.013) - (0.300 \pm 0.008)i$, $h = 1$. Note that the coefficients f and g , which are only allowed by chirality, have significant out-of-phase parts with respect to the dominant coefficient h that does not rely on chirality. Such phase differences between the chiral and achiral coefficients are the origin of the circular-difference response evident in Figure 9.20.

It is noteworthy that the value of g is different from zero and relatively large. This result suggests that the electric and magnetic contributions to the nonlinearity are essentially of the same order of magnitude. This large value of the magnetic contributions is probably due to the near centrosymmetric arrangement of the monomer units in the helical polymer structure

that tends to suppress the electric dipole nonlinearity. To further illustrate the failure of the electric dipole approximation, we have also tried to fit the results by assuming that g vanishes. This fit is also shown in Figure 9.20 (dashed line) and clearly cannot explain the features of the experimental data. The importance of the expansion coefficient g was also verified for the other s -polarized signals (reflected direction and both reflected and transmitted directions for film-side incidence). In all cases the fitted value of g was found to be of the same order of magnitude than for the case of Figure 9.20.

4.4 Chiral 1,1'-Binaphthyl-Based Helical Polymers as Nonlinear Optical Materials

Binaphthyl molecules (chiral 2,2'-dihydroxy-1,1'-binaphthyl) have been studied by Hicks et al., who reported the first experimental observation of CD-SHG on surfaces.^{4,29,43} In this section, we investigate the nonlinear optical properties of a chiral 1,1'-binaphthyl-based helical polymer.

The polymer was prepared from chiral 1,1'-binaphthyl-based monomeric units and optimized for nonlinear optics by adding a π -conjugated bridge and electron donor and acceptor groups (see Figure 9.21). The monomer units can be considered as an ensemble of rigid electric dipole units that form a propellerlike three-dimensional conformation due to the chirality of the binaphthyl units.⁴⁴⁻⁴⁷ Therefore, the chirality of these systems is derived from the main-chain conformation. Again, the sample studied consisted of an LB film of the enantiomerically pure material and was investigated by continuous polarization measurements with a quarter waveplate. The symmetry of the LB film was also determined using SHG. The sample was irradiated with p -polarized fundamental light under 45° of incidence and the p -polarized SH light was

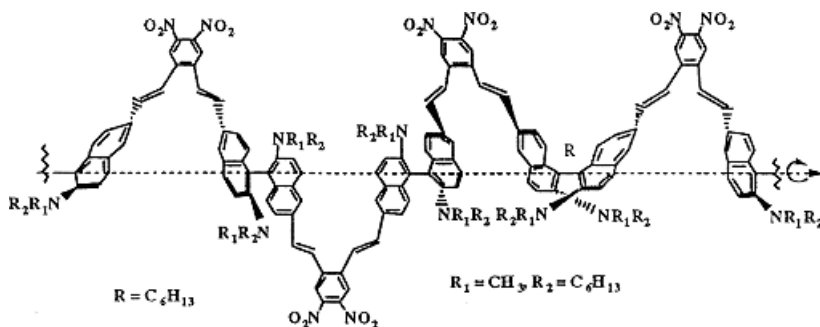


Figure 9.21 Chemical structures of helical polymer.

detected in transmission while rotating the samples about their surface normal. The shape of the rotation pattern is connected to the symmetry of the samples.⁴⁸ The symmetry of the films was found to be C_∞ with the surface normal as the ∞ -fold rotation axis.

A detailed analysis of the experimentally obtained polarization patterns allows to determine all susceptibility components of the LB films.^{16,49} The values of the susceptibility were calibrated using a quartz wedge ($d_{33} = 0.3$ pm/V) as reference.⁵⁰

From an analysis of the polarization dependence of the second-harmonic signals, we calculated the tensor components of the nonlinear susceptibility, $\chi_{ijk}^{(2)}$. Since the film has C_∞ symmetry, the nonvanishing components ijk are zzz , $zxx = zyy$, $xxz = xzx = yyz = yzy$, $xyz = xzy = -yxz = -yzx$ where z is along the surface normal, and x and y are the in-plane coordinates. The absolute values of the susceptibility components are given in Table 9.7. In remarkable contrast to the polyisocyanides⁵ and polythiophenes¹⁷ described in previous sections, no indications of magnetic contributions to the nonlinearity have been detected. We note also that in the study of monomeric binaphthyl molecules magnetic effects were also absent.

The values of the susceptibility components, between 2 and 35 pm/V, although resonantly enhanced, are quite large for a polymer system that differs significantly in chemical structure from the side-chain polymers traditionally used in nonlinear optics.⁵¹ Furthermore, the high values of the xxz , zxx , and zzz components suggest favorable ordering of the polymer chromophores in the LB films, which is rather unexpected based on the chemical structure of the polymer. The chirality of the LB film is reflected by the presence of a nonnegligible xyz component of 2 pm/V. Chirality also manifests itself in a difference in second-harmonic efficiency when the films are irradiated with left- and right-hand circularly polarized light. The CD effects were as high as 60%,⁵² expressing the role of chirality in these films. No CD effects were observed for films of the racemic mixtures.

Table 9.7
Absolute Values of Second-Order Susceptibility Components of Helical Polymer
Shown in Figure 9.21, Classification of Components as Chiral or Achiral

Second-Order Susceptibility Component χ_{ijk}	Absolute Value (pm/V)	Classification
xyz	2	Chiral
xxz	7	Achiral
zxx	5	Achiral
zzz	35	Achiral

4.5 Study of Chiral Helicenebisquinone Derivative

The systems discussed up to now all showed chiral susceptibilities that were of the same order of magnitude or smaller than the achiral susceptibility components. The system that we discuss in this section has chiral susceptibilities that dominate the nonlinear optical response.⁵³ The material is a chiral helicenebisquinone derivative shown in Figure 9.22. In bulk samples, the nonracemic, but not the racemic, form of the material spontaneously organizes into long fibers clearly visible under an optical microscope. These fibers comprise columnar stacks of helicene molecules.^{54,55} Similar columnar stacks self-assemble in appropriate solvents, such as *n*-dodecane, when the concentration exceeds ~ 1 mM. This association can be observed by a large increase in the circular dichroism (CD) of the solutions.

Langmuir–Blodgett films were prepared by spreading a 2×10^{-4} M solution of the enantiomerically pure helicenebisquinone in chloroform onto a water surface. After evaporation of the solvent, the monolayer was compressed to a surface pressure of 20 mN/m. After stabilization for 30 min, the monolayers were transferred by the horizontal dipping method onto glass substrates, treated with octadecyltrichlorosilane to make them hydrophobic.

The symmetry of the LB films was determined by polarized ultraviolet–visible (UV–Vis) absorption spectroscopy, optical rotation, and second-harmonic generation. All studies showed that the constructed LB films are anisotropic in the plane of the film and that the symmetry of the film is C_2 with the twofold rotation axis perpendicular to the film plane. For example, when the SH intensity is plotted as a function of the azimuthal rotation angle (rotation around an axis perpendicular to the plane of the film), the twofold symmetry becomes evident (Figure 9.23). Isotropic films generate an SH signal independent of the azimuthal rotation angle. On the other hand, the LB

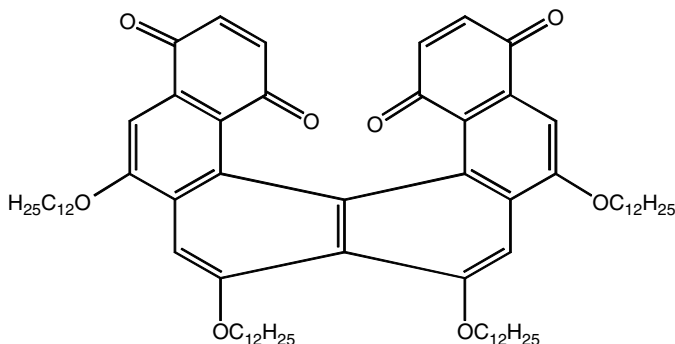


Figure 9.22 Chemical structure of the helicenebisquinone derivative.

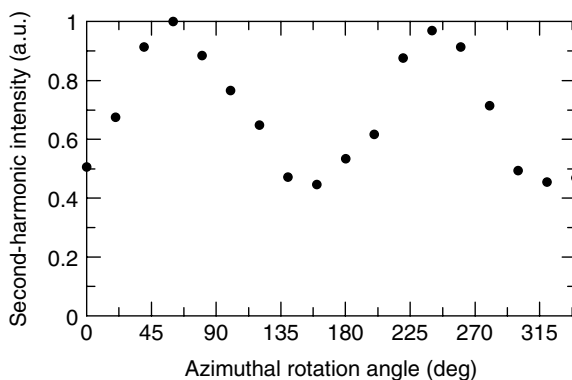


Figure 9.23 *s*-Polarized second-harmonic signal detected in transmitted direction as function of the azimuthal rotation angle. Twofold pattern clearly indicates C_2 symmetry of sample.

films of the helicene generate an orientation-dependent signal. The twofold symmetry pattern clearly suggests a C_2 symmetry.

A striking observation was that the strongest second-harmonic signal from a nonracemic film was approximately 1000 times as intense as that from a similar racemic film. This corresponds to a ~ 30 -fold enhancement in the value of the susceptibility. This enhancement is extraordinary because the individual molecules in both films have the same chemical structure. This observation is an important indication of the role of supramolecular organization for enhancing chirality effects. For the nonracemic sample, the second-harmonic signal was the strongest when the incident beam was *p* polarized and the second-harmonic beam was *s* polarized (*p* in–*s* out), whereas, for the racemic sample, the signal was strongest when both beams were *p* polarized (*p* in–*p* out). The presence of a nonvanishing *p* in–*s* out signal is due to components of the second-order susceptibility tensor that are nonvanishing only in the presence of chirality (chiral components).⁵³ The *p* in–*p* out signal, however, is allowed for all types of films and thus is due to the achiral components of the susceptibility tensor. These results suggest that in the nonracemic samples, the dominant part of the susceptibility tensor is associated with chirality. In the racemic samples, this part must cancel. To analyze this issue further, we investigated whether the dominant components of the second-order susceptibility tensor are only allowed by chirality. Although separating the chiral and achiral tensor components is straightforward for thin films that are isotropic, in-plane anisotropy significantly complicates such separation.⁵⁶ For such samples, the analysis of the nonlinear optical response becomes more involved because lowering of the in-plane symmetry introduces more independent components of the susceptibility tensor, which must be accounted for in the analysis. A slightly

modified measurement technique was used to analyze chiral anisotropic thin films, which allows the determination of the second-order susceptibility components and the separation between the contributions from both chirality and anisotropy. The analysis shows that the nonlinearity of the nonracemic samples is dominated by the chiral tensor components. Thus, the chirality of the nonracemic sample contributes significantly to the different NLO responses of the racemic and nonracemic samples. That it is essentially the sole factor responsible for the difference was verified by observing that the absolute signal levels of the p in- p out signals averaged over the in-plane rotation angle, were, within 20% error, equal for the racemic and nonracemic samples. Hence the achiral parts of the nonlinearity are essentially the same for the racemic and nonracemic samples. Why the chiral susceptibility components are large is, however, not explained by these results. A series of spectroscopic measurements combined with AFM (atomic force microscopy) and X-ray diffraction studies suggested that the primary explanation for the high second-order NLO response of the helicenes is the supramolecular aggregation into columnar stacks with large chiral (χ_{xyz} -type) nonlinear tensor components. Examples of such stacks, visualized by AFM, are shown in Figure 9.24 for racemic and nonracemic films. Spontaneous chiral segregation⁵⁷ probably occurs in the racemic films, with each enantiomer aggregating with itself and maintaining the large chiral components. In the racemic sample, however, these dominant components of the two enantiomers are equal in magnitude but opposite in sign, which lowers the overall NLO response. This principle is demonstrated in Figure 9.25. We prepared a series of multilayer LB films of the helicenebisquinone comprised of both enantiomers. The films were made of units of four molecular layers of a single enantiomer. We had two different

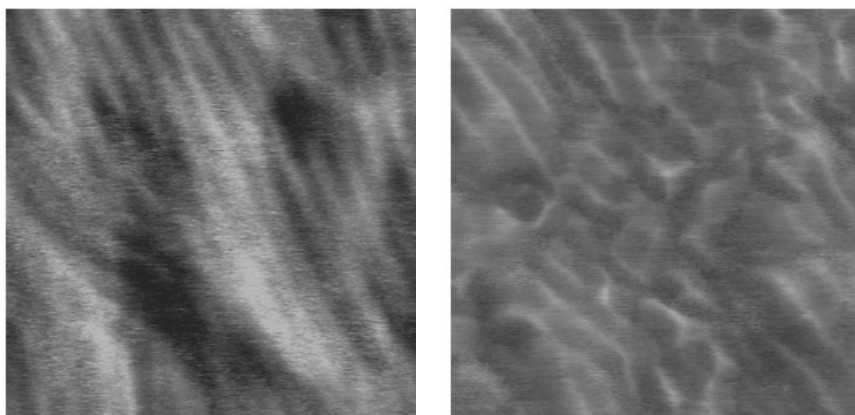


Figure 9.24 AFM images of racemic and nonracemic LB film of helicenebisquinone.

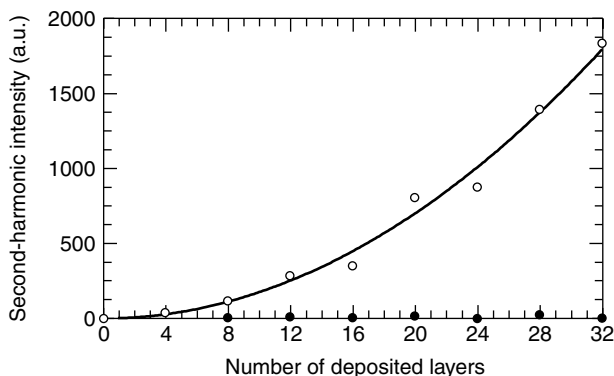


Figure 9.25 Second-harmonic intensity of LB films as function of number of layers: $R/S\dots$ structures (open dots) and $R/R\dots$ structures (filled dots). Solid line is quadratic fit of data points for $R/R\dots$ structures.

units as building blocks: One unit composed of the R enantiomer and one of the S enantiomer. As such, films were made with up to 8 units, that is, 32 layers. We used either the same units ($R/R/R\dots$) or alternated the units ($R/S/R\dots$). For the first type of film the signal should increase quadratically with the number of layers. On the other hand, the signal should vanish if the number of R units is equal to the number of S units. This behavior was experimentally observed and is shown in Figure 9.25.

4.6 Study of Biological Sample with Nonlinear Optical Activity

The combination of the surface specificity of SHG and nonlinear optical activity suggests a new tool to study biological samples. For example, the strength of nonlinear optical activity as a probe of chiral environment of biological samples was recently demonstrated by studying circular-difference effects in second-harmonic generation from bacteriorhodopsin.⁵⁸ Bacteriorhodopsin is the light-energy transducing protein present in the purple membrane of halophilic bacteria. In the membrane the protein is arranged into clusters of three that show stronger optical activity than individual protein molecules. Traditional CD spectra of suspensions of purple membrane in water typically show a relative circular-difference effect $\Delta\epsilon/\epsilon = 0.1\%$. The sample investigated consisted of bacteriorhodopsin molecules embedded in Langmuir–Blodgett films of soya phosphatidylcholine. In such a film the bacteriorhodopsin molecules can exhibit local ordering in a lattice similar to the one that occurs in purple membrane. These samples were investigated by continuous polarization measurements. The chirality of the sample was clearly reflected by a strong asymmetry in the polarization patterns.

Crawford et al.²⁴ explored the possibility of SHG-CD and SHG-ORD to study biological samples. They studied the dipeptide (*tert*-butyloxycarbonyl)tryptophanyltryptophan adsorbed at an air–water and a heptane–water interface. A dye laser that operated in the wavelength region 550–580 nm was used to record SHG-CD and SHG-ORD spectra. The SHG spectra from the *LL* and *DD* enantiomers showed equal but opposite dependences on the handedness of the fundamental laser beam and the *DL* diastereoisomer gave rise to different SHG spectra.²⁴

5 CHIRAL MATERIALS FOR SECOND-ORDER NONLINEAR OPTICAL APPLICATIONS

Second-order nonlinear optics (NLO) has several applications in the field of optoelectronics.¹¹ Several of these nonlinear processes are straightforward to experimentally demonstrate but their application in devices has been hampered by the lack of appropriate materials. Necessary requirements for second-order nonlinear optical materials include the absence of centrosymmetry, stability (thermal and mechanical), low optical loss, and large and fast nonlinearities.⁸

Perhaps the most stringent requirement for second-order NLO is the absence of centrosymmetry. On a molecular level, this has been achieved by connecting electron donor and acceptor groups by a highly polarizable π -conjugated system, yielding strongly dipolar molecules. On a macroscopic level the centrosymmetry must be broken artificially by techniques such as aligning molecular dipoles in an external electric field (poling) or by depositing Langmuir–Blodgett films or self-assembled films.^{8,11} These techniques result in noncentrosymmetric media with polar order. Unfortunately, several of these systems are thermodynamically unstable and therefore often not useful for applications. It would be beneficial to have noncentrosymmetric systems with no polar order. In fact, polar order is not required for a material to be noncentrosymmetric.⁹ For example, chiral materials comprised of enantiomerically pure chiral molecules are inherently noncentrosymmetric. Accordingly they give rise to second-order nonlinear optical effects even in the absence of polar order. In fact, frequency mixing has been observed in isotropic solutions of chiral sugar molecules and the electro-optic effect has been predicted to occur in isotropic media.^{59,60} A significant advantage of chiral apolar media as compared to traditional polar materials is their inherent thermodynamic stability. Furthermore, the susceptibility coefficients related to chirality can be quite large. In addition, the nonlinear optical properties of chiral molecules and polymers can be significantly enhanced by optimizing magnetic dipole contributions to the nonlinearity, as was shown in the previous section for chiral poly(isocyanide)s and polythiophenes. Therefore, chirality can be a valuable

alternative in the search for new second-order NLO materials. In the next section, we give an overview of the role of chirality in the field of second-order nonlinear optics and the potential applications of chiral materials in this field.

5.1 Second-Order Nonlinear Optics in Chiral Isotropic Bulk Media

As a particular example of materials with high spatial symmetry, we consider first an isotropic chiral bulk medium. Such a medium is, for example, an isotropic solution of enantiomerically pure molecules. Such material has arbitrary rotations in three dimensions as symmetry operations. Under rotations, the electric and magnetic quantities transform similarly. As a consequence, the nonvanishing components of $\chi^{(2),eee}$, $\chi^{(2),eem}$, and $\chi^{(2),mee}$ are the same. Due to the isotropy of the medium, each tensor has only one independent component of the xyz type:

$$\chi = \chi_{xyz} = \chi_{yzx} = \chi_{zxy} = -\chi_{xzy} = -\chi_{yxz} = -\chi_{zyx}$$

However, the components of the $\chi^{(2),eee}$ tensor are chiral (i.e., only present in a chiral isotropic medium), whereas the components of the tensors $\chi^{(2),eem}$ and $\chi^{(2),mee}$ are achiral (i.e., present in any isotropic medium, chiral or achiral). Hence, only the electric dipole response of chiral isotropic materials is related to chirality. The experimental work on chiral polymers described in Section 4 showed that large magnetic contributions to the nonlinearity are due to chirality. However, such contributions will therefore not survive in chiral isotropic media. In this respect, the electric dipole contributions associated with chirality may prove more interesting for applications.

In the electric dipole approximation, the polarization can in general (for any second-order nonlinear optical process) be written as⁹

$$\mathbf{P}(\omega_p + \omega_q) = 2\chi^{eee} \mathbf{E}(\omega_p) \times \mathbf{E}(\omega_q)$$

From the form of the polarization it is clear that in order to observe any nonlinear optical effect, the input beams must not be copropagating. Furthermore, nonlinear optical effects through the tensor χ^{eee} requires two different input frequencies (otherwise, the tensor components would vanish because of permutation symmetry in the last two indices, i.e., $\chi_{ijk}^{(2),eee} = \chi_{ikj}^{(2),eee}$). For example, sum-frequency generation in isotropic solutions of chiral molecules through the tensor χ^{eee} has been experimentally observed, and the technique has been proposed as a new tool to study chiral molecules in solution.^{59,61} From an NLO applications point of view, however, this effect is probably not very useful because recent results suggest that the response is actually very low.⁶²

Another related effect is the possibility of the electro-optic effect in chiral isotropic media through the tensor χ^{eee} .⁶⁰ The effect will be nonvanishing when material damping is properly accounted for. By using a standard density matrix treatment of nonlinear optics to calculate the electro-optic susceptibility of chiral isotropic media, several interesting effects were predicted, including the reversal of the real and imaginary parts of the susceptibility, dephasing induced resonances and electro-optically induced gain. However, the validity of the density matrix formalism in treating quantum-mechanical damping in general and the existence of the electro-optic effect in chiral isotropic media in particular has recently been challenged.⁶³ Although the use of isotropic materials in second-order nonlinear optics would be beneficial in the sense that such materials are thermodynamically stable, we are not aware of any isotropic system with a second-order NLO response that is actually useful for applications.

5.2 Second-Order Nonlinear Optics in Chiral Thin Films

Traditional materials used for second-order nonlinear optics usually consist of thin films in which the molecules have a net orientation along the film normal, and the samples thus have polar ordering. However, in several practical situations it would be beneficial to relax the requirement of polar ordering along the surface normal. Removal in polar ordering would introduce a twofold rotation axis in the plane of the film. For chiral molecules this would result in a sample belonging to the D_∞ symmetry group. For achiral molecules the sample would have a $D_{\infty h}$ symmetry. However, only the D_∞ symmetry allows for second-order nonlinear optical processes within the electric dipole approximation. Therefore, chirality can be used to significantly relax the requirement of polar ordering. The nonvanishing tensor components for a film with D_∞ symmetry are the same as for a chiral isotropic bulk material. The nonlinear optical properties of such a system have recently been investigated. The material used was the chiral helicenebisquinone shown in Figure 9.1.⁶⁴ The material was spin coated from a concentrated solution of chloroform onto hydrophobic glass slides, yielding films with thicknesses from 0.1 to 1.2 μm . Alternatively, similar films were prepared by placing a small amount of material between two glass slides followed by heating above the melting point of the helicenebisquinone (211°C).

To analyze the second-order susceptibility, the symmetry of the films was first analyzed by measuring the intensities of the second-harmonic light. The sample was irradiated with polarized light from a Nd:YAG laser incident at 45°, and the second-harmonic light emanating from the sample was detected while the sample was rotated around its surface normal. No variation in the second-harmonic intensity was observed as the sample was rotated, indicating

that the samples were isotropic in the plane of film. Hence, the symmetry of the sample is either C_∞ or D_∞ . To discriminate between these symmetries, the dependence of the polarization of the second-harmonic light on the polarization of the fundamental beam was analyzed. For an s -polarized fundamental, the p - and s -polarized second-harmonic signals were always zero. For a p -polarized fundamental, only the s -polarized second-harmonic was nonvanishing. The only symmetry compatible with this observation is D_∞ , which is chiral. For this symmetry there is only one nonvanishing susceptibility component, χ_{xyz} (the z coordinate was taken perpendicular to the film plane, and x and y in the plane of the film). By calibrating the p - s signal against a quartz reference, a value of 2 pm/V was found for the χ_{xyz} . Such a value is remarkably high, considering that no external force (such as from electric field poling) was used to align the sample. The remarkable stability of such a sample was demonstrated as follows: Heating the films up to 211°C has no significant effect on their SH efficiency. Above 211°C, that is, the melting point of the material, the SH signal drops to zero. However, after cooling the samples again below 211°C, the SH signal regains its original value.

Because of their acceptable nonlinearity and because they are so thermally stable, this type of compounds might be useful in nonlinear optical and photonic applications.

The same material can also be used to achieve a new way of quasi-phase matching.⁶⁵ Quasi-phase matching is important in frequency conversion processes in which the phase relation between the nonlinear source polarization and the generated field can only be maintained over the distance of a coherence length. However, by reversing the sign of the nonlinearity after each coherence length, the phase relation between the source and the generated field will be restored, allowing the nonlinear signal to grow quasi-continuously. In systems with polar order, for example, electric-field-poled materials, this can be achieved by periodically poling the material. In chiral materials, the second-order nonlinear optical coefficients associated with chirality differ in sign for the two enantiomers. Therefore, quasi-phase-matched frequency conversion in periodically alternating stacks of the enantiomers of a chiral material should be possible. Since the nonlinearity in films of the helicenebisquinone is dominated by chirality, this material is an excellent candidate to demonstrate this new type of quasi-phase matching. In fact, quasi-phase matching in LB films of a helicenebisquinone has recently been demonstrated.⁶⁵ A series of samples was investigated in which equally thick stacks of the two enantiomers alternated. Quasi-phase-matching was verified by selecting the second-harmonic signal associated with chirality and measuring its intensity as a function of the thickness of the stacks. When the thickness of the stacks equals the coherence length, the second-harmonic signal grows continuously with the number of stacks.

6 CONCLUSIONS

In this chapter we have described the combination of two different fields of research, that is, second-order nonlinear optics and chirality. The first part of the chapter deals with nonlinear optical techniques that can be used to study chirality. We have shown that optical activity effects in second-order nonlinear optics, and more specifically in second-harmonic generation, provide a new tool to study chirality. These nonlinear optical activity effects manifest themselves as rotation of the polarization of the second-harmonic light with respect to the fundamental light, a different efficiency of second-harmonic generation for excitation with left- or right-hand circularly polarized light (circular-difference effects) or a different efficiency of second-harmonic generation for excitation with $+45^\circ$ and -45° linearly polarized light (linear-difference effects). We have given an overview of the theoretical formalism that has been used to treat such effects and the experimental procedures that can be used to study nonlinear optical activity. From the experimental examples, it is clear that nonlinear optical activity has the potential to evolve into an extremely valuable method to study surface chirality since traditional methods such as circular dichroism or optical rotation are not surface sensitive. However, several important issues still need to be resolved. For example, the relation between the magnitude of magnetic susceptibility components and molecular structure is largely unknown. We are presently at a point where we have established the existence and importance of such contributions in chiral materials, but in order to use nonlinear optical activity as a routine characterization method, a better understanding is needed. Furthermore, a clear relation between traditional optical activity and nonlinear optical activity is needed to establish nonlinear optical activity as a chiral characterization tool. Future research in this field will need to focus on several different aspects. The usefulness of nonlinear optical activity should be clearly demonstrated in research fields such as biochemistry, catalysis, or pharmacology. For example, the study of configurational changes in proteins adsorbed at surfaces or the determination of the enantiomeric excess in pharmaceutical products should help in establishing nonlinear optical activity as a powerful tool of research.

The study of chiral materials with nonlinear optical properties might lead to new insights to design completely new materials for applications in the field of nonlinear optics and photonics. For example, we showed that chiral supramolecular organization can significantly enhance the second-order nonlinear optical response of materials and that magnetic contributions to the nonlinearity can further optimize the second-order nonlinearity. Again, a clear relationship between molecular structure, chirality, and nonlinearity is needed to fully exploit the properties of chiral materials in nonlinear optics.

ACKNOWLEDGMENTS

This work was made possible by research grants from the Fund for Scientific Research—Flanders (FWO-V, Nos. G.0338.98 and 9.0407.98), from the Belgian government (IUAP P4/11), and from the University of Leuven (GOA/2000/03). T.V. is a postdoctoral fellow of the Fund for Scientific Research—Flanders. We gratefully acknowledge the research groups of T. J. Katz, E. W. Meijer, R. J. M. Nolte, and L. Pu for providing us with the chiral polymers and molecules described in this work.

REFERENCES

1. Lakhtakie, A. (Ed.). *Selected Papers on Natural Optical Activity*, SPIE, Bellingham, Washington, 1990.
2. Wagnière, G. *J. Chem. Phys.* **1982**, *77*, 2786.
3. Meijer, E. X.; Havinga, E. E.; Rikken, G. L. J. A. *Phys. Rev. Lett.* **1990**, *65*, 37.
4. Petralli-Mallow T.; Wong, T. M.; Byers, J. D.; Yee, H. I.; Hicks, J. M. *J. Phys. Chem.* **1993**, *97*, 1383.
5. Kauranen, M.; Verbiest, T.; Meijer, E. W.; Havinga, E. E.; Teerenstra, M. N.; Schouten, A. J.; Nolte, R. J. M.; Persoons, A. *Adv. Mater.*, **1995**, *7*, 641.
6. Verbiest, T.; Kauranen, M.; Maki, J. J.; Teerenstra, M. N.; Nolte, R. J. M.; Persoons, A. *J. Chem. Phys.* **1995**, *103*, 8296.
7. Byers, J. D.; Yee, H. I.; Hicks, J. M. *J. Chem. Phys.* **1994**, *101*, 6233.
8. Verbiest, T.; Houbrechts, S.; Kauranen, M.; Clays, K.; Persoons, A. *J. Mater. Chem.* **1997**, *7*, 2175.
9. Kauranen, M.; Verbiest, T.; Persoons, A. *J. Nonlinear Opt. Phys. Mater.* **1999**, *8*, 171.
10. Pattanayak, D. N.; Birman, J. L. *Phys. Rev. B* **1981**, *24*, 4271.
11. Prasad, P. N.; Williams, D. J. *Introduction to Nonlinear Optical Effects in Molecules and Polymers*. Wiley Interscience, New York, 1991.
12. Shen, Y. R. *The Principles of Nonlinear Optics*, Wiley Interscience, New York, 1984.
13. Andrews, D. L.; Thirunamachandran, T. *J. Chem. Phys.* **1979**, *70*, 1027.
14. Lam, Y. T.; Thirunamachandran, T. *J. Chem. Phys.* **1982**, *77*, 3810.
15. Wagnière G. *Chem. Phys.* **1981**, *54*, 411.
16. Kauranen, M.; Maki, J. J.; Verbiest, T.; Van Elshocht S.; Persoons, A. *Phys. Rev. B* **1996**, *55*, R1985.
17. Van Elshocht S.; Verbiest, T.; Kauranen, M.; Persoons, A.; Langeveld-Voss B. M. W.; Meijer, E. W. *J. Chem. Phys.* **1997**, *107*, 8201.
18. Maki, J. J.; Persoons, A. *J. Chem. Phys.* **1996**, *104*, 9340.
19. Bloembergen, N.; Pershan, P. S. *Phys. Rev.* **1962**, *128*, 606.
20. Jackson, J. D., *Classical Electrodynamics*, Wiley, New York, 1962.
21. Kauranen, M.; Verbiest, T.; Maki, J. J.; Persoons, A. *J. Chem. Phys.* **1994**, *101*, 8193.
22. Kauranen, M.; Verbiest, T.; Persoons, A. *J. Mod. Opt.* **1998**, *45*, 403.

23. Maki, J. J.; Verbiest, T.; Kauranen, M.; Van Elshocht S.; Persoons, A. *J. Chem. Phys.* **1996**, *105*, 767.
24. Crawford, M. J.; Haslam, S.; Probert, J. M.; Gruzdkov, Y. A.; Frey, J. G. *Chem. Phys. Lett.* **1994**, *229*, 260.
25. Maki, J. J.; Kauranen, M.; Verbiest, T.; Persoons, A. *Phys. Rev. B* **1997**, *55*, 5021.
26. Verbiest, T.; Kauranen, M.; Van Rompaey Y.; Persoons, A., *Phys. Rev. Lett.* **1996**, *77*, 1456.
27. Fox, J. M.; Katz, T. J.; Van Elshocht S.; Verbiest, T.; Kauranen, M.; Persoons, A.; Thongpanchang, T.; Krauss, T.; Brus, L. *J. Am. Chem. Soc.* **1999**, *121*, 3453.
28. Verbiest, T.; Kauranen, M.; Maki, J. J.; Teerenstra, M. N.; Nolte, R. J. M.; Persoons, A. *J. Chem. Phys.* **1995**, *103*, 8296.
29. Byers, J. D.; Yee, H. I.; Petralli-Mallow T.; Hicks, J. M. *Phys. Rev. B* **1994**, *49*, 14643.
30. Teerenstra, M. N.; Hagting, J. G.; Oostergetel, G. T.; Schouten, A. J.; Devillers, M. A. C.; Nolte, R. J. M. *Thin Solid Films* **1994**, *248*, 110.
31. Byers, J. D.; Yee, H. I.; Hicks, J. M. *J. Chem. Phys.* **1994**, *101*, 6233.
32. Hecht, L.; Barron, L. D. *Mol. Phys.* **1996**, *89*, 61.
33. Maki, J. J.; Kauranen, M.; Persoons, A. *Phys. Rev. B* **1995**, *51*, 1425.
34. Kauranen, M.; Verbiest, T.; Persoons, A. *Nonlinear Opt.* **1994**, *8*, 243.
35. Pershan, P. S. *Phys. Rev.* **1963**, *130*, 919.
36. Roders, O.; Befort, O.; Marowsky, G.; Mobius, D.; Bratz, A. *Appl. Phys. B* **1994**, *59*, 537.
37. Geiger, F.; Stolle, R.; Marowsky, G.; Palenberg, M.; Felderhof, B. U. *Appl. Phys. B* **1995**, *61*, 135.
38. Dick, B.; Gierrulski, A.; Marowsky, G.; Reider, G. A. *Appl. Phys. B* **1985**, *38*, 107.
39. Heinz, T. F.; Tom, H. W. K.; Shen, Y. R. *Phys. Rev. A* **1983**, *28*, 1883.
40. Bouman, M. M.; Meijer, E. W. *Adv. Mater.* **1995**, *7*, 385.
41. Bouman, M. M.; Havinga, E. E.; Janssen, R. A. J.; Meijer, E. W. *Mol. Crystallogr. Liq. Crystallogr* **1994**, *256*, 439.
42. Roberts, G. *Langmuir-Blodgett Films*. Plenum, New York, 1990.
43. Byers, J. D.; Hicks, J. M. *Chem. Phys. Lett.* **1994**, *231*, 216.
44. Van Elshocht S.; Verbiest, T.; Kauranen, M.; Ma, L.; Cheng, H.; Musick, K. Y.; Pu, L.; Persoons, A. *Chem. Phys. Lett.* **1999**, *309*, 315.
45. Pu, L. *Acta Polymer* **1997**, *48*, 116.
46. Sheng, H.; Pu, L. *Macromol. Chem. Phys.* **1999**, *200*, 1274.
47. Musick, K. Y.; Hu, Q.-S.; Pu, L. *Macromolecules* **1998**, *31*, 2933; Ma, L.; Hu, Q.-S.; Vitharana, D.; Wu, C.; Kwan, C. M. S.; Pu, L. *Macromolecules* **1997**, *30*, 204.
48. Zhuang, X.; Wilk, D.; Marucci, L.; Shen, Y. R. *Phys. Rev. Lett.* **1995**, *75*, 2144.
49. Kauranen, M.; Maki, J. J.; Persoons, A. In *Nonlinear Optical Properties of Organic Materials VIII, Proceedings of the SPIE*, Vol. 2527. Möhlmann G. R. (Ed.). SPIE, Bellingham, Washington, 1995, p. 328.
50. Roberts, D. *IEEE J. Quantum Electron.* **1992**, *28*, 2057.
51. Wijekoon, W. M. K. P.; Wijaya, S. K.; Bhawalkar, J. D.; Prasad, P. N.; Penner, T. L.; Armstrong, N. J.; Ezenyilimba, M. C.; Williams, D. J. *J. Am. Chem. Soc.* **1995**, *118*, 4480.
52. Persoons, A.; Kauranen, M.; Van Elshocht S.; Verbiest, T.; Ma, L.; Pu, L.; Langeveld-Voss B. M. W.; Meijer, E. W. *Mol. Cryst. Liq. Cryst.* **1998**, *315*, 93.
53. Verbiest, T.; Van Elshocht S.; Kauranen, M.; Hellemans, L.; Snauwaert, J.; Nuckolls, C.; Katz, T. J.; Persoons, A. *Science* **1998**, *282*, 913.

54. Nuckolls, C.; Katz, T. J.; Castellanos, L. *J. Am. Chem. Soc.* **1996**, *118*, 3767.
55. Lovinger, A. J.; Nuckolls, C.; Katz, T. J. *J. Am. Chem. Soc.* **1998**, *120*, 264.
56. Sioncke, S.; Van Elshocht S.; Verbiest, T.; Persoons, A.; Kauranen, M.; Phillips, K. E. S.; Katz, T. J. *J. Chem. Phys.* **2000**, *113*, 7578.
57. Nassoy, P.; Goldman, M.; Bouloussa, O.; Rondelez, F. *Phys. Rev. Lett.* **1995**, *75*, 457.
58. Verbiest, T.; Kauranen, M.; Persoons, A.; Ikonen, M.; Kurkela, J.; Lemmetyinen, H. *J. Am. Chem. Soc.* **1994**, *116*, 9203.
59. Rentzepis, P. M.; Giorgmaine, J. A.; Wecht, K. W. *Phys. Rev. Lett.* **1966**, *16*, 792.
60. Beljonne, D.; Shuai, Z.; Brédas J. L.; Kauranen, M.; Verbiest, T.; Persoons, A. *J. Chem. Phys.* **1998**, *108*, 1301.
61. Yang, P.-K.; Huang, J. Y. *J. Opt. Soc. Am. B* **1998**, *15*, 1698.
62. Fischer, P.; Wiersma, D. S.; Righini, R.; Champagne, B.; Buckingham, A. D. *Phys. Rev. Lett.* **2000**, *85*, 4253.
63. Andrews, D. L.; Naguleswaran, S.; Stedman, G. E. *Phys. Rev.* **1998**, *A57*, 4925.
64. Verbiest, T.; Van Elshocht S.; Persoons, A.; Nuckolls, C.; Phillips, K. E.; Katz, T. J. *Langmuir* **2001**, *17*, 4685.
65. Busson, B.; Kauranen, M.; Nuckolls, C.; Katz, T. J.; Persoons, A. *Phys. Rev. Lett.* **2000**, *16*, 792.

SUBJECT INDEX

- A₆D peptide, self-assembled molecules, chirality characteristics, 317
- Absolute energy minima, growing chain chiral orientation, stereoselectivity, 14–21
- Accordion texture, ferroelectric banana phases, 510–512
- Achiral antiferroelectric smectic LC (AFLC):
bilayer smectics, 478–483
SmC₅P_A/SmC_AP_A antiferroelectric phases, 497–500
- Achiral systems:
liquid crystals:
B4 phase, 487–489
bent-core mesogens, 484–486
bilayer smectics, 478–483
Matsunaga diesters, 486–487
self-assembled discotics, 398–399
helicene self-assembly, 416–418
spontaneous reflection symmetry breaking, liquid crystals, 477–478
- Acrylate monomers, achiral liquid crystals, 481–483
- α-Agostic bond, homogeneous metallocenes, growing chain chiral orientation, 19–21
- Aldonamides, chiral self-assembly, 287–294
- 1-Alkenes:
chain-end controlled olefin polymerizations:
primary insertions, 49–51
secondary insertions, 51–54
homogeneous metallocenes, growing chain chiral orientation, 19–21
stereospecific polymerization, evolution, 7
- Alkene intermediates, site-controlled stereospecific polymerizations, homogeneous metallocenes, 14
- Alkyl(alkoxyphenyl)polysilane, optically active groups:
enantiopure chiral chains, 239
global-local conformation:
main-chain helicity, remote chiral group control, 242–243
substituent effects and cooperative helical order effect, 240–242
poly chiral aggregates:
chiroptical properties, 244–246
solvent effects, 248
switching and memory, 243–244
temperature effects, 246–248
poly molecular chirality recognition, 248–251
- Alkyl(phenyl)polysilane, optically active groups, 251–259
chiral-chiral substituents, copolymer UV and CD spectra, 253–254
copolymer UV and CD spectra, 255–256
Ising model, CD spectral analysis, 256–258
molecular mechanics calculation, 254–255
optically inactive homopolymer UV absorption, fluorescence spectra, and fluorescence anisotropy, 252–253
research issues, 258–259
- Amino acids, amphiphiles, chiral molecular self-assembly, 302–311
- Amorphous crystalline materials, disordered conformation, 121–124
- Amphiphiles, chiral molecular self-assembly:
carbohydrate amphiphiles, 287–301
aldonamides, 287–293
cerebrosides, 300–301
glycolipids, 293–299
peptide-based amphiphiles, 302–317
amino acids, 302–311
peptides, 311–317
- Amyloid fibrils, peptide amphiphiles, chiral molecular self-assembly, 311–317
- Amylose arylalkylcarbamates, chiral recognition, 179–180
- Amylose cycloalkylcarbamates, chiral recognition, 181
- Amylose phenylcarbamates, chiral recognition, 172–179
- Anisotropic chiral interactions:
cerebroside chirality, 300–301
nonlinear optics, helicenebisquinone derivative, 560–562
second-harmonic generation nonlinear optics (NLO), continuous polarization measurements, 540–541
self-assembled molecules, chirality characteristics, uniformly tilted membranes, 352–353
- Antichiral structures, crystalline polymers, macromolecular packing, 111–113
- Anticlinicity:
achiral smectic phases, 480–483

Materials-Chirality: Volume 24 of Topics in Stereochemistry,

Edited by Mark M. Green, R.J.M. Nolte, and E.W. Meijer

ISBN 0-471-05497-6 Copyright © 2003 John Wiley & Sons, Inc.

- Anticlinicity: (*Continued*)
 antiferroelectric liquid crystals, SmC_A^* phase, 471–474
 ferroelectric banana phase design, 504–512
 long-range positional three-dimensional order, up and down chains, 129–130
- Antiferroelectric liquid crystals:
 achiral structures, bilayer smectics, 478–483
 banana design, 493–495, 502–512
 SmC_A^* phase, 470–474
 $\text{SmC}_S\text{P}_A/\text{SmC}_A\text{P}_A$ phase, 496–500
 stereogenic elements, SmCP supermolecular diastereomers, 500–502
- Apolar media, chiral nonlinear optics, second-order applications, 563–566
- Approximated transition states, growing chain chiral orientation, stereoselectivity, 16–21
- Arylalkylcarbamates, chiral recognition, cellulose/amylose derivatives, 179–180
- Aspartic acid, self-assembled molecules, chirality characteristics, amino acid amphiphiles, 302–311
- Asymmetric patterns:
 chiral crystallization, helical chain conformation, 142–147
 crystalline polymers, symmetry breaking, 117–118
- Atactic polymers, chain conformation, 112–113
- Atomic force microscopy (AFM):
 nonlinear optics, helicenebisquinone derivative, 561–562
 optically active dialkylpolysilanes, molecular imaging, rodlike polysilanes, 222
 self-assembled molecules, chirality characteristics:
 aldonamides, 291–293
 amino acid amphiphiles, 309–311
 diacetylenic phosphonate lipids, 328–331
 peptide amphiphiles, 314–317
- Average long axis, banana phases, 490–495
- “Azimuthal anchoring”:
 banana phases, 491–495
 spontaneous reflection symmetry breaking, liquid crystals, 475–478
- B2 smectic phase:
 ferroelectric properties, 509–512
 spontaneous reflection symmetry breaking, 489–495
- B4 phase, achiral smectic phases, 487–489
- B7 phase, ferroelectric banana phases, 507–512
- Backbone structures:
 cholesteric handedness, helical polymers, 438–441
 helical self-assembly, chiral columns, 387–389
- Back-skip mechanism, growing chains, homogeneous metallocenes, 25–26
- “Banana leaf” texture, ferroelectric banana phases, 509–512
- Banana phases:
 achiral liquid crystals:
 B4 phase, 487–489
 bent-core mesogens, 484–486
 bilayer smectics, 478–483
 Matsunaga diesters, 486–487
 ferroelectric design, 502–512
- B-DNA, cholesteric handedness, helical polymers, 439–441
- Beer-Lambert law, optically active polysilanes, helical structure, 213–214
- Bent-core mesogens, achirality, 484–486
- Benzoate derivatives, chiral recognition, 170–172
- Bernoullian statistics, chirality polymerization mechanisms, 11
- Biaryl dopants:
 chiral molecule comparisons, 450–451
 thermotropic cholesterics, 443–446
 biaryl moiety, 447–450
- Biased chiral symmetry breaking, self-assembled molecules, 360–363
- Bilayered structures:
 ferroelectric banana phase design, 503–512
 long-range positional three-dimensional order, up and down chains, 128–130
 self-assembled molecules:
 chiral symmetry breaking, 359–360
 cylindrical vs. Gaussian curvature, 358–359
 diacetylenic phospholipids, 321–327
 nonchiral models, electrostatics, 343–344
 smectics, achiral antiferroelectric liquid crystals, 478–483
- Bile models, self-assembled molecules, chirality characteristics, steroid-based systems, 338–340
- 1,1'-Binaphthyl-based helical polymer, nonlinear optics (NLO), 557–558
- Biopolymers:
 nonlinear optics, 562–563
 optically active compounds, 210–211
- Biphenyl derivatives, thermotropic cholesterics, 448–450
- Birefringence:
 ferroelectric liquid crystals, smectic C phase (SmC), 470
 $\text{SmC}_S\text{P}_A/\text{SmC}_A\text{P}_A$ antiferroelectric phases, 499–500
- Bisignate Cotton circular dichroism:
 optically active polysilanes:
 dialkylpolysilanes, 230
 helical structure, 214
 poly chiral aggregates, switching and memory functions, 244
- Bistable blue texture, ferroelectric banana phases, 510–512
- Bistable switching, ferroelectric liquid crystals, smectic C phase (SmC), 470
- Bmcm space group, disordered conformation, crystalline polymers, 123
- Bolaamphiphiles, self-assembled molecules, chirality characteristics:
 amino acids, 309–311
 glycolipid, 293, 296–299
 nucleotides, 335–337
 peptide-based structures, 308–311
- Bow plane structures, banana phases, 491–495
 ferroelectricity, 502–512

- Bragg scattering technique, cholesteric handedness, 436
- Brookhart-type nickel catalyst, chain-end controlled polymerizations, primary 1-alkene insertions, 50–51
- β -sheets, self-assembled molecules, chirality characteristics, peptides, 311–317
- “Bulgy double helix,” self-assembled molecules, chirality characteristics, aldonamides, 289–293
- Bulk media, second-order nonlinear optics, 564–565
- 2-Butene copolymerization, metallocene symmetry, *E*–*Z* selectivity, 34–38
- Cahn-Ingold-Prelog rules, chirality polymerization mechanisms, 9–10
- Calorimetry data, diacetylenic phospholipid chiral self-assembly, 323–327
- Capacity factors, chiral recognition, 159–161
- ^{13}C NMR:
chiral recognition studies, 193–199
crystalline polymers, symmetry breaking, 114–118
disordered chain conformation, 103–105
kink-band disorder, 136–140
growing chain chiral orientation, stereoselectivity, 17–21
isotactic/syndiotactic structures, conformational energy calculations, 91
titanium trichloride catalysts, 40–42
- Carbamates, chiral recognition:
arylalkylcarbamates, 179–180
chromatographic studies, 187–190
cycloalkylcarbamates, 181
NMR studies, 190–199
phenylcarbamates, 172–179
- Carbohydrate amphiphiles, chiral self-assembly, 287–301
aldonamides, 287–293
cerebrosides, 300–301
glycolipids, 293–299
- Carbon triple bonds, phospholipid chiral molecular self-assembly, diacetylenic phospholipids, 318–327
- Cardanol compounds, self-assembled molecules, chirality characteristics, 298–299
- Catalyst chirality, stereospecific polymerizations:
chain-end controlled polymerizations, 48–61
conjugated diene, 57–61
olefins, 48–54
primary 1-alkene insertions, 49–51
secondary 1-alkene insertions, 51–54
styrene/substituted styrene syndiotactic polymerization, 54–57
mechanisms and elements, 9–13
site-controlled polymerizations, 13–48
heterogeneous catalysts, 38–46
magnesium chloride systems, 42–46
titanium trichloride systems, 39–42
homogeneous metallocenes, 13–38
back-skip of growing chain, 25–26
2-butene cyclopolymers, *E*–*Z* selectivity, 34–38
chain migratory insertion mechanism, 21–24
nonconjugated dienes, cyclopolymerization, 26–27
regioirregular insertion stereospecificity, 27–31
regiospecificity, symmetry dependence, 31–34
stereoselectivity mechanism, 14–21
stereospecific heterogeneous/homogeneous comparisons, 46–48
structure and properties, 2–9
- Cellulose aralkylcarbamates, chiral recognition, 179–180
- Cellulose cycloalkylcarbamates, chiral recognition, 181
- Cellulose esters, chiral recognition, 168–172
- Cellulose phenylcarbamates, chiral recognition, 172–179
- Central metal atom, chirality polymerization mechanisms, 9–10
- Centrosymmetry, chiral molecule nonlinear optics, 525–527
1,1'-binaphthyl-based helical polymer, 557–558
linear/circular polarized probes, comparison, 545–550
second-harmonic generation, 528–529
second-order applications, 563–566
isotropic bulk media, 564–565
thin films, 565–566
- Cerebrosides, chiral self-assembly, 300–301
- Chain-chain packing, cerebroside chirality, 300–301
- Chain conformation:
crystalline polymers:
alternating copolymers, 105–109
basic principles, 74–78
disordered conformations, 102–105
isotactic/syndiotactic polymers:
energy calculations, 84–92
helical conformation, 78–84
macromolecular packing, 110–113
optical activity and helical conformation, 93–94
polydienes, 94–102
optically active polysilanes, 211–213
self-assembled molecules, chirality characteristics:
aldonamides, 288–293
amino acid amphiphiles, 302–311
nucleotides, 335–337
- Chain-end controlled polymerizations:
catalyst chirality, 48–61
conjugated diene, 57–61
olefins, 48–54
primary 1-alkene insertions, 49–51
secondary 1-alkene insertions, 51–54
styrene/substituted styrene syndiotactic polymerization, 54–57
future research issues, 61–62
stereocontrol mechanisms, 10–11
- Chain migratory insertion mechanism, homogeneous metallocenes, site-controlled stereospecific polymerizations, 21–24

- Chemically defined lipid concentrate (CDLC), self-assembled molecules, chirality characteristics, steroid-based systems, 339–340
- “Chevron” structure:
achiral liquid crystals, 481–483
B2 smectic phases, 489–495
- Chiral crystalline, helical chain conformations, 142–147
- Chiral dopants:
biaryl comparisons, 450–451
cholesteric handedness, thermotropic characteristics, 441–451
noncooperative self-assembly, 399–407
- Chiral molecules:
nonlinear optics (NLO):
basic principles, 523–527
future research issues, 567
linear optics research, 521–522
magnetic dipole contributions, 529–530
molecular origins, 530–532
optical activity, 522–523
research background, 520–521
second-harmonic generation, 527–529, 535–541
1,1'-binaphthyl-based helical polymers, 557–558
biological sampling, 562–563
continuous polarization measurements, 538–541
electric dipole approximation failure, 554–557
electromagnetic second-order susceptibility tensors, quantitative determinations, 550–554
expansion coefficient determination, 541–544
experimental studies, 544–563
helicenebisquinone derivatives, 559–562
linearly/circularly polarized probes, 545–550
optical rotation effects, 537–538
second-order applications, 563–566
isotropic bulk media, 564–565
thin films, 565–566
theoretical formalism, 532–535
optically active polymers, 159–161
natural polymer derivatives:
polysaccharides, 168–201
cellulose/amylose arylalkylcarbamates, 179–180
cellulose/amylose
cycloalkylcarbamates, 181
cellulose/amylose phenylcarbamates, 172–179
cellulose esters, 168–172
chromatographic studies, 186–190
computational studies, 199–201
NMR studies, 190–199
oligosaccharides and cyclodextrins, 182–183
phenylcarbamates, 183–184
recognition mechanism, 185–201
proteins, 167–168
polyamides, 166
synthetic polymers, 166–167
vinyl polymers, 161–166
polymethacrylates, 161–165
poly chiral aggregates, 248–251
Chiral site stereocontrol, chirality polymerization mechanisms, 10–11
Chiral stationary phases (CSPs):
carbamate derivatives:
arylalkylcarbamates, 179–180
cycloalkylcarbamates, 181
phenylcarbamates, 172–179
cellulose/amylose phenylcarbamates, 172–179
cellulose esters, 170–172
computational studies, 199–201
optically active polymers, 158–161
poly chiral aggregates, 248–251
polyamides, 166
polysaccharide derivatives:
chromatographic studies, 186–190
computational studies, 199–201
NMR studies, 190–199
phenylcarbamates, 183–185
recognition mechanism, 185–201
proteins, 167–168
synthetic polymers, 167
vinyl polymers, 161–166
Chiroptical properties, poly chiral aggregates:
basic principles, 244–246
switching and memory functions, 243–244
Cholesteric handedness, molecular correlations:
future research issues, 451–452
lyotropic cholesterics, helical polymer formation, 436–441
research background, 425–431
techniques and protocols, 431–436
thermotropic-induced cholesterics, 441–451
biaryl moiety, 447–450
chiral/biaryl molecule comparisons, 450–451
empirical approach, 442–446
theoretical background, 446–447
Cholesteric phase, thermotropic liquid crystals:
nematic discotic (N_D) mesophase, chiral induction, 380–382
research background, 377–378
Chromophores, self-assembled molecules, chirality characteristics, amino acid amphiphiles, 304–311
Circular dichroism (CD). *See also* Second-harmonic generation circular dichroism (SHG-CD)
chiral molecules:
nonlinear optics, 520–521, 527–529
biological samples, 562–563
helicenebisquinone derivative, 559–562
oligosaccharides and cyclodextrins, 182–183
synthetic polymers, 167
vinyl polymers, 161–166
cholesteric handedness, 427–431
planar conformation, 432–436
discotic liquid crystals:
chiral core, 392
chiral phthalocyanines, side-chain packing, 390–391

- helical self-assembly, chiral columns, 384–387
 noncooperative self-assembly, 400–407
 optically active polysilanes, 211–213
 alkyl(alkoxyphenyl)polysilanes, global-local conformation, 241–243
 alkyl(phenyl)polysilane:
 chiral-achiral substituent copolymers, 253–254
 Ising model, 256–258
 dialkylpolysilanes:
 diastereomeric helicities, screw senses and pitches, 223–224
 enantiopure chiral termini, sergeants-and-soldiers cooperativity, 228–230
 “majority rule” principle, preferential screw sense, 227–228
 preferential screw sense homopolymers, 220–222
 “sergeants-and-soldiers” principle, preferential screw sense, copolymers, 225–226
 switching preferential screw sense, helix-helix transition, 230–238
 diarylpolysilanes:
 copolymer cooperativity, 266–269
 homopolymers, 259–263
 thermo-driven helix-helix transition, 270–272
 helical structure, 213–214
 poly(diarylsilane) aggregates, 272–273
 preferential screw sense ordering, 215–216
 poly chiral aggregates:
 chiroptical properties, 244–246
 solvent effects, 248
 temperature effects, 246–248
 self-assembled molecules, chirality characteristics:
 amino acid amphiphiles, 302–311
 diacetylenic phospholipids, 319–327
 guanine- and pterine-related molecules, 412–415
 mixed phospholipids, 331–333, 332–333
 nucleotides, 335–337
 Circularly polarized electroluminescence (CPEL):
 cholesteric handedness, 427–431
 planar conformation, 432–436
 diarylpolysilanes, 274
 Circularly polarized photoluminescence (CPPL), poly(diarylsilane) aggregates, 273–274
Cis-1,4-poly(isoprene), 102–105
Cis configuration:
 alternating copolymers, 105–109
 chain conformation, polydienes, 94–102
 nonconjugated diene cyclopolymerization, 26–27
 Clincity. *See also* Anticlinicity; Synclincity
 achiral smectic phases, 480–483
 antiferroelectric liquid crystals, SmC_A^* phase, 471–474
 SmCP supermolecular diastereomers, 501–502
 $\text{SmC}_S\text{P}_A/\text{SmC}_A\text{P}_A$ antiferroelectric phases, 499–500
 Close packing principle, polymer crystal macromolecules, 109–113
 Collagen fibrils, cholesteric handedness, 431
 Columnar mesophases:
 discotic liquid crystals, 375–376
 chiral core, 391–392
 ferroelectricity:
 cone-shaped molecules, 395–396
 flat discotics, 392–395
 helical self-assembly, 382–391
 helical core, 382–387
 polymer backbone-controlled helicity, 387–389
 side-chain packing, 389–391
 helicene self-assembly, 415–418
 self-assembled molecules, 397–411
 achiral expression, 398–399
 cooperative self-assembly, 407–411
 noncooperative self-assembly, 399–407
 thermotropic liquid crystals, nematic discotic (N_D) mesophase, chiral induction, 379–382
 Computational studies, chiral recognition, 199–201
 Cone-shaped discotic molecules:
 banana phases, 493–495
 ferroelectric banana phases, 509–512
 ferroelectricity, 395–396
 $\text{SmC}_S\text{P}_A/\text{SmC}_A\text{P}_A$ antiferroelectric phases, 499–500
 Conformational energy calculations:
 ferroelectric banana phase design, 505–512
 isotactic/syndiotactic polymers, 84–92
 Conglomerate structures:
 reflection symmetry breaking, 474–475
 SmCP supermolecular diastereomers, 501–502
 Conjugated dienes, chain-end controlled polymerizations, 57–61
 Continuous polarization measurements,
 second-harmonic generation nonlinear optics, 538–541
 linear/circular polarized probes, comparison, 545–550
 Continuum elastic theory, self-assembled molecules, chirality characteristics:
 molecular models, 348–349
 uniformly tilted membranes, 349–353
 Cooperative self-assembly, chiral columns, 407–411
 Cooperativity:
 dialkylpolysilanes, “sergeants-and-soldiers” principle:
 enantiopure chiral termini effects, 228–230
 preferential screw sense, copolymers, 224–226
 diarylpolysilanes, 266–269
 helical chain conformation, chiral crystallization, 145–147
 Coordinated ligands, chirality polymerization mechanisms, 9
 Copolymers:
 chain conformation, alternating copolymers, 105–109
 crystalline constitution and conformation, 72–74
 kink-band disordered conformation, 140

- Copolymers: (*Continued*)
- optically active polysilanes:
 - alkyl(alkoxyphenyl)polysilanes, global-local conformation, 241–243
 - alkyl(phenyl)polysilane:
 - chiral-achiral substituent copolymers, 253–254
 - UV/CD spectra comparisons, 255–256
 - dialkylpolysilanes, preferential screw sense:
 - “majority rule” principle, 226–228
 - “sergeants-and-soldiers” principle, 224–226
 - diarylpolysilanes, CD/UV spectra and cooperativity, 266–269
 - Cotton effects:
 - discotic liquid crystals:
 - chiral phthalocyanines, side-chain packing, 390–391
 - guanine- and pterine-related molecular self-assembly, 412–415
 - helical self-assembly, chiral columns, 384–387
 - helicene self-assembly, 415–418
 - noncooperative self-assembly, 401–407
 - polymer backbone-controlled helicity, 387–389
 - self-assembled molecules, achiral expression, 399
 - optically active polysilanes:
 - alkyl(phenyl)polysilane, circular dichroism (CD) spectra, 257–258
 - diarylpolysilanes, 261–263
 - thermo-driven helix-helix transition, 270–272
 - helical structure, 214
 - preferential screw sense ordering, 215–216
 - poly chiral aggregates, chiroptical properties, 244–246
 - Covalent bonding, molecular structures vs. liquid crystals, 459–462
 - CPMAS spectroscopy, crystalline polymers, symmetry breaking, 117–118
 - Crosslinked polymer gels, chiral recognition, 159–161
 - Crossover angle, discotic liquid crystals, noncooperative self-assembly, 404–407
 - Cryo-electron microscopy (EM) studies, self-assembled molecules, chirality characteristics:
 - aldonamides, 290–293
 - amino acid amphiphiles, 304–311
 - Crystal conglomerates, reflection symmetry breaking, 474–475
 - Crystalline polymers:
 - chain conformation:
 - alternating copolymers, 105–109
 - basic principles, 74–78
 - disordered conformations, 102–105
 - isotactic/syndiotactic polymers:
 - energy calculations, 84–92
 - helical conformation, 78–84
 - optical activity and helical conformation, 93–94
 - polydienes, 94–102
 - constitution and configuration, 72–74
 - macromolecular packing:
 - basic principles, 109–113
 - frustrated structures, 118–121
 - helical chain conformation, chiral crystallization, 142–147
 - long-range periodicity, 124–140
 - positional disorder, 121–124
 - conformational kink-band disorder, 136–140
 - ordered layer stacking, single lattice direction, 131–136
 - right- and left-handed chains, 124–125
 - up and down chains, 125–130
 - solid mesomorphic forms, 140–142
 - symmetry breaking, 113–118
 - Crystallites, chiral crystallization, helical chain conformation, 143–147
 - “Cut-and-paste” technique, optically active dialkylpolysilanes, diastereomeric helicities, screw senses and pitches, 224
 - p-n*-octyl-*p'*-Cyanobiphenyl (8CB), achiral structure, 480–483
 - Cycloalkylcarbamates, chiral recognition, cellulose/amylose derivatives, 181
 - Cyclodextrins, chiral recognition, 182–183
 - Cyclopentadienyl compounds:
 - conjugated diene polymerization, 60–61
 - syndiotactic polymerization, styrene/substituted styrenes, 54–57
 - Cyclopolymerization, nonconjugated dienes, homogeneous metallocene catalysts, 26–27
 - Cylinder of radius (*r*), crystalline polymers, macromolecular packing, 110–113
 - Cylindrical curvature, self-assembled molecules, chirality characteristics, 358–359
 - Decyloxybenzylideneaminomethylbutylcinnamate (DOBAMBC):
 - antiferroelectric liquid crystals, SmC_A^{*} phase, 471–474
 - ferroelectric banana phases, 512
 - ferroelectric liquid crystals, smectic C phase (SmC), 465–470
 - Degree of polymerization (DP), discotic liquid crystals, cooperative self-assembly, 408–411
 - guanine- and pterine-related molecules, 412–415
 - Density functional studies, conjugated diene polymerization, 58–61
 - Depolarized reflected light microscopy (DRLM):
 - achiral liquid crystals, 482–483
 - SmC₅P_A/SmC_AP_A antiferroelectric phases, 496–500
 - Diacetylene compounds, self-assembled molecules, chirality characteristics:
 - aldonamides, 293–294
 - biased chiral symmetry breaking, 361–363
 - phospholipids, 318–327
 - phosphonate lipids, 327–331
 - Diacetylenic glutamate lipids (DGLs), self-assembled molecules, chirality

- characteristics, amino acid amphiphiles, 306–311
- Dialkylpolysilanes, optically active groups: copolymers, preferential screw sense and “majority rule” principle, 226–228 diastereomeric helicities, 223–224 enantiopure termini effects, sergeants-and-soldiers cooperativity, 228–230 helix-helix switching, preferential screw sense, 230–238 preferential screw sense copolymers, “sergeants-and-soldiers” principle, 224–226 preferential screw sense homopolymers, enantiopure chiral side chains, 219–222 research issues, 238–239 rodlike single molecule imaging, 222
- Diarylpolysilanes, optically active groups, 259–274 circularly polarized photoluminescence, 273–274 copolymer CD and UV spectroscopy and cooperativity, 266–269 homopolymer CD and UV spectroscopy, 259–263 molecular mechanics calculations, 264–265 poly(diarylsilane) aggregates, 272–273 research issues, 274 thermo-driven helix-helix transition, 270–272
- Diastereomeric sites: chain-end controlled polymerizations: primary 1-alkene insertions, 49–51 secondary 1-alkene insertions, 52–54 ferroelectric banana phases, 502–512 homogeneous metallocenes, chain migratory insertion mechanism, 24 optically active dialkylpolysilanes, diastereomeric helicities, screw senses and pitches, 223–224 self-assembled molecules, chirality characteristics, aldonamides, 289–293 SmCP stereogenic phases, 500–502
- Dibenzopyrene compounds, ferroelectricity, 392–395
- Dienes, chain-end controlled polymerizations, conjugated dienes, 57–61
- Dilauryl-phosphotidylcholine (DLPC), chiral molecular self-assembly, 331–333
- Dimeric structures, smectic phases, 485–486
- Dimyristoyl-5'-phosphatidylcytidine (DMPC), nucleotide chiral molecular self-assembly, 334–337
- Dimyristoyl-5'-phosphatidyluridine (DMPU), nucleotide chiral molecular self-assembly, 335–337
- Dinonanoyl-phosphotidylcholine (DNPC), self-assembled molecules, chirality characteristics, mixed phospholipids, 331–333
- 1,2-Dipalmitoyl-*sn*-glycero-3-phosphocholine (L-DPPC), chiral molecular self-assembly, 322–327
- Discotic liquid crystals: lyotropic structures, self-assembly, dilute solution, 396–418 research background, 375–376 thermotropic mesophase, 377–396 chiral core discotics, 391–392 ferroelectricity, 392–396 cone-shaped molecules, 395–396 flat discotics, 392–395 helical self-assembly, 382–391 helical core, 382–387 polymer backbone-controlled helicity, 387–389 side-chain packing, 389–391 N_D mesophase, 379–382 research background, 374–376
- Disordered conformations: crystalline polymers, 102–105 chemical defects, 121–124 long-range positional three-dimensional order: conformational kink-band disorder, 136–140 macromolecular stacks, single lattice direction, 131–136 right- and left-handed helical chains, 124–125 up and down chains, 125–130 liquid crystals, 461–462 mesomorphic modifications, 140–142
- Dissymmetry ratios, optically active polysilanes: alkyl(phenyl)polysilane, circular dichroism (CD) spectra, 256–258 dialkylpolysilanes, switching preferential screw sense, helix-helix transition, 232–238 diarylpolysilanes: copolymer cooperativity, 267–269 thermo-driven helix-helix transition, 270–272
- DN1 peptide, peptide amphiphiles, chiral molecular self-assembly, 313–317
- DNA: cholesteric handedness, 429–431 helical self-assembly, chiral columns, 382–391 cooperative self-assembly, 411 nucleotide chiral molecular self-assembly, 333–337
- Double *gauche* conformation, isotactic/syndiotactic structures, energy calculations, 91
- EAK16 protein, peptide amphiphiles, chiral molecular self-assembly, 313–317
- EFK8 protein, peptide amphiphiles, chiral molecular self-assembly, 313–317
- Elasticity: nonchiral self-assembly models, orientational order, 345–346 self-assembled molecules, chirality characteristics, uniformly tilted membranes, 352–353
- Electric dipole susceptibility, nonlinear optics, 523 failure in polymer films, 554–557 quantitative determination, 550–554

- Electric field poling, second-harmonic generation
nonlinear optics, 526–527
- Electroless metallization, self-assembled molecules,
applications, 285–286
- Electro-optic (Pockels effect), chiral molecule
nonlinear optics, 524–527
isotropic bulk media, 565
- Electrostatics, nonchiral models, molecular
self-assembly, 343–344
- Eluents, chiral recognition:
cellulose/amylose arylalkylcarbamates, 180
cellulose/amylose phenylcarbamates, 176–179
polysaccharide phenylcarbamates, 184–185
- Empirical techniques, thermotropic cholesterics,
442–446
- Enantiomers:
chiral recognition:
cellulose/amylose phenylcarbamates, 179
computational studies, 199–201
NMR studies, 192–199
polysaccharide phenylcarbamates, 184–185
homogeneous metallocenes, chain migratory
insertion mechanism, 23–24
self-assembled molecules, chirality
characteristics, 282
diacetylenic phospholipid chiral
self-assembly, 324–327
uniformly tilted membranes, 352–353
- Enantiomorphous helices:
crystalline polymers, macromolecular packing,
111–113
isotactic polymers, 83–84
- Enantiopure chiral side chains:
alkyl(alkoxyphenyl)polysilanes, 239
optically active dialkylpolysilanes:
preferential screw sense homopolymers,
219–222
“sergeants-and-soldiers” principle:
copolymer preferential screw sense,
224–226
termini effects, 228–230
- Enantioselective mechanism:
growing chain chiral orientation, 17–21
optically active polymers, 158–159
- Enantiotropic phase, ferroelectric liquid crystals,
smectic C phase (SmC), 466–470
- Energy calculations, isotactic/syndiotactic polymers,
84–92
- Energy difference, chiral recognition, 159–161
- Energy mapping, disordered chain conformation,
103–105
- Entropic factors:
INAC phase sequence, 462–464
optically active dialkylpolysilanes, switching
preferential screw sense, helix-helix
transition, 236–238
polymer crystals, macromolecule packing,
110–113
- EO switching:
banana phases, 490–495
SmC₅P_A/SmC_AP_A antiferroelectric phases,
498–500
- Equilibrium constant, molecular structures vs. liquid
crystals, 460–462
- Equivalence principle:
crystalline constitution and conformation, 76
macromolecular packing, 109–113
disordered conformations, 102–105
- Erythro* structures:
alternating copolymers, 105–109
chain conformation, polydienes, 94–102
crystalline constitution and conformation,
73–75
- Ethylenes, olefin alternating copolymers, 105–109
- Ethylene-tetrafluoroethylene (ETFE), chain
conformation, mesomorphic modifications,
141–142
- Ewen catalysts, chain-end controlled
polymerizations, primary 1-alkene insertions,
49–51
- Expansion coefficients, nonlinear optics (NLO):
continuous polarization measurements,
538–541
electric dipole approximation failure, 555–557
experimental determination, 541–544
linear/circular polarized probes, comparison,
548–550
theoretical formalism, 534–535
- E-Z* selectivity, metallocene symmetry, 34–38
- Ferroelectricity:
banana phases, 502–512
discotic liquid crystals, thermotropic mesophase,
392–396
cone-shaped molecules, 395–396
flat discotics, 392–395
liquid crystals:
INAC phase sequence, 462–464
macroscopic racemate, unichiral mesogen,
512–514
molecular characteristics, 459–462
research background, 457–458
SmC* phase, 464–470
- Fibril formation, peptide amphiphiles, chiral
molecular self-assembly, 311–317
- Fingerprint measurements:
banana phases, 491–495
cholesteric handedness, 433–436
- Flat discotics, ferroelectricity, 392–395
- Flat membranes, self-assembled molecules, chirality
characteristics, tilt variations, 355–358
- Fluorescence anisotropy, optically active
alkyl(phenyl)polysilane, 252–253
- Fluorescence excitation (FE), optically active
polysilanes, dialkylpolysilanes, preferential
screw sense homopolymers, 220–222
- Fluorescence (FL) studies, optically active
polysilanes, 211–213
alkyl(phenyl)polysilane, 252–253, 255–256
dialkylpolysilanes:
preferential screw sense homopolymers,
220–222
switching preferential screw sense,
helix-helix transition, 230–238
- Fourier transform infrared (FTIR) studies,
self-assembled molecules, chirality
characteristics, glycolipids, 296–299

- Frank constants, self-assembled molecules, chirality characteristics:
 membrane tilt variations, 354–358
 uniformly tilted membranes, 352–353
- Free energy calculations:
 ferroelectric liquid crystals, smectic C phase (SmC), 469–470
 liquid crystals, 460–462
 molecular hypersurface, 459–462
 self-assembled molecules, chirality characteristics:
 membrane tilt variations, 353–358
 uniformly tilted membranes, 350–353
- Frequency doubling, chiral molecule nonlinear optics, 524–527
- Frustrated polymer crystals, chain conformation, 118–121
- Full width at half maximum (FWHM) peaks, optically active polysilanes:
 alkyl(phenyl)polysilane studies, 252–253
 global conformation, 218–219
- Galactocerebrosides, self-assembled molecules, chirality characteristics, 300–301
- Galactonamides, self-assembled molecules, chirality characteristics, 289–293
- Gas chromatography (GC), chiral stationary phases (CSPs) optically active polymers, 158–159
- Gauche* conformation. *See also* Double *gauche* conformation
 crystalline structures, 77–78
 isotactic/syndiotactic structures, energy calculations, 84–92
 self-assembled molecules, chirality characteristics:
 aldonamides, 289–293
 glycolipids, 296–299
- Gaussian curvature, self-assembled molecules, chirality characteristics, 358–359
- Gemini surfactants, self-assembled molecules, chirality characteristics, 340–342
 cylindrical *vs.* Gaussian curvature, 358–359
- Geometric packing parameters, self-assembled molecules, chirality characteristics, molecular models, 349
- Gibbs energy, chiral recognition, NMR studies, 197–199
- Ginzburg-Landau expansion, self-assembled molecules, chirality characteristics, chiral symmetry breaking, 360
- Glide planes, crystalline polymers:
 macromolecular packing, 111–113
 symmetry breaking, 115–118
- Global conformation, optically active polysilanes, 216–219
 alkyl(alkoxyphenyl)polysilanes, global-local conformation, 240–243
- Gluconamides, self-assembled molecules, chirality characteristics, 289–293
- N*-octyl-D-Gluconamide (D-Glu-8), self-assembled molecules, chirality characteristics, 287–293
- Glu-PDA-lipids, amino acid amphiphile chirality, 309–311
- Glutamic acid, self-assembled molecules, chirality characteristics, amino acid amphiphiles, 302–311
- Glycolipids, chiral self-assembly, 293–299
- Grandjean-Cano wedge method, cholesteric handedness, 433–436
- Growing chain:
 chiral orientation, 8–9
 future research issues, 62
 regioirregular insertion stereoselectivity, 30–31
 homogeneous metallocene stereoselectivity, 14–21
 back-skip mechanism, 25–26
- Guanine-related molecules, self-assembly mechanisms, 412–415
- Guanosine derivatives, cholesteric handedness, helical polymers, 436–441
- Half waveplate technique, nonlinear optics (NLO):
 continuous polarization measurements, 538–541, 544–545
 linear/circular polarized probes, comparison, 545–550
- Halogenated compounds, chiral core discotics, 391–392
- Hammitt parameter, chiral stationary phases (CSPs), chromatographic studies, 186–190
- Handedness:
 cholesteric correlations:
 future research issues, 451–452
 lyotropic cholesterics, helical polymer formation, 436–441
 research background, 425–431
 techniques and protocols, 431–436
 thermotropic-induced cholesterics, 441–451
 biaryl moiety, 447–450
 chiral/biaryl molecule comparisons, 450–451
 empirical approach, 442–446
 theoretical background, 446–447
 discotic liquid crystals:
 noncooperative self-assembly, 404–407
 polymer backbone-controlled helicity, 388–389
 molecular and cholesteric correlations:
 future research issues, 451–452
 lyotropic cholesterics, helical polymer formation, 436–441
 research background, 425–431
 techniques and protocols, 431–436
 thermotropic-induced cholesterics, 441–451
 biaryl moiety, 447–450
 chiral/biaryl molecule comparisons, 450–451
 empirical approach, 442–446
 theoretical background, 446–447
 self-assembled molecules, chirality characteristics, 284
 diacetylenic phospholipids, 325–327
 diacetylenic phosphonate lipids, 328–331

- Head group stereochemistry, self-assembled molecules, chirality characteristics:
aldonamides, 289–293
amino acid amphiphiles, 303–311
cerebrosides, 300–301
- Helfrich-Prost model, self-assembled molecules, chirality characteristics, 349–353
- Helical conformation:
basic principles, 77–78
cholesteric handedness, 426–431
helical polymers, 436–441
crystalline polymers:
chiral crystallization, 142–147
frustrated structures, 118–121
kink-band disorder, 138–140
macromolecular packing, 110–113
optical activity, 93–94
symmetry breaking, 115–118
up and down chains, positional disorder, 125–130
isotactic/syndiotactic polymers, 78–84
conformational energy calculations, 84–92
long-range positional three-dimensional order, right- and left-handed helical chains, 124–125
nonlinear optics (NLO), 1,1'-binaphthyl-based helical polymer, 557–558
optically active polymers, 93–94
alkyl(alkoxyphenyl)polysilanes:
cooperative helical order, substituent effects, 240–242
enantiopure chiral side chains, 239
alkyl(phenyl)polysilane, 251–252
dialkylpolysilanes:
diastereomeric helicities, screw senses and pitches, 223–224
switching preferential screw sense, helix-helix transition, 230–238
diarylpolysilanes, 261–263
polysilanes, 211–213
circular dichroism spectroscopy, 213–214
preferential screw sense ordering, 214–216
self-assembled molecules, chirality characteristics, 282, 285
amino acid amphiphiles, 302–311
biased chiral symmetry breaking, 360–363
cerebrosides, 300–301
chiral symmetry breaking, 359–360
cylindrical vs. Gaussian curvature, 358–359
diacetylenic phospholipids, 321–327
diacetylenic phosphonate lipids, 329–331
discotic liquid crystal helicity, 415–418
gemini surfactants, 340–342
glycolipids, 293, 295–299
membrane tilt variations, 355–358
nonchiral models:
electrostatics, 343–344
spontaneous curvature, 347
nucleotides, 335–337
peptide amphiphiles, 316–317
steroid-based systems, 337–340
thermotropic cholesterics, biaryl moiety, 447–450
thermotropic liquid crystals, chiral column self-assembly, 382–391
helical core, 382–387
polymer backbone-controlled helicity, 387–389
side-chain packing, 389–391
Helical core, helical self-assembly, chiral columns, 382–387
Helical twisting power (HTP):
ferroelectric liquid crystals, smectic C phase (SmC), 468–470
thermotropic cholesterics, 443–446
thermotropic liquid crystals, nematic discotic (N_D) mesophase, chiral induction, 379–382
Helicenebiquinone derivative, nonlinear optics, 559–562
Helicenes:
cholesteric handedness, 450–451
self-assembly, columnar mesophases, 415–418
Helix-helix transition:
optically active dialkylpolysilanes, switching preferential screw sense, 230–238
optically active diarylpolysilanes, thermo-driven transitions, 270–272
Heterogeneous catalysts, site-controlled stereospecific polymerizations:
catalyst chirality, 38–46
magnesium chloride systems, 42–46
titanium trichloride systems, 39–42
homogeneous catalyst comparisons, 46–48
Hexabenzocoronene, chiral discotic induction, side-chain packing, 390–391
2,4-Hexadienoyl groups, self-assembled molecules, chirality characteristics, amino acid amphiphiles, 306–311
Hexa-hexylthiotriphenylene, helical self-assembly, chiral columns, 382–391
Hexakis-porphyrinato benzenes, noncooperative self-assembly, 405–407
High-axial-ratio microstructures (HARMs), cerebroside chirality, 300–301
High-density polyethylene (HDPE):
ethene catalysts, 5
structure and properties, 1–2
Highest occupied molecular orbital-lowest unoccupied molecular orbital (HOMO-LUMO), diarylpolysilanes, 259
High-performance liquid chromatography (HPLC):
chiral recognition, 169–172
NMR studies, 194–199
polysaccharide phenylcarbamates, 183–185
chiral stationary phases (CSPs) optically active polymers, 158–159
High-resolution cross polarization, self-assembled molecules, chirality characteristics, aldonamides, 290–293
Homochiral side chains:
chiral phthalocyanines, side-chain packing, 389–391
discotic liquid crystals:
guanine- and pterine-related molecular self-assembly, 412–415
noncooperative self-assembly, 400–407

- Homogeneous catalysts:**
alternating copolymers, 105–109
evolution of, 4–9
site-controlled stereospecific polymerizations:
heterogeneous catalyst comparisons, 46–48
metallocenes, 13–38
backskip of growing chain, 25–26
2-butene cyclopolymers, *E-Z* selectivity,
34–38
chain migratory insertion mechanism,
21–24
nonconjugated dienes,
cyclopolymerization, 26–27
regioirregular insertion stereospecificity,
27–31
regiospecificity, symmetry dependence,
31–34
stereoselectivity mechanism, 14–21
- Homopolymers:**
dialkylpolysilanes optical activity, preferential
screw sense, enantiopure chiral side
chains, 219–222
diarylpolysilanes optical activity, UV/CD
spectra, 259–263
optically inactive groups, alkyl(phenyl)polysilane
studies, 252–253
- Host-guest complexes, molecular structures vs.**
liquid crystals, 460–462
- ¹H NMR, chiral recognition studies, 187–190**
phenylcarbamates, 190–199
- Hydrogen bonding:**
chiral recognition:
chromatographic studies, 187–190
NMR studies, 193–199
helical self-assembly, chiral columns, helical
core, 383–387
polymer backbone-controlled helicity, 388–389
self-assembled molecules, chirality
characteristics, 284–285
aldonamides, 287–293
cooperative self-assembly, 410–411
peptide-based amphiphiles, 302–317
amino acids, 302–311
peptides, 311–317
- Hydrophilic interactions, self-assembled molecules,**
chirality characteristics, 282
glycolipids, 293, 295–299
peptides, 311–317
- Hydrophobic interactions, self-assembled molecules,**
chirality characteristics, 282, 284–285
peptides, 311–317
- Hydroxy fatty acid cerebroside (HFA-Cer), chiral
self-assembly, 300–301**
- Hyperpolarizability tensors, nonlinear optical
activity, molecular origins, 530–532**
- Hypersurfaces, molecular structure, 459–462**
- Ibca space group, crystalline polymers, symmetry
breaking, 113–118**
- Identical sites, homogeneous metallocenes, chain
migratory insertion mechanism, 22–24**
- INAC phase sequence, liquid crystal mesogens,
462–464**
- Indium-tin oxide (ITO) films:**
banana phases, 491–495
SmC₅P_A/SmC_AP_A antiferroelectric phases,
498–500
- Induced circular dichroism (ICD), poly chiral
aggregates, molecular chiral recognition,
250–251**
- Induced dipole moment:**
nonlinear optics, 523–527
second-harmonic generation, 529–530
optical activity, 522–523
- Induced magnetic moment:**
nonlinear optics, second-harmonic generation,
529–530
optical activity, 522–523
- Infrared (IR) spectroscopy, ferroelectric banana
phase design, 505–512**
- Insertion mechanisms:**
chain-end controlled olefin polymerizations:
primary 1-alkene insertions, 51–54
secondary 1-alkene insertions, 51–54
homogeneous metallocenes:
chain migratory insertion mechanism, 21–24
regioirregular insertion stereoselectivity,
27–31
regiospecificity dependence, 31–34
- Intensity-difference effects, nonlinear optics (NLO),
continuous polarization measurements,
538–541**
- Inter axial crossing, discotic liquid crystals,
noncooperative self-assembly, 404–407**
- Intercalated smectics, achirality, 485–486**
- Intermolecular interaction:**
poly chiral aggregates, chiroptical properties,
244–246
self-assembled discotic liquid crystals, 397
- Intramolecular hydrogen bonding, helical
self-assembly, chiral columns, 383–387**
- Inversion centers, crystalline polymers,
macromolecular packing, 111–113**
- Ising model, optically active
alkyl(phenyl)polysilane, circular dichroism
(CD) spectra, 256–258**
- Isomers:**
bent-core mesogens, achirality, 484–486
molecular structures vs. liquid crystals, 459–462
SmCP supermolecular diastereomers, 500–502
- Isotactic structures:**
alternating copolymers, *erythro/threo*
configurations, 105–109
chain conformation:
energy calculations, 84–93
frustrated structures, 119–121
long-range positional three-dimensional
order, up and down chains, 125–130
macromolecular stacking disorder, single
lattice direction, 131–136
mesomorphic modifications, 141–142
polydienes, 94–102
crystalline constitution and conformation, 73–78
macromolecular packing, 111–113
helical conformation, 78–84
optical activity, 93–94

- Isotactic structures: (*Continued*)
 propene monomers, 2
 styrene-carbon monoxide (i-STCO) copolymers,
 107–109
- Isotropic bulk media, second-order nonlinear optics,
 564–565
- KFE8 peptide, peptide amphiphiles, chiral molecular
 self-assembly, 314–317
- Kink-band disorder:
 biased chiral symmetry breaking, 360–363
 crystalline polymers, 136–140
 self-assembled molecules, chirality
 characteristics, bolaamphiphiles, 297–299
- Kuhn's dissymmetry ratio, optically active
 polysilanes:
 alkyl(phenyl)polysilane, circular dichroism (CD)
 spectra, 256–258
 diarylpolysilanes, 262–263
 helical structure, 214
- KYOBOW, ferroelectric macroscopic racemate,
 unichiral mesogens, 513–514
- Langmuir-Blodgett films:
 helical self-assembly, chiral columns, 387
 nonlinear optics:
 1,1'-binaphthyl-based helical polymer,
 557–558
 biological samples, 562–563
 electric dipole approximation failure,
 554–557
 expansion coefficient determination, 543–544
 helicenebisquinone derivative, 559–562
 linear/circular polarized probes, comparison,
 545–550
 research background, 520–521
 second-harmonic generation (SHG), 526–527
 theoretical formalism, 532–535
- Langmuir monolayers:
 chiral symmetry breaking, 359–360
 crystal conglomerates, 475
- Layer interfaces, ferroelectric macroscopic
 racemate, unichiral mesogens, 514
- Least nuclear motion principle, chirality
 polymerization mechanisms, 13
- Lennard-Jones interaction, self-assembled
 molecules, chirality characteristics, molecular
 models, 348–349
- Lewis base, magnesium chloride catalysts,
 site-controlled stereospecific polymerizations,
 42–46
- Limit-disordered models:
 disordered conformation, crystalline polymers,
 123
 long-range positional three-dimensional order,
 macromolecular stacking disorder, single
 lattice direction, 131–136
 up and down chains, positional disorder,
 125–130
- Limit-ordered models:
 disordered conformation, crystalline polymers,
 123
- long-range positional three-dimensional order:
 macromolecular stacking disorder, single
 lattice direction, 131–136
 up and down chains, 125–130
- Linear optics. *See also* Second-harmonic generation
 linear dichroism (SHG-LD)
 chiral molecules, basic properties, 521–522
- Linear susceptibility, linear optics, chiral molecules,
 521–522
- Line repetition symmetry, chain conformation,
 polydienes, 94–102
- Liquid crystals:
 achiral molecules:
 B4 phase, 487–489
 banana phases, bilayer smectics, 478–483
 bent-core mesogens, 484–486
 Matsunaga diesters, 486–487
- antiferroelectricity:
 banana design, 502–512
 SmC_A^{*} phase, 470–474
 SmC_SP_A/SmC_AP_A phase, 496–500
 stereogenic elements, SmCP supermolecular
 diastereomers, 500–502
- chiral discotic molecules:
 applications, 376–377
 basic properties, 374–375
 future research issues, 418–419
 lyotropic structures, self-assembly, dilute
 solution, 396–418
 research background, 374
 self-assembly, 397–411
 absence of positional order, 398–399
 cooperative self-assembly, 407–411
 guanine and pterine-related molecules,
 412–415
 helices, 415–418
 noncooperative self-assembly, chiral
 columns, 399–407
 synthesis and characterization, 375–376
 thermotropic structures, 377–396
 chiral core discotics, 391–392
 ferroelectricity, 392–396
 cone-shaped molecules, 395–396
 flat discotics, 392–395
 helical self-assembly, 382–391
 helical core, 382–387
 polymer backbone-controlled helicity,
 387–389
 side-chain packing, 389–391
 N_D mesophase, 379–382
- cholesteric handedness, 427–431
- ferroelectricity:
 INAC phase sequence, 462–464
 macroscopic racemate, unichiral mesogen,
 512–514
 molecular characteristics, 459–462
 research background, 457–458
 SmC^{*} phase, 464–470
 supermolecular stereochemistry, 458–464
- self-assembled molecules, chirality
 characteristics, membrane tilt variations,
 354–358
- spontaneous reflection symmetry breaking,
 475–478

- symmetry breaking:
 - B2 spontaneous reflections, 489–495
 - organic crystal conglomerates, 474–475
 - SmCP phases, 495–496
 - spontaneous reflection, 475–476
- Local conformation, optically active
 - alkyl(alkoxyphenyl)polysilanes, 240–243
- Longitudinal polarization, antiferroelectric liquid crystals, bilayer smectics, 478–483
- Long-range positional three-dimensional order:
 - conformational kink-band disorder, 136–140
 - disordered conformation, crystalline polymers, 122–124
 - macromolecular stacking, single lattice disorder, 131–136
 - right- and left-handed helical chains, 124–125
 - up and down chains, disorder, 125–130
- Low-density polyethylene (LDPE), structure and properties, 1–2
- Lower critical solution temperature (LCST), discotic liquid crystals, cooperative self-assembly, 408–411
- Lyotropic discotic liquid crystals:
 - cholesteric handedness, 429–431
 - helical polymers, 436–441
 - cooperative self-assembly, 407–411
 - self-assembly, dilute solution, 396–418
 - guanine- and pterine-related molecules, 412–415
- M6R8 monomer, achiral liquid crystals, 481–483
- Macromolecular packing:
 - crystalline polymers:
 - basic principles, 109–113
 - frustrated structures, 118–121
 - helical chain conformation, chiral crystallization, 142–147
 - long-range periodicity, 124–140
 - positional disorder, 121–124
 - conformational kink-band disorder, 136–140
 - ordered layer stacking, single lattice direction, 131–136
 - right- and left-handed chains, 124–125
 - up and down chains, 125–130
 - solid mesomorphic forms, 140–142
 - symmetry breaking, 113–118
 - disordered conformation, single lattice direction, 131–136
- Macromolecules, semicrystalline polymer synthesis, 1
- Macroscopic chirality:
 - antiferroelectric liquid crystals, SmC_A^* phase, 471–474
 - ferroelectric liquid crystals, smectic C phase (SmC), 467–470
 - nonlinear optical activity, molecular origins, 530–532
 - spontaneous reflection symmetry breaking, liquid crystals, 477–478
- Macroscopic racemate:
 - ferroelectric unichiral mesogens, 512–514
 - reflection symmetry breaking, 475
- SmCP supermolecular diastereomers, 501–502
- $\text{SmC}_5\text{P}_A/\text{SmC}_A\text{P}_A$ antiferroelectric phases, 497–500
- Magnesium chloride systems, heterogeneous catalysts, site-controlled stereospecific polymerizations, 42–46
- Magnetic dipole susceptibility:
 - chiral molecule optical activity, 523
 - quantitative determination, 550–554
 - nonlinear optics, electric dipole approximation failure, 554–557
 - second-generation nonlinear optics, 529–530
- Magnetic induction field:
 - chiral molecule optical activity, 522–523
 - nonlinear optics (NLO), theoretical formalism, 532–535
- Main-chain chirality:
 - diarylpolysilanes, 259
 - optically active polysilanes, 211–213
 - alkyl(alkoxyphenyl)polysilanes, helicity control, remote chiral groups, 242–243
 - alkyl(phenyl)polysilane, 251–252
 - basic principles, 210–213
 - dialkylpolysilanes, switching preferential screw sense, helix-helix transition, 230–238
 - dialkylpolysilanes, molecular mechanics, 264–265
 - diarylpolysilanes, UV/CD spectra, 261–263
 - global conformation, 216–219
 - preferential screw sense ordering, 214–216
- Majority domains, $\text{SmC}_5\text{P}_A/\text{SmC}_A\text{P}_A$ antiferroelectric phases, 497–500
- “Majority rule” principle, dialkylpolysilanes, preferential screw sense, 226–228
- Mannonamides, self-assembled molecules, chirality characteristics, 289–293
- MAO (methylalumoxane) systems, site-controlled stereospecific polymerizations, 13–38
- Mark-Houwink-Sakurada plot, 217–219
- Matsunaga diesters, ferroelectricity, 486–487
- Mauguin limit, spontaneous reflection symmetry breaking, liquid crystals, 476–478
- Mechanistic studies, chiral recognition, 185–201
 - chromatographic studies, 186–190
 - computational studies, 199–201
 - NMR studies, 190–199
- Melting thermodynamics, diacetylenic phospholipid chiral self-assembly, 323–327
- Membrane modeling, self-assembled molecules, chirality characteristics, 348–349
 - chiral symmetry breaking, 359–360
 - tilt variations, 353–358
 - uniformly tilted membranes, 349–353
- Meso-diiotactic configuration, alternating copolymers, 105–109
- Mesogens:
 - bent-core mesogens, achirality, 484–486
 - ferroelectricity, 395
 - unichiral mesogens, macroscopic racemates, 512–514
 - INAC phase sequence, 462–464

- Mesogens: (*Continued*)
 molecules vs. liquid crystals, 460–462
 self-assembled discotic liquid crystals, 397
- Meso-isotactic/syndiotactic configurations,
 alternating copolymers, 105–109
- Mesomorphic modifications:
 disordered conformation, crystalline polymers,
 122–124
 macromolecule conformations, 140–142
- Metallocenes:
 homogeneous catalysts:
 alternating copolymers, 105–109
 site-controlled stereospecific polymerizations,
 13–38
 back-skip of growing chain, 25–26
 2-butene cyclopolymers, *E–Z* selectivity,
 34–38
 chain migratory insertion mechanism,
 21–24
 nonconjugated dienes,
 cyclopolymerization, 26–27
 regioirregular insertion stereospecificity,
 27–31
 regiospecificity, symmetry dependence,
 31–34
 stereoselectivity mechanism, 14–21
 stereospecific homogeneous catalysts, evolution
 of, 8–9
- Metallomesogens:
 ferroelectricity, 395
 self-assembled discotic liquid crystals, 397
- Metastable phase structure, banana phases, 495
- Methacrylates, chiral recognition, cellulose/amylose
 phenylcarbamates, 173–179
- 1-Methylheptyloxy carbonyl (MHOC) tail,
 ferroelectric banana phase design, 504–512
- 4-[(1-Methylheptyloxy) carbonyl]phenyl-4'-octyloxy-
 4-biphenyl carboxylate
 (MHPOBC):
 antiferroelectric liquid crystals:
 bilayer smectics, 478–483
 SmC_A^{*} phase, 470–474
 ferroelectric banana phase design, 504–512
- MHOBOW, ferroelectric macroscopic racemate,
 unichiral mesogens, 512–514
- Microcrystalline cellulose triacetate (CTA-I), chiral
 recognition, 168–172
- Microtubules, self-assembled molecules, chirality
 characteristics, 285–287
- Minimum-energy conditions:
 achiral liquid crystals, bilayer smectics, 479–483
 chain conformation:
 mesomorphic modifications, 141–142
 polydienes, 96–102
 chain-end controlled polymerizations, primary
 1-alkene insertions, 49–51
 crystalline constitution and conformation, 76
 macromolecular packing, 109–113
 disordered chain conformation, 103–105
 growing chain chiral orientation,
 stereoselectivity, 14–21
 isotactic/syndiotactic structures, conformational
 energy calculations, 84–92
 regiospecificity dependence, primary/secondary
 insertions, 33–34
- Minimum inertia axis, banana phases, 491–495
- Minority domains, banana phases, 493–495
- "Molecular" arrowheads, ferroelectric banana phase
 design, 503–512
- Molecular dynamics (MD), chiral recognition
 studies, 199–201
- Molecular imaging, optically active
 dialkylpolysilanes, rodlike single molecule,
 222
- Molecular length scale, self-assembled molecules,
 chirality characteristics, membrane tilt
 variations, 353–358
- Molecular mechanics. *See also* Self-assembled
 molecules
 chirality polymerization mechanisms, 11–13
 chiral recognition studies, 199–201
 self-assembly models, 347–349
 conjugated diene polymerization, 58–61
 growing chain chiral orientation,
 stereoselectivity, 17–21
 liquid crystals, 459–462
 nonlinear optical activity, 530–532
 optically active polysilanes:
 alkyl(phenyl)polysilane, 254–255
 dialkylpolysilanes, switching preferential
 screw sense, helix-helix transition,
 234–238
 diarylpolysilanes, 264–265
 site-controlled stereospecific polymerizations,
 titanium trichloride catalysts, 40–42
- Molecular polarizability, linear optics, chiral
 molecules, 521–522
- Monomeric copolymers:
 chiral crystallization, helical chain conformation,
 142–147
 chiral recognition, 159–161
 crystalline constitution and conformation, 72–74
 helical conformation, 84
- Monotropic phase, ferroelectric liquid crystals,
 smectic C phase (SmC), 466–470
- Monte Carlo technique:
 chiral recognition, computational studies,
 200–201
 thermotropic cholesterics, 446–447
- Nanoparticle imaging, self-assembled molecules,
 chirality characteristics, diacytlenic
 phospholipids, 326–327
- Nanotubular morphology, self-assembled molecules,
 chirality characteristics, mixed phospholipids,
 331–333
- Natural polymer derivatives, chiral recognition:
 polysaccharides, 168–201
 cellulose/amylose arylalkylcarbamates,
 179–180
 cellulose/amylose cycloalkylcarbamates, 181
 cellulose/amylose phenylcarbamates,
 172–179
 cellulose esters, 168–172
 chromatographic studies, 186–190
 computational studies, 199–201

- NMR studies, 190–199
 - oligosaccharides and cyclodextrins, 182–183
 - phenylcarbamates, 183–184
 - recognition mechanism, 185–201
- proteins, 167–168
- Nd:YAG laser experiments, nonlinear optics (NLO):
 - expansion coefficient determination, 541–544
 - thin films, 565–566
- Nematic discotic (N_D) mesophase:
 - cholesteric handedness, 426–431
 - thermotropic cholesterics, 444–446
 - thermotropic liquid crystals:
 - chiral induction, 379–382
 - research background, 377–378
- Nematic mesophase, INAC phase sequence, 463–464
- NH protons, chiral recognition studies, 187–190
- Nonbridged binaphthyls, thermotropic cholesterics, 448–450
- Nonchiral systems:
 - chiral molecular self-assembly models, 343–347
 - electrostatics, 343–344
 - orientational elasticity, 345–346
 - spontaneous curvature, 346–347
 - helical chain conformation, 143–147
- Nonconjugated dienes, homogeneous metallocene catalysts, cyclopolymerization, 26–27
- Noncooperative self-assembly, discotic chiral columns, 399–407
- Nonhexagonal lattices, helical chain conformation, chiral crystallization, 145–147
- Nonhydroxy fatty acid cerebroside (NFA-Cer), chiral self-assembly, 300–301
- Nonlinear optics (NLO):
 - chiral molecules:
 - basic principles, 523–527
 - future research issues, 567
 - linear optics research, 521–522
 - magnetic dipole contributions, 529–530
 - molecular origins, 530–532
 - optical activity, 522–523
 - research background, 520–521
 - second-harmonic generation, 527–529, 535–541
 - 1,1'-binaphthyl-based helical polymers, 557–558
 - biological sampling, 562–563
 - continuous polarization measurements, 538–541
 - electric dipole approximation failure, 554–557
 - electromagnetic second-order susceptibility tensors, quantitative determinations, 550–554
 - expansion coefficient determination, 541–544
 - experimental studies, 544–563
 - helicenebisquinone derivatives, 559–562
 - linearly/circularly polarized probes, 545–550
 - optical rotation effects, 537–538
 - second-order applications, 563–566
 - isotropic bulk media, 564–565
 - thin films, 565–566
 - theoretical formalism, 532–535
 - helical self-assembly, chiral columns, 387
- Nonparallel chains:
 - crystalline polymers, 112–113
 - self-assembled molecules, chirality characteristics, 283
- Nonracemic samples, nonlinear optics, helicenebisquinone derivative, 560–562
- NonylOxyBOW (NOBOW):
 - banana phases, 487, 491–495
 - ferroelectric macroscopic racemate, unichiral mesogens, 512–514
 - future research applications, 514
 - SmCP phases, 495–496
 - supermolecular diastereomers, 500–502
 - SmC_sP_A/SmC_AP_A antiferroelectric phases, 496–500
- NORABOW materials, ferroelectric banana phases, 508–512
- Nuclear magnetic resonance (NMR):
 - chiral recognition studies, 190–199
 - chiral stationary phases (CSPs) optically active polymers, 158–159
 - optically active polysilanes, 211–213
 - self-assembled molecules, chirality characteristics:
 - aldonamides, 289–293
 - mixed phospholipids, 332–333
- Nucleotides, chiral molecular self-assembly, 333–337
- “Odd-even” effect, poly chiral aggregates, molecular chiral recognition, 250–251
- Olefins:
 - alternating copolymers, 105–109
 - chain-end controlled polymerizations:
 - primary 1-alkene insertions, 49–51
 - secondary 1-alkene insertions, 51–54
 - chirality polymerization mechanisms, molecular modeling, 13
- Oligomer side chains, self-assembled discotic liquid crystals, 416–418
- Oligosaccharides, chiral recognition, 182–183
- Optical activity:
 - alkyl(alkoxyphenyl)polysilane:
 - enantiopure chiral chains, 239
 - global-local conformation:
 - main-chain helicity, remote chiral group control, 242–243
 - substituent effects and cooperative helical order effect, 240–242
 - poly chiral aggregates:
 - chiroptical properties, 244–246
 - chiroptical switching and memory, 243–244
 - solvent effects, 248
 - temperature effects, 246–248
 - poly molecular chirality recognition, 248–251
 - alkyl(phenyl)polysilane, 251–259
 - chiral-achiral substituents, copolymer UV and CD spectra, 253–254

- Optical activity: (*Continued*)
- copolymer UV and CD spectra, 255–256
 - Ising model, CD spectral analysis, 256–258
 - molecular mechanics calculation, 254–255
 - optically inactive homopolymer UV
 - absorption, fluorescence spectra, and fluorescence anisotropy, 252–253
 - research issues, 258–259
 - chiral molecules, basic principles, 522–523
 - chiral recognition ability, 159–161
 - natural polymer derivatives:
 - polysaccharides, 168–201
 - cellulose/amylose arylalkylcarbamates, 179–180
 - cellulose/amylose
 - cycloalkylcarbamates, 181
 - cellulose/amylose phenylcarbamates, 172–179
 - cellulose esters, 168–172
 - chromatographic studies, 186–190
 - computational studies, 199–201
 - NMR studies, 190–199
 - oligosaccharides and cyclodextrins, 182–183
 - phenylcarbamates, 183–184
 - recognition mechanism, 185–201
 - proteins, 167–168
 - polyamides, 166
 - synthetic polymers, 166–167
 - vinyl polymers, 161–166
 - polymethacrylates, 161–165
 - dialkylpolysilanes:
 - copolymers, preferential screw sense and “majority rule” principle, 226–228
 - diastereomeric helicities, 223–224
 - enantiopure termini effects,
 - sergeants-and-soldiers cooperativity, 228–230
 - helix-helix switching, preferential screw sense, 230–238
 - preferential screw sense copolymers,
 - “sergeants-and-soldiers” principle, 224–226
 - preferential screw sense homopolymers,
 - enantiopure chiral side chains, 219–222
 - research issues, 238–239
 - rodlike single molecule imaging, 222
 - diarylpolysilanes, 259–274
 - circularly polarized photoluminescence, 273–274
 - copolymer CD and UV spectroscopy and cooperativity, 266–269
 - homopolymer CD and UV spectroscopy, 259–263
 - molecular mechanics calculations, 264–265
 - poly(diarylsilane) aggregates, 272–273
 - research issues, 274
 - thermo-driven helix-helix transition, 270–272
 - helical conformation, 93–94
 - historical background, 210–211
 - polysilanes:
 - global conformation, optical correlation, 216–219
 - helical conformation, circular dichroism, 213–214
 - preferential screw sense helical ordering, 214–216
 - preparation, 213
 - structure, 211–213
 - structure and properties, 157–159
 - Optical rotation measurements:
 - chiral stationary phases (CSPs) optically active polymers, 158–159
 - cholesteric handedness, 433–436
 - second-harmonic generation, chiral molecules, 537–538
 - Optical rotatory dispersion (ORD), second-harmonic generation (SHG-ORD), 538
 - biological samples, 563
 - Organic materials, reflection symmetry breaking:
 - B2 spontaneous reflections, 489–495
 - crystal conglomerates, 474–475
 - SmCP phases, 495–496
 - spontaneous reflection, 475–478
 - Oriental order, nonchiral self-assembly models, 345–346
 - Packing mechanisms:
 - helical self-assembly, chiral columns, side-chain packing, 389–391
 - self-assembled molecules, chirality
 - characteristics, 283–284
 - diacetylenic phospholipids, 319–327
 - molecular chiral models, 347–349
 - Palladium catalysts, linear alternating copolymers, 106–109
 - 1-Palmitoyl-2-oleoyl-*sn*-glycero-3-phosphocholine (L-POPC), chiral molecular self-assembly, 322–327
 - Paracrystalline modifications, disordered conformation, crystalline polymers, 122–124
 - Peptide-based amphiphiles, chiral molecular self-assembly, 302–317
 - amino acids, 302–311
 - peptides, 311–317
 - Peptides, self-assembled molecules, chirality
 - characteristics, 311–317
 - Phenanthrenes, ferroelectricity, 394–395
 - Phenylcarbamates, chiral recognition:
 - cellulose/amylose derivatives, 172–179
 - chromatographic studies, 189–190
 - NMR studies, 190–199
 - polysaccharide derivatives, 183–185
 - Phosphatidylcholine, nonlinear optics, 562–563
 - Phospholipids, chiral molecular self-assembly, 317–333
 - diacetylenic phospholipids, 318–327
 - diacetylenic phosphonate lipids, 327–331
 - mixtures, 331–333
 - Photoluminescence, poly(diarylsilane) aggregates, 273–274
 - Photon annihilation and creation, chiral molecule
 - optical activity, 523
 - Phthalocyanines:
 - helical self-assembly, chiral columns, side-chain packing, 389–391
 - noncooperative self-assembly, 401–407

- π -coordinated ligands, homogeneous metallocenes:
 - chain migratory insertion mechanism, 22–24
 - growing chain chiral orientation, 16–21
 - regioirregular insertion stereoselectivity, 29–31
 - regiospecificity dependence, primary/secondary insertions, 32–34
 - site-controlled stereospecific polymerizations, 14
- π – π interactions:
 - nonlinear optics, electric dipole approximation failure, 554–557
 - self-assembled discotic liquid crystals, 397
- Pitch-to-diameter ratio, cholesteric handedness, helical polymers, 437–441
- Planar conformation:
 - banana phases, molecular bow plane, 491–495
 - cholesteric handedness, 431–436
 - isotactic/syndiotactic structures, energy calculations, 88–92
- PM6R8 monomer, achiral liquid crystals, 481–483
- Poincaré method, spontaneous reflection symmetry breaking, liquid crystals, 476–478
- Polarization measurements, nonlinear optics (NLO):
 - 1,1'-binaphthyl-based helical polymer, 557–558
 - expansion coefficients, 543–544
- Polar symmetry:
 - chiral nonlinear optics, second-order applications, 563–566
 - ferroelectric liquid crystals, smectic C phase (SmC), 464–470, 466–470
- Poly(2-vinylpyridine), frustrated structures, 120–121
- Poly(4-methyl-1-pentene):
 - isotactic/syndiotactic structures, conformational energy calculations, 84–92
 - symmetry breaking, 116–118
- Polyacetylenes, chiral recognition, 167
- Polyacrylamides, chiral recognition, 165–166
- Poly chiral aggregates:
 - chiroptical properties, 244–246
 - chiroptical switching and memory, 243–244
 - molecular chiral recognition, 248–251
 - solvent effects, 248
 - temperature effects, 246–248
- Poly(alkyl(aryl)silane)s, optically active properties, 258–259
- Polyamides, chiral recognition, 166
- Polybutene, isotactic/syndiotactic structures, conformational energy calculations, 84–92
- Poly(diarylsilane) aggregates, optically active functions, 272–273
- Polydienes, chain conformation, 94–102
- Poly- γ -benzyl-L-glutamate (PBLG), cholesteric handedness, 429–431
- Poly(isocyanide), nonlinear optics, linear/circular polarized probes, comparison, 545–550
- Polymer backbones:
 - cholesteric handedness, helical polymers, 438–441
 - helical self-assembly, chiral columns, 387–389
- Polymethacrylates, chiral recognition, 161–166
- Polymethylacrylamides, chiral recognition, 165–166
- Poly(*N*-benzyl-L-glutamine), chiral recognition, 166
- Polypropylene:
 - chain conformation, 3–6
 - frustrated structures, 119–121
 - kink-band disorder, 136–140
 - isotactic/syndiotactic structures, conformational energy calculations, 84–92
- Poly((*S*)-3-methyl-1-pentene), helical conformation, optical activity, 93–94
- Polysaccharides, chiral recognition, 168–201
- cellulose/amylose complexes:
 - arylalkylcarbamates, 179–180
 - cycloalkylcarbamates, 181
 - phenylcarbamates, 172–179
- cellulose esters, 168–172
- chromatographic studies, 186–190
- computational studies, 199–201
- NMR studies, 190–199
- oligosaccharides and cyclodextrins, 182–183
- phenylcarbamates, 183–184
- recognition mechanism, 185–201
- Polysilanes:
 - helical conformation, 213–214
 - optically active compounds:
 - alkyl(alkoxyphenyl)polysilane:
 - enantiopure chiral chains, 239
 - global-local conformation
 - main-chain helicity, remote chiral group control, 242–243
 - substituent effects and cooperative helical order effect, 240–242
 - poly chiral aggregates
 - chiroptical properties, 244–246
 - chiroptical switching and memory, 243–244
 - solvent effects, 248
 - temperature effects, 246–248
 - poly molecular chirality recognition, 248–251
 - alkyl(phenyl)polysilane, 251–259
 - chiral-achiral substituents, copolymer UV and CD spectra, 253–254
 - copolymer UV and CD spectra, 255–256
 - Ising model, CD spectral analysis, 256–258
 - molecular mechanics calculation, 254–255
 - optically inactive homopolymer UV absorption, fluorescence spectra, and fluorescence anisotropy, 252–253
 - research issues, 258–259
- dialkylpolysilanes:
 - copolymers, preferential screw sense and “majority rule” principle, 226–228
 - diastereomeric helicities, 223–224
 - enantiopure termini effects, sergeants-and-soldiers cooperativity, 228–230
 - helix-helix switching, preferential screw sense, 230–238
 - preferential screw sense copolymers, “sergeants-and-soldiers” principle, 224–226

- Polysilanes: (*Continued*)
- preferential screw sense homopolymers, enantiopure chiral side chains, 219–222
 - research issues, 238–239
 - rodlike single molecule imaging, 222
 - diarylpolysilanes, 259–274
 - circularly polarized photoluminescence, 273–274
 - copolymer CD and UV spectroscopy and cooperativity, 266–269
 - homopolymer CD and UV spectroscopy, 259–263
 - molecular mechanics calculations, 264–265
 - poly(diarylsilane) aggregates, 272–273
 - research issues, 274
 - thermo-driven helix-helix transition, 270–272
 - preparation and structure, 213
- Polystyrene:
- isotactic/syndiotactic structures, conformational energy calculations, 85–92
 - symmetry breaking, 115–118
- Polytetrafluoroethylene (PTFE), disordered conformation, 102–105
- Poly(thiophene), nonlinear optics, electric dipole approximation failure, 554–557
- Polyurethanes, chiral recognition, 166–167
- Positional ordering, discotic liquid crystals:
- helical self-assembly, chiral columns, 385–387
 - helicene self-assembly, 415–418
 - self-assembly, achiral expression, 398–399
- Preferential screw sense, optically active polysilanes:
- dialkylpolysilanes:
 - copolymers, “sergeants and soldiers” principle, 224–226
 - homopolymers, enantiopure chiral side chains, 219–222
 - “majority rule” principle, 226–228
 - switching preferential screw sense, helix-helix transition, 230–238
 - diarylpolysilanes, 262–263
 - copolymer cooperativity, 268–269
 - helical ordering, 214–216
- Preinsertion intermediates:
- chirality polymerization mechanisms, 13
 - conjugated dienes, 59–61
 - growing chain chiral orientation, stereoselectivity, 14–21
 - regiospecificity dependence, primary/secondary insertions, 33–34
- Prions, peptide amphiphiles, chiral molecular self-assembly, 311–317
- Propeller mechanism:
- chiral recognition, vinyl polymers, 163–166
 - discotic liquid crystals, helical self-assembly, chiral columns, 386–387
- Propene monomers:
- crystalline properties, 2–9
 - isotacticity index, 5–7
- Proteins, chiral recognition, 167–168
- Pseudo-hexagonal packing, chain conformation, mesomorphic modifications, 141–142
- Pterine-related molecules, self-assembly mechanisms, 412–415
- PYP906 mesogen, INAC phase sequence, 462–464
- Pyramidal molecules, ferroelectricity, 395–396
- Quantitative techniques, nonlinear optics, electro-magnetic second-order susceptibility, quantitative determination, 550–554
- Quantum mechanics/molecular mechanics (QM/MM) techniques:
- chiral recognition, 199–201
 - metallocene symmetry, *E*–*Z* selectivity, 36–38
- Quarter waveplate technique:
- nonlinear optics (NLO):
 - continuous polarization measurements, 538–541, 544–545
 - electro-magnetic second-order susceptibility, quantitative determination, 550–554
 - linear/circular polarized probes, comparison, 545–550
- Quasi-phase matching, thin films, second-order nonlinear optics (NLO), 565–566
- Racemic acid, crystal conglomerates, reflection symmetry breaking, 474–475
- Racemic polymers:
- chiral crystallization, helical chain conformation, 142–147
 - chiral recognition, 163–166
 - cellulose/amylose arylalkylcarbamates, 180
 - cellulose/amylose phenylcarbamates, 176–179
 - NMR studies, 191–199
 - cone-shaped molecule ferroelectricity, 396
 - ferroelectric banana phase design, 505–512
 - nonlinear optics, helicenebiquinone derivative, 559–562
 - second-harmonic generation, optical rotation effects, 537–538
- Racemo*-isotactic/syndiotactic configurations, alternating copolymers, 105–109
- (*Rac*)-MHOBOW, ferroelectric banana phase design, 505–512
- re* coordinations, chirality polymerization mechanisms, 9
- Reflection symmetry, ferroelectric liquid crystals, smectic C phase (SmC), 465–470
- Reflection symmetry breaking, liquid crystals:
- B2 spontaneous reflections, 489–495
 - organic crystal conglomerates, 474–475
 - SmCP phases, 495–496
 - spontaneous reflection, 475–478
- Refractive index, banana phases, 491–495
- Regioirregular insertion stereospecificity, homogeneous metallocene catalyst chirality, 27–31
- Regiospecificity, metallocene symmetry, 31–34
- Remote chiral groups, optically active alkyl(alkoxyphenyl)polysilanes, helicity control, 242–243

- Resolution factor, chiral recognition, 159–161
- Resonant conditions, nonlinear optics (NLO),
linear/circular polarized probes, comparison,
549–550
- Rodlike single molecule, optically active
dialkylpolysilanes:
enantiopure chiral termini, sergeants-and-soldiers
cooperativity, 230
molecular imaging, 222
“sergeants-and-soldiers” principle, preferential
screw sense, 225–226
switching preferential screw sense, helix-helix
transition, 230–238
- Rotational echo double-resonance NMR,
self-assembled molecules, chirality
characteristics, aldonamides, 290–293
- Rotation symmetry:
B4 smectic phases, 488–489
ferroelectric liquid crystals, smectic C phase
(SmC), 465–470
- r/R* ratio, crystalline polymers, macromolecular
packing, 110–113
- “Sergeants-and-soldiers” principle:
disclotic liquid crystals:
cooperative self-assembly, 409–411
noncooperative self-assembly, 400–407
optically active alkyl(alkoxyphenyl)polysilanes,
global-local conformation, 241–243
optically active dialkylpolysilane copolymers,
224–226
enantiopure chiral termini effects, 228–230
- Scanning electron microscopy (SEM),
self-assembled molecules, 285–287
- Scanning tunneling microscopy (STM), optically
active dialkylpolysilanes, molecular imaging,
rodlike polysilanes, 222
- Schiff base moieties:
ferroelectric banana phase design, 505–512
SmC₅P_A/SmC_AP_A antiferroelectric phases,
499–500
- Schoenflies symbols, ferroelectric liquid crystals,
smectic C phase (SmC), 464–470
- Screw models:
cholesteric handedness, helical polymers,
436–441
optically active polysilanes, 211–213
dialkylpolysilanes:
diastereomeric helicities, screw senses
and pitches, 223–224
preferential screw sense
copolymers, “sergeants and soldiers”
principle, 224–226
enantiopure chiral side chains,
219–222
“majority rule” principle, 226–228
switching preferential screw sense,
helix-helix transition, 230–238
diarylpolysilanes, 262–263
preferential screw sense ordering, 214–216
- Second-harmonic generation circular dichroism
(SHG-CD):
continuous polarization measurements, 538–541
- nonlinear optics:
1,1'-binaphthyl-based helical polymer,
557–558
biological samples, 563
chirality signatures, 535–536
chiral surfaces, 545–550
expansion coefficient determination, 543–544
helicenebisquinone derivative, 559–562
research background, 520–521, 527–529
- Second-harmonic generation linear difference
(SHG-LD):
continuous polarization measurements, 538–541
- nonlinear optics:
chirality signatures, 536–537
chiral surfaces, 545–550
research background, 520–521, 527–529
- Second-harmonic generation optical rotatory
dispersion (SHG-ORD):
basic principles, 538
biological samples, 563
- Second-harmonic generation (SHG), nonlinear
optics (NLO):
basic principles, 524–527
chiral molecules:
basic properties, 527–529, 535–541
1,1'-binaphthyl-based helical polymers,
557–558
biological sampling, 562–563
continuous polarization measurements,
538–541
electric dipole approximation failure,
554–557
electromagnetic second-order susceptibility
tensors, quantitative determinations,
550–554
expansion coefficient determination, 541–544
experimental studies, 544–563
helicenebisquinone derivatives, 559–562
linearly/circularly polarized probes,
545–550
optical rotation effects, 537–538
magnetic dipole contributions, 529–530
theoretical formalism, 532–535
- Self-assembled molecules:
applications, 285–286
chirality:
carbohydrate amphiphiles, 287–301
aldonamides, 287–293
cerebrosides, 300–301
glycolipids, 293–299
future issues, 364–365
gemini surfactants, 340–342
models, 342–363
biased symmetry breaking, 360–363
continuum elastic theory, uniformly tilted
membranes, 349–353
cylindrical vs. Gaussian curvature,
358–359
membrane tilt variations, 353–358
molecular techniques, 347–349
nonchiral models, 343–347
electrostatics, 343–344
orientational elasticity, 345–346

- Self-assembled molecules: (*Continued*)
 spontaneous curvature, 346–347
 symmetry breaking, 359–360
 nucleotide systems, 333–337
 peptide-based amphiphiles, 302–317
 amino acids, 302–311
 peptides, 311–317
 phospholipids, 317–333
 diacetylenic phospholipids, 318–327
 diacetylenic phosphonate lipids, 327–331
 mixtures, 331–333
 research background, 282–287
 steroid-based systems, 337–340
 cholesteric handedness, helical polymers, 436–441
 discotic liquid crystals, 396–411
 absence of positional order, 398–399
 cooperative self-assembly, 407–411
 guanine and pterine-related molecules, 412–415
 helices, 415–418
 noncooperative self-assembly, chiral columns, 399–407
 nonlinear optics, second-harmonic generation (SHG), 526–527
- Separation factor, chiral recognition, 159–161
- Shape models, thermotropic cholesterics, 446–447
- si* coordinations:
 chirality polymerization mechanisms, 9
 growing chain chiral orientation, stereoselectivity, 15–21
 homogeneous metallocenes, regioirregular insertion stereoselectivity, 27–31
- Side chains:
 alkyl(alkoxyphenyl)polysilanes, enantiopure chiral side chains, 239
 helical self-assembly, chiral columns, side-chain packing, 389–391
 optically active dialkylpolysilanes:
 preferential screw sense homopolymers, 219–222
 switching preferential screw sense, helix-helix transition, 230–238
 self-assembled molecules:
 cooperative self-assembly, 407–411
 helicene self-assembly, 416–418
- σ -coordinated ligands, site-controlled stereospecific polymerizations, homogeneous metallocenes, 14
- ²⁹Si NMR:
 optically active alkyl(alkoxyphenyl)polysilanes, helicity control, remote chiral groups, 243
 optically active dialkylpolysilanes, switching preferential screw sense, helix-helix transition, 232–238
- Silica gel, chiral recognition, vinyl polymers, 161–166
- Single-molecule moieties, optically active dialkylpolysilanes, molecular imaging, rodlike polysilanes, 222
- Single-site catalysts, structure and properties, 7–9
- Site-controlled stereospecific polymerizations, catalyst chirality, 13–48
 heterogeneous catalysts, 38–46
 magnesium chloride systems, 42–46
 titanium trichloride systems, 39–42
 homogeneous metallocenes, 13–38
 back-skip of growing chain, 25–26
 2-butene cyclopolymers, *E-Z* selectivity, 34–38
 chain migratory insertion mechanism, 21–24
 nonconjugated dienes, cyclopolymerization, 26–27
 regioirregular insertion stereospecificity, 27–31
 regioselectivity, symmetry dependence, 31–34
 stereoselectivity mechanism, 14–21
 stereospecific heterogeneous/homogeneous comparisons, 46–48
- Size-exclusion chromatography (SEC), optically active polysilanes, global conformation, 216–219
- Small-angle neutron scattering (SANS), self-assembled discotic liquid crystals:
 achiral expression, 398–399
 cooperative self-assembly, 409–411
 guanine- and pterine-related molecules, 412–415
- SmAP_A:
 achiral structure, 480–483
 ferroelectric banana phase design, 502–512
- SmAP_F, achiral structure, 480–483
- SmC_AP_A antiferroelectric phases, structural properties, 496–500
- SmCP phases:
 chiral structure, 495–496
 ferroelectric banana phase design, 503–512
- SmC_SP_A antiferroelectric phases:
 ferroelectric banana phase design, 502–512
 structural properties, 496–500
- Smectic A phase (SmA):
 achiral structures, 479–483
 INAC phase sequence, 463–464
- Smectic C phase (SmC):
 ferroelectric liquid crystals, 464–470
 INAC phase sequence, 463–464
 Matsunaga diesters, 486–487
- SmC* phase:
 achiral structures, 483
 antiferroelectric liquid crystals, 470–474
- Smectic CP phases, stereogenic elements, 500–502
- Sodium dodecyl sulfate (SDS), self-assembled molecules, chirality characteristics, aldonamides, 292–293
- Softness parameters, self-assembled molecules, chirality characteristics, membrane tilt variations, 357–358
- Solid-state nuclear magnetic resonance (NMR), self-assembled molecules, chirality characteristics, aldonamides, 290–293
- Solvatochromism, nonlinear optics, electric dipole approximation failure, 554–557
- Solvent effects:
 poly chiral aggregates, 248

- self-assembled molecules, chirality
 - characteristics, aldonamides, 292–293
 - thermotropic cholesterics, 445–446
- Sto Bustamante-Blinov achiral antiferroelectric bilayer, ferroelectric banana phase design, 502–512
- Sphingolipids, self-assembled molecules, chirality characteristics, 300–301
- Spontaneous curvature, nonchiral self-assembly models, 346–347
- Spontaneous reflection symmetry breaking:
 - B2 phases, 489–495
 - liquid crystals, 475–478
- Staggered conformations, discotic liquid crystals, noncooperative self-assembly, 402–407
- Statistical mechanics, thermotropic cholesterics, 446–447
- Stereochemistry, liquid crystals, supermolecular structure and, 458–464
- Stereogenic properties, SmCP supermolecular diastereomers, 500–502
- Stereoselectivity, homogeneous metallocenes:
 - growing chain chiral orientation, 14–21
 - regioirregular insertions, 29–31
- Stereospecific polymerizations:
 - catalyst chirality:
 - chain-end controlled polymerizations, 48–61
 - conjugated diene, 57–61
 - olefins, 48–54
 - primary 1-alkene insertions, 49–51
 - secondary 1-alkene insertions, 51–54
 - styrene/substituted styrene syndiotactic polymerization, 54–57
 - mechanisms and elements, 9–13
 - site-controlled polymerizations, 13–48
 - heterogeneous catalysts, 38–46
 - magnesium chloride systems, 42–46
 - titanium trichloride systems, 39–42
 - homogeneous metallocenes, 13–38
 - back-skip of growing chain, 25–26
 - 2-butene cyclopolymers, *E-Z* selectivity, 34–38
 - chain migratory insertion mechanism, 21–24
 - nonconjugated dienes,
 - cyclopolymerization, 26–27
 - regioirregular insertion
 - stereospecificity, 27–31
 - regiospecificity, symmetry dependence, 31–34
 - stereoselectivity mechanism, 14–21
 - stereospecific
 - heterogeneous/homogeneous comparisons, 46–48
 - structure and properties, 2–9
 - crystalline constitution and conformation, 72–74
- Steric hindrance:
 - flat discotics, ferroelectricity, 392–395
 - self-assembled molecules, chirality characteristics:
 - aldonamides, 289–293
 - noncooperative self-assembly, 403–407
- Steroid-based systems, chiral molecular self-assembly, 337–340
- Styrene-carbon monoxide copolymers, constitution, 106–109
- Styrene/substituted styrenes:
 - chain-end controlled polymerizations, catalyst chirality, 54–57
 - linear alternating copolymers, 106–109
- Submicrometer particles, self-assembled molecules, applications, 285–286
- Substituents:
 - chiral recognition studies, 188–190
 - optically active alkyl(alkoxyphenyl)polysilanes, global-local conformation, 240–242
 - optically active alkyl(phenyl)polysilane:
 - chiral-achiral substituent copolymers, 253–254
 - circular dichroism (CD) spectra, 257–258
- Supercoiled structures, discotic liquid crystals, noncooperative self-assembly, 403–407
- Supermolecular stereochemistry:
 - banana phases, 490–495
 - ferroelectric banana phase design, 505–512
 - ferroelectric liquid crystals, smectic C phase (SmC), 466–470
 - liquid crystals, 458–464
 - SmCP stereogenic phases, 500–502
- Supramolecular structures:
 - discotic liquid crystals, 377
 - helical self-assembly, chiral columns, 384–387
 - self-assembled lyotropic molecules, 396–411
 - liquid crystals as, 459–462
 - self-assembled molecules, chirality characteristics, 283–284
 - aldonamides, 287–293
 - guanaine- and pterine-related molecules, 412–415
 - noncooperative self-assembly, 399–407
 - steroid-based systems, 338–340
- Surface stabilized FLC (SSFLC) geometry:
 - antiferroelectric liquid crystals, SmC_A^{*} phase, 470–474
 - ferroelectric banana phases, 506–512
 - ferroelectric liquid crystals, smectic C phase (SmC), 468–470
 - SmC_SP_A/SmC_AP_A antiferroelectric phases, 498–500
- Surfactants, self-assembled molecules, chirality characteristics, gemini surfactants, 340–342
- Susceptibility tensors, nonlinear optics, electro-magnetic second-order susceptibility, quantitative determination, 550–554
- Switching phenomenon, poly chiral aggregates, chiroptical properties, 243–246
- Symmetry breaking:
 - crystalline polymers, 113–118
 - liquid crystals:
 - B2 spontaneous reflections, 489–495
 - organic crystal conglomerates, 474–475
 - SmCP phases, 495–496
 - spontaneous reflection, 475–476
 - self-assembled molecules, chirality characteristics:
 - biased chiral models, 360–363

- Symmetry breaking: (*Continued*)
 chiral models, 359–360
 nonchiral models, spontaneous curvature, 346–347
 research background, 285
- Symmetry elements:
 chiral molecule nonlinear optics, 525–527
 1,1'-binaphthyl-based helical polymer, 557–558
 linear/circular polarized probes, comparison, 545–550
 second-harmonic generation, 528–529
 second-order applications, 563–566
 isotropic bulk media, 564–565
 thin films, 565–566
 crystalline polymers, macromolecular packing, 112–113
- Synclincity:
 achiral smectic phases, 480–483
 ferroelectric banana phases, 502–512
 $\text{SmC}_S\text{P}_A/\text{SmC}_A\text{P}_A$ antiferroelectric phases, 497–500
- Syndiospecific systems:
 chain-end controlled olefin polymerizations, 48–49
 secondary 1-alkene insertions, 51–54
 conjugated diene polymerization, 58–61
 homogeneous metallocenes, regioirregular insertion stereoselectivity, 30–31
 regiospecificity dependence, primary/secondary insertions, 33–34
- Syndiotactic structures:
 chain conformation:
 energy calculations, 84–92
 frustrated structures, 123
 kink-band disorder, 136–140
 macromolecular stacking disorder, single lattice direction, 131–136
 mesomorphic modifications, 141–142
 polydienes, 94–102
 conjugated dienes, 58–61
 crystalline constitution and conformation, 73–78
 helical conformation, 78–84
 styrene-carbon monoxide (s-STCO) copolymers, 107–109
 styrene/substituted styrenes, 54–57
 symmetry breaking, sPP, 113–118
- Synthetic polymers:
 chiral recognition, 166–167
 optically active compounds, 210–211
- Talonamide, self-assembled molecules, chirality characteristics, 289–293
- Temperature dependence:
 cholesteric handedness, helical polymers, 439–441
 optically active dialkylpolysilanes, switching preferential screw sense, helix-helix transition, 231–238
 poly chiral aggregates, 246–248
 racemization and, cone-shaped molecule ferroelectricity, 396
- self-assembled molecules, chirality characteristics:
 amino acid amphiphiles, 303–311
 diacetylenic phospholipids, 318–327
 thermotropic liquid crystals, nematic discotic (N_D) mesophase, chiral induction, 380–382
- Tensor components, nonlinear optics:
 electro-magnetic second-order susceptibility, quantitative determination, 550–554
 expansion coefficient determination, 543–544
 isotropic bulk media, 564–565
 second-harmonic generation (SHG), 526–527, 529–530
- Tetrahydrofuran (THF):
 chiral recognition, cellulose/amylose phenylcarbamates, 177–179
 poly chiral aggregates, chiroptical properties, 243–248
- Tetrazole complexes, noncooperative self-assembly, 400–407
- Thermo-driven helix-helix transition, optically active diarylpolysilanes, 270–272
- Thermotropic mesophase:
 chiral discotic liquid crystals, 377–396
 chiral core discotics, 391–392
 ferroelectricity, 392–396
 cone-shaped molecules, 395–396
 flat discotics, 392–395
 helical self-assembly, 382–391
 helical core, 382–387
 polymer backbone-controlled helicity, 387–389
 side-chain packing, 389–391
 N_D mesophase, 379–382
 research background, 374–376
 cholesteric handedness:
 biaryl moiety, 447–450
 chiral/biaryl molecule comparisons, 450–451
 empirical methods, 442–446
 models and techniques, 441–451
 research background, 425–431
- Thin films, second-order nonlinear optics, 565–566
- Three-dimensional periodicity, disordered conformation, crystalline polymers, 121–124
- Threo* structures:
 alternating copolymers, 105–109
 chain conformation, polydienes, 94–102
 crystalline constitution and conformation, 73–75
- Tilt-induced dipole moment, flat discotics, ferroelectricity, 392–395
- Tilt plane:
 antiferroelectric liquid crystals:
 bilayer smectics, 478–483
 SmC_A^* phase, 474
 banana phases, ferroelectricity, 502–512
 ferroelectric liquid crystals, smectic C phase (SmC), 466–470
 membrane self-assembly, 353–358
 $\text{SmC}_S\text{P}_A/\text{SmC}_A\text{P}_A$ antiferroelectric phases, 499–500
- Titanium trichloride catalysts:
 site-controlled stereospecific polymerizations, 39–42

- magnesium chloride catalysts and, 43–46
- stereospecificity mechanism, 5
- Torsion angles:
 - chain conformation, polydienes, 96–102
 - isotactic/syndiotactic structures, conformational energy calculations, 92
- Trans*-1,4-poly(1,3-butadiene), disordered conformation, 102–105
- Trans* conformation:
 - crystalline structures, 77–78
 - kink-band disorder, 138–140
 - macromolecular stacking disorder, single lattice direction, 134–136
 - symmetry breaking, 115–118
 - helical chain conformation, chiral crystallization, 145–147
 - isotactic/syndiotactic structures, energy calculations, 84–92
 - mesomorphic modifications, 140–142
 - optically active alkyl(phenyl)polysilane, chiral-achiral substituent copolymers, 253–254
 - polydienes, 94–102
 - self-assembled molecules, chirality characteristics:
 - aldonamides, 289–293
 - glycolipids, 296–299
- Transmission electron microscopy (TEM), self-assembled molecules, chirality characteristics:
 - amino acid amphiphiles, 310–311
 - glycolipids, 295–299
- Trigonal packing:
 - crystalline polymers, 111–113
 - frustrated structures, 119–121
- Triphenylenes, self-assembled molecules, achiral expression, 399
- Triphenylmethyl methacrylate (TrMA), chiral recognition, 161–166
- Tris(hydroxymethyl)aminomethane (Tris), self-assembled molecules, chirality characteristics, amino acid amphiphiles, 306–311
- Tröger's base enantiomers, cellulose esters, chiral recognition, 169–172
- Tubular formations, self-assembled molecules, chirality characteristics, 285–286
 - aldonamides, 293
 - amino acid amphiphiles, 303–311
 - biased chiral symmetry breaking, 360–363
 - chiral symmetry breaking, 359–360
 - cylindrical *vs.* Gaussian curvature, 358–359
 - diacetylenic phospholipids, 318–327
 - diacetylenic phosphonate lipids, 327–331
 - glycolipids, 293, 295–299
 - membrane tilt variation, 353–358
 - mixed phospholipids, 331–333
 - nonchiral models:
 - electrostatics, 343–344
 - orientational elasticity, 345–346
 - spontaneous curvature, 346–347
 - uniformly tilted membranes, 349–353
- Twisted nematic cells, spontaneous reflection symmetry breaking, liquid crystals, 476–478
- Twist-grain boundary (TGB) structure, B4 smectic phases, 489
- Two-dimensional NMR, chiral recognition studies, 194–199
- Two-dimensional NOESY spectroscopy, chiral recognition studies, 194–199
- Twofold helical conformation, isotactic/syndiotactic polymers, 88–92
- Ultraviolet (UV) spectra, optically active polysilanes, 211–213
 - alkyl(alkoxyphenyl)polysilanes:
 - enantiopure side chains, 239
 - global-local conformation, 240–243
 - alkyl(phenyl)polysilane, 252–253
 - chiral-achiral substituent copolymers, 253–254
 - dialkylpolysilanes:
 - diastereomeric helicities, screw senses and pitches, 223–224
 - enantiopure chiral termini, sergeants-and-soldiers cooperativity, 228–230
 - “majority rule” principle, preferential screw sense, 227–228
 - preferential screw sense homopolymers, 220–222
 - “sergeants-and-soldiers” principle, preferential screw sense, copolymers, 225–226
 - switching preferential screw sense, helix-helix transition, 230–238
 - diarylpolysilanes:
 - basic properties, 259
 - copolymer cooperativity, 266–269
 - homopolymers, 259–263
 - thermo-driven helix-helix transition, 271–272
 - global conformation, 216–219
 - poly(alkyl(aryl)silane)s, 258–259
 - poly(diarylsilane) aggregates, 272–273
- Ultraviolet-visible (UV-Vis) spectroscopy:
 - nonlinear optics, helicenebisquinone derivative, 559–562
 - self-assembled discotic liquid crystals:
 - achiral expression, 399
 - noncooperative self-assembly, 401–407
- Unichiral mesogens, ferroelectric macroscopic racemate, 512–514
- Unit twist/height, isotactic polymers, helical conformation, 83–84
- Up/down disorder, chain conformations, 125–130
- Ureidotriazines, cooperative self-assembly, 411
- van der Waals radii:
 - helical self-assembly, chiral columns, 383–387
 - noncooperative self-assembly, discotic liquid crystals, 403–407
 - polymer crystal macromolecule packing, 109–113
- Vesicle structures:
 - amino acid amphiphile chirality, 303–311
 - nonchiral self-assembly models:

- Vesicle structures: (*Continued*)
 orientational elasticity, 345–346
 spontaneous curvature, 346–347
 phospholipid chiral molecular self-assembly,
 331–333
- Vinyl polymers:
 chiral recognition, polymethacrylates, 161–166
 crystalline configuration, 2–9
 helical conformation, optical activity, 93–94
- Water-dimethylformamide (DMF) solutions,
 cerebroside chirality, 300–301
- Waveplate techniques, nonlinear optics (NLO):
 continuous polarization measurements, 538–541,
 544–545
 electro-magnetic second-order susceptibility,
 quantitative determination, 550–554
 linear/circular polarized probes, comparison,
 545–550
- X-ray diffraction patterns:
 B4 smectic phases, 488–489
 chiral phthalocyanines, side-chain packing,
 390–391
 chiral recognition studies, 187–190
 discotic liquid crystals, 375–376
 chiral core, 392
 helical self-assembly, chiral columns,
 383–387
 disordered conformation, crystalline polymers,
 121–124
 kink-band disorder, 136–140
 long-range positional three-dimensional order,
 up and down chains, 125–130
 mesomorphic forms, 140–142
 nonlinear optics, helicenebisquinone derivative,
 561–562
 self-assembled molecules, chirality
 characteristics:
 aldonamides, 290–293
 diacetylenic phosphonate lipids, 327–331
- YAG laser, nonlinear optics, electric dipole
 approximation failure, 555–557
- Ziegler-Natta catalysts:
 alternating copolymers, 105–109
 future research issues, 61–62
 site-controlled stereospecific polymerizations,
 magnesium chloride catalysts, 43–46
 stereospecificity, 7–9
 structure and properties, 1–9
 syndiotactic polymerization, styrene/substituted
 styrenes, 55–57
- “Zigzag” conformation, ferroelectric liquid crystals,
 smectic C phase (SmC), 465–470
- Zimm-Bragg theory, cooperative self-assembly,
 discotic liquid crystals, 409–411

CUMULATIVE AUTHOR INDEX

Index comprises the names of contributors to Volumes 1–24 of **Topics in Stereochemistry**.

- Aaron, Herbert S., *Conformational Analysis of Intramolecular-Hydrogen-Bonded Compounds in Dilute Solution by Infrared Spectroscopy*, **11**, 1.
- Addadi, L., *A Link Between Macroscopic Phenomena and Molecular Chirality, Crystals as Probes for the Direct Assignment of Absolute Configuration of Chiral Molecules*, **16**, 1.
- Allen, L. C., *see* Buss, V., **7**, 253.
- Altona, C., *see* Romers, C., **4**, 39.
- Arad-Yellin, R., *see* Green, B. S., **16**, 131.
- Arigoni, D., *Chirality Due to the Presence of Hydrogen Isotopes at Noncyclic Positions*, **4**, 127.
- Arnett, E. M., *see* Stewart, M. V., **13**, 195.
- Ashby, E. C., *see* Boone, J. R., **11**, 53.
- Barton, D. H. R., *Conformational Analysis—The Fundamental Contributions of D. H. R. Barton and O. Hassel*, **6**, 1.
- Bauman, L. E., *see* Malloy, T. B. Jr., **11**, 97.
- Bell, R. A., *Some Chemical Applications of the Nuclear Overhauser Effect*, **7**, 1.
- Benfield, R. E., *see* Johnson, B. F. G., **12**, 253.
- Benner, S. A., *Stereospecificity in Enzymology: Its Place in Evolution*, **19**, 127.
- Berkovitch-Yellin, Z., *see* Addadi, L., **16**, 1.
- Berti, G., *Stereochemical Aspects of the Synthesis of 1,2-Epoxides*, **7**, 93.
- Binsch, G., *The Study of Intramolecular Rate Processes by Dynamic Nuclear Magnetic Resonance*, **3**, 97.
- Blanco, M.-J., *Transition-Metal-Templated Synthesis of Rotaxanes*, **23**, 125.
- Blaney, J. M., *see* Ripka, W. C., **20**, 1.
- Bonne, J. R., *Reduction of Cyclic and Bicyclic Ketones by Complex Metal Hydrides*, **11**, 53.
- Bonner, W. A., *Origins of Chiral Homogeneity in Nature*, **18**, 1.
- Bosnich, B., *Asymmetric Synthesis Mediated by Transition Metal Complexes*, **12**, 119.
- Brewster, J. H., *Helix Models of Optical Activity*, **2**, 1.
- Brunner, H., *Enantioselective Synthesis of Organic Compounds with Optically Active Transition Metal Catalysts in Substoichiometric Quantities*, **18**, 129.
- Brunsveld, L., *Chiral Discotic Molecules: Expression and Amplification of Chirality*, **24**, 373.
- Buckingham, D. A., *Conformational Analysis and Configurational Effects for Chelate Complexes*, **6**, 219.
- Bucourt, R., *The Torsion Angle Concept in Conformational Analysis*, **8**, 159.
- Bures, M. G., *Searching Techniques for Databases of Three-Dimensional Chemical Structures*, **21**, 467.

Materials-Chirality: Volume 24 of Topics in Stereochemistry,
Edited by Mark M. Green, R.J.M. Nolte, and E.W. Meijer
ISBN 0-471-05497-6 Copyright © 2003 John Wiley & Sons, Inc.

- Buss, V., *The Electronic Structure and Stereochemistry of Simple Carbonium Ions*, **7**, 253.
Buys, H. R., *see* Romers, C., **4**, 39.
- Carreira, L. A., *see* Malloy, T. B. Jr., **11**, 97.
Cavallo, Luigi., *see* Guerra, Gaetano, **24**, 1.
Chambron, J.-C., *see* Blanco, M.-J., **23**, 125.
Choi, N. S., *see* Goodman, M., **5**, 69.
Clark, C. I., *see* White, J. M. **22**, 137.
Closs, G. L., *Structures of Carbenes and the Stereochemistry of Carbene Additions to Olefins*, **3**, 193.
Cohen, M. D., *see* Green, B. S. **16**, 131.
Corradini, Paolo., *see* Guerra, Gaetano, **24**, 1.
Corriu, R. J. P., *Stereochemistry at Silicon*, **15**, 43.
Crabbé, P., *Applications of Optical Rotatory Dispersion and Optical Circular Dichroism in Organic Chemistry*, **1**, 93.
- Dale, J., *Multistep Conformational Interconversion Mechanism*, **9**, 199.
De Rosa, Claudio, *Chain Conformation, Crystal Structures, and Structural Disorder in Stereoregular Polymers*, **24**, 71.
DeSantis, G., *see* Silvestri, M. G., **23**, 267.
Diederich, F., *see* Thilgen, C., **23**, 1.
Dodziuk, H., *Unusual Saturated Hydrocarbons: Interaction Between Theoretical and Synthetic Chemistry*, **21**, 351.
Drabowicz, J., *see* Mikolajczyk, M., **13**, 333.
Duax, W. L., *Crystal Structures of Steroids*, **9**, 271.
Duddeck, H., *Substituent Effects on ¹³C Chemical Shifts in Aliphatic Molecular Systems. Dependence on Constitution and Stereochemistry*, **16**, 219.
- Eliel, E. L., *see* Arigoni, D., **4**, 127.
Enemark, J. H., *see* Feltham, R. D., **12**, 155.
Evans, D. A., *Stereoselective Aldol Condensation*, **13**, 1.
- Facelli, J. C., *Molecular Structure and Carbon-13 Chemical Shielding Tensors Obtained from Nuclear Magnetic Resonance*, **19**, 1.
Fahey, R. C., *The Stereochemistry of Electrophilic Additions to Olefins and Acetylenes*, **3**, 237.
Farina, M., *The Stereochemistry of Linear Macromolecules*, **17**, 1.
Feltham, R. C., *Structures of Metal Nitrosyls*, **12**, 155.
Fenoglio, D. J., *see* Karabatsos, G. J., **5**, 167.
Fenwick, D. R., *Asymmetric Amplification*, **22**, 257.
Fiaud, J. C., *see* Kagan, H. B., **10**, 175; **18**, 249.
Flood, Thomas C., *Stereochemistry of Reactions of Transition Metal-Carbon Sigma Bonds*, **12**, 37.
Floss, Heinz G., *Stereochemistry of Biological Reactions at Prochiral Centers*, **15**, 253.
Freedman, T. B., *Stereochemical Aspects of Vibrational Optical Activity*, **17**, 113.
Fryzuk, M. D., *see* Bosnich, B., **12**, 119.
Fuchs, B., *Conformations of Five-Membered Rings*, **10**, 1.
Fuji, K., *see* Kawabata, T., **23**, 175.
Fujiki, Michiya, *Chirality in Polysilanes*, **24**, 209.
- Gallagher, M. J., *Stereochemical Aspects of Phosphorus Chemistry*, **3**, 1.
Gielen, M., *The Stereochemistry of Germanium and Tin Compounds*, **12**, 217.

- Glasfield, A., *see* Benner, S. A., **19**, 127.
- Goodman, M., *Concepts of Polymer Stereochemistry*, **2**, 73; *Polypeptide Stereochemistry*, **5**, 69.
- Gosse, I., *see* Thilgen, C., **23**, 1.
- Gottarelli, Giovanni, *Some Correlations Between Molecular and Cholesteric Handedness*, **24**, 425.
- Graczyk, P. R., *Anomeric Effect: Origin and Consequences*, **21**, 159.
- Grant, D. M., *see* Facelli, J. C., **19**, 1.
- Green, B. S., *Stereochemistry and Organic Solid-State Reactions*, **16**, 131.
- Green, M. M., *Mass Spectrometry and the Stereochemistry of Organic Molecules*, **9**, 35.
- Guérin, C., *see* Corriu, R. J. P., **15**, 43.
- Guerra, Gaetano, *Chirality of Catalysts for Stereospecific Polymerizations*, **24**, 1.
- Hanson, K. R., *see* Hirschmann, H., **14**, 183.
- Hassel, O., *see* Barton, D. H. R., **6**, 1.
- Haubenstock, H., *Asymmetric Reductions with Chiral Complex Aluminum Hydrides and Tricordinate Aluminum Reagents*, **14**, 231.
- Havinga, E., *see* Romers, C., **4**, 39.
- Heathcock, C. H., *see* Oare, D. A., **19**, 227; **20**, 87.
- Hilvert, D., *Stereoselective Reactions with Catalytic Antibodies*, **22**, 83.
- Hirsch, J. A., *Table of Conformational Energies–1967*, **1**, 199.
- Hirschmann, H., *On Factoring Chirality and Stereoisomerism*, **14**, 183.
- Hofer, O., *The Lanthanide Induced Shift Technique: Applications in Conformational Analysis*, **9**, 111.
- Hoover, D. J., *see* Pirkle, W. H., **13**, 263.
- Hutchins, R. O., *see* Maryanoff, B. E., **11**, 187.
- Janzen, E. G., *Stereochemistry of Nitroxides*, **6**, 177.
- Jenkins, I. D., *see* Gallagher, M. J., **3**, 1.
- Jimenez, M. C., *see* Blanco, M.-J., **23**, 125.
- Johnson, B. F. G., *Stereochemistry of Transition Metal Carbonyl Clusters*, **12**, 253.
- Kagan, H. B., *see* Fenwick, D. R., **22**, 257.
- Kagan, H. B., *New Approaches in Asymmetric Synthesis*, **10**, 175; *Kinetic Resolution*, **18**, 249.
- Kalinowski, H.-O., *Fast Isomerizations about Double Bonds*, **7**, 295.
- Karabatsos, G. J., *Rotational Isomerism about sp^2 - sp^3 Carbon–Carbon Single Bonds*, **5**, 167.
- Kawabata, T., *Memory of Chirality: Asymmetric Induction Based on the Dynamic Chirality of Enolates*, **23**, 175.
- Keese, R., *see* Luef, W., **20**, 231.
- Kellie, G. M., *Nonchair Conformations of Six-Membered Rings*, **8**, 225.
- Kessler, H., *see* Kalinowski, H.-O., **7**, 295.
- Kinbara, K., *Chiral Discrimination During Crystallization*, **23**, 207.
- Klärner, F.-G., *Walk Rearrangements in [n.1.0] Bicyclic Compounds*, **15**, 1.
- Koe, Julian R., *see* Fujiki, Michiya, **24**, 209.
- Krebs, P. J., *see* Porter, N. A., **18**, 97.
- Krow, G., *The Determination of Absolute Configuration of Planar and Axially Dissymmetric Molecules*, **5**, 31.
- Lahav, M., *see* Addadi, L., **16**, 1.
- Lambert, J. B., *Pyramidal Atomic Inversion*, **6**, 19.
- Leiserowitz, L., *see* Addadi, L., **16**, 1.

- Luef, W., *Strained Olefins: Structure and Reactivity of Nonplanar Carbon–Carbon Double Bonds*, **20**, 231.
- Malloy, T. B., Jr., *Conformational Barriers and Interconversion Pathways in some Small-Ring Molecules*, **11**, 97.
- Martin, Y. C., *see* Bures, M. G., **21**, 467.
- Maryanoff, B. E., *Stereochemical Aspects of Phosphorus-Containing Cyclohexanes*, **11**, 187.
- Maryanoff, C. A., *see* Maryanoff, B. E., **11**, 187.
- Mason, S. F., *The Foundations of Classical Stereochemistry*, **9**, 1.
- Masuda, Y., *see* Goodman, M., **5**, 69.
- McKenna, J., *The Stereochemistry of the Quaternization of Piperidines*, **5**, 275.
- Meijer, E. W., *see* Brunsveld, L., **24**, 373.
- Mikolajczyk, M., *Chiral Organosulfur Compounds*, **13**, 333.
- Mikolajczyk, M., *see* Graczyk, P. R., **21**, 159.
- Mislow, K., *Molecular Chirality*, **22**, 1.
- Mislow, K., *Stereoisomeric Relationships of Groups in Molecules*, **1**, 1. *See also* Raban, M., **2**, 199.
- Mitchell, M., *see* Silvestri, M. G., **23**, 267.
- Moreau, J. J. E., *see* Corriu, R. J. P., **15**, 43.
- Moriarity, R. M., *Stereochemistry of Cyclobutane and Heterocyclic Analogs*, **8**, 271.
- Musso, H., *see* Osawa, E., **13**, 117.
- Nafie, L. A., *see* Freedman, T. B., **17**, 113.
- Nakashima, Hiroshi., *see* Fujiki, Michiya, **24**, 209.
- Nakazaki, M., *The Synthesis and Stereochemistry of Chiral Organic Molecules with High Symmetry*, **15**, 199.
- Nelson, J. V., *see* Evans, D. A., **13**, 1.
- Nolte, R. J. M., *see* Brunsveld, L., **24**, 373.
- Oare, D. A., *Stereochemistry of the Base-Promoted Michael Addition Reaction*, **19**, 227; *Acyclic Stereocontrol in Michael Addition Reactions of Enamines and Enol Ethers*, **20**, 87
- Okamoto, Yoshio, *Optically Active Polymers with Chiral Recognition Ability*, **24**, 157.
- Oki, M., *Recent Advances in Atropisomerism*, **14**, 1.
- Osawa, E., *Applications of Molecular Mechanics Calculations to Organic Chemistry*, **13**, 117.
- Palyulin, V. A., *see* Zefirov, N. S., **20**, 171.
- Persoons, André., *see* Verbiest, Thierry, **24**, 519.
- Peterson, M. J., *see* Vedejs, E., **21**, 1.
- Pethrick, R. A., *see* Wyn-Jones, E., **5**, 205.
- Piccirilli, J. A., *see* Benner, S. A., **19**, 127.
- Pirkle, W. H., *NMR Chiral Solvating Agents*, **13**, 263.
- Porter, N. A., *Stereochemical Aspects of Radical Pair Reactions*, **18**, 97.
- Raban, M., *Modern Methods for the Determination of Optical Purity*, **2**, 199; *See also* Mislow, K., **1**, 1.
- Riddell, F. G., *see* Kellie, G. M., **8**, 225.
- Ripka, W. G., *Computer Graphics and Molecular Modeling in the Analysis of Synthetic Targets*, **20**, 1.
- Rohrer, D. C., *see* Duax, W. L., **9**, 271.

- Romers, C., *Geometry and Conformational Properties of Some Five- and Six-Membered Heterocyclic Compounds Containing Oxygen and Sulfur*, **4**, 39.
- Rowan, A. E., *see* Brunsveld, L., **24**, 373.
- Ruch, E., *The Stereochemical Analogy Model—A Mathematical Theory of Dynamic Stereochemistry*, **4**, 99.
- Saigo, K., *see* Kinbara, K., **23**, 207.
- Saito, Y., *Absolute Stereochemistry of Chelate Complexes*, **10**, 95.
- Sandström, J., *Static and Dynamic Stereochemistry of Push-Pull and Strained Ethylenes*, **14**, 83.
- Sargeson, A. M., *see* Buckingham, D. A., **6**, 219.
- Sasai, H., *see* Shibasaki, M., **22**, 201.
- Saunders, J. K., *see* Bell, R. A., **7**, 1.
- Sauvage, J.-P., *see* Blanco, M.-J., **23**, 125.
- Schleyer, P. V. Ragué, *see* Buss, V., **7**, 253.
- Schlögl, K., *Stereochemistry of Metallocenes*, **1**, 39.
- Schlosser, M., *The Stereochemistry of the Wittig Reaction*, **5**, 1.
- Schnur, Joel M., *see* Spector, Mark S., **24**, 281.
- Scott, J. W., *Enantioselective Synthesis of Non-Racemic Chiral Molecules on an Industrial Scale*, **19**, 209.
- Selinger, Jonathan V., *see* Spector, Mark S., **24**, 281.
- Shibasaki, M., *Asymmetric Catalysis with Chiral Lanthanoid Complexes*, **22**, 201.
- Sih, C. J., *Resolution of Enantiomers via Biocatalysis*, **19**, 63.
- Silvestri, M. G., *Asymmetric Aldol Reactions Using Aldolases*, **23**, 267.
- Simamura, O., *The Stereochemistry of Cyclohexyl and Vinylic Radicals*, **4**, 1.
- Sloan, T. E., *Stereochemical Nomenclature and Notation in Inorganic Chemistry*, **12**, 1.
- Spada, Gian Piero, *see* Gottarelli, Giovanni, **24**, 425.
- Spector, Mark S., *Chiral Molecular Self-Assembly*, **24**, 281.
- Stewart, M. V., *Chiral Monolayers at the Air-Water Interface*, **13**, 195.
- Stoddart, J. F., *Chiral Crown Ethers*, **17**, 207.
- Stothers, J. B., *see* Wilson, N. K., **8**, 1.
- Sullivan, G. R., *Chiral Lanthanide Shift Reagents*, **10**, 287.
- Taber, T. R., *see* Evans, D. A., **13**, 1.
- Thilgen, C., *Chirality in Fullerene Chemistry*, **23**, 1.
- Toromanoff, E., *Steric Course of the Kinetic 1,2 Addition of Anions to Conjugated Cyclohexenones*, **2**, 157.
- Toyoda, Seth., *see* Fujiki, Michiya, **24**, 209.
- Tsai, M.-D., *see* Floss, Heinz G., **15**, 253.
- Ugi, L., *see* Ruch, E., **4**, 99.
- Vedejs, E., *Stereochemistry and Mechanism of the Wittig Reaction*, **21**, 1.
- Verbiest, Thierry, *Nonlinear Optics and Chirality*, **24**, 519.
- Verdini, A. S., *see* Goodman, M., **5**, 69.
- Walba, David M., *Ferroelectric Liquid Crystal Conglomerates*, **24**, 457.
- Weeks, C. M., *see* Duax, W. L., **9**, 271.
- Weissbuch, I., *see* Addadi, L., **16**, 1.
- White, J. M., *Stereoelectronic Effects of the Group 4 Metal Substituents in Organic Chemistry*, **22**, 137.

- Wilen, S. H., *Resolving Agents and Resolutions in Organic Chemistry*, **6**, 107.
- Willett, P., *see* Bures, M. G., **21**, 467.
- Wilson, N. K., *Stereochemical Aspects of ^{13}C NMR Spectroscopy*, **8**, 1.
- Wong, C.-H., *see* Silvestri, M. G., **23**, 267.
- Woodard, R. W., *see* Floss, Heinz G., **15**, 253.
- Wu, S.-H., *see* Sih, C. J., **19**, 63.
- Wynberg, H., *Asymmetric Catalysis by Alkaloids*, **16**, 87.
- Wyn-Jones, E., *The Use of Ultrasonic Absorption and Vibrational Spectroscopy to Determine the Energies Associated with Conformational Changes*, **5**, 205.
- Yamamoto, Chiyo., *see* Okamoto, Yoshio, **24**, 157.
- Yashima, Eiji., *see* Okamoto, Yoshio, **24**, 157.
- Young, D. W., *Stereochemistry of Metabolic Reactions of Amino Acids*, **21**, 381.
- Zefirov, N. S., *Conformational Analysis of Bicyclo[3.3.1]nonanes and their Hetero Analogs*, **20**, 171.

CUMULATIVE TITLE INDEX

	VOL.	PAGE
Absolute Configuration of Chiral Molecules, Crystals as Probes for the Direct Assignment of (<i>Addadi, Berkovitch-Yellin, Weissbuch, Lahav, and Leiserowitz</i>)	16	1
Absolute Configuration of Planar and Axially Dissymmetric Molecules (<i>Krow</i>)	5	31
Absolute Stereochemistry of Chelate Complexes (<i>Saito</i>)	10	95
Acetylenes, Stereochemistry of Electrophilic Additions (<i>Fahey</i>)	3	237
Acyclic Stereocontrol in Michael Addition Reaction of Enamines and Enol Ethers (<i>Oare and Heathcock</i>)	20	87
Aldolases, Asymmetric Aldol Reactions Using (<i>Silvestri, DeSantis, Mitchell and Wong</i>)	23	267
Aldol Condensations, Stereoselective (<i>Evans, Nelson, and Taber</i>)	13	1
Alkaloids, Asymmetric Catalysis by (<i>Wynberg</i>)	16	87
Aluminum Hydrides and Tricoordinate Aluminum Reagents, Asymmetric Reductions with Chiral Complex (<i>Haubenstock</i>)	14	231
Amino Acids, Stereochemistry of Metabolic Reactions of (<i>Young</i>)	21	381
Analogy Model, Stereochemical (<i>Ugi and Ruch</i>)	4	99
Anomeric Effect: Origin and Consequences (<i>Graczyk and Mikolajczyk</i>)	21	159
Antibodies, Catalytic, Stereoselective Reactions with (<i>Hilvert</i>)	22	83
Asymmetric Aldol Reactions Using Aldolases (<i>Silvestri, DeSantis, Mitchell and Wong</i>)	23	267
Asymmetric Amplification (<i>Fenwick and Kagan</i>)	22	257
Asymmetric Catalysis by Alkaloids (<i>Wynberg</i>)	16	87
Asymmetric Catalysis with Chiral Lanthanoid Complexes (<i>Shibasaki and Sasai</i>)	22	201
Asymmetric Reductions with Chiral Complex Aluminum Hydrides and Tricoordinate Aluminum Reagents (<i>Haubenstock</i>)	14	231
Asymmetric Synthesis, New Approaches in (<i>Kagan and Fiaud</i>)	10	175
Asymmetric Synthesis Mediated by Transition Metal Complexes (<i>Bosnich and Fryzuk</i>)	12	119
Atomic Inversion, Pyramidal (<i>Lambert</i>)	6	19
Atropisomerism, Recent Advances in (<i>Oki</i>)	14	1
Axially and Planar Dissymmetric Molecules, Absolute Configuration of (<i>Krow</i>)	5	31
Barriers, Conformational, and Interconversion Pathways in Some Small Ring Molecules (<i>Malloy, Bauman, and Carreira</i>)	11	97
Barton, D. H. R., and Hassel, O., Fundamental Contributions to Conformational Analysis (<i>Barton and Hassel</i>)	6	19
Bicyclic Compounds, Walk Rearrangements in [n.1.0] (<i>Kärner</i>)	15	1

Materials-Chirality: Volume 24 of Topics in Stereochemistry,
 Edited by Mark M. Green, R.J.M. Nolte, and E.W. Meijer
 ISBN 0-471-05497-6 Copyright © 2003 John Wiley & Sons, Inc.

	VOL.	PAGE
Carbene Additions to Olefins, Stereochemistry of (<i>Closs</i>)	3	193
Carbenes, Structure of (<i>Closs</i>)	3	193
sp ² -sp ³ Carbon-Carbon Single Bonds, Rotational Isomerism about (<i>Karabatsos</i> and <i>Fenoglio</i>)	5	167
Carbonium Ions, Simple, the Electronic St Hydrogen Isotopes at Noncyclic Positions Chelate Complexes, Absolute Stereochemistry of (<i>Saito</i>)	10	95
Catalysis, Asymmetric, with Chiral Lanthanoid Complexes (<i>Shibasaki</i> and <i>Sasai</i>)	22	201
Catalytic Antibodies, Stereoselective Reactions with (<i>Hilvert</i>)	22	83
¹³ C Chemical Shielding Tensors Obtained from NMR, Molecular Structure and (<i>Facelli</i> and <i>Grant</i>)	19	1
¹³ C Chemical Shifts in Aliphatic Molecular Systems, Substituent Effects on. Dependence on Constitution and Stereochemistry (<i>Duddeck</i>)	16	219
Chiral Crown Ethers (<i>Stoddart</i>)	17	207
Chiral Discotic Molecules: Expression and Amplification of Chirality (<i>Brunsveld</i> , <i>Rowan</i> , <i>Nolte</i> , and <i>Meijer</i>)	24	373
Chiral Discrimination during Crystallization (<i>Kinbara</i> and <i>Saigo</i>)	23	207
Chiral Homogeneity in Nature, Origins of (<i>Bonner</i>)	18	1
Chirality Due to the Presence of Hydrogen Isotopes at Noncyclic Positions (<i>Arigoni</i> and <i>Eliel</i>)	4	127
Chirality in Fullerene Chemistry (<i>Thilgen</i> , <i>Gosse</i> and <i>Diederich</i>)	23	1
Chirality, Molecular (<i>Mislow</i>)	22	1
Chiral Lanthanide Shift Reagents (<i>Sullivan</i>)	10	287
Chiral Lanthanoid Complexes, Asymmetric Catalysis with (<i>Shibasaki</i> and <i>Sasai</i>)	22	201
Chiral Monolayers at the Air-Water Interface (<i>Stewart</i> and <i>Arnett</i>)	13	195
Chiral Organic Molecules with High Symmetry, The Synthesis and Stereochemistry of (<i>Nakazaki</i>)	15	199
Chiral Organosulfur Compounds (<i>Mikołajczyk</i> and <i>Drabowicz</i>)	13	333
Chiral Recognition Ability, Optically Active Polymers with (<i>Okamoto</i> , <i>Yashima</i> , and <i>Yamamoto</i>)	24	157
Chiral Solvating Agents, in NMR (<i>Pirkle</i> and <i>Hoover</i>)	13	263
Cholesteric Handedness, Some Correlations Between Molecular and (<i>Gottarelli</i> and <i>Spada</i>)	24	425
Classical Stereochemistry, The Foundations of (<i>Mason</i>)	9	1
Conformational Analysis, Applications of the Lanthanide-induced Shift Technique in (<i>Hofer</i>)	9	111
Conformational Analysis of Bicyclo[3.3.1]nonanes and Their Hetero Analogs (<i>Zefirov</i> and <i>Palyulin</i>)	20	171
Conformational Analysis, The Fundamental Contributions of D. H. R. Barton and O. Hassell (<i>Barton</i> and <i>Hassel</i>)	6	1
Conformational Analysis of Intramolecular Hydrogen-Bonded Compounds in Dilute Solution by Infrared Spectroscopy (<i>Aáron</i>)	11	1
Conformational Analysis of Six-membered Rings (<i>Kellie</i> and <i>Riddell</i>)	8	225
Conformational Analysis of Steric Effects in Metal Chelates (<i>Buckingham</i> and <i>Sargeson</i>)	6	219
Conformational Analysis and Torsion Angles (<i>Bucourt</i>)	8	159

	VOL.	PAGE
Conformational Barriers and Interconversion Pathways in Some Small Ring Molecules (<i>Malloy, Bauman and Carreira</i>)	11	97
Conformational Changes, Determination of Associated Energy by Ultrasonic Absorption and Vibrational Spectroscopy (<i>Wyn-Jones and Pethrick</i>)	5	205
Conformational Changes by Rotation about sp^2 - sp^3 Carbon-Carbon Single Bonds (<i>Karabatsos and Fenoglio</i>)	5	167
Conformational Energies, Table of (<i>Hirsch</i>)	1	199
Conformational Interconversion Mechanisms, Multi-step (<i>Dale</i>)	9	199
Conformations of 5-Membered Rings (<i>Fuchs</i>)	10	1
Conjugated Cyclohexenones, Kinetic 1,2 Addition of Anions to, Steric Course of (<i>Toromanoff</i>)	2	157
Crystals as Probes for the Direct Assignment of Absolute Configuration of Chiral Molecules, A Link Between Macroscopic Phenomena and Molecular Chirality (<i>Addadi, Berkovitch-Yellin, Weissbuch, Lahav, and Leiserowitz</i>)	16	1
Crystal Structures of Steroids (<i>Duax, Weeks, and Rohrer</i>)	9	271
Cyclobutane and Heterocyclic Analogs, Stereochemistry of (<i>Moriarty</i>)	8	271
Cyclohexyl Radicals, and Vinylic, The Stereochemistry of (<i>Simamura</i>)	4	1
Databases of Three-Dimensional Chemical Structures, Searching Techniques for (<i>Bures, Martin and Willett</i>)	21	467
Double Bonds, Fast Isomerization about (<i>Kalinowski and Kessler</i>)	7	295
Electronic Structure and Stereochemistry of Simple Carbonium Ion, (<i>Buss, Schleyer, and Allen</i>)	7	253
Electrophilic Additions to Olefins and Acetylenes, Stereochemistry of (<i>Fahey</i>)	3	237
Enantioselective Synthesis of Non-Racemic Chiral Molecules on an Industrial Scale (<i>Scott</i>)	19	209
Enantioselective Synthesis of Organic Compounds with Optically Active Transition Metal Catalysts in Substoichiometric Quantities (<i>Brunner</i>)	18	129
Enzymatic Reactions, Stereochemistry of, by Use of Hydrogen Isotopes (<i>Arigoni and Eliel</i>)	4	127
Enzymology, Stereospecificity in: Its Place in Evolution (<i>Benner, Glasfeld and Piccirilli</i>)	19	127
1,2-Epoxides, Stereochemistry Aspects of the Synthesis of (<i>Berti</i>)	7	93
EPR, in Stereochemistry of Nitroxides (<i>Janzen</i>)	6	177
Ethylenes, Static and Dynamic Stereochemistry of Push-Pull and Strained (<i>Sandstrom</i>)	14	83
Five-Membered Rings, Conformations of (<i>Fuchs</i>)	10	1
Foundations of Classical Stereochemistry (<i>Mason</i>)	9	1
Fullerene Chemistry, Chirality in (<i>Thilgen, Gosse and Diederich</i>)	23	1
Geometry and Conformational Properties of Some Five- and Six-Membered Heterocyclic Compounds Containing Oxygen or Sulfur (<i>Romers, Altona, Buys, and Havinga</i>)	4	39
Group 4 Metal Substituents, Stereoelectronic Effects of the (<i>White and Clark</i>)	22	137

	VOL.	PAGE
Hassel, O. and Barton, D. H. R., Fundamental Contributions to Conformational Analysis (<i>Hassel and Barton</i>)	6	1
Helix Models, of Optical Activity (<i>Brewster</i>)	2	1
Heterocyclic Compounds, Five- and Six-Membered, Containing Oxygen or Sulfur, Geometry and Conformational Properties of (<i>Romers, Altona, Buys, and Havinga</i>)	4	39
Heterocyclic Four-Membered Rings, Stereochemistry of (<i>Moriarty</i>)	8	271
Heterotopism (<i>Mislow and Raban</i>)	1	1
Hydrocarbons, Unusual Saturated: Interaction between Theoretical and Synthetic Chemistry (<i>Dodziak</i>)	21	351
Hydrogen-Bonded Compounds, Intramolecular, in Dilute Solution, Conformational Analysis of, by Infrared Spectroscopy (<i>Aaron</i>)	11	1
Hydrogen Isotopes at Noncyclic Positions, Chirality Due to the Presence of (<i>Arigoni and Eliel</i>)	4	127
Infrared Spectroscopy, Conformational Analysis of Intramolecular Hydrogen-Bonded Compounds in Dilute Solution by (<i>Aaron</i>)	11	1
Intramolecular Hydrogen-Bonded Compounds, in Dilute Solution, Conformational Analysis of, by Infrared Spectroscopy (<i>Aaron</i>)	11	1
Intramolecular Rate Processes (<i>Binsch</i>)	3	97
Inversion, Atomic, Pyramidal (<i>Lambert</i>)	6	19
Isomerization, Fast, About Double Bonds (<i>Kalinowski and Kessler</i>)	7	295
Ketones, Cyclic and Bicyclic, Reduction of, by Complex Metal Hydrides (<i>Boone and Ashby</i>)	11	53
Lanthanide-induced Shift Technique—Applications in Conformational Analysis (<i>Hofer</i>)	9	111
Lanthanide Shift Reagents, Chiral (<i>Sullivan</i>)	10	287
Lanthanoid Complexes, Chiral, Asymmetric Catalysis with (<i>Shibasaki and Sasai</i>)	22	201
Liquid Crystal Conglomerates, Ferroelectric (<i>Walba</i>)	24	457
Mass Spectrometry and the Stereochemistry of Organic Molecules (<i>Green</i>)	9	35
Memory of Chirality: Asymmetric Induction Based on the Dynamic Chirality of Enolates (<i>Kawabata and Fuji</i>)	23	175
Metal Chelates, Conformational Analysis and Steric Effects in (<i>Buckingham and Sargeson</i>)	6	219
Metal Hydrides, Complex, Reduction of Cyclic and Bicyclic Ketones by (<i>Boone and Ashby</i>)	11	53
Metallocenes, Stereochemistry of (<i>Schlogl</i>)	1	39
Metal Nitrosyls, Structures of (<i>Feltham and Enemark</i>)	12	155
Michael Addition Reaction, Stereochemistry of the Base-Promoted (<i>Oare and Heathcock</i>)	19	227
Michael Addition Reactions of Enamines and Enol Ethers, Acyclic Stereocontrol in (<i>Oare and Heathcock</i>)	20	87
Molecular Chirality (<i>Mislow</i>)	22	1

	VOL.	PAGE
Molecular Mechanics Calculations—Applications to Organic Chemistry (<i>Osawa and Musso</i>)	13	117
Molecular Modeling, Computer Graphics and, in the Analysis of Synthetic Targets (<i>Ripka and Blaney</i>)	20	1
Monolayers, Chiral, at the Air-Water Interface (<i>Stewart and Arnett</i>)	13	195
Multi-step Conformational Interconversion Mechanisms (<i>Dale</i>)	9	199
Nitroxides, Stereochemistry of (<i>Janzen</i>)	6	177
Non-Chair Conformations of Six-Membered Rings (<i>Kellie and Riddell</i>)	8	225
Nuclear Magnetic Resonance, ¹³ C Chemical Shifts in Aliphatic Molecular Systems, Substituent Effects on. Dependence on Constitution and Stereochemistry (<i>Duddeck</i>)	16	219
Nuclear Magnetic Resonance Chiral Lanthanide Shift Reagents (<i>Sullivan</i>)	10	287
Nuclear Magnetic Resonance, ¹³ C Stereochemical Aspects of (<i>Wilson and Siothers</i>)	8	1
Nuclear Magnetic Resonance, Chiral Solvating Agents in (<i>Pirkle and Hoover</i>)	13	263
Nuclear Magnetic Resonance, for Study of Intra-Molecular Rate Processes (<i>Binsch</i>)	3	97
Nuclear Magnetic Resonance, Molecular Structure and Carbon-13 Chemical Shielding Tensors Obtained from (<i>Facelli and Grant</i>)	19	1
Nuclear Overhauser Effect, Some Chemical Applications of (<i>Bell and Saunders</i>).	7	1
Olefins, Stereochemistry of Carbene Additions to (<i>Class</i>)	3	193
Olefins, Stereochemistry of Electrophilic Additions to (<i>Fahey</i>)	3	237
Olefins, Strained: Structure and Reactivity of Nonplanar Carbon-Carbon Double Bonds (<i>Luef and Keese</i>)	20	231
Optical Activity, Helix Models of (<i>Brewster</i>)	2	1
Optical Circular Dichroism, Recent Applications in Organic Chemistry (<i>Crabbé</i>).	1	93
Optical Purity, Modern Methods for the Determination of (<i>Raban and Mislow</i>)	2	199
Optical Rotary Dispersion, Recent Applications in Organic Chemistry (<i>Crabbé</i>)	1	93
Optics, Nonlinear, and Chirality (<i>Verbiest and Persoons</i>)	24	519
Organic Solid-State, Stereochemistry and Reactions (<i>Green, Arad-Yellin, and Cohen</i>)	16	131
Organosulfur Compounds, Chiral (<i>Mikołajczyk and Drabowicz</i>)	13	333
Origins of Chiral Homogeneity in Nature (<i>Bonner</i>)	18	1
Overhauser Effect, Nuclear, Some Chemical Applications of (<i>Bell and Saunders</i>).	7	1
Phosphorus Chemistry, Stereochemical Aspects of (<i>Gallagher and Jenkins</i>)	3	1
Phosphorus-containing Cyclohexanes, Stereochemical Aspects of (<i>Maryanoff, Hutchins, and Maryanoff</i>)	11	186
Piperidines, Quaternization Stereochemistry of (<i>McKenna</i>)	5	275
Planar and Axially Dissymmetric Molecules, Absolute Configuration of (<i>Krow</i>)	5	31
Polymerizations, Chirality of Catalysts for Stereospecific (<i>Guerra, Cavallo, and Corradini</i>)	24	1

	VOL.	PAGE
Polymers, Chain Conformation, Crystal Structures, and Structural Disorder in Stereoregular (<i>De Rosa</i>)	24	71
Polymer Stereochemistry, Concepts of (<i>Goodman</i>)	2	73
Polypeptide Stereochemistry (<i>Goodman, Verdini, Choi, and Masuda</i>)	5	69
Polysilanes, Chirality in the (<i>Fujiki, Koe, Nakashima, and Toyoda</i>)	24	209
Pyramidal Atomic Inversion (<i>Lambert</i>)	6	19
Quaternization of Piperidines, Stereochemistry of (<i>McKenna</i>)	5	75
Radical Pair Reactions, Stereochemical Aspects of (<i>Porter and Krebs</i>)	18	97
Radicals, Cyclohexyl and Vinyllic, The Stereochemistry of (<i>Simamura</i>)	4	1
Reduction, of Cyclic and Bicyclic Ketones by (<i>Sih and Wu</i>)	19	63
Resolution, Kinetic (<i>Kagan and Fiaud</i>)	18	249
Resolving Agents and Resolutions in Organic Chemistry (<i>Wilen</i>)	6	107
Rotational Isomerism about sp^2 - sp^3 Carbon-Carbon Single Bonds (<i>Karabatsos</i> and <i>Fenoglio</i>)	5	167
Rotaxanes, Transition-Metal-Templated Synthesis of (<i>Blanco, Chambron,</i> <i>Jiménez and Sauvage</i>)	23	125
Self-Assembly, Chiral Molecular (<i>Spector, Selinger, and Schnur</i>)	24	281
Silicon, Stereochemistry at (<i>Corriu, Guerin, Mauman, and Carreira</i>)	11	97
Stereochemical Aspects of ^{13}C NMR Spectroscopy (<i>Wilson and Stothers</i>)	8	1
Stereochemical Aspects of Phosphorus-containing Cyclohexanes (<i>Maryanoff,</i> <i>Hutchins, and Maryanoff</i>)	11	186
Stereochemical Aspects of Radical Pair Reactions (<i>Porter and Krebs</i>)	18	97
Stereochemical Aspects of Vibrational Optical Activity (<i>Freedman and Nafie</i>)	17	113
Stereochemical Nomenclature and Notation in Inorganic Chemistry (<i>Sloan</i>)	12	1
Stereochemistry, Classical, The Foundations of (<i>Mason</i>)	9	1
Stereochemistry, Dynamic, A Mathematical Theory of (<i>Ugi and Ruch</i>)	4	99
Stereochemistry of Biological Reactions at Propochiral Centers (<i>Floss, Tsai,</i> and <i>Woodard</i>)	15	253
Stereochemistry of Chelate Complexes (<i>Saito</i>)	10	95
Stereochemistry of Cyclobutane and Heterocyclic Analogs (<i>Moriarty</i>)	8	271
Stereochemistry of Germanium and Tin Compounds (<i>Gielen</i>)	12	217
Stereochemistry of Linear Macromolecules (<i>Farina</i>)	17	1
Stereochemistry of Nitroxides (<i>Janzen</i>)	6	177
Stereochemistry of Organic Molecules, and Mass Spectrometry (<i>Green</i>)	9	35
Stereochemistry of Push-Pull and Strained Ethylenes, Static and Dynamic (<i>Sandström</i>)	14	83
Stereochemistry of Reactions of Transition Metal-Carbon Sigma Bonds (<i>Flood</i>)	12	37
Stereochemistry at Silicon (<i>Corriu, Guérin, and Moreau</i>)	15	43
Stereochemistry of Transition Metal Carbonyl Clusters (<i>Johnson and Benfield</i>)	12	253
Stereoselective Reactions with Catalytic Antibodies (<i>Hilvert</i>)	22	83
Stereoisomeric Relationships, of Groups in Molecules (<i>Mislow and Raban</i>)	1	1
Stereoisomerism, On Factoring Chirality and (<i>Hirschmann and Hanson</i>)	14	183
Stereoselective Aldol Condensations (<i>Evans, Nelson, and Taber</i>)	13	1

	VOL.	PAGE
Stereoelectronic Effects of the Group 4 Metal Substituents in Organic Chemistry (<i>White and Clark</i>)	22	137
Stereospecificity in Enzymology: Its Place in Evolution (<i>Benner, Glasfeld, and Piccirilli</i>)	19	127
Steroids, Crystal Structures of (<i>Duax, Weeks, and Rohrer</i>)	9	271
Strained Olefins: Structure and Reactivity of Nonplanar Carbon-Carbon Double Bonds (<i>Luef and Keese</i>)	20	231
Transition-Metal-Templated Synthesis of Rotaxanes (<i>Blanco, Chambron, Jiménez and Sauvage</i>)	23	125
Torsion Angle Concept in Conformational Analysis (<i>Bucourt</i>)	8	159
Ultrasonic Absorption and Vibrational Spectroscopy Use of, to Determine the Energies Associated with Conformational Changes (<i>Wyn-Jones and Pethrick</i>)	5	205
Unusual Saturated Hydrocarbons: Interaction Between Theoretical and Synthetic Chemistry (<i>Dodziuk</i>)	21	351
Vibrational Optical Activity, Stereochemical Aspects of (<i>Freedman and Nafie</i>)	17	113
Vibrational Spectroscopy and Ultrasonic Absorption, Use of, to Determine the Energies Associated with Conformational Changes (<i>Wyn-Jones and Pethrick</i>)	5	205
Vinylic Radicals, and Cyclohexyl. The Stereochemistry of (<i>Simamura</i>)	4	1
Wittig Reaction, Stereochemistry of (<i>Schlosser</i>)	5	1
Wittig Reaction, Stereochemistry and Mechanism of the (<i>Vedejs and Peterson</i>)	21	1